Advances in Intelligent Systems and Computing 479

Rajesh Singh
Sushabhan Choudhury *Editors*

Proceeding of International Conference on Intelligent Communication, Control and Devices

ICICCD 2016

Springer

Advances in Intelligent Systems and Computing

Volume 479

Series editor

Janusz Kacprzyk, Polish Academy of Sciences, Warsaw, Poland
e-mail: kacprzyk@ibspan.waw.pl

About this Series

The series "Advances in Intelligent Systems and Computing" contains publications on theory, applications, and design methods of Intelligent Systems and Intelligent Computing. Virtually all disciplines such as engineering, natural sciences, computer and information science, ICT, economics, business, e-commerce, environment, healthcare, life science are covered. The list of topics spans all the areas of modern intelligent systems and computing.

The publications within "Advances in Intelligent Systems and Computing" are primarily textbooks and proceedings of important conferences, symposia and congresses. They cover significant recent developments in the field, both of a foundational and applicable character. An important characteristic feature of the series is the short publication time and world-wide distribution. This permits a rapid and broad dissemination of research results.

Advisory Board

Chairman

Nikhil R. Pal, Indian Statistical Institute, Kolkata, India
e-mail: nikhil@isical.ac.in

Members

Rafael Bello, Universidad Central "Marta Abreu" de Las Villas, Santa Clara, Cuba
e-mail: rbellop@uclv.edu.cu

Emilio S. Corchado, University of Salamanca, Salamanca, Spain
e-mail: escorchado@usal.es

Hani Hagras, University of Essex, Colchester, UK
e-mail: hani@essex.ac.uk

László T. Kóczy, Széchenyi István University, Győr, Hungary
e-mail: koczy@sze.hu

Vladik Kreinovich, University of Texas at El Paso, El Paso, USA
e-mail: vladik@utep.edu

Chin-Teng Lin, National Chiao Tung University, Hsinchu, Taiwan
e-mail: ctlin@mail.nctu.edu.tw

Jie Lu, University of Technology, Sydney, Australia
e-mail: Jie.Lu@uts.edu.au

Patricia Melin, Tijuana Institute of Technology, Tijuana, Mexico
e-mail: epmelin@hafsamx.org

Nadia Nedjah, State University of Rio de Janeiro, Rio de Janeiro, Brazil
e-mail: nadia@eng.uerj.br

Ngoc Thanh Nguyen, Wroclaw University of Technology, Wroclaw, Poland
e-mail: Ngoc-Thanh.Nguyen@pwr.edu.pl

Jun Wang, The Chinese University of Hong Kong, Shatin, Hong Kong
e-mail: jwang@mae.cuhk.edu.hk

More information about this series at http://www.springer.com/series/11156

Rajesh Singh · Sushabhan Choudhury
Editors

Proceeding of International Conference on Intelligent Communication, Control and Devices

ICICCD 2016

Springer

Editors
Rajesh Singh
Department of Electronics, Instrumentation and Control Engineering
University of Petroleum and Energy Studies
Dehradun, Uttarakhand
India

Sushabhan Choudhury
Department of Electronics, Instrumentation and Control Engineering
University of Petroleum and Energy Studies
Dehradun, Uttarakhand
India

ISSN 2194-5357 ISSN 2194-5365 (electronic)
Advances in Intelligent Systems and Computing
ISBN 978-981-10-1707-0 ISBN 978-981-10-1708-7 (eBook)
DOI 10.1007/978-981-10-1708-7

Library of Congress Control Number: 2016944912

© Springer Science+Business Media Singapore 2017
This work is subject to copyright. All rights are reserved by the Publisher, whether the whole or part of the material is concerned, specifically the rights of translation, reprinting, reuse of illustrations, recitation, broadcasting, reproduction on microfilms or in any other physical way, and transmission or information storage and retrieval, electronic adaptation, computer software, or by similar or dissimilar methodology now known or hereafter developed.
The use of general descriptive names, registered names, trademarks, service marks, etc. in this publication does not imply, even in the absence of a specific statement, that such names are exempt from the relevant protective laws and regulations and therefore free for general use.
The publisher, the authors and the editors are safe to assume that the advice and information in this book are believed to be true and accurate at the date of publication. Neither the publisher nor the authors or the editors give a warranty, express or implied, with respect to the material contained herein or for any errors or omissions that may have been made.

Printed on acid-free paper

This Springer imprint is published by Springer Nature
The registered company is Springer Science+Business Media Singapore Pte Ltd.

Preface

The Department of Electronics, Instrumentation and Control Engineering, University of Petroleum and Energy Studies, Dehradun, takes immense pleasure in announcing the first International Conference on Intelligent Communication, Control and Devices (ICICCD 2016) held on 2nd and 3rd April 2016. ICICCD focus on the integration of intelligent communication systems, control systems and devices related to all aspects of engineering and sciences. ICICCD 2016 aims to provide an opportune forum and vibrant platform for researchers, academicians, scientists and industrial practitioners to share their original research work, findings and practical development experiences. The proceedings will be published in the Advances in Intelligent Systems and Computing (AISC) book series of Springer.

The general aim of the conference is to promote international collaboration in education and research in all fields and disciplines of engineering. More than 200 delegates from various countries attended the conference. ICICCD 2016 is an international forum for those who present their projects and innovations, having also the opportunity to discuss the main aspects and the latest results in the field of education and research.

The Organizing Committee is extremely grateful to the authors who had shown tremendous response to the call for papers. Over 270 papers were submitted from the researchers, academicians and students on wide area of three parallel tracks in Intelligent Communication, Intelligent Control and Intelligent Devices, along with a poster presentation session. Total 136 papers are accepted for publication with Springer.

We are obliged to our Honorable Chancellor Dr. S.J. Chopra, Vice Chancellor Dr. Shrihari Honwad, Vice President—Academic Affairs Dr. S.R. Das, Dean Dr. Kamal Bansal, for their confidence they have invested on us for organizing this international conference.

We extend our thanks to all faculty members and staffs with different committees for their support in organizing the conference and for making it a grand success.

Dehradun, India

Rajesh Singh
Sushabhan Choudhury

Conference Organizing Committee

Steering Committee

Chief Patron
Dr. S.J. Chopra, Chancellor, UPES, Dehradun, India

Patron(s)
Mr. Utpal Ghosh, President and CEO, UPES, Dehradun, India
Dr. Shrihari Honwad, Vice Chancellor, UPES, Dehradun, India
Dr. S.R. Das, Vice President, Academic Affairs, UPES, Dehradun, India

General Chair
Dr. Kamal Bansal, Dean, College of Engineering Studies, UPES, Dehradun, India

Program Chair
Dr. O.P.N. Calla, Director, International Center for Radio Science, India

Organizing Chair
Dr. Piyush Kuchhal, Associate Dean (COES), UPES, Dehradun, India
Dr. Manish Parteek, Associate Dean (COES), UPES, Dehradun, India
Dr. S.K. Banerjee, Associate Dean (COES), UPES, Dehradun, India
Dr. S.C. Gupta, Associate Dean (COES), UPES, Dehradun, India
Dr. Suresh Kumar, Associate Dean (COES), UPES, Dehradun, India

Organizing Co-Chair
Mr. Sushabhan Choudhury, HOD (EIC), UPES
Mr. Rajesh Singh, A.P. (SG) and Head, Institute of Robotics Technology (R&D), UPES

Publicity Chair
Dr. N.A. Siddiqui, HoD (HSE), UPES
Dr. Adesh Kumar, A.P. (SS), EIC, UPES
Dr. Vikas Garg, HoD, Civil Engineering, UPES

Public Relation Chair
Dr. Jitendra Kumar Pandey, Head (R&D), UPES
Dr. Paawan Sharma, A.P. (SS), EIC, UPES
Dr. Mukul Kumar Gupta, A.P. (SS), EIC, UPES

Session Management Chair
Dr. N. Prasanthi, Associate Professor, EIC, UPES
Mr. Ranjan Mishra, A.P. (SG), EIC, UPES

Editors
Mr. Sushabhan Choudhury, HOD (EIC), UPES
Mr. Rajesh Singh, A.P. (SG) and Head, Institute of Robotics Technology (R&D), UPES

Organizing Committee

Convener
Mr. Sushabhan Choudhury, HOD (EIC), UPES
Mr. Rajesh Singh, A.P. (SG) and Head, Institute of Robotics Technology (R&D), UPES

Conference Secretary
Ms. Anita Gehlot, A.P, EIC, UPES
Dr. Adesh Kumar, A.P. (SS), EIC, UPES

Finance Committee
Mr. Roushan Kumar, A.P. (SS), EIC, UPES
Dr. Mukul Kumar Gupta, A.P. (SS), EIC, UPES
Mr. Vinay Chowdhary, A.P., EIC, UPES
Mr. Raj Gaurav, A.P. (SG), EIC, UPES

Technical Support
Mr. Rajesh Singh, A.P. (SG) and Head, Institute of Robotics Technology (R&D), UPES
Dr. Adesh Kumar, A.P. (SS), EIC, UPES
Mr. Ranjan Mishra, A.P. (SG), EIC, UPES
Dr. Madhu Sharma, A.P. (SG), UPES
Dr. Gagan Anand, Associate Professor, UPES
Ms. Anita Gehlot, A.P, EIC, UPES
Mr. Vivek kaundal, A.P. (SS), EIC, UPES
Dr. Rishi Dewan, A.P. (SG), UPES
Mr. Roushan Kumar, A.P. (SS), EIC, UPES
Mr. Arpit Jain, A.P. (SS), EIC, UPES
Mr. Tarun Kumar, A.P. (SS), EIC, UPES
Mr. Raj Gaurav, A.P. (SG), EIC, UPES

Dr. Paawan Sharma, A.P. (SS), EIC, UPES
Mr. Ankur Dumka, A.P., CIT, UPES
Mr. Vishal Kaushik, A.P. (SG), CIT, UPES
Dr. Inder Singh, A.P. (SS), CIT, UPES
Dr. OM Parkash, HOD, Aerospace Engineering, UPES
Mr. Sudhir Kumar Chaturvedi, A.P. (SS), Aerospace Engineering, UPES

Sponsorship Committee
Dr. Nihal Anwar Siddiqui, HOD (HSE), UPES
Mr. Arpit Jain, A.P. (SS), EIC, UPES
Mr. Vivek Kaundal, A.P. (SS), EIC, UPES
Mr. Roushan Kumar, A.P. (SS), EIC, UPES
Dr. Mukul Kumar Gupta, A.P. (SS), EIC, UPES
Mr. Deepak Kumar, A.P. (SS), EIC, UPES
Dr. Amit Kumar Mondal, A.P., EIC, UPES
Mr. Raj Gaurav Mishra, A.P. (SG), EIC, UPES

Registration Committee
Dr. Adesh Kumar, A.P. (SS), EIC, UPES
Dr. N. Prasanthi, Associate Professor, EIC, UPES
Mr. Vinay Chowdhary, A.P., EIC, UPES
Mr. B. Khaleelu Rehman, A.P., EIC, UPES
Mr. Bhan Parkash, A.P. (SS), EIC, UPES
Mr. Abhishek Sharma, A.P., EIC, UPES

Session Management Committee
Dr. N. Prasanthi, Associate Professor, EIC, UPES
Ms. Anita Gehlot, A.P., EIC, UPES
Mr. Arpit Jain, A.P. (SS), EIC, UPES
Mr. B. Khaleelu Rehman, A.P., EIC, UPES
Dr. Madhu Sharma, Associate Professor, EPG, UPES
Ms. Meera C.S., DRF, EIC, UPES
Mr. Amit Kumar, JRF, CIT, UPES

Hospitality Committee
Mr. B. Khaleelu Rehman, A.P., EIC, UPES
Md. Salauddin, A.P., EIC, UPES
Mr. Vinay Chowdhary, A.P., EIC, UPES
Mr. Arpit Jain, A.P. (SS), EIC, UPES
Mr. Vivek Kaundal, A.P. (SS), EIC, UPES
Mr. Deepak Kumar, A.P. (SS), EIC, UPES

Venue Arrangement Committee
Mr. Arpit Jain, A.P. (SS), EIC, UPES
Mr. Vivek Kaundal, A.P. (SS), EIC, UPES
Mr. B. Khaleelu Rehman, A.P., EIC, UPES
Md. Salauddin A.P., EIC, UPES

Mr. Vinay Chowdhary, A.P., EIC, UPES
Mr. Bhan Parkash, A.P. (SS), EIC, UPES

Transport Committee
Mr. B. Khaleelu Rehman, A.P., EIC, UPES
Md. Salauddin, A.P., EIC, UPES
Mr. Vinay Chowdhary, A.P., EIC, UPES
Mr. Arpit Jain, A.P. (SS), EIC, UPES
Mr. Vivek Kaundal, A.P. (SS), EIC, UPES

International Committee

Dr. Pieter Jonker, DU Delft University of Technology, The Netherlands
Dr. Karl Heinz Steinke, Hochshule Hannover University of Applied Sciences and Arts, Germany
Dr. Sumeet S. Aphale, University of Aberdeen, Aberdeen, UK
Dr. Jai Ragunathan, Marine Institute, Canada
Dr. P. Arun Babu, Marie Curie Fellow, ResilTechs.r.l, Pisa, Italy
Dr. Babu Sena Paul, Johansberg University, South Africa
Dr. Ashraf Darwish, Helwan University, Cairo, Egypt
Dr. E.G. Rajan, Founder President, Pentagram Research Centre (P) Limited, Hyderabad, India
Dr. J. Manuel Moreno Arostegui, Technical University of Catalunya
Mr. Sérgio Ricardo Xavier da Silva, UNIFACS—Universidade Salvador, Bahia
Mr. Yashvardhan Rolyan, Rockwell Automation, Project Manager, USA
Dr. Mritunjoy Chakraborty, IIT Kharagpur
Dr. Arun Mahindrakar, IIT Madras, India
Dr. M.P. Poonia, Director, NITTTR, Chandigarh, India
Prof. D.V. Gadre, NSIT, Delhi, India
Dr. Ravi Gangwar, ISM Dhanbad, India
Dr. Debashish De, WBTU, Calcutta, India
Dr. A.K Singh, VNIT, Nagpur, India
Dr. Vijay Nath, Birla Institute of Technology, Mesra Ranchi, India
Dr. Yogendra Kumar Prajapati, MNIT Allahabad, India
Dr. Ramesh Lalwani, Vice Chancellor, ICFAI University, India
Dr. Vrijendra Singh, Associate Professor, IIIT, Allahabad, India
Dr. Loviraj Gupta, Lovely Professional University, India
Dr. M.R. Tripathy, Professor, Amity School of Engineering and Technology, Noida (UP), India
Dr. Hishmi Jamil Husain
Mr. Bryan Chong, Inti International College, Penang, Malaysia
Dr. Jaydeep Chakarvorty, Baddi University, Baddi, Solan (HP)
Dr. Sandeep Chakarvorty, Baddi University, Baddi, Solan (HP)

Dr. M.S. Yadav, Kurukshetra University, Kurukshetra, India
Dr. I.A. Pasha, Dean (R&D), BVRIT, India
Dr. Lini Mathew, NITTTR, Chandigarh, India
Dr. N.M. Singh, VJTI Mumbai, India
Dr. Faruk Kazi, VJTI Mumbai, India
Dr. Rupendra Pachauri, Gautam Budha University, Greater Noida, India
Dr. Yogesh Chauhan, Gautam Budha University, Greater Noida, India
Dr. Prabhat sharma, NIT, Nagpur, India
Dr. Sonal Singhal, Shiv Nadar University, NCR, GB Nagar, India
Dr. Debdatta Kandar, NEHU, India
Dr. M.D. Singh, Thapar University, Patiala, India
Dr. Preeti Singh, Panjab University, Chandigarh, India
Dr. L.M. saini, Professor, NIT, Krushetra, India
Dr. Babita Saini, NIT, Kurushetra, India
Dr. R. Gowri, Dean (Engineering), Graphic Era University, Dehradun, India
Dr. Namit Gupta, Shri Vaishnav Institue of Technology and Science, Indore, India
Dr. Vinay Bhatia, Baddi University, Baddi, Solan (HP), India
Dr. Himashu Monga, Director, SIET, Bilaspur, India
Dr. Chandra Mohan, Bapatla Engineering College, India
Dr. Vijaynath, Birla Institute of Technology, Mesra, India
Dr. Mayank Srivastava, Amity University, Noida, India
Mr. Shailesh Mishra, NSIT, Delhi, India
Mr. Ankur Kumar, ST Microelectronics, Noida, India
Mr. Manish Sharma, Amity University, Noida, India
Dr. Y.K. Awasthi, M.R. University, Faridabad, India
Mr. Purnendu Shekhar Pandey, THDC IHET, Tehri Garhwal, India
Mr. Vinod Kumar Yadav, HRIT, Ghaziabad, India
Dr. S. SRI Gowri, Professor and Head, ECE Department, SRK Institute of Technology, Enikepadu, Vijayawada, India
Mr. Harbinder Singh, Baddi University, Baddi, Solan (HP), India
Mr. Dileep Jaiswal, Maya Institute of Technolgy, Dehradun, India
Mr. Kuldeep Singh, Baddi University, Baddi, Solan (HP), India
Mr. Gaurav Verma, Jaypee University of Information Technology, Noida, India
Mr. Sushil Kumar, Bhushan Steel Limited, Engineer, Ghaziabad, India
Mr. Anuj Kumar Sharma, DIT University, Dehradun, India
Mr. Ravindra Sharma, Nimbus Academy of Management, Dehradun, India
Ms. Sunita Chandel, Uttrakhand Technical University, Dehradun, India
Mr. Kulshrest Paraliya, JBIT, Dehradun, India
Dr. Mayank Singh, KEC, Ghaziabad, UP, India
Mr. Anand Nayyar, KCL Institute of Management and Technology, Jalandhar, India
Mr. Vishal Jain, BMIET, Sonepat, India

Keynote Speakers



Program Chair
Dr. O.P.N. Calla
Director, International Center for Radio Science,
Jodhpur, India



Dr.ir. Pieter. P. Jonker
Professor, Faculty of Mechanical, Maritime and Materials Engineering, Delft University of Technology, Delft, The Netherlands



Dr. E.G. Rajan
Founder President Pentagram Research Centre (P) Limited, Partner Company, SUN Micro Systems, USA, Hyderabad, India



Dr. Jai Ragunathan
Professor
Marine Institute of Memorial University of Newfoundland, Canada



Prof. D.V. Gadre
NSIT, New Delhi Coordinator,
Centre for Electronics
Design and Technology Director,
TI Centre for Embedded Product Design

Contents

Differential Voltage Current Conveyor-Based One-Shot Pulse Generator Circuit Implementation 1
Amit Bhattacharyya

Sign Language Interpretation Using Pseudo Glove 9
Mukul Singh Kushwah, Manish Sharma, Kunal Jain and Anish Chopra

Commercial Aviation: The Legal Travails of Automation, Future Shock and the Zen of Machine Take Over 19
Sampath Kumar Karai Pattabiram

Prediction Models for Global Solar Radiations, Diffused Radiations and Direct Solar Radiations Using ANFIS 27
Anand Mohan, Piyush Kuchhal and M.G. Sharma

Forensic Analysis of Residual Artifacts from Private Browsing Sessions in Linux 39
A. Sankara Narayanan, T. Rajkumar and N.V. Sobhana

Prediction of Voltage Collapse in Power System Using Voltage Stability Indices 51
Pallavi Choudekar, Divya Asija and Ruchira

Adaptive Routing Mechanism for Real-Time Wireless Sensor Networks Based on Two-Hop Information 59
Sandhya Rachamalla and Anitha Sheela Kancherla

Mitigation and Analysis of Very Fast Transient over Voltages (VFTOs) of Transformer in 1000 KV Gas-Insulated Substation (GIS) Using Wavelet Transform 69
K. Prakasam, M. Surya Kalavathi and D. Prabhavathi

Application of PSO Technique in Multiarea Automatic Generation Control 89
Mohan Kashyap, Anu Chaudhary and Satish Kansal

Toward EEG Spectral Analysis of Tomographic Neurofeedback for Depression 97
Chamandeep Kaur and Preeti Singh

Comparison of Performance Metrics of ModAODV with DSDV and AODV 105
Mrinal Kanti Deb Barma, Rajib Chowdhuri, Sudipta Roy and Santanu Kumar Sen

Detection and Location of Faults in Three-Phase 11 kV Underground Power Cables by Discrete Wavelet Transform 113
D. Prabhavathi, M. Surya Kalavathi and K. Prakasam

Comparative Study of the Methodologies Used in Low-Power Master–Slave Flip-Flops 127
Arpita Sengupta and Peyush Pande

Wrist Pulse Signal Features Extraction: Virtual Instrumentation 135
Nidhi Garg, Ramandeep Kaur, Harry Garg, Hardeep S. Ryait and Amod Kumar

Optimized Swarm Architectures in Airborne Internet 143
Pardeep Kaur, Preeti and Amit Gupta

Operational Amplifier-Based Fractional Device of Order $s^{\pm 0.5}$ 151
Huirem Tarunkumar, Ashish Ranjan, Ravi Kumar and P. Subrahmanyam

A Novel Approach for Designing PID Controller for Set-Point Tracking for a HVAC Process 161
Nitin Sundriyal, Pratibha Yadav and Mayank Chaturvedi

Performance Analysis of FSO Link Using CO-OFDM Under the Effect of Atmospheric Turbulence 167
Saruchi Attri, Charu Narula and Sanjiv Kumar

Reliable and Fast Data Transmission Mechanism for Congested Wireless Sensor Network 173
Roshan Jahan and Preetam Suman

Performance Analysis of FSO System for Different Fog Conditions 181
Ritu Gupta and Preeti Singh

Performance Analysis of Multibeam WDM-FSO System in Clear and Hazy Weather Conditions 189
Marvi Grover, Preeti Singh and Pardeep Kaur

Triangular Inset Fed C-, X-, and Ku-Band Antenna for Satellite and Radar Applications 197
Vipin Choudhary, Aastha Gupta, Garima Mahendru and Malay Ranjan Tripathy

In-service Pipeline Inspection Crawler 203
Vimal Upadhyay and Sonali Agrawal

Femtocell-Based Load Balancing Using a Noncooperative Game 211
Asmita Roy, Priti Deb, Sadip Midya, Debashis De and Koushik Majumder

Study of Conventional Control Algorithms for PV-Based Grid-Connected Microgrid 219
Nikita Gupta, Rachana Garg and Parmod Kumar

Design of 10.24 Tb/s DWDM System Using NRZ Modulation Format with Narrow Channel Spacing 227
Kuldeep Singh and Sandeep K. Arya

Validation of ANN-Based Model for Binary Distillation Column 235
Amit Kumar Singh, H.P. Singh and Sachin Mishra

A VDVTA-Based Novel Configuration for Realizing Grounded Inductance 243
Ghanshyam Singh, Dinesh Prasad, Data Ram Bhaskar and Mayank Srivastava

In-campus Generator-Substation Monitoring and Control Using LabVIEW 251
Abhinav Shukla, Abhas, Rajesh Singh and Anita Gehlot

Performance Analysis of Interleaved Coupled Inductor Boost DC–DC Converter Fed Induction Motor Drive 259
Vivek Sharma, Ashutosh Bhatt, Nikita Rawat and Shobhit Garg

RSSI-Based Indoor Robot Localization System Using LabVIEW 267
Varchas Choudhry, Rajesh Singh and Anita Gehlot

Performance Estimation of WDM Radio-over-Fiber Links Under the Influence of SRS Induced Crosstalk 279
Abhimanyu Nain, Suresh Kumar and Shelly Singla

Design and FPGA Implementation of 32-Point FFT Processor 285
Amit Kumar, Adesh Kumar, Aakanksha Devrari and Shraddha Singh

Performance Enhancement in WDM-FSO System Using Optical Amplifiers Under Different Rain Conditions 293
Navneet Dayal, Preeti Singh and Pardeep Kaur

Fuzzy-Based Multi-Objective Optimization for Subjection and Diagnosis of Hybrid Energy Storage System of an Electric Vehicle 299
Kurukuru Varaha Satya Bharath and Kamlesh Pandey

MDS^{3}C: Modified Digital Signature Scheme for Secure Communication 309
Gulista Khan, Bhumika Gupta and Kamal Kumar Gola

Autonomous Operation of Wind-Battery Hybrid Power System with Intelligent Power Management Capability 317
Diwaker Pathak, Ankit Gupta, Rupendra Kumar Pachauri and Yogesh K. Chauhan

Performance Analysis of a Novel Text Watermarking Technique for Devanagari Text 325
Nitin Namdeo Patil and Jayantrao Bhaurao Patil

Evaluation of Entropy-Based Segmentation Techniques for Automated Skin Disease Detection 335
Ishita Bhakta and Santanu Phadikar

Futuristic Automobile Accident and Theft Notifier with Location Tracker 343
Archit Agarwal and Ayush Agarwal

Design and Comparative Analysis of Controllers for Continuous Stirred Tank Reactor (CSTR) 351
Parvesh Saini, Rajesh Kumar, Priyanka Sharma and Nalini Rajput

Performance Analysis of Reactive, Proactive and Hybrid Routing Protocol Used in Petroleum Tank Over Network Control Systems 367
S.K. Agarwal, Sachi Bansal and Anwar S. Siddiqui

Dead Time Compensation in Sugar Crystallization Process 375
Sandeep Kumar Sunori, Pradeep K. Juneja, Mayank Chaturvedi and Jeevanshi Mittal

Performance Analysis of AMC-Based Bowtie-Shaped Slotted Antenna for Terahertz (THz) Applications 383
Devesh Kumar, Malay Ranjan Tripathy, Manish Sharma, Amit Kumar and Umesh Kumar

ANFIS-Based Fault Diagnosis Tool for a Typical Small Aircraft Fuel System 391
Vijaylakshmi S. Jigajinni and Vanam Upendranath

Control of Reactive Power of RES-Based Hybrid Isolated Power System Using UPFC 407
Abhishek Gandhar, Balwinder Singh and Rintu Khanna

Intelligent Image Interpreter: A Semi-automatic Detection of Ships by Image Analysis of Space-Borne SAR Image Using SVM 417
S. Senthil Kumar and H.K. Anasuya Devi

Design and FPGA Implementation of DSSS for Near-Far Effect in MANET 425
Aakanksha Devrari, Adesh Kumar, Amit Kumar and Shraddha Singh

Air Mouse: An Everyday Mouse for the Ease of Computing 435
P.S. Venkateswaran, Vivek Kaundal, Amit Kumar Mondal, Abhishek Sharma, Vindhya Devalla and Shival Dubey

A Novel Approach for Continuous Pain Intensity Estimation 443
Neeru Rathee and Dinesh Ganotra

A Design and Application of Forest Fire Detection and Surveillance System Based on GSM and RF Modules 451
Aditya Agarwal, Vishal Sharma, Rajesh Singh, Anita Ghelot and Kanchan Bahukhandi

Generation of Electricity by Piezoelectric Crystal in Dance Floor 461
Pankaj Aswal, Suyash Kumar Singh and Apurv Thakur

Cylindrical Metallic Pin Structure Microstrip Patch Antenna for Wideband Application 471
Praful Ranjan, Mahesh Kumar Aghwariya, Purnendu Shekhar Pandey and N. Prasanthi

Low THD ±0.75 V 32 nm CNFET Quadrature VCO for PLL and Costas-Loop Applications 479
Jyoti Sharma and Md. Samar Ansari

Design of Quadratic Equations Multiplier (for upto 2-Bit Number) Using Vedic Technique 489
Parth Sharma, Raj Pratap Singh, Rohit Singh and Peyush Pande

Design Improvement and Assessment of Efficiency of Three Phase Induction Motor Operating Under the Rated Voltage 495
Rajeev Gupta, Devender Kumar Saini, Raj Kumar Saini and Piush Verma

Finite Element Analysis of Wing Design 503
Nitin Chandola and Rohit Singh Rawat

A Minimal Realization Universal Filter Employing Third-Generation Current Conveyor and Operational Transconductance Amplifier 511
Tajinder Singh Arora, Varkha Rani and Manish Gupta

Design of 30 MHz CMOS Operational Amplifier 519
Deepak Prasad, Ashutosh Pranav, Apoorva Nimbargi, Jyoti Singh, Vijay Nath, Abhishek Pandey, Madhu Kumari Ray, Manish Kumar and Manish Mishra

Line Flow Indices for Placement of Distributed Energy Sources in Relieving Transmission Line Congestion 527
Rajagopal Peesapati, Niranjan Kumar, Vinod Kumar Yadav and Gitanjali Mehta

Design and Development of Android-Based BOT for Medicine and Food Distribution to Patients 537
Tanvi Mehta, Anita Gehlot and Dolly Sharma

Integration of Renewable Energy Resources for Rural Electrification 545
Sheikh Suhail Mohammad, Sachin Mishra, Sanjay Kumar Sinha and Vijay Kumar Tayal

A Vision of IoT: Applications, Challenges, and Opportunities with Dehradun Perspective 553
Mainak Mukherjee, Isha Adhikary, Surajit Mondal, Amit Kumar Mondal, Meenakshi Pundir and Vinay Chowdary

LQR and PID Design Technique for an Electric Furnace Temperature Control System 561
Devendra Rawat, Kritika Bansal and Alok Kumar Pandey

Design and Development of Low-Cost Wireless Parameter Monitoring System for Nuclear Power Plant 569
Tanisha Gupta, Rohit Sanket, Rajesh Singh, Anita Gehlot, Eesh Mehandiratta, Ateev Agarwal and Sushabhan Choudhury

The Real-Time Hardware Design and Simulation of Thermoelectric Refrigerator System Based on Peltier Effect 581
Purnendu Shekhar Pandey, Mahesh Kumar Aghwariya, Praful Ranjan and Ginne Rani

Smart Geyser with Usage Profiling to Reduce Electricity Consumption 591
Rohit Samkaria, Ambujaksh Shah, Bhupinder Singh and Sushaban Choudhury

Stabilization of Underactuated Mechanical System Using LQR Technique 601
Akash Gupta, Varnita Verma, Adesh Kumar, Paawan Sharma, Mukul Kumar Gupta and C.S. Meera

A Particle Swarm Optimization Based Switching Scheme for Seven-Level Cascaded Hybrid Bridge Inverter 609
Parul Gaur, Yajvender Pal Verma and Preeti Singh

Analysis of Wavelet Transform and ANFIS-Based Fault Detection and Classification 617
Puja Bharti, M.A. Ansari, Y.K. Chauhan and Ashish Kumar

Study of Power Spectrum Estimation of Steady-State Visual Evoked Potential-Based BCI System Using AR Model Approach 625
Mukesh Kumar Ojha and Anshuman Prakash

Market-Clearing Price Forecasting for Indian Electricity Markets 633
Anamika and Niranjan Kumar

Outage Capacity Performance Analysis of Dual-Hop Multiple-Relay Decode-and-Forward System for Generalized η-μ Fading Channel 643
Manoj Bisht and P. Palanisamy

Design for Structured Uncertainty of Mass Spring System Using Robust Control Technique 653
Kapil Shukla, Mayank Ranakoti, Vivek Kaundal, Amit Mondal, Abhishek Sharma and Mukul Kumar Gupta

Scalable Design and Synthesis of 3D Mesh Network on Chip 661
Arpit Jain, Rakesh Dwivedi, Adesh Kumar and Sanjeev Sharma

Application of Remote Sensing in the Monitoring of Biogas Production 667
Shailey Singhal, Rajan Sharma, Madhu Sharma, Shilpi Agarwal and Naveen Singhal

Parallel Algorithm for LaGrange's Interpolation on BSN-Mesh 673
Ashish Gupta and Bikash Kanti Sarkar

Design of Broadband Monopole Microstrip Antenna Using Rectangular Slot 683
Raj Gaurav Mishra, Ranjan Mishra and Piyush Kuchhal

HAAR like Feature-Based Car Key Detection Using Cascade Classifier 689
Paawan Sharma, Mukul K. Gupta, Amit K. Mondal and Vivek Kaundal

Global Stability of Dynamic Model for Worm Propagation in Wireless Sensor Network 695
Rudra Pratap Ojha, Pramod Kumar Srivastava, Shashank Awasthi and Goutam Sanyal

WPAN-Based Energy Efficient Automation System for Buildings 705
Manish Kumar Mishra, Rajesh Singh, Anita and Rohit Samkaria

An Intelligent GA-Optimized Fuzzy Controller for Automatic Generation Control for a Two-Area Interconnected System 715
Vishal Jain, Devendra Saini, K.N. Dinesh Babu and J.S. Saini

Design and Verification of 16-Bit Vedic Multiplier Using 3:2 Compressors and 4-Bit Novel Adder 723
K. Venkata Siva Reddy, P. Vishnu Kumar, K. Maheswari and B. Khaleelu Rehman

Brain Tumor Segmentation in Glioma Images Using Multimodal MR Imagery 733
Shashwat Goel, Aastha Sehgal, Parthasarathi Mangipudi and Anu Mehra

Design and Sizing of Decentralized Grid-Connected Solar Power Plant 741
Vineet Mediratta, Kamal Bansal, Piyush Kuchhhal and Vinay Chandna

Effect of Faults on Power Electronic Devices for ZSI-Fed Induction Motor Drive System 747
Bhawana Negi, Vivek Sharma, Ankit Bhatt and Pratibha Yadav

Design of a Multiband Filter for Future Wireless Communication 753
Jagadish Baburao Jadhav and Pramod Jagan Deore

Gait-Based Human Recognition by Multiple Wavelet Coherence 761
Sagar Arun More and Pramod Jagan Deore

Automatic Segmentation of Brain MRI of Newborn and Premature Infants Using Neural Network 771
Tushar H. Jaware, K.B. Khanchandani and Anita Zurani

An Efficient Handoff Using RFID Tags 779
Sadip Midya, Asmita Roy, Koushik Majumder, Debashis De and Santanu Phadikar

A Robust and Fast Technique to Detect Copy Move Forgery in Digital Images Using SLIC Segmentation and SURF Keypoints 787
Kanica Sachdev, Mandeep Kaur and Savita Gupta

VPBC: A Varying Probability-Based Clustering for Energy Enhancement in WSN 795
Shaveta Gupta, Vinay Bhatia and Vishal Puri

Biosignal Acquisition of Stress Monitoring Through Wearable Device 803
Ritika Saxena, Sushabhan Choudhary, Rajesh Singh and Anshuman Prakash

Implementation of Heartbeat Sensing Using PSoC3 811
Ramesh Babu Chukka, D. Madhavi, N. Jyothi and Ch Sumanth Kumar

Design and Implementation of Wearable Device for Water Management System for Household Usage 817
Manpreet Kaur Khurana, Rajesh Singh, Vivek Kaundal and Nikhil Gupta

High Speed-Low Power Divide-by-16/17 Dual Modulus Prescaler Using C^2MOS 825
Anupriya Chakraborty, Akanksha Agrawal, Snehil Gupta, Sachin Kumar Rajput and Anu Mehra

Design and Optimization of Luggage Tracking System on Airport 833
Varun Gupta, Roushan Kumar, Raj Gaurav Mishra, Anirudha Semwal and Sweety Siwach

Contact Thickness Variation Effect on Performance of Novel Organic Thin Film Transistor 839
Aanchal Verma and Poornima Mittal

Comparative Analysis of Various Adaptive Filter Structures Using Simulink 847
Mahesh B. Dembrani, K.B. Khanchandani and Anita Zurani

Experimental Investigations on the Effects of Dust Fouling on PV Module 855
Ankit Batra, Ankit Gupta, Rupendra Kumar Pachauri and Athar Hussain

Study of Parametric Effects on Solid Oxide Fuel Cell 863
Kevi Singh, Rupendra Kumar Pachauri, Yogesh K. Chauhan and Ankit Gupta

Performance Investigation of ANN Controller-Assisted Small Hydro Power Generation System 871
Durgesh Kumar, Ankit Gupta, Rupendra Kumar Pachauri and Yogesh K. Chauhan

GA-Tuned 2DOFPID-Based Biomass Concentration Control of Bioreactor 879
Nikhil Pachauri, Asha Rani and Vijander Singh

Microcontroller and FPGA-Based Analysis of 8 $\times$ 48 LED Matrix Display with Keyboard Interface 887
Adesh Kumar, Vivek Kaundal, Rajesh Singh, Anita Gehlot, Nikhil Gupta and Mohit Suyal

Software Reliability Prediction Based on Ensemble Models 895
Pravas Ranjan Bal, Nachiketa Jena and Durga Prasad Mohapatra

Wireless Sensor Network Based Patient Health Monitoring and Tracking System 903
Amitabh Yadav, Vivek Kaundal, Abhishek Sharma, Paawan Sharma, Deepak Kumar and Pankaj Badoni

Maple Leaf Planar Fractal Antenna for Energy Harvesting Applications 919
Ila Verma, Pratima Singh, Hemant Kumar and Malay Ranjan Tripathy

Performance of Dual Metal-Double Gate Tunnel Field Effect Transistor with Different Dielectrics 927
Deepak Kumar and Prateek Jain

An In-Memory-Based Big Data Analytics with Two-Level Storage on Private Cloud 935
Nikkita Shekhar and Ambika Pawar

Drive Current Boosting Using Pocket Implant Near to the Strained SiGe/Si Source with Single-Metal/Dual-Metal Double-Gate Tunnel Field-Effect Transistor 943
Prateek Jain and Deepak Kumar

Distributed Intrusion Detection System for TCP Flood Attack 951
Deepak Kshirsagar, Suraj Sawant, Ravi Wadje and Pravin Gayal

An Optimized Approach: Air Energy Trap System in Railways for Power Generation 959
Nikhil Raj, Rohan Sharma, Sagar Majumdar, Rajesh Singh and Anita Gehlot

Implementation of Ladder Logic for Control of Pipeline Inspection Robot Using PLC 965
Varnita Verma, Roushan Kumar and Vivek Kaundal

Design of Wearable Device for Muscle Fatigue Monitoring 973
Sweety Siwach, Anita Gehlot and Anshuman Prakash

A Novel Design of Inexpensive, Heavy Payload and High Mobility ORQ Robot 979
Praveen Kumar, Parag Verma, Rajesh Singh and Ravi Kumar Patel

Hindi Dialect (Bangro) Spoken Language Recognition (HD-SLR) System Using Sphinx3 991
Virender Kadyan, Amitoj Singh and Parth Wadhwa

Fingerprint-Based Attendance System Using MATLAB 999
Anushka Swarup, Kottapalli Dheeraj and Adesh Kumar

Investigations on the Effects of Partial Shading and Dust Accumulation on PV Module Performance 1005
Pankaj Yadav, Amit Kumar, Ankit Gupta, Rupendra Kumar Pachauri, Yogesh K. Chauhan and Vinod Kumar Yadav

Design and Development an Embedded System for Multichannel Data Acquisition for Use in Networked Monitoring System 1013
Ashi Rastogi and Aastha Dadheech

Early Stage Identification of Localized Brain Atrophy Using Bioimage Processing Algorithms 1019
Abhishek Raj and Swati Kadlag

Dual Gate Organic Inverter Circuit Behavior Analysis Based on Diode Load Logic Configuration 1027
Yamini Pandey, Shubham Negi, Srishti, A.K. Baliga and Brijesh Kumar

Substrate Integrated Waveguide Leaky Wave Antenna with Backward to Forward Scanning Capability 1035
Anumeha Badoni, Nitin Kumar and S.C. Gupta

Optimal Power Dispatch in Competitive Market 1043
Aayush Shrivastava, Manjaree Pandit, Devender Saini and Raj Gaurav Mishra

Improvement in Performance of OLED by Introducing Additional Hole Blocking Layer 1051
Akanksha Uniyal and Poornima Mittal

Background Subtraction Method for Object Detection and Tracking 1057
Satrughan Kumar and Jigyendra Sen Yadav

Impact of Gate Thickness Variation and Dielectric on the Performance of Vertical Organic Thin Film Transistor 1065
Srishti, Yamini Pandey, A.K. Baliga and Brijesh Kumar

Depth Analysis of Organic Bilayer Solar Cell and Their Performance Parameters Extraction 1073
Kamlesh Kukreti, Arun Pratap Singh Rathod and Brijesh Kumar

Four-Stage Telecommunication Switching Design and Synthesis 1079
Adesh Kumar, Piyush Kuchhal and Sonal Singhal

Nanoferrite Embeddedin Poly(O-Toluidine) and Polyaniline Matrix for EMI Shielding 1087
Preeti, M. Farukh, Balesh Vasisth, Shaily Singhal, Lalit Gaur, Vivek Verma, S.P. Gairola and S.K. Dhawan

Design and Performance Analysis of Bowtie-Shaped Slotted Rectangular Patch Antenna for Terahertz (THz) Applications 1095
Devesh Kumar, Malay Ranjan Tripathy, Sachin K. Rajput, Amit Kumar and Manish Sharma

FPGA Implementation of UDP/IP Stack Using TSE IP Core and Transfer Data at 1 Gbps 1103
Deeksha Jain and Swati Shrivastava

Channel Capacity in MIMO OFDM System 1113
Nishu Baliyan, Manish Verma and Adesh Kumar

Digital Image Processing-Based Water Pollution Control System 1121
Ramandeep Singh, Toolika Srivastava, Anuj Sharma, Sandeep Sharma and Santosh Kumar

Switched Capacitor Circuit Realization of Sigma-Delta ADC for Temperature Sensor 1129
Abhishek Pandey, Mohd. Javed Khan, Deepak Prasad, Vijay Nath, S.S. Solanki and L.K. Singh

Calculation of Aircraft Altitude Using RADAR Dataset: A Basic Study and Implementation of FM Concept 1137
Shagun Bishnoi, Hutanshu Kamal, Sudhir Kumar Chaturvedi and Anirudh Katyal

Development and Analysis of FSR and RFID Based Authentication System 1145
Anita Gehlot, Piyush Kuchhal, Adesh Singh and Rajesh Singh

Author Index 1153

About the Editors



Dr. Rajesh Singh received his Ph.D from the University of Petroleum and Energy Studies, M.Tech. (Gold Medalist) in Digital Communication from Rajeev Gandhi Technical University, Bhopal, India and B.E. degree in Electronics and Communication Engineering from B.R. Ambedkar University Agra, India. He is currently associated with the University of Petroleum and Energy Studies, Dehradun, as an Assistant Professor (SG) and with additional responsibility as the Head of Institute of Robotics Technology (R&D). He has 14 years of teaching experience in reputed institutes. His area of expertise includes embedded systems, robotics, and wireless sensor networks. He has won the young scientist award in 2012. He has organized and conducted special sessions at different conferences, a number of workshops, summer internships, and expert lectures for students as well as the faculty. He is an active member of syllabus designing and course development activities. He has total six patents filed and more than 50 research papers published in various refereed journals/conferences. He is a peer reviewer for conferences and journals and has submitted eight research proposals to various funding agencies as the principal investigator. He got a Certificate of Appreciation from Texas Centre at NSIT, New Delhi and Laureate Award of Excellence in Robotics Engineering in Spain for his mentorship to students who have participated in national/international competitions. In the last 4 years, he has been awarded twice with the Certificate of Appreciation from the University of Petroleum and Energy Studies for exemplary work. He has supervised 15 postgraduate thesis and more than 50 undergraduate projects. His sole aim is to motivate students to come with innovative ideas and make them feel free to think and to enhance their skills.



Dr. Sushaban Choudhury is the Head of the Department of Electronics, Instrumentation, and Control in the University of Petroleum and Energy Studies. He has teaching experience of 26 years and he has completed his Ph.D from the University of Petroleum and Energy Studies, M.Tech from Tezpur Central University, Tezpur, India and received his B.E. degree from NIT, Silchar University, India. He has published more than 50 papers in various national/international conferences/journals. He has filed seven patents. His area of interest is Zigbee-based wireless networks. He has been selected as the outstanding scientist of the twenty-first century by the Cambridge Biographical Centre, UK. He has also been selected in the who's who of the world in science by Marquis Who's Who, USA.

Differential Voltage Current Conveyor-Based One-Shot Pulse Generator Circuit Implementation

Amit Bhattacharyya

Abstract This paper presents a novel One-shot pulse Generator Circuit, which is composed of only one differential voltage current conveyor (DVCC) as the active element. The application circuits utilizing the DVCC are introduced and implemented. Only one DVCC and two resistors and one capacitor are required to construct every circuit. Each circuit is able to provide a pulse-shaped response having changeable width via a positive-edge triggered signal. The first one is a general one-shot pulse generating circuit. The second design can reduce the recovery time after applying triggered signals. Is-Spice is the simulation software to simulate every model. To fabricate the models commercially available ICs (AD844AN) and passive elements are required. Program and experimental outputs satisfy theoretical results.

Keywords One-shot pulse generator · Differential voltage current conveyor · Positive-edge trigger · Recovery time · Parasitic effects

1 Introduction

One-shot pulse generators are widely used in instrumentation, communication, phase-locked loop circuits, power conversion control circuits, and signal processing applications [1]. Generally, one-shot pulse generator circuit consists of operational amplifier basically in voltage comparator mode, one capacitor, and three resistors [2] as shown in Fig. 1. This paper presents a novel one-shot pulse Generator Circuit composed of only one DVCC as active element. The application circuits utilizing the DVCC are introduced and implemented. The first one is a general one-shot pulse generating circuit. The second design can reduce the recovery time for triggering signals. Due to wide popularity of DVCC-based application circuits in the present era having larger width of the band, greater exactness, higher active range,

Amit Bhattacharyya (✉)
Department of Electronics and Communication Engineering,
Haldia Institute of Technology, Haldia, WB 721657, India
e-mail: amit_elec06@yahoo.com

© Springer Science+Business Media Singapore 2017

R. Singh and S. Choudhury (eds.), *Proceeding of International Conference on Intelligent Communication, Control and Devices*, Advances in Intelligent Systems and Computing 479, DOI 10.1007/978-981-10-1708-7_1

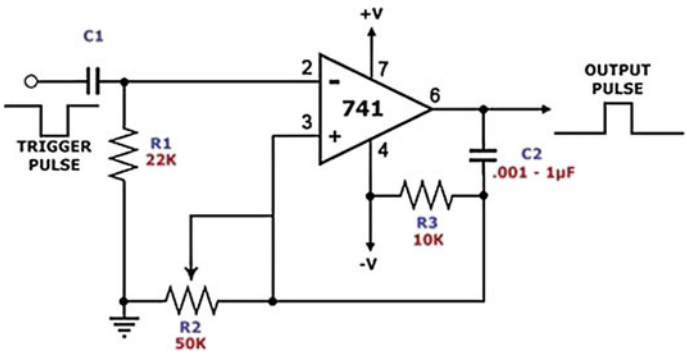


Fig. 1 Traditional approach of One-shot pulse generator circuit

and ease of fabrication [3–6] over traditional operational amplifiers, the presented one-shot pulse generator circuit is more applicable than the traditional designs to DVCC-based circuit systems. The proposed model has a number of advantages over the traditional design due to following reasons:

(1) Number of active devices used in the model are less or same.
(2) Most of the passive components are grounded rather than floating structure to obtain the advantages of IC fabrication techniques and enhanced parasitic properties.
(3) Obtained operating frequency is higher than OPA-based structure.
(4) The design can shorten the recovery time for triggering signals.
(5) Temperature sensitivity is less.
(6) Applicability in fully DVCC-based systems increases (Fig. 1).

2 Circuit Discussions and Working Ideology

2.1 Fundamental Idea and Construction of DVCC

The DVCC is useful for performing various superior presentations of continuous signal processed fields where voltage terminals require high input impedance and current terminals require high output impedance. Circuit symbol of DVCC having four

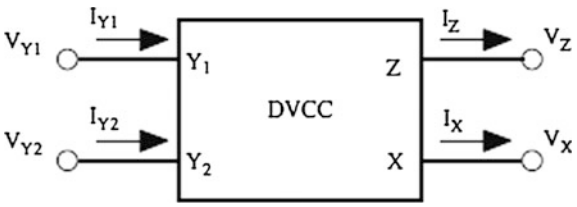


Fig. 2 Circuit symbol of DVCC

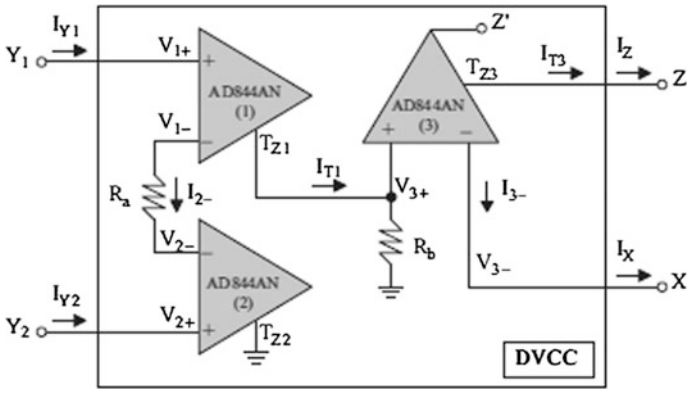


Fig. 3 Implementation of DVCC using IC844AN

terminals is used here. The voltage drop at *X* terminal equals the difference of voltage between two *Y* terminals, and the current flowing through *X* terminal is same as that of *Z* terminal. DVCC has zero *X* terminal input impedance and infinite impedances at two *Y* and one *Z* terminals. The circuit symbol of DVCC is shown in the Fig. 2.

To check the effectivity of projected model, Fig. 3 shows a realistic construction of DVCC using IC844AN which is easily accessible in the market.

The difference between AD844AN and OPAs is that it has a virtual short property between the inverting and non-inverting input terminals. Current flow through inverting terminal and current flow through T_Z terminal are same. Infinite resistances at two *Y* terminals are taken from non-inverting input terminals of the first two AD844ANs of DVCC structure. By connecting the T_Z terminal of the first IC AD844AN to the non-inverting input terminal of the third through resistor R_b which is grounded, voltage drop at *X* terminal equals the difference of voltage between two *Y* terminals, and the current flowing through *X* terminal is same as that of *Z* terminal, is obtained. From Fig. 3 the following *V*−*I* characteristic equations can be written as follows:

$$V_{Y1} = V_{1+} = V_{1-} \tag{1}$$

$$V_{Y2} = V_{2+} = V_{2-} \tag{2}$$

$$I_{Y1} = I_{Y2} = 0 \tag{3}$$

$$I_{TI} = I_{2-} = \frac{V_{1-} - V_{2-}}{R_a} = \frac{V_{Y1} - V_{Y2}}{R_a} \tag{4}$$

$$I_X = I_{3-} = I_{T3} = I_Z \tag{5}$$

$$V_X = V_{3-} = V_{3+} = I_{T1} R_b = \frac{R_b}{R_a}(V_{Y1} - V_{Y2}) \tag{6}$$

Therefore, the V–I characteristic equations of ideal DVCC can be obtained by setting $R_a = R_b$. Figure 3 shows a realistic construction of DVCC using IC844AN which is easily accessible in the market.

2.2 Proposed DVCC-Based Model Discussions

Figure 4 shows the models of the proposed DVCC-based One-shot pulse Generator. Figure 4(a) is a diode-clamping circuit. A modified model is shown in Fig. 4(b) reduces the recovery time. An oscillator provides rising-edged signal Vtrg for triggering the circuits for producing pulse-shaped waveform having fixed width. To form a regenerative-feedback in two projected models connects Y_1–Z together with the grounded resistor R_2. DVCC swings between two constant levels V_{o+} and V_{o-}. Figure 5 shows the related responses of the projected models in Fig. 4. T represents the pulse width, and Tr is considered as the required time of recovery until later pulse is fired. The working ideology of every proposed model has three conditions: stable condition, quasi stable condition, and recovery time condition. During stable condition, capacitor C is open-circuited and capacitor voltage VC drop is secured by the diode D or the analog switch M. By adjusting R_2 greater than R_1 stable state operation is maintained, for which I_Z is less positive than I_X. Hence the output voltage V_O reaches upper constant level V_{o+}.

This state will continue up to $t = T_1$, where a trigger pulse is fired and then, the quasi stable condition will start. At present, I_z is greater than I_x and consequently the output voltage V_o jumps abruptly from V_{o+} to V_{o-}. Since V_o remains at V_{o-}, C starts to discharge through R_1 from $t = T_1$. In this state, the currents through X and Z terminals, i.e., I_x and I_z and the capacitor voltage $V_C(t)$ are expressed as follows:

$$V_C(t) = V_{O-}\left(1 - e^{-\frac{(t-T_1)}{R_1 C}}\right) \tag{7}$$

$$I_X = \frac{V_O - V_C}{R_1} = \frac{V_{O-} - V_C}{R_1} \tag{8}$$

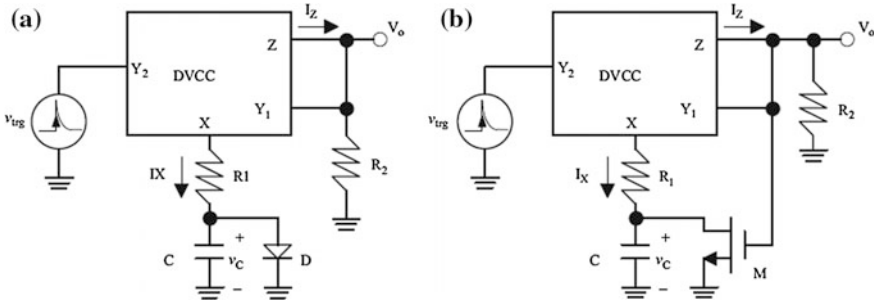


Fig. 4 **a** First projected model and **b** Second projected model to reduce recovery

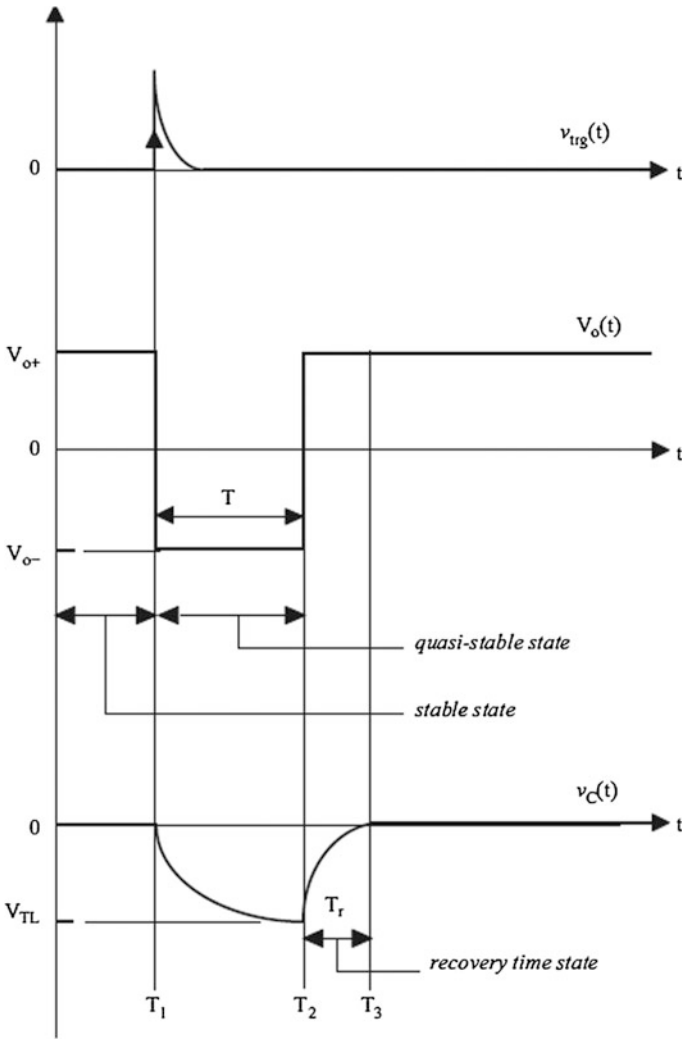


Fig. 5 Generated waveforms of the proposed models

$$I_Z = \frac{V_O}{R_2} = \frac{V_{O-}}{R_2} \tag{9}$$

when $t = T_2$, capacitor voltage V_C reaches minimum voltage V_{TL}. By solving (8) and (9) the equation of minimum voltage V_{TL} is obtained for $I_x = I_z$:

$$V_{TL} = V_C(T_2) = \left(1 - \frac{R_1}{R_2}\right) V_{O-} \tag{10}$$

Solving (7) and (10), size of the pulse, T, is obtained as given in Eq. (11). Equation (11) shows that the size of the pulse is changed for broad range of frequency by changing R_1 and C, and R_2 is used for accurate-tuning:

$$T = T_2 - T_1 = R_1 C \ln\left(1 - \frac{V_{TL}}{V_{O-}}\right) = R_1 C \ln\left(\frac{R_2}{R_1}\right) \tag{11}$$

3 Fabrication Criteria and Examined Outputs

Laboratory examination is performed by using easily accessible AD844AN ICs, analog switch CD4066, two resistors and one capacitor to build projected model. Is-Spice is the simulation software to simulate structure. The circuit simulations and experiments are maintained at supply voltages of ±10 V with saturation levels $\boldsymbol{Vo+ = Vo- = 9.4\ V}$. From an external function generator the triggering signal *Vtrg* is applied. For the proposed one-shot pulse generator models, the width of the pulse is considered as $T = 1$ ms, and impedance ratio of $R_2/R_1 = 10$ is adjusted. C is considered as 100 nF. Consider R_1 is much greater than R_x. Figure 6 shows the simulated and measured waveforms of V_{trg}, V_o, and V_C for two projected models

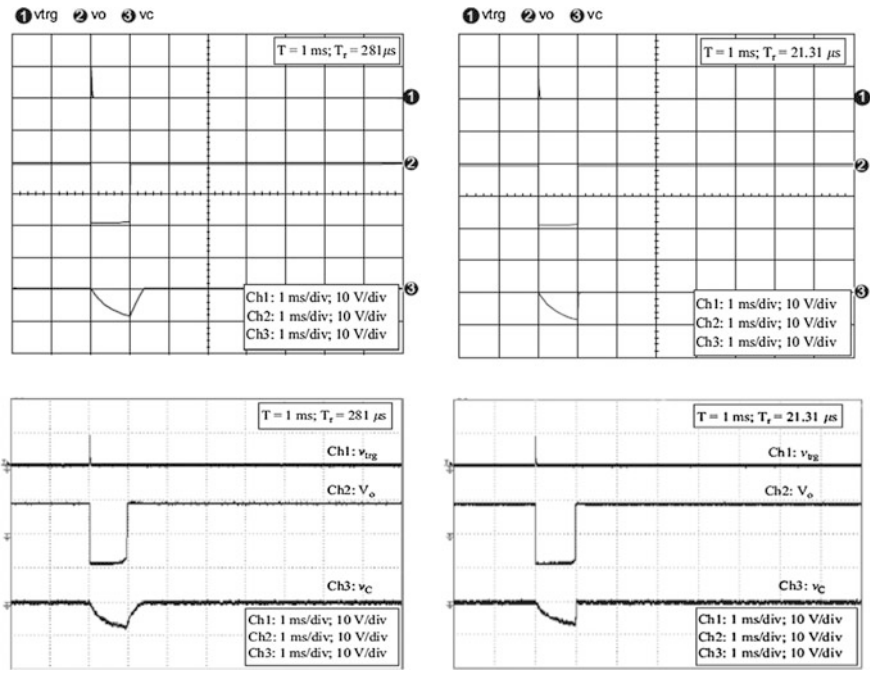


Fig. 6 Simulated and measured outputs of the corresponding waveforms with T = 1 ms for the first and second proposed model

with $T = 1$ ms and it is clearly observed, that even the design parameters are same, the second proposed circuit is able to reduce the recovery time. The measurements show that recovery time Tr is 281 μs for the first proposed model, and Tr is 21.3 μs for the second proposed model.

4 Conclusions

In this paper, the projected models consist of only one DVCC and several resistors and capacitors. The second proposed model can shorten the recovery time. The effectivity of the projected circuits is examined as program and experimental outputs satisfy theoretical results. The projected models provide new applications for the DVCC-based systems. They have wide applications in the instrumentation, measurement, and communication systems.

References

1. J.M. Jacob, Analog Integrated Circuit Applications, Prentice-Hall, New Jersey, 2000.
2. F. Giuseppe, C.G. Nicola, Low-Voltage Low-Power CMOS Current Conveyor, Kluwer Press, UK, 2003.
3. P. Tuwanut, J. Koseeyaporn, P. Wardkein, A novel monostable multivibrator circuit, IEEE Tencon 2005, pp. 1–4.
4. Y.K. Lo, H.C. Chien, Current-mode monostable multivibrators using OTRAs, IEEE Trans. Circuits Syst. II 53 (11) (2006) 1274–1278. Press, New York, 2004.
5. K. Lo, H.C. Chien, Single OTRA-based current-mode monostable multivibrator with two triggering modes and a reduced recovery time, IET Proc.-Circuits Devices Syst. 1 (3) (2007) 257–261.
6. Y.K. Lo, H.C. Chien, Current-controllable monostable multivibrator with retriggerable function, Microelectron. J. 40 (8) (2009) 1184–1191.

Sign Language Interpretation Using Pseudo Glove

Mukul Singh Kushwah, Manish Sharma, Kunal Jain and Anish Chopra

Abstract The research work presented in this paper explores the ways in which, people who are unable to speak, can communicate easily with the people around. The research incorporates a system comprising of a glove-based mechanism, constituting sensors and a controlling system to recognize the hand gestures and movements and communicate accordingly. This research work is significant as there are a number of ways to convey the message, which includes, display on LCD, on a Bluetooth device and as well as via a speaker. This hardware is integrated with a program embedded in a microcontroller chip capable of correctly determining the specified alphabets from the hand positions with the use of flex sensors. With the use of minimum tools and maintaining the efficiency certain alphabets and few common words used in conversations have been implemented, further scope for more with complex glove system.

Keywords ATmega16 · Microcontroller · Playback IC · Flex sensors

1 Introduction

Sign language is a language through which communication is possible without the means of acoustic sounds. Instead, sign language relies on sign patterns, i.e., body language, orientation, and hand movements such as a wave, to facilitate understanding between people. It requires a special training to learn the sign language, so the research presented would be able to bridge the gap between the differently abled people and the people who are unable to understand their language.

M.S. Kushwah (✉) · Manish Sharma · Kunal Jain · Anish Chopra
Electronics and Communication Engineering, Amity University,
Sector – 125, Noida, Uttar Pradesh, India
e-mail: mukul.singh8447@gmail.com

Manish Sharma
e-mail: manish.nsit07@gmail.com

© Springer Science+Business Media Singapore 2017

R. Singh and S. Choudhury (eds.), *Proceeding of International Conference on Intelligent Communication, Control and Devices*, Advances in Intelligent Systems and Computing 479, DOI 10.1007/978-981-10-1708-7_2

1.1 Background Information

Many research works related to Sign languages detection have been done as for example the American Sign Language (ASL), the British Sign Language (BSL), the Japanese Sign Language (JSL), and so on. But very little research has been done in Indian Sign Language (ISL) recognition till date [1].

There are, originally, two approaches toward the interpretation of sign language. One of them is through the use of glove-based systems which can be used for measuring different parameters of gestures such as hand and finger position, angles, and tip recognitions, which is known as glove-based method. The second approach revolves around the use of machine vision and image processing techniques to formulate vision-based hand recognition systems, known as vision-based method. Sensor gloves for measurements of finger movements are a promising tool for objective assessments of kinematic parameters and new rehabilitation strategies [1]. What we have implemented in our project is glove-based method due to various advantages of it, discussed further in the paper.

2 Objective

The objective in this research is to create a system comprising of a glove fitted with flex sensors on all the fingers. These sensors would be connected to a microcontroller, which would be interfaced with an LCD screen for the alphabets to be displayed, as well as a Bluetooth module so that the alphabets can be displayed on a Bluetooth-enabled device. For each alphabet and word, there being a different recorded sound.

3 Components Used

The model that we have come up with consists of several components integrated with each other to fulfill the objective. Following is the description of each of them.

3.1 Flex Sensors

These sensors depict the change in terms of resistance on bending, resistance being the greatest when bent maximum. They convert the change in bend to electrical resistance; the more the bend, the more will be the resistance value.

They are usually in the form thin strips, with length ranging from 1 to 5 in. [2]. Since, the sensors show the change in output in terms of resistance, we use a reference resistance of 10 kΩ and applying the voltage divider rule, send in a variable voltage, in accordance with the output resistance from the sensor, to the ADC ports of the microcontroller.

3.2 Bluetooth Module

We have incorporated the use of Bluetooth technology to get the output on any Bluetooth-enabled device. There are applications that connect via Bluetooth for mobile devices. When connected to a mobile device, any output from the glove can be seen on the user application. This gives the model a wireless connectivity with ease of use.

3.3 Playback IC

This is an IC which stores voice clips and plays when a certain signal is passed onto it. Whenever an alphabet or a word is recognized, the speaker connected to this IC will play the clip stored corresponding to that alphabet. Also, no extra programming is needed to store the voice clips. The recording is available from the chip only.

3.4 16 × 2 LCD Screen

A 16 × 2 LCD screen is used to display the alphabets decided on the basis of sensor values, i.e., according to the hand positions.

3.5 Microcontroller

The microcontroller used here is ATmega16. It is a 40-pin IC with low power consumption and 16 K bytes of In-System Programmable Flash Memory. In addition to this, it has 32 × 8 general purpose registers, 32 programmable I/O lines along with 8 channel 10bit ADC ports (Fig. 1).

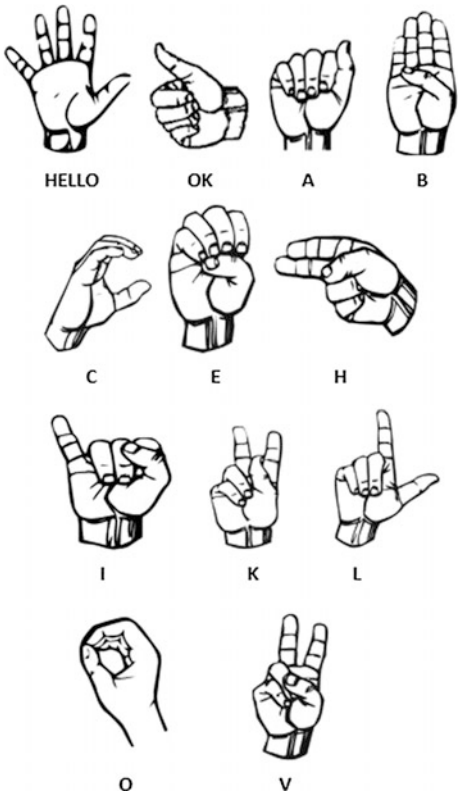


Fig. 1 Hand positions for different alphabets as key

4 Proposed Model

The primary component, the flex sensors are placed at each of the finger and the thumb. Figure 2 shows the connections of flex sensors with the microcontroller.

The flex sensors are connected via 10 kΩ resistances to obtain a voltage value instead of the resistance measure, using the voltage divider rule. The ADC (analog to digital) ports convert the analog output from sensors to feed in a digital input to the microcontroller (Fig. 3).

The main circuit board contains the microcontroller as well as an LCD screen and Bluetooth module interfaced with it. The playback IC and the development board, containing the microcontroller, share a power source.

The LCD is interfaced onto the port C of the microcontroller along with any required power source through AVCC and GND terminals. The code developed has functions that transfer data in parallel mode. The Playback IC for the sound output is connected through the port B of the microcontroller. The Bluetooth communication is provided through the serial communication via UART (universal asynchronous receiver/transmitter) interface (Figs. 4 and 5).

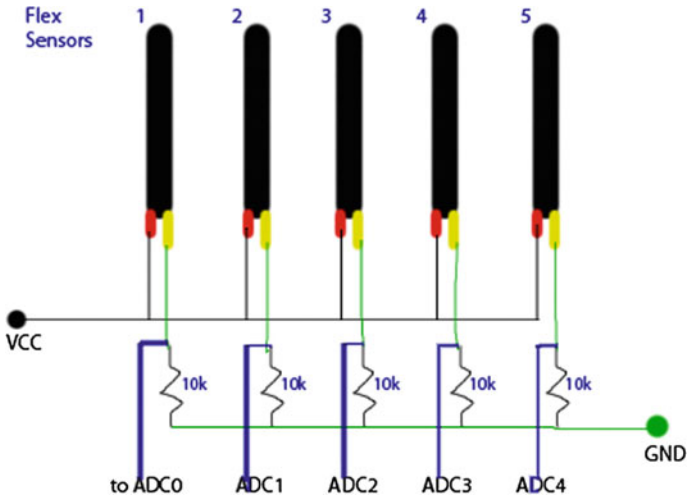


Fig. 2 Flex sensors connections

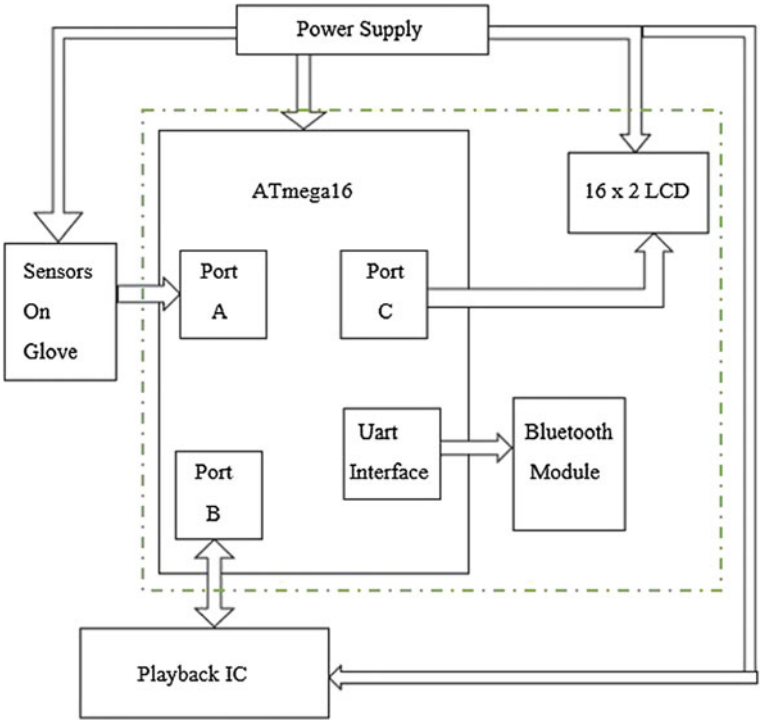


Fig. 3 Block diagram

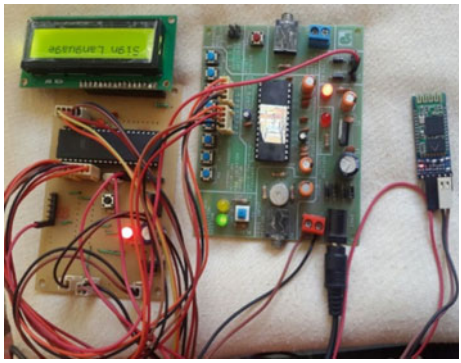


Fig. 4 Image of all the components



Fig. 5 Image of the glove fitted with flex sensors

The microcontroller is loaded with a program code designed to recognize the chosen alphabets and words and demonstrate output through various means on a number of devices. The program is designed such that it keeps on taking input from the flex sensors at certain intervals of time. The code generates an output corresponding to that set of predefined values and sends it to LCD and via Bluetooth. The port B is programmed such that each stored sound for an alphabet is played on detection of that alphabet. When an alphabet is detected, that port in enabled for a certain time and then it is disabled.

5 Computation, Testing, and Results

The flex sensors here play the primary role. With each of the step in the process and output determination depends on the values coming out of the flex sensors. The ADC ports convert the analog value (in terms of voltage measure) from the flex sensor to a digital one by the following formula:

$$\text{Digital value} = (V_{\text{in}}/V_{\text{ref}}) * 1024 \quad (1)$$

- The value V_{in} here referring to the value input to ADC port.
- V_{ref} being the reference value of the voltage. Here we have used internal source of reference and the value of this is 2.56 V.
- 1024 signifies that the microcontroller has 10bit ADC ports.

It was found that upon bending, the output resistance from the flex sensors increased as prescribed in the component specifications. Thereby, the output voltage, in converted form, decreased. By the Eq. 1, we can see that the input value to the microcontroller will decrease upon bending (Fig. 6).

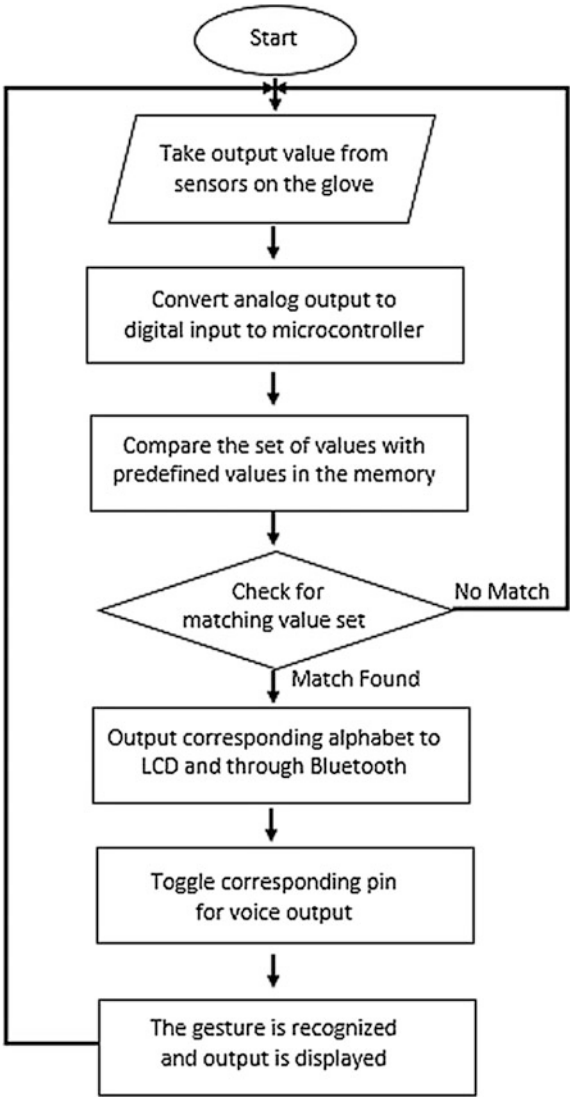


Fig. 6 Flow chart for the system

According to the provided key of the hand positions, the range is specified for each alphabet/word. When the flex sensors value set matches with the specified range set, the output is displayed (Figs. 7 and 8).

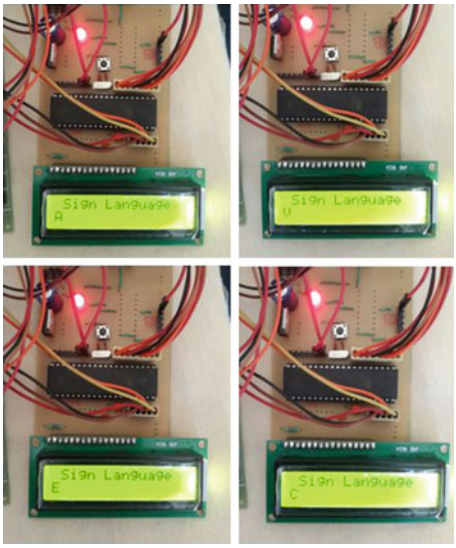


Fig. 7 Some results during testing phase

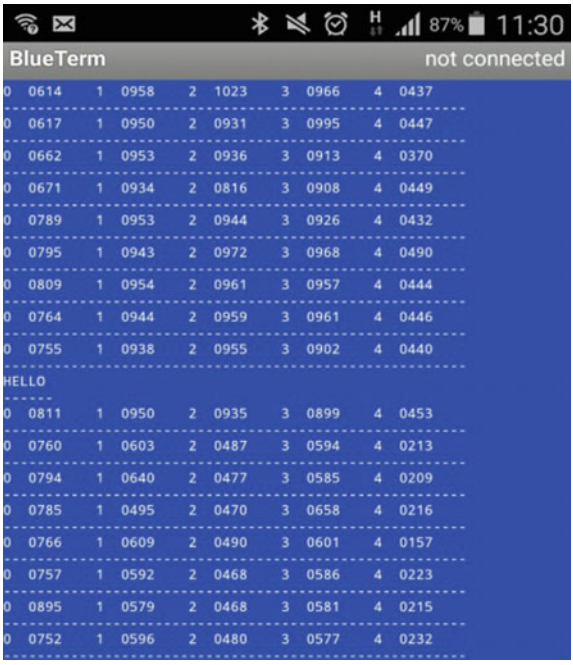


Fig. 8 Output on mobile screen

6 Comparison with Related Work

- As we have learned that, in of the gesture recognition methods, vision-based methods, computer camera is required as the input device for observing the movements of hands or fingers. Since, the movements to be captured must be of the hands only, there is a challenge of designing the system and incorporating heavy imaging processing tools to make the system background invariant, light insensitive, and also achieve efficient real-time performance. Thus, vision-based methods tend to prove complex and costly [3].
- Unlike other models available in the market, our model is capable to communicate in various ways, like, through Bluetooth, sound output, and also the output is visible on the generic LCD screen, which is mostly the only output form available in other models.
- Other models, in which wireless communication is used, come with RF (Radio Frequency) technology implementation. The performance of an RF module will depend on a number of factors such as a rise in the transmitter power and greater communication distance. However, this will also result in a greater electrical power drain on the transmitter device, which will result in shorter working life for battery-operated devices. Likewise, using a higher transmit power will make the system more prone to interference with other RF devices and also by increasing the receiver sensitivity will also increase the effective communication range, but will also potentially cause malfunction due to interference with other RF devices [4]. This problem is solved using Bluetooth instead of RF to communicate.

7 Conclusion

Summing up the research work here, the glove designed has a lot of benefit for a person with speech disability. Our model is of the simplest form. By using just the flex sensors, the complexity of the project is minimized. Covering all the alphabets is a bit difficult with the number of sensors we have used, because with the increase in number of outputs the sensitivity increases, thereby making it difficult for the user. It is not just one hand position will convey one word, but with suitable programming we can also map one position to even a word, thereby easing it out for the user. Also, with the use of Bluetooth, it is very easy and useful for anyone to use it, extending its compatibility and connectivity.

8 Future Scope

- With the implementation of more kinds of sensors, we can achieve a system comprising of all the alphabets. Moreover, with extensive use of this glove, all the circuit boards could be synthesized on one board, eliminating the complexity

altogether. Also, because of the use of one of the latest technologies available, i.e., Bluetooth, the glove is highly compatible, further the Bluetooth app can be specifically programed for this purpose to achieve more from the application itself, which would add up to the functions the glove can perform.

- This glove can also be used to control various other appliances like a T.V., computer, etc. Just like the microcontroller is programmed to convert the finger movements into recognizable alphabets, it can also be programed to do various other things upon certain movements of the hand.

References

1. Patil, K., Pendharkar, G., Gaikwad, P.: American Sign Language Detection. International Journal of Scientific and Research Publications 4(11) (2014)
2. Haydar, J., Dalal, B., Hussainy, S., Khansa, L., Fahs, W.: ASL Fingerspelling Translator Glove. International Journal of Computer Science Issues 9(6) (2012)
3. Patil, K., Pendharkar, G., Gaikwad, P.: Finger Detection for Sign Language Recognition
4. Abinayaa, V., Jayan, A.: Case Study on Comparison of Wireless Technologies in Industrial Applications. International Journal of Scientific and Research Publications 4(2) (2014)
5. Singha, J., Das, K.: Indian Sign Language Recognition Using Eigen Value Weighted Euclidean Distance Based Classification Technique. International Journal of Advanced Computer Science and Applications 4(2) (2013)

Commercial Aviation: The Legal Travails of Automation, Future Shock and the Zen of Machine Take Over

Sampath Kumar Karai Pattabiram

Abstract This is a study of human-level problems vis-a-vis automation in the air Law regulation. The article addresses various legal issues concerning automation in the context of pilot, airport tower managers, design/maintenance management, passenger ticketing, and cargo handling. Case laws and international conventions are discussed along with social paradigm of the more generic position of the entire field of automation and man's inability to cope with reference to Alvin Toffler's "Future shock." The question how much of automation is at balance with comfort levels and the probability of risk avoidance is addressed. Negligence concepts in warranty and torts are still evolving and remain in limbo at international air conventions. Future shock is revisited man's possible redundancy in the face of automations questioned. The article crescendos to the future of automation and into the Zen of machine takeover and leaves many questions still unanswered.

Keywords Aviation · Aircraft · Automation · Design · Future · Human

1 Introduction

Ever since Elvin Toffler's book "Future Shock" that first appeared in a magazine [1], the world has been concerned about man's ability to adapt to the pace of change in technology. Much of this comes as a shock to society unable to cope with its speed in terms of mental and physical interactivities. This seems to be the most prevalent in the case of the aviation industry that outpaces most other industries in automation for the critical operations of navigation, communication, and airworthiness. The aforesaid parameters are the primary regulatory concerns of both the Director General of Civil Aviation in India (DGCA) and the International Civil Aviation Organization (ICAO) along with the several conventions that our nation is heir to by multilateral ratifications. The standards that are set are as per the market

S.K.K. Pattabiram (✉)
University of Petroleum and Energy Studies, Dehradun, Uttarakhand, India
e-mail: Sampath@ddn.upes.ac.in

© Springer Science+Business Media Singapore 2017

R. Singh and S. Choudhury (eds.), *Proceeding of International Conference on Intelligent Communication, Control and Devices*, Advances in Intelligent Systems and Computing 479, DOI 10.1007/978-981-10-1708-7_3

leaders in the manufacturing of commercial aircraft predominantly in the west, to name a few Boeing, McDonnel Douglas, Airbus, United Technologies, and Lockheed Martin. As the telecommunication, GSP and Information technology systems get more and more sophisticated—the aircraft industry has most readily included automation at several levels of operation in the industry. This article features the pros and cons of such sophistication taking into account the factors that contribute to risk and legal liability exposure.

2 The Operative Concerns in Automation

The areas affected substantially by automation are the following [2]: (1) aircraft handling, (2) air traffic control, (3) aircraft design, construction, and maintenance, (4) passenger handling, and (5) cargo handling. Each of these concerns vis-a-vis is automation is discussed as follows.

2.1 The View at the Cockpit of the Pilot

The Pilot as per the Warsaw convention [3] is the commander of the aircraft under his control. In a given set of circumstances, he is accountable for action or inaction as the case may be. The control, however, is not merely mechanical landing and smooth take off, but also a complex maze of instrumentation and guidance systems that have to be reckoned in his inflight decision making. A broad recital of these activities that necessitate automation include among other things automatic pilot, navigation, correction of aircrafts course, collision avoidance, aircraft location pin pointer, automatic hijack alarm, automated landing in inclement weather, and so on. In fact owing to the nature of the air traffic and its inherent risks, such automation is not merely a novelty but a necessary prerequisite in the context of today's high density traffic. Instrument landing systems also include the "Enhanced vision system" [4].

Notwithstanding the fact that these instruments bring about a reduction in decisional making role of the captain, yet it is only the captain under the Chicago convention that is primarily responsible for its consequences. Is it possible that the human pilot has become completely redundant apart from bearing the burden of such legal responsibility? Not at all—computers and instrumentation can fail and the human factor in taking over when events demand it seems not completely extinguished. Many cases of instrument faults have come to be noticed [5] which otherwise would have led to disaster. The case involved a Korean Airlines flight which inadvertently strayed into Soviet territory and got shot down. In fact, the complex information and data provided by the automation may indeed prove overwhelming to the pilot and have caused a panic situation, which otherwise would have enabled him to react intelligibly based on gut instinct. In general, human travel by air has never been supported genetically by our evolution and is

not the same as sea travel from which life originated. Flying has always been the exclusive premise of the birds and this is perhaps the reason for the humans to feel strange at the subliminal level. Mostly, such skills are acquired without genetic support. In plain words, flying does not come natural to man but is an acquired ability. Another medico physical phenomenon that is worth discussing here is the aspect of 'Vertigo' [6]. Vertigo even to the most well-trained pilot results in the aircraft to be envisioned as tilted to one side, while actually this is an optical illusion. The pilots in such cases are advised to trust their instruments while landing. Many accidents have been caused by such distortion in vision. The automation has reduced the burden of the pilot, but has the legal responsibility shifted from pilot to the burgeoning instrumentation? The answer is a resounding, No! The legal onus still rests with the captain and the conventions and ICAO has yet to come to a consensus among nations for addressing the vexing uncertainty.

2.2 Air Traffic Control

From its early inception in the west and the early part of the twentieth century, air transport and with it the commerce of airline activity has come a long way. In its wake, air traffic density has increased to gargantuan proportions bringing unimaginable conditions in airports and their tarmacs if not for the facilitating automation. Airports like Chicago's O' hare airport, New York and London boast traffic rates around 1.5 to 1.7 operations per minute [7] both landing and takeoff. In such dense conditions, the role of the control tower for orderly movement is paramount and is not less complicated than that of the pilots on flight. The automation and GSP systems in place is perhaps even more complicated then at the cockpit. The Chicago convention annex 2 "Rule of the Air" specifies that the pilot is bound to obey the instructions of the traffic controller except on emergency conditions. Here the term "emergency" is still a gray area in many a situation to fix the legal liability. The role of the air traffic controller becomes additionally onerous considering that these are nationally controlled by government personnel. There are international cases that have penalized the negligence of Air controllers such as the mishap in the infamous Milan—Linate Airport disaster in 2001 when two aircrafts one a Scandinavian airlines (SAS) and the other a corporate aircraft which collided on the runaway during a foggy day resulting in the death of several passengers. The air controllers were booked for negligence for keeping faulty equipment and were sentenced to jail imprisonment. As in most government organizations, a strict regimen of penalization lead to a 'Cabal' of organized cover-ups of incidents that require to be brought to the notice of the management as a matter of preventive proactivity in safety procedures. The cover-up that surfaced in Schiphol airport [8], for instance, brought to light such cover-ups and on discovery controllers were prosecuted. A safety case-oriented airport is a feature indispensable for a modern aviation. Such cover-ups would not further the development safe commercial air travel.

It is almost axiomatic that following the rapid growth of the industry need-based technology is concurrently developed. Airport traffic management received its first attention in the ICAO in 1963 in the form of "Future Air Navigation systems" (FANS). FANS were the use of navigation systems based on satellites for navigation, control and communications. FANS were renamed as ICAO CNS/ATM systems (Communication, Navigation and Surveillance/Air Traffic Management systems).

Further, other systems developed such as the US Global Positioning system (GPS) and the Russian GLOSNASS. Both the systems were developed during the cold war between the USA and USSR, which later became imbibed into the lore of Airport traffic management systems. Other mutations of the above systems were the European EGNOS, MSAS (Japan), and WAAS (USA). However, the ICAO has to streamline all of such systems into one common system under the Global Navigation Satellite systems (GNSS). The liability of negligence in the absence of multilateral agreements by nations is still in a limbo as to a common standard for legal audit.

2.3 Aircraft Design and Maintenance Issues

Computer-aided design (CAD) has become the norm in engineering design and the aviation industry is no exception. Taking into account the complexity of aircraft manufacture, maintenance and avionics in particular automation was almost inevitable. To the manufacturing assembly, line was brought in the extensive use of robotics.

The use of robotics has created precisions both in terms of manufacture and specification compliances hitherto unknown to handcraftsmanship. In this regard, the product liability standard comes in two variants, the first is through warranties, which is a relationship between seller and buyer, and the other is through the medium of tortious liability. The first is the outcome of contracts but the other is more about fulfilling the role of social obligation to the unwary passenger or lay public. Product liability under tort is the remedy for social contracts to the consumer or public at large that has no knowledge of the implicit requirement of professional craftsmanship in the aviation industry. Despite the automation and its precision, yet there is always the aspect of defects. Automation creates its own level of encountered failure that has to be accounted both for intended as well as unintended effects. The law has not really stretched itself to take into account all failures. The history of tort liability has also undertaken sea changes taking into the nature of the business of aircraft design that pass through several contractual joint ventures involving many parties which then has the effect of diluting third party strict liability. In this regard, ever since the landmark case in the United States in Kaiser Steel versus Westinghouse Electric [9] has impacted also the aviation industry. The case exemplifies the limitation or even obfuscation of product liability in cases where there are joint agreements on design involving parties of equal economic

strength in a commercial setting bargain on specifications and their risk assessment. Such joint assemblies or Joint ventures are almost a common feature in the aviation industry as between seller and buyer. The legal position, therefore, is still effected by warranty clauses that specify the penalty for defect contractually rather than to a third party liability. The other feature effecting aircraft manufacture is that of the role of the underwriter insurance that are now willing to quantify the liability on quality assurance to the manufacturer and thus transferring some of the onerous duties on quality control to less than 100 % sampling. The manufacturer would normally check whether the product does not have any inherent defects prior to leaving the factory premises and there is no negligence in its production. These have also been diluted to some extent by insurance covers that now enable manufacturers to cut costs on an otherwise rigorous inspection. Where does this leave the grand stand of safe travel for the aviation industry in general taking into account such hedges provided by insurance coverages? The aspect of safety controls gain some mitigation in the compliance mechanisms both enforced through ICAO conventions and the routine maintenance under "Routine Maintenance and overhaul" (RMO) that are enforced through national agencies Director General of Civil Aviation (DGCA).

2.4 Aircraft Maintenance and the Assembly Line

As in design, routine aircraft maintenance is both regulatory in compliance and includes among other things Engine line management, Engine overhaul, Rotable components maintenance (Attrition parts tire, brakes, landing gear, etc.), Avionics (Instrumentation, electronics navigation, etc.), and other non-critical items such as paint and cleaning. These are preventive based maintenance of the aircraft which have to take place on time line pressures and schedules. There are dwell times at the hangar having competing interests both in time and qualitative workmanship on various aircrafts of diverse manufacture and airline schedules. The regulative mechanism s is enforced through national regulations (DGCA) as well as international agreement (ICAO). The ICAO on the other hand has its own check list of compliance documents to pass muster on vehicle safety namely written manuals on fixing operator maintenance responsibility on deeming an aircraft airworthy, mobilization of requisite emergency equipment and finally a certification for airworthiness for the intended voyage. Maintenance records are kept for inspection as airport hangar activity and RMO operations also have to be endorsed by approved independent third party inspectors as satisfactory compliance to standards prior to their subsequent release for actual functioning of the Aircraft. Whether due to compulsions of pressure or in terms of meeting deadlines that tend to feature the "Business as usual" syndrome rather than the qualitative effort is priority is a matter of conjecture from Airport to airport. In this context, automation of the maintenance function may tend to a certain complacence and an over dependence on support mechanisms such as automation.

2.5 Passenger Handling

The internet world of today has created jurisdiction problems where air ticketing is concerned. Take the case of Polanski versus KLM Royal Dutch Airlines [10] when a KLM ticket purchased from a home computer at Los Angeles through KLM website for a flight from Los Angeles to Warsaw by redeeming mileage coupons. A dispute as to this ticket and the jurisdiction sought by KLM was Netherlands and the passenger sought Poland. Ultimately the jurisdiction fell on the United States considering that the issue of ticket was done on the basis of KLM's partner Northwest Airline. The no cost tickets taxes that were paid in the United States was the clincher as to the jurisdiction of the dispute—the meeting of minds that constitute contract took place in Los Angeles. The internet booking can therefore jurisdictional problems in the context of litigation. The internet may also be a source of biased information generation by leaving out rival airlines schedules out of the loop of information on flights.

2.6 Cargo Handling

The problems of cargo handling is not as simple as the handling of passengers, which involve only two parties the passenger himself and another the carrier. The cargo on the other hand involves the sender (Consignor), carrier, and Consignee. Further operationally three more elements are included the consolidator, break bulk agent and the customs authority. Each of these requires exacting details and electronic air cargo handling systems have been successfully used to provide a central resource from which the cargo are not only tracked but information is available as to its shipped out locus. Information is also made available to the customs authorities and systematizes the cargo handling operations at all stages. Cargonaut [11], a cargo handling system evolved in Netherland has been successfully being operated for several years. Such modern data exchange systems makes for instantaneous communications complete in all ways and allows corrections to the systems flow and avoids paperless transactions.

3 Conclusion or the Zen of Machine Takeover

The Warsaw convention has put a lid on the aspect of the liability of the carrier through maxima minima monetary liability payable for death or injury to passenger or the loss of on board and "checked in" baggage during transit. Having effectively contained the issue, it paved the way for commercialization and proliferation of the industry despite inherent risk at all stages of the supply chain from design to manufacture and service to the consumer. However, a reigning equation of the

application of the tort of negligence still remains unaddressed. The issue connected with the uncertainties in particular of automation in the industry underpins central areas of jurisprudence. The concluding para of this article highlights some of these concerns that have emerged from the technology.

The first discussion is whether twenty first century has matured the initial infantile enthusiasm of its new toys of invention/technology to a more rational use of them? In this regard, the environment is one example of how years of abuse of the natural ecosystem have stretched the limits and now the world seems to wake up to its reality by cutting down use or modifying technologies that create greenhouse gases. We are in fact talking about the Brunt Land sustainability of saving the environment for future generations [12]. Reaching maturity levels? Henry Ford's assembly heralded as the great administrative operative system for mass production was later decried as a human rights abuse. Today its avatar is about the use of robotics for manufacture of all kinds of mass production. The question today of the assembly line has mutated to asking not about human rights, but whether the human effort has been rendered redundant. The answer to this question is if we consider the scenario of unmanned rockets that travel to outer space man seems to be comfortable. But would the scenario be the same for unmanned tramcars/automobiles traversing the pedestrian in city traffic? How would humans like to Air travel by a robotic pilot instead of a human? More so would such a replacement be trusted by human society? Time will tell, but there is lurking suspicion of its efficacy. The movie Space odyssey 2001 [13] enumerates the point when a computer is discovered to have made a fault and astronauts in their attempt to shut it down have to resist the onslaughts of the takeover from a vengeful computer. The point here is that computers that rely on mathematical equations are really unsuitable as far as the human social situations are concerned. The problem really is about the options that we get from the automaton namely great precision or complete failure. This is not really an Hobson's choice but more a trading for either human leisure or one of a time total disaster due to failure. The central problem is that society is not built on precision. One of the outstanding criticisms on operations research-based management science is about its mathematical precision as an unfit tool for executive decision in the human context. As an example of ineptitude of modern robotics is to recreate the multifarious functions of say a human hand—this is still an insurmountable problem. Hence, the high end of unimaginable complexity would be recreating the functions of the human brain. It will take eons before cybernetics actually manages to replicate it. In that sense the human brain may be far superior to any computer that human scientific society had or will be able to make. The contrary view is that man is not to be judged in isolation from nature. Automaton is also the product of a nature constructed through the medium of the "Collective scientific and engineering mind".

In this scenario, we have to revisit the futuristic premonitions of the Alvin Toffler model of "future shock" that puts Man in a position of a sitting duck on the receiving end rather than in a brave new world Darwinian evolutionary mode. Hard to believe that man is unable to cope. Certainly some humans may fall behind but it

is really farfetched to think that all human beings fail to reach their promised zenith as supermen as postulated by Nietzsche [14].

Whatever may be the outcome, time will tell. Interestingly, the economics of wealth of Thorsten Veblen [15] that proclaims that increasing leisure is the measure of effluence. The auto pilot, the automation and take over by machines, may yet succeed due to the overwhelming power of commercial interests that rest upon profit maximization and the end is efficiency or human leisure at its cheapest costs.

References

1. Toffler, Alvin, "The Future as a Way of Life", Horizon magazine, Summer 1965, Vol VII, Num 3
2. Isabella Henrietta Philepina Diederiks-Verschoor & Pablo Mendes de Leon, An introduction to Air law (2006) Kluwer Law International, Eighth edition
3. Available at https://www.iata.org/policy/Documents/MC99_en.pdf (As last seen on December 29th, 2015)
4. Available at https://en.wikipedia.org/wiki/Enhanced_flight_vision_system (As last seen on January 3rd, 2016)
5. See Bin Cheng, The destruction of KAL flight KE007 and article 3 bis of the Chicago convention in Air worthy, pp 47–74 (1994)
6. Available at http://www.airspacemag.com/military-aviation/the-disorient-express-474780/?no-ist (As last seen on December 31st, 2015)
7. Refer to http://aviation.stackexchange.com/questions/11575/at-what-intervals-do-planes-land-and-take-off-from-chicago-ohare (As Last seen on January 9th, 2016)
8. http://www.skybrary.aero/index.php/B763,_Delta_Air_Lines,_Amsterdam_Schiphol_Netherlands,_1998_(Legal_Process_-_Air_Traffic_Controller) (As Last seen on December 28th, 2015)
9. Kaiser Steel Corp. v. Westinghouse Electric Corp., 55 Cal.App.3d 737; Cal. Reptr. 838 (1976)
10. Polanski v. KLM Royal Dutch Airlines, US District Court, SD California, 378 F. Supp. 3d 1222 (2005)
11. https://www.schiphol.nl/B2B/Cargo/NewsPublications/CargoNews5/Cargonaut1.htm (As Last seen on December 28th, 2015)
12. Gro Harlem Brundtland, Our Common Future (Report of the World Commission on Environment and Development, submitted by the World Commission on Environment and Development) 1987. http://www.channelingreality.com/Documents/Brundtland_Searchable.pdf (As Last seen on December 28th, 2015)
13. Watch Space odyssey Stanley Kubrick, available at http://www.tft.ucla.edu/wp-content/uploads/pdfs/Mamber-Kubrick-in-Space.pdf (As last seen on December 28th, 2015)
14. See http://www.britannica.com/topic/superman-philosophy (As Last seen on December 28, 2015)
15. See http://www.britannica.com/biography/Thorstein-Veblen (As Last seen on December 28th, 2015)

Prediction Models for Global Solar Radiations, Diffused Radiations and Direct Solar Radiations Using ANFIS

Anand Mohan, Piyush Kuchhal and M.G. Sharma

Abstract In this study, the meteorological parameters of weather station of University of Petroleum and Energy Studies (UPES), Dehradun, India, has been considered for solar radiation prediction models based on adaptive neuro fuzzy inference system (ANFIS) have been proposed considering different inputs on daily basis for the year 2015. There are different metrological variables considered for solar energy prediction. To check the different suitable input parameters and different outputs like global radiation prediction, direct radiation prediction and diffused radiation, three models have been proposed in this paper.

Keywords Solar radiation prediction · ANFIS · Climatic conditions

1 Introduction

Solar energy is one of the most abundant and clean source of non-conventional energy. India is passing through the phase of solar development. Apart from many socioeconomic problems associated with Indian solar electrification, there are a number of other problems too. Thus, the proposed research is an attempt towards developing a greater understanding on the issue of solar energy generation potential and giving a possible solution for addressing the above said gap. Before developing a solar energy system for a site-specific, it is compulsory to know the potential of that energy available at that site.

Anand Mohan (✉) · Piyush Kuchhal
University of Petroleum and Energy Studies, Dehradun, India
e-mail: anand1mohan@gmail.com

Piyush Kuchhal
e-mail: pkuchhal@ddn.upes.ac.in

M.G. Sharma
Himachal Pradesh State Electricity Board Limited, Hamirpur, India
e-mail: madangopal_hpseb@yahoo.com

© Springer Science+Business Media Singapore 2017

R. Singh and S. Choudhury (eds.), *Proceeding of International Conference on Intelligent Communication, Control and Devices*, Advances in Intelligent Systems and Computing 479, DOI 10.1007/978-981-10-1708-7_4

Almost correct knowledge of different sun radiation and weather data at particular site is very important. However, in most of the places this data is not available or available inaccurately. A number of empirical as well as artificial neural networks (ANN) and ANFIS-based models have been suggested by researchers previously. So by selecting a particular site for prediction of solar radiation, an attempt has been made to know the most relevant solar radiation input parameters required for any potential solar generating station.

In process to check the prediction correctness of the solar models and to find out different parameters like global radiation prediction, direct radiation prediction and diffused radiation prediction different ANFIS-based models have been suggested using all and specifically selected input parameters for a specific location, i.e., University of Petroleum and Energy Studies (UPES), Dehradun, India. The data for the same has been collected from weather station at UPES. The objective of this study is to find the global radiations, diffused radiations and direct solar radiations for above said site as case study under different climatic conditions.

This paper is arranged as follows: literature survey has been presented in Sect. 1. The data used and the proposed methodology have been given in Sect. 2. The output and results have been discussed in Sects. 3 and 4 contains conclusion. Different ANFIS models have been suggested and analyzed in this research article.

Many researchers have done research on the solar radiation predictions. Few of most related research have been discussed below.

In [1], it has been suggested that a number of metrological and geographical factors influence the sun radiations. Different input parameters like temperature, humidity, longitude, latitude, etc., have been taken to suggest three different ANN-based models with most relevant inputs for different models considered.

A new method is proposed in [2] for estimating daily global sun radiation on a plane surface by the time of the year.

The paper [3] shows the evaluation of different models using only the sunshine for estimating global sun radiations.

In this paper [4], Meta-Heuristis Harmony Search method has been proposed to determine the Angstrom equation coefficients using daily solar radiation and daily sunshine duration data of Mashhad Synoptic station from 1997–2003.

An application of multilayer perceptron has been used to obtain solar radiation in Spain in this paper [5].

ANN-based modelling of daily global radiation data has been done in this research paper [6]. Six ANN models have been developed using different combinations as inputs. It has been found that the model using the sunshine duration and air temperature as inputs, give good results.

Paper [7] introduced ANN for modelling the spatial variation of global solar radiation for Saudi Arabia. The data from 41 locations is used and divided into 31 locations for the ANN and ten sites for the testing. The results indicate a relatively good relation between obtained and predicted values.

2 Data Used and Proposed Methodology

Different input variables used for prediction models and ANFIS-based prediction models are discussed in the following points:

2.1 Input Variables Used for Prediction Models

Different input variables used for different predictions are temperature (maximum and minimum), rainfall, relative humidity, global solar radiations, direct solar radiations, and diffused solar radiations. In the process of variable selection for different models suggested for solar radiation prediction different inputs have been given to the same targets. As the longitude and latitude is considered for the specific place, they have been omitted from the input variables. The prediction models have been developed using the above said inputs.

After the completion of variable selection process, the next is to predict the models using different number of input variables for different ANFIS predictions.

2.2 ANFIS Based Solar Radiation Prediction

Three ANFIS-based models have been developed using anfis edit tool of MATLAB. They have been given names as ANFIS-1, ANNFIS-2 and ANFIS-3. In this tool of MATLAB Simulink software, there are standards of uploading the file of different variables to anfis edit tool. 75 % data has been used for the purpose of training and remaining 25 % has been used for testing of data. After this the fuzzy inference system has been generated using grid partitioning. Then the system is trained by taking into consideration the hybrid type of system using zero error tolerance and different number of epochs for different models. When the training is complete, the ANFIS structure is generated. The rule base has been prepared depending upon the output required.

Different models have been trained using hybrid algorithm of ANFIS tool. Testing data does not affect the training rather it provides an independent performance during and after different numbers of epochs are obtained during training, testing and validation of data. Each epoch is one complete sweep of training, testing and validation of data. The number of hidden layers selected can be increased or decreased depending upon the error obtained. Plot of mean square error (MSE) with respect to epochs is called the performance of the network.

2.3 *Proposed Methodology for Solar Radiation Prediction Model*

The methodology used for ANFIS-based predictions is given as flowchart in Fig. 1. In the proposed methodology used for prediction models anfisedit is selected in nftool of MATLAB SIMULINK software. The selected inputs are loaded to the tool from workspace. The grid partition type is used with three no. of membership functions. Then the developed fuzzy rules are used to obtain the fuzzy inference system. Then model is trained by hybrid type of learning. The number of epochs can be changed between 1 and 20 to get the efficient and desired models based on

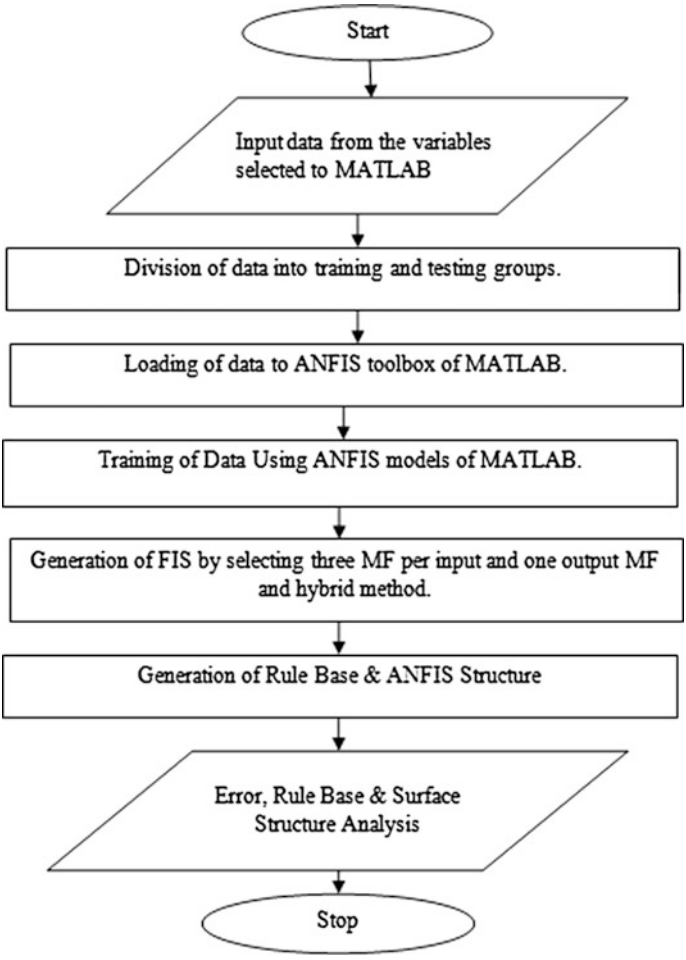


Fig. 1 Proposed methodology for prediction models

different inputs, then the output can be obtained in the form of final structure. Rules generated and the surface distribution can also be obtained using the said process.

3 Different ANFIS Prediction Models Analysis

Three ANFIS models have been proposed namely ANFIS-1, ANFIS-2 and ANFIS-3.

3.1 ANFIS-1 Radiation Prediction Model

In this predicted model, the direct radiations received on earth have been predicted using rainfall, relative humidity, temperature (maximum and minimum), global solar radiation and diffused radiations as input variables obtained from UPES weather station for 257 days of year 2015 has been used to predict the model. In Fig. 2, MATLAB output of model is shown as the rule base prepared for the said model. Number of epochs used are 10. There is a total number of 101 rules, which have been framed to get the desired output. Six inputs and one output is obtained and is shown in Fig. 2. By changing the inputs, we can get the desired output for the said model.

Figure 3 shows the error plot when plotted the fuzzy inference system (FIS) against the testing variables. The blue are the inputs obtained from the data are red are the values obtained after developing the model. Figure 4 shows the two

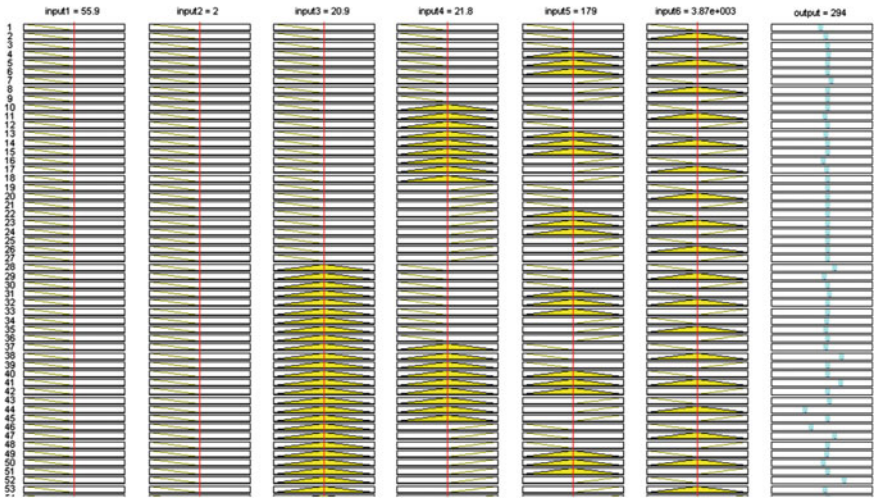


Fig. 2 Rule base for ANFIS-1 prediction model using MATLAB

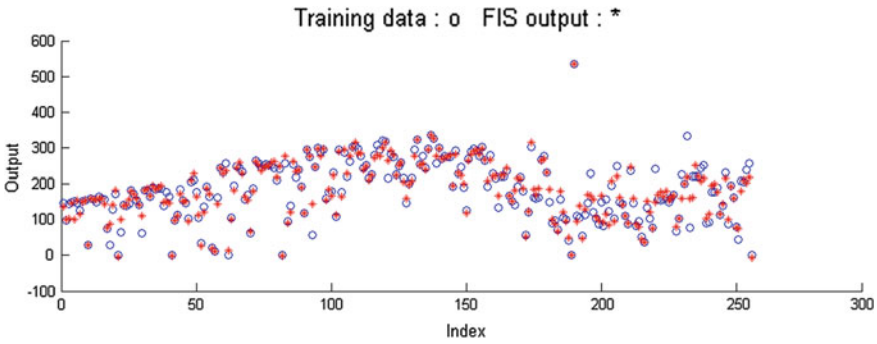


Fig. 3 Error analysis between training data and FIS output for ANFIS-1 model (Color figure online)

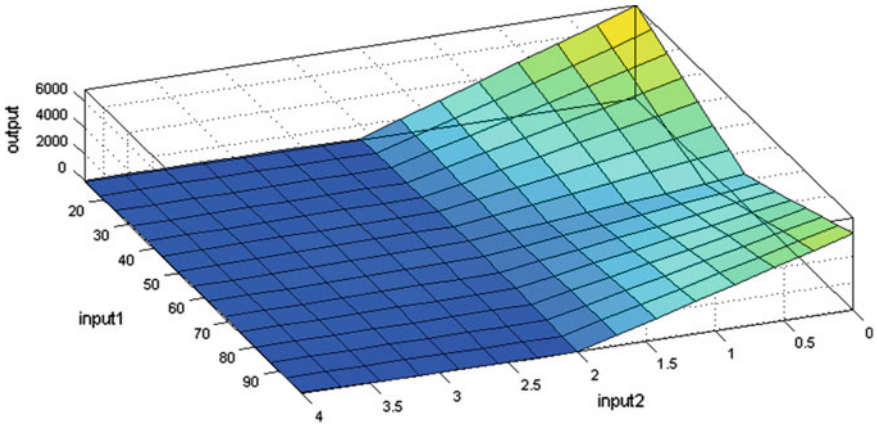


Fig. 4 3-D surface representation between two inputs and output for ANFIS-1 model

inputs plotted against the output and the researcher get a 3-D surface model. This model can be plotted by taking any two of the six inputs given to the model against the desired output. In this case, the inputs 1 and 2 have been plotted against output.

3.2 ANFIS-2 Radiation Prediction Model

In this predicted model, the diffused radiations received on earth have been predicted using rainfall, relative humidity, temperature (maximum and minimum), global solar radiation and direct radiations as input variables. Same 257 days values for variables have been taken into consideration like in ANFIS-1 model. Number of epochs used are 5. Figure 5 shows the rule base, Fig. 6 shows the error analysis

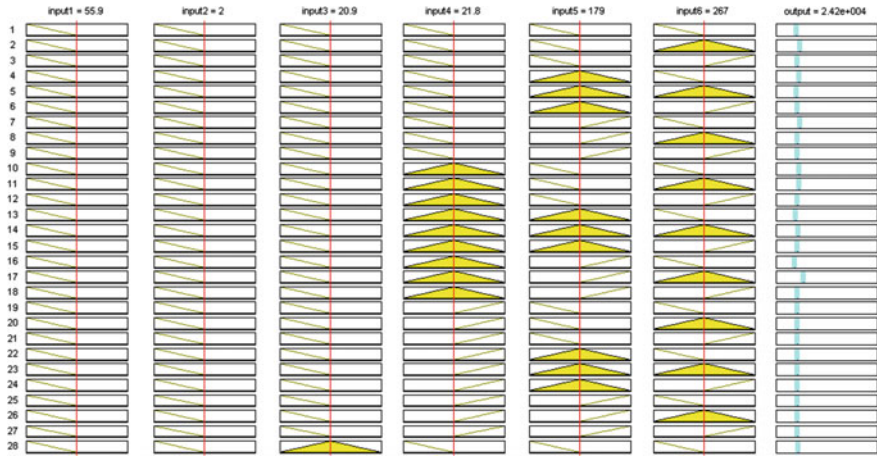


Fig. 5 Rule base for ANFIS-1 prediction model using MATLAB

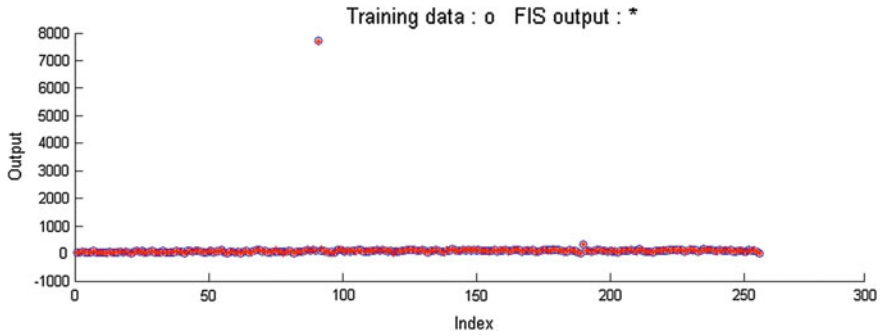


Fig. 6 Error analysis between training data and FIS output for ANFIS-2 prediction Model

with respect to the input variables and Fig. 7 shows the surface analysis of two inputs w.r.t. output that is diffused radiations in this case using the Matlab Simulink software.

3.3 ANFIS-3 Radiation Prediction Model

The global solar energy received on earth have been predicted using rainfall, relative humidity, temperature (maximum and minimum), diffused radiation and direct radiations as input variables in this third model.

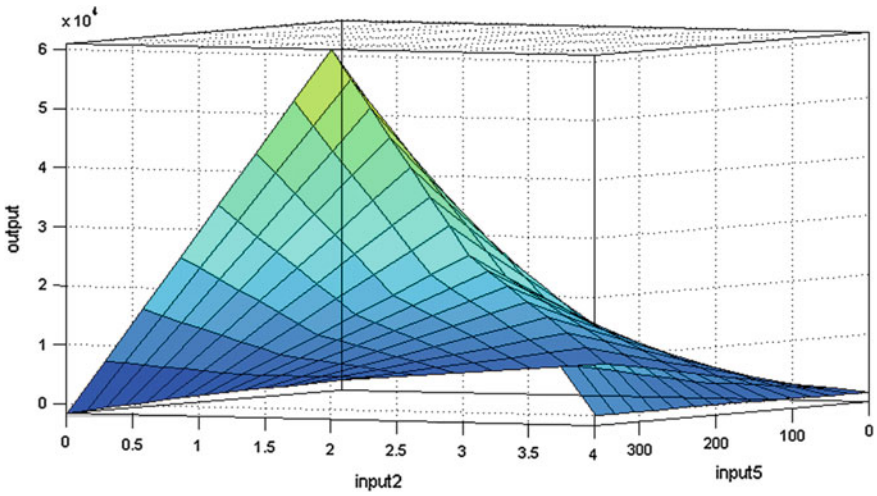


Fig. 7 3-D surface representation between two inputs and output for ANFIS-2 model

Rule base for the prediction of global sun radiations is given in Fig. 8. Total of 140 rules has been designed by the researcher to get the desired results using MATLAB. Three number of epochs have been selected in this case.

Figure 9 shows the error plot between indexed inputs and desired output using training data and FIS. They have been shown by different colours. The distribution

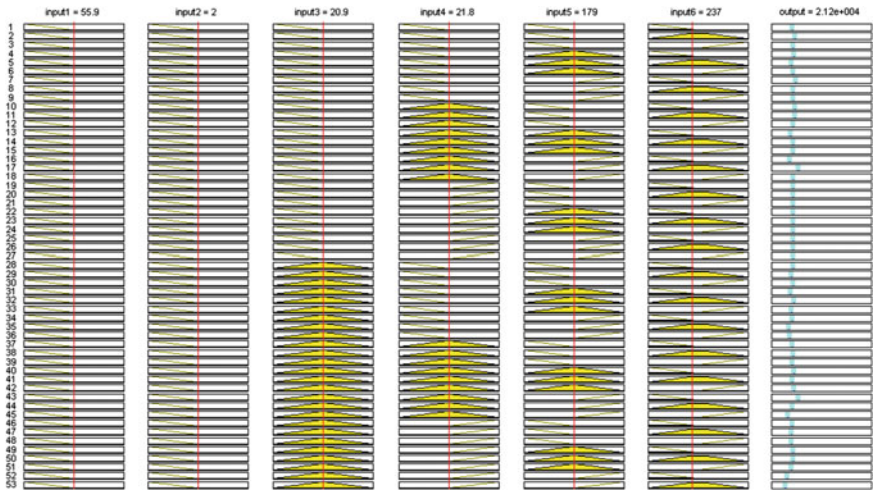


Fig. 8 Rule base for ANFIS-3 prediction model using MATLAB

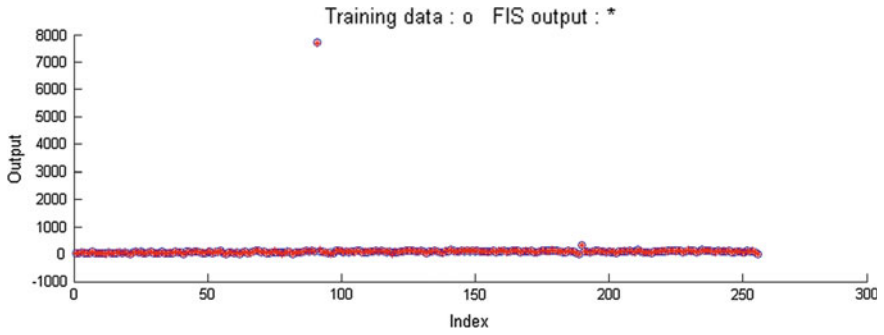


Fig. 9 Error analysis between training data and FIS output for ANFIS-3 prediction model

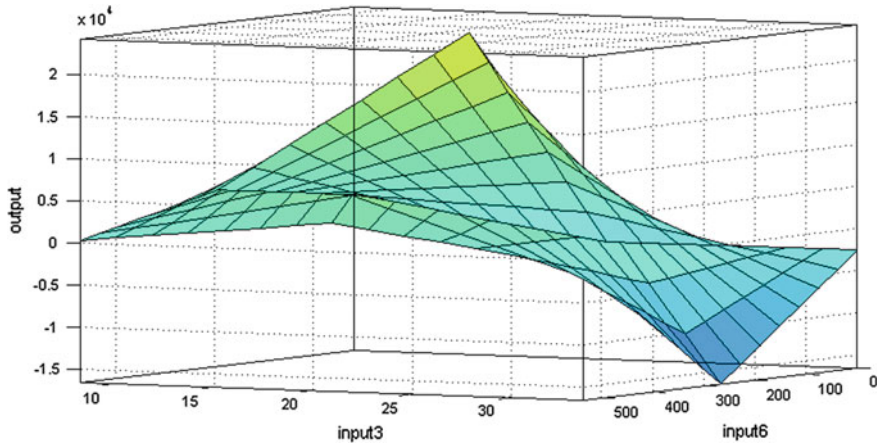


Fig. 10 3-D surface representation between two inputs and output for ANFIS-3 Model

of two inputs against the desired output has been shown in surface plot in 3-D format in Fig. 10.

4 Conclusion and Final Analysis

It can be analyzed that the radiations can be predicted using and developing only one model at different locations. The research gives the prediction of different parameters for setting up of solar generation plants at different remote as well as other locations, where solar and other climatic data are not so easily available. The final structure is shown in Fig. 11. It can be concluded from this final structure that by giving different available climatic inputs, the desired outputs can be obtained. The range of each and every input can be fixed from minimum to maximum.

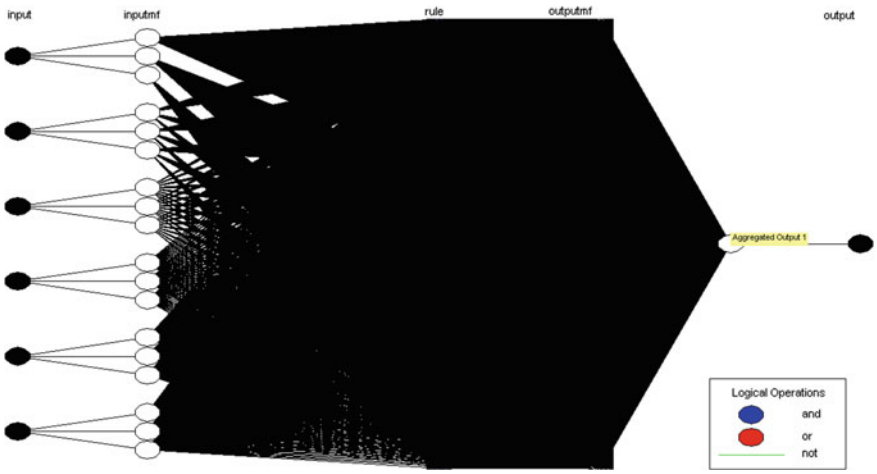


Fig. 11 ANFIS prediction model structure with six inputs and single output

The MATLAB SIMULINK software gives the researchers the access to change the range which has been fixed between minimum and maximum. Also the different desired output as in this research paper like diffused radiations, global solar radiations and direct radiations can be obtained. Further research can be done using the data for more than one city/location, which can be compared with one another and more specific results for particular sites can be obtained.

References

1. AK Yadav, H. Malik, S.S.Chandel, "Selection of most relevant input parameters using WEKA for artificial neural network based solar radiation prediction models", Renewable and Sustainable Energy Reviews, vol. 31, pp. 509–519, 2014.
2. Huashan Li, Weibin Ma, Yongwang Lian, Xianlong Wang, "Estimating daily global solar radiation by day of year in China," Applied Energy, vol. 87, issue 10, pp. 3011–3017, 2010.
3. Huashan Li, Weibin Maa, Yongwang Lian, Xianlong Wang, Liang Zhao, "Global solar radiation estimation with sunshine duration in Tibet, China", Renewable energy, vol. 36, issue 11, pp. 3141–3145, 2011.
4. Isaac Rahimia, Bahram Bakhtiarib, Kourosh Qaderib, Mehrdad Aghababaiec, "Calibration of Angstrom equation for estimating Solar Radiation using Meta-Heuristic Harmony Search Algorithm (Case study: Mashhad-East of Iran)", Energy Procedia, vol. 18, pp. 644–651, 2012.
5. Hontoria L., Aguilera J., Zufiria P., "An application of the multilayer perceptron: Solar radiation maps in Spain", Solar Energy, vol. 79, issue. 5, pp. 1–8, 2014.
6. Benghanem M, Mellit A, Alamri SN., "ANN-based modeling and estimation of daily global solar radiation data: a case study," Energy Consv. and Mang. vol. 50, issue 7, pp. 1644–1655, 2009.
7. Mohandes M., Rehman S., Halawani T.O., "Estimation of Global Solar Radiation using ANN", Renewable Energy, vol. 14, Nos 1–4, pp. 179-184, 1998.

8. Al-Salaymeh A., "Modelling of global daily Solar Radiation on Horizontal Surfaces for Amman City", Emirates Journal for Engineering Research, vol. 11, issue. 1., pp. 49–56, 2006.
9. Tadros M.T.Y., "Uses of sunshine duration to estimate the global solar radiation over eight meteorological stations in Egypt", Renewable Energy, vol. 21, pp. 231–246, 2000.
10. Mellit A., Kalogirou S.A., Shaari S., Salhi H., Hadj Arab A., "Methodology for predicting sequences of mean monthly clearness index and daily solar radiation data in remote areas: Application for sizing a stand-alone PV system", vol. 33, pp. 1570–1590, 2008.
11. Adnan Sozen, Erol Arcaklioglu, Mehme Ozalp, "Use od ANN for mapping of solar potential in Turkey", Applied Energy, vol. 77, pp. 273–286, 2004.
12. Abedelhak BEN Jemaa, Souad Rafa, Najib Essounbouli, Abdelaziz Hamzaoui, Faicel Hnaien, Farouk Yalaoui, "Estimation of Global Solar Radiation Using Three Simple Methods," Energy Procedia, vol. 42, pp. 406–415, 2013.
13. Hasni A, Sehli A, Draoui B, Bassou A, Amieur B., "Estimating global solar radiation using artificial neural network and climate data in the south western region of Algeria," Energy Procedia, vol. 18, pp. 531–537, 2012.

Forensic Analysis of Residual Artifacts from Private Browsing Sessions in Linux

A. Sankara Narayanan, T. Rajkumar and N.V. Sobhana

Abstract Private browsing is a common feature in modern web browsers to ensure the privacy of the user by disabling the history and other cached information about web browsing. User can browse the Internet after enabling private browsing feature in which no user data will be stored such as browsing history, auto fill data, user credentials, and cookie information. It is important to retrieve residual data related to one's normal and private browsing sessions available in his computer to prove his role in an offence or incident. This is critical and tricky in any cybercrime or physical crime where a computer is being used by the accused to browse Internet as conviction rates of cybercrimes are less than 10 % due to lack of proper evidences. This project is an analysis for residual artifacts from private browsing sessions in Linux platform using popular web browsers. Analysis result shows the possibility of retrieving evidences in such browsing scenarios and they are purely based on real-world web browsing sessions. Both Static and Live memory analysis are used. The tools and techniques used in this project are widely used and forensically sound.

Keywords Private browsing · Incognito mode · Linux · Fmem kernel module · dd tool · Dead acquisition · Live memory acquisition · Recently-used.xbel

A. Sankara Narayanan (✉) · T. Rajkumar
Department of Computer Science and Engineering,
College of Engineering Kallooppara, Thiruvalla, India
e-mail: sankaradhikarath@gmail.com

T. Rajkumar
e-mail: rajcek@gmail.com

N.V. Sobhana
Department of Computer Science and Engineering,
Rajiv Gandhi Institute of Technology, Kottayam, India
e-mail: Sobhana.nv@gmail.com

© Springer Science+Business Media Singapore 2017

R. Singh and S. Choudhury (eds.), *Proceeding of International Conference on Intelligent Communication, Control and Devices*, Advances in Intelligent Systems and Computing 479, DOI 10.1007/978-981-10-1708-7_5

1 Introduction

The rapid developments in the field of Information and Technology lead all the people into an online virtual world. The Internet is an essential tool for everyone for their daily tasks. Hence the nature of crimes gradually turned from its physical behavior into a virtual one which is called as cybercrimes. A cybercrime is a crime or incident in which a computer or Internet is directly or indirectly used for committing that crime. Physical crimes can easily become cybercrimes when the suspect is simply searching Internet from his PC or Smartphone for a method which is easy to do that particular crime. Numbers of cybercrimes are increasing day by day as the world rapidly turned into a virtual cyber world. As we all know, each and every one is using computers and Internet for both personal and official purpose as part of their job. In both case, there are lots of chances of violating cyber law which has been developed for limiting the misuse of Internet for annoying or harming others people or the society. This harm may be because of one's carelessness or lack of awareness about the policies and laws. But whatever may be the situation, the person who is the reason behind such activities and who is conducting such activities are equally considered as criminals by the law enforcement agencies and judiciary.

1.1 Web Browsers

A Web browser is now one of the ways for accessing the World Wide Web. It is a software program for interpreting, displaying, and allowing the users to actively interact with various contents hosted on web servers over internet [1]. The contents which are hosted in web servers are called as resources. These resources are identified by corresponding uniform resource identifier, also called as URL. User can make use of web browsers for accessing the contents in Internet and information stored in a local private network as well. We can see the increasing popularity of the browser Chrome nowadays which is developed by Google [1]. Also people are eager to use Internet using their mobile phones itself. Web browser helps us to make use of various Internet services such as email, messaging services, and social networks. The increasing popularity of Internet banking and online shopping applications and websites cause increase in the number of cyber-crimes and online fraudsters.

1.2 Private Browsing Mode or Incognito Mode

Private browsing is a common feature in modern web browsers to ensure the privacy of the user by disabling the history and other cached information about web

browsing. User can browse the Internet after enabling private browsing feature in which no user data will be stored such as browsing history, auto fill data, user credentials and cookie information. Private browsing is helping to disable the local storage of browsing information in user computer. Authorities who have privilege can easily collect the information from logs of remote web servers and other network devices like external firewall routers, proxy server, etc.

Internet users use private browsing with the following objectives:

- Avoid the storage of browsing history and auto fill data, user credential, browser cache, and cookies.
- For surfing the Internet without the effect of previous browsing histories by the same or other users.
- To avoid storage of user logon credentials and other web browser session information like cookies.
- For testing websites and their behavior.

2 Related Work

Internet is now an inevitable service for everyday activities with computers and other electronics devices like mobile phones and tablets. Major web browsers gradually introduced private mode of browsing for keeping users browsing details safe and private. This feature was first introduced in 2005. Private browsing is avoiding storing user browsing details either by deleting all browsing information immediately when the user terminates the browsing session, or by disabling writing the data into the permanent storage space of his computer at all. The main objective of the feature private browsing was to avoid disclosure of browsing information of one user to other users who share the same computers in home, office, etc. Researchers and analysts are always keen in analyzing the possibilities of retrieval of artifacts from private browsing sessions. Such studies and data retrieval are very much helpful for computer forensic investigators.

Surveys and studies among common people who regularly use Internet revealed relevant information to digital forensics world. Some users are unaware about such features and some users keep a lot of misconceptions about private browsing that may lead them to dangerous situations. Common people use private mode of browsing for doing illegal activities also. Some believe they are anonymous over the Internet and make use of private browsing for illegal acts like browsing pornography, child pornography, doing personal business during working hours etc. [2]. These are only because of their misconceptions about private browsing. Web browsers have been defined clear and specific user policies about the limitations of privacy that they are providing to the end users. They are not able to hide their activities over the Internet. They only hide browsing details of a user from his local computer only. Whenever a user connects to Internet, he could be tracked by the corresponding Internet Service Provider (ISP) or remote server from where he is

accessing web pages. ISPs are keeping log of the users who connect through that ISP to different websites over Internet. So using private mode of browsing, no user is anonymous over the Internet. He could be trapped by law enforcement officers.

Even if a person can be easily trapped by his browsing nature and URLs browsed from his IP address, investigating officers need traces from his computer to prove his involvement in a particular incident. This is where researches help investigators to follow different approaches.

Gao et al. conducted a survey for understanding whether the layman is really aware about the feature and limitations of private browsing which is available in their own web browsers. The result was disappointing because one third of the participants are not at all aware about such a feature available in their web browser and the rest who know about private browsing have many misunderstandings. They also found that people use this feature for illegal activities like watching pornography, personal business during working hours etc. [2].

Microsoft Windows is the most popular and widely used proprietary operating system in the world. Researchers mainly focus on windows platform for conducting their testing and research activities about private browsing sessions. In 2013, Ohana and Shashidhar proposed a methodology for analyzing evidences remaining from private and portable Internet browsing sessions in a user computer running Windows operating system [3]. It was a detailed analysis using four different popular web browsers. While going through the results of their research, it is clear that both private and portable web browsing sessions leave valuable evidences which will be helpful to accuse the user of a cybercrime. But it totally depends upon the type of web browser. Some browsers leave enough information even after the browsing session which helps the investigator to link the user to the incident and some do not. Internet Explorer is the one which leaving more private browsing-related information among the four popular browsers selected and used for research.

All researches discussed above analyzed the possibilities of retrieval of artifacts from private browsing sessions in Windows platform. Linux is another popular platform, which is a UNIX like POSIX compliant operating system for computers. UNIX is an old operating system platform. Linux and UNIX together offer security and reliability for professional applications and other organizations using the same platforms [4]. Popular and widely accepted websites such as Google, yahoo, etc. and organizations and professionals prefer Linux or UNIX-based servers to store their data. Android is the most popular operating system for touch screen smart phones is a Linux variant. It is developed by Google and is based on Linux Kernel. Even Apple OS x developed by Apple is based on UNIX operating system. Ubuntu operating system is also based on the Linux kernel.

Canonical Ltd is a UK-based company owned by South African entrepreneur Mark Shuttleworth who developed Ubuntu in 2004 [4]. Shuttleworth identified the power of Linux as an open source operating system. But at the same time, he was aware about the limitations and existing weaknesses in Linux which prevents its success as a mainstream operating system. He decided to address these issues and limitations and develop a mainstream operating system that is easy to use

and a competitor to existing other popular operating systems in the market. Ubuntu was developed as Debian as its base. They distributed the Ubuntu CDs for free. It became popular and the community and support increased rapidly. As a result of all these factors, Ubuntu became the most popular Linux distribution available. As the support and researches are more and free of cost, Ubuntu became favorite operating system for large organizations and educational bodies.

We identified that researchers conducted different kinds of analysis to extract the remaining evidences from private and web browsing sessions in windows platforms XP, 7. The OS and the file system used in windows and Linux are entirely different. So the possibility of getting evidences from these different platforms will be different. Researchers have not yet focused on the Linux platforms. As black hats are knowing these limitations and focusing into Linux variants, studies about the possibilities of retrieval of evidences from private browsing sessions in Linux platform is essential. This may enlighten the future investigation for trace analysis of browsing sessions.

3 Methodology

The proposed method is an analysis of private web browsing sessions for retrieval of residual artifacts in Linux platform. We selected latest version of Ubuntu, which is 14.04.1 operating system. The proposed method is to find out the possibilities of recovery of artifacts from a Linux machine which is helpful to create a link between a suspect and an incident. Popular web browsers in Linux platform are Google Chrome, Mozilla Firefox, and Open source project of Chrome called Chromium. Chromium is the open source initiative by Google itself. We selected Chrome and Firefox web browsers during creating the real-world scenario and analysis. The project expects a result based on the browser types used for the project because the behavior of browsers depends on the type of browser used.

We defined real-world browsing scenarios in this particular methodology. This is properly documented so that the method will not fail to find evidences of particular web browsing scenarios during the detailed analyses process. Both live and traditional forensic analyses were used in this project. That means live acquisition and traditional dead analysis which includes collecting the hard disk and RAM image files. This particular project analyzed the private browsing scenario for evidences and discussed various possibilities of evidence recovery and how to use them proficiently.

3.1 Tools and Techniques Required

Various hardware and software tools are required to perform the web browsing scenarios and analysis process. They are listed below.

Hardware Components

Computer with 500 GB *HDD and* 2 GB *RAM*: This computer is to perform real-world browsing scenarios. The hard disk needs to be of large storage capacity as it is to be used as target drive for collecting the image files of evidence drive and RAM.

40 GB *Hard disk*: It is the evidence drive in which we install fresh Ubuntu OS.

IDE—SATA converter: For connecting the IDE hard disk to SATA port in the mother board.

Forensic Workstation: Forensic workstation is nothing but a computer system installed with cyber forensic tools and other software tools required for the process of analysis.

Software Components

These are various system and application software required to complete the methodology.

Ubuntu 14.4.1 Operating System: Ubuntu 14.4.1 is the selected Linux platform for doing private browsing simulation.

Web Browsers: Google Chrome and Mozilla Firefox browsers are used for conducting real-world web browsing scenarios.

AccessData Forensic ToolKit: FTK is a computer forensic software made by AccessData. FTK has various tools such as data analyzer, data carving tool, disk imaging tool, etc.

DD Tool: DD is a command-line tool for UNIX and Linux operating systems and is used for copying and converting files. We mainly use DD tool for disk wipe and to capture the image of hard disk partitions. We need fresh sanitized hard disk for installing operating system and creating web browsing scenario. DD is one of the best wiping tools. It can be also used as an imaging tool. The output is a raw formatted disk image file. The use of dd tool is forensically sound as no GUI application is required to use dd tool in Ubuntu and running commands in terminal only.

Fmem Kernel Module: In old versions of Linux, the dd tool was able to read the contents of the RAM from the device file called /dev/mem. But in new versions of Linux distributions, access to the physical memory is restricted to a limited range of addresses only. So it is difficult to dump the entire physical memory from Ubuntu like operating system by simply using dd utility. Linux 2.6 kernel series is reducing the direct access of physical memory by pseudo-device files. Fmem is a kernel module that creates dev/fmem device which is similar to that of old dev/mem. But dev/fmem does not have any limitation for accessing the physical memory [8]. This device can be easily copied by using either dd or any other file copying tools.

3.2 Plan of Action

We are clear that the private browsing mode will not save any information into the database file (Palces.sqlite in the case of Mozilla Firefox) of web browser. So we are not focusing on browser's database file formats or table structure now.

Analyst's Perspective. Analyst needs to narrow down the possible locations where evidence can be obtained. We need to decide where we have to focus on. But first and foremost, no predictions will be there about the locations and possibilities of getting evidences. This may affect the analysis and analyst may miss some key locations containing valuable evidences which are not in his predictions.

Swap Area. Here is the important split of storage locations. Normally we divide the storage space within a computer into RAM and Hard disk. But when you closely analyze a Linux machine, users specify or reserve some amount of storage space in their hard disk as Swap area. This is the virtual memory used by any Linux OS. When memory hungry applications are running in Linux, the OS normally swap the inactive application details and files into swap area [5]. During the analysis process, we consider RAM, Swap space and Hard disk storage space. The logical splitting of storage locations of a Linux machine in this particular project is as shown in Fig. 1.

Dead Analysis. Dead analysis is the process of copying the entire bits of hard drive as it is from the suspect system when it is not working. Here the hard drive of the suspect system is removed first. Then a copy of the same I prepared for analysis and evidence collection. A dead acquisition copies the data without the assistance of suspect's operating system. This is to avoid investigators accidentally overwriting or modifying evidentiary data and to prevent data loses due to any harmful program or scripts present in the suspect's computer. A major difference between dead and live forensics is that dead forensic analysis cannot acquire live, volatile data from the physical memory as the computer as it is switched off.

Live Analysis. Live analysis is the process of collecting the volatile memory/RAM from suspect's system when it is alive or running. Hence the name live analysis. It helps us to know about the details of all running applications and various files and folders used by those applications and processes. Major limitation in live analysis is not always possible. Only if the investigator is present at the crime scene, he can go for a live acquisition. He needs to be very careful when conducting a live acquisition as he is accessing suspect system directly; there are chances of tampering important evidentiary data unknowingly.

Simulating Incident. The project is designed in such a way that real-world web browsing scenarios are created and the scenarios are then analyzed for obtaining evidences. We used two different scenarios in private or incognito browsing mode. First of all we created a Gmail account with username *testusercek@gmail.com* for

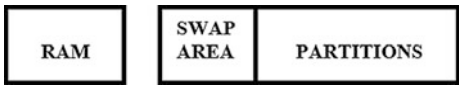


Fig. 1 Memory locations-logical splitting for analysis

accessing a Gmail account during each scenario. The following are the stepwise activities in the scenario I.

- Accessing mail account with user id *testusercek@gmail.com* and password *student@cek.*
- Creating a text file and send it to *sankaradhikarath@gmail.com* as an email attachment.
- Searching Google using the keyword *college of engineering kallooppara* and downloading some images of college of engineering kallooppara into the default downloads folder of the computer.

After performing these browsing scenarios, both live (RAM) and static memories are captured by the above said forensic tools. After acquisition process, we are analyzing the obtained image files for evidence collection based on the available information. The detailed process of incident simulation is given in next chapter as implementation details. Scenario 2 is the same as that of scenario 1 while the attached document is an image file instead of a text file. Also scenario 2 is used to analyze the behavior of Ubuntu when some memory hungry applications are running along with browser. We need to know whether there is any possibility of writing some physical memory data into swap area present in the hard drive storage space. The images files are then analyzed in detail using Forensic Toolkit (FTK).

4 Implementation

4.1 Sanitizing and Setting up Storage Device

The first and foremost thing we did was sanitizing the hard drive used as an evidence drive. We used DD tool for completing the task. As the hard drive is of large storage capacity, simple dd commands will not show any progress details of disk copying. We need to use PV tool for viewing the progress of copy or wiping.

$$\text{sudo cat/dev/zero 1 pv}-\text{brt 1 dd of} = /\text{dev/sdb1 bs} = 4096$$

The above command will write zeros into every bit present in the output file sdb1 (which is actually the hard disk here). Dev/zero are the input for writing process, which means it writes zero into the output location or bits. Block size bs is defining the size of each block collectively selecting for writing purpose [6]. Before executing the above command, you need to make sure that you selected the right output file which is the target drive, not any other drive or partition connected to the computer. It is easy to mess up the whole thing by a wrong output drive selection. Figure 2 shows the execution of dd command for wiping the hard disk.

We can use command *fdisk -l* for viewing the entire hard disks and storage devices connected to your Linux machine. We can also use *lsblk* command which will list out each storage device and their partitions along with their type as a tree

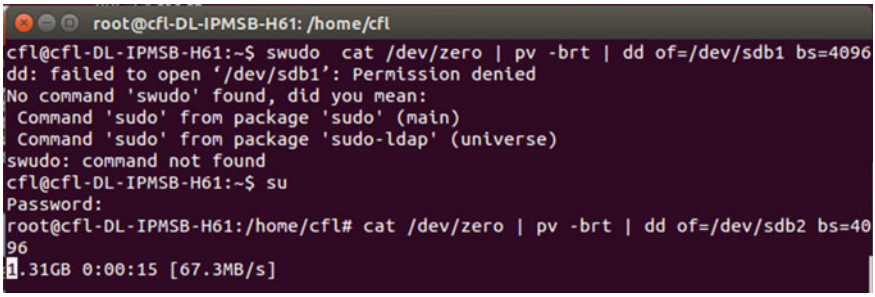


Fig. 2 Disk wiping using dd command

like structure [7]. I prefer the second one as the result is more readable and understandable. The figures show the use of these commands.

Next step is installing a fresh Ubuntu 14.04.1 OS into 10 GB partition present in the sanitized hard drive. Also we defined 2 GB Swap area. The size of RAM is also 2 GB.

4.2 Live Memory Acquisition

Fmem is a kernel module that creates dev/fmem device which is similar to that of old dev/mem. But dev/fmem does not have any limitation for accessing the physical memory. This device can be easily copied using either dd or any other file copying tools. This module works with Linux kernels 2.6 version. We can download kernel module and compile the same using make and /run.sh commands [8]. But the only thing you need is root access. Linux is providing an extreme security feature called root privilege.

Unlike windows, Linux is providing only a user access to their accounts. There is an administrative privilege that can be achieved by opening a terminal and typing the command sudo followed by the root password when asked. This root privilege is needed for compiling the kernel module. After successful compilation of fmem module, we can access the physical memory /dev/fmem. We are using dd tool for acquisition. The command used for live memory imaging is given below. The name of input file is given as /dev/fmem.

$$\begin{aligned} &\mathrm{Cat/dev/fmem|pv\,brt|dd\,of} = \mathrm{/desired_output_file_location.dd} \\ &\mathrm{bs\,4096\,iflag} = \mathrm{fullblock} \end{aligned}$$

4.3 Static or Dead Acquisition

Static acquisition is conducted after the down of the computer. The hard drive is removed and connected to the forensic workstation. Then FTK imager is used for imaging the entire hard drive. When we use FTK imager, we will get the entire hard drive including the swap area and unallocated space. To avoid this, in scenario 2 we used dd tool along with lsblk to differentiate different storage locations and to image them into separate raw image files.

5 Analysis Results

We used AccessData FTK for analyzing the acquired image files. FTK is a court-cited tool used in cyber forensic analysis process. We defined and executed a scenario so that we can analyze the obtained image files for evidences based on the incident (scenario) happened in that computer. As we used keyword search in Google and attached text and image files to the email created, a keyword search would be better. We also used the default tool provided by FTK for carving images. The results are in Table 1.

The result obtained is based on the type of browser used. Downloaded images and their URLs are present in the hard disk. This can be used for collecting the log information from the corresponding server. This can be obtained from the server administrator of particular organization or domain. Ubuntu operating system is maintaining an xml file for keeping track of most recently used files and their locations as URIs. This file is known as *Recently-used.xbel* (XML Bookmark Exchange Language). It also tracks the application which used the file with MAC timestamps in GMT format per application or per task. This is the key location from where we got the details of files that had been uploaded and downloaded by the web browsers. The *Recently-used.xbel* file is residing in.local/share directory which is a hidden folder in Ubuntu.

Table 1 Artifacts obtained during analysis and their locations

Type of artifact	Firefox		Chrome	
	Hard disk	RAM	Hard disk	RAM
Private browsing indication	✓	✓	✗	✓
Gmail access (username/password)	✗	✓	✗	✓
Downloaded files (URL/location)	✓	✓	✓	✓
Email attachments (contents/locations)	✓	✓	✓	✓
Internet connection details (IP address)	✓	✓	✓	✓

6 Conclusion and Future Scope

Even though people think private browsing does not save anything at all, still we are able to retrieve artifacts from the computer. It is really hard to obtain artifacts from a simple web surfing in private mode. But at the same time, there are lot of locations from where we can find the interconnecting artifacts if he or she is downloading of uploading any file during their browsing session. The results from both scenarios used for analysis were the same. Majority of details such as various image files and email attachments were successfully retrieved and carved from RAM. Investigators need to concentrate on live memory capturing as it is providing almost all information when compared to dead analysis. They should admit the fact that the obtained evidences are only an insight to the particular case or incident. They need to work further on that available leads to get the big picture of the incident.

The study has found the possibilities of evidence collection from private browsing sessions on Ubuntu platform in a scenario-based analysis process. It can be extended to a variety of different scenarios in other Linux distributions and Mac as well. Web browsers other than Chrome and Firefox can also be used for creating the browsing scenario.

References

1. Web browser, https://en.wikipedia.org/wiki/Web_browser (2015)
2. Xianyi Gaoy, Yulong Yangy, Huiqing Fuy, Janne Lindqvisty: Private Browsing: an Inquiry on Usability and Privacy Protection
3. Jacob Ohana, Narasimha Shashidhar: Do Private and Portable Web Browsers Leave Incriminating Evidence? A Forensic Analysis of Residual Artifacts from Private and Portable Web Browsing Sessions, EURASIP Journal on Information Security (2013)
4. Ubuntu Manual Team: Getting Started with Ubuntu 14.04 (2014)
5. Murukesh: https://help.ubuntu.com/community/SwapFaq (2015)
6. How do you monitor the progress of dd? http://askubuntu.com/questions/215505/how-do-you-monitor-the-progress-of-dd
7. How do I view all available HDD's/partitions? http://askubuntu.com/questions/182446/how-do-i-view-all-available-hdds-partitions (2012)
8. How can I dump all physical memory to a file? http://askubuntu.com/questions/147978/how-can-i-dump-all-physical-memory-to-a-file (2012)

Prediction of Voltage Collapse in Power System Using Voltage Stability Indices

Pallavi Choudekar, Divya Asija and Ruchira

Abstract Voltage collapse is the possible outcome of voltage instability. Voltage collapse occurs when the transmission lines are operating very close to their maximum capacity limits. This paper focuses on the usefulness of two voltage stability indices to find out the weak bus so that the appropriate measures can be taken in advance to avoid voltage collapse. In this paper, WSCC 3 Machine, nine bus test system has been considered and comparison of different voltage stability indices is done to predict voltage collapse.

Keywords Voltage collapse · Fast Voltage Stability Index (FVSI) · Line Stability Factor (LQP)

1 Introduction

Voltage instability happens in a power system due to overloading condition. Voltage collapse occurs due to voltage instability that ultimately results in blackout of the entire power system [1]. Forecasting of voltage collapse is significant in power system operation and planning. Voltage stability can be studied in static and dynamic stability methods [2]. Static analysis for voltage instability has been done in this paper. Prediction of voltage collapse at a particular bus can be found out by calculation of different indices [3–6]. The value of voltage stability indices lies between 0 and 1. Line whose stability index is closer to 1 is considered as a critical line.

This paper has been organized into six main sections. Section 2 represents the formulation of the voltage stability indices. Section 3 presents the description of WSCC nine bus test system. Section 4 describes the methodology to determine the

Pallavi Choudekar (✉) · Divya Asija · Ruchira
Amity University, Noida, Uttar Pradesh, India
e-mail: pallaveech@gmail.com

Divya Asija
e-mail: divyaasija83@gmail.com

© Springer Science+Business Media Singapore 2017

R. Singh and S. Choudhury (eds.), *Proceeding of International Conference on Intelligent Communication, Control and Devices*, Advances in Intelligent Systems and Computing 479, DOI 10.1007/978-981-10-1708-7_6

different stability indices. Section 5 presents the results obtained from the analysis. Section 6 presents the conclusion drawn from the results.

2 Formulation of Voltage Stability Indices

Analysis of voltage instability can be done by calculating values of different indices. Operators can use voltage stability indices to know when the system voltage will collapse. These indices may use online or offline to help operators in real-time operation of power system or in designing and planning operations. This paper discusses the two important indices namely FVSI and LQP.

(1) Line Stability Index FVSI: In this research, the voltage stability index referred to a line was formulated from the two bus representation of a system shown in Fig. 1 [7].
It shows voltages and power at two buses and impedance of line connected between the two buses.
Mathematically, the FVSI is given by

$$\text{FVSI} = \frac{4Z^2 Q_j}{V_i^2 X} \tag{1}$$

where X represents reactance, Z represents impedance of line, V_i represents the sending end voltage, and Q represents the reactive power flow at the receiving end. FVSI value is calculated by using results of load flow.
FVSI determines the maximum load that is possible to connect at a particular bus such that stability can be maintained. This point is referred as the maximum load ability of a particular bus, which after this limit system violation will be experienced. FVSI indices are sorted in ascending order and higher value of FVSI determines weak bus [8].

(2) Line Stability Index LQP: The LQP is obtained as follows:

$$\text{LQP} = 4\left(\frac{X}{V_i^2}\right)\left(\frac{X}{V_i^2}P_i^2 + Q_j\right) \tag{2}$$

where P_i represents active power flow at the sending bus; Q_j represents reactive power flow at the receiving bus; and X represents line reactance; V_i represents sending end bus voltage.

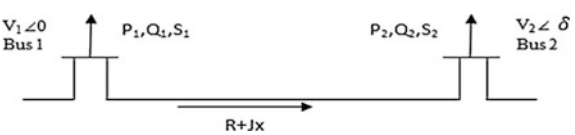


Fig. 1 Represents two bus power system model

Voltage stability indices can be calculated from results of power flow. Power flow calculations of nine bus system are done by power world simulator. Power world simulator is a simulation software, where can be designed interactive model of power system network for simulation of high voltage power system.

3 Description of Nine Bus Test System

The system under study is a typical WSCC nine bus three machine test system with 100 MVA base shown in Fig. 2 and Tables 1, 2, 3 and 4.

4 Methodology to Determine Different Stability Indices

Step 1: Create SLD for the nine bus system.
Step 2: Enter the data for all the components of test system.
Step 3: Save the above file and then load the system.
Step 4: Newton Raphson method is used for finding power flow solution.
Step 5: Calculate FVSI and LQP indices from the power flow results.
Step 6: Increase reactive power at load bus five, six and eight gradually by 30%.
Step 7: Again run power flow and evaluate new stability indices.
Step 8: Tabulate the value of indices and arrange them in descending order.

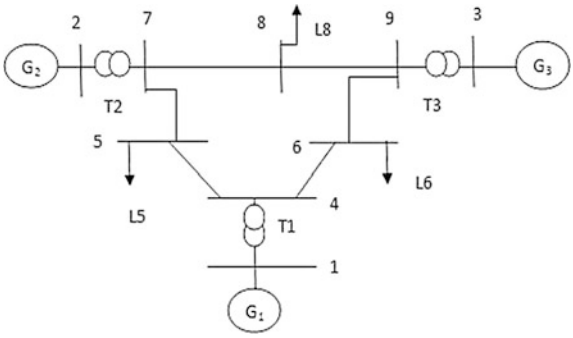


Fig. 2 Nine Bus Test system

Table 1 Rating of load

Bus no.	Voltage (pu)	Active power P(MW)	Reactive power (MVAR)
5	1	125	50
6	1	90	30
8	1	100	35

Table 2 Rating of transformer

Transformer no.	MVA rating	Reactance X	Voltage ratio
T1	77	0.0576	16.5/230
T2	163	0.0625	18/230
T3	86	0.0586	13.8/230

Table 3 Rating of transmission line

From bus to bus	Reactance (pu)	Resistance (pu)	Admittance (pu)
4 to 5	0.092	0.017	0.079
4 to 6	0.092	0.017	0.079
6 to 9	0.17	0.039	0.179
5 to 7	0.161	0.032	0.153
7 to 8	0.072	0.0085	0.0745
8 to 9	0.1008	0.0119	0.1045

Table 4 Rating of generator

Generator no.	Active power P(MW)	Reactive power (MVAR)	Voltage (pu)
G1	72	28	1.04
G2	163	5	1.025
G3	85	–11	1.025

5 Results

Calculation of different stability indices leads to prediction for collapse of voltage in power system. Value of FVSI close to one indicates instability of that particular line. Values of stability indices are found by increasing reactive power at each load bus. Table 5 shows increase of load at load bus five and carrying out load flow to find out FVSI and LQP indices for lines connected at bus five and voltage at bus five is also noted and procedure is repeated for bus six and results are shown in Table 6 and for also for bus eight and results shown in Table 7.

Table 8 shows values of different indices arranged in descending order. Values of these indices (FVSI and LQP) are found by increasing value of load at load buses. Transmission line with value of FVSI and LQP nearest to one indicates critical line and the bus at which this line is connected is considered as weakest bus.

Table 5 Stability indices values by increasing value of Q at load bus five

CASE 1 P = 125 MW, Q = 65 MVAR, V = 0.9135			CASE 2 P = 125 MW, Q = 85 MVAR, V = 0.8937			CASE 3 P = 125 MW, Q = 115 MVAR, V = 0.8618		
LINE	FVSI	LQP	LINE	FVSI	LQP	LINE	FVSI	LQP
4 to 5	0.3486	0.3586	4 TO 5	0.4492	0.4561	4 TO 5	0.6069	0.6093
5 to 7	0.4341	0.6901	5 TO 7	0.5451	0.7973	5 TO 7	0.7208	0.9671

Table 6 Stability indices values by increasing value of Q at load bus six

CASE 1 P = 90 MW, Q= 40 MVAR, V = 0.9280			CASE 2 P = 90 MW, Q = 55 MVAR, V = 0.9128			CASE 3 P = 90 MW, Q = 75 MVAR, V = 0.8916		
LINE	FVSI	LQP	LINE	FVSI	LQP	LINE	FVSI	LQP
4 to 6	0.2009	0.2057	4 TO 6	0.2725	0.2751	4 TO 6	0.3709	0.3704
6 to 9	0.2861	0.4253	6 TO 9	0.3722	0.5075	6 TO 9	0.4908	0.6209

Table 7 Stability indices values by increasing value of Q at load bus 8

CASE 1 P = 100 MW, Q = 50 MVAR, V = 0.9448			CASE 2 P = 90 MW, Q = 65 MVAR, V = 0.9323			CASE 3 P = 100 MW, Q = 85 MVAR, V = 0.9151		
LINE	FVSI	LQP	LINE	FVSI	LQP	LINE	FVSI	LQP
7 to 8	0.276	0.3154	7 TO 8	0.3281	0.3658	7 TO 8	0.3989	0.4346
8 to 9	0.1253	0.0616	8 TO 9	0.2443	0.1122	8 TO 9	0.4061	0.1812

Table 8 Values of different indices arranged in descending order

Rank	Line	FVSI	LQP
1	5–7	0.7208	0.9671
2	4–5	0.6069	0.6093
3	6–9	0.4908	0.6201
4	8–9	0.4061	0.1812
5	7–8	0.3989	0.4346
6	4–6	0.3709	0.3704

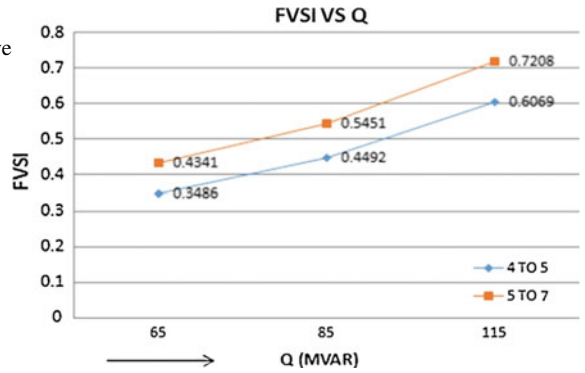


Fig. 3 FVSI versus reactive power at load bus five

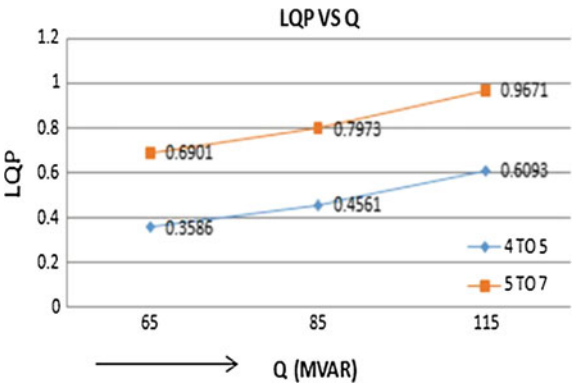


Fig. 4 LQP versus reactive power at load bus five

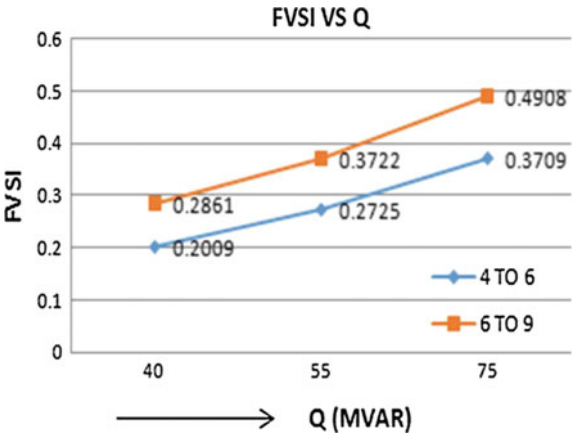


Fig. 5 FVSI versus reactive power at load bus six

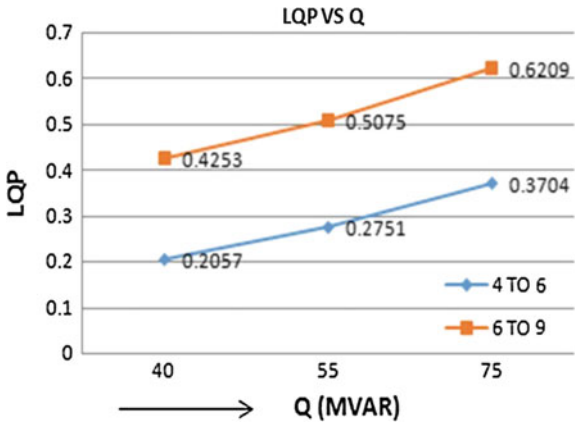


Fig. 6 LQP versus reactive power at load bus six

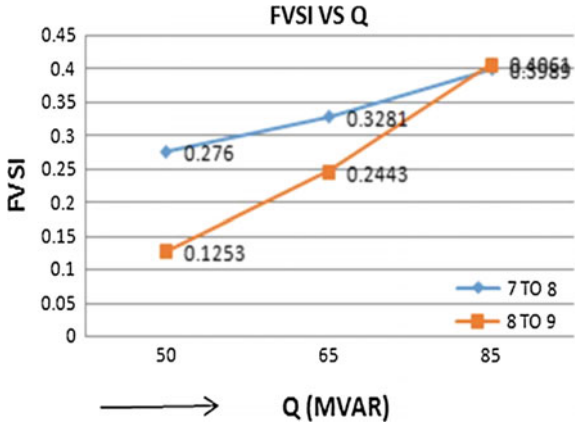


Fig. 7 FVSI versus reactive power at load bus eight

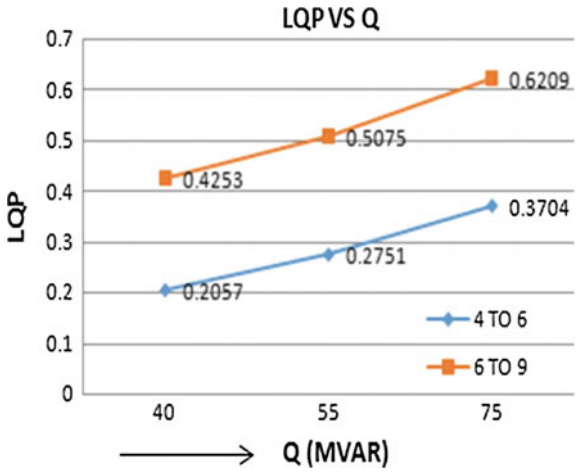


Fig. 8 LQP versus reactive power at load bus eight

6 Conclusion

Simulation of WSCC nine bus system has been done. Voltage stability indices have been calculated by changing reactive power at different load buses. Stability indices are used to find out the weak bus and early warning for blackout. Value of FVSI and LQP close to one that is weak bus and line corresponding to it is a critical line. From the Table 8, it is clear that transmission line 5–7 is having FVSI and LQP value close to one. From Figs. 3 and 4, it is concluded that FVSI and LQP values are higher (close to one) for bus five. Based on that value, bus five is the weak bus and that has to be protected to avoid voltage collapse and blackout Figs. 5, 6, 7, and 8.

References

1. P. S. Kundur, P. Pourbeik and C. W. Taylor, "The anatomy of a powergrid blackout-root causes and dynamics of recent major blackouts," IEEE Power and Energy Magazine, vol. 4 (2006)
2. G. K. Morison, B. Gao, and P. Kundur, "Voltage stability analysis using static and dynamic Approaches," IEEE Transactions on Power Systems, vol. 8 (1993) 1159–1171
3. M. Moghavvemi and F. M. Omar, "Technique for contingen monitoring and voltage collapse prediction," IEE Proceedings on Generation, Transmission and Distribution, vol. 145 (1998) 634–640
4. A. Andrade, C. Reis and F. Maciel, "Line stability indices for voltage collapse prediction," in Power Engineering, Energy and Electrical Drives, 2009. POWERENG'09 (2009) 239–243
5. A. Mohamed, G. Jasmon, and S. Yusoff, "A static voltage collapse indicator using line stability factors," Journal of Industrial Technology, vol. 7 (1989) 73–85
6. F. Karbalaei, H. Soleymani, and S. Afsharnia, "A comparison of voltage collapse proximity indicators," in IPEC, 201 Conference Proceedings, (2010) 432
7. T. A. Rahman, I. Musirin "Novel fast voltage stability index (Fvsi) for voltage stability analysis in power transmission system," in Research and Development, Student Conference on SCOReD (2002) 265–268
8. K. R. Vadivelu, and G. V. Marutheswar, "Maximum loadability estimation for weak bus identification using Fast Voltage stability index in a power transmission system by real-time approach" Int. J. Elec & Electr. Eng & Telecom (2014) Vol. 3, No. 1, 85–91

Adaptive Routing Mechanism for Real-Time Wireless Sensor Networks Based on Two-Hop Information

Sandhya Rachamalla and Anitha Sheela Kancherla

Abstract One of the critical and challenging aspects in wireless sensor networks (WSNs) is to optimally manage the limited energy of nodes without degrading the routing efficiency. In this paper, we propose an energy-efficient adaptive routing mechanism (EE-ARM) for WSNs which saves energy of nodes by removing the much delayed packets without degrading the real-time routing efficiency of the used routing protocol. It uses the adaptive transmission power algorithm which is based on the attenuation of the wireless link to improve the energy efficiency. Integrated in PATH, the well-known real-time routing protocol based on two-hop neighborhood information, the results show that the proposed routing mechanism perform good in terms of energy consumption per packet (ECPP) and deadline miss ratio (DMR).

Keywords Deadline miss ratio · Energy consumption per packet · Real-time routing · Adaptive transmission power

1 Introduction

Currently, WSNs are the latest research areas for the research community because of wide variety of applications that can be supported. Many WSN applications require real-time communication systems and examples of such applications can be found in many military areas, habitat monitoring, disaster management, and intelligent transportation systems [1]. Among several aspects of WSNs, energy conservation and delay, supporting real-time service is still gaining attention in research body [2]. Although efficient utilization of energy is the primary concern in WSNs

Sandhya Rachamalla (✉)
Department of ECE, University College of Engineering,
Osmania University, Hyderabad, India
e-mail: reddysandhya28@gmail.com

A.S. Kancherla
Department of ECE, University College of Engineering,
Jawaharlal Nehru Technological University, Hyderabad, India

© Springer Science+Business Media Singapore 2017

R. Singh and S. Choudhury (eds.), *Proceeding of International Conference on Intelligent Communication, Control and Devices*, Advances in Intelligent Systems and Computing 479, DOI 10.1007/978-981-10-1708-7_7

for longer network lifetime; the low latency communication is also gaining importance in new applications. Out-dated information will be irrelevant, mainly in real-time environments and may lead to serious effects to the applied systems [3]. Timeliness is important in sending crucial messages in industrial WSNs. And sensor nodes are battery operated which have limited energy. Hence energy efficiency and latency are the important design goals in WSNs. Real-time QoS in WSNs can be addressed through different layers and mechanisms of the network [4]. Cross-layer optimization can provide further improvement in the performance of the network and above all, routing protocol design by the network layer plays an important role in supporting real-time QoS [3].

To reduce the complexity of the systems, most of routing protocols are based on one-hop neighborhood information [5]. However, multi-hop information-based routing can perform better as more information about the neighbors of a node in the network is available and that is effectively utilized in broadcast operations, channel access methods, etc. [6–8]. It is observed from the study that two-hop based routing results in less number of hops from source to sink when compared with that of one-hop based routing [6]. However, it is not attractive to go for three-hop based routing, as it further increases the complexity which may not be affordable for the given network application. Hence in this paper, the proposed routing mechanism is integrated with PATH, the well-known two-hop based real-time routing algorithm for WSNs. The rest of the paper is organized as follows Sect. 2 summarizes related routing protocols and their performance measures. Section 3 presents our proposed mechanism which aims to improve energy consumption and real-time QoS. The performance of the proposed protocol is evaluated in Sect. 4. Section 5 concludes the paper and possible enhancements are discussed.

2 Real-Time Routing Protocols for WSNs

Many researchers have provided solutions for real-time routing in WSNs. This section provides the analysis of the various existing real-time routing protocols for WSNs emphasizing their strengths and weaknesses and various other challenges. AODV [9] is a reactive, on-demand routing protocol which builds route between the nodes with sequence numbers, only when the source node demands for routing the sensed data. DSR [10] protocol is another on-demand routing protocol which eliminates the periodic updating of routing tables as it is *beacon-less.* RAP [11] is the first real-time communication architecture that handles the deadline issues pertaining to large scale WSNs. It uses the high level 'query and event' services and the *velocity monotonic scheduling* (VMS) policy to schedule packets.

SPEED [12] protocol is an important real-time communication protocol to route packets with the desired speed for sensor networks. It does not consider the energy parameter in forwarding metric and single speed is considered. MMSPEED [13] extends the SPEED protocol to support different velocities and level of reliability for multiple probabilistic QoS guarantee in two domains, *timeliness* and *reliability*

in WSNs. RPAR [14] is the advance version of RAP. It is the first protocol that is designed to support the real-time routing for WSNs with power control. Application specific communication delays are handled in this protocol by adaptive transmission power and routing decisions are based on the system workload and packet deadlines. THVR [3] is a two-hop neighborhood information-based routing protocol for real-time WSNs proposed to support the QoS in terms of real-time packet delivery along with better energy efficiency. PATH [15] is another real-time protocol which uses the two-hop neighbor information for routing decisions. Dynamic adjustment of transmission power is adopted to reduce the packet dropping.

JiTS [16] shows that shortest path routing provides better performance than geographic routing and explores several policies for nonuniformly delaying data at several intermediate nodes for contention-free transmission. EARTOR [17] aims to increase the number of requests in the network and route requests are designed with specified latency constraints. Cross-layer design is adopted in EARTOR along with the routing mechanism at each relay node that takes into consideration remaining energy, position, and priority of relay node. EEOR [18] improves the throughput by allowing nodes that overhear the transmission to participate in forwarding the packet. The nodes are prioritized and low priority forwarder will discard the packet if the packet has been forwarded by high priority forwarder. The power control is done by sensors in the network using beacon messages and power loss is calculated in [19]. In [20], a two-hop based routing protocol is proposed with link reliability to reduce DMR with longer network lifetime. It implements the modules for estimating transmission delay and packet delivery ratios, but requires periodic update of these parameters with HELLO messages. In [21], packets are routed with differential delay constraints and reliability constraints along multiple paths, but one-hop neighborhood information is used.

In our proposed mechanism, we adopt the approach of identifying the slow packets, which are useless and cannot meet the prescribed deadline, and remove those packets from the queue of intermediate nodes located near to the sink. This conserves energy and improves the network lifetime. It also implements the adaptive transmission power algorithm, which dynamically changes the transmission power to be used in forwarding metric, instead of fixed transmission power as in THVR. Though power adaption scheme is used in PATH, it is invoked when it cannot find suitable two-hop neighbor and when it has sufficient choice of forwarding pair. During transmission, the power is adjusted according to the location of the receiver and the quality of the wireless link. This further improves energy efficiency. The forwarding metric is same as used in PATH, finding the suitable next forwarding pair based on the novel two-hop velocity integrated with energy balancing mechanism which maintains the routing efficiency without degrading the real-time behavior of the protocol. It is therefore named as energy-efficient adaptive routing protocol (EE-ARP). The proposed routing protocol details are given in the next section.

3 Design of EE-ARP for RT-WSN

The proposed protocol route the packets in three stages: (1) Identification and removal of much delayed packets (2) Adaptive transmission power algorithm and (3) Forwarding metric.

3.1 Identification and Removal of Much Delayed Packets

Not all the packets routed for transmission have the chance to reach their destination or sink within deadline. The deadline information is exploited in the proposed routing mechanism and the much delayed packets or slow packets are removed from the queue of intermediate nodes near the sink as it is useless to traverse those packets toward destination, thereby saving the energy of nodes. The queue is now maintained to have only packets with sufficient residual deadline. To identify the slow packet from the queue, EE-ARP calculates the expected delay for the current packet to reach the sink and decides whether to remove or not, the current packet based on this expected delay.

Expected Delay. The expected delay for the current packet p at the current node x to reach the destination d is $Txd(p)$ and is given by the formula (1).

$$Txd(p) = \frac{Dxd(p)}{Dsx(p)} * Tsx(p) \tag{1}$$

As shown in Fig. 1, $Dxd(p)$ denotes the remaining geographic distance that the current packet p has to traverse from current node x to the destination d and $Dsx(p)$ is the geographic distance traveled by the packet p from source s to current node x. $Tsx(p)$ gives the time delay for the packet to reach the current node x.

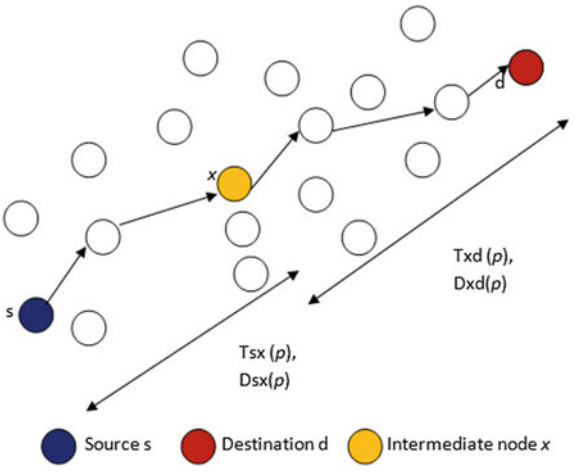


Fig. 1 Expected delay estimation

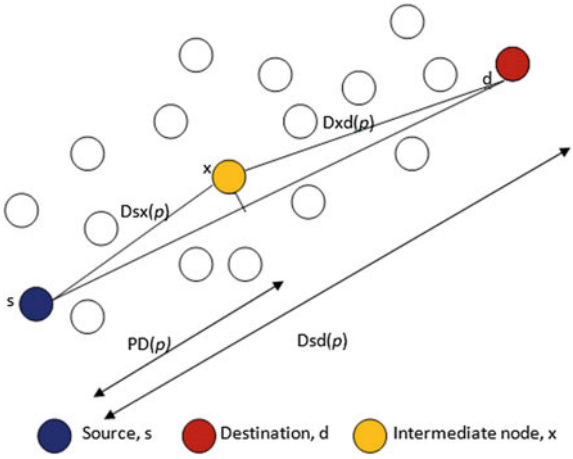


Fig. 2 Illustration of progressive distance PD(p)

3.2 *Removal of Much Delayed Packets*

After having the expected delay for the current packet p at current node x, it is to be decided whether the packet can be retained or not in the queue of intermediate node. The distance between the source s and the destination d, $Dsd(p)$ and progressive distance PD(p), the distance that the packet p progressed toward the destination, are used in the decision rule. Figure 2 shows the PD(p). The complete algorithm for the identification and removal of slow packets at each intermediate node is given in Algorithm 1.

The Algorithm 1 is as follows:

Algorithm 1 : Identification and Removal of slow packets

1. **For** each current packet p at the current node x,
2. **Calculate** expected delay $Txd(p)$
   # Packet removal decision rule.
3. **If** $PD(p) > \alpha * Dsd(p)$ **then**
4. **If** $Txd(p) > deadline\ (p)$ **then**
5. **Remove** packet p from the queue of current node x
6. **Endif**
7. **Else**
8. **If** $\frac{PD(p)}{\alpha * Dsd(p)} * Txd(p) > deadline\ (p)$ **then**
9. **Remove** packet p from the queue of current node x
10. **Endif**
11. **Endif**

The PD(p) is calculated as shown in formula (2).

$$PD(p) = \begin{cases} \frac{D^2sx(p) - D^2xd(p) + D^2sd(p)}{2 * Dsd(p)} & \text{if } Dsx(p) < Dsd(p) \\ Dsd(p) & \text{otherwise} \end{cases} \quad (2)$$

The Algorithm 1 explains the procedure to identify and remove the unwanted slow packets from reaching the destination because of insufficient deadline and to preserve energy of the nodes by not forwarding them toward the destination. After calculating the expected delay as shown in formula (1), the packet removal decision rule is applied.

While simulating the proposed algorithm, the parameter α is chosen 0.5 where α is the parameter chosen according to the application, it must be close to 1 for real-time applications and close to 0 for energy-efficient applications. So, the packet is tested only when it is progressed more than 50 % of the total distance. If the packet p cannot meet the deadline requirement then it is removed from the queue of current node x. Otherwise, more chance is given to the packet p to reach the destination with $Txd(p)$ multiplied with $\frac{PD(p)}{\alpha * Dsd(p)}$ and compared with given deadline. If the value exceeds the deadline, then the packet is removed.

3.3 Adaptive Transmission Power Algorithm

The queue of the current node now contains the useful packets after the removal of useless packets. The transmission power of each packet is adaptively varied based on the quality of wireless link and this power is used in forwarding metric for choosing the next candidate. In path loss model, the power transmitted from the transmitter falls as $1/d^n$, where d is the distance between the transmitter and receiver and n is the path loss exponent. This idea is exploited in the proposed routing mechanism. The adaptive transmission power algorithm is described in Algorithm 2.

Algorithm 2: Adaptive Transmission Power algorithm

1. While forwarding a packet p in a queue of intermediate node, the transmission power $P(x)$ is given by formula (3)
$$P(x) = t.d^n + C \quad (3)$$
where d is the distance from current intermediate node to the next forwarding node, n is the path loss exponent and depends on the quality of wireless link ($n \geq 2$). C is the system processing cost and t is prediction threshold.
2. The transmission energy $E(x)$ is given
$$E(x) = P(x) * T(x) \quad (4)$$
where $T(x)$ is the transmission time, the time required to send a packet by a node.

In the proposed routing protocol, the transmission power is varied based on the geographic position of next choice. During simulation, the path loss exponent n is chosen to be 2 and system processing cost C is assumed to be 0.

3.4 Forwarding Metric

The proposed routing mechanism is integrated with PATH [15] protocol and the same forwarding metric, which is based on velocity and energy metric, is used to select next forwarding pair for the packet p to get routed towards destination. But the transmission energies are adaptively calculated, as shown in formula (4), based on the distance between sender and receiver. This improves the energy efficiency and better forwarding pairs are selected in routing the packets.

4 Performance Evaluation

The EE-ARP is simulated in Network Simulator-2.35 [22]. We set the parameters close to practical WSN according to MicaZ motes [23] with MPR2400 (2.4 GHz) radio. Nodes are randomly deployed in a 500 m × 500 m sensing area and are fixed. We considered one source and one destination. The source node is chosen at the left-lower corner of the sensing area fixed at the location (95, 50 m), while the destination node is fixed at the location (43, 475 m) at right-top corner of the sensing area.

The EE-ARP is investigated and compared with THVR and PATH protocols. The source generates CBR traffic at 10 kbps rate with packet frame size 64 bytes (including header and CRC fields). The performance metrics are (i) ECPP, which is defined by the total energy expended divided by the number of successfully transmitted packets and (ii) DDMR, which is defined as the ratio of packets that miss the predefined deadline to the total transmitted packets. The deadline requirement is varied from 400 to 1,100 ms and in each run DMR is calculated for the three protocols. The results show that the proposed mechanism offers better energy efficiency than other two protocols as shown in Fig. 3. This is due to the adaptive transmission power algorithm and the novel method of removal of slow packets thereby saving the energy of nodes in the network.

The DMR is also improved in EE-ARP as shown in Fig. 4, because of the removal of much delayed packets at intermediate nodes and preventing them to reach the destination with large delay. In EE-ARP, the novel method of removal of much delayed packets is employed. This method helps in the removal of slow packets from the queue and only the packets which have sufficient residual deadline are retained for routing. Also the efficient utilization of energy results in better forwarding choice and the packets are routed effectively which further reduces DMR.

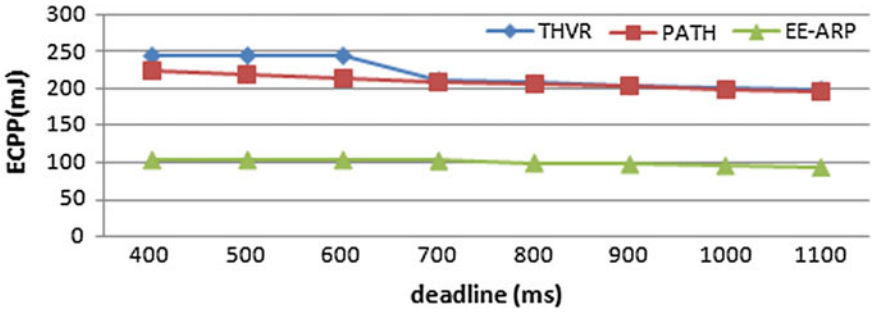


Fig. 3 ECPP comparison of THVR, PATH, and EE-ARP

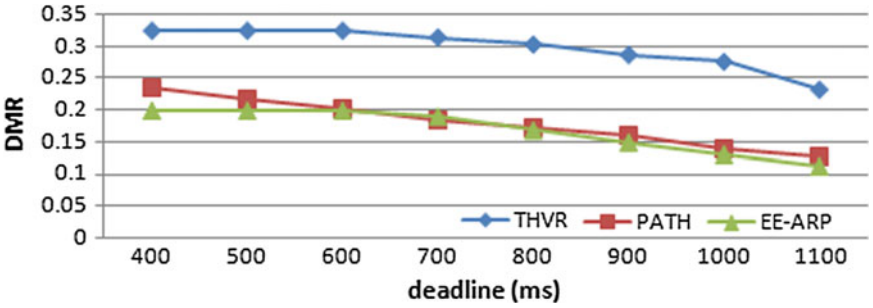


Fig. 4 DMR comparison of THVR, PATH, and EE-ARP

5 Conclusion and Future Scope

In this paper, an adaptive routing mechanism based on two-hop neighborhood information of the network is proposed. It employs a novel method of removal of much delayed packets and also the efficient adaptive transmission power algorithm to achieve better energy efficiency without degrading the real-time performance in WSNs. This integration reduces the energy consumption and improves DMR better than THVR and PATH. Our future work will consider multiple sources thereby increasing the traffic intensity in the network and the performance of the proposed mechanism is observed.

References

1. Chong CY, Kumar SP. "Sensor networks: evolution, opportunities, and challenges", Proceedings of the IEEE. 2003 Aug; 91(8), pp. 1247–56.
2. Chen W, Li W, Shou H, Yuan B. "A QoS-based adaptive clustering algorithm for wireless sensor networks. In Mechatronics and Automation", Proceedings of the 2006 IEEE International Conference on 2006 Jun 25 (pp. 1947–1952). IEEE.

3. Li Y, Chen CS, Song YQ, Wang Z, Sun Y. "Enhancing real-time delivery in wireless sensor networks with two-hop information". Industrial Informatics, IEEE Transactions on. 2009 May; 5(2):pp 113–22.
4. Li Y, Chen CS, Song YQ, Wang Z, Sun Y. "A two-hop based real-time routing protocol for wireless sensor networks". In Factory Communication Systems, 2008. WFCS 2008. IEEE International Workshop on 2008 May 21 (pp. 65–74). IEEE.
5. Li Y, Chen CS, Song YQ, Wang Z. "Real-time QoS support in wireless sensor networks: A survey". In 7th IFAC International Conference on Field buses & Networks in Industrial & Embedded Systems-FeT'2007, 2007.
6. Shue Chen C, Li Y, Song YQ. "An exploration of geographic routing with k-hop based searching in wireless sensor networks". In Communications and Networking in China, China Com 2008. Third International Conference on 2008 Aug 25 (pp. 376–381). IEEE.
7. Spohn MA, Garcia-Luna-Aceves JJ. "Enhancing broadcast operations in ad hoc networks with two-hop connected dominating sets". In Mobile Ad-hoc and Sensor Systems, 2004 IEEE International Conference on 2004 Oct 25 (pp. 543–545). IEEE.
8. Calinescu G. "Computing 2-hop neighborhoods in ad hoc wireless networks." In Ad-Hoc, Mobile, and Wireless Networks 2003 Jan 1 (pp. 175–186). Springer Berlin Heidelberg.
9. C.E. Perkins, E.M. Royer, "Ad hoc On-Demand Distance Vector Routing," Proc. of 2nd IEEE Workshop on Mobile Computing Systems and Applications, New Orleans, LA, February, 1999, pp 90–100.
10. David B. Johnson, David A Maltz, Josh Broch "DSR: The dynamic source routing protocol for multihop wireless adhoc networks", in Mobile Computing, Chapter 5, pp 153–181, Kluwer Academic publishers, 1996.
11. C lu, B. M. Blum, T.F. Abdelzaher, J.A. Stankonic and T. He, "RAP: A real time Architecture for large scale wireless sensor networks," in proceedings of RTA S, 2002, September, 2002.
12. Tian He, John A Stancovic, Chenyang Lu, Tarek Abdelzaher," Speed: A Stateless protocol for real time Communication in Sensor network", Proceedings of International Conference on Distributed Computing systems, Providence, RI, May 2003.
13. Emad Felemban, Chang Gun lee and Eylem Elcici, "MM SPEED: Multipath Mulit-speed protocol for QoS guarantee of reliability and Timeliness in Wireless sensor networks", IEEE transactions on Mobile computing [J], pp 738–754, 2006.
14. O. Chipura, Z. He, G. Xing, Q. Chen, Xiaorui Wang, C. Lu, J. Stankovic, T. Abdelzaher, "Real time Power Aware Routing Protocol in Sensor networks", in the proceedings of IWQoS 2006, June 2006.
15. P. Rezayat, M. Mahdavi, M. Ghasemzadeh, Agha. S, "A Novel Real time Power Aware Routing Protocol", in the proceedings of IJCSNS, Vol 10, April, 2010.
16. Liu K, Abu-Ghazaleh N, Kang KD. "JiTS: Just-in-time scheduling for real-time sensor data dissemination." In Pervasive Computing and Communications, 2006. PerCom 2006. Fourth Annual IEEE International Conference on 2006 Mar 13 (pp. 5-pp). IEEE.
17. Yang W, Liang W, Dou W. "Energy-aware real-time opportunistic routing for wireless ad hoc networks." InGlobal Telecommunications Conference (GLOBECOM 2010), 2010 IEEE 2010 Dec 6 (pp. 1–6). IEEE.
18. Mao X, Tang S, Xu X, Li XY, Ma H. "Energy-efficient opportunistic routing in wireless sensor networks." Parallel and Distributed Systems, IEEE Transactions on. 2011 Nov; 22 (11):1934–1942.
19. Trung Dung Nruyen, Van Duc Nruyen, Tien Pham Van, Wakasugi Koichiro and Ngoc Tuan Nguyen," Power Control Combined with Routing protocol for Wireless Sensor Networks", Computing, Management and Tele-communications (ComManTel), April, 2014.
20. Shiva, Prakash T., et al. "Link-reliability based two-hop routing for QoS guarantee in Wireless Sensor Networks." Wireless Personal Multimedia Communications (WPMC), 2013 16th International Symposium on. IEEE, 2013.

21. Rachamalla, Sandhya, and Anitha Sheela Kancharla. “Power-Control Delay-aware routing and MAC protocol for Wireless Sensor Networks.” Networking, Sensing and Control (ICNSC), 2015 IEEE 12th International Conference on. IEEE, 2015.
22. Network Simulator: http://www.isi.edu/nsnam/ns.
23. Crossbow Motes, http://www.xbow.com.

Mitigation and Analysis of Very Fast Transient over Voltages (VFTOs) of Transformer in 1000 KV Gas-Insulated Substation (GIS) Using Wavelet Transform

K. Prakasam, M. Surya Kalavathi and D. Prabhavathi

Abstract Mitigation and analysis of very fast transient over voltages (VFTO) is very important in gas-insulated substations (GIS). In this paper a power transformer rating of 1500 MVA in 1000 kV GIS has been considered and different techniques for mitigation and analysis of VFTOs at the transformer are applied and the same results are analyzed by the application of discrete wavelet transform (DWT) as wavelet transform gives the accurate results. The proposed system has been designed with Mat Lab software platform and the system is simulated to evaluate the peak values of VFTOs generated at the both at transformer and open end of the transformer with and without RC filter, ferrite ring, and a nonocrystilline. The results show that the peak value of VFTOs can be considerably reduced by introducing RC filter ferrite ring and nano crystalline methods. The outcomes are explored to wavelet transform for transient information. By the application of wavelet transform it has concluded that an exact measurement VFTOs can be obtained and is shown in the results.

Keywords Discrete · Damping · Ferrite ring · Crystalline · Wavelet

K. Prakasam · D. Prabhavathi (✉)
Department of EEE, JNTUA, Anantapuram, AP 515 002, India
e-mail: prabhavathi10@gmail.com

K. Prakasam
e-mail: gvitgem@gmail.com

M. Surya Kalavathi
Department of EEE, JNTUH, Hyderabad, TS 500 085, India
e-mail: munagala12@yahoo.co.in

© Springer Science+Business Media Singapore 2017

R. Singh and S. Choudhury (eds.), *Proceeding of International Conference on Intelligent Communication, Control and Devices*, Advances in Intelligent Systems and Computing 479, DOI 10.1007/978-981-10-1708-7_8

1 Introduction

The power system is large and interconnected one in which the transformer plays an important role and thereby it is very essential to protect it against the internal and external faults as well as from the over voltages due to any reason particularly when it is used in GIS since there is always possibility continuously the likelihood of reason for fast transient over voltages. Gas insulation substations (GIS) have been utilized as a part of force frameworks in the course of the most recent three decades on account of their high unwavering quality, simple support, and small ground space necessity, and so on. In India likewise, a couple GIS units are under different phases of establishment. The essential protection level (BIL) required for a gas protected substation (GIS) is not the same as that of the traditional substation on account of certain special properties of the previous. Gas protected substation has a surge impedance (70 Ω) more than that of the traditional oil filled links, however a great deal not as much as that of an over head line (300–400 Ω). In addition, the GIS is totally enclosed and therefore is free from any atmospheric contamination. Hence, in general the GIS permits lower BIL rating than the conventional one.

2 Scheme of Evaluation of Very Fast Transient over Voltages

As per the literature survey it has been observed that, the VFTOs can damp to a considerable level of peak using ferrite rings. The most of the authors tested the ferrite ring under low voltage and low frequency and conventional comparison given between the shunt resistor and ferrite ring, this paper presents a new method of analysis of VFTOs which is known as RC filter along with ferrite ring and nanocrystalline in association with wavelet transform as the VFTOs are concern to high frequency transients. In this work, VFTOs are produced by introducing disconnecting switch (DS) at both sides of power transformer. Disconnecting switch (DS) is represented by a PI segment which includes two voyaging wave models, two capacitors to ground, and a capacitor over the softening contacts as shown in Fig. 1. Disconnector is modeled in different manner for open and close positions. In the closed position, it has been modeled as a distributed transmission line. Open position of the DS has been modeled by a series capacitor demonstrating capacitance between contacts of the DS and is shown in Fig. 2. The parameters of proposed RC filter and ferrite ring and nanocrystalline are designed with the parameters as $R = 100\ \Omega$ and $L = 0.0022$ mH and $C = 1$ pF along with DS switching speed of 10 ms.

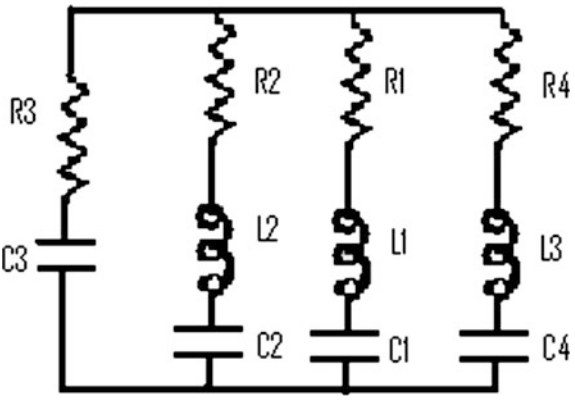


Fig. 1 Equivalent circuit of power transformer

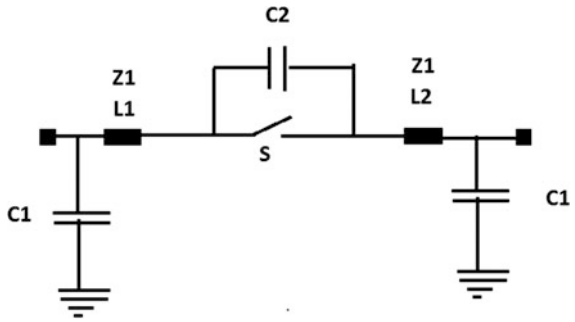


Fig. 2 Equivalent circuit of DS

2.1 Wavelet Transform

A wavelet is a scientific capacity used to separate a given capacity or constant time signal into various scales segments. Typically one can allot a recurrence extent to every scale part. Every scale part can then be contemplated with a determination that matches its scale. A wavelet change is the representation of a capacity by wavelets. The wavelets are scaled and deciphered duplicates (known as "girl wavelets") of a limited length or quick rotting wavering waveform (known as the "mother wavelet"). Wavelet changes have favorable circumstances over conventional Fourier changes for speaking to capacities that have discontinuities and sharp tops, and for precisely deconstructing and recreating limited, non-occasional and/or nonstationary signs.

Wavelet changes are grouped into discrete wavelet changes (DWTs) and consistent wavelet changes (CWTs). In the wavelet change we ought to note that both DWT and CWT are nonstop time (simple) changes. They can be utilized to speak to persistent time (simple) signals. CWTs work over each conceivable scale and interpretation while DWTs utilize a particular subset of scale and interpretation qualities or representation matrix. There are an expansive number of wavelet changes each

suitable for various applications. The wavelet change can be proficient in two unique courses relying upon what data is required out of this change process. The primary technique is a nonstop wavelet change (CWT), where one acquires a surface of wavelet Coefficients, CWT(b, a), for various benefits of scaling "a" and interpretation 'b', and the second is a DWT, where the scale and interpretation are defamed, however not are free variables of the first flag. In the CWT the variables "a" and "b" are nonstop. DWT results in a limited number of wavelet coefficients relying on the whole number of discretization venture in scale and interpretation, indicated by "m" and 'n'. In the event that and are the division step sizes for the scale and interpretation individually, the scale and interpretation regarding these parameters will be

$$a = a_0^m \text{ and } b = b_0 a_0^m \tag{1}$$

$$\psi_{b,a}(t) = \frac{1}{\sqrt{a\psi}\left(t - \frac{b}{a}\right)} \tag{2}$$

The above introduced mathematical statement speaks to the mother wavelet of persistent time wavelet arrangement. After discretization as far as the parameters, "m" and 'n,' the mother wavelet can be composed as,

$$\psi'_{b,a}(m,n) = \frac{1}{\sqrt{a_0}\Psi\left(t - \frac{nb_0 a_0^m}{a_0^m}\right)} \tag{3}$$

$$\psi'_{b,a}(m,n) = a_0^{\frac{m}{2}}\psi\left(ta_0^{-m} - nb_0\right) \tag{4}$$

After discretization, the wavelet space coefficients are no more spoken to by a basic "a" and 'b.' Rather they are spoken to as far as "m" and 'n.' The discrete wavelet coefficients DWT(m, n) are given by mathematical statement:

$$\mathrm{DWT}(m,n) = a_0^{m/2} \int_{-\infty}^{+\infty} f(t)\psi\left(ta_0^{-m} - nb_0\right)\mathrm{d}t \tag{5}$$

The change is over consistent time, however the wavelets are the change which is over nonstop time yet the wavelets are spoken to in a discrete manner. Like the CWT, these discrete wavelet coefficients speak to the connection between the first flag and wavelet for various blends of "m" and 'n.' In this study, the line current signs are utilized as the data signs of the wavelet examination. The DWT, utilizing a Daubechies-4 wavelet (db4), performed better at recognizing begin and end of an unsettling influence [1–4]. The Daubechies (Db) wavelet is extremely appropriate for recognizing brief time, high recurrence homeless people, and in addition low recurrence conduct over longer timeframes. In both cases the signs are non-occasional or nonstationary [1, 5]. The flaw drifters of the study cases are broken down through discrete wavelet change at levels one to five. Both estimate and points

of interest data related shortcoming current are removed from the first flag with the multidetermination examination.

2.2 Power Transformer

In this paper, the power transformer rating of 1500 MVA, in 1000 kV GIS has been considered and the transformer model is designed with the help of Mat lab platform. Since the transformer coil at high frequencies behaves as capacitive network the modeling of transformer has been designed based on very fast transients (VFT), i.e, the surge impedance, velocity of propagation, formative time, and length are considered, as well as the series capacitance between the turn and coil and the shunt capacitance between the turn [6], coil, and grounded core and transformer tank are considered for accurate results of the peak magnitude of VFTOs in the process of design of power transformer, due to high impedance at high frequencies the inductive branch toward ground has been neglected as well as the nonlinear behavior of the core also neglected.

2.3 Disconnecting Switch (DS)

During the closing operation of DS, the electric field increases but still sparking occurs and the sparking occurs at power frequency first. During the closing operation of the DS, the charging current flows and charge the load to the source voltage and voltage collapses and extinguish [7–9]. The sparking charge depends on the speed of the DS. The DS is represented to by a PI section which contains two traveling wave models, two capacitors to ground, and a capacitor across the contacts as shown up Fig. 2 with the parameters as $Z1 = 35\ \Omega$, $L1 = 640$ mm, $L2 = 450$ mm, $C1 = 25$ pF and $C2 = 2.5$ pF. The sparkle utilized as a part of DS restrike cases is displayed as an exponentially rotting resistance Ro $e^{(-t/\tau)}$ in arrangement with a little resistance, r of $0.5\ \Omega$ to deal with the lingering flash resistance. Disconnecting switch (DS) is modeled in different manner for open and close positions. In the closed position, it has been modeled as a distributed transmission line. Open position of the DS has been modeled by a series capacitor demonstrating capacitance between contacts of the DS and is shown in fig below. Value of fixed resistance r_s has been selected on the basis of the practical consideration as discussed.

$$L = \left(\frac{1}{1000}\right) l \left[\ln\frac{R1}{R3} + \ln C + \ln\left(\frac{R4}{R3}\right) + \frac{2 \times \left(\frac{R2}{R1}\right)^2}{1 - \left(\frac{R2}{R1}\right)^2} \times \ln\left(\frac{R1}{R2} - 1\right)\right] \quad (6)$$

$$C = \left(\frac{2\pi\varepsilon_0\varepsilon_r * l}{2.3 * \ln\left(\frac{b}{a}\right)} \right) \tag{7}$$

$$R_s = R_0 * e^{-t/\tau} + R_f, \tag{8}$$

where $R_0 = 10^6$ MΩ, fixed Resistance = 0.5 Ω. T (spark time constant) = 01 ns, open end section of GIS—The open ended section of GIS has been presented in the following figure where a lumped shunt capacitance has been considered. Assuming the same as a coaxial hemisphere, its capacitance has been estimated using following equation:

$$C = 2\pi\varepsilon_0\varepsilon_r * \frac{(R * r)}{(R - r)}, \tag{9}$$

where R = internal radius of enclosure, r = external radius of enclosure.

The DS can be modeled either as open end or closed end, in this paper the closed DS are modeled as a transmission line with distributed parameters. Capacitance of the switching contacts toward the ground is considered. For open condition switching, the DS are represented with inter electrode capacitance of the switching contacts toward the ground which is considered.

3 Methods of Mitigation and Analysis of Very Fast Transient over Voltages of Proposed System

As per the literature survey it has been observed that, the VFTOs can damp to a considerable level of peak using ferrite rings. The most of the authors tested the RC filter and ferrite ring under low voltage and low frequency and conventional comparison given between the shunt resistor and ferrite ring, this paper presents a new method of suppression and analysis of VFTOs which is known as RC filter, ferrite ring, and nano crystalline in association with wavelet transform as the VFTOs are concern to high frequency transients.

3.1 RC Filter Method

In the proposed work, the comparable circuit of 1000 kV GIS is considered with likeness *RC* channel. The parameters of R and C are picked as R = 100 Ω and C = 0.2 μF and recreations are completed. The RC channel has been associated in parallel with DS. The qualities decided for R = 100 Ω and C = 0.2 μF, since the capacitor ingests the high recurrence parts the greatness of voltage and steepness

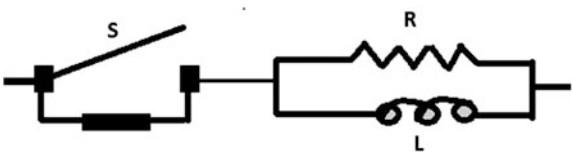


Fig. 3 Equivalent circuit of ferrite ring

falls quickly, because of this character of capacitor it has been executed as one of the strategy for mitigation and analysis.

3.2 Ferrite Ring Method

As per the literature survey [3] it has been observed that, the VFTOs can damp to a great considerable level of peak using ferrite rings. The most of the authors tested the ferrite ring under low voltage and low frequency and conventional comparison given between the shunt resistor and ferrite ring, this paper introduced a new method of analysis of VFTOs which is known as wavelet transform as the VFTOs are concern to high frequency transients. The comparable circuit of ferrite ring is shown in Fig. 3.

3.3 Nanocrystalline Method

Most of the authors tested the ferrite ring under low voltage and low frequency and conventional comparison given between the shunt resistor and ferrite ring and the ferrite ring has its own disadvantage that at high frequency it may gets saturation. Since the nanocrystalline exhibits enhanced electrical property in the high frequency range (100 kHz to 3 MHz) and have high dielectric strength. The nanocrystalline is modeled as R, L connected in series and connected in parallel with capacitor. The parameters of $R = 150\ \Omega$, $L = 0.002$ mH, and $C = 0.001$ nF chosen in the design of nanocrystalline. The equivalent circuit of nanocrystalline is shown in the following Fig. 4.

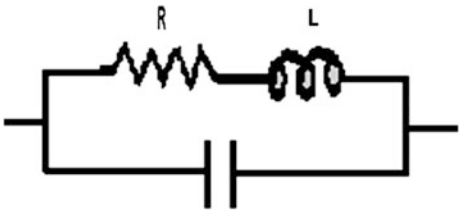


Fig. 4 Equivalent circuit nanocrystalline

4 Simulation Results of the Proposed System

The proposed system has been simulated with different mitigation methods like RC filter, ferrite ring, and nano crystalline by conventional and the results are analyses with wavelet transform and are shown in figures from Figs. 5, 6, 7, 8, 9, 10, 11, 12, 13, 14, 15, 16, 17, 18, 19, 20, 21, 22, 23 and 24. The peak values of VFTOs are tabulated in tables from Tables 1, 2, 3, 4 and 5.

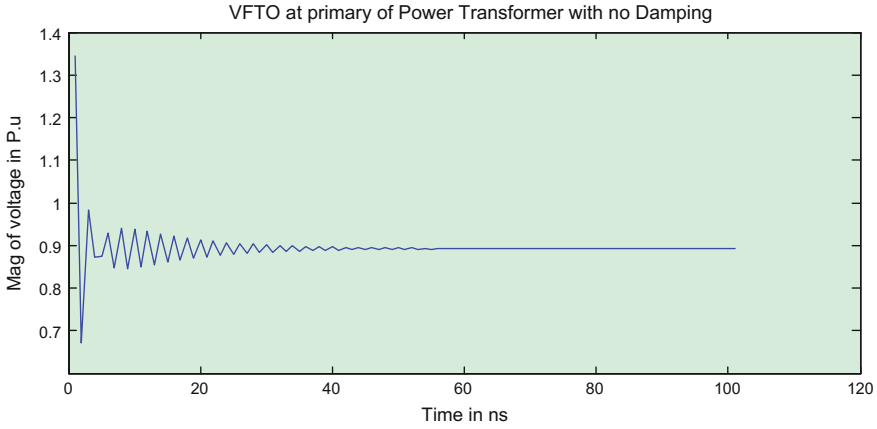


Fig. 5 Voltage peak at primary of transformer without damping

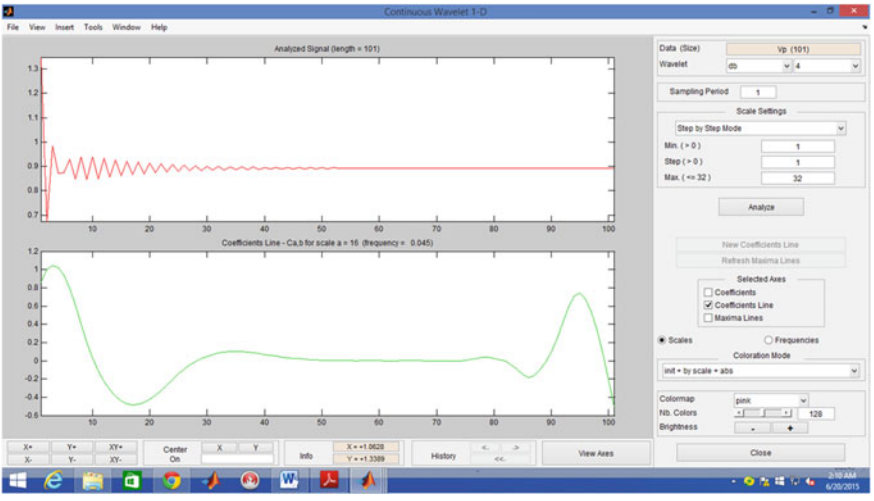


Fig. 6 Voltage peak at primary of transformer without damping with wavelet transform

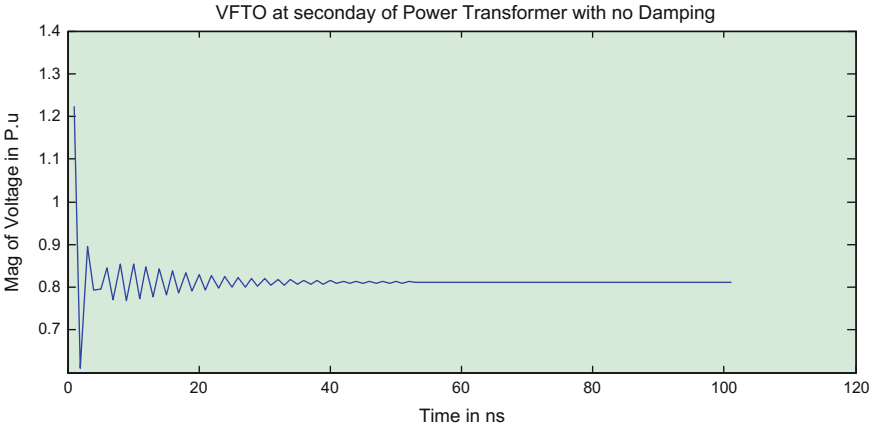


Fig. 7 Voltage peak at secondary of transformer without damping

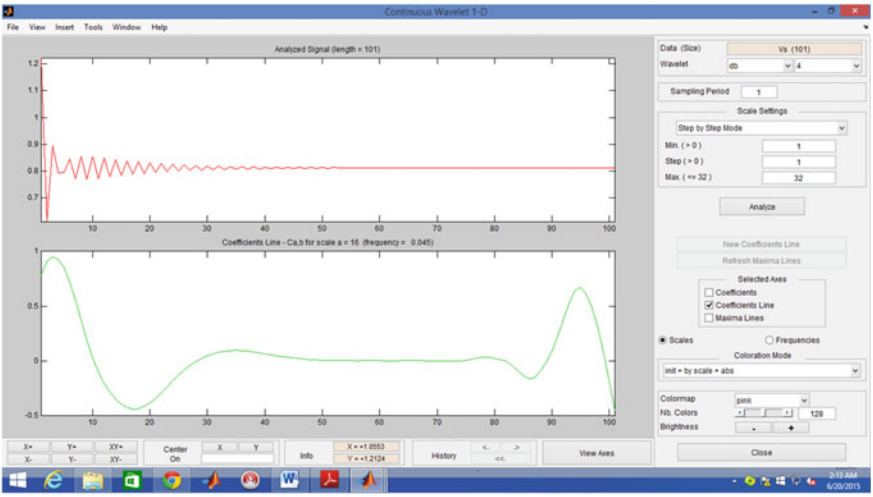


Fig. 8 Voltage peak at secondary of transformer without damping with wavelet transform

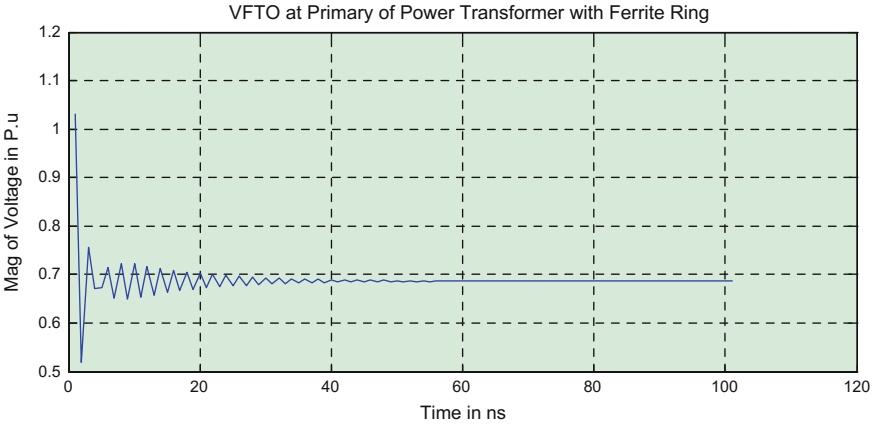


Fig. 9 Voltage peak at primary of transformer with ferrite ring

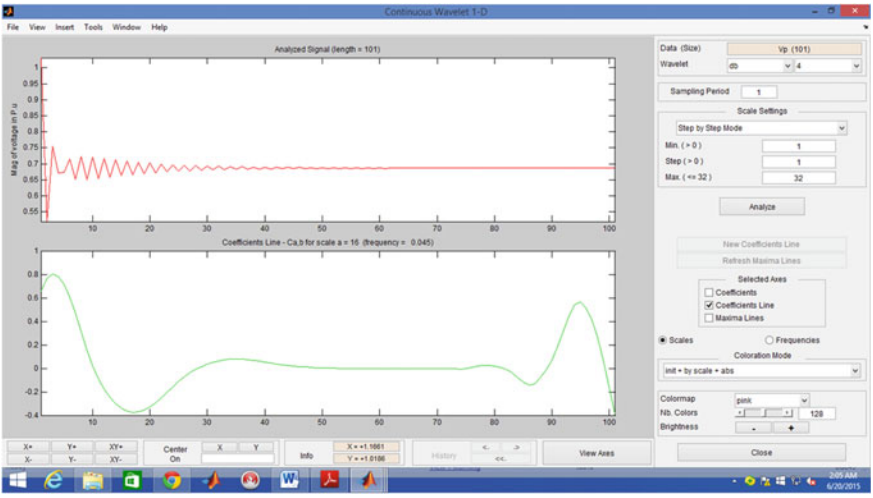


Fig. 10 Voltage peak at primary of transformer with ferrite ring with wavelet Transform

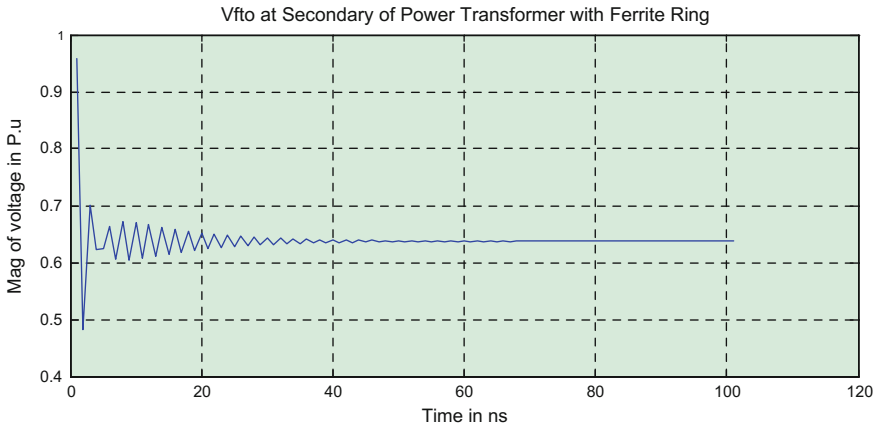


Fig. 11 Voltage peak at secondary of transformer with ferrite ring

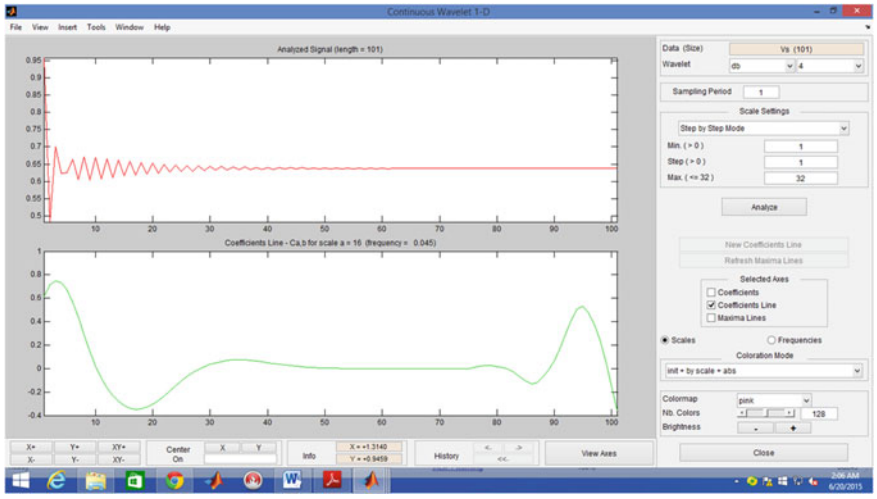


Fig. 12 Voltage peak at secondary of transformer with ferrite ring with wavelet transform

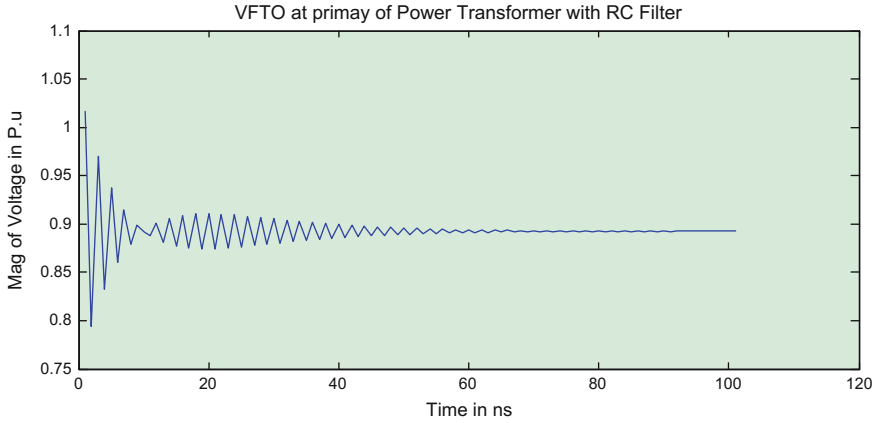


Fig. 13 VFTO peak at primary of transformer with RC filter

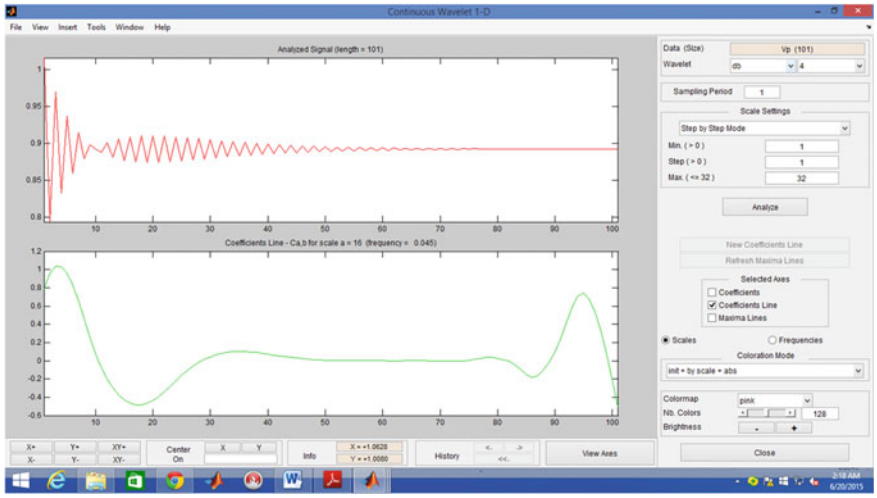


Fig. 14 VFTO peak at primary of transformer with RC filter with wavelet transform

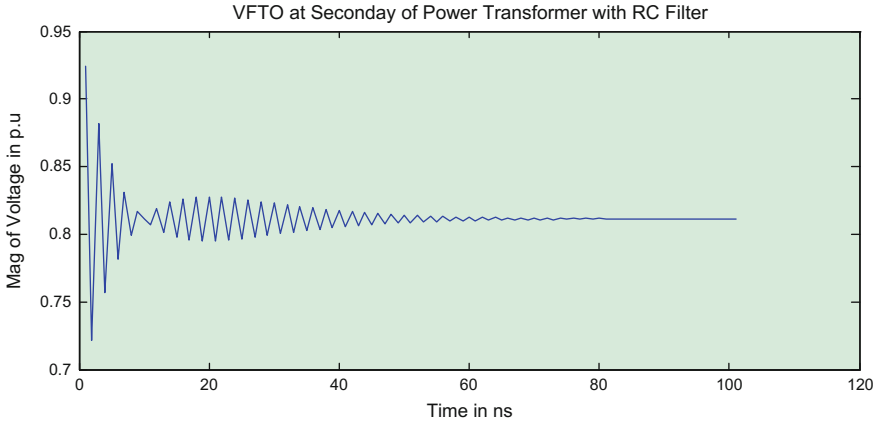


Fig. 15 VFTO peak at secondary of transformer with RC filter

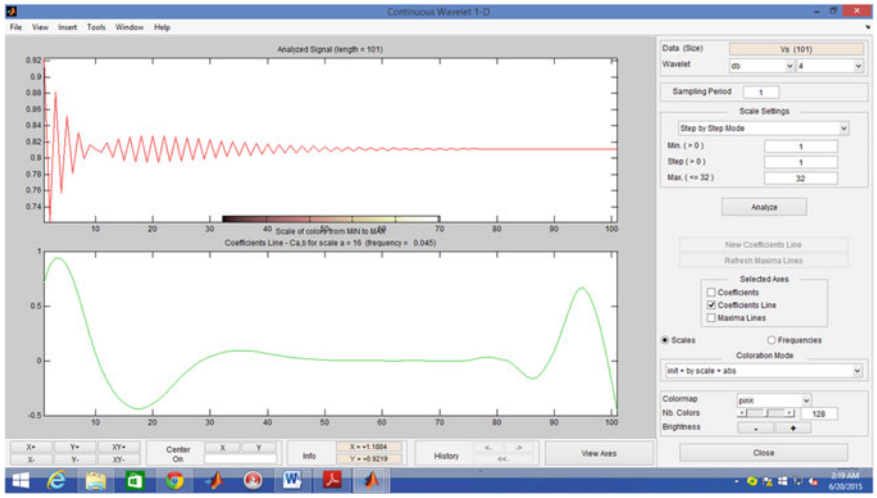


Fig. 16 VFTO peak at secondary of transformer with RC filter with wavelet transform

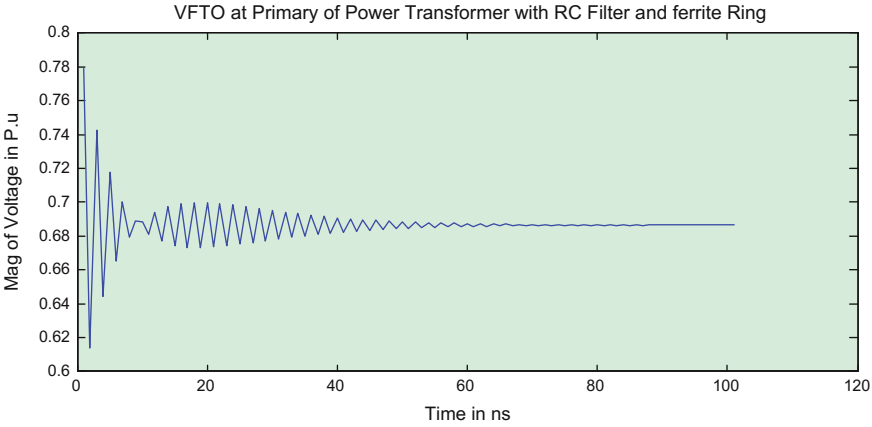


Fig. 17 VFTO peak at primary of transformer with RC filter and ferrite ring

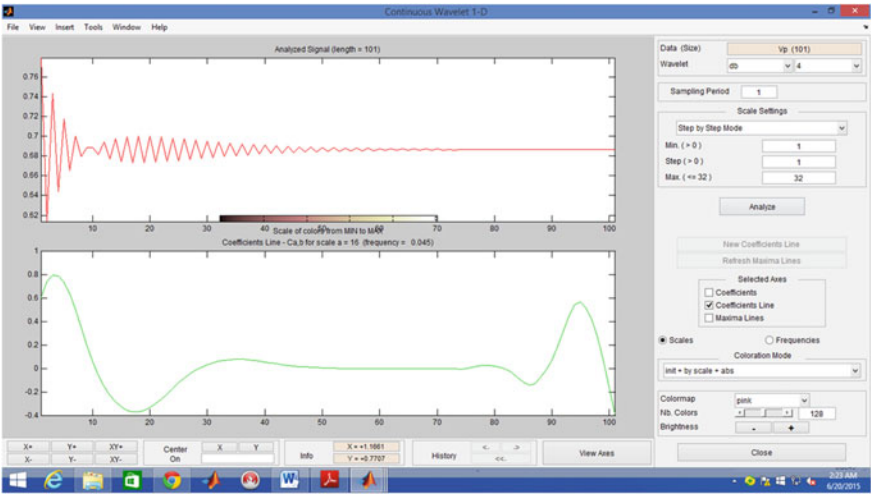


Fig. 18 VFTO peak at primary of transformer with RC filter and ferrite ring with wavelet transform

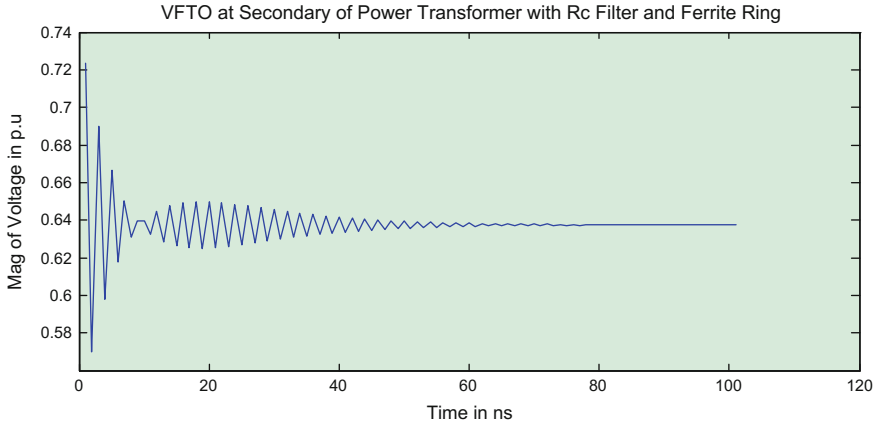


Fig. 19 VFTO peak at secondary of transformer with RC filter and ferrite ring

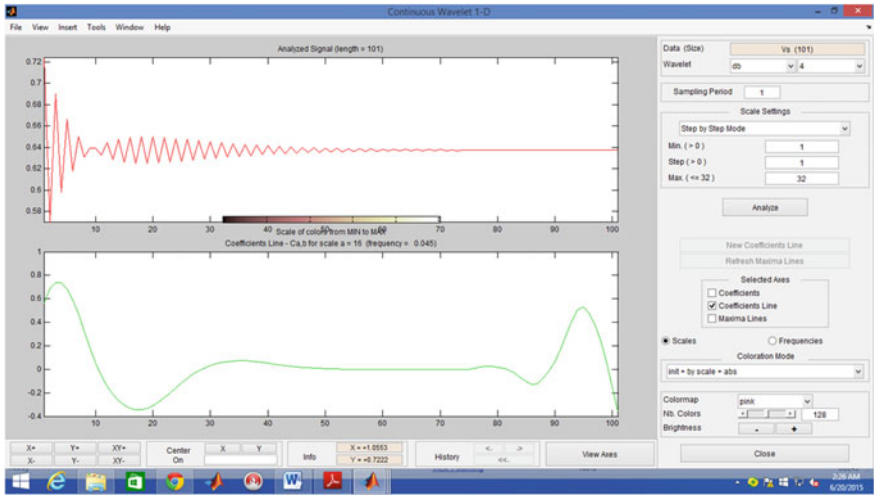


Fig. 20 VFTO peak at secondary of transformer with RC filter and ferrite ring with wavelet transform

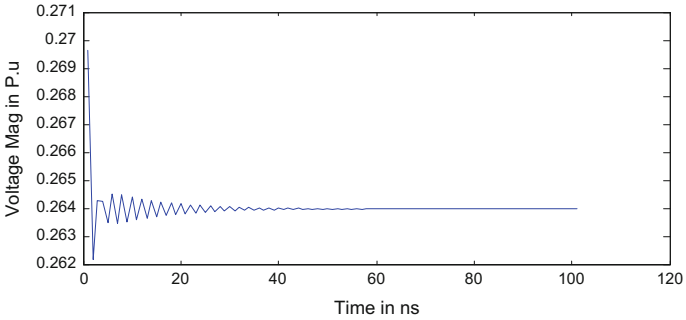


Fig. 21 VFTO peak at primary of transformer with RC filter and ferrite ring and nano crystalline

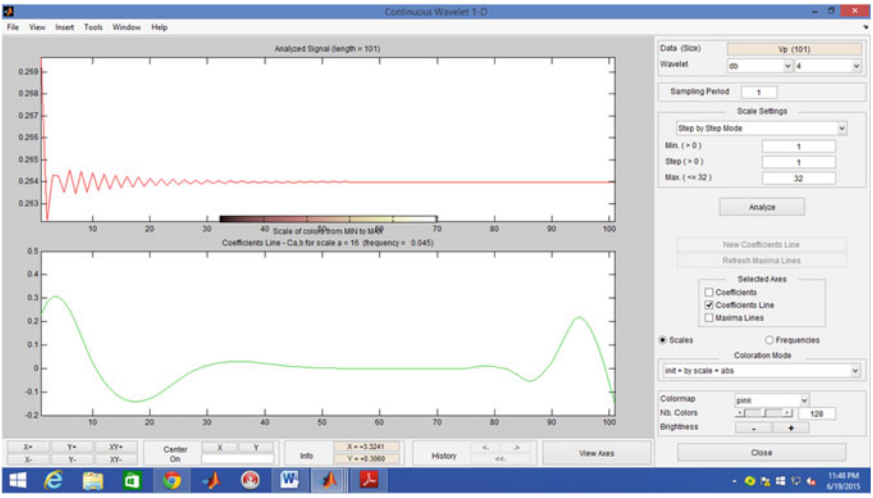


Fig. 22 VFTO peak at primary of transformer with RC filter and ferrite ring and nano crystalline with wavelet transform

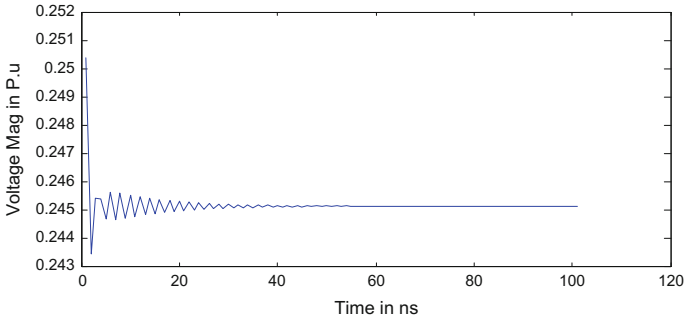


Fig. 23 VFTO peak at secondary of transformer with RC filter and ferrite ring and nano crystalline

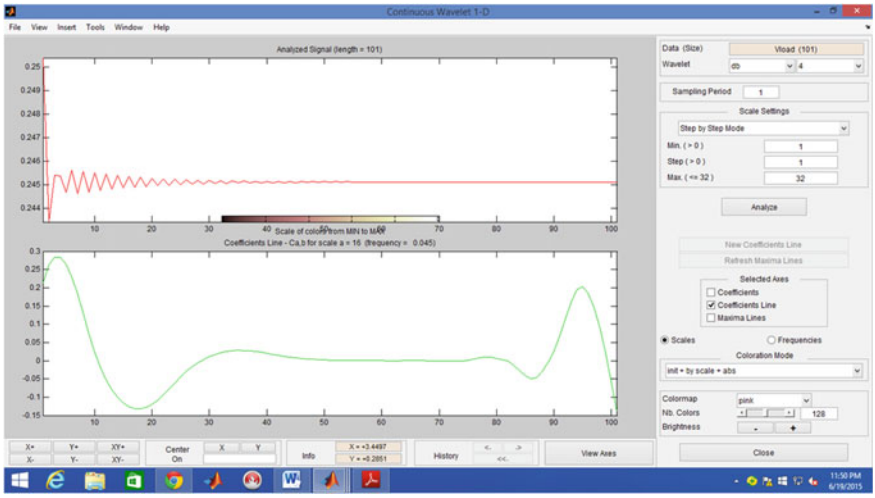


Fig. 24 VFTO peak at secondary of transformer with RC filter and ferrite ring and nano crystalline with wavelet transform

Table 1 Voltage peak without damping p.u

Transformer	Without wavelet *V* peak p.u	Wavelet (Db4)	Error
V_{tr}	1.324	1.448	0.124
V_{oc}	1.204	1.33	0.126

Table 2 Voltage peak with ferrite ring in p.u

Transformer	Without wavelet *V* Peak p.u	Wavelet (Db4)	Error
V_{tr}	1.028	1.12	0.092
V_{oc}	0.965	1.015	0.05

Table 3 Voltage peak with RC filter in p.u

Transformer	Without wavelet *V* peak p.u	Wavelet (Db4)	Error
V_{tr}	1.0122	1.125	0.112
V_{oc}	0.75	0.798	0.048

Table 4 Voltage peak with RC filter and ferrite ring in p.u

Transformer	Without wavelet *V* peak p.u	Wavelet (Db4)	Error
V_{tr}	0.768	0.9178	0.1498
V_{oc}	0.7245	0.9186	0.1941

Table 5 Voltage peak with RC filter and ferrite ring in and nanocrystilline p.u

Transformer	Without wavelet *V* peak p.u	Wavelet (Db4)	Error
V_{tr}	0.2695	0.27	0.0005
V_{oc}	0.2505	0.256	0.001

5 Conclusions

In this paper the power transformer of rating 1500 MVA, in 1000 kV GIS has been considered and is designed by utilizing Mat Lab platform for exact aftereffects of VFTOs. In the alleviation and examination prepare the DS, ferrite ring nanocrystilline were presented alongside the power transformer. This framework has been done for peak magnitude of VFTOs with no damping, RC channel, ferrite ring, and nanocrystalline strategies and are contrasted and also wavelet transform at level 4 (Db4) are shown in Figs. 5, 6, 7, 8, 9, 10, 11, 12, 13, 14, 15, 16, 17, 18, 19, 20, 21, 22, 23 and 24 and the reenacted results are shown in Tables 1, 2, 3, 4 and 5. From the results it can be observed that when there is no damping provided, the peak magnitude of VFTO at the transformer is 1.324p.u and at open end it is 1.204p.u but when the same is estimated using wavelet transform, it is 1.448p.u at transformer and 1.33p.u at open end. When ferrite ring is employed in the proposed system, the peak magnitude at transformer is 1.025p.u and at open end it is 0.965p.u, but with wavelet transform it is 1.12 and 1.015p.u, from this it can be concluded that there is a considerable reduction in magnitude of VFTO both at transformer and at open end by using the ferrite ring. In the next stage of this work, by RC filter, the peak magnitude of VFTO at transformer is 1.0122p.u and at open end it is 0.75p.um but with wavelet transform it is 1.1125p.u and 0.798p.u. In the further stage, the ferrite ring as well as RC filter combination has been implemented and peak magnitudes estimated both at transformer and at open end it is 0.768p.u at transformer and 0.7245p.u at the open end, but with wavelet transform it is 0.9178p.u and 0.9186p.u. The ferrite ring may get saturate at high frequency and RC filter is used for transformer protection only and there is no considerable effect on open end. In the next stage of the work, nanocrystalline is used for mitigation of VFTOs and peak magnitudes estimated at the transformer is 0.2695p.u and at open end it is

0.2505p.u. Tables 1, 2, 3, 4 and 5 give the estimated values of VFTOs with and without wavelet transform. From the results it can be concluded that by using different damping methods like RC filter, ferrite ring, and nanocrystalline the magnitude of VFTOs can be reduced to a considerable level, however from the results it is again proved that, by using wavelet transform an exact, accurate measurement can be done, since wavelet transform is a power full tool for high frequency nonstationary signals and it is superior than other conventional methods.

Acknowledgments I would like to express my gratitude to my Ph.D. guide, Prof. Dr M Surya Kalavathi madam garu, who encouraged me to pursue this work and taught me the art of VFT over voltages in GISs. It is my pleasure to acknowledge role of my co-author D. Prabhavathi in completion of this work.

References

1. Tiechen, Lu., Zhang Bo, "Calculation of Very Fast Transient Overvoltage in GIS", IEEE/PES Conference on Transmission and Distribution, Vol. 4 (2000), 1–5.
2. Boggs S.A., et al., "Disconnect switch induced transients and trapped charge in gas insulated", IEEE Trans. on Power Apparatus and Systems, vol. 101, no. 6, pp. 3593–3602.
3. Kamakshaiah, "Simulation and measurement of very fast transient over voltages in a 245 kv gis and research on suppressing method using ferrite rings" ARPN Journal of Engineering and Applied Sciences, vol. 5, No. 5 (2010). 88–95.
4. Vinod Kumar, V., Joy Thomas, M., and Naidu, M.S., "VFTO Computation in a 420 kV GIS", Eleventh International Symposium on High Voltage Engineering, (Conf. Publ. No. 467) (1999) 319–322.
5. Riechert, U.; Krüsi, U.; Sologuren-Sanchez, D.: "Very Fast Transient Overvoltages during Switching of Bus-Charging Currents by 1100 kV Disconnector", CIGRÉ Report A3-107, 43rd CIGRÉ Session (2010) 22–27.
6. Shibuya, Y., Fuji, S., and Hosokawa, N., " Analysis of very fast transient over voltage in transformer winding", IEE Proc. Generation transmission and distribution, Vol. 144, No. 5 (1997) 461–468.
7. Boggs, S.A., Chu F.Y and Fujimoto N., 'Disconnect Switch Induced Transients and Trapped charge in GIS', IEEE Transactions on Power Apparatus and Systems, Vol. PAS-101 (1998) 3593–3596.
8. Nobuhiro Shimoda, H., Murase, I. , Oshima, H., Aoyagi, I. , Miwa, "Measurement of transient voltages induced by disconnect switch operation", IEEE Transactions on Power Apparatus and Systems, PAS-104(1985) NO. 1.
9. Del Pozo, M.D.; Esteban, D.A.; Issouribehere, P.E.; Barbera, G.A.; Funes, A.; Ledesema, A.,"Field measurements and modeling of high frequency transients during disconnect switch operations in EHV Substations. Assessment of their effects on Current Transformers", CIGRÉ Report A3-207, 43rd CIGRÉ Session (2010) 22–27, Palais des Congrès, Paris, France.
10. Ozawa, J., Lalot, A., Sabot, J., Kieffer, S.W. mRowe, "Preventing earth faults during switching of disconnectors in gas insulated voltage Transformer", IEEE Transactions on Power Delivery, vol. 1 (1986). 434–441.
11. Martinez, J.A, P., Iravani, R., Keri, A., Povh, D., "Modelling guidelines for very fast transients in Gas Insulated substations", IEEE working group modeling and analysis of system transients, Vol. 11, no. 4 (1988) 2028–2047. Alvinson et al.
12. Hosokawa, N.,'Very fast Transient Phenomena associated with Gas Insulated Substations', CIGRE (1996) 33–53.

13. Bewley, L.V., NY 'Travelling waves on Transmission system', Dover pub Inc. Z. Haznadar,
14. Cariimavoid, S., Mahmutdehajid, R., "More accurate modeling of Gas insulated components in digital simulations of very fast transients", IEEE Transactions on Power delivery, Vol. 7, NO. 1 (1963) 434–441.
15. Ogawa S., Hanginomori E., 'Estimation of Restriking Transient overvoltage on Disconnecting Switch for GIS', IEEE Tans. P.S., Vol. PWRD-1, No. 2 (1986). 95–101.
16. Witzman R., 'Fast Transients in Gas Insulated substations—Modelling of Different GIS components', Fifth ISH, Braunschweig (1998) 12.06. Working Group 33/13–09, 'Very Fast Transient Phenomenon Associated With GIS, CIGRE.

Application of PSO Technique in Multiarea Automatic Generation Control

Mohan Kashyap, Anu Chaudhary and Satish Kansal

Abstract This paper proposes particle swarm optimization (PSO) technique to optimize the gains of an integral controller for automatic generation control (AGC) of a three unequal area thermal power system. Every control area takes into consideration dynamics of the thermal systems. Load frequency of interconnected multiarea thermal power system is also controlled for obtaining a better steady-state response of system. Further, results of PSO technique are compared with the bacterial-foraging (BF) technique that reveals superior performance of PSO technique over BF technique.

Keywords Particle swarm optimization · Integral controller · Three-area thermal power system

1 Introduction

One of the essential requirements for obtaining a continuous and healthy operation in the multiarea power system is automatic generation control [1, 2]. In large interconnected power systems, the frequency remains changing that leads to serious stability problems. Various factors like sudden changes in demand of power, different load characteristics, and various faults also increase such types of problems [3]. For obtaining a satisfactory operation, a balance between fixed frequency and

Mohan Kashyap (✉)
IKG Punjab Technical University, Jalandhar, Punjab, India
e-mail: mohan_kashyap80@rediff.com

Anu Chaudhary
Geeta Institute of Management and Technology, Kurukshetra, Haryana, India
e-mail: chaudharyanubattan60@gmail.com

Satish Kansal
Baba Hira Singh Bhattal Institute of Engineering and Technology,
Lehragaga, Sangrur, Punjab, India
e-mail: kansal.bhsb@gmail.com

© Springer Science+Business Media Singapore 2017

R. Singh and S. Choudhury (eds.), *Proceeding of International Conference on Intelligent Communication, Control and Devices*, Advances in Intelligent Systems and Computing 479, DOI 10.1007/978-981-10-1708-7_9

the active power is required [2]. In power system, power demand change or change in power generation results in change of system frequency. Modern power systems are interconnected to one another and power exchange takes place through tie-lines. For obtaining interconnected operation of power system, the desired operating level of system is characterized by voltage profile, load flow configuration, and the nominal frequency. This can be obtained by controlling the generated real and reactive powers [2, 4]. AGC plays an important role in power system by controlling the frequency of system and tie-line power flow under normal operating conditions and during small fluctuations.

Various classical approaches utilized for optimizing the value of integral gains are found to be time consuming. Also some new techniques like genetic algorithm, neural network, and fuzzy systems are nowadays utilized for obtaining optimum value of integral gains [5, 6]. In this paper, automatic generation control of a three-area thermal power system is achieved using integral controller. As the values of integral gains (K_{i1}, K_{i2}, K_{i3}) are needed to be optimized for obtaining the better steady-state response, PSO has been applied and proved to be a powerful and intelligent technique for optimizing the value of integral gains. It is a powerful optimization tool based on population-based approach. In this technique, particles fly in a multidimensional space. The direction of particle is defined by its history experience and the set of particles neighboring the particle. The convergence speed of PSO is very fast and it is easy to use [7–15].

2 System Investigated

Three-area interconnected system consists of three interconnected control areas. There is flow of tie-line power as per the changes in the load demand due to the interconnection made between the control areas. Thus the overall stability of the system is maintained at a balanced condition in spite of the constant variations in the load and load changes. Three unequal area of different MW capacity are considered. Integral controllers are used to improve system performance. The nominal parameters of system model are taken from Ref. [16]. Per unit values of the parameters of unequal areas are taken to be same on respective MW capacity bases. Therefore, while modeling interconnected areas of different capacities, quantities $a_{12} = -P_{r1}/P_{r2}$, $a_{23} = -P_{r2}/P_{r3}$ and $a_{13} = -P_{r1}/P_{r3}$ are taken into consideration [16]. State-space approach has been used for modeling the system. Then PSO is applied to get optimum values of the integral gains. The MATLAB simulation model of three-area system is shown in Fig. 1.

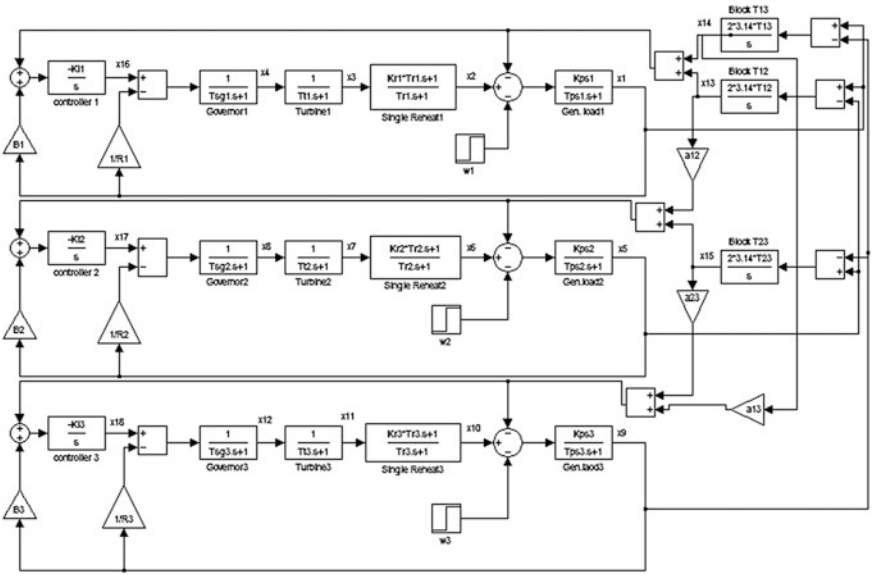


Fig. 1 MATLAB simulation model of three-area thermal power system

3 Simulation and Results

In this case, multiarea control system is unequal and consists of thermal system with reheat turbine. MATLAB version 7.10 is used to obtain dynamic response for Δf_1, Δf_2, Δf_3, $\Delta P_{\text{tie_line1-2}}$, $\Delta P_{\text{tie_line1-3}}$, and $\Delta P_{\text{tie_line2_3}}$ for 1 % step load perturbation (SLP) in either area. The MATLAB simulation model of a conventional three-area system is shown in Fig. 1 [16]. Following parameters have been used for PSO strategy [15, 17]:

$c_1 = 2$, $c_2 = 2$, $w_{\max} = 0.9$, $w_{\min} = 0.4$, $It_{\max} = 50$, Population Size = 20

Table 1 provides optimum values of integral controller gains.

The frequency deviation response of the area1, area2, and area3 are shown in Fig. 2a–c. Tie-line power deviation response is shown in Fig. 2d–f. Further, it is examined that dynamic response satisfies the requirement of AGC problem in term of settling time and steady-state error.

For same input model parameters, the output response of BF technique is different [16]. The output parameters of BF technique are obtained from Ref. [16] and compared with those of applied PSO technique. Table 2 provides the comparison of

Table 1 Optimum values of integral controller gains

Controller gains	Values
K_{i1}	0.3848
K_{i2}	0.2410
K_{i3}	0.2080

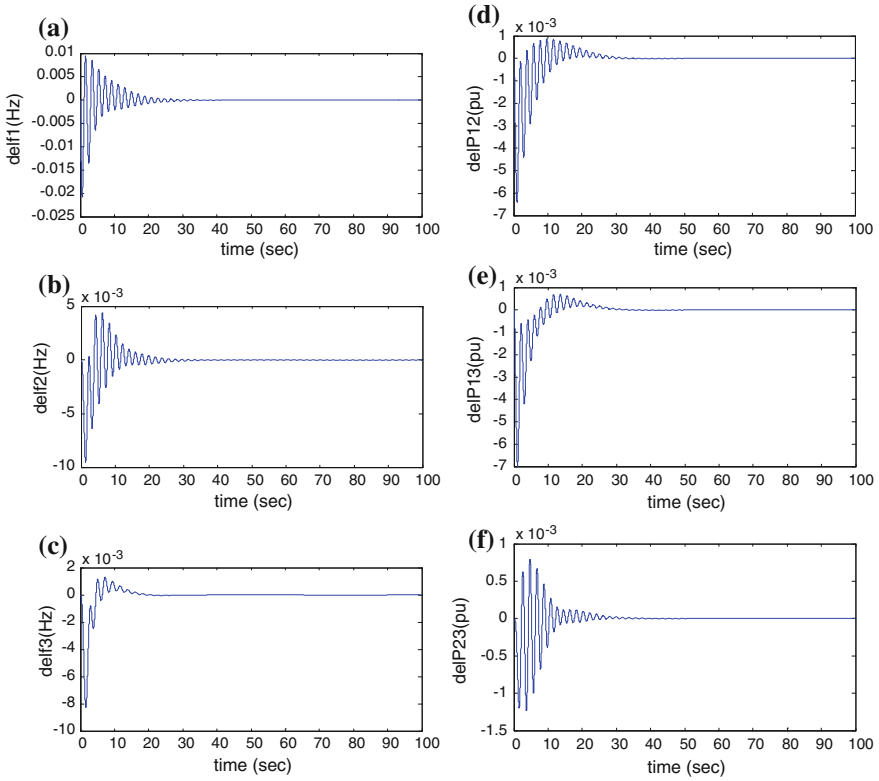


Fig. 2 **a** Frequency deviation in the area 1. **b** Frequency deviation in the area 2. **c** Frequency deviation in the area 3. **d** Power deviation in tie-line between area 1 and area 2. **e** Power deviation in tie-line between area 2 and area 3. **f** Power deviation in tie-line between area 1 and area 3

output integral gain values from both BF and PSO techniques. Table 3 provides the comparison of output parameters of BF and PSO techniques. Figure 3 shows combined output response of area1, area2, and area3 using BF and PSO.

Table 2 Comparison of output integral gains values

Optimum gains	BF	PSO
K_{i1}	0.4465	0.3848
K_{i2}	0.2191	0.2410
K_{i3}	0.2799	0.2080

Table 3 Comparison of output parameters

Output parameters	BF			PSO		
	Delf1	Delf2	Delf3	Delf1	Delf2	Delf3
Rise time	0.0030	2.6188	3.2231	0.000017	0.0232	0.000041
Settling time	26.4	37.6	40.8	23.9	24.9	16.5
Settling min	−0.0145	−0.0030	−0.0017	−0.0135	−0.0095	−0.00041
Settling max	0.0071	0.0015	0.00033	0.0094	0.0044	0.0013

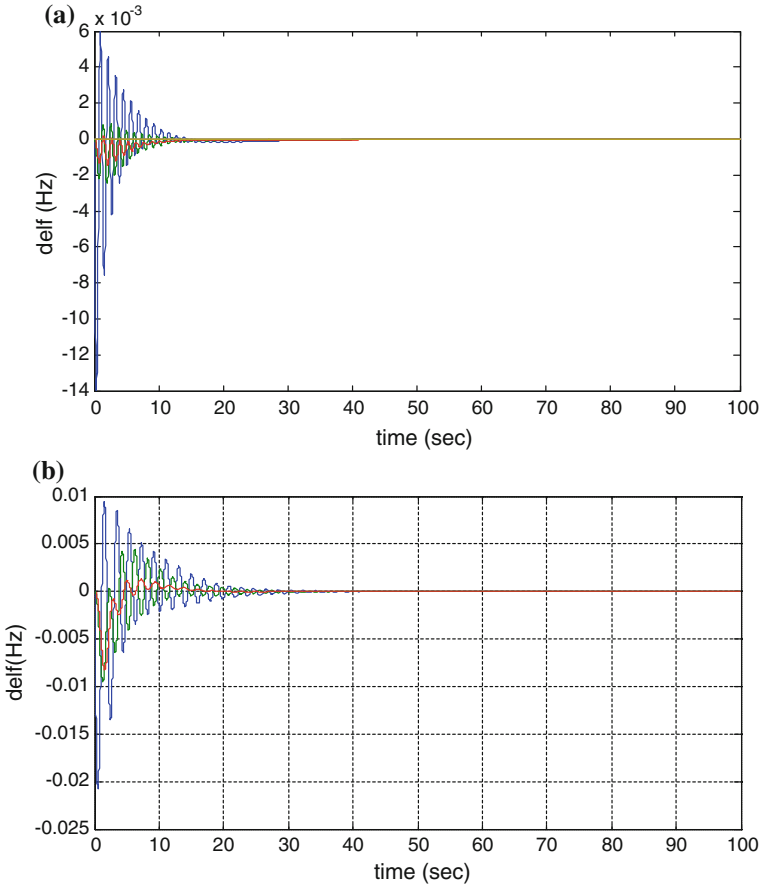


Fig. 3 Combined output response of area1, area2, area3 by using **a** BF and **b** PSO

4 Conclusion

In this paper, AGC of multiarea unequal thermal-thermal power system is presented. PSO technique is used to optimize the controller gains. In the multiarea power system, frequency response and power deviation response of tie-line are obtained for 1 % SLP. It is observed that frequency response and power deviation response settle with zero steady state error and satisfy the requirements. Also after comparison of results with Bacterial-foraging technique, it is found that PSO performs better than BF because of its fast convergence speed.

References

1. Kothari, D.P., Dhillon, J.S.: Power System Optimization, 2nd Edition, PHI, New Delhi (2010)
2. Gupta, S.K.: Power Systems Engineering, Umesh Publication (2009)
3. Kumar, C.H. Ravi, Rao, P.V. Ramana: PSO Based Fractional Order Automatic Generation Controller for Two Area Power System. Int. J. of Electrical Engg. and Tech., Vol. 5, Issue 9 (2014) 17–28
4. Kothari, D.P., Nagrath, I.J.: Modern Power System Analysis. 3rd edn., TMH, New Delhi (2009)
5. Chaturvedi, D.K., Satsangi, P.S., Kalra, P.K.: Load Frequency Control: A Generalized Neural Network Approach. Electr Power Energy Syst, Vol. 21, No. 6 (1999) 405–415
6. Demiroren, A., Sengor, N.S., Zeynelgil, H.L.: Automatic Generation Control by Using ANN Technique. Elect Power Compon Syst., Vol. 29, No. 10 (2001) 883–896
7. Ibrahim, H.E.A., Hassan, F.N., Shamer, Anas O.: Optimal PID Control of a Brushless DC Motor using PSO and BF Techniques. Ain Shams Engg. J. (2014) 391–398
8. Pandey, Shashi Kant, Mohanty, Soumya R., Kishor, Nand: A Literature Survey on Load–Frequency Control for Conventional and Distribution Generation Power Systems. Renewable and Sustainable Energy Reviews (2013) 318–334
9. Rani, Poonam, Jaswal, Ramavtar: Automatic Load Frequency Control of Multi-Area Power System using ANN Controller and Genetic Algorithm. Int. J. of Engg. Trends and Tech., Vol. 4, Issue 9 (2013)
10. Al-Hamouz, Z.M., Al-Duwaish, H.N.: A New Load Frequency Variable Structure Controller using Genetic Algorithms. Electr Power Syst Res, Vol. 55, No. 1 (2001) 1–6
11. Bevrani, H., Habibi, F., Babahajyani, P.M., Watanabe, Mitani, Y.: Intelligent Frequency Control in an AC Microgrid: Online PSO-Based Fuzzy Tuning Approach. IEEE Trans on Smart Grid, Vol. 3, Issue 4 (2012) 1935 – 1944
12. Feng, Hsuan-Ming, Horng, Ji-Hwei, Jou, Shiang-Min: Bacterial Foraging Particle Swarm Optimization Algorithm Based Fuzzy-VQ Compression Systems. J. of Information Hiding and Multimedia Signal Processing, Vol. 3, No. 3 (2012)
13. AlRashidi, M.R., EI-Hawary, M.E.: Hybrid Particle Swarm Optimization Approach for Solving the Discrete OPF Problem Considering the Valve Loading Effects. IEEE Trans on Power System, Vol. 22, Issue 4 (2007) 2030–2038
14. Das, T.K., Venayagamoorthy, G.K.: Optimal Design of Power System Stabilizers using a Small Population Based PSO. In: Proceeding of IEEE Power Engg. Society General Meeting. Montreal, Que (2006)
15. Eberhart, Russell C., Shi, Yuhui: Particle Swarm Optimization: Developments, Applications and Resources. In: Proceeding of IEEE Congress on Evolutionary Computation, Vol. 1, Seoul (2001) 81–86

16. Nanda, Janardan, Mishra, S., Saikia, Lalit Chandra: Maiden Application of Bacterial Foraging-Based Optimization Technique in Multiarea Automatic Generation Control. IEEE Trans on Power Systems, Vol. 24, No. 2 (2009)
17. Pain, Santigopal, Acharjee, Parimal: Multiobjective Optimization of Load Frequency Control using PSO. Int. J. of Emerging Tech. and Advanced Engg., Vol. 4, Issue 7 (2014)

Toward EEG Spectral Analysis of Tomographic Neurofeedback for Depression

Chamandeep Kaur and Preeti Singh

Abstract Neurofeedback (NF) or electroencephalography (EEG) biofeedback is a capable of expansion of brain–computer interface (BCI). It uses the fact of training subjects to achieve cortical oscillation modulations which has been facilitated using human–machine interface by making use of computer softwares. Up till now, many reports have focused on efficacy of NF in context of clinical and non clinical applications. In that direction, this work is focused to evaluate the spectral analysis of EEG signals for tomographic NF (a solution to EEG inverse problem). Z-score standardized low resolution electromagnetic tomography (sLORETA) NF has been provided to a patient detected with depression. Proposed work observed the increase in alpha, theta/beta ratio and decrease in beta after providing the 16 sessions. It illustrates the fact that tomographic NF could have greater impact on depression.

Keywords EEG · Neurofeedback · Human–machine interface · z-Scores · sLORETA

1 Introduction

One of the major challenges in modern society is to boost the cognitive functions, to improve cognitive impairments or psychosomatic ailments, thus, improving the quality of life. The knowledge of immense trouble linked with neurological and cognitive disorders is being considered. The progress of HMIs (Human–Machine Interfaces) has offered various strategies to provide neurorehabilitation. Neurofeedback (NF) based operant conditioning is one of them. Up till now, many reports have focused on efficacy of NF in context of clinical and non clinical

Chamandeep Kaur (✉) · Preeti Singh
UIET, Panjab University, Chandigarh, India
e-mail: ckchauhan.86@gmail.com

Preeti Singh
e-mail: preeti_singh@pu.ac.in

© Springer Science+Business Media Singapore 2017

R. Singh and S. Choudhury (eds.), *Proceeding of International Conference on Intelligent Communication, Control and Devices*, Advances in Intelligent Systems and Computing 479, DOI 10.1007/978-981-10-1708-7_10

applications. NF is achieving recognition for improving the signs of depression but more rigorous real-world researches are required to explore information of neural correlates of performance under NFT (Neurofeedback Training) to evaluate its effectivity. So, there is need to design and implement NF system to treat mild to moderate depression. Further, there have recently been developments in traditional NF procedures. The present work presents an advanced tomographic NF system based on electroencephalography (EEG) neuroimaging technique for depression. Here, superseding purpose is to examine rapidly building up evidence base for efficacy of z-score standardized low resolution electromagnetic tomography (sLORETA) NF in terms of EEG spectral power analysis.

2 What is Neurofeedback

Human–machine interface interprets various brain processes to derive external computer devices using software applications. NFT is state-of-the-art training that is based on principle of operant learning. NF accounts for permitting the individuals to change their cortical activity based on the biofeedback that is facilitated through HMIs using computer applications. The feedback is defined on the particular features of brain cortical action, so that the behavior should be influenced potentially. Subjects change their electrical activities such as amplitude, frequency, or the coherency. In this training, first of all, individual EEG signal is recorded; required intended frequency part is cut off using filtering, specified information concerned with that component is fed back using video and/or audio signal [1].

2.1 Tomographic Neurofeedback

EEG has the disadvantages of poor spatial resolution due to inverse problem and increased distance between source and the sensors. Such points account for limitations of traditional NF. Spatial nonspecificity of particular electrode site results in little spatial information from single channel EEG. This limitation can be improved by involving information that is more spatially specific and that can be achieved through electromagnetic tomographic method that is, an inverse solution method. So, major limitation of traditional method is spatial nonspecificity. General model of EEG source localization is generated expressing the experiential EEG data $S(t)$ as linear function of BES (Brain Electrical Sources) $J(t)$ according to quasi-static approximation of Maxwell's equation.

$$S(t) = GJ(t) + E \tag{1}$$

This is the branch of EEG inverse problem typical formulation [2]. So, the inverse problem deals with dilemma of estimating the distribution of BES (factors

such as orientation, position and the magnitude) from measurements of EEG that is noisy. In Eq. (1), G is gain matrix of lead fields of dipole sources and this transfer matrix is denoted as lead field matrix. E is additive noise. This estimation problem is very exigent because $J(t)$ is dimensionally much bigger than $S(t)$. Nonetheless, fairly accurate guess of $J(t)$ is possible to acquire. The nonparametric inverse solver methods include MNE (Minimum Norm Estimate), LORETA (Low Resolution Electromagnetic Tomography), sLORETA, and Bayesian approach [3], etc. Faster knowledge by low-cost EEG-based NF can be stimulated if a process is generated that provides training in a specific area of brain, which is termed as an inverse solution scheme.

2.2 z-Score sLORETA NFT

Various new methods are rising for enhancing the training designs and also it is possible in present time to identify definite brain procedures which lie beneath behavior and symptomatology so that targeted feedback can be directly provided like live z-scores. The live z-Score training is based on the normal equation given as,

$$z = \frac{x - \bar{x}}{\sigma}, \tag{2}$$

where x is current sample, $\bar{x}$ is the mean reference value and σ is the standard deviation. The amalgamating rationale of z-Score biofeedback is to emphasize extreme scores (outliers) in the direction of $Z = 0$, which is arithmetical center of a group of healthy normals.

The sLORETA is based on least square (min two norms) solution which is discrete, distributed, linear, and instantaneous solution of inverse problem. MNE can be changed to noise-normalized methods like sLORETA by conversion to statistical parametric maps considering the noise. It regiments the source distribution a posteriori by taking variance of each projected source,

$$\hat{J}_{\text{sLORETA}} = \hat{J}^{T}_{\text{MNE},l}\left\{\left|V_{\hat{J}}\right|_{ll}\right\}^{-1} \tag{3}$$

The $\hat{J}_{\text{MNE},l}$ is the density estimate of current density of lth voxel as defined by MNE. $V_{\hat{J}}$ is variance of current density estimate and $\left\{\left|V_{\hat{J}}\right|_{ll}\right\}$ is diagonal block at position l of resolution matrix $V_{\hat{J}}$. SLORETA is not the estimation of intensity of source but its probability to reveal high amplitude compared to others [4]. One study based on sLORETA concluded important aspects of tNF albeit no significant improvement observed in the ROT, which was, ACC (Anterior Cingulate Cortex) [5].

Another new domain of NF has been shown relevant to *z*-scores. LORETA and sLORETA can be shared with *z*-scores, so that each of the brain region is estimated in comparison with a database of brain action.

3 Literature Review

NF field was started in 1960s with experiment conducted by Kamiya et al. who proposed the possibility of learning brain activity controls with the help of feedback in the form of EEG-based frequency power, ERP (Event Related Potential), and SCP (Slow Cortical Potential) protocols [6]. Later on, various successive studies showed successful efficacy of NF for ADHD (Attention deficit hyperactivity disorder), epilepsy, schizophrenia, and many more applications [7–9]. It has been theorized that NF can be used as an alternate to antidepressants [10]. Baehr et al. theorized NF to be effective than psychotherapy for improving symptoms of depression disorders [11]. Hammond acknowledged intense declines in depression symptoms after providing NF and photic stimuli [12]. Another research concluded the alpha–theta NFT for alchoholics with symptoms of depression to be effective [13]. Also reducing the beta3 frequencies could have more impact on the analysis [14]. There are limited studies taking tomographical specificity into consideration. In that direction, an individualized protocol has been designed for depression in this paper by using new design measure like *z*-Score sLORETA-based NF training.

4 Methodology

4.1 Neurofeedback Protocol and Data Collection

EEG biofeedback has been provided using the BrainMaster Atlantis hardware to a single patient detected for depression on the basis of the (i) rating scale scores (ii) after comparing the deviances in standard deviations from normative database stored in Neuroguide software. Total 16 sessions, each of 20 min has been provided by using 19 electrode *z*-scores based PZOKUL sLORETA training. Individualized qEEG (quantitative EEG) protocol was provided for each session. Sampling rate of the data is 256 Hz.

4.2 EEG Signal Processing

First of all, EEG signals in edf (European data format) were preprocessed using EEGLAB toolbox. For analyzing the NF system, relative powers of EEG were

analyzed. The discrete wavelet transform with db5 wavelet function was used for calculating the relative powers. Also, for some of the bands, ratios of corresponding powers were evaluated for all the sessions.

5 Results and Discussion

Main aim of the present paper was to find out the relative power changes in EEG bands. Along with it, power ratio of theta/beta has been identified within each session and from session 1 to 16. For evaluating the importance of EEG changes within each session and with the number of sessions, statistical analysis using one-way ANOVA has been performed with $\alpha = 0.05$.

EEG spectral changes within each session: Results show that within a session, changes were significant for relative powers of theta, alpha, and beta. Within the session theta and alpha were increasing with more significant change for alpha with $F(1, 7)$ 11.8 with $p = 0.01$. The value of beta was decreasing with $p < 0.01$ as shown in Table 1. Figure 1a shows the average theta/beta ratio change within 20 min of a session.

EEG spectral changes across the sessions: ANOVA supports the changes in EEG powers with significant change in alpha with $F(1, 31) = 35.4$ and for theta/beta ratio as $F(1, 31) = 36.7$ with $p < 0.001$ as shown in Table 2. Increased alpha activity and decreased beta accounts for relaxation. Figure 1b shows the average change in theta/beta ratio from session 1–16. As overall alpha is increasing, it may represent alleviating the symptoms of depression after the training.

Table 1 ANOVA results for EEG changes within a session

EEG spectral measure	Degree of freedom	F statistic	P	Direction
Relative_Theta_Power	7	6.97	0.03	Increase
Relative_Alpha_Power	7	11.8	0.01	Increase
Relative_Beta_Power	7	14.7	0.008	Decrease
Theta/Beta ratio	7	12.07	0.01	Increase

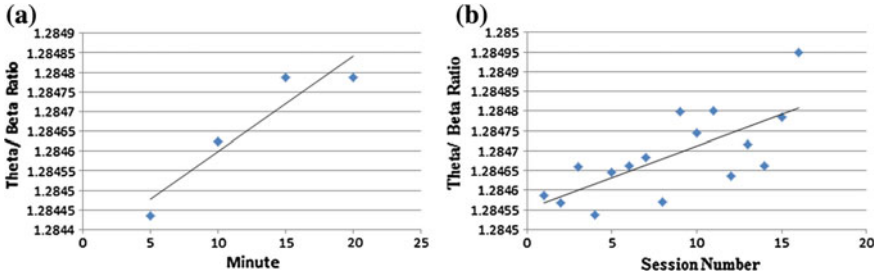


Fig. 1 Average variations in Theta/Beta ratio for **a** within a session for 1–20 min and **b** across 1–16 sessions

Table 2 ANOVA results for EEG band changes across 1–16 sessions

EEG spectral measure	Degree of freedom	F statistic	P	Direction
Relative_Theta_Power	31	14.4	0.006	Increase
Relative_Alpha_Power	31	35.4	<0.001	Increase
Relative_Beta_Power	31	20.6	<0.001	Decrease
Theta/Beta ratio	31	36.7	<0.001	Increase

6 Conclusion

In recent years, there has been a great deal on the progress of HMIs that have offered various strategies to provide neurorehabilitation. NF uses the fact of training subjects to achieve cortical oscillation modulations, which in the past has been extensively explored for treatment of conditions correlated with altered cortical oscillations. In this paper, it has been examined whether NF training can alter cognitive functions in depression disorder. To achieve this, pre and post qEEG analysis has been done after providing *z*-Score sLORETA NFT to a single subject. The power analysis has shown that there is an improvement in EEG measures. More alpha and theta activity with reduced beta activity accounts for reduction of symptoms of depression. Further, a larger effect size- based analysis with inclusion of control group is being planned. Also, more EEG measures can add up to the efficacy of the modality.

References

1. Gruzelier, J.H.: EEG-Neurofeedback for Optimising Performance. II: Creativity, the Performing Arts and Ecological Validity. Neuroscience and Biobehavioral Reviews, Vol. 44, No. 1 (2014) 142–158
2. Galka, A., Yamashita, O., Ozaki, T., Biscay, R. and Valdés-Sosa, P.: A Solution to the Dynamical Inverse Problem of EEG Generation Using Spatiotemporal Kalman Filtering. NeuroImage, Vol. 23, No. 2 (2004) 435–453
3. Grech, R., Cassar, T., Muscat, J., Camilleri, K.P., Fabri, S.G., Zervakis, M., Xanthopoulos, P., Sakkalis, V. and Vanrumste, B.: Review on Solving the Inverse Problem in EEG Source Analysis. Journal of NeuroEngineering and Rehabilitation, Vol. 5, No. 25 (2008) 1–33
4. Galka, A., Yamashita, O., Ozaki, T., Biscay, R., Valdés-Sosa, P.: A solution to the dynamical inverse problem of EEG generation using spatiotemporal Kalman filtering. NeuroImage 23 (2004) 435–453
5. Liechti, M.D., Maurizio, S., Heinrich, H., Jäncke, L., Meier, L., Steinhausen, H.C., Walitza, S., Drechsler, R. and Brandeis, D.: First clinical trial of tomographic neurofeedback in attention-deficit/hyperactivity disorder: evaluation of voluntary cortical control. Clin Neurophysiol., Vol. 123, No. 10 (2012) 1989–2005
6. Kamiya, J.: Operant Control of the EEG Alpha Rhythm and Some of Its Reported Effects on Consciousness. In: Tart C.T. (ed.), Altered States of Consciousness. Wiley, New York (1969) 519–529

7. Arns, M., de-Ridder, S., Streh, U., Breteler, M. and Coenen, A.: Efficacy of Neurofeedback Treatment in ADHD: The Effects on Inattention, Impulsivity and Hyperactivity: A Meta-Analysis. Clinical EEG Neuroscience, Vol. 40, No. 3 (2009) 180–9
8. Bakhtadze, S., Janelidze, M. and Khachapuridze, N.: Impact of Neurofeedback in Patients with Epilepsy. Epilepsy & Behavior, Vol. 17, No. 4 (2010) 598–599
9. Gruzelier, J.H.: EEG-Neurofeedback for Optimising Performance. I: A Review of Cognitive and Affective Outcome in Healthy Participants. Neuroscience and Biobehavioral Reviews, Vol. 44, No. 1 (2014) 124–141
10. Hammond, D.C.: Neurofeedback Treatment of Depression and Anxiety. Journal of Adult Development, Vol. 12, Nos. 2/3 (2005) 131–137
11. Baehr, E., Rosenfeld, J.P. and Baehr, R.: The Clinical Use of An Alpha Asymmetry Protocol in the Neurofeedback Treatment of Depression. Journal of Neurotherapy: Investigations in Neuromodulation, Neurofeedback and Applied Neuroscience,Vol. 2, No. 3 (1997) 11–18
12. Hammond, D.C.: Neurofeedback Treatment of Depression with the Roshi. Journal of Neurotherapy: Investigations in Neuromodulation, Neurofeedback and Applied Neuroscience, Vol. 4, No. 2 (2000) 45–56
13. Saxby, E. and Peniston, E.G.: Alpha-Theta Brainwave Neurofeedback Training: An Effective Treatment for Male and Female Alcoholics with Depressive Symptoms. Journal of Clinical Psychology, Vol. 51, No. 1 (1995) 685–693
14. Dias, A.M. and Deusen, A.V.: A New Neurofeedback Protocol for Depression. The Spanish Journal of Psychology, Vol. 14, No. 1 (2011) 374–384

Comparison of Performance Metrics of ModAODV with DSDV and AODV

Mrinal Kanti Deb Barma, Rajib Chowdhuri, Sudipta Roy and Santanu Kumar Sen

Abstract In this paper, an adaptive routing in Mobile Adhoc Network (MANET) is presented using special neighbors on different routes. The routing table of each node is computed and stored in a metric. The path with the minimum cost is selected as the primary routing path among all feasible paths. The Adhoc On—Demand Distance Vector (AODV) Routing protocol is modified in such a way that only the destination node will respond to a route request which greatly reduces the transmission of control data packets in a network. The performance of modified AODV is evaluated based on metrics such as throughput, packet delivery ratio, and normalized routing overhead.

Keywords MANET · Throughput · Packet delivery ratio · Normalized routing overhead

1 Introduction

The primary motivation toward the design and development of a Distance Vector Routing (DVR)-based hybrid protocol for Mobile Adhoc Network (MANET) and WSN kind of networks is mainly because of the simplicity and elegance of the DVR algorithm, which is a traditional routing protocol based on Bellman Ford's

M.K.D. Barma (✉) · Rajib Chowdhuri
Department of Computer Science and Engineering, NIT Agartala, Jirania, Tripura, India
e-mail: mkdb06@gmail.com

Rajib Chowdhuri
e-mail: rjbchwdhri@gmail.com

Sudipta Roy
Department of Computer Science and Engineering, Assam University, Silchar, India
e-mail: sudipta.it@gmail.com

S.K. Sen
Department of Computer Science and Engineering, GNIT Kolkata, Kolkata, India
e-mail: santanu.sen@ieee.org

© Springer Science+Business Media Singapore 2017

R. Singh and S. Choudhury (eds.), *Proceeding of International Conference on Intelligent Communication, Control and Devices*, Advances in Intelligent Systems and Computing 479, DOI 10.1007/978-981-10-1708-7_11

algorithm that later on got rejected mainly because of the Count-To Infinity (CTI) problem of the DVRA. The second motivation forwards the development of DVR-based routing algorithm for MANETs because of its neighbor exchange-based routing technique, through which a route can view its whole world only through a neighbor, and hence, need not to keep track of the whole network, thereby reducing the burden of bandwidth and battery supply. Routing is the heart of a network and optimality and reliability are the keen requirements for the success of such routing protocol.

The goal of this paper is to modify the routing table of original Adhoc On—Demand Distance Vector (AODV) protocol based on special neighbors of each route to obtain a modified version of AODV protocol termed as ModAODV whose performance is compared with that of AODV and DSDV in terms of throughput, packet delivery ratio, and normalized routing overhead.

2 Comparison of ModAODV Protocol with DVR Protocol

The important disadvantages of DVR protocol is as follows:

Slow Convergence Problem: When there is an increase in the cost of any link or there is a link failure between two neighboring nodes in a network or internetwork, the algorithm, in the worst case, may require an excessive number of iterations to converge or to terminate. The slow convergence phenomenon actually results from the propagation of a bad news which implies a loss or increased distance of a route. In the DVRA, the bad news travels slowly unlike the good news [1, 2].

Count to Infinity problem: DVR Algorithm suffers from the serious problem of CTI [1, 3–5] which sometimes occurs following a link or router failure, due to unending routing loops involving two or more routers. IP packets going round in loops are ultimately dropped after expiry of the Time-to-Live (TTL), but they generate considerable amount of unproductive traffic before being dropped.

Oscillation Problem: Because of the need to always use the shortest path, there may be frequent switching of routes caused by even small increase or decrease in the link costs. This frequent route switching gives rise to instability in routing and this problem is known as the route oscillation problem [2].

3 Identification and Utilization of Special Neighbors

Distance Vector Routing Table (DVRT) is primarily used for identifying special neighbors which are used in making ModAODV efficient and practical with fast convergence and no CTI problem. The procedure of identification of special neighbor and its method of utilization in case of both topological and traffic change is based on the example network shown in Fig. 1.

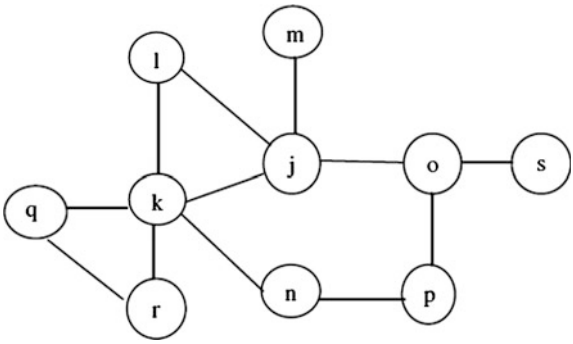


Fig. 1 Sample network with special neighbors of router *j*

3.1 Forwarding Neighbor (FN)

Identification—A router R_j identifies its current FNs for different destinations by processing the entries in its own routing table $DVRT_j$. If, in the *i*th entry in $DVRT_j$, R_j finds that $DEST_i = R_i$ but Next Hop $NH_i = R_k$ where $R_k \neq R_i$, then R_j identifies R_k as its FN for reaching R_i and notes it down in its Neighbor Table NT_j. However, if R_j finds that $DEST_i = R_i = NH_i$, then it identifies R_i as a neighboring router.

3.2 Dependent Neighbor (DN)

Identification—If a router R_k presently reaches a destination R_i via its neighbor R_j, i.e., if R_k depends on R_j for reaching R_i, then R_k is a Dependent Neighbor (DN) of R_j for reaching R_i. The routers R_k, R_l, and R_m, but not R_n, in Fig. 1 are all DNs of R_j for reaching the destination R_i.

Utilization—Router R_j utilizes its DNs in the ModAODV protocol when R_j is unable to find an alternative shortest path to destination. In such scenario, it permits some time to R_k to discover and advertise a new route (not via R_j) to reach destination. Only, thereafter, R_j considers that route as a contender for becoming the alternative shortest path to reach Destination.

3.3 Co-Neighbor (CN)

Identification—If three routers R_j, R_k, and R_l, form a triangle in a network graph, then any two of the three routers are mutual CNs of each other for the third one, e.g., in Fig. 1, R_k is a CN of R_j for R_l, R_l is a CN of R_j for R_k, R_j is a CN of R_k for R_l, and so on.

Utilization—The utility of a CN is enormous because it can help to isolate a link failure from a router failure to yield an extremely rapid convergence. In case R_j ever

loses its direct communication with a Multi Connected Neighbor (MCN) R_k, and has at least one CN say, R_l, then, R_j can statistically decide, with the help of its CN R_l, whether the router R_k itself has failed or the connecting link R_j, R_k has failed. Thus if R_j, being unable to communicate directly with its MCN neighbor R_k, discovers that R_l, its CN for R_k, is also unable to communicate with R_k, then both R_j as well as R_l, conclude that R_k itself has failed. On the other hand, if R_l can still communicate with R_k, then R_j concludes that its link R_j, R_k has failed. In the former case, both R_j and R_k will recognize the failed router R_k as a Lost Destination and will quickly disseminate this vital information throughout the network to achieve an extremely fast convergence. In the latter case, R_j will simply choose to reach R_k indirectly via its CN R_l and this indirect route to R_k will be shortest if the distance metric is hop count.

ModAODV is implemented based on the following general assumptions:

(i) Each router maintains an interval timer called Periodic Update Interval Timer that will periodically interrupt it for performing the periodic update of its DVRT and for sending copies of this updated DVRT to all neighbors.
(ii) Each router has, one interval timer called the Neighbor Interval Timer for all its neighbors to check that at least one DVRT is received from that neighbor within each Periodic Update Interval.
(iii) Each router has one Echo Timer for each neighbor which times out if any neighbor fails to send back an ECHO RESPONSE packet in response to an ECHO REQUEST packet sent by the router to that neighbor.
(iv) A DVRT has N entries where each entry corresponds to each known router in the N-node network. Each entry has 3 fields, namely, the identity of a destination router, the estimated distance (metric) of this router and, finally, the identity of the Next-Hop (NH) router, i.e., the FN in case of any remote router, for reaching that destination.

4 Results and Analysis

We use network simulator ns-2.34 [6, 7] and the simulations were performed with a minimum of 11 nodes to a maximum of 30 nodes and the nodes were of unicast type. The maximum number of packets in an interface queue which is known as Interface Queue Length (IFQLEN) is varied from 10 to 50 (Table 1).

4.1 Measuring Throughput

Throughput = (Total number of successfully received data packet/(Time of received data packet − Time of sent data packet)).

Table 1 Parameters used in simulation

Parameter	Value
Area of the network	500 m × 400 m
Simulation time	150 s
Packet size	512 Bytes
MAC type	IEEE 802.11
Interface queue type	Queue/DropTail/Priqueue
Mobility model	Random waypoint
Traffic type	CBR

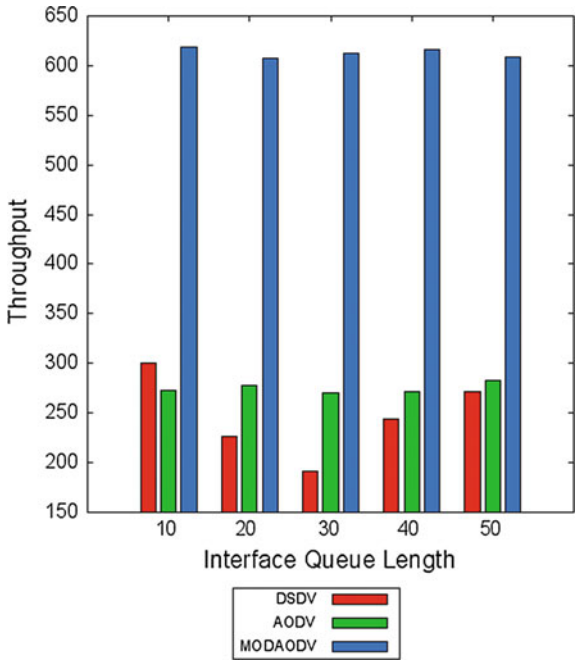


Fig. 2 Measurement of throughput with increase in interface queue length

In the first experiment, 5 (five) simulations were performed for each routing protocol to obtain the values of throughput by varying the size of IFQLEN from 10 to 50.

Figure 2 shows the impact of increasing IFQLEN on throughput. The number of nodes used in this experiment was 11. The maximum speed was V_m = 20.0 m/s and pause time was 2.0 s and it is observed that throughput of modified AODV doubles the throughput of original AODV and DSDV with increase in the number of packets in the interface queue.

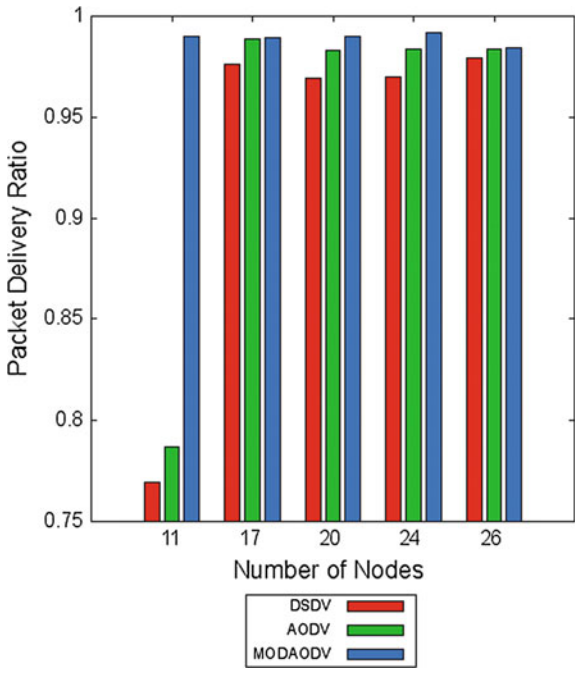


Fig. 3 Measurement of packet delivery ratio with increase in number of nodes

4.2 Measuring Packet Delivery Ratio

PDR = $\sum$ (Number of packets received by all sinks)/$\sum$ (Number of packets send by all sources).

In the second experiment, 5 (five) simulations were conducted for each routing protocol to obtain the values of PDR by varying the number of nodes from 11 to 26 and in the third experiment, the speed of nodes was varied from 40 to 90 m/s.

Figure 3 shows the impact of increasing the number of nodes on PDR. ModAODV delivers much higher data packets which is almost 5.62 % higher than that of AODV and by 4.38 % higher than DSDV. In this experiment, pause time was 2.0 s and the speed of nodes was 20 m/s.

Figure 4 shows the impact of increasing the speed of nodes on PDR. ModAODV delivers higher data packets which is almost 2.22 % higher than original AODV and 1.14 % higher than DSDV. In this experiment, 30 (thirty) nodes were taken and pause time was 20 m/s.

4.3 Measuring Normalized Routing Overhead

Normalized Routing Load (NRL) = (Amount of routing-related transmission)/(Total amount of data-related transmission).

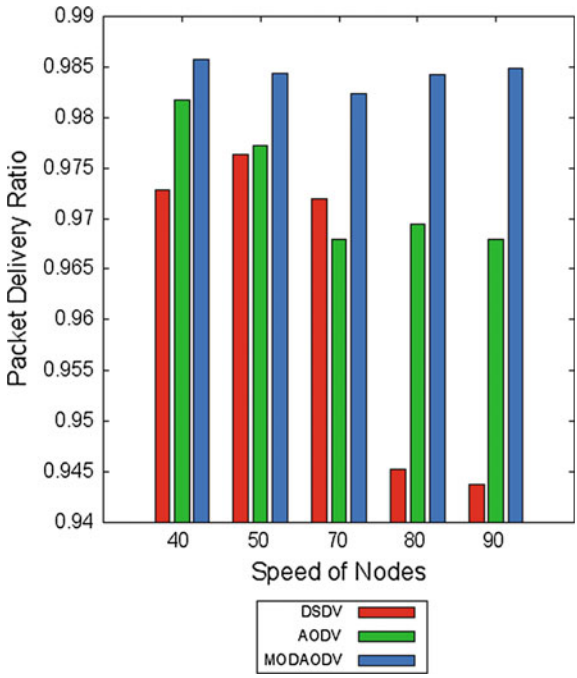


Fig. 4 Measurement of packet delivery ratio with increase in speed of nodes

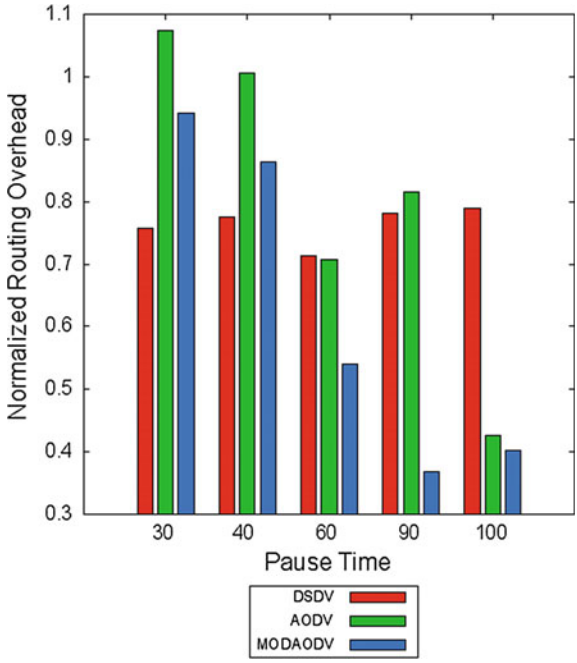


Fig. 5 Measurement of routing overhead with increase in pause time

In this experiment, 5(five) simulations were performed for each routing protocol to obtain the values of NRL by varying the pause time of nodes from 30 to 100 s.

Figure 5 shows the impact of increasing pause time of nodes on NRL which clearly depicts that the routing overhead of ModAODV is much lower than that of original AODV and DSDV except when pause time were 30 s and 40 s, overhead of ModAODV is a bit higher compared to DSDV. In this experiment, 30 (thirty) nodes were taken, speed of nodes was 20 m/s, and the size of IFQLEN was 50.

5 Conclusion

This paper compares the performance of a new routing protocol called ModAODV with two foremost routing protocols DSDV and AODV using ns-2 simulations. The results show that throughput of ModAODV doubles the throughput of original AODV and DSDV with increase in IFQLEN. The impact of increasing the number of nodes and speed of nodes depicts that ModAODV delivers much higher data packets compared to AODV and DSDV. The impact of increasing the pause time of nodes depicts that original AODV and DSDV has highest routing overhead compared to ModAODV. Throughput decreases in case of DSDV since it needs to advertise both periodic and event-driven updates but throughput of AODV remains stable. Thus DSDV consumes more bandwidth compared to DSDV.

As our future work, we will try to include one more additional feature to this ModAODV protocol like acknowledgement of data by the destination to the source.

References

1. A.S. Tenenbaum, “Computer Networks”, 5th Ed., Pearson Education Asea, 2010.
2. D.E. Comer, “Internetworking with TCP/IP”, 4th Ed., Pearson Education, Singapore, 2005.
3. S. K. Ray, S. K. Paira and S. K. Sen, “Modified Distance Vector Routing Avoids Counting - To-Infinity Problem”, Proc. Intl. Conf. CODIS 2004, Kolkata, pp. 31–34, 2004.
4. S. K. Ray, J. Kumar, S. K. Sen and J. Nath, “Modified Distance Vector Routing Scheme for a MANET”, Proc. Of the 13th National Conference on Communications (NCC), IIT Kanpur, pp. 197–201, 2007.
5. A. Leon-Garcia and Indra Widjaja, “Communication Networks”, 2nd Ed., Tata McGraw-Hill, 2004.
6. K. Fall and K. Varadhan, “The NS Manual, (formerly ns Notes and Documentation)”, The VINT Project: A Collaboration between Researchers at UC Berkeley, LBL, USC/ISI and Xerox PARC, 2011.
7. Yan Li, “Mobile Ad Hoc Network Simulation: Analysis and Enhancements”, PhD thesis, Heriot-Watt University, Edinburgh, UK, 2008.

Detection and Location of Faults in Three-Phase 11 kV Underground Power Cables by Discrete Wavelet Transform

D. Prabhavathi, M. Surya Kalavathi and K. Prakasam

Abstract This chapter presents the discovery and area of deficiency in underground links by wavelet change as it is a standout among the most effective instruments for dissecting nonstationary signs. The wavelet technique is productive and intense to assess issues when they occur in underground links, and it has been broadly utilized as a part of electrical force frameworks. Estimation and determination of the issue in an underground link is critical to clear the shortcoming rapidly and to restore the supply with the least intrusion. The high voltage power link 11 kV, 100 km is demonstrated using a MATLAB® platform. Mexican Hat and coif let wavelet transform are utilized to extract the transient signals and the waveforms are demonstrated. The outcomes demonstrate that the wavelet transform is superior to all other conventional methods.

Keywords Cable · Fault · Traveling · Mexican Hat

1 Introduction

When all is said in done there are three dominating sorts of faults in underground power links: single line to ground (LG) deficiency, double line to ground (LLG) shortcoming, and the triple line to ground (LLLG) issue. The single line to earth deficiency is the most widely recognized issue and happens generally every now and again. Shortcoming recognition and area taking into account the issue-instigated current or voltage voyaging waves have been contemplated for

D. Prabhavathi (✉) · K. Prakasam
Department of EEE, JNTUA, Anantapuram, AP 515 002, India
e-mail: prabhavathi10@gmail.com

K. Prakasam
e-mail: gvitgem@gmail.com

M. Surya Kalavathi
Department of EEE, JNTUH, Hyderabad, TS 500 085, India
e-mail: munagala12@yahoo.co.in

© Springer Science+Business Media Singapore 2017

R. Singh and S. Choudhury (eds.), *Proceeding of International Conference on Intelligent Communication, Control and Devices*, Advances in Intelligent Systems and Computing 479, DOI 10.1007/978-981-10-1708-7_12

quite a long time. In every one of these systems, the area of the flaw is resolved utilizing the high recurrence drifters. The shortcoming area in light of the voyaging waves can for the most part be sorted into two: single finished and twofold finished. For single finished, the current or voltage signs are measured toward one side of the line and the blame area depends on the investigation of these signs to distinguish the reflections that happen between the measuring point and the issue. For the twofold finished technique, the season of entry of the primary shortcoming produced signs is measured at both closures of the lines utilizing synchronized timers.

2 Strategies for Fault Detection and Localization

By examination of the transient signs at all stages demonstrated in the force link, the characterization of deficiency can be made. On the off chance that the transient sign shows up at only one stage the shortcoming is a single line to ground issue (if it shows up at two stages, LLG, at three stages, an LLLG issue). As a rule, the created transient signs brought on because of the deficiency are observed to be nonstationary and are of a wide band of recurrence; when a flaw happens in the system, the produced transient signs go into the system. On landing in an irregular position, the transient wave is by and large reflected somewhat and the rest of the occurrence to the line impedance. The transient signs reflected from the end of the line fly out back to the flaw point where another reflection happens because of the irregularity of impedance. Here in this flaw distinguishing proof and confinement plan, to catch these transient flags the wavelet investigation approaches have been utilized all the more definitely for wavelet examination. The flaw area can be done by contrasting the flying mode wavelet coefficient with deciding the moment when the vitality of the signals achieves its crest quality. The separation between the shortcoming point and the transport of the blamed branch is expressed by the accompanying comparison (1).

$$D = v\,X\left(\frac{t_{\mathrm{d}}}{2}\right) \tag{1}$$

where D speaks to the distance and t_{d} is the time distinction between two back-to-back tops of the wavelet change coefficients of the recorded current and is the wave proliferation speed in the airborne mode. An underground link of length 100 km has been utilized for issue examination. The velocity of a propagation transient wave in the 11 kV underground link framework is 1.9557×10^5 km/s, and examining time of 10 μs has been utilized. The accompanying figure shows the single line graph of the re-created framework with an 11 kV, 50 Hz, 50 km underground link. To perform the framework examination, different flaw conditions, for example, LG, LLG, and LLLG shortcomings have been considered and related identification parameters have been achieved. The execution has been assessed as far as % mistake and the deviation from genuine qualities. The general

procedure of shortcoming discovery and area has been expert. Consider a three-stage link line of length associated between transport A and transport B, with trademark impedance and voyaging wave speed of. In this re-creation model it has been found that if a shortcoming happens at a separation from transport, this will show up as a sudden infusion at the issue point. This infusion will travel like a wave "surge" along the line in both bearings and will keep on skipping forward and backward between the issue point and the two terminal transports until arriving at the post-blame unfaltering state. The separation to the issue point can be ascertained utilizing the voyaging wave hypothesis. Let and relates to the times at which the modular signs wavelet coefficients in scale 1 demonstrate their introductory crests for signs recorder at transport and transport B. The postponement between the flaw discovery times at the two closures can be resolved. Once the parameter is resolved, the flaw area from transport A can be assessed according to the accompanying expression (2).

$$X_2 = X - \frac{(t_1 - t_2)V}{2} \tag{2}$$

On the other hand the deficiency area can be figured from transport B as it takes after expression (3).

$$X_1 = X - \frac{(t_2 - t_1)V}{2} \tag{3}$$

Here is thought to be 1.9557×10^5 km/s, with examining time of 10 μs and the aggregate line length 50 km. In the above scientific model the variable and the separation to the deficiency is the time distinction between two back-to-back crests of the wavelet change coefficients of the recorded current and is the wavespread speed (propagation velocity).

2.1 Wavelet Transform

A wavelet is a scientific capacity used to isolate a given capacity or nonstop time signal into various scale parts. Normally one can dole out a recurrence reach to every scale part. Every scale part can then be considered with a determination that matches its scale. A wavelet change is the representation of a capacity by wavelets. The wavelets are scaled and deciphered duplicates (known as "little girl wavelets") of a limited length or quick rotting wavering waveform (known as the "mother wavelet"). Wavelet changes have points of interest over conventional Fourier changes for speaking to capacities that have discontinuities and sharp crests, and for precisely deconstructing and recreating limited, nonoccasional, and/or nonstationary signs.

Wavelet changes are grouped into discrete wavelet changes (DWTs) and persistent wavelet changes (CWTs). In the wavelet change we ought to note that both

DWT and CWT are nonstop time (simple) changes. They can be utilized to speak to ceaseless time (simple) signals. CWTs work over each conceivable scale and interpretation whereas DWTs utilize a particular subset of scale and interpretation qualities or representation matrix. There are a substantial number of wavelet changes each suitable for various applications.

3 Scheme of Evaluation of Proposed System

In the proposed framework, the creators select all the conceivable instances of ground flaws to delineate the execution of the proposed method under deficiency conditions. The deficiency area for LG, LLG, and LLLG is achieved by ordinary technique for both 25 and 50 km and the rate of blunder is assessed according to the formulae as appear underneath in Eq. (4) and is classified in Tables 1 and 2. In the following stage LG deficiency is chosen as the re-creation case and blame areas are organized alongside % mistake to analyze the deviation from the genuine qualities utilizing wavelet change (Mexican Hat and coif let), also in the second stage the LLG flaw is chosen and in the last stage the LLLG issue is chosen (Figs. 1 and 2).

$$D = \left(\frac{\text{Actual distance} - \text{Estimated distance}}{\text{Actual Length of the cable}} \right) 100 \tag{4}$$

4 Simulation Results of the Proposed System

The outcomes from the customary strategy and also wavelet transform (Mexican Hat and coif let) appear in Figs. 3, 4, 5, 6, 7, 8, 9, 10, 11, 12, 13, 14, 15, 16, 17, 18, 19 and 20 and are contrasted with real separation and organized in Tables 1 and 2.

Table 1 Percentage error evaluated for 25 km

Fault type	Actual distance (km)	Estimated distance (without wavelet) (km)	Mexican Hat (km)	Coif let (km)
LG	25	29	25.02	25.11
LLG	25	27.12	25.04	22.07
LLLG	25	31.22	25.09	25.05

Table 2 Percentage error evaluated for 50 km

Fault type	Actual distance (km)	Estimated distance (without wavelet) (km)	Mexican Hat (km)	Coif let (km)
LG	50	57	50.04	50.71
LLG	50	48.61	50.06	50.19
LLLG	50	59.45	50.14	50.13

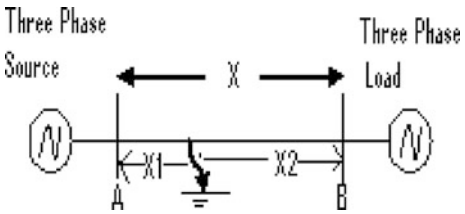


Fig. 1 Single line diagram of three-phase 11 kV, 100 km underground cable

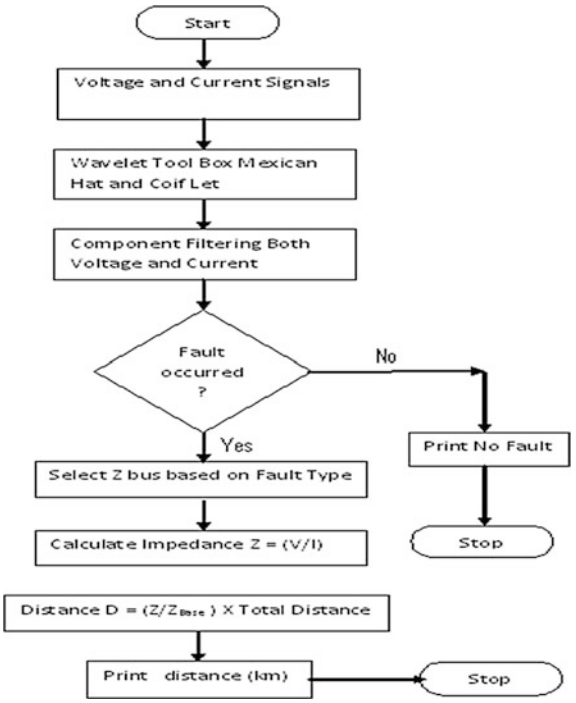


Fig. 2 The overall flowchart of the proposed algorithm

It is found that this calculation can identify flaws with 100 % precision. Subsequently, it is found that the use of the wavelet change (Mexican Hat and coif let) is a preferred tool for identifying and finding the shortcoming focuses in underground links precisely.

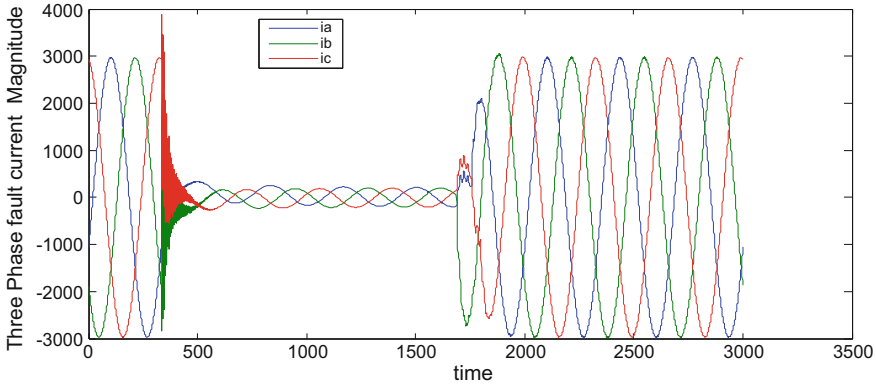


Fig. 3 Three-phase current for LLLG issue at 25 km

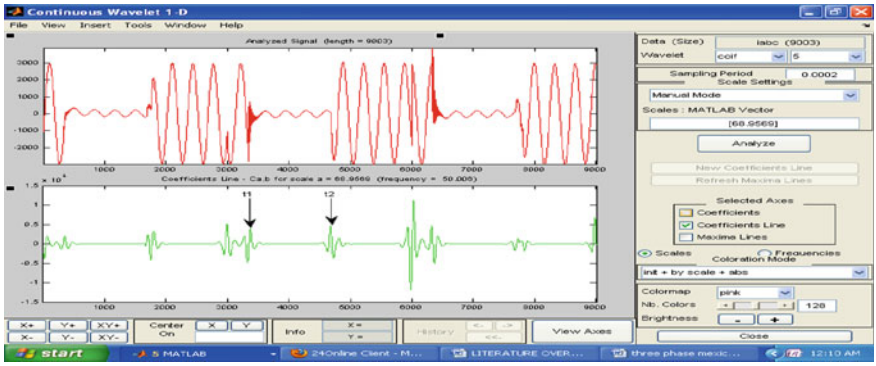


Fig. 4 Three-phase current for LLLG issue at 25 km (Coif let)

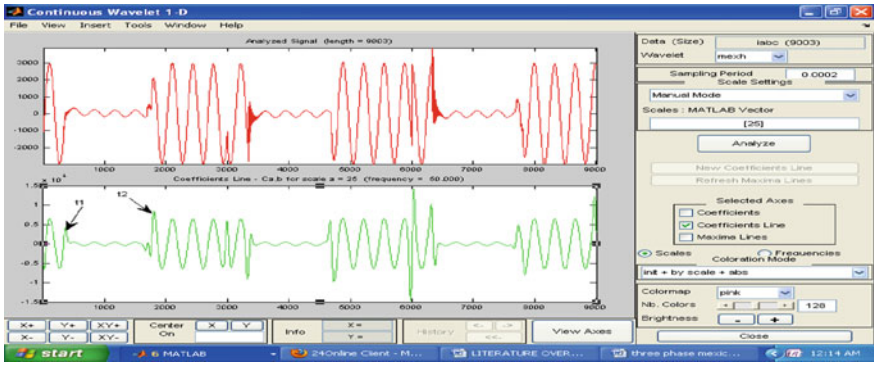


Fig. 5 Three-phase current for LLLG deficiency at 25 km (Mexican Hat)

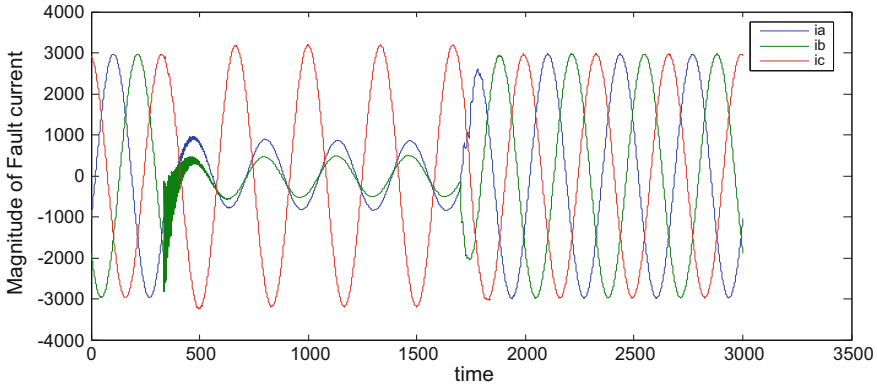


Fig. 6 Two-phase current for LLG deficiency at 25 km

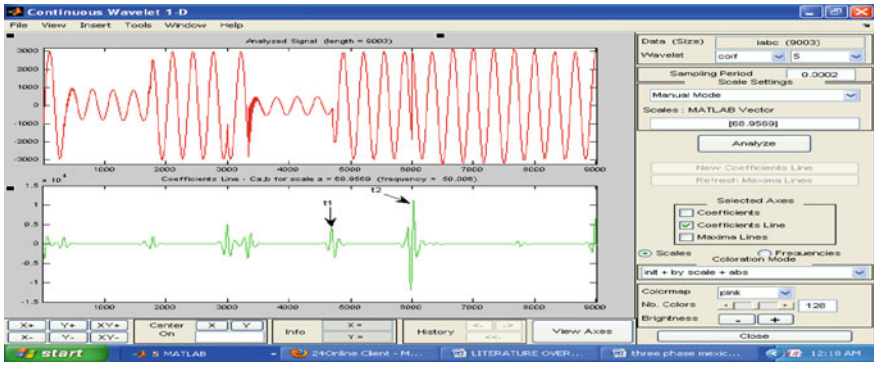


Fig. 7 Two-phase current for LLG shortcoming at 25 km (Coif let)

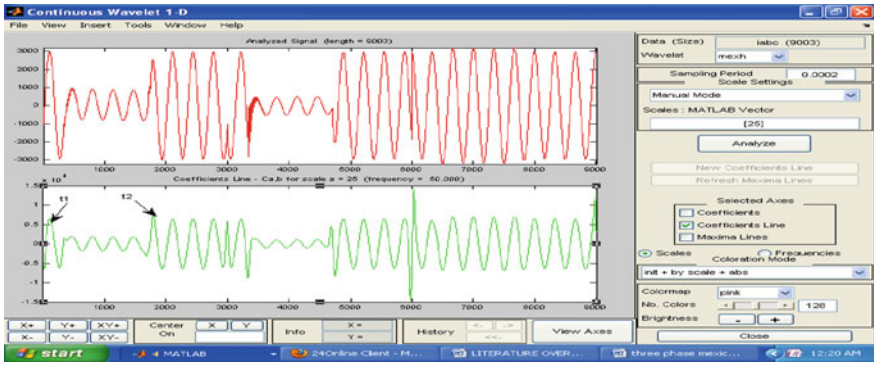


Fig. 8 Two-phase current for LLG shortcoming at 25 km (Mexican Hat)

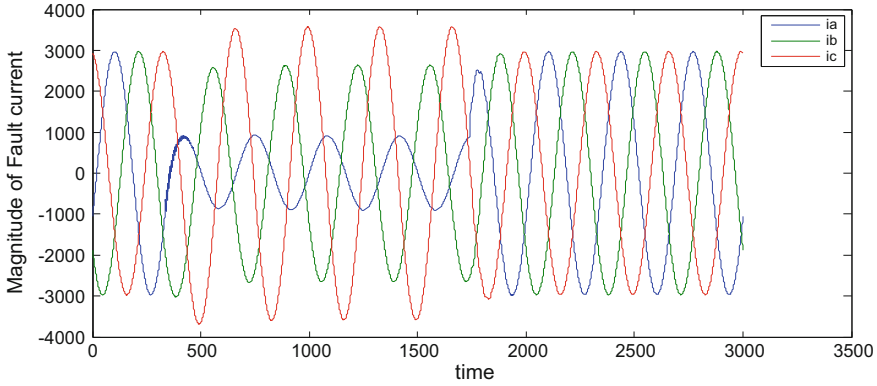


Fig. 9 Single-phase current for LG deficiency at 25 km

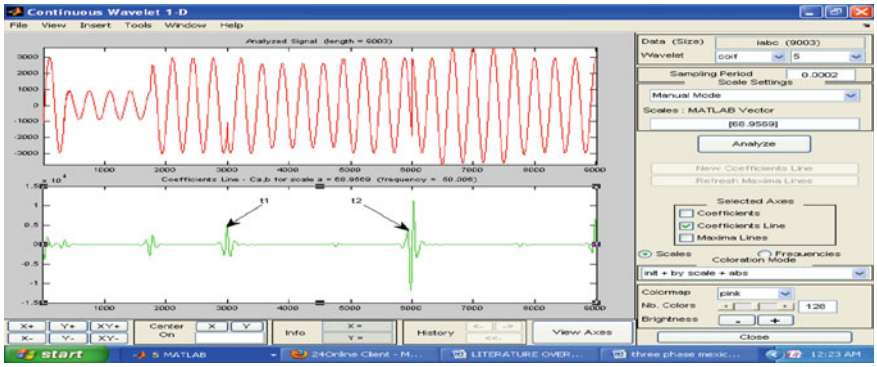


Fig. 10 Single-phase current for LG deficiency at 25 km (Coif let)

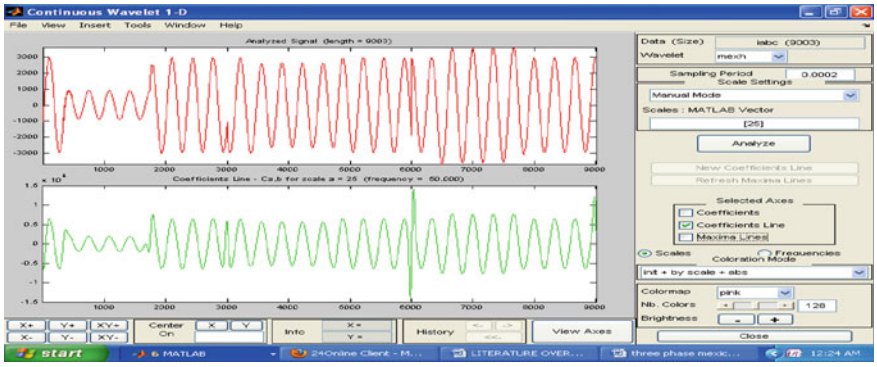


Fig. 11 Single-phase current for LG issue at 25 km (Mexican Hat)

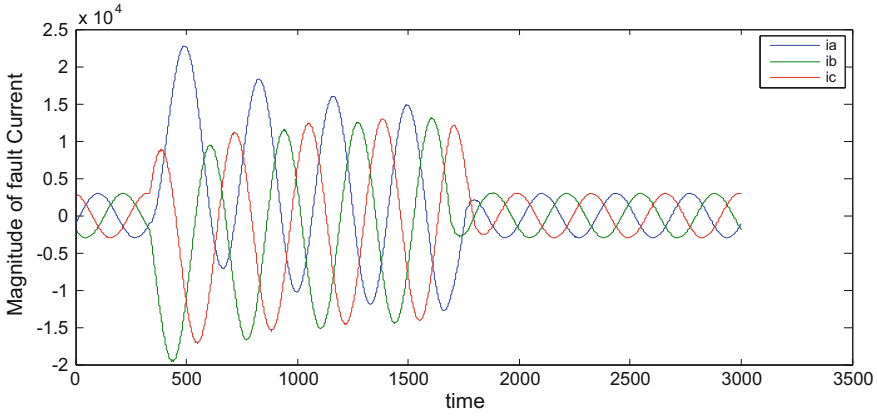


Fig. 12 Three-phase current for LLLG fault at 50 km

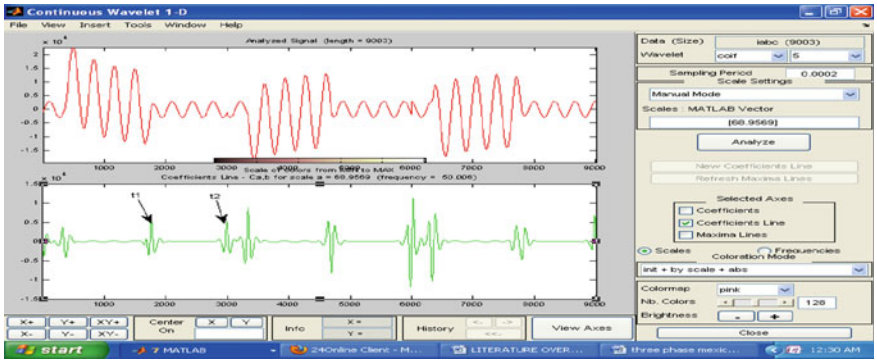


Fig. 13 Three-phase current for LLLG shortcoming at 50 km (Coif let)

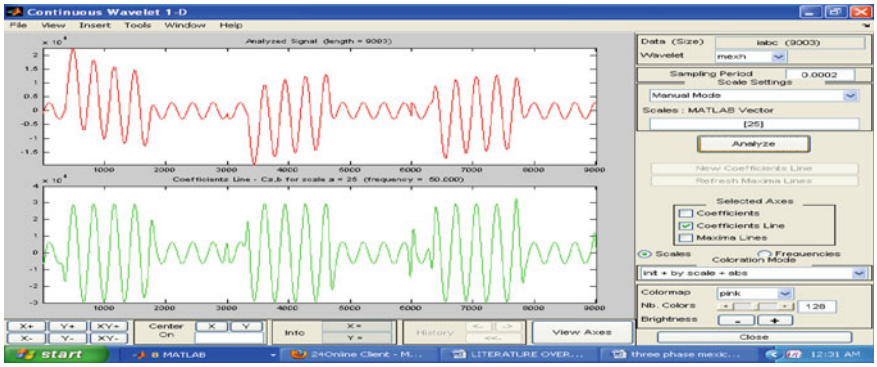


Fig. 14 Three-phase current for LLLG shortcoming at 50 km (Mexican Hat)

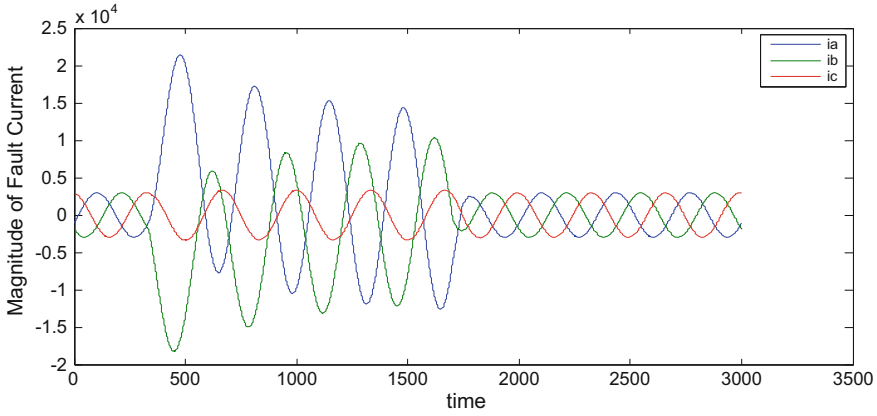


Fig. 15 Two-phase current for LLG flaw at 50 km

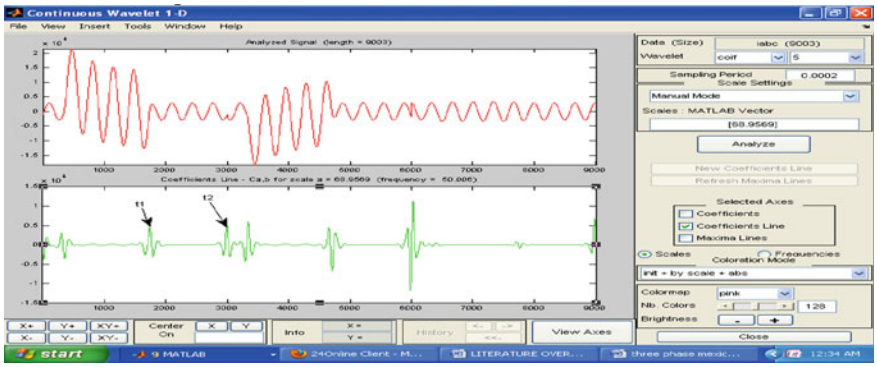


Fig. 16 Two-phase current for LLG flaw at 50 km (Coif let)

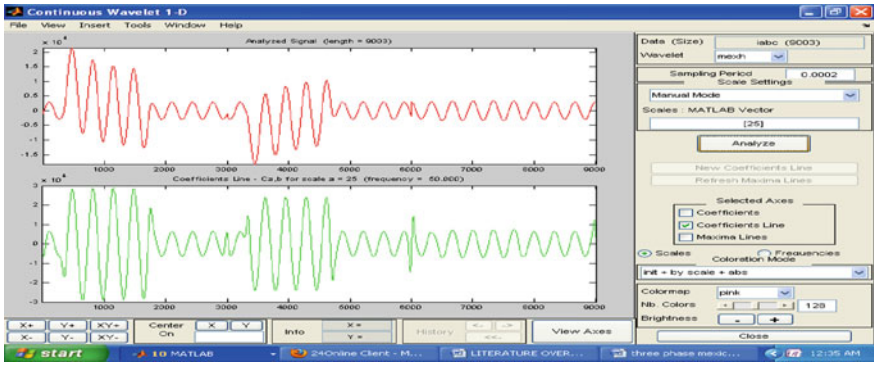


Fig. 17 Two-phase current for LLG deficiency at 50 km (Mexican Hat)

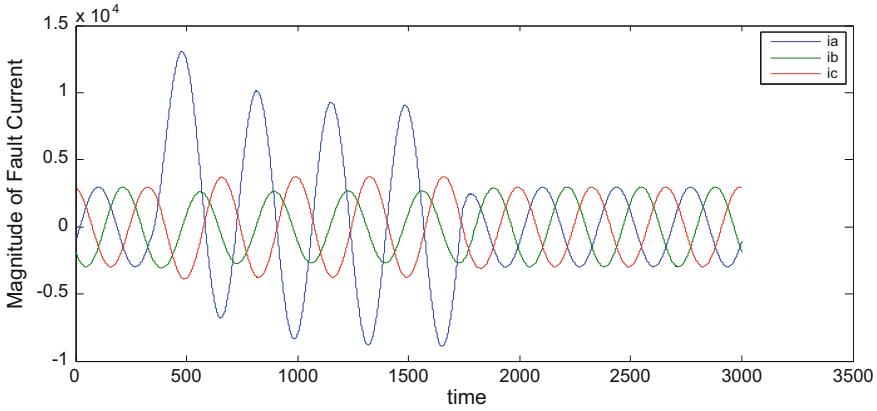


Fig. 18 Single-phase current for LG deficiency at 50 km

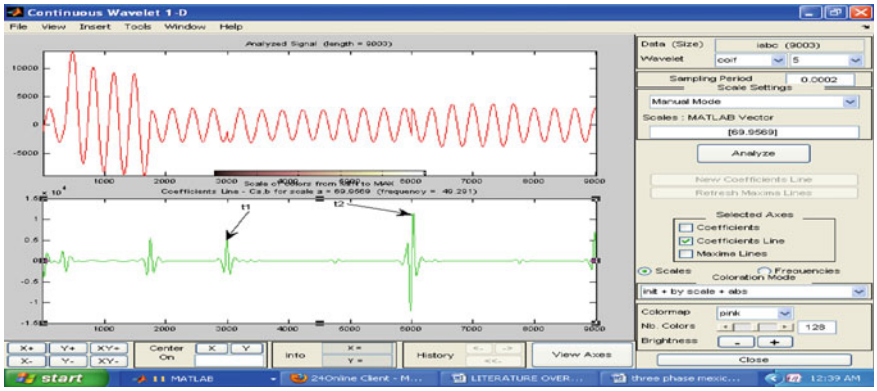


Fig. 19 Single-phase current for LG flaw at 50 km (Coif let)

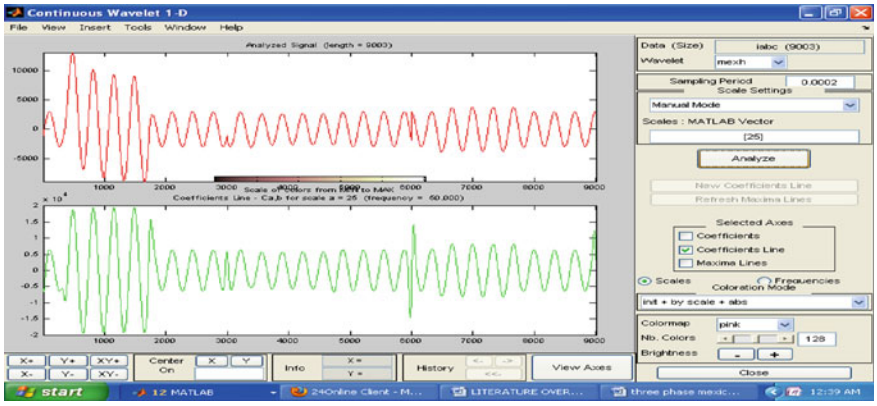


Fig. 20 Single-phase current for LG flaw at 50 km (Mexican Hat)

5 Conclusions

In this chapter an 11 kV 100 km long underground cable has been considered and is designed using a Matlab platform. The simulation work has been carried out for different faults with and without the wavelet transform technique. This method offers important advantages over other methods such as FFT and STFT due to good time and frequency localization characteristics. Analysis results presented clearly show that particular wavelet components can be used as the features to locate the fault in underground cables in the distribution system. This study shows that the scheme is insensitive to fault type, and fault position on the cable. Studies also show that the wavelet technique is able to offer a very high accuracy in fault detection and fault location on underground cable. The simulation work carried out for different faults single line to ground (LG), double line to ground (LLG), and triple line to ground (LLLG) at different points 25 km and 50 km from the source end and the simulation results are shown in Figs. 3, 4, 5, 6, 7, 8, 9, 10, 11, 12, 13, 14, 15, 16, 17, 18, 19 and 20. From the results it can be observed that the estimated distance by impedance method for the LG fault at 25 km is 29 km, but it is 25.03 km with Mexican Hat and is 25.11 km with coif let; that is, 4 km difference between the impedance method and Mexican Hat and 3.89 km difference between the impedance method and coif let. In the next stage when the double line to ground fault (LLG) occurs at 25 km, the estimated distance by the impedance method is 27.12, but it is 25.04 with Mexican Hat and 22.07 with coif let, that is, 2.08 km difference between the impedance method and Mexican Hat and 5.05 km difference between the impedance method and coif let. Similarly for the triple line to ground (LLLG) fault, there is 6.13 km difference between the impedance method and Mexican Hat and 6.17 km difference between the impedance method and coif let. The same analysis has been done for faults at 50 km. From the simulation work carried out with the wavelet transform it is proved that the wavelet transform gives much better results as the wavelet transform is a powerful tool for high-frequency nonstationary signals. As a result, the application of the discrete wavelet transform (DWT) based on the traveling wave is a good choice to detect the faults in underground power cable.

Acknowledgments I would like to express my gratitude to my Ph.D. guide, Prof. Dr. M. Surya Kalavathi madam garu, who encouraged me to pursue this work and taught me the art of fault location and identification in underground power cables. It is my pleasure to acknowledge the role of my co-author K. Prakasam in the completion of this work.

References

1. Din, E.S.T.E.; Gilany, M.; Abdel Aziz, M.M.; Ibrahim, D.K., 2005 "A wavelet-based faul location technique for aged power cables," *Power Engineering Society General Meeting. IEEE*, (2005), 2485–2491
2. Prasanna Kumar, K., Durga Syam Prasad, K., Sravanthi. K., "Wavelet-Based Fault Location and Distance Protection Method for Transmission Lines" Int. Journal of Engineering Research and Applications (2014), 05–16
3. Hassan Pourvali Souraki "A New Approach to Series Fault Location in Underground Distribution System Using Combined Neural Networks & Wavelet Analysis" International Conference on Electric Power and Energy Conversion Systems (EPECS), American University of Sharjah (2009)
4. El Sayed, Tag El Din., Mohamed Mamdouh, Abdel Aziz., Doaa khalil Ibrahim, Mahmoud., Gilany "Fault location scheme for combined overhead line with underground power cable" Electric Power Systems Research (2006)
5. Zhentao, Xin., Lei Wang, Hongyan Jiang., Baodong Chai, Jun Yang., "Smart re-close scheme of combined overhead line with underground power cable" Power System Technology (POWERCON), 2010 International Conference on (2010)
6. Apisit, C., Positharn, C., Ngaopitakkul, A., "Discrete wavelet transform and probabilistic neural network algorithm for fault location in underground cable," *Fuzzy Theory and it's Applications (iFUZZY), 2012 International Conference on*, (2012), 16–18
7. Apisit, C., Pothisarn, C., Ngaopitakkul, A., "An Application of Discrete Wavelet Transform and Support Vector Machines Algorithm for Fault Locations in Underground Cable," *Innovations in Bio-Inspired Computing and Applications (IBICA), 2012 Third International Conference on*, (2012) 26–28
8. Chul-Hwan Kim., Young-Bum Lim., Woo-Gon Chung, Tae-Won Kwon, Jong-Young Hwang, Il-Dong., Kim "A study on the fault identification of underground cable using neural networks "Energy Management and Power Delivery, 1995. Proceedings of EMPD'95. 1995 International Conference on (1995)
9. Wiggins, C.M., Thomas, D.E., Salas, T.M., Nickel, F.S., W Ng, H., "On-line fault location system for 66 kv underground cables with fast O/E and A/D technique". IEEE Trans. Power Delivery (1994) 579–584
10. Chen Ping, Wang Kuixin., "Fault location technology for high-voltage overhead lines combined with underground power cables based on travelling wave principle," *Advanced Power System Automation and Protection (APAP), International Conference on*, vol.1, (2011), 16–20
11. Katsuta, G., Muraoka, K., Inoue, N., Sakai, S., Tsunekage, T., Ando, K., "Fault section detection system for 66 kV underground branch transmission lines using optical magnetic field sensors," *Power Delivery, IEEE Transactions on*, (1992), 1–9
12. Mousa, Lee H., GPS travelling wave fault locator systems: investigation into the anomalous measurements related to lightning strikes. IEEE Trans on Power Delivery, (1996) 1214–122
13. Gale P F, Taylor, P V., Naidu, P., et al. Traveling wave fault locator experience on Eskom's transmission network. Proc. Seventh International Conference on Developments in Power System Protection, (2001), 327–330

Comparative Study of the Methodologies Used in Low-Power Master–Slave Flip-Flops

Arpita Sengupta and Peyush Pande

Abstract Low-power flip-flop plays a crucial role in low-power digital system. Flip-flops are the basic unit in the design of digital circuits which consumes a large amount of power in redundant transitions and clocking. In order to achieve power-efficient designs, reducing its power to improve the performance is an important issue in very large scale integration field. In this paper, the comparative study of few existing design techniques of master–slave falling edge triggering of D flip-flops are done. The synchronous nature of clock signal used to activate along with the input data signal in the techniques is used. Among different techniques, push-pull isolation flip-flop provides least transition delay and high performance which improves the overall efficiency. Simulations were performed in cadence virtuoso gpdk 180 nm/1.8 V CMOS technology.

Keywords Flip-Flop · Low power · Delay · Transistor · Circuit

1 Introduction

The eminence of portable systems is increasing day-by-day, which results in the need of constraining the power and heat dissipation in high-density chips. It guides us in the development of novel low-power design criteria. The motivation behind the advancement is battery-operated devices. The temperature along with the power dissipation of the chip increases due to the clocking part of the digital circuit [1]. In sequential digital systems, flip-flops are the basic building block of any device. For selection of any flip-flop designs, transistor count, power delay, high performance and low power are the main parameters which must be considered. About 30–70 % of the total power of the chip area accounts for clock distribution and flip-flops [2]. Flip-flops can be categorized as differential, pulse-triggered and master–slave flip-flops.

Arpita Sengupta (✉) · Peyush Pande
Department of Electronics and Communication,
Graphic Era University, Dehradun, India
e-mail: arpitasengupta151@gmail.com

© Springer Science+Business Media Singapore 2017

R. Singh and S. Choudhury (eds.), *Proceeding of International Conference on Intelligent Communication, Control and Devices*, Advances in Intelligent Systems and Computing 479, DOI 10.1007/978-981-10-1708-7_13

Master–slave consists of two latches called master and slave [3]. There can be three major factors of average power dissipation as follows:

$$P_{\text{avg}} = p_{\text{t}} C_{\text{L}} V_{\text{dd}}^2 f_{\text{clk}} + I_{\text{sc}} V_{\text{dd}} + I_{\text{leakage}} V_{\text{dd}} \quad (1)$$

The first term in the Eq. 1 [4] is the switching part where p_{t} is the transition probability, C_{L} is the load capacitance and f_{clk} is the frequency of the clock. The second term represents short circuit current and third term is the leakage power. Power dissipation is directly related to the number of clocked transistors of design so reduction in the transistor count minimizes the load capacitance and thus lessen power can be obtained [5]. The research paper is structured in the following way:

The subsequent section demonstrates the study of different master–slave techniques and short description about each flip-flop has been provided. In Sect. 3, the assessment of these flip-flops on the basis of parameters such as device count, power dissipation and transition delay is accomplished. In Sect. 4 paper ends with the concluding remarks.

2 Different Modes of Single Edge-Triggered D Flip-Flops

The methodology described herein consists of two stages, one master and other slave. The master part is controlled by clock signal and slave part by inverted clock signal. Here the discussions of some single edge-triggered D flip-flops techniques which are implemented through falling edge triggering have been done.

2.1 Transmission Gate Flip-Flop (TGFF)

The basic falling edge-triggered flip-flop comprises of two-stage latches is illustrated in Fig. 1. The two gate delays limit the speed of the flip-flop. The merit of

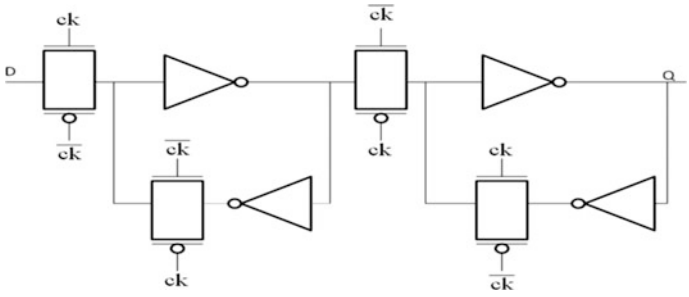


Fig. 1 Transmission gate flip-flop [6]

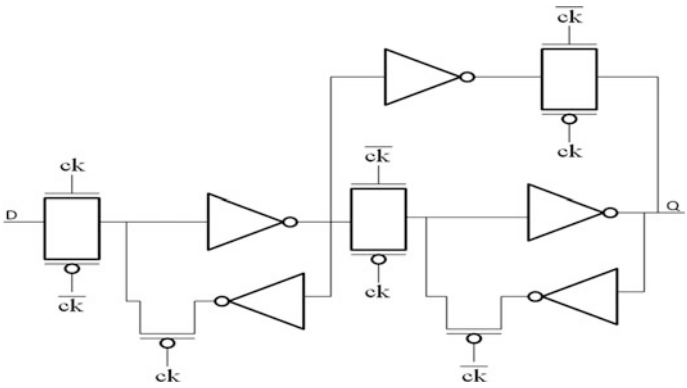


Fig. 2 High-performance flip-flop [7]

using TG flip-flop is that it requires simple design technique, small area and lesser power consumption [6].

2.2 High-Performance Flip-Flop (HPFF)

Figure 2 illustrates the technique. The merit of this technique is that it decreases the inside chip area, unwanted capacitance existing at the internal node and also reduces the device count which improves the power delay product [7].

2.3 Push-Pull Isolation Flip-Flop (PPIFF)

PPIFF circuit is illustrated in Fig. 3. It enhances the transistor count, but total power dissipation is reduced and a speed is increased up in comparison of the push-pull flip-flop. PPIFF provides more speed at a cost of more power and thus used in high-speed applications [8].

2.4 Low-Power D Flip-Flop (LPDFF)

Figure 4 shows the low-power DFF. The approach is used to eradicate the power dissipation due to short circuit from the feedback path and results in reducing power with a slight amount compared to the conventional transmission gate flip-flop [9].

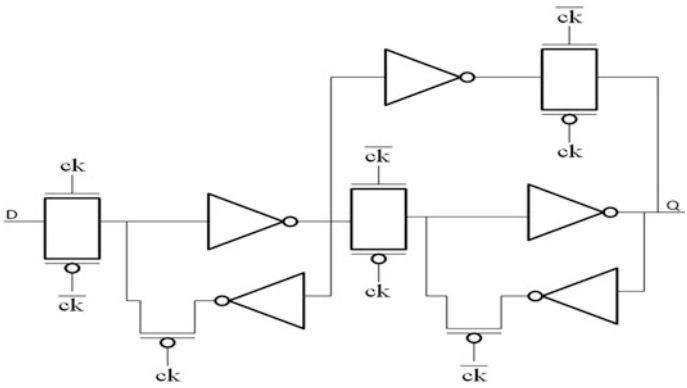


Fig. 3 Push-pull isolation flip-flop [8]

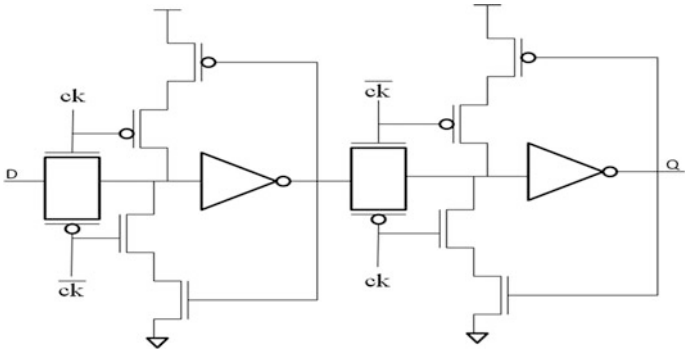


Fig. 4 Low-power D flip-flop [9]

2.5 Pass Transistor Flip-Flop (PTLFF)

Figure 5 shows the circuit diagram of PTLFF [10]. The NMOS transistors are used in the feedback path instead of PMOS because it performs static behavior when clock is stopped [11]. There is improvement in the overall power delay product.

3 Result and Analysis

As power is also dependent on the number of transistors, the transistor count along with the clocked transistors is compared with the speed and power. The simulations are done in cadence virtuoso 6.1.5 at gpdk 180 nm CMOS technology with voltage supply of 1.8 V.

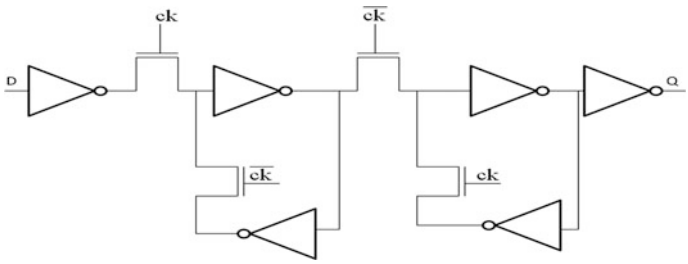


Fig. 5 Pass transistor logic flip-flop [10]

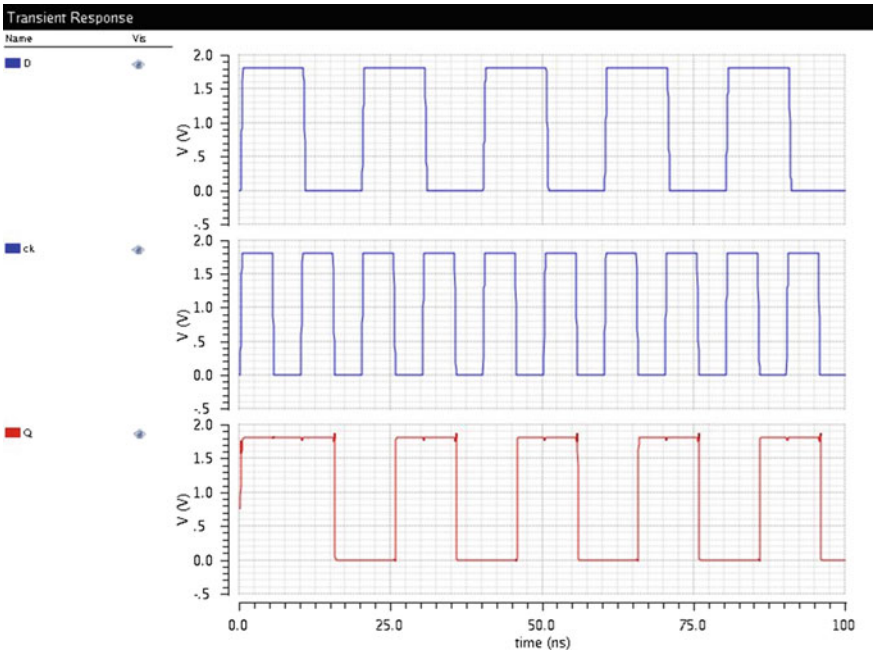


Fig. 6 Waveform of conventional falling edge-triggered D flip-flop

From Fig. 6 it can be inferred that output signal *Q* only follows input signal *D* when clock signal ck is at falling edge otherwise it remains stay at its previous state. The comparison Table 1 illustrates that according to the application needed corresponding flip-flop technique can be used.

Table 1 Comparison chart of various flip-flops

Parameters: 1.8 v	TGFF	HPFF	LPDFF	PPIFF	PTLFF
No. of total transistors	18	11	20	18	18
Data (*D*) to output (*Q*) delay (*ps*)	200.5	160.3	176.7	114.9	26.75
Clock (*C*) to output (*Q*) delay (*ps*)	95.49	55.3	71.69	9.889	51.75
Average power (μW)	26	26.3	24.23	36.59	42.23
Power delay product (fJ)	5.213	4.216	4.281	4.204	1.130

4 Conclusion

A contrast study of single edge-triggered master–slave D flip-flops has been prepared. Among the projected D flip-flops, TGFF is simplest in terms of design and also dissipate less power. The main problem arises in it is that the delay is more due to addition of two gate delays which limit its speed. HPFF also known as low-voltage flip-flop provide high performance both in terms of less power consumption and speed. The device count is also reduced in this case. LPDFF helps in power optimization and also a better method over TGFF. It reduces both delay and power as compared to conventional TGFF. PTLFF improves the overall power delay product. PPIFF proves best in terms of delay but power dissipation is little high. So according to the design and application need, the corresponding technique can be used. The sequential part, mainly the flip-flop along with the clock, consumes majority of the total power and so it should be minimized as much as possible.

5 Future Scope

A lot of research is still going on in this topic for designing more optimized techniques which scaled down up to 16 μm of technology node. Dual-mode techniques have been developing which can switch between single- and double-edge triggering.

References

1. Kang, S.M., Leblebici, Y.: CMOS Digital Integrated Circuits: Analysis and Design. Reading, Tata McGraw –Hill Edition. 2nd edn (2003)
2. Singh, K., Tiwari, S.C., Gupta, M.: A Modified Implementation of Tristate Inverter Based Static Master-Slave Flip-Flop with Improved Power-Delay-Area Product. A Research Article published on The Scientific World Journal (2014) 1–14
3. Khan, I.A., Shah, O.A., Beg, M.T.: Analysis of Different Techniques for Low Power Single Edge Triggered Flip Flops. IEEE Conference published on World Congress of Information and Communication Technologies (2011) 1363–1367

4. Consoli, E., Palumbo, G., Pennisi, M.: Reconsidering high speed design criteria for transmission-gate-based master-slave flip-flops. Vol.20. IEEE Transactions on Very Large Scale Integration (VLSI) Systems (2012) 284–295
5. Stojanovic, V., Oklobdzija, V.G.: Comparative analysis of master-slave latches and flip-flops for high-performance and low-power systems. Vol.34. IEEE Journal of Solid-State Circuits (1999) 536–548
6. Weste, N., Eshraghian, V.: Principles of CMOS VLSI Design: A Systems Perspective. Reading, MA: Addison-Wesley. 4th edn (1993).
7. Singh, K., Tiwari, S.C., Gupta, M.: A High Performance Flip Flop for Low Power Low Voltage Systems. World Congress on Information and Communication Technologies (WICT), IEEE conference (2011) 257–262
8. Ko, U., Balsara, P.T.: High-Performance Energy-Efficient D-Flip-Flop Circuits. Vol.8. IEEE Transaction on Very Large Scale Integration (VLSI) Systems. IEEE Transaction on Very Large Scale Integration (VLSI) Systems (2000) 94–98
9. Gerosa, G., Gary, S., Dietz, C., Pham, D., Hoover, K., et al.: 2.2 W, 80 MHz superscalar RISC processor. Vol.29. IEEE Journal of Solid-State Circuits (1994) 1440–1454
10. Khan, I.A., Beg, M.T.: Design and Analysis of Low Power Master Slave Flip-Flops. Vol.43. Informacije Midem-Journal of Microelectronics Electronic Components and Materials (2013) 41–49
11. Khan, I.A., Beg, M.T.: Comparative Analysis of Low Power Master Slave Single Edge Triggered Flip Flops. Vol.16. World Applied Analysis of Different Techniques for Low Power Single Edge Triggered Flip Flops Science Journal (2012) 15–21

Wrist Pulse Signal Features Extraction: Virtual Instrumentation

Nidhi Garg, Ramandeep Kaur, Harry Garg, Hardeep S. Ryait and Amod Kumar

Abstract Wrist Pulse Signal (Pulse Diagnosis) has successfully established an influential impact all over the world for promoting health conditions. With the increase in belief of traditional pulse diagnosis method, the need of computer-generated pulse signal waveforms for wrist pulse analysis has become an essential stage. The paper focuses primarily on the traditional feature extraction method for the study and analysis of pulse waveforms by means of virtual instrumentation (VI). The authors presented a first derivative method to obtain various time domain features using VI's. Digital Signal Processing techniques have been implemented and processed successfully to extract justifiable and valuable features from the wrist pulse waveforms.

Keywords Derivative method · Digital signal processing · LabVIEW · Pulse diagnosis · Time domain features

Nidhi Garg (✉)
I.K. Gujral PTU, Jalandhar 144001, Punjab, India
e-mail: nidhi_garg@pu.ac.in

Nidhi Garg · Ramandeep Kaur
UIET, PU, Chandigarh 160023, India
e-mail: ramandeepkr163@gmail.com

Harry Garg · Amod Kumar
Central Scientific Instruments Organisation (CSIR-CSIO), Chandigarh 160030, India
e-mail: harry.garg@gmail.com

Amod Kumar
e-mail: csioamod@yahoo.com

H.S. Ryait
BBSBEC, Fatehgarh Sahib 140407, Punjab, India
e-mail: hardeepsryait@gmail.com

© Springer Science+Business Media Singapore 2017

R. Singh and S. Choudhury (eds.), *Proceeding of International Conference on Intelligent Communication, Control and Devices*, Advances in Intelligent Systems and Computing 479, DOI 10.1007/978-981-10-1708-7_14

1 Introduction

Pulse diagnosis is one of the powerful and influential tools of Ayurveda. The key features like convenient to use, painless treatments and non-invasive diagnosis of diseases makes this method inevitable. An abundant number of diseases can be diagnosed by sensing the wrist (radial) pulse by placing the fingers at only three positions as shown in Fig. 1.

These three positions on wrist are used to acquire pulse signals and correspond to three doshas [1, 2]. The tactile vibratory qualities of these three doshas indicate the imbalance that is responsible for the subject's condition. Many investigations related to radial pulse have revealed a strong connection between health of a patient and radial pulse features. The features of pulse signal represent the state of heart and reflect the conditions of other organs. The blood flows a long way from the heart through the radial arteries and changes under different environments inside a body. Consequently, the features of the radial signals are important from diagnostic point of view. With the advancement of science and technology, different techniques using digital signal processing have been invented and utilized for analyzing and drawing out the significant parameters from computerized pulse signals. MATLAB and LabVIEW are two most effective tools commonly used to accomplish these objectives with adequate accuracy. Researchers studied photoplethysmographic (PPG) signals using LabVIEW software [3]. Authors in [4] worked on automated derivative-based time domain feature analysis of wrist pulse waveforms using MATLAB. Detection of sub-peaks using second derivative-based method was conducted by authors of [5]. Researchers in [6] have been acquired the ECG signals using LabVIEW then filtered and pre-processed using wavelet transform and finally analyzed to calculate heart beat rate using MATLAB. Advanced Signal Processing Tool kit (ASPT) and biomedical tool kit of LabVIEW were used to extract various ECG features [7]. Analysis of radial pulse data through NI LabVIEW software was conducted by many authors [8, 9]. Various prominent researches have been conducted in the past for time domain feature extraction [10–14].



Fig. 1 Traditional way of diagnosing three doshas

LabVIEW is the trademark of National Instrument, which is used as application software for extracting important parameters from a pre-processed radial pulse signal in this work. The paper is organized as follows: Sect. 2 gives overview of steps followed during preprocessing. In Sect. 3, implementation technique of first derivative method using LabVIEW has been explained for locating continuous peak and valley points. Time domain features are depicted in Sect. 4. Finally, we concluded the paper in Sect. 5.

2 Pulse Signal Preprocessing

The raw pulse signals were acquired to filter, amplify, and store data information in the computer using National Instrument's data acquisition (DAQ) card. The radial pulse signals were sampled at a rate of 4 k. The incoming data was collected using LabVIEW Virtual Instrument (VI). The acquired signal represented in Fig. 2b resembles well with the standard pulse taken from the radial artery [15] as shown in Fig. 2a. The recorded raw signal shown in Fig. 2b is most often affected by noise and artifacts. Processing the contaminated or noisy signal, give false information that generates incorrect results. To keep away such problem, preprocessing of raw pulse signal is required. Various steps are carried out in preprocessing stage [16]. The whole process of preprocessing of radial pulse signal is represented in Fig. 3.

3 Implementation Technique: First Derivative Method in LabVIEW

To reveal the pulse signal information, various parameters have to be derived from the pulse signal. Studies have been conducted in past to locate the peak points, valley points and onset points of the pulse waveform using derivative based method in MATLAB. We have approached the same derivative-based method in a simple way using ®LabVIEW tool.

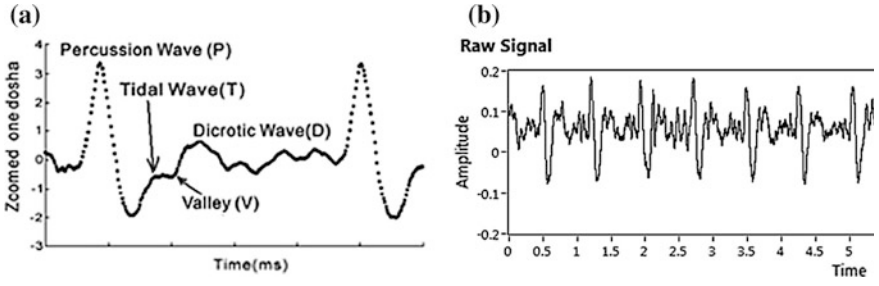


Fig. 2 **a** Standard signal from the radial artery [13]; **b** Collected raw signal

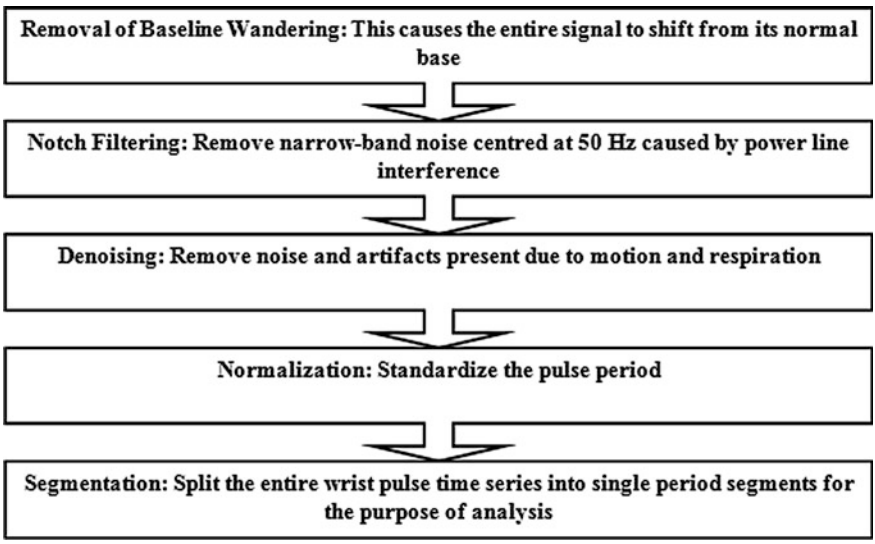


Fig. 3 Preprocessing flow chart

3.1 Implementation Technique

The main steps for the implementation of derivative method that has been carried out in LabVIEW to extract features of pulse signal are explained in steps.

1. Develop the preprocessed pulse signal by following the steps mentioned in the flow chart as shown in Fig. 3.
2. Derive the derivative pulse signal from preprocessed pulse signal using a LabVIEW Express VI: Derivative (d*X*/d*t*) as illustrated in Fig. 4. It is taken from Integration and Differentiation palette of LabVIEW to obtain the derivative signal from the preprocessed pulse signal.
3. Sequentially explore the zero-crossing points by first derivative based zero crossing detector and then determine their relevant amplitude and time as represented in Fig. 5.

Figure 6 represents the relation among pre-processed pulse signal and derivative of the identical pulse signal. On the preprocessed signal the first, third, and fifth

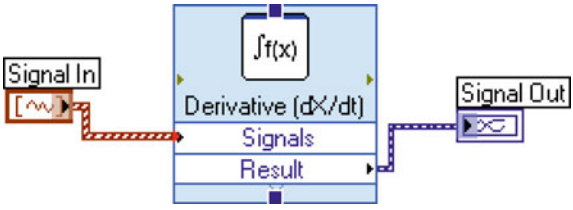


Fig. 4 Derivative (d*X*/d*t*) VI

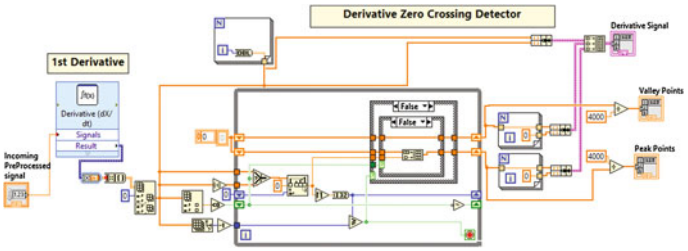


Fig. 5 Zero crossing detector program

doted lines represent peak points and the second and third dotted lines represent valley points.

Moreover, at this juncture, continuous zero crossings on the derivative signal indicates the concave and convex regions. The finding of positive and negative derivative signifies the existence of local minimum and local maximum points, respectively. These points are further used to determine various amplitude and time associated parameters of pulse signals. By implementing this technique in LabVIEW tool with an ease further features extraction method was executed.

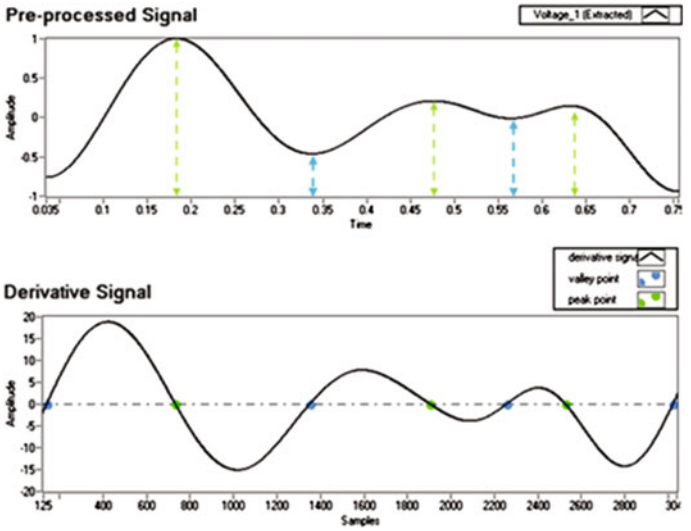


Fig. 6 Preprocessed signal and Derivative signal

4 Time Domain Features

The wrist pulse typically possesses three maxima and three minima points in one cycle of wrist pulse signal. The magnitudes and time indices of these extreme points and various combinations among them are entitled as time domain features of the wrist pulse wave with graphical representation in Fig. 7. In total, 12 features were extracted in this study. List of features extracted with their specifications are shown in Table 1. Magnitude related features were: *Hp*, *Hq*, *Hr*, *Hs*, *Ht,* and time-related features were: *Tp*, *Tq*, *Tr*, *Ts*, *Tt*, *w*, *TP*. The selection of appropriate features makes the analysis of pulse signal efficient.

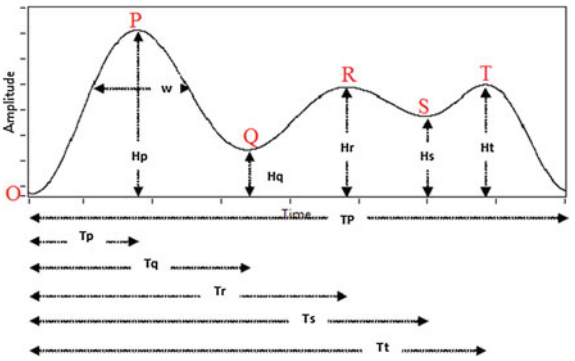


Fig. 7 Representation of derived features

Table 1 Parameters extracted from pulse signal

Parameters	Specifications
Hp	Amplitude of percussion wave peak point (P)—Amplitude of offset point (O)
Hq	Amplitude of 1st valley point (Q)—Amplitude of offset point (O)
Hr	Amplitude of 1st sub-peak point (R)—Amplitude of offset point (O)
Hs	Amplitude of 2nd valley point (S)—Amplitude of offset point (O)
Ht	Amplitude of 2nd sub-peak peak point (T)—Amplitude of offset point (O)
Tp	Time of percussion wave peak point (P)—Time of offset point (O)
Tq	Time of 1st valley point (Q)—Time of offset point (O)
Tr	Time of 1st sub-peak peak point (R)—Time of offset point (O)
Ts	Time of 2nd valley point (S)—Time of offset point (O)
Tt	Time of 2nd sub-peak peak point (T)—Time of offset point (O)
w	Time width between two points of percussion wave present at the amplitude level of 2/3 of Hp
TP	Time of next pulse offset point—Time of present pulse offset point

5 Conclusion

Computer-generated radial pulse waveform is commonly being utilized for pulse diagnosis in time series. Initially, observed the acquired pulse by comparing it with standardized pulse signal of the radial artery and afterwards preprocessed it using step by step procedure. This paper gave an insight on simple first derivative based method implementation in virtual instrumentation. Various parameters were derived from the radial pulse with an effortlessness and straightforward manner by analyzing continuous zero crossings on the derived signal. The entire research work was carried out in LabVIEW due to its simple and convenient to use traits. Finally, 12 time domain features were extracted with the purpose of doing further analysis in future.

References

1. Lad, V.D.: Secrets of the Pulse: The ancient art of Ayurvedic pulse diagnosis. Motilal Banarsidass, Delhi (2005).
2. Kaur, R., Chopra, M., Garg, N., Ryait, H.S.: Role of pulse diagnosis: A review. In: International Conference on Computing, Communication & Automation. pp. 152–155. IEEE (2015).
3. Deepa, N., Ganesh, A.B.: Optical Sensor for Indian Siddha Diagnosis System. Procedia Eng. 38, 1126–1131 (2012).
4. Xia, C., Li, Y., Yan, J., Wang, Y., Yan, H., Guo, R., Li, F.: Wrist Pulse Waveform Feature Extraction and Dimension Reduction with Feature Variability Analysis. In: 2008 2nd International Conference on Bioinformatics and Biomedical Engineering. pp. 2048–2051. IEEE (2008).
5. Calisto, A., Galeano, M., Serrano, S., Calisto, A., Azzerboni, B.: A new approach for investigating intracranial pressure signal: filtering and morphological features extraction from continuous recording. IEEE Trans. Biomed. Eng. 60, 830–837 (2013).
6. M.K. Islam, A.N.M.M. Haque, G. Tangim, T. Ahammad, and M.R.H.K.: Study and Analysis of ECG Signal Using MATLAB & LABVIEW as Effective Tools. Int. J. Comput. Electr. Eng. 4, 404–408 (2012).
7. Purohit, A., Khan, K., Bohra, G.K.: Calculate ECG Parameters through Labview. IJCA Proc. Natl. Conf. Innov. Recent Trends Eng. Technol. NCIRET, 18–20.
8. Devi, S.K., Shankar, K., Abudhahir, A.: Acquisition of Radial Artery Pulses (NADI). In: 2014 International Conference on Electronics and Communication Systems (ICECS). pp. 1–6. IEEE (2014).
9. Akshita Baisware, S.N.J.: Design of Non Invasive Pulse Rate Detector using LabVIEW. Int. J. Emerg. Trends Eng. Technol. 3, 71–75 (2015).
10. Wang, D., Zhang, D., Chan, J.C.: Feature Extraction of Radial Arterial Pulse. In: 2014 International Conference on Medical Biometrics. pp. 41–46. IEEE (2014).
11. Rangaprakash, D., Narayana Dutt, D.: Study of wrist pulse signals using time domain spatial features. Comput. Electr. Eng. 45, 100–107 (2015).
12. Rangaprakash, D., Narayana Dutt, D.: Analysis of wrist pulse signals using spatial features in time domain. In: 2014 International Conference on Communication and Signal Processing. pp. 345–348. IEEE (2014).

13. Sareen, M., Prakash, P., Anand, S.: Wavelet Decomposition and Feature Extraction from Pulse Signals of the Radial Artery. In: 2008 International Conference on Advanced Computer Theory and Engineering. pp. 551–555. IEEE (2008).
14. Chen, Y., Zhang, L., Zhang, D., Zhang, D.: Wrist pulse signal diagnosis using modified Gaussian models and Fuzzy C-Means classification. Med. Eng. Phys. 31, 1283–1289 (2009).
15. Abhinav, Sareen, M., Kumar, M., Santhosh, J., Salhan, A., Anand, S.: Nadi Yantra: a robust system design to capture the signals from the radial artery for assessment of the autonomic nervous system non-invasively. J. Biomed. Sci. Eng. 02, 471–479 (2009).
16. Chopra, M., Kaur, R., Garg, N.: Study and evaluation of denoising and baseline wandering of computerized wrist pulse signal using virtual instrument. In: 2015 1st International Conference on Next Generation Computing Technologies (NGCT). pp. 576–579. IEEE (2015).

Optimized Swarm Architectures in Airborne Internet

Pardeep Kaur, Preeti and Amit Gupta

Abstract There is a tremendous growth in telecommunication networks due to the emergence of various communication techniques. Optical communications have been the major contributors to it. Free space optical communication (FSO) is a technique based on transmission of data by propagating the light in free space. This is an effective technique to transmit the data at high bit rate over short distance with the added advantage of easy and fast installation and high security. Hybrid RF/FSO technique improve the overall reliability of the system. In this paper, aerial application of the RF/FSO system, i.e., airborne Internet which includes the use of optical links in the network of unmanned aerial vehicles (UAVs) is given. Different formations of UAV swarms, few methods to combat the problems faced by unmanned aerial vehicles (UAVs) and high altitude platform (HAPs) for research work have been discussed. A model is also proposed to improve the reliability of the swarm network.

Keywords FSO · Hybrid FSO/RF · Unmanned aerial vehicles (UAVs) · High altitude platforms (HAPs) · Airborne Internet

1 Introduction

Since the evolution of mankind has been taken place, communication has become an important way to send and exchange views throughout the world as one of the principal interest of human beings. The information is sent via an electromagnetic carrier wave whose frequency can vary from MHz to THz in a communication system. As we are beginning towards a new era, various dramatic changes in communication have been coming across. For example, businesses today rely on high-speed networks to do their daily affairs [1, 2]. Large MNCs which were once

Pardeep Kaur (✉) · Preeti
UIET, PU, Chandigarh, India
e-mail: pardeep.tur@gmail.com

Amit Gupta
Chandigarh University, Gharaun, Punjab, India

© Springer Science+Business Media Singapore 2017

R. Singh and S. Choudhury (eds.), *Proceeding of International Conference on Intelligent Communication, Control and Devices*, Advances in Intelligent Systems and Computing 479, DOI 10.1007/978-981-10-1708-7_15

using 155 Mbps are now using 1 Gbps connections. Thus, demand for bandwidth has been increased and at the same time the usage of those technologies which could be cost effective are to be promoted.

Free Space Optics is a new technique which is similar to optical fiber infrastructure but no cable is involved [3]. It requires line of sight connectivity between receiver and transmitter with a capability of sending up to 125 Gbps of data, voice, video communication simultaneously through air and even enable WDM like technologies to operate through free space. It has distinct advantages like no license requirement, easily upgradable, immune to RF interference, requires no safety upgrades, can be deployed everywhere, economical [4, 5]. Although FSO is gaining wide market acceptance as a functional wireless, high bandwidth access tool with license free access but still suffers from serious drawbacks. To combat that another thing becoming popular is hybrid FSO [6, 7]. It is the use of FSO with Radio Frequency (RF) link as backup. For link distances greater than approximately 140 m FSO/RF links could be used which would also solve the problem of line of sight (LOS), i.e., when there is no LOS access RF link can be used [8]. So, efficiency of the network connection would be improved but the only weather that could affect transmission of hybrid FSO/RF is heavy rain and dense fog [9, 10]. These systems fit precisely in emergency situation, for instance, earthquakes, tsunamis. In FSO/RF link system, the data rates for FSO and RF are 1.25 Gbps and 100 Mbps, respectively, with an average overall data rate of 183 Mbps [11]. Such a system would help to combat all the challenges posed to RF approach. The best utilization of this communication is between airborne and ground-based network nodes.

2 Airborne Internet

Airborne Internet means to provide high-speed wireless Internet connection by placing aircraft in fixed patters over hundreds of cities. As shown in Fig. 1, aircrafts are carrying data which they can project directly to the end user, to the other aircraft



Fig. 1 Airborne Internet

or within the plane itself for the passengers. To implement these networks, first option is using: HALO: in which lightweight planes will circle overhead and provide high-speed Internet to consumers. These HALO networks can cover the area up to 120 km in diameter but still this has to receive the approval from the aviation administration. Each city in the halo network will be allotted three piloted planes and will fly for 8 hr before next plane takes off. Second venture is to provide solar-powered, UAV that would work in similar manner to HALO. NASA is carrying out research to have solar powered lightweight planes that could fly over a city for six months at a stretch without landing and covering area up to 40 km [12].

3 FSO in Airborne Networks

Prof Nawaz has proposed the airborne Internet access through the sub marine optic cables. Internet access for passengers traveling in aircrafts is thought to be one of the unresolved major challenges for ubiquitous Internet provision [13]. Vast oceanic remote regions along the busy air routes of the world require low-cost, reliable, and high-speed Internet for the aircraft [14]. Satellite links can provide Internet coverage in such remote areas; however, their services are still costly with low bandwidth and longer delays. Fortunately, the submarine optical cables deployed across the oceans pass along the same busy air routes. These cables can be utilized as high-speed Internet backbone for wireless Internet access to the aircraft. Vehicles flying at some height from the ground can use FSO as a means of communication among themselves or to the base station at the ground. In Fig. 2, an aircraft as network hub is communicating with the ground-based halo gateway and to the end user directly, if we do not want to dig the infrastructure or need of quick network installation is there. The best utilization of aerial application o is in the 'Disaster recovery' [15, 16].

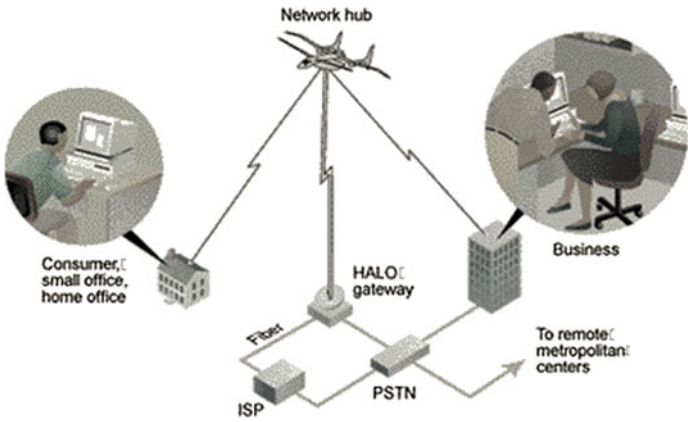


Fig. 2 Various nodes of airborne Internet

In case of a disaster, infrastructure completely collapses and air is the only means of communication with rest of the world. RF alone cannot provide the required bandwidth that is needed to transmit the live images of the disaster recovery area. So, hybrid FSO or ROFSO can be best solution for them. Hence, aerial vehicles with optimal placement of FSO transceivers form the best combination to accomplish quicker network recovery. Military uses FSO between airborne vehicles to observe hostile environments. Defense Advanced Research Projects Agency (DARPA) of U.S. has recently demonstrated aerial connection range up to 200 km and air to ground slant connection range up to 130 km exhibiting data rates from 3 to 9 Gbps on a hybrid FSO/RF link [15].

4 Unmanned Aerial Vehicles

In airborne Internet, UAV flying in swarm formations are predominantly used in civil and military applications like observing the battle field, monitoring traffic, protecting important buildings and many more. In order to have better end-to-end communication with good coordination and navigation, the number of UAVs are used which in turn also increases the range of distance by employing various topologies. UAVs have multiple wireless sensors which collect the data from ground and share it with the other UAVs in the swarm. As each UAV is equipped with numerous sensors, large data transfer takes place within the swarm, which is best suited through FSO links. Security of confidential information like battlefield arrangement and map information has led to the extensive use of these UAVs in military applications. But the greatest challenges faced by these airborne vehicles using FSO are the loss of sight due to the relative motion between them and atmospheric turbulences. So, we need to have a backup of RF transceivers in each vehicle to maintain communication even in foggy and hazy conditions and also in case of lost line of sight between them.

5 Ground–Aircraft Link

The communication for aerial vehicles start from ground station and then the information reaches UAVs or HAPs whichever are equipped. The rays have to travel different layers of atmosphere so various weather phenomenons are there which obstruct the path of optical waves namely fog, rain, snow. For optimal placement the number of trans-receivers to be used could be decided precisely so that both in good and worst weather conditions they could give better performance. The use of visibility codes have been proposed for switching to particular trans-receiver. The lifetime of hybrid FSO/RF is two times that of single RF link.

6 Inter-Airborne Communication

Inter-airborne communication means that two airplanes are communicating with each other instead of first communicating with centralized hub/station as shown in Fig. 3. We can efficiently use the FSO between the two nodes, i.e., earth station and central hub in the air in which one is stationary and utilize the best bandwidth out of these.

But between two moving airplanes, this will be tedious task so for that sub part we can use RF signals or smart tracking algorithms need to be devised, so as to capture the relative motion of two aircrafts w.r.t each other. Idea is not to replace the RF with the FSO but to create a combined smart architecture of two, so as to get the best utilization out of the two technologies.

7 Intra-Airborne Communication

In addition to this intra-airborne network is also gaining importance, i.e., in-flight communication network to provide Wi-Fi access in airplanes for videos, songs. For high data rate, control of surface illumination and FOV of receiver improves bandwidth, as proposed in, to at least 100 MHz [17]. To distinguish users in the same cell, Walsh–Hadamard codes could be used for 'movies on demand' [15]. A new method of using optical codes in FSO and indoor Visible Light Communication (VLC) is used parallel which gives better performance in terms of BER and SNR.

8 Proposed UAV Architecture

Low altitude UAV swarm can exchange the information of the battlefield with the high altitude mother ship through optical links. This swarm formation can be used in traffic regulation, tracking individual vehicles and other applications to increase

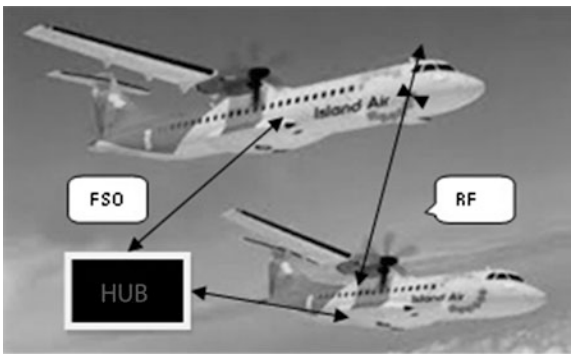


Fig. 3 Inter-airborne communication

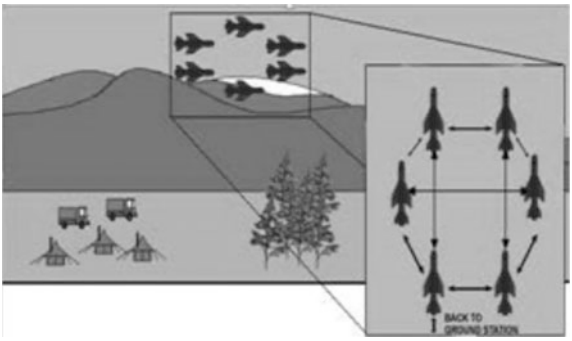


Fig. 4 Partial mesh topology

the reliability and achievability of links. The efficiency of the swarm network varies with the formations in which they are connected. These formations are called topologies or UAV architectures. A partial mesh topology is proposed as shown in Fig. 4. Here, UAVs have lesser links as compared to the full mesh topology thus reducing the network complexity and implementation cost.

This architecture combines the advantages of ring, star and mesh topology at an expectable cost and tolerable network congestion. It can be transformed into a more sophisticated network by using routing algorithms which switch the network back to shorter links of ring topology in case longer mesh links are unavailable due to obscure atmospheric conditions. Radio over Free Space optics (ROFSO), the latest development in the free space optics, in which we first modulate the data using RF modulation schemes like CDMA and then covert it to the FSO format, so as to further combine the advantages of RF and optical can also be investigated for the inter-UAV links. The connection between the HAP and the ground station using FSO/RF/ROFSO is proposed. The proposed airborne network is shown in Fig. 5. If the weather conditions are favorable then FSO and ROFSO can be used and it will automatically shift to RF alone in case the turbulence is there. By this the link availability as well as the bandwidth it supports increased many fold. For Ground station to aircraft communication, different error correcting codes can be used

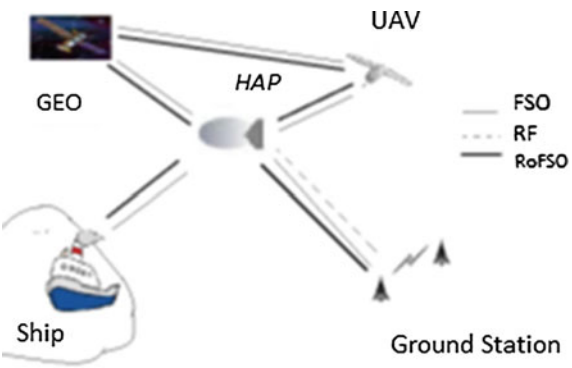


Fig. 5 Proposed airborne network

which could decrease BER and scintillation effects. RF link along with FSO link would give better performance in rain and increase the range where there would be no line of sight and using ROFSO gives good results than FSO on clear weather. For inter-airborne different wavelengths and hybrid codes can be used.

References

1. Noel Schmidt, Dan Ball, Frank Adelstein, Matt Stillerman: Development of an Airborne Internet Architecture to Support SATS: Trends and Issues, pages 1145–1151, IEEE (2002).
2. Kedar, D Arnon: Urban optical wireless communication networks-the main challenges and possible solutions, Communications Magazine, IEEE, vol 42, no 5 (2004).
3. Aditi Malik, Preeti Singh: Comparative Analysis of point to point FSO system under clear and haze weather conditions, Wireless personal communications, vol 78, no 3 (2014).
4. Peng Yan, Sluss, J, Refai, Lo Presti: An initial study of mobile ad hoc networks with free space optical capabilities, Digital Avionics Systems Conference, IEEE, Vol 14, DASC (2005).
5. Matsumoto, M. Osawa, Hotta, S. Wakamori: Innovative tracking system for next generation FSO systems under massive earthquakes, Optical Network Design and Modeling (ONDM), Pages 233–238, IEEE (2015).
6. D. Büchter: Drivers and Elements of Future Airborne Communication Networks, in Proc. DLRK, Berlin (2012).
7. D. Medina, F. Hoffmann: The Airborne Internet, *Future Aeronautical Communications*. Germany InTech, 2011, Chap. 17.
8. A. Solheim, J. Frodsham: Next generation backbone network metrics, NFOEC, Baltimore, MD (2001)
9. Jason Derenick, Christopher Thorne, John Spletzer: Hybrid Free-Space Optics/Radio Frequency (FSO/RF) Networks for Mobile Robot Teams, Multi-robot Systems, Swarms to Intelligent Automata Volume 3, pp 263–268 (2010).
10. Aditi, Preeti Singh: Free Space Optics: Current Applications and Future Challenges, International Journal of Optics (2015).
11. Zabidi, S.A, Khateeb, W.A. Islam, M.R Naji: The effect of weather on free space optics communicatin (FSO) under tropical weather conditions and a proposed setup for measurement, Computer and Communication Engineering (2010).
12. Long, Dou, David Lee, Jesse Johnson, and Peter Kostiuk: A Small Aircraft Transportation System (SATS) Demand Model, Logistics Management Institute, McLean, Virginia NASAlCR (2001).
13. E. Sakhaee, A. Jamalipour: The Global In-Flight Internet, IEEE Journal on Selected Areas in Communications (2006).
14. Syed nawaz: Airborne internet access through submarine cables, IEEE transactions on aerospace and electronic systems, vol 51(2015).
15. E. Sakhaee, A. Jamalipour, N. Kato: Aeronautical Ad Hoc Networks, IEEE WCNC (2006).
16. Sivathasan, S, O'Brien, D: Lifetime Comparison of Rf only and Hybrid RF/FSO wireless Sensor Networks, Computer and Communication Engineering (2008)
17. Deva K Borah, Anthony C Boucouvalas, Christopher C Davis, Steve Hranilovic and Konstantin's Yiannopoulos: A review of communication-oriented optical wireless systems, EURASIP Journal on Wireless Communications and Networking (2012).

Operational Amplifier-Based Fractional Device of Order $s^{\pm 0.5}$

Huirem Tarunkumar, Ashish Ranjan, Ravi Kumar and P. Subrahmanyam

Abstract This paper brings an active fractional order device realization using an Op-amp (LM741) and few passive components. The fractional device model is derived from the rational approximation of fractional-order operator. Here continued fraction expansion is used to obtain the transfer function for the active realization of $s^{\pm 0.5}$. RC-RC decomposition technique is used to synthesize the transfer function. The verification of the design is done using PSPICE to validate the theoretical as well as ideal result.

Keywords Continued fraction expansion · Op-amp (LM741) · Fractional device

1 Introduction

Over the years, integer-based systems were being modelled and designed to replicate real-life phenomena, until it was found that a more accurate description can be provided by using fractional calculus. The surge of interest in fractional order systems is a recent trend. As per the literature survey, it is found that fractional calculus deals with non-integer differentiations and integrations. This is because it provides accurate modelling in various fields like biomedical [1], controllers [2], filters [3],

Huirem Tarunkumar (✉) · Ashish Ranjan · Ravi Kumar · P. Subrahmanyam
National Institute of Technology Manipur, Imphal 795001, India
e-mail: connect2tarunh@gmail.com

Ashish Ranjan
e-mail: ashish.ism@rediffmail.com

Ravi Kumar
e-mail: rksingh.15892@gmail.com

P. Subrahmanyam
e-mail: subbu54.india@gmail.com

© Springer Science+Business Media Singapore 2017

R. Singh and S. Choudhury (eds.), *Proceeding of International Conference on Intelligent Communication, Control and Devices*, Advances in Intelligent Systems and Computing 479, DOI 10.1007/978-981-10-1708-7_16

oscillators [4], bioengineering [5] and many more. The Caputo derivative [6] gives the fractional derivative of any order as

$$aD_t^{\alpha} f(t) = \frac{1}{\Gamma(1-\alpha)} \frac{\mathrm{d}}{\mathrm{d}t} \int_a^t (t-\tau) f(\tau)\, \mathrm{d}\tau, \quad 0 < \alpha < 1 \tag{1}$$

At zero initial condition, the Laplace transform of (1) is

$$L\{a\, D^{\alpha}\, f(t)\} = s^{\alpha}\, F(s). \tag{2}$$

Therefore, a fractance device has an impedance $Z(s)$ proportional to $k_0 s^{\alpha}$ where α is the fractional order and it exhibits fractional capacitance, resistance and inductance at $\alpha = -1$, 0 and 1 respectively [7].

A number of fractional devices have been realized as ladder, RC network, grid type and tree as presented in [8–11], but apart from the inherent complexity of such realizations of fractance device, it also suffers from high cost and area. Another important criterion in the realization of fractional-order devices is finding the rational approximation of its function. Many methods have been used to find the rational approximation of fractance device, e.g. Newton's method, Matsuda approximation, Oustaloup approximation and continued fraction expansion (CFE) [12–17]. Here, CFE formulae are used to obtain the rational approximation of a fractional-order device. Apart from that, CFE method is more suitable for the modelling of fractance device. Also RC-RC decomposition technique is used to synthesize the circuit.

This paper presents a fractional device of orders ± 0.5 using an Op-amp (LM741) with some passive components. This work is organized as follows. In Sect. 2, a brief discussion on CFE and the procedure for the design of the fractional order device is discussed. In Sect. 3, simulation results of the fractional-order device are presented. Finally, Sect. 4 comes with conclusion.

2 Proposed Design Procedure

2.1 Continued Fraction Expansion

A number can be represented iteratively as the sum of its integer part and the reciprocal of another number. Such expressions are known as Continued Fractions. The CFE for $(1 + x)^{\alpha}$ is given by [18]

$$(1+x)^{\alpha} = \frac{1}{1-}\,\frac{x\alpha}{1+}\,\frac{(1+\alpha)x}{2+}\,\frac{(1-\alpha)x}{3+}\,\frac{(2+\alpha)x}{2+}\,\frac{(2-\alpha)x}{5+\,-\,-} \tag{3}$$

Table 1 Second-order rational approximation of s

No. of terms	Order	Rational approximation
4	+0.5	$\frac{5s^2+10s+1}{s^2+10s+5}$
4	−0.5	$\frac{s^2+10s+5}{5s^2+10s+1}$

Which converges in the finite complex s-plane, with negative real axis from $x = -\infty$ to $x = -1$. To calculate the rational approximations, put $x = s-1$ and taking the number of terms in Eq. (3) as four, the obtained rational approximation of s^{α}, where $\alpha = \pm 0.5$ are given in Table 1.

2.2 Circuit Description

The rational approximation of $\sqrt{s}$, may be considered as a ratio of two admittance terms, in which the numerator of rational function represents a parallel combination of resistive and capacitive terms. Similarly, the denominator consists of resistive and capacitive terms but the gain is negative when we consider the output across first Op-amp. Hence to achieve the second-order approximation of $\sqrt{s}$, we have to insert an inverting amplifier as shown in Fig. 1. The above process is also valid for $\frac{1}{\sqrt{s}}$, the combined circuit is similar to Fig. 1. RC-RC decomposition is used to decompose the above approximations of s^{α}, which yields the normalized component values.

If the rational approximation of $\sqrt{s}$ is $T(s) = \frac{5s^2+10s+1}{s^2+10s+5}$, then RC-RC decomposition technique [19] is used by taking an arbitrarily chosen polynomial as $D(s) = (s + 1)$. Hence $T(s)$ can be written as

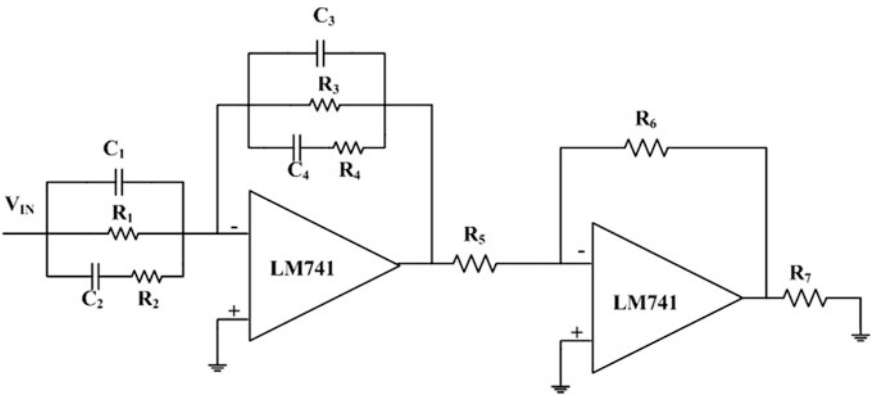


Fig. 1 Proposed fractional-order device using Op-amp

$$T(s) = \frac{(5s^2 + 10s + 1)/(s+1)}{(s^2 + 10s + 5)/(s+1)} \tag{4}$$

Solving the above equation will result in

$$T(s) = \frac{5s + 1 + \frac{4s}{s+1}}{s + 5 + \frac{4s}{s+1}} \tag{5}$$

By choosing proper Impedance Scaling Factor (ZSF) and Frequency Scaling Factor (FSF) we can get the exact component values from the normalized values. The exact values of resistance and capacitance is given by

$$R = R_{\mathrm{N}} \times \mathrm{ZSF}\,\Omega \tag{6}$$

$$C = C_{\mathrm{N}} \times C_{\mathrm{M}} F \tag{7}$$

Here R_{N} and C_{N} are the normalized values of resistance and capacitance respectively. C_{M} is the capacitance multiplication factor given by

$$C_{\mathrm{M}} = \frac{1}{2\pi(\mathrm{ZSF} \times \mathrm{FSF})} \tag{8}$$

The exact component values are obtained after scaling and some modifications. The different component values are listed in Table 2. Here, ZSF and FSF are 40 kΩ and 160 MHz.

Table 2 Normalized and exact component values

No. of terms	Fractional order	Normalized values	Component values
4	$s^{0.5}$	R_1 = 1	R_1 = 40 KΩ
		R_2 = 1/4	R_2 = 10 KΩ
		R_3 = 1/5	R_3 = 8 KΩ
		R_4 = 1/4	R_4 = 10 KΩ
		C_1 = 5	C_1 = 124.3 μF
		C_2 = 4	C_2 = 99.44 μF
		C_3 = 1	C_3 = 24.86 μF
		C_4 = 4	C_4 = 99.44 μF
	$s^{-0.5}$	R_1 = 1/5	R_1 = 8 KΩ
		R_2 = ¼	R_2 = 10 KΩ
		R_3 = 1	R_3 = 40 KΩ
		R_4 = ¼	R_4 = 10 KΩ
		C_1 = 1	C_1 = 24.86 μF
		C_2 = 4	C_2 = 99.44 μF
		C_3 = 5	C_3 = 124.3 μF
		C_4 = 4	C_4 = 99.44 μF

3 Simulation Results

To verify the circuit, it is simulated by PSPICE in which the active device is an operational amplifier (LM741) with some passive components. The passive elements for the proposed fractional device are listed in Table 2 and the component values for the additional inverting amplifier are taken as $R_5 = R_6 = R_7 = 1\ \text{k}\Omega$. First part of the simulation shows the magnitude and phase response of $\sqrt{s}$ which is given in Figs. 2 and 3 respectively.

After that Figs. 4 and 5 shows the magnitude and phase response for the fractional device for $\frac{1}{\sqrt{s}}$. From the plots, we can observe that the response of the proposed design matches with the theoretical plots. The phase angle of the proposed fractional device with $\alpha = +0.5$ and $\alpha = -0.5$ are $\pm 45^{\circ}$.

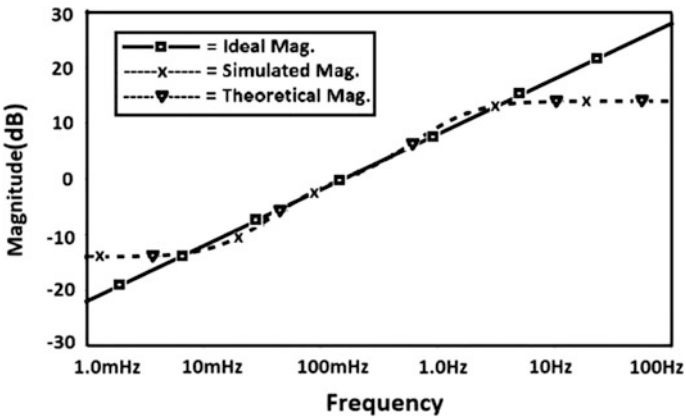


Fig. 2 Magnitude response of $\alpha = 0.5$

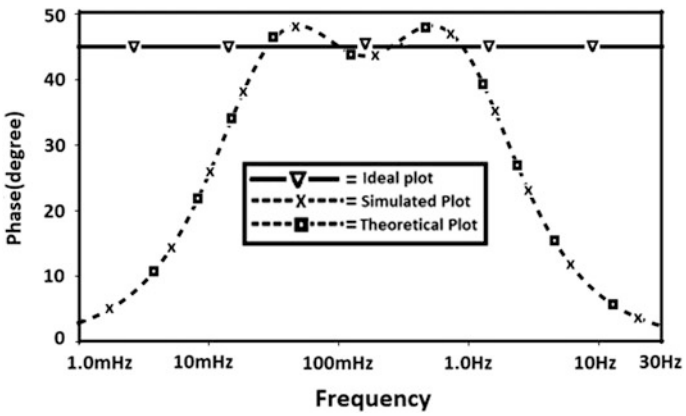


Fig. 3 Phase response of $\alpha = 0.5$

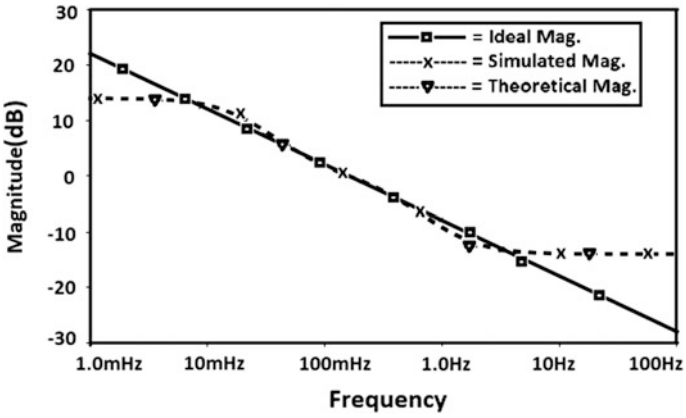


Fig. 4 Magnitude response of $\alpha = -0.5$

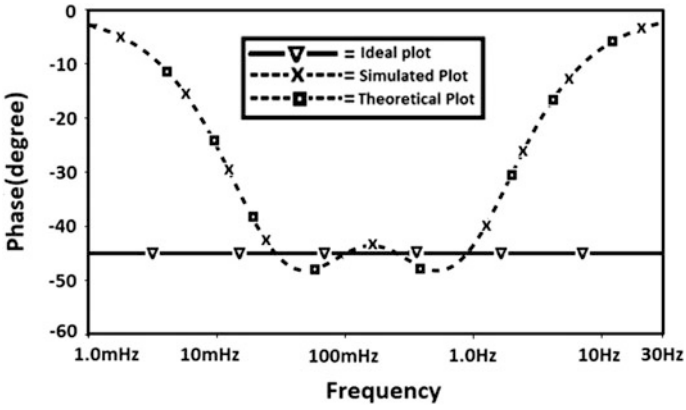


Fig. 5 Phase response of $\alpha = -0.5$

For $\alpha = -0.5$, the proposed design acts as a fractional capacitor. In order to verify the behaviour of the fractional capacitor, the circuit of Fig. 6 is simulated by applying a pulse. The fractional capacitor is replaced by a fractance element "F" that is simply a block model of the proposed fractional capacitor. The input pulse is applied to the fractional capacitor through a 20 kΩ resistor. The charging and discharging characteristics of the simulated fractance device are shown in Fig. 7.

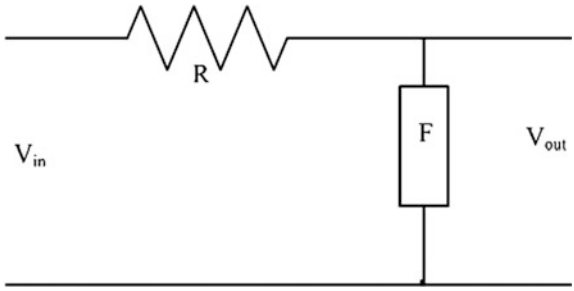


Fig. 6 Circuit for verification of the proposed fractional capacitor

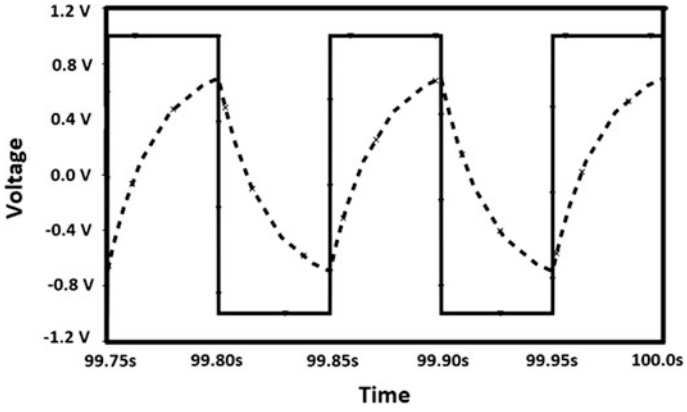


Fig. 7 Simulation result of fractional capacitor of order −0.5

3.1 Figures

The behaviour of the fractional capacitor can also be verified by incorporating in a low-pass filter (LPF) circuit. The circuit of Fig. 6 also corresponds to a first-order low-pass filter if an AC input is applied. An AC input is applied to the fractional capacitor through a 1 kΩ resistor. The magnitude and phase response of the simulated LPF with the fractional capacitor are shown in Fig. 8.

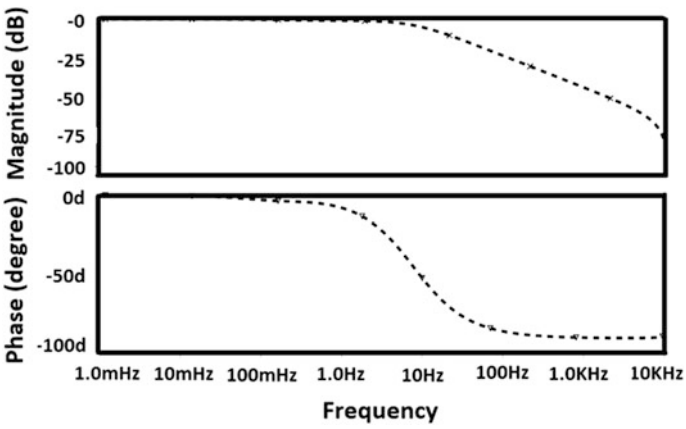


Fig. 8 Simulation result of the proposed fractional order low pass filter

4 Conclusion

The proposed method presents the design of a fractional-order device using an op-amp of order ± 0.5. Simulation results agree well with theory. Also the use of the proposed fractional device as a fractional-order capacitor is shown. Using the proposed method, fractional devices of different orders can be realized with op-amps and other active devices.

References

1. Freeborn, T.J: A survey of fractional order circuit models for biology and biomedicine. Emerging and Selected Topics in Circuits and Systems, IEEE Journal on, 3, 3, 416–424 (2013)
2. Pakhira, Anindya and Das, Saptarshi and Pan, Indranil and Das, Shantanu.: Symbolic representation for analog realization of a family of fractional order controller structures via continued fraction expansion. ISA transactions. 57, 390–402 (2015)
3. Ali, Akram Syed and Radwan, Ahmed Gomaa and Soliman, Ahmed M.: Fractional order Butterworth filter: active and passive realizations. Emerging and Selected Topics in Circuits and Systems, IEEE Journal on. 3, 346–354 (2013)
4. Said, Lobna and Madian, Ahmed H and Radwan, Ahmed G and Soliman, Ahmed M and others.: Current feedback operational amplifier (CFOA) based fractional order oscillators. In: 21st IEEE International Conference on Electronics, Circuits and Systems (ICECS), pp. 510–513 (2014)
5. Aguilar, José Francisco Gomez and Alvarado, J Jesús Bernal and Garcia, J Juan Rosales and Fraga, Teodoro Cordova.: Modeling and simulation of equivalent circuits in description of biological systems-a fractional calculus approach. Journal of Electrical Bioimpedance. 3, 2–11 (2012)
6. Podlubny, Igor.: Fractional differential equations. Academic Press, San Diego, CA (1999)

7. Machado, JA Tenreiro and Jesus, Isabel S and Galhano, Alexandra and Cunha, J Boaventura.: Fractional order electromagnetics. Signal Processing. 86, 10, 2637–2644 (2006)
8. Nakagawa, Masahiro and Sorimachi, Kazuyuki.: Basic characteristics of a fractance device. IEICE Transactions on Fundamentals of Electronics, Communications and Computer Sciences.75, 12, 1814–1819 (1992)
9. Yifei, Pu and Xiao, Yuan and Ke, Liao and Jiliu, Zhou and Ni, Zhang and Yi, Zeng and Xiaoxian, Pu.: Structuring analog fractance circuit for 1/2 order fractional calculus. In: 6th International Conference on ASIC (ASICON), pp. 1136–1139 (2005)
10. Pu, Yifei and Yuan, Xiao and Liao, Ke and Zhou, Jiliu and Zhang, Ni and Pu, Xiaoxian and Zeng, Yi.: A recursive two-circuits series analog fractance circuit for any order fractional calculus. In: ICO20: Optical Information Processing, pp. 60271Y–60271Y (2006)
11. Valsa, Juraj and Vlach, Jiri.: RC models of a constant phase element. International Journal of Circuit Theory and Applications. 41, 1, 59–67 (2013)
12. Krishna, BT and Reddy, KVVS.: Active and passive realization of fractance device of order 1/2. Active and passive electronic components (2008)
13. Vinagre, BM and Podlubny, I and Hernandez, A and Feliu, V.: Some approximations of fractional order operators used in control theory and applications. Fractional calculus and applied analysis. 3, 3, 231–248 (2000)
14. Matsuda, Khoichi and Fujii, Hironori.: H (infinity) optimized wave-absorbing control-Analytical and experimental results. Journal of Guidance, Control, and Dynamics. 16, 6, 1146–1153 (1993)
15. Podlubny, Igor and Petraš, I and Vinagre, Blas M and O'leary, P and Dorčak, L'.: Analogue realizations of fractional-order controllers. Nonlinear dynamics. 29, 1–4, 281–296 (2002)
16. Carlson, Gordon Eugene and Halijak, C.: Approximation of Fractional Capacitors $(1/s)^{1/n}$ by a regular Newton process. Circuit Theory, IEEE Transactions on. 11, 2, 210–213 (1964)
17. Oustaloup, A.: Fractional order sinusoidal oscillators: optimization and their use in highly linear FM modulation. Circuits and Systems, IEEE Transactions on. 28, 10, 1007–1009 (1981)
18. Khovanskii, Alexey Nikolaevitch and Wynn, Peter.: The application of continued fractions and their generalizations to problems in approximation theory. Noordhoff Groningen (1963)
19. Kilinç, Selcuk and Çam, Ugur.: Realization of nth-order voltage transfer function using single operational transresistance amplifier. Etri Journal. 27, 5, 647–650 (2005)

A Novel Approach for Designing PID Controller for Set-Point Tracking for a HVAC Process

Nitin Sundriyal, Pratibha Yadav and Mayank Chaturvedi

Abstract It is seen that most of the industrial processes are delayed processes. In this work, a first-order mathematical system with dead time has been obtained from second-order plus dead time system using Skogestad's half rule for HVAC process. For PID controller designing different tuning techniques have been used. On the basis of the comparison of the set-point tracking of the controller for step response, best tuning technique has been examined for the selected process model.

Keywords Controller tuning · FOPDT · HVAC systems · PID controller · SOPDT · Skogestad's half rule · Set-point tracking

1 Introduction

Process control enables mass production of consistent products from incessantly operated processes, such as paper manufacturing, oil refining, chemicals, power plants, and many others and therefore, it is mainly used in industries. In order to develop a control system, an important step is the specification of CVs, MVs, DVs [1]. The order of a system can be defined as the highest order of numerator or denominator polynomial, whichever is greater [2]. The transportation lag of the energy or matter in a process is termed as delay time. The presence of delay in a system, makes the control system perform in a sluggish manner [3]. Two dead time models, i.e., the FOPDT and SOPDT model is represented as:

Nitin Sundriyal (✉) · Pratibha Yadav · Mayank Chaturvedi
Department of Electrical Engineering, Graphic Era University, Dehradun, India
e-mail: nitinssundriyal@gmail.com

Pratibha Yadav
e-mail: pratibhayadavddn@gmail.com

Mayank Chaturvedi
e-mail: mayankchaturvedi.geit@gmail.com

© Springer Science+Business Media Singapore 2017

R. Singh and S. Choudhury (eds.), *Proceeding of International Conference on Intelligent Communication, Control and Devices*, Advances in Intelligent Systems and Computing 479, DOI 10.1007/978-981-10-1708-7_17

$$G(s) = \frac{K\mathrm{e}^{-\theta s}}{1+\tau s} \tag{1}$$

where, K is the system gain, θ is the time delay and τ is the time constant.

$$G(s) = \frac{k\mathrm{e}^{-\theta s}}{(1+\tau_1 s)(1+\tau_2 s)} \tag{2}$$

where k is the gain, θ is the time delay, and τ_1, τ_2 are the time constants [2].

In the process control applications, the most commonly used controller is the PID controller and can indemnify both the delayed and non-delayed effects [4]. Controller tuning minimizes the error between the process variable and the input [1]. The three principle control effects and the PID controller tuning methods presented by Ziegler and Nichols [5].

The process taken in this paper is the supply air pressure loop of HVAC (heating, ventilation, and air-conditioning) systems. For setting environmental variables which includes pressure, temperature, and moisture HVAC mechanism is used. The processes which are associated with HVAC have been controlled by PID controllers [6].

Skogestad [7] presented the simple analytic tuning procedure for model reduction by using Skogestad's half rule in order to find the time delay.

Wen Tan et al. [8] performed some well-known tuning formulas comparison.

Pradeep Kumar Juneja et al. [9] commented that most of the industrial processes are first-order plus dead time in nature for tuning purposes.

2 PID Controller Tuning Formulas (Standard)

PID controller can be represented as:

$$G(s) = K_{\mathrm{c}}(1 + 1/T_{\mathrm{is}} + T_{\mathrm{ds}}) \tag{3}$$

where, K_{c} represents proportional gain, T_{i} is the integral time, and T_{d} is the derivative time.

Table 1 contains various PID controller tuning techniques for SOPDT process model. Where K_{cu} represents the critical gain or ultimate gain and T_{u} is the ultimate

Table 1 PID tuning formulas for SOPDT

Controllers tuning methods	K_{c}	T_{i}	T_{d}
Ziegler-Nichols	$0.6k_{\mathrm{cu}}$	$T_{\mathrm{u}}/2$	$T_{\mathrm{u}}/8$
Tyreus-Luyben	$0.45K_{\mathrm{cu}}$	$2.2T_{\mathrm{u}}$	$T_{\mathrm{u}}/6.3$
Skogestad	$\frac{0.5(\tau_1+\tau_2)}{K_\theta}$	$\tau_1 + \tau_2$	$\frac{\tau_1\tau_2}{\tau_1+\tau_2}$
IMC	$\frac{(\tau_1+\tau_2)}{K(\tau_c+\theta)}$	$\tau_1 + \tau_2$	$\frac{\tau_1\tau_2}{\tau_1+\tau_2}$

Table 2 FOPDT PID tuning formulas

Controller tuning methods	K_c	T_i	T_d
Ziegler-Nichols	$0.6K_{cu}$	$0.5T_u$	$0.125T_u$
Tyreus-Luyben	$0.45K_{cu}$	$2.2T_u$	$T_u/6.3$
Skogestad	$\frac{0.5\tau}{K\theta}$	8θ	0.5θ
IMC	$\frac{(\tau+\theta/2)}{K(\tau_c+\theta/2)}$	$(\tau + \theta/2)$	$\frac{\tau\theta}{2\tau+\theta}$

period. The condition ($\tau_c < \tau_1$) given in IMC tuning method and τ_c is the closed-loop time constant [1]. Table 2 shows the PID controller tuning methods for FOPDT process and ($\mathcal{T}_c < \mathcal{T}$) given by IMC tuning method [1].

3 Methodology

Figure 1 shows the proposed methodology, in which the first step is to consider a SOPDT process, then delay in the selected model is approximated using Taylor series expansion. Skogestad half rule is implemented in order to convert SOPDT model into FOPDT model. PID controller is designed using various tuning techniques. The controller is implemented in a closed loop with the process models, i.e., SOPDT and FOPDT with unity feedback. By using different tuning techniques set-point tracking performance of the controllers is compared for step response.

The SOPDT model [6] is shown as:

$$G(s) = \frac{0.81e^{-2s}}{(0.97s+1)(0.1s+1)} \tag{4}$$

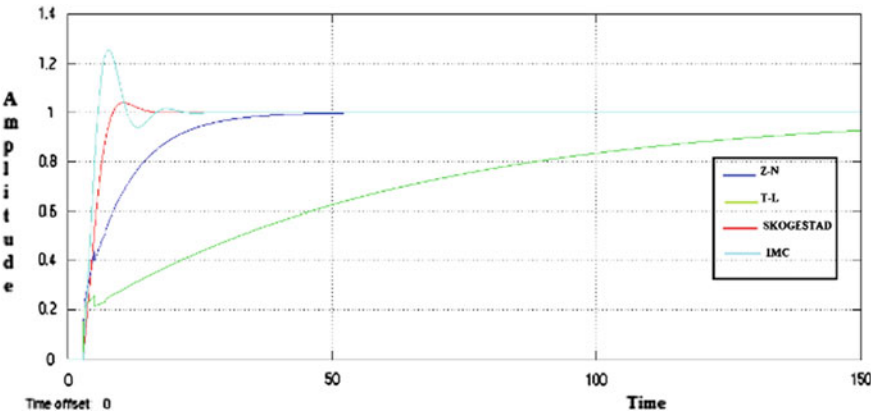


Fig. 1 Combined response of Z-N, T-L, Skogestad, IMC for SOPDT process model

Table 3 Controller parameters for SOPDT

Controller tuning method	K_c	T_i	T_d
Ziegler-Nichols	0.396	2.741	0.685
Tyreus-Luyben	0.297	12.06	0.8701
Skogestad	0.3302	1.07	0.0906
IMC	0.503	1.07	0.0906

The SOPDT transfer function after using the Taylor series expansion is:

$$G(s) = \frac{0.81(1 - 2s + 2s^2)}{(0.97s + 1)(0.1s + 1)} \tag{5}$$

Using different tuning techniques the PID controllers parameters are (Table 3):

The above table shows the controller parameters for SOPDT process model. For IMC tuning method, $\tau_c = 0.62$.

Defining Skogestad's half rule:

(i) A new time constant is generated by adding half of the largest neglected time constant value to the next largest retained time constant.
(ii) The other half of the neglected time constant provides a new time delay.

Thus the transfer function of FOPDT process model obtained from Skogestad half rule is given as

$$G(s) = \frac{0.81e^{-2.05s}}{(1.02s + 1)} \tag{6}$$

The Pade's approximation of the delay term for first-order system is given as:

$$e^{-\theta s} = \frac{1 - \theta_s/2}{1 + \theta_s/2} \tag{7}$$

Thus, the FOPDT process model obtained is (Table 4):

$$G(s) = \frac{0.81(1 - 1.025s)}{(1 + 1.02s)(1 + 1.025s)} \tag{8}$$

For IMC tuning method, the value of $\tau_c = 0.5$ s

Table 4 FOPDT PID controller parameters

Controller tuning methods	K_c	T_i	T_d
Ziegler-Nichols	1.4778	1.8565	0.464
Tyreus-Luyben	1.1083	8.1686	0.5893
Skogestad	0.3071	16.4	1.025
IMC	1.655	2.045	0.511

4 Results

The set-point tracking capability of the controller and different unit step response characteristics, i.e., gradual increase time, settling time, maximum overshoot is analyzed by performing simulation. Figure 1 shows the comparative response among the different controller tuning techniques values, i.e., Z-N, T-L, Skogestad, and IMC for SOPDT process model with step input. Figure 2 shows comparison response for FOPDT process model for different controller tuning techniques values, i.e., Z-N, T-L, Skogestad, and IMC with step input. Table 5 shows the combined time response characteristics of Z-N, T-L, Skogestad, IMC for SOPDT process model with step-input. Table 6 represents the combined time response characteristics of Z-N, T-L, Skogestad, IMC for FOPDT process model with step-input.

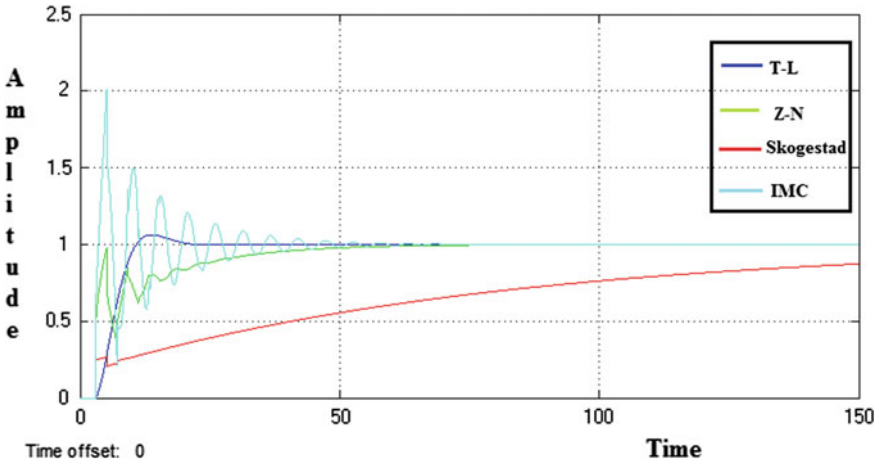


Fig. 2 Combined response of Z-N, T-L, Skogestad, IMC for FOPDT process model

Table 5 Comparison of time response characteristics for SOPDT model

Controller methods	Rise time (sec)	Settling time (sec)	Maximum overshoot (%)
Ziegler-Nichols	17.3	32.9	0
Tyreus-Luyben	128	228	0
Skogestad	3.82	12.1	3.96
IMC	2.13	14.6	26.4

Table 6 Comparison of time response characteristics for FOPDT model

Controller methods	Rise time (sec)	Settling time (sec)	Maximum overshoot (%)
Ziegler-Nichols	0.547	27.4	82.4
Tyreus-Luyben	1.56	50.7	0
Skogestad	166	296	0
IMC	0.336	46.8	101

5 Conclusion

In this paper, we have performed various tuning methods, i.e., Z-N, T-L, Skogestad, IMC for tuning PID controller for SOPDT model and approximated FOPDT model. In case of SOPDT process, Skogestad tuning technique gives the best response but in case of approximated FOPDT process using Skogestad half rule, Z-N tuning technique gives the best response.

References

1. D.E. Seborg, T.F. Edgar, D.A. Mellichamp: Process Dynamics and Control. 2nd ed., United States: John Wiley and Sons Publications (2004).
2. Dr. S. Palani and Prof. Anoop K. Jairath.: Automatic Control Systems. New Delhi Ane Books Publications.
3. Aidan O'dwyer.: A classification of techniques for the compensation of time delayed processes. Modern Applied Mathematical Techniques in Circuits, Systems and Control, World Scientific and Engineering Society Press (1999).
4. K.J. Astrom and T. Hagglund.: Automatic Tuning of PID controllers. Instrument society of America (1998).
5. J.G. Ziegler, N.B. Nichols.: Optimum settings for automatic controllers. Transactions. A.S.M.E. 64, pp. 759–768 (1942).
6. Mohammad Hassan Khooban, Davood Nazari Maryam Abadi, Alireza Alfi, Mehdi Siahi.: Optimal Type-2 Fuzzy Controller For HVAC Systems. AUTOMATICA 55(1), pp. 69–78 (2014).
7. Sigurd Skogestad.: Simple analytic rules for model reduction and PID controller tuning. Journal of process control, vol. 13, pp. 291–309 (2003).
8. Wen Tan, Jizhen Liu, Tongwen Chen, Horacio J. Marquez.: Comparison of some well-known PID tuning formulas. Computers and Chemical Engineering, vol. 30, pp. 1416–1423 in ELSEVER (2006).
9. Pradeep Kumar Juneja, AK Ray and RMitra.: Various Controller Design and Tuning Methods for a First Order plus Dead Time Process. Published in the International Journal of Computer Science and Communication, vol. 1, no. 2, pp. 161–165 (2010).

Performance Analysis of FSO Link Using CO-OFDM Under the Effect of Atmospheric Turbulence

Saruchi Attri, Charu Narula and Sanjiv Kumar

Abstract Free space optical communication (FSO) is a promising technology where optical fiber installation is not feasible. Performance of FSO system is affected by atmospheric attenuation caused by changing weather condition, such as haze, fog, snow, rain, etc., and scintillation induced by atmospheric turbulence. This article demonstrated the performance of coherent optical orthogonal frequency division multiplexing FSO (CO-OFDM FSO) system under the atmospheric turbulences and haze weather condition which performs better than traditional direct detection system. System is analyzed for different number of subcarriers under the influence of moderate to strong turbulence by adjusting the value of refractive index structure parameter. There is a degradation of 2–8 dB in SNR from moderate to strong turbulence up to the range of 30 km.

Keywords FSO · CO-OFDM · Atmospheric turbulence · Refractive index structure parameter

1 Introduction

Free space optical communication (FSO) is being studied as suitable alternate for optical fiber communication especially due to its ease of deployment where fiber installation is not feasible. Recently, it is an active area of research due to its advantages like high transmission rates, license-free operation, full duplex system, and high transmission security [1, 2]. However, the turbulences and attenuations

Saruchi Attri (✉) · Charu Narula · Sanjiv Kumar
UIET, PU, Chandigarh 160023, India
e-mail: saruchi.attri@gmail.com

Charu Narula
e-mail: charu_uiet@pu.ac.in

Sanjiv Kumar
e-mail: sanjivsam81@gmail.com

© Springer Science+Business Media Singapore 2017

R. Singh and S. Choudhury (eds.), *Proceeding of International Conference on Intelligent Communication, Control and Devices*, Advances in Intelligent Systems and Computing 479, DOI 10.1007/978-981-10-1708-7_18

generated in the atmosphere seriously affect the accuracy of the optical signal when transmitted over atmospheric channel.

OFDM can not only effectively suppress the inter symbol interference (ISI) but also provide high data rates. This communication technique has robustness against frequency selective fading and better utilization of frequency spectrum [3, 4]. OFDM is considered as exclusive case of multi carrier modulation (MCM) scheme, where information signal is modulated onto subcarriers appearing in different frequencies. These subcarriers are orthogonal to each other and thus do not interfere with each other [5, 6]. Coherent optical OFDM (CO-OFDM) produces the better receiver sensitivity and spectral efficiency by using the local oscillator with photodetection system. The incoming signal is optically mixed with optical field of local oscillator, can track the phase and amplitude of the original transmitted signal [7, 8].

The outdoor system performance of the FSO depends upon the climatic conditions and transmission path, i.e., scintillation effects and atmospheric attenuation. Scintillation causes the fluctuations in the irradiance of received signal due to change in the refractive index of the air. Many statistical distributions have been studied to model these fluctuations [9–11]. In this research article, we have demonstrated the performance of coherent optical orthogonal frequency division multiplexing FSO (CO-OFDM-FSO) system under the effect of scintillation by varying channel's refractive index structure parameter for different link lengths at haze weather condition. Moderate to strong turbulence is considered; SNR and received powers are analyzed over different link lengths. Rest of the article is organized as follows: in Sect. 2 a brief description of the simulative setup is provided, Sect. 3 presents the results and discussion and then Sect. 4 outlines conclusion.

2 Model Description

The FSO system is composed of three major communication parts that are transmitter, receiver, and propagation channel. The proposed CO-OFDM FSO system is designed using OPTISYSTEM v12 software generated 10 Gbps data rate. Data is generated by using 4-level QAM sequence generator with 2 bits per symbol. This QAM data is then modulates by using OFDM modulator with different number of subcarriers, i.e., 128, 512 and FFT size of 256 and 1024, respectively.

Sometimes subcarriers may lose their orthogonality and results in inter carrier interference (ICI), to over this effect cyclic prefix of 32 points is added [12, 13]. These OFDM analog signals are then optically modulated with light carrier generated by CW laser of –4 dBm power and wavelength of 1550 nm by means of two Mach–Zehnder modulators (MZM) to convert electrical signal to optical. Optical signal generated by MZM is transmitted through FSO channel having moderate and strong turbulences characterized by the value of refractive index structure parameter that is responsible for the scintillation effect. At the receiver base station signal is

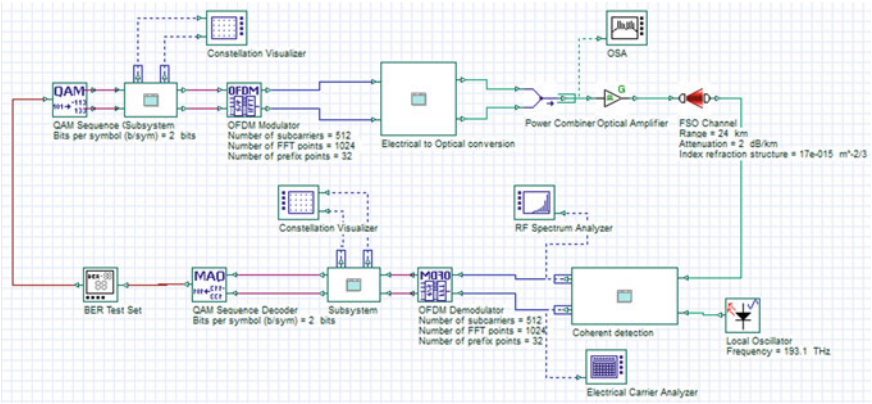


Fig. 1 OPTISYSTEM layout of CO-OFDM FSO system

received by two PIN photodetectors derived by a local oscillator having same wavelength as that of transmitter is used to realize the coherent detection. After that OFDM demodulator and QAM decoder is used to decode the signal into its original form. To visualize the constellation diagram an electrical constellation visualizer is attached after OFDM demodulator. A BER test set is connected after QAM decoder having inbuilt pseudo random bit sequence (PRBS) generator used to generate the random data bits. Figure 1 shows the OPTISYSTEM layout of the system.

3 Results and Discussion

The results are conferred in this section characterized the total received power and SNR at moderate and strong turbulences under haze weather condition. Comparison of number of subcarriers at moderate and strong turbulences is done. Parameter values for the analysis are shown [14] (Table 1):

Table 1 Parametric values for simulation

S. no.	Parameter	Value
1	Transmitter aperture diameter	10 cm
2	Receiver aperture diameter	30 cm
3	Additional losses	1 dB/km
4	Attenuation (haze)	2 dB/Km
5	Refractive index structure parameter for moderate and strong turbulence	1.7×10^{-14} and 5×10^{-14} ($m^{-2/3}$)
6	Number of subcarriers	128, 512

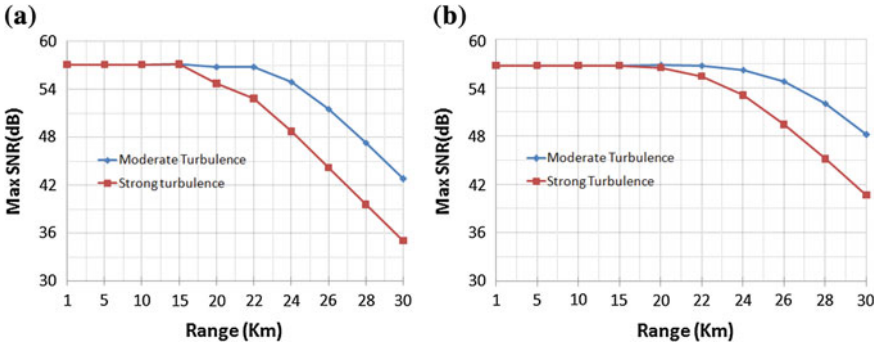


Fig. 2 Evaluation of SNR of CO-OFDM FSO link for different subcarriers **a** 128, and **b** 512

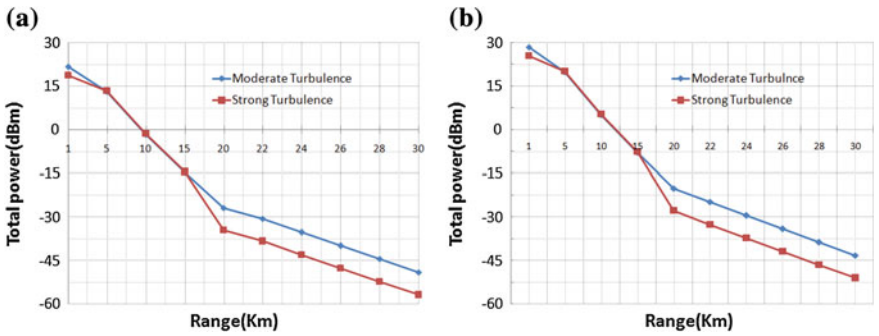


Fig. 3 Evaluation of received power of CO-OFDM FSO link for different subcarriers **a** 128, and **b** 512

It has been shown in Fig. 2 that SNR for first 15 km has very small variation from moderate to strong turbulences. After that moderate turbulence has better SNR than strong turbulence, there is 2–8 dB deterioration in SNR from moderate to strong turbulence. As we increase the number of subcarriers there is an improvement of 6 dB in SNR.

Figure 3 shows the total power at different link lengths and reduction in power from moderate to strong turbulence. Table 2 illustrates the values for SNR and total power for different ranges under different turbulences. RF power decreases as we are increasing the link range. It is depicted from the Table 2 that system performs better when number of subcarriers is increased from 128 to 512.

At moderate turbulence value of SNR for subcarriers [512, 128] is [48.19, 42.78] and for strong turbulence values are [40.71, 35.02], respectively at 30 km range. These are acceptable values for SNR for successful transmission.

Electrical constellation diagram for FSO link after 20 km is shown in Fig. 4.

Table 2 Illustration of total power received (dBm) and SNR (dB) for different turbulences

Range (km)	Number of subcarriers-512				Number of subcarriers-128			
	Moderate turbulence		Strong turbulence		Moderate turbulence		Strong turbulence	
	SNR	Power	SNR	Power	SNR	Power	SNR	Power
15	56.79	–7.81	56.79	–7.65	57.14	–14.52	57.14	–14.41
20	56.84	–20.04	56.5	–27.77	56.81	–26.8	54.72	–34.52
22	56.74	–24.79	55.45	–32.55	56.83	–30.54	52.83	–38.28
24	56.24	–29.48	53.09	–37.22	54.91	–35.23	48.71	–42.97
26	54.82	–34.12	49.45	–41.85	51.53	–39.87	44.18	–47.62
28	52.05	–38.71	45.17	–46.47	47.29	–44.46	39.57	–52.22
30	48.19	–43.27	40.71	–51.03	42.78	–49.02	35.02	–56.78

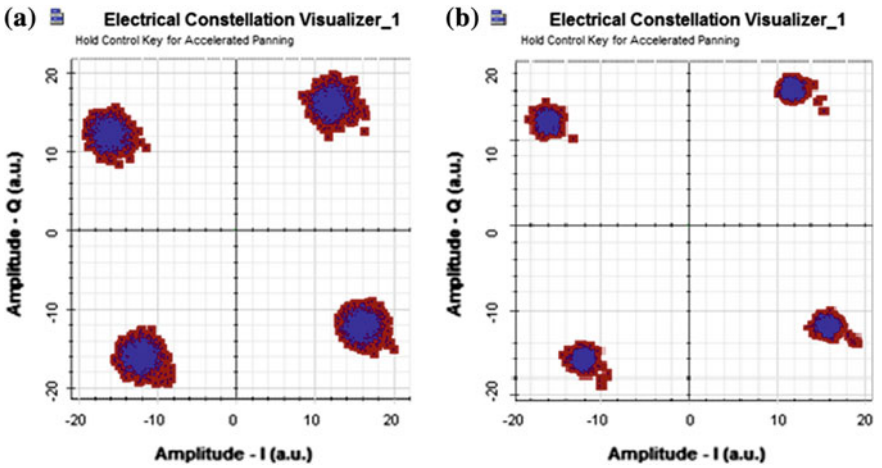


Fig. 4 Constellation diagram after 20 km FSO Transmission for subcarriers **a** 128, **b** 512

Constellation diagram in Fig. 4 shows the noise present in signal, it is observed that large amount of noise is present when subcarriers are 128 and can be reduced by increasing the number of subcarriers to 512. Results of coherent detection system that are shown above are better in terms of SNR and received power as compared of direct detection system demonstrated in [14].

4 Conclusion

In this work, we combine the advantages of coherent detection and OFDM technology in conventional FSO system and provide the data rate of 10 Gbps up to 30 km under the influence of turbulence in atmospheric channel and haze weather

condition. From our simulation results, it is concluded that there is an improvement of 6 dB in SNR when we increase the number of subcarriers. As we increase the turbulence from moderate to strong there is degradation in the received power and SNR of the system. Proposed coherent system provides the better receiver sensitivity and SNR as compared to direct detection system.

Acknowledgments The authors would like to acknowledge the support by UIET, Panjab University. They wish to thank the Electronics and Communication department for providing the lab facilities and required software.

References

1. V.W.S., Chan: Free-space optical communications. J. Lightwave Technol, vol. 24, no. 12, Dec (2006) 4750–4762
2. H., Willebrand, B., Ghuman: Free Space Optics: Enabling Optical Connectivity in Today's Networks. London, U.K.: Sams (2002)
3. F., Buchali, R., Dischler, X., Liu: Optical OFDM: A Promising High-speed Optical Transport Technology. Bell Labs Technical Journal 14(1), (2009) 125–146
4. S., Attri, C., Narula, S., Kumar: Techniques to Mitigate Fading Effect in FSO using OFDM. Proceedings of 2015 RAECS, IEEE, (2015)
5. F.B., Frederiksen, R., Prasad: An overview of OFDM and Related Techniques Towards Development of Future Wireless Multimedia Communications. Radio and Wireless conference, IEEE, (2002) 19–22
6. Bahai, B.R., Saltzberg: Multi-carrier Digital Communication: Theory and Applications of OFDM. 2nd ed., Springer-Verlag, New York (2004)
7. V., Sharma, Sushank: High speed CO-OFDM-FSO transmission system. Optik, vol.125, no. 6, Mar (2014) 1761–1763
8. W., Shich, C., Athaudage: Coherent optical orthogonal frequency division multiplexing. Electron. Lett., vol. 40, no. 10, May (2006) 587–588
9. Y., Wang, D., Wang, J., Ma: On the Performance of Coherent OFDM Systems in Free-Space Optical Communications. IEEE Photonic Journal, Vol. 7, no. 4, Aug (2015) Art ID 7902410
10. H.E., Nistazakis, A.N., Stassinakis, H.G., Sandalidis, G.S., Tombras: QAM and PSK OFDM RoFSO over M-turbulence induced fading channels. IEEE Photonic journal, vol. 7, no. 1, Feb (2015) Art ID. 7900411
11. A., Bekkali, C., Ben Naila: Transmission analysis of OFDM-based wireless services over turbulent radio-on-FSO links modeled by gamma–gamma distribution. IEEE Photonic Journal, vol. 2, no. 3, May (2010) 510–520
12. S., Choudhary, A., Amphawan, K., Nisar: "Realization of free space optics with OFDM under atmospheric turbulence", Elsevier Optic 125 (2014) 5196–5198
13. P., Patel, V., Mishra, V., Singh: Performance analysis of CO-OFDM FSO system under different weather conditions. 2nd International conference on emerging trends in Electronics, Communication and Networking, IEEE (2014) 1–5
14. P., Kumar, A., Srivastava: Enhanced Performance of FSO Link Using OFDM and Comparison with Traditional TDM-FSO Link. International Broadband and Photonics Conference, Bali, April (2015) 23–25

Reliable and Fast Data Transmission Mechanism for Congested Wireless Sensor Network

Roshan Jahan and Preetam Suman

Abstract Communication in large area wireless sensor networks that consists of more than 1000 nodes should be reliable in real-time event detection system. All nodes are active and transmit event information to the base station. Due to large number of packet transmission, network gets congested. This causes large number of packet loss. Missing of single packet of information can cause a big event. This paper presents a reliable and fast data transmission protocol for WSN. There are two improvements in this mechanism over previous mechanisms. First is the utilization of packet transmission waiting time and second is adjustment of sending window size according to packet drop ratio. The network capacity is measured according to packet loss ratio. The implementation of proposed technique is done in QualNet 5.0. Results are described in the paper.

Keywords Wireless ad hoc network · Wireless sensor network · Congestion control · TCP variants

1 Introduction

Wireless sensor networks [1] can be described in terms of thousands of small devices responsible of computation, communication, and sensing. These small devices are called MOTE [2]. The MOTEs are deployable in real-time application to protect large area. The sensor attached with the MOTE senses the environmental signals, processor/microcontroller perform computing to identify the events. The communication devices are transceivers, which receive and transmit event information to the base station through multihoping [3]. The packets of event information transmitted in network required certain protocols to reach the destination.

Roshan Jahan (✉) · Preetam Suman
Computer Science and Engineering, Integral University, Lucknow, India
e-mail: roshan@iul.ac.in

Preetam Suman
e-mail: psuman@iul.ac.in

© Springer Science+Business Media Singapore 2017

R. Singh and S. Choudhury (eds.), *Proceeding of International Conference on Intelligent Communication, Control and Devices*, Advances in Intelligent Systems and Computing 479, DOI 10.1007/978-981-10-1708-7_19

There are several routing protocols that exist for WSN. Static routing [4] is preferable in the case of multihop transmission.

The other required protocol is MAC [5] protocol. Energy of MOTE to sense and transmit the information in WSN is a major issue. Various protocols exist for MAC, but till now none of the MAC protocols is suitable for WSN. Still development and research are going on. Other than energy saving protocol, few media access protocol with collision detection and avoidance are used for WSN.

After MAC protocol, the most important protocol is TCP [6], which is required for reliable packet transmission. The successful packet transmission to the base station is very essential. Any serious event can take place, if packet transmission fails. There are many nodes which can transmit event information at the same time. It may cause congestion in network. There are various variants that have been proposed to reduce congestion effects, TCP Tahoe [7–9], TCP Reno [8], TCP Reno with Selective Acknowledgement (SACK) [7, 8], TCP NewReno [10, 11], TCP Westwood [11] TCP Vegas [12], and TCP FACK [13] are examples of proposed end-to-end solutions. These variants are proposed to improve network performance, but still we are facing problems of packet drop and packet loss.

This paper presents a new variant of TCP for wireless sensor network to reduce the effect of congestion in network. The proposed technique is based on utilizing waiting time for packet transmission and adjustment of sending window size according to the packet drop ratio.

There are various researches going on to reduce the effect of congestion and to make reliable communication by implementing transmission control protocol. Few of the research are as follows.

Kumar et al. [14] has proposed a congestion control mechanism for MANET. The author has calculated various parameters to monitor the congestion status and developed routing protocol. The proposed routing protocol with conventional TCP has been implemented and compared by the author. As results shows proposed technique is better.

Sharma et al. [15] has implemented various parameters to identify the non-congestion losses of TCP in MANET. Author has implemented parameters in NS-3 simulator, simulate the communication, and then observe the performance of MANET in different scenarios.

Above literatures shows development of TCP variants for various purposes. This paper presents implementation of protocol to reduce the packet drops in congested network.

Organization of paper: Sect. 2 transmission control protocol, Sect. 3 presents the proposed mechanism, and Sect. 4 presents results of simulation.

2 Transmission Control Protocol

Transmission control protocol (TCP) is known for reliable communication. It is a protocol of transport layer in TCP/IP layers [16]. The size of congestion window either increases or decreases according to the network capacity.

Slow Start: The first step in TCP is slow start. The size of congestion window starts from either 4380 byte or maximum of segment size. The congestion window grows exponentially. After a certain period network get congested and at that time size of congestion window becomes half. At the same time congestion avoidance phase starts.

Congestion avoidance phase: In this phase size of congestion window becomes half and congestion avoidance algorithm executes.

Fast retransmission: In this phase TCP transmits all those packets which are dropped or not acknowledged. After fast retransmission phase again slow start phase starts.

There are various improvements has been done for better performance. The improvements are based on avoiding the congestion and retransmit the packets. There are two demerits of TCP which are not covered by other variants.

The first demerit is waiting of acknowledgement. TCP does not transmit new packet until it gets acknowledgement of previous packet or timeout occurs. There is wastage of time. The second demerit is calculation of congestion window in congestion avoidance phase.

Proposed mechanism of TCP is trying to solve these both issues, described in next section.

3 Proposed Mechanism

The proposed mechanism is divided into two segments. The first segment is based on calculation of retransmission timeout. Sender has to wait until it gets acknowledgement for sent packet. Sender has no option to send packet even it has to send any important information. TCP start a timeout timer when it transmit a packet, and wait for acknowledgement. In the case of loss of acknowledgement in the network, TCP retransmits the packet and double the timeout timer. Reliability of packet transmission is costing enough time waste during communication. The enhance mechanism for data transmission calculates retransmission timeout, so that it can reduce time wastage during retransmission of packets. The round trip time (RTT) and retransmission timer overtime (RTO) can be calculated with following formula:

$$\mathtt{Retrans}_{\mathtt{new}} = 1 + (\mathtt{rtt} - \mathtt{min_rtt}) \,/\, (\mathtt{max_rtt} - \mathtt{min_rtt})$$

$$\mathtt{Reset_RTO} = \mathtt{Retrans}_{\mathtt{new}} * \mathtt{RTO}_{\mathtt{old}}$$

The second segment is based on calculation of congestion window according to packet loss in network. Packet loss rate is defined as ratio of total packet sent and total packet received. It can be denoted by P_L.

$$P_L = \texttt{total packet send} \,/\, \texttt{total packet received} \tag{1}$$

The packet loss rate also can be decided by the bit error rate (*BER*) of wireless link layer and the length (*Length*) of data frame:

$$P_L = 1 - (1 - \texttt{Bit Error Rate})\ \texttt{Length} \tag{2}$$

Avoidable BER ($P_{\text{loss_min}}$) is 0.4. If BER is greater than $P_{\text{loss_min}}$ the size of sending window should be decreased otherwise sending window size can increase. The algorithm is as follows.

```
Initial window size (cwnd)= 4* SMSS;
//smss: sender maximum segment size
//cwnd: congestion window
cwnd = cwnd+1;
PL = total packet send / total packet received
P_Loss_min=0.4
If (P_L  < P_Loss_min)
      cwnd=cwnd + cwnd* P_Loss_min;
else
      cwnd=cwnd - cwnd* P_Loss_min;
};
```

4 Results

The implementation and simulation had been done in QualNet 5.0 [17] network simulator with variation in number of nodes and pause time. Following graphs show the output of simulation after implementation of proposed protocol. The new algorithm is named as RTCP. The result of RTCP is compared with result of TCP RENO, TCP SACK, and TCP TAHOE.

Figure 1a shows the throughput of TCP variants (*y*-axis) with variation in number of nodes (*x*-axis) in network. Number of nodes indicates the traffic in network. It can be observed that throughput of RTCP (proposed routing protocol) is similar to TCP Tahoe, but it is better when number of nodes are 10.

Figure 1b shows the signal received with error by receiver (*y*-axis) with variation in number of nodes (*x*-axis) in network. It can be observed that RTCP (proposed routing protocol) is having less number of signals with error than other variants.

Figure 1c shows the total packet loss by receiver (*y*-axis) with variation in number of nodes (*x*-axis) in network. It can be observed that RTCP (proposed routing protocol) has lost less number of packets than other TCP variants, even in the case of heavy traffic.

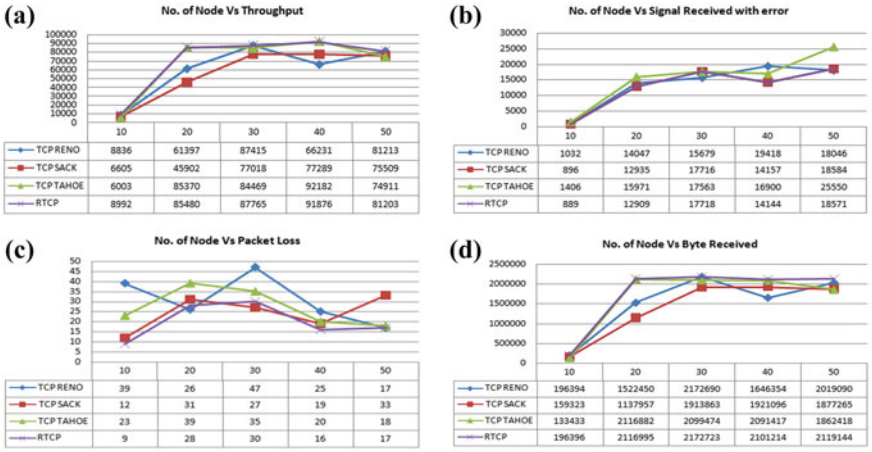


Fig. 1 Variation in number of nodes

Figure 1d shows the total byte received by receiver (*y*-axis) with variation in number of nodes (*x*-axis) in network. It can be observed that RTCP (proposed routing protocol) has received maximum bytes. The performance of RTCP is similar to TCP Tahoe.

Figure 2a shows the throughput analysis (*y*-axis) with variation in pause time (*x*-axis) in network. It can be observed that throughput of RTCP (proposed routing protocol) is better than other TCP variants.

Figure 2b shows total byte received by receiver (*y*-axis) with variation in pause time (*x*-axis) in network. It can be observed that RTCP (proposed routing protocol) has received more number of bytes than other TCP variants.

Figure 2c shows total packet loss by receiver (*y*-axis) with variation in pause time (*x*-axis) in network. It can be observed that RTCP (proposed routing protocol) has dropped less numbers of packets than other TCP variants.

Figure 2d shows total signals received with error by receiver (*y*-axis) with variation in pause time (*x*-axis) in network. It can be observed that RTCP (proposed routing protocol) has received less numbers signal with error than other TCP variants.

According to results, it can be observed that in most of the cases either in dense network or variation in pause time, the performance of RTCP is better than other TCP variants. The simulation result shows that RTCP is more reliable and can be used in sensitive networks.

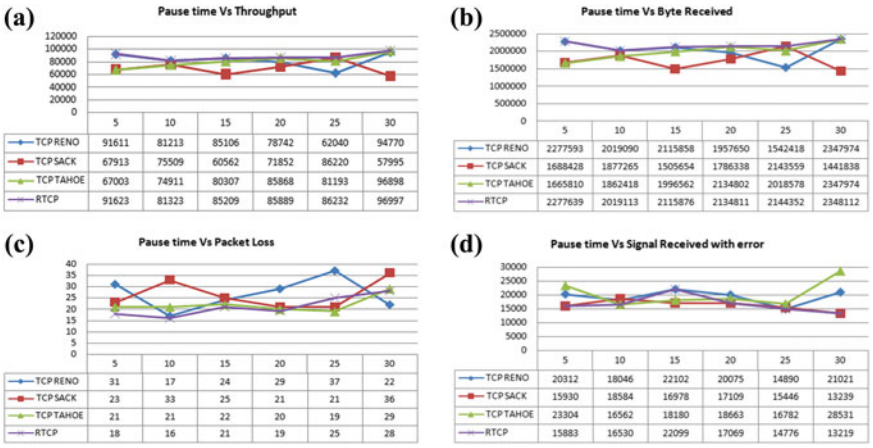


Fig. 2 Variation in pause time

5 Conclusion

Communication in large network is very complex, due to congestion in network. For a reliable and fast packet transmission, this paper presents a transmission algorithm. The proposed algorithm is based on utilizing time of packet retransmission and also on resizing the sending window according to the network capacity. The network capacity has been measured according to the number of packet drops. The mechanism was implemented on QualNet 5.0. According to the simulation results the proposed algorithm (RTCP) is performing better than other TCP variants. RTCP is more reliable, so it can be used in most sensitive places, where real time event monitoring is required.

References

1. Feng Zhao; Leonidas J. Guibas, "Wireless Sensor Networks: An Information Processing Approach" Morgan Kaufmann, 2004
2. C.S. Raghavendra; Krishna M. Sivalingam; Taieb Znati, "Wireless Sensor Networks" Springer Science & Business Media, 2005
3. Nishiyama, H.; Ito, M.; Kato, N., "Relay-by-smartphone: realizing multihop device-to-device communications," in Communications Magazine, IEEE, vol.52, no.4, pp. 56–65, April 2014
4. Bhaskar Krishnamachari, "Networking Wireless Sensors" Cambridge University Press, 2005
5. Ben Nacef, A.; Senouci, S.; Ghamri-Doudane, Y.; Beylot, A.-L., "A Cooperative Low Power Mac Protocol for Wireless Sensor Networks," in Communications (ICC), 2011 IEEE International Conference on, pp. 1–6, 5–9 June 2011
6. Zhaojuan Yue; Xiaodan Zhang; Yongmao Ren; Jun Li; Qianli Zhong, "The performance evaluation and comparison of TCP-based high-speed transport protocols," in Software Engineering and Service Science (ICSESS), 2012 IEEE 3rd International Conference on, pp. 509–512, 22–24 June 2012

7. Sikdar, B.; Kalyanaraman, S.; Vastola, K.S., "Analytic models and comparative study of the latency and steady-state throughput of TCP Tahoe, Reno and SACK," in Global Telecommunications Conference, 2001. GLOBECOM '01. IEEE, vol. 3, pp. 1781–1787, 2001
8. Jinwen Zhu; Tianrui Bai, "Performance of Tahoe, Reno, and SACK TCP at Different Scenarios," in Communication Technology, 2006. ICCT '06. International Conference on, pp. 1–4, 27–30 Nov. 2006
9. Hassani, M.M.; Berangi, Reza; Tavakolaie, H., "An analytical model for evaluating utilization of TCP TAHOE using markovian model," International Conference on Networking, Architecture, and Storage, 2007. NAS 2007, pp. 257–258, 29–31 July 2007
10. Parvez, N.; Mahanti, A.; Williamson, C., "An Analytic Throughput Model for TCP NewReno," in Networking, IEEE/ACM Transactions on, vol. 18, no.2, pp. 448–461, April 2010
11. Ratna Pavani, K.; Sreenath, N., "Performance evaluation of TCP-Reno, TCP-Newreno and TCP-Westwood on burstification in an OBS network," 18th Annual International Conference on Advanced Computing and Communications (ADCOM), pp. 19–24, 14–16 Dec. 2012
12. Srijith, K.N.; Jacob, L.; Ananda, A.L., "TCP Vegas-A: solving the fairness and rerouting issues of TCP Vegas," in Performance, Computing, and Communications Conference, pp. 309–316, 9–11 April 2003
13. Raza, I.; Hussain, S.A.; Ali, A.; Hassan Raza, M., "Persistent packet reordering attack in TCP based Ad hoc wireless networks," International Conference on Information and Emerging Technologies (ICIET), pp. 1–6, 14–16 June 2010
14. Kumar, H.; Singh, P., "TCP congestion control with delay minimization in MANET," International Conference on Information Communication and Embedded Systems (ICICES), 2014, pp. 1–6, 27–28 Feb. 2014
15. Sharma, N.; Chakrawarti, R.K., "Simulation for congestion-less losses control over MANET using TCP scheme," in Issues and Challenges in Intelligent Computing Techniques (ICICT), 2014 International Conference on, pp. 410–415, 7–8 Feb. 2014
16. Stefano Basagni; Marco Conti; Silvia Giordano; Ivan Stojmenovic, "Mobile Ad Hoc Networking" John Wiley & Sons, 2004
17. QualNet 5.0: "http://web.scalable-networks.com/content/qualnet" last accessed on 24/10/2015

Performance Analysis of FSO System for Different Fog Conditions

Ritu Gupta and Preeti Singh

Abstract Free-space optics (FSO) proved to be a complete replacement of radio frequency (RF) communications in recent years. The performance characteristics of FSO channel is affected by varying climate conditions such as fog, haze, rain, etc. due to their major influence on the laser beam quality propagation through the atmosphere. Attenuation due to fog conditions results in severe effect on the received power. Because of this still FSO has not achieved a mass success in the market. The quality of FSO system is analysed in terms of its signal-to-noise ratio. In this paper, the performance is analysed for different foggy weather conditions like dense, continental, maritime, stable, advection and dense haze using Kim and Kruse models. The density of the fog is governed by liquid water content (LWC) present in the atmosphere. The data rate at an optical wavelength of 1550 nm has also been studied here.

Keywords FSO · Kim · Kruse · Atmospheric turbulence · Fog

1 Introduction

Free-space optics (FSO) is also known as optical wireless and lasercom. Initially the attention on FSO was boosted by military purposes for defense applications. But today's market interest to FSO refers to civil applications also due to highest data rates in terms of Gbps. Because of these features FSO has the incredible potential to provide complete communication link. This technology endows with the way out to last mile problem such as for disaster recovery, broadband internet connectivity in rural areas, etc. in infrared and visible spectrum. Recently, FSO is being investigated

Ritu Gupta (✉)
Rayat Bahra University, Mohali, India
e-mail: erritugupta02@gmail.com

Preeti Singh
UIET, PU, Chandigarh, India
e-mail: preeti_singh@pu.ac.in

© Springer Science+Business Media Singapore 2017

R. Singh and S. Choudhury (eds.), *Proceeding of International Conference on Intelligent Communication, Control and Devices*, Advances in Intelligent Systems and Computing 479, DOI 10.1007/978-981-10-1708-7_20

for high speed data transfer applications comprising links between fixed and mobile platforms and found suitable for last mile access, optical fibre back-up link, cellular communication backhaul, temporary links, difficult terrains, high definition television and multi-campus communication network. The major challenges that affect the communication are surrounding light sources, obstructive and shadowing, alignment and tracking or adverse atmospheric climate conditions. If IR light source is operated incorrectly it can pose as potential safety hazards to human [1–3].

FSO and radio frequency (RF) link has complementary nature. The highly weather dependence is the major issue in FSO link and among all atmospheric attenuation factors fog is the key attenuating factor. When RF link fails during heavy rainfall FSO works well, but when FSO link fails during fog RF works well. To provide good signal quality to the user, both FSO and RF technologies are used as one in hybrid FSO/RF system [4]. It has been reported that attenuation has peak values of 480 dB/km under dense maritime fog. The bit error rate (BER) of FSO-WDM system increases with increase in distance [5]. The empirical and theoretical analysis for the fog, rain, snow, haze, etc. on light propagation in the visible and IR spectral range has been reported [6–8]. The performance of FSO depends upon several internal and external parameters. Optical power, wavelength, transmission bandwidth, divergence angle, optical loss on the transmitter and receiver sensitivity, receiver lens diameter and BER are the internal parameters that are concerned with design of an FSO system. External parameters are connected to the environment conditions such as line of sight, atmospheric attenuation, scintillation, etc. The atmosphere is a varying medium, so to get the best performance it is important to understand all these parameters before designing a system.

2 Performance Parameters of FSO Link

The performance of the link always depends on the conditions of the atmosphere in which the signal has to travel. The existence of drizzle, fog, snow, rain, haze, dust is the prime factor to scattering and absorption of the transmitted signal. Some other parameters such as alignment of antennas, transceiver also affect the performance of system. Analysis of Link budgets gives the performance of FSO system. There is an approximate relationship between wavelength and scatter "s" attenuation coefficient. Scattering depends upon the scatter "s" size with respect to the transmission wavelength λ.

Various parameters which must be included in link budget analysis are sensitivity losses (due to scattering, absorption, reflections and receive sensitivity), alignment loss, optical system loss, geometric loss and input power [9–11]. The spreading of transmitted beam between transmitter and the receiver causes geometric losses. The link budget analysis can be done in terms of received power.

$$\alpha = (3.91/V) \times (\lambda/550)^{-q} \tag{1}$$

V is visibility (km), λ is wavelength (nm) and q is a coefficient dependent on the size distribution of the scattering particles and visibility [12].

P_r, the received power is given as

$$P_r = P_t\, e_t\, e_r (\lambda/4\pi Z)^2 G_t\, G_r \exp(-\alpha \times Z) \tag{2}$$

P_t is the transmitted power, e_t and e_r are efficiency of transmitting and receiving antenna, respectively. G_t and G_r are geometric losses at the transmitter at receiver, respectively. Z is the distance between the transmitter and receiver. For a given laser transmitter power P_t, θ is the transmitter divergence, D, diameter of receiver and the achievable data rate DR is [13]

$$DR \approx P_r \tag{3}$$

Data rate can be calculated as given equation

$$DR = (4/\pi\, Ep\, N_b)\, P_r \tag{4}$$

Ep hc/λ, Photon energy
h Planck's constant
c light velocity
N_b −20 dBm receiver sensitivity.

Various theoretical models have been proposed which have been analysed here to describe the signal degradation and intensity fluctuations due to induced turbulence. In literature, two different fog models, i.e. Kruse and Kim models. The Kim model is used to find signal attenuation for fog weather [12]. These models have a predetermined value of q, which shows that as the wavelength increases the attenuation decreases. The attenuation coefficient has been reported as per visibility coefficient at different wavelengths, i.e. 850, 950 and 1550 nm. The Kruse model is similar to Kim model [13, 14]. However, originally the Kruse model was designed for dense fog. Due to which it is not suitable for visibility less than or equal to one kilometres. For both the reported models it has been found that the 1550 nm wavelength gives minimum attenuation. This range is also safe for eyes because as reported the eye safety regulations are less stringent in third wavelength window. Although the devices available for this range are relatively costly. Over modest distances lasers operating at 850 nm are much less expensive.

3 Simulation Results

In free-space optical communication system the receiver power is based on link budget analysis. In the present paper, the system analysis has been considered under different fog conditions at 1550 nm and the performance has been estimated in terms of received signal power and data rate. The investigation is based on the modelling equations. The received signal power is compared for dense fog, continental fog, maritime fog, dense haze, stable fog and advection fog using Kim and Kruse models. It has been proved that the received signal power decreases with decreasing visibility as being effected by weather conditions. High received signal power and data rate are also been perceived at wavelength 1550 nm for clear sky due to maximum visibility as compared to the other weather conditions.

Figure 1 shows the received power and Fig. 2 shows data rate with respect to visibility for different fog conditions using Kruse model. Figure 3 shows the received power and Fig. 4 shows data rate with respect to visibility for different fog conditions using Kim model. Data rate is dependent on received power as per Eq. 4. It has been observed for both the models that as the distance increases, visibility (depending on the fog and haze level) decreases and hence the received power and data rate also decreases.

4 Conclusion

Communication through FSO under atmosphere turbulence is a part of dynamic research in present scenario. Numerous ways have been recommended to mitigate signal fading during communication due to induced turbulence. In this paper, the

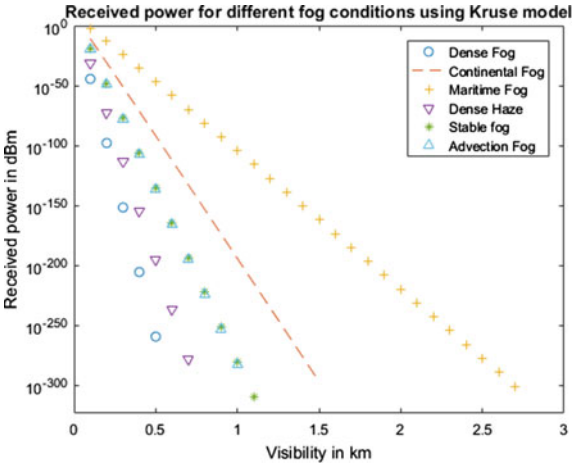


Fig. 1 Received power versus visibility for Kruse model

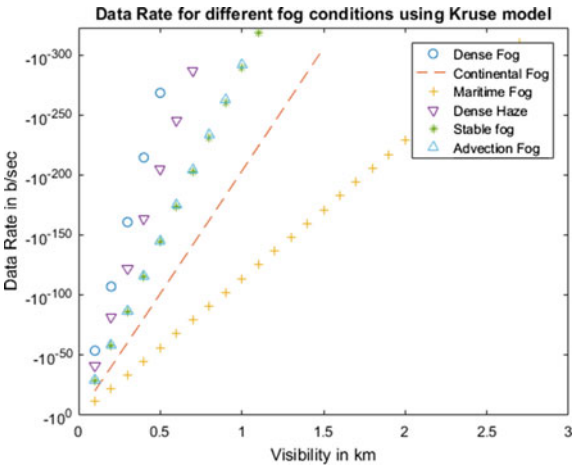


Fig. 2 Data rate versus visibility for Kruse model

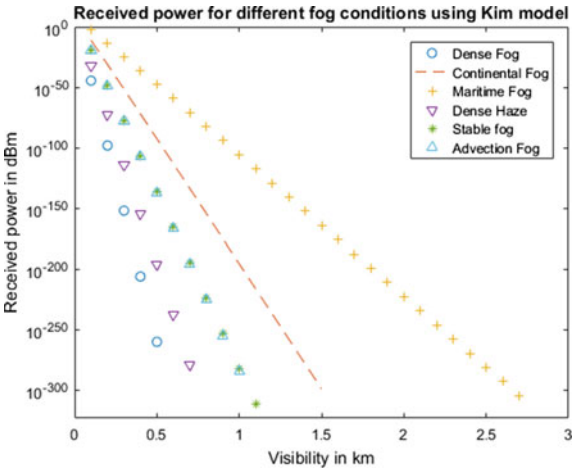


Fig. 3 Received power versus visibility for Kim model

performance of the FSO system has been analysed during fog and haze atmospheric conditions and it has been found that a 1550 nm wavelength range is suitable for FSO communication because of less BER during fog. The other advantages and disadvantages of FSO have also been discussed. It has been analysed that the dense fog severely affects FSO system received power and data rate. It has been observed from the study that FSO has a bright future and various advancements can be made in order to increase its efficiency and bandwidth. One option to improve visibility is

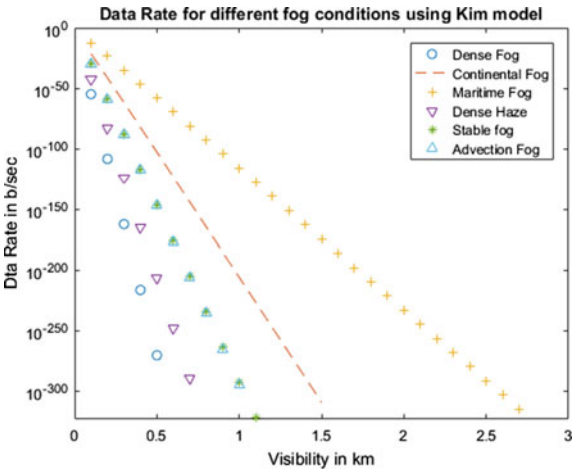


Fig. 4 Data rate versus visibility for Kim model

to make the light brighter. But this is not possible because the light then becomes unsafe to the eyes. In telecommunication, FSO will be proved as the preferred high-bandwidth wireless technology with the laser communication in use within its capabilities.

References

1. Akhil Gupta, Pankaj Anand, Rohit Khajuria, Sonam Bhagat, Rakesh Kumar Jha, "A Survey of Free Space Optical Communication Network Channel over Optical Fiber Cable Communication" International Journal of Computer Applications, Vol. 105, No. 10, Nov. 2014, pp 32–36.
2. Hennes Henniger, Otakar Wilfert, "An Introduction to Free-space Optical Communications" Radio Engineering, Vol. 19, No. 2, June 2010.
3. Aditi Malik, Preeti Singh, "Free Space Optics: Current Applications and Future Challenges", International Journal of Optics, Vol. 2015, pp 1–7, Nov. 2015.
4. Ritu Gupta, Preeti Singh, "Hybrid FSO - RF System: A Solution to Atmospheric Turbulences in Long Haul Communication" International Journal of Scientific & Engineering Research, Vol. 5, No. 11, pp 602–605, Nov. 2014.
5. Aditi, Preeti, "An Effort to Design a Power Efficient, Long Reach WDM-FSO System", International Conference on Signal Propagation and Computer Technology, pp 791–796, 2014.
6. Aditi Malik, Preeti Singh, "Comparative Analysis of Point to Point FSO System Under Clear and Haze Weather Conditions" Wireless Personal Communications An International Journal, SPRINGER, Aug. 2014.
7. K. W. Fischer, M. R. Witiw, and E. Eisenberg, "Optical attenuation in fog at a wavelength of 1.55 micrometers," Atmospheric Research, vol. 87, pp. 252–258, 2008.
8. I. I. Kim, B. McArthur, and E. Korevaar, "Comparison of laser beam propagation at 785 nm and 1550 nm in fog and haze for optical wireless communications," in Proc. SPIE 4214, Boston, MA, USA, 2001.

9. F. Nadeem, T. Javornik, E. Leitgeb, V. Kvicera, and G.Kandus, “Continental fog attenuation empirical relationship from measured visibility data,” of Radio Engineering, Vol. 19, No. 4, 2010.
10. Mazin Ali A. Ali “Analysis of Data Rate for Free Space Optical Communications System” IJECT, Vol. 5, Issue Spl-1, Jan - March 2014.
11. R. M. Pierce, J. Ramapras, and E. C. Eisenberg, “Optical attenuation in fog and clouds”, Proc. SPIE 4530, Vol. 58, 2001.
12. Dheeraj Duvey, Ritu Gupta, “Analysis Of Fog Attenuation Models For Multitransceiver FSO System For Different Frequencies”, International Journal of Application or Innovation in Engineering & Management (IJAIEM), Vol. 3, No. 6, June 2014, pp 216–220.
13. Xiaoming Zhu and Joseph M. Kahn, “Free-Space Optical Communication Through Atmospheric Turbulence Channels”, IEEE Transactions on Communications, Vol. 50, No. 8, Aug. 2002 pp 1293–1300.
14. Bloom, S., Korevaar, E., Shuster, J., and Willebrand, H., “Understanding the performance of free-space optics”, Journal of Networking, Vol. 2, pp. 178–200, 2003.

Performance Analysis of Multibeam WDM-FSO System in Clear and Hazy Weather Conditions

Marvi Grover, Preeti Singh and Pardeep Kaur

Abstract Free space optics has proved out to be an exalted technique for fast and cost-effective information exchange. Proficient in removing bandwidth limitation, it also solves the last mile problem. But as air is used as medium, it suffers from atmospheric effects which limit its achievable link distance. In this paper, a system is proposed to increase the maximum link range under different weather conditions and results have been compared with those of the previously existing system.

Keywords FSO · WDM-FSO · Singlebeam · Multibeam

1 Introduction

Free Space Optics is a communication technique which has engrossed the researchers due to its aspects like high bandwidth and enormous speed. As communication happens through air, FSO transmission is much faster than its fiber counterparts where glass is used as the medium for transmission [1]. Secure links, immunity to RF interference, larger bandwidth, and unlicensed spectrums are some key traits of FSO which have allured the telecom industry towards it [2]. But there are some stringent requirements for establishment of an efficient FSO link, these include a proper line of sight (LOS) between transmitter and receiver and clear weather conditions [3]. Atmospheric effects like scintillation, fog, haze, rain, absorption by water vapors, scattering of beam, fading, etc., have to be considered while designing an FSO network [4]. These factors attenuate the signal, thus deteriorating the quality of received signal. They play a major role in determining

Marvi Grover (✉) · Preeti Singh · Pardeep Kaur
UIET, PU, Chandigarh, India
e-mail: marvi310191@gmail.com

Preeti Singh
e-mail: preeti_singh@pu.ac.in

Pardeep Kaur
e-mail: pardeep.tur@gmail.com

© Springer Science+Business Media Singapore 2017

R. Singh and S. Choudhury (eds.), *Proceeding of International Conference on Intelligent Communication, Control and Devices*, Advances in Intelligent Systems and Computing 479, DOI 10.1007/978-981-10-1708-7_21

the link length, i.e., the distance up to which successful communication can take place. Also the power levels of the laser source used in the transmitter should be within the permissible limits to avoid any harm to human eyes. Applications of FSO include building to building communication, ship to ship, aircraft to ground links, ground to satellite links, and many more [5].

1.1 WDM-FSO Systems

Wavelength Division Multiplexing (WDM) refers to the technique in which more than one signals are multiplexed together and transmitted as one signal [6]. So, in WDM-FSO, multiple modulating signals modulate different optical carriers (channels) which are then multiplexed and sent through a single laser beam. WDM systems best utilize the channel capacity ameliorating the data transfer ability of FSO systems. These systems are flexible as channels can be added or removed at any point in the link using add/drop multiplexers [6]. However they also suffer from weather effects and atmospheric turbulences. This paper proposes a Hybrid multibeam WDM-FSO system which aims at mitigating the impact of weather suffered by a single beam WDM-FSO.

1.2 Multibeam WDM-FSO System

Multibeam WDM-FSO is designed to reduce the effect of atmospheric attenuation and obstacles in the path of light beam [7]. In this system, more than one beam of the multiplexed signal traverse through the free space and reach the receiver [8]. As each beam travels a different path, each of them undergoes different amount of attenuation. The multiplexed signal is split using a power splitter at the transmitter and the received power of all the beams is combined using a power combiner at the receiver [9]. Among the different weather effects, fog and haze play the major deterrents for the light beam [10]; the following sections of this paper analyze the efficiency of a multibeam WDM-FSO system in enduring the haze effect.

2 System Design

2.1 System Considerations

WDM-FSO system consists of a transmitter, receiver, and free space channel. Transmitter has a single CW laser for carrier generation, a pseudorandom bit sequence generator for generation of information signal, NRZ pulse generator,

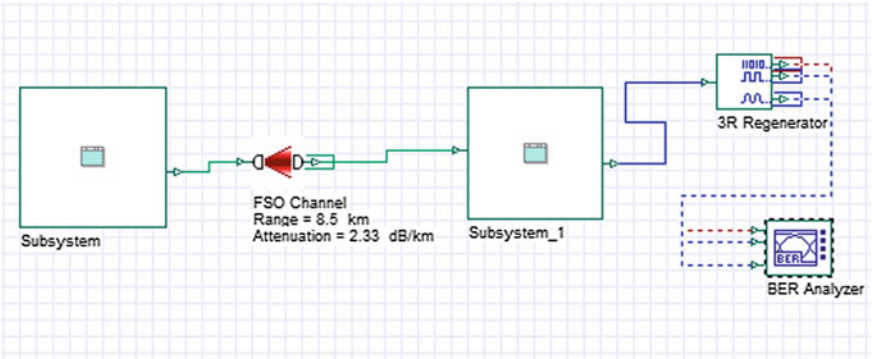


Fig. 1 Single beam WDM-FSO system

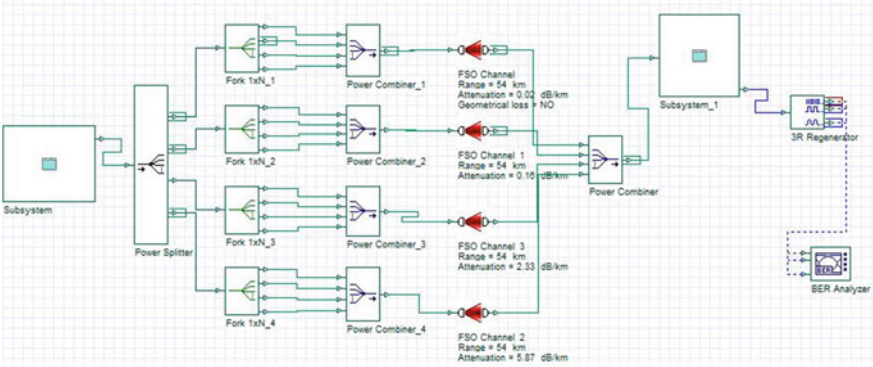


Fig. 2 Multibeam WDM-FSO system

a Mach-zehnder modulator, and a 32 channel WDM multiplexer. "Subsystem" shown in Figs. 1 and 2 have the transmitter module. On the other side, the receiver module is present in subsystem_1 which has a WDM demultiplexer, followed by a selector, an APD detector, and a low pass Gaussian filter. A bit error rate (BER) analyzer is used at the reception which gives the Quality factor and the BER of the received signal.

2.2 Haze Effect

Haze particles present in the air reduce the intensity of the light beam thus hindering the transmission. Attenuation caused by haze depends on the visibility level and is calculated by the famous Kim and Kruse model [11, 12] given by Eq. 1

$$\alpha = \frac{3.91}{V}\left(\frac{\lambda}{550\,\text{nm}}\right)^{-q} \tag{1}$$

where α is attenuation, V is visibility in km, and λ is the wavelength of light in nm. In this paper, attenuation has been calculated using Kim's model which is used for dense haze. According to the Kim model, the particle size distribution q is given as

$$q = \begin{cases} 1.6 & \text{for } V > 50\,\text{km} \\ 1.3 & \text{for } 6 < V > 50\,\text{km} \\ 0.16V + 0.34 & \text{for } 1 < V > 6\,\text{km} \\ V - 0.5 & \text{for } 0.5 < V > 1\,\text{km} \\ 0 & \text{for } V < 0.5\,\text{km} \end{cases}$$

2.3 Design Parameters

The analysis has been done by comparing a four beam WDM-FSO system with a single beam WDM-FSO. A single Continuous Wave Laser is used which operates at 1,550 nm, data rate used is 10 Gbps, lenses' aperture is set at 15 cm [11]. Performance of both the systems is analyzed for clear and haze weather conditions including the geometrical losses taking beam divergence to be 2 mrad. Simulations have been done in OPTISYSTEM v 12.

2.3.1 System 1 (Preexisting System)

Mach-zehnder modulator present in 'subsystem' modulates the multiplexed output and transmits a single beam which is received by the receiver having a WDM Demux followed by an APD. Q factor is given by the BER analyzer. Attenuation value for clear weather is 0.233 db/km and for haze is 2.33 db/km. The set up is shown in Fig. 1.

2.3.2 System 2

Transmitter consists of a CW laser, a demultiplexer and a Mach–Zehnder modulator. A 4:1 power splitter splits the output of the modulator into four beams which travel independently through air to reach the power combiner which combines the received power of all the four beams and gives it to the DEMUX. The analysis has been done by taking different attenuation values for different beams. For clear weather, these values are 0.065 and 0.233 db/km and for haze, the attenuation values have been calculated, assuming nonuniformity in haze particles, using Kim's model at different visibility level and these are 0.02, 0.16, 2.33, and 5.87 db/km for the four beams. System set up is shown in Fig. 2.

3 Results and Discussion

Simulations have been carried out for clear and hazy weather and performance of both systems is discussed below.

3.1 System 1 Versus System 2

Both the systems have been compared in terms of achievable link distance using same system parameters. The analysis has been done up to the acceptable values of Quality factor (Q) and minimum BER for successful communication. Table 1 gives the comparison of the two systems. The values of maximum range show that in clear and haze weather conditions; signal can be transmitted to a larger distance using system 2 as compared to system 1.

Table 1 Comparison of system 1 and system 2 under clear and haze weather condition

	Clear weather			Haze		
	Laser power used = 10 dBm			Laser power used = 40dBm		
	Max range (km)	Min BER	Q factor	Max range (km)	Min BER	Q factor
System 1	2.4	2.20e −09	5.8644	8.5	2.67e −09	5.8320
System 2	4.75	1.44e −09	5.9342	53	3.08e −09	5.8089

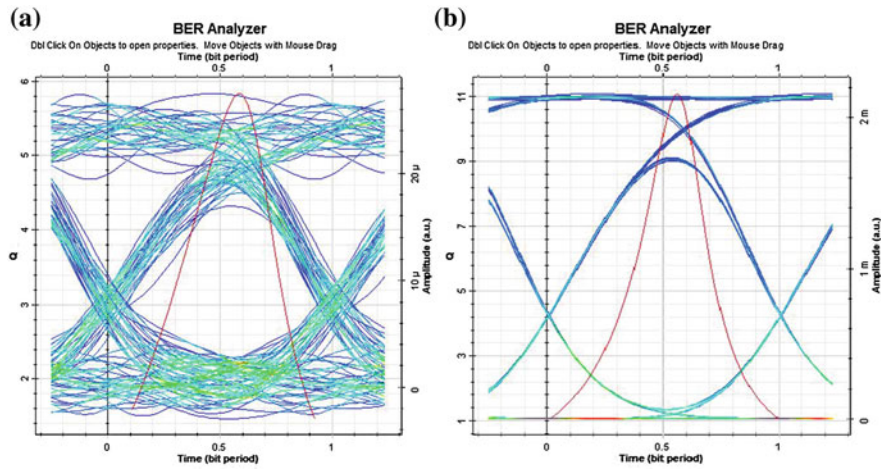


Fig. 3 Eye diagrams for **a** system 1 **b** system 2

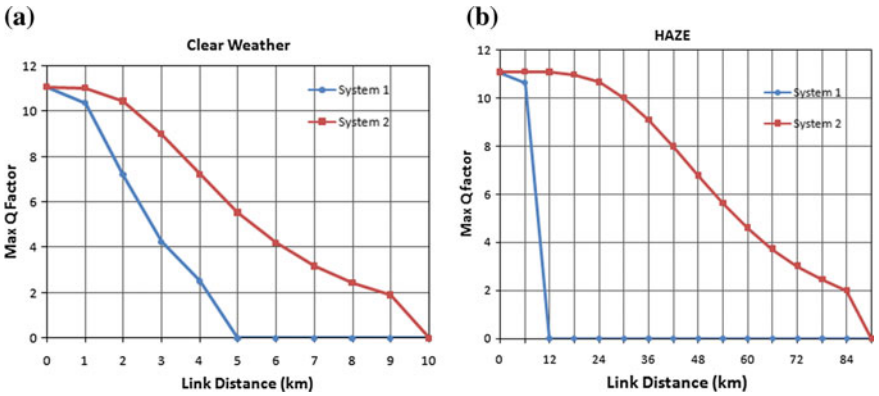


Fig. 4 Graphs for Q versus link distance for system 1 and system 2 in **a** Clear weather **b** Hazy weather

The eye diagrams (Fig. 3) obtained using the BER analyser clearly depict that in clear weather, at same link distance (8.5 km), the quality of reception of system 2 is much higher than that of system 1. Also, graphs shown in Fig. 4 analogize the two systems in terms of Q factor variation with link distance. It can be inferred that system 2 can work for very larger distance compared to system 1 and the Q factor at any distance for system 2 is more than that of system 1 at the corresponding distance. In both the weather conditions, system 2 out performs system 1 in terms of link distance.

4 Conclusion

Atmospheric effects play a major hurdle in FSO communication system limiting its use in distant communication. Studies for amalgamating various techniques are being carried out to reduce these effects. One such hybrid technique has been analyzed in this paper which combines a multibeam FSO system with a WDM-FSO system. Two systems have been investigated for clear and hazy weather condition, where system 1 uses a single beam WDM-FSO and system 2 uses a multibeam WDM-FSO. When simulated using same system parameters, results show that system 2 can communicate up to 53 km under haze whereas system 1 can establish a successful link for only 8.5 km. Also for clear weather system 2 performs better than system 1.

Acknowledgments Author expresses her deep gratitude towards the teachers of UIET, Punjab University for their help and support in completing the work presented in this paper.

References

1. Aditi, Preeti Singh: An effort to design a power efficient, long reach wdm-fso system, International conference on signal propagation and computer technology, IEEE, ajmer, JULY (2014).
2. Deva K Borah, Anthony C Boucouvalas, Christopher C Davis, Steve Hranilovic and Konstantinos Yiannopoulos: A Review of communication-oriented optical wireless systems, EURASIP Journal on Wireless Communications and Networking (2012).
3. N., Kumar and A., K., Rana: Impact of various parameters on the performance of free space optics communication system, Optik, vol. 124. no. 22 (2013) pp. 5774–5776.
4. D., Kedar, S., Arnon: Urban optical wireless communication networks: The main challenges and possible solutions, Communications Magazine, IEEE, Vol. 42. Issue: 5 (2004).
5. A., Malik, P., Singh: Free Space Optics: Current Applications and Future Challenges, International Journal of Optics, Vol. 7. Article ID 945483 (2015).
6. Stamatios V. Kartalopoulos: WDM Technology and Networks, Next Generation Intelligent Optical Networks, pp 55–99.
7. Al-Gailani, A., B., Mohammad., & R., Q., Shaddad: Enhancement of free space optical link in heavy rain attenuation using multiple beam concept, Elsevier, Optik, 124 (2013), pp. 4798–4801.
8. J., A., Anguita, J., E., Cisternas: Experimental evaluation of transmitter and receiver diversity in a terrestrial FSO link, GLOBECOM Workshops (GC Wkshps), IEEE (2010).
9. Mohammad A., B.,: Optimization of FSO system in tropical weather using multiple beams, Photonics (ICP), IEEE 5th International Conference on Photonics (2014).
10. H., A., Fadhil, A., Amphawan, H., A., B., Shamsuddin, Thanaa Hussein Abd, Hamza Al-Khafaji M., R., S., A., Aljunid, & N., Ahmed: Optimisation of free space optics parameters: An optimum solution for bad weather conditions, Elsevier, Optik, 124 (2012), 3969–3973.
11. Aditi malik, Preeti singh: Comparative Analysis of Point to Point FSO system under Clear and Haze weather conditions, Wireless Personal Communications, vol. 78. number 3, October (2014).
12. Muhammad Ijaz; Zabih Ghassemlooy; Jiri Pesek; Ondrej Fiser; Hoa Le Minh; Edward Bentley: Modeling of Fog and Smoke Attenuation in Free Space Optical Communications Link Under Controlled Laboratory Conditions, Journal of Lightwave Technology (2013), Vol. 31, Issue: 11, Pages: 1720–1726.

Triangular Inset Fed C-, X-, and Ku-Band Antenna for Satellite and Radar Applications

Vipin Choudhary, Aastha Gupta, Garima Mahendru and Malay Ranjan Tripathy

Abstract A compact multiband antenna is designed using HFSS on FR4 substrate with permittivity of 4.4. The dimension of substrate is $50 \times 75 \times 1.6$ mm^3. An M-shaped antenna with symmetrical slots is proposed in this paper. Inset feeding is made to make it simple and compact. Multibands are obtained in S_{11} versus frequency plots. Lower bands are obtained from 3.7–3.9 to 5.5–5.9 GHz. The higher bands are 9.3–10.3, 11.4–12.7, and 12.9–13.5 GHz. The higher bands are highly useful for X-band and Ku-band radar applications.

Keywords X-band · Ku-band · C-band · Microstrip patch antenna

1 Introduction

In recent years, wireless communication systems have increased rapidly, and the demand for higher data rates has been of prime importance [1–5]. With wireless communication heading toward advanced technologies, usage of smaller and multiband antennas is the need of the hour. Microstrip antennas are the best candidates for the present requirement of consumers for multiband wireless phones validating more than one network [6–8]. Apart from these, variegated work on microstrip antennas suitable for radar and satellite communication applications has been accomplished [9–11]. This field has been largely supported by the microstrip antennas due to its distinct advantages such as low profile, low cost, ease of fabrication, and ease of integration with accompanying electronics. Also, these provide multiband operation with better return losses.

Vipin Choudhary (✉) · Aastha Gupta · Garima Mahendru · M.R. Tripathy
Department of Electronics and Communication, ASET,
Amity University Uttar Pradesh, Noida 201313, India
e-mail: choudhary.vip77@gmail.com

Aastha Gupta
e-mail: gupta.aastha16@gmail.com

© Springer Science+Business Media Singapore 2017

R. Singh and S. Choudhury (eds.), *Proceeding of International Conference on Intelligent Communication, Control and Devices*, Advances in Intelligent Systems and Computing 479, DOI 10.1007/978-981-10-1708-7_22

In this paper, an M-shaped microstrip patch antenna has been designed for satellite and radar applications. Three different slots were made in the patch. Apart from these, two symmetric triangular slots were made for inset feeding. Detailed parametric studies were carried out for different configurations of patch antenna. Multibands with different return loss and impedance bandwidth are obtained from the design.

The paper is organized as follows. Section 2 describes antenna design and characteristics. Results and discussion are made in the Sect. 3. Conclusion is made in Sect. 4.

2 Antenna Design

Figure 1 represents an antenna that can be utilized in various radar applications. To design an M-shaped patch antenna, first a rectangular patch antenna is considered and a U-shaped patch is created by cutting out a rectangular slot from the rectangular monopole antenna. After creating a U-shaped patch, two rectangular slots are cut out from the corners of U-shape, as shown in the Fig. 1 above, thereby creating an M-shaped monopole patch antenna. The dimensions for the patch antenna are given to be A = 30 mm, B = 35 mm, C = 30.8 mm, D = 2 mm, G = 15 mm, and H = 17.5 mm. E and F are the dimensions of the two symmetric rectangular slots that are varied in order to achieve the desirable and useful results. The various values taken for the symmetric rectangular slots (E and F) are listed in Table 1 and the resulting antennas are shown in Fig. 2.

The feed provided to the patch antenna is an inset feed having feed line width (C) of 30.8 mm and a feed line inset distance (D) of 2 mm. The resonant frequency is independent of the inset length, but varies with the inset width.

The substrate allotted to this patch antenna has dimensions of 50 × 75 mm^2 and a thickness of h = 1.6 mm.

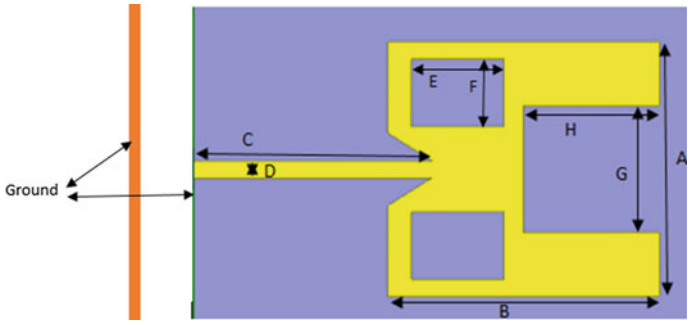


Fig. 1 Configuration of inset feed microstrip patch antenna

Table 1 The dimensions of the symmetrical rectangular slots different designs of M-shaped patch antenna

Design	E (mm)	F (mm)
1	8	12
2	8	10
3	8	8
4	8	6

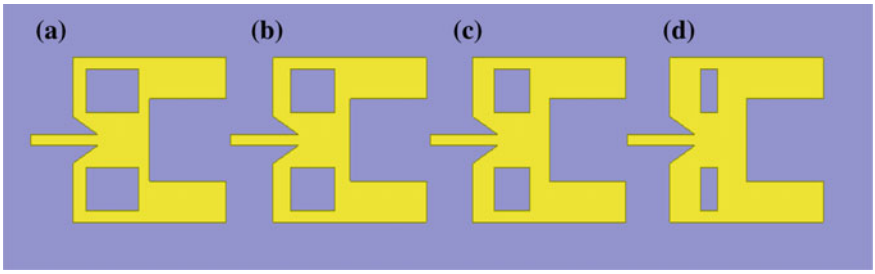


Fig. 2 Antenna design, **a** 8 × 12 mm^2, **b** 8 × 10 mm^2, **c** 8 × 8 mm^2 and **d** 8 × 6 mm^2

3 Results and Discussion

The antenna has been analyzed for the different dimensions of the slots as mentioned in Table 1. The return loss and gain obtained for different configurations in various frequency bands were studied, in order to understand its performance better. With the help of HFSS, the recorded outcome of return loss (S_{11}) parameter for different antennas is depicted in Table 2.

From the detailed analysis, it was found that better antenna characteristics were obtained as the size of the two symmetrical rectangular slots (with dimensions

Table 2 S_{11} parameter of design 1, 2, 3, and 4 in different frequency bands

Design	3–5 (GHz) band	5–6 (GHz) band	7–9 (GHz) band	10–14 (GHz) band
1	−20.8 dB (3.8 GHz)	−22.5 dB (5.6 GHz)	–	−24 dB (10 GHz)
				−23.6 dB (12.5 GHz)
				−15.5 dB (13 GHz)
2	–	–	−12.9 dB (7.7 GHz)	–
3	−20 dB (4.1 GHz)	−32.5 dB (5.6 GHz)	–	−18.5 dB (12.6 GHz)
4	−18.2 dB (4.5 GHz)	−14.3 dB (5.7 GHz)	–	−22 dB (10.5 GHz)
				−16.6 dB (13 GHz)

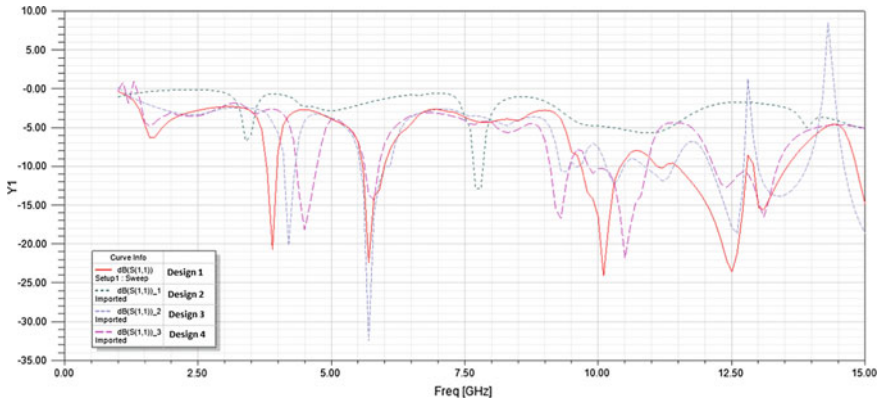


Fig. 3 Return loss (S_{11}) versus frequency plot for different antenna design

$E \times F$ mm) in the M-shaped patch antenna was increased. This can be concluded with the help of Fig. 3.

On closely studying the outcome values of return loss for different configurations (as shown in Table 2), design 1 was found to be of more useful. Design 1 provides multiband response which covers C-, X-, and Ku-bands and suitable for radar and satellite applications.

The design parameters for design 1 are tabulated in Table 3. The substrate in this design has a permittivity of $\varepsilon_r = 4.4$. The permittivity of the substrate should be in the range of 2.2–12, in order to have a good, larger bandwidth antenna. This triband antenna shows interesting results at 10, 12.5 and 13 GHz, with maximum gain of 16.3 dB at 13 GHz.

Analysis of the M-shaped antenna also showed some competent results in the design 2, i.e., the antenna with two symmetrical rectangular slots of 8×10 mm dimension. This design of antenna possesses a return loss of −12.9 dB and a gain of 8.4 dB at frequency 7.7 GHz.

Design 1 resonates at 10, 12.5, and 13 GHz with an optimum gain of 2, 7.9 and 16.3 dB and return loss of −24.1, −23.5, and −15.6 dB and bandwidth of 900, 1,300 and 600 MHz, respectively. Therefore, it can be deduced that the design 1 is appropriate for high frequency radar as well as satellite applications.

Figure 3 shows the return loss versus frequency plot for different M-shaped antennas with design 1, 2, 3, and 4. Table 2 describes detail parameters of $s11$ for different bands obtained in different designs. It can be observed that as the size of the symmetric rectangular slots were increased from 8×6 to 8×12 mm^2, improved return loss values are obtained. For the application frequency of 12.5 GHz in the radar range, design 4 has a return loss of −12 dB, whereas design 3 has the value of return loss as −17.8 dB. Further, design 1 with maximum slot size of 8×12 mm^2, has a return loss of −23.6 dB that was found useful for the required application. Thus, increasing the slot size led the design of the antenna to be more practical with interesting results in the field of return loss.

The return loss, gain, and VSWR values for the resonant frequencies and respective bands are listed in Table 3. It is seen that the best return loss of −24.1 dB is obtained at 10 GHz. The maximum gain is obtained at 12.9 GHz as 22 dB.

The obtained E-plane and H-plane radiation patterns for the proposed antenna (Design 1) at frequency 12.5 GHz are shown in Fig. 4. It is noticed that the E-plane

Table 3 Various parameters for design 1

Bandwidth range (GHz)	Frequency (GHz)	Return loss (S_{11})	VSWR	Gain (dB)
3.7–3.9	3.8	−20.8 dB	1.4	−2.9
5.5–5.9	5.6	−22.5 dB	1.2	−1.7
9.6–10.3	10	−24.1 dB	1.02	2
11.4–12.7	12.5	−23.6 dB	1.02	7.9
12.9–13.5	12.9	−15.6 dB	2.5	22

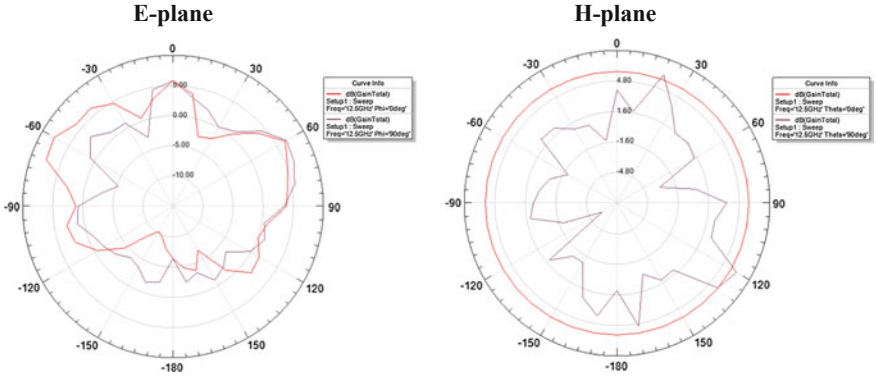


Fig. 4 E-plane and H-plane radiation pattern at 12.5 GHz for design 1

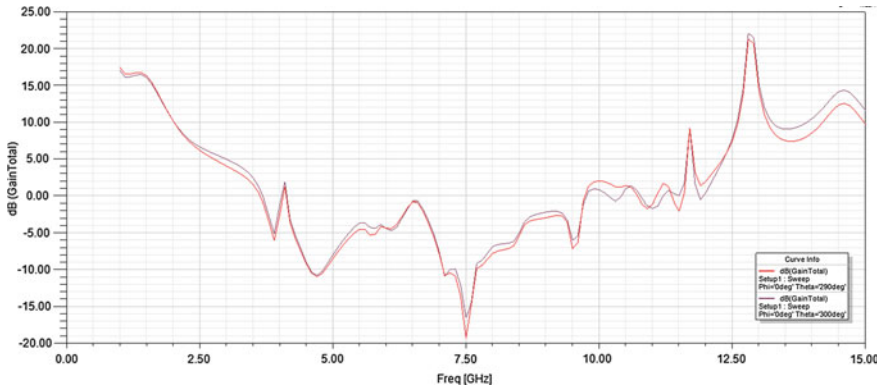


Fig. 5 Gain versus frequency plot for design 1

radiation pattern is omnidirectional with maximum gain of 7.9 dB at 12.5 GHz and also the H-plane radiation pattern is very stable with change in frequency.

Whereas the gain versus frequency plots at 10, 12.5 and 13 GHz for design 1 are depicted in Fig. 5. The peak gain is seen as 22 dB at 12.9 GHz.

4 Conclusion

In this paper, a highly efficient and compact design of antenna has been proposed. The designed antenna can be applied in the field of civilian as well as military applications involving radar and satellite communication, such as air traffic control, weather monitoring, defense tracking, etc. It works at resonant frequencies of 10, 12.5, and 13 GHz in the X-band and Ku-band.

References

1. Kaddoum, G.; Ahmed, M.F.A.; Nijsure, Y., "Code Index Modulation: A High Data Rate and Energy Efficient Communication System," in *Communications Letters, IEEE*, vol. 19, no. 2 (2015) pp. 175–178.
2. Tall, Abdoulaye, Zwi Altman, and Eitan Altman. "Multilevel beamforming for high data rate communication in 5G networks." *arXiv preprint* arXiv:1504.00280 (2015).
3. Seeds, Alwyn J., et al. "TeraHertz Photonics for Wireless Communications." *Journal of Lightwave Technology* 33.3 (2015): 579–587.
4. Xu, Zhiwei, et al. "Integrated D-band transmitter and receiver for wireless data communication in 65 nm CMOS." *Analog Integrated Circuits and Signal Processing* 82.1 (2015): 171–179.
5. Hansen, Christopher J., et al. "WLAN transmitter having high data throughput." U.S. Patent No. 8,964,895 (2015).
6. Sajad Mohammad Ali Nezhad and Hamid Reza Hassani, "A Novel Triband E-Shaped Printed Monopole Antenna for MIMO Application", *IEEE ANTENNAS AND WIRELESS PROPAGATION LETTERS, VOL. 9,(2010), Pg 576.*
7. Mondal, Tapas, et al. "A Novel Tri-Band Hexagonal Microstrip Patch Antenna Using Modified Sierpinski Fractal for Vehicular Communication." *Progress In Electromagnetics Research C* 57 (2015): 25–34.
8. Smyth, Braden, Stuart Barth, and Ashwin K. Iyer. "Design of multi-band microstrip patch antennas using miniaturized 1D metamaterial-based EBGs." *Radio Science Meeting (Joint with AP-S Symposium), 2015 USNC-URSI*. IEEE (2015).
9. Long, Jiang, and Daniel F. Sievenpiper. "A Compact Broadband Dual-Polarized Patch Antenna for Satellite Communication/Navigation Applications." *Antennas and Wireless Propagation Letters, IEEE* 14 (2015): 273–276.
10. So, Kwok Kan, et al. "Miniaturized Circularly Polarized Patch Antenna With Low Back Radiation for GPS Satellite Communications." *Antennas and Propagation, IEEE Transactions on* 63.12 (2015): 5934–5938.
11. Gao, S., et al. "A Ka/X-band digital beamforming synthetic aperture radar for earth observation." *Recent Advances in Space Technologies (RAST), 2015 7th International Conference on*. IEEE (2015).

In-service Pipeline Inspection Crawler

Vimal Upadhyay and Sonali Agrawal

Abstract In order to conduct health assessment of refinery process piping which undergo extensive corrosion damage, periodic inspections are carried out by refiners. However, such inspection of inaccessible regions is very difficult, time consuming, and labor intensive. Therefore, as a part of aiding such inspections, a robotic carrier is desired to be made that can provide access to inaccessible regions for conducting dimensional measurements as well as carry other handheld inspection tools. The present work aims at development of a prototype of a robotic carrier with a suitable mechanical design as well as electronics.

Keywords Preventive · Non-destructive testing · In-service · Over-headed

1 Introduction

In Current scenario, robots have become an imperative part of imminent social machinery that is why automated, autonomous, self-directed machines are covering the whole globe under their influence. Primarily the functional area of robotics was only limited to industrial automation which began with the industrial automation with the introduction of machinery. Individual construction continued to have some drawbacks ever since every new design has been created. From the very initial creations to newer automated techniques like aircrafts, bridges, etc., everything have some shortcomings and to overcome all these minor human faults which are inevitable, these field inspection techniques have been considered. Initial inspection of any design generally involve emphasizing on its mechanical properties, in extreme cases it could involve damage of entire prototype during measuring techniques, like hardness and ductility, etc. Though inspection techniques which are

Vimal Upadhyay (✉) · Sonali Agrawal
Indian Institute of Information Technology, Allahabad, India
e-mail: vimalupadhyay2002@gmail.com

Sonali Agrawal
e-mail: sonali@iiita.ac.in

© Springer Science+Business Media Singapore 2017

R. Singh and S. Choudhury (eds.), *Proceeding of International Conference on Intelligent Communication, Control and Devices*, Advances in Intelligent Systems and Computing 479, DOI 10.1007/978-981-10-1708-7_23

used during operating conditions demands nondestructive mode of Inspection as it is not possible every time to have a shutdown before having any inspection, which could results in heavy economic loses, even some industrial machinery requires a lot of human efforts for shutdown and restarting which could not be possible for a frequent scheduled inspections [1]. In this paper, nondestructive evaluation technique is used as an inspection of corrosion, erosion and physical defects without doing any harm to sample. Nondestructive testing assumes greater significance in dangerous zone or unapproachable zone for human being whose failure take a human life, or monetarily and loss of valuable recourses [2–4]. Common examples are energy pipes in petrochemical plant or nuclear plant, high risk buildings, aircrafts, complex structure of rail, road bridges, etc [5, 6].

2 Main Components of Crawler with Chosen Justification

There are four main components of crawler as follows:

(i) **Power Supply**: Lithium battery pack provided by IOCL. CSC93DD Lithium batteries pack is used to make a crawler and inspection tool operations energy efficient. The specifications of Lithium battery is shown in Table 1. Table 2 discusses the reasons for choosing Lithium batteries power pack:

(ii) **Magnetic Wheels Selection with Justification "Neodymium Magnet"**: Neodymium Magnet also known as neo magnet, NIB, NdFeB, and rare to earth magnet is the strongest permanent magnet. This magnet has the highest magnetic force in compare to currently available magnets. In neo magnet high magnetic forces can be obtained from small volume. Most common disadvantage of this magnet is its property easy to rust. Neo magnet first developed by General Motors and Sumitomo special metals in 1982. In present situation these magnets are widely used in electric motors (in cordless tools) and hard disk drivers. This magnet made from an alloy neodymium (Nd), iron (Fe), and boron (B). 2. Samarium or Cobalt Magnet: cobalt magnet second in strength or we can say after neo magnet. Most common advantages are (1) resistance to rusting (2) resistance to temperature. Disadvantages of cobalt magnet shown below: (1) brittle (2) mechanically low in strength (3) caution is required for handling. 3. Ferrite Magnet: ferrite magnet has low magnetic force. 4. Alnico Magnet: alnico magnet has superior power to work against high temperature and mechanical strength [7].

Table 1 Lithium battery with specifications

Type of battery	Specifications
Electrochem non rechargeable type lithium battery	1. Light in weight
	2. Discharge rate 1A
	3. Capacity 250C–30Ah
	4. Weight of each cell 213 gms

Table 2 Features of lithium batteries

Features	Description
High energy density	1. Inspect pipeline up to 70 km in single run
	2. Energy density up to 915 W hour per liter
	3. Provide power to data storage and sensors
Rugged construction	Capable to withstand against high shock and vibration
Safety features	Reliable power to overcome harsh operating conditions
Temperature operating range	Easily provide power to inspection tool at high temperature found in oil industries
High power with less weight	Very low in weight in comparison to other cells only 213 gm

In materials science, the coercive force or coercive field also known as coercivity is define as a measure of ferromagnetic material or ferroelectric material to withstand against external magnetic or electric field. High coercivity materials are called magnetically hard and mostly used in making permanent magnet. Permanent magnet is used in following applications: electric motors/magnetic separation/hard drives/floppy/magnetic tape. In the other end low coercivity materials are called magnetically soft; they are used in magnetic shielding/recording heads/transformer/microwave (Fig. 1).
Caution in handling of magnetic wheels:

1. Since these magnetic materials wheels are very fragile, no variation is available.
2. Magnetic wheel is vulnerable to impact. Be alert during fitting.
3. Magnetic fields generated by magnetic wheels cause's negative effects on electronic devices, i.e., Watch, phones, PCs etc.

(iii) **Justification for Chosen Resisting Flat Belt and Pulley**: MISUMI produce seven types of flat belts in market. (1) General Purpose (2) Sliding (3) Inclination (4) Electronic Parts Conveyer (5) Food Conveyer (6) Heat-Resisting and (7) Oil-Resisting. Following are the storage cautions of flat belt:

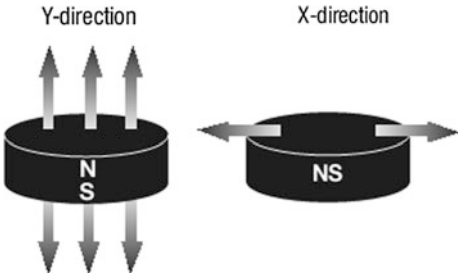


Fig. 1 Magnetization direction

- Avoid direct sunlight and store in dark place.
- Save from water or rain fall.
- Store in dark place where humidity less than 80 %, temperature lies in the range of 0° ~ 40°.

(iv) **L293D**: L293D is a quadruple high-current half-H driver. The L293D is designed for providing a bidirectional drive current up to the range limit 600-mA at voltages varies from 4.5 to 36 V. L293D device is designed to drive inductive loads, i.e., relays, high current/high voltage loads in supply applications, bipolar stepping motors, and solenoids. All inputs are TTL compatible. If the input is high its means driver is enabling and their output is active. When the value of enable input is low it means driver is disabled and their output is not active.

3 Software and Coding Platform for Crawler

From Fig. 2 it shows the complete set of components hardware as well as software will be used in development of entire system. Pipe crawler is an intelligent robot that simulates the traversing of robot over ferromagnetic oil pipeline. The intelligent simulated model robot works on feedback control system. The output of sensor array is an analog signal which with inbuilt analog to digital converter (ADC) in microcontroller converts analog sensor output to digital signal and provide it to microcontroller. The digital value generated by ADC of microcontroller can also be seen in a 16*2 LCD display interfaced with the microcontroller. The output of the microcontroller is given to the dc motors attached with it via H Bridge I.C.

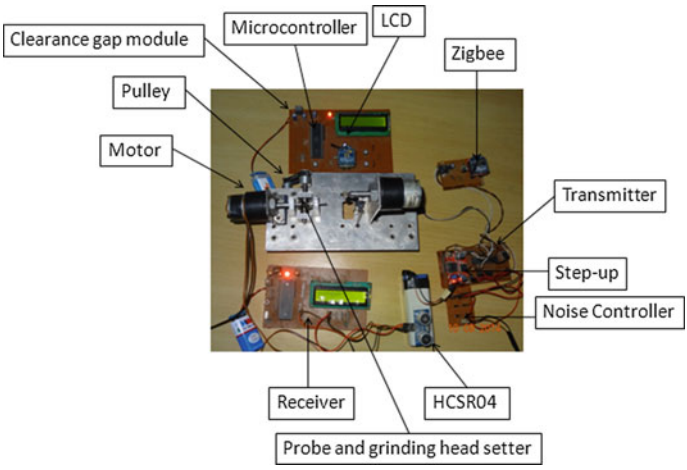


Fig. 2 Complete set of crawler

Software Description
Microcontroller only understands hexadecimal language and writing code in hexadecimal format is very tough task. So the code for controlling the robot is written in C language on keil platform. This software has a note pad to write code in it and has inbuilt complier which generates hexadecimal code for written *c* code. Through this platform the generated hexadecimal code also get transferred to microcontroller via USB programmer. This code reads the digital values received from analog to digital converter which gets analog values of sensors as input. With respect to these values microcontroller take its decision of motion of robot and decide the polarity of the motors which are connected to the microcontroller via H bridge IC. The digital values obtained from ADC also get displayed on 16*2 LCD display attached with microcontroller at PORT C.

4 Results and Discussion

This paper deals with the results and discussion of the present investigation on "To Develop an Autonomous Device Remotely Operable for Thickness Measurement" with the following end objectives:

(1) In case of horizontal direction:

- Record readings of crawler on the external surface of 24″ diameter pipe.
- Record readings of crawler on the internal surface of 24″ diameter pipe.

Record readings of crawler on the external surface of 24″ diameter pipe: The crawler was tested by traveling the same on the external surface of a 24″ diameter pipe. Markings of 0.5 m spacing were made on the surface of the pipe. The 12 V Dc power supply to the crawler was given an external source. In Fig. 3 crawler runs externally at 12 O'Clock position on a pipeline and 6 O'clock position in internal case.

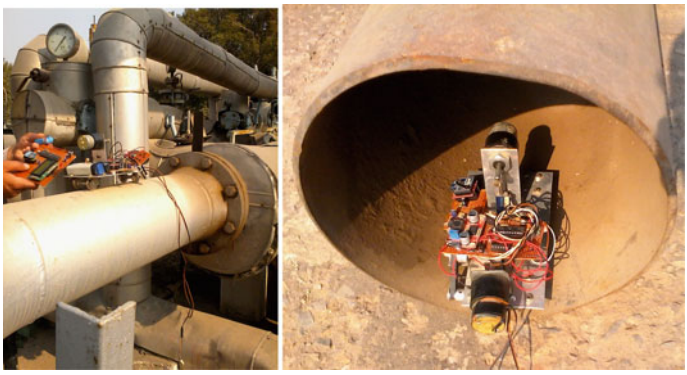


Fig. 3 Crawler runs externally and internally on horizontal pipe

Table 3 Readings of crawler run externally on horizontal pipe

S. no.	O'Clock	Distance (m)	Time (sec)	Load (gm)	Thickness (mm)	Remarks
1	12	0.5	4	0	30	System is remarkable
2	12	1.0	8	0	29	System is remarkable
3	12	0.5	4	500	30	System is remarkable
4	12	1.0	8	1000	29	System is remarkable
5	12	1.0	8	1500	29	System is remarkable
6	6	1.0	8	0	30	System is remarkable
7	6	0.5	4	500	29.5	System is remarkable
8	6	–	–	1000	29.5	Not able to hold beyond few seconds
9	3	0.5	4	0	30	System is remarkable
10	3	1.0	8	500	29	System is remarkable
11	3	–	–	1000	30	Not able to hold beyond few seconds

Table 4 Readings of Crawler run internally on horizontal pipe

S. no.	O'Clock	Distance (m)	Time (sec)	Load (gm)	Thickness (mm)	Remarks
1	12	0.5	4	0	30	System is remarkable
2	12	1.0	8	0	29	System is remarkable
3	12	0.5	4	500	30	System is remarkable
4	12	1.0	8	1000	29	System is remarkable
5	12	1.0	8	1500	29	System is remarkable
6	6	1.0	8	0	30	System is remarkable
7	6	0.5	4	500	29.5	System is remarkable
8	6	–	–	1000	29.5	Not able to hold beyond few seconds
9	3	0.5	4	0	30	System is remarkable
10	3	1.0	8	500	29	System is remarkable
11	3	–	–	1000	30	Not able to hold beyond few seconds

The crawler was run on the pipe surface at 12 O'Clock, 9 O'Clock, 6 O'Clock positions. The readings are as follows are shown in Fig. 3 indicate system is remarkable: (Table 3).

Record readings of crawler on the internal surface of 24″ diameter pipe: The crawler was tested by travelling the same on the internal surface of a 24″ diameter pipe. Markings of 0.5 m spacing were made on the surface of the pipe. The 12 V Dc power supply to the crawler was given an external source. The crawler was run on the pipe surface at 12 O'Clock, 9 O'Clock, 6 O'Clock positions. The readings are as follows shown in Table 4 indicate system is remarkable for industrial application point of view: (Table 4).

5 Conclusion

In other words we could say that our system moves 45 degree elbows, 90 degree elbows, but- joints, T-branches, brass hurdles, supports, and Y-branches. The distinctiveness of this paper is to design and implement a crawler with pipe inspection system, experimented the system in different diameter pipelines, complex network and pipeline layouts. The crawler is based on NdFeB magnet wheels with a drive motor. The choice of this magnet has been made for its highest energy product. The magnet has a curie temperature of 310 °C thereby limiting the application temperature.

References

1. José A. Gálvez, Pablo González de Santos, and Friedrich Pfeiffer, "Intrinsic Tactile Sensing for the Optimization of Force Distribution in a Pipe Crawling Robot" proceedings of IEEE/ASME TRANSACTIONS ON MECHATRONICS, VOL. 6, NO. 1, MARCH 2001.
2. Puneet Singh and G.K. Ananthasuresh, "A Compact and Compliant External Pipe-Crawling Robot", proceedings of IEEE TRANSACTIONS ON ROBOTICS, VOL. 29, NO. 1, FEBRUARY 2013.
3. Chen Jun, ZongQuan Deng, ShengYuan Jiang, "Study of Locomotion Control Characteristics for Six Wheels Driven In-Pipe Robot". Proceedings of the 2004 IEEE International Conference on Robotics and Biomimetics August 22–26, 2004, Shenyang, China.
4. Hyoukryeol Choi*, Jaejun Park, Taehun Kang, " A Self-contained Wall Climbing Robot with Closed Link Mechanism," KSME International Journal, VoL 18 No. 4, pp. 573–581, 2004.
5. Geoffrey A. Hollinger Jeri M. Briscoe, "Genetic Optimization and Simulation of a Piezoelectric Pipe-Crawling Inspection Robot," Proceedings of the 2005 IEEE International Conference on Robotics and Automation Barcelona, Spain, April 2005.
6. Fengping Xu and Jun Zhao, Zongquan Deng, "Research Influence Factor on Pipeline Robot Driving Force in Elbow of Pipe", Proceedings of the 2007 IEEE International Conference on Robotics and Biomimetics December 15 –18, 2007, Sanya, China.
7. Baeksuk Chu1, Kyungmo Jung1, Chang-Soo Han2 and Daehie Hong1, "A Survey of Climbing Robots: Locomotion and Adhesion", International journal of precision engineering and manufacturing vol. 11, no. 4, pp. 633–647 August 2010.

Femtocell-Based Load Balancing Using a Noncooperative Game

Asmita Roy, Priti Deb, Sadip Midya, Debashis De and Koushik Majumder

Abstract The increase in smart phone devices has lead to an exponential growth in the number of MUs (mobile user). With increasing number of MUs, the demand for data rate also increases. So, femtocells are deployed in indoor regions to give efficient coverage. Users on entering the system gets randomly connected to one of the femtocell under its coverage. This leads to some femtocell being overloaded and some femtocells remaining underutilized. In this paper, a non-cooperative game is played between the users for deciding among the femtocells under its coverage which gives an optimum performance; without hampering the performance of other users. The critical selection is based on reaching Nash Equilibrium of the game with the help of the utility function. This function is based on two important network parameters path loss and data rate of the femtocell. Simulations shows this approach helps in balancing the overall load of the system.

Keywords Femtocell · Path loss · NLOS · Noncooperative game · Nash equilibrium

1 Introduction

Heterogeneous environment is desirable in today's wireless network scenario for achieving high data rates. This further leads to the development of tier networks. Macrocell provides maximum area coverage. Better coverage in indoor regions is

Asmita Roy (✉) · Priti Deb · Sadip Midya · Debashis De · Koushik Majumder
Department of Computer Science and Engineering, West Bengal University of Technology, BF 142 Salt Lake Sector 1, Kolkata, India
e-mail: asmitaroy2002@gmail.com

Sadip Midya
e-mail: sadip20@gmail.com

Debashis De
e-mail: dr.debashis.de@gmail.com

Koushik Majumder
e-mail: koushikzone@yahoo.com

© Springer Science+Business Media Singapore 2017

R. Singh and S. Choudhury (eds.), *Proceeding of International Conference on Intelligent Communication, Control and Devices*, Advances in Intelligent Systems and Computing 479, DOI 10.1007/978-981-10-1708-7_24

achieved by Femtocell Access Point (FAP). Femtocell covers small areas typically (10–20 m) [1]. In order to get a seamless connection, the user needs to connect to the femtocell that gives the optimum service. In indoor regions, femtocells are deployed non uniformly due to varying building structure. Due to this type of deployment of femtocells, it becomes difficult for a Mobile User (MU) with no background knowledge to choose between available FAPs for optimum performance. If the load of one particular femtocell goes on increasing, then the Quality of Service (QoS) provided by the femtocell to its users decreases. On the other hand, many femtocells in the building remain unutilized. In present scenario where the demand for data rate is so high, user QoS and Quality of Experience (QoE) is also an important issue which cannot be compromised. Game theory can be used to help the users in making the correct decision as to which FAP needs to be selected to get the optimal performance. Game theory can be used for efficient power management in a network [2]. But choosing the correct femtocell is also a prime concern to serve the user with a good QoS. In [3] how a 4G network can be modeled using a game theoretic approach is shown. Game theory is also used in selecting the optimized network in today's heterogeneous radio access technology environment [4, 5].

In our approach, we have used non-cooperative game theory in modeling our system. A utility function is designed based on fairness, data rate of that femtocell, and the path loss between the user and FAP. A users' decision as to which FAP to select is based on reaching the Nash equilibrium in the game.

2 System Architecture for Femtocell Selection

In this model as shown in Fig 1, femtocell base stations are deployed inside the building for efficient network coverage. There are two types of femtocells: (a) closed access FAP, (b) open access FAP [1]. For our system model, we consider closed access, to monitor which user register to which FAP. At any point, the number of users connected to a FAP_i is expressed as N_i. In indoor region which is geographically not uniform, femtocells are placed randomly. Since indoor areas have many obstacles (e.g., wall, furniture) the signal from FAP to the Mobile Station (MS) does not follow Line Of Sight (LOS) mainly they are Non-Line Of Sight (NLOS). In their course of traversal, the signal faces a loss in power. So there is a difference between transmit power and received power. This difference in power is referred to as path loss of the signal.

Therefore path loss helps in measuring the signal strength. The path loss between the MS and FAP_i is given by WINNER NLOS model [6].

$$PL_W = 20\log(d) + 46.4 + 20\log(f/5) + N \quad (1)$$

where $N = 5(n_w - 1)$ for light wall and $N = 12(n_w - 1)$ for heavy wall, f is the frequency represented in GHz, d is the separation distance between femtocell access

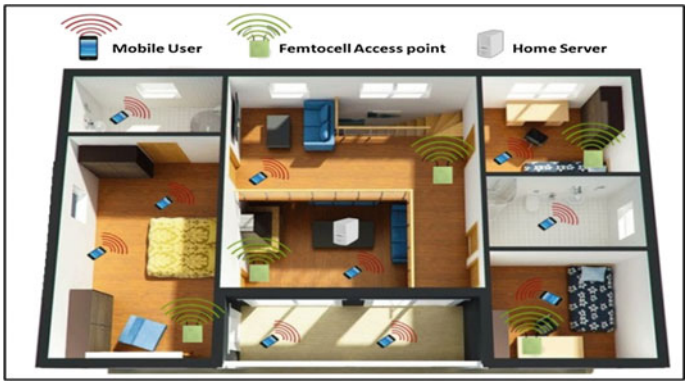


Fig. 1 Indoor scenario for femtocell deployment

points and the mobile device in meter, and n_w denotes the number of walls in the area where femtocell is placed.

Since FAP has smaller area of coverage so many FAPs are normally deployed for better coverage. This leads to co-tier interference [1]. SINR denotes the signal interference to noise ratio. The SINR for a femtocell is expressed as

$$\mathrm{SINR}_{i,j} = \frac{P_{\mathrm{tr}}}{\sum_{f_n} P_{\mathrm{tr}} + N_w} \tag{2}$$

where P_{tr} is the transmitted power of the FBS, f_n is the number of neighboring FBSs of the particular FBS and N_w is the noise. So the receiving data rate of user j connected to femtocell i is given by

$$C_j = X \cdot \log_2\left(1 + \mathrm{SINR}_{i,j}\right) \tag{3}$$

where X is the total available bandwidth of femtocell i divided by the number of users associated with the femtocell. Considering all users connected to a FAP have same network utilization, the achievable data rate of a FAP for each users connected to it can be expressed by $C_{j.}$

The best FAP selection by a MU depends on two network parameters: (a) path loss encountered by the user and the FAP under its coverage, and (b) available data rate of each FAP. So when many users enter the building there is a competition in choosing the best FAP. If it is done in an ad hoc manner some MU will benefit while others will suffer. To ensure that this decision is taken wisely, game theory is used in optimizing the decision.

3 Noncooperative Game

In our scenario let us say there are N numbers of MU spread across the building, M number of FAP having the same capabilities. The cost of associating a MU to the FAP is determined with the help of utility function or pay off function. So the utility function for a user i for selecting a particular access point j in a multiple user scenario can be given by

$$\mathrm{UF}_{i,j}(M) = \mathrm{PL}_{i,j} + w_t * 1/C_j \tag{4}$$

where $\mathrm{PL}_{i,j}$ denotes the path loss for MU i and FAP j given by Eq. (1). C_j is the current data rate of femto cell access point j given by Eq. (3). w_t is a weight assigned which can be configured according to user preference. The game is played between MU that have the same FAPs under its coverage. So the association decision as to which FAP will connect to which MU such that the load of the system remains maintained becomes critical. The way of selecting the correct FAP using the game theoretic approach is explained below with the help of an algorithm. The algorithm is divided in two stages

- Stage 1
  1. At the very first stage, the users are divided in two groups Real Time (RT) users and Non-Real Time (NRT) users.
  2. A higher priority is assigned to RT compared to NRT users. This allows us in serving the RT users before NRT users.
- Stage 2
  3. The associations are carried out for RT users before NRT users. Each of the MUs calculates their own utility function value using Eq. (4).
  4. The nash point of the game is found out with the help of a MXM matrix where M is the number of FAPs present under the coverage of the MU.
  5. Every MU present in the network is assigned to a FAP determined from the nash point in the game.

Nash equilibrium is a solution concept of a game [7]. In this game nash equilibrium is reached when the nash point is determined. A nash point between two players is found when given the strategies of the players, each player chooses a strategy such that both the players benefit from it. Since for our game payoff function is directly related to cost of associating the MU to a FAP, so minimum payoff value is desired for the players.

4 Results and Discussion

Path loss is measured using WINNER II model. Figure 2 shows how path loss affects a signal. In Fig. 2 a, b the frequency response of an LTE-A signal is shown before path loss and after path loss using WINNER II model. This experiment is done using EXA Vector Signal Analyzer (VSA) 9010A with center frequency 2 GHz.

The cost of each mobile nodes connecting every FAP under its coverage is calculated using MATLAB 2010b. The MUs get connected to that FAP which helps the game in reaching the nash equilibrium. Our area is divided into six rooms and a corridor. We deployed a femtocell base station inside each room. So there is a total of six femtocell access point in the area. Now in each room there are already some MUs from beforehand which connects to their respective femtocell access point. There are about 20 MUs distributed across six rooms marked by blue dots in the Figs. 3 and 4. Now, about 15 MUs (marked by red dots) enter the corridor and switch on their mobile phones. Which user connects to which FAP is decided using the above-illustrated game.

4.1 Comparative Study

The resultant load distribution of the system is compared without using game theory approach and with using game theory and is shown in Figs. 3a, b and 4a, b respectively.

It is noted that how most users get connected to FAP_1 as shown in Fig. 3 since it is nearer to all MU. So FAP_1 becomes over utilized reducing its capacity while FAP_6 and FAP_3 becomes underutilized.

According to our approach at the very first stage 15 users are divided in two subsets RT users and NRT users. Two users namely N_1 and N_2 belong to RT subset. The two users have four AP (AP1, AP2, AP3, AP4) under its coverage. Which AP will be chosen is determined by the nash point as shown in Table 1.

Figure 4 shows the entire scenario of 15 MUs connecting to the six AP using game approach. It is noted that the access points in the room, previously containing

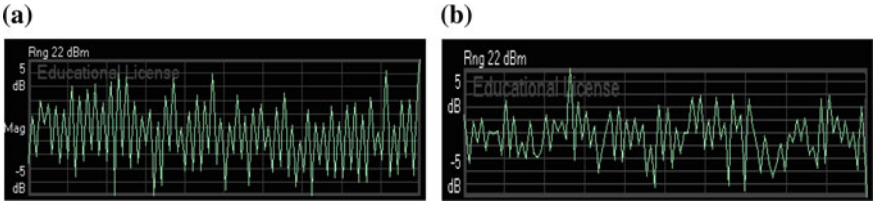


Fig. 2 **a** Signal before path loss. **b** Signal after path loss

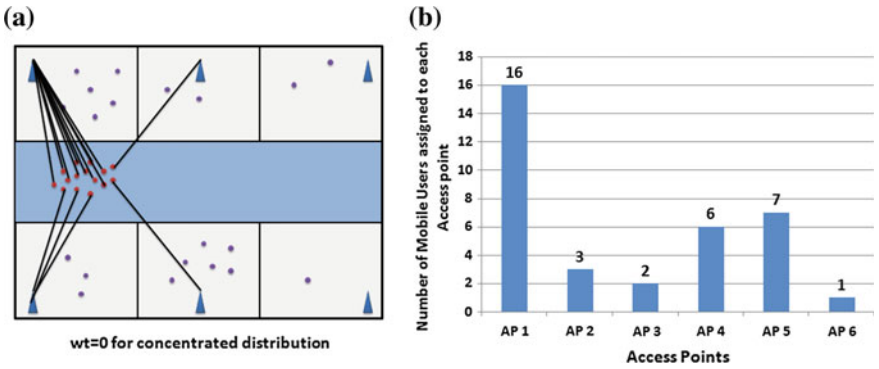


Fig. 3 **a** Simulation scenario. **b** Load of the overall system without using noncooperative game

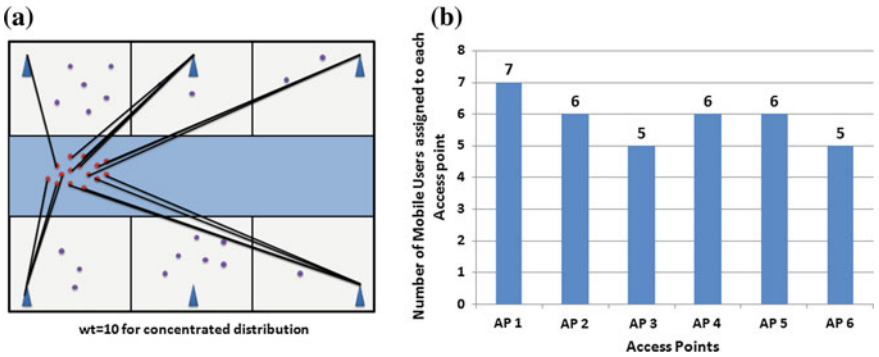


Fig. 4 **a** Simulation scenario. **b** Load of the overall system using noncooperative game

Table 1 Showing the cost of associating MUs N_1 and N_2 to the four AP under its coverage

Players	N_2				
N_1	Access point	AP1	AP2	AP3	AP4
	AP1	(203, 203)	(203, 111)	(203, 127)	(203, 132)
	AP2	(110, 203)	**(110, 111)**	(110, 127)	(110, 132)
	AP3	(127, 203)	(127, 111)	(127, 127)	(127, 132)
	AP4	(133, 203)	(133, 111)	(133, 133)	(133, 132)

The bold area shows the nash point

the minimum amount of MUs are assigned most of the newly arrived mobile nodes. Thereby distributing the network load across all the access points. Thus our scheme is proved to distribute the load and optimize the network. It is a win-win situation for all the MUs as well as the access points.

5 Conclusion

In this work, we aim to balance the load of the overall system using noncooperative game played between MUs. The MU gets connected to the FAP that gives the best performance. This work considers the correct selection of FAP in indoor NLOS region. It can be seen from the simulation that with our approach the network load is being balanced and all the femtocell inside the building are used equally. Even due to the uneven distribution of femtocells no femtocell is at a dead point. So resources are not underutilized enhancing the overall throughput of the system.

Acknowledgments The authors are grateful to West Bengal University of Technology TEQIP II program and DST FIST program with reference number FIST/ETI/296/2011.

References

1. Chandrasekhar, V., Andrews, J, G., Gatherer, A.: Femtocell networks: a survey. Communication Magazine, Vol. 46. IEEE (2008) 59–67.
2. Huang, J., Berry, R, A., Honig, M, L.: A game theoretic analysis of distributed power control for spread spectrum ad hoc networks. Proceedings of International Symposium on Information Theory, IEEE (2005).
3. Antoniou, J., & Pitsillides, A.: 4G converged environment: Modeling network selection as a game. 16th IST Mobile and Wireless Communications Summit, IEEE (2007) 1–5.
4. Chang, C.J., Tsai, T.L. and Chen, Y.H.:Utility and game-theory based network selection scheme in heterogeneous wireless networks. Wireless Communications and Networking Conference, IEEE (2009) 1–5.
5. Yang, C., Yubin, X., Rongqing, X. and Xuejun, S.: A heterogeneous wireless network selection algorithm based on non-cooperative game theory. Communications and Networking in China, 6th Int. conference ICST, IEEE (2011) 720–724.
6. IST-4-027756, WINNER II D1.1.2 Vol.2, WINNER II Channel Models, Part I Channel Models, (2008).
7. Trestian, R., Ormond, O., Muntean, G.M.: Game theory-based network selection: solutions and challenges. Communications Surveys & Tutorials, Vol. 14. IEEE (2012) 1212–1231.

Study of Conventional Control Algorithms for PV-Based Grid-Connected Microgrid

Nikita Gupta, Rachana Garg and Parmod Kumar

Abstract This paper evaluates four conventional algorithms of determining the compensating current for a PV inverter used for integrating PV array with grid. The algorithms studied are synchronous reference frame (SRF) theory, unit template, instantaneous reactive power (IRP) theory, and conductance Fryze. The system has been modeled and implemented in MATLAB along with Simulink toolbox. Simulation results of the performance of four algorithms are presented and analyzed for control of power flow and harmonics reduction in PV-based grid-connected microgrid system.

Keywords Photovoltaic array · Microgrid · Control algorithms · PV inverter

1 Introduction

In the last two decades, awareness of consumers about green technologies, environment concerns, and depletion of the stock of fossil fuel has forced the planners and grid designers to explore the renewable energy sources and alternative sources viz. Photovoltaic (PV) Cell, wind turbine generator, storage battery, microhydropower. In India due to abundance of sunlight, solar energy is gaining lots of importance. The output of PV cell is DC voltage and integration with conventional AC microgrid requires semiconductor inverters along with their controllers. Power generated from PV modules faces the problems concerning power quality like waveform distortion, unbalance, and fluctuations in voltage and/or current.

Nikita Gupta (✉) · Rachana Garg
Delhi Technological University, Delhi, India
e-mail: guptanikita08@gmail.com

Rachana Garg
e-mail: rachana16100@yahoo.co.in

Parmod Kumar
Maharaja Agrasen Institute of Technology, Delhi, India
e-mail: pramodk2003@gmail.com

© Springer Science+Business Media Singapore 2017

R. Singh and S. Choudhury (eds.), *Proceeding of International Conference on Intelligent Communication, Control and Devices*, Advances in Intelligent Systems and Computing 479, DOI 10.1007/978-981-10-1708-7_25

So, utilization of PV module efficiently needs output voltage and current to be tracked and optimized using appropriate control algorithm [1, 2]. Inverter plays a vital role for processing, control, and synchronization of generated power with grid. Performance of PV inverter is based on active, reactive, and harmonic current estimation. Accuracy of performance is decided by control algorithm. Several control schemes have been designed and reported in literature [3, 4]. In this paper, the author(s) have discussed and compared synchronous reference frame (SRF) theory, unit template, instantaneous reactive power (IRP) theory, and conductance Fryze based control algorithms. MATLAB and Simulink toolbox-based simulation analysis is presented for demonstration of effectiveness of these control techniques for PV-based grid-connected microgrid system.

2 Design of Control Algorithms

The different control algorithms are applied in the closed-loop control of PV inverter to generate gating pulse signals. Difference lies in the sensed parameters and their processing to generate the reference current signal for gating pulse generation. Once the reference signals (i_{ra}*, i_{rb}*, i_{rc}*) are obtained, they are processed with measured currents using hysteresis current controller (HCC). HCC generates the six gating pulse signal for the PV inverter. The proposed algorithms are implemented on a 10 kW PV-based grid connected microgrid as shown in Fig. 1 [5].

2.1 Synchronous Reference Frame Theory

In the SRF theory-based algorithm, sensed i_{la}, i_{lb} and i_{lc}; V_{terma}, V_{termb} and V_{termc} and v_{dc} are fed to controller for extracting the reference currents [6]. SRFT algorithm

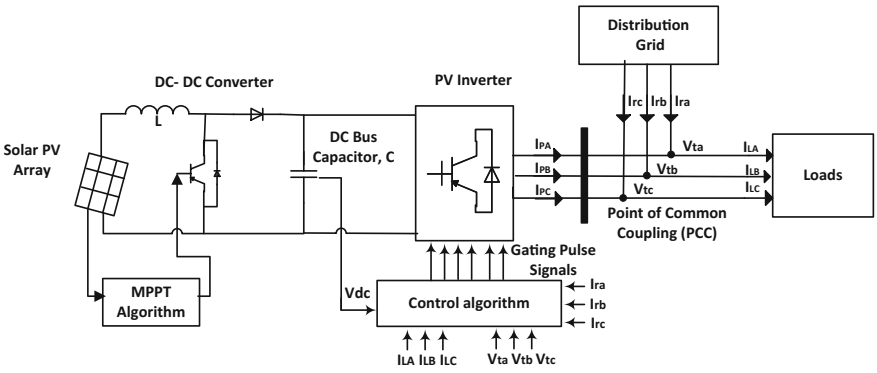


Fig. 1 Schematic diagram of PV-based grid-connected microgrid

uses Park's transformation to reduce three-phase AC quantities to two DC quantities for simplified calculations, given by Eqs. (1) and (2):

$$i_d = \frac{2}{3}\left(i_a \mathrm{Re}\{e^{i\alpha}\} + i_b \mathrm{Re}\{e^{i\beta}\} + i_c \mathrm{Re}\{e^{i\gamma}\}\right) \tag{1}$$

$$i_q = \frac{2}{3}\left(i_a \mathrm{Im}\{e^{i\alpha}\} + i_b \mathrm{Im}\{e^{i\beta}\} + i_c \mathrm{Im}\{e^{i\gamma}\}\right) \tag{2}$$

where α is (ωt), β is ($\alpha - 2\pi/3$), and γ is ($\alpha + 2\pi/3$). The two DC quantities, I_d (d-axis) current and I_q (q-axis) current are used to control the real and reactive power respectively. The PV inverter generated AC supply has to be synchronized with the grid supply before connection. The generated signals are synchronized with the grid using phase-locked loop (PLL). A PI controller is used for the DC bus voltage regulation. Output of PI is loss current (i_{loss}) component of power of system. To generate the reference currents inverse Park's transformation is carried out using Eqs. (3–5)

$$i^*_{\mathrm{ra}} = \left(i^*_d \mathrm{Re}\{e^{i\alpha}\} + i^*_q \mathrm{Im}\{e^{i\alpha}\}\right) \tag{3}$$

$$i^*_{\mathrm{rb}} = \left(i^*_d \mathrm{Re}\{e^{i\beta}\} + i^*_q \mathrm{Im}\{e^{i\beta}\}\right) \tag{4}$$

$$i^*_{\mathrm{rc}} = \left(i^*_d \mathrm{Re}\{e^{i\gamma}\} + i^*_q \mathrm{Im}\{e^{i\gamma}\}\right) \tag{5}$$

2.2 Unit Template Algorithm

In the unit template control algorithm, sensed inputs $i_{\mathrm{la}}, i_{\mathrm{lb}}$ and i_{lc}; $i_{\mathrm{ra}}, i_{\mathrm{rb}}$ and i_{rc}; V_{terma}, V_{termb} and V_{termc} and v_{dc} are fed to controller for extracting the reference currents [7]. Unit vectors in phase and in quadrature with terminal voltages are calculated using terminal voltage amplitude (V_{term}) as shown in Eqs. (6–8)

$$V_{\mathrm{term}} = \sqrt{\frac{2}{3}\left(V^2_{\mathrm{terma}} + V^2_{\mathrm{termb}} + V^2_{\mathrm{termc}}\right)} \tag{6}$$

$$p_a = v_{\mathrm{sa}}/v_{\mathrm{term}}, p_b = v_{\mathrm{sb}}/v_{\mathrm{term}}, p_c = v_{\mathrm{sc}}/v_{\mathrm{term}} \tag{7}$$

$$q_a = p_c - p_b/\sqrt{3}, q_b = p_a/\sqrt{2} + (p_b - p_c)/\sqrt{6}, q_c = -p_a/\sqrt{2} + (p_b - p_c)/\sqrt{6} \tag{8}$$

The unit vectors obtained are used to obtain the active load power and reactive load power given by Eqs. (9) and (10).

$$P = V_{\text{term}} \times (p_a * i_{\text{la}} + p_b * i_{\text{lb}} + p_c * i_{\text{lc}}) \tag{9}$$

$$Q = V_{\text{term}} \times (q_a * i_{\text{la}} + q_b * i_{\text{lb}} + q_c * i_{\text{lc}}) \tag{10}$$

The total load power calculated has two components, DC component (P_{dc}, Q_{dc}) and oscillating AC component (P_{ac}, Q_{ac}). AC component is harmonic component, which is removed using filter and active (I_{pf}) and reactive (I_{qf}) load current components are obtained. PV inverter is used to supply active load power as well as losses to maintain the unity power factor. PI controller helps in DC bus voltage regulation. Output of PI is loss current (i_{loss}) component of power of system. The unit vectors are then used to calculate the active and reactive components of reference grid currents, using Eqs. (11) and (12)

$$i_{\text{pra}} = p_a \times \left(i_{\text{pf}} + i_{\text{loss}}\right), i_{\text{prb}} = p_b \times \left(i_{\text{pf}} + i_{\text{loss}}\right), i_{\text{prc}} = p_c \times \left(i_{\text{pf}} + i_{\text{loss}}\right) \tag{11}$$

$$i_{\text{qra}} = q_a \times \left(i_{\text{qf}} + i_{\text{acq}}\right), i_{\text{qrb}} = q_b \times \left(i_{\text{qf}} + i_{\text{acq}}\right), i_{\text{qrc}} = q_c \times \left(i_{\text{qf}} + i_{\text{acq}}\right) \tag{12}$$

The addition of the above two components provide the total reference currents.

2.3 Instantaneous Reactive Power Theory

In the IRP theory-based algorithm, sensed $i_{\text{la}}, i_{\text{lb}}$ and i_{lc}; $v_{\text{la}}, v_{\text{lb}}$ and v_{lc} and v_{dc} are fed to controller for extracting the reference currents [8]. In IRPT, active and reactive power are calculated in α–β frame using Clarke's transformation given by Eqs. (13) and (14)

$$v_\alpha + jv_\beta = \sqrt{\frac{2}{3}}\left(v_a + v_b e^{\frac{j2\Pi}{3}} + v_c e^{-\frac{j2\Pi}{3}}\right) \tag{13}$$

$$i_\alpha + ji_\beta = \sqrt{\frac{2}{3}}\left(i_a + i_b e^{\frac{j2\Pi}{3}} + i_c e^{-\frac{j2\Pi}{3}}\right) \tag{14}$$

The estimated active power and reactive power are given by Eqs. (15) and (16).

$$P = v_\alpha i_\alpha + v_\beta i_\beta = P_{\text{dc}} + P_{\text{ac}} \tag{15}$$

$$Q = v_\alpha i_\beta - v_\beta i_\alpha = Q_{\text{dc}} + Q_{\text{ac}} \tag{16}$$

Calculated active and reactive power consists of fundamental component (P_{dc}, Q_{dc}) and harmonic component (P_{ac}, Q_{ac}). To remove the harmonic component, these instantaneous powers are passed through low-pass filter. Filter allows only fundamental signal to pass through. The reference currents are then obtained from

fundamental power signals which are in α, β frame. Inverse Clarke's transform is used to recover three-phase AC quantities of reference currents.

2.4 Conductance Fryze Algorithm

In the conductance Fryze control algorithm, sensed i_{la}, i_{lb} and i_{lc} and v_{terma}, v_{termb} and v_{termc} are fed to controller for extracting the reference currents [9]. In conductance Fryze algorithm, the average conductance value (G_{avg}) is calculated form three-phase terminal voltages and load currents using Eq. (17).

$$G_{avg} = (v_{terma} i_{la} + v_{termb} i_{lb} + v_{termc} i_{lc})/(v_{terma}^2 + v_{termb}^2 + v_{termc}^2) \tag{17}$$

The calculated value of average conductance value is passed through low-pass filter (LPF) that allows only fundamental signal to pass through. PI controller helps in DC bus voltage regulation, generating a loss component (G_{loss}) which is provided by PV inverter to the system. The net conductance G is obtained using Eq. (18)

$$G = G_{avg} + G_{loss} \tag{18}$$

Reference currents are obtained by multiplying the net conductance with the terminal voltages as shown in Eq. (19).

$$i_{ra}^* = G \times v_{terma}, i_{rb}^* = G \times v_{termb}, i_{rc}^* = G \times v_{termc} \tag{19}$$

3 Simulation Results

The solar PV system connected to the grid is simulated in MATLAB along with Simulink toolbox. The simulation results of grid side voltage (V_{grid}), grid side current (I_{grid}), DC link voltage (V_{dc}), load current (I_{la}, I_{lb}, I_{lc}), PCC current (I_{pa}, I_{pb}, I_{pc}), PV voltage (V_{pv}), PV current (I_{pv}), and PV power (P_{pv}) for different algorithms are shown in Figs. 2 and 3. Nonlinear load (universal bridge with 10 Ω, 100 mH) is used. Due to nonlinearity, THD of load current is 10.96 %. Simulation for different algorithms are performed taking into consideration the standard test condition of 1000 W/m^2 and 25 °C.

For performance under transient conditions, load unbalancing is introduced at 0.3–0.45 s. As seen from the figures, for all the algorithms V_{dc} remains constant and PCC voltage is regulated. A comparative analysis THD level of PCC voltage and grid current are presented in Table 1, which are well within IEEE limits [10].

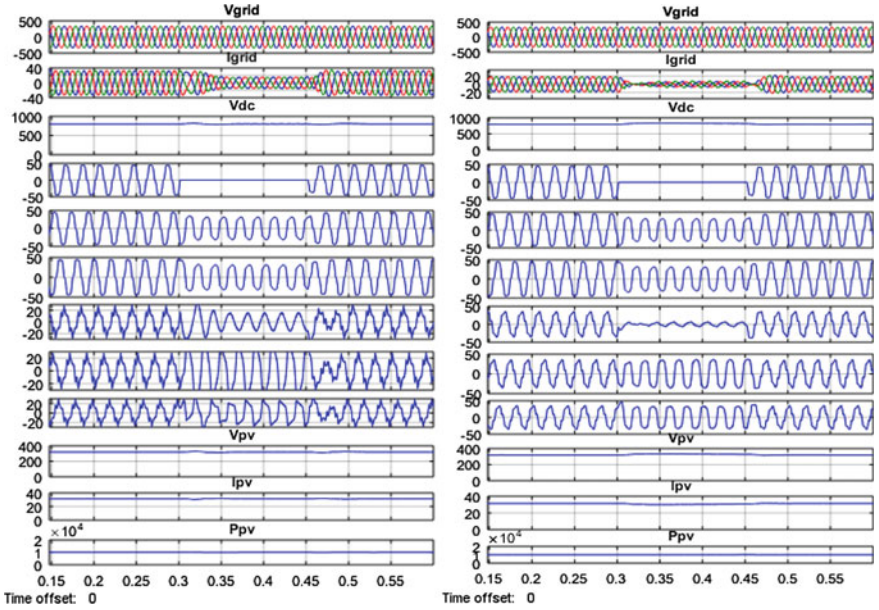


Fig. 2 Performance of SRF and unit template-based controller

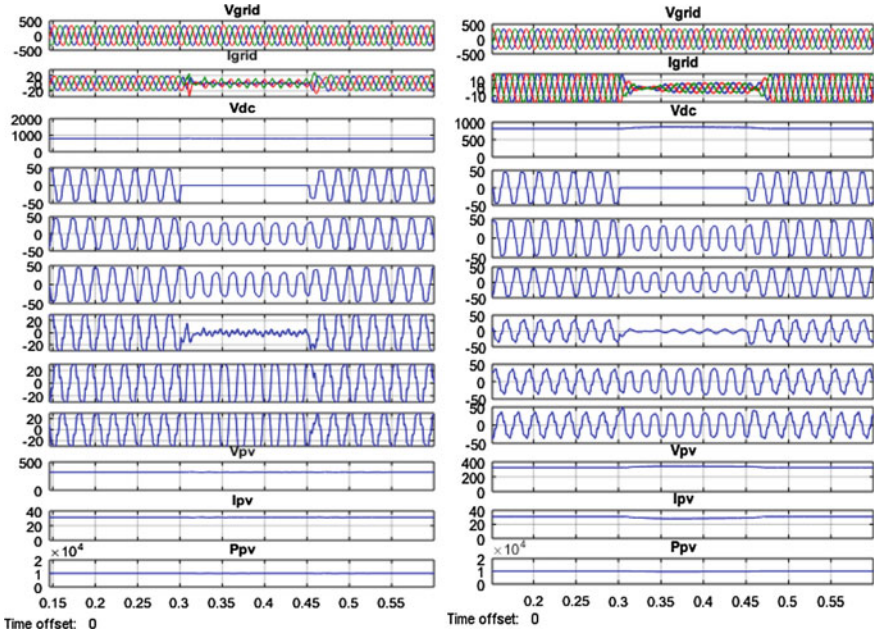


Fig. 3 Performance of IRP and conductance Fryze-based controller

Table 1 Performance of different algorithms under condition of load change

S. no.	Algorithm	Under load unbalancing		Under load increase	
		THD (%) of PCC voltage	THD (%) of supply current	THD (%) of PCC voltage	THD (%) of supply current
1	SRFT	3.07	2.37	2.56	6.90
2	Unit template	2.41	3.12	2.04	4.98
3	IRPT	3.02	2.52	2.42	7.00
4	Conductance Fryze	1.49	2.03	1.59	4.68

4 Conclusions

This paper presents four conventional control algorithms for control of PV inverter to integrate PV module with microgrid. The mathematical analysis of the four algorithms, i.e., SRFT, unit template, IRPT, and conductance Fryze have been presented to demonstrate the behavior of PV inverter. Conductance Fryze control algorithms have been found most suitable among all discussed algorithms. PCC and DC bus voltages of the PV inverter have also been regulated to reference values under all load conditions.

References

1. McEvoy A., Markvart T., Castaner L.: Practical Handbook of Photovoltaics-Fundamentals and Applications. 2nd ed. Wyman Street, USA: Elsevier (2012).
2. Rub H.A., Malinowski M., Al-Hadad K.: Power electronics of renewable energy systems, transportation, and industrial application. 1st ed. United Kingdom: IEEE press and John Wiley and Sons publication (2014).
3. Singh B., Chandra A., Al-Haddad K.: Power Quality: Problems and Mitigation Techniques. United Kingdom: John Wiley & Sons (2014).
4. Singh B., Solanki J.: A Comparison of Control Algorithms for DSTATCOM. IEEE Transaction on Industrial electronics, vol.56 no. 7 (July 2009).
5. Gupta N., Garg R., Kumar P.: Characterization Study of PV module Connected to Microgrid. In: Proceedings of the IEEE India International Conference JMI, India. (Dec. 2015).
6. Verma A.K., Singh B., Sahani D.T.: Grid Interfaced Photovoltaic power generating system with Power Quality Improvement at AC mains. In: Proceedings of the IEEE Third International Conference on Sustainable Energy Technologies (ICSET), Kathmandu (Sept. 2012).
7. Singh B., Kumar S.: Modified Power Balance Theory for Control of DSTATCOM. In: Proceedings of the Joint International Conference on Power Electronics, Drives and Energy Systems (PEDES) & 2010 Power India, New Delhi (Dec. 2010).
8. Hirofumi A., Edson W., Aredes M.: Instantaneous power theory and applications to power conditioning. 1st Ed. New Jersey: IEEE Press-Wiley Press Pvt. Ltd. (2007).
9. Rowey C.N., Summersz T.J., Betz R.E., Cornforth D.: A Comparison of Instantaneous and Fryze Power Calculations on P-F and Q-V Droop in Microgrids. In: Proceedings of the 20th Australasian Universities Power Engineering Conference, Christchurch (Dec. 2010).
10. IEEE Recommended Practices and Requirements for Harmonics Control in Electric Power Systems, IEEE Standard 519 (1992).

Design of 10.24 Tb/s DWDM System Using NRZ Modulation Format with Narrow Channel Spacing

Kuldeep Singh and Sandeep K. Arya

Abstract In this paper, optical communication system at 10.24 Tb/s using NRZ modulation for 1024 channels with channel spacing of 0.2 nm has been simulated. The performance of the designed dense wavelength division multiplexing (DWDM) system has been executed for evaluation in terms of BER, Q-factor, and eye diagrams. It has been observed that signal received at highest distance without dispersion compensation in good quality is 90 km with an average BER of 10^{-9} in S, C, L, U-bands and up to 1728.3 nm wavelength; moreover Q-factor is above the threshold value for DWDM system to implement an optical communication link. The system with NRZ modulation format shows good performance up to 90 km in all spectral bands designated for optical fiber communication, but at the distance of 120 km communication link is possible in S, C, and L-bands and at 150 km up to 1565 nm, i.e., C-band only.

Keywords Optical fiber communication · DWDM · Optical modulation · BER · Dispersion · Optimum bandwidth

1 Introduction

It is acknowledged that fiber optics technology is savior in networking industry to fulfill the user demand for huge bandwidth and high data rate to access the information in terms of voice over high definition (HD) videos and use of internet when we need it, where we need it, and in whatever format we need it. The need of enormous bandwidth and capacity may be exploited in applications like dense wavelength division multiplexing (DWDM) by using many numbers of wavelengths multiplexed [1]. From the extensive literature studied it is learned that there

Kuldeep Singh (✉) · S.K. Arya
Guru Jambheshwar University of Science and Technology, Hisar 125001, Haryana, India
e-mail: kuldeep.elect@gmail.com

S.K. Arya
e-mail: arya1sandeep@gmail.com

© Springer Science+Business Media Singapore 2017

R. Singh and S. Choudhury (eds.), *Proceeding of International Conference on Intelligent Communication, Control and Devices*, Advances in Intelligent Systems and Computing 479, DOI 10.1007/978-981-10-1708-7_26

are numbers of modulation formats like NRZ, RZ, CRZ, CS-RZ, DRZ, and MDRZ to support long distance transmission system in optical communication technology for up gradation of system performance in terms of spectral efficiency, data volume and bandwidth. Jun et al. [2] developed a WDM system spaced at 5 GHz for transmission of 2.5 Gb/s rate for 480 km in C (1530–1565 nm) and L (1565–1625 nm) bands and reported that a transmission of 1000 2.5 Gb/s WDM channels is possible. Bosco et al. [3] investigated a narrow channel DWDM system at a rate of 40 Gb/s by using different modulation formats NRZ, RZ and CS-RZ. They demonstrated that the standard setup of fibers do not allow good performance by taking 0.4 nm channel spacing, but an improvement have been seen by the use of RZ and CS-RZ modulation formats. Hoshida et al. [4] described a DWDM system of 43 Gb/s with density of 120 channels spaced at 75 GHz evaluated the performance using NRZ modulation and reported in low cost configuration and small dependence on fiber type in terms nonlinear tolerance. Kaler et al. [5] reported simulation of DWDM system of 1.28 Tb/s capacity and 0.4 bit/s/Hz spectral efficiency. They described the impact of SNR on channel spacing, length of fiber, dispersion and number of channels. Sharma et al. [6] demonstrated simulated analysis of DWDM system of 40 Gb/s using CS-RZ, DRZ, and MDRZ modulation formats for pre, post and symmetrical compensation schemes. They reported that using MDRZ modulation format on optical transmission link beyond 1550 km is possible. Garrett et al. [7] demonstrated a bidirectional transmission system with 16 channels at the rate of 10 Gb/s over 5000 km of nonzero dispersion shifted fiber, for a full duplex capacity distance product of 800 Tb-km/s.

It is learnt that modulation formats, fiber length and dispersion compensation schemes are the key components in the design of high-capacity optimal DWDM system. The research till now for different modulation formats like NRZ, RZ, CRZ, CS-RZ, DRZ, MDRZ is up to 100–120 channels in C (1530–1565 nm) and L (1565–1625 nm) bands have been evaluated [2, 4–6]. In this paper performance of 1024 channels at reference bit rate of 10 Gb/s DWDM system using NRZ modulation format is evaluated by analyzing the possibility for implementation of an optical communication link. Section 2 demonstrates experimental setup configuration and system design hierarchy. Section 3 explains the results of performance evaluation. Section 4 presents conclusion.

2 Experimental Setup

To design optimal ultra-dense WDM system with the possibility of narrow channel spacing, we used the experimental schematic layout shown in the Fig. 1 in RSOFT Commercial Package OptSim to implement an optical communication link.

The experimental setup is composed of 64 transmitters, combiner, booster, iteration loop, 10 single channel receiver blocks, and a scope in the output to measure BER, Q-factor and to plot eye diagrams. The complete configuration of 1024 channels in the transmission section is defined with 64 transmitter blocks

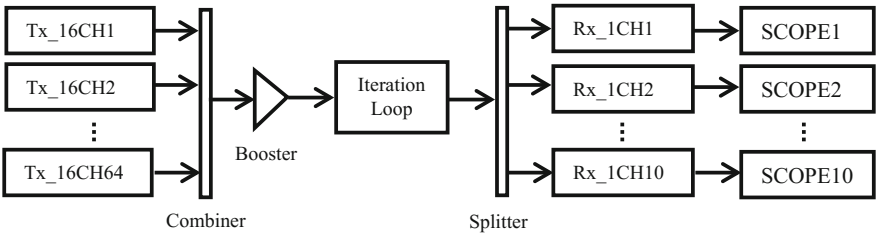


Fig. 1 Schematic layout of proposed optical link with 1024 channels

comprises of 16 individual single channel blocks. The simulation setup at 10 Gb/s with center wavelength 1511.2 nm for first channel and 1730.3 nm for the last channel simulated a DWDM optical link by using NRZ modulation format. The system simulation parameters are listed in Table 1.

In optical link, fix gain output power booster has been added to compensate the losses that occurred during transmission. After that fiber is used. The transmission of each span comprises of DS_Anomalous single mode fiber (SMF) type with the parameters given in Table 2. The nonlinearity coefficient of fiber accountable for Kerr's effect is restricted via "n_2" (fiber nonlinear refractive index) in OptSim by the functional relation [8]:

$$\gamma = \frac{2\pi F_r n_2}{c a_{\text{eff}}} \tag{1}$$

where F_r = reference frequency, a_{eff} = effective area of fiber and c = speed of light.

Pre-amplifier has been used after fiber link, to compensate wavelength dependent noise. The simulation is performed with Lorentzian Raman profile. The amplifier model properties can allow inclusion or exclusion of noise. The system configuration is simulated with a noisy link of 4.5 dB noise figure.

Table 1 System parameters

Data capacity	10 Gb/s × 1024 ch.
Channel allocation	1511.2–1524 nm (S-band)
	1531.5–1560.3 nm (C-band)
	1568–1619.2 nm (L-band)
	1628.2–1669.8 nm (U-band)
	1677.5–1730.3 nm
VBS center frequency (nm)	1620.74
VBS center frequency (THz)	185.82
Channel spacing (nm)	0.2
Bit rate (Gb/s)	10
PRBS	7
Transmission distance (km)	30, 60, 90, 120, 150

Table 2 Fiber parameters

Parameter name	Value	Unit
Length	10	km
Dispersion, D	2	ps/nm/km
Dispersion Slope, S_o	0.7	ps/nm^2/km
β_2	–2.255	ps^2/km
Effective area, A_{eff}	55	μm^2
Nonlinearity coefficient, γ	1.84	W^{-1}/km
Loss, α	0.2	dB/km
PMD	0.1	ps/km$^{1/2}$
Nonlinear refractive index, n_2	2.55	$\times 10^{-20}$ m^2/W

3 Results and Discussion

The results have obtained for 10.24 Tb/s DWDM system using NRZ modulation format with narrow channel spacing to evaluate the performance in terms of BER, Q-factor and eye diagrams. The Q-factor and BER graphs plotted against transmission distance for different wavelengths are shown in Figs. 2 and 3, respectively. The plots show that a band of wavelengths from 1511.2 to 1730.3 nm has been taken to cover the complete spectrum of frequencies designated for optical fiber communication. Ten different wavelengths (1511.2, 1524, 1531.5, 1560.3, 1568, 1619.2, 1628.2, 1669.8, 1677.5 and 1728.8 nm) from whole spectrum have been taken for the performance evaluation of the DWDM system in terms of BER, Q-factor and eye diagrams.

Table 3 shows the observed values of BER and Q-factors over the fiber length. In optical system, BER maximum threshold level at which signal can be recovered is 10^{-09}. Signal having value of BER less than 10^{-9} can be transmitted successfully and detected at receiver end. It has been observed that signal received at highest distance without dispersion compensation in good quality is 90 km with an average BER of 10^{-09} in S, C, L, and U-bands; moreover Q-factor is above the threshold value for DWDM system to implement an optical communication link.

The system with NRZ modulation format shows good performance up to 90 km in all spectral bands designated for optical fiber communication, but at the distance of 120 km, the transmission is possible in S, C, and L-bands. Further at the distance

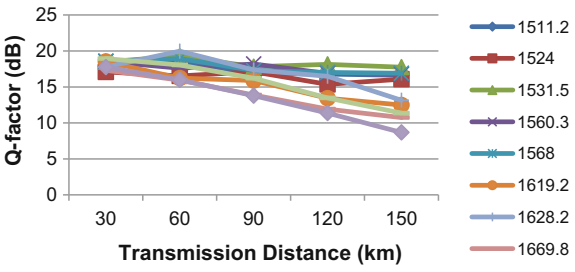


Fig. 2 Q-factor plotted against transmission distance at different wavelengths

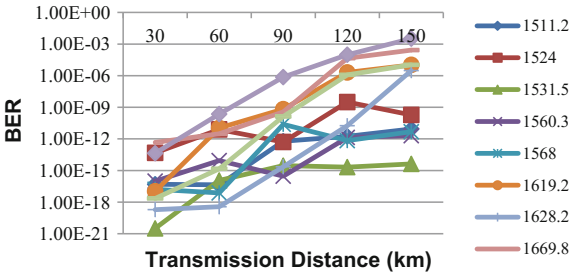


Fig. 3 BER plotted against transmission distance at different wavelengths

of 150 km up to 1565 nm, i.e., in S and C-bands only. At distance of 120 km, BER level is very high, Average BER reported is 10^{-05}. At wavelengths 1619.2, 1669.8, 1677.5 and 1728.8 nm the BER values are 10^{-6}, 10^{-5}, 10^{-6} and 10^{-5} respectively. This shows at 120 km and above for these wavelengths signal cannot be transmitted successfully. Q-factor at which signal can be transmitted successfully is 16 dB (corresponds to BER threshold level 10^{-9}). For NRZ format, Q-factor has been reported at different wavelengths at distance from 30 to 150 km. The average value of Q-Factor is 18 dB, which is above the threshold value, so signal can be received successfully with less distortion. At 60 km, Q-factor starts to decrease and is at value of 17.7 dB which is again above than threshold. At 90 km, the average Q-factor is close to threshold limit, moreover at wavelengths 1669.8, 1677.5 and 1728.8 nm the Q-factor has very low values. Thus signal cannot be transmitted successfully here. This shows that with NRZ format, the signal has good Q-factors up to 60 km, but at 90 km and above distances Q-factor tends to decrease.

Figure 4 shows the eye diagrams for a transmission link of 90 km for different wavelengths. The system behavior was evaluated by vary the length of the fiber from 30 to 150 km. It was reported that the increase in length of the fiber reduces the opening of eye and so Q-factor reduces. So by using 0.2 nm channels spacing the performance observed for DWDM system using NRZ modulation after 90 km transmission was poor. Eye diagrams have been taken to judge whether the eye opening is more than threshold level or below to find out the level of noise. The eye opening in general view should be 50 % to confirm functionality of design according to ITU_T standards. In OptSim Scope shown in schematic layout of proposed optical link with 1024 channels helps in displaying the eye opening diagrams and reports the calculated results for BER and Q-factor.

In Fig. 4a–h, the eye diagram results show that signal transmission is successful up to 90 km because the eye opening percentage is more than 50 % at each wavelength. However, for wavelengths 1677.5 and 1728.8 nm the eye opening is below 50 %. Thus signal cannot be recovered successfully at the receiver end for these frequencies.

Table 3 Performance of optical communication system reported in terms of Q-factor (dB) and BER over the variable distance for different wavelengths in NRZ modulation format

Channel wavelengths (nm)	Q-factor (dB) versus distance (km)					BER versus distance (km)				
	30	60	90	120	150	30	60	90	120	150
1511.2	17.89	18.54	16.89	16.79	16.63	4.92E–17	4.39E–17	6.01E–13	1.73E–12	8.71E–12
1524	17.08	16.53	17.11	15.35	16.08	4.73E–14	7.84E–12	5.11E–13	3.13E–09	1.89E–10
1531.5	18.49	19.28	17.81	18.14	17.75	3.20E–21	1.14E–16	2.89E–15	2.11E–15	4.25E–15
1560.3	18.55	17.61	18.19	16.87	16.76	9.80E–17	8.77E–15	2.89E–16	1.37E–12	2.03E–12
1568	18.57	18.93	17.28	17.01	16.9	1.64E–17	7.46E–18	2.42E–11	6.91E–13	4.77E–12
1619.2	18.53	16.23	15.89	13.43	12.48	1.07E–17	1.09E–11	6.62E–10	2.03E–06	1.06E–05
1628.2	17.78	19.97	17.37	16.48	13.15	1.94E–19	3.63E–19	2.27E–15	1.79E–11	3.04E–06
1669.8	17.31	15.94	13.87	11.92	10.75	4.71E–13	3.03E–12	3.73E–10	4.56E–05	2.68E–04
1677.5	18.94	18.05	16.21	13.47	11.36	2.23E–18	1.46E–15	1.34E–10	1.21E–06	1.07E–05
1728.8	17.76	15.98	13.78	11.37	8.68	4.34E–14	2.27E–10	7.31E–07	9.71E–05	3.28E–03

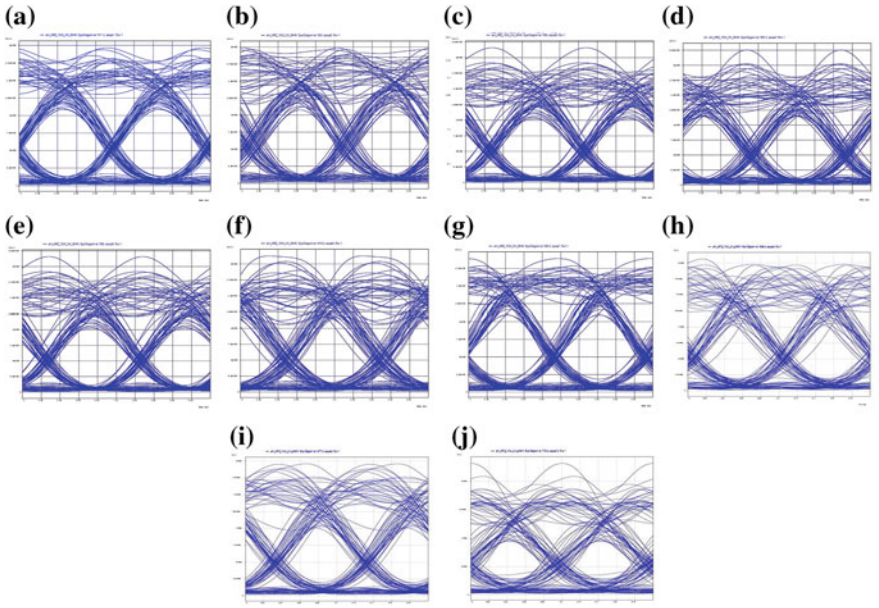


Fig. 4 Eye diagrams for NRZ modulation format at 0.2 nm channel spacing at for **a** 1511.2 nm, **b** 1524 nm, **c** 1531.5 nm, **d** 1560.3 nm, **e** 1568 nm, **f** 1619.2 nm, **g** 1628.2 nm, **h** 1669.8 nm, **i** 1677.5 nm, and **j** 1728.8 nm wavelength of a transmission link of 90 km

4 Conclusion

The performance of DWDM system can be characterized in terms of Q-factor, BER, channel spacing, channel density. In this study we have successfully evaluated 10.24 Tb/s DWDM system using NRZ modulation for 1024 channels with channel spacing of 0.2 nm for short haul (90 km) communication link. The impact of transmission distance on Q-factor, BER and eye diagrams has been reported. It is revealed that signal distortion starts increasing above 90 km. The results revel that at a transmission distance of 120 km communication link is possible in S, C, and L-bands with same simulation setup. At distance of 150 km a link is possible up to 1565 nm i.e., C-band only. Based on the simulation results, NRZ modulation format can be used with 10.24 Tb/s data rate over a common fiber. This provides an efficient way to increase the capacity to support user demands for high volume data information.

References

1. B. Mukherjee: WDM Optical Communication Networks: Progress and Challenges. IEEE Journal on Selected Areas in Communications, Vol. 18, No. 10, October 2000.
2. S. B. Jun, K. J. Park and Y. C. Chung: Transmission of 2.5 Gb/s WDM channel spaced at 5 GHz over 480 k of single fiber. IEEE Photonics Technology Letters, Vol.15, No.9, September 2003.
3. G. Bosco, A. Carena, V. Curri, R. Gaudino, and P. Poggiolini: On the Use of NRZ, RZ, and CSRZ Modulation at 40 Gb/s With Narrow DWDM Channel Spacing. IEEE Journal of Lightwave Technology Vol. 20, No. 9, September 2002.
4. T. Hoshida, O. Vassilieva, K. Yamada, S. Choudhary, R. Pecquer, H. Ksuwahara: Optimal 40 Gb/s modulation formats for spectrally efficient long haul DWDM systems. IEEE Journal of Lightwave Technology, Vol. 20, No. 12, December 2002.
5. R. S. Kaler, T. S. Kamal, A. K. Sharma: Simulation results for DWDM systems with ultra-high capacity. Fiber and Integrated Optics, 21:5, 361–369, Taylor & Francis, 2002.
6. Anu Sheetal, Ajay K. Sharma, R. S. Kaler: Simulation of high capacity 40 Gb/s long haul DWDM system using different modulation formats and dispersion compensation schemes in the presence of Kerr's effect. Optik- Int. J. Light Electron. Opt, 121, 739–749, Elsevier, 2010.
7. Lara D. Garrett, Michael H. Eiselt, Jay M. Wiesenfeld, Marvin R. Young, and Robert W. Tkach: Bidirectional ULH Transmission of 160-Gb/s Full Duplex Capacity Over 5000 km in a Fully Bidirectional Recirculating Loop. IEEE Photonics Technology Letters, Vol. 16, No. 7, August 2004.
8. OptSim Models Reference, RSoft Design Group, 2010.

Validation of ANN-Based Model for Binary Distillation Column

Amit Kumar Singh, H.P. Singh and Sachin Mishra

Abstract An artificial neural network model for Binary Distillation Column (BDC) is presented in this work. The recurrent neural networks have been used for the modeling to represent the nonlinear behavior of distillation process. The data for neural network training has been acquired from continuous BDC setup available in laboratory. The available model contains nine trays. The neural network model is composed of two layers. The activation function chosen for the first layer is a hyperbolic tangent sigmoid function, whereas a pure linear function is utilized as activation functions in the second layer. The validation of developed neural network based model has been done by an extensive data set of real-time data acquired from the BDC set up.

Keywords Binary distillation column · Modeling · Neural network

1 Introduction

Distillation columns are well known chemical processes which are majorly used in different chemical applications, i.e., food industry are concentrating essential oils. The basic schematic of a continuous binary distillation column is shown in Fig. 1.

The control of binary distillation column is discussed in literature. Reflux flow rate and reboiler heat duty are selected as manipulated variables and top and bottom compositions have been selected as controlled variable in most of the literature.

A.K. Singh (✉) · H.P. Singh · Sachin Mishra
Electrical and Electronics Engineering, Amity School of Engineering and Technology, Amity University Uttar Pradesh, Noida 201313, India
e-mail: aksingh20@amity.edu

H.P. Singh
e-mail: hpsingh2@amity.edu

Sachin Mishra
e-mail: smishra8@amity.edu

© Springer Science+Business Media Singapore 2017

R. Singh and S. Choudhury (eds.), *Proceeding of International Conference on Intelligent Communication, Control and Devices*, Advances in Intelligent Systems and Computing 479, DOI 10.1007/978-981-10-1708-7_27

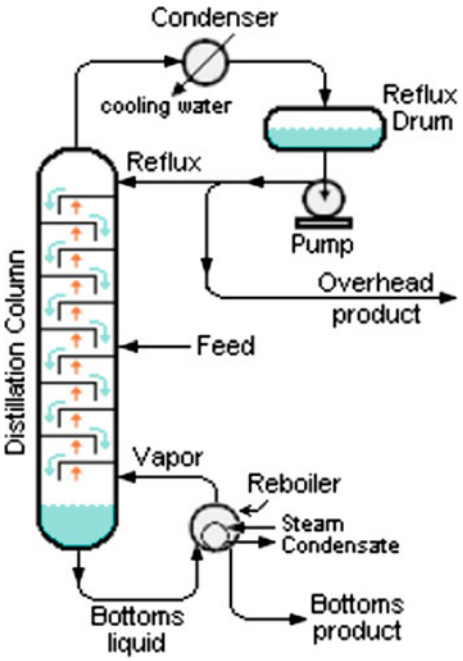


Fig. 1 Schematic of a binary continuous distillation column

Distillation process involved large time delays and nonlinear interaction between outputs and due to these factors distillation process is a difficult problem to control.

Artificial neural networks have been utilized effectively in different modeling and control applications because it is very advantageous than other conventional methods. ANN has adaptive learning capability and has the ability for nonlinear mapping. The applications of neural network to different problems of chemical control have been investigated in the literature. Neural network based control scheme has been compared with internal model control (IMC), global linearization and GMC by Piovoso et al. [1]. Radial basis function NN has been utilized by Seaborg and co-workers for nonlinear simulation and control [2, 3]. Neural network has been utilized in various applications like identification of nonlinear process [4], IMC [2, 5], adaptive control [6, 7]. It is also used in the tuning of conventional proportional–integral–derivative controllers [8]. Backpropagation algorithm is utilized in the adjustment of parameters for the training of neural networks. This trained neural network is used for identification and control of different nonlinear dynamic systems [9]. Bhat et al. discussed the application of multilayer Neural Network in the dynamic modeling and control of various chemical processes [10]. Two approaches have been proposed for modeling and control of nonlinear applications. A learned NN model of the system or plant is utilized in a model-based control in the first perspective, whereas, in the second perspective, an inverse NN-based model of the plant is utilized in the structure of IMC. Willis et al. explained some NN-based approaches in modeling and control applications [11].

Few nonlinear control problems have been solved by utilizing neural network based scheme [12]. A multilayered Neural Network model name emulator has been learned for the identification of the physical characteristics of the system while another multilayered NN has been learned for the emulator control. This trained controller is further utilized to control the real plant. A learning algorithm is developed by Shin and Ikeda [13]. It is concluded in the work [14] that the modular neural network can utilized as a substitute of multilayer FFN, especially for the sharp changing functions. The application of Back propagation algorithm is presented in this work to train the Feed forward neural network for BDC. The results of the developed NN model have been compared with the experimental results of existing BDC setup. The details of lab set up of BDC are discussed in second section. Section 3 discusses the development of the neural network model by the basic back propagation algorithm. In Sect. 4, training process of neural network model of BDC is discussed. Section 5 contains and simulation results. The work has been summarized and concluded in Sect. 6.

2 Lab Setup of BDC

The lab set up of nine-tray continuous binary distillation column unit with one input feed and two product output is utilized in this work. Mixture of different compositions of methanol and water is taken as feed to the column. The BDC contains a vertical column that has nine equally spaced bubble cap trays mounted inside of it. Every tray has one conduit on alternate side, called down comer. Liquid flows through these down comers by gravity from each tray to the one below. Every tray has a weir, which is present on one side of the tray to maintain the liquid level at a suitable height. A reboiler is connected which provides necessary heat for vaporization for distillation column operation. It has three electric heaters of 4, 2 and 2 kW. One condenser is connected to the column through another piping so as to condense the overhead vapors. Water is used as coolant in condenser. Three rota-meters are provided for measuring the liquid flow rate as well as for controlling the liquid flow of feed, the bottom product and the cooling water. A Compressor is provided to develop necessary pressure for circulating the feed. Transducers are interfaced in the BDC to facilitate monitoring and control of various parameters of the column under consideration.

3 Neural Network Model Development

The modeling of the BDC has been carried out with the use of MATLAB® neural network toolbox. The same toolbox is also used for the simulation. Predefined functions provided with the toolbox are utilized as activation functions in ANN modeling. A neural network contains artificial neurons which are operating in

parallel. The network function is defined by utilizing the weights between the neurons. The neural network has been trained to approximate a given function by regulating the weights. The structure of the designed network to model the Distillation Column is shown in Fig. 2. The developed neural network has two Layers, one is input or hidden layer and another is output layer. Number of hidden neurons affects the performance of the training. There is not a definite method to select the total number of hidden layer neurons. The numeral value of neurons in the input layer has been decided by trial and error method. Finally ten hidden neurons have been selected, since on this value the MSE between the trained output and desired target output is minimum. In the two-layer network, a *tansig* function has been chosen as first layer activation function whereas a linear function has been taken in the other layer. Pure linear function in the output layer has been utilized to model most nonlinearities.

These are the input variables of neural network: u_{R}: Reflux flow rate, u_{F}: Feed flow rate, $u_{\mathrm{T_1}}$: First tray temperature, $u_{\mathrm{Q_B}}$: Reboiler duty, $u_{\mathrm{P_T}}$: Reflux drum top pressure and, $u_{\mathrm{P_B}}$: Reboiler bottom pressure. The neural network model output is x_{D}, the output distillate composition. The correlation between s_1, the first layer output, and the input variables is given by (1)

$$\begin{aligned} s_1 = {} & IW\{1,1\}u_{\mathrm{R}} + IW\{1,1\}u_{\mathrm{F}} + IW\{1,1\}u_{\mathrm{T_1}} \\ & + IW\{1,1\}u_{\mathrm{Q_B}} + IW\{1,1\}u_{\mathrm{P_T}} + IW\{1,1\}u_{\mathrm{P_B}} + b\{1\} \end{aligned} \tag{1}$$

where s_1 is the weighted average of the input variables, which is augmented to hyperbolic tangent sigmoid activation function. The output of the hyperbolic tangent sigmoid function is $x_{1,}$ which is given by (2)

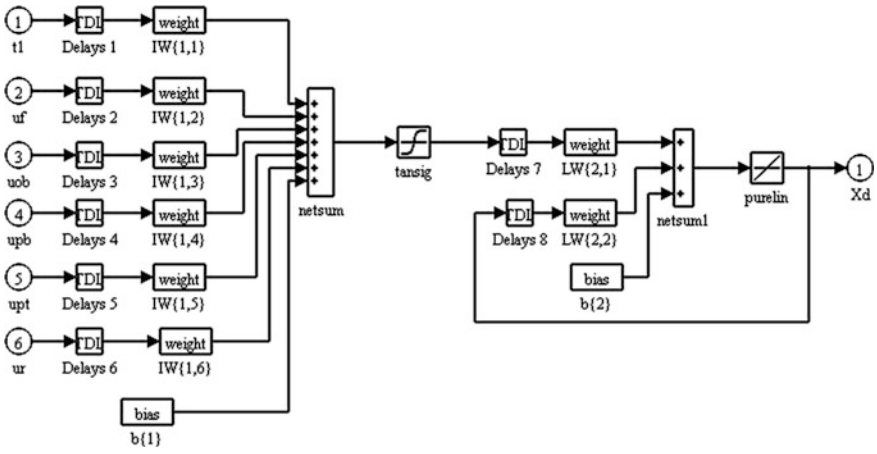


Fig. 2 Neural network model of the binary distillation column

$$x_1 = \tan \text{ sig}(s_1) = \left[\frac{2}{1+e^{-2s_1}} - 1\right] \tag{2}$$

The output of the first layer x_1 is then augmented as an input to the second layer. A *purelin* function has been selected as the activation function of the second layer. s_2 is the weighted sum which is used as input to the second layer of the network as shown by (3)

$$s_2 = LW\{2,1\}x_1 + LW\{2,2\}x_D + b\{2\} \tag{3}$$

where $x_D = purelin(s_2)$. The output x_D is utilized as a feedback signal augmented at the input of the second layer to design the recurrent network. This network helps to achieve the faster convergence rate. The *purelin* function is taken as an activation function in the output layer. Linear function has been chosen as it can distribute the target values.

4 Training for the Neural Network Model

The training and testing data of the neural network model has been acquired from the operation of the experimental set up of BDC existing in laboratory. Input–output data sets with divergent values of $u_{R,}$ $u_{F,}$ u_{T_1}, u_{Q_B}, u_{P_T} and u_{P_B} are used as the training and testing data sets. Each input vector contains 579 data samples. Each input and output variable operating in a range as given below u_R: 0.82–1.41 kmole/h, u_F: 2.5–3.5 kmole/h, u_{T_1}: 80–99 Deg C, u_{Q_B}: 0.019×10^6 (5.5 kW)–0.0241×10^6 kJ/h (7.0 kW), u_{P_T}: 101.42–106 kPa, u_{P_B}: 115.21–120 kPa. x_D: 0.84–0.92 %. Overall, 3447 data samples have been used to train the NN model for the BDC. The Levenberg–Marquardt (LM) based backpropagation algorithm is utilized for training. Training has been done by using the NN toolbox of MATLAB® (MathWorks). The criterion for convergence is set to 10^{-10} % methanol composition for training the model. The training process achieved the optimized value of mean squared error (MSE) as $6.50383e^{-008}$ % in 200 epochs.

5 Simulation Results

5.1 Training Performance

Table 1 shows the gradient value and the MSE of the different architectures of neural network. These two characteristics represent the performance of the model and are used for validation and testing of the developed neural network model.

Table 1 Gradient value and MSE of neural model

Architecture	Gradient	MSE	Architecture	Gradient	MSE
6-6-1	7.08754e-007	5.38178e-007	6-16-1	3.13599e-006	3.86997e-006
6-8-1	4.40621e-006	1.12582e-007	6-17-1	4.64871e-007	3.00008e-006
6-10-1	6.63989e-008	6.50383e-008	6-18-1	1.08061e-005	2.10534e-007
6-12-1	7.74967e-007	2.7823e-007	6-20-1	5.53205e-007	1.52098e-007
6-14-1	1.13615e-007	4.19688e-007	6-22-1	5.63932e-006	6.98418e-006

The numbers of hidden neurons considered are 6 to 22 because the neural network did not converge when the numbers of neurons were taken less than six. Training the network with more than 22 neurons produces the non-convergence.

5.2 *Comparison with Experimental Data*

The data for training, testing and validation of NN has been experimentally acquired from the BDC in laboratory. For modeling of the neural network, neural network toolbox of MATLAB® has been used.

Here 70 % data has been taken for training, 15 % data for testing and 15 % data for validation. From the comparison of neural model output with experimental result as shown in Fig. 3, it is observed that the model output closely followed the real data.

The MSE was $6.50383e^{-008}$ for the estimation of distillate product composition. The results show that the developed neural network was in good agreement with the

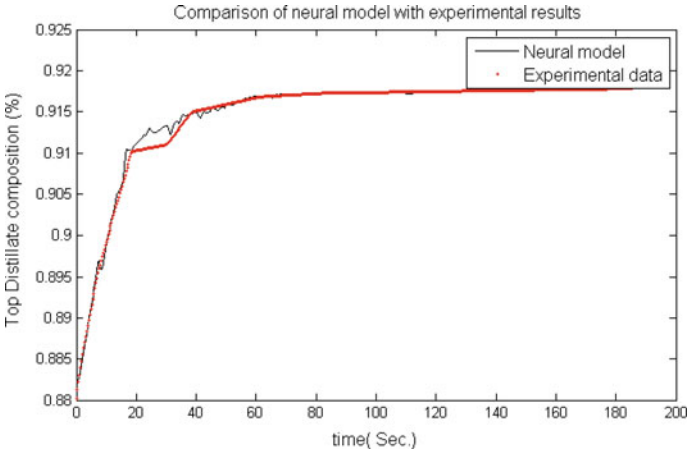


Fig. 3 Validation of NN model with experimental results

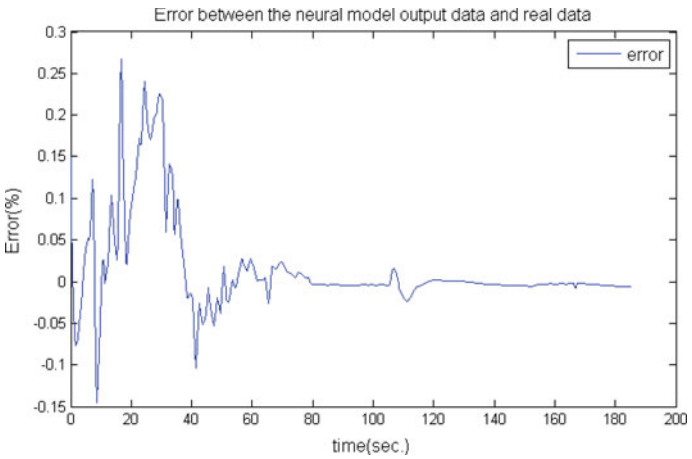


Fig. 4 Error between the NN model output and experimental output of BDC

experimental data. Error between the neural network model output and experimental results of BDC can be seen in Fig. 4. Error is maximum, i.e., 0.25 % in the initial phase of the simulation. It shows that model takes some time to minimize the error between the neural output and target.

6 Conclusion

In this paper, a neural network model of a continuous BDC is developed using recurrent neural networks. The presented two layer recurrent NN model incorporates the nonlinear behavior of BDC. The Training of the neural network has been done by the experimentally acquired real data from the lab setup of continuous BDC. The trained NN outputs distillate composition. The model has been validated with the experimental results. It is found that the ANN modeling for BDC is more suitable than mathematical modeling because of the involvement of the nonlinearities in distillation process.

References

1. Piovoso, M., Kosanovich, K., Rohhlenko, V., and Guez, A. (1992),"A comparison of three nonlinear controller designs applied to a nonadiabatic first-order exothermic reaction in a CSTR," *Proc. Amer. Cont. Conf.*, pp. 490–494.
2. Nehas, E.P., Henson, M.A., and Seborg, D.E. (1992), "Nonlinear internal model control strategy for neural network models," *Comput. and Chem. Eng.*, vol. 16, pp. 1039–1057.
3. Pottmann, M. and Seborg, D. (1992), "A nonlinear predictive control strategy based on radial basis function networks," *Proc. IFAC DYCORD Symposium*, pp. 536–544.

4. Chen, S., Billings, S.A. and Grant, P.M. (1990), "Nonlinear system identification using neural networks," *Int. J. of Control*, vol. 51, pp. 1191–1199.
5. Cutler, C.R. and Ramaker, B.L. (1979), "Dynamic matrix control–a computer control algorithm," *AIChE National Meeting*, Houston, Texas.
6. Boskovic, J.D. and Narendra, K.S. (1995), "Comparison of linear, nonlinear and neural network based adaptive controllers for a class of fed-batch fermentation processes," *Automatica*, vol. 31, pp. 817–840.
7. Etxebarria, V. (1994), "Adaptive control of discrete systems using neural networks," *IEE Proc. Control Theory Appl.*, vol. 141, pp. 209–215.
8. Wang, M. and Li, B.H. (1992), "Design of a neural network based controller for control system," *Proc. of SICICI'92*, pp. 1333–1339.
9. Narendra, K.S. and Parthasarathy, K. (1990), "Identification and control of dynamical systems using neural networks," *IEEE Trans. on Neural Networks*, vol. 1, pp. 1–16.
10. Bhat, N. and McAvoy, T.J. (1990), "Use of neural networks for dynamic modelling and control of chemical process systems," *Comput. and Chem. Eng*., vol. 14, pp. 573–583.
11. Willis, M.J., DiMassimo, C., Montague, G.A., Tham, M.T., and Morris, A.J. (1991), "Artificial neural networks in process engineering," *IEE Proc-D*, vol. 138, pp. 3–11.
12. Nguyen, D.H. and Widrow, B. (1991), "Neural networks for self training control system," *Int. J. Control*, vol. 54, pp. 1439–1451.
13. Ikeda, K., Shin, S., 1996. Boundedness of estimator with an improved back propagation algorithm, in: Proceedings of the IEEE IECON 22nd International Conference on Industrial Electronics, Control and Instrumentation, 5–10 August, vol. 1, pp. 309–314.
14. Fun, M.H., Hagan, M.T., 1996. Levenberg–Marquardt training for modular networks, in: IEEE International Conference on Neural Networks, 3–6 June, vol. 1, pp. 468–473.

A VDVTA-Based Novel Configuration for Realizing Grounded Inductance

Ghanshyam Singh, Dinesh Prasad, Data Ram Bhaskar and Mayank Srivastava

Abstract This paper proposes a new active simulator of grounded inductance using single voltage differencing voltage transconductance amplifier (VDVTA), one grounded capacitor and one grounded resistance. The presented configuration is electronically controllable, exhibits low nonideal effects and has low values of active and passive sensitivity. The working of the presented active inductor simulator is confirmed by employing it in designing of a voltage mode (VM) band-pass biquad filter. The performance of proposed inductor simulator and band-pass filter is demonstrated by SPICE simulations with TSMC CMOS 0.18 μm process parameters.

Keywords VDVTA · Grounded inductor simulator · Electronic control · Low nonideal effect

1 Introduction

Active simulation of inductors has been a popular research in the last three decades as conventional passive spiral inductor has several inherent drawbacks such as large size and weight, generation of unwanted harmonics, picking as well as radiation of

Ghanshyam Singh (✉)
Department of Electronics and Communication Engineering,
HMRITM, Hamidpur, New Delhi, Delhi, India
e-mail: ghanshyamsingh_09@rediffmail.com

Dinesh Prasad · D.R. Bhaskar
Department of Electronics and Communication Engineering,
Jamia Millia Islamia, New Delhi, India
e-mail: dprasad@jmi.ac.in

D.R. Bhaskar
e-mail: dbhaskar@jmi.ac.in

Mayank Srivastava
Department of Electrical, Electronics and Communication Engineering,
The Northcap University, Gurgaon, Haryana, India
e-mail: mayank2780@gmail.com

© Springer Science+Business Media Singapore 2017

R. Singh and S. Choudhury (eds.), *Proceeding of International Conference on Intelligent Communication, Control and Devices*, Advances in Intelligent Systems and Computing 479, DOI 10.1007/978-981-10-1708-7_28

electromagnetic waves and liner relationship between dimension and quality factor. In active inductors a grounded/floating inductor is simulated employing some active element(s) along with capacitor and/or resistor(s).

Several grounded inductance simulator circuits employing different active blocks such as operational amplifiers (Op-amp) [1–4, 6, 9], current conveyors (CC) [5, 7, 8, 10–16, 25, 27–29], current feedback operational amplifiers (CFOA) [17–19, 26], current differencing transconductance amplifiers (CDTA) [20], four terminal floating nullors (FTFN) [21], current feedback transconductance amplifier (CFTA) [22], voltage differencing differential input buffered amplifiers (VDDIBA) [24], operational transresistance amplifiers (OTRA) [30], voltage differencing current conveyors (VDCC) [31], and voltage differencing buffered amplifiers (VDBA) [32] have been proposed in the literature but unfortunately all the mentioned configurations have one or more disadvantageous features given below.

(i) Excessive (more than one) number of the active elements [1, 6, 7, 9, 12, 14–16, 18, 20, 22, 24, 30].
(ii) Excessive (more than one) use of the passive components [1–3, 5, 6, 8–11, 13, 15, 17–19, 21–23, 25–32].
(iii) Use of floating passive component(s) [1–11, 13, 15–19, 21, 25–30, 32].
(iv) Lack of electronic controllability [1–6, 8–11, 13–19, 21, 23, 25–30].
(v) Adverse nonideal effects [9, 12, 14–16, 18, 20–24, 30, 32].

Therefore, the purpose of this communication is to present a novel grounded inductor simulator configuration with following advantageous features: (i) low active and passive elements requirement (only one VDVTA, one capacitor, and one resistor), (ii) employment of all grounded passive components, (iii) electronically controllable inductance, and (iv) low nonideal effects.

The VDVTA is a recently proposed active building block [33] finds application in analog filter designing [34]. Figure 1 shows the symbolic representation VDVTA, where input terminals are *P*, *N,* and *V* along with *Z*, *X*+, and *X*− output terminals. All the terminals of VDVTA are high impedance terminals.

The terminal current voltage relationships of VDVTA are described by following given equations:

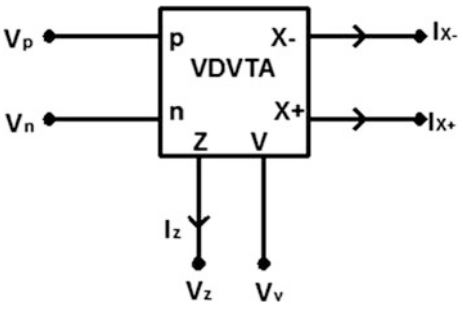


Fig. 1 Symbolic representation of VDVTA

$$I_z = g_{m_1}(V_p - V_n) \tag{1}$$

$$I_{x+} = g_{m_2}(V_z - V_v) \tag{2}$$

$$I_{x-} = -g_{m_2}(V_z - V_v) \tag{3}$$

The CMOS implementation of VDVTA [34] is shown in Fig. 2.

2 Proposed VDVTA-Based Grounded Inductor Simulator

Figure 3 shows the proposed grounded inductance simulation circuit. A straightforward circuit analysis of this configuration gives the input impedance Z_{in} as:

$$Z_{in} = \frac{sC_1}{g_{m_1} g_{m_2}} \tag{4}$$

where

$$g_{m_2} = \frac{1}{R_1} \tag{5}$$

Thus the circuit simulates a lossless grounded inductor with inductance value

$$L_{eq} = \frac{C_1}{g_{m_1} g_{m_2}} \tag{6}$$

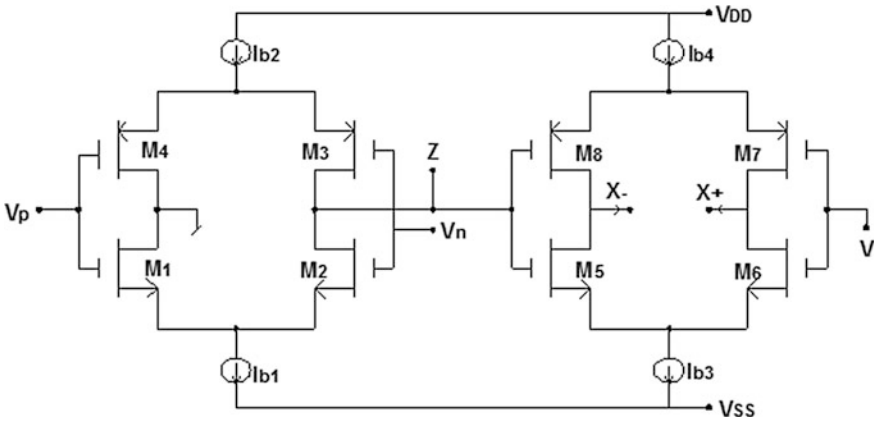


Fig. 2 CMOS implementation of VDVTA [34]

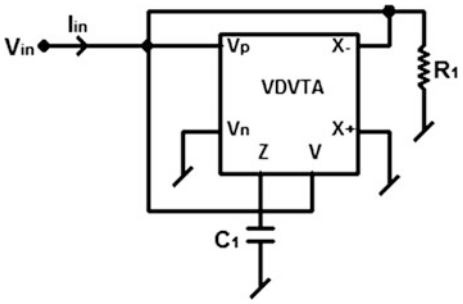


Fig. 3 Proposed VDVTA-based grounded inductor simulator

which is electronically tunable by g_{m1} or g_{m2}. The condition $g_{m_2} = \frac{1}{R_1}$ can be easily achieved in practice by adjusting g_{m2} (by varying the bias currents of VDVTA).

3 Nonideal Analysis and Sensitivity Calculations

Under the influence of VDVTA nonidealities, the defining equations of VDVTA are modified as

$$I_z = \beta_z g_{m_1}(V_p - V_n) \tag{7}$$

$$I_{x+} = \beta_{x+} g_{m_2}(V_z - V_v) \tag{8}$$

$$I_{x-} = -\beta_{x-} g_{m_2}(V_z - V_v) \tag{9}$$

where β_z, β_{x+}, and β_{x-} are the transconductance error gains and there values are very slightly less than unity. The expression of nonideal input impedance of proposed configuration under nonideal conditions is found to be;

$$Z_{\text{in}} = \frac{1}{g_{m_2}(1 - \beta_{x-}) + \frac{g_{m_1} g_{m_2} \beta_z \beta_{x-}}{sC_1}} \tag{10}$$

The nonideal equivalent circuit derived from Eq. (10) is shown in Fig. 4 where

$$R_{\text{eq}} = \text{g}_{\text{m}_2}(1 - \beta_{x-}) \tag{11}$$

and

$$L_{\text{eq}} = \frac{C_1}{\text{g}_{\text{m}_1}\text{g}_{\text{m}_2}\beta_z\beta_{x-}} \tag{12}$$

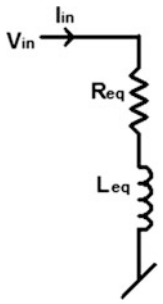


Fig. 4 Nonideal equivalent circuit of proposed inductor simulator

So, it is clear from Fig. 4 that proposed circuit simulates a series *R*–*L* circuit with equivalent resistor (R_{eq}) and equivalent inductor (L_{eq}) values given by Eqs. (11) and (12) respectively. We know that value of β_{x-} is very close to unity. So, from Eq. (11), R_{eq} will be equal to zero. This shows that even in nonideal condition the proposed circuit simulates a pure grounded inductor. Hence, the influence of nonideal conditions is very low. The various active and passive sensitivities of L_{eq} are;

$$S_{g_{m1}}^{L_{eq}} = -1,\ S_{g_{m2}}^{L_{eq}} = -1,\ S_{C_1}^{L_{eq}} = 1,\ S_{R_1}^{L_{eq}} = 0,\ S_{\beta_z}^{L_{eq}} = -1,\ S_{\beta_{x+}}^{L_{eq}} = 0,\ S_{\beta_{x-}}^{L_{eq}} = -1 \quad (13)$$

So, all the sensitivities of L_{eq} are low with their magnitudes not more than unity.

4 Application Example

To verify the working of proposed grounded inductor simulator, it has been employed in the realization of a second-order voltage mode (VM) band-pass filter shown in Fig. 5.

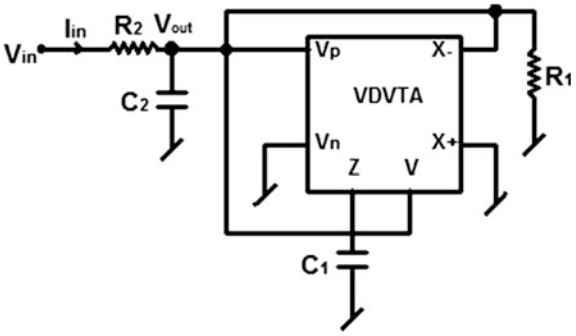


Fig. 5 VM second-order band-pass filter realized by proposed grounded inductor simulator

5 SPICE Simulation Results

The circuit proposed in Fig. 3 is tested by SPICE simulations with TSMC 0.18 μm process parameter model. The simulations were performed employing CMO VDVTA as shown in Fig. 2. The simulated frequency response of proposed inductor simulator is given in Fig. 6. The simulation is performed by selecting following values of passive elements: $C = 0.01$ nF and $R_1 = 1.583$ KΩ. From Fig. 6, it has been observed that up to 10 MHz, the simulated inductance value which is 25.09 μH, remains constant. Hence, the proposed configuration is working like a grounded inductor of value 25.09 μH up to frequency of 10 MHz.

The band-pass filter application circuit shown in Fig. 5 is also simulated with CMOS model of VDVTA and passive element values $C_1 = 0.005$ nF, $C_2 = 0.01$ nF, and $R_1 = R_2 = 1.583$ kΩ. In all the simulations the bias voltage of VDVTA is ±0.9 V D.C with bias currents $I_{B1} = I_{B2} = I_{B3} = 150$ μA. The simulated frequency response of filter given in Fig. 5 is shown in Fig. 7. These results,

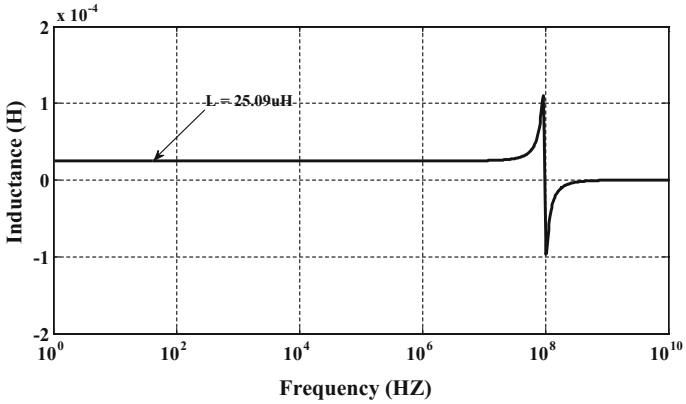


Fig. 6 One frequency response of the simulated grounded inductor

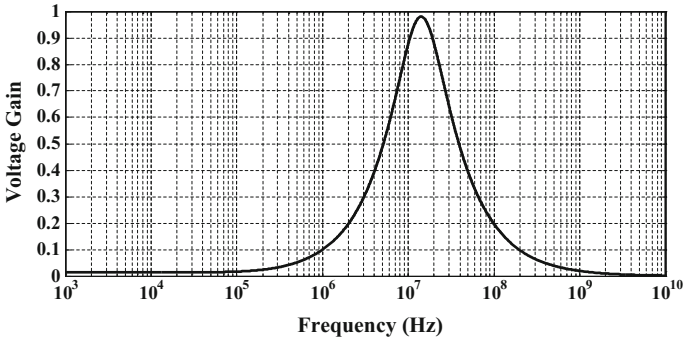


Fig. 7 One band-pass filter realized by the new grounded simulated inductor

thus, confirm the validity of the application of the proposed grounded simulated inductance circuit.

6 Conclusions

A VDVTA-based grounded inductance simulator circuit has been presented, which offers electronic control of inductance and low nonideal effects. To verify the validity of the proposed grounded inductor, a second-order band-pass filter has been realized. The SPICE simulation results confirm the theoretical predictions.

References

1. Ford, R.L., Girling, F.E.J.: Active filters and oscillators using simulated inductance. Electronics Letters, 2(2) (1966), 481–482.
2. Prescott, A.J.: Loss compensated active gyrator using differential input operational amplifier. Electronics Letters, 2(7) (1966), 283–284.
3. Orchard, H.J., Willson, A.N.: New active gyrator circuits. Electronics Letters, 10(13) (1974), 261–262.
4. Dutta Roy, S.C.: On operational amplifier simulation of grounded inductance. Archiv fuer Elektronik und Uebertragungstechnik, 29 (1975), 107–115.
5. Senani, R.: Active simulation of inductors using current conveyors. Electronics Letters, 14 (1978), 483–484.
6. Nandi, R.: Novel insensitive lossless inductor simulation through inverse function generation. Electronics Letters, 16(12) (1980), 481–482.
7. Nandi, R.: Lossless inductor simulation: novel configurations using DVCCS. Electronics Letters, 16(17) (1980), 666–667.
8. Paul, A. N., Patranabis, D.: Active simulation of grounded inductors using a single current conveyor. IEEE Trans. Circuits and Systems, 28(1981), 164–165.
9. Fabre, A.: Gyrator implementation from commercially available trans-impedance operational amplifiers. Electronics Letters, 28(3) (1992), 263–264.
10. Arslan, E., Cam, U., Cicekoglu, O.: Novel lossless grounded inductance simulators employing only a single first generation current conveyor. Frequenz; journal of RF engineering and telecommunications. 57(2003), 204–206.
11. Yuce, E., Minaei, S., Cicekoglu, O.: A novel grounded inductor realization using a minimum number of active and passive components. ETRI Journal, 27(4) (2005), 427–432.
12. Parveen, T., Ahmed, M.T.: Simulation of ideal grounded tunable inductor and its application in high quality multifunctional filter. Microelectronics International Journal, 23(3) (2006), 9–13.
13. Yuce, E., Minaei, S., Cicekoglu, O.: Limitations of the simulated inductors based on a single current conveyor. IEEE Trans. Circuits and Systems, 53(12) (2006), 2860–2867.
14. Psychalinos, C., Spanidou, A.: Current amplifier based grounded and floating inductance simulators. International Journal of Electronics and Communication (AEU), 60(2006), 168–171.
15. Yuce, E.: Grounded Inductor Simulators with Improved Low Frequency Performances. IEEE Trans. Instrumentation and Measurement, 57(5) (2008), 1079–1084.

16. Pal, K., Nigam, M.J.: Novel active impedances using current conveyors. Journal of Active and Passive Electronic Devices, 3(2008), 29–34.
17. Yuce, E., Minaei, S.: A modified CFOA and its applications to simulated inductors, capacitance multipliers, and analog filters. IEEE Trans. Circuits and Systems, 55(1) (2008), 254–263.
18. Yuce, E., Minaei, S.: On the realization of simulated inductors with reduced parasitic impedance effects. Circuits Systems and Signal Processing, 28(2009), 451–465.
19. Yuce, E.: Novel lossless and lossy grounded inductor simulators consisting of a canonical number of components. Analog Integrated Circuits and Signal Processing, 59(1) (2009), 77–82.
20. Prasad, D., Bhaskar, D.R., Singh, A.K.: New grounded and floating simulated inductance circuits using current differencing transconductance amplifiers. Radioengineering, 19(1) (2010), 194–198.
21. Kumar, P., Senani, R.: New grounded simulated inductance circuit using a single PFTFN. Analog Integrated Circuits and Signal Processing, 62(2010), 105–112.
22. Herencsar, N., Koton, J., Vrbra, K.: CFTA-based active-C grounded positive inductance simulator and its application, Elektrorevue, 1(1) (2010), 24–27.
23. Kacar, F.: New lossless inductance simulators realization using a minimum active and passive components. Microelectronics Journal, 41(2–3) (2010), 109–113.
24. Prasad, D., Bhaskar, D. R., Pushkar, K.L.: Realization of new electronically controllable grounded and floating simulated inductance circuits using voltage differencing differential input buffered amplifiers. Active and Passive Electronic Components, (2011), 8 pages.
25. Ibrahim, M.A., Minaei, S., Yuce, E., Herencsar, N., Koton, J.: Lossless grounded inductance simulation using only one modified dual output DDCC. Proc. of the 34thInternational Conference on Telecommunications and Signal Processing (TSP2011), (2011) 261–264.
26. Kacar, F., Kuntman, H.: CFOA-based lossless and lossy inductance simulators, *Radioengineering*, 20(3) (2011), 627–631.
27. Metin, B.: Supplementary inductance simulator topologies employing single DXCCII. *Radioengineering*, 20(3) (2011), 614–618.
28. Myderrizi, I., Minaei, S., Yuce, E.: DXCCII based grounded inductance simulators and filter applications. Microelectronics Journal, 42(9) (2011), 1074–1081.
29. Ibrahim, M.A., Minaei, S., Yuce, E., Herencsar, N., Koton, J.: Lossy/lossless floating/grounded inductance simulator using one DDCC. Radioengineering, 21(1) (2012), 2–10.
30. Gupta, A., Senani, R., Bhaskar, D. R., Singh, A. K.: OTRA-based grounded-FDNR and grounded-inductance simulators and their applications. *Circuits, Systems, and Signal Processing,* 31(2) (2012), 489–499.
31. Kacar. F., Yesil, A., Minaei, S., Kuntman, H.: Positive/negative lossy/lossless grounded inductance simulators employing single VDCC and only two passive elements. International Journal of Electronics and Communication (AEU), 68(1) (2014), 73–78.
32. Yesil. A., Kacar, F., Gurkan, K.: Lossless grounded inductance simulator employing single VDBA and its experimental band-pass filter application. International Journal of Electronics and Communication (AEU), 68(2) (2014), 143–150.
33. Shaktour, M.T.: Unconventional circuit elements for ladder filter design. PhD. Thesis, Brno Univ. Tech.
34. Singh, G., Prasad, D., Bhaskar, D. R.: Single VDVTA-based voltage-mode biquad filter. Circuits and Systems, 6 (2015), 55–59.

In-campus Generator-Substation Monitoring and Control Using LabVIEW

Abhinav Shukla, Abhas, Rajesh Singh and Anita Gehlot

Abstract The various parameters which are used to measure the generators (which are used in substation) are their input power (in KVA-kilo volt amperes), terminal voltage, current, and power factor. Various methods came into existence in order to measure these parameters and some of them are by the use of Heffron–Phillips model, load model, and so on. But here we are using LabVIEW software as DATA LOGGER which will be helpful to monitor these given parameters more effectively and efficiently. Proteus simulation model is also developed to check its accuracy. In order to monitor these parameters, received data will be again transmitted through virtual serial port at 9600 baud rate and it is being received and displayed in the graphical user interface. This system will be easy to use with the help of this software and further studies can also be conducted so as to make it easier to use in the future years.

Keywords LabVIEW software · DATA LOGGER · Virtual serial port · Proteus model

1 Introduction

In the present scenario of automation and control, most of the systems which were mostly running slowly due to analog systems are now digitalized and became more advanced which gives very fast response in the required time interval. Whenever the electrical power is generated in a power plant, then it is being transmitted toward load side by the means of transmission lines. From the main station, the generated voltage is stepped up by the means of step-up transformers (also called power transformers) and then these are propagated over long distance. Now here comes the actual picture, i.e., in a campus there is also a substation and also a

Abhinav Shukla (✉) · Abhas · Rajesh Singh · Anita Gehlot
Electronics, Instrumentation and Control Department,
University of Petroleum and Energy Studies, Dehradun, India
e-mail: shuklaabhinav1011@gmail.com

© Springer Science+Business Media Singapore 2017

R. Singh and S. Choudhury (eds.), *Proceeding of International Conference on Intelligent Communication, Control and Devices*, Advances in Intelligent Systems and Computing 479, DOI 10.1007/978-981-10-1708-7_29

generator which distributes the power in the different parts of the campus depending upon the need. Now, in order control and monitor the various parameters of the generator which is used in the substation are the important part. It is important to know because if any excess voltage which cannot be beard by the load side can be controlled and monitored so that the overall loss can be minimized. Here, in this method of monitoring and control of these parameters, LabVIEW software will be used as a data logger in the receiver side. "Laboratory Virtual Instrument Engineering Workbench" (LabVIEW) is a system design platform and development environment for visual programming language from National Instruments. And also a DATA LOGGER which is a device that stores information time to time through the external world like instruments and sensors.

2 Related Work

Various methods came into existence in order to measure and control these parameters. Some of them are as follows: Karrari and Malik stated that parameters of synchronous generator can be done through online measurement in which a multivariable Linear transfer function was created and was transformed to the parameters of Heffron–Phillips model [1]. Ma et al. stated a load model in the power system simulation and control in which according to their study the constant impedance, current, and power load together forms a composite load model whose parameters were detected through field measurements by using measurement-based modeling practices as a tool but nothing such as a research was conducted and they made a possibility to measure those by the reduction of combination load parameters [2]. Chen et al. mentioned that in order to realize real-time measurement of power angles of generators and bus voltage phasors of substations in various locations for its stability for stability control another method based on GPS can measure the bus voltages and current along with the power angles of generators when they in working conditions [3]. Ranvir et al. proposed an innovative design which was based on a micro controller which measures the required parameters of a distribution transformer and communicates it wirelessly by the means of GSM modem which sends the electrical packet in the form of SMS [4]. Liang et al. designed a kind of monitoring and alarming system which monitors substation based on ZigBee wireless technology in which the system uses GPRS for remote transmission and makes a wireless substation monitoring system which reduces cost and gets constructed [5]. Nasipuri et al. presented a design along with the performance of a wireless sensor network which consists of 45 low-power nodes for sensing temperature and a high power node which performs a more specialized computations, furthermore each and every node communicates over a multi-hop mesh network which uses dynamic link quality-based routing protocol [6]. So, these were the methods which were used till now controlling and monitoring the different parameters used in a generator of the substation. Now, in this paper, these parameters will be controlled and monitored more efficiently by the use of

LabVIEW software as a data logger. The main feature of LabVIEW which is different from other acquisition programs is its highly modular graphical language in which the code is flexible, re-useable, and self-documenting [7].

3 System Description

The monitoring system consists of transmitting side and receiving side. Transmitting side is in the substation side which consists of various types of sensors which usually consists of current sensor, voltage sensor, and power sensor which measures the corresponding values, respectively. Then a controller is used (Arduino) which processes the information and ZigBee is used for its transmission and a 20 × 4 LCD display is also there. And on coming to the receiver side again a ZigBee module along with the controller circuit and a 20 × 4 Display. An additional feature is also added which the Lab view Software which will be used as a data acquisition of the measured parameters in the system. Both the sides have been given a power supply. The system usually consists of a transmitting part and a receiving part. The transmitting part is placed at substation and the receiving part is in the energy block of the campus. In this diagram it is quite clear that the sensors which are named as SENSOR 1, SENSOR 2, and SENSOR 3 are supposed to measure the rated current, voltage and apparent power, respectively. Since the given parameters will give the analog output in the form of sinusoidal wave hence they are interfaced with the analog input pins of Arduino (which is the controller of the transmitting side) and since Arduino has inbuilt ADC which changes analog signal to digital signal And then the controller is further interfaced with the 20 × 4 LCD display which displays the results of output parameters and then further the data packet is transmitted wirelessly by the means of ZigBee module through serial communication. Then coming to receiver side, its received by the ZigBee module and then again fed back as a input for Arduino which displays it in the 20 × 4 LCD display and also seen in lab view software which provides a graphical user interface and controls the substation and studies the characteristics of current and voltages from time to time through data logging (or data acquisition). Current sensing is the important part and mostly functioned on a smart power chip, earlier method to sense current was done by inserting a resistor in their current path but now methods have come up which measures current without any heat dissipation [8]. Similarly voltage between two wires is measured by the means of voltage sensors. Power sensors are also used which measures the rated power which is in Kilo Volt Amperes (KVA) and the output of these sensors is interfaced with the analog input pins of Arduino (controller of the circuit). Arduino is a microcontroller which is easy to use which is platform-independent that its code runs in any of the operating system (e.g., Mac OS, LINUX, and Windows). Then these sensed values are further processed and transmitted serially by the means of ZigBee module and ZigBee mostly uses GPRS for transmitting data [5]. Now, the data packet which is generated is displayed in the 20 × 4 LCD of transmitting side of the system. Then the

data packet is transmitted serially and is received to the receiving part of the ZigBee then it is further send to controller and its being displayed in the LCD of the receiving side of the system. Then now the similar data can be also seen in the LabVIEW software which is used as a data logger (or sometimes it is also called data acquisition). In recent years, LabVIEW is replacing the embedded microprocessor control systems which were used in laboratory though a personal computer [9]. LabVIEW provides User, simple generated control software along with a professional GUI. Now let us see how we can use LabVIEW as a data logger/data acquisition. Data acquisition is an automated process of getting data in the form of voltage/current signal and storing them in the computer for analysis purposes. Here, VISA which refers to Virtual Instrument Software Architecture which provides the programing interface between hardware and developed environments such as LabVIEW. Now in the diagram which is given below is the demonstration of the LabVIEW in which we are doing some of the settings like we choose and control appropriate COM port by clicking on the VISA resource name, then adjusting the Baud rate at 9600, choosing the data bits 8 and placing parity and flow control at none (Figs. 1, 2 and 3).

Let us get interacted with the basic block diagram of data acquisition system. In this diagram we can see that it consists of a transducer (or any sensor say temperature/voltage) which changes it into a voltage signal (an electrical signal)

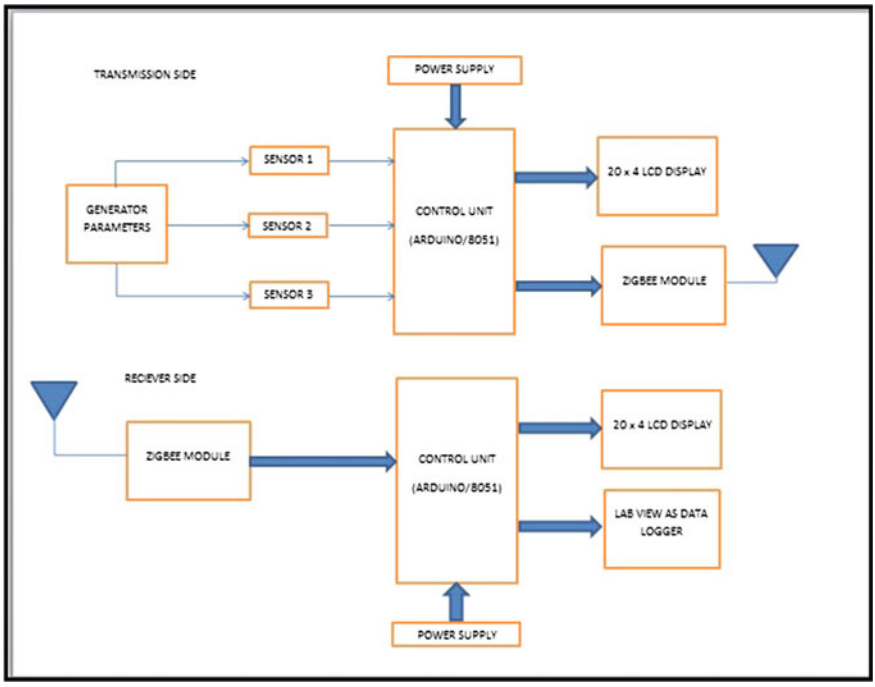


Fig. 1 Block diagram of the system

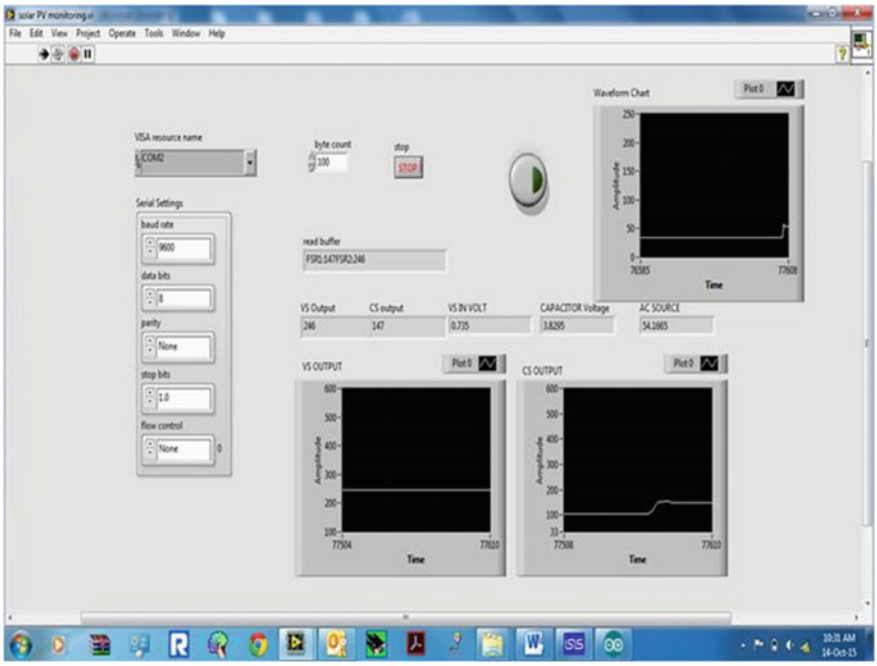
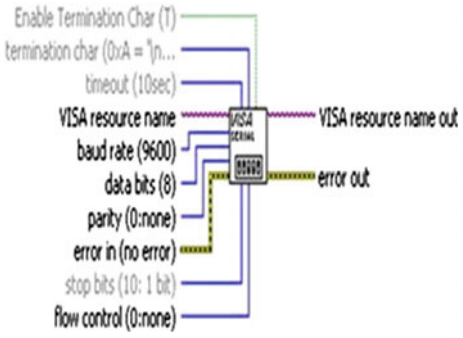


Fig. 2 GUI of LabVIEW

Fig. 3 VISA serial port



which is further amplified through means of signal conditioning (which is for amplification, filtering) and the amplified output is fed again as a input to the DAQ hardware and its interfaced with computer by means of a USB cable and then the output is seen in the computer and further analysis is also done in the received data (Figs. 4, 5 and 6).



Fig. 4 Block diagram of data acquisition system

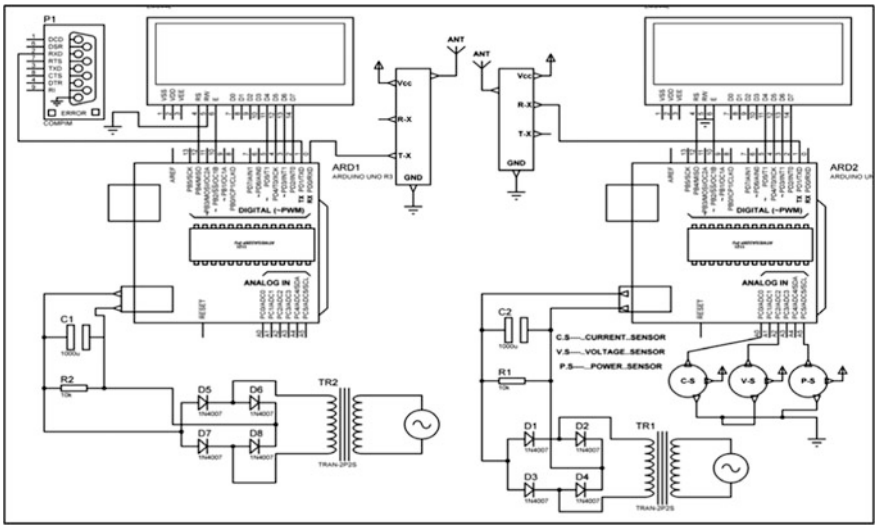


Fig. 5 Circuit diagram of the monitoring system

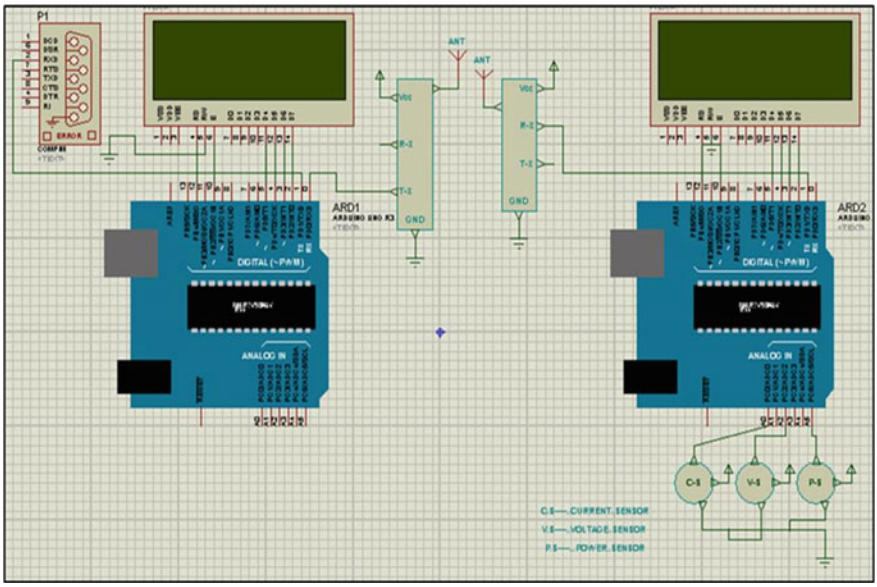


Fig. 6 Proteus model of the system

4 Results and Conclusions

Though previous researchers came up with methods which were useful for the measurement of parameters of the generator and substations, it had some disadvantages like the use of wireless sensor networks will increase the complexity and also becomes difficult to configure and also increase the cost of the hardware. Similarly, other methods also have some disadvantages. Hence, measurement of the various parameters of the generator-substation which is to be monitored and controlled by the using LabVIEW as a DATA LOGGER (or data acquisition) which is more efficient and is easy to use in LabVIEW. As LabVIEW mostly works on VISA serial port and provides a graphical user interface which is more easy to see and configure it and also displays the data more fast and accurately and supports extensively for interfacing with other equipment's like sensors and many more hardware at last we can say that use of LabVIEW is a useful and a perfect method which can be used and further modifications can be so as to reduce future gaps.

References

1. Karrari, M., and O. P. Malik. "Identification of physical parameters of a synchronous generator from online measurements." Energy Conversion, IEEE Transactions on 19.2 (2004): 407–415.
2. Ma, Jin, et al. "Reducing identified parameters of measurement-based composite load model." Power Systems, IEEE Transactions on 23.1 (2008): 76–83.
3. Chen, Yunping, et al. "A new approach to real time measurement of power angles of generators at different locations for stability control." Power Engineering Society Winter Meeting, 2000. IEEE. Vol. 2. IEEE, 2000.
4. Ranvir, Kunal V., et al. "Substation Monitoring System."
5. LIANG, Hu-hui, et al. "ZigBee-based substation monitoring and alarming system [J]." Power System Protection and Control 12 (2010).
6. Nasipuri, Asis, et al. "Wireless sensor network for substation monitoring: Design and deployment." Proceedings of the 6th ACM conference on Embedded network sensor systems. ACM, 2008.
7. Kalkman, Cor J. "LabVIEW: a software system for data acquisition, data analysis, and instrument control." Journal of clinical monitoring 11.1 (1995): 51–58.
8. Forghani-Zadeh, Hassan Pooya, and Gabriel Rincon-Mora. "Current-sensing techniques for DC-DC converters." Circuits and Systems, 2002. MWSCAS-2002. The 2002 45th Midwest Symposium on. Vol. 2. IEEE, 2002.
9. Krauß, A., U. Weimar, and W. Göpel. "LabView™ for sensor data acquisition." TrAC Trends in Analytical Chemistry 18.5 (1999): 312–318.

Performance Analysis of Interleaved Coupled Inductor Boost DC–DC Converter Fed Induction Motor Drive

Vivek Sharma, Ashutosh Bhatt, Nikita Rawat and Shobhit Garg

Abstract This paper provides detailed study of performance parameters of interleaved topology of coupled inductor boost system with induction motor load. This study emphasizes on measurement of harmonic distortions for faults introduced in the system. The faults under consideration are commonly occurring fault in practical established drive system. The simulation results are tabulated.

Keywords Interleaved · Converter · FFT spectrum · Total harmonic distortion (THD)

1 Introduction

DC and AC drives are used in practical scenario of power electronic industries. To obtain variable DC supply choppers are used. If the obtained voltage at output side is higher than supply side it is called term boost converter. Converters are systems used to transform or control electrical energy using the phase control of thyristor. A thyristor in these circuits periodically provides conducting and nonconducting states alternately which are used to control the output voltage or output frequency or both [1–4].

The novel concept of coupling inductor for boost converter operation topology is replacing the disadvantages of conventional boost converter. It can be achieved by varying the number of turns of primary components w.r.t secondary component.

Vivek Sharma (✉) · Ashutosh Bhatt · Nikita Rawat · Shobhit Garg
Department of Electrical Engineering, Graphic Era University, Dehradun, India
e-mail: mail.vivek21@gmail.com

Ashutosh Bhatt
e-mail: ashu.bhattengg@gmail.com

Nikita Rawat
e-mail: nikitarwt8@gmail.com

Shobhit Garg
e-mail: garg8834@gmail.com

© Springer Science+Business Media Singapore 2017

R. Singh and S. Choudhury (eds.), *Proceeding of International Conference on Intelligent Communication, Control and Devices*, Advances in Intelligent Systems and Computing 479, DOI 10.1007/978-981-10-1708-7_30

It also reduces the duty cycle and overcomes the sudden increase in voltage of the converter. The clamp diode is connected in series with the circuit of coupled inductor. Therefore the current, which flows through the clamp diode the leakage inductance current and called as the total current in the circuit [5, 6].

Interleaving the proposed converter enhances efficiency of the system as well as reliability of the system. In turn the size of inductor and capacitor is reduced by interleaving the conventional topology. In this topology cells are connected in parallel. Each converter cell is considered as a phase [7, 8]. In this paper, two coupled inductor boost converter are interleaved ($n = 2$) to achieve higher efficiency and connected to an induction motor through three-phase voltage source inverter (Fig. 1).

2 Simulation Results

2.1 Proposed Circuitry with R-Load

In this case interleaved proposed converter is simulated with linear load to show actual output waveform. In the proposed circuit 60 V DC voltage is given as input. The following simulation circuit produces a boosted output of 150 V. The simulation circuit of proposed system is presented in Fig. 2.

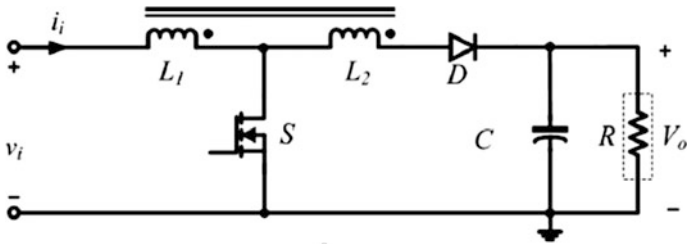


Fig. 1 Diagram of coupled inductor boost converter

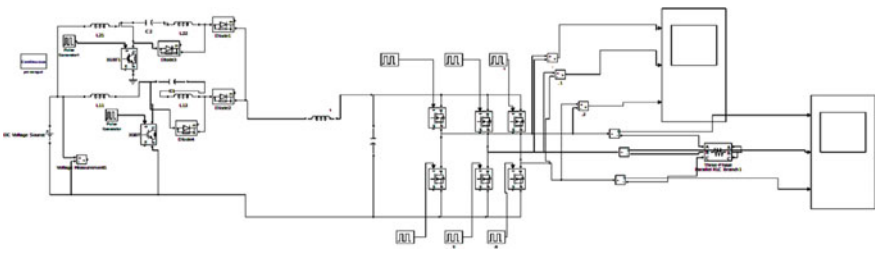


Fig. 2 Simulation circuit of interleaved converter fed R-load

The output current waveform with its FFT spectrum of circuit under consideration converter fed induction motor is given in Fig. 3a, b. The THD measured at 50 Hz is 31.39 % w.r.t. fundamental frequency.

2.2 *Interleaved Coupled Inductor Boost DC–DC Converter Fed Induction Motor*

To study variation of proposed system with practical applications, the proposed circuitry is simulated with induction motor load. Figure 4 presents the circuit diagram of considered circuitry with AC motor load system.

The output current waveform and FFT spectrum are shown in Fig. 5a, b. The harmonic distortion calculated at 50 Hz is 95.60 % for output current waveform.

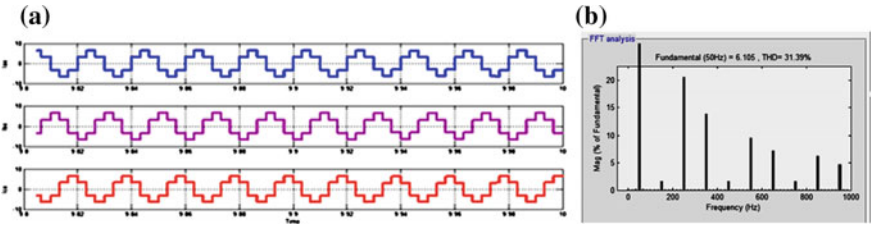


Fig. 3 **a** Output current waveform. **b** FFT spectrum

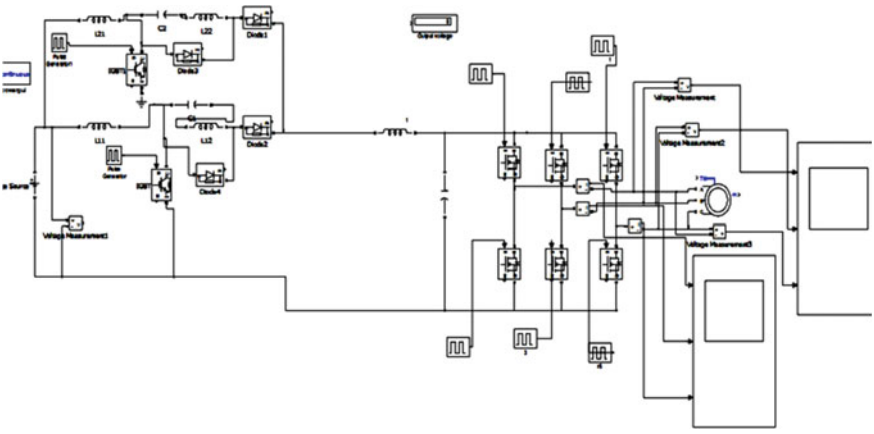


Fig. 4 Simulation circuit of interleaved system fed with induction motor

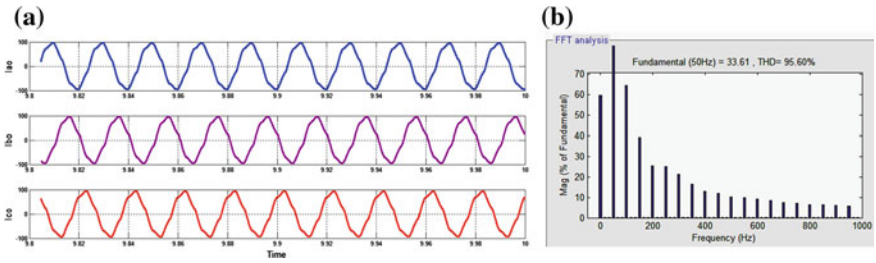


Fig. 5 **a** Output current waveform. **b** FFT spectrum

2.3 *Fault at Phase a MOSFET Gate Terminal*

In this case the novel topology is simulated for absence of gate pulse in phase A MOSFET. In order to achieve this, gate terminal of Phase A MOSFET is provided with grounded pulse. Figure 6 shows simulation circuit for the specified fault condition.

The output current waveform with its FFT spectrum is presented in Fig. 7a, b, respectively. The THD obtained under short circuit fault is 44.21 % for output current waveform for fundamental frequency.

2.4 *Phase a MOSFET Blown off Fault*

To achieve the condition of MOSFET blown off, the particular MOSFET is replaced by high resistance. The current through that MOSFET is very small which in turn results in distortions introduced to the system as shown in Fig. 8.

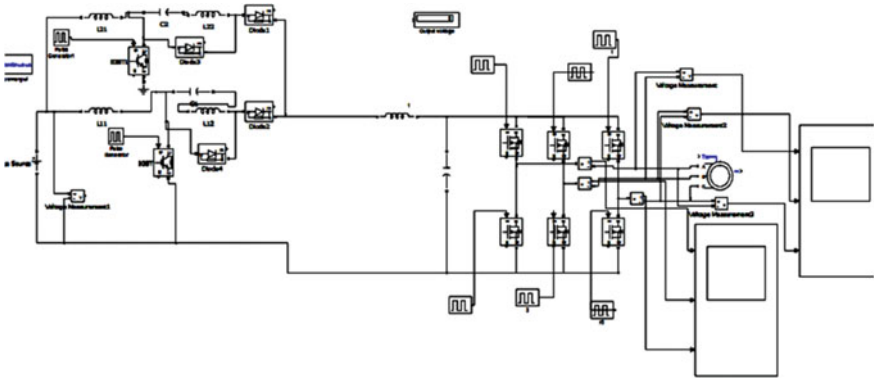


Fig. 6 Simulation circuit of interleaved boost DC–DC converter fed induction motor fault at phase A MOSFET gate terminal

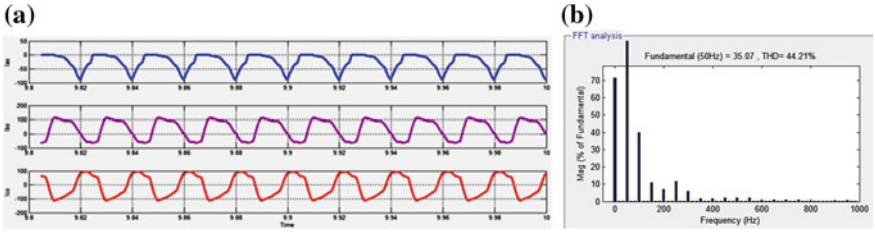


Fig. 7 **a** Output current waveform. **b** FFT spectrum of interleaved boost DC–DC converter fed induction motor with fault at MOSFET gate terminal

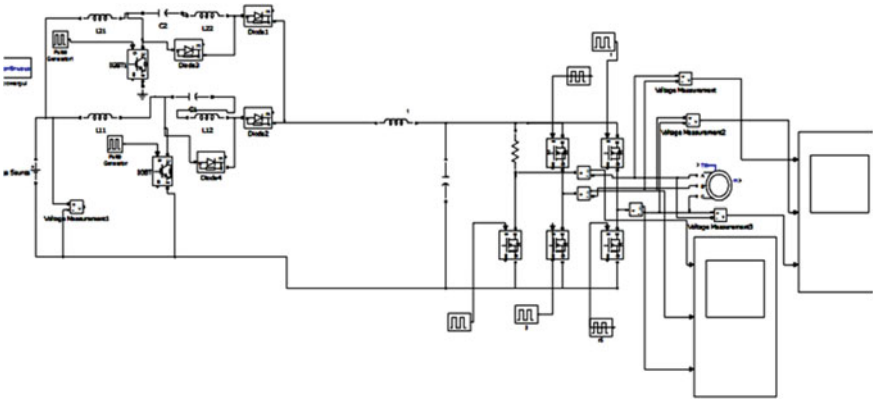


Fig. 8 Simulation circuit of proposed converter fed induction motor with MOSFET blown off fault

Figure 9a gives the output current waveform of interleaved coupled inductor converter fed induction motor under open-circuit fault condition. Its FFT analysis is also shown in Fig. 9b. The THD measured w.r.t fundamental frequency is 96.60 %.

2.5 Line to Ground Fault

Line to ground fault is the most common fault that occurs in drive system at high ratings. To simulate this condition, one of the phases is directly connected to ground. Figure 10 shows simulation circuit for this fault condition.

Figure 11a presents waveform of output current and Fig. 11b shows the Signature spectrum under line to ground fault. The THD measured under line to ground fault at fundamental frequency is 58.10 %. The summary of signature analysis of current for the research work is tabulated in Table 1.

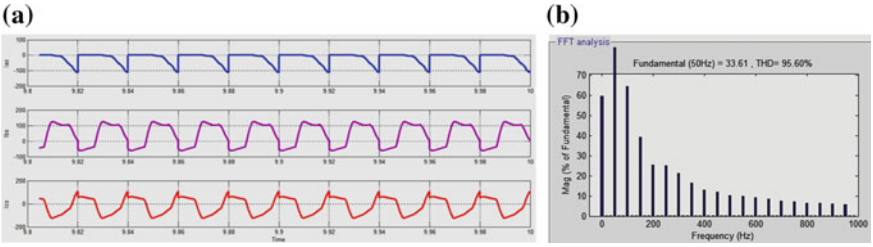


Fig. 9 **a** Output current waveform. **b** FFT spectrum

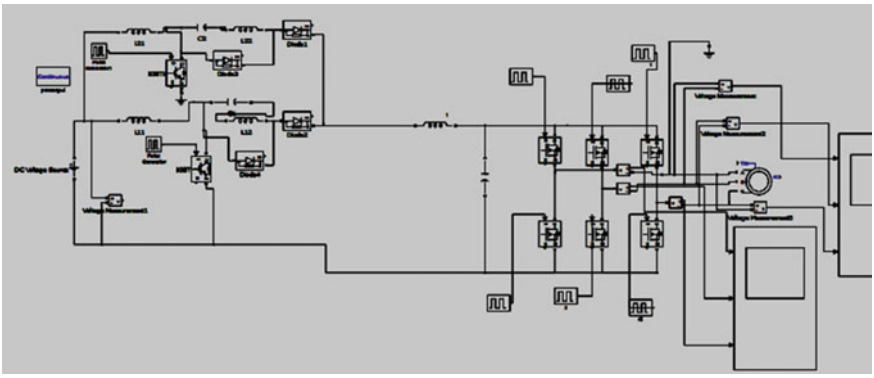


Fig. 10 Simulation circuit of boost DC–DC converter fed induction motor with line to ground fault

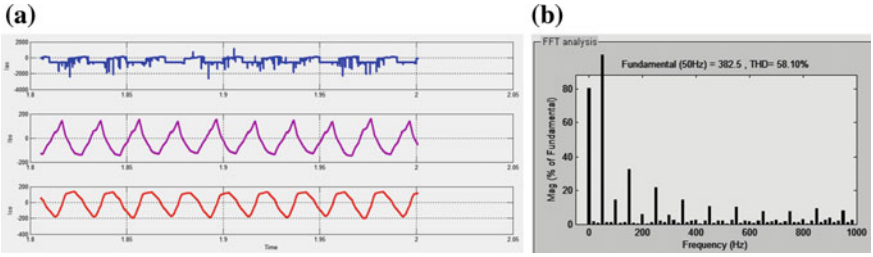


Fig. 11 **a** Output current waveform. **b** FFT spectrum

3 Result and Conclusion

In this paper, harmonic distortions are measured for various commonly occurring faults in practically established drive system. The results of circuit analysis are precisely covered. The comparative studies show that nonlinear system introduces more distortions compared to linear load system. Besides increasing value of load

Table 1 Comparative analysis of fault conditions

Condition	THD (%)	Current (A)
With linear load (R-load)	31.39	10A
Without fault (induction motor drive load)	95.60	100
Fault at MOSFET gate terminal	118.21	−50
MOSFET blown off fault	149.03	−100

current, harmonic currents leads to excessive heating in the induction motor connected with the thyristor system. Torque pulsations are also introduced with introduction of faults. With the above study, line to ground fault proves to be the most harmful fault for the system. The simulation results are tabulated.

The work reported in this paper can be extended for three-phase systems.

References

1. Suman Dwari, Leila Parsa: An efficient high-step-up interleaved DC–DC converter with a common active clamp, IEEE trans. On power electronics, vol.26, no. 1. Jan 2011.
2. Vivek Sharma, Gaurav Mendiratta: Harmonic Analysis of CSI-fed Induction Motor Drive", In Proceedings of the 8th INDIACom 2014 IEEE International Conference on "Computing for Sustainable Global Development", 5th–7th March, 2014.
3. Vivek Sharma, Chiranjeev Panwar: Comparative Analysis Of PV Fed DC–DC Converters, "in proceedings of IEEE International Conference on Green Computing, Communication and Electrical Engineering (ICGCCEE 2014)-Reg, March 2014.
4. Vivek Sharma, Lokesh Yadav: harmonic analysis of PWM full bridge converter," in proceedings of IEEE International Conference on Power, Control and Embedded System (ICPCES-2014) held at MNNIT, Allahabad, India, Dec 2014.
5. Vivek Sharma, Nikita Rawat: Comparison of Interleaved Coupled-Inductor Boost Converter with Conventional DC Converters," in IEEE sponsored 4th International Conference on Computing of Power, Energy & Communication", ICCPEIC 2015, April 2015.
6. Qun Zhao and F.C. Lee: High-efficiency, high step-up DC–DC convertes," IEEE trans. power electron., vol.18, no. 1, pp. 65–73, Jan.2003.
7. N. Mohan, T. M. Undeland, W. P Robbins, Power electronics: converters, applications, and design. New York: wiley, 1995.
8. M. M. Jovanovie and Y. Jang: A new soft-switched boost converter with isolated active snubber, IEEE Trans. Ind. Appl., vol. 35. no. Mar/Apr., PP. 496–502, 1999.

RSSI-Based Indoor Robot Localization System Using LabVIEW

Varchas Choudhry, Rajesh Singh and Anita Gehlot

Abstract Today in twenty-first century, we have totally migrated to highly efficient wireless sensor technology as it offers various advantages over the conventional wired technology. An important task of a wireless sensor network is to capture and forward data to the specified destination. This gives rise to a whole new area of research of localization system and technologies. It is highly imperative to out the location from where the data has been collected. Localization is a process of determining the location of sensor nodes with suitable algorithms. Localization of sensor nodes is an intriguing area of research, and many works have been done till date. Today in this fast evolving world, there is a requirement for developing and designing a low-cost and efficient localization technique for WSNs. In this paper, we discuss localization technique based on the RSSI and real-time data acquisition on LabVIEW (i.e., LabVIEW is used as a data logger). Then, received data gets analyzed using LabVIEW.

Keywords Data logger · LabVIEW · Localization · RSSI

1 Introduction

Today an area which interests researchers and scientists is indoor localization. According to the researchers, indoor localization has proved itself to be a demanding area for research. Wireless networks are deployed to perform indoor localization using a suitable algorithm. Sensor nodes are used to gather and forward data so that a particular task can be performed. Sensor nodes have a property to produce output on encountering some sort of physical change. WSNs have many applications such as security, civil, and environmental applications. Some important applications are Area Monitoring for security purpose. Deployment of such system is done in the area where any irregularity has to be monitored; for example, the

Varchas Choudhry (✉) · Rajesh Singh · Anita Gehlot
University of Petroleum and Energy Studies, Dehradun, India
e-mail: varchas.choudhry@gmail.com

© Springer Science+Business Media Singapore 2017

R. Singh and S. Choudhury (eds.), *Proceeding of International Conference on Intelligent Communication, Control and Devices*, Advances in Intelligent Systems and Computing 479, DOI 10.1007/978-981-10-1708-7_31

position of the intruder is monitored and the information collected is forwarded to security room for further processing. Vehicular movement can also be monitored using same approach. Another application is for Wildlife Monitoring, i.e., movement of animals to observe their habits can be deployed which can help the wildlife researcher about the various parameters associated. Localization system can also be used to track the status of traffic flow and number plates on vehicles and help locating their positions if needed.

1.1 Previous Works

Hara et al. discussed in his paper on the theoretical analysis and computer simulation, which compares the location estimation performances between RSSI-based and TDAO-based methods practically [1]. Awad et al. focused and analyzed the approaches relying on the RSSI, its advantages, and also explores one the most puzzling and essential issues in WSNs [2]. Ahn et al. altercates a typical technique for localizing the stationary object in an office. The method utilizes the RSSI of signals emanating from stationary nodes and tags placed at already known positions [3].

Paul et al. evaluates the feasibility of the same model, which can function over existing Wi-fi networks. Sigma Point Kalman Smoother-(SPKS) based location and tracking algorithm considered as a superior alternative for indoor positioning is proposed [4]. Cheng et al. explained a location estimation method, which includes two steps and is based on received signal strength in WSNs proposed. Further, the least square approach is applied to decide parameters of signal propagation model [5]. Saxena et al. counters the problem by presenting a thorough experimental analysis of RSSI models in WSN, Also, it implements a k-nearest signal space neighbor match algorithm for location estimation [6]. Catovic et al. draws the Cramer Rao-Bound(CRB) for location accuracy estimation for TOA/RSS and TDOA/RSS-based hybrid schemes. The hybrid scheme provides improved accuracy, especially in the proximity of the reference devices for short ranges [7]. Patwari et al. under the Gaussian and Log Normal models given for TOA and RSS in an indoor office environment demonstrates MLE(maximum-likelihood estimator) performance. Relative location estimation algorithms are finally implemented in a wireless sensor network tested and deployed in indoor and outdoor environment [8]. Cheng et al. proposes an efficient indoor localization technology of hybrid RSSI/TDOA which lowers the errors taking place during indoor RSSI localization and costly TDOA localization. Measurement of RSSI is done with iterative recursive weighted average filter, and polynomial model is derived to fitting the RSSI measurement [9]. Luo et al. aims at the assessment of the accuracy of several RSSI-based localization techniques on a live jobsite and does a comparison with results obtained in a target building. RSSI-based localization algorithms are better because of relative low cost and can show high level of accuracy [10]. Pathirana et al. discuss a distinctive scheme for localization of node in a Delay Tolerant Sensor Network (DTN). The scheme uses a robot which performs location

estimation based on RSS for the sensor nodes [11]. Goldoni et al. draws a comparison between some of the most used ranging localization methods based on the Received Signal Strength Indicator (RSSI) in low-power IEEE 802.15.4 wireless sensor networks [12]. Graefenstein et al. discuss that geo-referencing of the sensor information is done by determining the actual position of the radio nodes in a wireless sensor network. Its position is determined by a Real Time Kinematic (RTK) GPS [13]. Zanca et al. observe the performance of some of the best localization algorithms known to us. Other schemes prove to be costly and high energy demanding. RSSI-based scheme is efficient and does not require additional circuitry which reduces the cost [14]. Raghavan et al. give a description of localization of a mobile robot using Bluetooth technology. Innovative approaches were introduced for attaining distance estimates and trilateration that supersede the previously known limitations of using Bluetooth for localization [15]. Whitehouse et al. describe, radio signal strength (RSS) being a noisy signal induces difficulty for the use of ranging-based localization. RSS is used to localize a multi-hop sensor network, and we compute the effects of various environmental factors on the final localization error [16]. Scholl et al. discuss about the geo-referenced RSSI measurements, called fingerprints that are recorded to build for radio-mapping of the building during the offline phase which helps to estimate location of another nodes [17] (Fig. 1).

2 System Description

The above figure exhibits the block diagram of the proposed system. N1 and N2 are the nodes having the capability of motion using simple DC motors. S is the stationary node which is connected to the mobile nodes via Xbee modem and is further connected to a real-time computer system where the data of the RSSI signal is getting recorded. LabVIEW is used as a data acquisition software where the data of RSSI values of different mobile nodes at different instances of time are recorded to

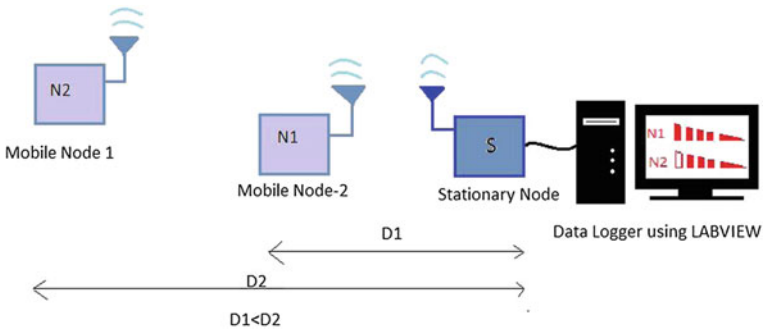


Fig. 1 System description

govern the position and location of each mobile node. In the above diagram D1 and D2 represents the physical distance of the mobile nodes N1 and N2 from the stationary node S respectively. Distance D1 is less than the distance D2, therefore the RSSI value of N1 will be higher than N2 as shown.

2.1 Hardware Description

The prime objective of this paper is analyzing the RSSI values of different nodes to stationary node communicating serially with LabVIEW via COM PORT for further analysis of RSSI values. So, the circuit diagram of the transmitter and receiver nodes has been shown in Fig. 2. Experimentation includes the setup of a stationary node in a room with multiple mobile nodes all around the stationary node and we recorded the RSSI values coming from different nodes and plotted the signal strength versus time graph with the help of the data (RSSI values) provided to LabVIEW via receiver stationary node. The embedded platform used to fabricate the robot localization system is AVR ATMega 32. Atmel's ATMega 32 is an 8-bit low-power microcontroller fabricated using CMOS technology and based on RISC architecture.

Transmitting Node—Transmitting node consists of a microcontroller unit mounted on a robot capable of motion with the help of two simple DC motors. The motors are interfaced to the microcontroller using motor driver IC L293D. 16 × 2

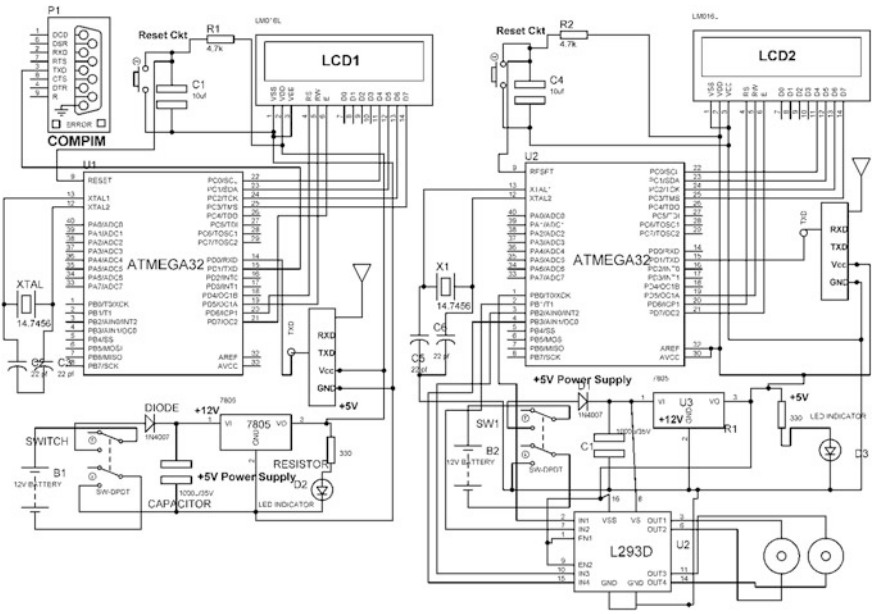


Fig. 2 Circuit diagram of transmitting and receiver modules

alphanumeric LCD is used to show the status of the transmitted data. Xigbee module is used because of its reliability as it adopts collision avoidance. It has advance time slot allocation for communications with fixed bandwidth requirement, so that conflicts between signals are eliminated when transmitting data. Confirmed data transmission is adopted by the MAC (i.e., each data packet sent waits for the confirm signal from the receiver). Receiver Node—It consists of a stationary node capable of receiving the signal from various mobile nodes and it transmits the data to LabVIEW via COMPIN for further analysis and evaluation of the RSSI values. The LCD connected to the stationary node is to represent the status of the signal received from different nodes. A power supply is also connected to provide 5 V Vcc to the microcontroller for its function. The power supply uses 7805 voltage regulator capable of giving a constant +5 V DC.

3 Methodology

Received signal strength indicator (RSSI) is used to measure the received signal strength of a radio signal. Mapping of RSSI according to the values of distance is done after calibration. RSSI value is 8- or 10-bit long generally, extracted from the physical layer, and is used for the issue of Clear to Send (CTS) message. Hardware is responsible for the number of bits used for RSSI. RSSI on the Analog to Digital Converter (ADC) channel 0 is available to the software and it is a 10-bit number. So the conversion from ADC_Counts to RSSI in dBm as given in [6]

$$\begin{aligned} \text{VRSSI} &= \text{Vbattery} \times \text{ADC_COUNTS}/1024. \\ \text{RSSI(dBm)} &= -51.3 \times \text{V(RSSI)} - 49.2. \\ \text{Signal Strength (dBm)} &= \text{y} = 10 \times \log 10(\text{Power(mw)}/1\text{mw}). \end{aligned}$$

Note: Signal quality is not implied as RSSI.

The value V(RSSI) always lies between 0 and 1.2 V and is inversely proportional to the input signal (i.e., higher the voltage in magnitude means lower the input signal). Thus RSSI in dBm is a function of V(RSSI) in Volts which is decreasing in nature. We assume signal propagation in free space and have the following expression for power per square meter.

Considering concentric spheres has radius R which increases around the antenna. Total power which emanates through the sphere remains constant, but the surface area increases as $R2$. So, absolute power in milliWatts will be proportional to $C/R2$ and that in dBm is defined as the variable y as

$$\begin{aligned} y &= 10 \times \log 10(C/R2) \\ y &= 10 \log 10\, C - 20 \log 10\, R2 \\ y &= (-51.3 \times \text{VRSSI}) - 49.2 \end{aligned}$$

where

$$K = (10 \log 10\, K + 51.3(\text{Vbattery} \times \text{ADC COUNTS}/1024) + 49.2)/2.$$
$$(\text{putting } R = 10\, K)$$

In the above equations,

V(RSSI) = RSSI Voltage measured from RSSI/IF pin of CC1000 chip, at the ADC of the μ controller.
Vbattery = Mote Battery Voltage.
ADC COUNTS = 10 bit ADC count of the μ controller.
C = Constant (Environment dependent).
R = Transmission Distance.

4 Software Development

The softwares used for developing both transmitter and receiver module are WinAVR compiler, AVR Studio, Proteus simulator, LabVIEW, and Virtual Serial Port. The programming language used to develop the program is C and the code is compiled using AVR-gcc which is an open source compiler.

LabVIEW: LabVIEW software consists of the two panels—front Panel and back panel. The programmed code has the VISA resource and VISA Read unit with defined data bits, baud rate, parity, stop bits, flow control parameters. The communication between the real-time hardware and the LabVIEW model is through serial virtual port (Figs. 3 and 4).

VISA stands for Virtual Instrument Software Architecture provides the programming interface between the real-time hardware and LabVIEW, Visa Configure Serial port is used to initialize the serial port the settings specified in Fig. 5.

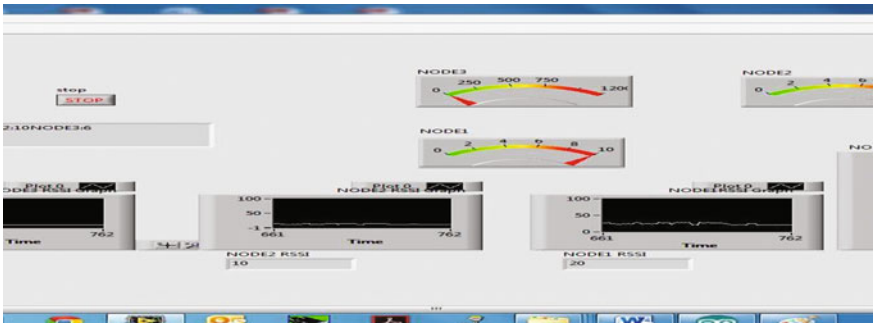


Fig. 3 LabVIEW front panel programing

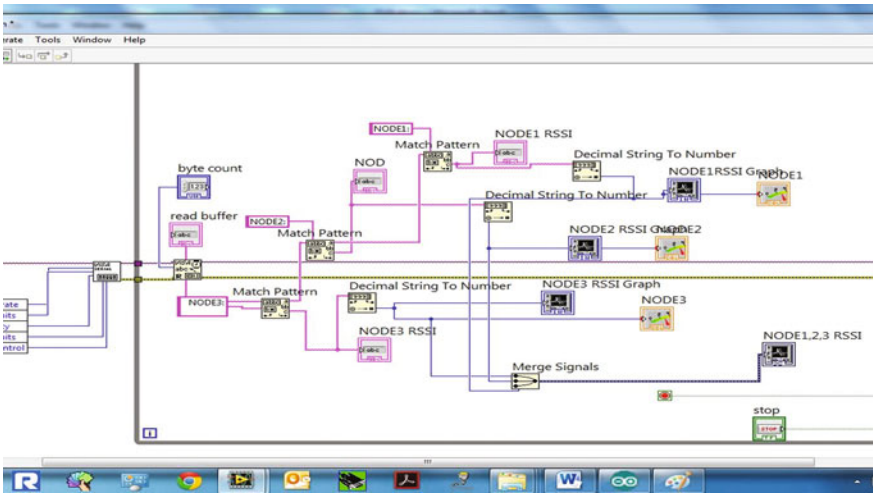


Fig. 4 LabVIEW back panel programing

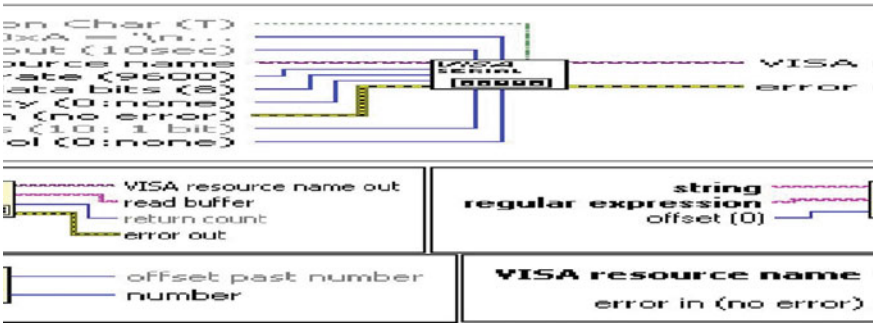


Fig. 5 LabVIEW programing blocks

VISA serial Read is used to read the already specified byte length from the device defined by VISA resource name and returns the data which gets stored in read buffer. At last VISA Close is used to Close a device session defined by VISA resource name.

Another software used is VSPE which is a useful software used to test/create/debug applications that use serial ports. It has the capability of creating various virtual devices capable of transmitting and receiving data. With the help of VSPE serial port, data for several applications can be shared, serial port to local network (via TCP protocol) can be exposed, virtual serial port device pairs can be created (Fig. 6).

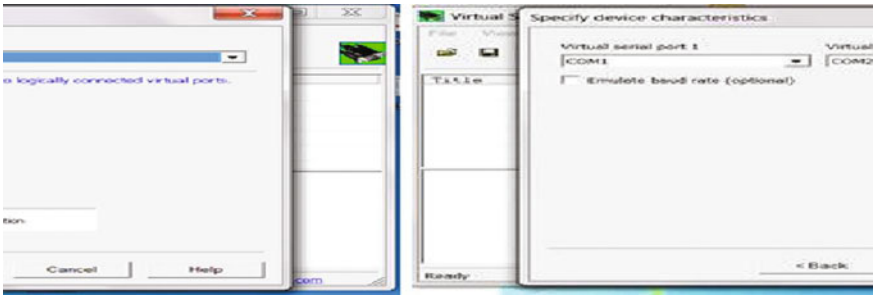


Fig. 6 Virtual serial port configuration

5 Results and Discussion

In this section, analysis of the results is discussed which we gathered during real-time experimentation of the proposed model. The experimentation for the proposed model was done in an indoor environment with four mobile nodes and one stationary node which is connected to a real-time computer for data collection. Every node has an Xbee modem and the stationary node receives different RSSI values from different mobile nodes according to the distance from the stationary node (Figs. 7 and 8).

XCTU is used in the following system as it is a free multi-platform software which provides a simple graphical user interface (GUI) to allow interaction with RF and Xbee modules. In the software, the PAN ID for the Xbee module stationed on the stationary node is set to 21. Similarly, the PAN ID for the Xbee modules on the mobile nodes is set to 21 (i.e., the PAN ID should be same for the transmitter and receiver). Along with the PAN ID, the software JN (join network) is enabled,

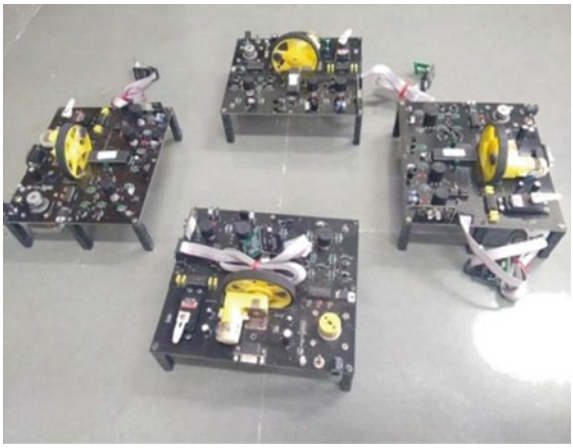


Fig. 7 Real hardware prototype for the system

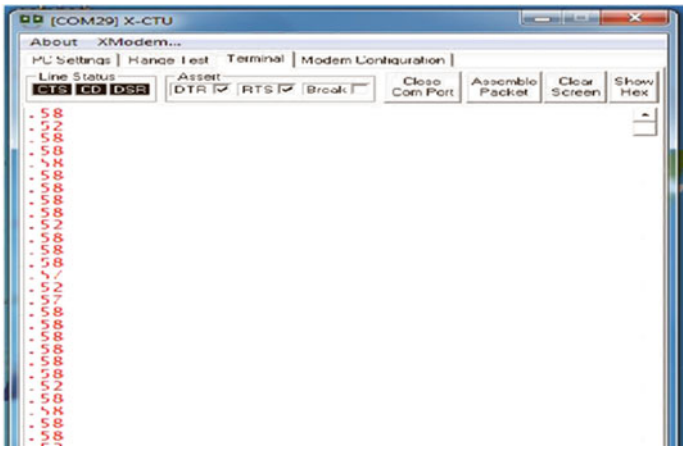


Fig. 8 RSSI values on XCTU terminal

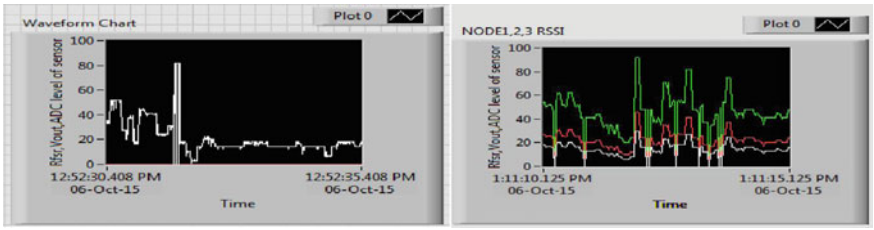


Fig. 9 Shows graph-1: the strength of signal received by stationary node connected to the computer vs time. In graph-2 three different nodes are used and the received signal strength vs time graph is plotted

D3-I/O setting 2 is set to ADC and IR-I/O sampling is fixed to 64 to facilitate connection between the stationary and mobile nodes (Fig. 9).

From all the above tools and softwares we developed an effective indoor robot localization system to find the location or the position of node moving in an indoor environment. This proposed model has further application in wildlife monitoring, area monitoring, traffic control system, and many more. The wireless node which is capable of motion when moves an instant change in RSSI value of that particular node changes accordingly which can be seen of the real time computer system which is recording the data continuously.

6 Conclusion

In this paper, our main objective is to demonstrate the capabilities of the RSSI-based Indoor Localization technique. RSSI-based localization system proves itself to be effective, efficient, and cost-effective alternatives to the already existing schemes for localization. The proposed model works effectively for the indoor environments and the accuracy can be increased to great extents by just increasing the number of stationary node. The data collected by larger number of stationary nodes can be analyzed using a suitable algorithm and mapping of exact position of the mobile robots can be done.

References

1. Hara, Shinsuke, and Daisuke Anzai. "Experimental performance comparison of RSSI-and TDOA-based location estimation methods." Vehicular Technology Conference, 2008. VTC Spring 2008. IEEE. IEEE, 2008.
2. Awad, Abdalkarim, Thorsten Frunzke, and Falko Dressler. "Adaptive distance estimation and localization in WSN using RSSI measures." Digital System Design Architectures, Methods and Tools, 2007. DSD 2007. 10th Euromicro Conference on. IEEE, 2007.
3. Ahn, Hyo-Sung, and Wonpil Yu. "Environmental-adaptive RSSI-based indoor localization." Automation Science and Engineering, IEEE Transactions on 6.4 (2009): 626–633.
4. Paul, Anindya S., and Eric Wan. "RSSI-based indoor localization and tracking using sigma-point Kalman smoothers." Selected Topics in Signal Processing, IEEE Journal of 3.5 (2009): 860–873.
5. Cheng, Yu-Yi, and Yi-Yuan Lin. "A new received signal strength based location estimation scheme for wireless sensor network." Consumer Electronics, IEEE Transactions on 55.3 (2009): 1295–1299.
6. Saxena, Mohit, Puneet Gupta, and Bijendra Nath Jain. "Experimental analysis of RSSI-based location estimation in wireless sensor networks."Communication Systems Software and Middleware and Workshops, 2008. COMSWARE 2008. 3rd International Conference on. IEEE, 2008.
7. Catovic, Amer, and Zafer Sahinoglu. "The Cramer-Rao bounds of hybrid TOA/RSS and TDOA/RSS location estimation schemes." IEEE Communications Letters 8.10 (2004): 626–628.
8. Patwari, Neal, et al. "Relative location estimation in wireless sensor networks."Signal Processing, IEEE Transactions on 51.8 (2003): 2137–2148.
9. Cheng, Long, Cheng-Dong Wu, and Yun-Zhou Zhang. "Indoor robot localization based on wireless sensor networks." Consumer Electronics, IEEE Transactions on 57.3 (2011): 1099–1104.
10. Luo, Xiaowei, William J. O'Brien, and Christine L. Julien. "Comparative evaluation of Received Signal-Strength Index (RSSI) based indoor localization techniques for construction jobsites." Advanced Engineering Informatics 25.2 (2011): 355–363.
11. Pathirana, Pubudu N., et al. "Node localization using mobile robots in delay-tolerant sensor networks." Mobile Computing, IEEE Transactions on 4.3 (2005): 285–296.
12. Goldoni, Emanuele, et al. "Experimental analysis of RSSI-based indoor localization with IEEE 802.15. 4." Wireless Conference (EW), 2010 European. IEEE, 2010.

13. Graefenstein, Juergen, et al. “Wireless node localization based on RSSI using a rotating antenna on a mobile robot.” Positioning, Navigation and Communication, 2009. WPNC 2009. 6th Workshop on. IEEE, 2009.
14. Zanca, Giovanni, et al. “Experimental comparison of RSSI-based localization algorithms for indoor wireless sensor networks.” Proceedings of the workshop on Real-world wireless sensor networks. ACM, 2008.
15. Raghavan, Aswin N., et al. “Accurate mobile robot localization in indoor environments using bluetooth.” Robotics and Automation (ICRA), 2010 IEEE International Conference on. IEEE, 2010.
16. Whitehouse, Kamin, Chris Karlof, and David Culler. “A practical evaluation of radio signal strength for ranging-based localization.” ACM SIGMOBILE Mobile Computing and Communications Review 11.1 (2007): 41–52.
17. Scholl, Philipp M., et al. “Fast indoor radio-map building for RSSI-based localization systems.” Networked Sensing Systems (INSS), 2012 Ninth International Conference on. IEEE, 2012.

Performance Estimation of WDM Radio-over-Fiber Links Under the Influence of SRS Induced Crosstalk

Abhimanyu Nain, Suresh Kumar and Shelly Singla

Abstract Stimulated Raman Scattering-(SRS) induced crosstalk is one of the sources of attenuation in optical fiber link. This paper focuses on the impact of modulation index on the SRS-induced crosstalk. The SRS-induced crosstalk has been reported against modulation frequency, optical power, and transmission length at varied modulation indexes. It is observed that there is significant effect of modulation index on the SRS-induced crosstalk. As the modulation index is increased from 0.3 to 0.9, the crosstalk levels are enhanced by 5 dB approx. It is also revealed that, when modulation frequency is increased, the crosstalk is decreased. Crosstalk increases with increasing optical power and minor increase in the crosstalk levels with increasing transmission length.

Keywords Radio over Fiber (RoF) · Wavelength Division Multiplexed (WDM) · Stimulated Raman Scattering (SRS) · Modulation index

1 Introduction

The wireless mobile communication has grown exponentially in the past few years. Optical fiber has been the key to this extraordinary growth. Radio-over-Fiber (RoF) technique has been the front runner to provide better wireless mobile services to the last mile as it offers a competent distribution and access network. It has plentiful advantages such as a centralized master station, small remote antenna units

Abhimanyu Nain (✉)
GJUS&T, Hisar, India
e-mail: nainabhi@gmail.com

Suresh Kumar
UIET, MDU, Rohtak, India

Shelly Singla
IIET, Jind, India

© Springer Science+Business Media Singapore 2017

R. Singh and S. Choudhury (eds.), *Proceeding of International Conference on Intelligent Communication, Control and Devices*, Advances in Intelligent Systems and Computing 479, DOI 10.1007/978-981-10-1708-7_32

which are connected to master station through optical fiber cable. Remote and dynamic frequency channel allocation schemes at master station which makes remote antenna units simple and effortless [1, 2]. RoF finds its application in diverse domains as millimeter waves and microwaves can be easily distributed through optical fiber over large distances. Wavelength Division Multiplexed (WDM) system can be brought to work in realizing full bandwidth of the fiber. But WDM system suffers from different kind of impairments such as dispersion, nonlinear effects including Stimulated Raman Scattering (SRS), Cross Phase Modulation (XPM), and Four Wave Mixing (FWM), etc.

The Raman gain which is constructive for designing fiber amplifiers can also prove lethal for WDM systems. The reason is that a high-frequency channel can act as a pump for lower frequency channels and thus transfer part of the pulse energy to neighboring channels. It leads to a crosstalk among channels which adversely affects the system performance [3]. This crosstalk is known as Raman-induced crosstalk. Intermediate frequency channels transfer energy to lower frequency channels and receive energy from higher frequency channels as well. Higher frequency channels are the most affected from Raman-induced crosstalk as energy is transferred to all the channels. This phenomenon results in a tilt in the spectral power distribution of the various channels and induces channel-to-channel crosstalk with a power penalty in the higher frequency channels [4, 5].

SRS induced crosstalk is governed by various factors like optical power, walk-off parameter, Raman gain coefficient, modulation index, etc. Jiang et al. [6] studied the relative intensity noise induced due to SRS effects. Yamamoto et al. [7] investigated the power penalty and power impairments caused by the SRS effect. Cantono et al. [8] developed the theory of Pump-to-Probe interaction caused by the SRS effect. In this paper, the effect of modulation index on the SRS-induced crosstalk is studied when modulation frequency, transmission length, and optical power is varied over a range. Theoretical modeling section describes the mathematical modeling for the crosstalk. Results section projects the impact of modulation index on the crosstalk. Graphical results are obtained through MATLAB platform in this section. Finally remarks are presented in the conclusion section.

2 Theoretical Modeling

The theoretical modeling is presented here explaining SRS-induced crosstalk for a 2-channel WDM system.

When two optical waves with same polarization are put together in a single mode fiber, then optical power at the output of fiber can be written as

$$Y_k = Y_c(1 + m \cdot x(t)) \tag{1}$$

where $k = 1(\lambda_1), 2(\lambda_2)$

and $\lambda_1 > \lambda_2$; Y_c is the average optical power; m is the modulation index and $x(t)$ is the modulating signal which is proportional to $\cos \omega t$ and ω is subcarrier angular frequency.

The SRS interaction for a 2-channel WDM system can be described through following equations [9, 10]:

$$\frac{\partial Y_1}{\partial z} + \frac{1}{V_{g1}}\frac{\partial Y_1}{\partial t} = (gY_2 - \alpha)Y_1 \tag{2}$$

$$\frac{\partial Y_2}{\partial z} + \frac{1}{V_{g2}}\frac{\partial Y_2}{\partial t} = (-gY_1 - \alpha)Y_2 \tag{3}$$

V_{gk} is group velocity for transmitted signal at λ_k, α is fiber loss coefficient.

$g = \frac{F_r}{A_{\text{ef}}}$; Raman gain coefficient divided by fiber effective area. Solving for Eqs. (2) and (3), Eq. (2) can be written as

$$Y_1(z, \tau_2) = Y_1(0, \tau_2)\mathrm{e}^{-\alpha z} \tag{4}$$

By putting the value from Eq. (4) into Eq. (3), we get

$$Y_2(z, \tau_2) = Y_2(0, \tau_2)\mathrm{e}^{-\alpha z} \cdot \mathrm{e}^{\left(-g\int_0^z Y_1(0, \tau_2 + d_{21})\mathrm{e}^{-\alpha z}\mathrm{d}z\right)} \tag{5}$$

Here $d_{21} = \frac{1}{V_{g2}} - \frac{1}{V_{g1}}$ is walk-off parameter and $\tau_2 = t - \frac{z}{V_{g2}}$.

Expanding the exponential in (5) and considering $Y_2(0, \tau_2)$ an unmodulated wave, the equation can be simplified to

$$Y_2(z, \tau_2) = Y_c\mathrm{e}^{-\alpha z}.\left[1 - gY_c\left(\frac{\mathrm{e}^{-\alpha L} - 1}{\alpha}\right) - mgY_c\int_0^L \mathrm{e}^{-\alpha z}\cos(\omega\tau_2 + \omega d_{21} z)\mathrm{d}z\right] \tag{6}$$

The third term in the bracket represents the crosstalk; second term in the bracket denotes interaction between optical carriers. Working for the crosstalk term only and solving the integral crosstalk effect at the second wavelength can be expressed as [10]

$$\mathrm{CT}_{\text{SRS}} = mg\,P_c\left[\frac{\mathrm{e}^{(-\alpha + i\omega d_{jk})L} - 1}{(\alpha - i\omega d_{jk})}\right] \tag{7}$$

3 Results and Discussions

The results for SRS-induced crosstalk against modulation frequency, optical power, and transmission length at varied modulation index are discussed here. The observations are made while considering the following values of different parameters. Equation (7) is exploited on MATLAB platform to obtain the results (Table 1).

Figure 1a shows the behavior of SRS-induced crosstalk against modulation frequency when modulation index is varied at different values. Modulation frequency is taken over a range of 0 to 2 GHz. Transmission length is fixed at 25 km and optical power is kept at 5 mW. It shows that the crosstalk decreases from −84 to −97 dB, −82 to −95 dB, −81 to −93 dB, and −79.5 to −92 dB when modulation index is kept fixed at 0.3, 0.5, 0.7, and 0.9, respectively.

Variation in the crosstalk when optical power is swept over a range of 2 to 6 mW is depicted in Fig. 1b. In this case modulation frequency is 1 GHz and transmission distance is 25 km. From the graph we observe that the crosstalk increases from −101 to −93 dB, −98.5 to 91 dB, −97 to −89.5 dB, and −96 to −88.5 dB when modulation index is 0.3, 0.5, 0.7, and 0.9 respectively.

Figure 2a indicates the SRS-induced crosstalk versus transmission length at varied modulation index. The transmission length is considered over the range of 10 to 50 km. The optical power is kept 5 mW and modulation frequency is 1 GHz. It is viewed that the changes in the crosstalk are minor over the transmission distance for a fixed modulation index value. Crosstalk increases by a value of 0.1 to 0.2 dB when we move from 10 to 50 km for each value of modulation index.

From Fig. 2b, it is observed that the SRS-induced crosstalk increases as the modulation index is increased from 0.3 to 0.9. When the modulation frequency is varied from 0 to 2 GHz, the maximum crosstalk levels are −84 and −79.5 dB at the modulation index values of 0.3 and 0.9, respectively. Similar trend is revealed when investigation is done against optical power. In this case, the maximum crosstalk levels are −93 and −88 dB at the modulation index values of 0.3 and 0.9, respectively. Though changes with respect to the transmission length are minor, but the similar pattern is indicated here also. The crosstalk increases as the modulation

Table 1 Various parameters values

Parameter	Value
Pump wavelength (λ_1)	1546 nm
Probe wavelength (λ_2)	1542 nm
Optical power (P_c)	0.02–0.06 W
Modulation frequency	0–2 GHz
Modulation index (m)	0.3, 0.5, 0.7, 0.9
Transmission length	10–50 km
g	$5.5 * 10^{-11}$
Fiber attenuation (α)	0.22 dB/km

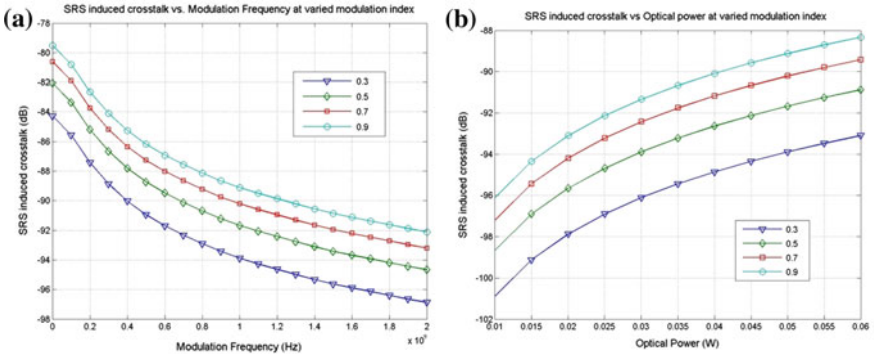


Fig. 1 SRS induced crosstalk versus **a** modulation Frequency at varied modulation index, **b** optical Power at varied modulation index

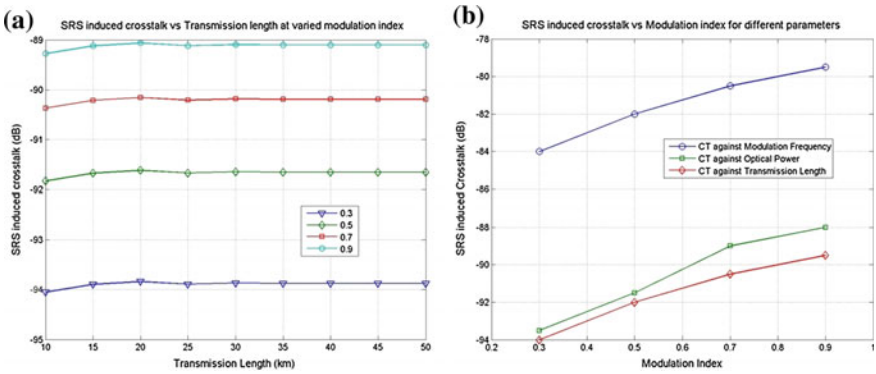


Fig. 2 SRS induced crosstalk versus **a** transmission length at varied modulation index, **b** modulation Index for different parameters

index is increased. The crosstalk levels are −94 and −89 dB at the modulation index values of 0.3 and 0.9, respectively.

4 Conclusion

This paper projects the impact of modulation index on the SRS-induced crosstalk. The study is done against modulation frequency, optical power, and transmission length. It is concluded that the crosstalk level decreases as the modulation frequency is increased whereas increasing the optical power increases the crosstalk induced. Transmission length effects are less severe where crosstalk level remains almost unchanged. But taking a broader view, increasing the modulation index

enhances the crosstalk induced. The crosstalk levels are increased by 5 dB when modulation index is increased from 0.3 to 0.9. The levels increase from −84 to −79.5 dB against modulation frequency, −93 to −88 dB against optical power and −94 to −89 dB against transmission length when modulation index is varied from 0.3 to 0.9. Results obtained help us to design better transmission system in order to improve transmission properties against SRS-induced crosstalk. So the performance of WDM RoF system can be optimized by carefully selecting the depth of modulation.

References

1. Shelly Singla, Sandeep K. Arya: Performance evaluation of up-converted radio-over-fiber signal transmission based on SOA-MZI using different recovery schemes, Optik 124, (2013), 4635–4638
2. Vishal Sharma, Amarpal Singh, Ajay K. Sharma: Challenges to radio over fiber (RoF) technology and its mitigation schemes—A review, Optik 123, (2012), 338–342
3. G.P. Agarwal: Application of Nonlinear Fiber Optics, Academic Press, San Deigo, CA, (2001)
4. Frédérique Vanholsbeeck, Stéphane Coen, Philippe Emplit, Marc Haelterman, and Thibaut Sylvestre: Raman-Induced Power Tilt in Arbitrarily Large Wavelength-Division-Multiplexed Systems, IEEE Photon. Technol. Lett, 17(1), (2005), 88–90
5. P. M. Krummrich and M. Birk: Experimental Investigation of Compensation of Raman-Induced Power Transients from WDM Channel Interactions, IEEE Photon. Technol. Lett, 17(5), (2005), 1094–1096
6. Zhi Jiang and Chongcheng Fan: A Comprehensive Study on XPM- and SRS-Induced Noise in Cascaded IM-DD Optical Fiber Transmission Systems. Journal of Lightwave Technology, 21 (4), (2003), 953–960
7. Toshiaki Yamamoto and Seiji Norimatsu: Statistical Analysis on Stimulated Raman Crosstalk in Dispersion-Managed Fiber Links, Journal of Lightwave Technology, 21(10), (2003), 2229–2240
8. Mattia Cantono, Vittorio Curri, Antonio Mecozzi and Roberto Gaudino: Polarization-related Statistics of Raman Cross-talk in Single-mode Optical Fibers, Journal of Lightwave Technology, (2015)
9. A.K. Sharma, S.K. Arya: Improved analysis for SRS and XPM induced crosstalk in SCM-WDM transmission link in the presence of HOD, Optik 120, (2009), 773–781
10. Frank S. Yang, Michel E. Marhic, Leonid G. Kazovsky: Nonlinear crosstalk and two countermeasures in SCM–WDM Optical communication systems, Journal of Lightwave Technology, 18(4), (2000), 512–520

Design and FPGA Implementation of 32-Point FFT Processor

Amit Kumar, Adesh Kumar, Aakanksha Devrari and Shraddha Singh

Abstract The research article presents the design and FPGA implementation of 32-point FFT algorithm. DFT has the symmetry and periodicity property, but requires more hardware, delay for the calculations in butterfly structure because twiddle factor is loaded in each stage. Twiddle factor has the real and imaginary parts and utilize inefficient memory. FFT computation requires less number of clock cycles because the periodicity and symmetry property of the twiddle factors in several stages together optimize the memory utilization and storage area due to twiddle factors. In the research article 32-point FFT processor is designed using VHDL programming language. It is based on pipelined architecture and can be used for high-speed applications and modulation techniques like Orthogonal Frequency Division Multiplexing in 4G mobile communication. The design is carried in Xilinx ISE 14.2 and functional checked in Modelsim 10.1 and synthesized on Virtex 5 FPGA.

Keywords Discrete Fourier transform (DFT) · Field programmable gate array (FPGA) · Fast Fourier transform (FFT) · Very High Speed Integrated Circuit Hardware Description Language (VHDL) · Integrated System Environment (ISE)

Amit Kumar (✉)
Faculty of Technology, Department of VLSI Design,
Uttarakhand Technical University (UTU), Dehradun, India
e-mail: amit989762@gmail.com

Adesh Kumar
Departments of Electronics Instrumentation and Control (EIC) Engineering,
University of Petroleum and Energy Studies (UPES), Dehradun, India

Aakanksha Devrari
Departments of Electronics and Communication Engineering,
Women Institute of Technology, Dehradun, India

Shraddha Singh
Departments of Electronics and Communication Engineering,
GLA University, Mathura, India

© Springer Science+Business Media Singapore 2017

R. Singh and S. Choudhury (eds.), *Proceeding of International Conference on Intelligent Communication, Control and Devices*, Advances in Intelligent Systems and Computing 479, DOI 10.1007/978-981-10-1708-7_33

1 Introduction

The FFT [1, 2] is a method that efficiently calculates the DFT. The DFT [1, 2] of an input sequence $x(n)$ over length 'N' is expressed by the relation which is a complex-valued sequence $X(k)$.

$$X(k) = \sum_{n=0}^{N-1} x(n) e^{-j2\pi nk/N}, \quad \text{where } 0 \leq k \leq N-1 \tag{1}$$

The same can be represented with the help of following equation:

$$X(k) = \sum_{n=0}^{N-1} x(n) e^{-j2\pi nk/N} = \sum_{n=0}^{N-1} x(n) W_N^{nk}, \quad \text{where } 0 \leq k \leq N-1 \tag{2}$$

Here W_N represents the complex-valued phase factor, which is the Nth root of unity and expressed as $W_N = e^{-j2\pi/N}$. In the same way, the equation of IDFT [1, 2] is expressed as

$$x(n) = \frac{1}{N} \sum_{k=0}^{N-1} X(k) W_N^{-nk}, \quad \text{where } 0 \leq n \leq N-1 \tag{3}$$

From Eq. (3), it is clear that the above equation requires *'N'* number of multiplication to calculate the direct values of $X(k)$ with respect to each discrete value of 'k'. It requires *4N* number of real multiplications, *(N−1)* number of complex additions, and *(4N−2)* number of real additions. Hence, the computation of 'N' point DFT [1, 2] requires N^2 complex multiplications and $N(N-1)$ complex additions. The 'N' point DFT [2, 3] is computed using Eq. (3), and can be represented in real and imaginary parts.

$$X(k) = X_R(k) + jX_I(k) = \sum_{n=0}^{N-1} X_R(n) + jX_I(n) \left[\cos \frac{2\pi nk}{N} - j \sin \frac{2\pi nk}{N} \right]$$

where $x(n)$ is a complex-valued sequence. The components X_R and X_I represent the real and imaginary parts. In the representation of real and imaginary values the above equation is expressed as

$$X_R(k) = \sum_{n=0}^{N-1} \left[X_R(n) \cos \frac{2\pi nk}{N} + X_I(n) \sin \frac{2\pi nk}{N} \right] \tag{4}$$

$$X_I(k) = -\sum_{n=0}^{N-1} \left[X_R(n) \cos \frac{2\pi nk}{N} - X_I(n) \sin \frac{2\pi nk}{N} \right] \tag{5}$$

In the direct computation of DFT [1, 4] there is the requirement of $2N^2$ trigonometric evaluations, $4N^2$ number of real multiplications, and $4N(N-1)$ number of real additions. It is primarily inefficient due to unexploited symmetry and periodicity properties of weight function or W_N (phase factor). The properties of W_N is given by

$$\text{Summetry Property [5] of Phase Factor } W_N^{k+N/2} = -W_N^k \tag{6}$$

$$\text{Periodicity Property [5] of Phase Factor } W_N^{k+N} = W_N^k \tag{7}$$

The solution of the two properties of DFT is the FFT, which is an efficient technique to exploit the above two Eqs. (4) and (5). The operations related to additions multiplication [2, 5] needed for the simple forms of DFT and IDFT are of order N^2. The calculation of *'N'* point data points need '*N'* complex arithmetic operations. FFT is an efficient algorithm to calculate DFT and its inverse transform IDFT and produces same Solution which is given by DFT. The only difference is that it is fast as FFT uses three properties, i.e., symmetric, periodic, and recursive properties of twiddle factor [6]. FFT is an optimized algorithm and increases the efficiency of DFT. Decimation in Time (DIT) and Decimation in Frequency (DIF) Fast Fourier transform algorithms rely on the decomposition of *'N'* point transform into two *(N/2)* point transformation [7]. The decomposition operations can be applied to any composite value *'N'*. When the FFT algorithm is applied in time domain, it is called DIT FFT algorithm. Decimation refers to the significant reduction in number of calculations performed on time domain data. The DIT FFT algorithm is used for 8-point FFT implementation which can be implemented using radix-2 FFT.

2 FFT Processor Design

The design and operation of the 32-point FFT processor [8, 9] consist of three main units. The operations are the input data, FFT computation module, and data output processing as shown in Fig. 1. The 32-point FFT processor can be designed using four 8-point FFT processors. Figure 2 shows the input sequence $x[0]...x[31]$ and output sequence $y[0]....y[31]$ of 32-point FFT with *clock* and *reset,* shown in Fig. 2. Instead of direct implementing 32-point FFT, it is possible to achieve faster speed of 32-bit processor because it will support parallel processing or pipelined architecture as shown in Fig. 3. In 32-point FFT computation, only 8-point FFT is computed one time. The operation can be controlled with the selection logic which processes 8 points at one time. Table 1 explains the selection and computation processing of 32-point FFT.

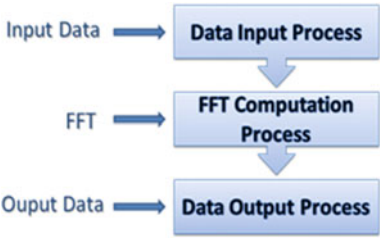


Fig. 1 FFT computation process

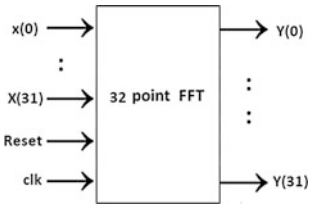


Fig. 2 32-point FFT processor

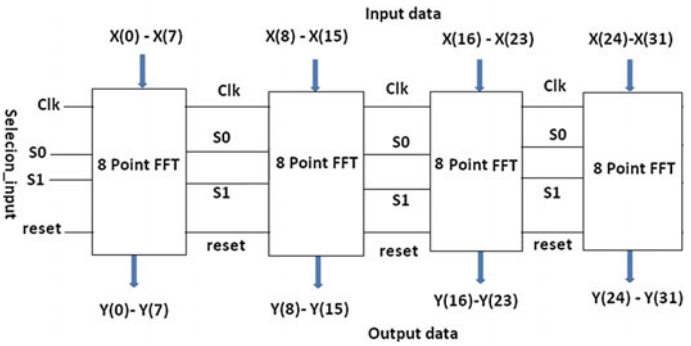


Fig. 3 Pipelined processing of 32-point FFT

Table 1 Computation and selection logic of 32-point FFT

(S_0 S_1) Selection	Computation
00	FFT 1 selection for input $X(0)$ to $X(7)$ and corresponding output $Y(0)$–$Y(7)$
01	FFT 2 selection for input $X(8)$ to $X(15)$ and corresponding output $Y(8)$–$Y(15)$
10	FFT 3 selection for input $X(16)$ to $X(23)$ and corresponding output $Y(16)$–$Y(23)$
11	FFT 4 selection for input $X(24)$ to $X(31)$ and corresponding output $Y(24)$–$Y(31)$

3 Simulation and Synthesis Results

The simulation of 32-point FFT is carried in modelSim 10.1 b software. Figure 4 shows the snapshot, which shows the computed values of FFT and corresponding data. The corresponding RTL is shown in Fig. 5 and the details of the pin are given in Table 3. In the snapshot, the input of 32-point FFT module is represented by $x(0)$ to $x(31)$ which are the discrete inputs of 32-bit data. The corresponding output of each input is subdivided into the real and imaginary components. The concept of 32-bit floating point representation is used to compute the values of Re_$y(0)$ to Re_$y(31)$ and imaginary parts of outputs are Im_$y(0)$ to Im_$y(31)$. Reset is sequential input when reset = 1, the output of 32-point FFT is zero and at Reset = '0' the clock pulse signal is synchronized to provide actual output (Table 2).

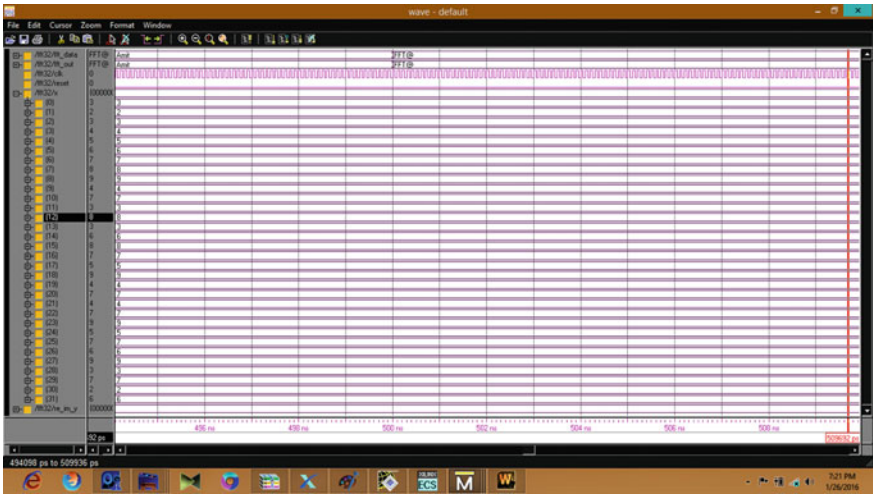


Fig. 4 Full data flow for 32-point FFT operation

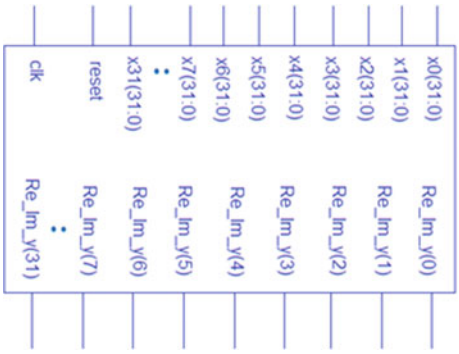


Fig. 5 Pin diagram RTL for 32-point FFT algorithm

Table 2 Details of pin used in RTL of 32-point FFT

Pin	Description
$x(0)$–$x(31)$	Input of 32-point FFT
Clk	Input to 32-point FFT used to provide positive (rising edge) of clock pulse
Reset	Input which is used to reset the FFT contents in memory
Re_Im_*y* (0) to im_ (31)	Represent the real and imaginary outputs of 32-point FFT, separated from output

The functional simulation depends on the clock pulse input and rest input. Initially, reset is kept to 1, reset = 1, and then all outputs will be zero. After that reset = '0' and force all values $X(0)$ to $X(31)$, the corresponding output of the FFT is obtained. In the simulation result the data transfer using FFT-32 is also shown in the same figure. The input data is fft_data (31:0) and output data is fft_out (31:0).

Test case 1: *fft_data (31:0) = 1'h46465440 (in hex) or = "0100 0110 0100 0110 0101 0100 0100 0000"* in binary and the same data is obtained *at fft_out (31:0)*. The data in 8-bit ASCII format is *FFT@*.
Test case 2: *fft_data (31:0) = 1'h416D6974 (in hex) "0100 0001 0110 1101 0110 1001 0111 0100"* and the same data is obtained at *fft_out (31:0)*. The data in 8-bit ASCII format is *Amit*.

The target FPGA is Virtex-5: xc5vlx20t-2-ff323 device. The same output data fft_out (31:0) is shown on the LCD of the corresponding FPGA.

4 Device Utilization Summary of 32-Point FFT

The summary report extracted directly from the Xilinx software about device utilization is the details of utilized FPGA device hardware parameters such as logic gates, flip-flops, slices, LUTs, memory, etc. The synthesis report shows the complete details of device utilization. If the designed chip is not having the optimized

Table 3 Device and time utilization summary (32-point FFT)

Device Part	Utilization	Parameter for timing	Utilization
Slices utilization	4642/6144 76 %	Frequency (maximum)	395 kHz
Slice flip-flops utilization	6146/12288 50 %	Arrival time before clk (minimum)	3.559 ns
4-input LUTs utilization	132/12288 55 %	Time after clk (maximum)	3.969 ns
Bonded IOBs utilization	132/240 73 %	Total path delay (combinational)	16.015 ns
GCLKs utilization	16/32 50 %	Memory utilization	244,608 KB

hardware parameters, further chip development is done in the Xilinx ISE design software. Table 3 shows the hardware and timing utilization for the FFT structure. The target device is xc5vlx20t-2-ff323, which is programmed in Virtex 5 FPGA. The details of timing parameters are described by frequency support (maximum), arrival time as input before clock pulse, output time after clock pulse, total path delay as combinational delay.

5 Conclusion

The VHDL implementation of FFT algorithm is done in Xilinx ISE 14.2 and functionally simulated in Modelsim 10.1 software. The implementation is done for 32-point FFT and synthesized on Virtex-5 FPGA. The implementation is tested on the different test cases. The special feature of pipelined and parallel execution of FFT makes the design faster and lesser more. The throughput of such FFT implementation is applicable for any wireless techniques such as OFDM, OFDMA, and WiMAX applications in which fast processing is required. The memory utilization is found to be 244,608 KB, maximum frequency is 395 MHz, minimum time before clock is 3.559 ns and minimum time required after clock is 3.969 ns, and minimum combination part delay is 16.015 ns. The implementation of such FFT can be applicable in high-speed communication system and their modulation schemes such as OFDM and OFDMA. The same architecture can be used to implement variable length FFT.

References

1. A. Raghunathan, S. Dey, N. K. Jha, "*High-level macro-modeling and estimation techniques for switching activity and power consumption*", Very Large Scale Integration (VLSI) Systems, IEEE Transactions on, Vol. 11, 2003 Page(s), pp (538–557).
2. S Salivahanan, C Gnanapriya "*Didital Signal Processing*" Second Edition Tata McGraw Hill Education Private Limited, New Delhi. 2011.
3. K. Harikrishna, T. Rama Rao, Vladimir A. Labay, "*FPGA Implementation of FFT Algorithm for IEEE 802.16e (Mobile WiMAX)*" International Journal of Computer Theory and Engineering, Vol. 3, No. 2, April 2011 pp (197–202).
4. S. Sood, A. Singh, A. Kumar "*VHDL Design of OFDM Transreceiver Chip using Variable FFT*"Journal of Selected Areas in Microelectronics (JSAM), Singaporean Journal of Scientific Research (SJSR) Vol 5. No. 2 2013 pp. (47–58).
5. S Sukhsawas, K Benkrid. A High-level Implementation of a High Performance Pipeline FFT on Virtex-E FPGAs. Proceedings of the IEEE Comp. Society Annual Symp. on VLSI Emerging Trends in Systems Design (ISVLSI'04). 0-7695-2097-9/2004.
6. María José Canet, Javier Valls, Vicenç Almenar, José Marín-Roig "*FPGA implementation of an OFDM-based WLAN receiver*" Microprocessors and Microsystems Vol. 36 (2012), pp. 232–244.

7. M. Merlyn, ECE, Jayaram College of Engg & Tech, Trichy, India "*FPGA Implementation Of FFT Processor With OFDM Transceiver*" 2010 International Conference on Signal and Image Processing page, IEEE Xplorer, 2010, pp (485–489*)*.
8. S. He and M. Torkelson. A new approach to pipeline FFT processor, 10th Int. Parallel Processing Symp. (IPPS'96), pp. 766–770, 1996.
9. WANG Xiu-fang, HOU Zhen-long *"Design and Implement of FFT Processor for OFDMA system using FPGA"* Northeast Petroleum University (ICMEE 2010).
10. Lenart and Viktor Öwall. "*Architectures for dynamic data scaling in 2/4/8 k pipeline FFT cores."* IEEE transactions on Very Large Scale Integration (VLSI) systems, vol. 14, no. 11, November 2006, pp: 1286–1290

Performance Enhancement in WDM-FSO System Using Optical Amplifiers Under Different Rain Conditions

Navneet Dayal, Preeti Singh and Pardeep Kaur

Abstract Free Space Optics (FSO) is gaining huge market due to its numerous advantages as compared to other communication networks. But the main drawback is attenuation caused by weather conditions. In this paper, different configurable arrangements of optical amplifiers in FSO have been analysed to get optimum performance for 2.5 Gbps data rate with 35 dB power level of laser for three rain conditions. The pre-existing system is compared with the proposed system and the results are analysed. It is noticed that the proposed system is more efficient both in performance and cost.

Keywords LED · APD · WDM-FSO · NRZ · Amplifier

1 Introduction

The increasing demand of high data rate and efficiency in communication field has led to the replacement of Radio frequency (RF) networks with Free Space Optics (FSO). It can be employed in any topology based on the requirement of the network. The basic blocks of FSO consist of a transmission section, channel and reception section. FSO requires line of sight configuration between transmitter and receiver. The optical source can be LEDs or lasers as a transmitter but the use of laser is effective due to high directivity as compared to former one [1–3]. The channel is air through which the message is sent. The receiver includes the detector which can be PIN or APD; out of which APD is preferred due to more sensitivity. FSO can be used as a last mile access to any situation thus providing with high data rate and security,

Navneet Dayal (✉) · Preeti Singh · Pardeep Kaur
UIET, PU, Chandigarh, India
e-mail: navidayal1992@gmail.com

Preeti Singh
e-mail: preeti_singh@pu.ac.in

Pardeep Kaur
e-mail: pardeeptur@gmail.com

© Springer Science+Business Media Singapore 2017

R. Singh and S. Choudhury (eds.), *Proceeding of International Conference on Intelligent Communication, Control and Devices*, Advances in Intelligent Systems and Computing 479, DOI 10.1007/978-981-10-1708-7_34

no license requirement, less power consumption and low cost of deployment. Due to all these merits of FSO, it has found applications in various fields of defence, enterprise connectivity, disaster recovery and communication, etc. Though the merits and application of FSO are many yet there are conditions which limit the efficiency of network. These mainly include the weather conditions. The atmospheric fluctuations of refractive index lead to the change in attenuation level thus variation in performance is observed. As the laser beam passes through the environment, different effects are observed like scattering, dispersion, scintillation [4, 5]. These depend on the size of particles which is responsible for such phenomenon. Various weather conditions like fog, haze, snow and rain lead to degradation of performance. The rate of rainfall varies from 85 to 100 mm/h. The scintillation effects are also observed in summer days [6]. It rains at maximum 50 dB/km attenuation for microwave link and 150 dB/km attenuation for FSO [7, 8].

$$\alpha_{\text{specific}} = 1.076R^{0.67}\,[\text{dB/km}]$$

It signifies specific attenuation of rain and R represents rainfall rate in mm/h. WDM is used to enhance the system capacity without letting any other device to be installed. Besides WDM some other techniques are also utilised to gain high performance level which includes the use of optical amplifiers. Optical amplifiers help to reduce the circuitry and the optical signal is amplified directly without converting it into electrical signal. It is just as a laser but without any optical cavity. Shah et al. designed a system, i.e. System I in which the performance for different rain conditions such as light, medium and heavy, has been analysed [6]. It has been reported that at transmitter side optical amplifiers are used with all laser sources. The proposed system, i.e. System II given here is the improved one over the existing. In the forthcoming sections, the analysis of two systems—System I and System II, has been discussed. The performance of the proposed system is compared with the existing one on the basis of Bit Error Rate (BER) and eye diagrams.

2 System Design

The system consists of three modules—transmitter, medium and receiver. The transmitter section includes pseudorandom bit sequence generator at 2.5 Gbps, continuous wave laser, NRZ pulse generator, Mach–Zehnder modulator. The medium is FSO channel and the receiver has APD detector and Gaussian low-pass filter.

The performance is analysed using BER analyser which gives the related BER, power level and eye diagrams. The system parameters are shown in Table 1. The system is analysed to have BER of 10^{-9} at 1550 nm wavelength as it is reported as low attenuation window. The system with present specifications is designed in OptiSystem software v12.

System II is the proposed system with all the parameters same as System I. The combination of FSO and WDM is used to get optimum performance in the system

Table 1 System parameters

S. No.	Parameter	Value
1	Beam divergence	2.5 mrad
2	Laser power	30 dBm
3	Receiver aperture	30 cm
4	Amplifier gain	35 dB
5	Attenuation level	Light rain: 3 dB/km
		Medium rain: 9 dB/km
		Heavy rain: 20 dB/km

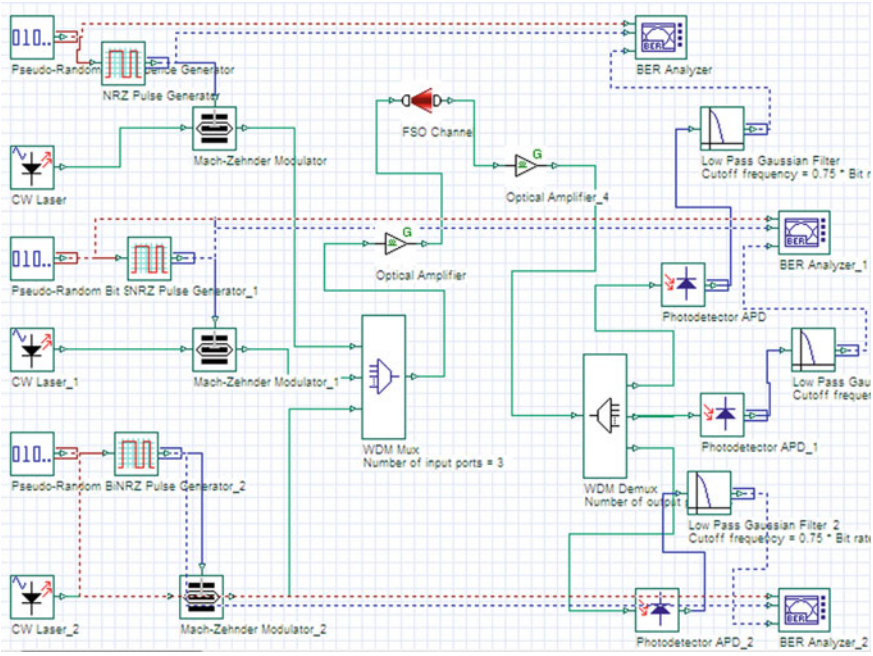


Fig. 1 Proposed System II with WDM-FSO (optical amplifier at transmitter and receiver)

by employing optical amplifiers at the transmitter and receiver sides as shown in Fig. 1. This system makes use of all the devices as in System I but the amplifier configuration is changed to have better results.

3 Analysis of Simulation Results

In the present paper, the effects of different parameters on the system under light, medium and heavy rain conditions are being observed in order to have an optimised system. The geometrical losses are considered in the simulation. It is noticed that

during light rain condition, acceptable transmission for System I is observed till 15.6 km and the range decreases as the attenuation level increases. The attenuation rises as the rainfall rate increases. An optimum Q factor is obtained and eye opening is analysed which shows that for medium rain the range is 6.1 km and it is 3 km for high rain.

The proposed system, System II is analysed using optical amplifiers at both sides, i.e. after multiplexer and before demultiplexer. It is observed that the link range increases in System II. The Signal-to-Noise Ratio (SNR) obtained is also better than the System I. It has also been analysed that the System II reduces the layout devices thus decreasing cost too with all other specifications being same.

3.1 Comparison of Two Systems

The comparison of range, minimum BER and Q factor values for two systems are shown in Table 2.

In order to enhance the performance levels, WDM with amplifiers in a FSO system is utilised in both the systems. The only difference is that in System II, the

Table 2 Comparison of performance values of System I and System II

Intensity of rain	System I			System II		
	Range (km)	Minimum BER	Q factor	Range (km)	Minimum BER	Q factor
Light	15.6	2.1508e-008	5.46805	25	2.7534e-021	9.39142
Medium	6.1	1.7071e-008	5.50883	9.3	2.70299e-020	9.14786
Heavy	3	8.21765e-012	6.72511	4.5	3.51199e-020	9.11953

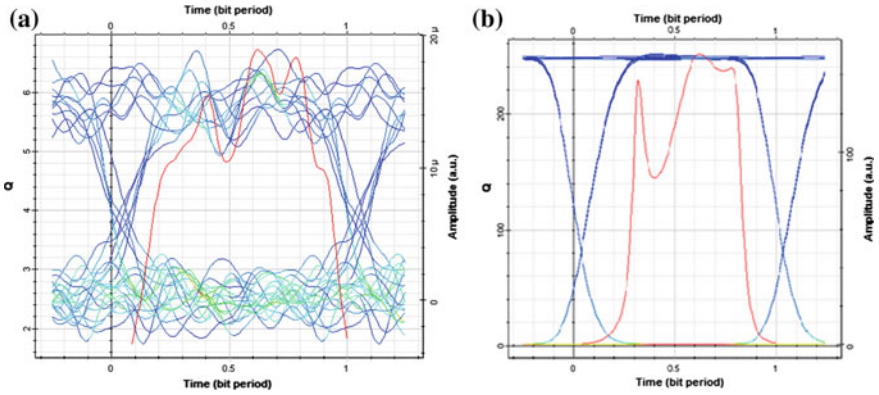


Fig. 2 BER analyser output in heavy rain condition for **a** System I **b** System II at 3 km

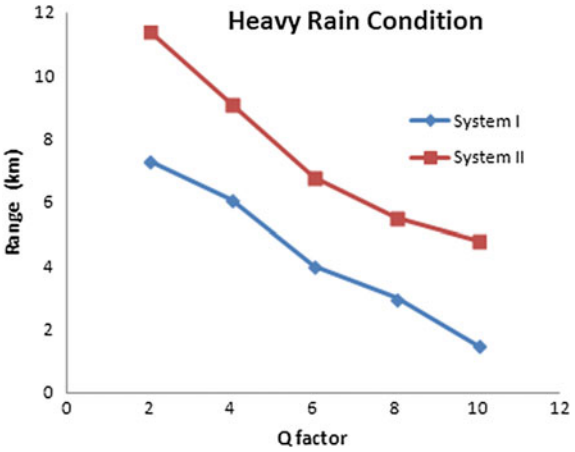


Fig. 3 Q factor versus range for two systems

arrangement of the amplifiers is changed. System II uses optical gain amplifiers after MUX and before DEMUX and it is noticed that the results analysed are better than System I. As observed from the tabulated results and simulations, it is reported that where the range for light rain condition is 15.6 for System I, it increases to 25 km for System II. The analysed results for medium and heavy rain conditions are also better than System I which shows maximum range of 9.3 km and 4.5 km, respectively, with acceptable transmission.

Thus, it can be stated that System II outperforms System I in terms of link distance as well as cost. While simulating the results the performance of eye diagrams is also analysed. It is reported that the eye opening in System II is more as it is clear from Fig. 2. The more the opening of eye, the more is the SNR at the reception side. The performance levels of both the systems are shown in Fig. 3.

4 Conclusion

FSO is used extensively nowadays in all areas as it shows better performance and reliability over other conventional systems with a large number of advantages. But due to worst weather conditions its performance can degrade, so efforts are made to achieve optimum performance level. One such technique is by the use of optical amplifiers as simulated. The use of optical amplifiers not only enhances SNR level but also increases the range of the system. It is clear from the simulations that System II offers good results with better range and quality factor for same power and other parameters than the existing System I. The proposed system not only increases system reliability and performance but also reduces cost of implementation.

References

1. Sushank Choudhary, Angela Amphawan, Kashif Nisar, "Realization of free space optics with OFDM under atmospheric turbulence", science direct, Optik-International Journal for Light and Electron Optics, vol 125, Issue 18, pp. 5196–5198, Sept 2014
2. Aditi, Preeti, "An effort to design a power efficient, long reach WDM-FSO system", ICSPCT, IEEE, pp. 791–796, July 2014
3. Aditi Malik and Preeti Singh, "Free space optics: current applications and future challenges", International Journal of Optics, Vol 2015, Article ID 945483, 7 pages, Hindawi publishing Corporation, Sept 2015
4. Swaminathan Parthasarathya, Andreas Kirstädterb, Dirk Giggenbacha,"Simulative Performance Analysis of ARQ Schemes for Free-Space Optical Inter-HAP Channel Model", Proceedings of photonic networks, ISBN, pp. 78–82, May 2015
5. Aditi Malik, Preeti Singh, "Comparative analysis of point to point FSO system under clear and haze weather conditions", Springer, Vol 80, Issue 2, pp. 483–492, Aug 2014
6. Dhaval Shah, Dilip Kumar Kothari, "Optimization of 2.5 Gbps WDM-FSO link range under different rain conditions in Ahmedabad", 2014 Annual IEEE India Conference (INDICON), pp. 1–4, Dec 2014
7. E.Leitgeb, T.Plank, M.Löschnigg, P.Mandl, "Free Space Optics in different (civil and military) application scenarios in combination with other wireless technologies", 16th International Telecommunications Network Strategy and Planning Symposium, IEEE, pp. 1–7, Sept 2015
8. A.J.Kshatriya, Dr.Y.B.Acharya, Dr.A.Aggarwal, "Analysis of Free Space Optical Link in Ahmedabad weather conditions", IEEE, ICT, pp. 272–276, Apr 2013

Fuzzy-Based Multi-Objective Optimization for Subjection and Diagnosis of Hybrid Energy Storage System of an Electric Vehicle

Kurukuru Varaha Satya Bharath and Kamlesh Pandey

Abstract Hybrid vehicles are widely considered as the emerging solutions for green technology in the field of transportation due to their user and eco-friendly interface. Generally speaking the hybrid energy system is prone to multiple types of faults and an intelligent monitoring layer can ensure smooth operation and inform any maintenance issues. In this work, we present an interface which integrates multiple AI and signal processing techniques to control the functioning of hybrid vehicles and detect the different faults interrupting smooth performance in a very short span of time. We demonstrate the thought process, simulation, final software interface, and test results to confirm its effectiveness.

Keywords Ultracapacitors (UCs) · Lithium-Ion Polymer Battery · Fuzzy inference system (FIS) · Hybrid electric vehicle (HEV)

1 Introduction

Increase in cost of energy sources along with the increase in awareness and acceptance of global warming, forced us to adapt green technology. Through this adaption the field of electrical is intensely overwhelmed to work for cleaner energy and transportation. Under such circumstances hybrid vehicles have loomed as a feasible solution for green technology in the world of transportation which itself consumes 40 % of world's energy sources. Irrespective of the thought that hybrid saves the fuel, but it has its flaws. The battery's composition consists of highly reactive substances, which are highly expensive, heavy, and difficult to replace. By addressing the flaws of the present day vehicle scenario, we can prove that hybrid

K.V.S. Bharath (✉) · Kamlesh Pandey
Department of Electrical and Electronics, ASET, Amity University Uttar Pradesh, Noida, UP, India
e-mail: kvsbharath@hotmail.com

Kamlesh Pandey
e-mail: pandey.1411@gmail.com

© Springer Science+Business Media Singapore 2017

R. Singh and S. Choudhury (eds.), *Proceeding of International Conference on Intelligent Communication, Control and Devices*, Advances in Intelligent Systems and Computing 479, DOI 10.1007/978-981-10-1708-7_35

electric vehicles are a best solution. The onset of latest, high-energy storage capacitor technologies, and light weight rechargeable batteries, with better energy density, has granted contemporary advancement in clean energy sector [1]. Quick fix to the problem can be battery-ultracapacitor system, where ultracapacitors act as a buffer due to their high power densities making it viable to handle oscillations without any impairment.

Our motive is to thrive an energy storage system that is suitable for use in Hybrid Electrical Vehicles (HEV) and can be used for remote or backup energy storage systems in absence of a working power grid. In order to get the highest efficiency from this system, ultracapacitors will be used in parallel with the battery and a pulsed load. The final product should use active circuit components to influence performance and efficiency in accordance with a varying load. The system is also integrated with highly intelligent control techniques like Fuzzy for control [2] and fault detection [3] in order to create an efficient system with an overall reduction in cost, size, and weight.

2 Ultracapacitors

Ultracapacitors are being considered as the emerging technologies with fast and efficient functionalities of charging and discharging. Benefitted from these functionalities, ultracapacitors are being preferred for thousands of applications and utilities and will been seen in most of the near future applications. Ultracapacitors correlate with various primary energy sources like an internal combustion engine, fuel cells, or various kinds of batteries which fallback in providing quick bursts of power. Ultracapacitors also provide high power density in comparison with the conventional storages providing them an ideal status for different applications which require quick power boost.

3 Hybrid Battery-Ultracapacitor

In the present section, we are comparing different systems which are formed individually and by combination of ultracapacitors and Lithium-Ion Polymer battery and we identified the better functionality among them [4].

Structure 1: This structure is only powered by ultracapacitors and is perfect for high power output because of ultracapacitor high power density. The problem lies in the exponential voltage drop of the ultracapacitor after a period of time one of these modules would be rendered useless because it would not be able to supply enough voltage.

Structure 2: This structure was battery powered, using Lithium-Ion Polymer battery cells. These batteries lack the properties of quick discharges of current and sometimes require high power densities.
Structure 3: This arrangement consists of Lithium-Ion Polymer batteries in parallel with a stack of ultracapacitors modules. This system implements current division rule on the batteries which has no efficiency. The system is also not feasible due to high costs [5].
Structure 4: The arrangement deals with Lithium-Ion Polymer batteries in parallel with a stack of ultracapacitor modules and utilizes active components in the circuit. This difference of using active components in the circuit allows switching of the power flow between the hybrid system and load. Battery life in such system is spared and the effects of a pulse signal are avoided. The structure was formulated from HESS concept [6]. The combination of high-energy-density batteries and high power density UC's in HEVs results in a good accomplishment, eminently productive, limited space occupancy, and better lifetime [7].

3.1 Comparing Systems

See Table 1.

Table 1 Comparison of different systems of ultracapacitors, battery's, and their combination to power 1 kW pulse load for 15 times for 18 s each up to 30 min [1]

SYSTEM#1	SYSTEM#2	SYSTEM#3	SYSTEM#4
Ultracapacitor	Battery	Battery/Ultracapacitor hybrid	Battery/Ultracapacitor hybrid with active circuit elements and control
Features: UC modules - 51.8 V - 905 F - 5 × 165F	**Features**: Lithium polymer (LiPo) Cells - 51.8 V - 56 LiPo Cells - 4 Protection Circuit Modules (PCMs)	**Features**: - 51.8 volts - 28 LiPo cells - 2 PCMs - 330 F total - 2 × 165 F UC modules	**Features**: - 51.8 V - 14 LiPo Cells - 1 PCM - 1 × 85 F UC Module - 3 Solid-state relays - 1 Digital relay controller
Limitations: - Excessive weight - High cost - Low energy	**Limitations**: - Limited cycle life - Low power - Excessive weight	**Limitations**: - Relatively high cost - Performance limited by voltage dependency	**Limitations**: - None

4 Fuzzy-Based Control

The control will be implemented through the GUI of fuzzy in MATLAB which has six input variables and two outputs. Power ratio acts as a controller in managing the proportion of power between two or multiple sources. As per our considerations the outputs are the sheer values of power which facilitates the energy flows directly between sources, and allows control on the state of charge of ultracapacitors [8] (Fig. 1).

The input variables denoted as error of resultant hybrid source voltage (Uerr), Power load (Pload), Speed (speed), ultracapacitors voltage (Ucap), normalized value to the square of speed (speed^2), normalized value of square of ultracapacitor voltage (Ucap^2), terrain slope (Slope) [9].

The value of slope factor is formulated as an average characterstic quotient from:

$$\text{Slope} = \frac{6H(100) + 3H(200) + 2H(300) - 18H(0)}{18} \tag{1}$$

where $H(n)$ – elevation in meters from current location.

Ultracapacitors power (Pcap), Battery power (Pbat) are the output variables and the membership functions are given as: negative Large (neg_L) $= -50$, negative Small (neg_s) $= -20$, zero = O, positive Small (pos_s) $= 20$, positive Large (pos_L) $=$ 50 (Fig. 2).

There were as many as 35 rules that were defined for the experimentation purpose. The first ten rules do not depend on ucap^2, Speed^2, s1ope which results in:

- Ultracapacitors power the system during acceleration and also store energy during regenerative braking.

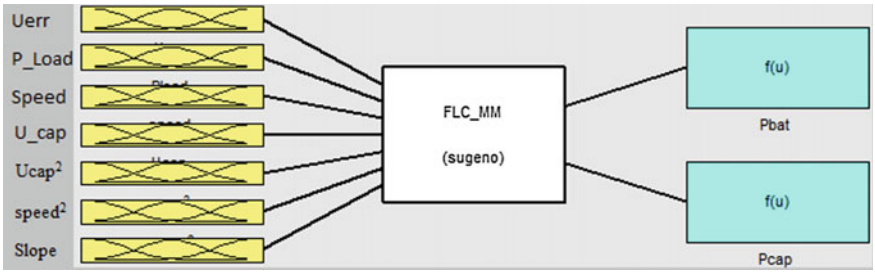


Fig. 1 Implementing input and output variable through GUI of fuzzy

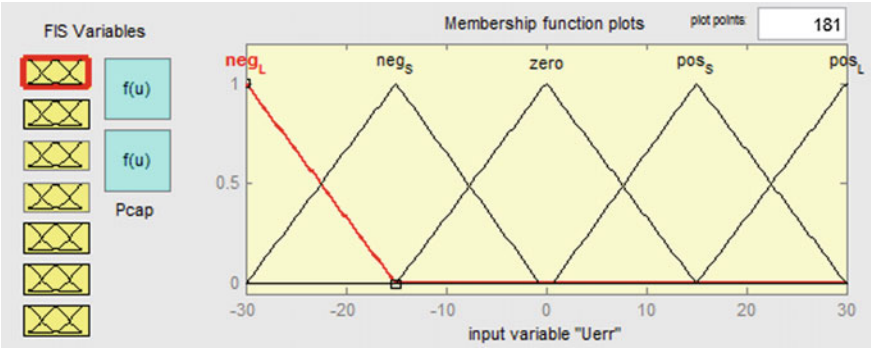


Fig. 2 Membership function plot of error of resultant hybrid source voltage (Uerr)

- Energy from regenerative braking after being stored in ultracapacitors is then stored in the batteries.
- While driving at constant speed battery acts as source.

The other rules has no dependency on inputs like Uerr, Pload, speed, Ucap which results in maintaining voltage of ultracapacitors at the convenient level with respect to the momentum of the vehicle. The sum of powers Battery power (Pbat) and Capacitor power (Pcap)] are calculated with the help of these rules is always zero [8]. The surface view of the fuzzy system depicts the relation between Pbat, Load power (Pload) with reference to the error of resultant hybrid source voltage (Uerr) (Fig. 3).

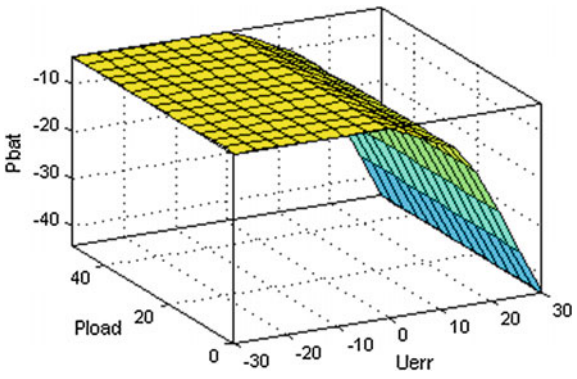


Fig. 3 Surface view of rules implemented in fuzzy

5 Simulation and Results

5.1 Control of Hybrid Energy Storage

The regulatory methods are depicted to bring about the eminent productivity working region of each and every power source and to control current and voltage at peak and average demands, without negotiating the overall performance of the system [10]. A multiple-input power electronic converter along with a generator, energy storage devices, and the voltage dc-link bus is integrated in the system [11]. The regulatory structure integrates the power flows between the power sources and the load. This supervisory control along knowledge-based system improvises the efficiency of the system by enhancing the fuel economy and increasing the mileage [12, 13] (Fig. 4).

The system performance was analyzed through the MATLAB Simulink and Plecs Standalone software. The results depict the driving conditions in different areas and particularly includes driving modes such as inconstant acceleration and deceleration. Figure 5 displays the ECE15 urban driving cycles power distribution storage [14]. The load power and the batteries maximum power are inversely proportional. Division of power between the sources is carried out as per the requirement. On an average the ultracapacitors power over a particular cycle is zero, which equates the average power of load and the battery. The operational framework of both batteries and UC's crumble with time and with the increment in number of charging-discharging cycles. The performance and life are strongly dependent on the conditions under which cells are being used. From the results we can conclude that discharge of battery power is limited and the charging power is almost eliminated.

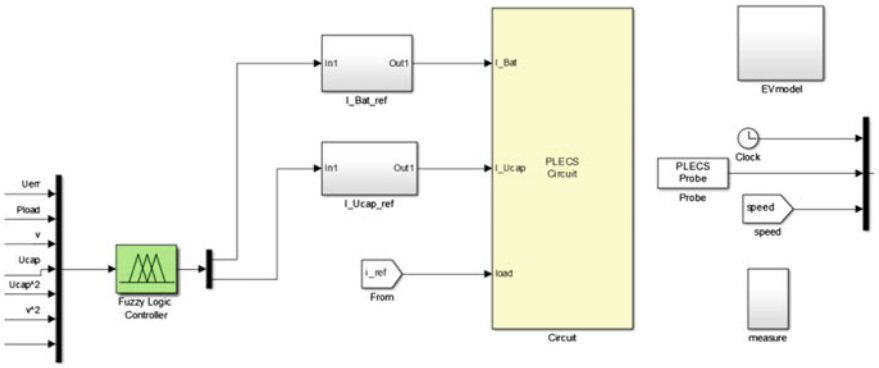


Fig. 4 Simulation circuit for fuzzy control of hybrid electric vehicle's energy storage system using PLECS standalone and MATLAB

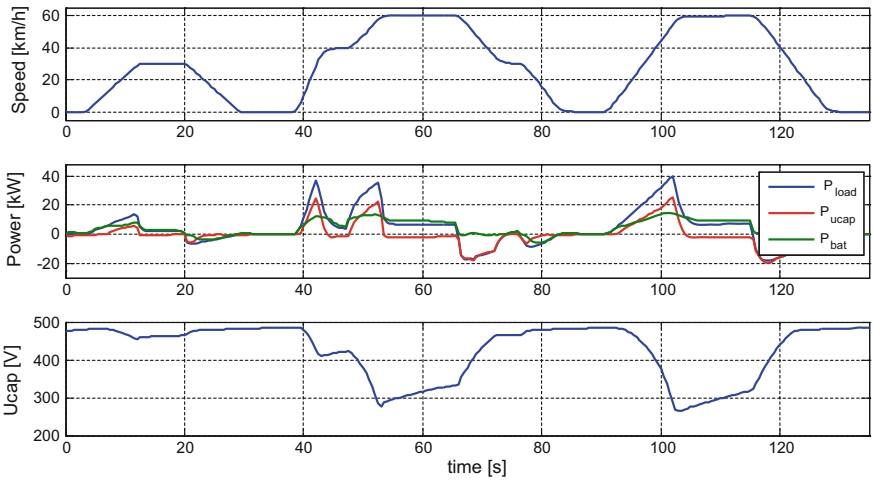


Fig. 5 ECE15 urban driving cycle speed, power, and ultracapacitors voltage

6 Failures of Ultracapacitors

Failing is termed as the inability of a fundamental to accomplish its intended operation as designed which results in one or many faults. In general, electrical stress and thermal stress affect the life of ultracapacitor. Such affects can be due to the external conditions, i.e., operating voltage and temperature [15, 16]. Summing up all the factors that distress the performance of ultracapacitors, the failure modes of the ultracapacitor stack are listed as:

Loss of Capacitance (more than 20 %). The capacitance decreases with respect to the utility and this is due to handy carbon surface and the availability of ions is diminished along with the electro-chemical cycling.

Effect of Over Pressure. The operating time is being increased by the pressure of gas inside the cell which was generated by the temperature and voltage. Under such conditions, the safety structure or arrangement which can be generally a groove on the wall may open up softly avoiding explosion. In such extreme cases of opening the component we have to keep an observation upon the increasing leakage current, internal resistance, and decrease of capacitance [17].

Open Circuit Failure. The pin of the ultracapacitor may break or corrode when working in a strong corrosive environment. In addition, a strong external force may cause the failure.

6.1 Fuzzy-Based Fault Detection

In this section, the proposed fuzzy inference approach is applied to the ultracapacitor stack. The fault diagnosis system consists of the preliminary circuit using plecs and fuzzy inference system combined implemented in MATLAB. The work demonstrates the voltage and current of every component in the stack of ultracapacitors. By utilizing fuzzy we are able to identify the current state of charge, discharge, which helps us in fault diagnosis using the difference method.

For the purpose of diagnosis the inputs are: (1) Voltage difference between the single and the average of the array in charge status ($V\tilde{C}$). (2) Voltage difference of the individual cell in charge status (ΔVC). (3) Voltage difference between the single and the average of the array in discharge status ($V\tilde{D}$). (4) Voltage difference of the individual cell in discharge status (ΔVD). The output variable is defined as the FC (Failure Cause).

Where $V\tilde{C}$ and $V\tilde{D}$ are obtained by calculating the voltage difference between single and the average of the array in 0.5 s on the other hand ΔVC and ΔVD are obtained by calculating the rising voltage value in 1 s. After simulating the features in the signal processing through PLECS and MATLAB, the fuzzy logic inference approach is used for fault diagnosis.

7 Conclusion

The paper provides an overview of different storage systems for electrical vehicles and provides the benefits of hybrid energy systems. The simulation results helped us to know about the behavior of various storage devices and how hybrid storage systems are efficient in comparison to others. Integrating the system with knowledge-based techniques such as multi-objective optimization using fuzzy helped us to reach out for both the control and diagnosis of the ultracapacitors. Implementing such techniques will provide an eco-friendly and maintenance free operation increasing the life and efficiency of the equipment. Further studies will be carried out on the prognosis and diagnosis for ultracapacitors and various intelligent techniques will be tested for better efficiency.

References

1. Marvel Mukongolo, Chi-Fai Lo, Michael Kovalcik, Jamal Adams, Dr. Fang Peng, Keld LLC: Battery-Super capacitor Hybrid energy systems, Design Team 10 Final Report.
2. Marek Michalczuk, Bartlomiej Ufnalski, Lech Grzesiak: Fuzzy logic control of a hybrid battery-ultracapacitor energy storage for an urban electric vehicle, 2013 Eighth International Conference and Exhibition on Ecological Vehicles and Renewable Energies.

3. J. Li, G. Wang, L. Wu, X. Li: Failure Prediction Of Ultracapacitor Stack Using Fuzzy Inference System, Engineering Review, Vol. 35, Issue 2, 103–111, 2015.
4. Marek Michalczuk, Lech M. Grzesiak, Bartłomiej Ufnalski: A lithium battery and ultracapacitor hybrid energy source for an urban electric vehicle, Przegląd Elektrotechniczny (Electrical Review), ISSN 0033-2097, R. 88 NR 4b/2012.
5. Amirabadi M: Fuzzy Control of a Hybrid Power Source for Fuel Cell Electric Vehicle using Regenerative Braking Ultracapacitor, Power Electronics and Motion Control Conference, 2006. EPE-PEMC 2006.
6. Mid-Eum Choi, Jun-Sik Lee, Seung-Woo Seo: Real-Time Optimization for Power Management Systems of a Battery/Supercapacitor Hybrid Energy Storage System in Electric Vehicles, Vehicular Technology, IEEE Transactions on (Volume: 63, Issue: 8).
7. Schaltz E; Khaligh A; Rasmussen P.O: Influence of Battery/Ultracapacitor Energy-Storage Sizing on Battery Lifetime in a Fuel Cell Hybrid Electric Vehicle, Vehicular Technology, IEEE Transactions on (Volume: 58, Issue: 8).
8. M. Mohammedia, O. Kraaa, M. Becherifb, A. Abouboua, M.Y. Ayadc, M. Bahria: Fuzzy Logic and Passivity-based Controller Applied to Electric Vehicle Using Fuel Cell and Supercapacitors Hybrid Source, Energy Procedia, Volume 50, 2014.
9. Yingming Lv; Haiwen Yuan; Yingyi Liu; Qiusheng Wang: Fuzzy Logic Based Energy Management Strategy of Battery-Ultracapacitor Composite Power Supply for HEV, Pervasive Computing Signal Processing and Applications (PCSPA), 2010.
10. Ferreira, A.A., Pomilio, J.A.; Spiazzi, G.; de Araujo Silva, L.: Energy Management Fuzzy Logic Supervisory for Electric Vehicle Power Supplies System, Power Electronics, IEEE Transactions on (Volume: 23, Issue: 1)
11. Amjadi, Z. Williamson, S.S-Power-Electronics-Based Solutions for Plug-in Hybrid Electric Vehicle Energy Storage and Management Systems, Industrial Electronics, IEEE Transactions on (Volume: 57, Issue: 2).
12. Qi Lia, Weirong Chena, Yankun Lia, Shukui Liub, Jin Huanga: Energy management strategy for fuel cell/battery/ultracapacitor hybrid vehicle based on fuzzy logic, International Journal of Electrical Power & Energy Systems, Volume 43, Issue 1, December 2012.
13. Jesús Armenta, Ciro Núñez, Nancy Visairo, Isabel Lázaro: An advanced energy management system for controlling the ultracapacitor discharge and improving the electric vehicle range, Journal of Power Sources, Volume 284, 15 June 2015.
14. DieselNet: https://www.dieselnet.com/standards/cycles/ece_eudc.php [25 january, 2015-10: 45AM].
15. Saponara S; Bove A; Baronti F; Roncella R; Saletti R; Dente D; Leonardi E; Marlia M; Taviani C: Thermal, electric and durability characterization of supercaps for energy back-up of automotive ECU, Industrial Electronics (ISIE), 2013 IEEE International Symposium.
16. Oliver Bohlen, Julia Kowal, Dirk Uwe Sauer: Ageing behaviour of electrochemical double layer capacitors: Part I. Experimental study and ageing model, Journal of Power Sources-Volume 172, Issue 1, 11 October 2007.
17. R. Kötz, P.W. Ruch, D. Cericola: Aging and failure mode of electrochemical double layer capacitors during accelerated constant load tests, Journal of Power Sources-Volume 195, Issue 3, 1 February 2010.

MDS^{3}C: Modified Digital Signature Scheme for Secure Communication

Gulista Khan, Bhumika Gupta and Kamal Kumar Gola

Abstract When it comes to security no one can be trusted, there may be situations, when sender's and receiver's authentication is required. Digital signature is used to provide the authentication to assure receiver about the message and its sender. Digital signature is an authentication mechanism which generates a unique code with the message, now this attached code (i.e., signature) is responsible for the validation of sender and message. As all know that digital signature provides authentication, message integrity, and non-repudiation services, but does not provide the confidentiality of data as well as signature which is most important during data transfer. This paper proposed a modified digital signature scheme for secure communication. This work includes the concept of public key encryption for secrecy of data. This work will reduce the well-known drawbacks of digital signature scheme. The aim of this technique is to provide the secure communication that includes the security for the data, private key, and digital signature.

Keywords Digital signature · Private key · Public key · Hash function · Prime numbers · Encryption and decryption

1 Introduction

Nowadays digital signature has the same valid importance as more traditional form of document. For software distribution and financial transaction, digital signatures are commonly used. It is a scheme using mathematical formulations for ensuring

Gulista Khan (✉) · K.K. Gola
Computer Science and Engineering, College of Engineering, TMU, Moradabad, India
e-mail: gulista.khan@gmail.com

K.K. Gola
e-mail: kkgolaa1503@gmail.com; kkgola1987@gmail.com

Bhumika Gupta
Computer Science and Engineering, GB Pant Engineering College, Pauri Garhwal, India
e-mail: bhumikamit6@gmail.com

© Springer Science+Business Media Singapore 2017

R. Singh and S. Choudhury (eds.), *Proceeding of International Conference on Intelligent Communication, Control and Devices*, Advances in Intelligent Systems and Computing 479, DOI 10.1007/978-981-10-1708-7_36

the verification of a document or document. A legal digital signature ensures the receiver that the document or message was sent by authenticated sender and not changed during transmission [1]. A digital signature having three phases, first is key generation algorithm, second is signing algorithm, and third is for verifying signature, that consists a message, public key, and a signature. Which is used to accept or rejects the message to prove the message authenticity [2]. Digital signatures are used widely in e-commerce applications, distribution of softwares, and banking applications [3].

1.1 Drawback of Digital Signature

There are some drawbacks associated with digital signature.

1. The private key must be secured because if someone get the key then he/she can use this key for the generation of digital signature and send to the receiver who will identify the message as correct.
2. In digital signature no one knows that whether the message is altered or the message is created using invalid private key. Sometime it may be happen that digital signature dose not verify with the public key, then the message will be consider as invalid and rejected by the receiver.
3. As we know digital signature provides authenticity but does not provide confidentiality.

2 Literature Review

In [3] the authors have proposed a modified RSA digital signature scheme for data confidentiality. In this work the authors used the two pair of keys. One of the sender and another of the receiver. To provide the authentication the sender used the private key of itself while to provide the confidentiality the sender used the public key of the receiver. In [4] the author has proposed a method to implement the public key cryptosystem. This algorithm is using factorization method of large numbers to secure transfer. This says if the method proves its acceptable security, then one cannot have to carry the keys. The encryption function of the proposed algorithm is the only function known to the two parties for communication. In [5] the author has proposed a new secure hash algorithm, which is based on fixed arrangement algorithm called Secure Hash Algorithm (SHA-192). Implementation results compares with the existing SHA-1 and it produces better results. In [6] the author has proposed ANSI X9.62 ECDSA here author explained its associated security issues. The main reason for using ECDSA is that there is no existing algorithm to solve the problem of elliptic curve discrete logarithm. This uses the full exponential

time to solve this problem. Expressively smaller parameters can be used in ECDSA. This takes full exponential time while RSA and DSA uses sub exponential time.

3 Algorithm

3.1 Algorithm Process

See Fig. 1.

3.2 Proposed Algorithm

Step-1 Key Generation Process at sender side

(a) Select a large prime number p
(b) Find the value of q where q should be a prime factor of $(p-1)$
(c) Sender calculates the value of g, where g is a public key at sender side
$g = h^{(p-1)/q} \bmod p$ where h is a number less than $(p-1)$ and $h^{(p-1)/q} \bmod p > 1$
(d) Calculate $n = p * q$
(e) Calculate the value of x, where x is a private key of the sender
$x = h^g \bmod q$ where $h < q$ and $0 < x < q$
(f) Calculate the value of y, where y is a public key of the sender
$y = g^x \bmod p$

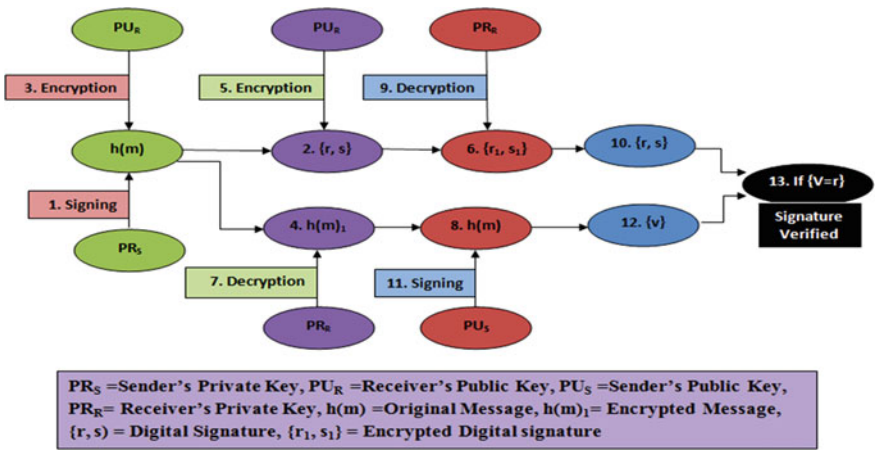


Fig. 1 Modified digital signature algorithm model

Step-2 Signing Process at sender side

(a) Select the value of $h(m)$ with condition $0 < h(m) < q$
(b) Calculate value of k with condition $1 < k < q$
$k = h(m)^x \bmod q$
(c) Calculate the value of r and s, where r and s are the signatures at sender side
$r = (g^k \bmod p) \bmod q$ and
$s = (((h(m)) + x * r)\ k^{-1}) \bmod q$

Step-3 Encryption Process at sender side

(a) Before sending the value of $h(m)$, r and s, encrypt these value using receiver's public key
$h(m)_1 = h(m)^e \bmod n$
$r_1 = r^e \bmod n$
$s_1 = s^e \bmod n$
(b) Now the encrypted values of $h(m)$, r and s will be sent to the receiver.

Step-4 Key Generation Process at receiver side same as RSA Public Key algorithm

Step-5 Decryption Process at receiver side

(a) First the receiver decrypts the values of $h(m)_1$, r_1 and s_1 using
$h(m) = h(m)_1^d \bmod n$
$r = r_1^d \bmod n$
$s = s_1^d \bmod n$

Step-6 Verifying Process at receiver side

(a) First the receiver checks that given condition for the value of r and s should be true.
$0 < r < q$ and $0 < s < q$ else reject the signature
(b) Calculate the value of t
$t = s^{-1} \bmod q$
(c) At last the receiver verifies the signature using given equation
$v = [(g^{h(m)} * y^r)^t \bmod p] \bmod q$
If $v = r$ then signature verified

4 Implementation

Step-1 Key Generation Process at sender side

(a) Select a large prime number $p = 23$
(b) Find the value of q where q should be a prime factor of $(p-1)$
$q = p-1 = 23-1 = 22$
$q = 11$

(c) Sender calculates the value of g where g is a public key at sender side
Let $h = 2$
$g = h^{(p-1)/q} \bmod p$
$g = 4$
(d) Calculate $n = p * q$
$n = 253$
(e) Calculate the value of x known as private key of the sender
$x = h^g \bmod q$ where $h < q$ and $0 < x < q$
$x = 2^4 \bmod 11$
$x = 5$
(f) Calculate the value of y where y is a public key of the sender
$y = g^x \bmod p$
$y = 12$

Step-2 Signing Process at sender side

(a) Select the value of $h(m)$ with condition $0 < h(m) < q$
let $h(m) = 8$
(b) Calculate value of k with condition $1 < k < q$
$k = h(m)^x \bmod q$
$k = 8^5 \bmod 11$
$k = 10$
(c) Calculate the value of r and s where r and s are the signatures at sender side
$r = (g^k \bmod p) \bmod q$
$r = 6$
$s = ((8 + 5 * 6)10^{-1}) \bmod 11$
$s * 10 = 38 \bmod 11$
$s = 6$

Step-3 Encryption Process at sender side

(a) Before sending the value of $h(m)$, r and s encrypts these value using receiver's public key
$h(m)_1 = 248$
$r_1 = r^e \bmod n$
$r_1 = 6^{13} \bmod 253$
$r_1 = 128$
$s_1 = s^e \bmod n$
$s_1 = 6^{13} \bmod 253$
$s_1 = 128$
(b) Now the encrypted values of $h(m)$, r and s will be sent to the receiver

Step-4 Key Generation Process at receiver side

(a) Public key (e, n)
(13,253)

(b) Private Key (d, n)
Private Key (17,253)

Step-5 Decryption Process at receiver side

(a) First the receiver decrypts the values of $h(m)_1$, r_1 and s_1 using
$h(m) = h(m)_1^d \bmod n$
$h(m) = 248^{17} \bmod 253$
$h(m) = 8$
$r = r_1^d \bmod n$
$r = 6$
$s = s_1^d \bmod n$
$s = 6$

Step-6 Verifying Process at receiver side

(a) First the receiver checks the condition for the value of r and s are true.
$0 < 6 < 11$ and $0 < 6 < 11$ condition is true
(b) Calculate the value of t
$t = s^{-1} \bmod q$
$t = 6^{-1} \bmod 11$
$t * 6 = 1 \bmod 11$
$t = 2$
(c) At last the receiver verifies the signature using given equation
$v = [(g^{h(m)} * y^r)^t \bmod p] \bmod q$
$v = [(4^8 * 12^6)^2 \bmod 23] \bmod 11$
$v = [((195689447424)^2 \bmod 23] \bmod 11$
$v = 6 \bmod 11$
$v = 6 = r$ Signature Verified

5 Conclusion

The digital signature algorithm proposed in this paper provides confidentiality as well as authentication, while regular digital signature algorithms only provide the authentication. Implementation of the proposed algorithm shows that the proposed technique provides better security to the private key and data as compared to existing digital signature algorithms. The key concept behind any effort in area of security is to provide the Confidentiality, Authenticity, and Message Integrity. The proposed algorithm fulfills all the given requirements in an efficient way. The proposed algorithm may not be effective in terms of time complexity for encryption or decryption but it will serve the main feature, i.e., security. In the existing scheme, there is no security for the private key generation and data, it only provides the user authentication, but the proposed techniques provides security to the private key generation as well as provide the security to the data and signature during transfer.

References

1. National Institute of Standards and Technology, Digital Signature Standard (DSS), Federal Information Processing Standards 186–3.
2. William Stallings, Cryptography and Network Security Principles and Practices, 4th Edition, Pearson Education.
3. Kamal Kr. Gola, Bhumika Gupta and Zubair Iqbal, "Modified RSA Digital Signature Scheme for Data confidentiality", International Journal of Computer Application, Volume-106, No. 13, November 2014.
4. R.L. Rivest, A. Shamir, and L. Adleman, "A Method for Obtaining Digital Signatures and Public-Key Cryptosystems", Magazine communications of the ACM, Volume 21, Issue 2, Page 120–126, Feb 1978.
5. Thulasimani Lakshmanan and Madheswaran Muthusamy, "A Novel Secure Hash Algorithm for Public Key Digital Signature Schemes", the International Arab Journal of Information Technology, Vol. 9, No. 3, May 2012.
6. Aqeel Khalique, Kuldip Singh Sandeep Sood, Implementation of Elliptic Curve Digital Signature Algorithm, International Journal of Computer Applications, May 2010.

Autonomous Operation of Wind-Battery Hybrid Power System with Intelligent Power Management Capability

Diwaker Pathak, Ankit Gupta, Rupendra Kumar Pachauri and Yogesh K. Chauhan

Abstract In this paper, a control scheme is proposed based on the fuzzy logic for a hybrid wind-battery power system under dynamic wind speed. The control scheme comprises three controllers such as blade pitch angle (BPA) control; voltage control and switching control. BPA control is utilized for constant wind turbine (WT) torque, voltage control maintains the voltage of the wind energy conversion system (WECS) at the reference voltage and switching control is used for switching between WECS and battery systems efficiently. The entire proposed system is implemented in MATLAB/Simulink. The overall system performance is estimated under dynamic wind speed in terms of WT torque, battery parameters, and duty ratio control of the buck/boost converter. The performance of overall system is found satisfactory under dynamic condition.

Keywords Wind turbine · Fuzzy logic · Permanent magnet synchronous generator · Blade pitch angle control · Battery system

1 Introduction

Renewable energy (RE) is generally represented as energy, which is composed from the sources that are naturally refilled etc. such as solar irradiation, wind, tides etc. [1]. Energy resources such as fossil fuels are depleting because of their high consumption. There is need to explore more energy sources [2]. In this context, wind energy is an economic source of energy for power generation. But the nature

Diwaker Pathak (✉) · Ankit Gupta · R.K. Pachauri · Y.K. Chauhan
Electrical Engineering Department (EED), School of Engineering,
Gautam Buddha University, Greater Noida 201312, India
e-mail: diwakergnit29@gmail.com

Ankit Gupta
e-mail: guptaankit299@gmail.com

R.K. Pachauri
e-mail: rupendra.gbu@gmail.com

© Springer Science+Business Media Singapore 2017

R. Singh and S. Choudhury (eds.), *Proceeding of International Conference on Intelligent Communication, Control and Devices*, Advances in Intelligent Systems and Computing 479, DOI 10.1007/978-981-10-1708-7_37

of wind speed is never constant [3]. In the proposed system a WECS integrated with battery system as a power backup source. The hybrid wind-battery system powered to the resistive load under dynamic condition for investigation.

In [4], the authors proposed a scheme for smooth wind power generation using Permanent Management Synchronous Generator (PMSG). In [5], the authors have developed the control scheme of WT operation by using BPA control. The authors in [6], proposed various maximum power point tracking for WT operations such as voltage, current, power, rotor speed, and BPA using PI controller. In [7], the authors have modeled an effective controller for smooth power generation under variable speed.

Based on the above literature review, the research addition of this research article is to integrate with battery system and investigate a hybrid WECS-battery system with a power management scheme under dynamic wind speed.

2 System Explanation

The proposed system is categorized into four foremost parts (a) WECS (i) WT (ii) PMSG, (b) Power electronics interface (i) Rectifier (ii) Buck/boost converter (c) Power management scheme (i) BPA controller (ii) Voltage controller (iii) Switching controller (d) Resistive load. The layout of proposed system is shown in Fig. 1.

3 Mathematical Modeling of WT and PMSG

The mechanical power (P_m) of WT system described by Eq. (1) as

$$P_m = \frac{1}{2}\rho A C_p(\lambda, \beta) V_w^3 \tag{1}$$

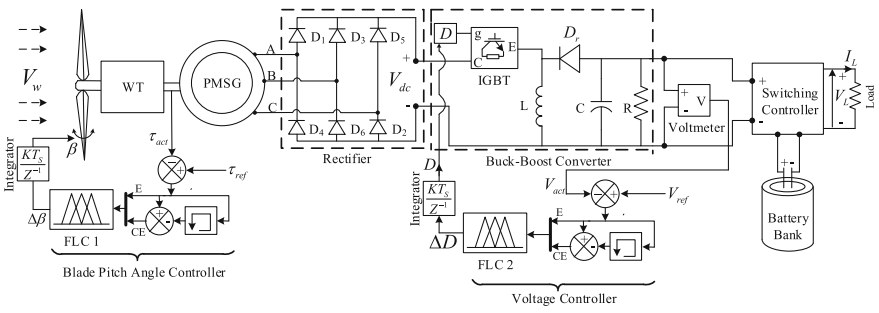


Fig. 1 Wind-battery hybrid power system

where ρ, A, $V_{w,}$ and C_p are represented for air density, blade swept area, wind speed, and performance coefficient respectively.

The C_p can be evaluated by Eq. (2) as

$$C_p(\lambda,\beta) = \mu_1\left(\frac{\mu_2}{\lambda_i} - \mu_3\beta - \mu_4\right)e^{\frac{-\mu_5}{\lambda_i}} + \mu_6\lambda, \frac{1}{\lambda_i} = \frac{1}{\lambda + 0.08\beta} - \frac{0.035}{\beta^3 + 1} \tag{2}$$

where $\mu_1, \mu_2 \ldots \mu_6$ are coefficients, β is BPA and λ_i is initial tip speed ratio. The tip speed ratio is calculated as [8],

$$\lambda = \frac{V_{\text{tip}}}{V_w} = \frac{\omega_r R}{V_w} \tag{3}$$

The current equations along d and q axis of PMSG is given by Eq. (4) [8] as,

$$\frac{\text{di}_q}{\text{dt}} = \frac{(-R_s i_q + \omega_e(L_q + L_l)i_d + u_q)}{L_q + L_l}, \frac{\text{di}_d}{\text{dt}} = \frac{(-R_s i_d + \omega_e(L_q + L_l)i_q + u_d)}{L_d + L_l} \tag{4}$$

where ω_r is the rotor speed of WT. R_s is stator resistance, L_q and L_d are the inductances along d and q axis and L_l represents the leakage inductance. Electrical speed is shown as ω_e of PMSG system as shown in Eq. (5) as

$$\omega_e = p\omega_g \tag{5}$$

The electromagnetic (EM) torque equation of PMSG are shown in Eq. (6) as

$$\tau_{em} = (3/2)p((L_d - L_l)i_d i_q + i_q\phi_f) \tag{6}$$

where, i_q and i_d are the currents of PMSG along d and q axis, p is the number of pole pairs, Φ_f is the flux of field, and τ_{em} is the EM torque of the PMSG.

4 Intelligent Power Management Scheme

The proposed intelligent power management scheme consists three controllers namely (a) BPA controller, (b) Voltage controller (c) Switching controller.

4.1 Blade Pitch Angle Controller

BPA has been controlled with the help of BPA controller by controlling the torque generated by WT. The proposed controller is based on fuzzy logic phenomenon.

Input is the error (E) and change in error (CE) between actual torque (τ_{act}) and reference torque (τ_{ref}) and change in BPA ($\Delta\beta$) is the output of the controller.

Components of a fuzzy logic controller (FLC) are described in Fig. 2,

E and CE that are the inputs of FLC are given in Eq. (7) as

$$E(k) = \tau_{ref}(k) - \tau_{act}(k),\ CE(k) = E(k) - E(k-1) \tag{7}$$

The rule base for FLC is given in Table 1.

The input and output membership functions are shown in Fig. 3a–c.

4.2 Voltage Controller

Voltage controller is also based on fuzzy logic, which is used to control the output voltage of the buck/boost converter (V_{DC}) to achieve the fixed voltage level at load side. The rule base and membership functions used in this scheme are similar to BPA controller. Input is error (E) and change in error (CE) between actual voltage (V_{act}) of the buck/boost converter and a reference voltage (V_{ref}), output is change in duty cycle (ΔD).

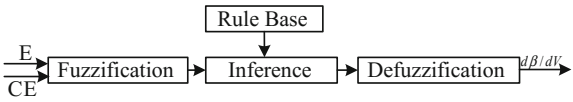


Fig. 2 Schematic diagram of FLC

Table 1 Rule base of FLC

CE	E				
	NL	NS	ZE	PS	PL
NL	NL	NL	NS	NS	ZE
NS	NL	NS	NS	ZE	PS
ZE	NS	NS	ZE	PS	PS
PS	NS	ZE	PS	PS	PL
PL	ZE	PS	PS	PL	PL

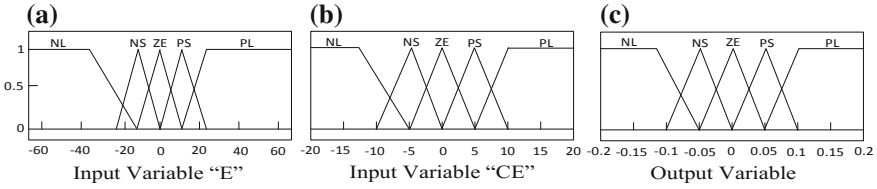


Fig. 3 **a–c** Membership functions of FLC

4.3 Switching Controller

Switching controller is designed to deliver the uninterrupted power supply to the resistive load. The proposed controller senses the operating condition and controls the switches ON/OFF condition.

5 Results and Discussion

The wind speed is varied from 9 to 10 m/s, as presented in Fig. 4a. The behavior of wind speed is given to WT system with FLC for BPA and voltage controlling. The transient response of intelligent power management scheme is shown in Figs. 4, 5, 6, 7 and 8.

In this work, wind speed incident on WT, as shown in Fig. 4a, is step changed in the range 9–10 m/s to determine the response of the system. The transient response is shown in Figs. 4b–c, 5a–c, 6a–b, 7a–b and 8a–b in terms of β, τ_{WT}, PMSG parameters (I_{abc}, ω_r, τ_{em}), buck/boost converter parameters (D, V_{DC}), switching

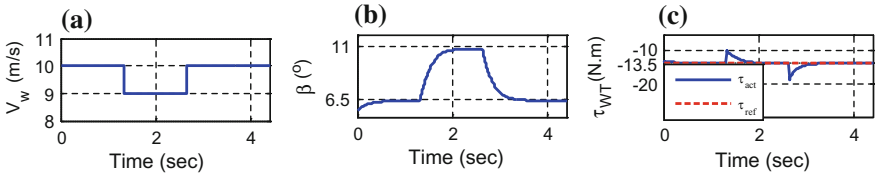


Fig. 4 **a–c** Wind speed variation and WECS parameters (β, τ_{WT}). **a** Wind speed (m/sec). **b** BPA (°). **c** WT torque (N.m)

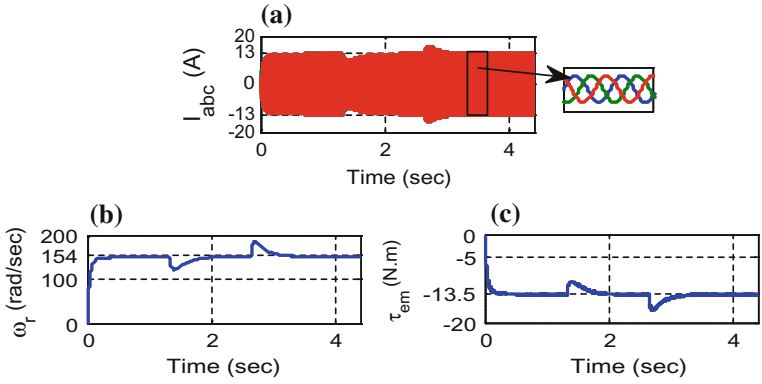


Fig. 5 **a–c** PMSG performance. **a** Stator currents (Amp). **b** Rotor speed (rad/sec). **c** Electromagnetic torque (N.m)

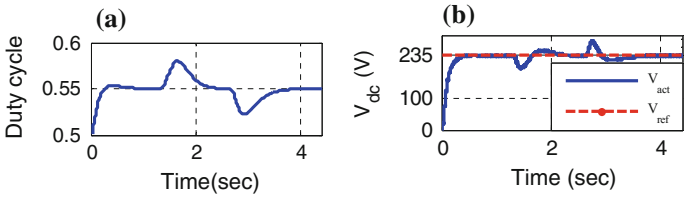


Fig. 6 **a–b** DC-DC Buck/boost converter performance. **a** Duty cycle. **b** Output voltage of the DC-DC buck/boost converter

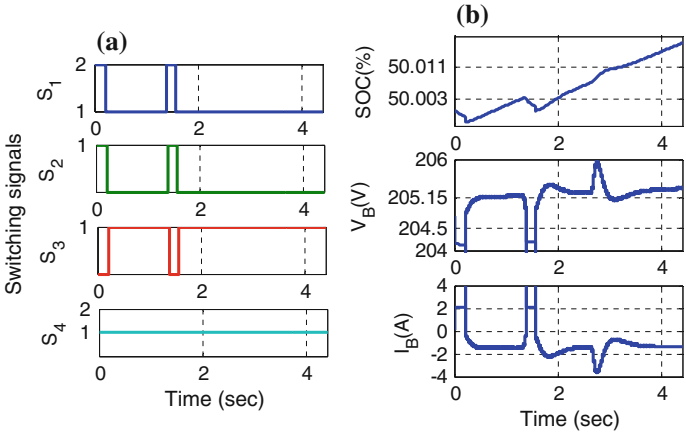


Fig. 7 **a–b** Battery performance. **a** Switching signals of battery. **b** Parameters of battery

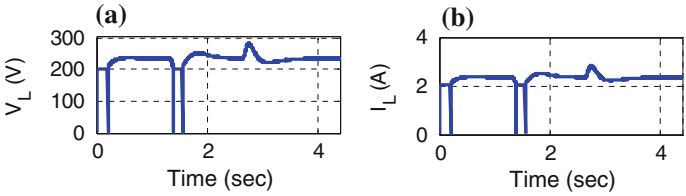


Fig. 8 **a–b** Performance of load parameters. **a** Load voltage (V). **b** Load current (A)

signals (S_1, S_2, S_3, S_4), battery parameters (SOC, V_B, I_B), and load parameters (V_L, I_L) respectively. From above stated figures it is observed that the change in wind speed is compensated by BPA and voltage controller using β and duty cycle. From Fig. 7a it can be concluded that the switching of the sources (WECS and battery) has been successfully achieved. The comprehensive study of the system constraints is depicted in Table 2.

Table 2 System parameters

	Time	β	τ_{WT}	D	V_{DC}	S_1	S_2	S_3	S_4	SOC	V_L	I_L
Steady state value	t = 0 s	6.5	13.5	0.55	235	0	1	0	1	50	200	2
	t = 1.3 s	10.75	13.5	0.55	235	1	0	1	1	50.003	235	2.2
	t = 2.6 s	6.5	13.5	0.55	235	1	0	1	1	50.011	235	2.2
Settling time (sec)	t = 0 s	0.8	0.3	0.8	0.3	–	–	–	–	–	0.3	0.3
	t = 1.3 s	0.8	0.68	1.3	1.4	–	–	–	–	–	0.04	0.04
	t = 2.6 s	1.1	0.4	0.6	1	–	–	–	–	–	0.4	0.4

6 Conclusion

A study of WT-based WECS for constant power generation has been carried out. The extensive simulation of WT system along with the system components has been done. The FLC-based BPA controller is designed to obtain the constant torque of WT. Another FLC scheme is also used to control the duty ratio of DC-DC buck/boost converter to control the voltage for resistive load. Furthermore, an autonomous power management scheme is implemented to control the switches for power flow among the energy sources. The transient analysis of simulated model has been done and it is found satisfactory.

Appendix

Blade radius (R) = 4.5 m, Number of blades = 3, Wind speed (V_w) = 9–10 m/s, Air density (ρ) = 1.2 kg/m^{3,} Power Coefficient (C_p) = 0.45, μ_1 = 0.5176, μ_2 = *116,* μ_3 = 4, μ_4 = *5,* μ_5, = *21,* μ_6 = *0.0068,* Stator Phase Resistance (R_s) = 0.4250 O, Inertia (J) = 0.001469 kg m^2, Inductance (L_d, L_q) = 0.0084 H, Pole pairs = 4.

References

1. Pachauri, R. K., Chauhan Y. K.: Assessment of Wind Energy Technology Potential in Indian Context: International Journal of Renewable Energy and Research, 2 (2012) 773–780
2. Kumar, H., Gupta, A., Pachauri, R. K., Chauhan, Y. K.: PI/FL Based Blade Pitch Angle Control for Wind Turbine used in Wind Energy Conversion System. In: IEEE Conference on Recent Developments in Control, Automation and Power Engineering, (2015) 15–20
3. Pachauri, R. K., Chauhan, Y. K.: Mechanical Control Methods in Wind Turbine Operations for Power Generation. Journal of Automation and Control Engineering, 2 (2014) 215–220
4. Uehara, A., Pratap A., Goya, T., Senjyu T., Yona, A., Urasaki, N., Funabashi T.: A Coordinated Control Method to Smooth Wind Power Fluctuations of a PMSG-Based WECS. IEEE Transactions on Energy Conversion, 26 (2011) 550–558

5. Senjyu, T., Sakamoto, R., Urasaki, N., Funabashi, T., Fujita, H., Sekine, H.: Output Power Leveling of Wind Turbine Generator for all Operating Regions by Pitch Angle Control. IEEE Transactions on Energy Conversion, 21 (2006) 467–475
6. Abdullah, M. A., Yatim, A. H. M., Tan, C. W., Saidur, R.: Review of Maximum Power Point Tracking Algorithms for Wind Energy Systems. Renewable and Sustainable Energy Reviews, 16 (2012) 3220–3227
7. Luo, C., Banakar, H., Shen, B., Ooi, B. T.: Strategies to Smooth Wind Power Fluctuations of Wind Turbine Generator. IEEE Transactions on Energy Conversion, 22 (2007) 341–349
8. Pachauri, R. K., Kumar, H., Gupta, A., Chauhan, Y. K.: Pitch Angle Controlling of Wind Turbine System Using Proportional-Integral/Fuzzy Logic Controller. In: International Conference on Advanced Computing, Networking and Informatics, 43 (2015) 55–63

Performance Analysis of a Novel Text Watermarking Technique for Devanagari Text

Nitin Namdeo Patil and Jayantrao Bhaurao Patil

Abstract Digital text watermarking is a challenging task which attempts to secure all types of digital text content. Specifically implementation of linguistic text watermarking experiences more difficulties because of variation in the appearance of the text information of different natural languages. This paper presents extended work of previously implemented Marathi language text watermarking technique. Here we test for performance analysis of the proposed technique. We further investigate this technique against different possible text watermarking attacks using standard corpus of varying lengths. Our aim is to verify whether the technique predominates the essential properties of typical text watermarking system. The constructive experimental outcomes confirm the effectiveness and the robustness of the proposed technique.

Keywords Natural language · Authorship · Certified Authority · Sarvanam · Robust

1 Introduction

The boundless world of Internet has afforded the digital format to numerous authors from diversified domains to express their views and knowledge. These authors' valuable data can be easily written and shared to intended readers in digital format rather than typical paper format. This digital format gives ease of editing, formatting, and quick sharing of the information. At the same time, it has the threat of sharing, distributing, coping, or reproducing of the genuine author content illegitimately. Compared to other existing solutions for information hiding of digital data

N.N. Patil (✉) · J.B. Patil
Department of Computer Engineering,
R. C. Patel Institute of Technology, Shirpur 425405, India
e-mail: er_nitinpatil@rediffmail.com

J.B. Patil
e-mail: jbpatil@hotmail.com

© Springer Science+Business Media Singapore 2017

R. Singh and S. Choudhury (eds.), *Proceeding of International Conference on Intelligent Communication, Control and Devices*, Advances in Intelligent Systems and Computing 479, DOI 10.1007/978-981-10-1708-7_38

like steganography and cryptography, watermarking is recognized as the appropriate solution amongst all. The basic characteristics and implementation methodology make the digital watermarking as the best suitable method against different security attacks. A watermarking technique has some basic properties like robustness, capacity, security, and imperceptibility [1, 2]. The watermarking process basically embeds watermark into the digital signal. This digital signal can be any type of digital media like image, audio, video, or text. The digital text watermarking is the process of embedding the watermark in the text to provide unique identity to the authentic user. The prime objective is to protect the authorship of the original author of the text information. An unauthorized user can attempt to reuse, redistribute some or all the text information of an authorized user and also can claim the authorship of the data. Our research work specifically concentrates on digital text watermarking. In this context, we have studied certain linguistic text watermarking techniques which claim to protect text information of various languages like Arabic, English, Chinese, Turkish, German, Korean, and Marathi [3–9]. Each of these uses the specialized feature(s) of respective language to implement the watermarking technique. Numerous types of Marathi text like literature, teaching-learning material, financial, spiritual knowledge, dictionaries, press articles, blogs, and many other are widely available in digital format over the Internet. In our previous paper, we demonstrated a novel text watermarking technique for Devanagari (Marathi) language. In this technique, we appropriately used the 'sarvanam' (pronoun) as the key feature of Marathi language text to generate the required watermark. We focused on protecting authorship of Marathi language text [9]. The experimental results revealed category-wise variation in occurrences of sarvanam for all considered text categories. These observations can be further used to study different expected features like the accuracy of the implemented technique. Also, it is expected to investigate the behavior of the technique in case of different possible text attacks. It should be evaluated to confirm whether the technique meets the essential basic important characteristics of a text watermarking technique or not.

2 Previous Work

The necessity of protection to various digital content which is explicitly accessible over the Internet encourages the need for a strong security mechanism to make them secure against different types of probable threats such as illegal copying, redistribution, reproduction, fingerprinting, tampering, and authentication. This led to the development of different watermarking techniques for image, video, audio, and text in last few years as prevention to the security issues.

As our aim is to investigate text watermarking methods, we explored several approaches accomplishing the security requirements. Basically, text watermarking can be normally classified as image-based, syntactic, semantic, and structural approach [10]. We further detail on linguistic watermarking which uses language specific feature(s) for effective implementation.

Gutub et al. proposed the watermarking method for Arabic text focusing on the secrecy of the key used. 'Kashida,' an extendable character is used to symbolize the watermarking bits. These special characters are used twice in these methods. The first time they are used to create confusion which results in security assurance. Second, some particular 'kashidas' are used in the standard watermarking process [3].

Alginahi et al. developed enhanced 'kashida'-based Arabic text watermarking method which places the 'kashidas' in between typical characters of words subjected to meet some condition in the generation of watermark [11].

Kim et al. introduced an enhanced word-shift algorithm based on classification and inter-word space statistics. This algorithm considers input text as segmented into words, lines, and pages. Watermark generation is dependent on satisfying predefined condition by some statistics. This statistics is formulated related to the inter-word spaces in between the segments [12].

Zhang et al. effectively used special properties of MS-Word document's word objects to hide the information. The embedding phase includes encryption, grouping, and packing of the genuine author and legal user's information circularly in the special attribute of word objects [5].

Halvani et al. used lexical and syntactic constructs of German text to develop four methods for German text watermarking. They fended off complicated Natural Language Processing. Instead, the authors effectively used some grammar rules for the proposed implementation. They claimed a good percentage of preserving original and the watermarked text [7].

Kim used syntactic analysis to propose a method which forms a syntactic dependency tree for the input Korean text. The watermark bits are compared with movement bit of the target constituent. If they do not overlap then the syntactic constituent is the part of the modified syntactic tree. The authors claimed the method better than previous systems but lacking in the capacity of information hiding [8].

Meral et al. explored agglutinative nature of Turkish language to develop syntax-based natural language watermarking approach. The Turkish language contents are having free word order and the wide range of morphosyntactic structures. The syntactic tree is built by converting a marked text. This tree uses coding of syntactic hierarchies and functional dependencies. Then watermarking software executes to exclude semantics drops. Appropriate security is insured by key controlled randomization and including void watermark [6].

Jalil et al. utilized structural components of text contents to implement the English language text watermarking. While implementing no alterations are done in the text but the features of the text are effectively utilized for creating watermark. The authors claim the algorithm to be robust, secure, and capable to protect against random tampering attacks [13].

Mir used natural language (English) rules such as verbs, articles, and prepositions to demonstrate a watermarking technique for web text [4].

3 Proposed Work

In our previous attempt, we proposed a novel technique including embedded algorithm and extraction algorithm. We effectively used 'Sarvanam' as the key construct of Marathi language. Although Marathi is a twisted language, our technique successfully preserved the meaning of original text throughout the implementation.

In embedding phase, the selected input text from the original author is provided a unique author id along with a security phrase and proper timestamping. The algorithm combines all the sarvanam, author id, and timestamp to generate a common string. Advanced Encryption Algorithm (AES) is applied to this string to produce encrypted string. The encrypted string is used as the watermark to embed into the input text.

3.1 The Embedding Algorithm

In this step, the embedding algorithm is designed to generate the required watermark to be embedded along with the necessary security measures.

1. Input Text and author name.
2. Generate Author_ID from A to Z, a to z, 0 to 9 of length equal to length of author name.
3. Provide file name, security phrase, and timestamp.
4. Count occurrence of Marathi sarvanam. Define and assign count to respective variables.
5. Repeat Step 4 for all occurrences of Marathi sarvanam.
6. Concatenate Author_ID and watermark timestamp to Marathi sarvanam.
7. Apply AES to raw string to generate encrypted key with security phrase.
8. Output protected file with Author key (watermark).

At the extraction stage, it is required to separate original text from watermark out of concatenated string. For this decryption is applied first then watermark gets disembodied from the string. This extraction is conducted by Certified Authority (CA) which is trusted third party [14]. CA acts to assure the authentication mechanism. In our implementation CA can register genuine user input file and provide unique authorization key and timestamping to the user. All this information is maintained along with originally created file as a unique record of the original author. In the case of conflict related to authorship, CA plays a vital role to verify the original user of any text document by performing the crosscheck with the record maintained for each registered user document. Table 1 represents some sample entries which are kept as records for each individual author's unique authorization claim.

Table 1 Sample entries for certified authority records

Author	Watermark in protected File	Date and time watermarking	Unique key for each author by CA	Watermarked file
Nitin	CNOotTRGhszAPveSGgby YRQVGX6Ule + 7xOFfzlIS6RVc2z6	31 Aug 2015 14:41:58:000	4e0b6c79	File1.pdf
Nitin Patil	o06akTmNB6W66DPb3mw SZJNieflMNAr6bF12DkIFzhCEis E5DOORxmXcwQpHtsVoI	27 Aug 2015 13:07:44:000	KeyByCALOL123	File2.pdf

3.2 The Extraction Algorithm

1. Input protected file (containing watermark).
2. Provide Author_ID, security phrase and Timestamp sequentially.
3. Separate encrypted watermark and original text from protected file.
4. Get raw string from encrypted watermark stored in protected file Applying AES and security phrase to raw string.
5. Isolate Marathi sarvanam and create temp string from original test.
6. Repeat Step 4 for all occurrences of Marathi sarvanam.
7. Concatenate Author_ID and watermark timestamp to Marathi sarvanam.
8. Compare temp string created from original text and raw string generated from watermark.
9. If match found, "You are Genuine Author of this Content!" else "You are not Author of this Content!"

As we already have demonstrated the above algorithms in our previous work [9], we here discuss the validation of our implementation. We used the corpus afforded by Center for Indian Language Technology (CFILT), Indian Institute of Technology, Bombay (IITB) and Technology Development for Indian Languages (TDIL). Our goal is to test this corpus against different possible attacks on the text namely; insertion, deletion, and combined attack. For this, we form four categories of the corpus. These four categories are: Category 1, Category 2, Category 3 and Category 4 which hold text with word count less than 100, in between 100 and 500, less than 1000 but greater than 500, and in between 1000 and 5000, respectively. We evaluated all three attacks on all these four categories.

4 Experimental Results and Discussion

The experimental results are expected to confirm whether our proposed technique fulfills the essential characteristics of text watermarking technique. Moreover, we test the technique against different possible attacks on text data. In this section, we

discuss the results obtained by performing text attacks on the selected corpus of CFILT and TDIL [15]. Table 2 summarizes the attack analysis.

In Table 2, the insertion-deletion and combined attacks are enforced on the considered four categories at localized and randomized location in text samples. In localized insertion, we can observe considerably good percentage recovery for all text categories. Besides large size text categories, we can observe the best percentage recovery of the watermark. In case of dispersed insertion, as the volume of text category increased the percentage retrieving accuracy also increases. We can confirm average recovery of watermark for all the four categories. For the deletion attack when it is localized deletion, the general observation is that the smaller volume text categories are more vulnerable they are for deletion attack compared to larger volume text categories. Whereas in dispersed deletion attack more the word count of the text category better is the percentage recovery of the watermark. Here for a very large size of sample text, the performance of retrieving accuracy is the best.

All the above observations are quite promising to substantiate the four most important characteristics of text watermarking specifically robustness, security, capacity, and imperceptibility. The encouraging results with a greater percentage of retrieving watermarks confirm the robustness of the technique. The effective implementation justifies that the watermark, its existence, and carrying media remain covert. None of the authorized entity can be able to detect the presence of watermark and its details. This meets the security property of text watermarking. The expected upper limit watermark length is quite high in our implementation so the capacity of the technique is sufficient enough. The technique also supports imperceptibility property as the watermark is not observed by the viewer and it does not alter the meaning of the text content. The watermarked file and the original file are indistinguishable in appearance.

Table 2 Attack analysis for different text categories

Attack type		Localized attack			Dispersed attack		
Attack (%)		5	10	30	5	10	30
Insertion attack	Category 1	95.9	95.8	97	95.2	94.5	96.4
	Category 2	94.7	96.4	97	95.7	96.5	97.2
	Category 3	96.6	98.2	97.2	95.5	96.8	97.2
	Category 4	97.8	98.1	97.4	98.8	97.2	98.1
Deletion attack	Category 1	96	96.5	97.4	95.6	96.8	95.2
	Category 2	96.6	96.6	97.4	96.7	96.9	95.3
	Category 3	97.7	96.6	98.1	96.8	97.1	96.7
	Category 4	98.8	98.2	98.7	97.1	97.4	96.8
Combined attack	Category 1	95.35	96.2	97.2	95.65	95.8	95.85
	Category 2	96.6	96.45	97.4	96.1	96.85	96.2
	Category 3	96.8	97.4	97.55	96.15	96.95	96.95
	Category 4	98.3	98.15	97.95	98	97	97.45

There cannot be the direct comparison of the results of the proposed technique with other existing techniques due to different implementation approaches. We compare the results of our experiments with results produced by Jalil et al. [13] for English text watermarking and we can comment that our technique is comparatively better.

The following graphs in Figs. 1 and 2 demonstrate percentage accuracy of retrieved watermarks for different categories of text variable lengths. These graphical illustrations of the experimental results also validate that watermark retrieving accuracy greatly depends upon the size of the sample text and the type of attack. This conclusion is valid for 5, 10, and 30 % attacks on the selected text samples, respectively.

5 Conclusion

In recent decades, the rapid digitalization of text information has also caused security threats to copyrights of original authors. In this paper, we have successfully conducted performance analysis of novel text watermarking technique for Marathi text. The discussed technique is found to be the most suitable watermarking technique. The testing was done using standard corpus. The technique incorporates all the required important properties of the text watermarking. It can be further concluded that it has outstanding watermark retrieving ability in probable attack scenarios.

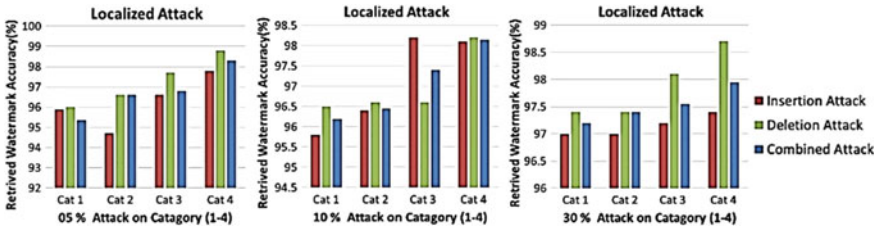


Fig. 1 Localized attack (5, 10 and 30 %) on Marathi language text

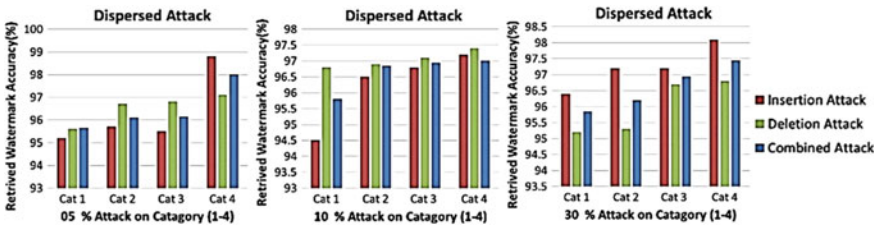


Fig. 2 Dispersed attack (5, 10 and 30 %) on Marathi language text

Acknowledgments We the authors of this paper express our sincere thanks to Government of Maharashtra (India) and North Maharashtra University, Jalgaon (M. S.) for providing funding and resources to accomplish this work under the scheme 'Research Grant Assistance for Science & Technology Projects (RGSTC).'

We are thankful to 'Indian Institute of Technology, Bombay' (IITB) and also to 'Technology Development for Indian Languages' (TDIL) Programme initiated by the Department of Electronics & Information Technology (DeitY), Ministry of Communication & Information Technology (MC&IT), Govt. of India for providing valuable resources of Marathi Language corpus to experiment with our proposed technique and to evaluate the experimental results.

References

1. F. A. P. Petitcolas, R. Anderson, and M. G. Kuhn, "Information hiding - A survey", Proc. of the IEEE, 1999, pp. 1062–1077.
2. F. Hartung, and M. Kutter, "Multimedia watermarking techniques", Proc. of the IEEE, 1999, pp. 1079–1107.
3. Adnan Gutub, Fahd Al-Haidari, Khalid Al-Kahsah, and Jameel Hamodi, "e-Text Watermarking: Utilizing 'Kashida' Extensions in Arabic Language Electronic Writing", Journal of Emerging Technologies in Web Intelligence (JETWI), 2010, pp. 48–55.
4. Nighat Mir, "Robust Techniques of Web Watermarking Using Verbs, Articles and Prepositions", International Journal of Computer Science and Information Security, Vol. 9, No. 2, 2011, pp. 248–252.
5. Yingli Zhang, and Huaiqing Qin, "A Novel Robust Text Watermarking For Word Document", 3rd International Congress on Image and Signal Processing, 2010 pp. 38–42.
6. Hasan Mesut Meral, Bulent Sankur, A. Sumru Ozsoy, Tunga Gungor, and Emre Sevinç. 2009. Natural language watermarking via morphosyntactic alterations. *Computer. Speech Lang.* 23, 1 (January 2009), 107–125.
7. Oren Halvani, Martin Steinebach, Patrick Wolf, and Ralf Zimmermann, Natural language watermarking for german texts. In *Proceedings of the first ACM workshop on Information hiding and multimedia security* (IH&MMSec '13). ACM, New York, NY, USA, 2013, pp. 193–202.
8. Mi-Young Kim. Text watermarking by syntactic analysis. In *Proceedings of the 12th WSEAS international conference on Computers* (ICCOMP'08), World Scientific and Engineering Academy and Society (WSEAS), USA, 2008, pp. 904–909.
9. Nitin N. Patil and J. B. Patil, "Implementation of a Novel Watermarking Technique for Devanagari Text", International Journal of Information and Electronics Engineering, Vol. 5, No. 5, 2015, pp. 353–355.
10. Jalil, Z., and Mirza, A.M., and Sabir, M., "Content based Zero-Watermarking Algorithm for Authentication of Text Documents," International Journal of Computer Science and Information Security, Vol. 7, No. 2,2010, pp. 212–217.
11. Alginahi, Yasser M., Muhammad N. Kabir, & Omar Tayan, (2014) "An Enhanced Kashida-Based Watermarking Approach for Increased Protection in Arabic Text-Documents Based on Frequency Recurrence of Characters", International Journal of Computer and Electrical Engineering, Boston, London,vol.6,2014, pp. 381–392.
12. Young-Won Kim, Kyung-Ae Moon, and Il-Seok Oh. 2003. A Text Watermarking Algorithm based on Word Classification and Inter-word Space Statistics. In Proceedings of the Seventh International Conference on Document Analysis and Recognition - Volume 2 (ICDAR '03), Vol. 2. IEEE Computer Society, Washington, DC, USA,2003, 775.

13. Jalil, Z.; Mirza, A.M.; Iqbal, T., "A zero-watermarking algorithm for text documents based on structural components," in Information and Emerging Technologies (ICIET), 2010 International Conference on, vol., no., 2010, pp. 1–5, doi:10.1109/ICIET.2010.5625705.
14. Ministry of Law, Justice and Company Affairs (Legislative Department), The Information Technology Act, New Delhi, Vol. 21 of 2000, 2000.
15. Technology Development for Indian Languages Programme [Online] Available: http://tdil.mit.gov.in/.

Evaluation of Entropy-Based Segmentation Techniques for Automated Skin Disease Detection

Ishita Bhakta and Santanu Phadikar

Abstract Image segmentation is a crucial part of medical imaging technology. Threshold-based image segmentation is very effective for medical images. A good segmentation helps in correct diagnosis. In this paper, entropy-based thresholding is used for automatic segmentation of hypo and hyperpigmented skin disease. Here threshold values are selected based on Shannon and Gini entropy. A comparison study with Otsu and Fuzzy C-Means (FCM) method is carried out based on rand index (RI) to prove efficiency of entropy-based thresholding. The rand index value indicates that Gini entropy-based thresholding is the best choice for hypo and hyperpigmented skin diseases segmentation.

Keywords Image segmentation · Shannon entropy · Gini entropy

1 Introduction

Automation of skin disease diagnosis is an interesting field of medical imaging technology. There are four steps in an automated skin disease detection system, e.g., image acquisition cum preprocessing, segmentation, feature extraction, and classification. Image preprocessing is required to enhance the color information, contrast of the image, and remove artifact and noise. For correct diagnosis diseased area should be detected accurately and automatically in such an automated system. Image segmentation is used to separate the diseased area and normal skin. Change of skin disease color according to skin types, depressed and raised surface of skin disease, irregular boundaries, patchy skin disease, and various types of shape and size make segmentation procedure more complex. Several segmentation methods

Ishita Bhakta (✉) · Santanu Phadikar
Department of Computer Science and Engineering, West Bengal University of Technology, BF 142 Salt Lake Sector 1, Kolkata, India
e-mail: ishita.official@gmail.com

Santanu Phadikar
e-mail: sphadikar@yahoo.com

© Springer Science+Business Media Singapore 2017

R. Singh and S. Choudhury (eds.), *Proceeding of International Conference on Intelligent Communication, Control and Devices*, Advances in Intelligent Systems and Computing 479, DOI 10.1007/978-981-10-1708-7_39

are proposed in literature to overcome these problems. They are broadly categorized into three types, threshold-based, edge-based, and region-based segmentation. Otsu is a simple threshold-based segmentation approach used in literature [1, 2]. It causes a partial loss of image information by considering probability distribution of two regions separately instead of global probability distribution of image. Gradient vector flow is an example of edge-based segmentation method [3]. This method detects false edges when there is a smooth transition between normal skin and infected region or artifacts in boundary of diseased area. Region-based method like adaptive snake (AS), level set method of Chan et al. (C-LS), and expectation-maximization level set (EM-LS) [3] have also been used for segmentation of skin diseases in the literature. But all these methods have high computational complexity and require two initial mouse clicks on infected region for segmentation which is not effective for an automated system. Fuzzy C-means (FCM) and K-means are other two region-based segmentation approaches used in [2] to track diseased area. Main disadvantages of FCM and k-means are large computation time and high sensitivity to noise. For K-means segmentation method, value of k should be known which is very difficult in case of skin disease automation system. To overcome all these problems, we have used entropy-based thresholding approach for segmentation of hypo- and hyperpigmented skin disease in this paper. Entropy-based method has the following advantages: easy implementation, entropy not only includes color information but also considers texture of the diseased area; entropy maximizes the degree of homogeneity of diseased region and fast computation. In this paper, the threshold value is calculated using two different entropy measures like Shannon [4] and Gini [5]. Hypo- and hyperpigmented images are also segmented using Otsu and FCM method for the performance analysis with entropy-based methods. An objective evaluation of entropy-based methods is carried out based on rand index. Gini index is mainly used to measure degree of inequality. At the border of pigmented skin disease degree of inequality is high so Gini index can detect the border efficiently. The purpose of this work is to find out which entropy measure performs better for hypo- and hyperpigmented skin disease.

The rest of the paper is organized as follows: Sect. 2 gives the details of preprocessing of acquired images and proposed image segmentation technique using entropy thresholding method, Sect. 3 discusses the results and gives an objective evaluation of used techniques and finally Sect. 4 concludes the paper.

2 Proposed Method

This section provides the details of proposed methodology of this study. First subsection gives an overview of image acquisition and preprocessing and next section details out the entropy calculation, segmentation algorithm, and advantages of entropy-based segmentation.

2.1 Image Acquisition and Preprocessing

Some images are collected from a consultant dermatologist at Haldia Dock Complex Hospital, some are captured using a digital camera of 20.1 megapixel with CCD sensor and rests of the images are taken from dermis [6] and dermnet [7] database. Here five different preprocessing steps are applied on images—remove hair from diseased area using dullRazor software [8], convert the RGB image to grayscale as only intensity values are required for further processing, adjust illumination of images to avoid over and under segmentation due to wrong illumination, sharpening to get detailed shape of diseased area, and remove noise using median filter.

2.2 Segmentation Using Entropy-Based Method

Threshold-based segmentation is one of the best choice for any type of medical images. In this paper threshold is chosen using entropy calculation based on information theory. Two types of entropy calculation (Gini and Shannon) are used here to measure the uniformity of pixel characteristics of disease images. Calculated threshold value is applied on hypo- and hyperpigmented skin disease images and result is carried out and discussed. Entropy selects intensity level with maximum information content which provides correct segmentation. For hypo- and hyperpigmented skin disease entropy-based segmentation is best choice as it is easy to compute, not time consuming and has low complexity. Equations (1) and (2) represent the formula of Shannon and Gini entropy calculation, respectively.

Shannon entropy is defined by

$$H_s = -\sum p(x) \log_2 p(x), \tag{1}$$

where $p(x)$ is the probability of an event occurs.

Gini index is used to measure information gain. It is defined as

$$G(T) = 1 - \sum_{j=1}^{n} p_j^2, \tag{2}$$

where T denotes dataset, n = number of classes from which datasets are taken, p_j is the relative frequency of class j in dataset T. The general algorithm of calculating threshold using these two types of entropy calculation is described in Algorithm 1.

```
Algorithm 1.
  1. Read Image and Convert the image into grayscale im-
  age.
  2. Calculate image size, histogram and normalize it.
  3. for i = 1 to 256
        Calculate cumulative distribution function.
        for j = 1 to i
            Calculate class 1 entropy
        end
        for k = (i+1) to 256
           Calculate class 2 entropy
        end
     end
  4. Calculate entropy.
  5. Threshold = intensity level with maximum entropy.
```

3 Results and Discussion

This section discusses the result of entropy-based image segmentation. Experiment has been done in MATLAB 2014b on a dataset of total 40 images of which 20 for hypopigmented skin disease and 20 for hyperpigmented skin disease. Images have been segmented using Otsu, FCM, and entropy-based thresholding (Gini, Shannon). Standard dataset has been prepared manually using Adobe Photoshop and further verified by experience dermatologist for objective evaluation of threshold-based image segmentation using entropy. For objective evaluation rand index [9] has been calculated for Otsu, FCM, and entropy-based method with standard dataset. Rand index (RI) measures the degree of similarity between two sets of data. RI values vary between 0 and 1 where RI 0 means two datasets are completely disagree and RI 1 means two datasets are exactly same. RI values for entropy-based segmentation are compared with RI values in Otsu and FCM method. Comparison results are shown in Figs. 1 and 2 for hypo- and hyperpigmented skin diseases, respectively.

Figure 1 shows that Gini provides better result in 70 % (p-value 0.011) cases compared to Otsu and 65 % (p-value 0.057) cases compared to FCM for hypopigmented skin disease. Whether Shannon provides better result 55 % (p-value 0.528) cases compared to Otsu and equal result with FCM. In case of hyperpigmented skin disease (Fig. 2), Gini provides better result in 60 % (p-value

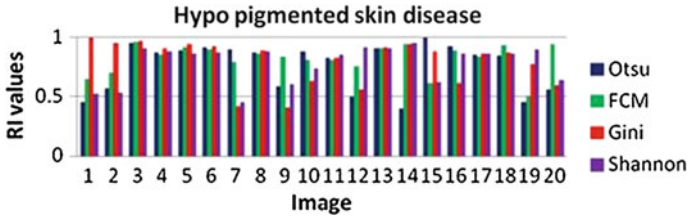


Fig. 1 RI values for hypopigmented skin diseases

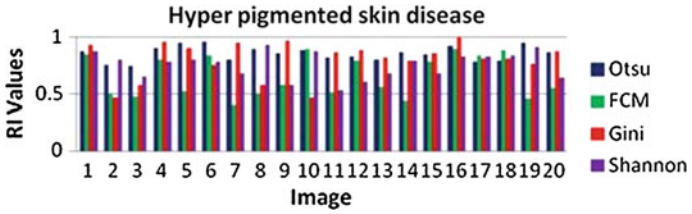


Fig. 2 RI values for hyperpigmented skin diseases

0.208) cases compared to Otsu and 75 % (p-value 0.001) cases compared to FCM. But Shannon entropy does not provide better result compared to Otsu and FCM for hyperpigmented skin disease.

Figure 3 represents the result of segmentation using Gini, Shannon, FCM, and Otsu. Here Otsu and FCM are mainly considered to establish the efficiency of entropy-based segmentation method. Gini and Shannon entropy-based segmentation methods are compared with Otsu and FCM individually. Comparison is done on the basis of RI values. RI values of each of these methods are calculated comparing with the ground truth (Fig. 3b, h). For hypopigmented skin disease image (a) in Fig. 3 RI values of Gini, Shannon, FCM and Otsu methods are 0.932560194, 0.863144845, 0.874945486 and 0.847052963, respectively. For hyperpigmented skin disease image (g) in Fig. 3 RI values of Gini, Shannon, FCM and Otsu method are 0.934409422, 0.87548358, 0.852464 and 0.877894565, respectively.

From the above discussion, it can be concluded that overall Gini entropy is more acceptable as threshold-based method for automatic segmentation of hypo- and hyperpigmented skin diseases.

4 Conclusion

This research work proves that entropy-based segmentation technique is more effective than standard method like Otsu and FCM for automated hypo- and hyperpigmented skin disease detection system. Two entropy measures—Gini and

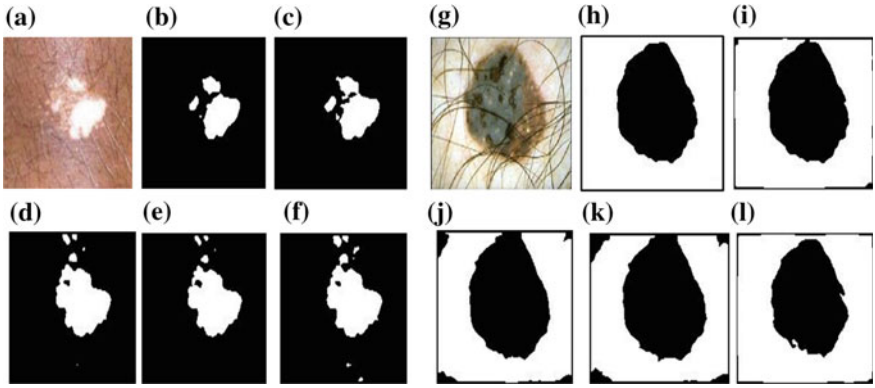


Fig. 3 Result of segmentation. **a** Original hypopigmented skin disease, **b** Ground truth of hypopigmented image, **c** Gini entropy, **d** Shannon entropy, **e** FCM, **f** Otsu, **g** Original hyperpigmented skin disease, **h** Ground truth of hyperpigmented image, **i** Gini entropy, **j** Shannon entropy, **k** FCM, **l** Otsu

Shannon have been considered here for comparison. Efficiency of each of these methods has been evaluated using rand index. Result of evaluation proves that Gini entropy is the best entropy-based segmentation method for automated hypo- and hyperpigmented skin disease detection system.

Acknowledgments I would like to thank Dr. Sanjib Chowdhury, Consultant Dermatologist, Haldia Port Haspital, Haldia, West Bengal for providing me with the dataset. I also want to thank West Bengal University of Technology's TEQIP II program and DST FIST with reference number FIST/ETI/296/2011.

References

1. Alcón, José Fernández, et al.: Automatic imaging system with decision support for inspection of pigmented skin skin diseases and melanoma diagnosis. In: Selected Topics in Signal Processing, Vol. 3(1), pp. 14–25, IEEE Journal, February 2009.
2. Trabelsi, O., Tlig, L., Sayadi, M., & Fnaiech, F.: Skin disease analysis and tracking based on image segmentation. In: Electrical Engineering and Software Applications (ICEESA), pp. 1–7, International Conference on IEEE, March 2013.
3. Silveira, M., Nascimento, J. C., Marques, J. S., Marçal, A. R., Mendonça, T., Yamauchi, S. & Rozeira, J.: Comparison of segmentation methods for melanoma diagnosis in de moscopy images. In: IEEE Journal of Selected Topics in Signal Processing, Vol. 3(1), pp. 35–45, IEEE, February 2009.
4. Pandey, Varshika, and Vipin Gupta.: MRI Image Segmentation Using Shannon and Non-Shannon Entropy Measures. In: International Journal of Application or Innovation in Engineering & Management, Vol. 3(7), pp 41–46, July 2014.
5. Singh, H., & Zwiggelaar.: G-Images: Towards Multilevel Unsupervised Image Segmentation. In: ICVGIP, pp. 473–478, 2004.

6. Dermis.net, (2016). DermIS: Dermatology Pictures - Skin Disease Pictures. Retrieved 30 January 2016, from http://www.dermis.net/dermisroot/en/home/index.htm.
7. Dermnet.com, (2016). Dermnet: Dermatology Pictures - Skin Disease Pictures. Retrieved 30 January 2016, from http://www.dermnet.com/dermatology-pictures-skin-disease-pictures/.
8. Lee, T., Ng, V., Gallagher, R., Coldman, A., & McLean, D.: Dullrazor®: A software approach to hair removal from images. In: Computers in Biology and Medicine, Vol. 27(6), pp. 533–543, Elsevier, 1997.
9. Manisha Sharma, Vandana Chouhan.: Objective Evaluation Parameters of Image Segmentation Algorithms. In: International Journal of Engineering and Advanced Technology (IJEAT), Vol. 2 (2), pp. 2249–8958, December 2012.

Futuristic Automobile Accident and Theft Notifier with Location Tracker

Archit Agarwal and Ayush Agarwal

Abstract In today's life, road traffic accidents are increasing at alarming rate. Most of the people lost their life due to unavailability of medical services. A device has been developed for any two-wheeler automobile that can send the SMS of the location of the incident as soon as accident occurs. As to make our vehicle safe from theft, anti-theft feature is added to the device. Another feature is added that corresponds to the people who used to forget to park their vehicle. To deal with this problem added third feature to the system can send the location of the vehicle automatically as soon as vehicle is parked. An effective system is developed that deals with these situations with the help of sensors, GPS, GSM and embedded system technology.

Keywords Accident · Anti-theft · Sensors · GPS · GSM · Vehicle

1 Introduction

Today modern living is creating binge drinking rush driving. Most of the people forget to follow the basic traffic rules in this humdrum of life therefore result accidents. We cannot change the people mind set towards the cause of accidents but a contribution to rescue the accidental cases by appropriate medical services can be done [1]. A device is proposed in this paper for specific two wheelers that is capable to detect the vehicular accidents instantly and send SMS to the Fire rescue unit, medication unit and driver registered contacts [2]. This system includes various sensors which are capable to observe and analysis the output parameter of the vehicle to determine the present status thereby take actions [3]. A wireless and

Archit Agarwal (✉) · Ayush Agarwal
Electronic Engineering Department,
University of Petroleum and Energy Studies, Dehradun, India
e-mail: architagarwal280@gmail.com

Ayush Agarwal
e-mail: ayushagarwal.bly360@gmail.com

© Springer Science+Business Media Singapore 2017

R. Singh and S. Choudhury (eds.), *Proceeding of International Conference on Intelligent Communication, Control and Devices*, Advances in Intelligent Systems and Computing 479, DOI 10.1007/978-981-10-1708-7_40

location tracking unit consists of GPS and GSM capable to find the location and send the SMS to the saved emergency contacts [4]. The sensor unit consists of accelerometer and vibration sensor. As soon as vehicle is in speed accident mode is automatically switched on and this is possible through inbuilt accelerometer and vibration sensor measurement and senses the abnormal activity. If the readings exceed the predefined value of the sensors an SMS is sent with the location of the incident happen through the GPS/GSM to the emergence receiving unit consist of ambulance, owner-related known contacts [5].

Theft in automobiles is increasing exponentially in present scenario that reinforce to design of anti-theft system. The proposed device includes the feature to deal with this problem. System is activated when the user switched the device into antitheft mode by pressing the antitheft button. In case of any abnormal condition governed by the sensor parameters through sensor unit which comprises of accelerometer and vibration sensor, anti-theft mode is activated [6]. As soon as parameters of the sensor goes beyond the limit a repeated transmission of location of the vehicle through SMS send continuously with pre-set delay [7]. These SMS does not stop until the device is turned off. Through wireless location tracking unit of the system, location of the stolen automobile can be tracked [8].

Most of the people do not remember their parking location. To overcome this problem a feature is added to the system which examines the Vehicle running condition [9]. Parking location tracker feature activates automatically as soon as vehicle is stopped for a specific period of time system and assume the vehicle in parking mode. Then device automatically switched into parking mode and sends the location of the vehicle of the last lock in position via SMS to the owner number or to the registered numbers through wireless and location tracking unit [10].

Every possibility regarding incidents have been taken into considerations in prospective of two wheelers that can be accidents, thefts even parking location. These proposed systems can be implemented in any two wheelers without need to change the internal of the two wheelers. Various positions of the two wheelers observed correspondingly desired actions have implemented through embedded system through programming.

2 Internal Subdivision of the Device

See Fig. 1.

2.1 Internal Subdivision Is Divided into Four Units

1. **Sensor unit:** This unit is consist of sensors which will be use to observe the status of the vehicle. There are two analog sensors which interface to analog port of the microcontroller one is vibration sensor and other is accelerometer. We can

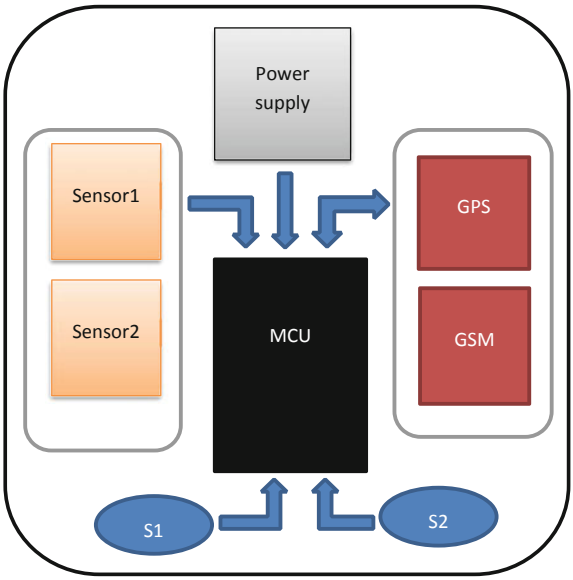


Fig. 1 Various subdivision of the entire system

use any categories of these sensors which are readily available online. But in our proposed device we are dealing with Triple Axis Accelerometer—ADXL335, vibration detecting module that are accelerometer and vibration sensor, respectively.

2. **GPS/GSM unit:** This unit includes the wireless location tracking and sending subsystem consists of GPS that can measure the latitude and longitude for location tracking and other is GSM that basically use for communication purpose and able to send message to recipients. There can be any such types of GPS/GSM model can be use that are readily available in market but we are dealing with GPS receiver with active antenna, RS232 and GSM modem—RS232—SIM900A which are GPS, GSM modules, respectively.
3. **Microcontroller**: System is built around AVR microcontroller atmega16 which is the heart of the device. It can be programmed based upon the specific situation and can interface any input and output devices.
4. **Power supply and switching system**: System runs on 12 V DC power supply where 12 V DC is required by GPS/GSM and 5 V is required by microcontroller that can be obtained by internal power supply circuit that can converts from 12 V DC to 5 V. Inputs to the device is given by 12 V battery internally in vehicle and 7812, 7805 for exact voltage. There are two switches in total one is use for power the device other is use to switch the antitheft mode.

3 Circuit Diagram

3.1 Description of the Circuit

Circuit of the device is based upon AVR as shown in Fig. 2. It is build around AVR atmega16 MCU, GPS, GSM, vibration sensor, accelerometer, switches, ICs 7812, 7805, Max232, a multiplexor, and few other components.

The device which is proposed in this paper uses AVR Atmega16 microcontroller which is the heart of the system. It is used for interfacing to various hardware peripherals. Atmga16 has interfaced serially with GPS/GSM, sensors are interfaced through ADC port of the microcontroller. SYSTEM use two sensors one is vibration sensor and other is accelerometer both are analog sensor. These sensors work as input to microcontroller and interface with build in analog to digital converter in microcontroller. Sensor 1 which is accelerometer connected to PA0 pin and sensor 2 is connected to PA1, PA2, PA3 pin. Vibration sensor have three terminals, out of which two are vcc (5 V), ground (0 V) and third terminal is analog output pins. If we consider about accelerometer pin configuration then there are total 5 pin in use out of which three pins are input named as X, Y, Z pins are analog output pins corresponding to x, y, z coordinate, respectively, and other two are vcc (5 V), ground (0 V). For location tracker gps receiver module is taken in use which includes antenna and a built in processor. This processor calculates the required information in form of NMEA code which output serially in form of string. These strings are received by microcontroller. GPS module have three terminal vcc (12 V), ground (0 V), tx (transmitter) and interface to USART port. It gives series

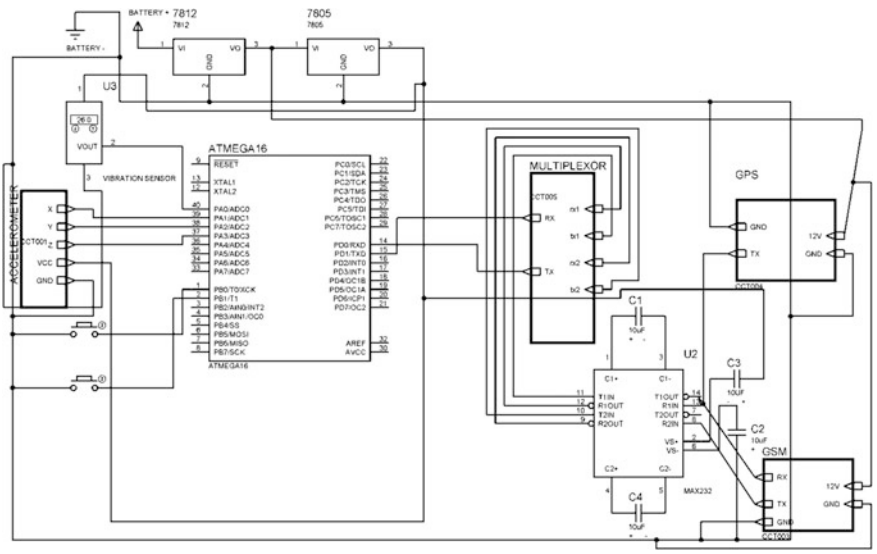


Fig. 2 Circuit diagram simulated in proteus

of serial output which is given to PD0/RXD pin. Another communication module GSM module is a specialized type of modem that accept the sim card and operates over a paid network and interface to USART port. This module accepts At commands set for sending and receiving SMS messages. As GSM module and GPS are works on RS232 logic whereas microcontroller works on TTL logic. IC MAX232 converts TTL logic to RS232 logic. There is only one USART port in total. But there is need of two USART port so a two channel multiplexor is used to deal with this problem. Transmit pin of TXD and receive pin RXD of both GSM and GPS are connected to two channel multiplexor to which multiplexor rx and tx is connected to microcontroller via Max232. Port pin PD0 and port pin PD1 of the microcontroller are connected to 12 and 10 of Max232, respectively. The circuit can be powered by any 12 V battery which gives the exact 12 V output after the input of battery is connected to 7812 and its output gives exact 12 V power to GPS/GSM and output 12V is connected as input to 7805 to give 5 V as output and power microcontroller. Switches S1, S2 are interfaced digitally as input to PC0 and PC1, respectively, whereas S1 corresponds to power the device and S2 corresponds to to switched the device to antitheft mode (Table 1).

4 Software Development Process

4.1 Description of the Program

Figure 3 flowchart clearly define the software algorithm in which variables X, Y, Z, V can be change according to the type of vehicle and specific condition. The program for the proposed device is written in c language that has been compiled using AVR studio. As soon device is powered on by pressing the switch(s1) both sensors are activated. There are four parameters according to which situation are change. The X, Y, Z parameters for accelerometer sensor and another V parameter

Table 1 Components required for the system

Components	Quantity	Specification/model
Microcontroller	1	AVR ATMEGA16,5 V
GPS	1	GPS Receiver with active antenna, RS232, 12 V
GSM	1	GSM modem - RS232 - SIM900A, 12 V
Vibration sensor	1	RK1-307, 5 V
Accelerometer	1	ADXL345, 3.3–5 V
Regulator ICS	1	7812,7805
Capcitor	4	10 µf, 16 V
MAX232	1	5 V
Multiplexor	1	2 channel multiplexor
Miscellaneous	–	–

for vibration sensor. Then three ways to proceed one if antitheft switch is pressed or based upon the readings of the sensor device automatically switched to accident mode or switched automatically to parking. If switch (S2) is pressed, system will process through microcontroller the value of input sensors. If the change in any X, Y, Z and V value is taken place which then an abnormal condition is detected. A continuous string SMS is send to recipients which includes owner, police or any registered contacts in the program until device is switched off that can be done only by owner. As device is safe in metallic case. If the above given condition (2) in flowchart is satisfy then system is switched into accident mode. System process the GPS and GSM instantly and send the location of the vehicle via SMS to the recipients includes driver-related contacts and ambulance number. If in the system there is no change in X, Y, Z and V parameters then system automatically switched to parking mode. It processes the GPS and GSM and location of the vehicle is send to registered driver mobile number via SMS. The recipients, user, ambulance and other emergency number should be include in the program before debugging the program in order to receives the calls from SIM using the GSM module. Using AVR programmer debug the program in the microcontroller through any AVR programmer software. GPS module with 9600 baud rate (defined in the program) receives data from satellite. Our software is developed to decode NMEA

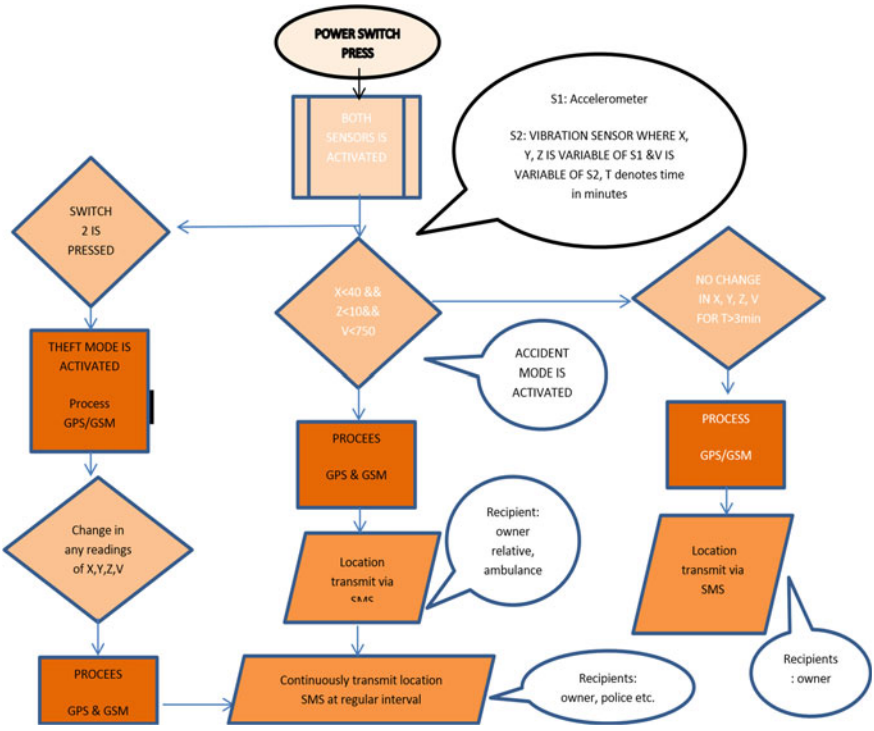


Fig. 3 Algorithm of the program

protocol. The GPS module provides the data in the form of ASCII message. In which each string starts with $ and with <CR><LF>. The software output protocols include geographic latitude and longitude (GLL), global positioning system fixed data (GGA) but in this device we are extracting only GLL readings only. As we are working on AVR separate libraries including ANALOG, DIGITAL, USART and many other libraries used in the programing.

5 Conclusion

A new multifunction-based system is introduced in this paper. The proposed system is designed to overcome the multiple problems related to any two wheelers vehicles. The main prospective of this system is to make simple, cost effective, reliable and multiple task-related system. It works well in any adverse situation of the vehicle independently according to the various predefined situations. Another reason was to make three in one situation device that resolves most likely situation based upon automobiles. This proposed device can be having much further implication in software and hardware by increasing the no of inputs to outputs relations in real time in sake of budget.

References

1. Rathinakumar, R., and D. Manivannan. "Wireless Accident Information System Using GSM and GPS." *Research Journal of Applied Sciences, Engineering and Technology* 4.18 (2012): 3323–3326.
2. Montague, Albert. "Mobile wireless phone with impact senoisor, detects vehicle accidents/thefts, transmiremedical exigency-automatically notifies authorities." U.S. Patent Application No. 10/915,819.
3. Gehlot, Narayan L. "System and method for preventing automobile accidents." U.S. Patent No. 6,060,989. 9 May 2000.
4. Khawam, Maurice A. "Wireless vehicle location and emergency notification system." U.S. Patent No. 6,678,612. 13 Jan. 2004.
5. Goud, Varsha. "Vehicle accident automatic detection and remote alarm device." *International Journal of Reconfigurable and Embedded Systems (IJRES)* 1.2 (2012): 49–54.
6. Song, Hui, Sencun Zhu, and Guohong Cao. "Svats: A sensor-network-based vehicle anti-theft system." *INFOCOM 2008. The 27th Conference on Computer Communications. IEEE*. IEEE, 2008.
7. Stählin, Ulrich. "Emergency call receiving unit for task forces for expediting rescue operations by transmitting a locating signal repeatedly from a vehicle involved in an emergency." U.S. Patent No. 8,606,221. 10 Dec. 2013.
8. Gioia, Thomas A. "Method and apparatus for detection, notification and location of vehicle theft." U.S. Patent No. 6,067,007. 23 May 2000.
9. Zeng, Jun, Minbo Li, and Jia Liang. "An Anti-theft Electric Bicycle Tracking System Supporting Large-Scale Users." *Identification, Information and Knowledge in the Internet of Things (IIKI), 2014 International Conference on*. IEEE, 2014.
10. Rodriguez, Albert. "GPS location finding device." U.S. Patent No. 7,233,863. 19 Jun. 2007.

Design and Comparative Analysis of Controllers for Continuous Stirred Tank Reactor (CSTR)

Parvesh Saini, Rajesh Kumar, Priyanka Sharma and Nalini Rajput

Abstract The most crucial section in chemical processes based industries is Continuous stirred tank reactor (CSTR). CSTR is the example of non-linear dynamical systems. In order to obtain the desired product, it is necessary to have the proper analysis of CSTR in chemical industries. Temperature is the important parameter which is required to be controlled in exothermic CSTRs. The reason for this is the huge temperature variations. These variations are the cause of side reactions which in turn can result in wrong final product. It is desirable that CSTR operates on the desired temperature. Hence, controlling the temperature of CSTR is of prime concern for any process engineer. This paper presents two controllers (viz., Proportional–Integral–Derivative (PID), Fuzzy Logic Controller (FLC)) designed to control the temperature of the CSTR and a comparative analysis of both the controllers have been presented. The behaviour of CSTR has been tested in presence of step disturbance and then the control methodologies have been developed to control the temperature.

Keywords CSTR · Temperature · Step disturbance · PID · Fuzzy logic control (FLC)

1 Introduction

The control systems employed in industries is to boost the economy of the industry. There are numerous processing units connected to each other in chemical industries. These units are actually the various stages of transformation of the raw material into

Parvesh Saini (✉) · Priyanka Sharma · Nalini Rajput
Department of Electrical Engineering, Graphic Era University, Dehradun 248002, Uttarakhand, India
e-mail: parv1606@gmail.com

Rajesh Kumar
Department of Instrumentation and Control Engineering, Graphic Era University, Dehradun 248002, Uttarakhand, India

© Springer Science+Business Media Singapore 2017

R. Singh and S. Choudhury (eds.), *Proceeding of International Conference on Intelligent Communication, Control and Devices*, Advances in Intelligent Systems and Computing 479, DOI 10.1007/978-981-10-1708-7_41

the final product. One of these units is (CSTR's) [1]. CSTR is a unique section in chemical process industries which shows extremely non-linear behaviour and generally has varied operating range [2]. One of the key parameters of CSTR is its temperature (*T*). Since a CSTR possess high non-linear dynamics, so it becomes important to precisely control the temperature of an exothermic chemical reactor, such as, hydrolysis of propylene oxide to produce propylene glycol is an exothermic reaction and requires proper control of reactor's temperature [3]. If the temperature of the CSTR is not as per the set point, then it can adversely affect the final product. Also the large variations such as undershoot and overshoot are undesirable and it is required to achieve steady state quickly at given set point temperature range. However, due to high non-linearity and uncertainty in its response, the parameters of CSTR are not easy to control precisely [4]. During the past few years, the process control techniques used in industries have made inordinate and significant improvements. A number of control methodologies, for example, intelligent control techniques (ANN, FLC etc.) have been discussed in [2–11], various robust controllers have been proposed and discussed in [12–14], Robust PID in [15], Optimal PID controller using Particle Swarm Optimisation in [16], Optimal Control techniques in [17–19], Adaptive control in [3, 5, 20–22] and cascade controllers in [8, 23]. Some comparative studies of various control techniques for CSTR have also been discussed in [2, 9, 24–26] and many more to mention. However, this paper presents a design and comparison of the performance of the different controllers, such as: (PID), (FLC), and Cascade Controller, for controlling the reactor's temperature.

2 Modelling of CSTR

Though there are many types of reactors generally used in chemical industries, the CSTR has an edge on all. The reason for this is that is has most of the features which are encountered in many reaction systems [27]. In this paper, A simple CSTR [4] with cooling jacket is considered which has irreversible exothermic reaction as given below:

$$\mathrm{A} \rightarrow \mathrm{B} + \Delta\mathrm{H} \tag{1}$$

The coolant medium that flows through the jacket of the CSTR (A schematic of CSTR is shown in Fig. 1) removes the heat of reaction [4]. The purpose is to uphold the CSTR's temperature (*T*) set point value. To control the CSTR temperature (*T*), the coolant temperature (*Tc*) is manipulated. However, inlet temperature (*Ti*) and inlet flow (*Fi*) may act as disturbances. For this paper, the feed temperature (*Ti*) is taken as a disturbance variable.

However, the following assumptions have been made regarding the CSTR process [28]:

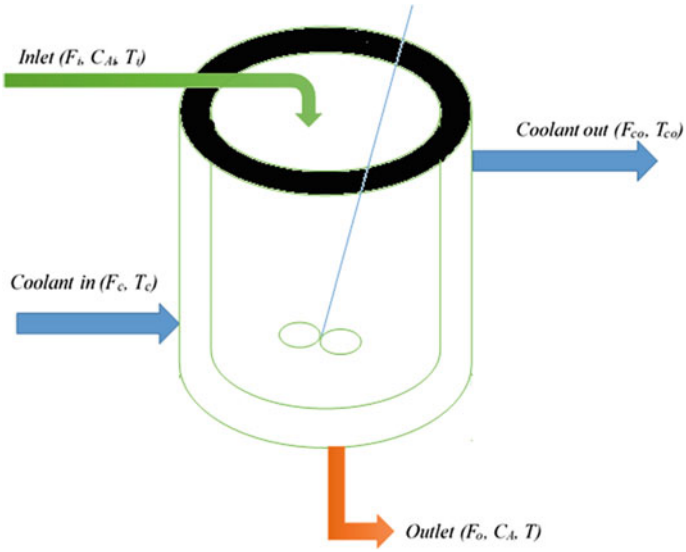


Fig. 1 CSTR system

(i) Perfect Mixing
(ii) Constant density of the liquid (ρ) and Constant heat capacity (Cp)
(iii) Reactor's jacket if perfectly insulated and Perfect mixing of coolant in jacket
(iv) Reactor's and Jacket volume are constant

The material and energy balance equations of a CSTR can be summarised in the state equations, after considering the steady state conditions, are given below:

$$\frac{dx_1}{dt} + \alpha_{11}x_1 + \alpha_{12}x_2 = \beta_1 x_{1i} \tag{2}$$

$$\frac{dx_2}{dt} + \alpha_{21}x_1 + \alpha_{22}x_2 = \beta_1 x_{2i} + \beta_2 x_{2c} \tag{3}$$

where; $\alpha_{11} = \frac{1}{\tau} + k_0 e^{\frac{-E}{RT_0}}$; $\alpha_{12} = \frac{k_0 E}{RT_0^2} e^{\frac{-E}{RT_0}} c_{A,0}$; $\alpha_{21} = -Jk_0 e^{\frac{-E}{RT_0}}$; $\alpha_{22} = \frac{1}{\tau} - J\frac{k_0 E}{RT_0^2} e^{\frac{-E}{RT_0}} c_{A,0} + \frac{UA_t}{\rho C_P V}$; $\beta_1 = \frac{1}{\tau}$; $\beta_2 = \frac{UA_t}{\rho C_P V}$; $x_{1i} = c_{Ai} - c_{A0}$; $x_1 = c_A - c_{A0}$; $x_2 = T - T_0$; $x_{2i} = T_i - T_{i0}$ and $x_{2c} = T_c - T_{c0}$.

The above mathematical equations of CSTR, the whole system can be expressed in matrix form as (Fig. 2):

$$\begin{bmatrix} \dot{x}_1 \\ \dot{x}_2 \end{bmatrix} = \begin{bmatrix} -\alpha_{11} & -\alpha_{12} \\ -\alpha_{21} & -\alpha_{22} \end{bmatrix} \begin{bmatrix} x_1 \\ x_2 \end{bmatrix} + \begin{bmatrix} 0 & 0 & \beta_1 \\ \beta_2 & \beta_1 & 0 \end{bmatrix} \begin{bmatrix} x_{2c} \\ x_{2i} \\ x_{1i} \end{bmatrix} \tag{4}$$

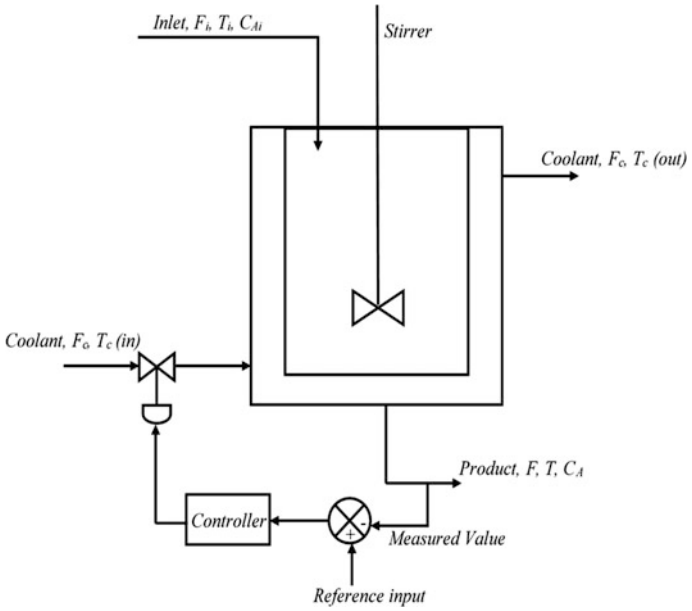


Fig. 2 Temperature control methodology for CSTR

And the output equation of is:

$$y = \mathbb{C}\begin{bmatrix} x_1 \\ x_2 \end{bmatrix} \tag{5}$$

$$\text{where;} A = \begin{bmatrix} -\alpha_{11} & -\alpha_{12} \\ -\alpha_{21} & -\alpha_{22} \end{bmatrix}; B = \begin{bmatrix} 0 & 0 & \beta_1 \\ \beta_2 & \beta_1 & 0 \end{bmatrix}; C = [0 \quad 1]; \text{and} D = 0 \tag{6}$$

The various model parameters of CSTR and their respective values are taken from [28]. These values of CSTR parameters and Eqs. 2–6 can be used to evaluate the A, B, C and D matrices which are mentioned below:

$$A = \begin{bmatrix} -7.991 & -0.0137 \\ 2922.9 & 4.5564 \end{bmatrix}; B = \begin{bmatrix} 0 \\ 1.4582 \end{bmatrix}; C = [0 \quad 1]; D = 0$$

Using the above matrices, the transfer function of the *CSTR* and disturbance is given as below:

$$G_{\text{CSTR}}(s) = \frac{x_2}{x_{2c}} = \frac{1.4582s + 11.6524762}{s^2 + 3.4376s + 3.6635376} \tag{7}$$

$$G_{\text{Disturbance}}(s) = \frac{x_2}{x_{2i}} = \frac{4s + 31.964}{s^2 + 3.4346s + 3.6335} \tag{8}$$

The CSTR transfer function exhibits complex Eigen values and the real part is negative which indicates the stability of the system (CSTR).

3 Controller Design

Controller is a device that generates a control signal to actuate the final control element which in turn manipulates some variables to control the process. From [3–24], there have been many controller types or control schemes used to control the process (CSTR). However, the most common type of controllers which are used in industries is P, I, D or composite form such as PI, PD, or PID (depends upon the type of process to be controlled). There have been some intelligent controllers (such as FLC, Neural Network Controller, etc.) designed and developed in recent years and are being used to control various processes. The ultimate goal of any type of controller in process is to manipulate or regulate the process in such a way that the desired performance is achieved with some proper trade-off between transient and steady state characteristics of the system. In this section, the controllers which have been used to study the behaviour of CSTR are discussed.

3.1 PID Controller

PID is a three mode controller PID which is commercially available since 1930s [29]. During that decade only the first research papers were published on process control [30, 31]. PID controller is the simplest and highly efficient type of controller and has been popular since its invention and is being used in about 90 % of the industries [32]. Along with its simplicity, a PID controller offers many other advantages such as perfect functionality and applicability, user friendly, etc. [33]. However, it appears to be intuitive to design and tune a PID controller. But if many objectives like perfect stability and small transients are to be attained then, it is hard to implement a PID controller practically (Figs. 3 and 4).

A PID controller is form of a phase lead–lag compensator with one pole at origin and other at infinity. A standard PID controller can be expressed by the transfer function generally written in parallel form as:

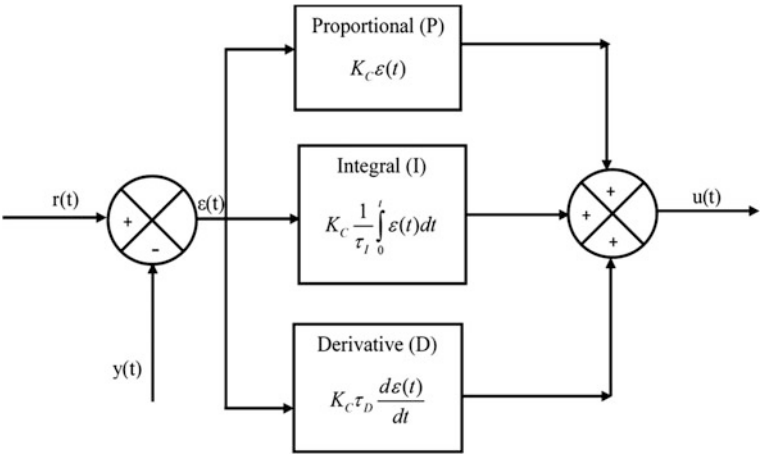


Fig. 3 Configuration of PID controller

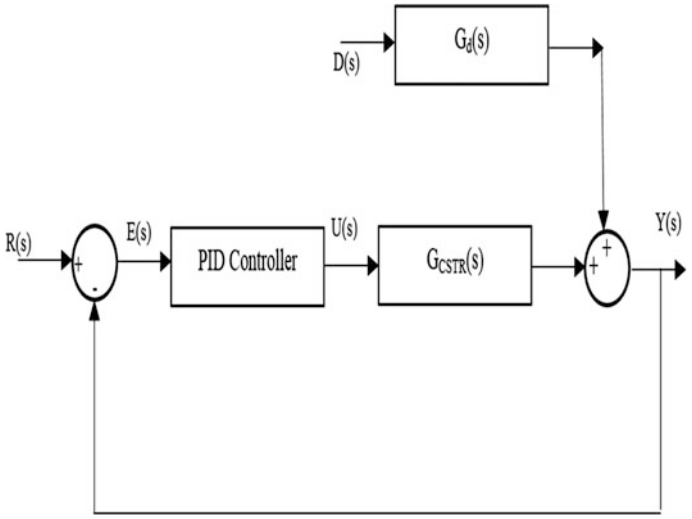


Fig. 4 Block diagram PID control system

$$\mathbb{C}(s) = \frac{\psi(s)}{\varepsilon(s)} = \kappa\left[1 + \frac{1}{\chi_I s} + \chi_D s\right] \quad \text{Or, } \mathbb{C}(s) = \kappa_P + \frac{\kappa_I}{s} + \kappa_D s \tag{9}$$

where, $\kappa_P = \kappa$, $\kappa_I = \frac{\kappa}{\chi_I}$ and $\kappa_D = \kappa\chi_D$ are Proportional, Integral and Derivative gain, respectively. $\chi_I = \tau_I$ and $\chi_D = \tau_D$ are integral and derivative time constants, respectively. In this research paper, κ_P,κ_I and κ_D, respectively are 0.4048, 0.40077 and 0.102 used to tune PID controller.

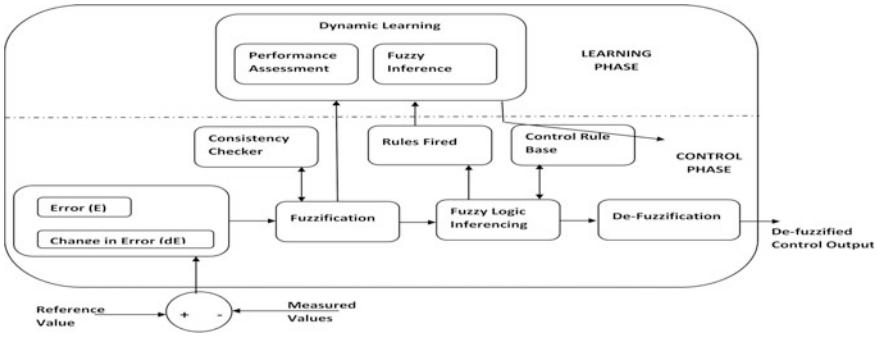


Fig. 5 Structure of fuzzy logic controller [35]

3.2 *Fuzzy Control*

In this section, the application of fuzzy logic control to the complex processes (CSTR's Temperature) has been discussed. It is quite difficult to control various complex industrial processes because of the non-linear and time varying behaviour and the quality of the measurements available for such processes is very poor. The solution for such problems is automatic control. The complex and poorly defined processes are automated by directly implementing the linguistically expressed fuzzy control algorithms [34]. The heuristics and human perceptions are integrated by using particular set of rules of fuzzy logic control as required by the conventional FLCs. However, any such system which has highly complex dynamic characteristics is difficult to control because of the difficulty in determining the best and least reasonable fuzzy rule [35]. The basic structure of a FLC is as shown in Fig. 5.

The overall performance of a FLC depends on the selection of the parameter for the tuning of the fuzzy controllers because there is no established rule or procedure for their tuning [36]. A general block diagram of fuzzy logic control system is as shown in Fig. 6. The objective of designing fuzzy logic control system is to use in problems where there is inaccuracy and uncertainty in the available information [34]. This section presents the design of FLC for the control of reactor's temperature. Figure 7 shows the design FLC for CSTR. The membership functions designed for the error, change in error and control output along with the surface viewer have been shown in Figs. 8 and 9.

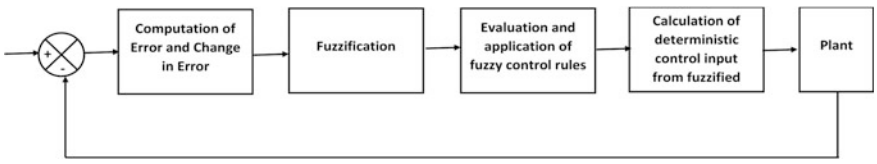


Fig. 6 Fuzzy logic control system block diagram [34]

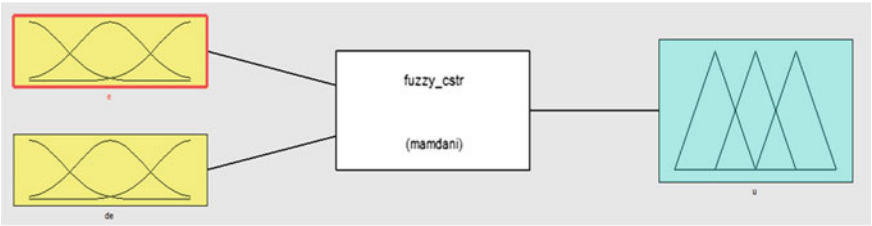


Fig. 7 Fuzzy logic controller (FLC)

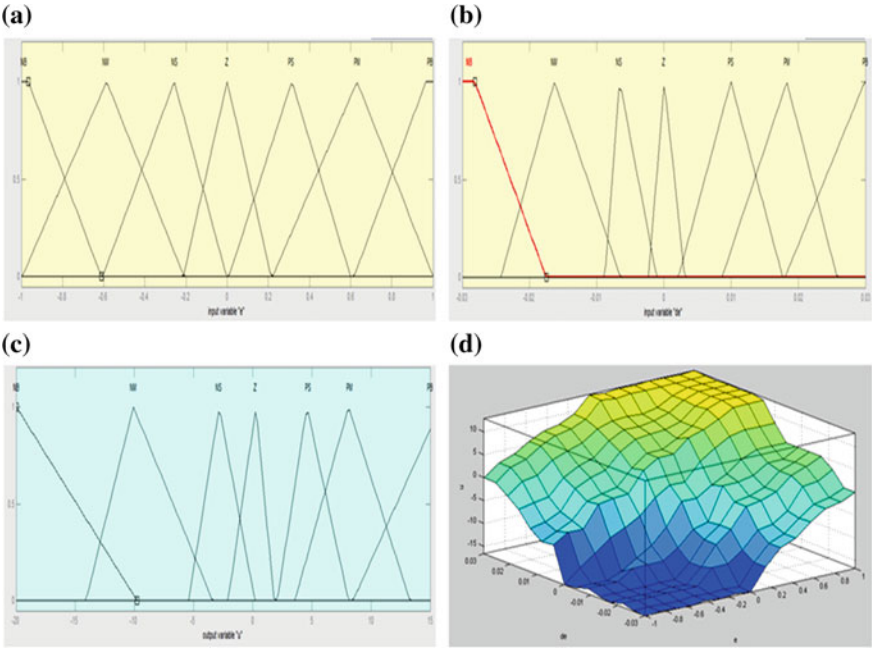


Fig. 8 **(a)** error **(e)** membership function, **(b)** change in error (de) membership function; **(c)** Control variable (u) membership function; **(d)** Surface viewer

4 Result Analysis

This section discusses the results obtained for the CSTR using the two controllers (viz., PID and FLC). The results of both controllers have been compared. Figure 10 shows the open loop response of the CSTR. Figure 11 shows the undisturbed step response of the CSTR using PID controller. Since, the response of PID controller on CSTR has also been analysed by subjecting the CSTR to step disturbance. The step disturbance has been applied on CSTR at the beginning and PID controller is tuned accordingly. The response in Fig. 12 shows an overshoot of 325 %, which is never

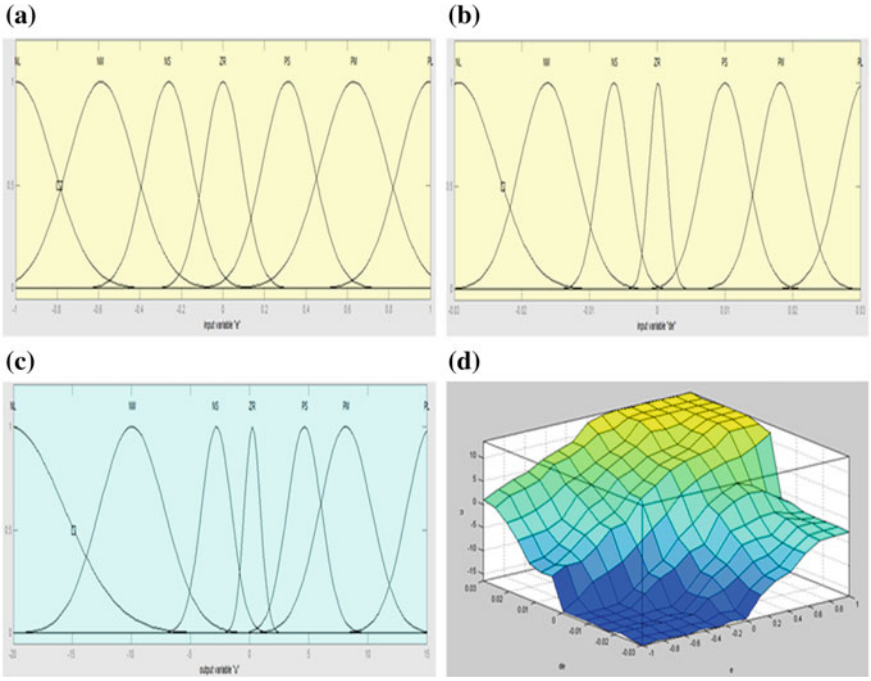


Fig. 9 **(a)** error **(e)** membership function, **(b)** change in error (de) membership function; **(c)** Control variable (u) membership function; **(d)** Surface viewer (These membership functions are used when CSTR is subjected to step disturbance)

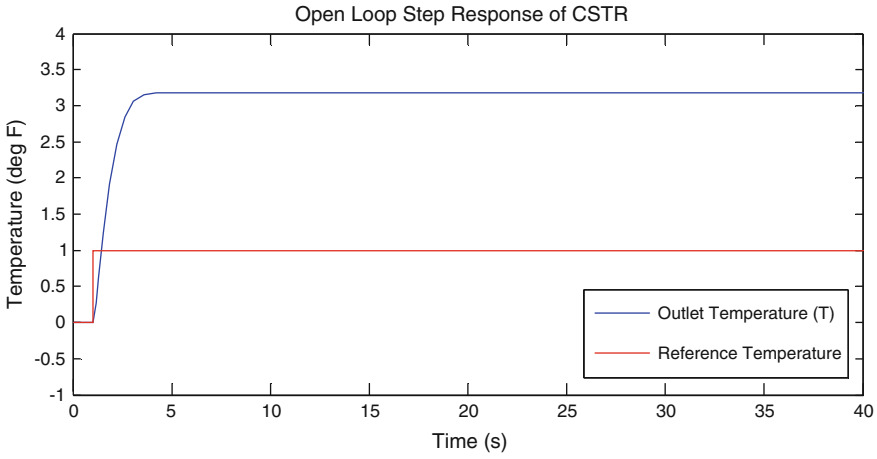


Fig. 10 Step response (Open loop)

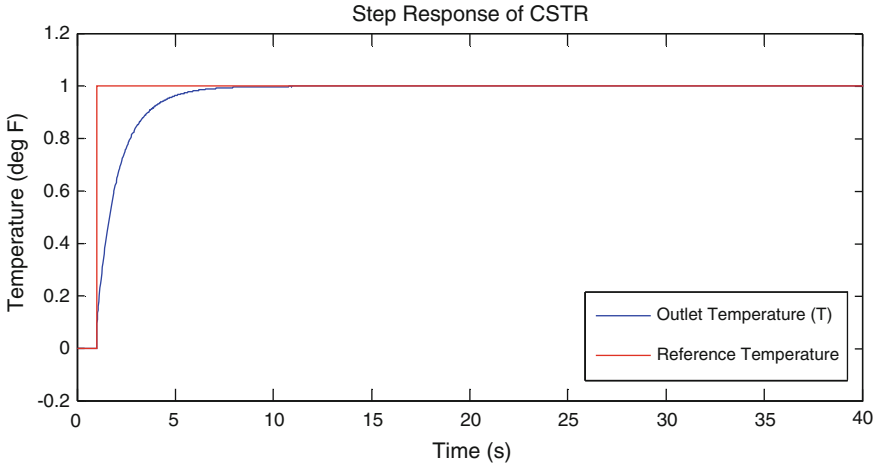


Fig. 11 PID-controlled step response (Disturbance considered: No)

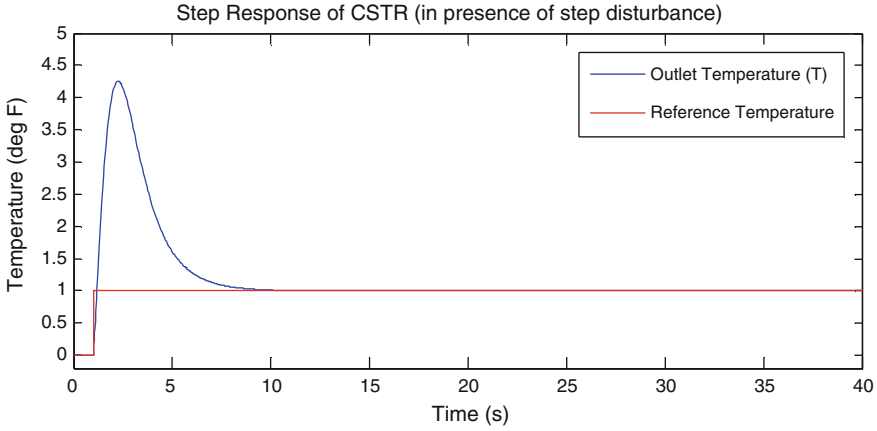


Fig. 12 PID-controlled step response (Disturbance considered: Yes)

desirable. This depicts that if the reference temperature of the reactor is 100 °C, the overshoot of 325 % will raise the temperature to 325 °C. However, the PID controller is capable of controlling the response of CSTR even in presence of step disturbance but the effect of disturbance remains for almost 10 s. If the original scaled time response of CSTR is evaluated then these 10 s are equivalent to few hours. This means that the CSTR remain under the effect of very high temperature for almost 2–3 h. A very high temperature sustained for some hours in CSTR give rise to side reactions and the overall product's concentration changes which eventually change the final product. During the designing of PID controller for suppressing the effect of step disturbance on CSTR, it was found that the parameters

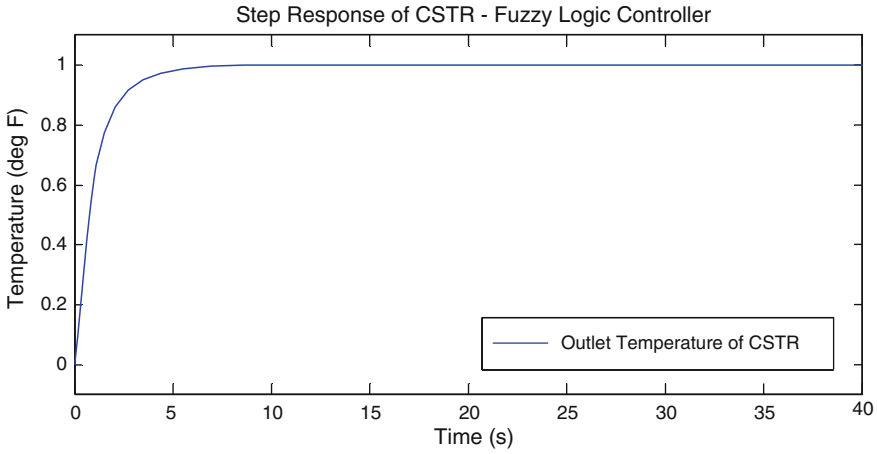


Fig. 13 Fuzzy-controlled step response (Disturbance considered: No)

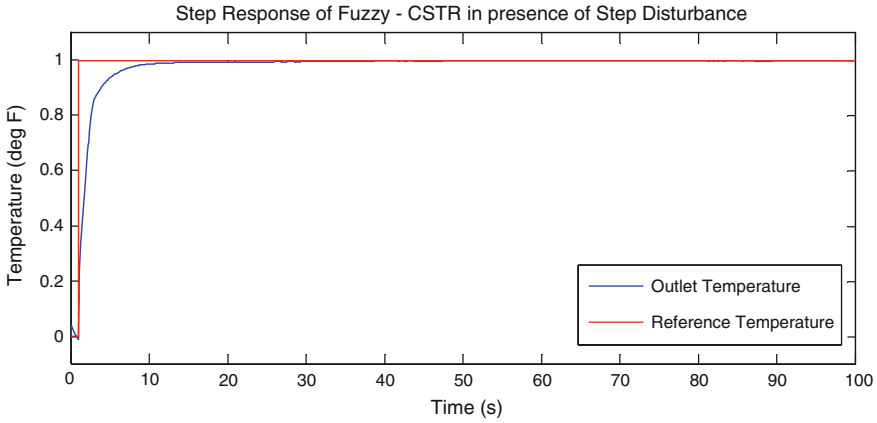


Fig. 14 Fuzzy-controlled step response (Disturbance considered: Yes)

of PID (viz., K_P, K_I, K_D) are kept very high (in range of hundreds to few thousands). Such high values of PID gains are not desirable as it may cause instability in the system and also such high gains are practically difficult to achieve. Then FLC is used to control the reactor's temperature. The step response of CSTR using FLC has been shown in Fig. 13. It is clear from the response that FLC has controlled the system efficiently. The main difference between PID and FLC can be understood from Fig. 14, which depicts the step response of CSTR using FLC in presence of step disturbance. Figure 14 clearly shows that the FLC is an efficient controller for suppressing the effect of step disturbance on CSTR as compared to PID Controller, since there is no overshoot in the response of CSTR in presence of step disturbance when FLC is used. A comparison of the response of CSTR for both controllers has

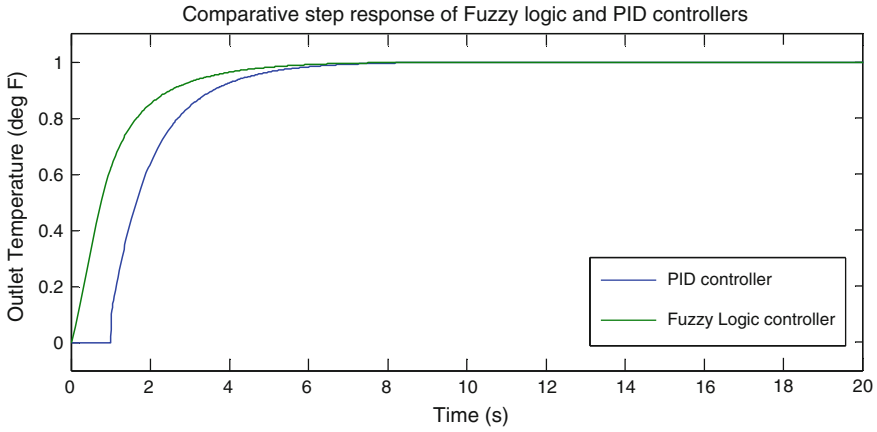


Fig. 15 Comparison of FLC and PID response (Disturbance considered: No)

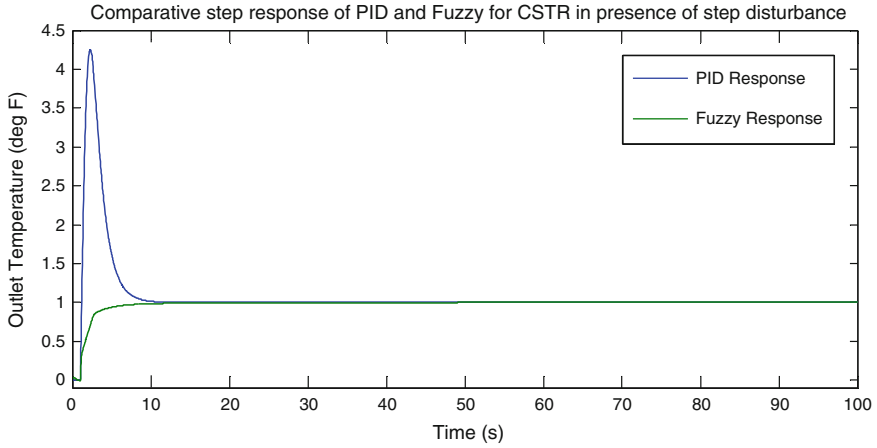


Fig. 16 Comparison of FLC and PID response (Disturbance considered: Yes)

been shown in Fig. 15 (in absence of disturbance) and Fig. 16 (in presence of step disturbance). A comparison of response of CSTR for set point changes using PID and FLC have been shown in Fig. 17. The response in Fig. 17 depicts that PID controller is more efficient that FLC when CSTR is subjected to set point changes. Also, it is seen in Fig. 17 that initially an FLC shows an extreme overshoot in the response which means that as compared to PID controller, an FLC is least efficient and desirable. Though (as shown in Fig. 17) the FLC is showing command following characteristics later on. But still the response of FLC for changes in set point is slow as compared to PID. The reason for this is the non-linearity and vagueness in the linguistic and heuristic rules of FLC (Table 1).

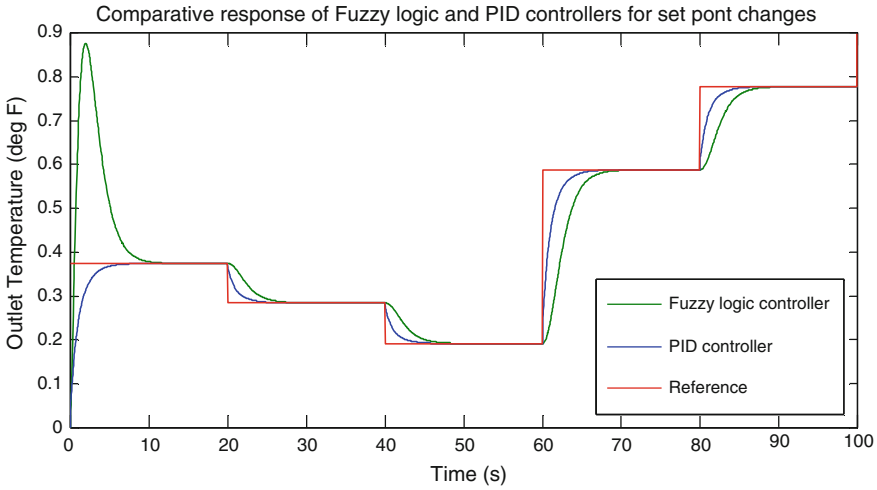


Fig. 17 Set point changes response by FLC and PID controller

Table 1 Performance index of PID controller and FLC

Controller type		ISE	IAE	ITAE
PID	In absence of disturbance	1.5434	2.9852	3.4731
	In presence of disturbance	16.9800	7.9841	26.9902
FLC	In absence of disturbance	0.2261	0.6736	1.2491
	In presence of disturbance	0.4518	1.5241	8.9520

5 Conclusion

This paper has presented the design and analysis of two controllers (viz., PID and FLC) for temperature control of (CSTR). The comparative analysis of two controllers has been done on the basis of performance indices. It has been observed from the results that FLC has better response in all respects as compared to PID controller. However, for set point changes, FLC fails to accept the changes in set points and shows sluggish behaviour as compared to PID controller. A better FLC has been designed over conventional PID controller to control the reactor's temperature.

References

1. Pysal, Y.; Becerikli, Y., "Optimal control of nonlinear exothermic reactor," 9th Mediterranean in Electrotechnical Conference (MELECON 98), vol.1, no., pp. 580–584 vol.1, (1998)

2. Stephanopoulos, G.: Chemical Process Control: A Introduction to Theory and Practice, 1st edn, pp. 395–402. PHI Learning, Upper Saddle River (1984)
3. Zuhwar, Z.F.: The control of non-isothermal CSTR using different controller strategies. Iraqi J. Chem. Pet. Eng. 13(3), (2012) 35–45
4. Om Prakash Verma, Sonu Kumar & Gaurav Manik, "Analysis of Hybrid temperature control for nonlinear continuous stirred tank reactor", 4th international conference on soft computing for problem solving, advances in intelligent systems & computing, (2015) 103–121
5. Ge, S.S., Hang, C.C., Zhang, T., "Nonlinear adaptive control using neural networks and its application to CSTR systems" Journal of Process Control, Vol. 9, issue 4 (1998) 313–323
6. Mose Galluzzo, Bartolomeo Cosenza, "Control of a non-isothermal continuous stirred tank reactor by a feedback–feedforward structure using type-2 fuzzy logic controllers", Information Sciences (Elsevier), Vol. 181, Issue 17 (2011) 3535–3550
7. Khalil Jouili, Houssem Jerbi, Naceur Benhadj Braiek, "An advanced fuzzy logic gain scheduling trajectory control for nonlinear systems", Journal of Process Control, Vol. 20, Issue 4 (2010) 426–440
8. A.Vasickaninova & M.Bakosova, (2005), "Cascade fuzzy logic control of a chemical reactor", 15th international conference process control (2005) 175-1–175-5
9. Mohd Fuaad Rahmat, Amir Mehdi Yazdani, Mohammad Ahmadi Movahed and Somaiyeh Mahmoudzadeh, 2011"Temperature control of a continuous stirred tank reactor by means of two different intelligent strategies", international journal on smart sensing & intelligent systems, Vol. 4, No.2 (2011) 244–267
10. A. M. Yazdani, M. A. Movahed, and S. Mahmoudzadeh, 2011, "Applying a Novel Fuzzy-PI Controller on the Model of Continuous Stirred Tank Reactor", International Journal of Machine Learning and Computing, Vol. 1, No. 2 (2011) 218–223
11. R. Suja Mani Malar & T. Thyagarajan (2009), "Artificial Neural Networks Based Modelling and Control of Continuous Stirred Tank Reactor", American J. of Engineering and Applied Sciences, Vol. 2, No. 1 (2009) 229–235
12. Stephen Piche, Bijan Sayyar-Rodsari, Doug Johnson, arid Mark Gerules, "Nonlinear model predictive control using Neural Networks", IEEE Control Systems Magazine, (2000) 53 – 62
13. Doyle III, F.J., Packard, A.K., Morari, M.: Robust controller design for a nonlinear CSTR. Chem. Eng. Sci. 44(9) (1989) 1929–1947
14. Elisante, E., Rangaiah, G.P., Palanki, S., "Robust controller synthesis for multivariable nonlinear systems with unmeasured disturbances", Chemical Engineering Science (Elsevier), Vol. 59, Issue 5 (2004) 977–986
15. Monika Bakosova, Dalibor Puna and Alojz Meszaros, "Robust Controller Design for a Chemical Reactor", European Symposium on Computer Aided Process Engineering – 15 (Elsevier), Vol. 20 (2005) 1303–1308
16. Zhicheng Xu, "A novel robust PID controller design method," International Conference on Computer Application and System Modeling (ICCASM), vol.6 (2010) V6-332–V6-337
17. Mohammad Ali Nekoui, Mohammad Ali Khameneh and Mohammad Hosein Kazemi, "Optimal Design of PID Controller for a CSTR System Using Particle Swarm Optimization", 14th International Power Electronics and Motion Control Conference, EPE-PEMC, (2010) T7-63–T7-66
18. A. Soukkou1, A. Khellaf, S. Leulmi and K. Boudeghdegh, "OPTIMAL CONTROL OF A CSTR PROCESS", Brazilian Journal of Chemical Engineering, Vol. 25, No. 04 (2008) 799–812
19. Jan Mikles, Lubos Cirka, and Miroslav Fikar, "H2 - Optimal Controller with Integral Action for a Chemical Reactor", Proceedings of the 2006 IEEE International Conference on Control Applications (2006) 2127–2131.
20. Zhang, T.; Guay, M., "Adaptive nonlinear control of continuously stirred tank reactor systems," Proceedings of the American Control Conference, vol.2 (2001) 1274–1279
21. Abatneh, Y., Sahu, O., "Adaptive control design for a Mimo chemical reactor" Autom. Control Intel. Syst. Vol. 1, Issue 3 (2013) 64–70

22. Chaal, Hamza, "A chemical reactor benchmark for adaptive control using U-Model and NARMA-L2 techniques" International Conference on Control, Automation and Systems (2007) 1710–1714
23. A.O.Ahmed, G.A.Gasmelseed, A.B.Karama & A.E.Musa, 2013, "Cascade control of continuous stirred tank reactor", Journal of applied & Industrial Sciences, Vol. 1, No. 3 (2013) 16–23
24. Pankaj, S., Kumar, J.S., "Comparative analysis of MIT rule and Lyapunov rule in model reference adaptive control scheme", Innovative System Design and Engineering, Vol. 2, No. 4 (2011) 154–162
25. Ayush Sharma, Miroslav Fikar, Monika Bakosova, "Comparative study of Time Optimal Controller with PID Controller for a Continuous Stirred Tank Reactor" Acta Chimica Slovaca, Vol. 8, No. 1 (2015) 27—33
26. C. Jeyachandran and M. Rajaram, "Comparitive performance analysis of various training algorithms for control of CSTR process using narma-L2 control," 3rd International Conference on Trendz in Information Sciences and Computing (TISC) (2011) 5–10
27. Dale E.Seborg, Thomas F. Edgar, Duncan A. Mellichamp, Francis J. Doyle III, "Process Dynamics and Control", 3rd edition, John Wiley & Sons, (2010)
28. Bequette, B.W.: Process Control: Modeling, Analysis and Simulation, 1st edition, Prentice Hall, Upper Saddle River (2003)
29. Ziegler, J.G. "Those magnificent men and their controlling machines", Journal of Dynamic Systems, Measurement and Control, Transactions ASME, Vol. 97, No. 3 (1975) 279–280
30. Grebe, J.J., R. H. Boundy, R. W. Cermak, "The control of chemical processes, Transactions AIChE, Vol. 29 (1933) 211–255
31. Ivanoff, A., Theoretical foundations of the automatic regulation of temperature, J. Inst. Fuel, Vol. 7, No. 33 (1934) 117–130
32. Ang, K.H. and Chong, G.C.Y. and Li, Y., "PID control system analysis, design, and technology". IEEE Transactions on Control Systems Technology, Vol. 13, No. 4 (2005) 559–576
33. L. Wang, T. J. D. Barnes, and W. R. Cluett, "New frequency-domain design method for PID controllers," Proc. Inst. Elect. Eng. D—Control Theory Appl., vol. 142, no. 4, pp. 265–271, (1995)
34. P. J. Kin, E. H. Mamdani, "The Application of Fuzzy Control Systems to Industrial Processes" Automatica, Vol. 13, Pergamon Press (1977) 235–242
35. Jeong Jun Song and Sunwon Park, "A fuzzy dynamic learning controller for chemical process control", Fuzzy Sets and Systems Vol. 54 (2) (1993) 121–133
36. A.Vasickaninova, M.Bakosova, "Cascade fuzzy logic control of a chemical reactor", 15th international conference on process control, (2005) 175–1 – 175-5

Performance Analysis of Reactive, Proactive and Hybrid Routing Protocol Used in Petroleum Tank Over Network Control Systems

S.K. Agarwal, Sachi Bansal and Anwar S. Siddiqui

Abstract Remote controlling or wireless communication is emerging technology with innumerable applications. In process industry closing the control loop over the network adds value to the systems but time delay and packet dropout are the two significant constraints while designing the systems. In this paper, the tuning of control valves (actuators) of petroleum pipe line connected to the controller/s through internet is carried out by a method in which uses frequency response of the plant. The performance of the system is compared on the basis of time delay, jitter, and throughput using different protocols as dynamic source routing DSR protocol, ZRP and OLSR protocol. QualNet 5.0 and MATLAB10.0 is used to simulate the above model.

Keywords Networked control system · WSN · OLSR · DSR · ZRP · E2E delay · Jitter · Transient response

1 Introduction

In production industry [1], to improve the efficiency of traditional work process there is a need to upgrade the existing method of controlling a system. Due to the certainty in the behavior of Field-bus technologies, it has been used for a very long period in the automation industry. Different communication networks like Ethernet are used for conquering problems which are faced by Field-bus technologies like comparatively high-cost hardware and its difficulty in integration with different network protocols. In the new era automation industries [2, 3] are looking forward to use different communication network like internet besides Ethernet. Both technologies are uncertain in nature leading to degradation in the performance and

S.K. Agarwal · Sachi Bansal (✉)
Department of Electronics Engineering, YMCAUST, Faridabad, India
e-mail: shachida@yahoo.com

A.S. Siddiqui
Department of Electrical Engineering, Jamia Millia Islamia, New Delhi, India

© Springer Science+Business Media Singapore 2017

R. Singh and S. Choudhury (eds.), *Proceeding of International Conference on Intelligent Communication, Control and Devices*, Advances in Intelligent Systems and Computing 479, DOI 10.1007/978-981-10-1708-7_42

stability of the system because of many uncontrollable factors in this type of networks like time delay, packet loss, throughput, different energy consumption, etc. [4]. Time delay [5] also affects the performance of the system in terms of higher overshoot and larger settling time. Therefore for designing new closed loop systems there are more number of demands that have to be taken care and more intricacies that has to be solved out. Thus a mandatory demand for a new networked control system is to design a controller which guarantees stability in the control loop. The performance of the system does not depend on single parameter like quality of service but it also depends on how network has been engaged in the loop. Thus less sampling time does not guarantee better performance, because fast sampling leads to surplus network traffic leading to comparatively elongated delays and thus packet loss occurs. As a consequence there is a need of selecting an appropriate sampling rate taking into consideration for stability and performance of the system and network bandwidth is also as equal importance.

This paper shows the comparison of different routing protocols [6] used in network control system of a petroleum tank. The performance parameters such as E2E delay and jitter are measured through simulation of network in QualNet 5.0. Further performance parameters like Overshoot, Settling time, Rising Time are measured via simulation in MATLAB10.0 [7].

This paper is presented as follows. In Sect. 2, the problem formulation is carried through. It gives the brief view of the study system. Section 3 gives the outline of QualNet 5.0, Routing Protocols and the critical parameters of a wireless sensors network such as end to end time delay, jitter. Section 4 shows the setup of virtual network for the study system. Section 5 demonstrates the transient response of the network controlled petroleum tank system. Section 6 contains the conclusion.

2 Problem Formulation

2.1 Brief View of the Study System

The block diagram of network controlled petroleum tank is shown in Fig. 1. The Petroleum tank and PID controller are connected with one another via internet. Major delays in the above process include computation delay, measurement delay and process delay occurring at PID controller and plant. The network delay, introduced in communication channel between the two during data acquisition from

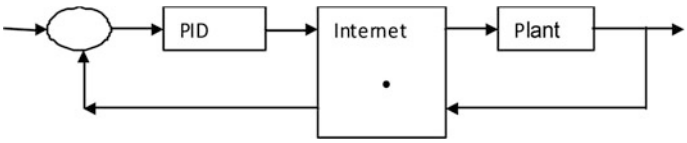


Fig. 1 Network controlled petroleum tank system

process and control command transfer between controller and actuators, leads to instability. Henceforth communication delays are simulated using QualNet 5.0 with different routing protocols. Different protocols [8] affect the performance of the petroleum tank system which is analyzed in MATLAB10.0.

3 QualNet 5.0

3.1 Protocols

3.1.1 DSR

The Dynamic Source Routing protocol (DSR) [9] is reactive unicast routing protocol, it is very simple and efficient routing protocol which was designed for specifically multihop wireless mobile ad hoc networks of mobile nodes. DSR allows the network to be entirely self-reliant and self-configuring, without the need for any existing network infrastructure or administration. In DSR, every data packet completes their routing information and sends to dissemination by using source routing to sending packets. DSR uses source routing this means that the source must know the complete hop sequence to the destination. Additionally, each node maintains a route cache, where all routes it knows are stored. The route discovery process is initiated only if the desired route cannot be found in the route cache in DSR each node uses caching technology to maintain the route information. There are two major phases in DSR:

(i) Route Discovery Phase
(ii) Route Maintenance Phase

3.1.2 Optimized Link State Protocol

The Optimized Link State Protocol (OLSR) [10] characterized as proactive routing protocol employs an efficient link state packet forwarding called multipoint relaying. The OLSR has many advantages make it superior option more other table driven protocols. OLSR is flat routing protocol no need of central administrative. This protocol provides routing information to all the participating hosts in the network. This protocol is appropriate for the application which inhibits the long delays.

3.1.3 Zone Routing Protocol

Zone Routing Protocol (ZRP) is hybrid (proactive and reactive combination) type of routing protocol which was developed for ad hoc networks (mobile). The main design purpose of hybrid protocols was reducing bandwidth and control overhead

in desired wireless network. The hybrid routing protocols approaches towards to decrease the latency caused by route search operations in reactive routing approaches [11, 12].

3.2 Performance Parameter

3.2.1 E2E Delays

E2E delay is defined the time taken to process the input and produce an output. The E2E delay should be deterministic but when communication network is introduced to connect controller to physical plant the end to end delay tend to become non deterministic [9]. It is easier to overcome the deterministic delay but difficult and complex circuitry is required to overcome non deterministic delay. If specific output signal produced do not occur within a specific time frame then it leads to malfunctions or catastrophic failure in the physical plant.

4 Setup of Virtual Network for the Study System

Communication of data from source node, i.e., PID controller to a remotely situated actuator of a petroleum tank and vice versa has been done by simulating the ad hoc network in QualNet 5.0 shown in Fig. 2 with the consideration as shown in Table 1.

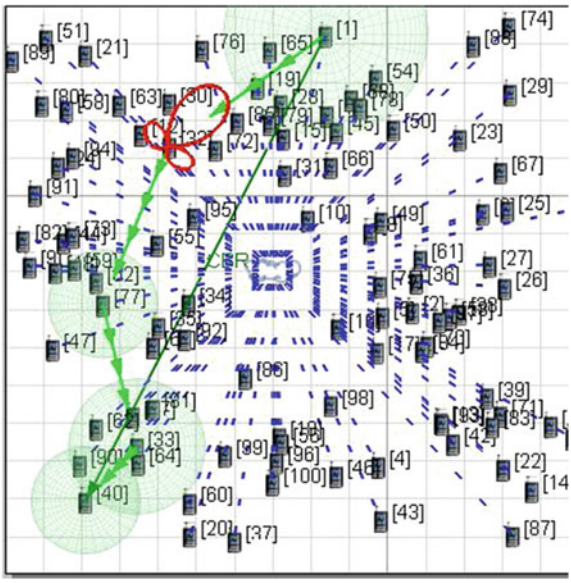


Fig. 2 Snapshot of QualNet animator to exploit DSR protocol of 100 nodes using route discovery mechanism

Table 1 Parametric values for selected Ad hoc network

Network parameter	Assigned value
Routing protocol	OLSR, DSR.ZRP
Number of nodes	100
Mobility model	Random way point
Transmission range	600 m
Simulation time	30 s
Simulation area	1500 × 1500
Traffic type	Constant-bit rate
MAC protocol	IEEE 802.11e
Size of packet	12288 bytes
Node placement	Random
Radio type	IEEEE 802.11b Radio
Total packet sent	24
Antenna model	Omni-directional
Channel frequency	2.4 GHZ

QualNet 5.0 is the simulation software use to find out the parameter like End to End delay, jitter, throughput etc. when communicate between the controller and petroleum tanks [9].

5 Performance Evaluation of a Remote Controlled Actuator of a Petroleum Tank

Considering transfer function of petroleum tank [13] with computation delay only in Eq. (1).

$$Gp(S) = \frac{3e^{-10S}}{10S + 1} \tag{1}$$

The transfer function of PID controller is given in Eq. (2). An arbitrary value of K_p = 0.2, the value of K_i and K_d is taken arbitrary from stability region as 0.02 and 1.0 respectively [14].

$$G_C(S) = \frac{K_P S + K_i + K_d S^2}{S} \tag{2}$$

Table 2 depicts the effects of different protocols.

Using Eqs. (1) and (2). Assuming arbitrary value of K_p, K_i, K_d as 0.2, 0.02 and 1.0 respectively in Eq (2). Step response of the system with computation delay and

Table 2 Effect of different protocols

Protocol	End to end delay	Jitter
OLSR	0.23901779	0.175369469
DSR	0.40202679	0.18200939
ZRP	0.36043164	0.153206493

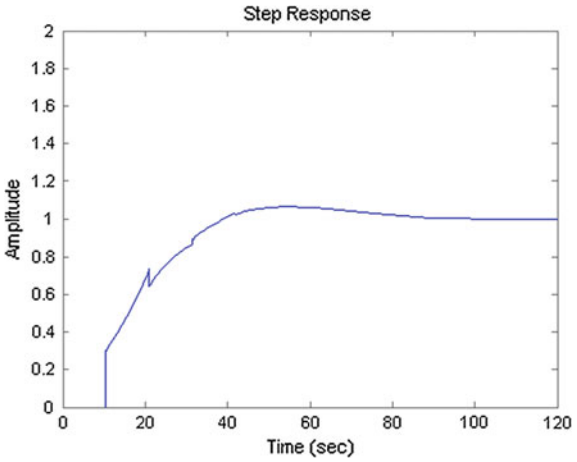


Fig. 3 Step response with OLSR protocol

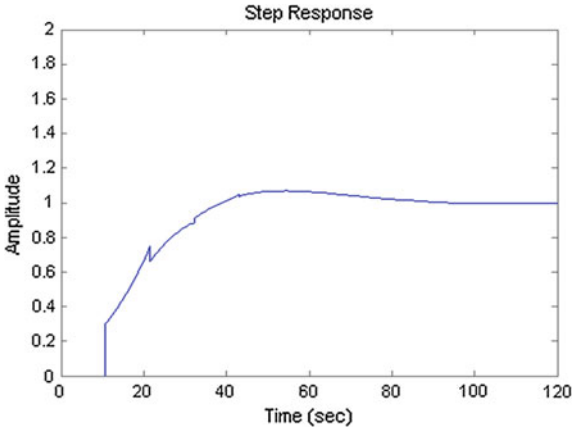


Fig. 4 Step response with DSR protocol

network delay due to OLSR, DSR and ZRP protocol is simulated in MATLAB is shown in Figs. 3, 4 and 5 respectively.

The following table shows the effect of protocol on the time response characteristics of the system.

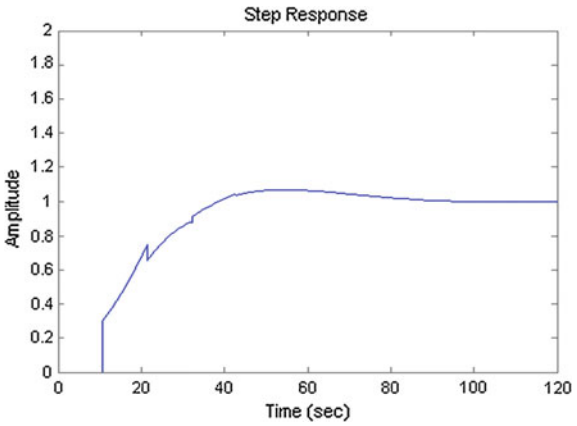


Fig. 5 Step response with ZRP protocol

Table 3 Effect of protocol on the time response characteristics of the system

Protocol	Rising time	Settling time	Overshoot (%)
OLSR	21.4691	79.6170	6.2778
DSR	21.6082	79.7207	6.8348
ZRP	21.4420	79.7011	6.7280

6 Conclusions

This paper reveals the impact of technology and the effect on time response characteristics of the system with the usage of different protocol in network. Tables 2 and 3 show that the use of OLSR protocol exhibits End to End delay as 0.2390 s, Rising time as 21.4 s and 6.2 % of overshoot, similarly in DSR exhibits End to End delay as 0.4020 s, Rising time as 21.6 s and 6.8 % of overshoot. ZRP exhibits end to end delay as 0.3604 s, Rising time as 21.44 s and 6.72 % of Overshoot. The analysis of Reactive, Proactive, and Hybrid Routing Protocol used in petroleum tank over network control systems for 100 nodes reveals no major changes in characteristics of the system. It is studied that for long delay OLSR is much suitable for such type of system. Further, to keep pace with latest trends the study of NCS [15–18] is interesting and challenging field of research and study of all available protocols is must to use NCS most efficiently.

References

1. Torre, M.,: Applied Automation supplement for Control Engineering and Plant Engineering, Halliburton, (2014).
2. Huang, F.D., Nguang, S.,: Robust H_∞ output feedback control of networked control systems with multiple quantizers, Journal of The Franklin Institute, Elsevier Ltd., (2012).
3. Luan, X., Shi, P., Liu, F.,: Stablisation of NCS with Random delays,IEEE, (2010).

4. Ling, W.E.I., D.X.U.E., Yu., Zhi, E.D.,: Some Basic Issues in Networked Control Systems, Second IEEE Conference on Industrial Electronics and Applications, (2007).
5. Mittal, S., Siddiqui,A.S.,: Networked Control System: Survey and Direction,: Journal of Engineering Research and Studies, vol I, Issue II, (2010), 35–50.
6. Prasad, KS, N., Puttamadappa, C.,: Design and performance analysis of energy aware routing protocol for delay sensitive applications for wirelessbsensors networks, International Journal of Computer Networks and Communications Security, Vol.1(2), (2013) 46–53, E-ISSN 2308-9830.
7. Vardhan, S., Kumar,R.,: An implementation of time-delay compensation scheme for Networked Control Systems using MATLAB/Simulink, International Conference on Computational Intelligence and Communication Systems IEEE, DOI 10.1109/CICN.2011.29, (2011).
8. Aggarwal, Ruchi., Kaur, Amanpreet.,: Energy Efficient Zone Based Location Aided Routing Protocol for MANE International Journal of Computer Science and Information Technologies, Vol. 5 (4), (2014), 4990–4994.
9. Vir, Dharam., Agarwal, S.K., Imam, S.A.,: Traffic Generator Based Power Analysis of Different Routing Protocol For Mobile Nodes in Wireless Sensor Network Using QualNet (IJERA) ISSN: 2248 –9622 Vol.3(4), (2013),.2548 -2554.
10. Perkins, C.E, Royer, E.M.,: Ad-Hoc On-Demand Distance Vector Routing, Proceedings of IEEE WMCSA'99, New Orleans, LA, (1999), 90–100 Hass, Z.J, Pearlman, M.R, Samar,P.,: The Zone Routing Protocol (ZRP) for Ad Hoc Networks, draft-ietf-manet-zone-zrp-04.txt, (2002).
11. Hass, Z.J, Pearlman, M.R, Samar, P.,: The Zone Routing Protocol (ZRP) for Ad Hoc Networks, draft-ietf-manet-zone-zrp-04.txt, (2002).
12. Pei, G., Gerla, M., Hong, X, Chiang, C.,: A wireless hierarchical routing protocol with group mobility, Wireless Communications and Networking, New Orleans, (1999), 11–18.
13. Choudhary Shoukat, M.A.A., Thorn Hill, NF, Shah, SL,: Modeling valves stiction, Control Engineering Practice, Vol. 13 (5), (2005) 641–658
14. Sujoldzic S, Watkins J,: Stabilization of an arbitrary order transfer function with time delay using PID controller, Proceedings of the 45th IEEE Conference on Decision &Control Manchester Grand Hyatt Hotel San Diego, CA, USA, (2006).
15. Figueredo, L.F.C., Santana, P.H.R.Q.A., Alves, E.S., Ishihara, J.Y., Borges, G.A., Bauchspicess,A.,: Robust Stability of Network control system, Robotics, Automation and computer Vision Group, Deptt of Electrical Engg, University of Brasilia, Brazil.
16. Dewivedi, A.K., Khushwaha, S., Vyas, O.P.,: Performance of Routing Protocols for MANETs and WSN:A Comparative Study, International. journal of recent trends in Engineering, Vol.2, No.4, (2009).
17. Cacho, M.D., Delgado, E., Barreiro, A.,: Intenet Adaptive Dead Band for NCS and Tele operation,18th Mediterranean Conference on Control and Automation Congress Palace Hotel, Marrakech, Morocco, (2010), 23–25.
18. Martins, E.C., Jota,F.G.,: Design of NCS with explicit compensation for time delay variations, IEEE, (2010).

Dead Time Compensation in Sugar Crystallization Process

Sandeep Kumar Sunori, Pradeep K. Juneja, Mayank Chaturvedi and Jeevanshi Mittal

Abstract The input to the sugar factory is the sugarcane billets and the output is the crystal sugar. There are many subprocesses with significant multivariable interaction involved within this process which is cane preparation, juice extraction by crushing mill, heating, clarification and filtration, evaporation, and crystallization. In the present paper, the Smith predictor is designed using MATLAB in order to compensate the dead time present in heat exchanger system of the crystallization process and its performance is compared to that of a conventional PI controller with no dead time compensation.

Keywords Smith predictor · Crystallization · Dead time · Disturbance rejection

1 Introduction

The extracted juice from the crushing mill is clarified and evaporated. The resulting syrup is then sent to the crystallization process. The flow diagram of the crystallization process, which is found in sugar factories are shown in Fig. 1. The objective is to maximize the crystal growth speed with minimum cost and losses.

Vacuum boiling pans are used for crystallization in which the syrup is boiled until it gets supersaturated. A sucrose solution is said to be saturated if it contains two parts of sucrose to one part of water at room temperature and five parts

S.K. Sunori (✉)
Graphic Era Hill University, Bhimtal, Uttarakhand, India
e-mail: sandeepsunori@gmail.com

P.K. Juneja · Mayank Chaturvedi · Jeevanshi Mittal
Graphic Era University, Dehradun, Uttarakhand, India
e-mail: mailjuneja@gmail.com

Mayank Chaturvedi
e-mail: mayankchaturvedi.geit@gmail.com

Jeevanshi Mittal
e-mail: mittaljeevanshi@gmail.com

© Springer Science+Business Media Singapore 2017

R. Singh and S. Choudhury (eds.), *Proceeding of International Conference on Intelligent Communication, Control and Devices*, Advances in Intelligent Systems and Computing 479, DOI 10.1007/978-981-10-1708-7_43

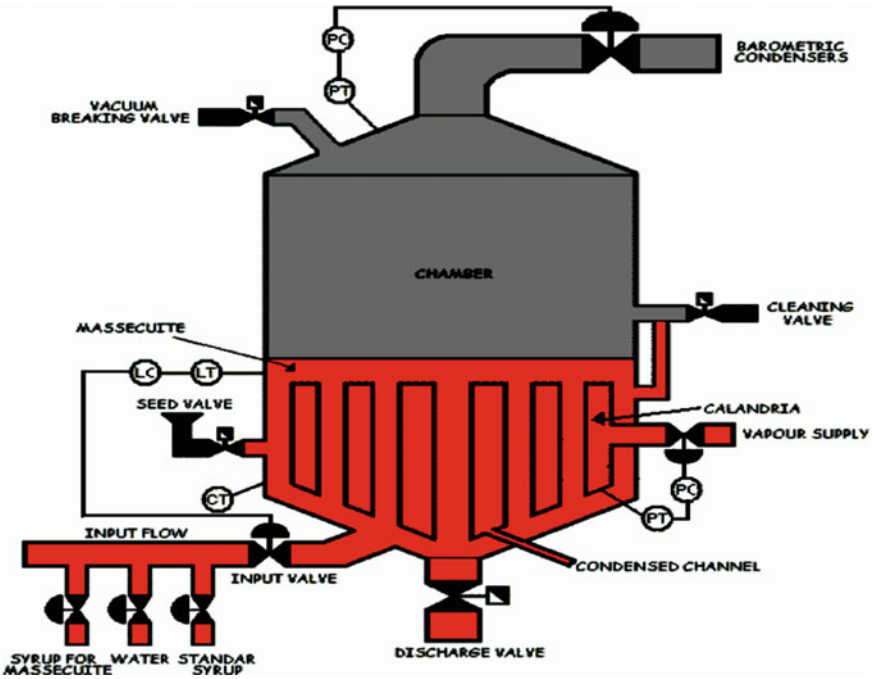


Fig. 1 Vacuum pan [1]

of sucrose to one part of water at 100 °C. If the concentration of sucrose is raised above this value, then it becomes supersaturated which is essential for crystallization to take place [2].

Now, the sugar crystals suspended in alcohol are added to it. These crystals behave as seed crystals. Sucrose gets deposited around these crystals. These crystals then grow in size. The sugar liquor is generally boiled in three stages A, B, and C.

The mixture containing syrup and sugar crystals which is called massecuite is evaporated until supersaturation takes place in vacuum pan 'A'. Now the centrifuging of this mixture is done at a high speed which separates the sucrose crystals from the syrup. The residual syrup is passed to 'B' vacuum pan where the same crystallization process is repeated. The sugar that is recovered from 'B' pan is added to the concentrated syrup fed to 'A' pan. The machine syrup of 'B' pan is passed to 'C' pan where it is again subjected to the crystallization process. The sugar that is recovered from 'C' pan is added to the concentrated syrup fed to 'B' pan. The machine syrup of 'C' pan is passed to the purifier for purification.

2 Process Model

The vacuum pan is cylindrical in shape with 20–60 m^3 volume as shown in Fig. 1. There is also a provision for additional water input for diluting the sugar solution, whenever required. A calandria type system of heat exchanger system is employed for exchange of heat between steam and solution. Steam flows in a spiral tube around the vacuum pan. A contact barometric condenser is used to generate the vacuum pressure of about 0.2–0.3 bar in the pan. The average operation cycle time is about 90 min [3]. The objective is to design a control system to maintain the temperature of solution with optimum value 105–110 °C.

The heat exchanger system is comprised of [4]:

(i) Control valve having transfer function given Eq. (1) with valve opening as the input and the amount of steam as the output. The output of control valve is fed as input to the heat exchanger.

$$G_1(s) = \frac{0.133}{3s + 1} \tag{1}$$

(ii) Heat exchanger having transfer function given in Eq. (2) with amount of incoming steam as the input and temperature of solution as the output.

$$G_2(s) = \frac{e^{-15.7s}}{22.35s + 1} \tag{2}$$

Combining Eqs. (1) and (2), the overall transfer function of the heat exchanger system is given by Eq. (3).

$$P(s) = \frac{0.133e^{-15.7s}}{(3s+1)(22.35s+1)} \tag{3}$$

3 Smith Predictor Design

The Smith predictor is employed in the conventional controller in order to cancel the undesired effects of the time delay. This scheme is designed for constant time delays and may therefore not perform as well for systems with time delays which vary significantly over time [5]. Empirical design formulas have been developed [6].

The effect of dead time of the process needs to be canceled since, besides delaying the effect of control action taken by the controller, time delay also makes the designed controller unstable. In the Bode diagram of a normal first-order system without time delay, the phase angle asymptotically approaches a limiting value

of −90° thus never reaches the critical value of −180° hence this system is always stable. On the other hand, in Bode diagram of first-order plus dead time system, the phase angle falls monotonically with frequency with no limits. There is now a limiting value of proportional controller gain at which the phase angle crosses −180° and the system becomes unstable. This limiting value of proportional gain decreases as the time delay of the system increases which is highly undesirable [7].

The block diagram of Smith predictor is depicted in Fig. 3 with the process P, controller C, internal model Gp to predict the response with the assumption of delay being not present and filter F. Here, τ, and d represent the time delay and the output disturbance respectively [8, 9].

Now, for the given process P, the tuned PI controller C is given in Eq. (4).

$$C(s) = 3 + 0.18s \tag{4}$$

The filter F is chosen to be first order as given in Eq. (5)

$$F(s) = \frac{1}{5s + 1} \tag{5}$$

The comparison plots for set-point tracking and disturbance rejection performance for simple PI controller C without dead time compensation and the Smith predictor designed with P, C, and F given by Eqs. (3), (4) and (5), respectively are depicted in Figs. 2 and 3 respectively. Table 1 is revealing the corresponding performance parameters showing clearly that there is a significant improvement in controller performance with dead time compensation by Smith predictor.

The comparison of Bode Plots for PI controller and the Smith predictor is shown in Fig. 4 showing that bandwidth is improved with Smith predictor as compared to simple PI controller.

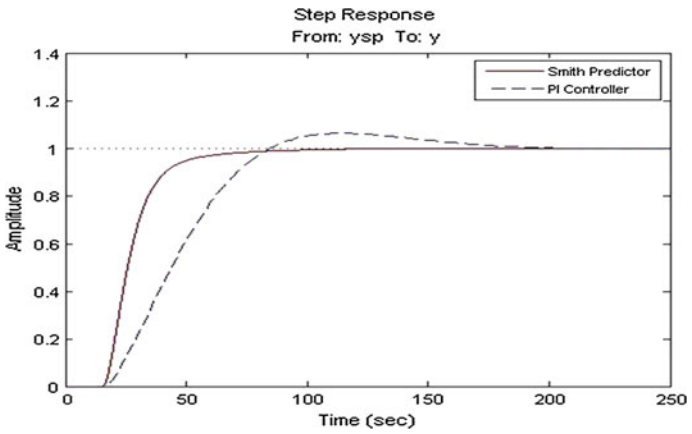


Fig. 2 Comparison of set-point tracking performance of PI controller and smith predictor

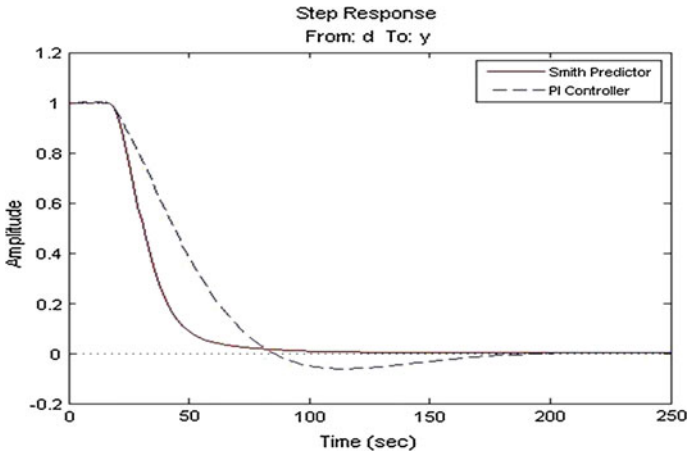


Fig. 3 Comparison of disturbance rejection performance of PI controller and smith predictor

Table 1 Comparision of performance parameters

Parameter	PI controller	Smith predictor
Settling time (s)	163	71.4
Overshoot (%)	6.19	0
Disturbance–rejection time (s)	163	77.3

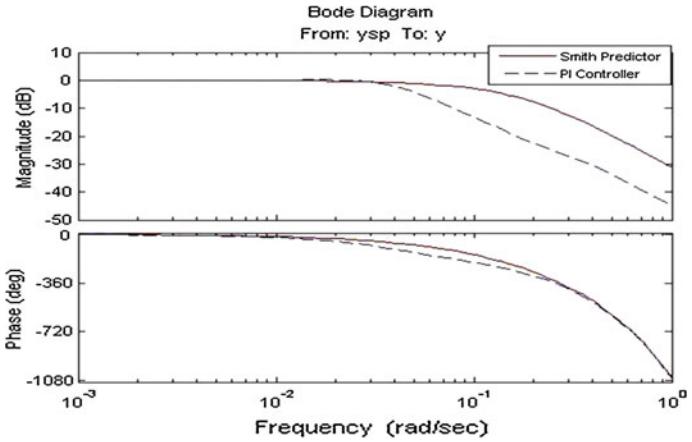


Fig. 4 Comparison of bode plots

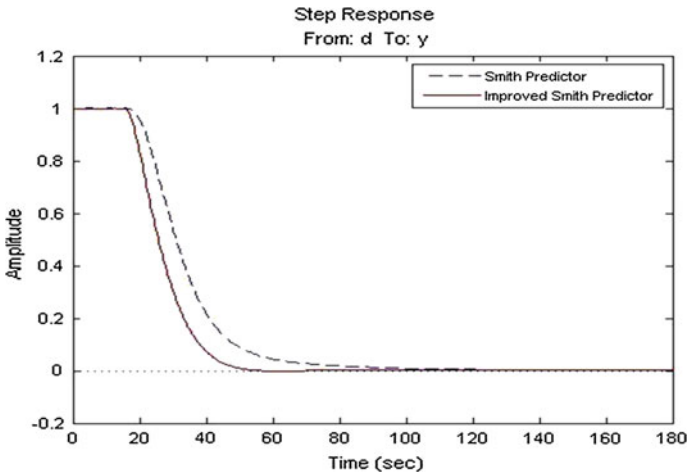


Fig. 5 Comparison of disturbance rejection performance of smith predictor and improved smith predictor

Table 2 Improvement in disturbance rejection performance

Parameter	Smith predictor	Improved smith predictor
Disturbance–rejection time (s)	77.3	46.8

4 Improvement in Disturbance Rejection

As per Huang, H.P. et al. [10], the best disturbance rejection performance of the Smith predictor can be achieved with criterion of selection of filter F given by Eq. (6),

$$F = \frac{(1 + B)}{(1 + B\mathrm{e}^{-\tau s})} \tag{6}$$

B being the state space representation of process P. The comparison of disturbance rejection performance of Smith predictor with filter F given by Eq. (5) and the improved Smith predictor with filter F given by Eq. (6) is depicted in Fig. 5 with corresponding performance parameters specified in Table 2.

5 Conclusion

In the present research work, an industrial process with a large dead time is considered and PI controller is designed for it with and without dead time compensation. A significant improvement in set-point tracking and disturbance rejection

performance has been exhibited by the Smith predictor as a dead time compensator. The disturbance rejection performance is further improved by modifying the characteristics of the filter used in Smith predictor.

References

1. Garcia, A., Acebes, L.F., de Prada, C.: Modeling and simulation of batch processes: A case study. 15th Triennial World Congress, Spain, (2002).
2. Yassien. M., Tenmark, El-Abdein, O.Z., Abdullah, I.D., Amin, S.T.: Sugar crystallization in low temperatures: The theory and practice by advanced sugar crystallization control programme. IJETR (2014) 41–48.
3. Suarez, L.A.P., Georgieva, P., de Azevedo, S.F., Model predictive control strategies for batch sugar crystallization process. Advanced Model Predictive Control chapter 11 225–244.
4. Singh, S.K., Boolchandi, D., Modani, S.G., Katal N.: Multi-objective optimization of PID controller for temperature control in centrifugal machines using genetic algorithm. Research Journal of Applied Sciences, Engineering and Technology (2014) 1794–1802.
5. BabatundeA.Ogunnaike B.A., Ray, W.H.: Process Dynamics, Modeling and Control. Oxford University Press (1994).
6. Watanabe, K., Ito, M.: A process model control for linear system with delay. IEEE Trans. Automat. Contr. 26 (1981) 1261–1266.
7. Sunori, S.K., Jethi, G.S., Juneja, P.K.: Control Strategy for Processes with Complex Dynamics. IJEMR (2015) 522–527.
8. Smith, O.J.M.: Close Control of Loops with Dead Time. Chem. Eng. Prog. Vol. 53. Issue 5. (1957) 217.
9. Huang, H.P., Chen, C.L., Chao, Y.C., Chen, P.L.: A Modified Smith Predictor with an Approximate Inverse of Dead Time," AiChE Journal (1990) 1025–1031.

Performance Analysis of AMC-Based Bowtie-Shaped Slotted Antenna for Terahertz (THz) Applications

Devesh Kumar, Malay Ranjan Tripathy, Manish Sharma, Amit Kumar and Umesh Kumar

Abstract This paper presents the design and performance analysis of AMC (artificial magnetic conductor)-based bowtie-shaped slotted antenna at a solution frequency 1.56 THz for a frequency range of 1.1–1.8 THz. In fact, a metamaterial-inspired structure, which acts as an artificial magnetic conductor (AMC), is used along with ground plane to enhance overall performance of the design. The characteristic parameters like return loss, VSWR, gain, and radiation pattern of proposed design have been presented and analyzed to exhibit the performance of the design proposed. The simulated results demonstrate that the designed antenna exhibits multiband in nature. The maximum gain of 6.14 dB and return loss of −20.14 dB are achieved at 1.56 and 1.4940 THz, respectively. HFSS simulation software is used for simulating the design.

Keywords Bowtie · AMC structure · Multiband · Return loss · Gain · Terahertz

Devesh Kumar (✉) · M.R. Tripathy · Manish Sharma · Amit Kumar · Umesh Kumar
Department of Electronics and Communication Engineering, ASET, Amity University Uttar Pradesh, Noida, India
e-mail: dvshkmr@gmail.com

M.R. Tripathy
e-mail: malay.amity@gmail.com

Manish Sharma
e-mail: manish.nsit07@gmail.com

Amit Kumar
e-mail: amitkumar5555@gmail.com

Umesh Kumar
e-mail: umeshknit@gmail.com

© Springer Science+Business Media Singapore 2017

R. Singh and S. Choudhury (eds.), *Proceeding of International Conference on Intelligent Communication, Control and Devices*, Advances in Intelligent Systems and Computing 479, DOI 10.1007/978-981-10-1708-7_44

1 Introduction

A lot of efforts are being made to design innovative antennas for THz applications. In most of the cases, the applications are seen in the areas of remote sensing and imaging. With these developments tremendous opportunities are available to obtain the images with super quality spatial resolutions. THz antenna design inherits many challenges starting from fabrication to interaction of electromagnetic waves with its nano-structures and limitations involving the way of signal generation and detection.

The review on THz photonics for wireless communications is reported in [1] and THz antenna for space application is mentioned in [2]. A field-effect transistor coupled bowtie antenna is used to detect and generate THz signals [3–5]. The detailed studies are made on frequency-division multiplexing in the terahertz range using a leaky-wave antenna in [6]. A trapezoidal microstrip patch antenna on photonic crystal substrate for high speed THz applications is described in [7]. A bowtie-shaped antenna with a finite ground plane and AMC (artificial magnetic conductor) structure is well designed to achieve better directivity [8]. The graphene metamaterials-based tunable terahertz absorber is designed by using effective surface conductivity approach [9]. An overview of the theory and applications of meta-surfaces is made in [10]. The design for THz antenna array, system and method for producing a THz antenna array is mentioned in an US patent [11]. The control of THz radiation is presented by using tunable metamaterials [12]. Low-index metamaterial is used to enhance the gain of the planar THz antenna [13]. The detailed review on graphene is made for THz optoelectronics [14]. Novel Design of Key-Shaped Fractal Antenna for UWB Applications is presented in [15]. THz communication can be used to achieve high data rate system line communication (which can go up to Gb/s) which is beneficial for a secure point to point and short distance communication. The transmission of THz waves through water and objects is still a concern but its upside is enormous with huge advantages for wireless communication. A lot of research has been done on antennas for THz applications but there is always green and healthy room for better designs and improved characteristics.

The proposed work of the paper is intended towards the designing of an antenna for THz application. The AMC structure is used to improve the performance characteristics of the antenna. Bowtie-shaped antenna with GaAs substrate is proposed to have multiband characteristics at THz frequencies. HFSS software is used for this simulation.

In the following manner, the paper is organized. Section 2 is devoted for description of antenna design. Simulated results and Discussions are presented in Sect. 3. Finally, the paper is concluded in Sect. 4.

2 Antenna Design

The bowtie-shaped slotted Terahertz Antenna (as shown in Fig. 1) is designed and simulated for frequency range 1.1–1.8 THz. The antenna designed is simulated at 1.56 THz. The feed used is micro-strip transmission line. Gallium-Arsenite material of dielectric permittivity 12.9 is used as substrate which is a semiconductor. The dimension of the substrate is 90 × 156 × 22 μm^3. A main radiating patch of dimension 64 × 148 μm^2 is placed on top of the substrate. The dimension of ground is 90 × 156 μm^2. A bowtie-shaped slot is created on radiating patch which covers 2/3 area of the patch. The strip lines which connect bowtie slot are of dimension 16 × 4 μm^2. Further the metamaterial-inspired square loop (FSS-based) structure is introduced in the ground plane. This is used to enhance directivity of design. The combination of the GaAs substrate and the square loop structure works as an AMC structure. Figure 1 shows various pictures of the designed antenna (Table 1).

3 Simulated Results and Discussion

The simulation of proposed antenna is done by using HFSS software platform at solution frequency 1.56 THz. The most of the results are analyzed and presented for the frequency range 1.1–1.8 THz.

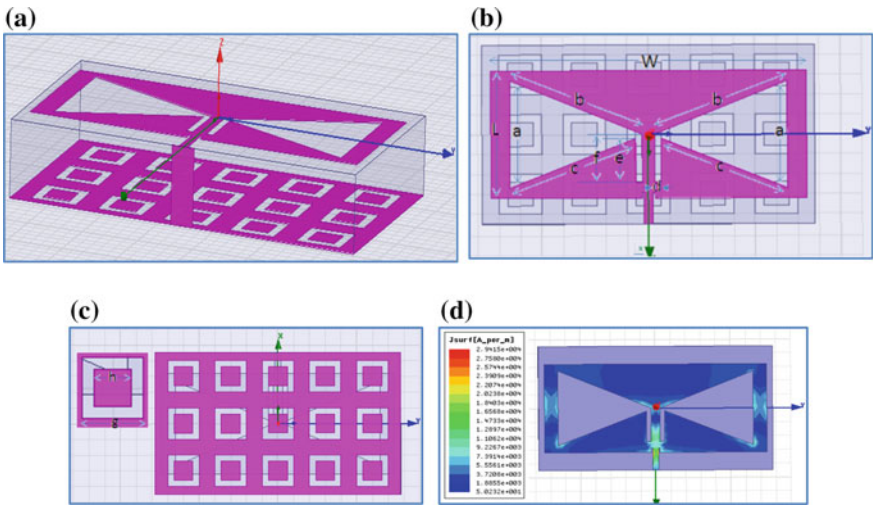


Fig. 1 Bowtie-shaped slotted antenna. **a** 3-D view. **b** Top view. **c** AMC structure in ground plane. **d** Current distribution in radiating patch

Table 1 Physical parameters of metamaterial-based bowtie-shaped slotted antenna

Parameters	Values (μm)				Parameters	Values (μm)	
Radiating patch ($L \times W$)	64 × 148				Square loop slot	g	20
Bowtie shaped slots	a	54.00	d	3		h	12
	b	66.70	e	22	Substrate ($L_S \times W_S \times H_S$)	90 × 156 × 22	
	c	63.16	f	24	Ground ($L_g \times W_g$)	90 × 156	
Feed ($L_f \times W_f$)	16 × 4				Wave port ($W_W \times H_W$)	10 × 22	

3.1 Return Loss of the Design

The return loss versus frequency graph of the proposed antenna is shown in Fig. 2. Three maximum peaks are obtained at frequencies 1.246 THz (RL = −13.92 dB), 1.4940 THz (RL = −20.14 dB), and 1.5960 THz (RL = −20.04 dB) with the acceptable value of RL. The observed impedance bandwidths corresponding to these peaks obtained are 11.8, 23.2, 10.1 GHz, respectively, with RL $\leq$ −10 dB.

3.2 VSWR of the Design

Figure 3 shows the VSWR versus frequency plots of the antenna. The acceptable value of VSWR is less than 2. The VSWR values of 1.5046 (abs), 1.2183 (abs) and 1.2211 (abs) are obtained at 1.1246 THz, 1.4940 THz, and 1.2211 THz, respectively.

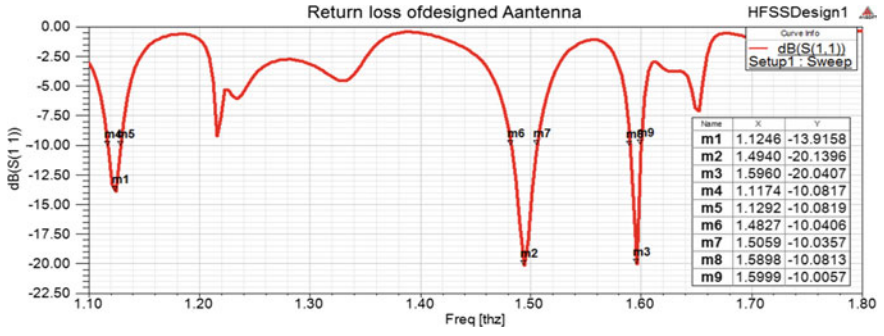


Fig. 2 Return loss of proposed antenna

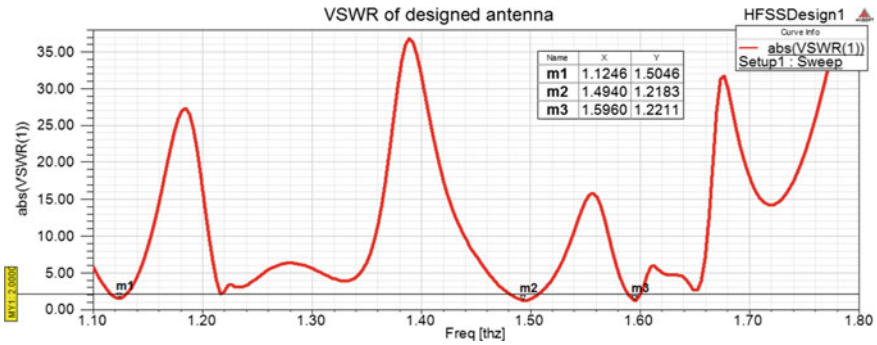


Fig. 3 VSWR of proposed antenna

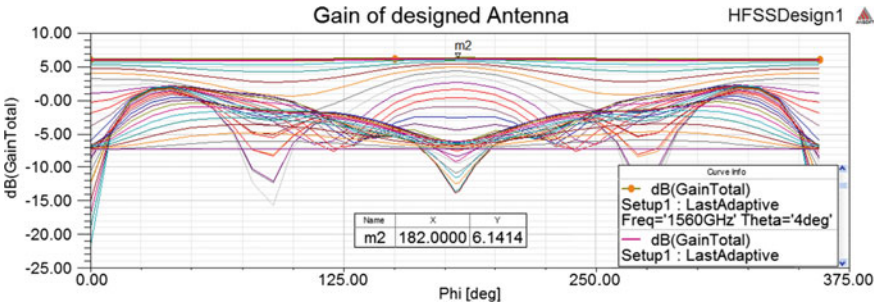


Fig. 4 Total gain of proposed antenna verses angle Φ for various angles θ

3.3 Gain of the Design

Figure 4 depicts the variation of total gain of the proposed design of antenna as an azimuthal angle Φ for various elevation angle θ at solution frequency 1.56 THz. It can be observed from figure that the maximum gain obtained is 6.14 dB in radial directions denoted by angles $\theta = 40°$ and $\Phi = 182°$ at solution frequency of 1.56 THz.

3.4 Radiation Pattern of the Design

The radiation pattern in E-plane and H-plane of the proposed antenna is shown in Fig. 5 at solution frequency 1.56 THz. It is observed that maximum gain obtained in E-plane is 4.95 dB in both vertical planes $\Phi = 0°$ and $\Phi = 90°$ at frequency 1.246 THz. Similarly, the maximum gain is obtained in H-plane as 3.75 dB at frequency 1.4940 THz (Table 2).

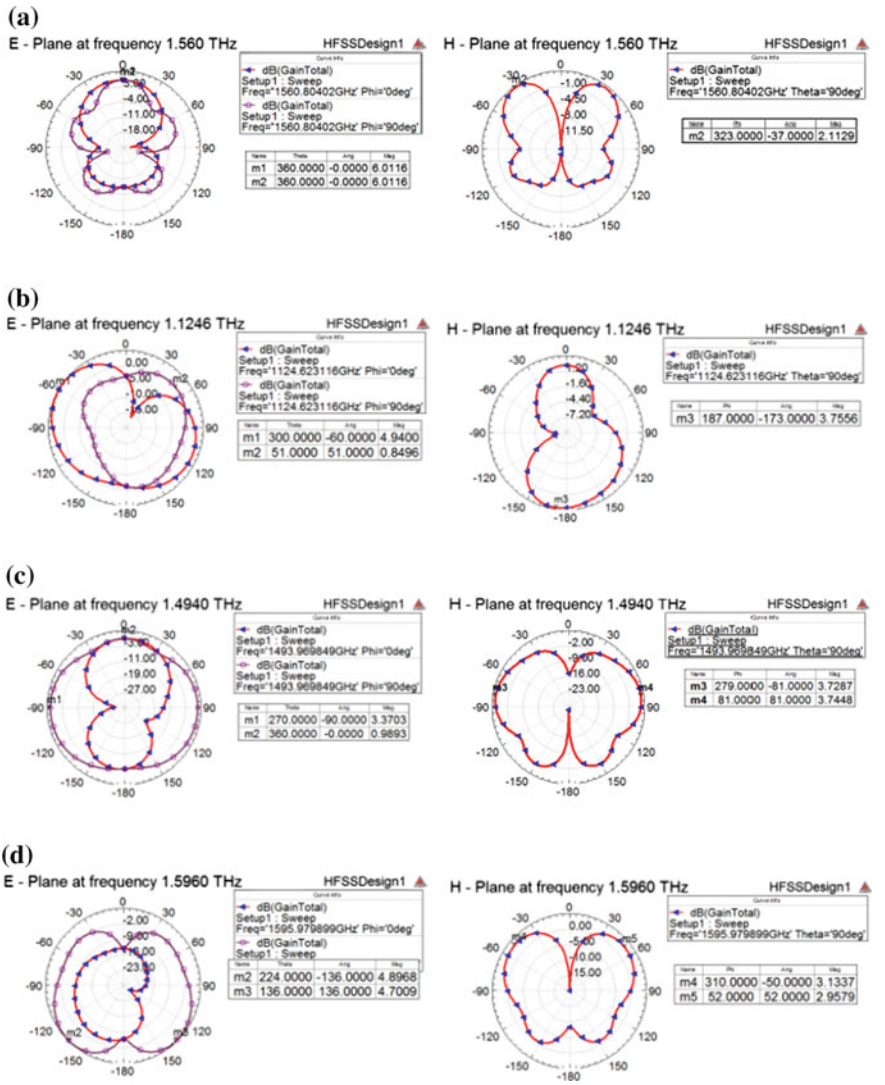


Fig. 5 Simulated radiation patterns in E and H Plane of the proposed antenna at **a** 1.56 THz, **b** 1.1246 THz, **c** 1.4940 THz, **d** 1.5960 THz

Table 2 Summary of parameters

Frequency (THz)	Return loss (dB)	Bandwidth (GHz)	Max. gain (dB)
1.1246	−13.92	11.8	4.49
1.4940	−20.14	23.2	3.74
1.5960	−20.04	10.1	4.96

4 Conclusion

In conclusion, bowtie-shaped antenna with GaAs substrate is proposed for THz application. It shows the multi band behavior in the frequency range of 1.1–1.8 THz. The AMC structure is used to improve the performance characteristics of the antenna. This design has three resonant frequencies at 1.246 THz (RL = −13.92 dB), 1.4940 THz (RL = −20.14 dB), and 1.5960 THz with return loss ≤ -10 dB and VSWR ≤ 2. It is seen that the maximum gain of 6.14 dB is obtained at 1.56 THz in radial directions denoted by angles $\theta = 40°$ and $\Phi = 182°$. This antenna has interesting E plane and H plane radiation patterns which can be useful for THz imaging and THz aerospace applications.

References

1. Seeds, Alwyn J., et al. "Tera Hertz Photonics for Wireless Communications" Journal of Lightwave Technology 33.3 (2015): 579–587.
2. Han, Huipeng, Jungang Yuan, and Jincheng Tong. "Design of THz Space Application System." Journal of Computer and Communications 3, no. 03 (2015): 61.
3. Ravaro, M., et al. "Detection of a 2.8 THz quantum cascade laser with a semiconductor nanowire field-effect transistor coupled to a bow-tie antenna." Applied Physics Letters 104.8 (2014): 083116.
4. Ríos, Rubén Darío Velásquez, et al. "A bow-tie photoconductive antenna using a low-temperature-grown GaAs thin-film on a silicon substrate for terahertz wave generation and detection." Journal of Optics 17.12 (2015): 125802.
5. Natrella, Michele, et al. "Modelling of surface waves on a THz antenna detected by a near-field probe." Optics express 20.14 (2012): 16023–16031.
6. Karl, Nicholas J., Robert W. McKinney, Yasuaki Monnai, Rajind Mendis, and Daniel M. Mittleman. "Frequency-division multiplexing in the terahertz range using a leaky-wave antenna." Nature Photonics (2015).
7. Singh, Amandeep, and Surinder Singh. "A trapezoidal microstrip patch antenna on photonic crystal substrate for high speed THz applications." Photonics and Nanostructures-Fundamentals and Applications 14 (2015): 52–62.
8. N. Zhu and R. W. Ziolkowski, "Progress toward THz antenna designs with high directivity and high efficiency," in Proc. IEEE AntennasPropagat. Soc. Int. Symp., Orlando, FL, USA, 2013, pp. 2271–2272.
9. Andryieuski, Andrei, and Andrei V. Lavrinenko. "Graphene metamaterials based tunable terahertz absorber: effective surface conductivity approach." Optics express 21, no. 7 (2013): 9144–9155.
10. Holloway, Christopher L., Edward F. Kuester, Joshua Gordon, John O. Hara, Jim Booth, and David R. Smith. "An overview of the theory and applications of metasurfaces: The two-dimensional equivalents of metamaterials." Antennas and Propagation Magazine, IEEE 54, no. 2 (2012): 10–35.
11. Nagel, M., Rwth Aachen University, 2013. THz antenna array, system and method for producing a THz antenna array. U.S. Patent 8,581,784.
12. Vendik, Irina B., Orest G. Vendik, Mikhail A. Odit, Dmitry V. Kholodnyak, Svetlana P. Zubko, Margarita F. Sitnikova, Pavel A. Turalchuk et al. "Tunable metamaterials for controlling THz radiation." IEEE Trans. THz Sci. Techn 2 (2012): 538–549.

13. Zhang, Qing-Le, Li-Ming Si, Yongjun Huang, Xin Lv, and Weiren Zhu. "Low-index-metamaterial for gain enhancement of planar terahertz antenna." AIP Advances 4, no. 3 (2014): 037103.
14. Sensale-Rodriguez, Berardi, Rusen Yan, Lei Liu, Debdeep Jena, and Huili Grace Xing. "Graphene for reconfigurable terahertz optoelectronics." Proceedings of the IEEE 101, no. 7 (2013): 1705–1716.
15. Devesh Kumar, Sakshi Bansal and Manish Sharma "Novel Design of Key-Shaped Fractal Antenna for UWB Applications" IEEE CICN 2014, Nov 2014, pp 41–45.

ANFIS-Based Fault Diagnosis Tool for a Typical Small Aircraft Fuel System

Vijaylakshmi S. Jigajinni and Vanam Upendranath

Abstract In the present paper, an Adaptive Neuro-Fuzzy Inference System (ANFIS) based intelligent diagnosis tool for investigating the health of a typical small aircraft fuel system simulation was proposed. The system was designed for identifying the faults present in the aircraft fuel system and to diagnose those conditions with a proper fuel flow to the engine. The ANFIS intelligent tool works based on the logical rules of an expert system, which are developed as per the engine's fuel consumption and the fuel flow from the tanks. The inputs to train the ANFIS are the fuel flow at the previous instant and the engine's fuel consumption and the corresponding target is the fuel tank's control signals. Training of ANFIS, generates the control signals as per the fuel requirement of the engine and the fuel flow to the tanks. The proposed intelligent controller model was implemented in the platform of MATLAB/Simulink and a comparison with the other techniques allowed the effectiveness of the proposed model.

Keywords Aircraft fuel system · Fuel flow · Fault diagnosis · ANFIS · Fuel tank

1 Introduction

The aircraft industry has an important socio-economic impact on society and world economy [1]. Based on the nonlinear systems, the aircraft systems are proposed as hybrid systems [2]. The normal cooperating systems in an aircraft are specified as, Flight Management System (FMS), Flight Warning Computer (FWC), Display

V.S. Jigajinni (✉)
Department of Electronics and Instrumentation Engineering,
Basaveshwar Engineering College, Bagalkot 587 102, Karnataka, India
e-mail: talk2vijusj@gmail.com

Vanam Upendranath
IVHM, Structural Technologies Division (STTD), CSIR-National Aerospace Laboratories,
Bangalore 560 017, Karnataka, India
e-mail: vanam@nal.res.in

© Springer Science+Business Media Singapore 2017

R. Singh and S. Choudhury (eds.), *Proceeding of International Conference on Intelligent Communication, Control and Devices*, Advances in Intelligent Systems and Computing 479, DOI 10.1007/978-981-10-1708-7_45

Management Computer (DMC), Overhead Fuel Panel (OFP), Inertial Navigation System (INS), Engine Master Switches, Landing Gear Status, Weight-On-Wheels (WOW) [3]. Every part of the above-stated cooperating systems are responsible for safe travel of the aircraft, either in commercial or combat or jet types. On the other hand, the internal combustion engine is the foundation of aircraft propulsion and it is exemplified by gas turbines and reciprocating engines, which employ fossil fuel [4]. As a result, in avionic system fuel is the most decisive fluid to handle [5]. Hence, aircraft fuel system is considered as an important nonlinear system of the aircraft.

Generally, an aircraft fuel system contains numerous internal, transfer, and wing tanks with a minimum of two engines. The fuel flow to the engines is devised through fuel transfer pipelines. There is a chance of failure in any of these components, like tank leakage, pump failure, pipeline leakage, filter blocks, valve stuck, etc. The malfunction in one of these subsystems effects in the crash of the aircraft system. Hence, interconnection among those tanks has been launched for eradicating an important shift in the centre of gravity and the possible loss of control over the aircraft [6]. In this regard, newly developed technological advancements in control engineering, signal processing, and computer sciences have noticeable potentials which helps to solve several issues associated to the aircraft systems with respect to improved guidance, navigation and control of the flying systems together with better flight performance, self-protection and enlarged life of structures [7]. As a result, to develop operation dependability and safety of aircraft systems, fault diagnosis tools have been effectively employed in technical processes of aircraft fuel system [8–12].

Fault diagnosis is a process that identifies the presence of fault and isolates it. It depends on the kind, location and time of detection of a fault. Fault identification chases fault isolation, and is the determination of the size and time deviation behaviour of a fault [13, 14]. Compared with the industry systems, application of fault diagnosis in aircraft control system is more realistic and significant [15]. Therefore, efficient measures avoid serious economic losses and help to mitigate the untimely and avoidable replacement of the components and parts in the aircraft [16]. Conversely, an early detection and analysis of anomalies and faults in an aircraft system makes it feasible to carry out significant decisions based on condition maintenance and actions as resisted to conventional time-based maintenance actions [17]. Moreover, in the case of commercial aircraft, competent diagnoses can reduce the disturbance caused to passenger travel and the financial cost of downtime maintenance [18]. The common structure of any diagnosis technique process includes three steps of the following system. In the first step some unique information of the fault is obtained. Second, constructive features from the gathered information are removed by means of a definite tool. Finally, by means of a recognition tool [19] the dissimilar kinds of fault patterns are recognized. Fault diagnosis algorithms are classified into two types, namely model-based and data-driven techniques. Both the techniques are broadly studied in the literature for health monitoring of aircraft systems [20].

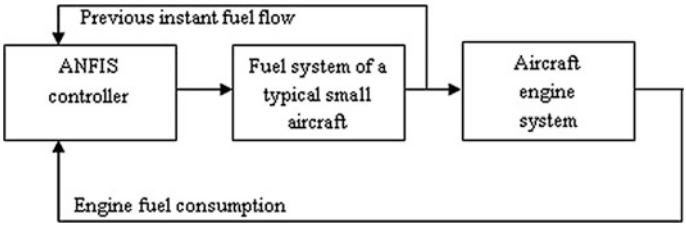


Fig. 1 Block diagram of ANFIS controller for a typical small aircraft fuel system

In this paper, fault diagnosis is carried out by hybrid ANFIS tool for the health investigation of a typical small aircraft fuel system. Figure 1 depicts the block diagram of the ANFIS-based fault diagnosis tool for investigating the health of a typical small aircraft fuel system. The suggested system is devised for recognizing the fault present in the fuel system of aircraft and analyse that condition with appropriate fuel flow to the engine. The ANFIS works based on the expert system logical rules, which are improved as per the engine fuel consumption and fuel flow from the tanks. The ANFIS algorithm is trained by two inputs, viz, earlier instant fuel flow and engine fuel consumption with the target output as control signals of fuel tank. By employing the training samples, the suggested intelligent controller improves the control signals as per the fuel requirement of the engine and the fuel flow of the tank, which helps to monitor the overall health of the fuel system.

In Sect. 3, the improvement of suggested ANFIS diagnosis tool for faults in the fuel system is specified. In addition, the current research work on fuel system diagnoses is assessed in Sect. 2. In Sect. 4, the justification of the suggested ANFIS diagnosis tool is demonstrated.

2 Recent Research Review

There has been a lot of research on diagnosis tools for fault detection approaches on aircraft fuel system. A few of the current research are assessed here. Papadopoulos [21] have used the knowledge of statecharts and fault trees for improving an online hazard-directed monitoring plan. In this plan, an appropriate specification was obtained from design models and a reference monitoring model was formed through safety analysis. For the justification of the suggested approach, a generic safety monitor was proposed to hold up online detection, analysis and control of hazardous failures in actual time. In order to offer a platform for the study of the entire fuel system logic and sequencing, a simulation of an aircraft fuel management system has been launched by Jimenez et al. [22]. They proposed the onboard executable programmes for normal flights and for failure cases. The suggested simulation environment could be effortlessly adapted and expanded to employ

novel components. In this document, a particular example was considered based on an aircraft with a tail tank and six tanks in the wings.

Narasimhan et al. [23] have performed the methods for online monitoring and analysis of complex hybrid system such as the fuel transfer system of aircraft. It employed model-based diagnosis (MBD) methodologies on the engine of the suggested hybrid system. It comprises a modelling methodology geared to the diagnosis task viewed and fault detectors for following system behaviour and recognizing discrepancies among predicted and observed behaviour, and fault isolation and identification plans for finding out the faulty component and computing the magnitude of the change. Bartlett et al. [24] have investigated on two approaches, namely, fault tree analysis technique and the method of digraphs to provide for the demands of diagnosis inside aircraft fuel system. Both the above-mentioned techniques use a comparative approach to consider variations among real system behaviour and anticipated one. Shen et al. [25] built the virtual simulation software of aircraft fuel Prognostic and Health Management (PHM) system which is an integrated approach of model-based method and signal processing technique. It is used to overcome the complexity of acquisition of fault information from the actual working system, where they examined the status parameters that used to recognize the failure modes. The important failure modes identified by this approach were nozzle clogging, joints looseness, pipe broken and leakage in fuel tanks of aircraft. The status parameters were fuel pressure and fuel flow. To replicate the performance of sensor the status parameter model was built to identifying the status of fuel system. Using the LabVIEW software with signal processing module, the outputs from the virtual sensors were collected to understand the modelling and simulation of failure detection and failure analysis.

Centre of Gravity (CoG) control of fuel system is one of the significant control systems in aircraft safety. Any abrupt changes in the CoG lead to the difficulty in control of aircraft flight. In order to avoid the CoG problem, aircraft fuel system control must be performed effectively and accurately without any shortcomings. To achieve such flawless performance and to avoid massive damages model-based fault diagnosis tools have been developed. The direct testing of fault diagnosis tools involves more expenditure. Hence, model-based aircraft fuel systems have been developed in simulation tools such as LabVIEW, MATLAB/Simulink, etc.

The recent literature studies and discussions showed various fault detection and diagnosis techniques, viz., statecharts, fault trees, digraphs, Extended Kalman Filter (EKF). Here, statecharts were based on the selected state variable of the system. It needs expert advice to select the state variables for the specific aircraft fuel system. Fault trees are derived from determining the possible fault conditions that appear during the undesired state of the system. It was developed to understand the risk involved in the aircraft and take the possible measures to avoid such risks in order to improve the aircraft system safety and reliability. But, it is different for each aircraft systems like transport, civil, etc. But it needs background knowledge of subsystems and its behaviour for feature extractions to determine the possible faults.

Digraphs involve the selection of proper nodes and possible paths towards neighbour nodes. Nodes considered are, locations in fuel system such as pump drive, tanks, engines, etc., and possible paths are connection pipelines for fuel flow. As the number of node selection increases in the fault diagnosis tool, the computations for fault analysis increases and burdens the monitoring systems with complex nature. EKF models have the limitations of improper estimations of system parameters in cases of wrong initial estimations or incorrect process models. From the above demerits of mentioned tools for fault diagnosis, it is evident that the design of fuel system of aircraft is a complex task and is the necessity of easy and intelligent diagnosis tool. Thus, ANFIS-based fault diagnosis technique helps in overcoming the limitations of the above-mentioned techniques. An ANFIS-based intelligent fault diagnosis method is designed, which is a robust scheme that comprises of both neural network and fuzzy logic. It is a hybrid framework which involves different methodologies where it compensates one weakness with the strength of other technique.

3 Proposed Fault Diagnosis Tool

In the proposed methodology ANFIS algorithm is used for fault diagnosis to recognize the faults present in the aircraft fuel system. The ANFIS algorithm works based on the expert system logical rules, which are trained as per the engine fuel consumption and fuel flow from the tanks. The ANFIS is trained by the earlier instant fuel flow and engine fuel consumption as input with the related target/output as fuel tank control signals. By employing the training samples, the suggested intelligent diagnosis tool improves the control signals as per the fuel requirement of the engine and the fuel flow of the tank.

3.1 Proposed Aircraft Fuel System Design

A block diagram of a typical small aircraft fuel system, which consists of aircraft fuel tanks, pumps, pipeline routes, the fuel controller, etc., is depicted in Fig. 2. Generally in aircraft fuel tanks are either located in the aircraft's fuselage or in the wings. The system contains a total of eight fuel pumps and there are four main pumps, two pumps for backup and two for delivery of fuel between wings at emergency conditions. The aircraft fuel system is controlled by the proposed intelligent fault diagnosis tool with its targeted control signals. The primary objective of the proposed model is to manage the fuel flow to the engine without fail, so as to reach at the required engine fuel consumption rate. If any fault occurs in any one of the fuel tanks, the controller model detects it and reacts as per the fuel requirement of the aircraft fuel engine.

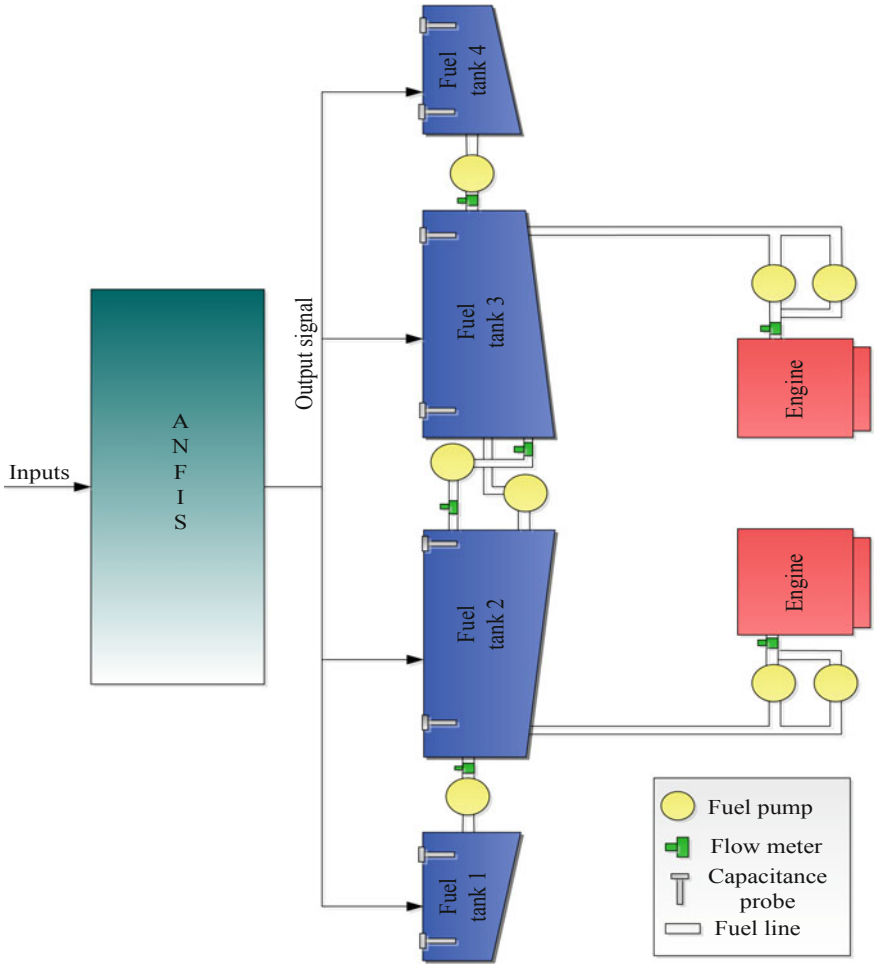


Fig. 2 Structure of the aircraft fuel system with controller

ANFIS is a machine learning tool to realize the human's decision-making capability for decades. It has the ability to learn from the fuzzy theory with a five layer structure, which depends on the antecedent as well as the consequent parameters, to approximate the nonlinear functions. ANFIS is well known for its robustness to changes in its parameters within the system and has faster performance than the conventional processing tools. ANFIS is used to diagnose the faults and also act as a controller to generate the targeted control signals. With the diagnosis rules derived from the user, the ANFIS tool processes the system parameters. It performs fault detection process and the corresponding suggestions are made. The structure of the proposed controller is explained in Fig. 3 and the brief explanations about the development of the ANFIS fault diagnosis tool are given in Sect. 3.2.

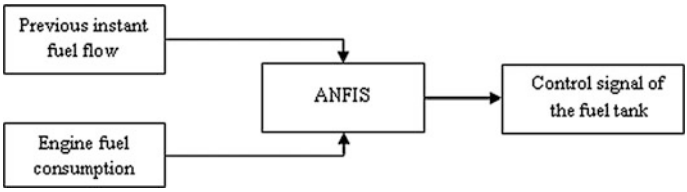


Fig. 3 The structure of the proposed controller

3.2 ANFIS Diagnosis Tool Development

ANFIS refers to a soft computing model, which is a hybrid technique of fuzzy logic as well as neural network. The significant features of ANFIS include the increasingly high reasoning ability with decreased level of computational power [26]. The fuzzy inference rules that are created in ANFIS rely on both the input and the target outcome. Tuning of the fuzzy inference mechanism can be accomplished with the learning ability of neural network. The ANFIS structure is a layered one as depicted in Fig. 5. There are totally five layers in the structure of ANFIS viz the input layer, the fuzzification layer, the product layer, the normalization layer and the defuzzification layer. The nodes may be adaptive or fixed. In this case, the inputs to the ANFIS may possibly be the fuel flow at a previous instant (X) and engine's fuel consumption (Y). Further, the control signals of the fuel tank (Z) are considered as the target output. Hence, the considered parameters aid the ANFIS in formulating the rules, in addition to achieving a better tuning performance.

A first order Takagi-Sugeno inference system consists of two fuzzy rule set which is expressed in Eqs. (1) and (2).

$$\text{Rule 1: If } X \text{ is } C_1 \text{ and } Y \text{ is } D_1 \text{ then } f_1 = m_1 X + n_1 Y + k_1 \tag{1}$$

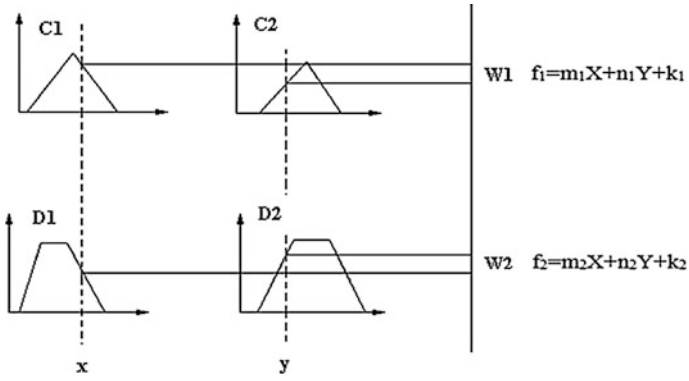


Fig. 4 First order Takagi-Sugeno fuse reasoning

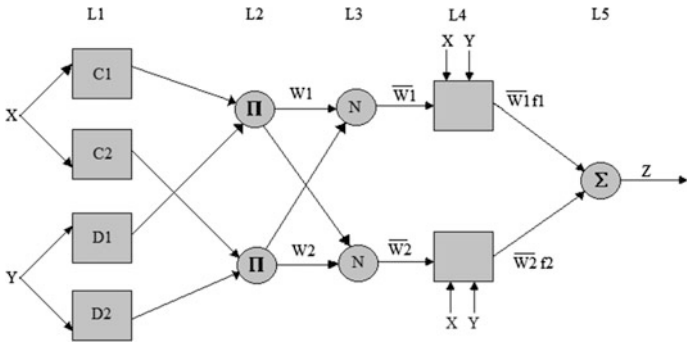


Fig. 5 Structure of the ANFIS

$$\text{Rule 2: If } X \text{ is } C_2 \text{ and } Y \text{ is } D_2 \text{ then } f_2 = m_2X + n_2Y + k_2, \tag{2}$$

where m_1, m_2, n_1, n_2, k_1 and k_2 are the linear parameters and C_1, C_2, D_1 and D_2 are the nonlinear parameters. Figure 4 shows the fuse reasoning of ANFIS diagnosis tool.

The activation levels that correspond to the fuzzy rules are computed with the expression, $W = C_i(x) * D_i(y)$. A continuous t-norm enables the modelling of the logical operator "and" and moreover, it is considered as a product. For every single rule, the computation of the individual output involves the linear combination of the antecedents' parameters and it is shown in Eq. (3) [27].

$$f_i = m_iX + n_iY + k_i, \quad i = 1, 2 \ldots n \tag{3}$$

The output of the model f can be produced with the multiplication between the individual output of each rule and activation degrees of the rules, as in Eq. (4).

$$f = \frac{\sum \overline{W_i} f_i}{\sum W_i}, \quad i = 1, 2 \ldots \tag{4}$$

where W_i indicates the normalized value obtained through the addition of W_1 and W_2. Figure 5 portrays the layered structure of ANFIS:

Fuzzification layer: Every single input layer denotes an input variable and they are forwarded to the fuzzification layer. The fuel flow at an earlier instant (X) and the engine's fuel consumption (Y) of nodes are C_1, C_2, D_1 and D_2, which characterizes the linguistic labels of fuzzy theory in order to divide the membership functions.

$$S_{L1,i} = \mu C_i(X), \quad i = 1, 2 \tag{5}$$

$$S_{L1,j} = \mu D_j(Y), \quad j = 1, 2, \tag{6}$$

where $S_{L1,i}$ and $S_{L1,j}$ indicate the outputs of the fuzzy layer: $\mu C_i(X)$ and $\mu D_j(Y)$ are the membership functions of the fuzzy layer.

Product layer: In this layer, the logical "and" operation that implies the product between the input membership functions is carried out. This operation is given by the labelπ. The outputs from the product layer act as the subsequent node's input weight functions. Equations (7) and (8) are the representations of the outputs from the product layer.

$$W_1 = S_{L2,i} = \mu C_i(X) \cdot \mu D_i(Y), \quad i = 1, 2 \tag{7}$$

$$W_2 = S_{L2,j} = \mu C_j(X) \cdot \mu D_j(Y), \quad j = 1, 2 \tag{8}$$

where, W_1 and W_2 specifies the outputs from the product layer.

Normalization layer: This layer forms the third layer in the ANFIS structure. Here, each and every node is fixed and points to the IF portion in the fuzzy rule. The input weights get normalized in this layer for permitting the execution of fuzzy "and" operation. N is the label of this layer and the outputs from this layer are depicted in Eqs. (9) and (10).

$$\overline{W_1} = S_{L3,i} = \frac{W_i}{W_1 + W_2}, \quad i = 1, 2 \tag{9}$$

$$\overline{W_2} = S_{L3,j} = \frac{W_j}{W_1 + W_2}, \quad j = 1, 2 \tag{10}$$

where, $\overline{W_1}$ and $\overline{W_2}$ refers to the outputs of the normalized layer.

Defuzzification layer: An adaptive action is conducted in this layer. The previously set fuzzy rules help in obtaining the output membership functions from this layer. The outputs are specified in Eqs. (11) and (12).

$$\overline{W_1} f_i = S_{L4,i} = \frac{W_i}{W_1 + W_2} \left[m_1 V_g + n_1 V_d + k_1 \right] \tag{11}$$

$$\overline{W_2} f_j = S_{L4,j} = \frac{W_j}{W_1 + W_2} \left[m_2 V_g + n_2 V_d + k_2 \right], \tag{12}$$

where $\overline{W_1} f_i$ and $\overline{W_2} f_j$ stands for the outputs of the defuzzification layer.

Total output layer: The THEN part of the fuzzy rule is represented using this layer of ANFIS. The outputs are evaluated and labelled as $\sum$.

$$f = S_{L5,i} = \sum \overline{W_i} f_i = \frac{\sum \overline{W_i} f_i}{\sum w_i}, \tag{13}$$

where the total output is f.

Upon completing the training phase, ANFIS is bestowed with the power to readily offer the control signals of the fuel system in the aircraft. The implementation is done using MATLAB/Simulink platform. By comparing with the existing methods, ANFIS proves to be an effective technique for health monitoring of a typical small aircraft fuel system. Section 4 deals with the implementation as well as the related descriptions of the proposed method.

4 Results and Discussion

In this paper, a model of a typical small aircraft fuel system is designed based on the reference paper [3] and the health of the fuel system is analysed using the proposed method. The proposed ANFIS controller model with the aircraft fuel system is shown in Fig. 6a, b. To perform the simulation, the fuel utilized is the liquid

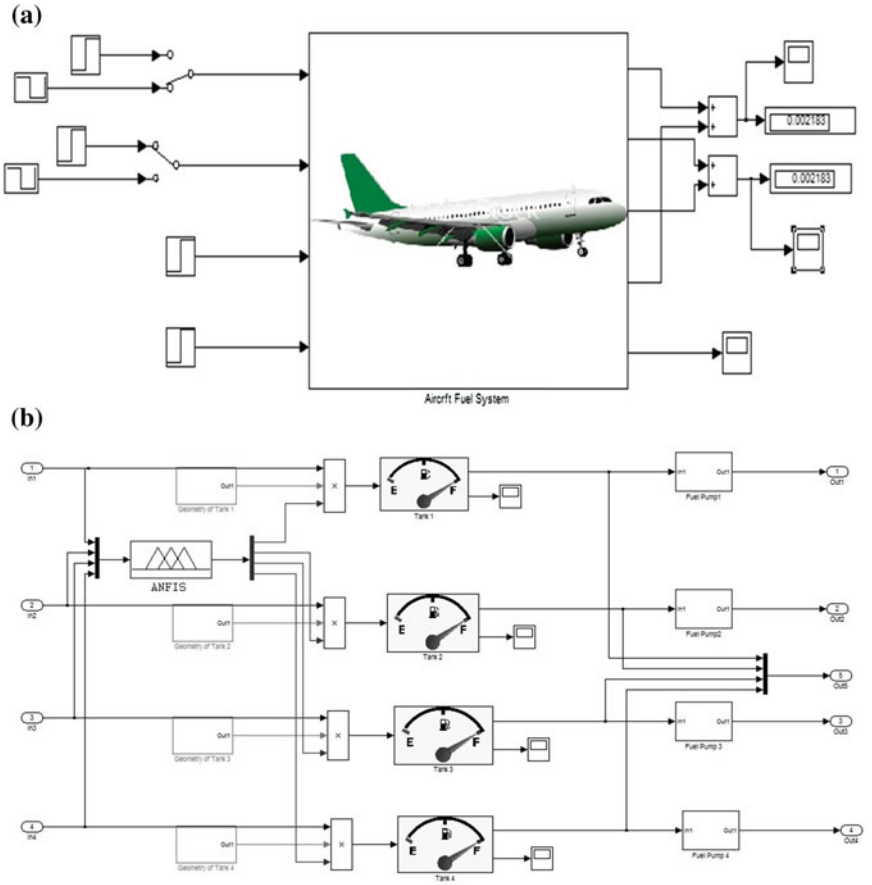


Fig. 6 **a** Simulation of outer model of the small aircraft fuel system. **b** The Simulink model of the aircraft fuel system with controller

Hyjet-4A. The characteristics of hyjet-4A available in the MATLab/Simulink were used to simulate the model.

The temperature and viscosity of hyjet-4A are found to be 22.72 °C and 1. The fuel line is built in the same manner as in the practical fuel systems using the metal pipes that are firm and fixed. The pipe length equals the length of 500 mm in between the wing tip tanks and the internal wing tanks while it is 7200 mm between the engines and the integral wing tanks. The pipes have an internal diameter of 10 mm and the pipes' shape is decided with a geometry factor, the value of which is set as 64. With this preset geometry factor, the pipe is found to have a circular cross-section. An axial pump containing the electric motor drive is being selected in the place of the fuel pump. For this particular pump, the reference angular velocity and the correction factor are set with a value of 1,770 rpm and 0.8, respectively.

A typical small aircraft fuel system model is interfaced with the ANFIS controller, which predicts the fault occurrences and diagnoses the problem in the fuel system via the control signals that are given to the fuel tanks. The effectiveness of the proposed method is evaluated using the comparison analysis with the existing techniques such as the Artificial Neral Network (ANN) and the aircraft fuel system without a controller. The simulation time that is used in this model is about 20 s. The fuel management and fuel consumption requirement in the aircraft system without a controller is described in Fig. 7. It shows that the fuel requirement in the aircraft engine is ≈2,800 kg/h, which is solved with the four fuel tanks. As per the fuel requirement, the fuel required from each tank is 700 kg/h. Here, the four tanks offer a solution to the engine requirement within 4–6.5 s. After 4 s, the fuel flow in the fuel tank 1 is reduced. As a result, the delivery of the fuel to the engine is affected. This fault is not correctly identified by the automatic fuel management

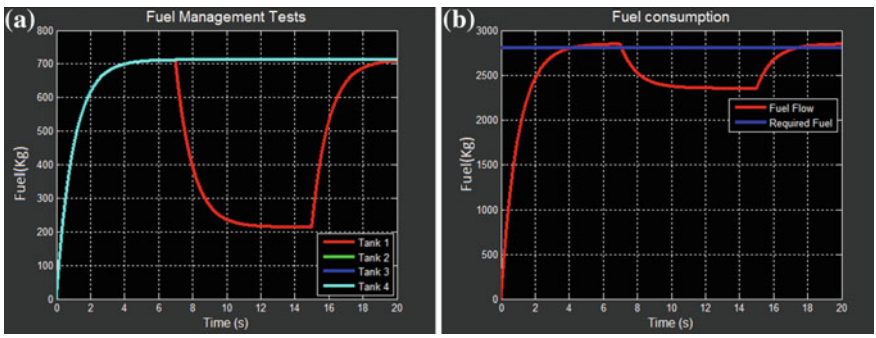


Fig. 7 **a** Fuel management and **b** fuel consumption without controller

system in the aircraft fuel system. Therefore, the performance of the system gets affected. A similar fault conditions through ANN technique is illustrated in Fig. 8. It shows that the ANN technique detects the time of fault and diagnoses the condition through the additional fuel injection from the other fuel tanks. But, the ANN technique is based on the historical dataset and the weight updation alone. The weight updation process utilized in the ANN technique is the back propagation algorithm, which is a traditional method. With this technique, the fuel flow to the engine becomes 2600 kg/h that is not the full requirement of the engine. The proposed controller for the aircraft fuel system is shown in Fig. 9. The fuel management using the different techniques, as per the fuel requirements of the engine, is described in Fig. 10. From these results, it is understood that the proposed method effectively detects the fault in the fuel tank and manages the fuel requirement of the aircraft engine, compared to other methods.

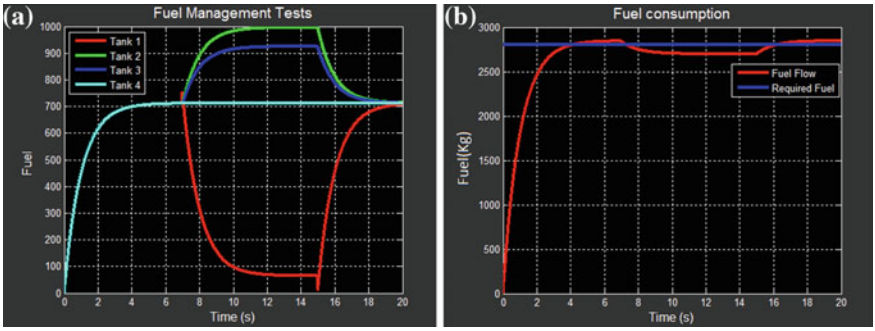


Fig. 8 **a** Fuel management and **b** fuel consumption using ANN

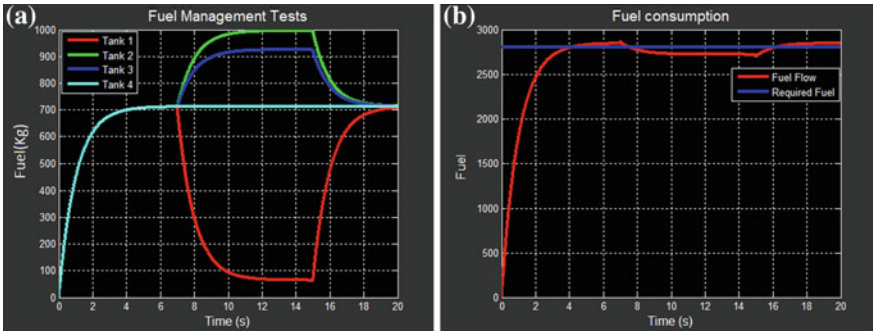


Fig. 9 **a** Fuel management and **b** fuel consumption using the proposed controller

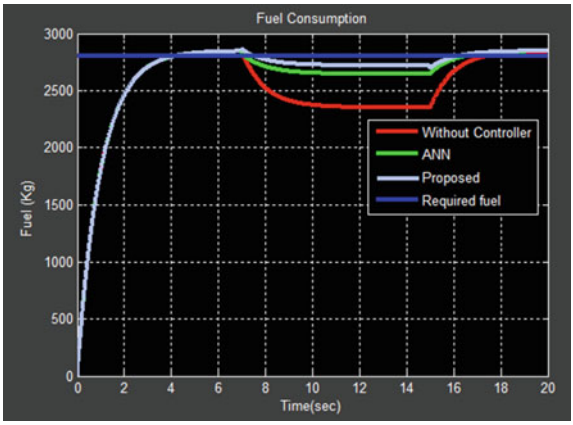


Fig. 10 Comparisons of fuel consumption

5 Conclusions

An ANFIS-based intelligent health monitoring model for a typical small aircraft fuel system is modelled. The proposed intelligent ANFIS controller was designed to generate the control signals of the fuel tanks based on the fuel requirement of the engine and the fuel flow to the tanks. The development of ANFIS is helpful for detecting the faults present in the aircraft fuel system and for diagnosing those faults using the expert's logical rules. The aircraft fuel system is designed with four fuel tanks and different types of tank faults were applied. During a fault condition in the tank, the controller's performance was analysed. The effectiveness of the proposed method was verified through a comparison analysis with the existing techniques. From the comparison analysis, it is apparent that the proposed method is an effective technique to detect and diagnosis the faults.

References

1. Zhi-Ling Yang, Wang Bin, Dong Xing-Hui, L I U Hao.: Expert system of fault diagnosis for gear box in wind turbine. In: Systems Engineering Procedia, Vol. 4, pp. 189–195, 2012
2. Biswas Gautam, Gyula Simon, Nagabhushan Mahadevan, Sriram Narasimhan, John Ramirez, Gabor Karsai.: A robust method for hybrid diagnosis of complex systems. In: Proceedings of the 5th Symposium on Fault Detection, Supervision and Safety for Technical Processes, pp. 1125–1131, 2003
3. Robert Breda, Vladimir Beno.: Modeling of Control Circuit of Aircraft fuel system. In: Przegląd Elektrotechniczny, Vol. 89, pp. 172–175, 2013
4. Bohwa Lee, Sejin Kwon, Poomin Park, Keunbae Kim.: Active power management system for an unmanned aerial vehicle powered by solar cells, a fuel cell, and batteries. In: IEEE Transactions on Aerospace and Electronic Systems, Vol. 50, No. 4, pp. 3167–3177, 2014
5. Insaurralde Carlos C, Miguel A Seminario, Juan F Jimenez, Jose M Giron-Sierra.: Computer tool with a code generator for avionic distributed fuel control systems with smart sensors and

actuators. In: IEEE Transactions on Systems, Man, and Cybernetics, Part C: Applications and Reviews, Vol. 38, No. 3, pp. 431–445, 2008
6. Timothy G Davis.: Aircraft fuel system simulation. In: Proceedings of the IEEE National Conference in Aerospace and Electronics, pp. 905–911, 1990
7. Ali Zolghadri.: Advanced model-based FDIR techniques for aerospace systems. Progress in Aerospace Sciences, Vol. 53, pp. 18–29, 2012
8. Kamal M M, D W Yu, D L Yu.: Fault detection and isolation for PEM fuel cell stack with independent RBF model. Engineering Applications of Artificial Intelligence, Vol. 28, pp. 52–63, 2014
9. Inseok Hwang, Sungwan Kim, Youdan Kim, Chze Eng Seah.: A survey of fault detection, isolation, and reconfiguration methods. In: IEEE Transactions on Control Systems Technology, Vol. 18, No. 3, pp. 636–653, 2010
10. Zhang Y M, Jin Jiang.: Active fault-tolerant control system against partial actuator failures. In: IEEE proceedings-Control Theory and applications, Vol. 149, No. 1, pp. 95–104, 2002
11. De Lillo Liliana, Lee Empringham, Pat W Wheeler, Sudarat Khwan-On, Chris Gerada, M Nazri Othman, Xiaoyan Huang.: Multiphase power converter drive for fault-tolerant machine development in aerospace applications. In: IEEE Transactions on Industrial Electronics, Vol. 57, No. 2, pp. 575–583, 2010
12. Yu Xiang, Jin Jiang.: Hybrid fault-tolerant flight control system design against partial actuator failures. In: IEEE Transactions on Control Systems Technology, Vol. 20, No. 4, pp. 871–886, 2012
13. Isermann Rolf, Peter Balle.: Trends in the application of model-based fault detection and diagnosis of technical processes. In: Control engineering practice, Vol. 5, No. 5, pp. 709–719, 1997
14. Zhang Xiaodong, Thomas Parisini, Marios M Polycarpou.: Sensor bias fault isolation in a class of nonlinear systems. In: IEEE Transactions on Automatic Control, Vol. 50, No. 3, pp. 370–376, 2005
15. Xu Yufei, Bin Jiang, Zhifeng Gao, Ke Zhang.: Fault tolerant control for near space vehicle: a survey and some new results. In: Journal of Systems Engineering and Electronics, Vol. 22, No. 1, pp. 88–94, 2011
16. Talebi H A, K Khorasani.: A neural network-based multiplicative actuator fault detection and isolation of nonlinear systems. In: IEEE Transactions on Control Systems Technology, Vol. 21, No. 3, pp. 842–851, 2013
17. Muenchhof Marco, Mark Beck, Rolf Isermann.: Fault-tolerant actuators and drives-Structures, fault detection principles and applications. In: Annual Reviews in Control, Vol. 33, No. 2, pp. 136–148, 2009
18. Kelly Emma M, L M Bartlett.: Improved fault diagnostics of a dynamic aircraft fuel system using the digraph approach. In: Proceedings of the European Safety and Reliability Conference, Risk, Reliability and Societal Safety, pp. 801–808, 2007
19. Yousef Shatnawi, Mahmood Al-Khassaweneh.: Fault Diagnosis in Internal Combustion Engines Using Extension Neural Network. In: IEEE Transactions on Industrial Electronics, Vol. 61, No. 3, pp. 1434–1443, 2014
20. Tayarani-Bathaie Seyed Sina, Zakieh Nasim Sadough Vanini, Khashayar Khorasani.: Dynamic neural network-based fault diagnosis of gas turbine engines. Neurocomputing, Vol. 125, No. 11, pp. 153–165, 2014
21. Papadopoulos Yiannis.: Model-based system monitoring and diagnosis of failures using state charts and fault trees. In: Reliability Engineering & System Safety, Vol. 81, No. 3, pp. 325–341, 2003
22. Jimenez Juan F, Jose M Giron-Sierra, C Insaurralde, M Seminario.: A simulation of aircraft fuel management system. In: Simulation Modelling Practice and Theory, Vol. 15, No. 5, pp. 544–564, 2007
23. Narasimhan Sriram, Gautam Biswas.: Model-based diagnosis of hybrid systems. In: IEEE Transactions on Systems, Man, and Cybernetics, Vol. 37, No. 3, pp. 348–361, 2007

24. Bartlett Lisa M, E E Hurdle, Emma M Kelly.: Integrated system fault diagnostics utilising digraph and fault tree-based approaches. In: Reliability Engineering & System Safety, Vol. 94, No. 6, pp. 1107–1115, 2009
25. Shen Ting, Fangyi Wan, Weimin Cui, Bifeng Song.: Application of prognostic and health management technology on aircraft fuel system. In: Prognostics and Health Management Conference of IEEE, pp. 1–7, 2010
26. T.R. Sumithira, A. Nirmal Kumar.: Elimination of Harmonics in Multilevel Inverters Connected to Solar Photovoltaic Systems Using ANFIS: An Experimental Case Study. In: Journal of Applied Research and Technology, vol. 11, pp. 124–132, February 2013
27. J.J. Mora, G. Carrillo, L. Perez.: Fault Location in Power Distribution Systems using ANFIS Nets and Current Patterns. In: Transmission and Distribution Conference and Exposition Latin America, pp. 1–6, 2006

Control of Reactive Power of RES-Based Hybrid Isolated Power System Using UPFC

Abhishek Gandhar, Balwinder Singh and Rintu Khanna

Abstract In India, Electric power system network becomes very complex and Flexible AC transmission Systems (FACTS) controllers are deployed for overall control of system. In this paper, most efficient FACTS controller Unified Power Flow Controllers (UPFC) is used for studying the dynamic control of reactive power of RES (Renewable Energy Sources)-based hybrid isolated power system (HIPS). The extensive time-domain simulations are carried out in the proposed HIPS test system. This paper presents the reactive power compensation capability and illustrating the other control features of this controller. UPFC has been implemented in test system for dynamic compensation and improving voltage regulation. The present paper describes the analysis of combination of the UPFC, machines, and the network has been done in SIM POWER SYSTEM/MATLAB software.

Keywords RES · HIPS · UPFC · MATLAB

1 Introduction

India is a developing country with a very large population. There are many remote locations in India which are still not connected with the grid. For social and economic development of these areas, the sufficient electrical power is necessary. The best way to provide electricity to these locations is with diesel power plants as this is a proven technology and its operational reliability is very high [1]. But, it affects

Abhishek Gandhar (✉) · Balwinder Singh · Rintu Khanna
PEC University of Technology, Chandigarh, India
e-mail: abhishek.gandhar@gmail.com

Balwinder Singh
e-mail: balwindersingh@pec.ac.in

Rintu Khanna
e-mail: rintukhanna@pec.ac.in

Abhishek Gandhar
BVCOE, New Delhi, India

© Springer Science+Business Media Singapore 2017

R. Singh and S. Choudhury (eds.), *Proceeding of International Conference on Intelligent Communication, Control and Devices*, Advances in Intelligent Systems and Computing 479, DOI 10.1007/978-981-10-1708-7_46

the environmental conditions and not a very cost effective solution as well. So, the solution to these problems is RESs (renewable energy sources) like wind, solar, hydro, biomass, etc. These RESs can be integrated with the other conventional energy sources. This integration is termed as HIPS (Hybrid Isolated Power System). In fact, HIPS can be an integration of several energy sources, such as solar, hydro, wind, biomass, diesel, etc. However, the penetration of these RES can cause some power quality and power related problems. (1) Power Fluctuations (2) Voltage regulation and power flow complications (3) Harmonics inserted in the network (4) Over voltage due to islanding (5) System vulnerability. Therefore, proper interfacing and control technologies must be used [2–4].

The power imbalance in between generation and the local loads affect the power quality and bring instability in the system. One of the main factors which affect the quality of supply is voltage variations. The variation in voltage is clearly a mismatch in the reactive power variations. This problem is termed as Voltage-KVAR problem of power system. Many studies have been carried out for the smooth integration of RES with conventional energy sources to maintain the reliability and quality of power supply. The conventional methods of reactive power control such as shunt capacitors or different power electronics-based controllers like SVCs and STATCOMs have been proposed. In this proposed work, the most advanced FACT controller, i.e., UPFC has been used to mitigate the imbalance in between the reactive powers of generation and load demand. Economically, the implementation of UPFC is quite expensive due to size of the power electronics converters used for islanded operation or for small load centers like remote areas. Therefore, instead of large thyristors, a small ratings IGBTs (insulated bipolar gate transistors), or any other small rating power semiconducting devices can be used to design the UPFC [5–8].

Here, the test system comprises of a combination of synchronous generator, wind turbine generator system, and a UPFC (Unified Power Flow Controller). The Time simulations studies are carried out including the effect of Excitation controller. AVR (Automatic Voltage Controller) and Exciter model for synchronous generator are modeled as standard IEEE model. This paper discusses the reactive power control capability of UPFC [9]. This simulation study clearly shows the reactive power balancing of synchronous and induction machine after insertion of UPFC in the test system. Simulations carried out in SIM POWER SYSTEM toolbox of MATLAB software package.

Proposed paper has these sections: Introduction in Sect. 1. The Basic theme of UPFC in Sect. 2. Test system Configuration in Sect. 3. Simulation results in Sect. 4, and Conclusion in Sect. 5.

2 Basic Structure of UPFC

FACTS controller consists of a large number of power electronics-based different controllers. In this group of power system controllers, unified power flow controllers (UPFC) is most accomplished FACTS controller. In fact it is a multifunctional

controller which can regulate many actions simultaneously, such as control of transmission voltage, line impedance, and phase angle, etc. It also provides controlled compensation to the power system. This is the advanced circuitry of power electronics technology which consists of two converters in shunt and series connections with the network. It is combined topology of a STATCOM and SSSC, it has the capability to achieve the objectives of both series and shunt controller like power flow control, increasing transient stability, and most important voltage (reactive power) regulation [10, 11].

The UPFC consists of two VSCs (voltage-source converters), connected in opposite manner and a DC capacitor is placed in between those VSCs (Fig. 1). It injects a synchronous voltage source of required amplitude and phase in the transmission line for controlling the power flow. The function of series converter is to inject synchronous voltages, V in series with the line, which results in the exchange of active power and reactive power with the line. The reactive power is locally generated by the series converter, whereas the active power is transferred to or from the line through the dc capacitor. On the other hand, the shunt converter generates the requirement of this DC terminal power to or from the line, thereby regulates the voltage profile of DC bus. The total active power consumed by the UPFC at the expense of total losses of converters and the coupling transformers. The exchange of reactive power is also done by shunt converter. The shunt converter draws a regulated current from the line. One component of this current is used to compensate the demand of active power supply of the series converter. The other part of this injected current is to generate the reactive power depending upon the demand of nature of

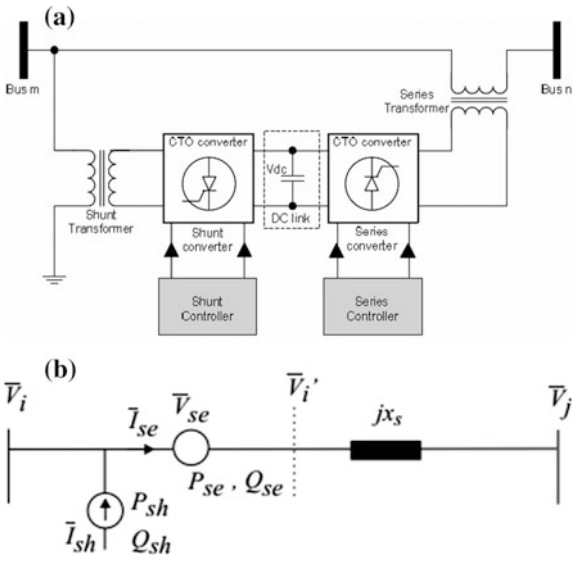


Fig. 1 **a** The schematic configuration of UPFC [9]. **b** The electric circuit diagram

reactance of system. The reactive compensation control technique of the shunt converter is synonymous to conventional static VAR compensators [11–13].

$$Q = V_1(V_1 - V_2\cos\delta)/X \quad P = V_1V_2\sin\delta)/X \tag{1}$$

3 Test System Configuration

The hybrid power system is designed using a wind energy source as nonconventional and diesel system as conventional method of generation of electricity. The proposed system comprises of different AC machines for different type of energy generations. Generally, Induction machines are used in wind energy conversion system while alternators are used for conventional way of energy generation. These generators are fulfilling the energy demand of load network. The reactive power demand of load and Induction machine is supplied by synchronous generator but because of intermittent nature of wind, an imbalance in reactive power demand has evolved in the system. For compensating this imbalance, a very powerful controller UPFC has been implemented here. The block diagram is as shown in Fig. 2 which shows the flow of reactive power. In this paper, the investigations are executed on the assumption that the wind turbine is operating at rated speed (9 m/s). The Induction Generator of Group 1 is of rating 1.5 KVA nominal powers. The diesel generator is having nominal power of 3.125 KVA (Fig. 3).

Therefore, the whole test system is divided in two parts/sections i.e. Wind induction generator section and diesel synchronous generator section. The FACT controller UPFC has been deployed between these sections. Thus, the UPFC

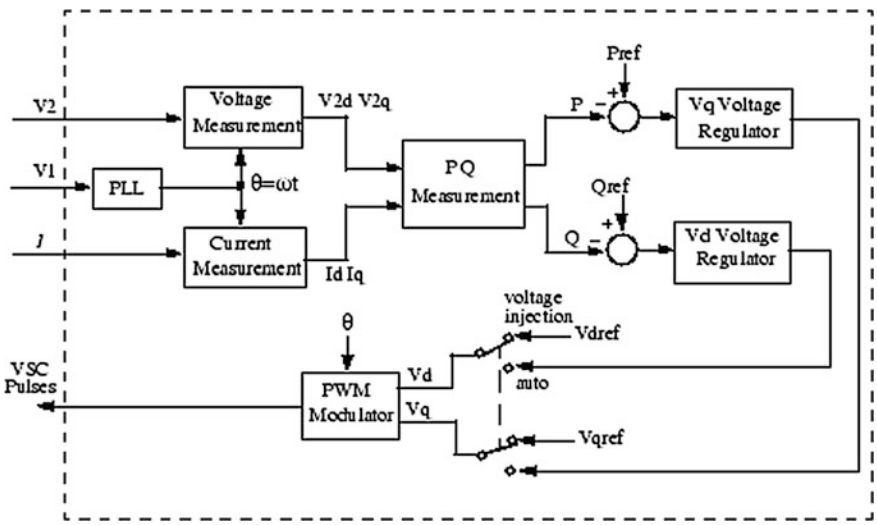


Fig. 2 Block diagram of control system for UPFC

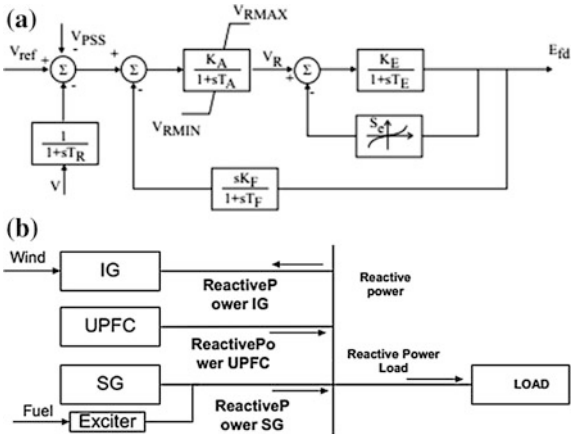


Fig. 3 **a** The AVR and exciter model of synchronous generator. **b** The HIPS model

Controller is relieving the power congestion of both systems in a very effective manner. Due to 1 % step variations in reactive power load ΔQ_L, the system voltage will vary accordingly. The Total reactive power of system will be $\Delta Q_{\mathrm{SG}} + \Delta Q_{\mathrm{UPFC}} - \Delta Q_L - \Delta Q_{\mathrm{IG}}$ and the resultant difference will reflect the voltage variations in the system [14]. The Governing equation of system is as follows:

$$P_{\mathrm{IG}} + P_{\mathrm{SG}} = P_L \tag{2}$$

$$Q_{\mathrm{SG}} + Q_{\mathrm{UPFC}} = Q_L + Q_{\mathrm{IG}} \tag{3}$$

$$\Delta V(s) = K_V/(1 + \mathrm{ST}_V)[\Delta Q_{\mathrm{SG}}(s) + \Delta Q_{\mathrm{UPFC}}(s) - \Delta Q_L(s) - Q_{\mathrm{IG}}(s) \tag{4}$$

where $T_V = 2H_r/D_V\, V^0$ and $K_V = 1/D_V$.

The equation of synchronous generator equation is given as:

$$Q_{\mathrm{SG}} = (E'_q V\cos\delta - V^2)/X'_d \tag{5}$$

For small change, the same equation is written as

$$\Delta Q_{\mathrm{SG}} = V\cos\delta/X'_d \Delta E'_q + (E'_q\cos\delta - 2V)/X'_d \Delta V \tag{6}$$

Taking the Laplace Equation (Fig. 4).

$$\Delta Q_{\mathrm{SG}}(s) = K_{a1}\Delta E'_q(s) + K_{b1}\Delta V(s) \tag{7}$$

where

$$K_{a1} = V\cos\delta/X'_d, K_{b1} = (E'q\cos\delta - 2V)/X'_d \tag{8}$$

It supplies the reactive power against the demand of Induction generator and load. Thus, UPFC offers the dynamic compensation and effectively controls the variations in the voltage profile of system.

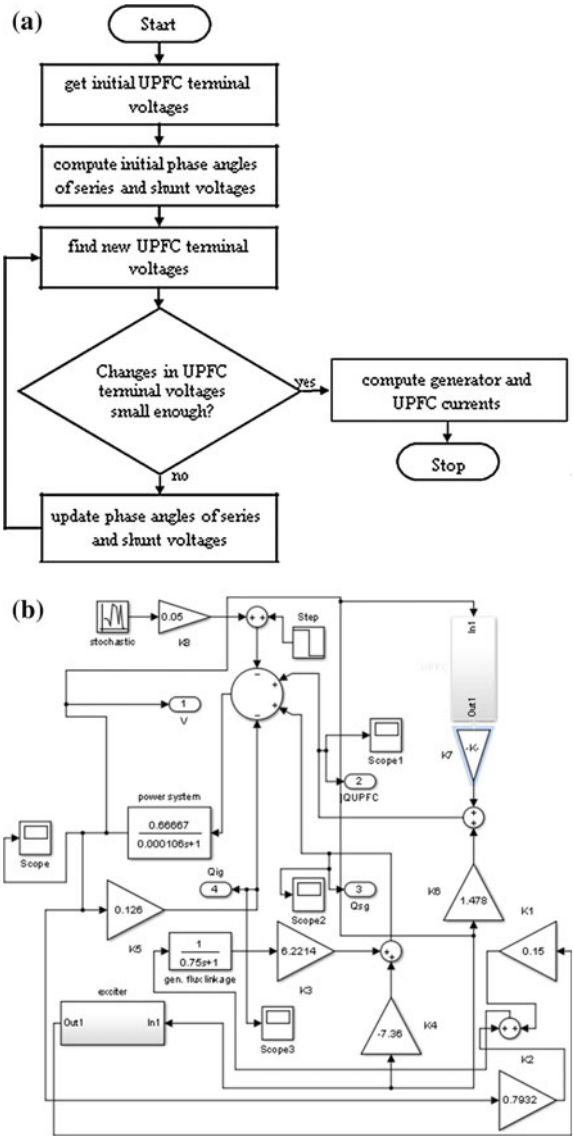


Fig. 4 **a** Algorithm for interfacing the UPFC. **b** Simulation test system of proposed HIPS

4 Simulation Results

The simulation study is carried out in SIM POWER tool box of MATLAB software. These studies are carried out for the 1 % step change in reactive power demand of system. The random variations are inserted in the system using the stochastic noise. The small variations in the change of reactive powers of induction generator of wind power system and synchronous generator of diesel power system are clearly presented

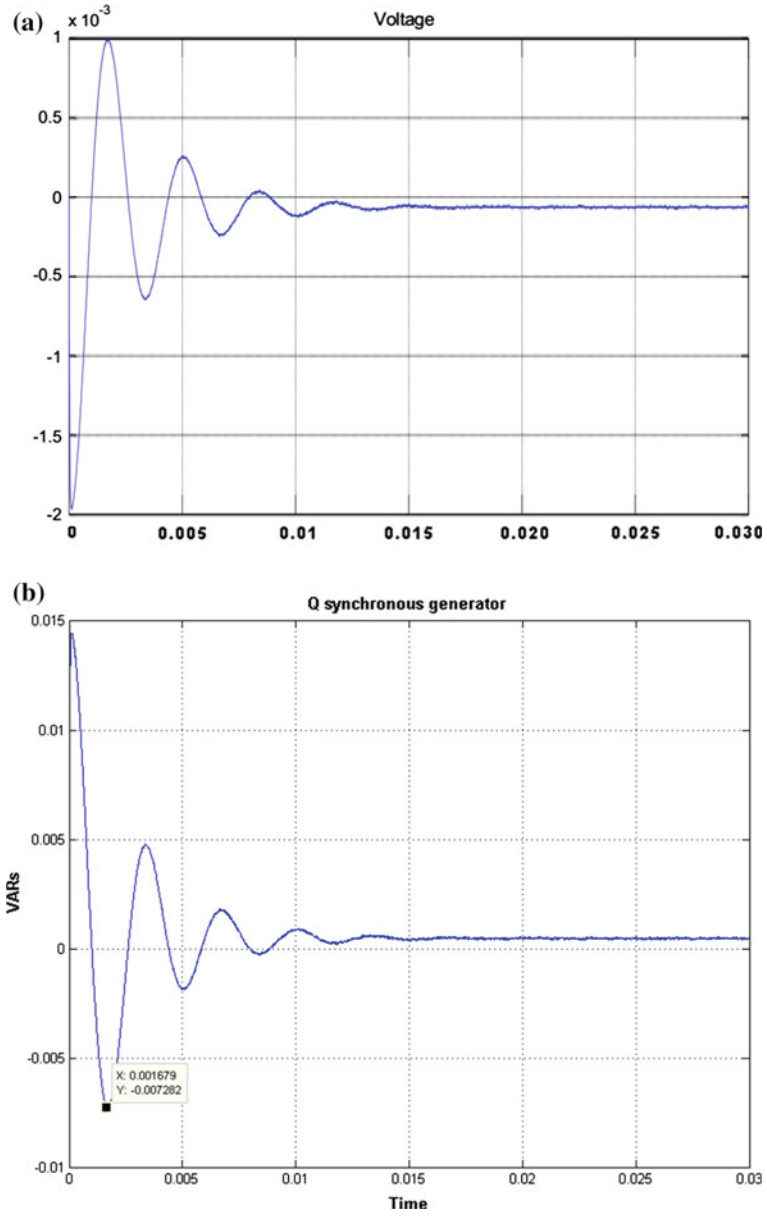


Fig. 5 **a** Change in voltage profile of HIPS. **b** Change in reactive power profile of synchronous generator

here. It shows that UPFC is clearly mitigating the imbalances of the reactive VARs of these machines. Thus providing a dynamic compensation to the network. The wind velocity fluctuations are continuously varying the demand of reactive VARs of

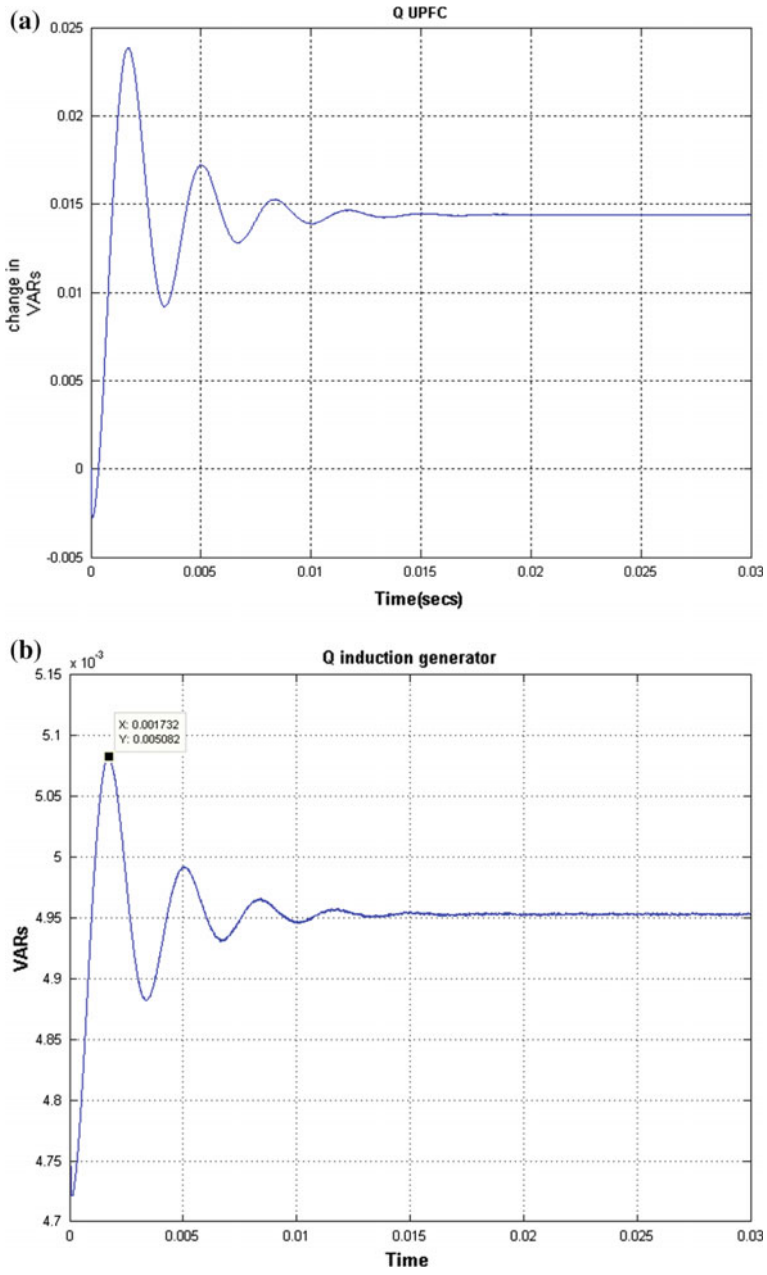


Fig. 6 **a** Change in reactive power profile of UPFC. **b** Change in reactive power profile of induction generator

system. Therefore, fixed capacitors are not enough to provide compensation to the proposed HIPS and this dynamic VAR requirement is to be supplied by UPFC. The compensation provided by UPFC is varied from no-load to full-load condition. In this study, it is also observed that UPFC provides better control over variation in voltage when the size of diesel generator is bigger than wind Generator. Thus, UPFC is playing a pivotal role in balancing reactive power of given test system and proved to be a most powerful FACT controller of the family (Figs. 5 and 6).

5 Conclusion

In this paper, the necessity of using an effective FACTS controller is analyzed. UPFC is used for improving the reactive power balancing of interconnection of wind power system and diesel power system. It is concluded that compensation with UPFC produces better results than conventional methods of compensation as it provides dynamic compensation. It also helps in relieving the considered HIPS from the reactive power congestion and voltage variations. The result reveals that dispensing of the existing capacitor banks cannot be effective in such cases, therefore only FACTS controllers like UPFC can compensate such hybrid system effectively. The paper has discussed the need of FACTS devices for the control of hybrid power system in detail.

Appendix

System parameter	HIPS	Synchronous generator	
RES	100 KW	P_{SG}, KW	0.5
Diesel sources	200 KW	Q_{SG}, KW	0.3
Base power	200 KVA	V (pu)	1.0
Load	200 KW	E_q (pu)	1.113
		Pitch angle regulator gains, $K_p = 5$, $K_i = 25$, max pitch angle = 45°	
		$X_d' = 0.296$, $X_d'' = 0.177$, $X_q = 1.04$, $X_q'' = 0.177$	
		$T_d' = 3.7$s, $T_d'' = 0.05$ s, $T_{qo} = 0.05$s	

UPFC data		Induction generator	
Series controller data:	Shunt controller data	Stator resistance = 0.004843 Pu	$K_p = 5$
R_{se}: 0.16 pu, X_{se}: 0.016 pu	R_{sh}: 0.22 pu, X_{sh}: 0.22 pu,	Rotor resistance = 0.004377 Pu	$K_i = 25$
K_{pse}: 0.025, K_{ise}: 1.5	K_{psh}: 0.01, K_{ish}: 20	Stator leakage reactance = 0.01248 Pu	Rotor leakage reactance = 0.0179

References

1. R,C.Bansal, T.S.Bhatti, and D.P.Kothari, "Automatic Reactive Power Control Of Wind-Diesel-Micro Hydro Autonomous Hybrid Power Systems Using ANN Tuned Static VAR Compensator", Proc.Int. Conf. on Large engineering System conference on Power Engineering (LESCOPE), Montreal, Canada, pp 182–188, May 7–9, 2003.
2. T. Aekcrmann et al., "Distributed generation: a definition", Electrical Power Systems Research, vol. 57, pp. 195–204, 2001.
3. Al-Majed S.I. and T. Fujigaki, "Wind power generation: An overview" Proceedings of the International Symposium Modern Electric Power Systems (MEPS), IEEE Xplore Press, Wroclaw, Poland, pp. 1–6, sept 20–22, 2010.
4. Ahilan, T., K.P. Mohammed and S. Arumugham, "A critical review of global wind power generation". American Journal of Applied Science, vol. 6, pp. 204–213. 2009.
5. John J. Paserba, Fellow, IEEE, "How FACTS Controllers Benefit AC Transmission Systems", IEEE Transactions on Power Delivery, vol. 1, pp. 949–957, 2003.
6. W. Breuer, D. Povh, D. Retzmann, E. Teltsch, "Role of HVDC and FACTS in Future Power Systems", Shanghai Power Conference, CEPSI- 2004, Shanghai.
7. Sandeep Gupta, R. K. Tripathi, and Rishabh Dev Shukla, "Voltage Stability Improvement in Power Systems using Facts Controllers: State-of-the-Art Review," IEEE Trans. On Power Systems, 2010.
8. Abhishek Gandhar, Balwinder Singh, Rintu Khanna "Impacts of FACTS technology-A state of Art Review," "International Journal of Innovative Technology and Exploring Engineering (IJITEE)", ISSN: 2278-3075, vol.1, Iss, 4, pp, 28–31, 2012.
9. L. Gyugyi, "A unified flow control concept for flexible AC transmission systems," International Conference on AC and DC Power Transmission, pp. 19–26,1991.
10. Papic, P. Zunko, D. Povh and W. Weinhold, "Basic control of unified power flow controller", IEEE Trans. on PS, vol. 12, no. 4, pp. 1734–1739, 1997.
11. Z.Y. Huang, Yixin Ni, C.M. Shen, F.F. Wu, S.S. Chen, and B. Zhang, "Application of unified power flow controller in interconnected power systems—modelling, interface, control strategy, and case study," *IEEE Trans. Power Syst.*, vol. 15, no. 2, pp. 817–824, May 2000.
12. Yashaswini. T., Poornima G. P, Vasantha Kumara T.M, T. R. Narasimhegowda "Grid Connected Wind Energy Conversion System Using Unified Power Flow Controller" International Journal of Science and Research (IJSR) ISSN (Online): 2319–7064, vol. 3 Iss. 6, June 2014.
13. N. Dizdarevic, M. Majstrovic, and *G.* Anderson, "Reactive power compensation of wind energy conversion system by using unified power flow controller", Int. J. Energy. Tech. & Policy, vol. 3, no. 3, pp. 269–298, 2005.
14. Asit Mohanty, Soumya R. Mohanty, Nand Kishor, Prakash K. Ray, "Adaptive Fuzzy Tuned PID and UPFC for Reactive Power Compensation in Distributed Generation System," Proc. of the Second Intl. Conf. on Advances in Electronics and Electrical Engineering — AEEE 2013, ISBN: 978-981-07-5939-1.

Intelligent Image Interpreter: A Semi-automatic Detection of Ships by Image Analysis of Space-Borne SAR Image Using SVM

S. Senthil Kumar and H.K. Anasuya Devi

Abstract The objective is to study the usability of microwave remote sensing in the detection of ships and evaluate the potential of SVM in improving the semi-automatic detection accuracy of ships. The research limits use of SAR-Synthetic Aperture Radar (TerraSAR-X High-Resolution Spotlight imagery), ERDAS Imagine, and MATLAB for analysis. EO image interpretation done manually is accurate but is limited by processing cost and time and adverse weather conditions like fog or clouding. While Microwave SAR remote sensing offers cost-effectiveness with better efficiency and flexibility for the identification of ship under all weather conditions. Large amounts of image data generated by SAR systems can quickly overburden a human observer. The paper discusses a robust method of image analysis for visualization and classification of image using SVM (support vector machines) to assess data toward detection of ships and ascertain the accuracy of feature detection in proposed method.

Keywords SAR · Ship detection · Semi-automation · TerraSAR-X · SVM · Matlab · ERDAS imagine

1 Introduction

The value of information/intelligence obtained is time-bound. Image interpretation from huge remote sensing data by qualified Image Analysts is time consuming in the absence of reliable automatic analysis tools. Hence an objective approach to the

S. Senthil Kumar (✉)
University of Petroleum and Energy Studies, Dehradun, India
e-mail: ersenkumars@yahoo.co.in

H.K. Anasuya Devi
CCE, Indian Institute of Science, Bangalore, India
e-mail: hkadevi@yahoo.com

© Springer Science+Business Media Singapore 2017

R. Singh and S. Choudhury (eds.), *Proceeding of International Conference on Intelligent Communication, Control and Devices*, Advances in Intelligent Systems and Computing 479, DOI 10.1007/978-981-10-1708-7_47

fundamental image analysis problem is rather an intelligent decision-making process with a required degree/probability of success. The observation of maritime activity is the need of time which has improved since inception of synthetic aperture radar (SAR) imagery from space and aerial platforms. The information derived from remote sensing imagery provides decision-makers, the valuable time with automatic methods to ease the human image interpretability.

1.1 Objective

The objective is to study the usability of microwave remote sensing in the detection of ships and evaluate the potential of SVMs in improving the semi-automatic detection accuracy of ships. The research limits use of TerraSAR-X spotlight image, ERDAS Imagine, and MATLAB for analysis.

2 Background

Microwave SAR remote sensing offers cost-effectiveness with better efficiency and flexibility for the identification of ship under all weather conditions. Large amounts of image data generated by SAR systems can quickly overburden a human observer. Recent developments in this field have introduced different nonlinear procedures and techniques of statistical learning [1–5]. Using statistical learning techniques [6–8], SVMs have reached the minimum of the upper bound in the error of probability of a classifier. This paper discusses a robust method of image analysis for visualization and classification of image using SVM to assess data toward detection of ships and ascertain the accuracy of feature detection in proposed method.

3 Study Area and Datasets Used

VHR SAR images (Fig. 1) of Visakhapatnam Naval Port, Andhra Pradesh, India have been used as sample images of TerraSAR-X spot light mode for study of a robust method by using SVMs for the image classification and the corresponding Electro Optical (EO) image by Google Earth (Fig. 2).

TerraSAR-X is specifically optimized to meet the requirements of commercial users around the globe, who require, high-quality and precise Earth observation data readily available. Image specification is as follows (Table 1):

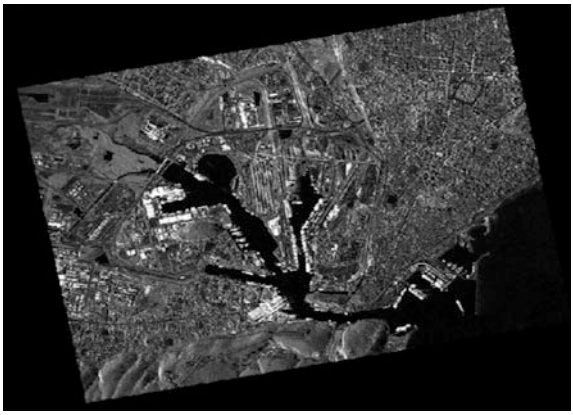


Fig. 1 VHR SAR imagery by TERRA SAR

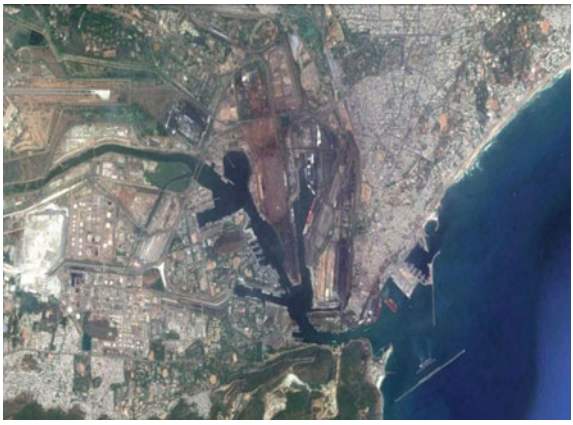


Fig. 2 EO image by Google earth

Table 1 Dataset specification

Location	India	Polarization mode	Single
File format	GeoTiff	Projection	UTM
Polarization channel	VV	Angle of incidence	41.90
Date of acquisition	12/10/2008	Azimuth resolution	1.1 m
Look direction	Right	Range resolution	0.9 m
Acquisition mode	SpotLight	Datum	WGS 84

4 Methodology

The architecture of the proposed enterprise level, methodology used for the image analysis and implementation of the Intelligent Image Interpreter (Fig. 3) is restricted to the conceptualization. The initial part of the implementation was carried out by ERDAS Imagine and SVMs train and classification in MATLAB.

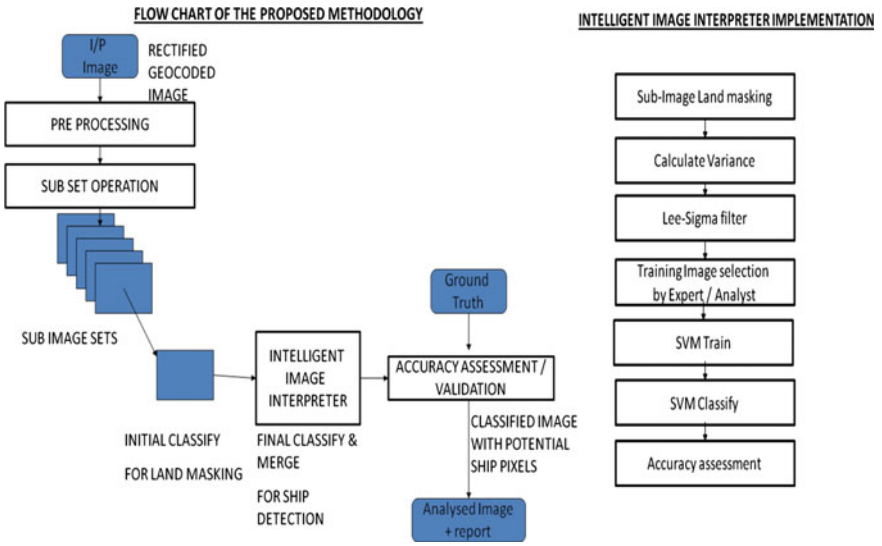


Fig. 3 Flow chart of the proposed methodology and implementation of intelligent image interpreter

4.1 Implementation of Algorithm

The following steps were utilized for implementation: The database is codified as two classes Ship (+1) and Water (–1). Two sets of training images for ship pixel and water pixels were selected in a folder/container. Read Training Images from the folder/container automatically (two each for each class in this case). SVM train. Test Image formation for ship detection from the same folder/container automatically. SVM Classify. Classified Image formation. Accuracy Assessment.

5 Results and Analysis

For this particular SAR image, the quality of the speckle suppression at the trade-off at smoothening the image for the purpose of the interpretation the Lee sigma filter is better than other because it has not only reduced the speckle but also highlighted the other features in surroundings. The semi-automatic implementation using MATLAB (Statistics and Machine Learning toolbox) has revealed that SVMs of using linear, quadratic basis revealed more error rate in classification when compared to the Gaussian radial basis function and multi layer perceptron models (Fig. 4). Hence it is deduced that while RBF produces greater accuracy with higher time cost which can be reduced by cross-validation quadratic gives a robust accuracy in lesser time (Fig. 5). It is interesting to note that linear function basis

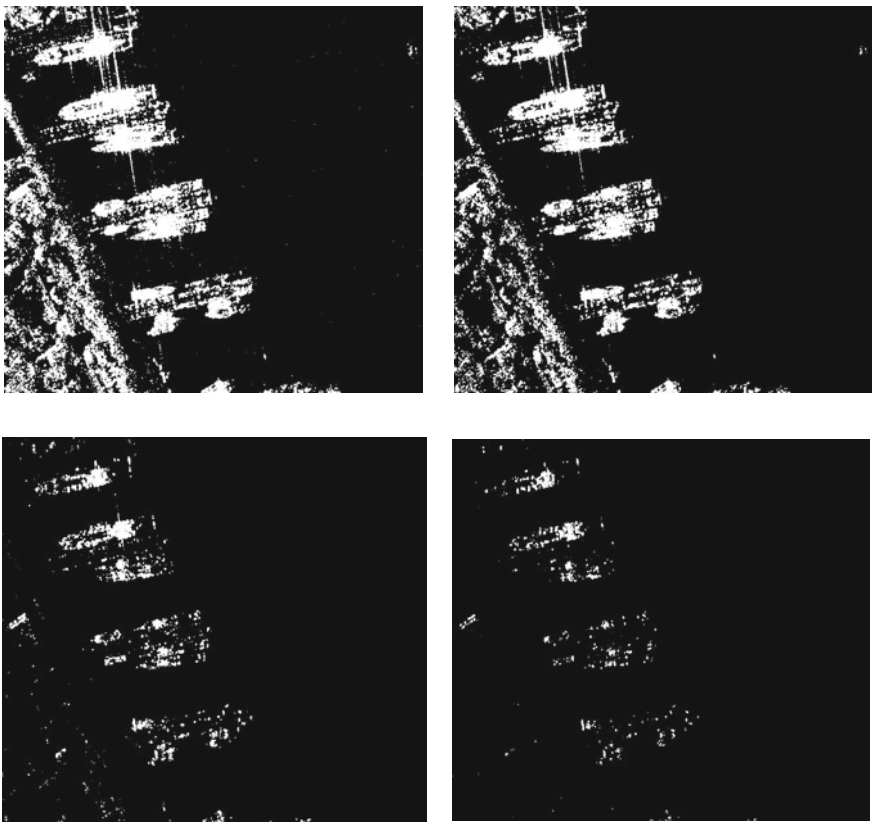
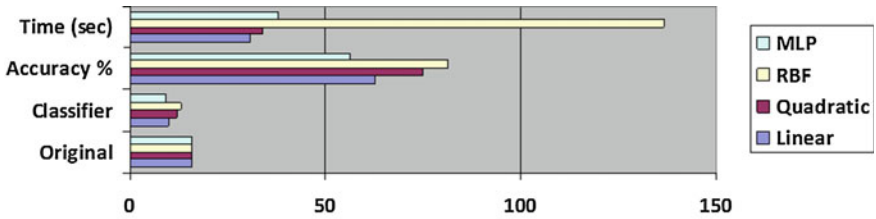


Fig. 4 SVMs classified images **a** Linear function. **b** Quadratic function. **c** Gaussian radial basis function. **d** Multi layer perceptron function

gives better visual appreciation of the finer details including portions of ever much smaller potential ship pixels; while MLP gives a clear indication of the ships by eliminating even portions of the jetty. Also RBF gives higher accuracy with reduced probability of false alarm and hence modification of the constraint, sigma, and with cross-validation, it will produce the best results. Finally, the Quadratic function basis gives the robust accuracy making it useful for detection and for further analysis it is the RBF which will effectively give the best results for learning about the target of interest for future detection.



	Original	Classifier	Accuracy %	Time (sec)
MLP	16	9	56.25	38.029
RBF	16	13	81.25	136.541
Quadratic	16	12	75	33.776
Linear	16	10	62.5	30.796

Fig. 5 Accuracy assessment

6 Accuracy Assessment

The number of ships identified on the processed image with the original image and assessment is tabulated.

7 Discussion

This section discusses some solutions that may help improve this method further, so that detection of naval features is carried out more accurately. The problem handled in this paper is a generic detection of ships in sea. The trade-offs have to be formulated to match the aim of the user specific to area of interest. Considerations of the Target include type, class, size, and velocity of target to be detected in the given user area. Environmental considerations of surveillance area include sea state and wind conditions. Finally time constraints and revisit rate against available computing resources is the bottleneck for decision-maker. Considerations of radar include frequency, resolution, incidence angle, and polarization [1]. The radar parameters would be chosen to match the user target and area of interest. Therefore taking all the considerations the ship detection algorithms are designed to match the data used for analysis. This paper is aimed to provide base to choose the best SVM techniques for ship detection in SAR imagery.

7.1 Human Supervision

As the importance of intelligence is time sensitive for the decision-maker, it is vital to include expert to reduce to false detections. This semi-automated algorithm's capability can be enhanced by the human supervision.

8 Conclusion

This paper presents improved methods for semi-automatic naval feature extraction using microwave remote sensing. For this purpose, Erdas Imagine software was used. This software was explored to define the best filters available for processing the microwave image. In this study, very high-resolution image of Terra SAR X is used and by using this image and by applying SVMs-based analysis of images for the semi-automatic interpretation of ships is explored.

8.1 Future Scope

SVM selection and parameter optimization using cross-validation of fit and avoidance of the over/under fitting to optimize the classification with trade-off between computational and time complexity for a given resources. Ship constructed with material like small wooden boats and fiber glass boats may also be picked up by the microwave imagery. Object-based image analysis may be carried out on the processed image for image segmentation for better extraction of naval features. Capability enhancement of ship detection algorithms can be done using of circular transmit, linear receive (CTLR) mode of RISAT 1 SAR data.

References

1. Crisp, D. J. (2004), "The state-of-the-art in ship detection in synthetic aperture radar imagery", DSTO Information Sciences Laboratory, DSTO–RR–0272.
2. M. Liao and C. Wang "Using SAR images to detect ships from sea clutter", *IEEE Geosci. Remote Sens. Lett.*, vol. 5, no. 2, pp. 194–198 2008.
3. Meyer, F., Automatic Ship Detection in Spaceborne SAR Imagery, ISPRS Hannover Workshop 2009, High-Resolution Earth Imaging for Geospatial Information.
4. Tonje Nanette Hannevik and Andreas N. Skauen, Ship detection using high resolution satellite imagery and space-based AIS, Norwegian Defence Research Establishment (FFI), 15 December 2011, FFI-rapport 2011/01693.
5. Angiulli, G., Barrile, V., and Cacciola, M., "SAR Imagery Classification using Multi-class Support Vector Machines", Progress in Electromagnetics Research Symposium, Hangzhou, 2005, August 22–26, pp. 218–222.
6. Vapnik, V. N., The Nature of Statistical Learning Theory, Springer Verlag, New York, 1995.
7. Vapnik, V. N., Statistical Learning Theory, Wiley, New York, 1998.
8. Cortes, C., V. N. Vapnik, "Support Vector Networks," Machine Learning 20, 273, 1995.

Design and FPGA Implementation of DSSS for Near-Far Effect in MANET

Aakanksha Devrari, Adesh Kumar, Amit Kumar and Shraddha Singh

Abstract The Direct Sequence Spread Spectrum, Code Division Multiple Access (DSSS-CDMA) is the one of the medium access technology in the future mobile communication systems because of its potential and immunity against noise. The CDMA has a unique feature, i.e., spectrum-spreading process which employs a pseudo random noise (PN) sequence. These systems suffer from Multiple Access Interference. The most important issue in spread spectrum approach is near-far effect. Spreading codes plays a very important role in DSSS-CDMA system. In this paper, DSSS-CDMA system is implemented in VHDL for field programmable gate array (FPGA) so as to remove near-far effect for Mobile Ad hoc Networks (MANET). Modelsim Xilinx Edition 10.2 (MXE) tool is used for functional simulation as well as logic verification. For synthesis, Xilinx Synthesis Technology (XST) of Xilinx ISE tool 14.2 is used for transmitter and receiver on Virtex 5 FPGA.

Keywords Binary phase shift keying (BPSK) · Code division multiple access (CDMA) · Direct sequence spread spectrum (DSSS) · Field programmable gate array (FPGA) · Mobile ad hoc networks (MANET)

Aakanksha Devrari (✉)
Department of Electronics and Communication Engineering,
Women Institute of Technology (WIT), Dehradun, India
e-mail: aks.uit08@gmail.com

Adesh Kumar
Department of Electronics, Instrumentation and Control Engineering (EIC),
University of Petroleum and Energy Studies (UPES), Dehradun, India

Amit Kumar
Faculty of Technology, Department of VLSI Design,
Uttarakhand Technical University (UTU), Dehradun, India

Shraddha Singh
Department of Electronics and Communication Engineering,
GLA University, Mathura, India

© Springer Science+Business Media Singapore 2017

R. Singh and S. Choudhury (eds.), *Proceeding of International Conference on Intelligent Communication, Control and Devices*, Advances in Intelligent Systems and Computing 479, DOI 10.1007/978-981-10-1708-7_48

1 Introduction

Radio systems utilize mainly two resources, frequency and time. Frequency Division Multiple Access [1] (FDMA) means division by frequency, in such a way that each user is allocated a part of the spectrum for all of the time. Time division multiple accesses (TDMA) mean division by time, so that each pair of user is allocated the entire spectrum for part of the time. Other multiple access scheme is the Code Division Multiple Access (CDMA) [1], where each user will be allocated the spectrum for the entire period of the time. CDMA uses pseudorandom codes to differentiate between users. CDMA is a spread spectrum technique, where the modulated coded signal has a much higher bandwidth compared to the bandwidth of the data to be transferred. Spread spectrum technique simply utilizes spectrum larger compared to the spectrum required to send the data (Figs. 1, 2 and 3).

The binary data $x(t)$ of low bandwidth is multiplied by the code sequence $c(t)$ in order to obtain the spectrum spreading. The baseband signal here $S_n(t)$ is then filtered to bandlimit it. The modulation technique used in spread spectrum system is phase shift keying for, e.g., Quadrature Phase Shift Keying (QPSK) [2], Minimum Shift Keying (MSK) [2], Binary Phase Shift Keying (BPSK), or Differential Binary Phase Shift keying (D-BPSK) [3] is employed. In the base band signal $S_n(t)$ is the product of input signal $x(t)$ and code sequence $c(t)$.

$$S_n(t) = x(t) \cdot C(t) \tag{1}$$

The baseband signal $S_n(t)$ is then convoluted with the impulse response $h(t)$ of the spectrum-shaping filter given by Eq. (2)

$$y(t) = S_n(t) \otimes h(t) \tag{2}$$

where symbol $\otimes$ denotes convolution. $S_s(t)$ is the bandpass signal given as

$$S_s(t) = S_n(t) \otimes h(t) \cdot \cos\ \omega t \tag{3}$$

The received signal $S_s(t)$ is converted to a lowpass signal $Y(t)$ by mixing it with a locally generated coherent carrier cos wt. The lowpass spread spectrum is combined

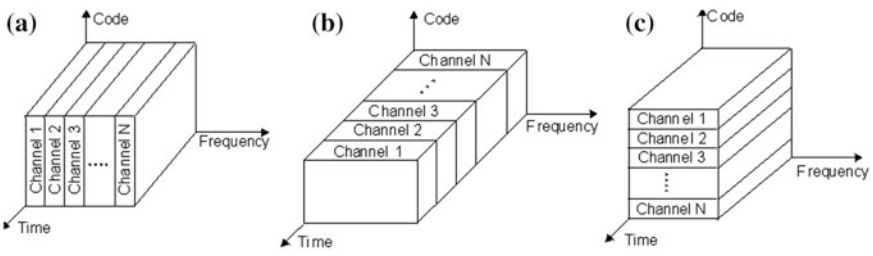


Fig. 1 Multiple access schemes. **a** FDMA, **b** TDMA, **c** CDMA

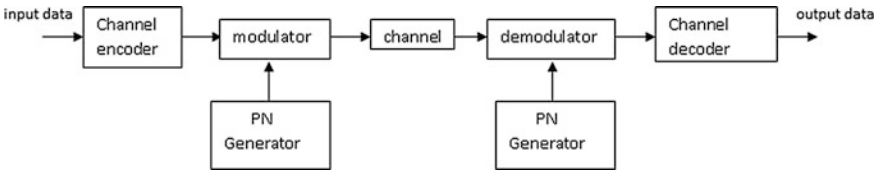


Fig. 2 Direct sequence spread spectrum system

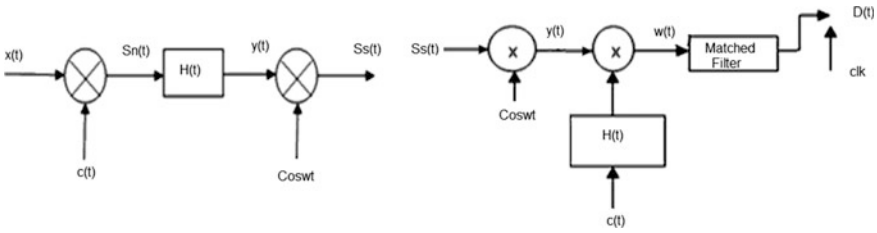


Fig. 3 **a** Block diagram of DSSS modulator. **b** Block diagram of DSSS demodulator

by a locally generated code sequence which is synchronized. The de-spread signal $W(t)$ is then matched filtered and sampled. The lowpass signal and de-spread signal are represented with the help of Eqs. (4) and (5), respectively.

$$Y(t) = S_s(t) \cdot \cos \omega t \tag{4}$$

$$W(t) = A(t) \cdot [c(t) \otimes h(t)] \tag{5}$$

The matched filter output is expressed using Eq. (6)

$$d(T) = \int_{(k-1)T}^{KT} W(t)\, \mathrm{d}t \tag{6}$$

The receiver decodes the data as follows: If ($d(T) > 0$), it decodes a binary '1' otherwise decodes a binary '0'.

2 Near-Far Effect

Near-far effect [3] occurs when the transmission power through the transmitters is equal, in such situation if a receiver is close in distance to transmitter/mobile station than other mobile station. The signal of near station will arrive at the receiver with a higher power compared to the farther one, which causes incorrect decoding of the data. This near-far problem affects packet reception, and thus network throughput.

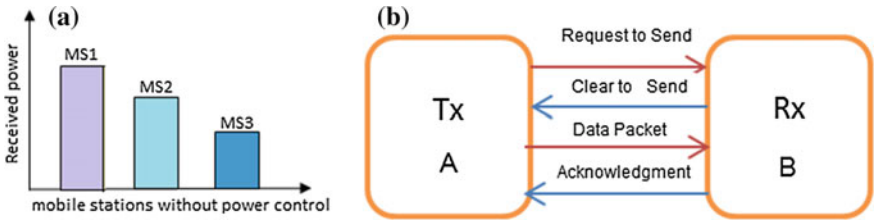


Fig. 4 **a** Near-far effect in different base stations. **b** Principle of MAC protocol

It is shown with the help of Fig. 4a, in which there are three mobile stations MS1, MS2, and MS3 in which the signal power is decreasing sequentially. Moreover, cross correlation between spreading codes may be another reason which can cause multiaccess interference.

Mobile ad hoc networks (MANET) are time asynchronous means so they have different time delays. Power control phenomena can be used so that signals reach at the base stations with the same power. Simultaneous transmissions cannot take place at the same time as the power will destroy the reception at neighboring terminal or node as well as any ongoing transmission. Therefore, power control in itself is not sufficient to overcome the near-far problem in MANET. A MAC [4] protocol moderates access to the shared medium by process rules that allow devices/nodes to communicate with each other in a proper order and economical manner. MAC-based direct sequence spread spectrum (DSSS) CDMA system provides a solution in which on receiving the ID from the transmitters, receiver first checks for the destination ID in the received signal. If the ID matches with the self-ID of the receiver then only it will allow the transmitter to send the data further. This process will always restrict the non-intended means that interfere the transmitter to transmit the data to the non-intended receiver by intimating the transmitter to reduce its transmission power if the ID match fails.

2.1 Channel Access Mechanism

The channel access mechanism can be understood with the help of RTS and CTS frame format shown in Figs. 5 and 6.

Step 1 The intended receiver '*B*' on receiving the RTS frame, uses a predefined value of power $W_{\max}$ and the received signal power $W_{\text{received}}^{\text{ab}}$ to calculate the channel gain G_{ab}.

$$G_{\text{ab}} = \left(W_{\text{received}}^{\text{ab}}\right)/(W_{\max}) \tag{7}$$

Step 2 Receiver '*b*' can correctly decode the data packet if it is transmitted at a power

Destination address (2 bit)	Transmitter address(2 bit)	Duration of transmission	Size of data (n bit)	Allowable power for transmission ($W^{ab}_{allowed}$)

Fig. 5 RTS frame

Transmitter Address (2 bit)	Destination Address (2 bit)	Duration of transmission	Interference tolerance Wb(noise)	Allowable power ($W^{ab}_{allowed}$)

Fig. 6 CTS frame

$$W_{\min}^{(ab)} \text{ given as } W_{\min}^{(ab)} = \mu^*(W_{\text{thermal}} + W_{\text{MAI}-\text{current}}^{(i)})/G_{ab} \tag{8}$$

where W_{thermal} = Thermal noise power, $W_{\text{MAIcurrent}}^{(b)}$ = Effective current MAI from ongoing (interfering) transmissions, G_{ab} = Channel Gain. All neighbors of the terminal '*b*' have to defer their transmissions during *b*'s ongoing reception.

Step 3 Calculate the Power of the terminal 'a' W_{allowed}^{ab} given as

$$W_{\text{allowed}}^{ab} = \xi_{\max}\mu^* W/G_{ab} \tag{9}$$

where W_{thermal} = Thermal noise power, μ^* = Effective bit energy-to-noise spectral density ratio, $\xi_{(\max)}$ = Maximum noise rise. If $W_{\text{allowed}}^{(ab)} < W_{\min}^{(ab)}$, '*b*' responds with a negative Clear to send (CTS) signal to inform '*a*' that '*b*' can't proceed b's transmission. If $W_{\text{allowed}}^{(ab)} > W_{\min}^{(ab)}$, terminal 'b' calculates the power tolerance $W_{\text{MAI}-\text{future}}^{(b)}$ that can be endured from future unintended transmitters.

$$W_{\text{MAI future}}^{(b)} = 3XG_{ji}\left(W_{\text{allowed}}^{(ab)} - W_{\min}^{(ab)}\right)/2\mu^* \tag{10}$$

where, X = Processing gain. '*b*' distributes this power tolerance among users that can interfere in future, μ^* = Effective bit energy-to-noise spectral density ratio. When responding to Request to send (RTS) signal of '*a*', terminal '*b*' indicates in its CTS signal the power level $W_{\text{allowed}}^{(ab)}$ that '*a*' can use. Also it adds $W_{\text{noise}}^{(b)}$ in the CTS packet and sends packet back to terminal '*a*' with maximum power. Where, $W_{\text{noise}}^{(b)}$ = Interference tolerance that each future neighbor can add to terminal '*b*'.

Step 4 Compute $W_{\text{map}}^{(y)}$: Interfering terminal '*y*' when sees the CTS message from '*b*' calculates the channel gain G_{yb} between '*s*' and '*b*' and also calculates the maximum power $W_{\text{map}}^{(y)}$ that can be used by '*s*' in future transmissions.

$$W_{\text{map}}^{(S)} = \min(W_{\text{noise}}^{(b)}/G_{\text{yb}}) \tag{11}$$

Step 5 '*a*' sends data to '*b*'. If *a*'s transmission is success, receiver '*b*' responds to '*a*' with Acknowledgement packet with the same power level which should be used if '*b*' has to send any data packet to '*a*'.

3 Block Diagram of DSSS MAC System

The block diagram of DSSS [5] system based on medium access control is shown in Fig. 7. The input to the system is discrete' bit data. The input data is a data stream in a discrete form of N bit data. Convolution Encoder encodes redundant bits into the incoming signal, thus improving the data capacity of the channel and making it immune to noise. Next state is Interleaver where shuffling (rearrangement) of the encoded data is done so as to remove any burst errors if present in the consecutive bits when data passes through channel.

At the same time Gold code sequence is generated using two pseudo noise sequences with the help of a feedback shift register regulated by a timing clock. This sequence goes to the Decimator which reduces the data rate from 1.22 Mbps to 19.2 Kbps in order to make it compatible with the data rate of the incoming bit stream. Data bits then goes to BPSK modulator where modulation is achieved. Next, a synchronized orthogonal code at the receiving end is again used to separate lowpass original signal back and it is achieved with the help of Walsh codes. In the next step, data goes to de-interleaver that rearranges the preshuffled data in the proper sequence order. In the last step, decoding of the de-interleaved data is achieved by Viterbi decoder and original sequence of data stream is obtained at the receiver side.

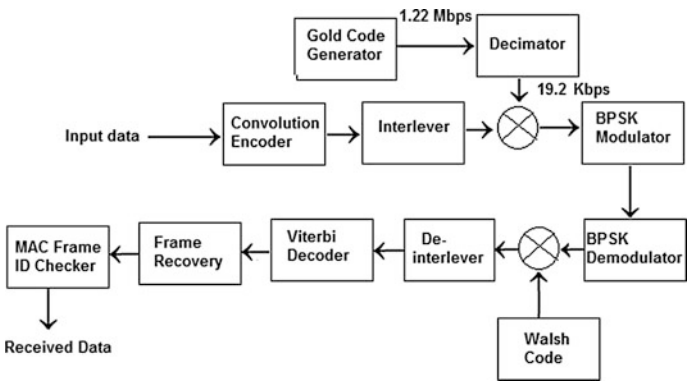


Fig. 7 MAC-based DSSS-CDMA system

4 Simulation Results

The designing and synthesis of chip is carried out in Xilinx 14.2 ISE software. The RTL schematic of the developed chip is shown in the Fig. 8 and the Modelsim simulation for the corresponding test vectors is shown in Fig. 9.

Table 1 gives the details supporting the RTL view. *Re*set is the input to reset, *Clock* (*clk*) is used to synchronize as well as provide a duty cycle to the transmitters

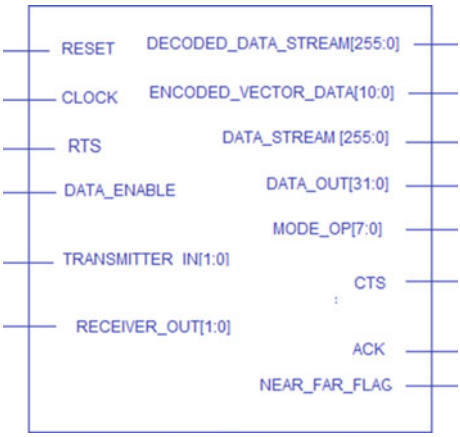


Fig. 8 RTL of the DSSS-CDMA

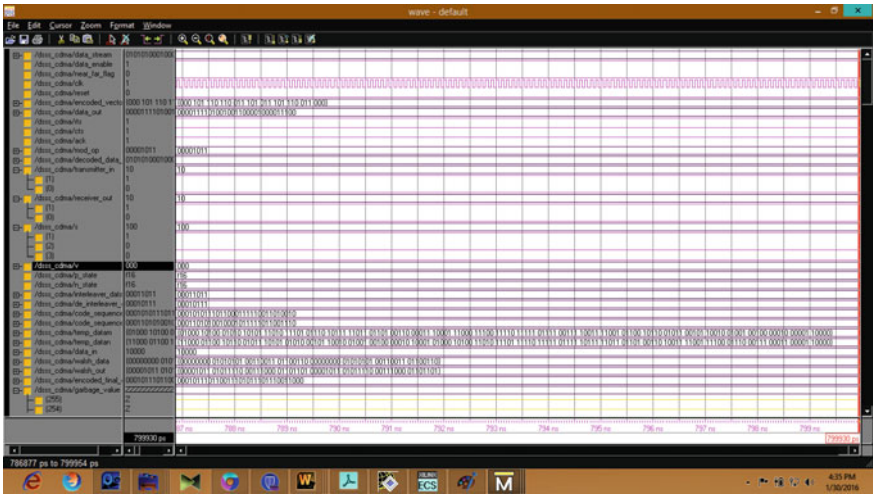


Fig. 9 Simulation results for solving near-far effect (when ID matches)

Table 1 Details of pins used in RTL of MAC based DSSS-CDMA forward link

Pins	Description
Reset	It is used to reset the data transmission states
Clock (1 bit)	Input to the DS-CDMA used to provide positive (rising edge) of clock pulse
RTS (1 bit)	Input signal for RTS frame from transmitter to receiver
Data_Enable (1 bit)	Enable input for transmitter to send data
Transmitter_in (2 bit)	Transmitters ID selection in RTS frame
Reciver_out (2 bit)	Receivers address to select the desired receiver
Encoded_vector_data (32 bit)	Encoded vector data of convolution encoder
Data_stream (256 bit)	Input data stream in packet from for the DS-CDMA system
Mode_op (8 bit)	Input sequence for modulated gold code
Data_out (32 bit)	Output of code sequence generator (gold code)
Decoded_data_stream (256 bit)	It is the output of the DS-CDMA system to verify the output data received corresponding to destination receiver
CTS (1 bit)	CTS signal frame from receiver to transmitter
ACK (1 bit)	Acknowledgement on successful data reception
Near_far_flag (1 bit)	Depicts near-far effect is present or not

and receivers. The transmitter and receivers are identified with their identity addresses, i.e., IDs, Transmitter_in is the address of transmitters, and Receiver_out is address of receivers. RTS is the frame sent by transmitter to the receiver. CTS is the frame sent to the transmitter by receiver. Once CTS frame is received by the transmitter, data packet is sent and on the successful data reception at the receiver end, an acknowledgement signal (Ack) is sent by the receiver. The simulation is carried out on an assumption of four transmitters with the Ids (00, 01, 10, and 11) and four receivers with their corresponding addresses (00, 01, 10, and 11).

5 Device Utilization Summary

The section provides the information of device utilization on Virtex 5 FPGA for different data streams tested on it (Table 2).

In the design every transmitter and receiver is allotted with the individual IDs and if the ID of a particular transmitter matches with the ID of receiver, it means that it is the intended transmitter and the intended receiver. In such case, only data can be transmitted and comes at the output. At the same time if the ID does not match a non-intended terminal is restricted and their data remains in a temporary state which means a garbage value.

Table 2 Device utilization and timing report for DSSS-CDMA system for MANETs

Device part	Utilization (%)	Parameter for timing	Utilization
Slices utilization	693/6144 11	Frequency (maximum)	395 kHz
Slice flip flops utilization	976/12288 7	Arrival time before clk (minimum)	3.643 ns
4 input LUTs utilization	963/12288 7	Time after clk (maximum)	4.593 ns
Bonded IOBs utilization	154/240 64	Total path delay (combinational)	6.438 ns
GCLKs utilization	8/32 25	Memory utilization	202,240 KB

6 Conclusions

In the paper, a DSSS-CDMA protocol-based system is implemented on Virtex-5 Field programmable gate array (FPGA) kit. It is found that the hardware utilization in terms of number of slices is 11 %, number of flip flops is 7 %, number of bonded IOB's is 64 %, number of GCLKS is 25 %, and number of 4 i/p LUTs is 7 % which is extracted from the design. It is seen that channel access mechanism approach acquires the transmission which is desired for the data packets to permit for the simultaneous transmissions which are interference limited, so that receiver terminal gets the data only due to intended transmitter. The protocol provides a solution to the near-far effect in DSSS Ad hoc systems at the same time also increases the throughput of network. Further research can be extended and same concept can be integrated on several number of transmitter and receivers.

References

1. B. Sreedev, V. Vijaya, Ch. Kranthi Reeks, Rama Valupadasu and B. Rama Rao Chunduri, "*FPGA implementation of DSSS-CDMA Transmitter and receiver For ad-hoc networks*" IEEE symposium on computer & Informatics, 2011, pp. 255–260.
2. Hasan and J.G. Andrews, "*The guard zone in wireless ad-hoc networks*," IEEE Trans. Wireless Commun., vol. 6, March 2007, pp. 897–906.
3. B.S. Tripathi, Monika kapoor, "*Review on DS-SS CDMA Tx and Rx for Ad-hoc Network*" International Journal of Advances in Engineering & Technology, Vol. 5, Issue 2, Jan. 2013, pp. 274–279.
4. D.D. Seth, Srikant Patnaik, Srikanta Pal, "*A Quality of Service Assured & Faired MAC protocol for Mobile Ad-hoc Network*", IEEE413, 2011, pp. 413–417.
5. Faisal Fayyaz Qureshi, "*REECR-MAC: Reliable and Energy Efficient Cognitive Radio MAC Protocol for Ad-hoc networks*" 2013 Fifth International Conference on Computational Intelligence, Modelling and Simulation, IEEE, 2013, pp. 339–344.
6. Lu Ying, Kang Feng-ju, Zhong Lian -jiong, liang Xiang-yang, "*Improvement Method of MAC Protocol Based on Ad-hoc Network Traffic Characteristic*",IEEE, 2011, pp. 464–467.

7. M. Habib Ullah, Akhmad Unggul Priantoro, M. Jasim Uddin, ICCIT, "*Design and Construction of Direct Sequence Spread Spectrum CDMA Transmitter and Receiver*" Proceedings of 11th International Conference on Computer and Information Technology, 2008.
8. MihirNyayate, Y.N Singh, "Dynamic *Safe Transmit Power MAC protocol in Wireless Ad-hoc MAC Protocol*", 2011 IEEE 179 TENCON 2011, pp. 179–183.

Air Mouse: An Everyday Mouse for the Ease of Computing

P.S. Venkateswaran, Vivek Kaundal, Amit Kumar Mondal, Abhishek Sharma, Vindhya Devalla and Shival Dubey

Abstract There are several ways for human computer interaction in the modern era of electronics. In the present day, computers motion recognition is used very efficiently for playing games. The work done in this paper presents a simple and low-cost device for the movement of cursor on computer screen or to rotate the three-dimensional images. For the movement of cursor the data of accelerometer sensor (according to hand movement) is fed to the controller unit and after processing it is sent serially to the computer through RS 232 protocol. The developed device is used for all applications as accomplished with mouse. The proposed device senses the end user action with the help of accelerometer and push buttons. The air mouse is comfortable to wear, and does not considerably obstruct entering. It functions completely as serial mouse available in the market, and even has the feature of scrolling as the conventional mouse. This innovative approach improves the end user's experience with day-to-day task and playing games in computer.

Keywords Mouse · ATmega32 · Dual-axis accelerometer · ADC

1 Introduction

A mouse is a representative device specially in computing. The operation of which depends on recognition of gestures in two-dimensional space. Materially, a mouse is a device made up of optical sensor embedded with electronic components. It at times features other elements, such as "wheels", which permit the user to execute various system-reliant processes, or additional controls or features can add extra dimensional input. The present technology in mouse needs it to rest on a hard surface and there will be variations in the sensitivity as and when the surface is changed and there is also a need for us to move back and forth between the mouse

P.S. Venkateswaran · Vivek Kaundal · A.K. Mondal (✉) · Abhishek Sharma · Vindhya Devalla · Shival Dubey
University of Petroleum and Energy Studies, Dehradun, India
e-mail: akmondal1603@gmail.com

© Springer Science+Business Media Singapore 2017

R. Singh and S. Choudhury (eds.), *Proceeding of International Conference on Intelligent Communication, Control and Devices*, Advances in Intelligent Systems and Computing 479, DOI 10.1007/978-981-10-1708-7_49

and the screen during presentations [1, 2]. By resting our hands on a hard surface, it weakens the muscles and creates carpel tunnel syndrome [1, 3, 4]. But air mouse which can be worn as a glove and one can type and at the same time by moving one's hands, user can move the mouse pointer on the screen.

2 Materials and Method

2.1 Design and Outlook

All the technologies which have been used so far needs the mouse to be placed on a hard surface and all these technologies uses optical or mechanical means for position tracking. Air mouse uses an accelerometer sensor which gives the acceleration of the hand in the XY plane in air and this motion is transformed to point the cursor on the screen. This transformation is done using a high-speed microcontroller with an inbuilt ADC and sending the serial data via a cable to the computer. There is a filtering circuit for removing noise and an amplifier circuit to increase the gain of the signal. The total functioning of the device is like a serial mouse to make it cost efficient but the special thing about it is that since it makes use of the accelerometer sensor it can be used in midair, as shown in Fig. 1.

2.2 Components and Fabrication

The air mouse device consists of the following components

a. Accelerometer: The ADXL 203 is sized at $5 \times 5 \times 2$ mm^3. The main features of it include the high rate of precision, low power consumption and dual-axis

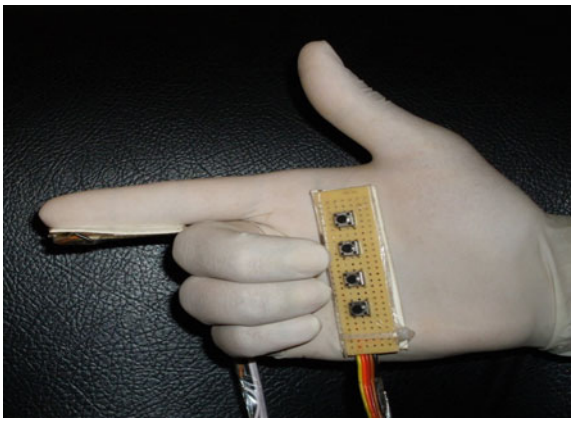


Fig. 1 Air mouse

accelerometer that gives signal-conditioned output voltage. It measures acceleration with a full-scale range of ±1.7 g. It is able to measure only two types of dynamic and static acceleration. Its bandwidth is less than 60 Hz and is been selected by the user by inbuilt capacitor and output pins.

b. Amplifier and Filter Circuit: In order to remove the unwanted frequency noise at the input terminals of ADXL IC, a lowpass filter was used. Then a dual-operational amplifier LM358 is used. It comprises of two-operational amplifiers having features including high gain and better stability. They work on same power supply. The differential part amplifies the accelerometer output. On providing suitable gain into the accelerometer, output results into higher resolution with the ADC.
c. ATmega32 microcontroller: The ATmega32 is an 8-bit microcontroller fabricated on the CMOS technology and its architecture is based on the advanced virtual RISC architecture. In a single clock cycle, with the help of executing instructions ATmega32 has the capability of providing the throughputs at the speed of 1 MIPS per MHz. This feature allows the system with optimized power consumption and high processing speed. It has a 10-bit ADC that converts the analog signal into digital using the successive approximation technique. PORT A is the ADC port in ATmega32. The controller used in this paper is used to convert the analog filtered signals to computer compatible format, i.e., 2's compliment format.
d. Max 232A (RS232 to TTL): Max232A [5] it requires +5 V dc voltage and also external capacitors for the proper operation. It uses a voltage inverter with the rating of 10 V. According to RS-232 protocol the 0 V is taken in the range of +5 to +15 V and for the 1 V range varies from –5 to –15 V. Most of the microcontrollers do not have capability to generate this range of voltage. In order to connect a microcontroller SCI port to a true RS-232 device, for this it is necessary to convert the range of TTL voltage (0 and +5 V) into voltage range of –10 to +10 V.

3 Operation and Program Design Flow

3.1 Hardware Operation

The operation of the air mouse is focused on information gathering and processing. Output of the accelerometer passes through three stages to pass through lowpass filter to remove noise due to high frequency. The second stage is known as differential amplifier stage. Second stage is of differential stage amplifier, it amplifies the signal by a factor of two and increases the accelerometer output from 1.5 to 3.5 V for –1 to 1G to 0.5 to 4.5 V. Thus by introducing the suitable gain into the output given by accelerometer will improve the resolution of the inbuilt ADC. There is generation of negative and positive voltage which is used as the differential

input for both accelerometer and potentiometer output. Potentiometer helps to tune the accelerometer 0 G level to a voltage of the desired choice. By providing the output of the amplifier through a resistor ADC circuit is prevented from exposure of high current. Combination of diode and resistor generates the +5 V output. The output is taken from the junction of potential divider circuit formed by the combination of resistor and diode. It also prevents the following things:

i. Generation of output voltage from amplifier not more than 5 V.
ii. The threshold voltage of the diode (0.67 V in case of Si).

Besides these two accelerometer inputs, there are four push-buttons inputs in the form of enable/disable functionality, left click, right click, and mouse scrolling of the mouse to the microcontroller, the same has been shown in Fig. 2.

3.2 *Program Operation Flow*

Figure 3 is representing the flow diagram of the air mouse program. Initially user has to wait for the computer to toggle the RTS line. When it does, "MZ" signal is

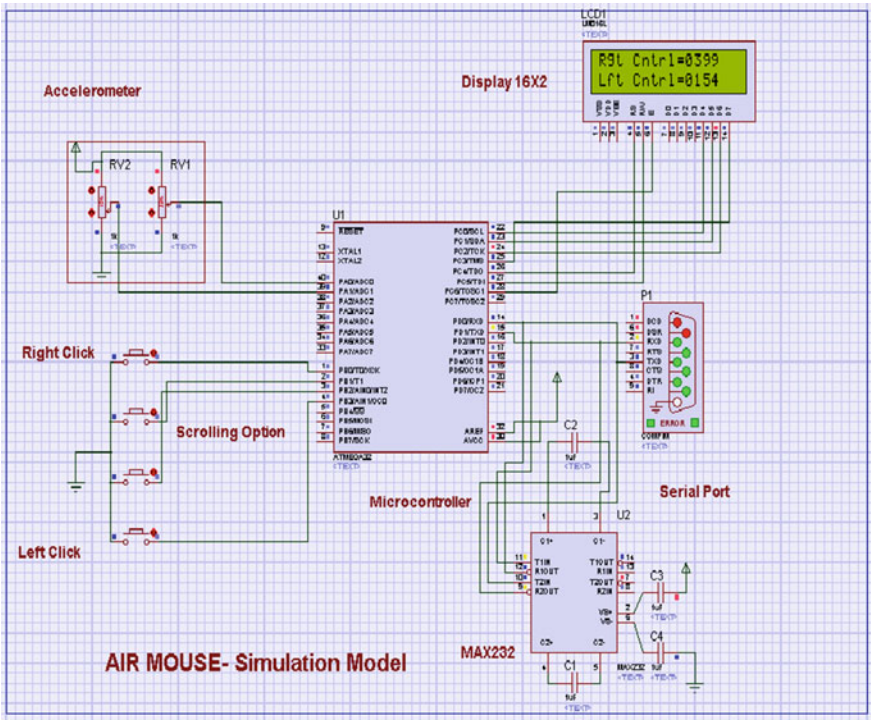


Fig. 2 Simulation model for air mouse

sent indicating that it is a Microsoft serial scroll mouse. The response for five queries is done, then deactivate query response is functionalized and finally the start mouse operation is performed.

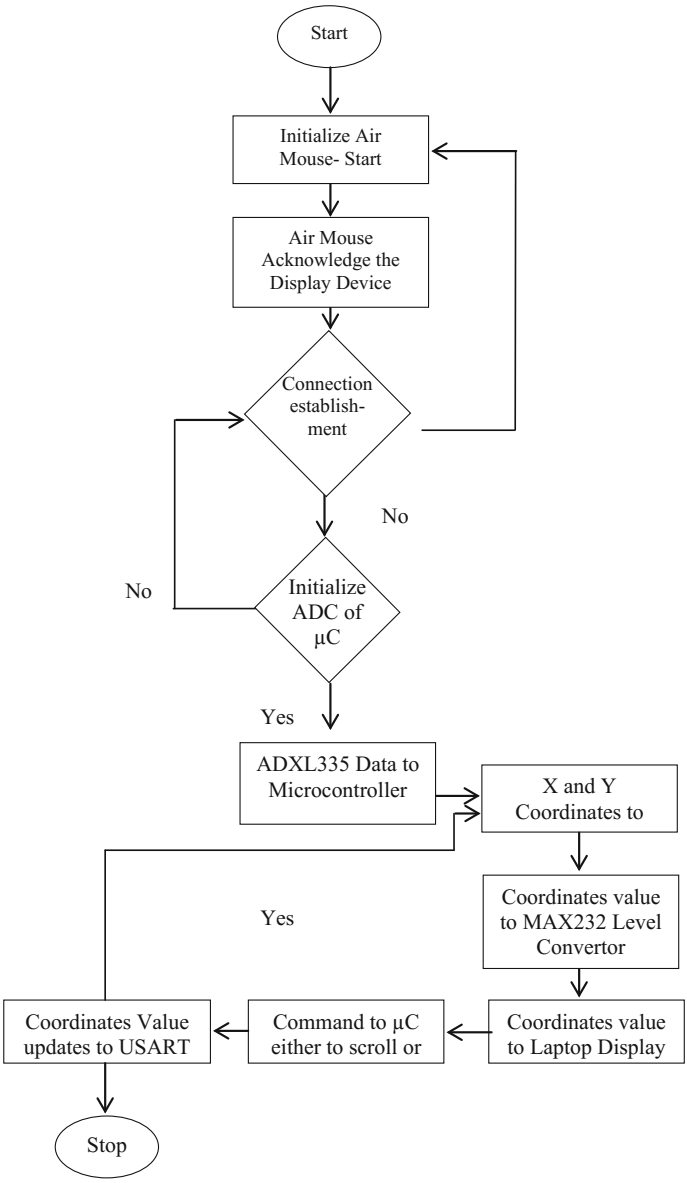


Fig. 3 Flowchart of the air mouse program operation

If the mouse is inactive, the program cycles through the button sampling until the mouse is active. After the sampling of button is made, mouse is empowered and acceleration axis checking is been done. If *X* has not been sampled, set the sample multiplexer to *Y*, sleep until *X* is prepared, and sample *X*. The multiplexer is fixed to *Y* before *X* is been sampled because the present sample being processed is continuously taken off of the current multiplexer value, which is *X,* if *X* has not been sampled. If *X* has been sampled, *Y* has to be checked to see whether it has been sampled or not. If it has not been, set the multiplexer to *X*, sleep until *Y* is prepared, and sample *Y*. If *Y* has been sampled, adjust the samples to the correct twos complement numbers, scale them, and create the serial packets. Send the serial packets, indicate that *X* needs to be sampled, and return to the beginning of the loop. The mouse is enabled and disabled by one of the sampled buttons.

Initialize ADC of µC
Initialize USART of µC
char data;
int main ( )
Calculate XYcor;
end for
Display to LCD
end for
Cmd to USART;
Locate ***XYcor*** to Screen;
end for
Updt_USART;
end for
Finding new ***XYcor;***
Return to finding XYcor;
end for

Notations:

char: Character initialization of 8 bit
XYcor: Locate coordinates of screen in two dimension
Updt_USART: updating of USART value
USART: Universal synchronous asynchronous Receiver Transmitter
ADXL_Sensor: Accelerometer Sensor value in XY coordinates

3.3 Applications

i. For ease of conducting seminars or official meetings in a large hall since it requires wearing of a simple glove which acts as the mouse. Also, many of the tasks where both the keyboard and mouse are required, makes the user frustrating and awkward to switch back and forth between them. The same can be easily solved by the proposed solution.
ii. Air mouse prevents its users from occupational disorders like Carpal Tunnel Syndrome. This is caused by resting wrist on a hard surface as in the case of conventional mouse. No need to move back and forth between the projected slide and the system to open or close any related files. It is an innovative way to maintain proper ergonomics.

The tricky part of this algorithm is its timing and the conversion of the accelerometer output to the proper 2's complement number. There might be some issues pertaining to the accelerometer readings probably when the sensor is moved on the NW–SE plane. But for getting good readings the microprocessor can be put to sleep until the reading becomes ready.

4 Conclusion

The design is aimed at the utilization of movement of hand to yield a cursor velocity, and the desired results are easily achievable. The device will work well if the pitch and roll functions are taken into consideration properly. Rolling the device counter-clockwise or clockwise moves the mouse to the left or to the right. Pitching the device towards one or away moves the mouse down or up. The vertical motion of the mouse is reversed, like a joystick. This type of gesture is simple to acclimatize to than having the pitch non-inverted. The present model of the Air mouse is a hand glove type hence there might be problems of varying size of human hands. Moreover there is always a need of a cable attached to the computer. This can be avoided by devising the circuitry in a wireless environment. In extended forms of this project, one can use a gyro the cost of which is very low. So that gravity in the motion sensing can also be taken into account for achieving perfection in positioning of the device in the free space.

References

1. Seelye, A., et al., *Computer mouse movement patterns: A potential marker of mild cognitive impairment.* Alzheimer's & Dementia: Diagnosis, Assessment & Disease Monitoring, 2015. **1**(4): p. 472–480.
2. Onyebeke, L.C., et al., *Effects of forearm and palm supports on the upper extremity during computer mouse use.* Applied Ergonomics, 2014. **45**(3): p. 564–570.
3. Fogleman, M. and G. Brogmus, *Computer mouse use and cumulative trauma disorders of the upper extremities.* Ergonomics, 1995. **38**(12): p. 2465–2475.
4. Van Niekerk, S.M., S.M. Fourie, and Q.A. Louw, *Postural dynamism during computer mouse and keyboard use: A pilot study.* Applied Ergonomics, 2015. **50**: p. 170–176.
5. Devalla, V., et al., *Design and Development of Object Recognition and Sorting Robot for Material Handling in Packaging and Logistic Industries.* International Journal of Science and Advanced Technology, 2012. **2**(9).

A Novel Approach for Continuous Pain Intensity Estimation

Neeru Rathee and Dinesh Ganotra

Abstract In this study, a novel approach for continuous pain intensity estimation based on facial feature deformations is presented. The proposed approach is based on the fact that the shape and appearance of facial features get deformed due to pain. The shape deformation caused due to pain is computed using Thin Plate Spline (TPS). The non-rigid parameters are used as representative of facial feature deformations and affine transformation parameters are ignored. The deformation of appearance features is extracted using local binary pattern features. The shape and appearance features are fed to relevance vector regression separately and jointly for pain intensity estimation. The pain intensity estimation is carried directly (by estimating the pain intensity from facial feature deformation) and indirectly by first estimating the Action Unit intensity and then computing the pain intensity. For assessment of the proposed approach, we have selected the popularly accepted UNBC-McMaster Shoulder Pain Expression Archive Database. Experimental results ensure the efficacy of the proposed approach for pain intensity estimation.

Keywords Thin plate spline · Local binary pattern · Pain detection · Pain intensity estimation · Relevance vector regression · Facial feature descriptors

1 Introduction

The reliable measure of pain intensity is the one of the major concern of medical practitioners and has drawn much attention. Earlier this task was done by analyzing the reports generated by patients themselves or by taking their interviews. Later,

Neeru Rathee (✉)
Maharaja Surajmal Institute of Technology, Guru Gobind Singh Indraprastha University, New Delhi, India
e-mail: neeru1rathee@gmail.com

Dinesh Ganotra
IGDTUW, New Delhi, India
e-mail: dinesh_ganotra@hotmail.com

© Springer Science+Business Media Singapore 2017

R. Singh and S. Choudhury (eds.), *Proceeding of International Conference on Intelligent Communication, Control and Devices*, Advances in Intelligent Systems and Computing 479, DOI 10.1007/978-981-10-1708-7_50

Visual Analog Scale (VAS) was used for evaluating pain intensity [16]. The above methods were very convenient and were being widely used as they did not use advance technology [2, 5, 9].

In late 1980s, when the development in the field of facial expression came into existence [14], then researchers focused on detection of pain from facial images. The pioneering work in this direction was done by measuring pain in terms of Facial Action Coding System (FACS) [18]. The fascinating feature of such systems is that they can be used in real time for taking care of the patients in intensive care unit [1, 12, 13]. Moreover, it was helpful to those who need continuous monitoring. The pain intensity estimation was a binary problem earlier and researchers achieved success diagnose whether pain is present or not [1, 8, 13]. Recently, researchers are working toward measuring the various levels of pain [7].

The above-mentioned methods represent facial features either by shape features or by appearance features for pain intensity detection. An attempt in this direction has been made to estimate continuous pain intensity by combining DCT features and Local Binary Pattern (LBP) features [10]. Recently, Histogram of Topological features has also been used for estimating pain intensity [6]. In the present work, we use TPS transformation parameters and LBP features for representing facial features. The motivations behind using TPS are its performance in point matching for image registration application [3] and pain intensity detection [19]. The reason behind using LBP features is its capability to represent facial features [10, 15].

We have performed continuous pain intensity estimation by using two different approaches: direct and indirect. In direct approach, pain intensity estimation is done directly from facial features. Another approach is to first estimate facial action unit intensity and then computing the pain intensity by using the formula proposed by [18]. The block diagram of the proposed approach is presented in Fig. 1.

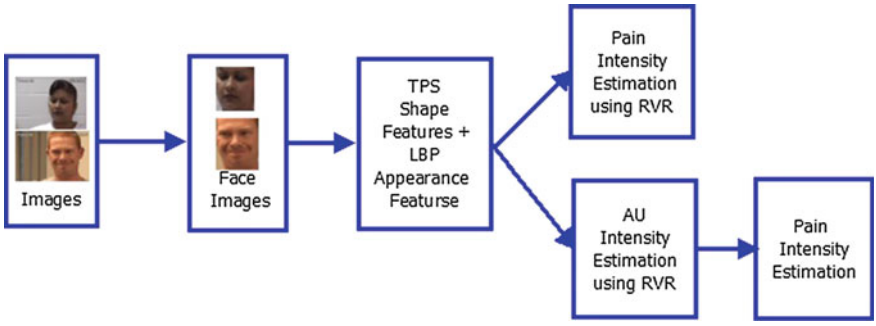


Fig. 1 Block diagram representation of pain intensity estimation approach

2 Feature Extraction

Feature extraction is the important step in any recognition task. The efficiency of the recognition engine is highly dependent on how effectively the features have been extracted. The feature extraction steps are listed well in this section.

2.1 Face Registration

Image registration is the primary step for feature extraction which is popularly used for aligning similar facial images. For alignment of facial images, we have used 66 landmark points around facial components provided along with the database. The reference landmark points are obtained by taking the average of the all the landmark points over the entire training data. A 2D similarity transformation and bilinear interpolation technique are utilized to transform the new image of the new reference coordinate system [11]. The registered facial images are then masked to extract various facial components. Face registration is required for pixel based features and is avoided for thin plate spline based feature extraction.

2.2 Thin Plate Spline Features

The TPS mapping function provides affine and non-affine mapping between two point sets and thus help in capturing the global rigid and local non-rigid transformations. This property of TPS is used by [3] for non-rigid point matching. Motivated by the promising results, we have investigated TPS to extract deformation of facial features caused due to different mindsets. TPS provides a single step closed form solution for measuring deformation of facial features in various pain intensity image frames. Due to lack of iterative algorithms in TPS mapping, it is computationally less complex.

2.3 Local Binary Pattern

The appearance features were extracted using local binary pattern by adopting the same approach as mentioned in [10]. LBP features were found to be a powerful method for texture feature extraction and has been popularly accepted for facial feature representation [4]. The most important properties of LBP were computation simplicity and illumination invariance [17]. Investigated many variants of LBP for multi-view facial expression recognition to investigate the importance of multi-resolution and orientation analysis for feature representation. We have used extended



Fig. 2 LBP features of facial images with different pain levels

LBP, which is rotation invariant. Rotation invariant LBP uses fewer bins as compared to regular LBP and reduces the number of components used for binary pattern representation. Feature extraction was implemented as follows: first, the face image was divided into several non-overlapping blocks of size 9×9. Then, LBP histograms were calculated for each block resulting in a feature vector of 59-D. Finally, the block LBP histograms were concatenated to generate a feature vector corresponding to an image framer. As a result, the facial expressions were represented by the LBP and the shape of the face was recovered by the concatenation of different local histograms. The LBP features for facial images are represented in Fig. 2.

3 Database

The assessment of the proposed model for pain intensity estimation was done using UNBC-McMaster Shoulder Pain expression archive. It contains face videos of patients (66 females and 63 males) suffering from shoulder pain while performing range-of-motion tests of their arms. Out of which videos of 25 subjects are available for research purposes. Movements of the arms were recorded in two different modes: (1) active mode where the subject moves the arm himself (with camera orientation frontal initially) and (2) passive mode where the subjects arm is moved by a physiotherapist (with camera orientation about 70° from the frontal). We have taken only frontal images with slight variation in angle.

4 Experimental Results

The TPS parameters were computed using 66 landmark points given with UNBC-McMaster shoulder pain archive database. The PSPI scores were used to label pain level in various frames of a video. The first frame of each video was used source image and the rest of the frames were used as target image. The non-affine transformation parameters were computed for all the frames of a video. The LBP features were also extracted for all the frames of video. The TPS parameters and LBP features were mapped to discriminative space by using the distance metric learning method proposed in [19]. The extracted features were fed to the relevance vector regression for pain intensity estimation. At first set of experiments, PSPI score of an image frame was used as label of pain intensity. The feature set was applied to relevance vector regression for pain intensity estimation. The reason behind using RVR instead of Support Vector Regression is that support vectors selected by former are less as compared to later [10], thus resulting in more sparse model. The TPS features and LBP features were applied separately and jointly. To combine the performance of both the feature RVR fusion strategy adopted by [10] was adopted in the proposed approach.

At first set of experiments, PSPI score of an image frame was used as label of pain intensity. The feature set was applied to relevance vector regression for pain intensity estimation. The reason behind using RVR instead of Support Vector Regression is that support vectors selected by former are less as compared to later [10], thus resulting in more sparse model. The TPS features and LBP features were applied separately and jointly. To combine the performance of both the feature RVR fusion strategy adopted by [10] was adopted in the proposed approach.

The regression was performed using leave-one-subject-out cross-validation approach. In this approach, the videos of one subject were used for testing and videos of remaining subjects were used for training. The evaluation parameters used to measure the performance of the proposed approach are Mean Square Error (MSE) and Pearson correlation coefficient (CORR). In second set of experiment, one RVR is used for detecting the intensity of each AU. In the present work, 6 different RVRs were used to estimate their intensity. For each frame, PSPI [18] score was computed using the following equation:

$$\text{Pain} = \text{AU}\,4 + \max(\text{AU}\,6, \text{AU}\,7) + \max(\text{AU}\,9, \text{AU}\,10) + \text{AU}\,43 \qquad (1)$$

To evaluate the performance of the proposed approach, MSE and CORR were computed for AUs mentioned in Eq. (1) by using TPS and LBP features separately and in combination with each other. The results are depicted in Figs. 3 and 4.

The intensity of the AUs was used to compute PSPI score of an image frame using the Eq. (1). The PSPI score referred to the pain level of the image frame and this was named as indirect pain intensity estimation. For direct pain intensity estimation, the TPS features and LBP features were fed to RVR for direct estimation of pain level.

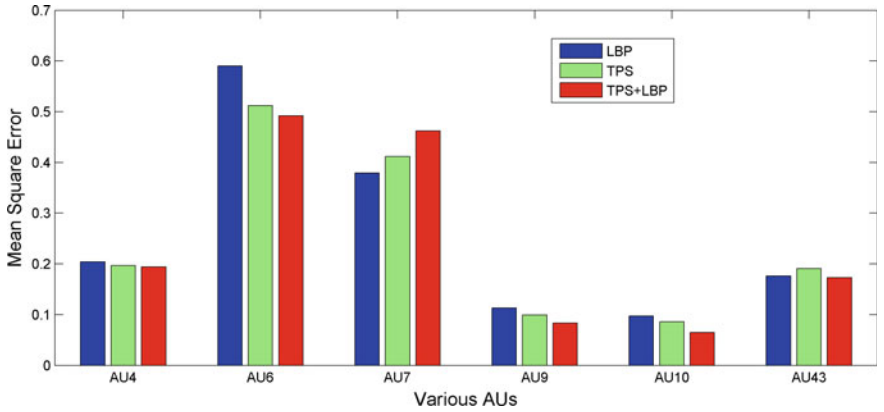


Fig. 3 MSE for AU intensity estimation using various feature

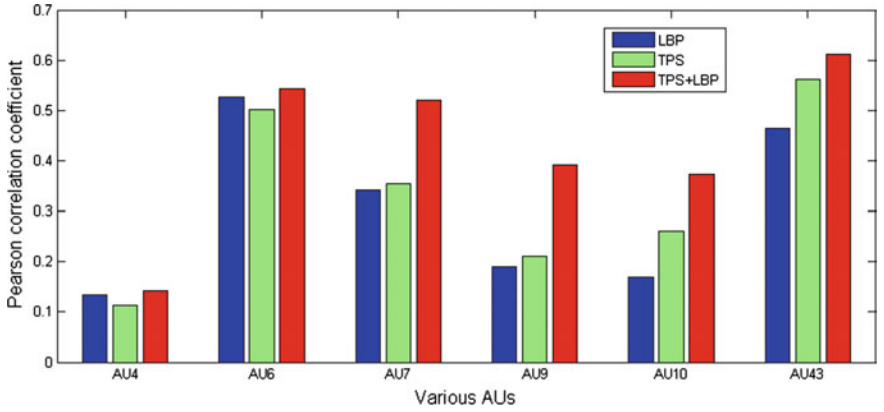


Fig. 4 Pearson correlation coefficient using various feature for AU intensity

MSE and CORR using combined features are better as compared to the features used alone. The TPS parameters results in better performance in terms of MSE as compared to LBP features, but their performance deteriorate in terms of CORR. We may also conclude from Table 1 that performance of the direct pain intensity estimation is better than the indirect pain intensity estimation.

Table 1 Continuous pain intensity estimation. Direct pain estimation refers to estimation of pain intensity directly from facial features. Indirect pain estimation refers to estimating AUs first and then computing pain intensity

		Direct method		Indirect method	
		MSE	CORR	MSE	CORR
Proposed approach	TPS	1.623	0.432	1.324	0.654
Proposed approach	TPS+LBP	1.283	0.623	1.594	0.401
Kaltwang et al.	DCT+LBP	1.386	0.59	1.633	0.471

MSE Mean Square Error, CORR Pearson Correlation Coefficient

5 Conclusion

Continuous pain intensity estimation by combining shape and appearance facial feature deformations is presented. The pain intensity estimation is performed using two different approaches. In the first approach, RVR predicts the PSPI score of image frames of a video by using TPS features and LBP features individually and in combination with each other. In the second approach, intensity of various AUs is predicted first and then PSPI score is computed to represent the pain level. Experimental results ensure the efficacy of the proposed approach for pain intensity estimation. The MSE is less in direct pain recognition and Pearson correlation coefficient is higher for direct pain recognition by combined feature set, thus proving the suitability of direct approach for pain intensity estimation.

References

1. Ashraf, A.B., Lucey, S., Cohn, J.F., Chen, T., Ambadar, Z., Prkachin, K.M., Solomon, P.E.: The painful face–pain expression recognition using active appearance models. Image and vision computing 27(12), 1788–1796 (2009)
2. Burckhardt, C.S., Jones, K.D.: Adult measures of pain: The mcgill pain questionnaire (mpq), rheumatoid arthritis pain scale (raps), short-form mcgill pain questionnaire (sf-mpq), verbal descriptive scale (vds), visual analog scale (vas), and west haven-yale multidisciplinary pain inventory (whympi). Arthritis Care & Research 49(S5), S96–S104 (2003)
3. Chui, H., Rangarajan, A.: A new point matching algorithm for non-rigid registration. Computer Vision and Image Understanding 89(2), 114–141 (2003)
4. Feng, X., Pietikainen, M., Hadid, A.: Facial expression recognition with local binary patterns and linear programming. Pattern Recognition and Image Analysis C/C of Raspoznavaniye Obrazov I Analiz Izobrazhenii 15(2), 546 (2005)
5. Ferraz, M.B., Quaresma, M., Aquino, L., Atra, E., Tugwell, P., Goldsmith, C.: Reliability of pain scales in the assessment of literate and illiterate patients with rheumatoid arthritis. The Journal of rheumatology 17(8), 1022–1024 (1990)
6. Florea, C., Florea, L., Vertan, C.: Learning pain from emotion: transferred hot data representation for pain intensity estimation. In: ECCV workshop on ACVR (2014)
7. Hammal, Z., Cohn, J.F.: Automatic detection of pain intensity. In: Proceedings of the 14th ACM international conference on Multimodal interaction. pp. 47–52. ACM (2012)

8. Hammal, Z., Kunz, M.: Pain monitoring: A dynamic and context-sensitive system Pattern Recognition 45(4), 1265–1280 (2012)
9. Jensen, M.P., Karoly, P., Braver, S.: The measurement of clinical pain intensity: a comparison of six methods. Pain 27(1), 117–126 (1986)
10. Kaltwang, S., Rudovic, O., Pantic, M.: Continuous pain intensity estimation from facial expressions. In: Advances in Visual Computing, pp. 368–377. Springer (2012)
11. Li, Y., Mavadati, S.M., Mahoor, M.H., Zhao, Y., Ji, Q.: Measuring the intensity of spontaneous facial action units with dynamic bayesian network. Pattern Recognition (0) (2015), http://www.sciencedirect.com/science/article/pii/S0031320315001612
12. Lucey, P., Cohn, J., Lucey, S., Matthews, I., Sridharan, S., Prkachin, K.M.: Automatically detecting pain using facial actions. In: Affective Computing and Intelligent Interaction and Workshops, 2009. ACII 2009. 3rd International Conference on. pp. 1–8. IEEE (2009)
13. Lucey, P., Cohn, J.F., Matthews, I., Lucey, S., Sridharan, S., Howlett, J., Prkachin, K.M.: Automatically detecting pain in video through facial action units. Systems, Man, and Cybernetics, Part B: Cybernetics, IEEE Transactions on 41(3), 664–674 (2011)
14. Lucey, P., Cohn, J.F., Prkachin, K.M., Solomon, P.E., Chew, S., Matthews, I.: Painful monitoring: Automatic pain monitoring using the UNBC-McMaster shoulder pain expression archive database. Image and Vision Computing 30(3), 197–205 (2012)
15. Mavadati, S., Mahoor, M., Bartlett, K., Trinh, P., Cohn, J.: Disfa: A spontaneous facial action intensity database. Affective Computing, IEEE Transactions on 4(2), 151–160 (April 2013)
16. McCormack, H.M., de L Horne, D.J., Sheather, S.: Clinical applications of visual analogue scales: a critical review. Psychological medicine 18(04), 1007–1019 (1988)
17. Moore, S., Bowden, R.: Local binary patterns for multi-view facial expression recognition. Computer Vision and Image Understanding 115(4), 541–558 (2011)
18. Prkachin, K.M., Solomon, P.E.: The structure, reliability and validity of pain expression: Evidence from patients with shoulder pain. Pain 139(2), 267–274 (2008)
19. Rathee, N., Ganotra, D.: A novel approach for pain intensity detection based on facial feature deformations. Journal of Visual Communication and Image Representation 33, 247–254 (2015)

A Design and Application of Forest Fire Detection and Surveillance System Based on GSM and RF Modules

Aditya Agarwal, Vishal Sharma, Rajesh Singh, Anita Ghelot and Kanchan Bahukhandi

Abstract Forest fires in recent years have been devastating both for natural ecosystem, biodiversity and forest economy. With increasing population pressure and change in global climate scenario, there is an increase in percentage of forest fires that are a major cause of declining Indian forests. According to forest survey report of India, 50 % of forest areas in country are fire prone (ranging from 50 to 90 % in some states of country). About 6 % of the forests are prone to severe fire damages. The designed system and research paper aims to identify forest fire in the initial stage. This system will monitor each tree and will give respective data to the control room. The hardware will be equipped with node, head and main server having application like exact location identifier (GSM Modem), fire detectors and RF system for data transferring and devices which will be helpful in forest surveillance.

Keywords GSM modem · RF system · Server · Node

1 Introduction

Fires are the widespread phenomenon in Indian forests. Most forest fires are the result of human interference or due to natural causes like lightening, recorded atmospheric temperature and low humidity which offer favorable circumstances for

Aditya Agarwal (✉) · Vishal Sharma · Rajesh Singh · Anita Ghelot · Kanchan Bahukhandi
University of Petroleum and Energy Studies, Dehradun, India
e-mail: adityaa235@gmail.com

Vishal Sharma
e-mail: vishalsharma7r@gmail.com

Rajesh Singh
e-mail: rsingh@ddn.upes.ac.in

Anita Ghelot
e-mail: anita@ddn.upes.ac.in

Kanchan Bahukhandi
e-mail: kanchanupes@gmail.com

© Springer Science+Business Media Singapore 2017

R. Singh and S. Choudhury (eds.), *Proceeding of International Conference on Intelligent Communication, Control and Devices*, Advances in Intelligent Systems and Computing 479, DOI 10.1007/978-981-10-1708-7_51

fire to start. Forests that are the lifeline help out the people who work and have dependency on forest products. India, having a forest cover of 7.3 million hectares has a variety of species which are distributed all over the country. The forests and the biodiversity of the country are at a greater risk and under tremendous pressure. Suppression of wildfires that occur in forest area demands large amount of federal resources, costing up to $1.59 billion per year, along with the lives of ten to twenty firefighters [1]. It is important to note that in order to control forest fire, early warning systems are essential. In India there are usually traditional ways to minimize the effect of forest fire. Combating forest fires are usually done in traditional way like fire traces and beating with branches. New technologies like fire extinguisher from water planes and demarcation to reduce the spread of fire is not usually followed in India. The country has the richness of 99 national parks and 442 wildlife sanctuaries. In order to protect these vast stretches of land and biodiversity there is an important need to have a good surveillance and early warning systems so that the forest fire while in its beginning stage of spreading shall be controlled so as to prevent its spread. Usually in order to control fire in forest area there is a huge dependency on man power. Tracing exact location, communication problems, transportation facilities, weather conditions, environmental and wildlife situation which are one of the various factors preventing the officials and responsible authority to act when forest fire occur. Proper mechanism to prevent forest fire can be laid down in a better way so that it may be helpful to officials and forest concerned authority. Through this research paper we create a system which will assist the forest fire safety people to control unwanted effects on forest ecosystem and wildlife. For this purpose a sensing environment will be deployed with a large number of wireless sensors that are composed of sensor nodes [2]. These networks are of great relevance as they facilitate human capabilities while monitoring wide-forest areas [3]. We validate that monitoring the wide area of forest by the use of modern electronic components can be very much helpful to the forest authority [4]. The system comprises a number of remote detectors which are placed collectively as an instrument within the forest area, linked to a central processing system [5]. Wireless Sensor Network (WSN) becomes an important source of receiving and transmitting collected data which is subdivided for environmental monitoring [6]. The controller is equipped with fire sensor, accelerometer, RF modem, and GSM modem which will monitor the periodic changes and will send signals to the control room for further actions. The purpose of surveillance by sensors and electronic devices is to provide a broad and precise overview of forest health and data for forest authorities and administration. This allows them to take appropriate strategic decisions and manage risks at earlier stage [7]. A simulation of this research and technique permits the researcher to take appropriate measures for estimating the maximum range of detection with appropriate sensibility of the system [8].

2 Proposed System

2.1 Node

This node consists of microcontroller (Atmega 16), RF Modem, Fire Sensor, Accelerometer and DC power supply. The controllers will be placed individually on the trees in a given required area which is highly prone to deforestation, poachers or forest fires. Fire sensors will identify and send signal if any trace of forest fire is close to proximity. Accelerometer will determine any vibration on angular displacement of tree coordinate, which can be due to cutting of tree by poachers or landslides (Fig. 1).

2.2 Head

Atmega 16 is the microcontroller which has been used in the head. The head will be placed in range of 1 km. In this the RF and GPS system will be helpful in determining the exact location of the given tree so that it is easy to send needed safety equipment's at the place of emergency. The controller provided in the head will be sending signals to the control room, where every detail will be analyzed with the exact co-ordinates by the help of GSM Modem (Fig. 2).

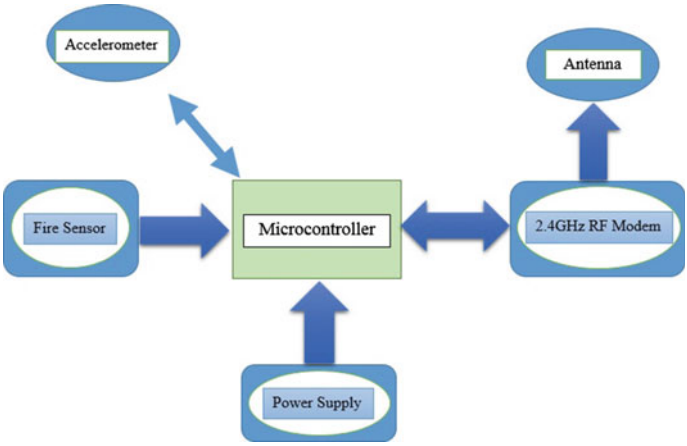


Fig. 1 Block diagram of node

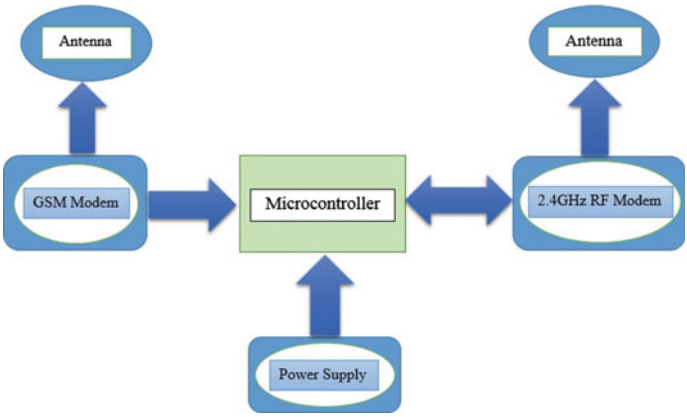


Fig. 2 Block diagram of head

2.3 Main Server

The main server consists of microcontroller (Atmega 16), Alarm, RF Modem, GSM Modem, MAX232, DB9 and a PC which is going to analyze all the incidents going around the forest. The main server will receive collected data from the head through GSM Modem. From here the manager can take proper and early steps to control forest fire or can stop illegal trade of trees (Fig. 3).

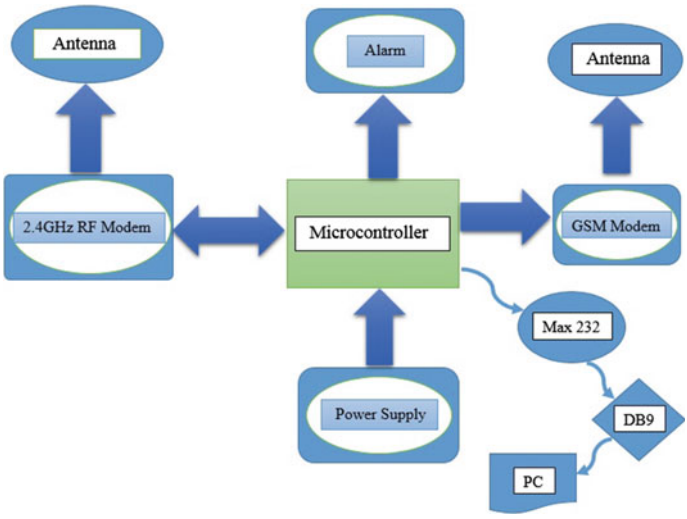


Fig. 3 Block diagram of main server

3 Hardware Development

3.1 Node

The main controlling system is Atmega 16 in which the Tx pin of controller is connected with Rx pin of RF Modem to transfer the signals and can be marked as an identity for getting the exact location. Three pins of Accelerometer are connected to PA0, PA1 and PA2 pins of Atmega 16 to transmit the signals. One pin of fire sensor is connected to pin PB0 of microcontroller which will help to sense the fire and a DC power source is connected to the controller (Fig. 4).

3.2 Head

In this the main controlling system is Atmega16. GSM is connected to Rx and Tx pin of DB9 which is used to receive and transfer signals of exact co-ordinates to MAX232 which is directly connected to the Atmega16. RF Modem is connected with Tx pin of controller which is used to transfer signals to the main server and a power supply is connected to microcontroller (Fig. 5).

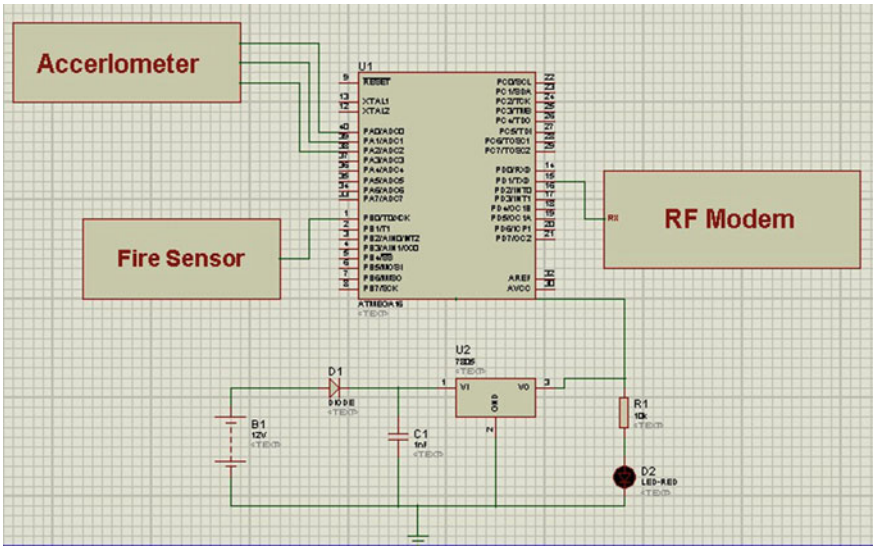


Fig. 4 Circuit diagram of node

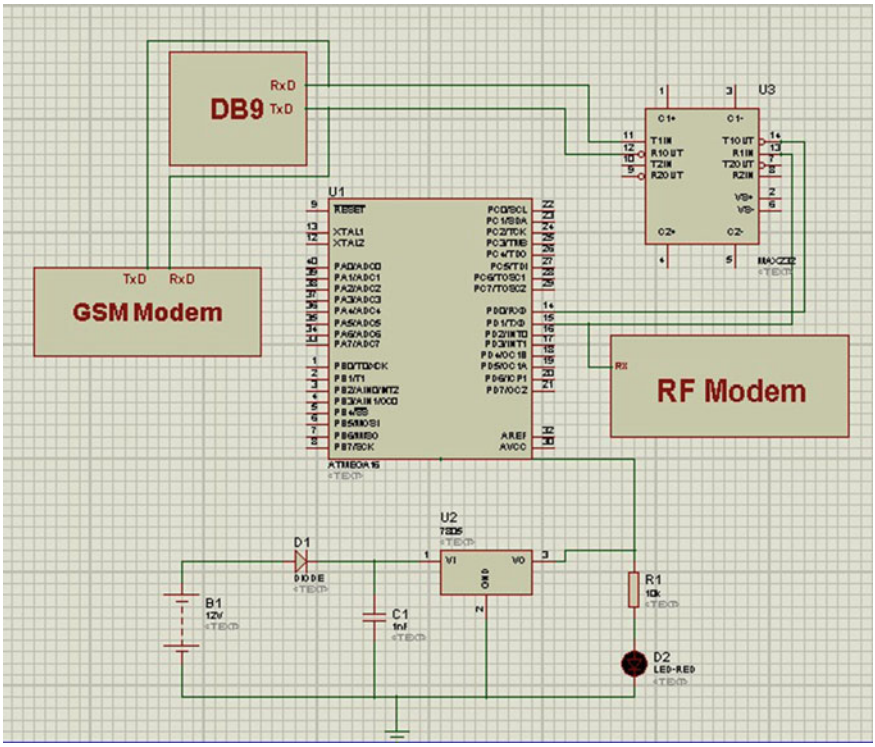


Fig. 5 Circuit diagram of head

3.3 Main Server

In the main server the main controlling system is Atmega16. In this system, GSM is connected to Rx and Tx pin of DB9 which is used to receive and transfer signals of exact co-ordinates to MAX232 that is directly connected to the Atmega16. RF Modem is used to receive the signals from the head. Alarm is also connected to the controller. Practical simulations and theoretical results are used to corroborate the control of system which is related with probability of false alarm (PFA). Probability of detection (PD) which is dependent on signal to noise ratio (SNR) are also used in the system [9] (Fig. 6).

4 Component Description

See Table 1.

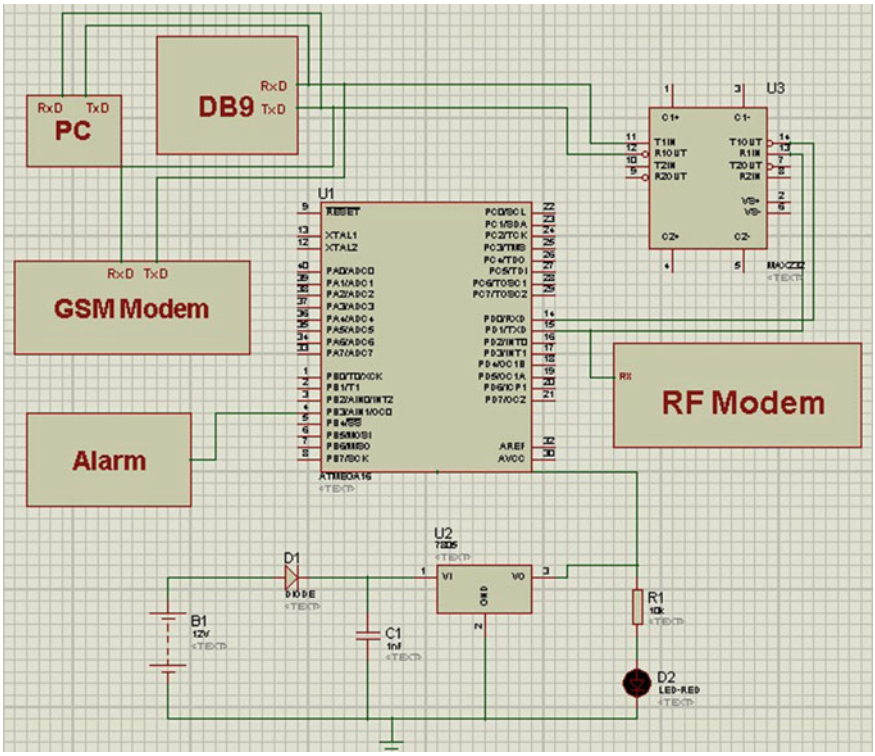


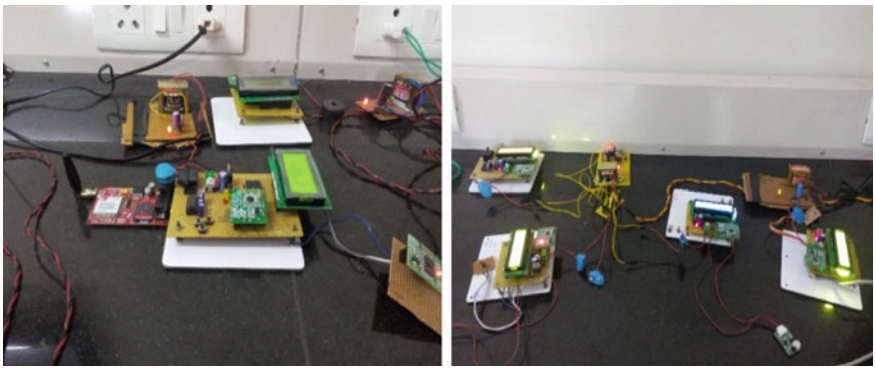
Fig. 6 Circuit diagram of main server

Table 1 Instruments used

S. No.	Device/module	Specifications and working
1.	Atmega 16	It is a CMOS 8-bit microcontroller based on the AVR RISC architecture
2.	RF modem	RF data modem working at 2.4 GHz frequency. Receives and Transmits serial data of adjustable baud rate of 9600/4800/2400/19200 bps at 5 or 3 V level for direct interfacing to microcontrollers
3.	GSM modem	GSM/GPRS Modem-TTL (5 V) is built with Tri-band GSM/GPRS engine, works on frequencies Tri-Band GSM/GPRS 900/1800/1900 MHz
4.	MAX 232	Level converter IC that is used in cluster head and main server to link the data in PC
5.	DB9	It's a 9 pin serial female port
6.	Fire sensor	A Fire sensor is designed to detect and respond to the presence of flame or fire
7.	Accelerometer	An accelerometer is an apparatus, either mechanical or electromechanical, for measuring acceleration or deceleration
8.	Alarm	This device gives us an audible, visual or other form of signal related to a problem or condition specifying a particular instant [10]
9.	Power supply	12 V/1A power supply, 12 V/1A lithium ion battery, AC power supply
10.	Relay	It's used to control circuits by low power signal

5 Result and Discussion

As computerized monitoring is now days very essential and useful, it is quiet understandable that by accepting the use of this technology we can achieve the way of surveillance and control of resources of forest more conveniently. This system is cost efficient, easy to handle, approachable and eco-friendly for the environment.



6 Future Scope of the Work

The project gives emphasis on using modern technology of remote sensing and other techniques to equip the forest authority and organizations in their work for forest conservation. Due to the lack of efficient staff and emergency plan there is a greater need to use much efficient systems. It is difficult for authorities to manage huge forest areas and to be present at a time of accidents. Due to human limitation and lack of modern technology, it is not possible to combat forest fire. The installation of this project in a better way can give a chance to organizations to have efficient control over forest by not interrupting its fragile ecosystem. The use of this forest surveillance system will be helpful in mapping emergency plan and making it more effective during the occurrence of any disaster. This system uses advance technology which will help in tracing out the forest fire in its initial stage. The poaching activities and illegal trade of forest goods can be stopped by the application of these sensors. Hence, with the complete information of incident and its nature, the administration can take the appropriate decisions to combat illicit trading of trees and preventing forest fires.

References

1. Zhou, Gouqing, Chaokui Li, and Penggen Cheng. "Unmanned aerial vehicle (UAV) real-time video registration for forest fire monitoring." *Geoscience and Remote Sensing Symposium, 2005. IGARSS'05. Proceedings. 2005 IEEE International*. Vol. 3. IEEE, 2005.
2. Liao, Wen-Hwa, Yucheng Kao, and Ying-Shan Li. "A sensor deployment approach using glowworm swarm optimization algorithm in wireless sensor networks." *Expert Systems with Applications* 38.10 (2011): 12180–12188.
3. Bosch, Ignacio, Soledad Gómez, and Luís Vergara. "Automatic forest surveillance based on infrared sensors." *Sensor Technologies and Applications, 2007. SensorComm 2007. International Conference on*. IEEE, 2007.
4. Hefeeda, Mohamed, and Majid Bagheri. "Wireless sensor networks for early detection of forest fires." *Mobile Adhoc and Sensor Systems, 2007. MASS 2007. IEEE International Conference on*. IEEE, 2007.
5. Brogi, Giulio, Luca Pietranera, and Francesco Frau. "Forest surveillance and monitoring system for the early detection and reporting of forest fires." U.S. Patent No. 5,734,335. 31 Mar. 1998.
6. Son, Byungrak, Yong-sork Her, and Jung-Gyu Kim. "A design and implementation of forest-fires surveillance system based on wireless sensor networks for South Korea Mountains." *International Journal of Computer Science and Network Security (IJCSNS)* 6.9 (2006): 124–130.
7. Smith, David, et al. "Forest health surveillance in Victoria." *Australian Forestry* 71.3 (2008): 188–195.
8. Bellecci, C., et al. "Reduction of false alarms in forest fire surveillance using water vapour concentration measurements." *Optics & Laser Technology* 41.4 (2009): 374–379.
9. Bosch, Ignacio, et al. "Infrared image processing and its application to forest fire surveillance." *Advanced Video and Signal Based Surveillance, 2007. AVSS 2007. IEEE Conference on*. IEEE, 2007.
10. Briz, S., et al. "Reduction of false alarm rate in automatic forest fire infrared surveillance systems." *Remote Sensing of Environment* 86.1 (2003): 19–29.

Generation of Electricity by Piezoelectric Crystal in Dance Floor

Pankaj Aswal, Suyash Kumar Singh and Apurv Thakur

Abstract The need to develop an alternative source of energy is increasing day by day. The fashion of youth going to the disco and clubs is also increasing. How is it if we make power generating dance floors and use it for a life time period to run the equipments of disco or night club using a piezoelectric crystal which is an alternate source of energy? It would also decrease the load of an area where the club is located and also there is saving of electricity without any pollution. Here we have shown how the power can be generated in a club using piezoelectric crystals.

Keywords Piezoelectric materials · Electrical energy · Piezoelectricity · Potential gradient · Young's modulation · Simulation · Crystalline structure

1 Introduction

There are certain solid-state materials such as photovoltaic materials, thermoelectric material, and piezoelectric material that can generate electricity by the action of heat, stress, and light as stated by Qing Li et al. [1]. Piezoelectric material is the material that can generate electricity by the action of stress (force/area). These materials are generally made up of silicon (Si) or germanium (Ge) in addition with other elements; examples of piezoelectric materials are tourmaline, lithium niobate ($LiNbO_3$), etc., the resource description given by F-Rubio Marcosl [2].

The output voltage obtained from a single piezoelectric crystal is in millivolts range, and the power in microwatt range. So in order to achieve higher voltages, the piezoelectric crystals can be arranged in cascading manner, i.e., series. The energy

Pankaj Aswal (✉) · S.K. Singh · Apurv Thakur
Graphic Era University, Dehradun 248002, India
e-mail: aswal_pankaj@rediffmail.com

S.K. Singh
e-mail: suyashsingh7132@gmail.com

Apurv Thakur
e-mail: Sweetapurv12@gmail.com

© Springer Science+Business Media Singapore 2017

R. Singh and S. Choudhury (eds.), *Proceeding of International Conference on Intelligent Communication, Control and Devices*, Advances in Intelligent Systems and Computing 479, DOI 10.1007/978-981-10-1708-7_52

thus obtained is stored in lithium batteries or capacitors. We have used this concept here in case of dance floor by laying the crystal beneath the tile, and using piezoelectric material from the jumping and walking of people on the dance floor is of great interest, because this vibration of energy is otherwise unused. Movement is everywhere; we just need to capture this energy for advancement in efficiency and cleaner energy production.

1.1 Power Generating Dance Floor

We can generate power while having fun at the dance floor, and use this power to run various equipments of the night club or disco. This can be done using piezoelectric crystals. Piezoelectric crystal is one of the renewable sources of energy as our fossil fuels are on the verge of extinction. We need to find out an alternate source energy which can overcome the need of our fossil fuels. Piezoelectric crystal is readily available in the market and is very cheap. A single crystal costs about 23–25 rupees only. It is also pollution free. The disco or night clubs consume lot of power in any area. If they can produce their own power, then it would be very helpful for the society as it can decrease the need of power in an area as concluded from Chowdhary [3].

The piezoelectric crystal can be laid below the tiles of a night club, and when the group of people uses this dance floor, expansive amount of voltage is produced. This voltage can be used to run equipments of a disco or a night club as stated by EDE RANIERI [4]. Let us consider a very small area 6 ft*3.5 ft, where 6 ft is the width and 3.5 ft is the length, i.e., the region of the floor is 21 square feet. The number of tiles covering this area is 1. Let the size of one crystal be 1 ft*1 ft, and 'n' number of crystals is laid below the tile. For this region we are going to study how much power is generated if we laid the piezoelectric crystals in this region.

2 Relation Between Potential Gradient and Pressure

Piezoelectricity is a material which charges when force (mechanical stress) is applied on it and discharges when stress is removed. It converts mechanical energy into electrical and vice versa.

From Fig. 1 if the force applied in the tile is F then:
we know that

$$\begin{aligned} Q &\propto F \\ Q &= d * F \end{aligned} \tag{1}$$

where d = charge sensitivity.

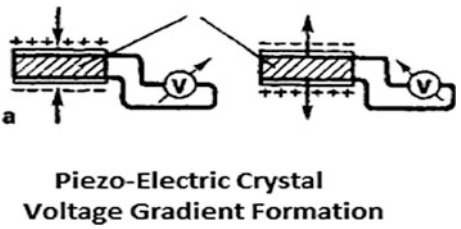


Fig. 1 Piezo-Electric Crystal Voltage Gradient Formation

$$\text{Young's modulus} = \frac{\text{stress}}{\text{strain}}$$
$$F = A\,\gamma\left(\frac{\Delta t}{t}\right) \tag{2}$$

From Eqs. (1) and (2) we get

$$Q = d\,A\,\gamma\left(\frac{\Delta t}{t}\right) \tag{3}$$

In Eq. (3) Q can be written as $C\ V_0$

$$V_0 = g * p * t \tag{4}$$

where $p = \frac{F}{A}$ = pressure; and g = voltage sensitivity; and t = gap between tile and a crystal (Fig. 2).

The second-degree RLC equation is given by

$$i(t) = v(t)\ R + \frac{1}{l}\int v(t) + c\frac{\mathrm{d}v(t)}{\mathrm{d}t} \tag{5}$$

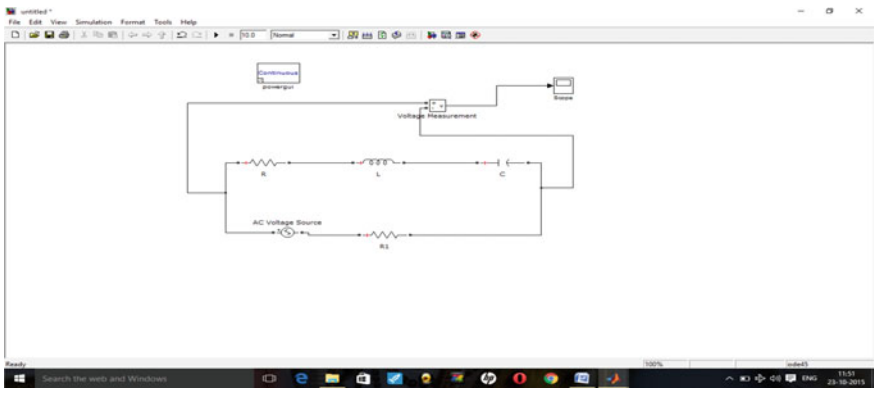
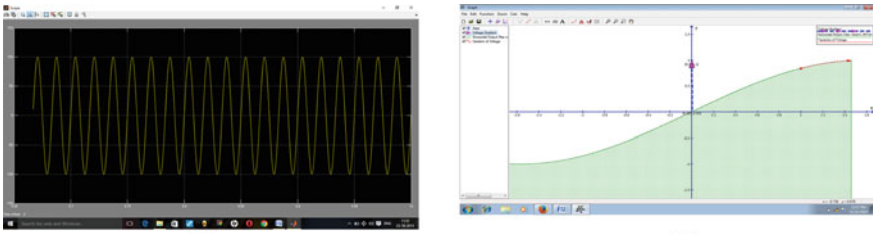


Fig. 2 The RLC model designed on Matlab



(a) (b)

Fig. 3 **a** The response of the RLC model. **b** The relationship between sensitivity g and develop voltage gradient

Taking Laplace transform of Eq. (1) we get

$$V(s) = \frac{s}{s^2\sigma + sR + \frac{1}{l}} \quad I(s) \tag{6}$$

With the help of equation number 2 the transient response can be calculated. The output of above scope is shown in Fig. 3.

2.1 *Resonator Model*

Solving the characteristic equation the output in terms of voltage is given below:
Substituting

$$R = 0.01\,\text{ohm} \quad L = 0.01\,\text{H} \quad C = 0.01\,\text{F}$$

The output is

$$\text{Voltage} = 1.46\,\text{V} \quad \text{Time} = 0.98\,\text{s}$$

Here the values of resistance, inductance, and capacitance substituted are as small as required for a unit of piezoelectric crystal; a pulse of electricity can affect the output of the small cell of crystal and work as a useful subsystem (Fig. 4).

2.2 *First-Generation Model Development*

Develop an analogous system and represent it to mechanical equivalent system. Implementing analogous system to that force is equally suitable, and Eq. (7) is written as

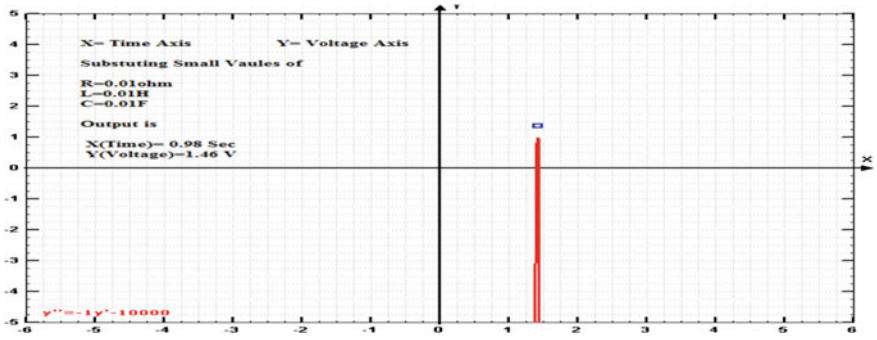


Fig. 4 The output of characteristic equation

$$Ms^2X(s) + KX(s) = F(s) \tag{7}$$

where

M mass;
K spring constant of the resonator;
$x(t)$ position of the oscillating spring relative to its static position;
$X(s)$ the frequency-domain representation of the spring position

$$G(s) = \frac{X(s)}{F(s)} = \frac{1}{Ms^2 + K} \tag{8}$$

2.3 Second-Generation Model Derivation

The problems were encountered. It was concluded that non-uniformity of spring–mass system internally damped the system; the article focuses on the ideal situation without application of external forces or its reaction to the analogous system. The new equation is shown in Eq. (9). The difference between these two equations derived the presence of α term, which is the damping constant, description given by Pankaj Aswal [5]:

$$Ms^2x(s) + \alpha x(s) + kx(s) = F(s) \tag{9}$$

The relative accurate system creating the gap between the results of undamped and damped transfer function (α) is the presence of f_v term in the damped function, where $G(s)$ is the second-order representation of damped transfer function:

$$G(s) = \frac{X(s)}{F(s)} = \frac{1}{Ms^2 + \varepsilon s + k} \tag{10}$$

2.4 Calculation of Damping Constant (α)

The damping constant can be calculated by Eq. (10). The calculation for damping constant is shown below:

$$\omega_o = \sqrt{\frac{k}{m}}$$

$$\omega_d = \sqrt{\frac{k(1-\theta)}{m}}$$

$$\theta = \frac{\alpha}{2m}$$

Now force equation can be given by

$$M\frac{d^2x}{dt^2} + \alpha\frac{dx}{dt} + Kx = F(t) \tag{11}$$

Graph in Fig. 5 depicts the value of given variables.

Damping coefficient (α) = 0.01/75 minimum is assigned for smallest vibration or fluctuation occurs due to pressure disturbance movement.

Spring constant (K) = 1/75 is assigned for smallest pressure which occurs due to variable stepping of foot in a minimal area.

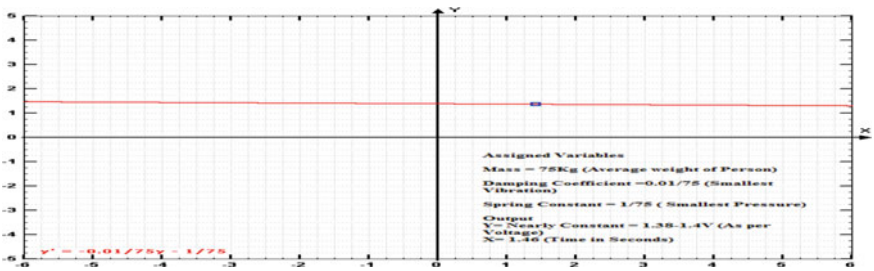


Fig. 5 Mass (M) = 75 kg is assigned for average weight person of age group of 21–30 years

2.5 Simulink

Figure 6 shows the simulated model that was used for analysis of the given abstract.

The figure determines the joint forces acting and comparing the commanded motion; the various components used are as follows:

(1) (Spring + Damper)
It represents one translational degree of freedom. The follower (F) body translates relative to the base (B) body along single translational axis connecting body coordinates origins. Sensor and actuator ports can be added.

(2) Trajectory
Trajectory is made using a pulse generator, add, and integrator. It applies a motion to the extremity of second mass as shown in Fig. 7.

(3) Scope
It is used to determine joint forces and compare command motion; the above Simulink shows how the electricity is produced when force is applied on the tile or in other word on the crystal which is beneath the tile of the dance floor.

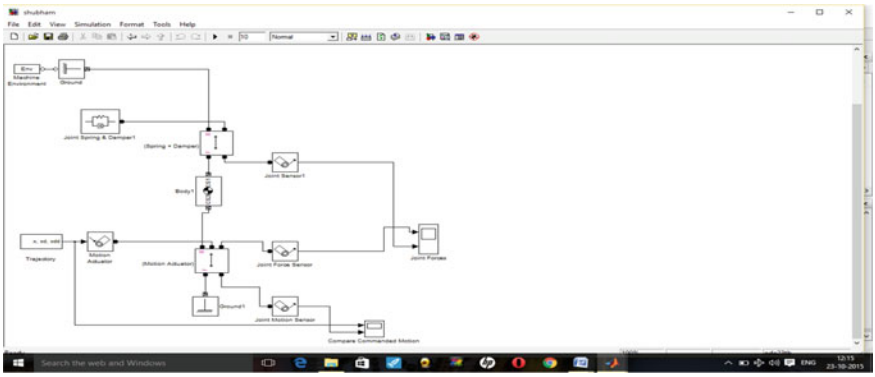


Fig. 6 Joint forces acting and comparing the commanded motion

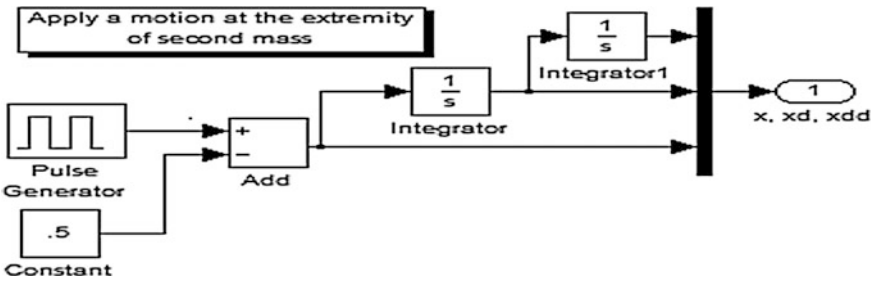


Fig. 7 Motion of Extrimity of Second Mass

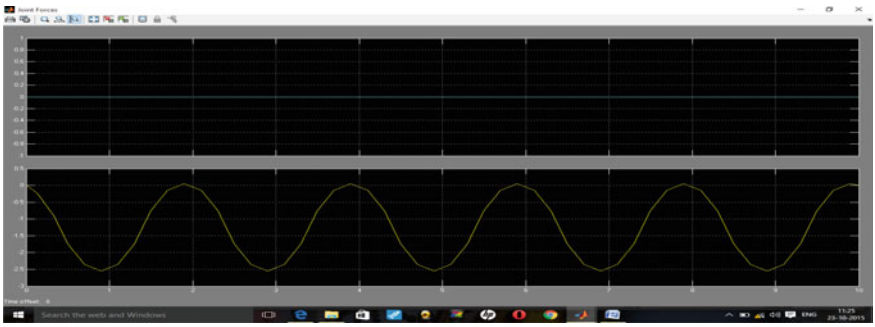


Fig. 8 Effect of joint forces

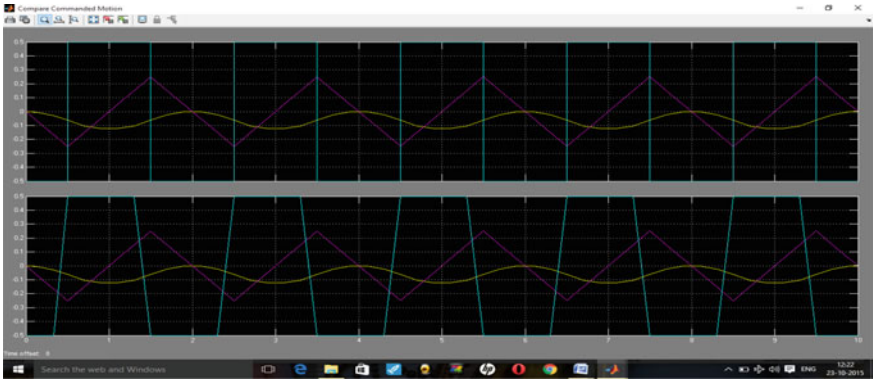


Fig. 9 Commanded motions

The outcomes of scope are as follows:

Graph in Fig. 8 shows the effect of joint forces. The straight line shows that there are no oscillations produced.
Graph in Fig. 9 has compared the commanded motions, i.e., how the sinusoidal waves are produced by combining the transient responses.

3 Conclusion

Generation of harmless energy is an upcoming sector in future energy and the development of electrical energy model for utilization of power resources with conserving throughout the extinction of natural resources. In this paper authors try to configure the utilization of piezoelectric crystal in a dance floor for conversion of pressure into electrical energy. The basic transducer model fabrication has been done to impart the fact about the conversion.

References

1. Qing-li Li; Piezoelectricity, Acoustic Waves, and Device Applications (SPAWDA) and 2009 China Symposium on Frequency Control Technology, Joint IEEE Conference of the 2009 Symposium on 17–20 doi: Dec. 2009 978-1-4244-4950-7 Beijing Chenjing Electron. Co., Ltd., Beijing, China.
2. F. Rubio-Marcos, P. Marchet, X. Vendrell, J.J. Romero, F. Rémondière, L. Mestres and J.F. Fernández Journal: Journal of Alloys and Compounds, 2011, Volume 509, Number 35, Page 8804, doi: 10.1016/j.jallcom.2011.06.080.
3. Chowdhury, R.R.; Dept. of Electrical, Electronics & Communication. Eng., Mil. Inst. of Sci. & Technology, Dhaka, Bangladesh; Kabir, M.S. Electrification of streets of Dhaka city using solar and Piezoelectric energy doi: May 2014 Informatics, Electronics & Vision (ICIEV), 2014 IEEE Print ISBN:978-1-4799-5179-6.
4. E. De Ranieri, P. E. Roy "Piezoelectric control of the mobility of a domain wall driven by adiabatic and non-adiabatic torques" Nature Materials 12, 808–814 doi: Research | 09 June 2013.
5. Aswal, P:, Dave, J:, Ansari, P. (2013). "Electricity Generation by Vibrating Piezoelectric Crystal in Roadway Using Simulink" American International Journal of Research - iasir.net.

Cylindrical Metallic Pin Structure Microstrip Patch Antenna for Wideband Application

Praful Ranjan, Mahesh Kumar Aghwariya, Purnendu Shekhar Pandey and N. Prasanthi

Abstract This paper presents a successful designing of microstrip patch antenna at the center frequency of 5.9 GHz with cylindrical metallic PINs structure in between two dielectric materials. The bandwidth is increased by inserting cylindrical PINs structure and using the capacitive coupled coplanar strip feed. The PINs are made by copper wire. The bandwidth of prototype is approximately 3.25 GHz. Prototype structure is on a RT/Duroid substrate, with the dielectric constant of 3.0, thickness of the substrate is 1.56 mm, and the feeding is provided by capacitive coupled feeding patch of the dimensions of 3.7 mm $\times$ 1.2 mm. The structure has then been modeled and simulated using Ansoft HFSS.

Keywords Metallic pins · RT/duroid substrate · Capacitive coupled feeding · Wide band

1 Introduction

Microstrip antennas play very important role in the wireless communication, satellite communication, and mobile communication. This increases the concentration of researchers to the direction of designing various microstrip antennas to achieve the desired specification of the communication system. The subjects of wireless communications are of wide interest in many research activities which uses the microwave band. In recent years, wireless communication links have gone through a tremendous growth. The micro strip antennas are very compact antenna

Praful Ranjan (✉) · M.K. Aghwariya · P.S. Pandey
Department of Electronics and Communication Engineering,
THDC Institute of Hydropower Engineering and Technology,
Bhagirathipuram, Tehri, India
e-mail: prf98354@rediffmail.com

N. Prasanthi
Department of Electronics and Communication Engineering,
UPES, Dehradun, India

© Springer Science+Business Media Singapore 2017

R. Singh and S. Choudhury (eds.), *Proceeding of International Conference on Intelligent Communication, Control and Devices*, Advances in Intelligent Systems and Computing 479, DOI 10.1007/978-981-10-1708-7_53

with very easy manufacturability and very low cost, which is a great advantage over the traditional big size antennas. Microstrip patch antennas are planar antenna with low cost and easy accessibility which has the application in high frequency communication system [1]. In designing of these antennas, thin layer of conduction material which is known as patch formed on the top surface of dielectric material with different dielectric constant. One more layer of conducting material also used at the other side of the dielectric material is known as ground plane. The patch can be of any size and shape; for the higher frequency application the size of the patch antenna should be minimum. The patch antennas can easily be operated in dual frequency band and multi frequency band and any type of polarization. However, microstrip patch antenna provides narrow bandwidth; so for higher frequency wideband operations the bandwidth should be enhanced which can be done by many methods like inserting cylindrical metallic PINs in between the dielectric material, which have been done in this paper [2].

2 Antenna Structure and Designing

The basic antenna structure is shown in Fig. 1a, b while Fig. 2 designed antenna (3D structure). The basic structure consist of microstrip patch antenna with coplanar capacitive coupled feeding [3–5], provided by SMA connector. Basic dielectric material is RT/Duroid with relative dielectric constant of 3.

Cylindrical metallic pins [1, 6, 7] of radius 0.5 mm and height 5.0 mm, mutually spaced by 7.75 mm, have been inserted between the two dielectric substrates which

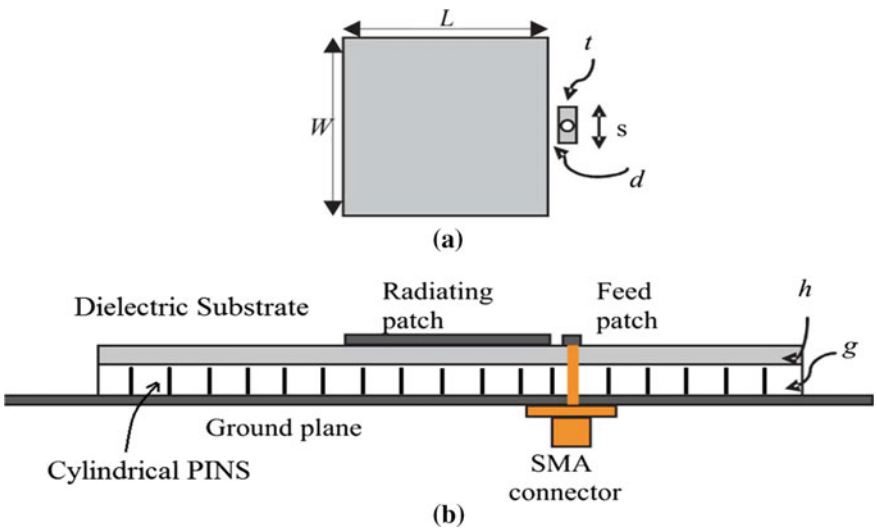


Fig. 1 Geometrical view of the antenna. **a** Top view. **b** Side view

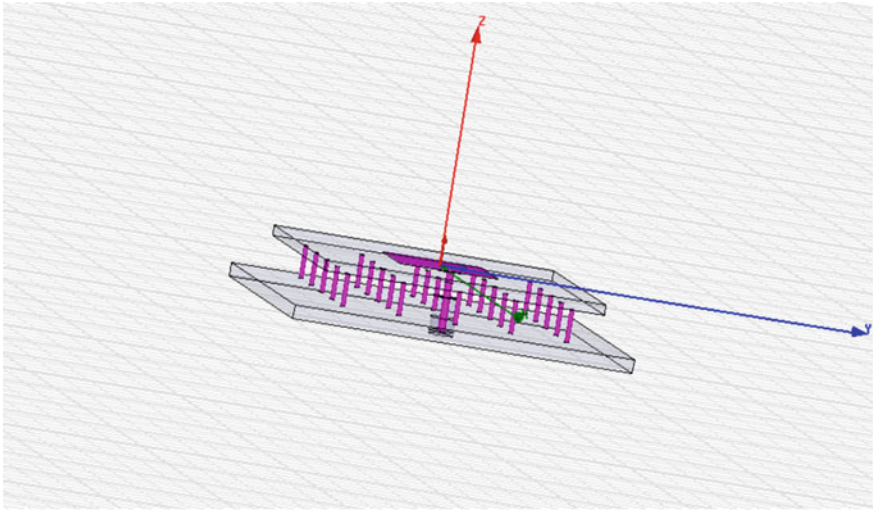


Fig. 2 3D structure of the antenna with cylindrical PINs

Table 1 Dimensions of the antenna with cylindrical metallic PINs designed at 5.9 GHz

Parameters	Value
Length (L)	15.5 mm
Width (W)	16.4 mm
Feed strip length (s)	3.7 mm
Feed strip width	1.2 mm
Distance between feed strip from the patch (d)	0.5 mm
Air gap between the substrates (g)	6.0 mm
Relative dielectric constant (ε_r)	3
Substrate thickness	1.56 mm
Ground plane size	70×70 mm^2
Conducting cylinders of radius (r)	0.5 mm
Obstacle spacing (b)	7.75 mm (6×6 matrix)
Cylindrical pin height	5.0 mm

improve the bandwidth and gain of the antenna, 6×6 matrix of cylindrical metallic pin have been used, arrangement of the PINS can be changed accordingly since the bandwidth and gain of the antenna will vary. Different parameters of the antenna and the parameters of the cylindrical metallic PINS [8–11] have been given in Tables 1 and 2.

Figure 3 shows the variation on bandwidth of the antenna with the feed strip length and width. Dimensions of the capacitive coplanar coupled feed strip [12], it has been chosen 3.7 mm $\times$ 1.2 mm for this structure for achieving higher bandwidth. Bandwidth of 3.25 GHz has been achieved at the length of 3.7 mm of the feed strip and width of 1.2 mm.

Table 2 Variation in bandwidth and gain with different radius of the cylindrical metallic PINs

Radius of Cylinder (mm)	Obstacle Space (mm)	Bandwidth (GHz)	Gain (dBi)
0.1	7.75	3.00	5.78
0.2	7.75	3.04	5.98
0.3	7.75	3.05	6.03
0.4	7.75	3.10	6.19
0.5	7.75	3.25	6.78
0.6	7.75	2.69	6.15
0.7	7.75	2.54	6.06
0.8	7.75	2.50	6.06
0.9	7.75	2.43	5.86
1.0	7.75	2.42	5.78
1.1	7.75	2.26	5.65

Air gap = 6 mm, Obstacle height = 5.0 mm, Cylindrical pin arrangement: 6 × 6 Matrix

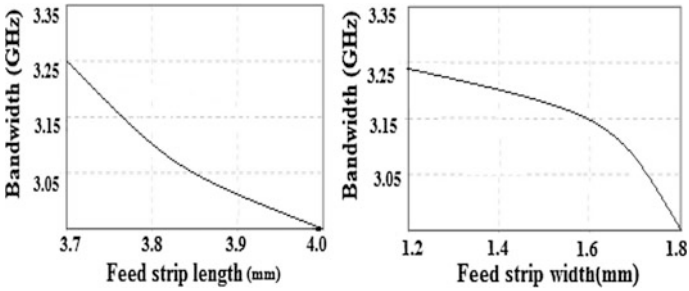


Fig. 3 Variation on bandwidth with the length and width of feed strip

A rod type artificial dielectric [13–16] is introduced. The substrate behaves as an anisotropic medium. For TM^z field configuration, the pass bands for the medium are defined by the relation [2].

$$\cos(\eta\theta) = \cos\theta + \frac{A}{\theta}\sin\theta \tag{1}$$

$\theta = k_r \cdot x$ is the electrical spacing, η is reflective index.

k_r is the wave number in embedding medium and

$$A = \pi / \ln(x/\pi r)$$

For square grid case, where 'x' is grid period and 'r' is the pins diameter.

For the above equation to remain valid, the grid spacing must satisfy the condition.

$r \ll x \ll \lambda_r/2$, where λ_r is the operating wavelength in the embedding medium. The pins dimensions and grid spacing are chosen in such a way so that the entire operating region is well above cut-off.

3 Simulation Results

The designed structure has been simulated by using HFSS simulation software. Figure 4 shows the return loss of the antenna which has been achieved −22 dB after simulation. Figure 5 shows the Electric field pattern (E-Field) and magnetic field (H-Field) pattern of the antenna.

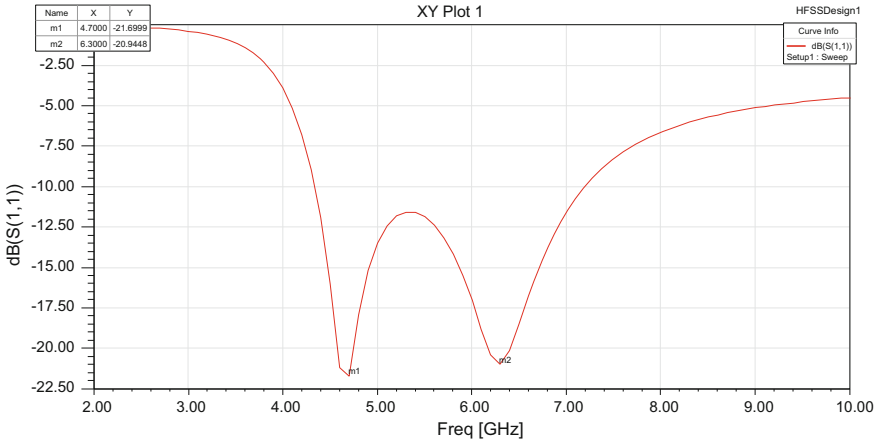


Fig. 4 Return loss versus frequency plot of the antenna

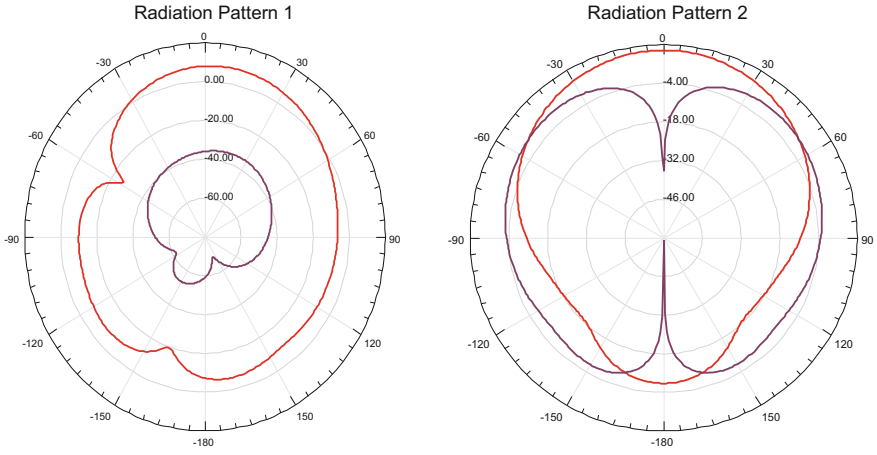


Fig. 5 E-Field pattern and H-Field pattern of the antenna

4 Conclusions

A microstrip patch antenna has been successfully designed at the center frequency of 5.9 GHz. The bandwidth of the antenna has been increased by using cylindrical metallic PINs in 6×6 matrix in between two dielectric substrates air and Rogers RT/duroid 3003 ($\varepsilon_r = 3$), all the PINs are of same radius 0.5 mm and height of 5 mm. Coplanar capacitive coupled feed strip have been used to provide feeding to the antenna. Ground plane of cross section are of 70×70 mm^2 and substrate thickness 1.56 mm. Feeding is provided by capacitive coupled feed strip cross sectional area of 3.7×1.2 mm^2. Simulating in HFSS, return loss have been achieved -22 dB and the bandwidth of the antenna have been achieved as 3.25 GHz which may be increased by varying the height and width of the metallic cylindrical PINs and area of feeding strip for future application.

References

1. S. B. Cohn, "Analysis of the metal-strip delay structure for microwave lenses," J. Appl. Phys., vol. 20, pp. 257–262, 1949.
2. Prateek Juyal, Ashok Mittal, Asok De,"*WideBand Compact Rectangular Patch Antenna Using. Artificial Dielectrics", IJMOT, vol. 5, no. 5, September 2010.*
3. J. M. Schellenberg, "CAD models for suspended and inverted microstrip," IEEE Trans. Microw. Theory Tech., vol. 43, no. 6, pp. 1247–1252, 1995.
4. K. Verma, N. V. Tyagi, and D. Chakraverty, "Input impedance of probe fed multilayer rectangular microstrip patch antenna using the modified Wolff model," Microw. Opt. Technol. Lett., vol. 31, no. 3, pp. 237–239, 2001.
5. F. Abboud, J. P. Damiano, and A. Papiernik, "Simple model for the input impedance of the coax-feed rectangular microstrip patch antenna for CAD," Proc. Inst. Elect. Eng., vol. 135, no. 5, pp. 323–326, 1988.
6. M. Kirschning, R. H. Jansen, Jansen, and N. H. L. Koster, "Measurement and computer aided modeling of microstrip discontinuities by an improved resonator method," IEEE MTT-S Digest, pp. 495–497, 1983.
7. "Experimental verification of the metal-strip delay-lens theory," J. Appl. Phys., vol. 24, no. 7, pp. 839–841, 1953.
8. J. Brown, "Artificial dielectrics," in Progress in dielectrics, vol. 2, pp. 195–225, 1960.
9. W. Rotman, "Plasma simulation by artificial dielectrics and parallel plate media," IRE Trans. Antennas Propagat., vol. 10, pp. 82–95, 1962.
10. C. A. Moses and N. Engheta, "Electromagnetic wave propagation in the wire medium: a complex medium with long thin inclusions," Wave Motion, vol. 34, pp. 301–317, 2001.
11. P. A. Belov and S. A. Tretyakov, "Dispersion and reflection properties of artificial media formed by regular lattices of ideally conducting wires," J. Electromagnetic Waves and Applications, vol. 16, no. 8, pp. 1153–1170, 2002.
12. Veeresh G. Kasabegoudar and K. J. Vinoy," Coplanar Capacitively Coupled Probe Fed Microstrip Antennas for Wideband Applications," IEEE Transan antenna and propg. vol. 58, no. 10, October 2010.
13. R. J. King et al., "The synthesis of surface reactance using an artificial dielectric," IEEE Trans. Antennas Propagat. vol. 31, no. 3, pp. 471–476, 1983.

14. G. Poilasne et al., “Influence of metallic photonic bandgap (MPBG) materials interface on dipole radiation characteristics,” Microwave Opt. Technol. Lett., vol. 18, no. 6, pp. 407–410, 1998.
15. C. R. Simovski and S. He, “Antennas based on modified metallic photonic bandgap structures consisting of capacitively loaded wires,” Microwave Opt. Technol. Lett., vol. 31, no. 3, pp. 214–221, 2001.
16. J. Brown, “Artificial dielectrics having refractive indices less than unity,” Proc. Inst. Elec. Eng., vol. 100, pt IV, pp. 51–62, 1953.

Low THD ±0.75 V 32 nm CNFET Quadrature VCO for PLL and Costas-Loop Applications

Jyoti Sharma and Md. Samar Ansari

Abstract In this paper, first a new Analog Building Block (ABB) viz. the Carbon Nanotube Field Effect Transistor (CNFET)-based voltage-controlled current conveyor (VCCC) is presented. Thereafter, a voltage-mode resistor-less quadrature oscillator is proposed which employs three CNFET-based VCCCs and three capacitors. The proposed Voltage-Controlled Oscillator (VCO) can provide two sinusoidal quadrature voltage outputs. The bias voltage of VCCC can be adjusted to electronically control the frequency of oscillation and condition of oscillation of the Quadrature Voltage-Controlled Oscillator (QVCO). VCOs find applications in Phase-Locked Loops (PLLs) and receivers for amplitude modulation systems. The VCO output can also be used to generate a clock signal for a digital system. Results of HSPICE simulations using 32 nm CNFET parameters at ±0.75 V biasing voltages show good agreement to theoretical assumptions. The THD performance of the proposed quadrature VCO was found to be excellent with the distortion values lying well below 3 % for both the voltage outputs.

Keywords Carbon nanotube field effect transistor · Voltage-controlled current conveyor · Current mode · Low-voltage design · Quadrature oscillator

1 Introduction

In the past few decades, the electronics industry witnessed a remarkable miniaturization of devices, according to Moore's law. Innovation and integration of new materials, such as high-K gate dielectrics, silicides, and nitrides have been the key for this evolutionary path of CMOS device scaling [1]. However, as device dimensions are shrunk down to sub-10 nm range, direct tunneling between source

Jyoti Sharma (✉)
Department of ECE, BIT Mesra, Jaipur Campus, Jaipur, India
e-mail: jyotisharma@bitmesra.ac.in

Md. Samar Ansari
Department of Electronics Engineering, Aligarh Muslim University, Aligarh, India

© Springer Science+Business Media Singapore 2017

R. Singh and S. Choudhury (eds.), *Proceeding of International Conference on Intelligent Communication, Control and Devices*, Advances in Intelligent Systems and Computing 479, DOI 10.1007/978-981-10-1708-7_54

and drain, non-scalability of the MOSFET V_{th} with power supply scaling, and severe second-order effects present virtually unsurmountable primary challenges. As a result, a lot of research has been directed toward the exploration of new channel structures to enable (i) ballistic transport (i.e., higher mobility) and (ii) improved electrostatics at nanoscale (i.e., nonplanar channel materials). One viable alternative that has emerged amongst a multitude of options is the use of carbon nanotubes (CNT) as the channel material, resulting in the Carbon Nanotube Field Effect Transistor (CNFET). With ultra-long mean free path ensuring elastic scattering, near-ballistic transport phenomenon can be attained by a CNT under very low-voltage bias which results in high performance in terms of lower power dissipation and extended bandwidth in comparison to CMOS. There have been several attempts to utilize CNFETs for designing circuits, both digital and analog. However, some application areas still remain unaddressed [2–9]. Examples include precision rectifiers, high-frequency oscillators, and continuous-time analog filters.

Sinusoidal oscillators constitute an imperative building block which finds various applications in analog signal processing. One particular type, i.e., the VCO forms an integral part of the Phase-Locked Loop (PLL); and when designed with phase-quadrature outputs, is employed in various communication applications, e.g., quadrature mixers and single-sideband modulators. Various CMOS-based sinusoidal oscillators have been proposed widely in the technical literature [1, 10–17]. However, as mentioned earlier, CMOS scaling dictates alternative designs.

As shown in Fig. 1, this paper deals with the design of VCO for use in PLLs and the Costas—Loop receiver for Double-Sideband Suppressed Carrier (DSB-SC) modulation setups. Toward that end, first a new Analog Building Block (ABB) viz. the CNFET-based Voltage-Controlled Current Conveyor (VCCC) is proposed which is then utilized in the design of a VCO capable of two voltage outputs in phase quadrature. Additionally, two 90° separated current-mode outputs are also available. Being based on CNFETs, the both the ABB and the VCO are low-power designs operating with only ±0.75 V. The bias voltage of VCCC can be adjusted to electronically control the frequency of oscillation and condition of oscillation of the

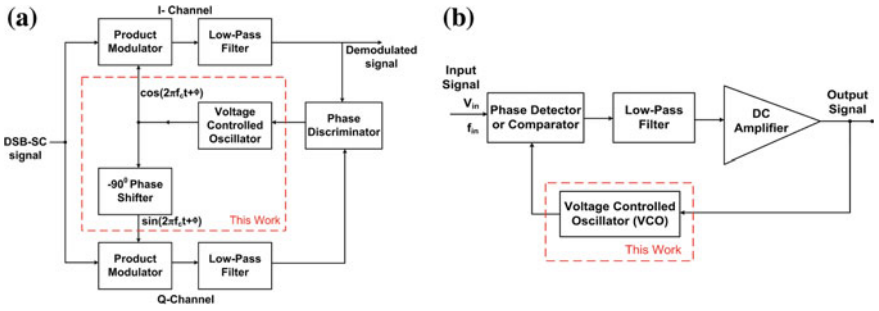


Fig. 1 Voltage-controlled oscillator applications. **a** Costas-Loop receiver for DSB-SC demodulators. **b** Phase-Locked Loop (PLL)

QVCO. Both the VCCC and the VCO circuits are resistorless, and the VCO employs only grounded capacitors, thereby facilitating monolithic implementation.

In this paper, details of the proposed new ABB viz. CNFET-based VCCC along with results of functionality verification are presented in Sect. 2. Section 3 contains the particulars of the resistor-less QVCO along with the design equations for the frequency of oscillation and condition of oscillation. Nonideal and parasitic effects have been analyzed in Sect. 4. Simulation Results using HSPICE are presented in Sect. 5. Concluding remarks appear in Sect. 6.

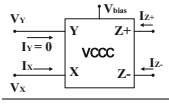
2 Proposed CNFET Voltage-Controlled Current Conveyor (CNFET-VCCC)

The proposed VCCC is designed by using a CNFET-based current controlled conveyor, with its bias current generated using a CNFET-based voltage-controlled current source. A symbolic representation of the VCCC, along with pertinent mathematical expressions for port relationships, port-X resistance, and relationship of the control current with the bias voltage applied, are presented in Table 1. Transistor-level implementation is presented in Fig. 2 with the two subparts of the complete circuit marked in red and blue. From (2) and (3), it can be observed that at port-X, the parasitic resistance is proportional to $I_B^{-½}$ and hence it is possible to control its value by changing the biasing current I_B, whereas the bias current itself may be controlled by the bias voltage V_{bias} of the VCCC, making it an attractive building block for designing circuits with great functional versatility, since it does not require any external resistors (except the one used in the biasing of VCCS).

Performance evaluation via HSPICE simulations for the proposed CNFET-based VCCC of Fig. 2 was carried out using Stanford 32-nm CNFET model [7]. The VCCC circuit has been optimized in terms of number of CNT and inter-CNT pitch. For the purpose of simulations, voltage supplies were kept at ±0.75 V and the biasing voltage was set to V_{bias} = 0.5 V. Some relevant device and technology parameters related to CNFETs which were used in the HSPICE simulations are listed in Table 2.

In order to ascertain the correct operation of the proposed CNFET-based VCCC, DC, transient and AC analyses were carried out using HSPICE simulations. Results of the various device verification tests are presented in Fig. 3 from where the following observations are made:

Table 1 Pertinent expressions for VCCC parameters

Symbol	Port relationships of VCCC	Port-X resistance	Bias current
	$\begin{bmatrix} I_Y \\ I_Z \\ V_X \end{bmatrix} = \begin{bmatrix} 0 & 0 & 0 \\ 0 & 0 & \pm 1 \\ 1 & 0 & R_X \end{bmatrix} \begin{bmatrix} V_Y \\ V_Z \\ I_X \end{bmatrix}$ (1)	$R_X = \frac{1}{\sqrt{8\mu_n C_{ox} \frac{W}{L} I_B}}$ (2)	$I_B = \frac{\beta_2}{2}\left[\left(\frac{C_2/C_1}{1+C_2/C_1}\right)V_{bias} - V_T\right]^2$ (3)

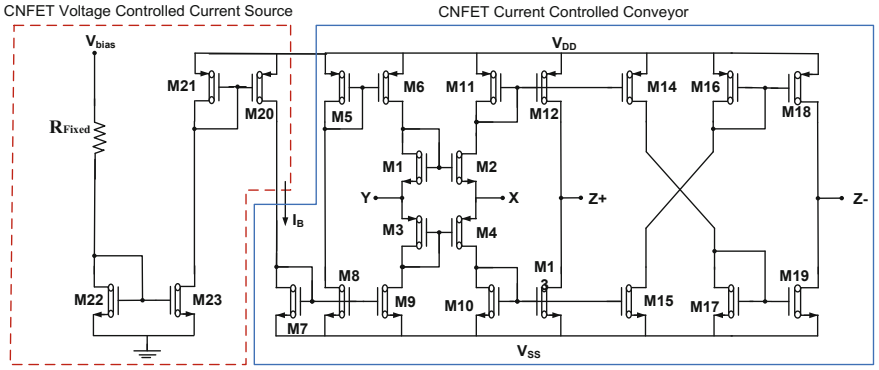


Fig. 2 Proposed CNFET-based voltage-controlled conveyor implementation with *Z*+ and *Z*– outputs

Table 2 Technology parameters of CNFET used for HSPICE simulations

Parameter	Value	Parameter	Value	Parameter	Value
Diameter of CNT	1.5 nm	Number of CNTs	3	Inter-CNT pitch	20 nm
Chirality vector	(19, 0)	Oxide thickness	4 nm	Dielectric constant	16
Power supplies	±0.75 V	Threshold voltage	0.49	Technology node	32 nm

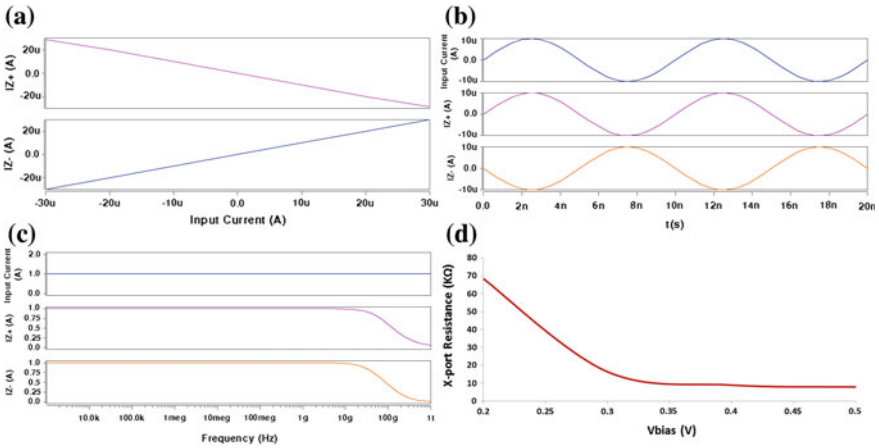


Fig. 3 Simulation results for the noninverted and inverted outputs of the VCCC using HSPICE. **a** DC analysis. **b** Transient analysis. **c** AC analysis. **d** Variation of port-X resistance with the bias voltage

- Figure 3a: DC analysis of the CNFET-based VCCC, carried out by sweeping the current at X terminal via the control voltage V_{bias}, reveals that the currents at the $Z+$ and Z terminal (I_{Z+} and I_{Z-}) are in agreement with Eq. (1).
- Figure 3b: Transient analysis of the CNFET-based VCCC has been done using 100 MHz frequency sinusoid as an input. It is observed that the proposed VCCC circuit has verified the current relationship equation given by Eq. (1).
- Figure 3c: AC analysis for the CNFET-based VCCC reveals excellent conformity between the input current (I_X) and the output currents (I_{Z+}) and (I_{Z-}) till frequencies well beyond 10 GHz.
- Figure 3d: Variation of the port-X resistance of the proposed CNFET-VCCC is shown, which is in agreement with the relationships given in (2) and (3).

3 Proposed Quadrature Vco

In this section, the design of the proposed CNFET-based QVCO is presented. An all-pass filter is first designed using two VCCCs (Numbered 1 and 2 in Fig. 4) and two capacitors. Thereafter, APF is coupled with an integrator (using VCCC no. 3 in Fig. 4 and the grounded capacitor C_3). As can be seen from Fig. 4, the circuit does not require any passive resistor, and has maximally grounded capacitors, making it amenable for integrated circuit implementation. The auxiliary equation of the QVCO of this paper has been obtained by routine analysis of Fig. 4 and is given by

$$s^2 R_{X1} R_{X3} C_1 C_3 + s(R_{X3} C_3 - R_{X1} C_1) + 1 = 0 \tag{4}$$

The frequency of oscillation and condition of oscillation of the proposed second-order QVCO, as obtained from (4) are given in (5) and (6).

$$\text{FO: } f_0 = \frac{1}{2\pi\sqrt{R_{X1} R_{X3} C_1 C_3}} \tag{5}$$

$$\text{CO: } R_{X1} C_1 = R_{X3} C_3 \tag{6}$$

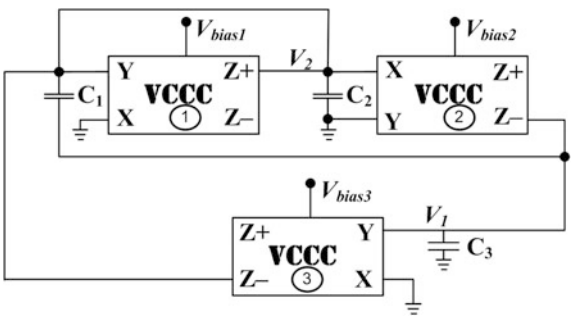


Fig. 4 Proposed CNFET-based Quadrature VCO utilizing the proposed analog building block CNFET-VCCC

Equations (5) and (6) show that the frequency of oscillation can be adjusted by varying R_{X1} and R_{X3}, i.e., by varying the value of bias voltages V_{Bias1} and V_{Bias3}. If all capacitances chosen to have the same value, i.e., $C_1 = C_2 = C_3 = C$, the frequency of oscillation and condition of oscillation are simplified and given by Eqs. (7) and (8).

$$\text{FO: } f_0 = \frac{1}{2\pi C\sqrt{R_{X1}R_{X3}}} \tag{7}$$

$$\text{CO: } R_{X1} = R_{X3} \tag{8}$$

4 Nonideal and Parasitic Analysis

The nonidealities, if any, of the active elements present in the circuit may deteriorate the performance of the actual current conveyor. For the case of the present work, the nonidealities in the VCCC are described by the port relationships as shown in Table 3. On reanalysing the second-order QVCO of Fig. 4 including the nonideal characteristics of the CNFET-VCCC, the characteristics Eq. (10), simplified expression for frequency of oscillation (11), and condition of oscillation (12) are presented in Table 3.

Parasitic capacitances also perform vital role in the behavior of the circuit. Let the parasitic capacitances at port X, Y, and Z be modeled as C_X, C_Y, and C_Z, respectively. In this work, the QVCO consists of an all-pass filter and an integrator thus there are capacitors at the input and output ports of each VCCC. The externally applied capacitors become enhanced by the values of parasitics as shown in Eqs. (13a)–(13c). It can be observed from (13a)–(13c) that the altered values of the capacitors would certainly introduce some deviations in the oscillation frequency but the same may be corrected by varying the bias voltage V_{bias} of the VCCCs. Such calibration of oscillation frequency is easily accomplished with availability of a tuning voltage.

Table 3 Expressions for nonideal analysis of the proposed CNFET QVCO

	Ideal	Nonideal
Port relationships of VCCC	$\begin{bmatrix} V_X \\ I_Y \\ I_Z \end{bmatrix} = \begin{bmatrix} R_X & 1 & 0 \\ 0 & 0 & 0 \\ \pm 1 & 0 & 0 \end{bmatrix} \begin{bmatrix} I_X \\ V_Y \\ V_Z \end{bmatrix}$	$\begin{bmatrix} V_X \\ I_Y \\ I_Z \end{bmatrix} = \begin{bmatrix} R_X & \beta & 0 \\ 0 & 0 & 0 \\ \pm\alpha & 0 & 0 \end{bmatrix} \begin{bmatrix} I_X \\ V_Y \\ V_Z \end{bmatrix}$ (9)
Characteristic equation	$s^2R_{X1}R_{X3}C_1C_3 + s(R_{X3}C_3 - R_{X1}C_1) + 1 = 0$	$s^2R_{X1}R_{X3}C_1C_3 + \beta s(R_{X3}C_3 - R_{X1}C_1) + \alpha\beta = 0$ (10)
FO	$f_0 = \frac{1}{2\pi\sqrt{R_{X1}R_{X3}C_1C_3}}$	$f_0 = \frac{\alpha\beta}{2\pi\sqrt{R_{X1}R_{X3}C_1C_3}}$ (11)
CO	$R_{X1} = R_{X3}$	$R_{X1}C_1 = R_{X3}C_3$ (12)

$$C_1' = C_1 + C_{Y1} + C_{Z2} + C_{Y3} + C_{Z3} \tag{13a}$$

$$C_2' = C_2 + C_{Z1} + C_{X2} + C_{Y1} \tag{13b}$$

$$C_3' = C_3 + C_{Y1} + C_{Y3} + C_{Z2} \tag{13c}$$

5 Simulation Results

The proposed second-order quadrature oscillator shown in Fig. 4 has been simulated in HSPICE using the CNFET-based VCCC (shown in Fig. 2) as the active element. The circuit is implemented using 32 nm CNFET technology parameters with ±0.75 V voltage supplies. The second-order QVCO has been designed with equal capacitor values of 100 fF each. The bias voltages were taken to be $V_{\text{bias1}} = V_{\text{bias2}} = V_{\text{bias3}} = 0.5$ V for the start-up of oscillations so that the loop gain is greater than unity and the oscillations build. The frequency of oscillation and condition of oscillation can be adjusted electronically by varying the values of bias voltage. The simulated frequency obtained is 93 MHz. The simulated results for the voltage waveforms are shown in Fig. 5a. Tuning results, i.e., variation of frequency of oscillation with the control voltage, are presented in Fig. 5b which depicts an (almost) linear variation. The low-THD performance of the proposed QVCO can be observed from Fig. 5c which shows that the distortion values for all frequencies obtained are well below the 3 % mark.

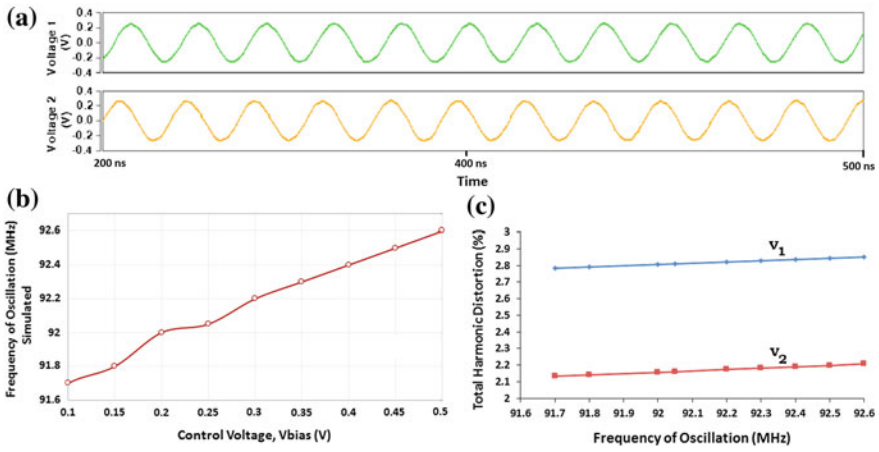


Fig. 5 **a** Simulated quadrature voltage outputs obtained from the proposed CNFET QVCO. **b** Variation of frequency of oscillation with control voltage V_{bias} of the VCO. **c** Noise characteristics of proposed CNFET QVCO

Table 4 Comparison of the proposed circuit with existing works

Reference	Process	Tech. Node	Supply voltage (V)	IB1 (μA)	IB2 (μA)	IB3 (μA)	C1	C2	C3	THD (%)	Simulated frequency
[13]	CMOS	0.5 μm	±2.5	100	108	100	100 pF	100 pF	100 pF	<2	4 MHz
[1]	CMOS	0.35 μm	±2.5	150	149	150	1 nF	1 nF	–	<3	499 kHz
[16]	CMOS	45 nm	±1	3	3	3	1 pF	1 pF	–	<3	38.5 MHz
This work	CNFET	32 nm	±0.75	1.5	1.5	1.5	100 fF	100 fF	100 fF	<3	93 MHz

To highlight the superiority of the QVCO circuit proposed, it is compared with existing circuits implemented in [1, 13, 16], on various parameters such as bias currents, capacitors, power supply, total harmonic distortion, and simulated frequency. The comparison is given in Table 4 from where it can be seen that the power supply, bias current, and capacitors used are very small as compared to those taken in [1, 13, 16].

6 Conclusion

In this paper, an electronically tunable quadrature VCO employing only a new CNFET-based VCCC as an active element and grounded capacitors was proposed. This circuit provides the two quadrature sinusoidal voltage outputs. The circuit employs only grounded capacitors and no resistors; therefore it is well suited for IC implementation. Power supply used was ±0.75 V. The frequency of oscillation can be electronically tuned independently of the condition of oscillation through the bias voltage of the proposed VCCC. Nonideal and parasitic considerations are included. The simulated frequency was found to be around 93 MHz. The THD performance of the proposed quadrature VCO was found to be excellent with the distortion values lying well below 3 % for both the voltage outputs. The circuit shows good high frequency performance and a linear tunability of frequency, and is likely to find applications in PLLs and Costas-Loops.

References

1. A. Lahiri: Deriving (MO)(I)CCCII based second-order sinusoidal oscillators with non-interactive tuning laws using state variable method: Radioengineering vol. 20, no. 1 (April 2011) pp. 349–353.
2. S. Iijima: Helical microtubules of graphitic carbon: Nature vol. 354 (1991) pp. 56–58.
3. M. S. Dresselhaus, G. Dresselhaus, P. Avouris: Carbon nanotube: Springer-Verlag.
4. P. L. McEuen, M. S. Fuhrer, P. Hongkun: Single-walled carbon nanotube electronics: IEEE Trans. Nanotechnology vol. 1, no. 1 (Mar. 2002) 78–85.
5. H. S. P. Wong: Beyond the conventional transistor: Solid-State Electronics, vol. 49 (2004) pp. 755–762.
6. H. H. Kuntman: New advances and possibilities in active circuit design: International conference on development and application systems, Romania.
7. Stanford university: CNFET model, http://nano.stanford.edu/model.php/id=23.
8. J. Deng, H. S. P.Wong: A compact SPICE model for carbon nanotube field effect transistors including nonidealities and its application—part II: Full device model and circuit performance benchmarking, IEEE Trans. Electron Devices Vol. 54, No. 12 (Dec. 2007) pp. 3195–3205.
9. H. S. P. Deng, J. & Wong: A compact SPICE model for carbon nanotube field effect transistors including nonidealities and its application—part I: Model of the intrinsic channel region, IEEE Trans. Electron Devices Vol. 54, No. 12 (Dec. 2007) pp. 3186–3194.

10. P. Beg, M. A. Siddiqi, M. S. Ansari: Multi output filter and four phase sinusoidal oscillator using cmos dx-MOCCII: International Journal of Electronics vol. 98, no. 9 (September 2011) pp. 1185–1198.
11. I. A. Khan, P. Beg, M. T. Ahmed: First order current mode filters and multiphase sinusoidal oscillators using CMOS MOCCIIs: The Arabian Journal for Science and Engineering Vol. 32, No. 2C (December 2007) pp. 119–126.
12. S. Maheshwari, I. Khan: Current controlled third order quadrature oscillator: IEEE Proceedings-Circuits Devices Systems Vol. 152, No. 6 (December 2005) pp. 605–607.
13. S. Maheshwari: Current-mode third-order quadrature oscillator: IET Circuits, Devices and Systems Vol. 4, No. 3 (September 2010) pp. 188–195.
14. S. Siripongdee, P. Suwanjan, S. Tuntrakool, W. Jaikla: Electronically controllable current-mode multiphase sinusoidal oscillator for biomedical tissue measurement systems: International Journal of Bioscience, Biochemistry and Bioinformatics Vol. 4, No. 1 (January 2014) 57–59.
15. P. Bodade, D. Meshram: Design of 2.4 Ghz oscillators in CMOS technology: International Journal of Computer Science and Engineering Technology Vol. 4, No.6 (June 2013) pp. 799–807.
16. M. Y. Yasin, B. Gopal: High frequency oscillator design using a single 45 nm CMOS current controlled current conveyor (CCCII +) with minimum passive components: Journal of Circuits and Systems Vol. 2 (April 2011) pp. 53–59.
17. F. A. Usmani, M. Hasan: Design and parametric analysis of 32 nm OPAMP in CMOS and CNFET technologies for optimum performance: Proceedings of the Argentine School of Micro-Nanoelectronics, Technology and Applications (Oct. 2009) pp. 87–92.

Design of Quadratic Equations Multiplier (for upto 2-Bit Number) Using Vedic Technique

Parth Sharma, Raj Pratap Singh, Rohit Singh and Peyush Pande

Abstract Vedic mathematics is an illustration of 16 mathematical sutras which were introduced by Sri Bharti Krishna Tirthaji. Vedic mathematics defines the distinctive methods of calculation on the basis of 16 sutras. This paper proposes the design of a 2-bit multiplier for multiplying two quadratic equations using Vedic Technique 'Urdhva Tiryakbhyam'. This paper presents implementation and simulation of Vedic multiplier circuit using Cadence Virtuoso on 180 nm process technology and this is CMOS logic designing. Further, the power consumption of the proposed circuit is also being observed.

Keywords Quadratic equation · Vedic mathematics · Vedic multiplier · Urdhava Tiryagbhyam sutra · Cadance virtuoso

1 Introduction

Multiplication is the most frequently used and important ALU operation having vast implementations in various domains of Engineering and Technology. In early twentieth century, Vedic techniques were used by Indian mathematicians. Vedic mathematics is mainly based on 16 rules or formulas which are defined as Sutras. In this design, Vedic mathematics is used for multiplication of quadratic equations.

Parth Sharma (✉) · R.P. Singh · Rohit Singh · Peyush Pande
Department of Electronics and Communication Engineering, Graphic Era University, Dehradun, India
e-mail: parthsharma005@gmail.com

R.P. Singh
e-mail: th.rajpratapsingh8@gmail.com

Rohit Singh
e-mail: rohitthakur499@gmail.com

Peyush Pande
e-mail: peyushpandit@rediffmail.com

© Springer Science+Business Media Singapore 2017

R. Singh and S. Choudhury (eds.), *Proceeding of International Conference on Intelligent Communication, Control and Devices*, Advances in Intelligent Systems and Computing 479, DOI 10.1007/978-981-10-1708-7_55

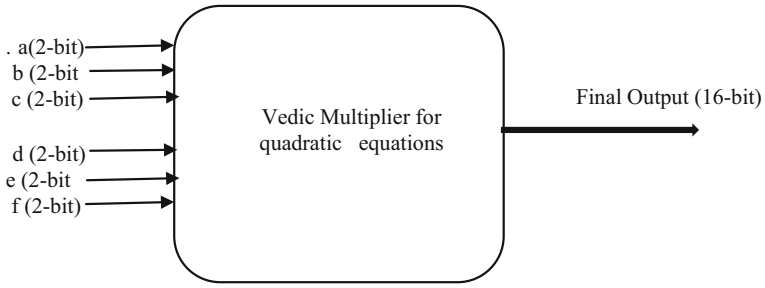


Fig. 1 Basic structure of multiplier for multiplying quadratic equation

Urdhava Tiryagbhyam was used in order to acquire multiplication of decimal numbers in comparatively less time. This algorithm is more efficient as compared to its counterparts. In [1], this sutra has been proven to be effective in reducing NXN multiplier into a 2 × 2 multiplier. In this paper, after an introduction to basic principle of this Sutra, it is applied for multiplying two quadratic equations. The hardware architecture and simulated output of the Vedic multiplier are also presented in this paper. The figure below gives a basic idea about the multiplier for multiplying quadratic equation which is proposed in this paper. In this figure *a*, *b,* and *c* are the variables of first quadratic equation and *d*, *e,* and f are the variables of second quadratic equations. Constant *x* is common for both equations. As the proposed multiplier is of 2 bit, so all the constants and variables of both equations will be of 2 bit (Fig. 1).

This paper has been divided in sections as follows: Sect. 2 explains the methodology behind the Urdhva Triyagbhyam sutra that is used for multiplying two quadratic equations in this paper. Section 3 explains the architecture of proposed multiplier. Section 4 presents the simulated result and the average power ratings of multiplier, Sect. 5 provides the conclusion and the references.

2 Design Methodology

The general formula of Urdhava Tiryagbhyam can be applied in almost all cases of multiplication. It means horizontally and vertically. This section explains how two quadratic equations will be multiplied by using the Urdhva Triyakbhyam sutra. In the multiplication shown below, we start process from left and move toward right. It is to be noted that if vice versa of above is done, that is, if we start process from right and moves toward left, the answer obtained in this case will be same as that obtained in previous case.

Now to demonstrate how two quadratic equations will be multiplied using Vedic multiplier, consider the following quadratic equations:

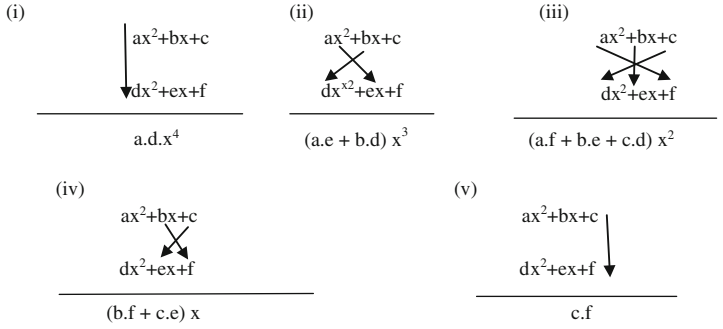
$$\left(ax^2+bx+c\right) \tag{1}$$

$$\left(dx^2+ex+f\right) \tag{2}$$

So, when both are multiplied, the answer is

$$(ax^2+bx+c)\,X\,(dx^2+ex+f) = a\cdot d\cdot x^4+(b\cdot d+a\cdot e)\cdot x^3+(c\cdot d+b\cdot e+a\cdot f)\cdot x^2+(c\cdot e+b\cdot f)\cdot x+c\cdot f$$

2.1 Multiplying by Vedic Multiplication Method



i. Coefficient of x^4, that is, '$a\cdot d$' is obtained by multiplying coefficient 'a' of multiplicand with coefficient 'd' of multiplier, starting from the left side.
ii. Coefficient of x^3, that is, '$(a\cdot e+b\cdot d)$ is obtained by multiplying coefficient 'a' and 'b' of multiplicand with coefficient 'e' and 'd' of multiplier and then adding obtained products.
iii. Coefficient of x^2, that is, '$(a\cdot f+b\cdot e+c\cdot f)$' is obtained by multiplying coefficients 'a,' 'b,' and 'c' of multiplicand with coefficients 'f,' 'e,' and 'd' of multiplier, respectively, and then adding obtained products.
iv. '$(b\cdot f+c\cdot e)$' is obtained through multiplication of coefficient 'b' and 'c' of the multiplicand with coefficient 'f' and 'e' of the multiplier and then adding the obtained products.
v. '$c\cdot f$' is obtained by multiplying coefficient 'c' of multiplicand with coefficient 'f' of multiplier. So the final equation, after multiplication, which will be obtained is $a\cdot d\cdot x^4+(b\cdot d+a\cdot e)\cdot x^3+(c\cdot d+b\cdot e+a\cdot f)\cdot x^2+(c\cdot e+b\cdot f)\cdot x+c\cdot f$.

3 Internal Architecture of Multiplier

This section explains the hardware architecture of Vedic multiplier for quadratic equations. This architecture will give the equation proven in Sect. 2 as the output. Also it is to be noted that the values of constants and variables in above equation are of 2 bits, i.e., from 0(00) to 3(11).

3.1 Explanation of Architecture

In first part of quadratic equation, that is, $a \cdot d \cdot x^4$, $a \cdot d$ is simply obtained by 2-bit Urdhava Tiryagbhyam multiplication technique. For x^4, first x (2 bit) and x (2 bit) are multiplied using 2-bit Urdhava Tiryagbhyam multiplication technique to obtain x^2(4 bit). Similarly remaining two x are multiplied to obtain x^2(4 bit). After this, x^2 and x^2 are multiplied using 4-bit Urdhava Tiryagbhyam multiplication technique to obtain x^4(8 bit). While designing multiplier for x^4, two adders of 4 input and 5 input, respectively, are required. These adders are designed using Karnaugh map (*k*-map) technique.[1] The following table shows the truth table for 4-bit and 5-bit adder. Here, it is to be noted that, in both cases, each bit is taken as single input.

The *k*-map equation of 4 input adder for sum is $ac(d + b) + bd(a + c) + c\ d\ (a\ b + b\ a) + a\ b\ (c\ d + c\ d)$ and equation for carry is $(a + c)(b + d) + bd + ac$. Similarly the *k*-map equation of 5 input adder for sum is $(a\ b + a\ b)(c\ d\ e + c\ d\ e) + c\ d(a\ b\ e + a\ b\ e + a\ b\ e + a\ b\ e) + a\ b\ (c\ d\ e + c\ d\ e + c\ d\ e) + ab(c\ d\ e + c\ d\ e + c\ d\ e) + cd(a\ b\ e + a\ b\ e) + abcde$ and equation for carry is $c(a + c + d + e) + d(a + b + e) + b(a + e) + (ae)$. We implemented these equations on gate level to design 4 input and 5 input adder, respectively.

In second part of quadratic equation, that is, $(b \cdot d + a \cdot e) \cdot x^3$, $(b \cdot d + a \cdot e)$ is obtained by using two 2-bit Vedic multiplier, one for multiplying b with d and another for multiplying a with e. Outputs of both multiplier are in 4 bit which are then given as inputs to a 4-bit adder. To obtain x^3, first x (2 bit) is multiplied by x (2 bit) to give x^2(4 bit) as output. The remaining x (2 bit) is converted to x (4 bit) by adding two zeros at MSB in its binary form. After this x^2(4 bit) is multiplied by x (4 bit) through 4-bit Vedic multiplier in the same manner as x^4 is obtained in first part. Now $(b \cdot d + a \cdot e) \cdot x^3$ is acquired by applying the outputs of 4-bit adder and 4-bit Vedic multiplier in 8×8 multiplier [2] after converting them into 8-bit binary numbers.

[1]The adders designed by cascading half adders and full adders gives more than two outputs. So, Karnaugh map (*k*-map) is used in order to obtain output in 2 bit, one for carry and one for sum. But for some exception we are getting output in 3 bit and our requirement is that output should come in single bit as sum and carry.

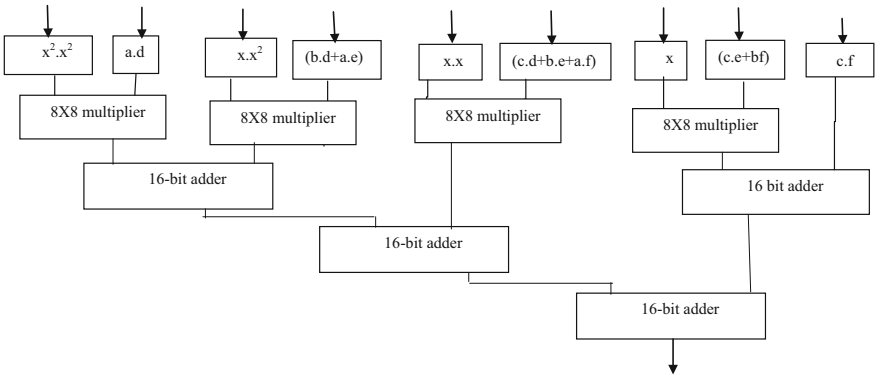


Fig. 2 Hardware architecture of Vedic multiplier for quadratic equations

In third part of equation, that is, $(c \cdot d + b \cdot e + a \cdot f) \cdot x^2$, $(c \cdot d + b \cdot e + a \cdot f)$ is obtained by using three 2-bit Vedic multipliers, one multiplying c with d, second one for multiplying b with e and last one for multiplying a with f. Outputs of every multiplier are then given as inputs to a 6-bit adder. After this, x (2 bit) and x (2 bit) are multiplied with each other using 2-bit Vedic multiplier to obtain x^2 (4 bit). Now $(c \cdot d + b \cdot e + a \cdot f) \cdot x^2$ is acquired by applying outputs of 6-bit adder and 2-bit Vedic multiplier in 8×8 multiplier after converting them into 8-bit binary numbers.

In fourth part of equation, that is, $(c \cdot e + b \cdot f) \cdot x$, $(c \cdot e + b \cdot f)$ is obtained in similar manner as $(b \cdot d + a \cdot e)$ was obtained in second part of equation. Now x and $(c \cdot d + b \cdot f)$ are converted into 8-bit binary numbers and then both are applied to the inputs of 8×8 multiplier.

The last part of the equation, that is, c.f is obtained simply through 2-bit Vedic multiplier. The outputs of 8-bit multipliers are $a \cdot d \cdot x^4$, $(b \cdot d + a \cdot e) \cdot x^3$, and $(c \cdot d + b \cdot e + a \cdot f) \cdot x^2$ and $(c \cdot e + b \cdot f) \cdot x$, respectively. To obtain final output, all the parts of the equation are added with the help of 16-bit adders as shown in Fig. 2.

4 Simulated Result

In this case, all the inputs from $a0$ to $x1$ are taken as '1' which means values of all variables (a, b, c, d, e, f) and constant (x) is '3'(11). The output in this case will be '1521' which can be represented in binary form as '1000111110100000' and is shown in Fig. 3.

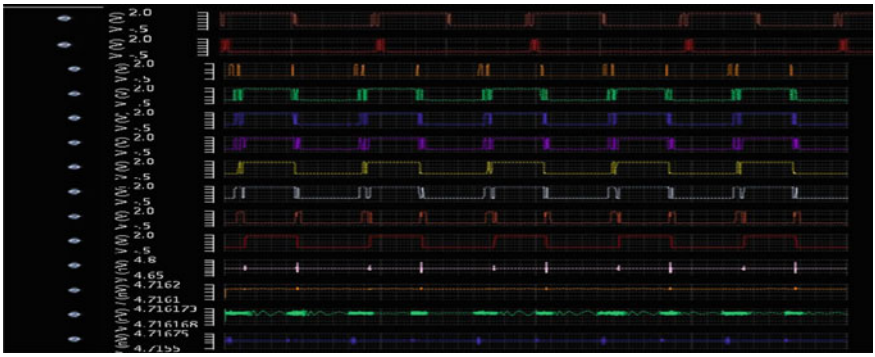


Fig. 3 Waveform of 2×2 Quadratic multiplier

5 Conclusion and Future Scope

This paper proposed a unique design of multiplier for multiplying quadratic equations with the help of Vedic mathematics. The method proposed in this paper is effective, time saving, and a simple way of multiplying quadratic equations. This design will make it very easy to multiply two quadratic equations in practical scenarios, if we know the values of variables and constant of quadratic equation, we can obtain the final product just by applying those values as inputs of the proposed multiplier. Further the power consumption of the proposed design is calculated. In proposed design the power consumption is 6.44 mV. It can be seen that due to Vedic multiplication method, the power consumption of the multiplier is very low.

In future, 4×4 multiplier and 8×8 multiplier for multiplying quadratic equations can be designed using same logic.

References

1. Poornima M, Shivaraj kumar Patil, Shivukumar, Shridhar K P, Sanjay H: "Implementation of multiplier using Vedic Algorithm, vol. 2", International Journal of Innovative Technology and Exploring Engineering, ISSN: 2278–3075, issued on 5, may 2013
2. Premananda B.S, Samarth S. Pai, Shashank B., Shashank s. Bhat.: "Design and Implementation of 8-Bit Vedic multiplier", International Journal of Advanced Research in Electrical, Electronics and Instrumentation Engineering, issued on 12, dec 2013

Design Improvement and Assessment of Efficiency of Three Phase Induction Motor Operating Under the Rated Voltage

Rajeev Gupta, Devender Kumar Saini, Raj Kumar Saini and Piush Verma

Abstract Three-phase induction motors which are designed for rated voltages but operating under the rated voltages particular in the rural areas increases stator and copper losses which leads to reduction in efficiency, temperature rise, and shorter life time of the machine. Far from the utility centers the voltage profile in most of the distribution networks is poor due to reactive power demand. This paper describe a consideration in design of a three-phase induction motor which can give desirable performance under the rated voltages even when operating without any protection system. The objective of this paper is to improve the design of the induction motors to get its rated performances which are designed for the rated voltage, but generally operating under the rated voltages.

Keywords Three-phase induction motor · Improved design · Efficiency · Under rated voltages · Ampere conductor

Rajeev Gupta
Faculty of Applied Sciences, University of Petroleum and Energy Study, Dehradun, Uttarakhand, India
e-mail: rajeevgupta@ddn.upes.ac.in

D.K. Saini
Faculty of Electrical Engineering, University of Petroleum and Energy Study, Dehradun, Uttarakhand, India
e-mail: dksaini@ddn.upes.ac.in

R.K. Saini (✉)
Department of Electrical Engineering, University of Petroleum and Energy Study, Dehradun, Uttarakhand, India
e-mail: rajsaini.acet@gmail.com

Piush Verma
Rayat–Bahra Group of Institutes, Patiala Campus (Pb.), Mohali, India
e-mail: pverma19@yahoo.co.uk

© Springer Science+Business Media Singapore 2017

R. Singh and S. Choudhury (eds.), *Proceeding of International Conference on Intelligent Communication, Control and Devices*, Advances in Intelligent Systems and Computing 479, DOI 10.1007/978-981-10-1708-7_56

1 Introduction

Apart from the industrial sector, induction motors find extensive use in the agricultural sector to drive irrigation pumps in rural areas even operating under the rated voltage. In Ref. [1], the author describes some methods to improve the efficiency of three-phase induction motors operating at low voltages in industry and for the general purposes. In this paper, twenty five elements have been taken in order to calculate the design of the motor and twelve variable elements have been taken which affects the efficiency of the machine. These twelve variables are valued independently to study the effects on the efficiency and characteristic of the motor. The author of Ref. [2], carried out a detailed study for the modification of a three-phase induction motor under the wide range of load and supply voltage and proofed that the efficiency of a new design is about 2.5 % more than that of the standard motor and also find that the input kva is about 3 % less than that of standard motor, but also investigated that the cost of proposed design is about 15 % more than that of the standard design and said that this extra cost is pay back within a reasonable period of time. In Ref [3], the author describes that the unbalanced voltages reduces the efficiency and power factor of the machine. By increasing the positive sequence of the voltage, a reduction in power factor also has been absorbed. In Ref. [4], author proofed that the worst scenario will appear when under voltages and over voltages appear with unbalanced voltages. Jawad Faiz a senior member of IEEE, in Ref [5], pointed out that the available definitions of unbalanced voltages are uncompleted. To prove the claim, a three phase 25-hp squirrel cage induction motor is analyzed under the unbalanced voltage and verified the theoretical results with experimental results. In Ref. [6], the IEEE112-B, IEC34-2, and JEC37 international standard for induction motor efficiency are evaluated and found that the rated efficiency of the machine depends upon the standard followed. On the bases of the results IEEE112-B can be considered the best suitable standard for the stray load loss measurement, hence for the motor efficiency measurement IEC34-2 and JEC 37 overestimate the motor efficiency because they only define instead of measuring the stray load losses. The author aided that stray load loss calculations are very important to calculate the correct value of efficiency. In Ref. [7], the author pointed out that the energy efficiency of continuous motor (S1) is a subject of more interest compared to intermittent duty motors (S3). The efficiency of such types of motors can be increased by proper selection of stack length and rotor material of the machine. In Ref. [8], the author concluded with the help of analytical and experimental study that the derating factor depends upon voltage unbalanced factor and magnitude of positive sequence voltage and also suggested that positive sequence voltage must be consider together with unbalanced voltage factor. In Ref. [9], the main focus of this paper is to calculate the efficiency of the induction motor under the variation of load with the variation of unbalanced, over and under voltages. In Ref. [10, 11], the authors of these research papers describe the various effects and definitions of unbalanced voltages on the operation performance of induction motors. The major effects of unbalanced voltages will lead to change in characteristic of an induction

Table 1 Input Specifications

Particulars	Inputs
Rating of the machine (Pi)	2.2 Kw
Number of phases (m)	3
Supply voltage (Es)	415 V
Power factor (pf)	0.825
Supply frequency (f)	50 Hz
Full load efficiency (n)	0.8 %
Synchronous speed (Ns)	1500 R.P.M
Electric loading (ac)	21,000

motor, due to this reason the real and reactive power consumption of an induction motor will be changed which will affect the voltage stability margin. Due to positive sequence voltage which is higher than that of the rated voltage, may be another cause of unbalance of voltages. The voltage unbalance cases may be due to single phase under voltage unbalance, two phases under voltage unbalanced, three phases under-voltage unbalanced, single phase over-voltage unbalanced, two phases over voltage unbalanced, three phases over voltage unbalanced, unequal single phase and angle displacement and unequal two phase angle displacement. To calculate the unbalanced voltages, different definitions are discussed by different authors. The definition of voltage unbalanced generally used by the power community is the ratio of negative sequence voltage to the positive sequence voltage. However in electrical machine community IEEE and NEMA use the following definitions of voltage unbalanced.

$$\%\,\text{unbalanced} = \text{Maximum deviation from average voltages}/\text{Average voltage}*100$$

In order to investigate the performance of the three-phase squirrel cage induction motor in terms of rated voltage and under the rated voltage, the input parameters of the three phase induction motor are shown in Table 1.

1.1 Analysis of Efficiency Under the Rated Supply Voltage

In this research, article the performance of three-phase induction motor operating under the rated voltage mostly due to the presence of unbalanced voltage present in the three phases have been investigated. This is studied that in the rural areas the phase-to-phase voltage in the three phases are less than the normal voltage. The variable losses and efficiency of the motor are analyzed at rated and under the rated voltages as discussed in Table 2. Constant losses have been taken as 2.5 % of the output of the machine. Still up to date research on the induction motors, the effects of the unbalanced voltages have been pointed out, the remedies of the system is still pending. The rectification of the voltage from the utility side is not much possible,

Table 2 Calculation of efficiency under the rated voltage

S. no.	% Unbalanced	Ave(v)	% below the rated voltage	Stator copper losses (w)	Rotor copper losses (w)	% Efficiency
1	0.55	363	12.30	226.96	145.22	80.69
2	1.97	370.67	10.68	22.27	142.25	80.91
3	1.70	371.67	11.65	226.34	144.82	80.72
4	2.70	370	10.84	222.18	142.50	80.89
5	1.16	370.67	11.95	222.27	142.25	80.91
6	1.33	374	9.87	220.29	141.00	81.00
7	0.18	365.67	11.96	225.51	144.30	80.76
8	0.09	365.67	11.88	225.30	144.17	80.77
9	1.06	376	9.38	219.12	140.26	81.06
10	1.15	375.67	9.48	219.31	140.38	81.05
11	2.51	370.67	10.68	222.27	142.25	80.91
12	1.2	367.33	11.48	224.28	143.52	80.81
13	0.36	365.67	11.88	225.30	144.17	80.77
14	1.10	362	12.77	227.59	145.61	80.66

but to save the energy crises the modification in the design of the motor is possible to achieve the desired performance of the machines operating under the rated voltage. The aim of this research paper is to modify the design of the machine by adjusting the ampere conductors and others parameters. In Table 2 the efficiency of the machine is worked out under the rated voltage (by taking the average voltage of the three unbalanced phases) without modifying the ampere conductors and other related parameters, while in Table 3 parameters are calculated by applying the rated voltage 415 V and under the rated voltage 368 V. 368 V is the approximate average voltage of all the average of 14 observations.

The voltage in all the three phases have been calculated regularly, discussed in Table 2. From this unbalanced voltage average voltage of all the three phases, percentage below the rated voltage, stator and copper losses are calculated to calculate the efficiency.

1.2 Results and Discussions

The calculations for the average voltage of the three phases which generally lies under the rated voltage due to the presence of unbalanced voltages in the three phases have been discussed in Table 2. Variation of supply voltage gives rise to additional losses in the machines. It means that millions of induction motors in the rural areas are running under the rated voltages which directly affect the efficiency of the machines. The proposed efficiency of the machine can be maintained up to

Table 3 Calculations of stator and rotor parameters at rated voltage and under rated voltage

Parameters	Computer added parameters (415 V)	Unmodified parameters (368 V)	Modified parameters (368 V)	% change in parameters
Output coefficient	97.066	97.066	92.444	−4.99
Product of *D*^2 L	0.00137 m	0.00137 m	0.00144 m	4.86
Diameter of core	0.10527 m	0.10527 m	0.10699 m	1.60
Length of core	0.1239 m	0.1239 m	0.1259 m	1.58
Net iron length	0.1023 m	0.1023 m	0.1039 m	1.53
Flux per pole	0.004507	0.004507	0.004656	3.20
Stator turns/phase	434	434	373	−16.35
Stator slot pitch	0.01377 m	0.01377 m	0.01399 m	1.57
Stator conductors	2604	2604	2238	−16.35
Conductors/slot	2604	2604	2238	−16.35
Slot pitch	13.785 mm	13.785 mm	14.0113 mm	1.61
Teeth width	4.985 mm	4.985 mm	5.211 mm	4.33
Flux density	1.473 web	1.473 web	1.432 web	−2.86
Length of turns	0.6779 m	0.6779 m	0.6851 m	1.19
Area of stator core	0.00187 m^2	0.00187 m^2	0.00194 m^2	3.60
Depth of stator core	0.01836 m	0.01836 m	0.01866 m	1.60
Stator resistance	9.231 Ω	8.1860 ohms	7.1099 Ω	−15.13
Outer diameter of laminations	159.59 mm	183.997 mm	186.325 mm	1.24
Total copper loss in stator	198.524 w	233.879 w	194.45 w	−20.27
Air gap length	0.428 mm	0.428 mm	0.432 mm	0.925
Diameter of rotor core	104.413 mm	104.41 mm	106.131 mm	1.61
Rotor pole pitch	12.609 mm	12.609 mm	12.817 mm	1.62
Current in each rotor bar	206.589 A	232.974 A	200.229 A	−16.35
Area of each bar	34.431 mm^2	38.82 mm^2	33.371 mm^2	−16.35
Width of rotor slots	4.130 mm	4.529 mm	4.0337 mm	−12.29
Copper loss in bars	117.73 W	132.766 W	115.439 W	−15.0
End ring current	427.652 A	482.271 A	414.486 A	−16.35
Area of each end ring	71.275 mm^2	80.37 mm^2	69.081 mm^2	−16.35
Depth of end ring	7.919 mm	8.931 mm	7.675 mm	−16.35
Total copper loss	127.239 w	143.269 w	124.88 w	−14.72
Rotor frequency	2.708 Hz	3.0286 Hz	2.66 Hz	−13.83
Full load efficiency	82.05 %	80.83 %	82.24 %	1.71

Table 4 Analysis of copper losses and efficiency

S. no	Average voltage	Modified ampere conductors	Losses (S + R) without modified parameters	Losses (S + R) with modified parameters	% Efficiency without modified parameters	% Modified efficiency
6	374	20000	361.29	319.25	81.00	82.24
11	370.67	19080	364.52	319.57	80.01	82.24
12	367.33	19070	367.8	319.05	80.81	82.25
13	365.67	19065	369.47	318.77	80.77	82.26
1	363	19061	372.18	319.38	80.69	82.24
14	362	19059	373.2	319.39	80.66	82.24

desirable limit by selecting the proper selection of the electric loading, and others parameters as discussed in Table 3, generally when the machine is operating under the rated voltage.

In Table 3. The change in parameters has been investigated without modified and with modified ampere conductors under the rated voltage 368 V. To study the performance of the motor and other characteristics under the rated voltage approximately 56 parameters are observed by putting the input data into the computer with the help of Mat Lab-Gui as a research tool, out of which 32 major parameters are modified to increase the efficiency.

In Table 4 six values of average voltage are exerted from Table 2 to observe the variation of efficiency with and without modifying the value of ampere conductors and other parameters. This is observed that the efficiency of the motor can be improved up to its rated efficiency with the modification of the ampere conductors.

Figures 1 and 2 show that the efficiency of the machine can be achieved up to its rated efficiency by modifying the ampere conductors and controlling all others parameters discussed in Table 3.

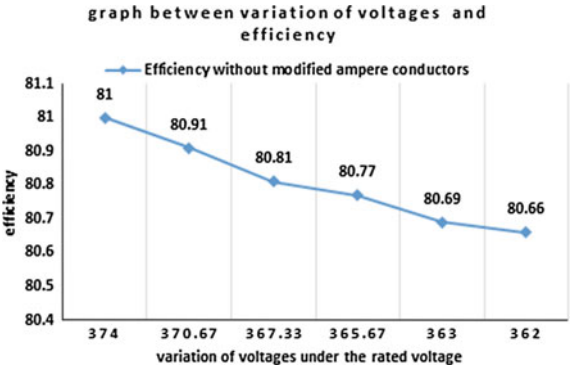


Fig. 1 Variation of voltages Vs Unmodified efficiency

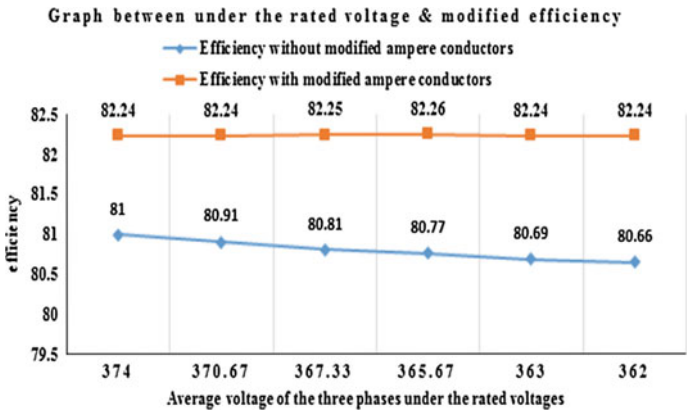


Fig. 2 Variation of voltages Vs Modified efficiency

2 Conclusion

The efficiency of three phase induction motor decreases while operating under the rated voltages. This reduction leads to an increase of total power losses. The present study shows that if a motor operating under the rated voltage is properly derated, even then the efficiency of the motors can be improved up to its rated efficiency. This can be achieved by reducing the value of electric loading thereby controlling the copper losses and 32 others parameters as discussed in Table 3. This type of study is very important for those rural areas where the network of power distribution is poor. To get the maximum efficiency, further scope of research related to this article is to optimize the ampere conductors and other related parameters of three phase induction motor operating under the variation of voltages by adding more experimental results.

References

1. Hasuike, K: Efficiency improvement study of low voltage three phase squirrel cage induction motor for general purpose. IEEE Trans on power apparatus system, VOL.PAS-102, No.12, (1993).
2. Sridhar, L: Design of energy efficient motor for irrigation pumps operating under realistic conduction IEE Roc.-Electr. Power Appl., Vol. 141, No. 6, (1994) 269–274.
3. Lee CY: Effect of unbalanced voltages on the operation of performance of a three phase induction motor. IEEE Trans Energy Convers (1999) 202–208.
4. Gnacinski, p: Winding temperature and loss of life of an induction machine under voltage unbalanced combined with over or under voltages. IEEE Trans Energy (2008) 363–371.
5. Jawad Faiz: Influence of Unbalanced Voltage on the Steady-State performance of a Three-Phase Squirrel-Cage Induction Motor. IEEE Trans on Energy conversion, vol. 19, no. 4 (2004) 657–662.

6. Aldo Boglietti: International Standards for the Induction Motor Efficiency Evaluation: A Critical Analysis of the Stray-Load Loss Determination. IEEE Trans on industry applications, VOL. 40, no. 5, (2004) 1294–1301.
7. Yaw-Juen Wang: Analysis of Effects of Three-Phase Voltage Unbalance on Induction Motors with Emphasis on the Angle of the Complex Voltage Unbalance Factor. IEEE transactions on Energy Conversion, vol. 16, no. 3, September 2001, pp 270–275.
8. Repo, A: Energy efficiency of hoisting motors. Electrical Machines (ICEM), IEEE International conference on 2–5 Sept (2014) 144–149.
9. Enrique C. Quispe: Influence of the Positive Sequence Voltage on the Derating of Three-Phase Induction Motors under Voltage Unbalance Electric Machines & Drives Conference (IEMDC), 2013 IEEE International on 12–15 May(2015) 100–105.
10. Giridhar Kini, P: Effect of Voltage and Load Variations on Efficiencies of a Motor-Pump System. IEEE Transactions on Energy Conversion, vol. 25, no. 2 (2010) 287–292.
11. Jawad Faiz: Precise derating of three phase induction motors with unbalanced voltages. Elsevier, Energy conversion and management (2007) 2579–2586.

Finite Element Analysis of Wing Design

Nitin Chandola and Rohit Singh Rawat

Abstract The present analysis is based upon evaluation and optimization of the structural behavior of wings used in airplanes, as given by advanced material and transport aircraft structure. The main goal is to reduce mass and volume cum the stress and deformation in the plane geometry. The main focus of the analysis is on the factor of safety or level of safety, which is optimized to remain constant for both standard and new model. The analysis of the wing is kept organized only as far as structural and stress analysis is concerned. The aerodynamics analysis can be done for this geometry.

Keywords Computational fluid dynamics · AMTAS · ANSYS · Factor of safety

1 Introduction

The stiffness/weight is one of the most important factor which describes the reliability and endurance of a wing of an airplane or a drone [1]. Higher stiffness/weight indicates higher reliability and endurance of the wing. Two types of design changes are generally considered to achieve high stiffness/weight ratio:

1. Structural design
2. Aerodynamic design
3. The structural design is mainly based on the change in the geometry of the wing design. The developments have been done in this sector by Vinson in 1986 [2] by using hexagonal cells and honey comb shapes for uniaxial compressive loads. Iyengar and Joshi [3] designed the way for weight optimization by using

Nitin Chandola (✉) · R.S. Rawat
Department of Mechanical Engineering,
Graphic Era University, Dehradun, India
e-mail: nitinchandola7@gmail.com

R.S. Rawat
e-mail: rohitsinghrawat276@gmail.com

© Springer Science+Business Media Singapore 2017

R. Singh and S. Choudhury (eds.), *Proceeding of International Conference on Intelligent Communication, Control and Devices*, Advances in Intelligent Systems and Computing 479, DOI 10.1007/978-981-10-1708-7_57

Table 1 Parameters of standard design by AMTAS

Bounding box	
Length *X*	557.97 mm
Length *Y*	347.25 mm
Length *Z*	28.45 mm
Properties	
Volume	1.0032 × 106 mm^2
Mass	2.7086 kg

reinforced fiber composites. By the introduction of ANSYS, Ubaid [1] found the way of static stress analysis effects the critical zones in a wing of a plane. The introduction of Unmanned Aircraft Vehicle (UAV) researched by Jabur in 2003 [1] was carried out by calculating displacement and stress in ANSYS 5.4. The torsional rigidity also plays a vital role in designing of a wing structure because the decrease in the weight of wing can cause decrease in rigidity [4]

4. The objective of this paper is to curb the problem shown by the advanced material and transport aircraft structure (AMTAS) by only considering structural analysis in static load condition. Parameters of standard design by AMTAS are given by Table 1. The wing model is to be optimized in following categories
5. The basic length of the new wing is taken as standard given by AMTAS
6. The analysis done by using factors during static structural analysis are taken constant for both model
7. The temperature of the wing is considered and not of the environment.

2 Methodology

In present work, a suitable model of drone or UAV is selected for analysis. The AMTAS model is selected for comparison with proposed model, due to its popularity and practical implementation. The proposed model is compared with the model given by AMTAS, considering structural analysis in static load condition. After checking the reliability of the design, stability analysis is done, evaluating important mechanical characteristics, like normal stress, deformation, and factor of safety (FOS). Then, implement the angle obtained for reliability until the FOS is greater than 2. Compare the important mechanical characteristics of proposed design and standard design.

3 Motivation

The turbulence in the air plane wing is the most dangerous situation for an aircraft. The optimization of wing is necessary to overcome the adverse effect of the turbulence on the aircraft. The bird strike causes the most of the damages on the wings

and engine of airplane [5]. Also birds are the prime cause of the emergency landings in aerospace industry [6]. The vortex formation by the end of wing tail in a subsonic aircraft structure is one of the key factor for designing an aircraft.

The reduction of mass and increasing the FOS of the wing is the real motivation of the present analysis. Imparting the force of above 5000 N on the plane made at the ratio 1:2 of the AMTAS wing design [7]. The considered value is taken as average for both rear and front span [8]. The material used on the one part one body of both standard and proposed design is 6061-T6 that is commonly used for manufacture for wing. The probability of damage is taken into consideration according to the reliability assessment done by AMTAS on their wing [9]. As the FOS is the factor to change and establish more reliable designs.

4 Design Optimization

The design proposed by the AMTAS is taken into consideration. The geometry was created as one part one body in ANSYS 14 modeler and the modal analysis at an assumed condition of plane during dynamic conditions. The pros and cons were calculated and the proposed design is established by redesigning it by taking length as proposed by standard model of AMTAS. The design has been optimized when the normal stress will act directly on the upper surface of the plane wing and according to it the optimized wing is increased in FOS. The methodology of wing structure optimization includes the changing of angles. The taper wing can have lower tip chord which can affect the behavior of impact, turbulence and vortex formation at the end [10]. The angle taken into consideration is $\pm 10°$ to the standard designs. The mesh was optimized in form of tetrahedrons using computational fluid dynamics (CFD) module instead of mechanical module [11]. Factors considered for analysis of airplane wing are given by Table 2. The wing design is checked for following categories:

i. **Low wing**: The angle is checked only for one plane, i.e., X-axis in $\pm 10°$ of the original. The $+10°$ in the wing showed the larger reliability than $-10°$.
ii. **High wing:** The high wing design is similar to low wing and the $+10°$ criteria seems to be reliable enough for this arrangement as FOS is high.

Table 2 Factors considered for analysis of airplane wing

Factors	AMTAS design	Proposed design
Nodes	420979	249589
Elements	380640	1351825
Type	Fixed support	Fixed support
Suppressed	No	No
Define by	Vector	Vector
Magnitude of force	5000 N (ramped)	5000 N (ramped)
Direction	Defined	Defined

iii. **Gull wing:** The gull wing are drawn by taking $\pm 10°$ in y-axis direction at which both wing's tail and fixed ends were tested for the static analysis and its FOS.
iv. **Inverted gull wing:** The inverted gull wing are the gull wing inverted as the only difference is in the symmetry but, the structural load changes its behavior.

5 Material

As the wing of plane is not made of one material but the basic part, i.e., air foil is made of the AISI6061-T6 so the material is taken in both design were common.

Among these only 6061-T6 was found to be more reliable than others. As 7075-T6 was used before in the aircrafts and were expensive so the 6061-T6 was chosen according to its availability in the market. But the ribs and flanges are to be made by graphite or epoxy [1].

6 Results and Discussion

The results were obtained under the constant temperature for both proposed body and standard body given by AMTAS. The basic length of proposed design and standard design were also constant. The results were analysed for normal stresses mainly because in normal stresses the AMTAS design shows critical stress concentration area at fixed end. The check for FOS was also done for the fixed end to optimize. Figure 1 shows the analysis of FOS for proposed design and the analysis of FOS for slandered design is given by Fig. 2.

The results obtained are for the factors analyzed at both tail end and fixed end of the wing respectively. An optimal rise in the accuracy and reliability is noted in the new design in comparison to standard design. The expected air foil for the analyzed

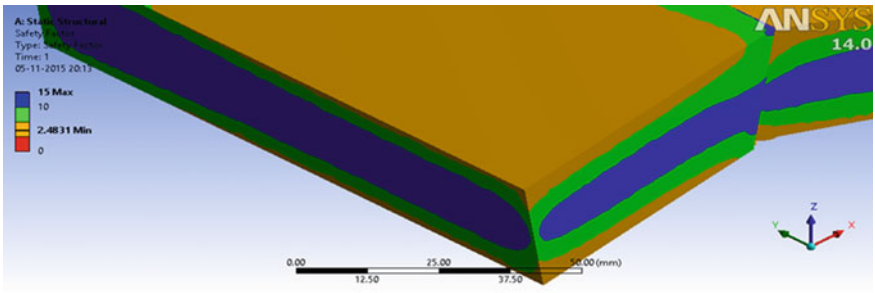


Fig. 1 Analysis of FOS for proposed design

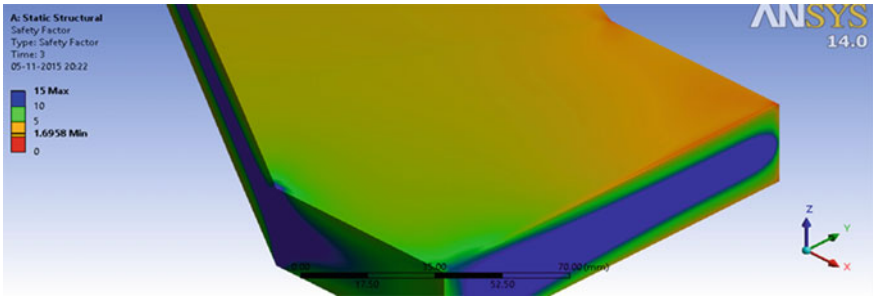


Fig. 2 Analysis of FOS for standard AMTAS design

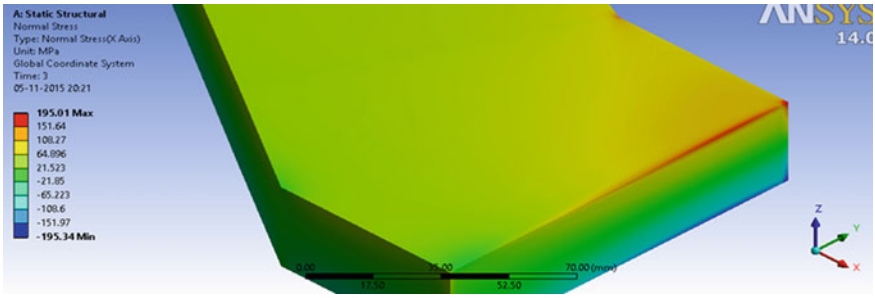


Fig. 3 Normal stress in AMTAS design

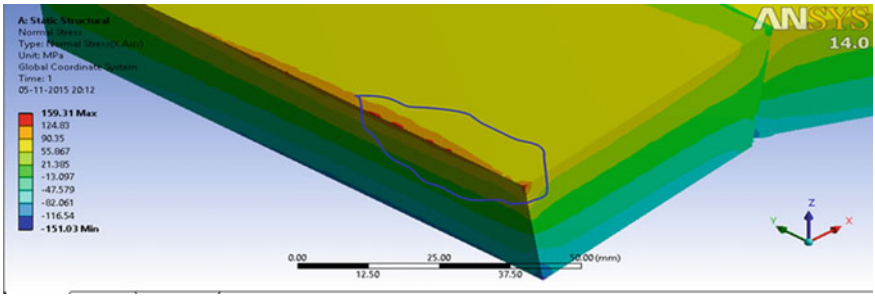


Fig. 4 Normal stress in proposed design

wing can be six digit NACA air foils because it gives lift favorable on both surfaces [12]. The number of nodes and elements has also shown a gradual deviation in standard design.

Figures 3 and 4 exhibits the normal stress at the fixed end of airplane wing for standard design and proposed design, respectively. Tables 3 and 4 shows the comparative results for the important mechanical factors between proposed design and standard design, at tail end and fixed end, respectively.

Table 3 Analysis of important mechanical characteristics at tail end

Factors	AMTAS	Proposed design	Percentage change (%)
Total deformation	15.62 mm	10.45 mm	33.27
Normal stress	-2.0656×10^{-2} MPa	-6.1887×10^{-3} MPa	70.39
Equivalent stress	0.52947 MPa	0.2005 MPa	62.13
Equivalent elastic strain	9.1653×10^{-6}	2.9138×10^{-6}	68.2
Factor of safety	15	15	0

Table 4 Analysis of important mechanical characteristics at fixed end

Factors	AMTAS	Proposed design	Percentage change (%)
Total deformation	5.4778×10^{-3} mm	1.993×10^{-3} mm	63.61
Normal stress	157 MPa	57.164 MPa	63.5
Equivalent stress	145.29 MPa	43.754 MPa	69.88
Equivalent elastic strain	7.0849×10^{-4}	1.2145×10^{-3}	−71.4
Factor of safety	2.4354	3.4835	43

7 Conclusion

In the present analysis, the model of drone or UAV given by AMTAS is selected and analyzed for important mechanical factors like normal stress, total deformation, etc. using ANSYS 14.0 package. A new model is also proposed by changing the angle of inclination by $\pm 10°$ in fixed end and tail end of the airplane wing. The proposed model is also compared with standard AMATAS design, for important mechanical factors using ANSYS 14.0 package.

The proposed design increases FOS, at fixed end by 43 % in comparison with AMTAS design. Hence it increases the reliability of proposed design over AMTAS design if the normal stress over the plane surface of the airplane wing is considered under the static structural analysis. The results can also be verified in aerodynamic systems as the present analysis is based on the static structural analysis.

References

1. Jweeg, M.J., Abid-Aun, S.H.: Optimization of Light Weight Aircraft Wing Structure. Journal of Engineering & Development, Vol. 12, No. 1, March (2008).
2. Vinson, J.R.: Optimum Design of Composite Honeycomb Sandwich Panels Subjected to Uniaxial Compression. University of Delaware, AIAA Journal, Vol. 24, No. 10, October 1986, p. 1690–1696.

3. Iyengar, N.G.R., Joshi, S.P.: Optimal Design of Antisymmetric Laminated Composite Plates. Journal of Aircraft, Vol. 23, No. 5, May 1986, pp. 359–360.
4. Guo, S.J., Banerjee, J.R., Cheung, C.W.: The effect of laminate lay-up on the flutter speed of composite wings. Proceedings of the Institution of Mechanical Engineers, Part G: journal of aerospace engineering, Vol. 217, No. 3, 2003, pp. 115–122.
5. Belega, B.A.: Bird-strike impact simulation with an aircraft wing using SPH bird model. INCAS Bulletin. Vol. 7 Issue 3, pp. 51–58, 2015.
6. Katukam, R.: Comprehensive bird strike simulation approach for aircraft structure certification. cyient white paper, 2014.
7. Chitte, P., Jadhav, P.K., Bansode, S.S.: Statistic and Dynamic Analysis of Typical Wing Structure of Aircraft using Nastran. IJAIEM Journal, Volume 2, Issue 7, July 2013.
8. Raj, N.S.N., Koti, H., Channankaiah: Static Stress Analysis for Aircraft Wing and Its Weight Reduction using Composite Material. International Journal of Engineering Research & Technology, Vol. 3 Issue 3, March – 2014, 2300–2303.
9. Huang, C.K., Lin K.Y.: A method for reliability assessment of aircraft structures subject to accidental damage. American Institute of Aeronautics and Astronautics Paper, pp. 1–10, 2005.
10. Prabhu, M.S., Raj J.N., Vignesh, G.: Optimization of Unmanned Aerial Vehicle Wing Structure. IJISET - International Journal of Innovative Science, Engineering & Technology, Vol. 2 Issue 3, March 2015, pp. 28–34.
11. Khan, H.N., Usama, M.W., Ahmad, R., Rasool, I.: 3-D CAD Modeling and Analysis of Aircraft Wing Using CATIA Software And Its Comparison With ANSYS Software. proceedings of the 4th international conference on Automation and Transportation Systems, Brasov, Romania, pp. 19–22, 2013.
12. Goud, T.S.K. Kumar A.S., Prasad, S.S.: Analysis of Fluid-Structure Interaction on an Aircraft Wing. International Journal of Engineering and Innovative Technology (IJEIT) Volume 3, Issue 9, March 2014, pp. 146–152.

A Minimal Realization Universal Filter Employing Third-Generation Current Conveyor and Operational Transconductance Amplifier

Tajinder Singh Arora, Varkha Rani and Manish Gupta

Abstract This paper proposes a new current-mode universal filter utilizing third-generation current conveyor (CCIII) and an operational transconductance amplifier (OTA) as an active device. This current-mode filter requires a minimum and all grounded passive elements. Only one grounded resistor and two grounded capacitors are required to get all the five, i.e., low pass, high pass, band pass, band reject, and all pass responses, without changing any hardware configuration. The current input is at low impedance port and current output is at high impedance port which makes this circuit a better composition. PSPICE simulation has been done to test and verify the theoretical and simulated results.

Keywords Universal filter · Third-generation current conveyor · Active filters

1 Introduction

Despite the advancement in digital signal processing and their applications in real world, analog signal processing still cannot be replaced with it, because of their certain advantageous. There are various processing of natural signals that should be carried out with analog signal processing only such as amplification, rectification, etc. [1]. Electronic filter is one of the important application of analog signal processing. A filter allows electrical signals having certain frequencies to pass through

T.S. Arora (✉)
Department of Electronics and Communication Engineering,
Maharaja Surajmal Institute of Technology, C-4 Janakpuri, New Delhi 110058, India
e-mail: tajarora@msit.in

V. Rani · M. Gupta
Department of Electronics and Communication Engineering, Greater Noida Institute of Technology, Plot no. 7, Knowledge Park II, Greater Noida 201306, Uttar Pradesh, India
e-mail: vrani.ec@gmail.com

M. Gupta
e-mail: guptamanish2004@gmail.com

© Springer Science+Business Media Singapore 2017

R. Singh and S. Choudhury (eds.), *Proceeding of International Conference on Intelligent Communication, Control and Devices*, Advances in Intelligent Systems and Computing 479, DOI 10.1007/978-981-10-1708-7_58

depending upon their type, which can be low pass (LP), high pass(HP), band pass (BP), band reject (BR), or all pass (AP) filter. The filters may vary from mode of operation such as current-mode (CM), voltage-mode (VM), Transconductancemode (TC) and trans-resistance-mode (TR) filters. A filter that is capable of performing two or more types of filtering is called a multifunction filter, whereas the one that can perform all five types of filtering is called a universal filter.

Various universal filters based on OTA has been available in literature, for instance [2–4] and there cited in. In [2] Tsukutani et al. proposes a universal filter using OTA and current conveyor but they employed three OTA to get all the responses. In [3] only three active devices has been utilized but suffers from the drawback of using floating capacitors. In [4] simple OTA has been employed to get a second-order standard filtering function, but uses a large number of active devices.

The authors proposes one such proposition that eliminates all the above-mentioned criteria. This circuit proposes a universal filter that gives all the five basic responses, i.e., LP, HP, BP, BR, and AP, simultaneously. This CM circuit offers electronic tunability of quality factor and frequency of operation. The proposed circuit uses a minimum number of passive component. All the employed passive components are grounded in nature, makes this circuit useful for its implementation as an integrated circuit. The current-mode output is available explicitly, which makes the circuit good for the use of making higher order filter.

In this paper, Sect. 2 gives the introduction to the active devices used in the designed filter. Section 3 shows the block diagram and transfer functions of the proposed circuit. Sect. 4 demonstrates the simulation results of the proposed biquad circuit carried out with the help of PSPICE. At last the concluding remarks have been given in Sect. 5.

2 Introduction to Ota and CCIII

The operational transconductance amplifier (OTA), symbolically shown in Fig. 1, is characterized by

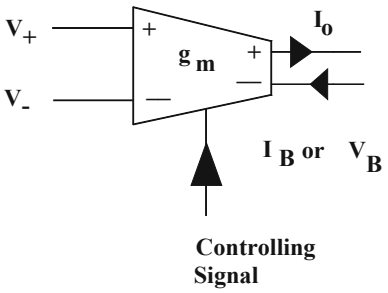


Fig. 1 Symbolic notation of OTA

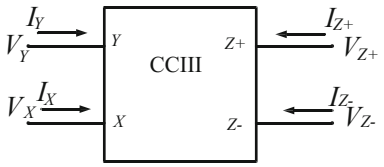


Fig. 2 Symbolic notation of CCIII

$$I_o = \pm g_m(V_+ - V_-) \tag{1}$$

The transconducatnce factor is defined by g_m and it is controlled by the bias current inside the circuitry of the OTA. The polarity symbol + or − used before the transconductance parameter represents the direction of the current at the output.

A third-generation current conveyor (CCIII), symbolically shown in Fig. 2, is characterized by

$$\begin{bmatrix} I_y \\ V_x \\ I_{z\pm} \end{bmatrix} = \begin{bmatrix} 0 & -\alpha & 0 \\ \beta & 0 & 0 \\ 0 & \pm\gamma & 0 \end{bmatrix} \begin{bmatrix} V_y \\ I_x \\ V_{z\pm} \end{bmatrix} \tag{2}$$

where α, β and γ represent nonideal port transfer ratios of X, Y, and Z terminals, respectively, and ideally $\alpha = \beta = \gamma = 1$.

3 Circuit Configuration

The proposed second order universal filter using OTA and CCIII, by utilizing all grounded passive components is shown in Fig. 3. By using the port's relationships given in (1) and (2), routine analysis yields derivation of all the transfer functions as given in (3–6). The natural angular frequency ω and the quality factor Q of the filter are given in (7).

$$\frac{I_{o1}}{I_{in}} = \frac{\left(\frac{g_{m2}}{R_1C_1C_2}\right)}{D(s)} \tag{3}$$

$$\frac{I_{o2}}{I_{in}} = -\frac{\frac{s}{R_1C_1}}{D(s)} \tag{4}$$

$$\frac{I_{o3}}{I_{in}} = \frac{s^2}{D(s)} \tag{5}$$

$$D(s) = s^2 + \frac{s}{R_1C_1} + \frac{g_{m2}}{R_1C_1C_2} \tag{6}$$

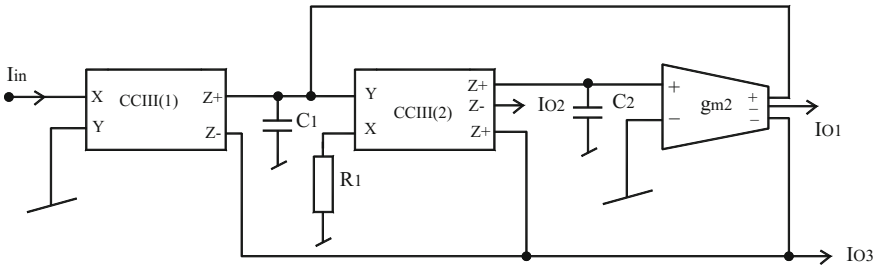


Fig. 3 Proposed universal filter configuration

$$\omega = \sqrt{\frac{g_{m2}}{R_1 C_1 C_2}} \quad \text{and} \quad Q = \sqrt{\frac{R_1 g_{m2} C_1}{C_2}} \tag{7}$$

The summation of I_{o1} and I_{o3} will give the BR response, whereas summation of currents I_{o1}, I_{o2}, and I_{o3} will provide an AP response. It is clearly visible from Eq. (3–7) that all the filter responses, namely high pass (HP), band pass (BP),low pass (LP), band pass (BP), and all pass (AP) can easily be realized using the proposed filter configuration. These are the filter responses that may be required from any of the designed universal filter. It can be seen from (7) that Q has electronic tunability and its value can be changed by varying the value of g_{m2}. Simulation results based on the same is given in Sect. 4.

4 Simulation Results

The testing and the workability have been checked, of current-mode response of the proposed circuit configuration of Fig. 3, on PSPICE software. The CMOS versions of OTA and CCIII, respectively, are shown in Figs. 4 and 5 for the use of making a universal filter. All MOS devices operate in saturation. The aspect ratios of all the MOS transistors, utilized in Fig. 4, are given in Table 1. The model parameters used for the PSPICE simulations have been taken from [5]. The selected supply voltage has been $V_{DD} = -V_{SS} = 1.0$ V for OTA and $V_{DD} = -V_{SS} = 1.65$ V for the CCIII. The bias current are taken as 2.8 μ A for the OTA to get the values of g_{m2} as 31.57 μ A/V. The ω chosen for the design was 1 MHz and the passive component values selected were $R_1 = 17.1$ K, $C_1 = C_2 = 6.8$ pF. Simulation results of the proposed current-mode filter for LP, BP, HP, and BR is shown in Fig. 6. Continuous line in Fig. 6 shows the simulated outputs, whereas dashed line represents the ideal or theoretical outputs of the derived filter configuration. For AP response, the magnitude as well as phase response is shown in Fig. 7. One can see in Fig. 6 the simulated and ideal responses are in good agreement to each other.

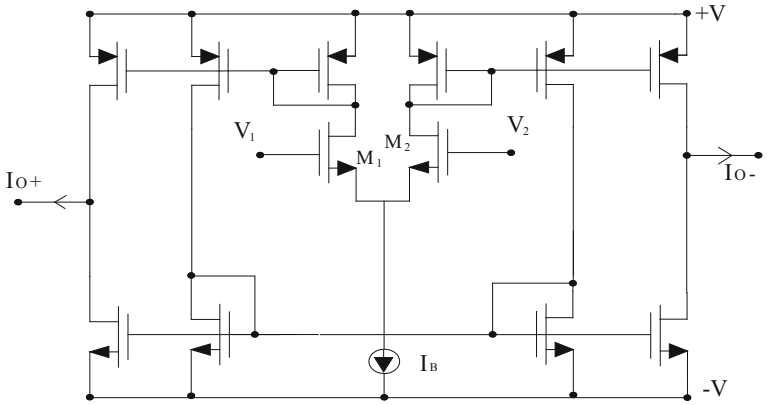


Fig. 4 CMOS realization of the OTA [5]

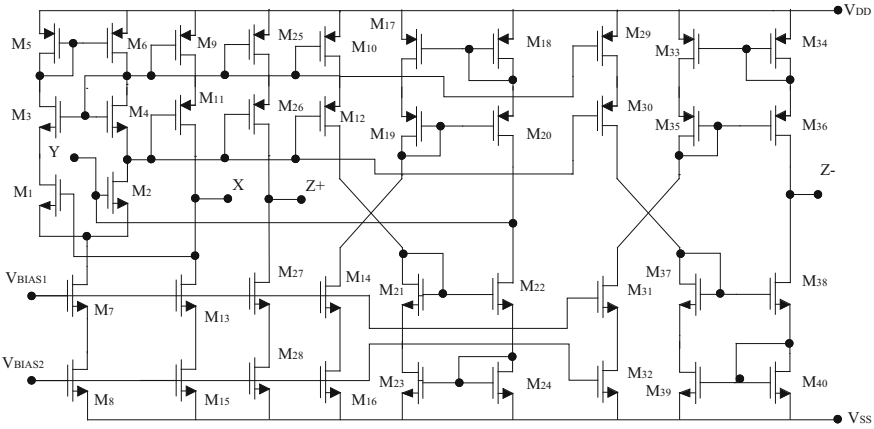


Fig. 5 Third-generation current conveyor (CCIII) [6]

Table 1 Aspect ratios of OTA

MOSFET	W(μm)	L(μm)
M1, M2	5.76	0.72
M3, M4, M5, M6, M7, M8	2.16	0.72
M9, M10, M11, M12	1.44	0.72

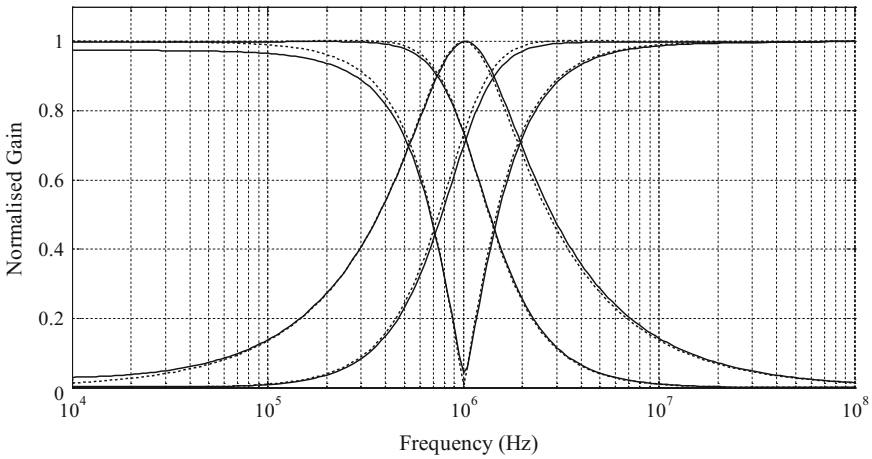


Fig. 6 Frequency response curves of the proposed filter circuits

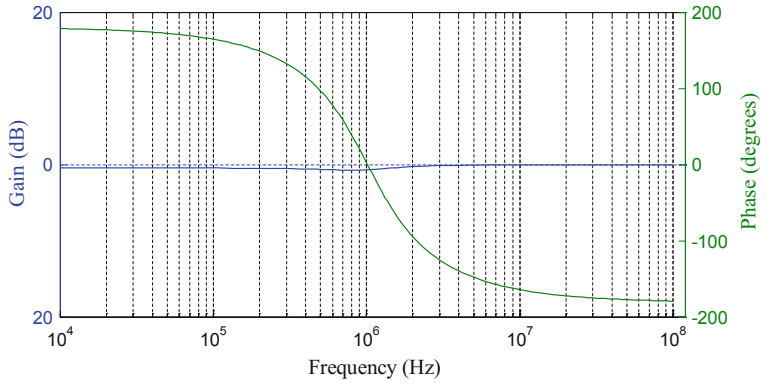


Fig. 7 Frequency response of an all pass filter configuration

5 Conclusion

This paper proposes a new universal filter based on OTA and a CCIII. It has been simulated using PSPICE software. The circuit offers several advantageous (1) requirement of minimum number of passive components, i.e., only three, (2) all the five responses can be achieved without changing any hardware configuration, (3) to achieve all five responses it does not require any matching conditions for passive components, (4) the use of all grounded passive components, (5) this current-mode circuit electronic tunability of Q, (6) explicit output available at high impedance port make is a better proposition for cascading, (7) This circuit works at a considerable high frequency. The simulated result agrees with the theoretical analysis to a high degree.

References

1. Senani, Raj, D. R. Bhaskar, and A. K. Singh. *Current conveyors: variants, applications and hardware implementations*. Springer, 2014.
2. Tsukutani, T., Y. Sumi, and Y. Fukui. "Novel current-mode biquad filter using OTAs and DO-CCII." *International journal of electronics* 94, no. 2 (2007): 99–105.
3. Horng, Jiun-Wei. "High input impedance voltage-mode universal biquadratic filter using two OTAs and one CCII." *International Journal of Electronics* 90, no. 3 (2003): 185–191.
4. Kumngern, Montree, Peerawut Suwanjan, and Kobchai Dejhan. "Electronically tunable voltage-mode universal filter with single-input five-output using simple OTAs." *International Journal of Electronics* 100, no. 8 (2013): 1118–1133.
5. Senani, Raj, Manish Gupta, Data Ram Bhaskar, and Abdhesh Kumar Singh. "Generation of equivalent forms of operational trans-conductance amplifier-RC sinusoidal oscillators: the nullor approach." *The Journal of Engineering* 1, no. 1 (2014).
6. Abdalla, Kasim K., Data Ram Bhaskar, and Raj Senani. "Configuration for realising a current-mode universal filter and dual-mode quadrature single resistor controlled oscillator." *Circuits, Devices & Systems, IET* 6, no. 3 (2012): 159–167.

Design of 30 MHz CMOS Operational Amplifier

Deepak Prasad, Ashutosh Pranav, Apoorva Nimbargi, Jyoti Singh, Vijay Nath, Abhishek Pandey, Madhu Kumari Ray, Manish Kumar and Manish Mishra

Abstract CMOS operational amplifier is now an integral part of analog and mixed mode designs. In this article, CMOS op-amp with 30 MHz bandwidth is designed. This configuration of op-amps finds huge application in active filters. The op-amp showed the unity gain bandwidth of about 30 MHz and DC gain of about 56.94 dB and slew rate of about 29.9 V/μs. This circuit is designed using Cadence virtuoso environment gpdk 045 nm CMOS technology.

Keywords CMOS (complementary metal oxide semiconductor field effect transistor) · Op-amp (operational amplifier) · Gain · Bandwidth · Slew rate

1 Introduction

With relentless miniaturization of MOSFET, electronics industry has had a tremendous development, which has enabled several emerging multi-GHz wireless and wire line applications. Now, operational amplifier is as useful in analog environment as logic gates in digital electronics [1, 2]. This advancement has helped in improving the performance of digital circuits without posing much penalty on design and implementation, but analog and mixed signal circuits' designers have faced

Deepak Prasad (✉) · Ashutosh Pranav · Vijay Nath
Abhishek Pandey · Madhu Kumari Ray
Dept. of ECE, BIT Mesra Ranchi, Ranchi, Jharkhand, India
e-mail: prasaddeepak007@gmail.com

Vijay Nath
e-mail: vijaynath@bitmesra.ac.in

Apoorva Nimbargi · Jyoti Singh
Dept. of ECE, PESIT, Bangalore, Karnatka, India

Manish Kumar
Dept. of ECE, NERIST, Nirjuli, Arunachal Pradesh, India

Manish Mishra
Dept. of Electronics, DDUGU, Gorakhapur, Uttar Pradesh, India

© Springer Science+Business Media Singapore 2017

R. Singh and S. Choudhury (eds.), *Proceeding of International Conference on Intelligent Communication, Control and Devices*, Advances in Intelligent Systems and Computing 479, DOI 10.1007/978-981-10-1708-7_59

problems like short channel effects, cross talk, increased channel length modulation constant, leakage etc. [3–5]. Other than the problems faced in fabricating analog circuits there are design trade-offs such as DC gain versus bandwidth and power versus speed that pose substantial analog design challenges [3]. Of late analog designers are trying to solve many of these problems by using many non-classical design procedures of basic building blocks of analog design. One such important basic building block of many analog circuits is amplifier. Amplifiers having high gain and wide bandwidth, in excess of 100 MHz, with low amplitude distortion and stable gain, are of increasing importance in modern electronics. Most of the classical amplifier designs use emitter-degenerated configuration which suffer from current- and temperature dependent emitter impedance which in turn lead to distortion and gain instability. Negative feedback technique can't be used in more than two stage amplifier at this bandwidth as it causes excess phase shift around the loop. Further, such amplifiers have voltage swing at the signal frequencies are present throughout the chain and parasitic capacitances limit the bandwidth. One other popular way to realize wideband amplifier is to have two stage amplifiers combined in parallel, unfortunately such an implementation has a penalty on area. There are op-amps designed for good bandwidth, but with high voltage supply [6], which is not feasible in today's development of low power circuits. Devices with less technology value can produce high bandwidth [5], but can hamper gain of the amplifier. All these problems hamper the bandwidth of the amplifier. It was not possible to realize wide bandwidth amplifiers in older process but with the latest advancements in transistor fabrication like FINFETs, carbon nanotubes, nanowires, etc., the same is very promising. This paper proposes a non-classical two stage, one path operational amplifier design which can provide high gain even at a wide bandwidth while making sure it maintains high dynamic range and output swing.

2 Op-amp Architecture

Op-amps being an important integral part of various analog and mixed mode circuits and systems, its design is very crucial in various applications. Figure 1 is the basic block diagram of op-amp circuit.

Op-amps have sufficiently high gain such that even when negative feedback is applied, the effect on the gain is less. A critical part of many analog circuits, op-amp

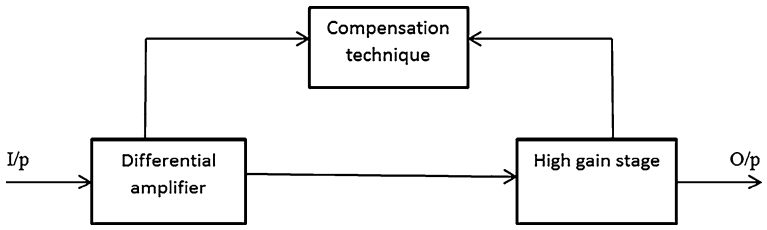


Fig. 1 Generic op-amp structure

has a lot of specifications to be met to work as required in our application. There are several things like bandwidth, gain, slew rate, CMRR, PSRR, etc., which decides in which application the op-amp can be used. The op-amp also exhibits trade-off in bandwidth and gain specifications, where increase in one factor may result into degradation of another. Similar is the case with speed and power factors. Keeping all these factors into account, a suitable op-amp has to be designed.

Basically, an op-amp consists of a differential amplifier which is the basic block and one of the most versatile circuits that amplifies the difference between the two signals given. The differential amplifier will give considerable gain required. It consists of a transconductance amplifier with current-mirror active load.

The second stage is a simple common source stage used to improvise the gain of the op-amp. There is a frequency compensation technique included for the stability of closed loop op-amp. Miller compensation technique is adopted here. A Miller capacitor is placed between the output of differential amplifier and the input of common source amplifier.

3 Design Methodology

The op-amps work based on the specifications took, for any particular application. Feedback in op-amps helps in making the transfer function independent of the gain. But with increase in frequency, the gain degrades making closed loop transfer function dependent on gain. In order to avoid this, op-amps must be of wide band for radio frequency applications.

After finding the transfer function of the op-amp designed, we can find the value of two poles in the circuit, each contributed by the differential amplifier and the common source amplifier. We can also find the gain and it is the product of the gains of the two stages. The op-amp circuit block diagram is shown in Fig. 2.

The design procedure begins with choosing the device length of the transistors to be used in the entire op-amp circuit. Next, the compensation capacitor value is chosen such that it satisfies the following equation [7, 8]

$$C_{\mathrm{c}} > (2.2/10)C_{\mathrm{L}} \tag{1}$$

where, C_{c} = coupling capacitor and C_{L} = load capacitor. Similarly, the gain bandwidth product is given by,

$$\mathrm{GB} = \frac{g_{m1}}{C_{\mathrm{c}}} \tag{2}$$

where, g_{m1} is the input transconductance. For the gain bandwidth product to be high, the input transconductance should be high. And similarly, the output capacitance should be low. For the input transconductance to be high, the transistor MN1

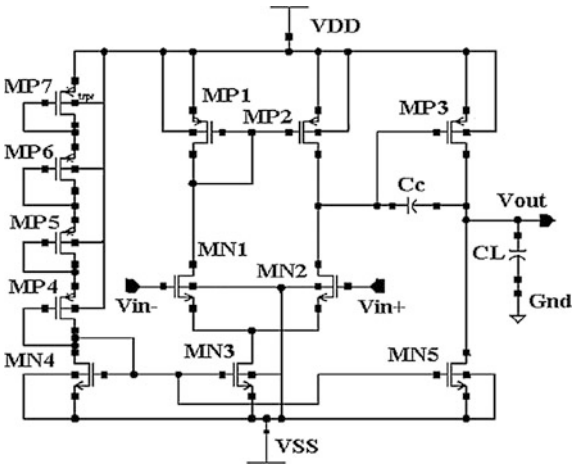


Fig. 2 Schematic of proposed CMOS op-amp

and MN2 channel widths are made large, which is evident by the following equation

$$g_m = \sqrt{2\mu_p C_{ox} \frac{W}{L} I_d} \tag{3}$$

Slew rate decides the current flowing in the transistor MN3, and is given by

$$\mathrm{SR} = \frac{I_{\mathrm{MN3}}}{C_{\mathrm{c}}} \tag{4}$$

Since the transistors MP1 and MP2 are connected in current-mirror mode the aspect ratio of both transistors is same. Transistor MP4, MP5, MP6, and MP7 are used for current bias, while MP3 and MN5 used for compensating the output gain.

For a phase margin of 60°, the output pole is assumed to be at the location which is 2.2 times. So, g_{mMP3} is determined by the following equation

$$g_{m\mathrm{MP3}} = 2.2 g_{m\mathrm{MN2}} \left(\frac{C_{\mathrm{L}}}{C_{\mathrm{C}}} \right) \tag{5}$$

The aspect ratio of transistor MN5 is obtained using

$$S_{\mathrm{MN5}} = (S_{\mathrm{MN3}}) \left(\frac{I_{\mathrm{MP3}}}{I_{\mathrm{MN3}}} \right) \tag{6}$$

where, S_{MN3} and S_{MN5} are the aspect ratio of transistors MN3 and MN5, respectively.

4 Simulation and Results

The op-amp designed is simulated using Cadence analog and digital system tools gpdk45 nm CMOS technology. The power supply used is 2 V. The op-amp shows the unity gain bandwidth of about 30 MHz and DC gain of about 56.94 dB and slew rate of about 29.9 V/μs. In AC analysis, the phase margin, gain and unity gain bandwidth is determined. The slopes are measured between the 20 % of the rising/falling edge to the 80 % of the rising/falling edge. While doing this calculation the negative input of the op-amp is connected to the output, where as a finite input impedance is given to the positive input of the op-amp. Simulation results of slew rate are shown in Figs. 3 and 4, respectively. Gain & Phase versus frequency plots are shown in Fig. 5 which are used to calculate DC gain and phase margin. The layout of proposed of op-amp circuit shown in Fig. 5 (Table 1).

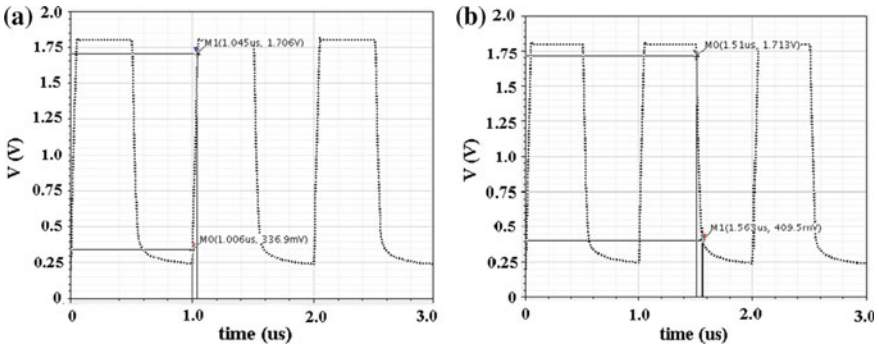


Fig. 3 **a** Measurement of positive slope of the transient curve (slope = 35.4 V/μs) and **b** negative slope of the transient curve (slope = 24.4 V/μs)

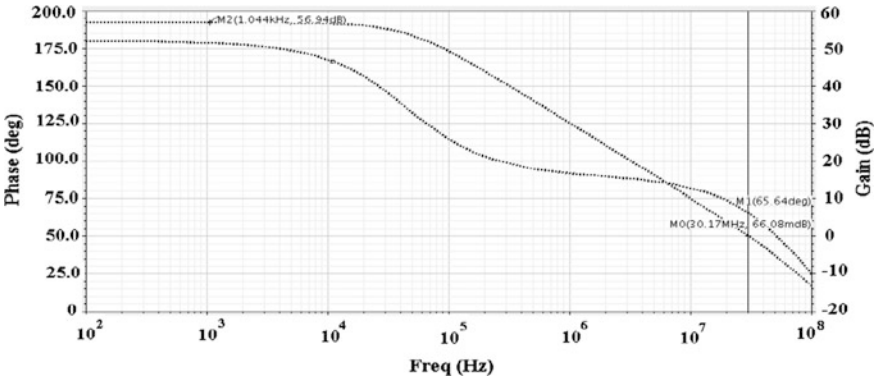


Fig. 4 Gain and phase versus frequency plots

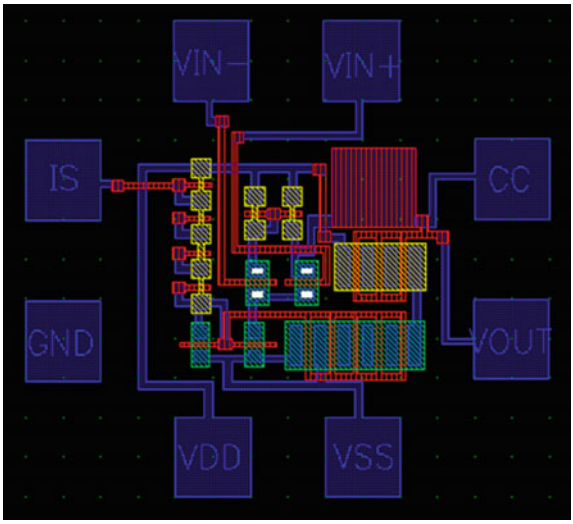


Fig. 5 Layout of proposed CMOS op-amp

Table 1 Performance analysis of op-amp

Parameters	This design	[9]	[6]
Technology	45 nm	180 nm	180 nm
DC gain	56.94 dB	70 dB	57.18 dB
Unity gain bandwidth	30.17 MHz	10 MHz	10 MHz
Phase margin	65.64°	–	56°
ICMR	0.4 V–1.8 V	1.5 V–2.8 V	–
CMRR	37.33 dB	>60 dB	–
Slew rate	29.9 V/μs	10 V/μs	11.5 V/μs
Power dissipated	1.667 mW	–	–

5 Conclusion

This circuit consumes minimum power around 1.6 mW and providing good bandwidth of around 30 MHz. This op-amp is used in wide range of applications. Bandwidth of this op-amp is more suitable for analog filters and in medical and instrumentation applications such as diagnosis equipment and power line monitors. It covered very less area and it can also be used in portable devices. The large bandwidth will give additional filtering and thereby reducing additional components in wireless devices. So, it serves as a key circuit in many applications. The layout of proposed op-amp circuit is verified by DRC, LVS, and RCX. The pre layout and post layout result are giving nearly the same result.

Acknowledgment We are thankful to RESPOND ISRO, Bangalore for funding this research work. We are also thankful to Prof. V.R. Gupta, HOD ECE, Prof. T.Ghosh, Dean(SR) and Prof. R.Sukesh Kumar, Dean(FA) & Prof. M.K. Mishra, Vice-chancellor, BIT Mesra Ranchi for providing infrastructure facility to carry out this research work.

References

1. Abhishek Pandey, Subhra Chakraborty, Suraj Kumar Saw and Vijay Nath.: A Darlington Pair Transistor Based OperationalAmplifier. Proceedings of 2015 Global Conference on Communication Technologies(2015) 273–276.
2. Abhishek Pandey, Subhra Chakraborty and Vijay Nath,: Slew rate enhancing technique in darlington pair based cmos op-amp. ARPN Journal of Engineering and Applied Sciences Vol. 10 (2015) 3970–3973.
3. D Gangopadhyay, T.K. Bhattacharyya.: A 2.3 GHz gm-boosted high swing class AB ultra wide band op-amp in 0.18um CMOS technology. IEEE 53rd Int.midwest symposium on circuit and systems. (2010) 713–716.
4. T.K.Bhattacharyya, M.K.Hati.: A Power Efficient and constant-gm 1.8 V CMOS Operational Transconductance Amplifier with Rail to Rail input and output ranges for charge pump in Phase locked loop. IEEE Int.conference on Circuit and Systems. Vol. 134 (2012) 38–43.
5. Ramkrishna Kundu, Abhishek Pandey, Dipayan Ghosh, Jyoti Singh, Vijay Nath.: A 4.596 GHz, High slew rate, ultra lowpower cascade operational amplifier in 45 nm CMOS for wireless communication. Int.journal of computer applications in engineering sciences. Vol. 3, (2014).
6. Shilpa Goyal, Nitin Sachdeva, Tarun Sachdeva.: Analysis and Design of a Two Stage CMOS OP-AMP with 180 nm using Miller Compensation Technique. Int.Journal on Recent and Innovation Trends in Computing and Communication, Vol. 3 (2015).
7. P.E.Allen, D.R. Holberg, CMOS Circuit Design, Oxford Indian Edition, (2009).
8. Razavi B.: Design of CMOS Analog Integrated Circuits, McGraw Hill, California, (1998).
9. Amana Yadav.: A review paper on design and synthesis of two-stage op-amp. Int.journal of advances in engineering and technology. Vol. 2, (2012) 677–688.

Line Flow Indices for Placement of Distributed Energy Sources in Relieving Transmission Line Congestion

Rajagopal Peesapati, Niranjan Kumar, Vinod Kumar Yadav and Gitanjali Mehta

Abstract In the present work, intelligent approach is presented for the placement of distributed generation (DG) unit in order to relieve congestion in transmission lines. Loss flow index is employed to find the optimal locations for the incorporation of DG unit to the existing network. The index presented in this work is based on mathematical form of real power losses which is drawn from conventional power flow solution. The proposed method of obtaining optimal placement is applied on IEEE 30 bus system, and obtained results are compared with respect to DGs. The suboptimal places are also determined in view of geographical suitability of the DG installation with respect to the optimal location. Results conveyed that the approach of optimal placement is good enough in comparison to other approaches presented in the past literature.

Keywords Congestion · Loss flow index · Distributed generation · Transmission lines

Rajagopal Peesapati (✉) · Niranjan Kumar
Department of Electrical and Electronics Engineering,
National Institute of Technology Jamshedpur, Jamshedpur, India
e-mail: gopal.12rsee009@nitjsr.ac.in

Niranjan Kumar
e-mail: nkumar.ee@nitjsr.ac.in

V.K. Yadav · Gitanjali Mehta
School of Electrical Electronics and Communication Engineering,
Galgotias University, Greater Noida, India
e-mail: v3k5y7@gmail.com

Gitanjali Mehta
e-mail: gitanjali.iitr@gmail.com

© Springer Science+Business Media Singapore 2017

R. Singh and S. Choudhury (eds.), *Proceeding of International Conference on Intelligent Communication, Control and Devices*, Advances in Intelligent Systems and Computing 479, DOI 10.1007/978-981-10-1708-7_60

1 Introduction

In restructured environment, electric utilities are availed with new technologies to improve the quality and reliability of the power supplied to consumers. The uncertainties like fuel costs, estimation of demand, transmission network operations; imperfect scheduling and contingencies should be captured and relieved at the earliest to make maximum usage of available transmission resources for gaining the maximum profit [1–3]. Load shedding, generator rescheduling with adaptive bacterial foraging incorporate including Nelder–Mead are shown as alternatives to alleviate the congestion in network lines [4–10]. The congestion management problem is solved by the optimal placement of the series flexible alternative current transmission systems (FACTs) controller and static VAR compensators are proposed [11, 12]. The benders decomposition is used to find the optimal places for the static VARs [12]. Congestion management problem for bilateral markets is solved using evolutionary bipartite network in [13]. It is found that multilateral congestion management is effective than the bilateral congestion management [14–16]. Load side governing is more effective in congestion management than the supply side governing due to the heavy competition, load variation, and load growth [17]. Methodologies for congestion management with optimal placement of Distributed Generation (DG) have been proposed in [18–20]. Hybrid particle swarm optimization (HPSO) technique is proposed for obtaining the optimal sizing and placements of DGs [21]. Big bang–big crunch method is applied in optimizing multiobjective function for optimal planning of dispatchable distributed generator [22]. Fireworks optimization algorithm is presented for both distribution network reconfiguration and DGs placement [23]. Bacterial foraging algorithm (BFA) is proposed to obtain the optimal capacities of DGs by minimizing the power loss, operational costs and improving voltage profile [24]. The search space for the above algorithms has been reduced in [25]. Combined heuristic constructive algorithm-based DG allocation along with network reconfiguration by adding the new bus bars are proposed in [26, 27]. In the present work, a demand side management technique based-congestion management is proposed for an IEEE 30 bus system. A new loss flow index is introduced to incorporate the DG into existing electrical power network for relieving congestion in the transmission line. The loss flow indices also evaluate the suboptimal locations based on the priorities to incorporate the DG if the optimal location is geographically not suitable. Further, article is arranged as: the congestion management problem and its solution methodology are presented in Sect. 2. The steps for solving the congestion are presented as an algorithm in Sect. 3. The results and related discussions are presented in Sect. 4 and the findings of the work are presented as conclusions in Sect. 5.

2 Problem Formulation

The present section provides the mathematical modeling of the congestion management problem with and without DG placement (considering fixed demand) and loss flow indexes for the DG placement.

2.1 Congestion Management Problem Without DG Placement Considering Fixed Demand

The cost function (G_{di}) in \$ /hr of a distribution company can be obtained from its bid. Similarly the cost function $\left(G_{\mathrm{gi}}\right)$ in \$ /hr of a generation company can be obtained from its offer. These functions can be mathematically represented by

$$G_{\mathrm{di}} = -\frac{1}{2}c_{\mathrm{di}}P_{\mathrm{di}}^2 + d_{\mathrm{di}}P_{\mathrm{di}}(\$\ /\mathrm{hr}) \tag{1}$$

$$G_{\mathrm{gi}} = \frac{1}{2}a_{\mathrm{gi}}P_{\mathrm{gi}}^2 + b_{\mathrm{gi}}P_{\mathrm{gi}}(\$\ /\mathrm{hr}) \tag{2}$$

where, $-c_{\mathrm{di}}$ is slope of the distribution company cost function, d_{di} is intercept of the ith distribution company cost function, a_{gi} is slope of the ith generation company cost function, b_{gi} is intercept of the ith generation company cost function, P_{di}, P_{gi} is real power demand and generation of the ith distribution company and generation company, respectively.

In deregulated environment, the congestion management problem is structured by maximizing the distribution company's costs minus generation company's costs subjected to equilibrium constraints and transmission congestion constraints. The problem of congestion management without DG fixed demand can be formulated as

$$\text{Min} \quad J = \sum_{i=1}^{N_{\mathrm{g}}} G_{\mathrm{gi}} \tag{3}$$

Subject to

$$P_{\mathrm{gi}} = P_{\mathrm{di}} + \sum_{\mathrm{j}=1}^{N} \frac{\left(\delta_{\mathrm{i}} - \delta_{\mathrm{j}}\right)}{x_{\mathrm{ij}}} \quad \forall i \tag{4}$$

$$\left|Pl_{\mathrm{ij}}\right| \leq Pl_{\mathrm{ij}}^{\max} \quad \forall i, j \in N_{\mathrm{l}} \tag{5}$$

$$0 \leq P_{\mathrm{gi}} \leq P_{\mathrm{gi}}^{\max} \quad \forall i = 1, , 2, \ldots, N_{\mathrm{g}} \tag{6}$$

$$\delta_{\min} \leq \delta_{\mathrm{i}} \leq \delta_{\max} \quad \forall \mathrm{i} = 1, 2, \ldots, \mathrm{N} \tag{7}$$

where, N, N_{l}, N_{g} are the number of system buses, lines, and generators, respectively, δ_{i}, $\delta_{\min}$, $\delta_{\max}$ are voltage angles of the ith bus and its minimum and maximum limits, respectively, x_{ij} is series inductive reactance between the buses $i-j$,Pl_{ij} is real power flow over the line between $i-j$, $Pl_{\mathrm{ij}}^{\max}$ is thermal limit of the line between the buses $i-j$, $P_{\mathrm{gi}}^{\max}$ is maximum limit of P_{gi}, Pl_{km} is real power flow in the line between $k-m$ and $Pl_{\mathrm{km}}^{\max}$ is maximum limit of real power flow in the line between $k-m$.

2.2 Loss Flow Indexes for DG Placement

Consider a π network illustration of transmission line connected between buses k and m as shown in Fig. 1. The real power (P_{km}) and reactive power (Q_{km}) in the line can be expressed as below

$$P_{\mathrm{km}} = V_{\mathrm{k}}^2 g_{\mathrm{km}} - V_{\mathrm{k}} V_{\mathrm{m}} g_{\mathrm{km}} \cos(\theta_{\mathrm{km}}) - V_{\mathrm{k}} V_{\mathrm{m}} b_{\mathrm{km}} \sin(\theta_{\mathrm{km}}) \tag{8}$$

$$Q_{\mathrm{km}} = -V_{\mathrm{k}}^2 \left(b_{\mathrm{km}} + b_{\mathrm{km}}^{\mathrm{sh}}\right) + V_{\mathrm{k}} V_{\mathrm{m}} b_{\mathrm{km}} \cos(\theta_{\mathrm{km}}) + V_{\mathrm{k}} V_{\mathrm{m}} g_{\mathrm{km}} \sin(\theta_{\mathrm{km}}) \tag{9}$$

where, $\theta_{\mathrm{km}} = \theta_{\mathrm{k}} - \theta_{\mathrm{m}}$. The real power losses (P_{loss}) can be obtained by the summation of the P_{mk} and P_{km}

$$P_{\mathrm{loss}} = P_{\mathrm{mk}} + P_{\mathrm{km}} = \mathrm{g}_{\mathrm{km}} \left(V_{\mathrm{k}}^2 + V_{\mathrm{m}}^2 - 2V_{\mathrm{k}} V_{\mathrm{m}} \cos(\theta_{\mathrm{km}})\right) \tag{10}$$

$$P_{\mathrm{loss}} = g_{\mathrm{km}} \left|\overline{V_{\mathrm{k}}} - \overline{V_{\mathrm{m}}}\right|^2 \tag{11}$$

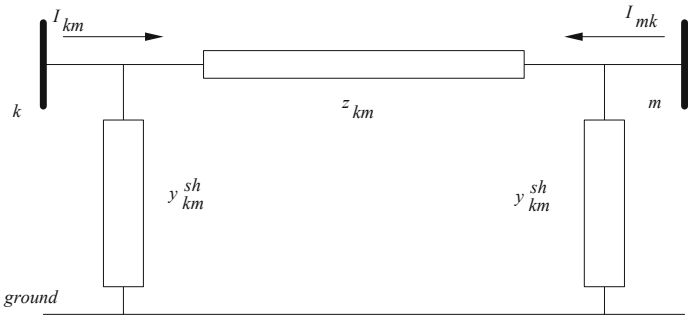


Fig. 1 Simple test bus system

The loss flow index covers both the line flows and losses based on voltage deviation from 1.0 p. u. at each of the buses. The loss flow index $\left(T_{ij}^{k}\right)$ for the allocation of DG can be expressed as below

$$T_{ij}^{k} = \left[\text{Maximum}\left|\frac{Pl_{\text{km}}}{Pl_{\text{km}}^{\max}}\right|\right] * \left[g_{\text{km}}|V_{\text{k}} - 1|^{2}\right] \tag{12}$$

where V_{k} is the peak voltage magnitude at bus k, g_{km} is the shunt suspectance and b_{km} is shunt conductance.

2.3 Congestion Management Problem Considering DG

The congestion in transmission lines is solved after placing the DGs at appropriate locations using the modified equations of (3)–(7) as expressed below

$$\text{Min} \sum_{i=1}^{N_{\text{g}}} G_{\text{gi}} + \sum_{p=1}^{N_{\text{DG}}} G_{\text{DGp}} \tag{13}$$

Here, the congestion management problem is solved after placing distributed generators at suitable locations based on the equations presented in (14)–(17) along with Eqs. (5) and (6) respectively.

$$P_{\text{gi}} = P_{\text{di}} + \sum_{j=1}^{N} \frac{\left(\delta_i - \delta_j\right)}{x_{ij}} \quad \forall i,\ i \neq p \tag{14}$$

$$P_{\text{gi}} + P_{\text{DGp}} = P_{\text{di}} + \sum_{j=1}^{N} \frac{\left(\delta_i - \delta_j\right)}{x_{ij}} \qquad \forall i = p \tag{15}$$

$$0 \leq P_{\text{DGp}} \leq P_{\text{DG}}^{\max} \quad \forall i = 1, \ , 2, \ldots, N_{\text{DG}} \tag{16}$$

$$G_{\text{DGp}} = \frac{1}{2} a_{\text{DGp}} P_{\text{DGp}}^{2} + b_{\text{DG}} P_{\text{DGp}} (\$ \text{ /hr}) \tag{17}$$

where, P_{DGp} is real power generated by DG placed at bus p, $P_{\text{DG}}^{\max}$ is maximum limit of real power generated by DG, N_{DG} is total number of DG units, a_{DGp}, b_{DGp} are emission coefficients of DG p.

3 Algorithm for Relieving Congestion in Transmission Lines

The present section depicts the steps in solving the congestion management problem using the proposed approach.

1. Study the data and obtain the solution for DC-OPF
2. Perform the load flow and obtain system conditions
3. Obtain the loss flow indices for the each bus with respect to each congested line
4. Place DG and solve the congestion management problem using modified equation as presented in Sect. 2.3
5. Perform load flow to check the congestion in line and stop.

4 Results

The methodology described above is simulated on IEEE-30 bus system which has six generators, 21 demands and 41 transmission lines. In its initial condition (base case), the test system has no DG allocation. The base MVA considered for the entire study is 100 MVA. For the base case, the congestion management problem is solved exclusive of DG. The results of DC-OPF produces the real power flows in each of the transmission lines, voltages at every bus, and total real and reactive power losses of the system. The maximum voltage magnitude of 1.082 p. u. is obtained at bus 11 and minimum voltage magnitude of 0.98 p. u. is obtained at bus 30. The total real power losses obtained in the base case are 11.834 MW. The line connected between the buses 1 and 3 is considered to be congested by adjusting its thermal limit to 60 MW. This implies the congested line connected between bus 1 and 3 is loaded with 105.65 % of its line limit. In this work, remedial action for reliving the congestion in transmission line has been taken by placing DG at the optimal locations. The load flow analysis for the base case depicts the state of the power system and helps in evaluating the loss flow indices. These are evaluated for each of the buses corresponding to congested line connected between the buses

Table 1 Preferred locations for DG placement by the loss flow index $\left(T_{ij}^{k}\right)$, Z_{bus} contribution factors and LMP-based approaches

Loss flow factor		Z_{bus} contribution factors [20]		LMP approach [28]	
T_{ij}^{k}	Priority	P_{ij}^{k}	Priority	LMP at bus k	Priority
−0.263	3	−0.2271	3	42.99	3
−0.0424	4	−0.1137	4	41.13	4
−0.0195	29	−0.0923	12	40.78	12
−0.0192	30	−0.0922	13	40.78	13
−0.0183	24	−0.0903	14	40.74	14

1–3. The top five results of the loss flow indices corresponding to the congested line in the network are presented in Table 1. This shows that the maximum negative value of loss flow index is obtained for the bus 3. Therefore, the DG placement at bus 3 would cause considerable shrinkage of real power flow in the line 1–3. The optimal location for the DG placement agrees with the locational marginal pricing-(LMP)based approach [28]. In LMP-based approach, rank of each bus for DG placement are decided according to descending values of respective LMPs. Table 1 shows the first five preferred locations for DG placement according to the loss factors, Z_{bus} based contribution factors [20], and LMP-based [28] approaches. It can be noticed that the optimal location and first suboptimal for the DG allocation agrees with other works as in [20, 28] but the second, third, and fourth suboptimal locations are differentiated form the previous research results. The transmission line congestion is relieved by solving Eqs. (13)–(17) considering 60 MW DG at optimal location. The values like real power flow and real power losses after placing DG are presented in Table 2. It has been observed that the congestion in the line is relieved by 11.51 % with critical contingency condition. This implies that the congestion in the line has been relived completely and can be loaded up to a greater extent for the future transmission transaction purposes. The results obtained after placing 60 MW DG at preferred locations are presented in Table 2 and Fig. 2. Figure 2 reveals that the magnitudes of voltages have been improved greatly after connecting the 60 MW DG at buses 29, 30, and 24, respectively. It is revealed that the line flow is more than its limit when a DG is incorporated at different suboptimal locations. Hence, increased rating of DG is connected at the suboptimal locations in order to relieve the congestion in transmission line.

Various capacities like 60, 70, and 80 MW are considered for the incorporation at the suboptimal locations and the results obtained are presented in Fig. 3. It is observed that line flows have been reduced after incorporation of higher capacity DGs at both optimal and suboptimal locations determined by the loss flow indices. It is also observed that 80 MW DG is found to be sufficient in reducing the congestion in the line 1–3 by placing at the preferred buses. However, the present study can easily be extended in this regard to choose an optimal capacity of DG.

Table 2 Comparison of various factors with and without DG placement

	Power flow in line 1–3 (Pl_{13})	Real power losses (P_{loss})
Without DG	63.36 MW	11.834 MW
60 MW DG at bus 3	56.82 MW	14.097 MW
60 MW DG at bus 4	63.06 MW	12.652 MW
60 MW DG at bus 29	67.78 MW	16.920 MW
60 MW DG at bus 30	67.78 MW	16.941 MW
60 MW DG at bus 24	65.72 MW	12.825 MW

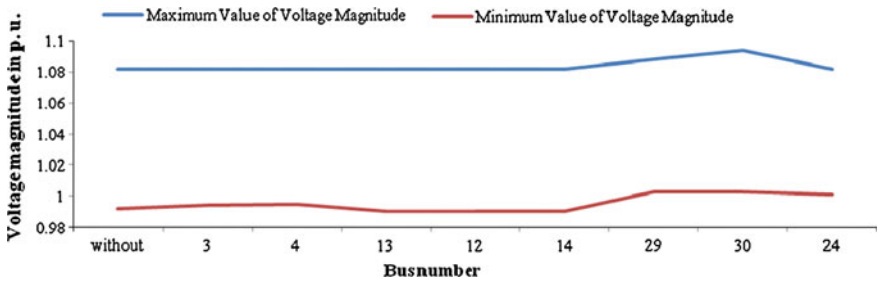


Fig. 2 Voltage profile of the buses in the electrical power network at different stages

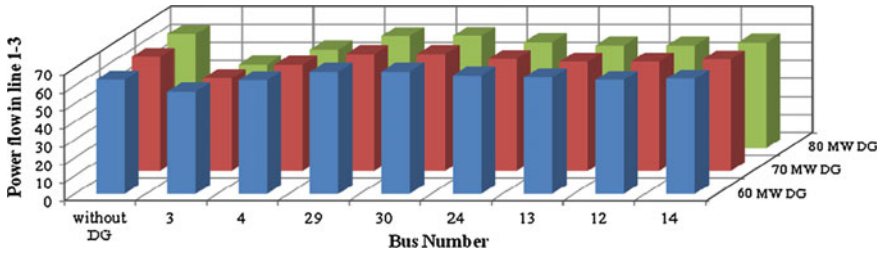


Fig. 3 Practical line flow in the congested line after placement of various capacities of DGs

5 Conclusion

In the present work, a new approach is introduced for finding the optimal locations of renewable DGs to relive the congestion in transmission line of the electrical power network. Loss flow indexes are recommended to obtain the optimal locations for incorporation of DGs into the existing network. It is observed that the real power losses are reduced up to 11.15 % when DG with 60 MW is connected to the electrical power network. It is observed that voltage profile is improved at all load buses significantly. The critical contingency condition has been relived and wide scope has been unlocked for further transmission line transactions. The methodology proposed in the work is advantageous in terms of improving the technical performance of the network and providing a larger scope for future transmission transaction purposes. Finally the results obtained were very effective and the effort made in this work was feasible for power system optimization problems.

References

1. Anbazhagan, S., Kumarappan, N.: Day Ahead deregulated electricity market price forecasting using neural network input featured by DCT. Energy conversion and management, 78 (2014) 711–719
2. Vinod Kumar Yadav, Padhy, N. P., Gupta, H.O.: Performance evaluation and improvement directions for an Indian electric utility. Energy policy 39 (2011) 7112–7120
3. Vinod Kumar Yadav, Padhy, N. P., Gupta, H.O.: A micro level study of an Indian electric utility for efficiency enhancement. Energy 35 (2010) 4053–4063
4. Medicherla, T. K. P., Billinton, R., Sachdev, M. S.: Generation rescheduling and load shedding to alleviate line overload-analysis. IEEE Trans. Power Appl. Syst. 98 (1979) 1876–84
5. Chan, S. M., Schweppe, F. C.: A generation reallocation and load shedding algorithm. IEEE Trans. Power Appl. Syst. 90 (1979) 26–34
6. Hazra, J., Sinha, A. K.: Congestion management using multi objective particle swarm optimization. IEEE Trans. Power Syst., 22 (2007) 1726–1734
7. Dutta, S., Singh, S. P.: Optimal rescheduling of generators for congestion management based on particle swarm optimization. IEEE Trans. Power Syst., 23 (2008) 1560–1569
8. Talukdar, B. K., Sinha, A. K., Mukhopadhya, S., Bose, A.: A computationally simple method for cost-efficient generation rescheduling and load shedding for congestion management. Int. J. Elect. Power Energy Syst., 27 (2005) 379–388
9. Kumar, A., Srivastava, S. C., Singh, S. N.: A zonal congestion management approach using real and reactive power rescheduling. IEEE Trans. Power Syst., 19 (2004) 554–562
10. Panigrahi, A. K., Ravi Kumar Pandi, V.: Congestion management using adaptive bacterial foraging algorithm. Energy conversion and management 50 (2009) 1202 – 1209
11. Acharya, N., Mithulananthan, N.: Locating series FACTS devices for congestion management in deregulated electricity markets. Electric Power System Research 77 (2007) 352–360
12. Yorino, N., El-Araby, E. E., Sasaki, H., Harada, S.: A new formulation for FACTS allocation for security enhancement against voltage collapse. IEEE Trans. Power Syst. 18 (2003) 3–10
13. Huang, T., Bompard, E., Yan, Z.: Congestion management impacts on bilateral electricity markets under strategic negotiation. Electric Power System Research 81 (2011) 1161–1170
14. Rodrigues, A. B., Da Silva, M. G.: Impact of multilateral congestion management on the reliability of power transactions. Electric power and energy systems 25 (2003) 113–122
15. Masoud Esmaili, Nima Amjady, Heidar Ali Shayanfar: Stochastic congestion management in power markets using efficient scenario approach. Energy conversion and management 51 (2010) 2285–2293
16. Subhasish Deb, Sadhan Gope, Arup Kumar Goswami: Congestion Management considering wind energy sources using evolutionary algorithm. Electric Power Components and Systems 43 (2015) 723–732
17. Masoud Esmaili, Esmail Chaktan Firozjaee, Hieder Ali Shayanfar: Optimal placement of distributed generations considering voltage stability and power losses with observing voltage related constraints. Applied energy 113 (2014) 1252–1260
18. Liu, J., Salama, M. M. A., Mansour, R. R.: Identify the impact of distributed resources on congestion management. IEEE Trans. Power Delivery 20 (2005) 1998–2005
19. Shahidehpour, M.: Distributed resources for transmission congestion and expansion management. Proceedings of IEEE Power Engineering Society Summer Meeting, pp. 1045–1048, Chicago, IL, 25 July 2002.
20. Singh, K., Yadav, V. K., Padhy, N. P., Sharma, J.: Congestion Management considering optimal placement of distributed generator in deregulated power system network. Electric power components and systems 42 (2014) 13–22

21. Aman, M. M., Jamson, G. B., Bakar, A. H. A., Mokhils, H.: A new approach for optimum simultaneous multi-DG distributed generation units placement and sizing based on maximization of system loadability using HFPA (hybrid particle swarm optimization) algorithm. Energy 66 (2014) 202–215
22. Almotaz Y. Abdelaziz, Yasser G. Hegazy, Walid El-khattam, Mahmoud M. Othman: A multi objective optimization for sizing and placement of voltage controlled distributed generation using supervised big bang-big crunch method. Electric Power Components and Systems 43 (2015) 105–117
23. Mohamed Imran, A., Kowsalya, M., Kothari, D. P.: A novel integration technique for optimal network reconfiguration and distributed generation placement in power distribution networks. Electrical power and energy systems 63 (2014) 461–472
24. Mohamed Imran, A., Kowsalya, M.: Optimal size and sitting of multiple distributed generators in distribution system using bacterial foraging optimization. Swarm and Evolutionary computation 15 (2014) 58–65
25. Antonio Jose Gil Mena, Juan Andres Martin Garcia: An efficient approach for the sitting and sizing problem of distributed generation. Electrical power and energy systems 69 (2015) 167–172
26. Gustavo Rosseti, J. S., Edimar J. de Oliveira, Leonardo W. de Oliveira, Ivo C. Silva Jr., Wesley Peres: Optimal allocation of distributed generation with reconfiguration in electric distribution systems. Electric power system research 103 (2013) 178–183
27. Mahmoud Pesaran, Abdullah Asuhaimi Mohd Zin, Azhar Khairuddin, Omid Shariti: Optimal sizing and siting of distributed generators by a exhaustive search. Electric Power Components and Systems 42 (2014) 1131 – 1142
28. Gautam, D., Mithulananthan, N.: Locating distributed generator in the LMP - based electricity market for social welfare maximization. Electric Power Components and Systems 35 (2007) 489 – 503

Design and Development of Android-Based BOT for Medicine and Food Distribution to Patients

Tanvi Mehta, Anita Gehlot and Dolly Sharma

Abstract The Android-based robot can be used for applications such as spy bots, it can also be used for supplying medicines to the patients. This Android-based robot which is driven by the "to and fro" movement of Android phone can also distribute medicines to the suffering patients. The robot is connected to the Android phone through Bluetooth module. In this research, a wireless robot is designed by using serial communication and Bluetooth process for wireless transmission of data and an Android mobile. A Bluetooth module has been interfaced with CPLD device and connected with Android operating system-based mobile. By using this mobile APP transmission of data to CPLD is done and it will receive data by using Bluetooth module and according to the requirement the robot will work. This application in mobile will transmit ASCII of the characters—"W," "A," "S," and "D" to the robot. The robot will receive these characters using Bluetooth module and it will perform the operations—"Forward," "Backward," "Left," and "Right."

Keywords VLSI · Robot · Android · Medicine

1 Introduction

Human and Machine interaction is becoming very important these days [1]. Information transfer between more than two or two devices can be done with the help of technology known as wireless communication. In case of wireless

Tanvi Mehta (✉)
Department of ECE, Gian Jyoti Group of Institutions, Shambhukalan, India
e-mail: tanvi05.er@gmail.com

Anita Gehlot
University of Petroleum and Energy Studies, Dehradun, Uttarakhand, India

Dolly Sharma
Department of Computer Science, Chandigarh Group of Colleges,
Landran, Mohali, Punjab, India
e-mail: dolly.azure@gmail.com

© Springer Science+Business Media Singapore 2017

R. Singh and S. Choudhury (eds.), *Proceeding of International Conference on Intelligent Communication, Control and Devices*, Advances in Intelligent Systems and Computing 479, DOI 10.1007/978-981-10-1708-7_61

communication, transference is done without the actual physical connection. Radio waves are best suited for the connectionless technology. It is suitable for both short as well as long distances. Radio technology is used worldwide in many eras of life such as wireless mice, satellite television, GPS units, PDAs, landline, and mobile phones, etc.

Robotics deals in designing such kind of bots that can replace human beings from uncomfortable environment, hazardous areas, also human fatigue is minimized. Moreover robotics focuses on the physical appearance of bots and emphasis that especially they should look more or less like us.

Biorobotics is completely inspired by the natural environment and conditions [2–5].

Robots mostly are implied for respective tasks, which human beings avoid, or they are fit into the places where size limitations are the issue or bottom of sea, also in the disastrous conditions, gesture-controlled robots can be targeted [6].

2 Proposed Model

In this research work a wireless robot is made by using serial communication. In this Bluetooth process for wireless transmission of data and an Android mobile is used [7]. Usually Bluetooth range is 10 m [8]. A Bluetooth module has been interfaced with our CPLD device and connected with Android operating system-based mobile. By using this mobile APP, we will transmit data to CPLD and it will receive data by using Bluetooth module and according to our requirement the robot will work. This application in mobile will transmit ASCII of the characters—"W," "A," "S," and "D" to the robot. And the robot will receive these characters using Bluetooth module and perform the operations—"Forward," "Backward," "Left," and "Right" [9].

2.1 Serial Communication Architecture

To obtain serial communication architecture by using VHDL serial communication logic is followed. According to this logic, to transmit data serially start and stop bits are to be sent to initialize communication. These bit functions are as follows:

- Start Bit: Start bit is use to initialize serial communication. It is initialized by sending bit "0" in data.
- Stop Bit: Stop bit is use to terminate serial communication. It is terminated by sending bit "1" in data.

Let us take an example, for transmitting data "A" serially, start bit is sent to initialize communication. And after transmission stop bit is sent to terminate serial

communication. ASCII code of the "A" is "01000001." To send this 8 bit data serially start and stop bits have to be sent with this. So total number of bits are going to transmit is 10.

Major point about the serial communication is that it is done on baud rates. There are several bauds which are used in serial transmitting of data. The hardware which we are going to use can transmit serial data over 9600 baud rate.

In our hardware we have used 8 MHz crystal oscillator, which means our oscillator is giving 80,00,000 pulses in one second. And at this rate timing delay is very small. So to increase our delay we will simply divide our frequency and make it 1 Hz. So that in one second it will give one pulse. So we will make a new clock for this. So we will place a counter for counting the pulses up to 40,00,000. After which new clock will change its phase.

To generate baud rate for serial communication, clock pulses are to be divided with baud rate. After this it will give us counter value for serial communication. VHDL code for generation of new clock and serial communication of data.

2.2 Bluetooth Module

Bluetooth acts as a boon for those people who share their media very frequently in their day-to-day life. Through this technique one can easily connect their personnel usage devices like smart phones, laptops by other peripheral [10]. One can also direct or transfer signals consuming low power using this. In the designing and development of this BOT, the signals of Android-based application are transferred to the main structure with the help of the Bluetooth module. It is not mandatory that structure should be in line of sight with the Bluetooth.

2.3 Algorithm of VHDL Coding for Robot

- Declare the libraries used for the program. In this all the libraries of VHDL are used.
- In the entity part of the code, the ports are declared. In this, two input ports clk (clock) and data are used with one output and one in out port as per the requirements.
- The architecture portion of the code consists of two processes. One process is for the generation of the clock signal and another process is for the further use of the clock signal.
- The second process consists of the main function of the robot. In this part four codes (ASCII of character "W," "A," "S," and "D") are provided which when combined with the Bluetooth application produce movements in the robot.

2.4 Technical Specifications of Bluetooth-Controlled Robot

This research work is accomplished by using the VLSI technology. CPLD of XC9500 series (CPLD XC9572) which consists of 72 macrocells has been used. The crystal oscillator of 8 MHz is used to give the clock pulse to CPLD. The 10 pin box header is used to make the connections between the CPLD and Bluetooth modem. In this 9 V batteries are used to give the power supply to the robot. Data is transmitted from Android phone via Bluetooth. L293D is used to drive motors of the rotating wheels.

2.5 Android Application of BT Robot Controller

Bluetooth of the smart phone is switched ON and it is paired with the circuit by using the password. The snapshot of the Smartphone Android Application window is shown in Fig. 3.

3 Results

Block diagram shown in Fig. 1 shows how the data is transmitted serially and robot is controlled. In this Android application BT ROBOT CONTROLLER is used (Fig. 2).

- Switch ON the Bluetooth of the smart phone and pair it by using the password 1234 or 0000 [11].
- Then select the device which is paired with the Bluetooth.
- As Bluetooth module is attached on the circuit, data. A is received by it on pressing UP key of the Smartphone Application. This received A signal is read by microcontroller and makes the BOT to move in FORWARD direction.
- Data B is received by the Bluetooth of the circuit, on pressing DOWN key of the Smartphone Application. This received B signal is read by microcontroller and makes the BOT to move in BACKWARD direction.
- Data C is received by the Bluetooth of the circuit, on pressing LEFT key of the Smartphone Application. This received C signal is read by microcontroller and makes the BOT to move in LEFT direction.
- Data D is received by the Bluetooth of the circuit, on pressing RIGHT key of the Smartphone Application. This received D signal is read by microcontroller and makes the BOT to move in RIGHT direction.
- As shown in Fig. 3 when STOP button is pressed, data E is received by the Bluetooth of the circuit, on pressing this Centre key of the Smartphone Application. This received E signal is read by microcontroller and STOPS the BOT.

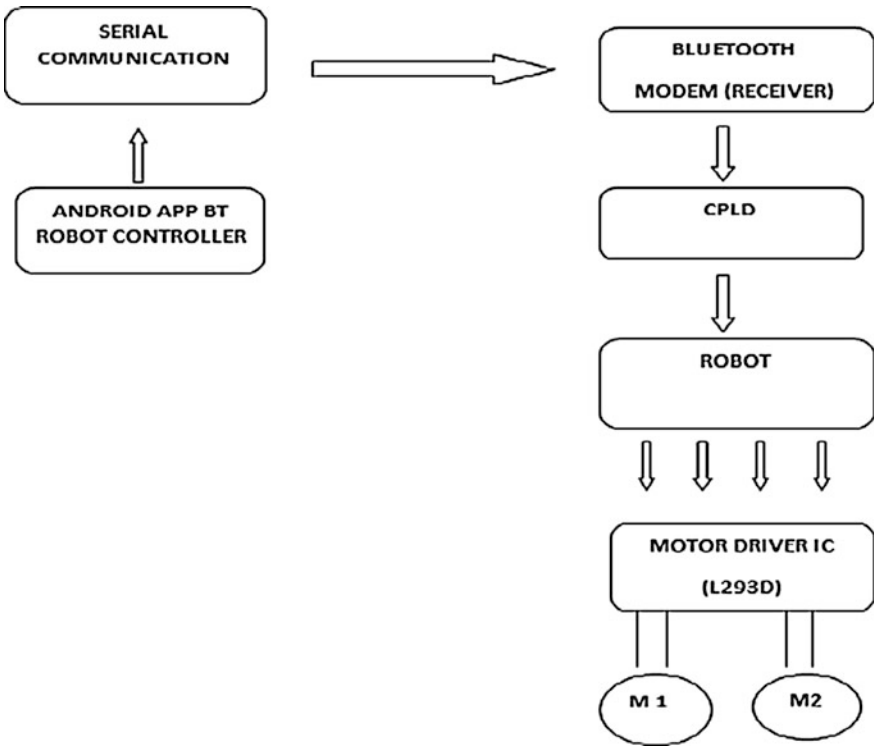


Fig. 1 Proposed model

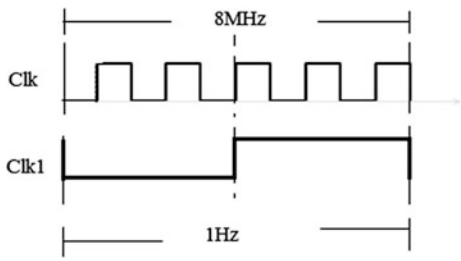


Fig. 2 Generation of new clock

3.1 Final Structure of Android-Based BOT

The final structure of Android-based BOT is shown in Fig. 4. Further this circuit can be placed into the mechanical structure of the trolley, as per the requirement of hospital for distributing the food and medicines to the hospitalized patients.

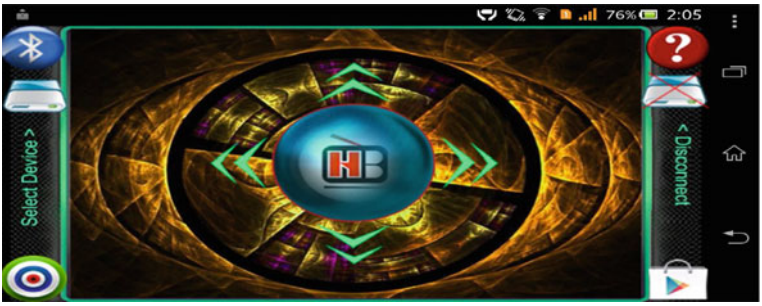
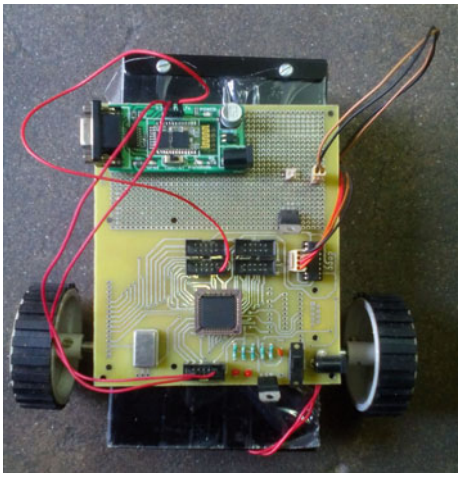


Fig. 3 Android application

Fig. 4 Bot architecture



4 Conclusion and Future Scope

A reliable smart phone-controlled BOT using VHDL is designed to distribute medicines and food in the hospitals. It can also act as spy robot in the fields with some additional features addition. This design and structure are quiet flexible in a sense that cameras and sensors can be used on it for using it in many other applications [12]. With few additions and modifications, this robot can be used in the borders for detecting and disposing hidden land mines.

References

1. Monika Jain, Aditi, Ashwani Lohiya, Mohammad Fahad Khan, Abhishek Maurya."Wireless Gesture control Robot: Analysis", in the proceedings of International Journal of Advanced Research in Computer and Communication Engineering Vol. 1, Issue 10, December 2012
2. Izaak D. Neveln1, Yang Bai, James B. Snyder, James R. Solberg, Oscar M. Curet, Kevin M. Lynch and Malcolm A. MacIver, "Biomimetic and bio-inspired robotics in electric fish research", The Journal of Experimental Biology 216, 2501–2514, 2013
3. Kevin Y. Ma, Pakpong Chirarattananon, Sawyer B. Fuller, Robert J. Wood, "Controlled Flight of a Biologically Inspired, Insect-Scale Robot", Science 03 May 2013: Vol. 340, Issue 6132, pp. 603–607 DOI:10.1126/science.1231806
4. Yoseph Bar-Cohen, "Biologically Inspired Intelligent Robotics", Paper 5051–02, Proceedings of the SPIE Smart Structures Conference San Diego, CA., Mar 2-6 2003
5. Ebrahim Abdulla Mattar, Khalid Al-mutib, "Bio-inspired Robotics Hands: A Work in Progress", Conference: 5th International ICST Conference on Bio-Inspired Models of Network, Information, and Computing Systems, At Boston, MA, Volume: 1, 667–675, 2012.
6. SwarnaPrabha Jena, Sworaj Kumar Nayak, Saroj Kumar Sahoo, Sibu Ranjan Sahoo, Saraswata Dash, Sunil Kumar Sahoo, "International Journal Of Engineering Sciences & Research Technology", IJESRT, Jena, 4(4): April 2015.
7. Arvind Kumar Saini, Garima Sharma, Kamal Kishor Choure, "BluBO: Bluetooth Controlled Robot", International Journal of Science and Research, National Conference on Knowledge, Innovation in Technology and Engineering (NCKITE), 10–11 April 2015, Kruti Institute of Technology & Engineering (KITE), Raipur, Chhattisgarh, India
8. Saliyah Kahar, Riza Sulaiman, Anton Satria Prabuwono, Nahdatul Akma Ahmad and Mohammad Ashri Abu Hassan "A Review of Wireless Technology Usage for Mobile Robot Controller", in the proceedings of International Conference on System Engineering and Modeling IPCSIT Vol. 34, 2012
9. Naga Phanindra, B. Suresh Ram' "Wireless Remote Control Car based Robot on ARM7", in the proceedings of International Journal of Engineering Trends & Technology (IJETT) volume 5 Numer 5, Nov 2013
10. Arita Dey, Akash Pal, Sayantan Nandi, Lusika Roy, "Three way controlled android Smartphone based robotic vehicle via Bluetooth", in the proceedings of International Journal of Advanced Research in Computer and Communication Engineering Vol. 4, Issue 9, September 2015
11. M. Selvam, "Smart Phone Based Robotic Control for surveillance applications", in the proceedings of International Journal of Research in Engineering &Technology, Vol. 3, Issue 3, March 2014.
12. Saurav Biswas, Umaima Rahman, Asoke Nath, "A New Approach to Control Robot using Android Phone and Color Detection Technique", in the proceedings of International Journal of Computer Science & Information Technologies, Vol. 6(3), 2015

Integration of Renewable Energy Resources for Rural Electrification

Sheikh Suhail Mohammad, Sachin Mishra, Sanjay Kumar Sinha and Vijay Kumar Tayal

Abstract Integration of renewable energy resources is a good solution for electrifying the remote unelectrified villages. In this paper, optimal and economical combination of renewable energy resources has been done using Homer software for the electrification of remote village, Kadura in the state of Jammu and Kashmir. The renewable energy resources that we have considered in our case are hydro, solar, and wind. First the commercial, domestic, industrial, agricultural, and irrigation load demand have been estimated of this particular area. The optimized combination provided cost-effective and reliable electricity to this remote unelectrified village. The paper also explains sensitive analysis of external disturbances like climatic changes or technical snags that would affect the overall optimal combination. The combination provided by integrating renewable energy resources is environment friendly which is the most challenging task for modern power sector.

Keywords Integrated systems · Off-grid electricity · Optimization · Cost-effective solution · Environment

1 Introduction

About 1.2 billion of the world's total population is without electricity until 2015 [1]. Providing cost-effective and reliable electricity to such remote areas is still a big challenge and wide open.

Taking a look on Indian topography, it is very diverse with its remote areas hilly in the north and east, desert in the west, coastal in the south, and plain in the central. As per census 2011 there are around 68,227 villages without electricity [2]. The most feasible solution in covering unelectrified areas is to do grid extension, but this

S.S. Mohammad (✉) · Sachin Mishra · S.K. Sinha · V.K. Tayal
Department of Electrical and Electronics, Amity University,
Noida, Uttar Pradesh, India
e-mail: ssuhail73@gmail.com

© Springer Science+Business Media Singapore 2017

R. Singh and S. Choudhury (eds.), *Proceeding of International Conference on Intelligent Communication, Control and Devices*, Advances in Intelligent Systems and Computing 479, DOI 10.1007/978-981-10-1708-7_62

solution works well where access is easy. Areas which are very remote grid-connected electricity options fail.

Providing electricity to such remote areas, by integrating different renewable energy sources proved to be a cost-effective and reliable solution. However before integrating renewable energy resources, we need to find which combination is going to be optimal one, for finding this optimal combination, we have used Homer. The goal of our study is to find the optimal combination of renewable sources for a particular village under study, which would provide cost-effective and reliable electricity to this village and met with its load demand effectively [3].

2 Methodology

The methodology adopted in this paper for integration of renewable energy resources for providing reliable electricity supply to a rural area considered is shown in Fig. 1.

2.1 Reconnaissance Survey

Before going for the analysis a survey of the case study has to be carried out. It includes the details of the village name, village load assessment, village resource assessment, and component assessment.

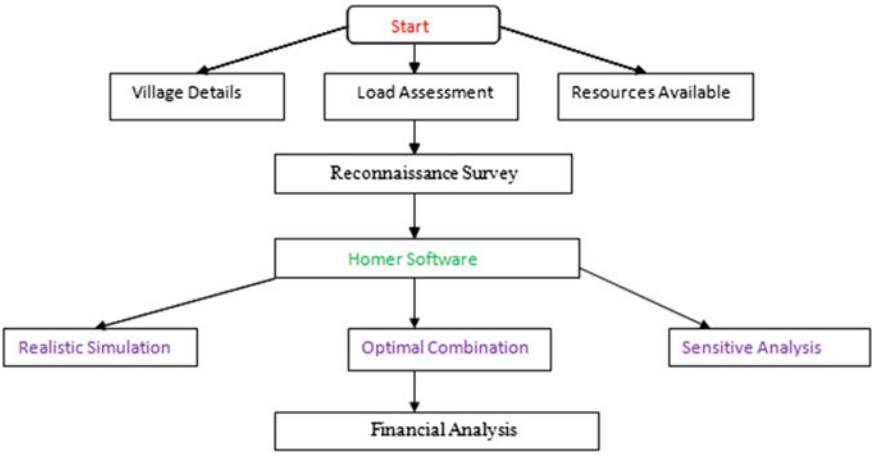


Fig. 1 Methodology flowchart

2.1.1 Village Details

The village considered for the case study is Kadura village under Bandipora district of Jammu and Kashmir (India) [4].

2.1.2 Resources Assessment

Figures 2 and 3 show the yearly solar and wind speed profiles, respectively [5].

2.1.3 Village Load Estimation/Prediction

The overall load estimated is shown in Table 1. Figure 4 shows the predicted load profile for the village considered.

2.1.4 Component Assessment

The solar photo voltaic (SPV) panels are connected in series. The capital cost for 1 kW SPV was considered to be $3000 with replacement cost $3000. Since there is little maintenance required, we have taken operation and maintenance cost equal to 10$/yr, we have considered life time and derating factor to be 20 % and 80 %, respectively.

A generic 10 kW horizontal- axis wind turbine is considered for simulation purposes. It gives a DC output of 10 kW. The capital and replacement cost for one unit was considered to be 10000$ and 90000$, respectively, with operation and maintenance cost equal to 500$/yr. Life time (yrs) and Hub height(m) were considered to be 15 and 25, respectively.

The SHP was designed for 363 kW AC output. The turbine was designed for 170 m head, 290L/S flow rate, 75 % efficiency, and pipe head-loss 5 %, The capital

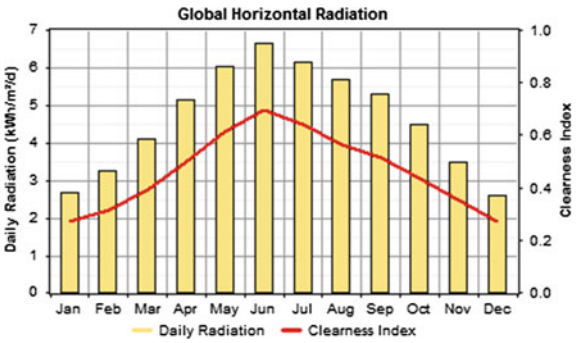


Fig. 2 Solar profile. *Source* https://eosweb.larc.nasa.gov/sse/RETScreen/

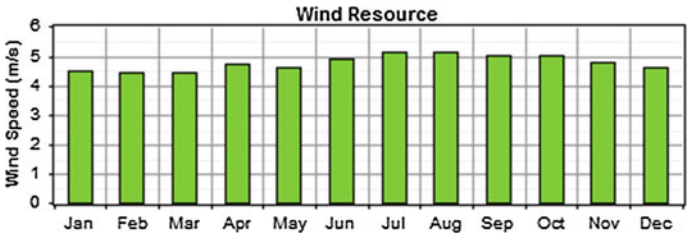
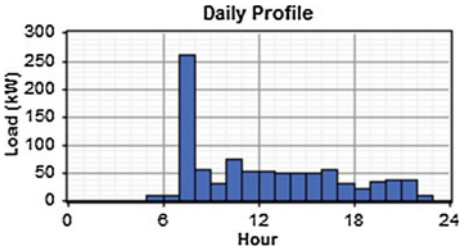


Fig. 3 Wind profile. *Source* https://eosweb.larc.nasa.gov/sse/RETScreen/

Table 1 Load profile

Load	No. in use	Summer (May to October) per day	Winter (November to April) per day
		Watt Hrs	Watt Hrs
Domestic purpose			
No. of house holds	468	563940	375804
Industrial/commercial/community purposes			
Total	–	84600	84600
School			
Total	01	2002	916
Health center (dispensary)			
Total	01	12912	8192
Irrigation and agriculture load			
Total	–	259988	236116

Fig. 4 Daily load profile



cost and replacement cost for 318 kW SHP were as taken 544500$ and 435600$, respectively, and operation and maintenance was considered 18.15 $/yr [6].

The battery type taken was Trojan L16P with quantity equal to 40, capital cost per battery is 300$, replacement cost taken was 300$ per battery, and operation and maintenance cost equal to 20$ per battery.

The converter size considered was 6 kW, with capital cost and replacement cost equal to 1000$ per converter, operation and maintenance cost taken was 600$ [6].

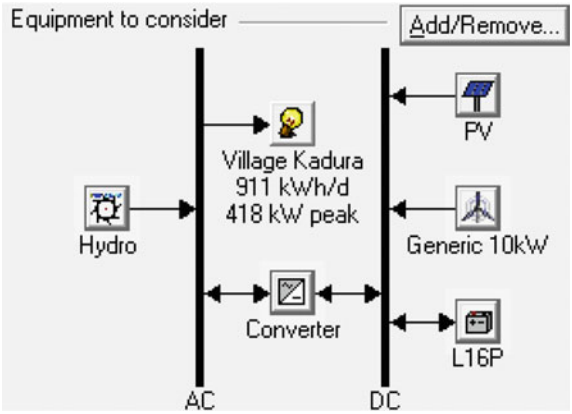


Fig. 5 Simulation model for integrated renewable energy system

2.1.5 Sensitive Inputs

For wind speed the two sensitivities entered are 4.5 m/s and 5.1 m/s. For daily solar radiation the two values entered are 2.6 kWh/m^2/d and 6.64 kWh/m^2/d. For hydro design flow rate 320 L/s and 4500 L/s are entered.

2.2 Simulation Model

After the survey of site, the data collected are used for the development of the simulation model of integrated renewable energy system which will be implemented for our case study. Figure 5 shows the required simulation model.

3 Results and Discussions

The optimal combination obtained is of 700 kW hydro, 60 Generic 10 kW, 363 kW PV, 40 Trojan L16P, 6 kW rectifier, and 6 kW inverter. The total net present cost (NPC), Levelized COE (Cost of Electricity), and capital cost for such an integrated scheme are $ 3,611,295, $0.850/kWh, and 3,262,500, respectively. The operating cost per year was found to be $ 27,285/yr. Figure 6 shows the monthly distribution of electricity produced by the optimal combination. As from the results it is very clear that from April to August, when the water discharge is good, the load is met by hydroelectricity. But from October to March the river discharge decreases and the peak load is met by the wind and solar power. It is evident that about 83 %, 9 %, and 7 % are shared by hydropower, wind power, solar power, respectively. Since by this combination, we are generating extra power it means that if number of household increase in future load can be met by this scheme.

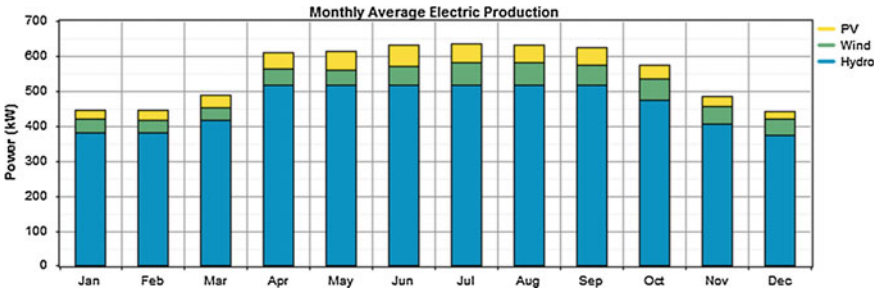


Fig. 6 Monthly average electricity production by integrated system

It is very clear from the cash flow summary that about 60 % of initial investment will go for photovoltaic's system. 18 % initial investment will go for wind power and 17 % will go for hydro power. Figure 7 shows cash flow summary.

Although the optimal combination obtained satisfies the demand, but the initial investment for the project is huge. There should be some utility, government organization, or some private authority, which could take the project for practical implementation. The solution which is technically feasible and also provides cost of each and every component, but a business model is not covered. So we need to form a team that would find the business model, which will decide the tariffs for this area. Business model is very important to take subsidy and discounts into consideration moreover, this area is unelectrified, so there is no electricity market experience. The realistic demand estimation, recovery cost, technical manpower, logistics, and poor transport facilities should be given a due consideration to avoid bad investments.

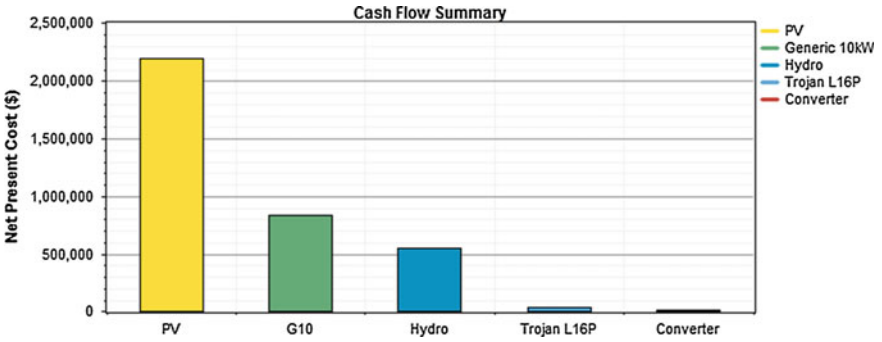


Fig. 7 Cash flow summary

4 Conclusion

The case study resulted in finding an optimal combination of renewable energy resources that will satisfy the predicted load demand of the remote border village. The optimal combination consists of solar, wind, and hydropower that satisfies demand at a cost of 0.850/kWh. The base load is met by hydroelectricity and peak load by combination of solar and wind power. The optimal combination was provided. The extra energy generated during summers could electrify neighboring unelectrified villages in combination with some other renewable energy source. In our case we are integrating renewable energy resources, therefore the proposed combination is environmental friendly because carbon dioxide, carbon monoxide, hydrocarbons, particulate matter, sulfur dioxide, and nitrogen dioxide are all zero in our case.

References

1. World energy outlook 2015: International Energy Agency; 2015
2. http://www.cea.nic.in/reports/others/planning/pdm/growth 2015 [Accessed 02,01,2016]
3. Rohit Sen, Subhes C. Bhattacharyya "Off-grid electricity generation with renewable energy technologies in India: An application of HOMER" Renewable Energy 2014;62:388–398
4. http://www.censusindia.gov.in/ [Accessed Feb 08, 2016]
5. https://eosweb.larc.nasa.gov/sse/RETScreen/ [Accessed Oct 10, 2015]
6. http://www.homerenergy.com/pdf/HOMERHelpManual.pdf [Accessed Feb 15, 2016]

A Vision of IoT: Applications, Challenges, and Opportunities with Dehradun Perspective

Mainak Mukherjee, Isha Adhikary, Surajit Mondal, Amit Kumar Mondal, Meenakshi Pundir and Vinay Chowdary

Abstract In this paper, the emphasis has been the application of Internet of the things (IoT) system on an urban (Dehradun) prospective, that is a broader category which has been subdivided into specific application domain. Urban IoT's are planned to support modern smart cities. The prime objective behind IoT-based smart cities is to harness the advanced communication technologies to support the value-added services of city administration for the citizen. This paper provides a proposed in-depth suitable technologies, protocol, and network architecture for Dehradun city.

Keywords Smart city · Network architecture · Sustainable development · Dehradun

1 Introduction

The Internet of Things (IoT) is a modern epitome, in which all the everyday objects equipped with communication module with suitable protocol communicate with each other as well as with the users, becoming an fundamental part of the internet [1, 2]. IoT grants access to the following devices: home appliances, monitoring sensors, surveillance cameras, displays, vehicles, actuators etc., which indeed can be applied to various other domains such as industrial automation, medical aid, home automation, mobile healthcare, smart grids, traffic management, energy management, assisting elderly people etc. By adoption of IoT for a city infrastructure, while decreasing the operating costs of public administration, proves the concept of smart city [3, 4]. Hence an IoT-based smart city provides the following benefits: optimization of traditional public services, salubrity of schools and hospitals, maintenance of public areas, lightning, surveillance, transport and parking,

Mainak Mukherjee · Isha Adhikary · Surajit Mondal · A.K. Mondal (✉) · Meenakshi Pundir · Vinay Chowdary
University of Petroleum and Energy Studies, Dehradun, India
e-mail: akmondal1603@gmail.com

© Springer Science+Business Media Singapore 2017

R. Singh and S. Choudhury (eds.), *Proceeding of International Conference on Intelligent Communication, Control and Devices*, Advances in Intelligent Systems and Computing 479, DOI 10.1007/978-981-10-1708-7_63

power distribution and energy management etc. In this paper, a comprehensive review-based solution has been provided for Dehradun (located between 30° 15′ 58″ N to 30° 24′ 16″ N latitude and 77° 58′ 56″ E to 78° 06′ 05″ E longitude, covering an approximate area of 350 km^2, with 93 % mountain and 64 % forest covering), Uttarakhand, India as a smart city for enabling technologies, protocols, and architecture for an IoT.

2 Smart City Concept and Services

In this section, we outline some of the key service sectors that might be facilitated by an IoT service to make Dehradun a smart city, as realizing them will increase the quality of the services presented to the citizens while providing an economical gain for the city admin. Keeping in mind the developmental economy of India, only those services that furnishes social value with clear return of investment have been produced here (same has been summarized in Table 1, with suggested type of network, traffic rate, delay, device powering etc.). From the geographical pattern of Dehradun it is clear that a single communication and service architecture is not feasible enough to solve the objective, indeed we need different mechanism on the basis of the region.

Table 1 Proposed services specification for Dehradun smart city

Service	Network type(s)	Delay	Energy source
Earthquake monitoring	802.15.4; WiFi, and Ethernet	30 min for data; 10 s for alarms	Battery powered
Building health		30 min for data; 10 s for alarms	Mains powered, battery powered, or photovoltaic panels
Landslide detection		30 min for data; 10 s for alarms	Battery powered
Energy management (smart parking, smart lighting)	Power line communication and Ethernet	5 min for data	Mains powered
Automation of public buildings	802.15.4; WiFi and Ethernet	10 min for data	Mains powered, battery powered or photovoltaic panels
Air quality and noise monitoring	802.15.4; Bluetooth; WiFi and Ethernet	5 min for data	Photovoltaic panels; battery powered

2.1 Earthquake Monitoring

Dehradun falls under seismic zone 5 and 4 of Indian seismic code (IS:1893-1984), which makes it susceptible to natural disasters. Dehradun has been short-listed by United Nations Development Program (UNDP) as one of the most earthquake prone city in India. Proper maintenance of buildings, city infrastructure, and its citizen requires continuous monitoring of seismic waves. Due to the harsh weather of Himalayan ecology, most of the building materials of Dehradun are category A2, A3, B, C1, but still built engineering are not perfect enough to sustain medium magnitude earthquake. Uttarakhand is already installed with earthquake monitoring system which detects the *p-wave* and generates alarm, providing a reaction time of 1–40 s [5]. Currently the system is not implemented in a full phase manner due to the high investment cost. Subsequently to monitor the structural health of the city buildings combination of seismic readings with vibration sensors implanted in buildings can lead us to better understanding of earthquake impacts on city buildings. The practical apprehension of this service demands installation of sensors in and around Dehradun and in its buildings which are interconnected with a control system.

2.2 Landslide and Forest Fire Monitoring

The stability of a slope is dependent on a variety of time independent and dependent factors, which lead to land sliding. Few of the factors are as follows:

i. Unfavorable geology like loosening of soil layers and increase or decrease in ground water level or continuous rainfall.
ii. Soil composition and topography and Seismic activities due to natural or artificial source.
iii. Stress-induced fatigue and chemical weathering.
iv. Cold Environment processes (permafrost degradation, freeze thaw processes).

An effective early warning system pertaining to landslides should possess the following features:

i. Monitoring, data acquisition, transmission, and health of the sensor.
ii. Analysis and forecasting based on the threshold values of the parameter assigned.
iii. Sufficient reaction time.

There are various types of sensors available to monitor the landslide, but considering Dehradun, Extensometers will be the best suited. Extensometers are positioned on vulnerable places on a slope to monitor its displacement. A set of extensometers are placed on the vulnerable site and they communicate wirelessly to a central node. Extensometers are kept inside tough steel shelters to limit the

instrumental (radio processors, transducers, analog to digital converter, data logger, and gateway) damage. On the basis of monitored per day shift (mm/day) of land, different set of alarms can be generated. Dehradun district receives an average annual rainfall of 2073.3 mm. Most of the annual rainfall in the district is received during the months from June to September, July and August being rainiest. As there is no clear correlation between precipitations and displacements, hence monitoring frequency during rainy weather has to be increased. Dehradun is covered 70 % with forest; hence by Identification of potential forest fire risk zones or mapping of vulnerable forest fire zones is necessary to implement warning system for forest fires.

2.3 Waste Management

Waste management is a major issue in a city like Dehradun. Being a major tourist attraction, a clean environment is a necessity. Use of IOT for smart waste management will significantly increase efficiency and economical and ecological benefits. Currently waste collection logistics are carried out by clearing containers or bins as and when found necessary. This system has many deficiencies:

i. Time consuming and also the operational efficiency is low.
ii. Improper cleaning due to inefficient human labor.
iii. High costs.
iv. Greater traffic congestion.
v. More fuel consumption, due to continuous movement of trucks, whether full or empty.
vi. Increased noise and air pollution as a result of more trucks on the road.

The optimisations of these services are required to reduce infrastructural, operating, and maintenance expenditures, as well as the contamination of directly associated with waste collection. Intelligent waste management solution includes applying technology (electronics and applications) to the existing operating system to empower bi-directional communication amid the infrastructure positioned in the city and service operators. The idea is to avert the focus on collection routes based on the fill levels of the containers. Intelligent and efficient waste logistics is possible today through:

i. A centralized real-time embedded system for control and analysis applications.
ii. Real-time information of waste deposition containers.
iii. Monitored truck routes using GPS, so that remote and dynamic arrangement of the routes can be decided on the basis of need and traffic on road.

This will create an optimized path for both Service Managers and citizens which results in major budgetry savings and less urban pollution.

2.4 Traffic Congestion

Due to the hilly topography of Dehradun, traffic congestion and frequent road accidents are prevailing factors. So traffic monitoring systems are of utmost necessity. Communication-based traffic monitoring is a potential Smart City service. This can be done using GPS trackers on vehicles and also air quality and acoustic sensors along the roadside. The city authorities can use the information to discipline traffic and send help quickly as and when needed. The local people can use the same to plan the route to be taken in advance.

2.5 Energy Management

Our world is changing, and as a result of continued urbanization, cities are playing an ever-greater role as the new 'units of change.' Cities are at risk from overcrowding and the security of basic utilities (public lighting, transportation, traffic lights, surveillance cameras, heating/cooling of buildings etc.), as well as pollution and natural or anthropogenic disasters, all of which are closely linked with energy, a basic 'lifeline.' The current energy chain has been built to operate in one direction—from source to consumer. We see four key elements that play important roles within that framework:

i. The ability to inform and shape demand so that energy is consumed when there is sufficient and affordable supply (and not vice versa, as is the case under the current paradigm); so that peak demand is reduced.
ii. Physical devices or gadgets, ranging from smart meters that measure energy consumption in real time to smartphones and in-home devices (IHDs) that make it easy to access data.
iii. An information platform which connects devices, from which progress can be measured, benefits can be pinpointed, financials are tracked and through which the necessary stakeholders are aligned.
iv. Integration of alternative (renewable) energy sources, as well as new consumption and storage devices such as the batteries of electric vehicles.

2.5.1 Urgency to Act

i. Worldwide CO_2 emissions rose by 1.4 % to 31.6 billion tons in 2012—reaching a record high, according to the International Energy Agency.
ii. According to the CDP Cities 2013 report, 39 cities reported increased efficiency of operations as a result of responding to climate change.

3 Urban IoT Architecture

From the analysis of the services mentioned above, it is clear that we need a centralized architecture having the ability of adding different technologies with existing facilities to support the progressive evolution using IoT. The fundamental benefit of using IoT-based urban infrastructure is easy accessibility of data by authorities and citizen, which increases the responsiveness and awareness in public matters.

3.1 Web Service-Based Architecture

In IoT domain many standards are available, but the Internet Engineering Task Force (IETF) standard is widely accepted due to open and royalty free nature, based on Internet's best practices and can count on a wide community. To realize the web services of IoT-based nodes, interoperability is required, which is met using Representational State Transfer (ReST). The current standards for internet communications are based on *unconstrained* protocol and are commonly used by internet hosts like eXtensible Markup Language (XML), HTTP, and IPV4. An urban IoT system entails both constrained and unconstrained protocol stack. But unconstrained protocol requires large data format and speed, to compensate it, *constrained* protocol are been used, which are mirrored of unconstrained protocol and in the same time they are not complex. In order to give insight detail of the protocol architecture, three distinct functional layers with interoperability among the layers are explained below as follows:

i. *Data Format*: In architecture based on IoT, data exchange is based on few standards set up by World Wide Web Consortium (W3C) and has proposed to use EXI format as constrained devices are also compatible with EXI format. Although XML is the common format but the size of XML messages are too large for constrained devices.
ii. *Application and Transport Layers*: For IoT-based architecture Constrained Application Protocol (CoAP) transported over User Datagram Protocol (UDP) is best suited due to the following reasons:

   (a) It supports ReST methods of HTTP (GET, PUT, POST, and DELETE)
   (b) One-to-one correspondence between different response codes of protocols.
   (c) Interoperation with native HTTP devices and applications.

iii. *Network Layer:* IoT networks demand billions of nodes with unique addresses, which is not possible by IPv4 due to its exhaustion, hence IPv6 addresses is the solution for it. But IPv6 are having overheads, which are not compatible with constrained devices, hence 6LoWPAN compression format is been used for IPv6 and UDP.

3.2 Link Layer

From Sect. 3.1 It is clear that constrained protocol best suits our purpose hence physical and link layers are described by low energy consuming and slow transfer rate types, i.e.,it exhibits long latencies. Prominent solutions will be Bluetooth Low Energy, IEEE 802.11 Low Power, Power line Communication (PLC), NFC, RFID, and IEEE 802.15.4.

3.3 IoT Peripheral Nodes

At the site level, IoT nodes deliver the data to control center. These nodes have to be cheap and low power consuming type. Mobile and radio devices can provide access to IoT devices in many ways: through IP connection, direct connection over short range wireless technology, low power Wi-Fi or Bluetooth.

4 Conclusion

In this paper we have analyzed the solutions recently available for the implementation of urban IOTs. For standardization the discussed technologies are closed and in respect to industry it will give an immense impact. There are numerous design options for IOT systems are available but the set of open and standardized protocols are limited. Regarding securely embrace to IOT new challenges required new thinking by that new possibilities can come through and it should avoid operational sides, as networking and convergence are the key. Security must be pervasive inside and outside the network and it should be devised and data agnostic, proactive and intelligent way. At last it can be said that focus must be given on timely passing of information, intelligence, not data convergence, additionally analytic speed is essential for real-time discussion.

References

1. Atzori, L., A. Iera, and G. Morabito, *The Internet of Things: A survey.* Computer Networks, 2010. **54**(15): p. 2787–2805.
2. Li, S., L. Da Xu, and S. Zhao, *The internet of things: a survey.* Information Systems Frontiers, 2014. **17**(2): p. 243–259.
3. Schaffers, H., et al., *Smart Cities and the Future Internet: Towards Cooperation Frameworks for Open Innovation.* Future Internet Assembly, 2011. **6656**: p. 431–446.
4. Walravens, N. and P. Ballon, *Platform business models for smart cities: from control and value to governance and public value.* Communications Magazine, IEEE, 2013. **51**(6): p. 72–79.
5. Talwar, G., *U'khand gets India's first fully functional quake warning system*, in *Times of India* 2015: Dehradun.

LQR and PID Design Technique for an Electric Furnace Temperature Control System

Devendra Rawat, Kritika Bansal and Alok Kumar Pandey

Abstract This paper presents a Linear Quadratic Regulator Controller design for Temperature Control of an Electric Furnace System using MATLAB. Also, Proportional-Integral-Derivative (PID) Controller is designed for control of an Electric Furnace. The three PID parameters K_p, K_i, and K_d are obtained using two tuning methods, Ziegler Nicholas and Tyreus Luyben. Performance of the system using LQR and PID (using Ziegler Nicholas and Tyreus Luyben) control techniques for an Electric Furnace Temperature System is compared by analyzing the Time Response of the system. The result of simulation shows that LQR technique gives better performance for the given system.

Keywords LQR · PID controller · Ziegler Nicholas tuning · Tyreus Luyben tuning · Electric furnace

1 Introduction

Electric Furnace is widely used in various industrial production processes. To generate heat, Electric Furnace uses electricity as its main power source. A few extremely complex methods for control of Electric Furnace Temperature System have already been proposed like Neural Network, Adaptive Fuzzy Control and Fuzzy PID [1–4]. However, many of these algorithms are highly complex and thus, difficult to be realized. Currently, PID controller is used for control of electric

Devendra Rawat (✉)
Department of Electrical Energy and Power, UPES, Dehradun, India
e-mail: d.rawat@ddn.upes.ac.in

Kritika Bansal
Electronics and Communication Department, JECRC, Jaipur, India
e-mail: kritikabansal.ece@jecrc.ac.in

A.K. Pandey
Electrical Department, KIET, Ghaziabad, India
e-mail: alok.pandey@kiet.edu

© Springer Science+Business Media Singapore 2017

R. Singh and S. Choudhury (eds.), *Proceeding of International Conference on Intelligent Communication, Control and Devices*, Advances in Intelligent Systems and Computing 479, DOI 10.1007/978-981-10-1708-7_64

furnace temperature systems. The PID control [5] design is very popular and there are many methods for tuning of PID parameters such as, Ziegler Nicholas [6], Tyreus Luyben [7], Cohen Coon [8], Direct Synthesis [9], Particle Swarm Optimization [10], Genetic Algorithm [11], and Differential Evolution [12].

In this paper, control of electric furnace temperature system has been done using PID control method and LQR technique. The PID controller parameters are obtained using Ziegler Nicholas tuning method and Tyreus Luyben tuning method. The results thus obtained using LQR technique and PID control method are compared by analyzing the Time Response of the system.

After a brief introduction, electric furnace temperature system is discussed in Sect. 2, followed by system stabilization using PID control technique and LQR technique in Sect. 3. In Sect. 4, the result of the stabilization techniques is compared. And finally, conclusions are drawn in Sect. 5.

2 Electric Furnace Temperature System

An electric furnace temperature control system consists of an electric furnace, a controller and a thermocouple as shown in Fig. 1 where w is the voltage given at the input of the system, R is the armature resistance, U is the controller output voltage and y is the thermocouple output voltage.

The transfer function of the electric furnace to be controlled is given as [13]

$$G(s) = \frac{0.15}{s^2 + 1.1s + 0.2}. \tag{1}$$

A delay of 1.5 is also used. Therefore, the transfer function of the electric furnace system with a time delay of 1.5 is [13]

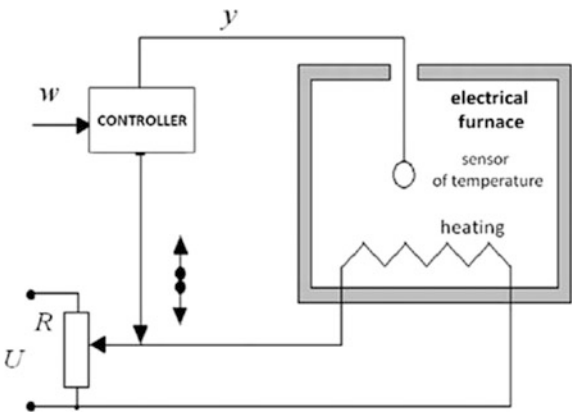


Fig. 1 Basic block diagram of an electric furnace temperature control system [13]

$$G(s) = \frac{0.15}{s^2 + 1.1s + 0.2} e^{-1.5s}. \quad (2)$$

After solving Eq. (2) the final transfer function will be,

$$G(s) = \frac{-0.1125s + 0.15}{0.75s^3 + 1.825s^2 + 1.25s + 0.2}. \quad (3)$$

3 Controller Design and Simulation Results

PID controller using Ziegler Nicholas and Tyreus Luyben tuning method and LQR technique is used for temperature control of an electric furnace system. Figure 2 shows the block diagram of an electric furnace system with temperature controller.

3.1 PID Controller

To implement a PID controller, three parameters needs be determined for the given process: proportional gain K_p, integral gain $K_{i,}$ and derivative gain K_d [14].

Increasing K_p reduces the steady state error and rise time but increases the overshoot. Integral control eliminates steady state error but it can increase the overshoot. K_d reduces overshoot but increases the settling time [14].

This controller has a transfer function as [6],

$$G_{PID} = K_p + \frac{K_i}{s} + sK_d \quad (4)$$

PID Controller is designed using Ziegler Nicholas tuning method and Tyreus Luyben tuning method. The parameters thus obtained using the two tuning techniques is given in Table 1.

The step response after using these values in Eq. (4) for the two tuning methods is shown in Figs. 3 and 4 respectively.

The time response in Fig. 3 shows that the system with PID controller using Ziegler Nicholas tuning method gives a peak overshoot of 43 % which is quite high

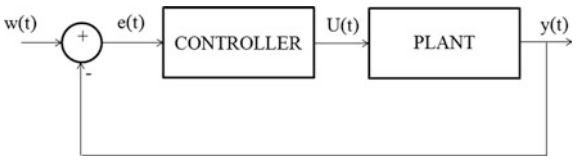


Fig. 2 Plant with controller

Table 1 PID parameters using Ziegler Nicholas and Tyreus Luyben tuning method

Parameters	Zeigler Nicholas method	Tyreus Luyben method
K_p	4.026	3.05
K_i	1.0323	0.177
K_d	3.925	3.776

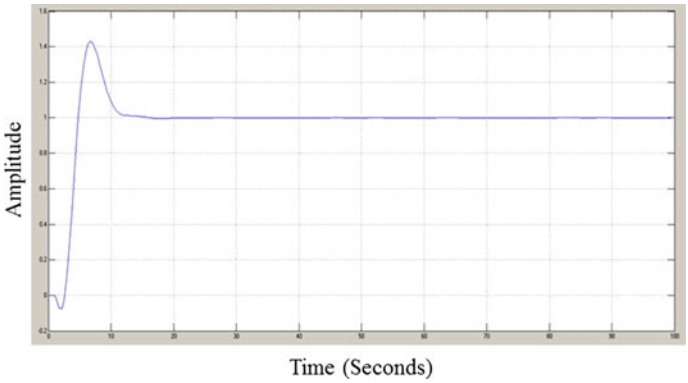


Fig. 3 Step response using Ziegler Nicholas tuning method

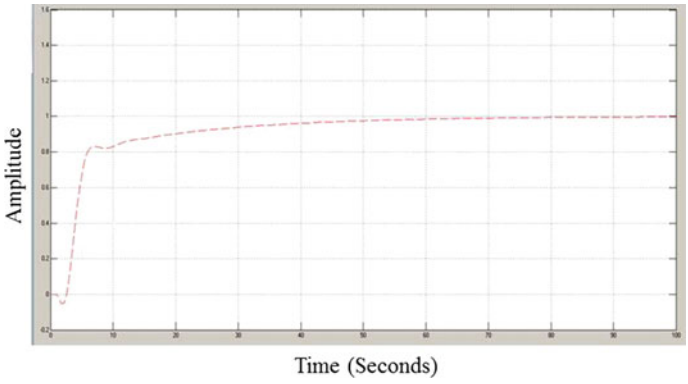


Fig. 4 Step response using Tyreus Luyben tuning method

with comparatively low rise time of 1.63 s. Also, system settles down at 11.6 s with zero steady state error whereas the step response in Fig. 4 shows that when Tyreus Luyben method is used a very high rise time of 16.4 s and settling time of 54 s.

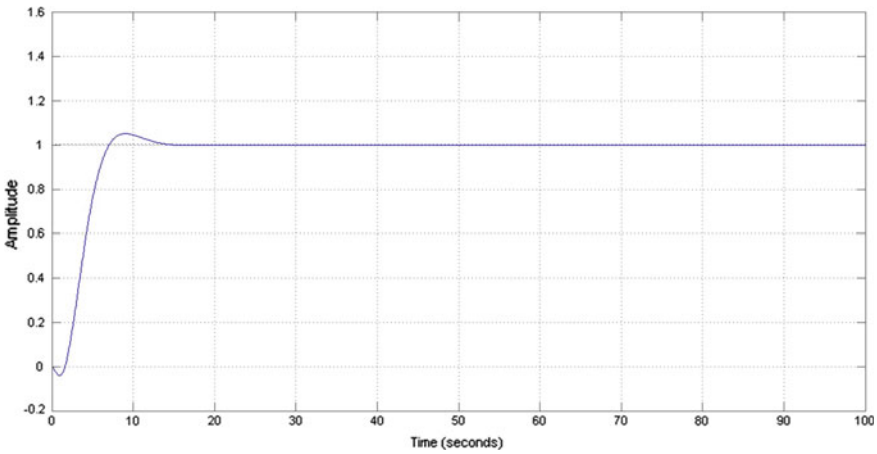


Fig. 5 Step response (LQR)

3.2 LQR Technique

Stabilizability of the pair (A, B) is a necessary condition for the existence of an optimal solution using LQR [15]. The gain matrix K calculated is given as

$$K = [0.0446 \quad 0.1094 \quad 0.0667]$$

Figure 5 illustrates the step response of the Electric Furnace Temperature system with LQR control technique. The time response shows that the system has a peak overshoot value of 5.03 % which is quite low with a rise time of 3.74 s. System settles down at 12 s and gives a zero error.

4 Performance Comparison and Discussion

On the basis of dynamic time response of the system, the quantitative comparison of PID control technique (Ziegler Nicholas and Tyreus Luyben tuning method) and LQR technique for Electric furnace temperature control system is illustrated. Table 2 gives the performance comparison on the basis of various parameters of the three techniques. LQR control technique is found to score over PID control technique. It is seen that the Electric Furnace System gives comparatively less peak overshoot with zero steady state error and almost equal settling time in case of LQR technique.

From Table 2, it can be seen that although the peak overshoot for LQR is more as compared to Tyreus Luyben PID control method but the rise time and settling

Table 2 Results of PID using Ziegler Nicholas, PID using Tyreus Luyben and LQR technique

Parameters	PID (Ziegler Nicholas)	PID (Tyreus Luyben)	LQR technique
Peak overshoot	43 %	–	5.03 %
Rise time	1.63 s	16.4 s	3.74 s
Settling time	11.6 s	54 s	12 s
Steady state error	0	0	0

time are considerably less. Also, even though the rise time for LQR is more than the Zeigler Nicholas PID controller, it has much less peak overshoot.

5 Conclusion

Controller for Electric furnace system is designed using PID control (Ziegler Nicholas and tyreus luyben tuning method) and LQR. Simulation result for the three techniques is presented. The temperature control of electric furnace using LQR controller gave better results when compared to PID control method.

References

1. Han, Y., Jinling, J., Guangjian, C., Xizhen, C.: Temperature Control of Electric Furnace Based on Fuzzy PID, Vol. 3. IEEE Trans. ICEOE (2011) 41–44
2. Junming, X., Haiming, Z., Lingyun, J., Rui, Z.: Based on Fuzzy – PID self-tuning temperature control system of the furnace. IEEE Trans. ICEICE (2011) 15–17
3. Ding-du, W.: Decoupling Control of Electric Heating Furnace Temperature Based on DRNN Neural Network. IEEE Trans. ICECT (2010) 261–264
4. Teng, F., Li, H.: Adaptive Fuzzy Control for the Electric Furnace. IEEE Trans. ICIS (2009) 439–443
5. Knospe, C.: PID Control. IEEE Control Systems Magazine (2006) 30–32
6. Bansal, K., Dewan L.: Comparison of Different Controllers for Line-of-Sight Stabilization of a Gimbal system. IEEE Conference on Engineering and Systems (2014)
7. Raut, K. H., Vaishnav, S. R.: Performance Analysis of PID Tuning Techniques based on Time Response Specifications, Vol. 2. IJIREEICE (2014) 616–619
8. Gamasu, R., Jasti, V. R. B.: Robust Cohen-Coon Controllers for Flexibility of Double Link Manipulators, Vol. 7. SERSC (2014) 357–368
9. Wang, H., Jin, X.: Direct Synthesis Approach of PID Controller for Second-Order Delayed Unstable Process, Vol. 1. IEEE Trans. WCICA (2004) 19–23
10. Rahimian, M., Raahemifar, K.: Optimal PID Controller Design for AVR System Using Particle Swarm Optimization Algorithm. IEEE Trans. CCECE (2011) 337–340
11. Zhang, H., Cai, Y., Chen, Y.: Parameter Optimization of PID Controllers Based on Genetic Algorithm, Vol. 1. IEEE Trans. EDT (2010) 47–49
12. Luo, Y., Che, X.: Tuning PID Control Parameters on Hydraulic Servo Control System Based on Differential Evolution Algorithm. IEEE Trans. ICACC (2010) 348–351

13. Sinlapakun, V., Assawinchaichote, W.: Optimized PID Controller design for Electric Furnace Temperature System with Nelder Mead Algorithm. 12th International Conference on ECTICON (2015) 15–18
14. Bennett, S.: Development of PID Controller. IEEE Control Systems (1973) 58–65
15. Gopal, M.: Digital Control and State Variable Methods. 2nd edn. Tata McGraw Hill, Inc. (2013)

Design and Development of Low-Cost Wireless Parameter Monitoring System for Nuclear Power Plant

Tanisha Gupta, Rohit Sanket, Rajesh Singh, Anita Gehlot, Eesh Mehandiratta, Ateev Agarwal and Sushabhan Choudhury

Abstract Safety is of utmost importance in any nuclear power plant, as even minor accidents may pose huge danger due to radiation leakage. The paper highlights the need of radiation leakage monitoring for nuclear power plant. Whenever radioactive radiations would increase beyond the safety level, alarms would indicate it. Thus, it will help to take safety measures before leading to serious problems. The system comprises of radiation sensor, fire sensors, and temperature sensors to detect any possibility of leakage and fire. XBee is used as communication media for the system. All the information is collected at a control room and analyzed through LabVIEW.

Keywords Fire sensor · Gas sensor · Radiation · Nuclear power plant · XBee

1 Introduction

Radiation leakage in nuclear power plants is posing health risks to people in and around nuclear power plants. This affects plant efficiency and harmful for animal life. Once any explosion takes place, repair takes a lot of time which reduces power generation. Fire in any part of the plant also leads to explosion and releases huge amount of radiations into the environment. Lin et al. discussed wireless sensor networks and used it to acquire and process data. This paper presents the current growth in WSN applications and its use in real-time monitoring of nuclear power plant [1]. Kim et al. discussed and analyzed internal parameters for nuclear power sites for two years [2]. Jang et al. deals with wireless sensor technology to monitor conditions in and around buildings. Sensor is programmed to process signals received in a suitable format through an open-source operating system [3]. Khedo et al. discussed the use of WSN-based air pollution monitoring system in Mauritius.

Tanisha Gupta · Rohit Sanket (✉) · Rajesh Singh · Anita Gehlot · Eesh Mehandiratta · Ateev Agarwal · Sushabhan Choudhury
University of Petroleum and Energy Studies, Dehradun, India
e-mail: rohitsanket@gmail.com

© Springer Science+Business Media Singapore 2017

R. Singh and S. Choudhury (eds.), *Proceeding of International Conference on Intelligent Communication, Control and Devices*, Advances in Intelligent Systems and Computing 479, DOI 10.1007/978-981-10-1708-7_65

Recursive Converging Quartiles algorithm merges data to remove duplicates, filter out invalid readings and convert it into simpler form which reduces the amount of data to be transmitted to the sink which helps in saving energy [4]. Lopez et al. describes the steps which are essential for developing a good WSN [5]. Ding et al. discussed the research deals in a GPS-enabled wireless sensor network as solution to monitor nuclear radiation. The node size is kept small to ensure the functions of communication. ZigBee multi-hop mesh routing protocol is used for wireless communication [6]. Shen et al. discussed a system, which is designed to predict wind power. Wireless sensor network is proposed for the collection and communication of the correlative real-time data [7]. Akyildiz et al. discussed sensor networks and the working of sensors, their potential applications and the communication setup for sensor networks [8]. Hashemian et al. discussed an integrated wireless system for condition monitoring with essential equipment in nuclear reactors by analysis and Measurement Services Corporation. AMS examined the electromagnetic compatibility of the wireless system with existing plant equipment [9]. Gomaa et al. discussed a WSN-based system for real-time monitoring of radiation levels at nuclear facilities by developing a prototype of wireless sensor node. The wireless node comprises of ZigBee technology for wireless communication, Arduino platform, TI CC2530 chips for implementation and Geiger Muller tube-based radiation detector [10]. Gomaa et al. discussed the prototype for a wireless sensor network that allows a real-time monitoring of radiation levels at nuclear facilities [11]. Bin et al. discussed the structure with a wireless system, compiled with a radiation sensor and associated peripherals implemented upon ZigBee technology using TI CC2530 chip to monitor radiation at nuclear facilities [12]. Chiti et al. discussed the main features of a wireless network and its use in disaster management system [13]. Fu et al. discussed the design of a wireless sensor network for gamma rays monitoring and also explains the requirements environment monitoring system for nuclear power plant [14]. Sav et al. discussed the mechanical properties of the prototype developed for sodium leakage in plant. Paper also discussed the fast breeder reactor component materials under the influence of sodium [15].

2 Proposed System

The concept is to design a low-cost system, which is capable of monitoring environmental parameters in the premises of the nuclear power plant. The information is collected with sensor nodes deployed at appropriate locations to monitor the radiation leakage, fire, gas temperature, and humidity of the surroundings to take action before leakage would take uncontrollable shape. All the data is collected at control room and analyzed with LabVIEW. A wireless sensor network is deployed with XBee as communication media. The system comprises of sensor nodes and a control room. If any of the parameter exceeds to its limit then the LED at control room will start blinking and hooter will on to alert about danger (Fig 1).

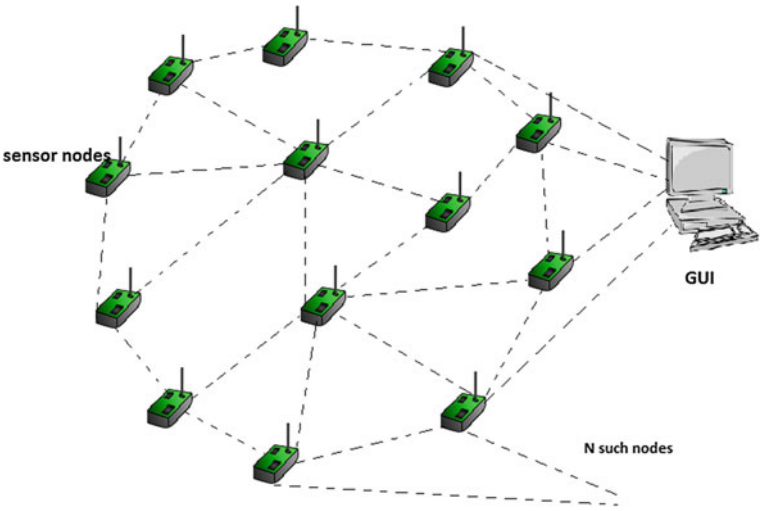
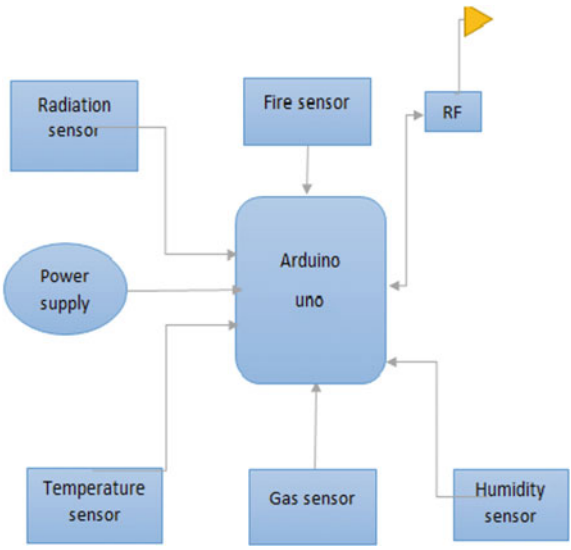


Fig. 1 Generalized block diagram

2.1 Sensor Node

It comprises of controller (Arduino uno), LCD (to display the content), RF modem (XBee), radiation sensor, fire sensor, gas sensor, temperature, and humidity sensor (as shown in Fig. 2).

Fig. 2 Block diagram for sensor node



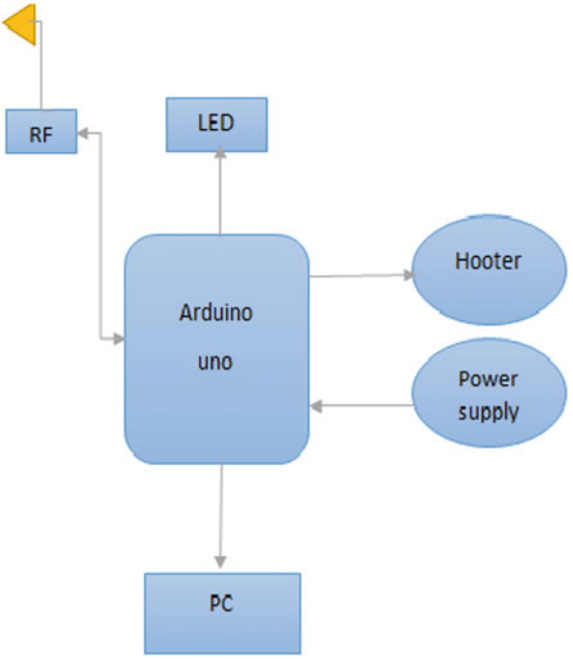


Fig. 3 Block diagram for control room

2.2 Radiation Sensor

It detects the radiation leakage in and around the plant. Temperature sensor—measures the temperature. Gas sensor—detects the harmful gases. Fire sensor—detects the occurrence of fire. Humidity sensor—measures the humidity inside the plant.

2.3 Control Room

All the data measured by sensor nodes is collected at control room wirelessly through XBee. The node comprises of controller (Arduino uno), LED, RF modem (XBee), hooter, and desktop for LabVIEW as data logger and analysis (Fig. 3).

3 Circuit and Simulation

The fire sensor is connected to digital pin as it activates only in case of fire and rest of the sensors are connected to analog pins which display the data continuously on the LCD attached to the node and transmits all the data to the receiver node via

XBee (RF modem) which can transmit data over long distance by passing data through a mesh network of intermediate devices.

The receiver has a GUI, sound alarm, LEDs, and a XBee attached to it. The receiver collects all the data from transmitter via XBee and displays it on the GUI. In case of fire, increased level of radiation or in presence on harmful gas—the sound alarm/hooter gets activated and the LED starts glowing (Figs. 4, 5 and 6).

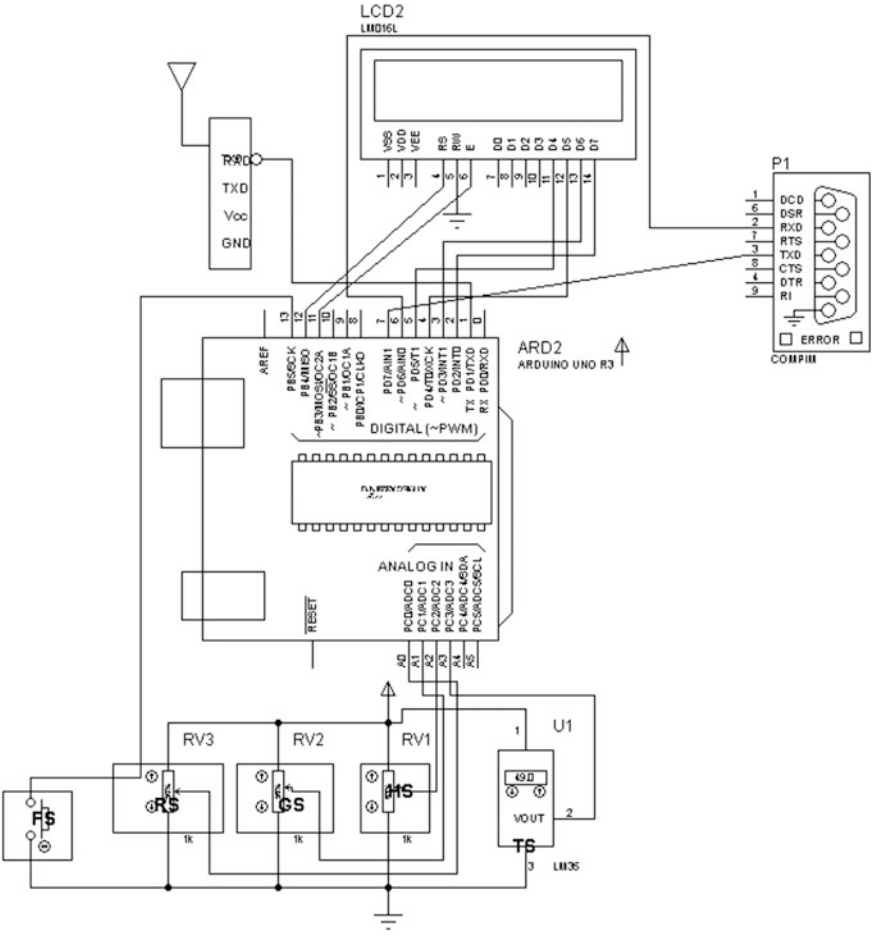


Fig. 4 Circuit diagram for sensor node

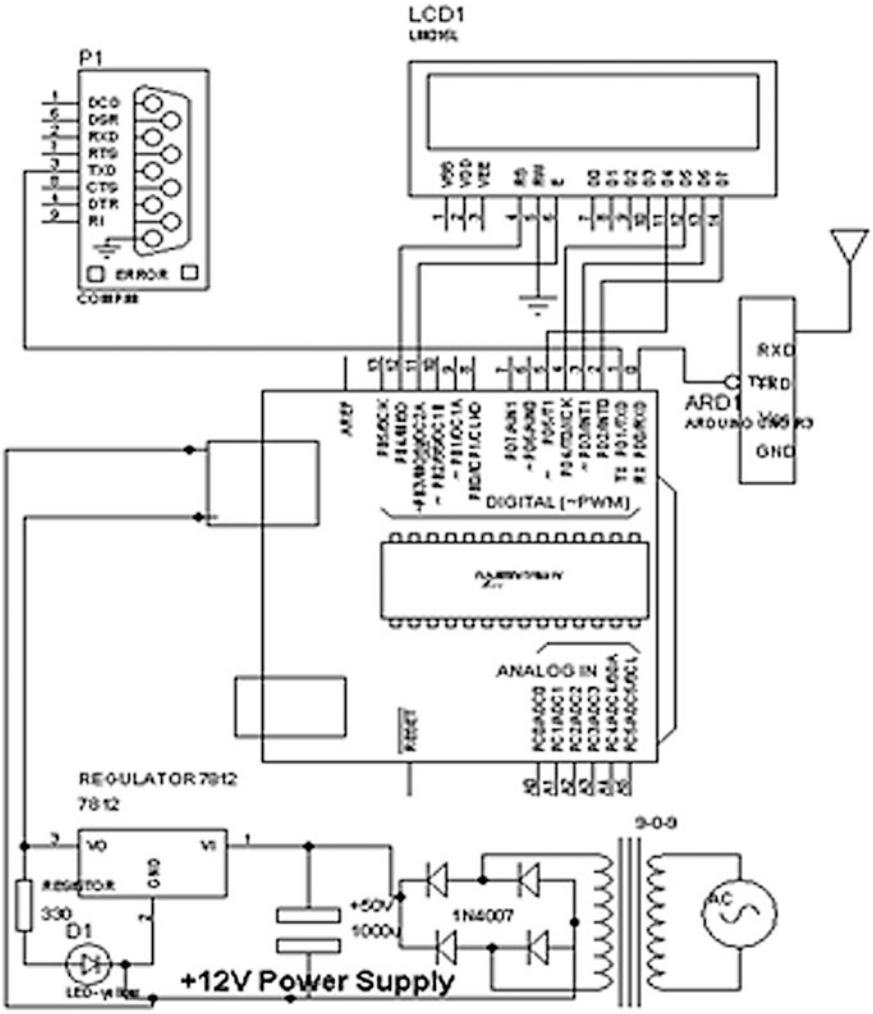


Fig. 5 Circuit diagram for receiver section/control room

4 Deployment Strategy of 'N' Nodes

Multiple sensor nodes are placed across the area. Let say A, B, C, D, E are five nodes placed at a location as shown in Fig. 7, have following duties:

A: Coordinator, B: End device, C: End device, D: End device, and E: End device

Node A acts as a coordinator for communicating to control room. All other nodes acts as transmitter node and communicate with coordinator. Node 'A' is in range of node 'B' and 'C' while node 'D' and 'E' are out of range for node 'A' but node 'E' and 'D' are in the range of node 'B' and 'C,' respectively. This network

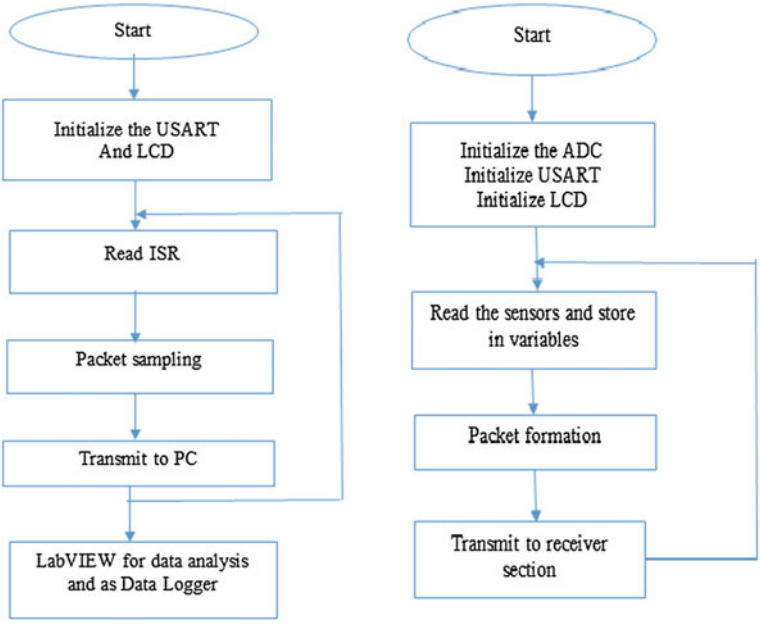


Fig. 6 Working flow chart for sensor node and control room

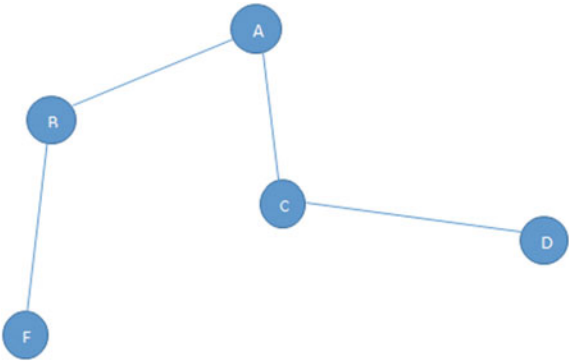


Fig. 7 Placement of sensor nodes

follows star and mesh networking to transmit the data. Node 'B' and 'C' directly transmits the data to node 'A,' forming a star network while node 'D' hop the data from node 'C' to 'A' similarly node E hops the data from node 'B' to 'A' forming a mesh network.

In the same way 'N' number of nodes communicate with each other and transmits their data by hopping the data from one node to another or directly transmitting the data when the node within the reach of receiver node.

5 Proteus Simulation

The sensor nodes are analyzed using Proteus professional software for integrated circuit designing. An Arduino uno board microcontroller is used for every node. Here we are presenting the working strategy making use of just two nodes—the transmitter node which transmits data received from the five sensors used, to the receiver node which further transmits the data to the data logger. The transmitter node uses an Arduino uno board which receives a constant power supply of 12 V. The four analog sensors namely fire sensor (represented by FS on the IC), gas sensor (represented by GS on the IC), radiation sensor(represented by RS on the IC), and the humidity sensor(represented by HS on the IC) are connected to the analog pins of the IC. The digital temperature sensor is connected to one of the digital pins of the IC. The five sensors run using a 5 V power supply. One LCD is attached to this node which simultaneously displays data of the sensors on the LCD screen. An RF modem simultaneously receives data displayed on LCD through its RXD pin and transmits it wirelessly via XBee to the receiver node. The receiver node also has similar structure as that of the transmitter node besides having a data logger (COMPIM). The receiver node transmits the data received from the transmitter node to the data logger besides sending its own sensors' data. It displays its own data simultaneously on the LCD attached to it. A code is used to give to command to the setup of the nodes on the Proteus professional software (Fig. 8 and Table 1).

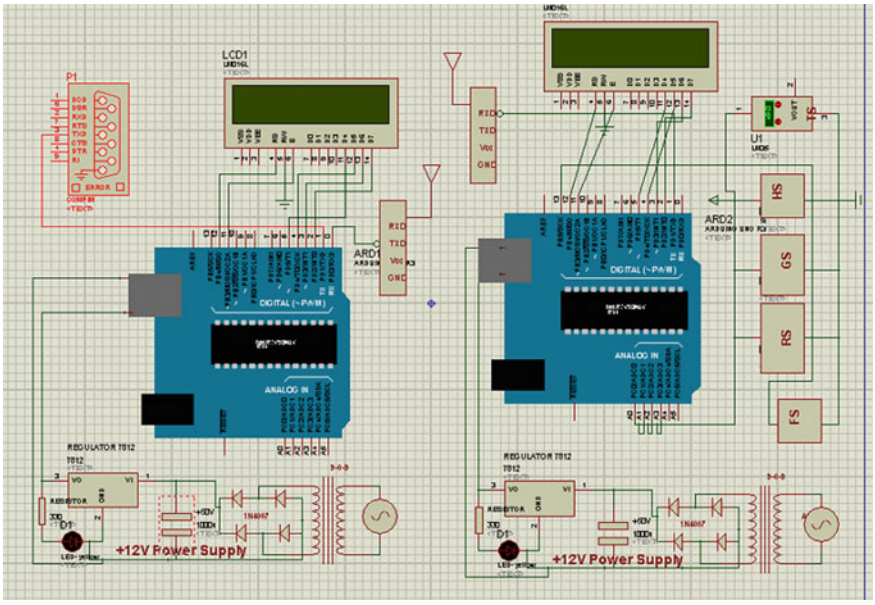


Fig. 8 Proteus simulation of model

Table 1 Components used for development

S. No.	Component	Model name	Description
1	Microcontroller board	ArduinUNO ATmega328P microprocessor	It is a 16 MHz, 8-bit microcontroller
2	XBee module	2.4 GHz XBee XB24Z7WIT-004 (ZigBee/802.15.4 modules) module from Digi. Series2	It has a frequency of 2.4 GHz, data range of 133–400 ft and transmits data at the rate of 250 kbps
3	Radiation sensor	RD2014 from Teviso Sensor Technologies Ltd.	It is a nuclear radiation sensor. It detects beta and gamma radiation and X-rays
4	Fire sensor	BE0010	It detects flame or wavelength at 760 nm range
5	Gas sensor	AS-MLV-P2 by ams	It is a multi-oxide semiconductor air quality sensor
6	Temperature sensor	1211 by Sunrom Technologies Ltd.	It can read temperatures from 2 to 60 °C
7	Humidity sensor	1211 by Sunrom Technologies Ltd.	It measures relative humidity from 1 to 100 %

6 Analysis with LabVIEW

The data of all the five sensors is displayed on the LabVIEW front panel. The graphs on the front panel indicate changes in the readings of the five sensors. The data from the designed system on Proteus professional is directly sent to LabVIEW using a visual serial ports emulator. The Proteus professional's data are sent from port designated as COM2. The LabVIEW receives this data on port designated COM1. The two ports are paired using visual serial ports emulator. Thus all the data sensed on one software is directly transmitted to another software using an emulator. Thus, LabVIEW actually displays the same data that was sensed by Proteus professional's setup (Figs. 9 and 10).

7 Results and Discussion

The prototype of the XBee-based wireless sensor network for nuclear radiation detection is successfully developed and tested. The prototype consisting of two sensor nodes—one as a transmitter node and the other as a receiver node has also been simulated using Proteus professional software and LabVIEW. The data for temperature, humidity, air quality, and radiation have been correctly obtained. Such sensor networks using sensor nodes transmitting data using XBee modules can be used in any desired area. The range of transmission can be changed by applying the specific network topology either mesh, star, and multi-mesh hop (Fig. 11).



Fig. 9 LabVIEW front panel

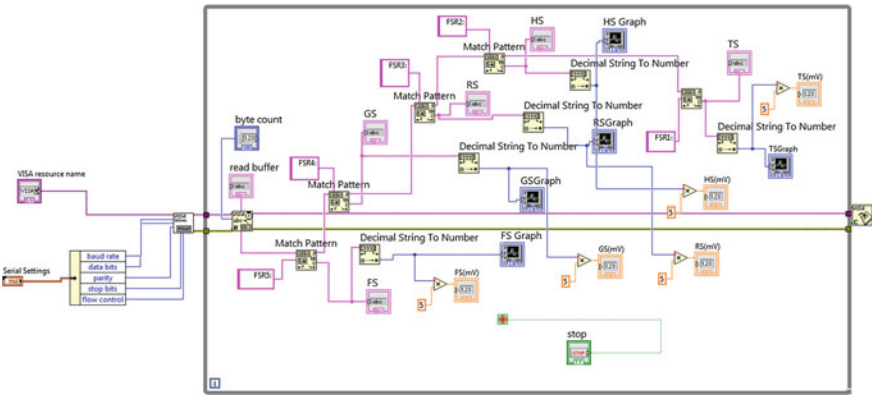


Fig. 10 LabVIEW back panel

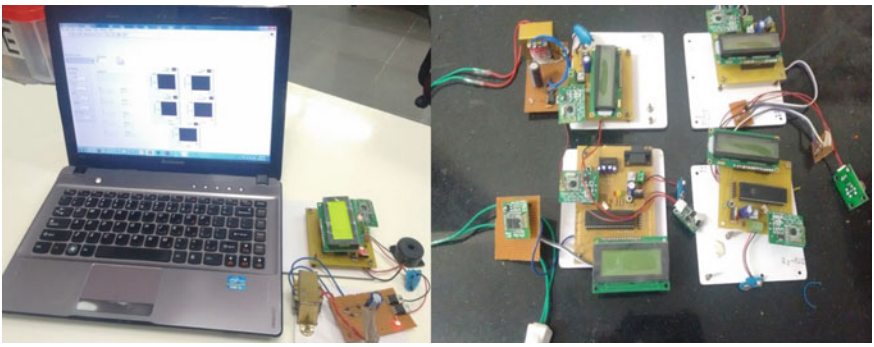


Fig. 11 Snapshot for developed prototype

8 Conclusion

This paper provides the study of XBee-based wireless sensor networks primarily for use in nuclear radiation detection, i.e., for safety purpose in nuclear power plant. It is just to provide alerts before any dangerous outcome like radiations going beyond the safety level. So, this WSN monitoring system helps to increase safety of the plant and prevent danger. These safety measures will reduce power plant repair cost because problem will be detected before it gets serious. Lives of people in and the around the plant would be saved. The environment would also be protected. Such high-level safety through WSN monitoring will popularize nuclear power as an alternative, clean source of power and reduce energy threats to the world. Also just by changing the type of sensor used, this type of WSN can be used for monitoring any kind of power plant or other area.

References

1. Lin, Ruizhong, Zhi Wang, and Youxian Sun. "Wireless sensor networks solutions for real time monitoring of nuclear power plant." Intelligent Control and Automation, 2004. WCICA 2004. Fifth World Congress on. Vol. 4. IEEE, 2004.
2. Kim, E. H., et al. "Analysis of the site characteristics of Korean nuclear power sites from the meteorological aspects." Annals of Nuclear Energy 34.9 (2007): 719–723.
3. Jang, Won-Suk, William M. Healy, and Mirosław J. Skibniewski. "Wireless sensor networks as part of a web-based building environmental monitoring system." Automation in Construction 17.6 (2008): 729–736.
4. Khedo, Kavi K., Rajiv Perseedoss, and Avinash Mungur. "A wireless sensor network air pollution monitoring system." arXiv preprint arXiv:1005.1737 (2010).
5. Lopez, Javier, et al. "Trust management systems for wireless sensor networks: Best practices." Computer Communications 33.9 (2010): 1086–1093.
6. Ding, Fei, et al. "A GPS-enabled wireless sensor network for monitoring radioactive materials." Sensors and Actuators A: Physical 155.1 (2009): 210–215.
7. Shen, Liangping, et al. "Application of wireless sensor networks in the prediction of wind power generation." Wireless Communications, Networking and Mobile Computing, 2008. WiCOM'08. 4th International Conference on. IEEE, 2008.
8. Akyildiz, Ian F., et al. "Wireless sensor networks: a survey." Computer networks 38.4 (2002): 393–422.
9. Hashemian, H. M., et al. "Wireless sensors for equipment health and condition monitoring in nuclear power plants." Future of Instrumentation International Workshop (FIIW), 2011. IEEE, 2011.
10. Gomaa, Rania, et al. "ZigBee wireless sensor network for radiation monitoring at nuclear facilities." Wireless and Mobile Networking Conference (WMNC), 2013 6th Joint IFIP. IEEE, 2013.
11. Gomaa, Rania Ibrahim, et al. "Real-Time Radiological Monitoring of Nuclear Facilities Using ZigBee Technology." Sensors Journal, IEEE 14.11 (2014): 4007–4013.
12. Bin, Cai, et al. "Application research on temperature WSN nodes in switchgear assemblies based on TinyOS and ZigBee." Electric Utility Deregulation and Restructuring and Power Technologies (DRPT), 2011 4th International Conference on. IEEE, 2011.

13. Chiti, Francesco, et al. “A broadband wireless communications system for emergency management.” Wireless Communications, IEEE 15.3 (2008): 8–14.
14. FU, Hai-long, Ming-chun JIA, and Gui-chu PENG. “Research on Continuous Environmental Radiation Monitoring System for NPP Based on Wireless Sensor Network [J].” Nuclear Electronics & Detection Technology 6 (2010): 028.
15. SAV, Satya Murty, et al. “Wireless sensor network for sodium leak detection.” Nuclear Engineering and Design 249 (2012): 432–437.

The Real-Time Hardware Design and Simulation of Thermoelectric Refrigerator System Based on Peltier Effect

Purnendu Shekhar Pandey, Mahesh Kumar Aghwariya, Praful Ranjan and Ginne Rani

Abstract This paper presents a successful designing of the theremoelectric refrigerator system based on Peltier effect at very low cost. In this system semiconductor-based electronic components are used which is the function of small heat pumps. On giving a low DC voltage (4 V) to the thermoelectric module system, heat moves through the module from one side to the other. One side of the module is therefore cooled, while the other side simultaneously heats up. The module can sink the heat from one side. The system is very useful for medicine which required the constant temperature such as insulin for diabetic patients.

Keywords Peltier effects · Thermocouple · Temperature sensors · Atmega16

1 Introduction

In the field of engineering, device may melt down or there may be a very low temperature required for working of the system so TE system is used to maintain temperature for a definite range. Thermoelectric refrigeration can be a useful system to contribute in minimizing the unnatural climate changes. Thermoelectric devices are not the one which demands higher energy consumption so in both ways to deal with energy crises as well as unnatural weather components can be lessening using TEC technology as replacement. Semiconductor thermoelectric coolers System or Peltier coolers offer a few focal points over customary frameworks. This system could be used to maintain lower temperature than the radiation. The system is utilized as a part of corner applications where their exceptional points of interest exceed their low effectiveness [1–5]. In this system, thermoelectric refrigerator can

P.S. Pandey (✉) · M.K. Aghwariya · Praful Ranjan · Ginne Rani
Department of Electronics and Communication Engineering, THDC Institute of Hydropower Engineering and Technology, Bhagirathipuram, Tehri, India
e-mail: purnendu12345@gmail.com

© Springer Science+Business Media Singapore 2017

R. Singh and S. Choudhury (eds.), *Proceeding of International Conference on Intelligent Communication, Control and Devices*, Advances in Intelligent Systems and Computing 479, DOI 10.1007/978-981-10-1708-7_66

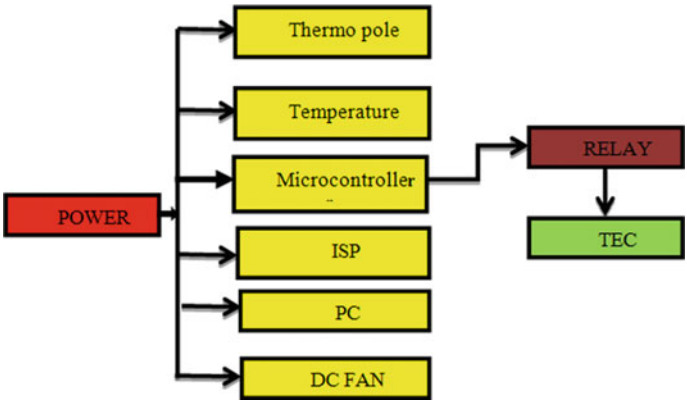


Fig. 1 Block diagram of the TE refrigerator

be manufactured with effortlessly accessible off-the-rack parts for minimal effort. The cooler will use around 60 W only. There is additionally a control framework in the cooler that screens and control the temperature. Block diagram of the system has been shown in Fig. 1.

2 Hardware Developments

The system Hardware implementation deals in drawing the schematic as per the application, testing the design over the breadboard using the IC's to find if the design meets the desired output, carrying out the PCB layout and of the schematic tested on breadboard, finally fabricate the PCB and testing the designed hardware [2]. Hardware of TE refrigerator System consists of the following components (Fig. 2).

2.1 Power Supply of 5 Volt

This circuit is basically designed to achieve 5 V output, 500 mA. This consists of a step-down transformer, IN4007 diodes, capacitor 1000 µF, 7805 regulator, 330 Ω resistance, LED as indicator [2]. Power supply shown in Fig. 3.

2.2 Embedded Microcontroller

This system is developing using AVR series of microcontroller (ATMEGA16). It is a CMOS 8-bit microcontroller based on the AVR RISC architecture [2]. By

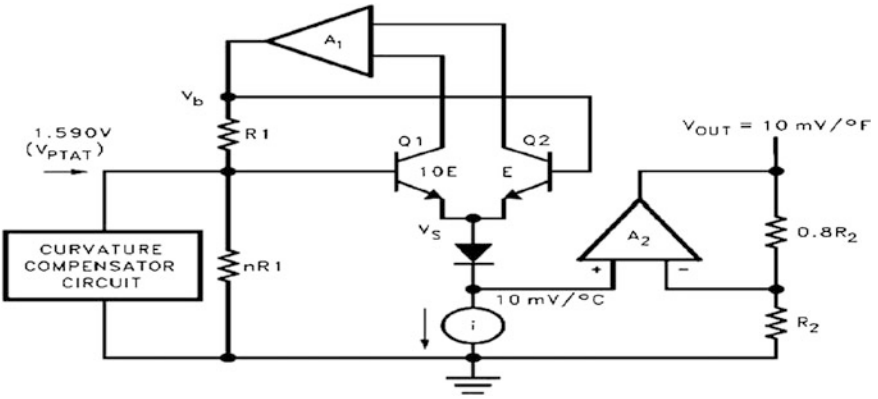


Fig. 2 LM35 inside working

executing commanding instructions in a single clock cycle, it attains throughputs approaching 1 MIPS per MHz, letting the system designed to improve power consumption versus processing speed.

2.3 Display Module

The microprocessor LCD unit receives character codes (8 bits/character), latches the codes to its display data RAM (80-byte) inbuilt DD RAM for storing 80 characters, and transmutes each character code into a 5 × 7 dot matrix. LCD pin connection as pin 1, 3, and 16 are connected to GND, pin 2 and 15 to +5 V pin 3, 4, 5 are RS, RW and enable respectively. Enable pins is always low. Data pins of LCD are 11–14 which are used for 4-bit parallel communication [2].

2.4 ISP Serial Programmers

It consist of a universal serial bus port which is connected to computer and it has small circuit whose second end has six pin connectors to connect with Atmega16 microcontroller programming pins. IPS programmer has been shown in Fig. 4.

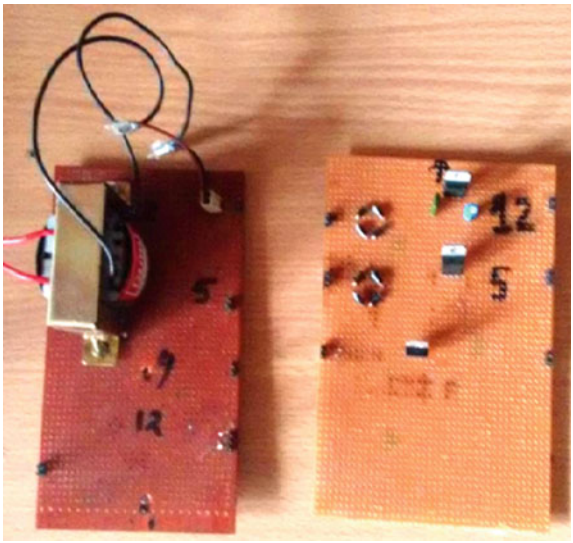


Fig. 3 Power supply board

2.5 Sensor Controller Circuit

The circuit is controlled by the TEC module. Sensor (LM35) measures the temperature of the TE refrigerator. On the basis of the sensor readings, microcontroller decides to on and off the TEC-12706 module.

It is essential to maintain the ambient temperature of refrigeration box in between 4 and 8 °C. The microcontroller polls the output coming from the sensor at regular intervals and matches against the fed values; if the temperature is found above 8 °C the module is turned in using relay, and if the temperature is found below 4 °C the module is turned off using the same.

2.6 LM35 Temperature Sensor

LM35 is the temperature sensor used in this system for measuring and maintaining required temperature inside the refrigerator box. It has two transistors in centre, the one transistor current density is 1/10th due to the fact one has 10 times greater area of the emitter than the other. It makes the R1 resistor voltage is linear to the absolute temperature. This linearity remains almost in its proportion by another circuit which makes the voltage, temperature curve straight [6–9]. Working of LM35 shown in Fig. 2.

Its output is in directly proportion with a scale of 0.01 V/1 °C. It's accuracy is of ±0.4 °C at room temperature and of ±0.8 °C up to 100 °C. It draws very small current.

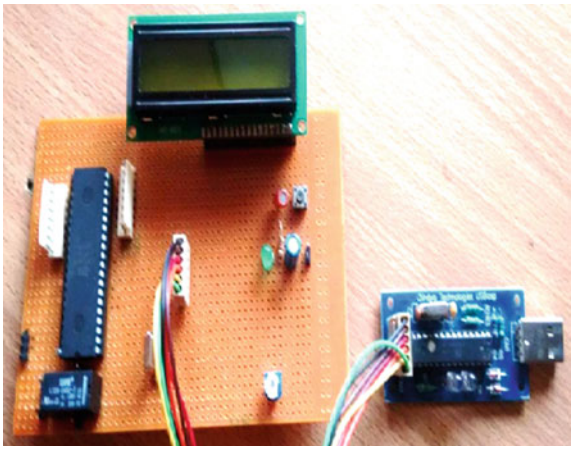


Fig. 4 ISP AVR programmer

2.7 TEC-12706 (Solid State Device)

This is the important component of the circuit; a solid state device works according to Peltier Effect with 12 V power supply turned on and off by the relay. The connections of relay are decided by the microcontroller by checking the values of temperature sensor, the range in this case is 4–8°, if it is found to be crossing either side the relay establishes the connection to maintain the required range of the Temperature. TEC module controller has been shown in Figs. 5 and 6 (Table 1).

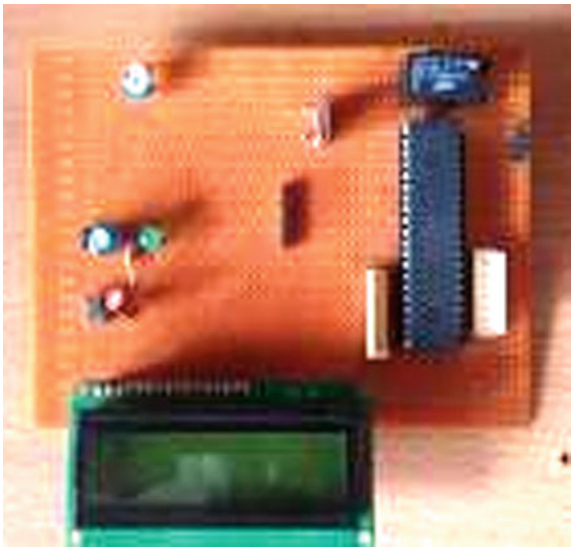


Fig. 5 TEC module controller

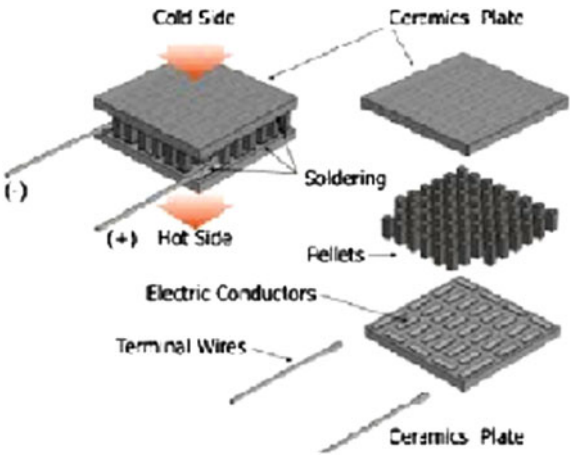


Fig. 6 Two stage of TEC constructions

Table 1 Following is the specification table for the TEC1-12706

Hot side temperature	25 °C	50 °C
Q_{max} (W)	50	57
Peltier T_{max} (°C)	60	75
I_{max} (Amp)	6.4	6.4
V_{max} (Volt)	14.4	16.4
Module resistance (ohms)	1.98	2.30

3 Software Development

The AVR Studio 4 is used for simulation. The AVR Studio uses a COF object file for simulation [2]. This file is created with through the C compiler by selecting COF as the output file type.

3.1 IDE Windows

The IDE has several windows that provide important information to the user. Irrespective of how the windows are produced, they can be moved and resized to fit the perception of the user. The main windows of interest are the Workspace, Source Code, Output, and Watch windows [5].

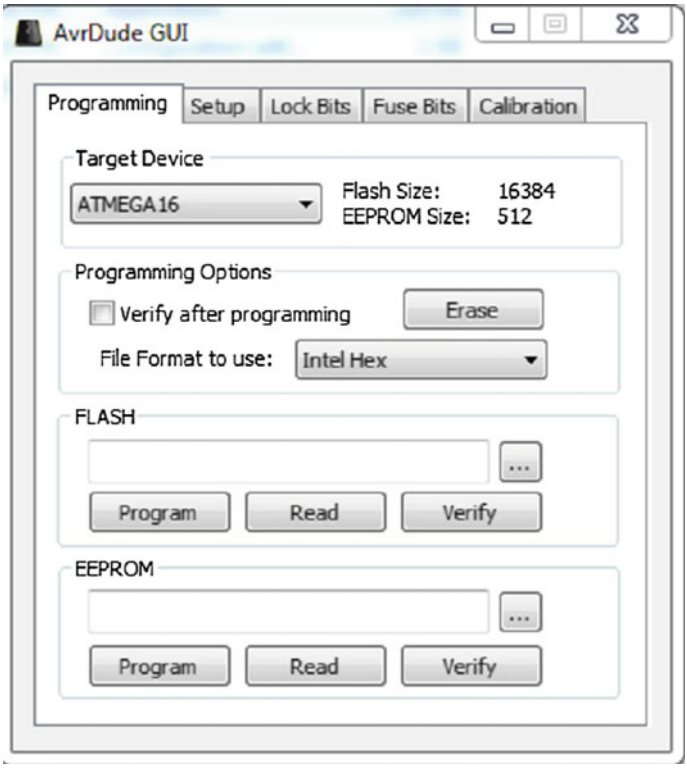


Fig. 7 AVR dude window

3.2 AVRDUDE

AVRDUDE is a GUI for AVRDUDE, a tool for programming Atmel microcontrollers. It supports all programmers and MCUs, allowing changing between devices and configurations quickly and easily, drags and drops files for easy uploading, automatically lists available COM ports. Shown in Fig. 7.

Figure 8 represents the simulation model of the system using Proteus trial software and Fig. 9 represents the overall hardware system having all the components interfaced.

4 Conclusion and Future Scope

The real-time thermoelectric refrigeration system based on Peltier effect has been designed. Efficiency of the system can be increased by making efficient heat sink and the mounting of the module. TER is capable of maintaining temperature

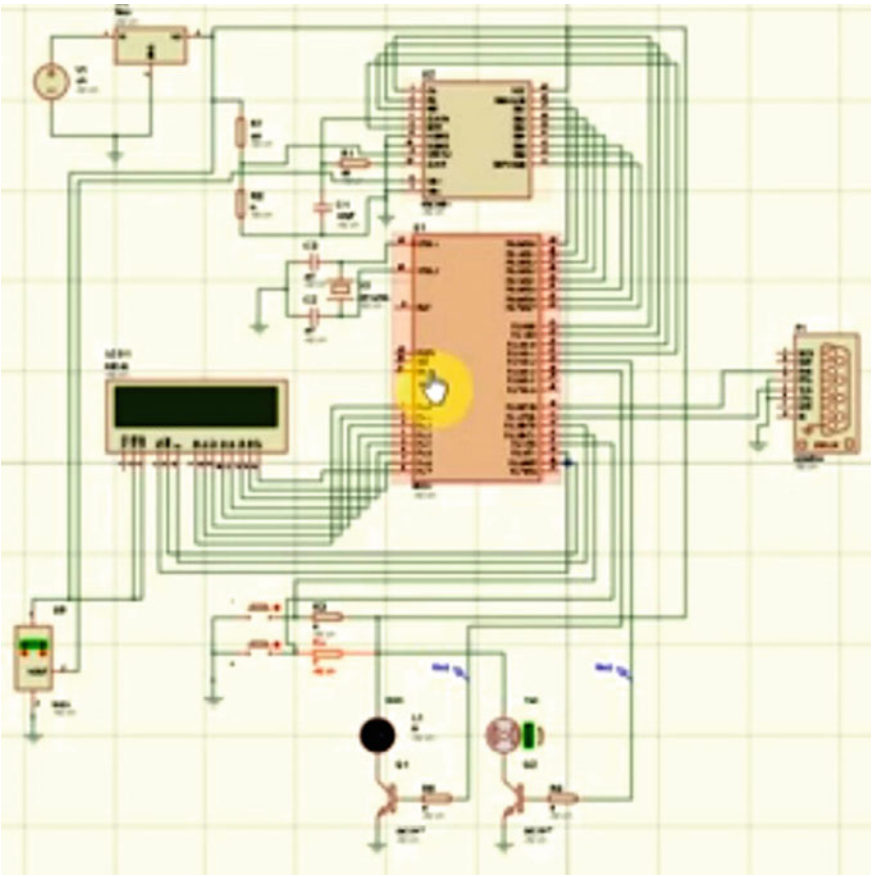


Fig. 8 Simulation model of the system using Proteus trial software

below 9 °C. LM35 works in efficient way to read the temperature. This can be used as a device to heat water in the winter while adding without additional components. Its sink part is capable of heating water as it is mounted on the hot side. Another way is reversing the terminal connection of the module, so cooling side can be effectively used as heating side. Increasing the number of TEC1-12706 modules or using latest TEC modules in series will increase the capacity. Heat sink plays an important rule to make effective cooling so an efficient way to take out the heat will make ice in less time. For the whole Circuit it only required 5 and 12 V for operation, it is possible to run it using a small solar panel. In summer, maximum output will be given by the solar panel.

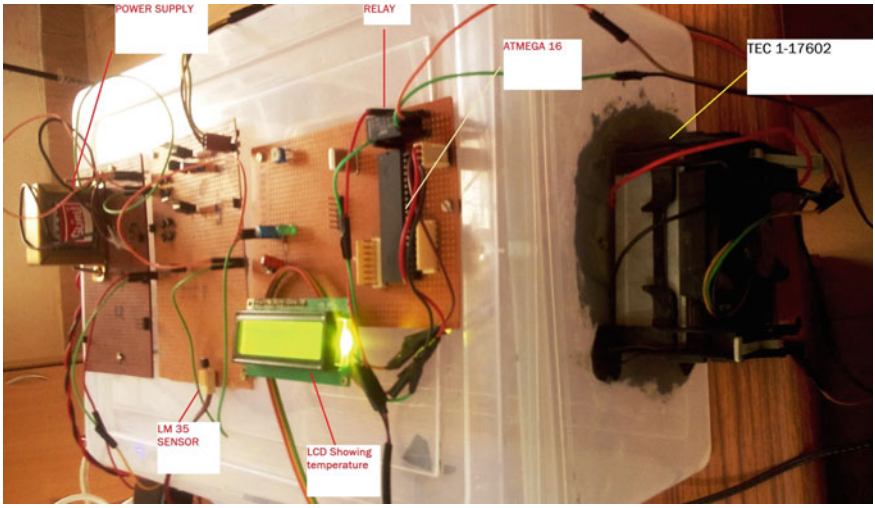


Fig. 9 Overall view of hardware system

References

1. Huang B.J., Chin C.J. & Duang C.L., 2000, "A design method of thermoelectric cooler", International Journal of Refrigeration, 23: 208–218.
2. Purnendu Shekhar Pandey, D.S Chauhan, Rajesh Singh, "The Real Time Hardware Design and simulation of moving message Display System Integrated with PLCC Modem" Innovative Systems Design and Engineering,ISSN 2222-1727 (Paper) ISSN 2222-2871 (Online), Vol 3, No 10, 2012.
3. Xi Hongxia, Luo Lingai and Fraisse Gilles, 2007, "Development and applications of solar-based thermoelectric technologies", Renewable and Sustainable Energy Reviews, 11(5): 923–936.
4. Gao Min and Rowe D.M., 2006, "Experimental evaluation of prototype thermoelectric domestic-refrigerators", Applied Energy, 83 (2):133–152.
5. Sabah A. Abdul-Wahab, Ali Elkamel, Ali M. Al-Damkhi, Is'haq A. Al-Habsi, Hilal S. Al-Rubai'ey', Abdulaziz K. Al-Battashi, Ali R. Al-Tamimi, Khamis H. Al-Mamari and Muhammad U. Chutani, 2009, "Design and experimental investigation of portable solar thermoelectric refrigerator", Renewable Energy, 34 (1): 30–34.
6. Bansal P.K. and Martin A., 2000, "Comparative study of vapour compression, thermoelectric and absorption refrigerators", International Journal of Energy Research, 24: 93–107.
7. Gillott Mark, Liben Jiang and Saffa Riffat, 2010, "An investigation of thermoelectric cooling devices for small-scale space conditioning applications in buildings", International Journal of Energy Research, 34: 776–786.
8. Lertsatitthanakorn C., Lamul Wiset and S. Atthajariyakul, 2009, "Evaluation of the Thermal Comfort of a Thermoelectric Ceiling Cooling Panel (TE-CCP"), System Journal of Electronic Materials, 38: (7) 1472–1477.
9. Putra N., 2009, "Design, manufacturing and testing of a portable vaccine carrier box employing thermoelectric module and heat pipe", Journal of Medical Engineering & Technology, 33 (3), 232–237.

Smart Geyser with Usage Profiling to Reduce Electricity Consumption

Rohit Samkaria, Ambujaksh Shah, Bhupinder Singh and Sushaban Choudhury

Abstract Geyser which is a pressurized hot water container utilized in household causes the high power consumption and at the same time degrading the efficiency of the heating element due to heat loses, i.e., overheating of the element. This paper presents the smart geyser which operates in two modes (i) Autonomous Mode (ii) User Mode. A temperature sensor probe is used as a control switch which is used to regulate the water temperature of geyser by adjusting the heating duration of the element. The study reveals the control topologies used to reduce the power consumption and to increases the efficiency of the geyser. The system consists of Atmega16 microcontroller which determines the hot water profile through temperature probe in Autonomous Mode and in User Mode the controller regulates the temperature of geyser as per the demand profile developed by user. From the result it is apparent that by controlling the temperature of the geyser, the heat loses in the Geyser element and saving of electricity power consumption can be made.

Keywords Geyser temperature control · Atmga16 microcontroller · Hot water profiling

1 Introduction

In daily life we use hot water for various purposes like cooking, bathing, or for industrial purposes and the process employed for the water heating uses the thermodynamics in which a source of energy is used to heat the water. Geysers used in households are pressurized hot water container which are operated by mains 220 V AC [1]. The element used for heating purposes inside the Geyser degrade due to

Rohit Samkaria (✉) · Sushaban Choudhury
University of Petroleum and Energy Studies,
Dehradun, India
e-mail: rohit.samkaria93@gmail.com

Ambujaksh Shah · Bhupinder Singh
Schematic Micro Electronics, Dehradun, India

© Springer Science+Business Media Singapore 2017

R. Singh and S. Choudhury (eds.), *Proceeding of International Conference on Intelligent Communication, Control and Devices*, Advances in Intelligent Systems and Computing 479, DOI 10.1007/978-981-10-1708-7_67

the overheating of water, i.e., heat loses and at the same time causes the major consumption of the electricity power. The objective of continuously monitoring the environmental data of geyser, i.e., water temperature is to lowering the power consumption of household and to increase the power efficiency of heating element of the geyser [2]. A temperature sensor probe is utilized to monitor the temperature of the water [3]. When the temperature profile reached the maximum value in the Autonomous mode, the electronic circuit which uses electromagnetic relay is actuated [4] and then the geyser is automatically put in off mode in order to avoid over heating of the element [5]. In the User Mode, the microcontroller tracks the temperature of the Geyser as per the demand profile developed by the user [6] and when this demand profile reached to the actual heat profile then Geyser is automatically put in off mode [7]. In most populated country like India, the use of electricity by domestic sector is substantial during peak times and hot water geyser is one of the devices which cause the largest power consumption. So by making a sophisticated geyser control system, it is possible to make a sufficient reduction in the consumption of electricity during the peak demand [8]. This paper represents the development, design, and testing of such a sophisticated device which can reduce the electricity consumption and increases the efficiency of the geyser by avoiding the heat loses in the heating element.

2 Proposed System

Automatic Smart Geyser having capability to heat the water in two modes, i.e., Autonomous Mode and User Mode with power saving capability is proposed. Figure 1 shows the schematic model of the proposed system. The water is heated in geyser by two modes. In first mode when user switches on the geyser it starts heating the water up to a desired temperature which is continuously monitored by the temperature sensor probe inside the geyser and after this desired temperature the controlled relay switched OFF the main supply of the geyser and in the same time the RED LED over the Geyser starts blinking with the buzzer beeping out which is the indication of the overheating of the water. In the User Mode if user wish to heat the water up to his own desire he/she can select the temperature limit through the temperature selector switch board. After putting the desired value, the geyser starts heating with GREEN LED blinking showing the normal water condition. When the water temperature reaches up to the user's defined limit the control relay switch board will cut the supply off the geyser and buzzer starts beeping with RED LED blinking over the geyser. In some cases, it is the contact volume editor that checks all the pdfs. In such cases, the authors are not involved in the checking phase.

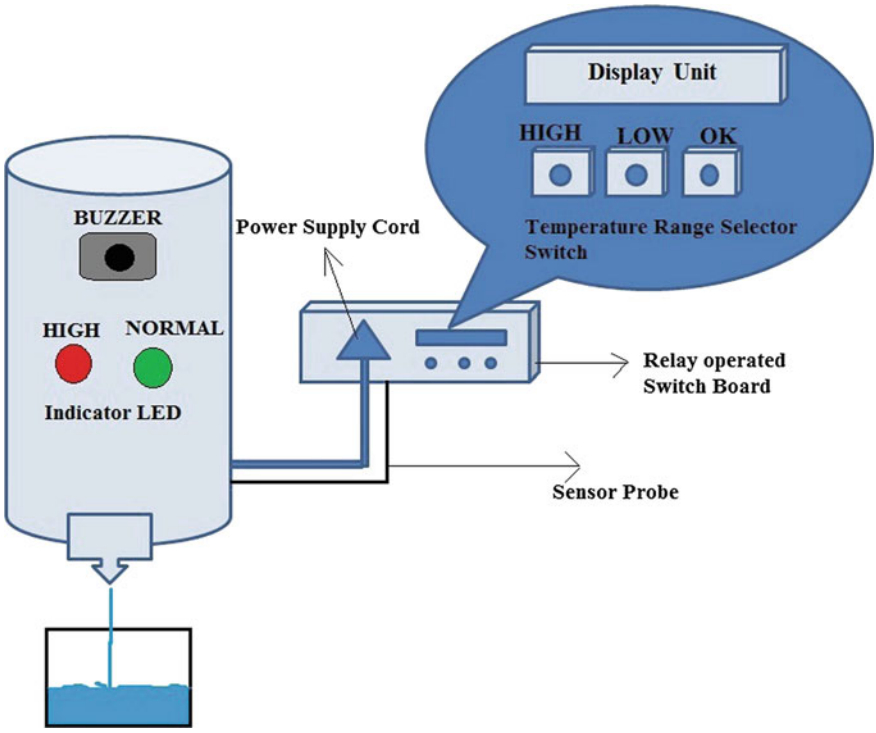


Fig. 1 Schematic diagram of model

3 Prototype Development

The hardware of the proposed system basically consists of the embedded system designed with a temperature monitor probe as a sensor unit for the system. Figure 2 shows the block diagram of the system having seven modules interconnected with each other.

In the block diagram, the main central control unit of the model is Atmega16 microcontroller which is termed as a single on chip computer which includes various numbers of peripherals device connected with it like EEPROM, RAM, etc., which perform some predefined task. Atmega16 having inbuilt 10-Bit ADC, SPI, PWM is much faster since it is modified RSIC processer. This microcontroller is capable of being programmed on board itself rather than first removing and then uploading the program. The monitoring and conditioning of data and taking the decision according to the predefined condition is done by the microcontroller unit. The temperature monitor probe which acts as the sensor unit for the module basically consists of the DS18B20 Programmable Resolution 1-wire digital thermometer which does not require external components and can be powered from the data line. The power supply required for the sensor is 3.0–5.0 V and measures the

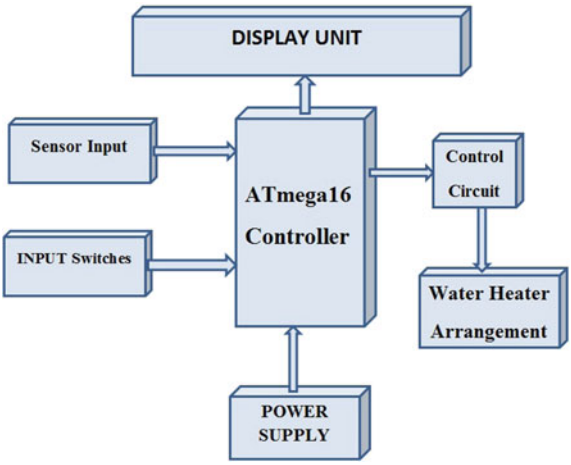


Fig. 2 Block diagram of the model

temperature from the –55 to +125 °C (Fahrenheit equivalent to –67 to +257 °F). The sensor is made of stainless steel tube 6 mm diameter by 30 mm long. The cable is 36″long/91 cm, 4 mm diameter (1 m long). Input switches module is utilized when the circuit is used in autonomous mode and it consists of push button (SPST) which is connected with the input port of the microcontroller. These push buttons are used to select the predefined level of the heating of the water marked as UP, DOWN, and OK. UP and DOWN push buttons slide the value from maximum to minimum and OK to set that particular value of heating. The control circuit consists of SPDT relay with transistor 2N2222 as a switch to operate the relay. The relay circuit connects the mains supply to the Geyser and this relay is operated through the microcontroller. The display unit consists of the 16 × 2 LCD (Liquid Crystal Display) which provides the visual display of the level of heating and is connected to the microcontroller unit. To power up the whole system, a power supply is needed which is provided by the regulated IC. The module consists of step-down transformer followed by bridge rectifier with filter circuit. To obtain the regulated supply IC7805 is used in this module with indication circuit that consist of LED in series with a resistance.

4 Hardware Development

The hardware of the model of sensor module and input switches module which decide the operation of the circuit. Figure 3 shows the circuit diagram of the model.

In the circuit diagram, the temperature sensor probe is connected to the ADC0 pin of the Atmega16 microcontroller. The temperature sensor probe has three pins VCC, DQ, and GND and is connected to the +5 V supply. The Atmega16 has 10-Bit ADC which convert this 5 V supply into 210 = 1024 levels and these levels

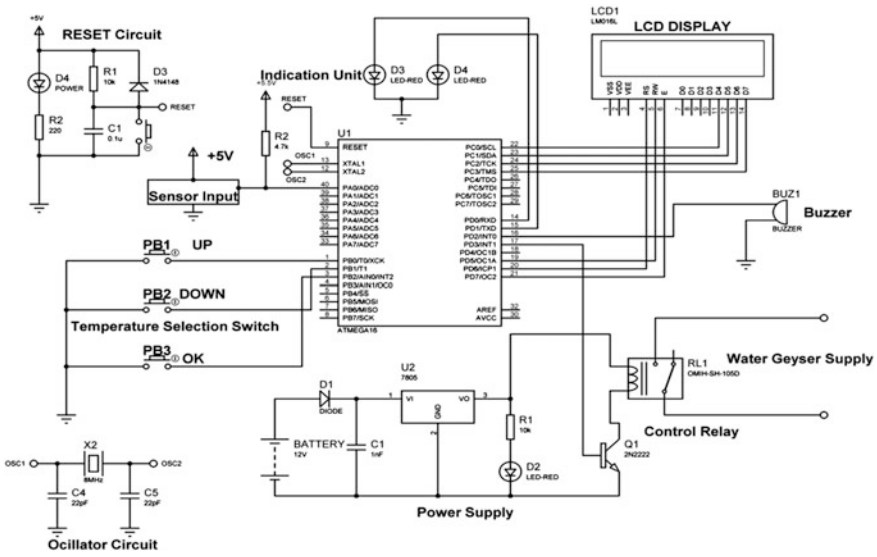


Fig. 3 Circuit diagram of the system

correspond to the temperature of the water. The input switches PB1, PB2, and PB3 are connected to the PB0, PB1, and PB2 pin of the microcontroller of the system. These three pins of the controller are internally pulled up and continuously read for a low voltage at these pins, so these push button are connected with the ground of the supply. LCD having 16 pins in which four data D11, D12, D13, D14 pins of the LCD are connected to the PC0, PC1, PC2, PC3 pin and the RS, R/W, and E pins are connected at PD6, PD5, and PD7 pin of the microcontroller. The two indications LED are connected at PD0 and PD1 pin of the controller which provides the status of the temperature. To provide the over temperature indication, the buzzer is connected to PD2 pin of the controller. The control circuit consists of 5 V operated relay which is controlled by a transistor 2N2222 that acts as a switch to ON/OFF the relay. The relay is connected at the collector of the transistor through a +5 V supply. The base of the transistor is connected at PD3 pin of the controller. By sending the high data over the PD3 pin, the transistor operates at saturation region and relay is connected at collector conducts. The whole circuit is powered up by regulated power supplies which consists of the regulated IC 7805.

5 Circuit Description

The circuit is operated in two modes (i) Autonomous Mode (ii) User Mode

(i) **Autonomous Mode**: In the autonomous mode, the circuit operates in automatic mode. The user switches ON the power supply and the control circuit gets activated which provides the bridge between the main supply and the geyser supply and geyser starts working. Now the water temperature inside the geyser starts to rise. The temperature probe inside the geyser measures this rise in water temperature and provides the corresponded level over the display. When water temperature reached the maximum level which is determined inside the controller program, the microcontroller deactivates the control circuit which cuts off the geyser supply from main and the buzzer provides the beep sound with RED LED blinking which provides the indication of the overheating of water.

(ii) **User Mode**: In the User Mode the predefined level of heating is selected from the selector switches, i.e., UP and DOWN switches can vary the range of the water heating and after that by pressing the OK button, system starts working. Now temperature probe monitors the rise in the temperature of the water and it compares the value defined by the user and the actual rise in temperature attained by the water. When the rise in temperature of water reaches equal to the defined value by the user, the microcontroller deactivates the control circuit which cuts off the geyser supply from the mains and buzzer starts beeping with RED LED blinking as an indication of overheating of the water.

The step-by-step working of the system is through algorithm in Fig. 4.

6 Software Development

The firmware for the system is developed using the WinAVR Compiler and AVR studio. The WinAVR is freeware, open source software development tool which is designed for the Atmel AVR series of RISC architecture microprocessor hosted on window platform and includes GCC compiler for C and C++. The software code for the desired system is written in the C language and the code is compiled by using the open source complier avr-gcc (Fig. 5).

7 Proteus Simulator

Proteus simulator is used as the hardware simulation platform which is a powerful design tool in which various virtual components from the libraries are placed in the work space and connected with each other and the code is loaded inside the microcontroller and real-time hardware simulation by using virtual components is taken. The Proteus simulator has the ability to define most of the aspects of the drawing appearance and hardware feasibility is checked on Proteus simulation before actual hardware implementation.

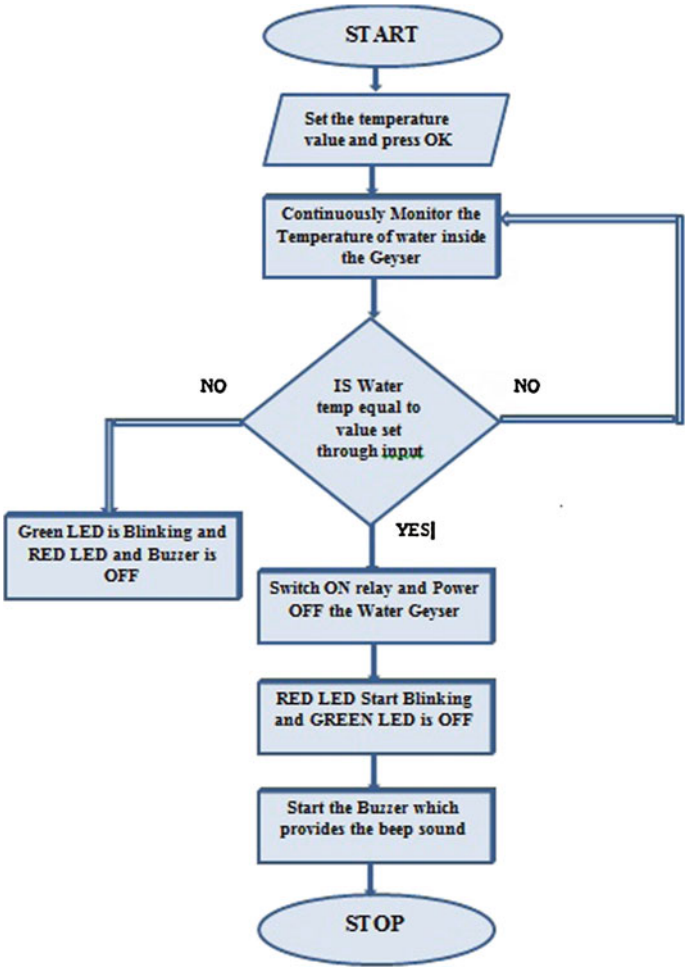


Fig. 4 Flow chart for working of the proposed system

Figure 6 shows the Proteus simulation of the model in which various virtual components from the Proteus libraries are placed on the work space and interconnected with each other. The code is loaded in the controller from the AVR studio in which coding is done by using C language. This code is compiled and the hex file created after compilation of the code is loaded into the microcontroller and then the Proteus simulation executed.

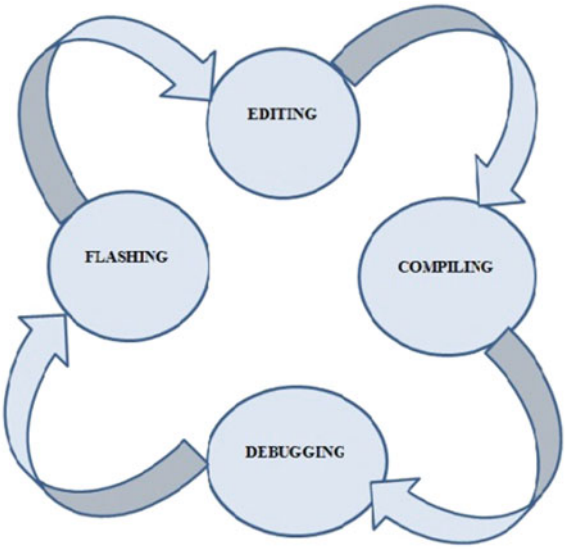


Fig. 5 Coding step

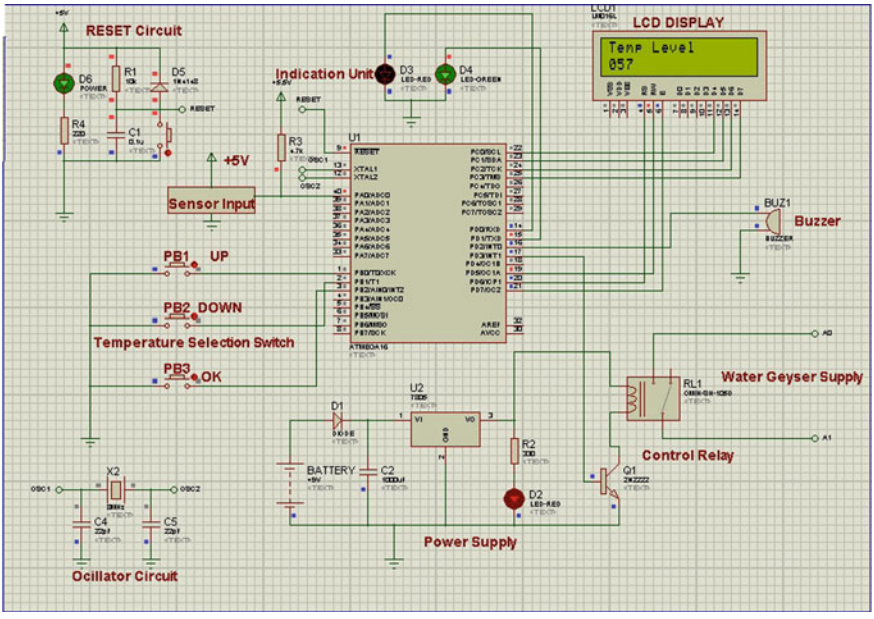


Fig. 6 Proteus simulation of the model

8 Result and Discussion

The proposed system is mainly focused to reduce the electric power consumption through smart geyser used in the domestic purposes which can save 7.48 (kWh) energy per month at a heating of 65 °C of heating element. There are two types of geyser which are mostly used in the domestic a 3 kW 150 L and 4 kW 200 L which causes an average energy loss of 2.3 kWh energy losses per day. So by this smart geyser these energy loss can be reduced and the efficiency of the heating elements can be increased three times that of the normal geyser where element degrades due to the heating loss.



9 Conclusion and Future Scope

From the result, we found that the average power consumption is reduced and at the same time the efficiency of the geyser increased by reducing the heat losses in the filament. Such type of geyser could in future also accommodate energy saving when connected with solar energy. By this system, it is possible to set predefined temperature profile.

As results have shown the net efficiency of geyser which would increase with reduction in the electricity consumption.

References

1. Catherine, Quinton, et al. “Hot water usage profiling to improve geyser efficiency.” Journal of Energy in Southern Africa 23.1 (2012): 39.
2. Hulsbos, R., et al. “Design of a smart geyser controller unit.” AFRICON, 2015. IEEE, 2015.

3. Haines, Eldon L., and Ralph E. Bartera. “Self-pumping solar heating system with geyser pumping action.” U.S. Patent No. 4,478,211. 23 Oct. 1984.
4. Hayashi, Toshikazu. “Ventilation fan system with smoke detector speed control.” U.S. Patent No. 3,826,180. 30 Jul. 1974.
5. Steyn, S. J. M., and R. Chetty. “Development of a residential appliance control interface (ACI) module using smart systems.” Industrial Technology (ICIT), 2013 IEEE International Conference on. IEEE, 2013.
6. Elmahalawy, Ahmed Mustafa, Newal Elfishawy, and Mohamed Nour El-Dien. “Anticipation the consumed electrical power in smart home using evolutionary algorithms.” Multimedia Computing and Information Technology (MCIT), 2010 International Conference on. IEEE, 2010.
7. Harris, James R. “Transistor circuit for operating a relay.” U.S. Patent No. 2,718,613. 20 Sep. 1955.
8. Anderson, Larry L., Lawrence W. Shumaker, and Russell J. Van Rens. “Circuit for a power operated machine.” U.S. Patent No. 4,195,722. 1 Apr. 1980.Appendix: Springer-Author Discount.

Stabilization of Underactuated Mechanical System Using LQR Technique

Akash Gupta, Varnita Verma, Adesh Kumar, Paawan Sharma, Mukul Kumar Gupta and C.S. Meera

Abstract The two-link inverted pendulum on cart (TLIPOC) is a widely known system having underactuation property. TLIPOC is a highly unstable and nonlinear system. The modelling of TLIPOC is obtained using Euler–Lagrangian approach. In this paper use of optimal control minimizing a quadratic cost functional is discussed. The aim of the paper is to stabilize the TLIPOC using linear quadratic regulator (LQR) technique. MATLAB simulations are used to show the efficiency and feasibility of proposed approach.

Keywords Underactuated system · Linear quadratic regulator

1 Introduction

The two-link inverted pendulum on cart (TLIPOC) constitutes a challenging control problem because of underactuation property [1]. In underactuated systems there are fewer actuators than their degrees of freedom. These systems have many applications like robotics, mobile systems, aerospace systems and locomotion. The underactuation

Akash Gupta (✉) · Varnita Verma · Adesh Kumar · Paawan Sharma · M.K. Gupta · C.S. Meera
University of Petroleum and Energy Studies, Dehradun, India
e-mail: akashgupta646@gmail.com

Varnita Verma
e-mail: varnitaverma@yahoo.in

Adesh Kumar
e-mail: adeshkumar@ddn.upes.ac.in

Paawan Sharma
e-mail: paawan.sharma@ddn.upes.ac.in

M.K. Gupta
e-mail: mkgupta@ddn.upes.ac.in

C.S. Meera
e-mail: meera.cs@ddn.upes.ac.in

© Springer Science+Business Media Singapore 2017

R. Singh and S. Choudhury (eds.), *Proceeding of International Conference on Intelligent Communication, Control and Devices*, Advances in Intelligent Systems and Computing 479, DOI 10.1007/978-981-10-1708-7_68

property is due to (i) dynamical property, (ii) failure of actuator, (iii) reduction of cost, (iv) forcefully reducing order of the system. Despite many control techniques, controlling of these systems remains challenging problem [1, 2]. The TLIPOC system is a highly nonlinear system so linear technique cannot be used. Linear quadratic regulator (LQR) is the technique to obtain the performance index function [3–6]. With the LQR technique, system stability can be achieved in a simpler manner as directly we can apply the LQR command whereas fuzzy logic or neural network is more challenging technique as compared to LQR.

2 A Two-Link Inverted Pendulum

The TLIPOC system is shown in Fig. 1. First we assume that the rod is lumped in nature and cart mass is denoted as M_0, rod mass are m_{10} and m_{20}. There is external force applied on the cart, $x(t)$ represents position of the cart, $\theta 1(t)$ and $\theta 2(t)$ are the angle from the vertical position.

The difference between kinetic energy (K) and potential energy (V) is known as the Lagrangian of a system [7].

The Lagrangian will be calculated as the follows:

$$L = \frac{1}{2}[M + m_{10} + m_{20}]\dot{x}^2 \frac{1}{2} m_{10}(l_1\dot{\theta}_1)^2 + \frac{1}{2} m_{20}\{(l_1\dot{\theta}_1)^2 + (l_2\dot{\theta}_2)^2 + 2l_1l_2\dot{\theta}_1\dot{\theta}_2\cos(\theta_1 - \theta_2)\}$$
$$+ [m_{10} + m_{20}]\dot{x}\dot{\theta}_1 l_1 \cos\theta_1 + m_{20}\dot{x}\dot{\theta}_2 l_2 \cos\theta_2 + (m_{10} + m_{20}gl_1(\cos\theta_1) + (m_{20})gl_2(\cos\theta_2) \quad (1)$$

The Lagrangian equations of motion will be calculated from the following:

$$\frac{\mathrm{d}}{\mathrm{d}t}\frac{\partial L}{\partial \dot{x}} - \frac{\partial L}{\partial x} = 0 \quad (2)$$

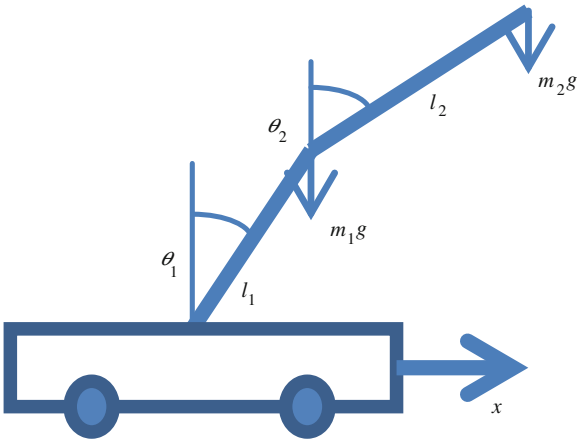


Fig. 1 The two-link inverted pendulum system

$$\frac{\mathrm{d}}{\mathrm{d}t}\frac{\partial L}{\partial \dot{\theta}_1} - \frac{\partial L}{\partial \theta_1} = 0 \tag{3}$$

$$\frac{\mathrm{d}}{\mathrm{d}t}\frac{\partial L}{\partial \dot{\theta}_2} - \frac{\partial L}{\partial \theta_2} = 0 \tag{4}$$

We get

$$\begin{aligned}(M + m_{10} + m_{20})\ddot{x} + (m_{10} + m_{20})\ddot{\theta}_1 l_1 \cos\theta_1 + m_{20} l_2 \ddot{\theta}_2 \cos\theta_2 \\ - (m_{10} + m_{20})\dot{\theta}_1^2 l_1 \sin\theta_1 - m_{20}\dot{\theta}_2^2 l_2 \sin\theta_2 = u\end{aligned} \tag{5}$$

$$\begin{aligned}(m_{10} + m_{20})l_1^2\ddot{\theta}_1 + m_{20} l_1 l_2 \ddot{\theta}_2 \cos(\theta_2 - \theta_1) \\ - m_{20} l_1 l_2 \dot{\theta}_2^2 \sin(\theta_2 - \theta_1) + (m_{10} + m_{20}) g l_1 (\sin\theta_1) = 0\end{aligned} \tag{6}$$

$$\begin{aligned}m_{20} l_2^2 \ddot{\theta}_2 + m_{20}\ddot{x} l_2 \cos(\theta_2 + l_1 l_2 \ddot{\theta}_1 \cos(\theta_1 - \theta_2) \\ - l_1 l_2 \dot{\theta}_1^2 \sin(\theta_1 - \theta_2 + m_{20} g l_2 \sin\theta_2) = 0\end{aligned} \tag{7}$$

After splitting the values of $\ddot{x}$, $\ddot{\theta}_1$, $\ddot{\theta}_2$ and substituting into nonlinear model as

$$\frac{\mathrm{d}}{\mathrm{d}t}(x) = f(x, u, t) \tag{8}$$

$$\begin{aligned}&x_1 = x, x_2 = \dot{x} = x_1, x_3 = \theta_1 \\ \text{Let } &x_4 = \dot{\theta}_1 = \dot{x}_3 \\ &x_5 = \theta_2, x_6 = \dot{\theta}_2 = \dot{x}_5\end{aligned} \tag{9}$$

State space representation is indicated as follows:

$$\frac{\mathrm{d}}{\mathrm{d}t}\begin{pmatrix} x_1 \\ x_2 \\ x_3 \\ x_4 \\ x_5 \\ x_6 \end{pmatrix} = \begin{pmatrix} x_2 \\ \dot{x}_2 \\ x_4 \\ \dot{x}_4 \\ x_6 \\ \dot{x}_6 \end{pmatrix} \tag{10}$$

Linearize the above equation at $(\underline{x}_0, \underline{u}_0) = (0, 0)$ and also taking the values of,

$$m_{10} = m_{20} = 0.2\,\text{kg},\ M = 0.5\ \text{kg},\ l_1 = l_2 = 1\,\text{m},\ g = 10\,(\text{ms}^{-2})$$

The linearized form of the system is

$$\frac{\mathrm{d}}{\mathrm{d}t}(\delta \underline{x}) = J_{\underline{x}}(\underline{x}_0, u_0)\delta \underline{x} + J_u(\underline{x}_0, u_0)\delta u \tag{11}$$

After solving the above equations we get the linearized matrix as [1]

$$\frac{\mathrm{d}}{\mathrm{d}t}(\delta \underline{x}) = \begin{bmatrix} 0 & 1 & 0 & 0 & 1 & 0 \\ 0 & 0 & -0.07 & 0 & 0.12 & 0 \\ 0 & 0 & 0 & 1 & 0 & 0 \\ 0 & 0 & -1.4 & 0 & -2.8 & 0 \\ 0 & 0 & 0 & 0 & 0 & 1 \\ 0 & 0 & 5.75 & 0 & 1.38 & 0 \end{bmatrix} \delta \underline{x} + \begin{bmatrix} 0 \\ 0.012 \\ 0 \\ -0.015 \\ 0 \\ -0.015 \end{bmatrix} \delta u \tag{12}$$

And the output matrix is

$$y = \begin{bmatrix} 1 & 0 & 0 & 0 & 0 & 0 \\ 0 & 0 & 1 & 0 & 0 & 0 \\ 0 & 0 & 0 & 0 & 0 & 0 \end{bmatrix} \begin{bmatrix} x \\ \dot{x} \\ \theta_1 \\ \dot{\theta}_1 \\ \theta_2 \\ \dot{\theta}_2 \end{bmatrix} \tag{13}$$

3 LQR Controller

For the design of LQR controller the main aim is to minimize the performance index J. The weighted matrix are positive definite in nature. The control input is taken as

$$u(t) = -Kx(t) \tag{14}$$

Weight matrices Q and R in performance index J are chosen randomly [8]. The selection that the elements of the matrix Q are larger than the matrix R means that controller is more sensitive to states than the control input. The elements of the Q and R matrices under consideration are

$$Q = \mathrm{diag}([100010001000]); \quad R = 1$$

Table 1 Eigen values of Matrix A and Ac

S.no	E.V. of A	E.V. of Ac
1	0	–1.3802 + 1.3828i
2	0	–1.3802 – 1.3828i
3	–1.3772 + 1.3845i	–1.3743 + 1.3862i
4	–1.3772 – 1.3845i	–1.3743 – 1.3862i
5	1.3772 + 1.3845i	–0.2211 + 0.2213i
6	1.3772 – 1.3845i	–0.2211 – 0.2213i

The gain matrix is

$$K = [1.0000 \quad 5.9638 \quad -674.0980 \quad -59.0284 \quad -499.6924 \quad -297.1697] \quad (15)$$

The E.V. of Matrix A and Ac is given in Table 1.

4 Results and Discussion

Various trajectory plots of TLIP system are as shown in various figures. From the results it is clear that systems settling time is very low in almost all the output which is a very good indication. Here all the possible output is shown including cart for double inverted pendulum. There are other techniques also available like fuzzy control, neural network or LOR fuzzy, but for stability point of view it is the simplest technique as directly we can apply this technique with the MATLAB command. The main use of this control technique is to make the system stable in a simpler and effective manner (Figs. 2, 3, 4, 5, 6 and 7).

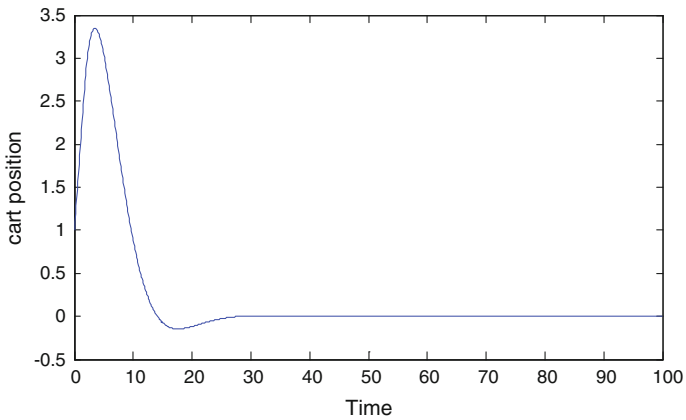


Fig. 2 Cart position

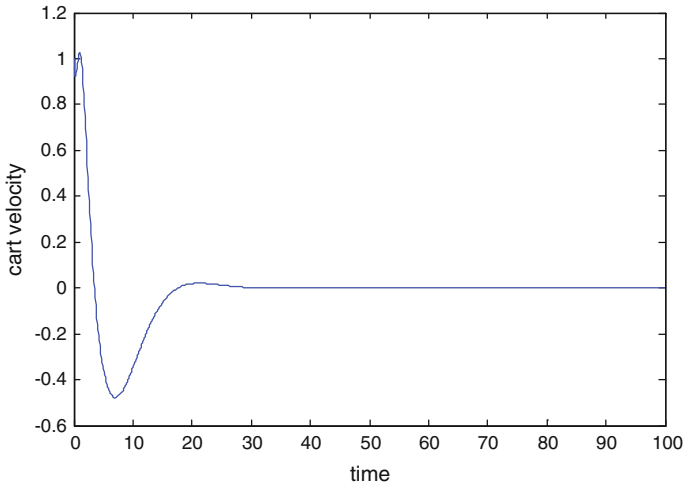


Fig. 3 Cart velocity

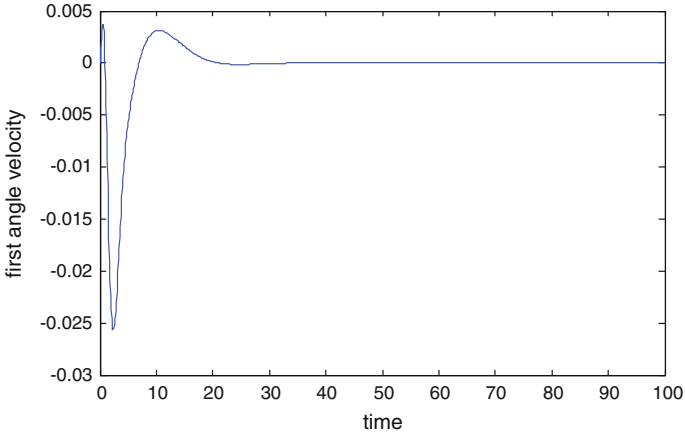


Fig. 4 First angle

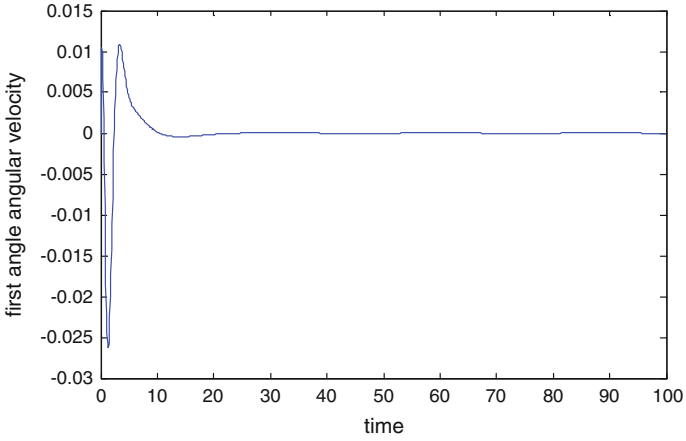


Fig. 5 First angle angular velocity

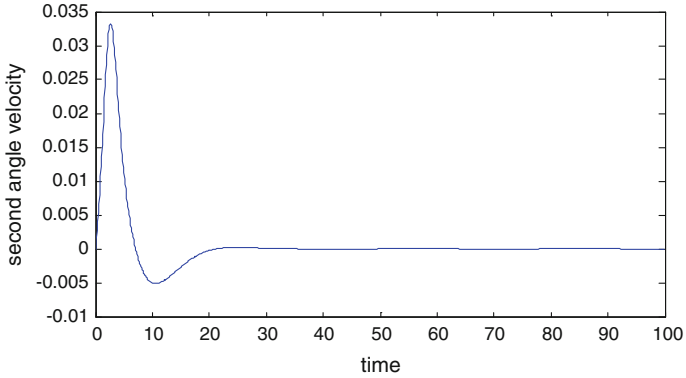


Fig. 6 Second angle

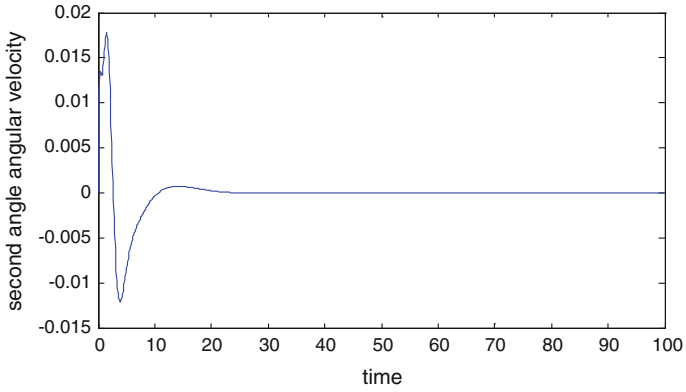


Fig. 7 Second angular velocity

5 Conclusion

The paper presents LQR technique to stabilize the TLIPOC system about its vertical position. The value of Q&R tried after various hit-and-trial methods and it is found that these are the most suitable value for optimal control. To balance a TLIP on a moving cart has been successfully designed using optimal control system. Simulation shows the validity of the suggested controller as the system's outputs are satisfactory. The main objective of this paper is to make output of TLIP stable in nature with least effort applied by the controller as compared with the other control techniques.

References

1. Abhaya Pal Singh, Faruk S. Kazi, N.M. Singh, Pallavi Srivastava, PIαDβ Controller Design for Underactuated Mechanical Systems, 2012 12th International Conference on Control, Automation, Robotics & Vision Guangzhou, China, 5–7th December 2012 (ICARCV 2012).
2. C. Chevallereau, J.W. Grizzle and C.H. Moog. Nonlinear Control of Mechanical Systems with one Degree of Underactuation."Robotics and automation", vol-3, 2222–2228, (2004).
3. Jinghu Xing, workers Chen, Ming Jiang. The study of inverted pendulum optimal control system based on LQR. Industrial Instrumentation and Automation. 2007.
4. Dan Huang, Shaowu Zhou, "Inverted pendulum control system based on the LQR optimal regulator. Micro Computer Information", 2004, 20(2): 37–39.
5. W. Zhong and H. Rock, Energy and passivity based control of the double inverted pendulum on a cart. In Proceedings of the IEEE international conference on control applications, Mexico City, Mexico, September 2001.
6. Desineni Subbaram Naidu, "Optimal Control Systems", Idaho State University, 2002, p. 129.
7. Lijuan Zhang, Yaqing Tu, "Research of Cart Inverted Pendulum Model Based on Lagrange Equation", Proceedings of the 6th World Congress on Intelligent Control and Automation, IEEE Press, June 2006, pp. 820–824.
8. Bogdanov Alexander, 2004, "Optimal Control of a Double Inverted Pendulum on a Cart", Technical Report CSE-04-006.Y.

A Particle Swarm Optimization Based Switching Scheme for Seven-Level Cascaded Hybrid Bridge Inverter

Parul Gaur, Yajvender Pal Verma and Preeti Singh

Abstract This paper presents a particle swarm optimization (PSO) based optimized switching scheme for seven-level cascaded hybrid bridge (CHB) inverter, which results in minimized total harmonic distortions (THD) in the output waveform. A set of transcendental equations characterizing the inverter's output waveform is solved by PSO. With aid of PSO, optimized three switching angles for seven-level inverter have been calculated. The proposed technique is validated in MATLAB simulink by designing a three-phase CHB inverter for seven-level. The results obtained through simulations show the minimized harmonics in the inverter's output waveform.

Keywords Cascaded hybrid bridge (CHB) · Seven-level inverter · Particle swarm optimization (PSO) · Harmonics · Total harmonic distortion (THD)

1 Introduction

As the concept of competitive electricity market is emerging, it is important for electric utilities to supply quality power to the consumers to compete in the market. Multilevel inverters (MLIs) are being used as interfaces to renewable energy sources particularly solar power. Numerous topologies of MLIs are available such as Flying Capacitor (FC), Neutral Point Clamped (NPC) and Cascaded Hybrid Bridge (CHB). MLIs synthesize the output waveform by dividing the waveform into several levels. With increase in levels, complexity and switching losses also increases as more and more switches are required. However, the Total Harmonic

Parul Gaur (✉) · Y.P. Verma · Preeti Singh
UIET, Panjab University, Chandigarh, India
e-mail: parul34@gmail.com

Y.P. Verma
e-mail: yajvender_verma@yahoo.com

Preeti Singh
e-mail: preeti_singh@pu.ac.in

© Springer Science+Business Media Singapore 2017

R. Singh and S. Choudhury (eds.), *Proceeding of International Conference on Intelligent Communication, Control and Devices*, Advances in Intelligent Systems and Computing 479, DOI 10.1007/978-981-10-1708-7_69

Distortion (THD) reduces with increase in the number of levels. To keep the harmonics within acceptable limits, generally medium voltage (2.2–6.3 kV) inverters are preferred [1–3]. MLIs are characterized by a set of transcendental equations. The solution of these transcendental equations can be determined by various iterative algorithms [4]. Newton Raphson (NR) is one of such technique, but it requires the initial guess of switching angles. Resultant theory can also be applied for solving the transcendental equations, which results in minimization of smaller number of harmonics. As the number of harmonics to be eliminated increases, solution of resultant theory becomes difficult. Other iterative techniques are Genetic Algorithm (GA) and Particle Swarm Optimization (PSO) [5]. In this paper, PSO technique has been applied for solution of transcendental equations characterizing a seven-level CHB inverter.

This paper is divided into six sections. Section 1 deals with introduction, gives an overview of MLIs and numerous techniques for solution of MLIs. Section 2 represents a seven-level CHB inverter. Section 3 enlists the concept of PSO and its algorithm. Simulink model and results for seven-level CHB inverter using PSO are presented in Sect. 4. Section 5 presents the conclusion and future scope.

2 Seven-Level Cascaded Hybrid Bridge Inverter

A CHB inverter makes use of m H-bridge cells for $(2m + 1)$ levels. Each H-bridge cell has a direct current (DC) source and four switches. Each cell produces three voltage levels, i.e., $+V_{dc}$, 0 and $-V_{dc}$ depending upon the on and off time of four switches. Figure 1 represents a seven-level CHB inverter per phase. A seven-level CHB inverter uses three hybrid bridges per phase. Each hybrid bridge has four

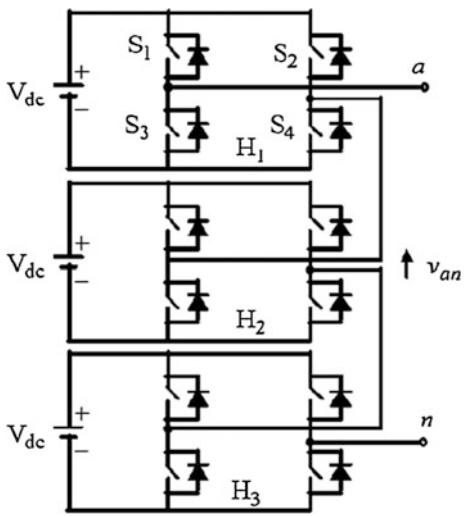


Fig. 1 Seven-level cascaded hybrid bridge inverter

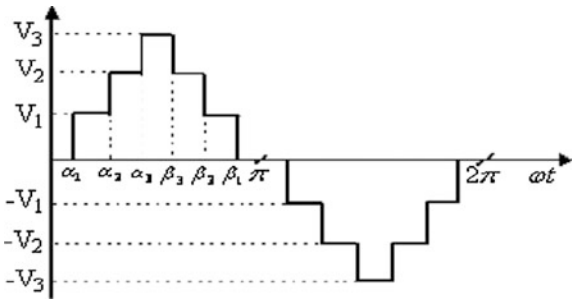


Fig. 2 Output waveform of seven-level CHB inverter

active switches and one DC source. The total phase voltage V_A is sum of individual cell voltages, i.e., $V_A = V_1 + V_2 + V_3$.

Figure 2 depicts the output obtained for a CHB inverter of seven-level. Generally, the output waveform of a MLI inverter is represented by the Fourier series expansion as given by Eq. (1):

$$Vo = \sum_{n=1}^{\infty} (a_n \sin n\theta_n + b_n \cos n\theta_n). \tag{1}$$

where $a_n = \frac{4V_{dc}}{n\Pi} \sum_{l=1}^{m} \cos n\theta_l$.

Using (1), the output equation for a CHB inverter of seven-level can be represented as follows:

$$V_0 = \sum_{n=1}^{\infty} \frac{4V_{dc}}{n\Pi} (\cos n\theta_1 + \cos n\theta_2 + \cos n\theta_3) \sin(nwt). \tag{2}$$

Analysis of output waveform indicates the harmonics in the waveform. By the quarter wave symmetry of the output waveform, triplen harmonics and even harmonics cancel automatically. However, non-triplen odd harmonics exist in the output waveform. Thus, for better results there is a need to design an MLI with minimum harmonics [6]. The harmonic contents depend upon the firing angles of an MLI. For seven-level CHB inverter, there exist three firing angles corresponding to three cells. In this paper, selective harmonic elimination (SHE) technique has been applied and using PSO three switching angles have been calculated. SHE works on fundamental switching frequency, which further results in minimum losses. Equation (2) can be converted into SHE equations as follows:

$$\begin{aligned} &\cos\theta_1 + \cos\theta_2 + \cos\theta_3 = 3M \\ &\cos 5\theta_1 + \cos 5\theta_2 + \cos 5\theta_3 = 0 \\ &\cos 7\theta_1 + \cos 7\theta_2 + \cos 7\theta_3 = 0 \end{aligned} . \tag{3}$$

In Eq. (3), M represents the modulation index and is defined as the ratio of fundamental output voltage to the maximum obtained fundamental voltage. Three switching angles must satisfy the constraint:

$$0 < \theta_1 < \theta_2 < \theta_3 < \frac{\Pi}{2} \tag{4}$$

3 Particle Swarm Optimization Algorithm

In this paper, PSO algorithm has been used for calculating the three switching angles. PSO methodology was discovered through simulation of a simplified social model via bird flocking, fish schooling, etc., and presently being used in various applications for optimization of non linear equations [7]. Figure 3 represents the flowchart of PSO algorithm.

3.1 PSO Algorithm for Seven-Level CHB Inverter

The proposed PSO algorithm for seven-level CHB inverter involves the following steps:

Step I: Objective function formulation
Fifth and seventh harmonics can be mathematically represented as follows:

$$\begin{aligned} V_5 &= \cos 5\theta_1 + \cos 5\theta_2 + \cos 5\theta_3 \\ V_7 &= \cos 7\theta_1 + \cos 7\theta_2 + \cos 7\theta_3. \end{aligned} \tag{5}$$

Objective function is to minimize these harmonics as follows:

$$y = (\text{abs}(V_5) + \text{abs}(V_7)) \tag{6}$$

Step II: Initialization
Initialize the parameters of optimization problem such as position, velocity, local best position of the particles and the global best position of the swarm by taking into consideration the constraints of the switching angles.

Step III: Update the personal best position w.r.t best position of the individual particles.

Step IV: Update the global best position w.r.t best position of the swarm.

Step V: Stop when a good fitness value is achieved, which further leads to optimized three switching angles for seven-level CHB inverter.

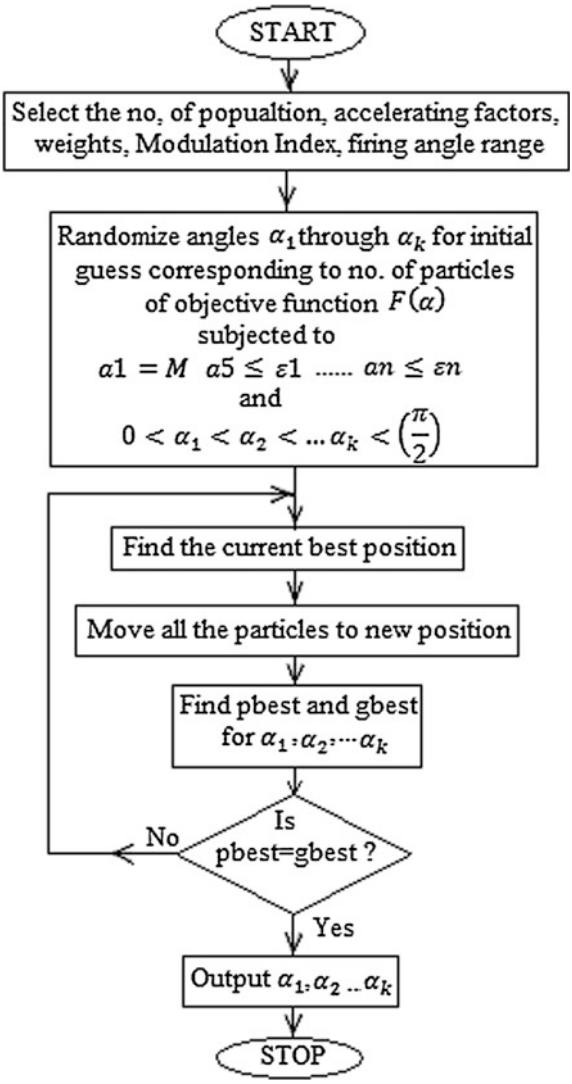


Fig. 3 Flowchart of PSO algorithm

4 Simulink Model and Results

Seven-level CHB inverter has been modeled and implemented in MATLAB simulink as shown in Fig. 4. The optimized switching angles were calculated from PSO algorithm at modulation index 0.87. Seven-level CHB inverter consists of 12 switches (IGBTs) with three separate DC sources per phase. Figure 5 depicts the line voltages for seven-level CHB inverter with minimum harmonics obtained after simulation.

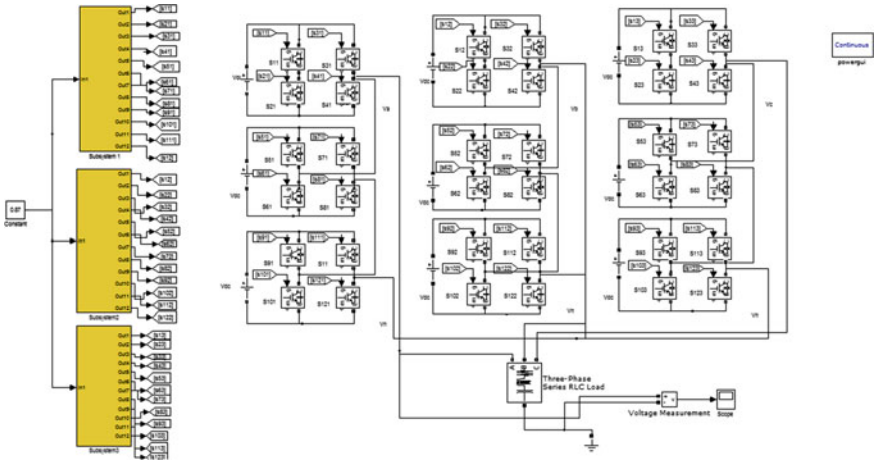


Fig. 4 Simulink model for seven-level CHB inverter

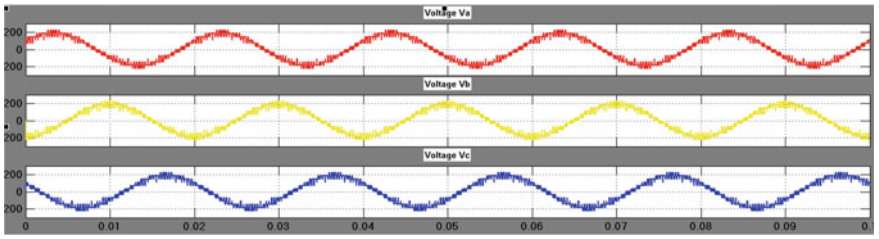


Fig. 5 Line voltages of three-phase seven-level CHB Inverter **a** V_a, **b** V_b, and **c** V_c

5 Conclusion and Future Scope

Various algorithms are available for finding out the optimum switching angles for seven-level CHB inverter. In this paper, PSO algorithm has been used. Based upon the optimum switching angles, seven-level inverter is fired and FFT analysis was done. PSO algorithm converges faster than the other existing iterative algorithms. Therefore, PSO can be used for quick and effective harmonic eliminations of MLIs. As a future scope, this algorithm can be used for higher levels of MLIs for better THD output waveform.

References

1. Rodriguez, J., Lai, J.S., Peng, F.Z.: Multilevel inverters: A survey of topologies, controls and applications. IEEE Transactions on Industrial Electronics, Vol. 49 (2002) 724–738
2. Sastry, J., Bakas, P., Kim, H., Wang, L., Marinopoulos, A.: Evaluation of cascaded H-bridge inverter for utility scale photovoltaic systems. Renewable Energy, Vol. 69 (2014) 208–218
3. Abu-Rub, H., Holtz, J., Rodriguez, J., Baoming, G.: Medium Voltage Multilevel Converters-State of the Art, Challenges and Requirements in Industrial Applications. IEEE Transactions on Industrial Electronics, Vol. 57 (2010) 2581–2596
4. Gaur, P., Singh, P.: Optimization Techniques for Harmonic Minimization in Cascaded Hybrid Multilevel Converters: A Review. International Journal of Research in Engineering and Technology, Vol. 4 (2015) 188–193
5. Gupta, V.K., Mahanty, R.: Optimized Switching Scheme of Cascaded H-bridge Multilevel Inverter using PSO. Electrical Power and Energy Systems, Vol. 64 (2015) 699–707
6. Kumar, J., Das, B., Agarwal, P.: Optimized Switching Scheme of a Cascaded Multilevel Inverter. Electric Power Components and Systems, Vol. 38 (2010) 445–464
7. Shen, K., Zhao, D., Mei, J., Tolbert, L.M., Wang, J., Ban, M., Ji, Y., Cai, X.: Elimination of Harmonics in a Modular Multilevel Converter Using Particle Swarm Optimization Based Staircase Modulation Strategy. IEEE Transactions on Industrial Electronics, Vol. 61 (2014) 5311–5322

Analysis of Wavelet Transform and ANFIS-Based Fault Detection and Classification

Puja Bharti, M.A. Ansari, Y.K. Chauhan and Ashish Kumar

Abstract Abnormal conditions occur in the power system. The intelligent techniques can be applied to know about the fault nature. The identification of fault in the power system is very important for the safeguard of the equipments from the abnormal conditions which arises due to fault. When the faults are identified, then the classification of the fault and after clearing the fault for studying the stability in the system is paramount. For the identification and classification, the use of intelligent techniques in which identification through wavelet transform and classification through ANFIS (Adaptive Neuro Fuzzy Inference System) is proposed in this paper. Wavelet transform identifies the fault in terms of energy and classification of fault by the ANFIS as well as fuzzy inference system which display the type of fault. The fault identifications are based on the fault current which is more dominant for line faults.

Keywords Power system · Fault identification · Classification · Wavelet transform · ANFIS

Puja Bharti (✉) · M.A. Ansari · Y.K. Chauhan · Ashish Kumar
Department of Electrical Engineering, Gautam Buddha University, Greater Noida, Uttar Pradesh, India
e-mail: pujabharti025@gmail.com

M.A. Ansari
e-mail: mahmadiitr@gmail.com

Y.K. Chauhan
e-mail: chauhanyk@yahoo.com

Ashish Kumar
e-mail: ashishelectrical025@gmail.com

© Springer Science+Business Media Singapore 2017

R. Singh and S. Choudhury (eds.), *Proceeding of International Conference on Intelligent Communication, Control and Devices*, Advances in Intelligent Systems and Computing 479, DOI 10.1007/978-981-10-1708-7_70

1 Introduction

The power system is divided into three main components namely generation, transmission, and distribution. Generation is very basic component like to generate the power to the system. In India, the generation of voltage level varies between 11 kV and 33 kV and distribution Voltage level varies between 11 kV and 415 V [2]. However, in the transmission, as the voltage level varies from high voltages to extra high voltage it creates the case of faults. So, the safety and stability of the transmission is necessary in the power system. Life without electricity is not possible and consumption of electricity increases gradually. So, first identify the fault and after that classify the fault. When the faults are clear then system comes under the stable condition [1]. Normally, the faults which occur in the system are symmetric and unsymmetrical. Symmetrical faults are also called balanced or three phase faults. These types of faults arise when three conductors touch each other with ground or without ground likely (a-b-c) or (a-b-c-g). It occurs 2–5 % in the power system [2]. When symmetric faults occur, then it remains in balance condition but it damages the system too much. Unsymmetrical faults are also called unbalanced fault. Unbalanced faults are of three types, namely; Single line to ground fault (a–g, b–g, c–g), Double line to ground fault (a-b-g, b-c-g, c-a-g), Line to Line fault (a-b, b-c, c-a). Single line to ground (SLG) fault occurs when one phase conductor touches with the ground then this type of fault are arises. These types of faults are very common in the power system and occur 65–70 % fault in the power system. Double line to ground (DLG) fault occurs when two phase conductor touches with the ground; then this type of fault arises in the power system. It occurs for 15–20 % fault in the power system. Line to Line (LL) fault arises when two phase conductor touches each other and it occurs in the power system for 5–10 % [2].

2 Detection of Faults Using Wavelet Transform

The wavelet transform helps to find the energy of various signals (currents) associated in the power system and due to that, the identification of faults is carried out. The wavelet transform takes the signal from the workspace and the workspace data comes from the simulation results and the current waveform is considered for identification and classification of the line fault. Wavelet transform decomposes the signal for more accurate studies [3]. At suitable level and wavelet are used to decompose the signal in the power system. In this paper, Daubechies (db.) wavelets are used in the level 8. The signal decomposed in two components likely, approximate and detail coefficient as shown in Fig. 1. In which approximate coefficient has the high scale and low frequency as well as detail coefficient has the low scale and high frequency [4]. Approximate (A) and detail (D) help to filter the signal and after that to find the energy for the power system that helps us to identify fault in the power system.

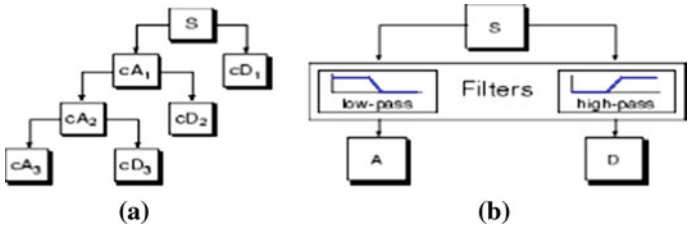


Fig. 1 **a** 'S' is the signal which is decomposed and it divided into two components A and D mean approximate and detail coefficient and c is the constant value. **b** A and D are filters

3 Classification of Fault Using ANFIS

ANFIS is used to classification of fault in the power system. ANFIS is a hybrid system which is the mixture of Fuzzy and ANN [5]. In the ANFIS, the data is trained for the results which contain the types of fault. ANFIS takes the data which is decomposed and filter by the wavelet transform [6]. The data is put into the ANFIS and check the result, and Fuzzy logic controller display the results. Fuzzy takes the signal in term of FISs (Fuzzy inference system) and then declares the type of fault [7].

4 Flow Chart for Detection and Classification of Faults in the Power System

See Fig. 2.

5 Simulink Model of Proposed Fault Detection in Power System

In Fig. 3, it has one generator and one transformer. There are three buses in which Bus-1 is slack bus and is called Swing or Reference bus. Three phase faults are connected in Bus-2 which is the creation of fault by these blocks. All the faults declared current base only. Scope is used to see the graph. All the calculations are for Bus-2 only.

In Figs. 4, 5, 6 and 7, there is current waveform in different situation. Variation of current which show abnormality in some graph has the sign of fault and these type of fault are also detected by putting the data into the wavelet transform and by doing this, energy of current will show that there is a fault. It means the detection of fault check by wavelet transform as well as scope graph Figs. 4, 5, 6 and 7 shows the fault current.

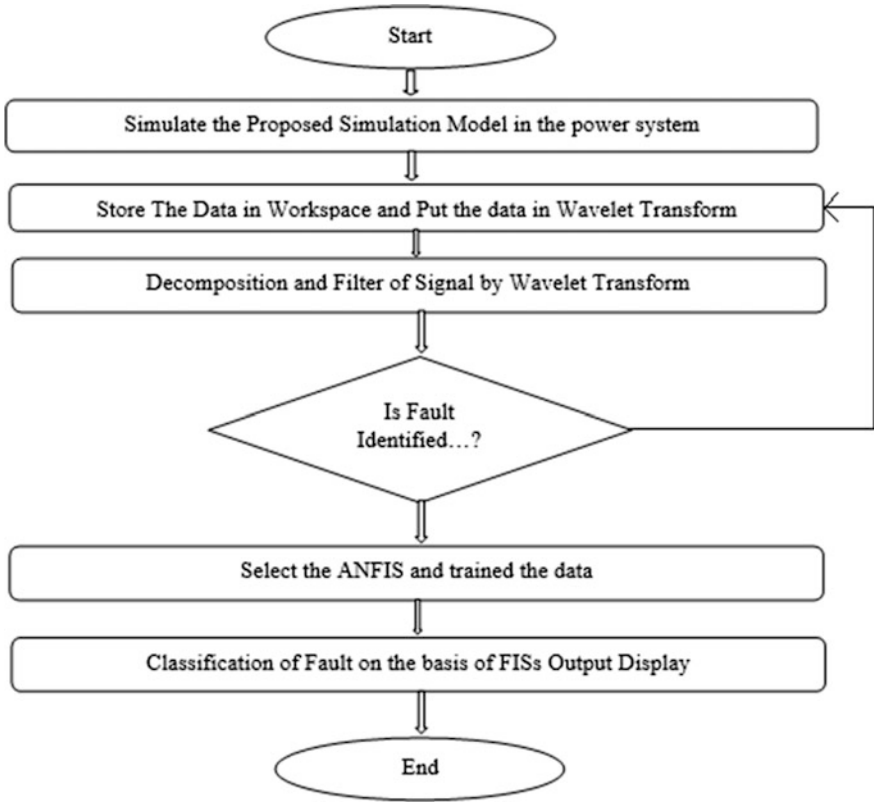


Fig. 2 Flow chart for detection and classification of faults

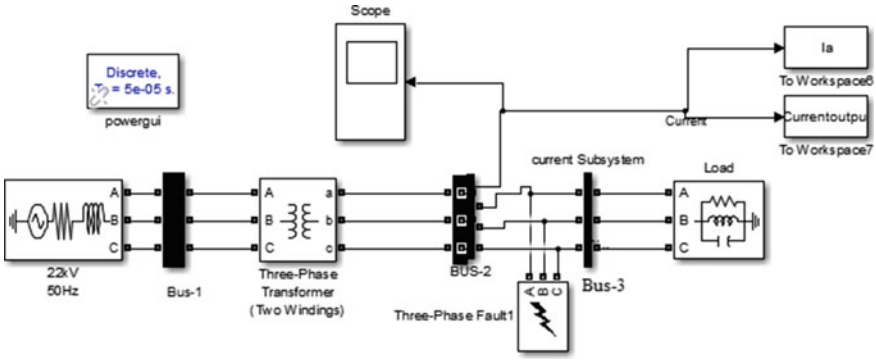


Fig. 3 Simulation of proposed model for fault identification and classification

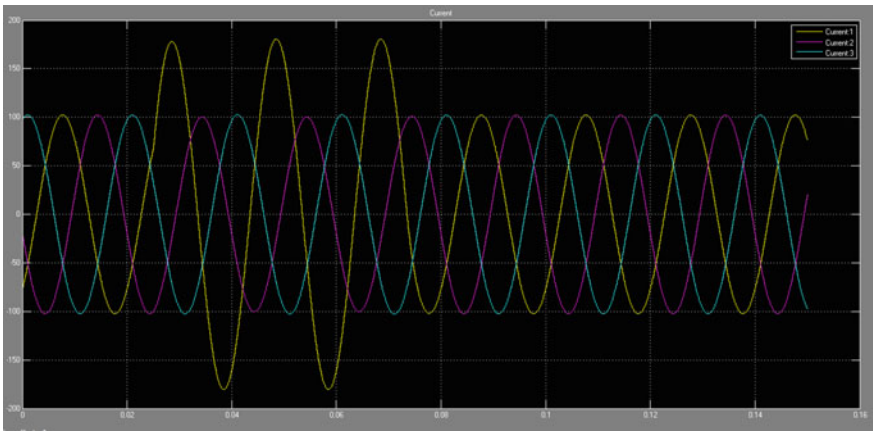


Fig. 4 Current waveform of SLG fault (abnormal condition of Bus-2). [$I_{a\ max}$ = 170A, $I_{b\ max}$ = $I_{c\ max}$ = 101.5A]

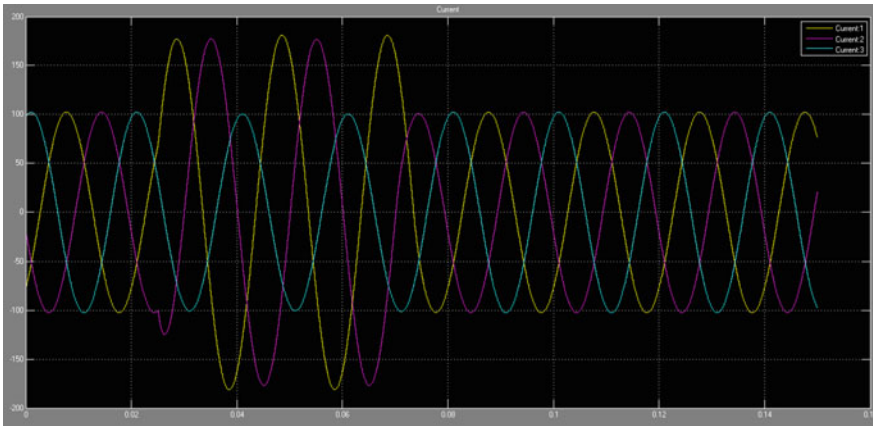


Fig. 5 Current waveform of DLG fault (abnormal condition of Bus-2) [$I_{a\ max}$ = $I_{b\ max}$ = 170A, $I_{c\ max}$ = 101.5A]

6 ANFIS Results and Discussion

In the ANFIS, the data is trained for the classification of fault. All the data is taken from the matrix form and the data is taken from the workspace which comes from wavelet transform that gives the energy of current waveform of bus-2.

In Fig. 8a Checking the data, checking data shows the output 1 "+" like this and "1" denotes the three phase fault and their phase (a-b-c or a-b-c-g). Similarly, all the faults are the output from 1 to 10. From this basis, classification of fault occurs. There are the surface view of the three phase fault where the phase (a-b-c or

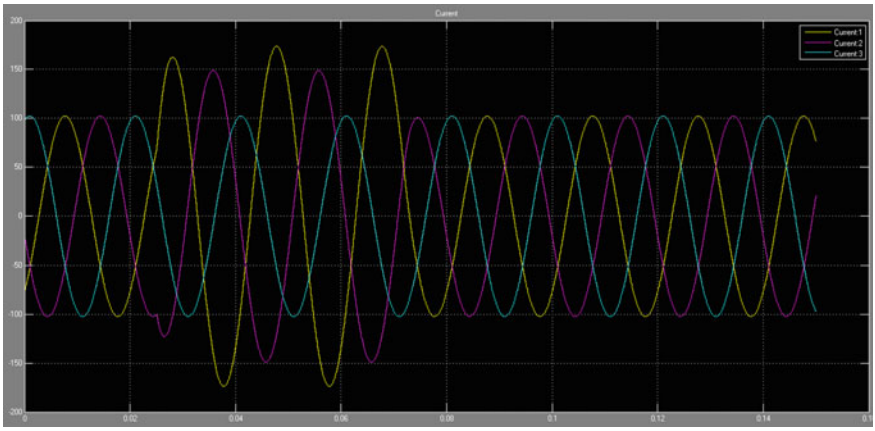


Fig. 6 Current waveform of LL fault (abnormal condition of Bus-2) [$I_{a\ max}$ = 160A, $I_{b\ max}$ = 150A, $I_{c\ max}$ = 100A]

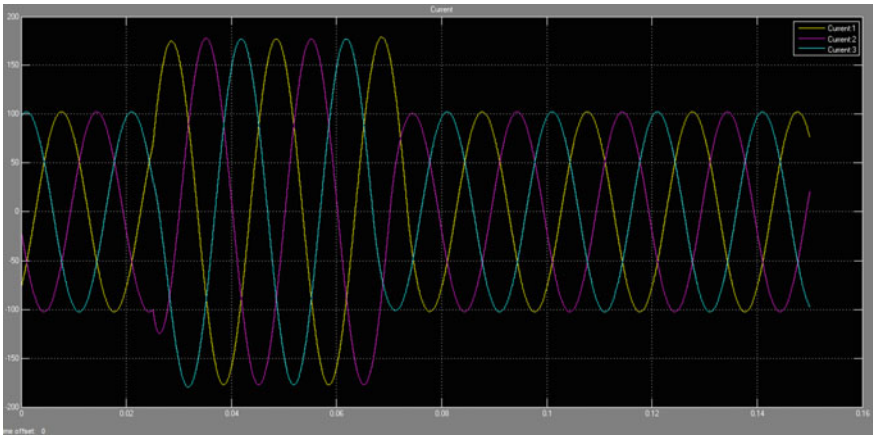


Fig. 7 Current waveform of three phase fault (abnormal condition of Bus-2) [$I_{a\ max}$ = $I_{b\ max}$ = hx00A0;$I_{c\ max}$ = 175A]

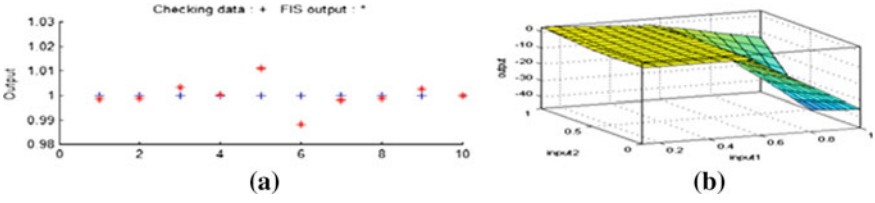


Fig. 8 **a** Checking data in ANFIS and graph shows in FIS output. **b** Surface view of three phase fault where the phase (a-b-c or a-b-c-g)

a-b-c-g). It start from 0 and to 1. Surface view starts from 0 and end with the value 1 for three phase fault.

In Fig. 9, the fuzzy logic controller displays the type of fault as shown in Table 1. Fuzzy logic controller takes the value from the workspace in FISs form whereas the constant value also takes from workspace in the matrix form. In Table 1, the display shows the output in display numerical value from 1 to 10, and from this value classification of faults occurs. Various types of line fault are classified by the FIS. When three phase fault occurs in the system then it shows the value "1" and from this display, classify the fault. Similarly, all these types of fault like the SLG fault are classified; when output come "8/9/10" then classify the fault and which phase are also classified by value "8/9/10". If 8 comes, then "A-G" Phase fault occurs and it is SLG fault. From this, classify all faults and after that clear the fault as soon as possible from damage the equipment from the hazard.

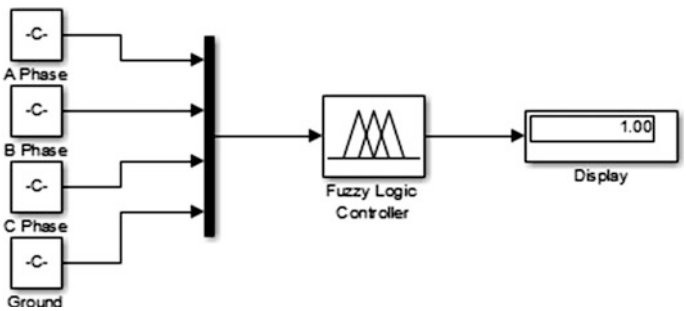


Fig. 9 Fuzzy inference system to display the type of fault

Table 1 Type of fault, phase conductor and display output for the classification of fault

Type of fault	Phase of conductor	Display output
Three phase fault	A-B-C or A-B-C-G	1
DLG	A-B-G	2
DLG	B-C-G	3
DLG	C-A-G	4
LL	A-B	5
LL	B-C	6
LL	C-A	7
SLG	A-G	8
SLG	B-G	9
SLG	C-G	10

7 Conclusion

Current is the most important factor for the line. For identification of faults, we used the wavelet transform and for classification of ANFIS. Wavelet Transform helps to find the energy of current and energy of current is varied in fault condition. In fault condition, energy of faulty phase is more compared to normal condition; due to this condition identify the fault. ANFIS helps to classify the fault by the displayed output in Table 1. In the FISs system, output display is controlled by the fuzzy logic controller.

References

1. C. L. Wadhwa: Electrical Power System. New Age International Publishers. 6th Edition, 2005.
2. Badri Ram and D N Vishwakarma: Power System Protection and Switchgear. Tata McGraw Hill. 2nd Edition, 2007.
3. Mayuresh Rao and R.P. Hasabe: Detection and Classification of Faults on Transmission Line Using Wavelet and Neural Network. International Journal of Advanced Electrical and Electronics Engineering, (IJAEEE). 2278–8948. Volume-2. Issue-5. 2013.
4. S. Saha, M. Aldeen and C.P.Tan: Fault detection in transmission networks of power systems. Scince Direct Electrical Power and Energy Systems 33. pp. 887–900. 2011.
5. Kevin M. Passino and Stephen Yurkovich: Fuzzy Control. 1st Edition. Addison Wesley Longman. Inc. California. 1998.
6. Huseyin Eristi: Fault diagnosis system for series compensated transmission line based on wavelet transform and adaptive neuro-fuzzy inference system. Elsevier. Measurement. Vol 46. pp. 393–401. 2013.
7. J. Zhang, Z.Y. He, S. Lin, Y.B. Zhang, Q.Q. Qian: An ANFIS-based fault classification approach in power distribution system. Elsevier. Electrical Power and Energy Systems. Vol. 49. pp. 243–252. 2013.

Study of Power Spectrum Estimation of Steady-State Visual Evoked Potential-Based BCI System Using AR Model Approach

Mukesh Kumar Ojha and Anshuman Prakash

Abstract Brain-computer interface (BCI) system is the direct interaction between the human brain and the external electronic devices like robotic arms, electronic wheel chair, etc., through desired mental tasks which enable the different amplitude of brainwaves inferring to humans' different mental activities. It uses the electrical activity of brain caused by the communication between the two neurons. The neurons communicate with each other in the form of electrical impulses which generate low amplitude and low frequency electromagnetic wave termed as electroencephalogram (EEG), In the past years, different Paradigms have been used to design BCI like Motor imaginary, P300, SSVEP, etc. The objective of this paper is to estimate the power spectral density (PSD) of the SSVEP signal (Steady-state Visual evoke Potential) from recoded EEG Data using AR Model approach.

Keywords BCI · SSVEP · EEG · Feature extraction

1 Introduction

Brain-computer interface (BCI) is a direct communication system between human brain and external device that enables a person to send the command to external device only by means of different brain activities [1, 2]. The functional activity of brain signal is measured by placing the sensors on the surface of the brain called electroencephalography (EEG). The appearance of different brain activity depends upon the location of sensor placement on the surface of head, mental status of the subject, and various other parameters. EEG approach to acquire the brain signal is broadly acceptable because of its simple and safe approach.

M.K. Ojha (✉)
BIT MESRA, Ranchi, India
e-mail: mukesh_cs07@yahoo.com

Anshuman Prakash
University of Petroleum and Energy Studies, Dehradun, India

© Springer Science+Business Media Singapore 2017

R. Singh and S. Choudhury (eds.), *Proceeding of International Conference on Intelligent Communication, Control and Devices*, Advances in Intelligent Systems and Computing 479, DOI 10.1007/978-981-10-1708-7_71

Different paradigms can be followed in the design of BCI Such as Motor Imagery, P300, and Steady-State Visual Evoked Potential (SSVEP) [3]. In recent years, SSVEP-Based BCI System become more popular among the various research groups because of high information Transfer Rate (ITR), short training time, high signal-to-noise ratio and simple system configuration [4, 5].

This paper is organized as follows; in Sect. 2 fundamental of SSVEP Signal and SSVEP-Based BCI System is presented in detail. In Sect. 3, FFT Approach and AR Model approach to estimate the power spectrum is explained in details. Result and future research work are presented in Sect. 4.

2 SSVEP System

2.1 Fundamentals of Steady-State Visual Evoked Potentials

The various research groups working on SSVEP-based BCI system have suggested that when subject focuses his/her attention on a visual stimulus that flicker at certain frequency, a periodic response occurs into the visual cortex of brain region known as steady-state visual evoked potential [4, 5]. The study of various research papers have explained that the EEG response produces brain signal with an increase in energy at frequency same as the frequency at which stimulus blinking. The SSVEP response is predominant into visual cortex region of brain while the other brain region is also activated with some amount of variation of degree [5]. The detection of SSVEP signal is done using various signals processing method that exploit the specific characteristics of signal such as timing, rhythmic information.

2.2 SSVEP-Based BCI System

Three fundamental modules are used to design SSVEP-Based BCI System as shown in Fig. 1. They are **Data Acquisition System, Signal Processing, and Classification** module. The function of data acquisition system is to acquire the brain signal from the surface of head. The technique used to acquire the brain signal from the surface of head is known as EEG.

Since EEG is an indirect approach to acquire the brain signal, it is often contaminated with noise. The most common noise in EEG is from muscles or electromyogram (EMG), Power line frequency (50–60 Hz), and electrooculogram (EOG). Electrooculogram mainly comes from eye blinking and eye movement. The next stage of BCI system is signal processing. The objective of signal processing approach to minimize the noise level and to detect the informative signal (SSVEP Signal) from recorded EEG signal. Signal processing approach is performed into three stages, i.e., preprocessing, feature extraction, and detection [6]. Finally, the

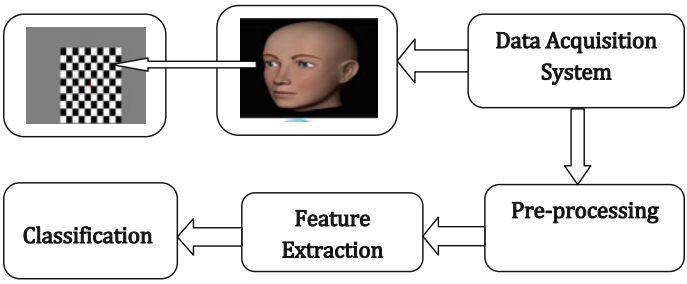


Fig. 1 SSVEP-based BCI system

detected signal is classified using various classification algorithms into certain command to operate the external machine. The main emphasis of this paper is extract the SSVEP signal which resides in the EEG recorded signal. This paper focus on the study of various methods such as FFT-based Periodogram and AR model approach to estimate the power spectrum density of recorded EEG signal corresponds to the stimulus frequency of SSVEP signal.

3 PSD Estimation Using FFT and AR Model

3.1 DFT Approach to Calculate the PSD

Discrete Fourier transform is a powerful tool for spectral analysis that can be applied to detect the SSVEP peak. The analysis signal is EEG recorded from the surface of head. Fourier states that any signal in time domain can be expressed into frequency domain as a sum of sinusoidal function with different frequency [7]. Mathematically, this is define as

$$x(n) = \sum_{n=-\frac{N}{2}}^{\frac{N}{2}} A_n \sin(2\pi f_n t + \varphi)$$

The discrete Fourier transform of the signal $x(n)$ at ith electrode recorded from the surface of head at discrete time t_n is given by

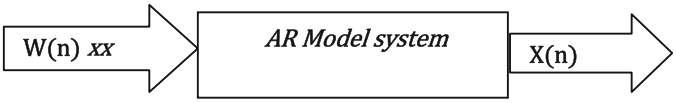
$$X(K) = \sum_{n=0}^{N-1} x(n) \mathrm{e}^{\frac{-j2\pi Kn}{N}} \tag{1}$$

The power spectrum of data sequence $x(n)$ is computed by

$$S_{xx}(f) = \frac{1}{N}|X(K)|^2 \tag{2}$$

3.2 AR Model to Calculate the PSD

The major drawback with DFT approach is that this method suffers from spectral leakage and also provides poor frequency resolution [7]. To overcome such problem, a model-based approach is used to estimate the power spectral density [7]. A model for the generation of signal is constructed and also the number of parameters can be estimated from the observed data. Based on model and estimated parameters, power spectral density is computed. Autoregressive model (AR-Model) is most widely used model and is suitable to represent the spectra with narrow peak and require simple linear equation to find the AR parameters [7].



Block Diagram AR Model System

The output data sequence $x(n)$ is obtained from difference equation which is given by

$$\begin{aligned} x(n) &= -\sum_{k=1}^{p} a_k x(n-k) + w(n); \quad \text{where } p \\ &= \text{model order and } w(n) \text{ is gaussian noise} \\ \text{or;} \quad & x(n) + \sum_{k=1}^{p} a_k x(n-k) = w(n) \end{aligned} \tag{3}$$

The Fourier transforms of above equation give the power spectral density that is given by

$$P_{xx(f)} = \frac{\sigma^2}{\left|1 + \sum_{k=1}^{p} a_k e^{-j2\pi k}\right|^2} \tag{4}$$

The estimation of power spectrum requires the selection of model order p and the estimation of model order parameters a_k. Here, Yule-Walker method is used to find the model parameters a_k.

Estimation of a_k Using Yule-Walker Method:

We know that a series of data sequence using AR model is represented as;

$$x(n) + a_1 x(n-1) + a_2 x(n-2) + \cdots \; a_N x(n-N) = w(n) \tag{5}$$

$$\text{or;} \; \sum_{k=0}^{N} a_k x(n-k) = w(n) \tag{6}$$

where $w(n)$ is white Gaussian noise and N is the length of data sequence.

The ensemble average of the above Eq. (6) is given by

$$\sum_{k=1}^{N} a_k E[x(n-k)x(n-l)] = E\{w(n)x(n-l)\};$$

$$\text{where} \;\; a_0 = 1 \;\; \text{and} \;\; l \;\text{is the order of system}$$

Finally

$$\sum_{k=1}^{N} a_k r_{xx}(l-k) = r_{xx}(l) \tag{7}$$

$$\begin{bmatrix} r_{xx}(0) & r_{xx}(-1)\ldots & r_{xx}(1-N) \\ r_{xx}(1) & r_{xx}(0)\ldots & r_{xx}(2-N) \\ r_{xx}(N-1) & r_{xx}(N-2)\ldots & r_{xx}(0) \end{bmatrix} \begin{bmatrix} a_1 \\ a_2 \\ a_N \end{bmatrix} = - \begin{bmatrix} r_{xx}(1) \\ r_{xx}(2) \\ r_{xx}(N) \end{bmatrix} \tag{8}$$

The solution of the above equation gives

$$a = -R^{-1} r \tag{9}$$

where R is a Toeplitz matrix of data sequence $x(n)$; r is the autocorrelation matrix of data sequence $x(n)$ and the 'a' is the AR Coefficient. These AR coefficients can be estimated by using Yule-Walker method and the corresponding PSD can be obtained from the frequency response of Yule-Walker method. Akalke information criteria are used for the selection of model order.

The order of system using Akaike information criteria is given by

$$\text{AIC}(P) = \ln\left(\sigma^2 p\right) + \frac{2(p+1)}{N}$$

where N is the length of data and $\sigma^2 p$ is the prediction error rate of AR Model with order p. The major challenges with AR Model approach is the selection of model order. If the selected order is low, there will be no definite peaks in the spectrum and hence frequency details of the signal cannot be identified. If the order is large, faulty peak may be seen into the spectrum that is not related to original signal [7]. In this paper, model order is considered as 16 to find the frequency spectrum of recorded data.

4 Result and Discussion

The data used in this paper is a single channel data set taken from internet which is available online for free to everyone. The copyright of data set is with Adnan vilic. The study of data set state that EEG signal is recorded by placing the electrode at OZ position on the surface of head by using 10–20 electrode placement system. The

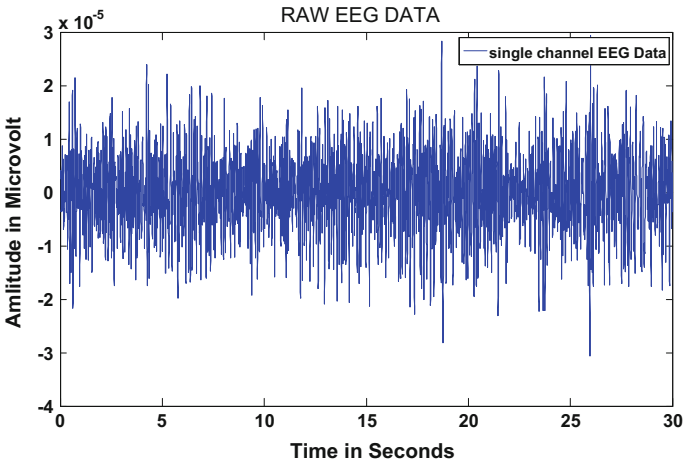


Fig. 2 EEG recorded data

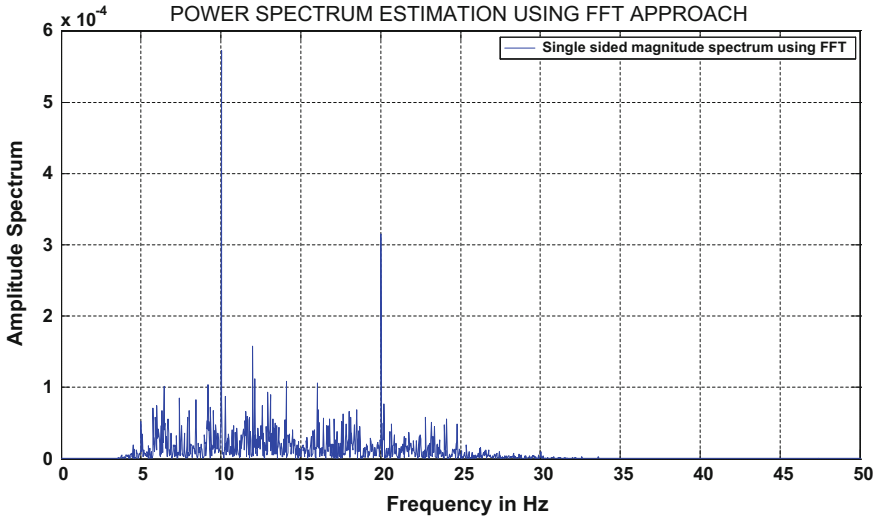


Fig. 3 Amplitude spectrum of SSVEP in response to 10 Hz, recorded from Oz channel using FFT approach

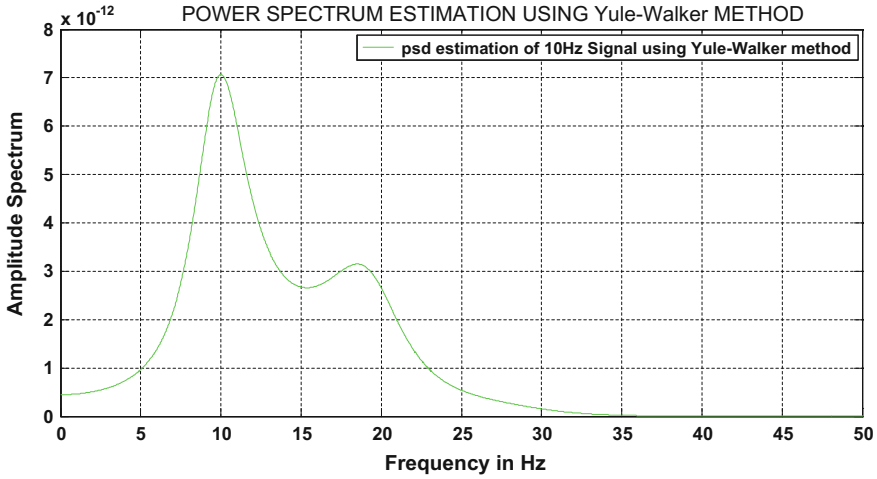


Fig. 4 Amplitude spectrum of SSVEP in response to 10 Hz, recorded from Oz channel using Yule-Walker method

available data set is recorded for 30 s at sampling rate of 512 Hz. The stimulus flickering frequency is 6, 6.5, 7, 7.5, 8.2, 9, and 10 Hz. The time series of recorded data set is shown in Fig. 2.

For each trail of above data set the power spectrum density using FFT approach and Auto regressive approach is estimated that is shown in Figs. 3 and 4.

The future steps in this research include:

- To study the various classification algorithm to find the detection accuracy of power spectrum estimated using above approach. Our plan is to work on the SSVEP data set recorded from multiple channel placed at the surface of head. Our objective in future work is on the study of the advance signal processing algorithm such as Non-linear Detection Algorithm to optimize the SSVEP detectability.

References

1. J.R. Wolpaw, N. Birbaumer, et al.: “Brain Computer Interfaces for communication and control”, Clinical Neurophysiology, Vol. 113, No. 6, pp. 767–791, 2002.
2. Henrik Gollee, Member, IEEE, Ivan Volosyak, Angus J. McLachlan, Kenneth J. Hunt, and Axel Gr¨aser “An SSVEP-Based Brain–Computer Interface for the Control of Functional Electrical Stimulation” IEEE Transactions on Biomedical Engineering, Vol. 57, No. 8, 2010, pp. 1847–1855.
3. Ming Cheng, Xiaorong Gao “Design and Implementation of a Brain computer Interface with High Transfer Rates” IEEE Transaction on Biomedical Engineering, 2002, PP.1181–1185.

4. Ola Friman, IvanVolosyak and Axel Graser, “Multichannel Detection of SSVEP for Brain Computer Interface” IEEE Transaction on Biomedical Engineering, 2007, PP. 742–749.
5. Danhua Zhu etc “A survey of Stimulation methods used in SSVEP Based BCIs” computational intelligence and Neuroscience, 2010.
6. Zhenghua Wu and Dezhong Yao “Frequency Detection with stability coefficient for SSVEP Based BCIs” journal of Neural Engineering, 2008. PP.506–512.
7. John G. Proakis “Digital Signal Processing Principles, Algorithms and Application” Fourth Edition Pearson Education, Prentice Hall.
8. Zhonglin Lin and Changshui Zhang “Frequency Recognition Based on Canonical Correlation Analysis for SSVEP-Based BCIs” Neural Engg. 2006, PP. 845–849.
9. Ivan Volosyak “SSVEP-based Bremen-BCI Interface-boosting information transfer rates” journal of Neural Engineering, 2011 pp-702–709.
10. Jie pan “Enhancing the classification accuracy of SSVEP Based brain computer interfaces using phase constrained canonical correlation Analysis” Journal of Neural Engineering, 2011.
11. Toshihisa Tanaka, Cheng Zhang, and Hiroshi Higashi “SSVEP frequency detection methods considering background EEG” journal of Neural Engineering, 2012.
12. Quan Liu, Kun chen “Review: Recent Development of Signal Processing Algorithms for SSVEP-based Brain computer interfaces” journal of Medical and Biological Engineering, pp 299–309, Aug 2013.
13. Sarah N. Carvalho, Thiago B.S. Costa “ Comparative analysis of strategies for feature extraction and classification in SSVEP BCIs.” Biomedical Signal Processing and control, 2015, pp 34–42.
14. YU Zhang, Guoxu Zhou “ Frequency Recognition in SSVEP-Based BCI using multiset canonical correlation Analysis.” International Journal of Neural Systems, 2014.
15. Kuo-kai shyu, Yun-jen chiu “Adaptive SSVEP-Based BCI System with frequency and pulse duty-cycle Stimuli tuning Design.” IEEE Transaction on neural systems and Rehabilitation Engineering, vol-21, 2013.
16. Guangyu Bin, Zheng Yan “An online multi-channel SSVEP-based brain Computer Interface using a canonical correlation analysis method.” Journal of Neural Engineering, 2009.
17. T. Tanaka, C. Zhang “SSVEP Frequency detection methods considering background EEG,” IEEE SCIS-ISIS, pp. 20–24, 2012.

Market-Clearing Price Forecasting for Indian Electricity Markets

Anamika and Niranjan Kumar

Abstract A robust market-clearing price (MCP) forecasting tool is needed for efficient and profitable power market execution. The work predicts MCPs for the months of April, May, and June using artificial neural networks (ANNs). A very large ANN with varying input data may lead to poor prediction in comparison with smaller ANN with similar input data due to its highly sensitive characteristic. Grouping of similar data accelerates the learning process of ANNs along with more accurate and efficient prediction result. In this paper, input data set is arranged into homogeneous groups of hours with similarity in prices, based on correlation matrix and peak, off-peak values of prices. Mean absolute percentage errors (MAPEs) are evaluated to find out the best grouping technique and forecasting model for Indian Electricity Markets. MAPE results are shown for the best two consecutive days and the whole month to demonstrate the effectiveness of grouping techniques.

Keywords Indian Electricity Markets · Artificial Neural Networks · Monotonic function · Correlation grouping · Peak and off-peak grouping

1 Introduction

Introduction of deregulation leads to customer-driven, organized electricity market, which offers opportunities for optimal resource utilization and efficient electricity procurement strategy. Electricity market-clearing price (MCP) is mutually agreeable price of electricity at equilibrium where the market is clear of shortage and surplus. For an Independent System Operator (ISO), MCP is obtained by solving Unit Commitment (UC) and Economic Dispatch (ED) problem with the bids and

Anamika (✉) · Niranjan Kumar
Department of Electrical and Electronics Engineering,
National Institute of Technology, Jamshedpur, India
e-mail: anamika.12rsee010@nitjsr.ac.in

Niranjan Kumar
e-mail: nkumar.ee@nitjsr.ac.in

© Springer Science+Business Media Singapore 2017

R. Singh and S. Choudhury (eds.), *Proceeding of International Conference on Intelligent Communication, Control and Devices*, Advances in Intelligent Systems and Computing 479, DOI 10.1007/978-981-10-1708-7_72

system conditions. The two forecasting procedures are considered largely. First one is forecasting based on average prices of similar days and, the other one is forecasting based on average prices of similar days plus ANN refinement. The forecasting models with specified inputs are applied to PJM electricity market to forecast the LMPs for a weekend day in winter, a holiday in spring, and a summer day. The best MAPEs are found to be 5.33, 5.53, and 3.32 % respectively [1]. The time series models dynamic regression (DR) and transfer function (TF) models are applied to forecast the actual prices in the electricity markets of Mainland Spain and California. The mean of the errors is calculated for all the weeks and for both DR and TF models [2]. The neural networks were first preprocessed through rough set theory. Correlation results show the relationships in weekly variation data on electricity prices. The %MAPE for the year in PJM market is found to be 11–33 % [3]. Comparative volatility indices analysis is conducted in the case of Ontario Market, where volatility indices are developed based on price velocity concepts and historical volatility [4]. Price cap regulation achieved the goal of lowering the price level at the cost of higher price volatility [5]. ANNs are combined with graphics processing units (GPUs) for forecasting of power system demand in Korean Electricity Markets. As GPU is incorporated with ANN, MAPE of forecasting result is around 1 % and forecasting result is produced fast [6]. Nonparametric regression methods are used for forecasting the electricity price and demand in the market of mainland Spain [7]. Least square support vector machine (LSSVM) is combined with auto-regressive moving average with external input (ARMAX) module to predict hourly electricity MCP for an entire month [8]. The LSSVM is being a strong regression tool to forecast electricity price in California's electricity markets. The data samples are collected, clustered, and passed through LSSVM to predict price [9]. Modeling for suitable forecasting model for Indian Electricity Markets using Day of the week, A time slot of Day, Forecasted Demand, Change in Demand, Price one day ago, Price one week ago, Price two weeks ago, Price three weeks ago, and Price four weeks ago. Data preprocessing by eliminating price spikes and normalizing the rest (three sigma rule is used to identify the price spikes and normalization is performed by linear scaling of data). Grouping of 24 h of a day based on correlation matrix and based on peak, off-peak values of MCPs are conducted. Significant improvement in prediction performance with a smaller and similar input data set. The rest of the paper is as follows: Sect. 2 illustrates methodologies used for forecasting the MCPs. The grouping of hours based on correlation matrix and peak, off-peak values of MCPs are described in Sect. 3. Inputs and outputs used for predicting the MCPs in Indian Electricity Markets are discussed in Sect. 4. The findings of the research are presented in Sect. 4 and conclusions are included in the Sect. 5.

2 Approaches

2.1 Artificial Neural Networks (ANN)

The interest in ANNs is largely due to their skill to imitate natural intelligence in its learning from experience. A multi-layered perceptron (MLP) neural network (NN) using three hidden layers is implemented in this research for accurate price forecasting. An MLP neural network can be viewed as three-layered feed forward neural network with a linear output mapping and without feedback. Let us consider an artificial neuron has n inputs as x_i $(i = 1, 2, 3. . .n)$ from the environment or adjacent neuron. Each input is weighted with w_{i} before reaching the processing body of the neuron. The total signal net inside the neuron could be calculated by

$$\text{net} = \sum_{i=1}^{n} x_i w_i = W^T X \tag{1}$$

The weighted signal will be mapped by the activation function $f(.)$. Hence the output can be calculated by (2). This output may either input to the other neuron in adjacent layer or final output at the output layer. The back propagation algorithm suggested in [1] is used as a supervised iterative training method of finding weights that can achieve best mapping between input and output. The weights revision was done based on rule stated in (3).

$$y = f(\text{net}) \tag{2}$$

$$w_{ji}^{\text{new}} = w_{ji}^{\text{old}} - \eta \frac{\partial E}{w_{ji}} \tag{3}$$

Here, E is the amount of error and it can be calculated as below

$$E = \sum_{k=1}^{L} \sum_{j=1}^{q} \left(b_{jk} - z_{kj}\right)^2 \tag{4}$$

2.2 Correlation Analysis

The correlation provides the degree of linear association between two variables, which entails how strongly the two variables are related to each other. It is performed by determining the correlation coefficient, whose value is bounded between −1 and 1. There are three possibilities of being positively correlated, negatively correlated and not correlated for the correlation coefficients with values near to 1, −1, and 0, respectively. The procedure to compute the correlation coefficients is as follows:

1. Consider two data sets X and Y and convert them to standard units and determine mean and standard deviation of each data set.
2. Compute the products of the standard units of the x-values and the y-values.
3. Take the average of the products.

The correlation coefficient is obtained by using a nonparametric measure of statistical dependence between two variables called Spearman rank-correlation coefficient, whose one important characteristic is that it utilizes rank-order of the data regardless of distribution between two data sets. The expression of Spearman rank-correlation coefficient for its calculation is given as

$$\rho = 1 - 6\sum_{i=1}^{n} D_i^2 / n\left(n^2 - 1\right) \tag{5}$$

where $D_i = x_i - y_i$

2.3 Performance Evaluation

Mean absolute percentage error (MAPE) is the most widely used measurements for performance evaluation of forecasting MCPs. The expression to evaluate the MAPE is as follows.

$$\text{MAPE} = \frac{1}{N}\sum_{t=1}^{N} \frac{|t_k - O_k|}{t_k} \times 100 \tag{6}$$

3 Grouping of Hours of the Day

This section provides the various grouping of hours for the implementation of forecasting MCPs for Indian Electricity Markets. Out of the two approaches the former being the grouping based on correlation matrix and later being the grouping based on peak and off-peak. The two methods are as follows.

3.1 Grouping Based on Correlation Matrix

A correlation matrix has been evaluated to find out the hours which are nearly correlated. The matrix has been evaluated based on the data from January 1, 2014 to

June 30, 2014 of Indian Electricity Markets. The correlation results reveal that the 24 h in a day can be divided into 5 groups and they are presented as follows. *Group 1* includes the hours from 1 to 5 depending upon the correlation factor 0.77. The hours 1, 2, 3, 4 are correlated as 0.79, 0.88, 0.91, and 0.95, respectively, with respect to hour 5 which is more than 0.77. *Group 2* consists of hours 6, 7, 8, and 9 which have the correlation factors as 0.78, 0.79, 0.938, and 1, respectively, with respect to hour 9. *Group 3* consists of hours 10 to 17 which have the correlation factor as 0.87, 0.87, 0.9, 0.9, 0.85, 0.88, 0.87, and 1, respectively, with respect to hour 17. The correlation factor of hour 18 with 19 is 0.68 and 17 is 0.83. This intends to insert the hour 18 with the group that contains hour 17. *Group 4* however the hour 19 is not correlated highly with any of the remaining hours. Therefore, this hour is considered separately as a group. *Group 5* constitutes of hours 20, 21, and 22 which have the correlation factor of 0.86, 0.93, and 1, respectively. The correlation factors of hour 23 with 22 and 24 are 0.9 and 0.84, respectively. This leads to insertion of the hour 23 into the group that contains hour 22.

3.2 Grouping Based on Peak and Off-Peak Values of MCP

A regular subdivision in only two time blocks is proposed to forecast the MCPs in the Indian Electricity Market. Table 1 represents the actual distribution of peak and off-peak hours of every month for considering the time period. Various combinations of hours are found out to discover peak and off-peak hours based on the similarity on price.

Table 1 Classification of hours for the peak, off-peak hours grouping technique

Data set	Month	Peak hours	Off-peak hours
Training	January	9, 10, 11, 12, 13	1, 2, 3, 4, 5, 6, 7, 8, 14, 15, 16, 17, 18, 19, 20, 21, 22, 23, 24
	February	9, 10, 11, 12, 13	1, 2, 3, 4, 5, 6, 7, 8, 14, 15, 16, 17, 18, 19, 20, 21, 22, 23, 24
	March	10, 11, 12, 13, 14, 19, 20, 21, 22	1, 2, 3, 4, 5, 6, 7, 8, 9, 15, 16, 17, 18, 23, 24
Testing	April	10, 11, 12, 13, 14, 19, 20, 21, 22	1, 2, 3, 4, 5, 6, 7, 8, 9, 15, 16, 17, 18, 23, 24
	May	10, 11, 12, 13, 14, 15, 16, 20, 21, 22, 23, 24	1, 2, 3, 4, 5, 6, 7, 8, 9, 17, 18, 19
	June	11, 12, 13, 14, 15, 16, 20, 21, 22, 23, 24	1, 2, 3, 4, 5, 6, 7, 8, 9, 10, 17, 18, 19

4 Data Collection

The inputs and outputs are selected for forecasting MCP in Indian Electricity Markets based on insight given by Singhal et al. [10]. The data are collected from the Indian Electricity Exchange (IEX) [11] for 6 months from January 2014 to June 2014. The neural networks are trained with 50 % data and tested with remaining 50 % data. Historical information on electricity prices and past load demand constitutes important inputs for predicting MCP. The various inputs considered for predicting the MCPs are *Day of the week, A time slot of Day, Forecasted Demand, Change in Demand*, *Price one day ago*, *Price one week ago, Price two weeks ago*, *Price three weeks ago,* and *Price four weeks ago.*

5 Results

The electricity price and demand data have been collected for 6 months from IEX [11]. 50 % data are used for training and the remaining 50 % is used for testing neural networks. The time steps are hourly, which means that each day consists of 24 steps (i.e., 24 h). The proposed model will take time indices, historical prices, and historical demand as inputs and predict MCP. Neural Networks are applied separately on different groups to forecast hourly MCPs for the months of April, May, and June of the year 2014 in the Indian Electricity Exchange. Data is preprocessed by eliminating outliers or price spikes and normalizing or limiting the rest. Presence of outliers or price spikes leads to vulnerable prediction result and unusual market behavior.

5.1 Correlation Grouping Results

Five separate ANNs are used to forecast the MCPs for the months of April, May, and June. The feed forward networks have been trained to estimate MCP based on

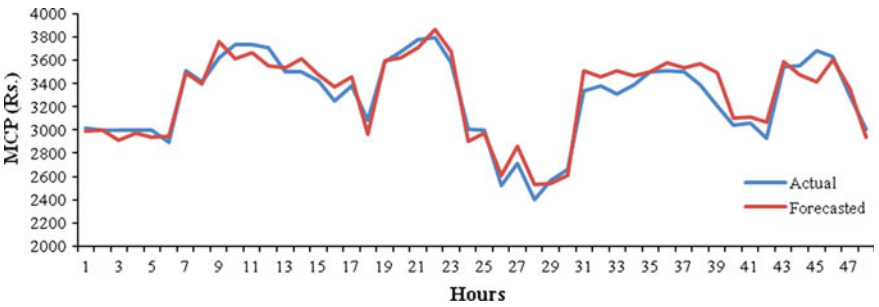


Fig. 1 Forecasted MCP and actual MCP for two consecutive days in month April using correlation grouping

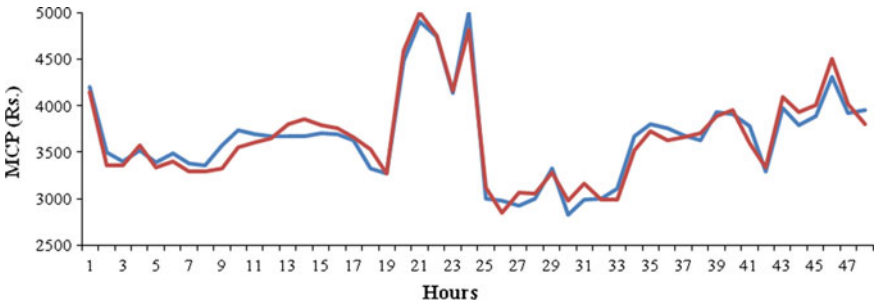


Fig. 2 Forecasted MCP and actual MCP for two consecutive days in the month May using correlation grouping

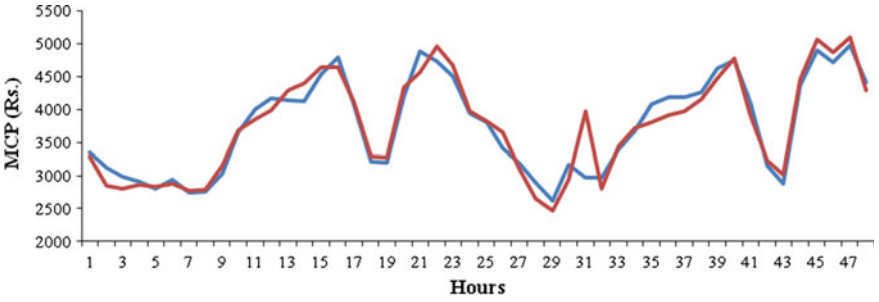


Fig. 3 Forecasted MCP and actual MCP for two consecutive days in month June using correlation grouping

the training data set. The best model is validated by comparison between estimated and measured values of MCPs as shown in (Figs. 1, 2 and 3).

5.2 Peak and Off-Peak Grouping Results

The peak and off-peak hours of grouping is applied to forecast prices of peak hours and off-peak hours of a day. This kind of grouping divides the total 24 h into two time blocks and these are forecasted separately. Hence two ANNs are used to forecast MCPs for the months of April, May, and June, respectively. Figure 4 describes the actual and estimated values of MCP for the IEX in the month of April (for only two consecutive days) using peak, off-peak grouping. The graph shows an acceptable agreement between estimated and actual values of MCPs. The figure also reveals that maximum MCP is available at 46th hour and minimum is at 28th hour. It reveals that MCPs at 29th hour and 22nd are forecasted with highest errors. The error obtained by peak, off-peak grouping at 45th hour is low when compared

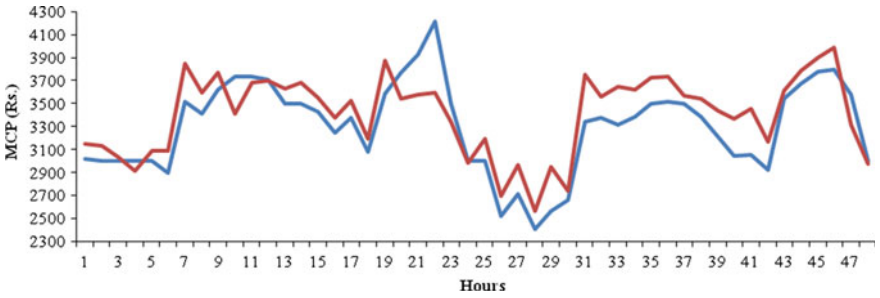


Fig. 4 Forecasted MCP and actual MCP for two consecutive days in month April using peak, off-peak grouping

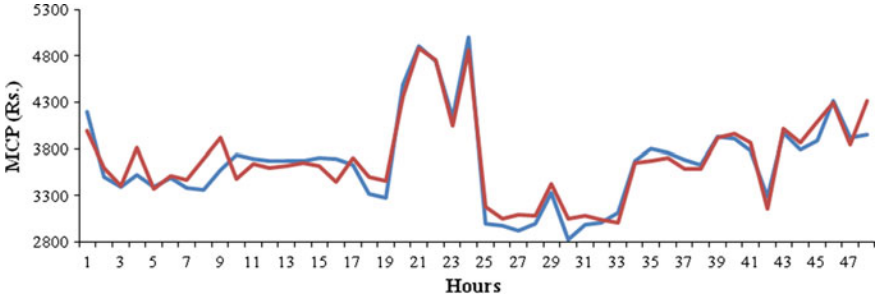


Fig. 5 Forecasted MCP and actual MCP for two consecutive days in the month May using peak, off-peak grouping

with error obtained by correlation grouping. The forecasted and actual values of MCPs for IEX in the month of May are presented in Fig. 5.

The figure shows a closest agreement between estimated and actual values of MCP for all the 48 h. The maximum of MCP is observed at 21st hour and minimum is observed at 33rd hour. This illustrates a good agreement between forecasted and actual values of MCP. The hours except 8th and 9th are forecasted with good accuracy. The Fig. 6 depicts the predicted and actual values of MCP for the month of June. The maximum and minimum values of MCP are observed at 16th hour and the 29th hour, respectively. The MAPE values are also evaluated for further favoritism in the analysis of accuracy. The values of absolute errors, according to the Eq. (5) for two consecutive days and for the whole month using both correlation and peak, off-peak grouping methods are evaluated. The MAPE, R^2 values obtained for 2 consecutive days and 3 months by both of grouping techniques are tabulated in Table 2, respectively. The R^2 values obtained by correlation grouping of hours are observed as 0.9175, 0.9438, and 0.9192 for the months of April, May, and June, respectively. Similarly, the values for months April, May, and June are observed as 0.7279, 0.9127, and 0.8934, respectively. This confirms good potentiality in predicting MCP by ANNs for Indian Electricity Markets.

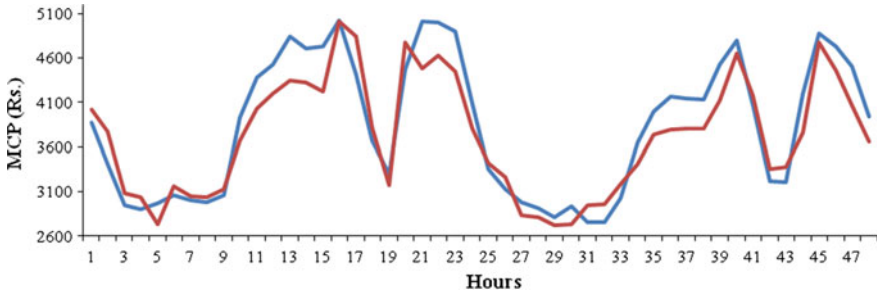


Fig. 6 Forecasted MCP and actual MCP for two consecutive days in month June using peak, off-peak grouping

Table 2 Summary of results obtained in two consecutive days and for whole month using both of the grouping techniques

Month	Correlation grouping			Peak, off-peak grouping		
	Two consecutive days (%)	R^2	Whole month (%)	Two consecutive days (%)	R^2	Whole month (%)
April	2.602	0.9175	09.9786	5.8838	0.7279	09.1938
May	2.776	0.9438	14.2805	3.2127	0.9127	32.0518
June	4.142	0.9192	14.0128	6.1237	0.8934	24.8935

6 Conclusion

In this paper, electricity MCPs estimation using neural networks is presented in deregulated electricity markets. The MCPs are estimated over the months of April, May, and June for Indian Electricity Exchange using an innovative technique. Various grouping modules are applied initially on collected data to group the 24 h of a day. The correlation grouping module and the peak, off-peak grouping module divides the 24 h of a day into 5 and 2 groups, respectively. Time slots, historical demands, and prices are utilized as inputs to the forecasting tool. The MLP network has been applied to forecast the MCPs for Indian Electricity Exchange. The validation of the proposed model was performed with unknown data, which the model did not see before. Analysis of MAPE values concludes that the prediction through the proposed MLP network is more appropriate and accurate as compared to the other empirical models.

References

1. Paras Mandal, Tomonobu Senjyu, Atsushi Yona, Jung-Wook Park and Anurag K. Srivastav: Sensitivity Analysis of Similar Days Parameters for Predicting Short Term Electricity Price. Proc. NAPS' 07 (2007) 568–574.
2. Francisco J. Nogales, Javier Contreras, Antonio J. Conejo and Rosario Espínola: Forecasting Next Day Electricity Prices by Time Series Models. IEEE Trans. Power Systems 17 (2002) 342–348.
3. Hirofumi Toyama, Tomonobu Senjyu, Phatchakorn Areekul, Shantanu Chakraborty, Atsushi Yona and Toshihisa Funabashi: Next Day Electricity Price Forecasting on Deregulated Power Market. Proc. T&D Asia (2009) 1–4.
4. Hamidreza Zareipoura, Kankar Bhattacharya and Claudio A. Can izares: Electricity Market Price Volatility: The case of Ontario. Energy Policy 35 (2007) 4739–4748.
5. Sherzod N. Tashpulatov: Estimating the Volatility of electricity prices: The case of England and Wales wholesale electricity market. Energy Policy 60 (2013) 81–90.
6. Ting He, Ke Meng, Zhao Yang Dong, Yong-Taek Oh and Yan Xu: Use of High Performance Graphics Processing Units for Power System Demand Forecasting. Journal of Electrical Engineering & Technology 5 (2010) 363–370.
7. Juan M. Vilar, Ricardo Cao and Germán Aneiros: Forecasting next day electricity demand and price using non parametric functional methods. Electrical Power and Energy Systems 39 (2012) 48–55.
8. Xing Yan and Nurul A. Chowdhury: Mid-term electricity market clearing price forecasting: A hybrid LSSVM and ARMAX approach. Electrical Power and Energy Systems 53 (2013) 20–26.
9. Li Xie and Hua Zeng: Electricity Price Forecasting by Clustering-Least Squares Support Vector Machine. Proc. CSIP (2013) 1357–1361.
10. Deepak Singhal and K. S. Swarup: Electricity Price Forecasting using Artificial Neural Networks. Electrical Power and Energy Systems 33 (2011) 550–555.
11. Prices at IEX INR/Mwh, http://www.iexindia.com/marketdata/areaprice.aspx. Date last accessed: 09.01.2016.

Outage Capacity Performance Analysis of Dual-Hop Multiple-Relay Decode-and-Forward System for Generalized η-μ Fading Channel

Manoj Bisht and P. Palanisamy

Abstract The outage performance of dual-hop multi-relay decode-and-forward system for generalized (η-μ) fading channels is analyzed with the help of outage capacity. The channels between source to destination, direct or through relays are assumed to be generalized (η-μ) fading channels. This derived expression of outage capacity is for the considered system model. This paper contributes an exact formula for outage capacity for dual-hop multiple-relay generalized fading channels. Derived formulation is in infinite series form nevertheless the series converges promptly and therefore can be precisely approximated by considering finite number of terms. Examples are presented for dissimilar values of parameters η and μ. The derived expression is upheld by simulation.

Keywords Outage capacity · Multi-relay system · Dual hop · Decode and forward

1 Introduction

Relay system and cooperative communications [1–3] have been one of the most widely explored topics in communications in recent years. In relaying, two users cooperate through relays and transmit each other's message to the destination, outage of communication occurs only when both users concurrently experience poor channels, consequently enhance the transmission trustworthiness. There are three main categories of relaying system, namely amplify-and-forward (AF), decode-and-forward (DF) [4] and compress-and-forward (CF). In cooperative communication, relay decodes and regenerates the message and transmits it to the destination in the subsequent time slot, in case of DF relaying scheme. This paper discusses the DF relaying system. η-μ distribution is suited for non-line of sight situation. Formulation for outage capacity of a dual-hop multi-relay DF relaying

Manoj Bisht (✉) · P. Palanisamy
Department of Electronics and Communication, National Institute of Technology, Tiruchirappalli 620015, Tamilnadu, India
e-mail: Manoj.Bisht@gmail.com; manojbishtcoer@gmail.com

© Springer Science+Business Media Singapore 2017

R. Singh and S. Choudhury (eds.), *Proceeding of International Conference on Intelligent Communication, Control and Devices*, Advances in Intelligent Systems and Computing 479, DOI 10.1007/978-981-10-1708-7_73

system model for η-μ faded channels is derived in this paper. In order to derive this expression, the equipment received signal-to-noise ratio (SNR) is obtained [5, 6] and with the help of this, cumulative distribution function (CDF) is evaluated. Selection combining diversity technique is used for signal selection at the receiver. It is assumed that the source (S), relays (R), and destination (D), everyone have one antenna and all channels of transmission are independent of each other. There are two stages [7] of transmission. In first stage, destination and relays receive the signal transmitted from source. In second stage, destination receives transmitted signals from source and relays. This expression is used to analyze the outage performance of dual-hop multi-relay cooperative decode-and-forward system.

2 System Model

Consider a dual-hop multiple-relay DF cooperative relaying model [8]. Figure 1, shows the system model. It is also considered that relays are operated in half-duplex mode.

Signal x broadcasted by source is received at destination and at all relays. Received signal at destination (D) is given by

$$y_{\mathrm{SD}} = h_{\mathrm{SD}}\sqrt{P_{\mathrm{S}}}x_{\mathrm{S}} + w_{\mathrm{SD}} \tag{1}$$

signal x received at relays R_i in the system of N relays is given by

$$y_{\mathrm{SR}_n} = h_{\mathrm{SR}_n}\sqrt{P_{\mathrm{S}}}x_{\mathrm{S}} + w_{\mathrm{SR}_n} \tag{2}$$

here P_{S} is the transmitted power of source terminal, h_{SD} and h_{SR_n} are fading channels coefficient between source-delay and source-relays, respectively. In second phase of transmission, since DF protocol is in use, the relays (R_n) decode the

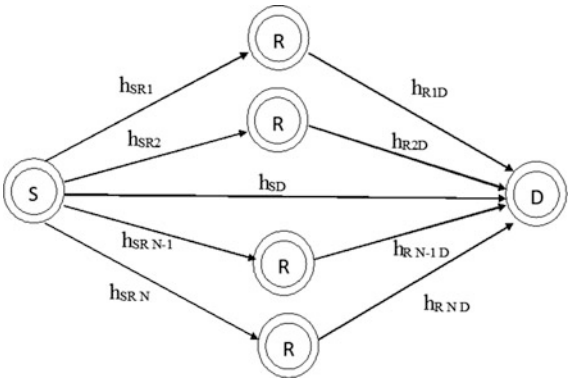


Fig. 1 System model for dual-hop multiple-relay cooperative decode-and-forward model

received signal from source and transmit it to destination (D) [8]. Finally destination (D) receives signal from relays (R_n), which can be written as

$$y_{R_nD} = h_{R_nD}\sqrt{P_{R_n}}x + w_{R_nD} \tag{3}$$

P_R is the transmitted power at relay $R_n \cdot h_{R_nD}$ are the η-μ fading channels coefficients between relays (R_n) and destination. N is the number of relays which decode-and-forward signal towards destination. Signal at destination node is received using selection combining as diversity technique, i.e., we are choosing the strongest signal, which has highest SNR [3] out of one straight path from source terminal to destination and N paths from relays (R_n) to destination.

$$\gamma_{SR} = \frac{|h_{SR}|^2 P_S}{w_{SR}} \tag{4}$$

$$\gamma_{RD} = \frac{|h_{RD}|^2 P_S}{w_{RD}} \tag{5}$$

for dual-hop DF relaying system model, the corresponding received SNR at node D is closely approximated at high SNR section [9] as follows $\gamma_{eq} = \min(\gamma_{SR_n}, \gamma_{R_nD})$. The probability density function of the instantaneous SNR (γ) [8, 10] in case of η-μ fading channel is written as

$$f_{\gamma_{\eta-\mu}}(\gamma) = \frac{2\sqrt{\pi}\mu^{\mu+\frac{1}{2}}h^{\mu}\gamma^{\mu-\frac{1}{2}}}{\Gamma(\mu)H^{\mu-\frac{1}{2}}\overline{\gamma}^{\mu+\frac{1}{2}}}\exp\left(\frac{-2\mu h\gamma}{\overline{\gamma}}\right)I_{\mu-\frac{1}{2}}\left(\frac{2\mu H\gamma}{\overline{\gamma}}\right) \tag{6}$$

where $\Gamma(\cdot)$ symbolizes the gamma function and modified Bessel function [11] is represented as $I_v(\cdot)$. $\overline{\gamma} = E(\gamma)$ is average SNR $E(\cdot)$ is expectation. μ indicates number of multipath cluster.

$$\mu = \frac{E^2(\gamma)}{2\mathrm{var}(\gamma)}\left[1 + \left(\frac{H}{h}\right)^2\right] \tag{7}$$

var($\cdot$) is variance. The functions of the parameter η are represented by H and h. These functions are expressed by two dissimilar cases [10]. First case is for $0 < \eta < \infty$, where it represents the scattered wave power ratio between the in phase and quadrature components of every cluster of multipath. For this case $h = \frac{(2+\eta^{-1}+\eta)}{4}$ and $H = \frac{(\eta^{-1}-\eta)}{4}$. Second case is for $-1 < \eta < 1$, which represents the correlation coefficient between the scattered wave in phase and quadrature components of every cluster of multipath. For second situation, $h = \frac{1}{(1-\eta^2)}$ and $H = \frac{\eta}{(1-\eta^2)}$. For both cases, $\mu > 0$. In addition, $\mu > 0$ indicates the number of multipath clusters in both situations. For this system, model first case is considered.

3 Performance Analysis

This part gives derivation of outage probability of dual-hop multi-relay DF cooperative (η-μ) fading channel. Outage is the event, that received signal cannot be reliably decoded at the destination terminal [3]. The probability, when the instantaneous SNR at destination terminal falls lower than the predetermined threshold value (sometimes called the protection ratio) γ_{th}, provide the outage probability (P_{outage}). Expected Quality of Service (QoS) and modulation techniques affects the value of protection ratio (threshold value) γ_{th} [12]. P_{outage} gives the indication of QoS level [3, 12]. The cumulative distribution function of γ_{eq} is evaluated as

$$\begin{aligned} F_{\gamma_{\text{eq}}}(\gamma_{\text{th}}) &= P\left(\gamma_{\text{eq}} \le \gamma_{\text{th}}\right) = 1 - P(\gamma_{\text{SR}} > \gamma_{\text{th}})P(\gamma_{\text{RD}} > \gamma_{\text{th}}) \\ &= P(\gamma_{\text{SR}} \le \gamma_{\text{th}}) + P(\gamma_{\text{RD}} \le \gamma_{\text{th}}) - P(\gamma_{\text{SR}} \le \gamma_{\text{th}})P(\gamma_{\text{RD}} \le \gamma_{\text{th}}) \end{aligned} \tag{8}$$

outage probability is obtained as

$$P_{\text{outage}} = F_{\text{eq}}(\gamma_{\text{th}}) = P\left(\gamma_{\text{eq}} < \gamma_{\text{th}}\right) \tag{9}$$

$P(\cdot)$ is the probability operator. Number of relays between source and destination are denoted by n. For source-relays channels

$$P\left(\gamma_{\text{SR}_n} \le \gamma_{\text{th}}\right) = \int_0^{\gamma_{\text{th}}} f_{\text{SR}_n}\left(\gamma_{\text{SR}_n}\right) \mathrm{d}\gamma_{\text{SR}_n} \tag{10}$$

putting the value of $f_{\gamma_{\text{SR}_n}}\left(\gamma_{\text{SR}_n}\right)$ using Eq. (6) in Eq. (10)

$$P\left(\gamma_{\text{SR}_n} \le \gamma_{\text{th}}\right) = \int_0^{\gamma_{\text{th}}} \frac{2\sqrt{\pi}\mu^{\mu+\frac{1}{2}} h^{\mu} \gamma_{\text{SR}_n}^{\mu-\frac{1}{2}}}{\Gamma(\mu) H^{\mu-\frac{1}{2}} \overline{\gamma}_{\text{SR}_n}^{\mu+\frac{1}{2}}} \exp\left[\frac{-2\mu\gamma_{\text{SR}_n} h}{\overline{\gamma}_{\text{SR}_n}}\right] I_{\mu-\frac{1}{2}}\left[\frac{2\mu\gamma_{\text{SR}_n} H}{\overline{\gamma}_{\text{SR}_n}}\right] \mathrm{d}\gamma_{\text{SR}_n} \tag{11}$$

the modified Bessel function [11] of the first kind in (11) is represented as

$$I_v(z) = \sum_{\alpha=0}^{\infty} \frac{z^{2\alpha+v}}{2^{2\alpha+v}\Gamma(\alpha+1)\Gamma(v+\alpha+1)} \tag{12}$$

using the definition of modified Bessel function of first kind form Eq. (12) and on simplification, we can write

$$I_{\mu-\frac{1}{2}}\left(\frac{2\mu H\gamma}{\overline{\gamma}}\right) = \left(\frac{\mu H\gamma}{\overline{\gamma}}\right)^{\mu-\frac{1}{2}} \sum_{\alpha=0}^{\infty} \frac{\left(\frac{\mu H\gamma}{\overline{\gamma}}\right)^{2\alpha}}{\Gamma(\alpha+1)\Gamma\left(\mu+\alpha+\frac{1}{2}\right)} \tag{13}$$

substituting Eq. (13) in Eq. (11) and on further simplification

$$P(\gamma<\gamma_{\text{th}})=\int_0^{\gamma_{\text{th}}}\frac{2\sqrt{\pi}\mu^{\mu+\frac{1}{2}}h^{\mu}\gamma^{\mu-\frac{1}{2}}}{\Gamma(\mu)H^{\mu-\frac{1}{2}}\overline{\gamma}^{\mu+\frac{1}{2}}}\exp\left(\frac{-2\mu h\gamma}{\overline{\gamma}}\right)\left(\frac{\mu H\gamma}{\overline{\gamma}}\right)^{\mu-\frac{1}{2}}\sum_{\alpha=0}^{\infty}\frac{(\mu H\gamma)^{2\alpha}}{\Gamma(\alpha+1)\Gamma\left(\mu+\alpha+\frac{1}{2}\right)}\mathrm{d}\gamma \quad (14)$$

after simplification

$$P(\gamma<\gamma_{\text{th}})=\sum_{\alpha=0}^{\infty}\frac{2\sqrt{\pi}\mu^{\mu+\frac{1}{2}}h^{\mu}}{\Gamma(\mu)H^{\mu-\frac{1}{2}}\overline{\gamma}^{\mu+\frac{1}{2}}}\frac{\left(\frac{\mu H}{\overline{\gamma}}\right)^{2\alpha+\mu-\frac{1}{2}}}{\Gamma(\alpha+1)\Gamma\left(\mu+\alpha+\frac{1}{2}\right)}\int_0^{\gamma_{\text{th}}}\gamma^{2\mu+2\alpha-1}\exp\left(\frac{-2\mu h\gamma}{\overline{\gamma}}\right)\mathrm{d}\gamma \quad (15)$$

by solving the above integral and simplifying the expression

$$P(\gamma<\gamma_{\text{th}})=\sum_{\alpha=0}^{\infty}\frac{2\sqrt{\pi}\mu^{\mu+\frac{1}{2}}h^{\mu}}{\Gamma(\mu)H^{\mu-\frac{1}{2}}\overline{\gamma}^{\mu+\frac{1}{2}}}\frac{\left(\frac{\mu H}{\overline{\gamma}}\right)^{2\alpha+\mu-\frac{1}{2}}}{\Gamma(\alpha+1)\Gamma\left(\mu+\alpha+\frac{1}{2}\right)}\left(\frac{(2\mu+2\alpha-1)!}{\left(\frac{2\mu h}{\overline{\gamma}}\right)^{2\mu+2\alpha}}-\exp\left(\frac{-2\mu h\gamma_{\text{th}}}{\overline{\gamma}}\right)(2\mu+2\alpha-1)!\sum_{m=0}^{2\mu+2\alpha-1}\frac{1}{m!}\frac{\gamma_{\text{th}}^{m}}{\left(\frac{2\mu h}{\overline{\gamma}}\right)^{2\mu+2\alpha-m}}\right) \quad (16)$$

from definition of incomplete gamma function [11],

$$\frac{\Gamma\left(2\mu+2\alpha,\frac{2\mu h\gamma_{\text{th}}}{\overline{\gamma}}\right)}{\Gamma(2\mu+2\alpha)}=\exp\left(\frac{-2\mu h\gamma_{\text{th}}}{\overline{\gamma}}\right)\sum_{m=0}^{2\mu+2\alpha-1}\frac{1}{m!}\left(\frac{2\mu h\gamma_{\text{th}}}{\overline{\gamma}}\right)^{m} \quad (17)$$

using Eqs. (16) and (17) we can get

$$P(\gamma<\gamma_{\text{th}})=\sum_{\alpha=0}^{\infty}\frac{1}{h^{\mu}}\left(\frac{H}{h}\right)^{2\alpha}\frac{\Gamma(\mu+\alpha)}{\Gamma(\mu)\Gamma(\alpha+1)}\left(1-\frac{\Gamma\left(2\mu+2\alpha,\frac{2\mu h\gamma_{\text{th}}}{\overline{\gamma}}\right)}{\Gamma(2\mu+2\alpha)}\right) \quad (18)$$

in multiple-relay system model, in the case of selection combining, the outage at receiver occurs only when all the paths, i.e., direct path from source terminal to destination terminal and paths via relay terminals R_n to destination terminal have outage. It means that when the output SNR of all the diversity branches falls below a defined protection ratio, i.e., threshold SNR γ_{th}, outage will occur in the system. Since we are assuming that all the channels are independent, the outage probability for system model can be easily calculated using basic addition and multiplication theorems of probability theory. The overall outage probability of system is represented as

$$P_{\text{outage}_{\eta-\mu}}=P_{\text{outage}_{\text{SD}}}\prod_{n=0}^{N}\left[1-\left\{\left(1-P\left(\gamma_{\text{SR}_n}<\gamma_{\text{th}}\right)\right)\left(1-P\left(\gamma_{\text{R}_n\text{D}}<\gamma_{\text{th}}\right)\right)\right\}\right] \quad (19)$$

$$P_{\text{outage}_{\eta-\mu}} = P_{\text{outage}_{\text{SD}}} \prod_{n=0}^{N} \left[P\left(\gamma_{\text{SR}_n} < \gamma_{\text{th}}\right) + P\left(\gamma_{\text{R}_n\text{D}} < \gamma_{\text{th}}\right) - P\left(\gamma_{\text{SR}_n} < \gamma_{\text{th}}\right) P\left(\gamma_{\text{R}_n\text{D}} < \gamma_{\text{th}}\right) \right] \quad (20)$$

3.1 Outage Capacity

The channel capacity for dual-hop corresponding link is given as

$$C = \frac{1}{2} \log_2\left(1 + \gamma_{\text{eq}}\right). \quad (21)$$

the rate loss due to the half-duplex function is given by factor $\frac{1}{2}$. The channel capacity from Eq. (21) is normalized to the bandwidth, thus having the unit of bps/Hz. The channel of the system model will be in outage if its achieved capacity (21) drops below a target transmission rate R. The outage capacity can be evaluated as

$$P_{\text{out}} = P(C < R) = P\left[\frac{1}{2} \log_2\left(1 + \gamma_{\text{eq}}\right) < R\right] \quad (22)$$

Using Eqs. (20) and (22), the outage capacity for dual-hop multiple-relay DF relaying system model over η-μ fading channels is calculated. The analytical expression (23) is new and can be calculated with the help of mathematical tools available in MATLAB.

$$P_{\text{outage}_{\eta-\mu}} = \sum_{q=0}^{\infty} \left(\frac{1}{h_{\text{SD}}}\right)^{\mu_{\text{SD}}} \left(\frac{H_{\text{SD}}}{h_{\text{SD}}}\right)^{2q} \frac{\Gamma(\mu_{\text{SD}} + q)}{\Gamma(\mu_{\text{SD}})\Gamma(q+1)} \left(1 - \frac{\Gamma\left(2\mu_{\text{SD}} + 2q, \frac{2\mu_{\text{SD}} h_{\text{SD}}\left(2^{2R}-1\right)}{\overline{\gamma}_{\text{SD}}}\right)}{\Gamma(2\mu_{\text{SD}} + 2q)}\right)$$

$$\prod_{n=1}^{N} \left[\begin{array}{l} \sum_{\alpha=0}^{\infty} \left(\frac{1}{h_{\text{SR}_n}}\right)^{\mu_{\text{SR}_n}} \left(\frac{H_{\text{SR}_n}}{h_{\text{SR}_n}}\right)^{2\alpha} \frac{\Gamma\left(\mu_{\text{SR}_n} + \alpha\right)}{\Gamma\left(\mu_{\text{SR}_n}\right)\Gamma(\alpha+1)} \left(1 - \frac{\Gamma\left(2\mu_{\text{SR}_n} + 2\alpha, \frac{2\mu_{\text{SR}_n} h_{\text{SR}_n}\left(2^{2R}-1\right)}{\overline{\gamma}_{\text{SR}_n}}\right)}{\Gamma\left(2\mu_{\text{SR}_n} + 2\alpha\right)}\right) \\ + \sum_{\beta=0}^{\infty} \left(\frac{1}{h_{\text{R}_n\text{D}}}\right)^{\mu_{\text{R}_n\text{D}}} \left(\frac{H_{\text{R}_n\text{D}}}{h_{\text{R}_n\text{D}}}\right)^{2\beta} \frac{\Gamma\left(\mu_{\text{R}_n\text{D}} + \beta\right)}{\Gamma\left(\mu_{\text{R}_n\text{D}}\right)\Gamma(\beta+1)} \left(1 - \frac{\Gamma\left(2\mu_{\text{R}_n\text{D}} + 2\beta, \frac{2\mu_{\text{R}_n\text{D}} h_{\text{R}_n\text{D}}\left(2^{2R}-1\right)}{\overline{\gamma}_{\text{R}_n\text{D}}}\right)}{\Gamma\left(2\mu_{\text{R}_n\text{D}} + 2\beta\right)}\right) \\ - \sum_{\alpha=0}^{\infty} \left(\frac{1}{h_{\text{SR}_n}}\right)^{\mu_{\text{SR}_n}} \left(\frac{H_{\text{SR}_n}}{h_{\text{SR}_n}}\right)^{2\alpha} \frac{\Gamma\left(\mu_{\text{SR}_n} + \alpha\right)}{\Gamma\left(\mu_{\text{SR}_n}\right)\Gamma(\alpha+1)} \left(1 - \frac{\Gamma\left(2\mu_{\text{SR}_n} + 2\alpha, \frac{2\mu_{\text{SR}_n} h_{\text{SR}_n}\left(2^{2R}-1\right)}{\overline{\gamma}_{\text{SR}_n}}\right)}{\Gamma\left(2\mu_{\text{SR}_n} + 2\alpha\right)}\right) \\ \sum_{\beta=0}^{\infty} \left(\frac{1}{h_{\text{R}_n\text{D}}}\right)^{\mu_{\text{R}_n\text{D}}} \left(\frac{H_{\text{R}_n\text{D}}}{h_{\text{R}_n\text{D}}}\right)^{2\beta} \frac{\Gamma\left(\mu_{\text{R}_n\text{D}} + \beta\right)}{\Gamma\left(\mu_{\text{R}_n\text{D}}\right)\Gamma(\beta+1)} \left(1 - \frac{\Gamma\left(2\mu_{\text{R}_n\text{D}} + 2\beta, \frac{2\mu_{\text{R}_n\text{D}} h_{\text{R}_n\text{D}}\left(2^{2R}-1\right)}{\overline{\gamma}_{\text{R}_n\text{D}}}\right)}{\Gamma\left(2\mu_{\text{R}_n\text{D}} + 2\beta\right)}\right) \end{array} \right] \quad (23)$$

4 Analytical Results

The analytical results of outage capacity is discussed in this part, for different values of parameters η and μ. In order to simplify, it is considered that the parameters of first hop (source-relay) and second hop (relay-destination) are same, i.e., $\eta_{\mathrm{SR}_n} = \eta_{\mathrm{R}_n\mathrm{D}} = \eta$ and $\mu_{SRn} = \mu_{RnD} = \mu$. The target transmission rate R = 1.0 bps/Hz. The derived expression is of infinite series, nevertheless, convergence of this expression is very rapid, thus $N = 4$ for precise outcomes. Parameter η gives correction. μ represents the number of multipath clusters.

Figure 2 illustrates the outage capacity as a function of average SNR (dB) for $\eta - \mu$ generalized fading channels when parameters η and μ are varying. It is clear by observing the results from Fig. 2 that increase in η causes the reduction in outage probability. Moreover, outage probability can be increased with the reduction of multipath clusters. Figure 3 shows graph between outage capacity and average SNR in dB for η-μ generalized fading channels when N is varying. It is discovered that outage capacity declines when the relay (N) in system model increases. Additional accessible diversity paths are forming virtual MIMO, hence increasing number of relays R results decrease in outage probability of system.

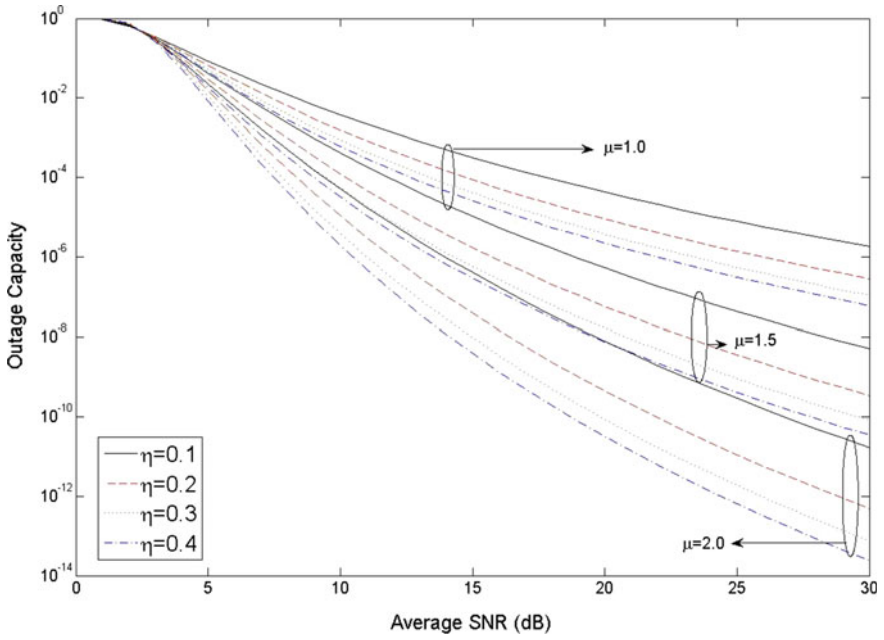


Fig. 2 Outage probability P_{outage} versus average SNR (dB) over dissimilar values of η and μ for γ_{th} = 4 dB

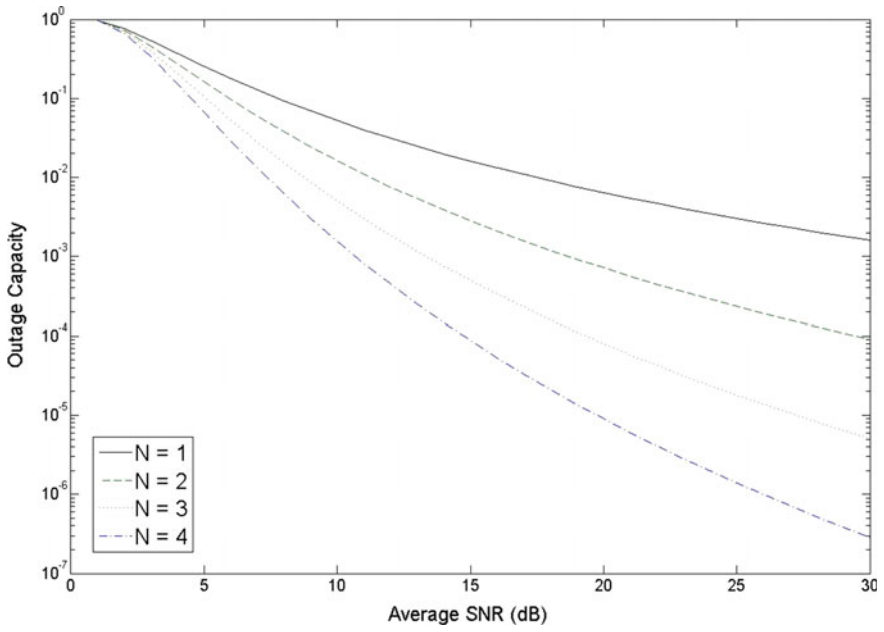


Fig. 3 Outage probability P_{outage} versus average SNR (dB) over dissimilar number of relays (N) for $\mu' = \mu'' = 1$ and $\gamma_{\text{th}} = 4$ dB

5 Conclusion

An expression for outage capacity of a dual-hop DF multiple-relaying system is derived for η-μ fading channels. With the help of this analytical expression, the system performance of dual-hop DF multiple-relay system model is evaluated. The obtained expression is analyzed for different channel parameters by considering different value of k, μ and η. From the result, it is realized that when the number of relays are increased the overall outage performance is getting enhanced due to improvement in system diversity.

References

1. Sendonaris, A., Erkip, E., Aazhang, B.: User co-operation diversity. Part I. system description. IEEE Trans. Commun., Vol. 51. (2003) 1927–1938.
2. Hasna, M.O., Alouini, M.S.: Optimal power allocation for relayed transmissions over Rayleigh-fading channels. IEEE Trans. Wireless Commun., Vol. 3. (2004) 1999–2004.
3. Hong, Y.W.P., Huang, W.J., Kuo, C.C.J.: Cooperative communications and networking: Technologies and System Design. (2010).

4. Li, W.G., Chen, M.: Outage capacity of dual hop decode and forward relaying system over generalized fading channels: 2nd international conference on future computer and communication. IEEE Wuhan, Vol. 3. (2010) 827–831.
5. Nakagami, M.: The m-distribution - A general formula for intensity distribution of rapid fading: Statistical Methods in Radio Wave propagation. W.G. Hoffman, Ed. Oxford, U.K. Pergamon. (1960) 3–36.
6. Laneman, J.N., Tse, D., Wornell, G.W.: Co-operative diversity in wireless networks: Efficient protocols and outage behavior. IEEE Trans. Info. Theory, Vol. 50. (2004) 3062–3080.
7. Kumar, P., Dhaka, K.: Performance analysis of a decade and forward relay system in k-μ and η-μ fading channels. IEEE vehicular technology society, Vol. 20. (2015) 1.
8. Yacoub, M.D.: The k-μ distribution and the η-μ distribution. IEEE Antennas propag. Mag., Vol. 49. (2007) 68–81.
9. Wang, T., Cano, A., Giannakis, G.B. Laneman, J.N.: High performance co-operative demodulation with decode-and-forward relays. IEEE Trans. Commun., Vol. 55. (2007) 1427–1438.
10. Yacoub, M.D.: The η-μ distribution: A General Fading Distribution. IEEE Boston Fall vehicular technology conference 2000, Boston, USA (2000).
11. Gradshteyn, I.S., Ryzhik, I.M.: Table of Integrals, Series and products: Academic press. Fifth edition, San Diego, (1994).
12. Rappaport, T.S.: Wireless communications: principles and practice, Vol. 2. Prentice hall PTR. (1996).

Design for Structured Uncertainty of Mass Spring System Using Robust Control Technique

Kapil Shukla, Mayank Ranakoti, Vivek Kaundal, Amit Mondal, Abhishek Sharma and Mukul Kumar Gupta

Abstract The main aim of the paper is to use the robust-based control design technique keeping the entire structured uncertainty model. Here mass spring system has been taken which is having numerous applications in real life. In Robust Control system, mainly sensitivity and disturbances are considered for the design of the system. Matlab software has been used for the frequency response analysis for calculating sensitivity and complementary function. Also the Bode and Nyquist plot has been obtained for the analysis of uncertain system.

Keywords Mass spring system · Singular value · Robust control · Complementary sensitivity · Uncertain system · Robust control system

1 Introduction

Robustness plays the crucial role in control design because real engineering system is vulnerable to disturbance and measurement noise and always there are differences from mathematical modelling and real-time modelling of the system; in control

Kapil Shukla · Mayank Ranakoti (✉) · Vivek Kaundal · Amit Mondal · Abhishek Sharma · M.K. Gupta
University of Petroleum and Energy Studies, Dehradun, India
e-mail: mayankranakoti978@gmail.com

Kapil Shukla
e-mail: shuklakapil108@gmail.com

Vivek Kaundal
e-mail: vkaundal@ddn.upes.ac.in

Amit Mondal
e-mail: adadakmondal1603@gmail.com

Abhishek Sharma
e-mail: abhishek@ddn.upes.ac.in

M.K. Gupta
e-mail: mkgupta@ddn.upes.ac.in

© Springer Science+Business Media Singapore 2017

R. Singh and S. Choudhury (eds.), *Proceeding of International Conference on Intelligent Communication, Control and Devices*, Advances in Intelligent Systems and Computing 479, DOI 10.1007/978-981-10-1708-7_74

system design typically we stabilize the system in a possible manner. In case of robust control design system, we consider all the disturbance and sensitivities that occur in real-life problem in the present paper a mass spring system is discussed considering all the uncertainties.

2 Robust Control

Robust control is a major area of research for a few decades with in control engineering community. Uncertainty in the physical parameter that define a structure may lead to extremely poor behaviour because of poor and incomplete dynamics of the structure. With the development of robust control system behaviour can be increased. The basic block diagram consisting of disturbance and noise is shown in Fig. 1.

Figure 1 consisting of the disturbances d_i, d and n is the noise available in the system. We are incorporating both the term in the design of robust structure. If the system is internally stable, then

$$y = T_0(r - n) + GS_i d_i + S_0 d \tag{1}$$

$$r - y = S_0(r - d) + T_0 n - GS_i d_i \tag{2}$$

$$u = KS_0(r - n) - KS_0 d - T_i d_i \tag{3}$$

$$u_g = KS_0(r - n) - KS_0 d - S_i d_i \tag{4}$$

The input loop transfer function (TF) matrix L_i and the output loop T/F L_0 are defined, respectively, as $L_i = KG, L_0 = GK$.

The input and output sensitivity matrix is defined as the following $S_i = (I + L_i)^{-1}, S_0 = (I + L_0)^{-1}$. The input and output complementary sensitivity

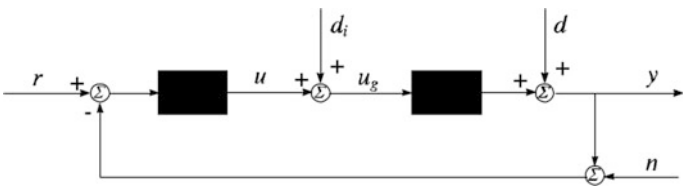


Fig. 1 Multivariable feedback control system

matrix is defined as $T_i = I - S_i, T_0 = I - S_0$ respectively. The closed loop system stability can be checked when stab = 1 means overall system is stable in nature and when stab zero means system is stable in nature.

Consider the two channel system has a TF matrix

$$G = \begin{bmatrix} \frac{5}{(8s+1)(0.1s+1)} & \frac{-0.04}{0.1s+1} \\ \frac{0.07}{0.2s+1} & \frac{4}{(1.8s-1)(0.6s+1)} \end{bmatrix} \tag{5}$$

And Controller has the following TF matrix form

$$K = \begin{bmatrix} 6(s+1) & 0 \\ 0 & \frac{15(s+2)}{(s+1)} \end{bmatrix} \tag{6}$$

The output loop transfer is shown in Fig. 2.

The singular Value (SV) plot of the output loop transfer matrix L_0 are shown in Fig. 2. The plots of input output sensitivity and complementary sensitivity function are shown in Figs. 3 and 4. In low frequency range the SV of the matrix are below −30 dB, which means that the input disturbance d_i is attenuated more than 29 times at input.

From Fig. 4 it is seen that frequency above −45 dB the noise n in this range is repressed more than 100 times at plant output.

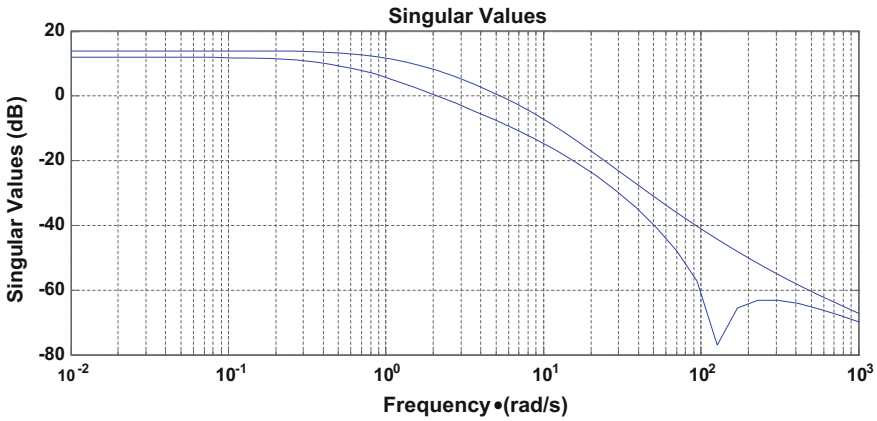


Fig. 2 Output loop TF

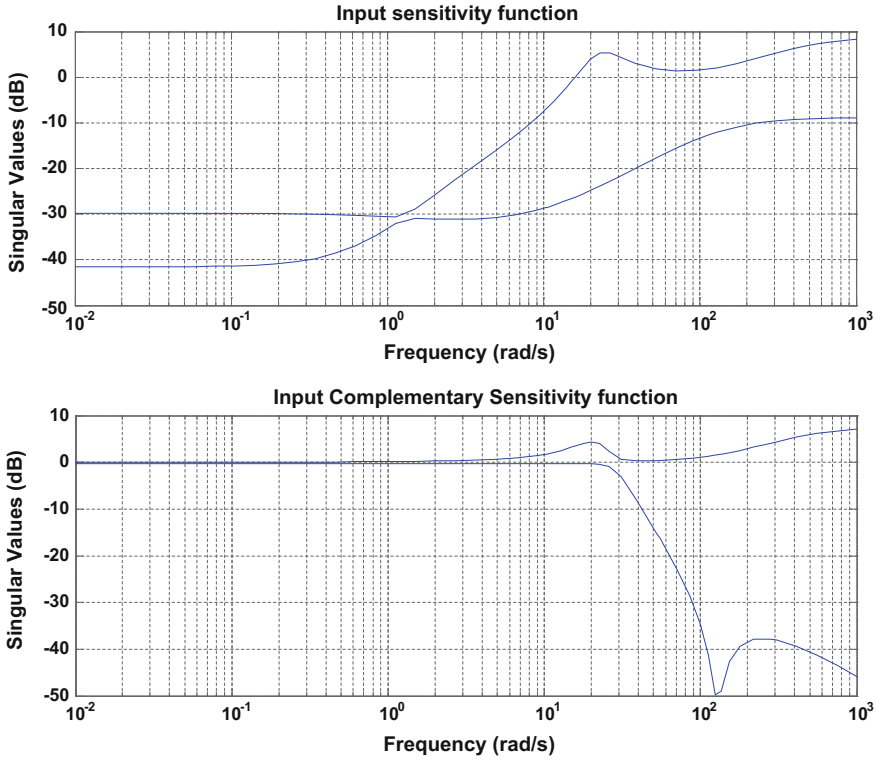


Fig. 3 Input sensitivity and input complementary sensitivity

The most widely used mechanical mass spring (M-S) system that we are considering is as follows. This system is described in Fig. 5.

The dynamics of (M-S) can be described as follows $m\ddot{x} + c\dot{x} + kx = u$. The state space form of the (M-S) can be obtained by putting $x_1 = x$, $x_2 = \dot{x}$.

And the following matrix can be obtained

$$A = \begin{bmatrix} 0 & 1 \\ -k/m & -c/m \end{bmatrix},\ B = \begin{bmatrix} 0 \\ 1/m \end{bmatrix},\ C = [10],\ D = 0$$

The T/F of the matrix if y is the displacement of the mass and u is the force acting on mass is

$$\frac{y(s)}{u(s)} = \frac{1}{ms^2 + cs + k} \tag{7}$$

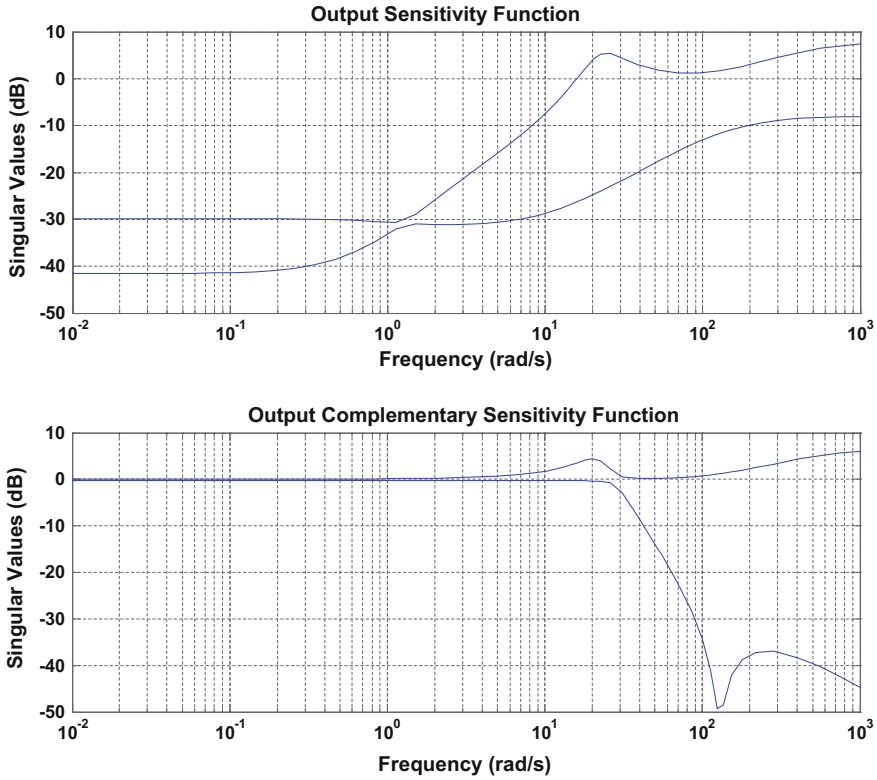
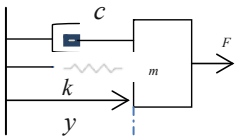


Fig. 4 Output sensitivity and input complementary sensitivity

Fig. 5 Mass spring system



In real-time system, the exact value of the parameter is exactly not known. They are always having some deviation from the modelling value. Let $m = \bar{m}(1 + \Delta p_m \Delta m)$, and $c = \bar{c}(1 + \Delta p_c \Delta c)$, $k = \bar{k}(1 + \Delta p_k \Delta k)$ where $\bar{m} = 4$, $\bar{c} = 1$, $\bar{k} = 3$ are called nominal value. The quantities $\Delta p_m, \Delta p_c, \Delta p_k$ and $\Delta m, \Delta c, \Delta k$ represent the possible changes on these three parameters. In the present case 20 % uncertainty in the mass, 20 % uncertainty in the damping coefficient and 30 % uncertainty in the spring constant.

3 Result

It is good to see the frequency response of the (M-S) system for dissimilar values of parameters mass, damper and spring constant. The results are shown in Fig. 6. Similarly the step response and Nyquist plot has been obtained for various values of these parameters (Figs. 7 and 8).

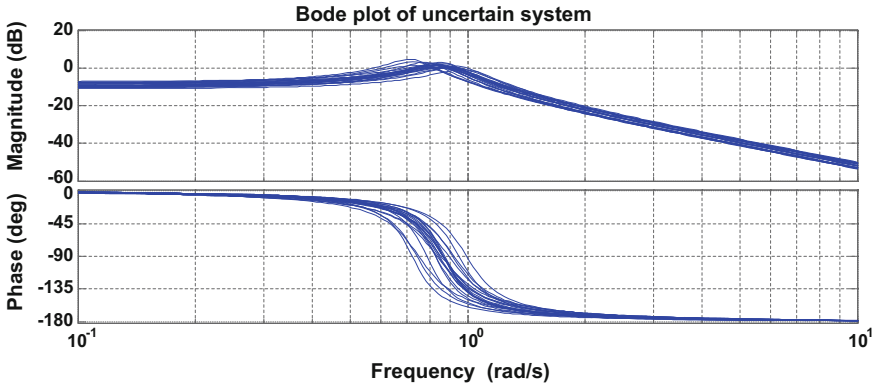


Fig. 6 Bode plot of uncertain system

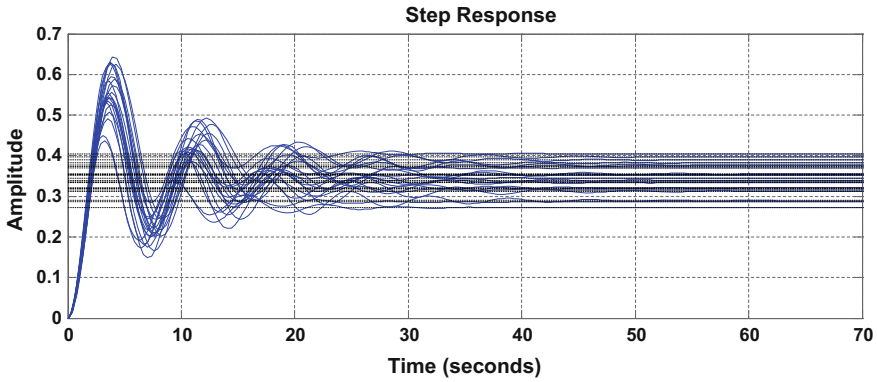


Fig. 7 Step response of uncertain system

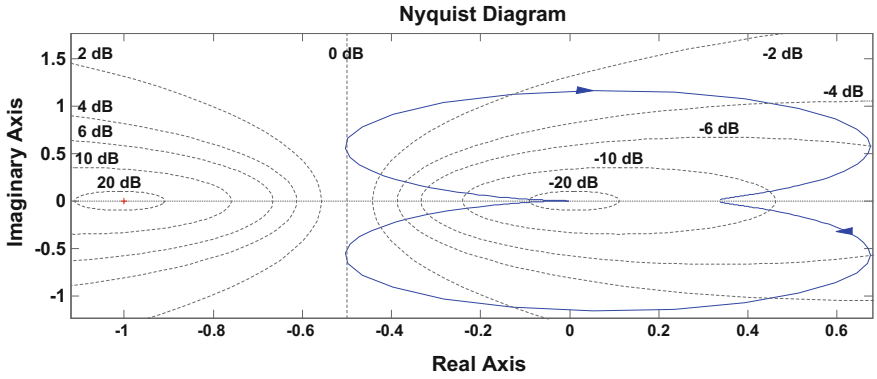


Fig. 8 Nyquist diagram of uncertain system

4 Conclusions

A parametric approach has been presented in the presence of uncertainties. Mass spring system has been discussed with all the possible uncertainties frequency response analysis like Bode Plot, Nyquist Analysis has been done for the parametric uncertainties for ensuring robust stability and robust performance.

References

1. D.W. Gu., P.H. Petkov and M. M. Konstantinov Robust Control Design with Matlab Springer–Verlag London 2013.
2. Paolo Venini Robust control of uncertain structures, Department of Structural.
3. Mechanics, University of Pavia, Computers and Structures 67 (1998).
4. K.J. Astrom & R.M. Murray, Feedback Theory An Introduction for Scientists and Engineers, Princeton University Press, 2008.
5. J.C. Zhou, J.C. Doyle, and K. Glover. Robust and Optimal Control. Prentice Hall, Englewood Cliffs, NJ, 1996.
6. D.C. McFarlane and K. Glover. Robust Controller Design Using Normalized Coprime Factor Plant Descriptions. Springer, New York, 1990.
7. M. Green and D.J.N. Limebeer. Linear Robust Control. Prentice Hall, Englewood Cliffs, NJ, 1995.

Scalable Design and Synthesis of 3D Mesh Network on Chip

Arpit Jain, Rakesh Dwivedi, Adesh Kumar and Sanjeev Sharma

Abstract The research article proposed the 3D mesh topological network on chip (NoC) and its hardware chip implementation. 3D NoC improves the performance of on-chip communication network because the connection of the switches and their length to connecting links is shorter and the data can be switched across the on-chip communication network with the help of less number of switches. The cluster size of the designed 3D mesh NoC is chosen as $4 \times 4 \times 4$. The addressing scheme and intercommunication among nodes is verified in the scalable design. The proposed 3D mesh NoC is designed with the help of VHDL programming language, simulated in ModelSim 10.1 and synthesized in Xilinx ISE 14.2 as software tools. The communication is realized based on look ahead XYZ routing algorithm. The targeted FPGA is Virtex-5 and hardware and timing parameters are also analyzed in the same design.

Keywords Network on chip (NoC) · Multiprocessors system on chip (MPSoC) · Many core chip multiprocessors (CMP) · Field-programmable gate array (FPGA)

Arpit Jain (✉) · Rakesh Dwivedi
Department of Computer Science Engineering,
Teerthanker Mahaveer University, Moradabad, India
e-mail: arpit.record@gmail.com

Adesh Kumar
Department of Electronics, Instrumentation and Control (EIC) Engineering,
University of Petroleum and Energy Studies (UPES), Dehradun, India

Sanjeev Sharma
Department of Computer Science and Engineering, JP Institute of Engineering and Technology, Meerut, India

© Springer Science+Business Media Singapore 2017

R. Singh and S. Choudhury (eds.), *Proceeding of International Conference on Intelligent Communication, Control and Devices*, Advances in Intelligent Systems and Computing 479, DOI 10.1007/978-981-10-1708-7_75

1 Introduction

Many core chip multiprocessors (CMP) are formed using multiprocessors system on chip (MPSoC). There is the need of high performance, scalable and low-power emerging system to provide intra-chip communication infrastructure. Network on chip (NoC) [1, 2, 5] is the promising solution to provide the scalable design and high performance can be achieved using topological structure. NoC interconnects the various cores such as CPU, DMA, SRAM, and DRAM. The computational operations in the NoC are performed using processing elements (PE). NoC has router [4] that forwards and decodes the packets from one PE to another PE. The storing and receiving of the packets are done with the help of input buffer. Arbiter decides the routes and services from source node to the destination node in case of multiple requests. There are some classical methods and topologies for communications among nodes such as crossbar technology [3, 7], bus-based communication at point to point, but NoC is the advance technology to provide fast and scalable routing. NoC architectures can be designed using different 2D and 3D network topologies such as mesh, star, tree, and butterfly. The topologies are applicable for 2D planner [6] structures. In the existing NoC challenges the design of 3D NoC topological architectures in which the several nodes are existing in different layers. The connection between these layers is provided using TSV [6]. The most benefit of 3D IC is the considerable reduction of global and length of wires that enhance the performance and reduce the power requirements. Another biggest advantage is that 3D IC provides CMOS integration [9] that disparate non-silicon and electro-mechanical switching systems. NoC supports simple interconnecting models, highly flexible, regular network supports, and high fault tolerance capability.

2 System Design

The design consideration and structure of the 3D mesh NoC [7, 8] is shown in Fig. 1. The mesh cluster configuration is $4 \times 4 \times 4$, which signifies that four nodes are placed in *X*, *Y,* and *Z* directions, respectively. The architecture is a 4-layer architecture. The addressing and node identification is based on the XYZ routing [7] method. For example in layer 1, the *X*-axis nodes are identified as 000, 001, 002, and 003 in *X* direction; 000, 010, 020, and 030 in *Y* direction; and 000, 100, 200, and 300 in *Z* direction. It may exist single hop to connect some nodes or more than one hop to connect same nodes. The flow control is maintained using wormhole routing. The packet is stored by the router and transmits it to neighboring routers before the next flit arrives. The communication is possible in the nodes within the layers or the nodes which are existing in interconnecting layers.

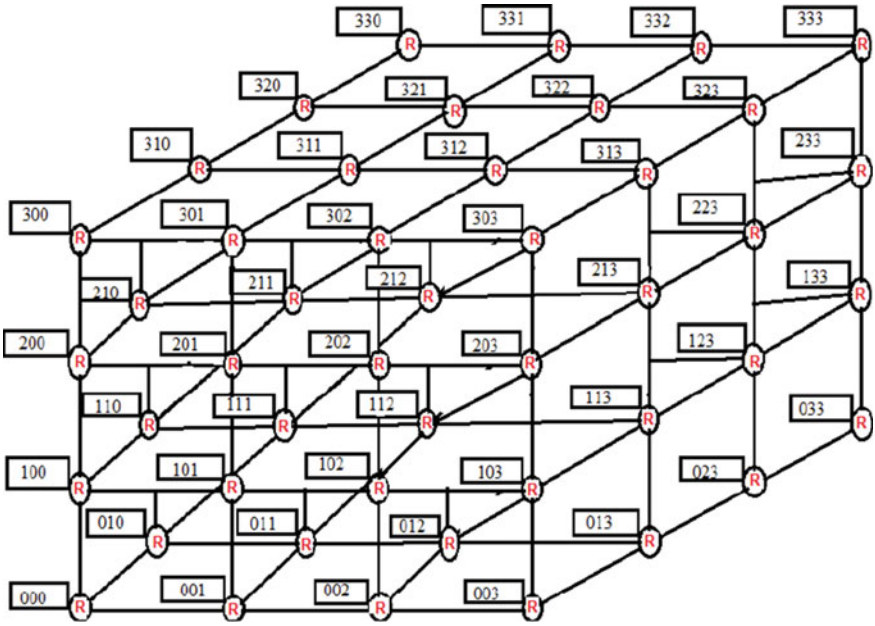


Fig. 1 3D NoC design considerations [7]

E (Enable)	D8-D0 Destination Node Address(9 bit)	S8-S0 Source Node Address(9 bit)	Layer address (2 bit)	Data (256 bit)

Fig. 2 Packet format

2.1 Frame Format

The packet is transferred which has enabled bit 'E.' It enables the node to transfer the data. Source node address is of 9 bits (S_8–S_0), and destination node address is of 9 bits (D_8–D_0). The layered architecture performs intercommunication based on layer address (00 to 11) for four layers, respectively. The data transfer can be on 'N' bit. In this case the size of data is 256 bit (Fig. 2).

3 Hardware Utilization on FPGA

The summary report extracted directly from the Xilinx software about device utilization is the detail of utilized FPGA device hardware parameters such as logic gates, flip flops, slices, LUTs, memory, etc. The synthesis report shows the

Table 1 Device and time utilization summary

Device part	Utilization	Parameter for timing	Utilization
Slices utilization	1236/12,480	Frequency (maximum)	400 MHz
Slice flip flops utilization	900/12,480	Arrival time before clk (minimum)	8.755 ns
4 input LUTs utilization	864/900	Time after clk (maximum)	12.169 ns
Bonded IOBs utilization	36/172	Total path delay (combinational)	16.015 ns
GCLKs utilization	1/32	Memory utilization	597,185 KB

complete details of device utilization. Table 1 shows the hardware and timing utilization for developed chip. The target device is xc5vlx20t-2-ff323, which is programmed in Virtex-5 FPGA. The details of timing parameters are descripted by frequency support (maximum), arrival time as input before clock pulse, output time after clock pulse, and total path delay as combinational delay.

4 Results and Discussions

The RTL view of the developed design is shown in Fig. 3. It descripts the pin used in the design. *Clk* is the rising edge input of the clock input. *Reset* is the input to keep the memory contends zero. *Data_in*[255:0] and *data_out*[255:0] are the data input and output of the corresponding node. The source node is identified by *souce_addr*[8:0] and destination node by *destination_add*[8:0]. The intercommunication is possible using *layer_add*[1:0]. The addressing of the 3D NoC is in *X, Y,*

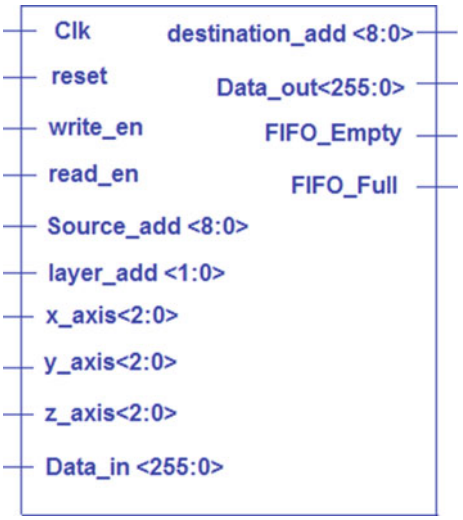


Fig. 3 RTL of (4 × 4 × 4) 3D NoC

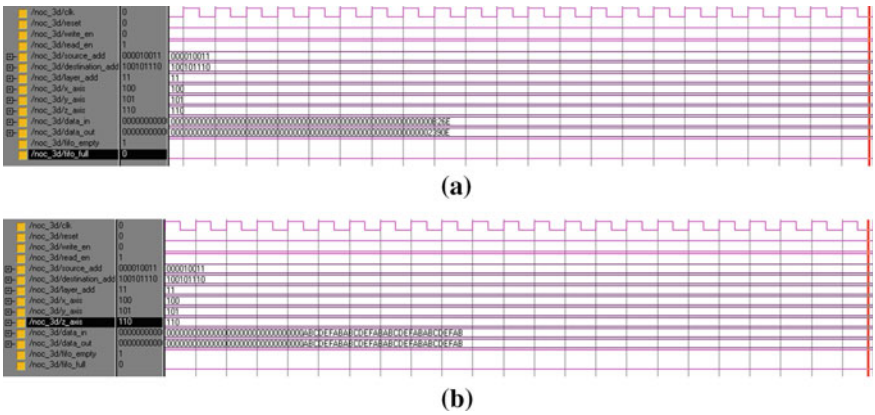


Fig. 4 **a** Simulation waveform of 3D NoC with 32-bit data (Modelsim). **b** Simulation waveform of 3D NoC with 256-bit data (Modelsim)

and *Z* direction which is done using *X_axis*[2;0], *Y_axis*[2:0], *and Z axis*[2:0]. Write_en and read_en are the two control inputs relating to memory that enable the destination node to write or read the data. In case of multiple accesses, the arbiter accesses the *FIFO_empty* and *FIFO_Full* signals. The priority of the nodes is decided using FIFO logic. The corresponding simulation of developed design is shown in Fig. 4a, b that expresses the inter-data transfer from layer 1 to layer 2.

5 Conclusions

3D NoC is evolved from 2D NoC, exhibiting good performance, latency, and low power consumption. The 3D mesh NoC for 4 × 4 × 4 cluster configuration for 4 layers is designed in Xilinx ISE 14.2 successfully and synthesized on Virtex-5 FPGA. The proposed NoC is applicable for small, medium, and larger network. It is a scalable architecture and based on packet switching. In future the same NoC can be implemented on larger cluster size and the concept of network security can be integrated within the same chip.

References

1. Aamir Zia, Sachhidh Kannan, H. Jonathan Chao, Garrett S. Rose "3D NoC for many-core processors" *Microelectronics Journal, Elsevier* Vol. 42, 2011, pp (1380–1390).
2. Amir-Mohammad Rahmani, Pasi Liljeberg, Juha Plosila, Hannu Tenhunen "Developing a power-efficient and low-cost 3DNoC using smart GALS-based vertical channels" *Journal of Computer and System Sciences, Elsevier* Vol. 79 (2013) pp (440–456).

3. A. Kumar, P. Kuchhal, S. Singhal "Network on Chip for 3D Mesh Structure with Enhanced Security Algorithm in HDL Environment" *International Journal of Computer Applications (IJCA)* Vol. 59– Number 17, (2012) pp (6–13).
4. Bouraoui Chemli and Abdelkrim Zitouni *"*A Turn Model Based Router Design for 3D Network on Chip*" World Applied Sciences Journal,* Vol. 32, No. 8, (2014), pp (1499–1505).
5. Haytham Elmiligi, Fayez Gebali, M. Watheq El-Kharashi "Power-Aware Mapping for 3D-NoC Designs using Genetic Algorithms" *Procedia Computer Science,* Elsevier Vol. 34 (2014), pp (538–543).
6. Konstantinos Tatas, Kostas Siozios Dimitrios Soudris, Axel Jantsch Book Ch-1, Ch-2 "Designing 2D and 3D Network-on-Chip Architectures" *Springer New York Heidelberg Dordrecht London*, (2014), pp (1–45).
7. Shalaka V. Parmar, Roshani B. Kharche, Payal V. Mamankar, Hasan M. Raza "Architecture and Design of 4 x 4 x 4 NoC for Multicore SoC" *International Journal of Engineering and Advanced Technology (IJEAT),* Vol. 4, No.-4, (2015) pp (2249–8958).
8. Vitor de Paulo and Cristinel Ababei "3D Network-on-Chip Architectures Using Homogeneous Meshes and Heterogeneous Floorplans" *International Journal of Reconfigurable Computing,* Hindawi Publishing Corporation Volume 2010, pp(1–12) doi:10.1155/2010/603059.
9. Vasilis F. Pavlidis, Eby G. Friedman, "3D Topologies for Networks-on-Chip*" IEEE Trans. On VLSI Systems,* Vol. 15, No.10, 2007, pp (1081–1090).

Application of Remote Sensing in the Monitoring of Biogas Production

Shailey Singhal, Rajan Sharma, Madhu Sharma, Shilpi Agarwal and Naveen Singhal

Abstract Anaerobic digestion (AD) systems are extremely sensitive to changes in environmental variables. Correct design and control of the system's parameters are essential to maximize process efficiency, increase stability, and prevent system failure. Automation systems can both raise plant availability and help meet the transparency requirements of the process. A fully automated continuous stirred tank reactor (CSTR) of 40 m^3 capacity was designed for jatropha waste and installed at University of Petroleum and Energy Studies, Dehradun (India). This is first fully automated digestor at pilot scale which can be monitored by remote sensing all over the country. Parameters (pH, temp, feeding rate, energy consumption) were attained from a CSTR plant online by using remote monitoring system. Pilot scale CSTR was operated using cow dung:jatropha de-oiled cake (CD:JDOC) in a optimized ratio of 1:3. The reactor was run continuously for 120 days. Average biogas produced per day was 25 m^3 per day.

Keywords Anaerobic digestion · Automation · Remote sensing · Biogas

Shailey Singhal · Shilpi Agarwal
Department of Chemistry, University of Petroleum and Engineering Studies, Dehradun, India

Rajan Sharma
Department of Chemistry, Uttarakhand University, Dehradun, India

Madhu Sharma (✉)
Department of Electrical Engineering, University of Petroleum and Engineering Studies, Dehradun, India
e-mail: madhusharma@ddn.upes.ac.in

Naveen Singhal
Department of Chemistry, DIT University, Dehradun, India

© Springer Science+Business Media Singapore 2017

R. Singh and S. Choudhury (eds.), *Proceeding of International Conference on Intelligent Communication, Control and Devices*, Advances in Intelligent Systems and Computing 479, DOI 10.1007/978-981-10-1708-7_76

1 Introduction

Biogas technology provides an alternative source of energy to be utilized either as transportation fuel or as cooking fuel or for electricity generation mainly from organic wastes, viz cattle dung, kitchen waste, etc. Apart from this huge amount of lignocellulosic waste is also available for its effective conversion to biogas. The potential of jatropha de-oiled seed cakes for the generation of methane has long been recognized [1–3]. Biochemical methane potential (BMP) of various parts of jatropha plant has been investigated by Gunaseelan [4]. Studies on anaerobic digestion of J. curcus fruit shells (Hulls) indicate the production of about 2.5 L biogas with 70 % CH_4 at 4 g VS (volatile solid) [5]. It has been reported that jatropha de-oiled cake (JDOC) produced biogas yield of 355 L kg^{-1} [6, 7]. Although not very popular, but awareness about the usage of biogas is increasing day-by-day resulting in the number of biogas plants in the country, that too at community level (plants bigger than 15 m^3 capacity). At such a large scale, it becomes difficult to monitor all the operating conditions of the plant manually. Thus integration of plant operation and its remote monitoring has become a necessity in the present scenario.

Automation systems have their unique advantages, like they help in raising plant availability and meeting the transparency requirements of the process. Operational efficiency and biogas yields are potentially raised through gathering various types of data, which must also be available for further processing. Information can include flow rates, pressures, or fill levels as well as motor performance data or methane content. Some parameters must be monitored cyclically. It is important, for instance, to ensure that the fermentation process runs smoothly. If the bacteria in the fermenter are not "fed" for 6 hours, methane production drops significantly. Gas and energy production must also be documented along with the quantities of all feed materials. By constantly checking ingredients, operators can monitor and control the fermentation process to maintain the quality of the generated biogas. To achieve this, all subsystems must communicate simply and securely with each other. For this purpose, industrial Ethernet has become the standard for meeting the industrial sector's need for robust communication systems that can reliably transfer data over long distances. If talked in long run, integrated robust complete systems based on durable, flexible industrial solutions are the best investment for plant operators.

Keeping in view the significance and necessity of automation in this technology, a fully automated CSTR of 40 m^3 capacity was designed for jatropha waste and installed at the campus of University of Petroleum and Energy Studies, Dehradun (India) in 2013. This is the first fully automated digestor at pilot scale which can be monitored by remote sensing from all over the country.

2 Experimental Details

The CSTR was designed taking the concentration of slurry and BMP of JDOC in consideration. The components of CSTR Biogas digester include 5 mm thick MS plate with angle support and fibers glass reinforced plastics (FRP) lining 1 mm thick, 2 HP Flange mounted vertical stirrer system, 3 HP shredder, 1/2 HP screw slurry pump, and remote monitoring system which allowed the constant monitoring of the operating parameters of the plant to understand its efficiency (Fig. 1).

Actual plant constructed on this basis is shown in Fig. 2.

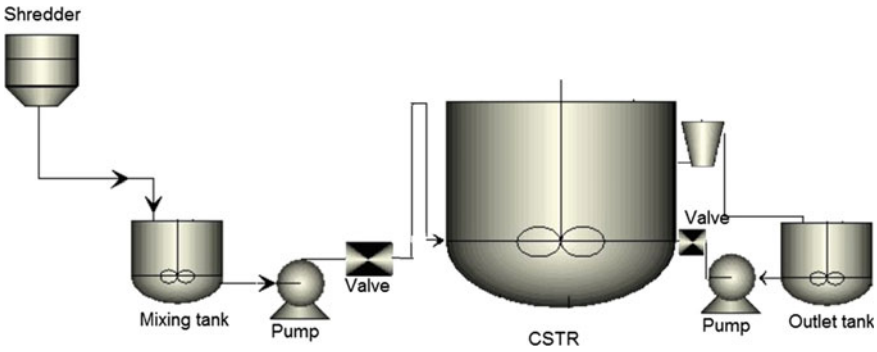


Fig. 1 Process flow diagram of CSTR



Fig. 2 40 m^3 CSTR at UPES campus

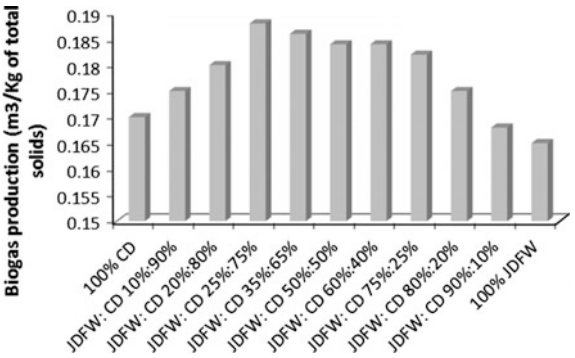


Fig. 3 Ratio optimization of feed stock at lab scale

Ratio of JDOC and cow dung (CD) (to be fed in pilot scale digester) was optimized at lab scale (Fig. 3).

Maximum production was observed in the mixture of JDOC and CD in a ratio of 25:75, but the objective was to shift the plant on JDOC up to the best possible extent. Hence, 75:25 ratio of JDOC and CD was chosen as an optimum ratio and fed in pilot scale plant, with a continuous monitoring of pH, temperature and gas production for 120 days.

3 Results and Discussion

Monitored data was stored in the automated system through remote sensing which was used to analyze the performance of the plant (Fig. 4).

Results indicate that initially production of biogas was lower which eventually increased with time. The possible reason for this is that initially decomposition of biomass was slow and it took around 15 days to start for gas production. Once the microorganisms were grown properly, the process was zoomed up leading to increased production of biogas. Later stages show continuously higher production of biogas which is also due to decreased HRT. In CSTR, out coming slurry (already containing grown microorganisms) was recycled to the digester, which helped in reducing the HRT from 15 to 5 days with the production of around 25 m^3 biogas/day.

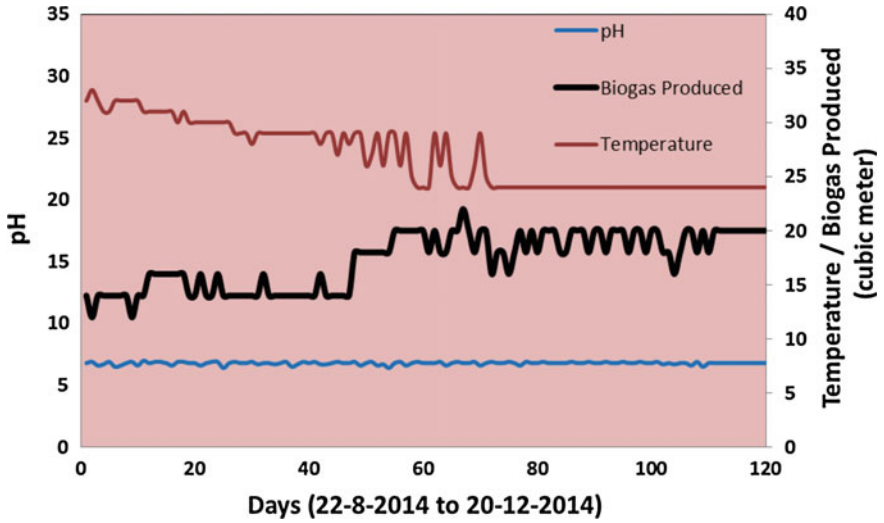


Fig. 4 Operational results of pilot scale CSTR for 04 months

4 Conclusion and Recommendation

Automated biogas plants are beneficial for community-based digesters in the villages. Successful implementation of the process at pilot scale can recommend the technology to be adopted at industrial level as two major advantages are associated with the use of CSTR, i.e., it helps in the reduction of hydraulic retention time; and the operation can be monitored and guided for better performance optimizing the production of biogas.

Acknowledgments Authors acknowledge the financial support provided by Ministry of New and Renewable Energy (MNRE), New Delhi, India (MNRE Sanction Order No: 19-1/2011-BE/R&D).

References

1. Gollakota KG, Jayalakshmi B. Biogas (natural gas) production by anaerobic digestion of oil cake by a mixed culture isolated from cow dung. Biochem Biophys Res Commun. 110, (1983) 32–35.
2. Lingaiah V, Rajasekaran P. Biodigestion of cow dung and organic wastes mixed with oil cake in relation to energy. Agric wastes. 17, (1986) 161–173.
3. Radhakrishna P, Gollakota KG. A pilot plant design and performance for biomethanation of non-edible oil cakes. Energy, 14, (1989) 771–772.
4. Gunaseelan VN, Biomass estimates, characteristics, biochemical methane potential, kinetics and energy flow from Jatropha curcus on dry lands, Biomass and bioenergy 33 (2009) 589–596.

5. Lopez O, Foidl G, Foidl N. Production of biogas from Jatropha curcus fruit shells. In: Symposium on Jatropha 97. Austria: Austrian Ministry of Foreign Affairs; 1997.
6. Staubmann R, Foidl G, Foidl N, Gubitz GM, Lafferty RM, Valencia VM, et al. Production of biogas from Jatropha curcus seeds press cake. In: Symposium on Jatropha 97. Austria: Austrian Ministry of Foreign Affairs; 1997.
7. Chandra R, Vijay VK, Subbarao PMV. A study on biogas generation from non-edible oil seed cakes: potential and prospects in India. In: Second joint International conference on sustainable energy and environment (SEE 2006). Bangkok, Thailand; 2006.

Parallel Algorithm for LaGrange's Interpolation on BSN-Mesh

Ashish Gupta and Bikash Kanti Sarkar

Abstract The efficient mapping of numerical problems over parallel architectures is a desirable and challenging task. Bi-Swapped Networks (BSN) is a new class of network architecture related to the family of Swapped or Optical Transpose Interconnection System (OTIS) Networks. The architectural advancement of BSN ensures vertex symmetry and thus improves algorithmic efficiency. Further, it ensures regularity, modularity, scalability, robustness of the network. In the present article, parallel implementation of Lagrange's interpolation over BSN-Mesh is performed. The architectural properties of BSN make it a desirable network for the efficient parallel mapping over it. The parallel algorithm for LaGrange's interpolation is designed over BSN-Mesh and then analyzed accordingly. The proposed parallel algorithm claims to map LaGrange's interpolation over BSN-Mesh in $12(n-1)$ electronic and five optical moves.

Keywords BSN · BSN-Mesh · Parallel algorithm · OTIS · Lagrange's interpolation

1 Introduction

Interconnection network is a way by which *processors* or *processing elements* are able to communicate among themselves. The algorithmic efficiency of network relies heavily over the architectural properties of network. Bi-Swapped is a regular, modular, scalable, and robust network. In addition, it also ensures symmetry of network. Therefore, it ultimately improves the algorithmic efficiency. The large network size of Bi-Swapped Networks (BSN) in comparison to Optical Transpose Interconnection System (OTIS) allows to map problem containing massive amount

Ashish Gupta (✉) · B.K. Sarkar
Birla Institute of Technology, Mesra, Ranchi 835215, Jharkhand, India
e-mail: aashish.parj@gmail.com

B.K. Sarkar
e-mail: bk_sarkarbit@hotmail.com

© Springer Science+Business Media Singapore 2017

R. Singh and S. Choudhury (eds.), *Proceeding of International Conference on Intelligent Communication, Control and Devices*, Advances in Intelligent Systems and Computing 479, DOI 10.1007/978-981-10-1708-7_77

of data. Besides the architectural properties of network, designing efficient parallel algorithms and mapping of it over parallel architectures is also an important criteria that need to be considered. BSN is related to the family of Swapped or OTIS Network. Simple connectivity of it with the vertex symmetrical nature of network improves algorithmic efficiency. However, there are some trade-offs such as increase of one unit of diameter in BSN in comparison to OTIS Network. In the present article, parallel algorithm for Lagrange's interpolation is performed and mapped over BSN-Mesh efficiently.

The general idea behind the interpolation is to find a function of a specified form which passes through a given list of data points. In general, polynomial of degree at most $(n - 1)$ is required to pass through the given list of n data points, $\{(x_1,y_1), (x_2,y_1), \ldots, (x_n,y_n)\}$ with all the x-coordinates different. The number of data points can be obtained by sampling or experimentation. Actually, these data points show function's value for limited values of the independent variable. It is often required to interpolate (estimate) the value of that function for an intermediate value of the independent variable. Polynomial interpolation is the interpolation of a given dataset (consisting of data points) by a polynomial or can say that finding of polynomial which exactly passes through the given set of data points. It may be noted that, Lagrange's interpolation uses polynomials.

Polynomials can be utilized in various fields, such as to approximate complicated curves, for shaping of letters in typography for a given set of data points, etc. Natural algorithm and trigonometric functions are also among the important applications of it. Several parallel algorithms have been proposed for Lagrange's interpolation over various parallel architectures [1–14]. In the present proposed article, parallel implementation of it demands $12(n - 1)$ electronic moves and five optical moves.

Section 1 of the present study gives general idea regarding the proposed article, whereas a background on network architectures of BSN-Mesh as a computational model is presented in Sect. 2. Langrage's interpolation methodology is briefly elaborated in Sect. 3. Finally, proposed parallel algorithm is performed for Lagrange's interpolation over BSN-Mesh architecture in Sect. 4.

2 Computational Model (BSN-MESH)

As name specifies, Bi-Swapped Networks follows Mesh pattern as its basic building block. In Mesh, each row and column processors are linearly connected. In fact, after processing of data values, shifting or pumping of it to the neighboring processors is possible in pipelined array.

Following are some of the most important properties with respect to the architectural point of view. Mesh Network does not have regular structure. Vertex degree is not similar for each processor. Therefore, property of vertex symmetry conflicted. It has balanced bipartite and Hamiltonian properties. Mesh satisfies

constant vertex degree property with $O(n)$ diameter and $O(n)$ bisection width. BSN-Mesh follows complete bipartite pattern for connectivity among the groups of processors in opposite parts and fulfills significant criteria of vertex symmetry. It may be noted that, if the basis network satisfies Hamiltonian property, it certainly satisfies the same for the entire architecture of BSN. Mesh does not have vertex (or say node) symmetry. However, it satisfies it for the entire architecture of BSN. For the better understanding, the architecture of BSN-Mesh is depicted in Fig. 1.

Definition 1 (*Horizontal Intra-Group Links*). In this architecture, $\forall g$ and $\forall p$, processor: $P(g, i, p)$ in each row follows linear pattern rooted from processor: $P(g, i \times n, p)$, $0 \leq i \leq n-1$. There exist n rows in each group with each row exhibits $n-1$ links. Therefore, $n \times n$ BSN-Mesh contains total $n \times (n-1)$ horizontal links in each group.

Definition 2 (*Vertical Intra-Group Links*). In this architecture, processor: $P(g, i, p)$ in each column follows linear pattern rooted from processor: $P(g, i, p)$, $0 \leq i \leq n-1$. There exist n columns in each group with each column exhibits $n-1$ links. Therefore, $n \times n$ BSN-Mesh contains total $n \times (n-1)$ vertical links in each group.

Definition 3 (*Inter-Part Links*). Inter-part links connect the processors among the groups of opposite part.

(i) If group number (g) does not match with processor number (i), then processor: $P(g, i, 0)$ is directly connected to processor: $P(g', i', 1)$, $0 \leq g', i \leq n^2-1$, where $g', = i, i' = g$, and vice versa.
(ii) If group number (g) match with processor number (i), then processor: $P(g, i, 0)$ is directly connected to processor: $P(g', i', 1)$, $0 \leq g, i \leq n^2-1$, where $g' = g, i' = i$, and vice versa.

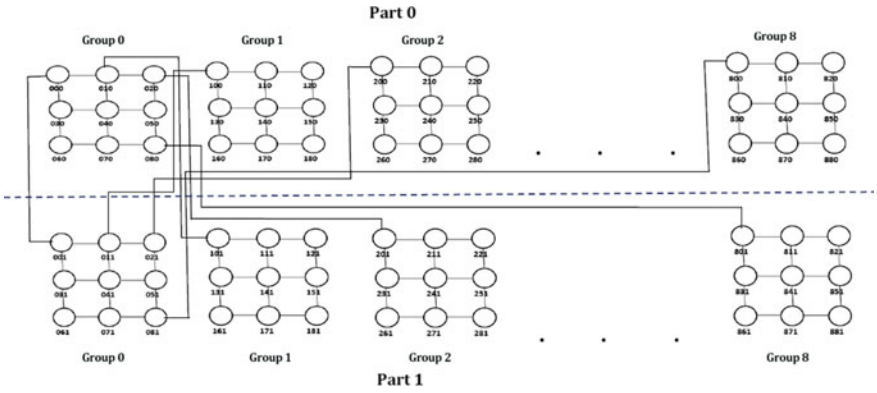


Fig. 1 3 × 3 BSN-Mesh architecture

3 Methodology

The LaGrange's interpolating polynomial is the polynomial $p(x)$ of the degree less than $(2n^2-1)$. Basically, it passes through the $2n^2$ points $(x_0, y_0 = f(x_0))$, $(x, y_1 = f(x_1))$, $(x_2, y_2 = f(x_2))$, ..., $(x^2_{2n-1}, y^2_{2n-1} = f(x^2_{2n-1}))$, and is given by

$$P(x) = \sum_{j=0}^{2n^2-1} p_j(x) \tag{1}$$

where

$$P_j(x) = y_j \sum_{\substack{k=0 \\ k\neq j}}^{2n^2-1} \frac{x - x_k}{x_j - x_k} \tag{2}$$

Written explicitly

$$\begin{aligned} P(x) = \sum_{k=0}^{2n^2-1} & \frac{(x-x_1)(x-x_2)(x-x_3)\ldots(x-x_{2n^2-1})}{(x_0-x_1)(x_0-x_2)(x_0-x_3)\ldots(x_0-x_{2n^2-1})} y_0 \\ & + \frac{(x-x_0)(x-x_2)(x-x_3)\ldots(x-x_{2n^2-1})}{(x_1-x_0)(x_1-x_2)(x_1-x_3)\ldots(x_1-x_{2n^2-1})} y_1 \\ & + \frac{(x-x_0)(x-x_1)(x-x_3)\ldots(x-x_{2n^2-1})}{(x_2-x_0)(x_2-x_1)(x_2-x_3)\ldots(x_2-x_{2n^2-1})} y_2 \\ & + \cdots + \frac{(x-x_0)(x-x_1)(x-x_2)\ldots(x-x_{2n^2-2})}{(x_{2n^2-1}-x_0)(x_{2n^2-1}-x_1)(x_{2n^2-1}-x_2)\ldots(x_{2n^2-1}-x_{2n^2-2})} y_{2n^2-1} \end{aligned} \tag{3}$$

It is important to note that, the degree would be higher of the resulting polynomial if performing over large number of data points. Therefore, greater oscillation exhibits between the data points. The high-degree interpolation improves accuracy at the data points. However, it may be a poor predictor of the function between data points. BSN (related to OTIS or swapped interconnection family) has large network size in comparison to OTIS Network (approximate double). It ultimately results in large number of data points which are used in the parallel implementation of interpolation with greater oscillation between the data points.

4 Parallel Algorithm

Performing LaGrange's interpolation over $2n^2$ data points where n represents the each group's row or column processors. Each processor has six registers namely $A(g,i,p)$, $A_1(g,i,p)$, $B(g,i,p)$, $B_1(g,i,p)$, $C(g,i,p)$, $C_1(g,i,p), 0 \leq g \leq n^2 - 1$,

$0 \le i \le n^2 - 1$, p is 0 and 1, where g represents group number, i represents processor number and p represents part number.

4.1 Proposed Parallel Algorithm

/*Feeding of Data*/.
Feed the following values in their respective registers according to Fig. 2.

$\forall p$, Feed the data value X in $A(g,0,p)$ register, $0 \le g \le n^2 - 1$.
$\forall p$, Feed the data value X in $A_1(g,0,p)$ register, $0 \le g \le n^2 - 1$.
$\forall p$, Feed the data value $X_{g+p(n^2)}$ in $B(g,0,p)$ register, $0 \le g \le n^2 - 1$.

Step 1. Perform Steps 1.1, 1.2, and 1.3 in parallel.

1.1. $\forall g$, $\forall p$, Perform parallel broadcast of data value X in each group from register $A(g,0,p)$.

1.2. $\forall g$, $\forall p$, Perform parallel broadcast of data value X in each group from register $A_1(g,0,p)$.

1.3. $\forall g$, $\forall p$, Perform parallel broadcast of data value $X_{g+p(n^2)}$ in each group from register $B(g,0,p)$.

The content of *A(g, i, p)*, $A_1(g, i, p)$ and *B(g, i, p)* registers are shown in Figure 3 and 4 respectively.

Step 2. Perform Optical moves in parallel from register: $B(g,i,p)$ to register: $C(i,g,p')$ $0 \le g, i \le n^2 - 1$, $p \ne p'$ and vice versa.

Step 3. $\forall g, \forall p$, Send data from register: $C(g,i,p)$ to register: $B_1(g',i',p')$, $g = i, g' = i', g = g', i = i', p \ne p'$ and vice versa.

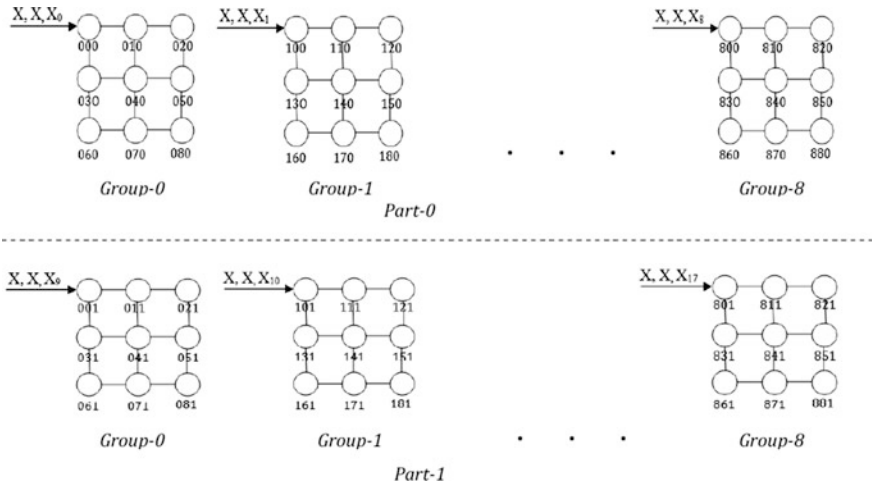


Fig. 2 Feeding of data values in their respective $A(g, i, p)$, $A_1(g, i, p)$ and $B(g, i, p)$ registers

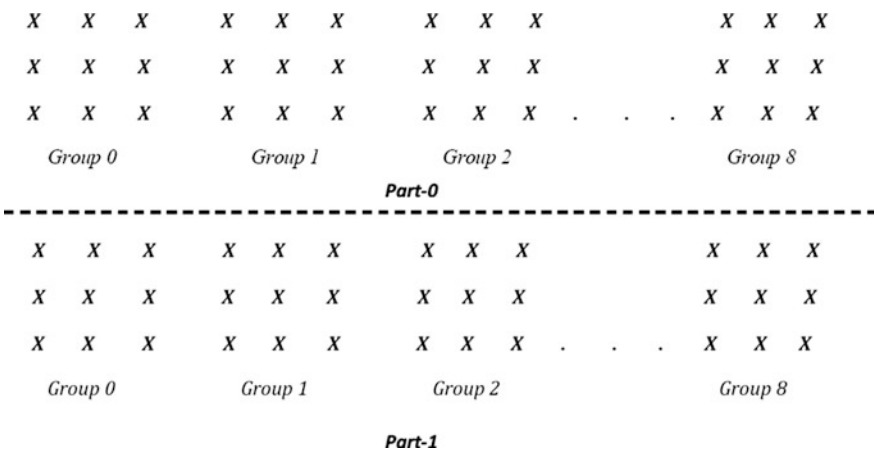


Fig. 3 Content of register $A(g, i, p)$ and $A_1(g, i, p)$

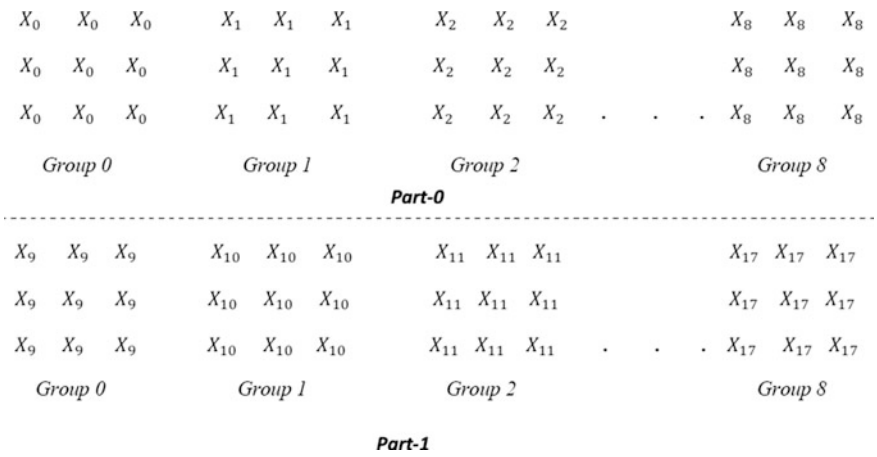


Fig. 4 Content of register $B(g, i, p)$

//The content of register: $C_1(g', i', p')$ *and register:* $B_1(g', i', p')$ *are shown in* Figs. 5 *and* 6 *respectively.*

Step 4. $\forall p, \forall g$, Perform parallel broadcasting of data in each group from register: $B_1(g, i, p)$, $g = i$.

Step 5. Perform the Steps 5.1, 5.2, 5.3, and 5.4 in parallel.

5.1. Perform subtraction: $[B_1(g, i, p) - C(g, i, p)]$, $0 \leq g$, $i \leq n^2 - 1$, $p = p'$. Store the result in their respective $B_1(g, i, p)$, register.

5.2. Perform Perform subtraction: $[A(g, i, p) - C(g, i, p)]$, $0 \leq g$, $i \leq n^2 - 1$, $p = p'$. Store the result in their respective $A(g, i, p)$ register.

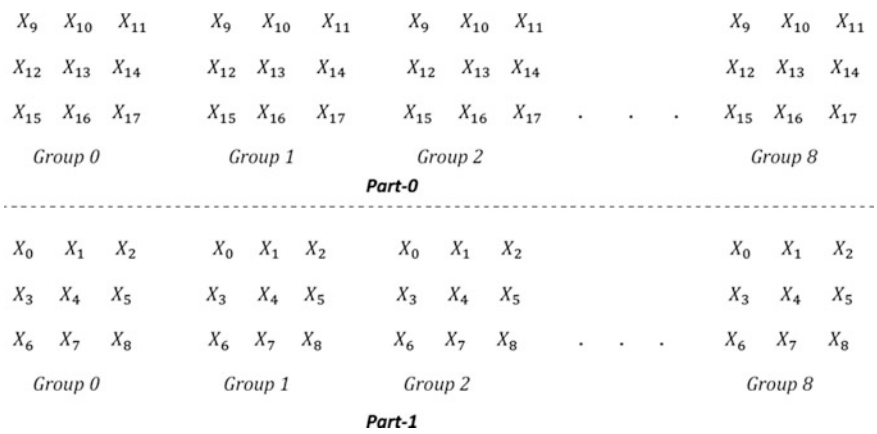


Fig. 5 Content of register $C(g, i, p)$

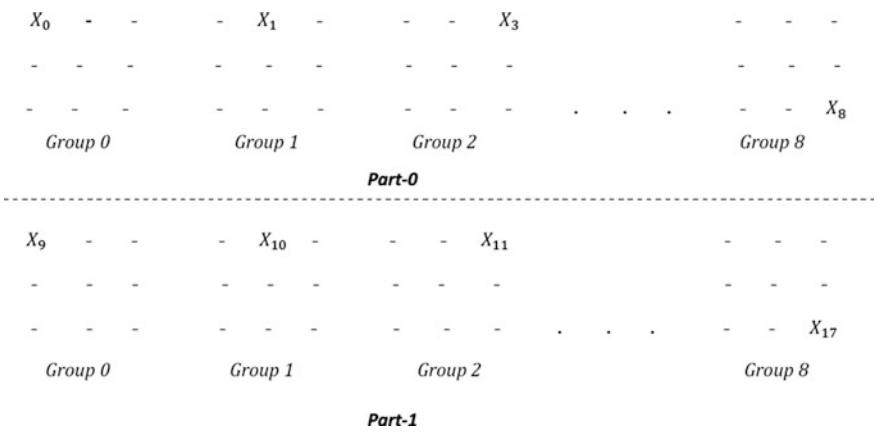


Fig. 6 Content of register $B_1(g', i', p')$

5.3. Perform subtraction: $[B(g,i,p) - C(g,i,p)]$, $0 \le g, i \le n^2 - 1$, $p = p'$. Store the result in their respective $B(g,i,p)$ register.

5.4. Perform Perform subtraction: $[A_1(g,i,p) - C(g,i,p)], 0 \le g$, $i \le n^2 - 1$, $p = p'$. Store the result in their respective $A_1(g,i,p)$, register.

Step 6. $\forall p, \forall g, \forall i$, Perform parallel addition as prefix [15] row wise in each group over registers: $B_1(g, i, p)$, $A(g, i, p)$, $B(g, i, p)$, *and* $A_1(g, i, p)$, $g \neq i$. Store the result in their respective first column processors.

Step 7. $\forall p, \forall g, \forall i$, Perform parallel addition as prefix [15] over the registers: $B_1(g, i, p)$, $A(g, i, p)$, $B(g, i, p)$, and $A_1(g, i, p)$ of first column processors of each group. Store the result in their respective registers of first processor: $P(g, 0, p)$ of each group.

Step 8. $\forall p, \forall g$, Perform parallel broadcast in each group from register: $B_1(g, 0, p)$, $A(g, 0, p)$, $B(g, 0, p)$, and $A_1(g, 0, p)$.

Step 9. Perform Steps 9.1 and 9.2 in parallel.

9.1. $\forall g, \forall i$, Perform parallel addition from register: $B_1(g, i, p)$ to register: $B(g', i', p')$, $g = i$, $g' = i'$, $g = g'$, $i = i'$.

9.2. $\forall g, \forall i$, Perform parallel addition from register: $A_1(g, i, p)$ to register: $A(g', i', p')$, $g = i$, $g' = i'$, $g = g'$, $i = i'$.

//$\forall p, \forall g$, Now register: $B(g, i, p)$, $g = i$ and register: $A(g, i, p)$, $g = i$ contain the new values.

Step 10. Perform Steps 10.1 and 10.2 in parallel.

10.1. $\forall g$, Perform parallel addition from register: $B(g, i, 0)$ to register: $B(g', i', 1)$, $g = i$, $g' = i'$, $g = g'$, $i = i'$.

10.2. $\forall \forall g$, Perform parallel addition from register: $A(g, i, 0)$ to register: $A(g', i', 1)$, $g = i$, $g' = i'$, $g = g'$, $i = i'$.

Step 11. $\forall g$, Perform parallel division: $A(g, i, 1)/B(g, i, 1)$, $g = i$. Store the result in their respective $A(g, i, 1)$ register.

Step 12. Multiply function y_i with register: $A(g, i, 1)$, $g = i$, $j = g$.

Step 13. $\forall g$, Perform parallel broadcast of data in each group from register: $A(g, i, 1)$, $g = i$.

Step 14. $\forall g$, Perform parallel optical moves from register: $A(g, 0, 1)$ to register: $A(0, g, 0)$.

Step 15. $\forall i$, Perform parallel addition as prefix [15] row wise over register: $A(0, i, 0)$.

Step 16. Perform parallel addition as prefix [15] over register: $A(0, i, 0)$ of first column processors in group 0. Finally store the outcome in register: $A(0, 0, 0)$.

4.2 Time Complexity Analysis

In the initial phase of parallel algorithm performed in Sect. 4.1, feeding of data values in respective registers demands constant step. In Step 1, parallel broadcast of data value in each group demands $2(n-1)$ steps. Further, Steps 2 and 3 each requires one optical move for inter-part communication. Again, Step 4 needs $2(n-1)$ steps for parallel broadcasting of data value in each group. Step-5 requires constant moves. Steps 6 and 7 each requires $(n-1)$ steps for computing parallel prefix addition. Step 8 demands $2(n-1)$ steps for parallel broadcasting of data in each group. Steps 9 and 10 each demands one optical move each for inter-part communication. Step 13 requires $2(n-1)$ steps for broadcasting of data values in each group. Step 14 demands one optical move. Steps 15 and 16 each needs $(n-1)$ steps for parallel prefix addition. Therefore, total 12 log n electronic and five optical moves are necessary for performing Lagrange's Interpolation on BSN-Mesh.

5 Result and Discussion

In the proposed work, parallel algorithm for Lagrange's interpolation is mapped over BSN-Mesh. The 12 logn electronic moves (intra-group) and five optical moves (inter-part) are required for an efficient implementation of Lagrange's interpolation over BSN-Mesh. Actually, the proper selection of efficient network for implementing numerical problems over it is a challenging task. Prior to designing parallel algorithm, certain network parameters such as diameter, bisection width, symmetry, network size, etc., need to be focused. Bi-Swapped Network is related to Swapped/OTIS interconnection network family. BSN preserves symmetrical nature and has large network size in comparison to OTIS Network. It satisfies the important properties of Cayley graph which is considered as a benchmark network for efficient designing of network. After analyzing the network properties, efficient designing of parallel algorithm is important.

6 Conclusion

Over the years, networks like Mesh, Mesh of Trees, Ring, Hypercube, Multi-Mesh of Trees, OTIS, etc., and their variation have been designed for implementing parallel algorithms (especially for numerical problems). From ad hoc to module-based networks, efficient parallel mapping of numerical problems over it is a challenging task. Bi-Swapped Network is a modular, scalable, symmetrical, and robust network. For parallel mapping of massive amount of data, large network size of it clearly shows an undue advantage over OTIS/Swapped interconnection networks. Further, symmetrical nature of Bi-Swapped Network also preserves the symmetrical properties of its basis network and thus the important properties of Cayley graphs as a benchmark network. In the present article, we have shown Parallel Algorithm for Lagrange's interpolation over BSN-Mesh. It demands 12 logn electronic and five optical moves.

Acknowledgments The author is indebted to Department of Computer Science and Engineering, BIT Mesra, Ranchi, for facilitating all necessary facilities for the accomplishment of research.

References

1. H. Sarbazi-Azad, M. Ould-Khaoua, L.M. Mackenzie and S.G. Akl, "A parallel algorithm for Lagrange interpolation on the star graph", Journal of Parallel and Distributed Computing 62, 605–621 (2002).
2. H. Sarbazi-Azad, M. Ould-Khaoua, L.M. Mackenzie and G. Min, "An efficient parallel algorithm for Lagrange interpolation and its performance", In The Fourth International Conference on High Performance Computing in the Asia-Pacific Region, Volume P, May 14–17, Beijing, China (2000).

3. S.S. Gupta, D. Das and B.P. Sinha, "A fast parallel algorithm for polynomial interpolation using Lagrange formula", In Proceedings of the International Conference on High Performance Computing, Dec. 27–30, New Delhi, India (1995).
4. H. Sarbazi-Azad, M. Ould-Khaoua and L.M. Mackenzie, "A parallel algorithm for Lagrange interpolation on *k*-ary *n*-cubes", ACPC Conference, 85–95, (1999).
5. B. Goertzel, "Lagrange interpolation on a processor tree with ring connections", J. Parallel Distributed. Comp. 22 (2) (1994) 321–323.
6. S. Sengupta, D. Das, B.P. Sinha, M. Ghosh, "A Fast parallel algorithm for polynomial interpolation using Lagrange's formula", in: Proceedings of the International Conference on High Performance Computing (HiPC), New Delhi (1995), pp. 701–706.
7. P.K. Jana, B.P. Sinha, "Efficient parallel algorithms for Lagrange and Hermite interpolation", Int. J. Appl. Sci. Comput. 4 (2) (1998) 118–136.
8. P.K. Jana, "Finding polynomial zeros on a multi-mesh of trees (MMT)", in: H. Mohanty, C. Baral (Eds.), Trends in Information Technology, Proceedings of the 2nd International Conference on Information Technology, (CIT'99), Bhubaneswar, India (1999), Tata Mc-Graw-Hill, December 20–22.
9. Wenjun. Xiao, Weidong. Chen, Mingxin. He, Wenhong. Wei and B. Parhami, "Biswapped Network and Their Topological Properties", Proceedings-Eighth ACIS International Conference on Software Eng., Artific. Intelligence, Networking, and Parallel/Distributed Computing, 2007, pp. 193–198.
10. Wenjun Xiaoa, Behrooz Parhamib*, Weidong Chena, Mingxin Hea and WenhongWeia, "Biswapped networks: a family of interconnection architectures with advantages over swapped or OTIS networks", International Journal of Computer Mathematics, Vol. 88, No. 13, September 2011, Taylor and francis, 2669–2684.
11. Wenhong Wei, Wenjun Xiao. "Algorithms of Basic Communication Operation on the Biswapped Network", The 8th International Conference on Computational Science, 2008, 5101: 347–354.
12. Yulian Yu, Wenhong Wei. "Load balancing on the biswapped network", Proceedings of the 2nd International Conference on Intelligent Networks and Intelligent Systems, 2009, pp. 146–149.
13. W. Xiao, B. Parhami, W. Chen, M. He, W. Wei, "Fully Symmetric Swapped Networks Based on Bipartite Cluster Connectivity," Information Processing Letters, vol. 110, 2010, pp. 211–215.
14. B. Parhami, "Swapped interconnection networks: Topological, performance, and robustness attributes", J. Parallel Distrib. Comput. 65 (2005), pp. 1443–1452.
15. S.G. Akl, The Design, Analysis of Parallel Algorithms, Prentice-Hall, Englewood Cliffs, NJ, 1989, New Delhi, 2000, pp. 202–206.
16. B. Goertzel, "Lagrange interpolation on a processor tree with ring connections", Journal of Parallel and Distributed Computing 22, 321–323 (1994).
17. H. Sarbazi-Azad, M. Ould-Khaoua, L.M. Mackenzie and S.C. Aki, "Parallel Lagrange interpolation on the star graph", In Proc. IEEE and ACM Int. Parallel Distributed Processing Symposium, (IPDPS'2000), May 1–5, Cancun, Mexico (2000), pp. 777–782.

Design of Broadband Monopole Microstrip Antenna Using Rectangular Slot

Raj Gaurav Mishra, Ranjan Mishra and Piyush Kuchhal

Abstract Microstrip antenna suffers from narrow bandwidth. The bandwidth would be enhanced by use of slot. Different sizes and shapes of slots on the patch are of great interest for obtaining optimum results in antenna design. A suitable dimension of the patch along with the position and dimension of the slot is critical in the broadening effect of the antenna. Present study proposed the method of a broadband microstrip patch antenna using slot. The slot used on the patch's surface affects the radiation characteristics of microstrip patch antenna. This study also presents the choice of size and position of the slot for the broadband antenna. The simulations are conducted using HFSS and ADS, and results of the simulation studies are discussed in this paper.

Keywords Microstrip antenna · Bandwidth · Slot · Patch dimension

1 Introduction

In last few years, microstrip patch antenna attracted considerable amount of attention of researchers due to demand of its large variety of applications in different fields such as radar, aircraft, missiles, satellite communications, biomedical telemetry, remote sensing, and different other wireless applications. Recently the advancement and spread of the technology in the wireless communication spur the demand for broadband microstrip antenna. The antenna should be compact and low

R.G. Mishra (✉) · Ranjan Mishra
CoES, University of Petroleum and Energy Studies, Dehradun, Uttarakhand, India
e-mail: rgmishra@ddn.upes.ac.in

Ranjan Mishra
e-mail: rmishra@ddn.upes.ac.in

Piyush Kuchhal
Department of Physics, CoES, University of Petroleum and Energy Studies, Dehradun, Uttarakhand, India
e-mail: pkuchhal@ddn.upes.ac.in

© Springer Science+Business Media Singapore 2017

R. Singh and S. Choudhury (eds.), *Proceeding of International Conference on Intelligent Communication, Control and Devices*, Advances in Intelligent Systems and Computing 479, DOI 10.1007/978-981-10-1708-7_78

volume. Its advantages lies in its low in volume, light weight, easily integration, ease in fabrication and low cost [1]. The conventional microstrip has narrow bandwidth. Its bandwidth is around 5 % and it stances a challenge in the design aspect of the patch to meet the broadband techniques [2]. Serious efforts have been made by the scientists, researchers, and designers to improve the bandwidth of the microstrip antenna [3].

The bandwidth improvement is achieved by loading a different shape and size of slots on the patch or in the ground plane. The impedance bandwidth of the antenna is a vital parameter of antenna. It is the range of frequencies satisfied by the desired antenna characteristics. Over this frequency range the input impedance of antenna is perfectly matched to the characteristic impedance of the feed line. The technique of imparting slot is simple in design and easy in loading and improving bandwidth [4, 5] without increasing the volume of the structures. Therefore, a number of papers have been reported by the researchers for wireless applications on the shape of the slot such as U-slot [6], stepped U-slot, half stepped U-slot, L-slot, C-slot, V-slot, W-shaped [7], M-slot [8], and E-H shaped slot [9]. We present a simple design aspect by choosing the slot to be single rectangular one. The performance of the antenna with varying meaningful length of the slot and varying position is presented. The design is also provided for the antenna broadening along with it.

2 Results and Discussion

The design of rectangular microstrip antenna is governed by the set of equations [1]. The dimension of the patch is dependent on the resonant frequency and the height of the substrate. The suitable height of the substrate is 1.6 mm [10]. The substrate chosen for this discussion is epoxy FR4 with a permittivity of 4.4. The selected feeding technique is microstrip line feeding method. It is very widely used because of its simplicity in designing and further analysis. This method is also simply matched [11] by controlling the inset position. In the first case of observation the height of the substrate and length of the patch is fixed. Both these are the function of the material permittivity and resonant frequency. The length of the patch, for the resonant frequency of 7 GHz, is kept fixed at 12 mm. In the initial discussion, to get the broadening effect, the width of the patch is changed from 14 mm onwards. Simulation result was observed by varying the width by an interval of 0.25 mm, and the results are plotted in Fig. 1. The results are for both the absolute magnitude of the return loss and the bandwidth. With 50 Ω line; the best impedance is observed at 16 mm of the patch width. It is quite obvious that with the changing width, both the return loss and bandwidth performance of the microstrip antenna changes. Beyond 18 mm, the performance dips below the significant value.

The width of the antenna is responsible for the fringing effect. With more width the fringing effect is more, but the higher order modes are also generated and this will results in the degradation after certain width.

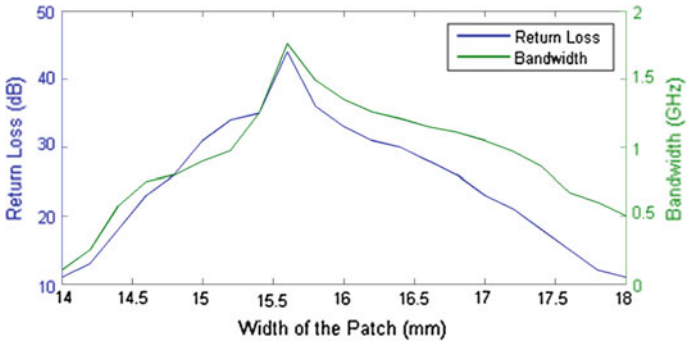


Fig. 1 Variation of antenna parameter with width of the patch

In the second set of observation the dimension of the patch is kept fixed and a slot is carved on it. Simulation results were observed with varying the position and height of the patch. The height of the slot is lower than the length of the patch [1]. The position of the slot is varying from the non-radiating side with an interval of 0.5 mm. Three set of length of the slots is chosen for the observation. These are 11, 10, and 9 mm. For the performance of the antenna two passive parameters viz. return loss and bandwidth is taken for the observation. The combined results of return loss and bandwidth are shown plotted in the Figs. 2, 3 and 4. Figure 2 is the result with 11 mm of slot length, whereas Fig. 3 is with 10 mm of slot length. The result obtained with 9 mm of slot length is shown in Fig. 4. All the three figures show similarity in the pattern.

Also the best return loss is obtained nearly to 4 and 8 mm from the non-radiating side of the patch antenna. After 10 mm distance the result drops to zero value. The distance 4 and 8 mm, where the best resonant occurs, is the harmonic multiple of the wavelength used. Similarly the bandwidth increased from 0 mm to reach to maximum near to 4 mm. Also as the distance increases, the bandwidth reduces and again maximum at 8 mm. Similar to return loss plot, it also drops to null value

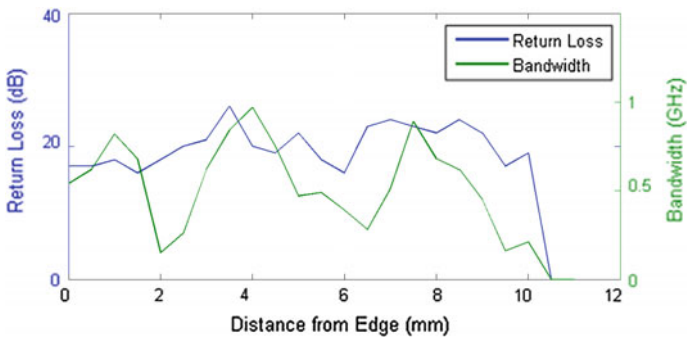


Fig. 2 Performance with 9 mm rectangular slot

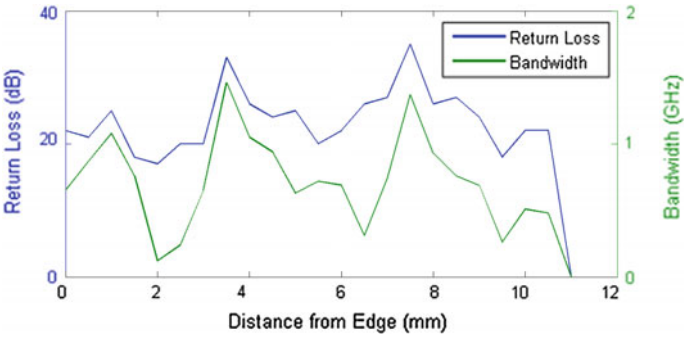


Fig. 3 Performance with 10 mm rectangular slot

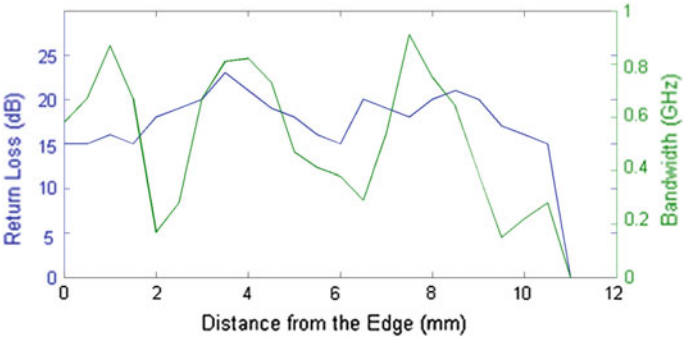


Fig. 4 Performance with 11 mm rectangular slot

beyond 10 mm from the side. So, it is obvious from the simulated result that the best matching occurs at near 4 mm distance from the side and with a slot dimension of 10 mm. With these results observed from the various simulation optimizations, the final result is taken with the following dimension of the antenna is shown in Table 1.

The image of the current distribution in the patch of the antenna fed with microstrip line is shown in the Fig. 5. It shows that the current has a higher value near the periphery of the slot that enhances the radiation pattern. This subsequently accounts for more bandwidth.

Table 1 Dimension of the proposed antenna

Parameters	Dimensions (mm)
Patch length	12
Patch width	16
Slot length	10
Slot width	0.5
Slot distance	4

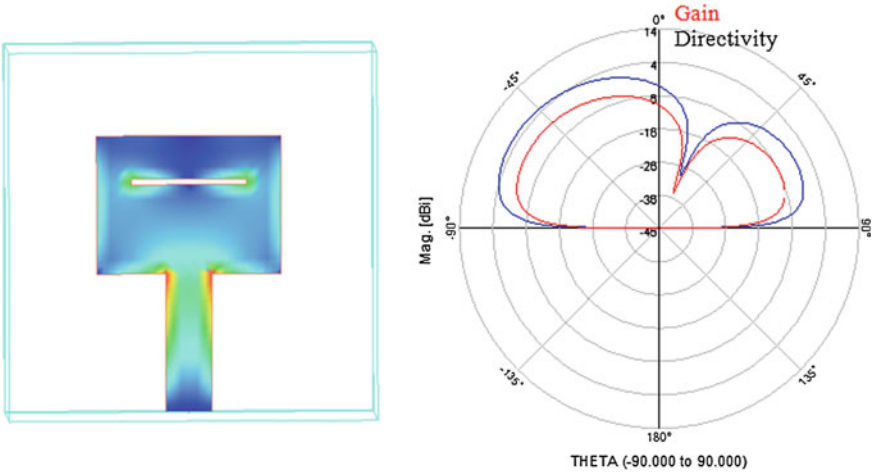


Fig. 5 Current distribution in the single slot-loaded patch and the radiation pattern of the proposed antenna

The return loss plot simulated in HFSS is shown in Fig. 6. It is clear that this prototype is giving a very high bandwidth (of 1.7 GHz) and a maximum return loss of –27 dB.

The antenna is showing a uniform power radiation with good omnidirectional pattern. The two dimensional antenna radiating pattern is shown in Fig. 1. The simulated result records a gain of 1.5 dB and directivity of 6.7 dB with a radiation efficiency of more than 27 %.

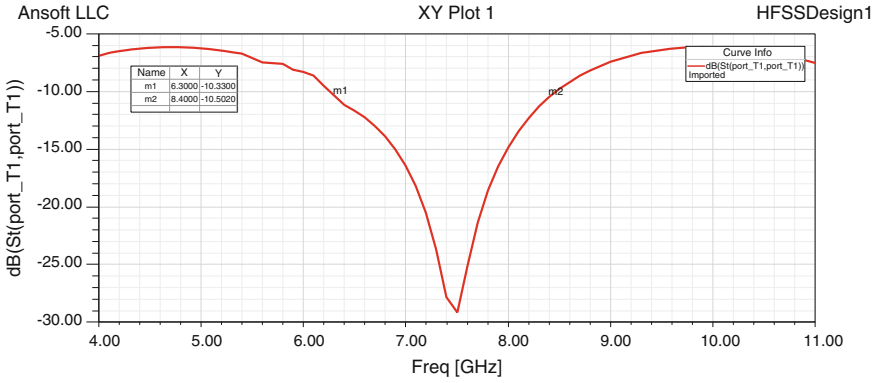


Fig. 6 Return loss plot of the proposed antenna

3 Conclusion

Imparting a slot of right dimension at the right distance will gives a perfect matching. This results in a good return loss and higher bandwidth. The slot intensifies the electric field and enhances the performance of the antenna. By proper selection of the patch dimension and the slot, a broadband antenna can be designed conveniently.

References

1. R. Garg, P. Bhartia, and I. Bahl, Ittipiboon, Microstrip Antenna Design Handbook, Artech House, Norwood, Mass, USA, 2001.
2. Pozar, D. M. and D. H. Schaubert, Microstrip Antennas: The Analysis and Design of Microstrip Antennas and Arrays, IEEE Press, New York, 1995.
3. A. A. Deshmukh and K. P. Ray, Compact broadband slotted rectangular microstrip antenna, IEEE Antennas and Wireless Propagation Letters, vol. 8, pp. 1410–1413, 2009.
4. Kang Woong, Kim Kangwook, Kim Woosu, A Broad-Band Conductively-Loaded Slot Antenna for Pulse Radiation, A Broad-Band Conductively-Loaded Slot Antenna for Pulse Radiation, IEEE transaction on Antenna and Propagation, vol 62, no 1, pp 33–39, 2014.
5. Jang Joon Won, Hwang Hee Yong, An Improved Band-Rejection UWB Antenna with Resonant Patches and a Slot, IEEE transaction on Antenna and Propagation, vol 57, no 8, pp 299–302, 2009.
6. A. A. Deshmukh and G. Kumar, Compact broadband U slot-loaded rectangular microstrip antennas, Microwave and Optical Technology Letters, vol. 46, no. 6, pp. 556–559, 2005.
7. A. A. Lotfi Neyestanak, F. Hojjat Kashani, and K. Barkeshli, W-shaped enhanced-bandwidth patch antenna for wireless communication, Wireless Personal Communications, vol. 43, no. 4, pp. 1257–1265, 2007.
8. F. Jolani, A. M. Dadgarpour, and H. R. Hassani, Compact M– slot folded patch antenna for WLAN, Progress in Electromagnetics Research Letters, vol. 3, pp. 35–42, 2008.
9. M. T. Islam, M. N. Shakib, and N. Misran, Broadband E-H shaped microstrip patch antenna for wireless systems, Progress in Electromagnetics Research, vol. 98, pp. 163–173, 2009.
10. R. Mishra, P. Kuchhal, A. Kumar, Effect of Height of the Substrate & Width of the Patch on the Performance Characteristics of Microstrip Antenna, International Journal of Electrical and Computer Engineering, vol 5, no 6, pp 1441–45, Dec 2015.
11. G. Zheng, T. Huiping, W. Xudong, L. Qun, et al, Bandwidth Enhancement of Monopole UWB Antenna With New Slots and EBG Structures, IEEE transaction on Antenna and Propagation, vol 61, no 12, 2013, pp 1550–1553.

HAAR like Feature-Based Car Key Detection Using Cascade Classifier

Paawan Sharma, Mukul K. Gupta, Amit K. Mondal and Vivek Kaundal

Abstract The paper reports effective real-time implementation for specific object detection in an image or sequence of images. For the present work, car key has been taken as an object under consideration. The classifier is developed using OpenCV-Python. The procedure encompasses training and detection. A wide variety of object images are used for training purpose. The developed xml classifier is then tested on separate test images. The classifier has a good success rate with minimal false object detection rate.

Keywords Classifier · Haar-like features · OpenCV · Python · Machine vision · Pattern recognition

1 Introduction

Machine vision is a very crucial component of robotics and automation for various systems such as manufacturing plants, smart robots, etc. [1]. OpenCV [2] is an open source library for computer vision. Specifically in real-time applications, OpenCV exhibits a good computational efficiency. Classifier design is an important aspect of any machine vision-based application, and is practiced to implement a decision rule [1]. Classifier behavior depends on features which are extracted from images.

Paawan Sharma (✉) · M.K. Gupta · A.K. Mondal · Vivek Kaundal
Department of Electronics, Instrumentation and Control Engineering, University of Petroleum and Energy Studies, Dehradun, India
e-mail: paawan.sharma@ddn.upes.ac.in

M.K. Gupta
e-mail: mkgupta@ddn.upes.ac.in

A.K. Mondal
e-mail: akmondal@ddn.upes.ac.in

Vivek Kaundal
e-mail: vkaundal@ddn.upes.ac.in

© Springer Science+Business Media Singapore 2017

R. Singh and S. Choudhury (eds.), *Proceeding of International Conference on Intelligent Communication, Control and Devices*, Advances in Intelligent Systems and Computing 479, DOI 10.1007/978-981-10-1708-7_79

Every classifier has some description, which can be obtained using supervised or unsupervised learning [3]. In supervised learning, a training set of images is used to develop class representation in terms of various statistical parameters. An unsupervised learning is basically a clustering algorithm which links samples to the nearest cluster.

Viola-Jones generated [4] Haar-like features from Haar basis function $f(x)$ described in Eqs. (1) and (2), and constructed classifier using Adaboost [5] by successive combination in a cascade fashion resulting into detection speed improvement.

$$f(x) = \begin{cases} 1 & 0 \le x < \frac{1}{2} \\ -1 & \frac{1}{2} \le x \le 1 \\ 0 & \text{else} \end{cases}; \tag{1}$$

$$f(x)_j^k \equiv f\left(2^j x - k\right) \tag{2}$$

In such process, a weak learning algorithm selects the single feature which best differentiates between positive and negative samples. This optimal function results into minimum number of wrong classifications.

2 Methodology

This section describes the overall process of generating a classifier as shown in Fig. 1. It starts with creating a vector file (.vec file) from positive and negative samples (images). Positive images are those which contain the desired object (car keys in this case), while negative images are those which do not contain the object. The utility opencv_createsamples in OpenCV [6] creates a vector file according to various options. The second utility opencv_traincascade [6] uses the *.vec file generated in previous step and set of background images to create the classifier (*.xml file).

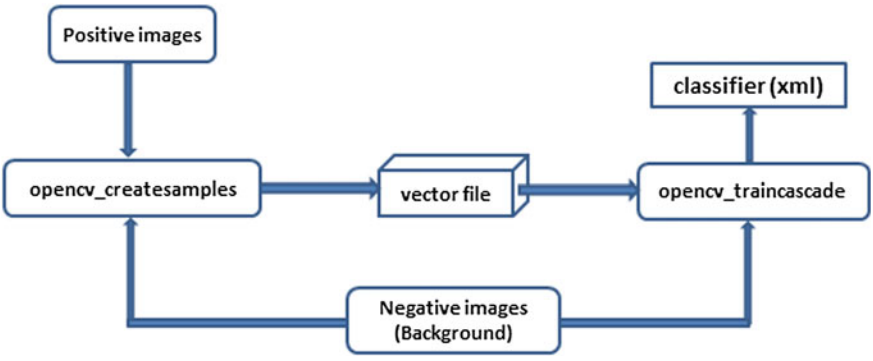


Fig. 1 OpenCV classifier (.xml) design process

Table 1 opencv_createsamples parameters

Parameter	Value	Description
-maxxangle	1.1	Maximum X-axis rotation angle
-maxyangle	1.1	Maximum Y-axis rotation angle
-maxzangle	0.5	Maximum Z-axis rotation angle
-w	24	Sample width in pixels
-h	24	Sample height in pixels

Table 2 Opencv_traincascade parameters

Parameter	Value	Description
-numPos	18	No. of positive samples
-numNeg	18	No. of negative samples
-numStages	20	Trainable cascade stages
-w	24	Sample width in pixels
-h	24	Sample height in pixels

Then, the classifier is applied on various test images using a simple Python program. The code for this purpose is expected to draw a polygon at the location where object is detected in the image.

As discussed in Sect. 2.1, the OpenCV utilities have many optional parameters which alters the training process. opencv_createsamples has -vec, -info, -img, -bg, -num, -bgcolor -bgthresh, -inv, -randinv, -maxidev, -maxxangle, -maxyangle, -maxzangle, -show, -w, -h as parameters, the values for which are mentioned in Table 1. opencv_traincascade has -data, -vec, -info, -img, -bg, -numPos, -numNeg, -numStages, -mode, -w, -h, -minHitRate as parameters, the values for which are mentioned in Table 2.

2.1 Code Syntax

OpenCV command usage

```
 opencv_createsamples -info
E:\machine_vision\haarclassifier\imagess \info.dat -bg
E:\machine_vision\haarclassifier\imagess\bg.txt -vec
op_ft.vec -num 18
 opencv_traincascade -data E:\machine_vision\ -vec
op_ft.vec -bg
E:\machine_vision\haarclassifier\imagess\bg.txt -numPos
18 -numNeg 18
```

Python code [7]

```
import numpy as np
import cv2
carkeys_cascade = cv2.CascadeClassifier('carkeys.xml')
img1 = cv2.imread('img1.jpg')
img2 = cv2.imread('img2.jpg')
gray1 = cv2.cvtColor(img1, cv2.COLOR_BGR2GRAY)
gray2 = cv2.cvtColor(img2, cv2.COLOR_BGR2GRAY)
faces1 = carkeys_cascade.detectMultiScale(gray1, 1.05,
1)
faces2 = carkeys_cascade.detectMultiScale(gray2, 1.05,
1)
for (x,y,w,h) in faces1:
      cv2.rectangle(img1 , (x,y) , (x+w, y+h) , (255,0,0)
, 2)
for (x,y,w,h) in faces2:
      cv2.rectangle(img2 , (x,y) , (x+w, y+h) , (255,0,0)
, 2)
cv2.imshow('img1',img1)
cv2.imshow('img2',img2)
cv2.imwrite('det1.png',img1)
cv2.imwrite('det2.png',img2)
cv2.waitKey(0) cv2.destroyAllWindows()
```

3 Results

Figure 2 shows the output of Python program, which clearly indicates the detection of car keys. However, a better success rate and minimal false object detection can be achieved by increasing the number of positive as well as negative samples. For present study, 18 images for each category were chosen for training purpose.

4 Conclusion

A practical method of object detection was analyzed in real-time yielding positive results. The biggest advantage of using OpenCV-Python for such purpose lies in the fact that both tools are available for Linux operating system also. This makes it possible to implement it on hardware platform such as Raspberry pi, etc., since users can select OS of their choice for the hardware platform. Hence, a combination of Linux-OpenCV-Python can be easily exploited over a hardware platform.

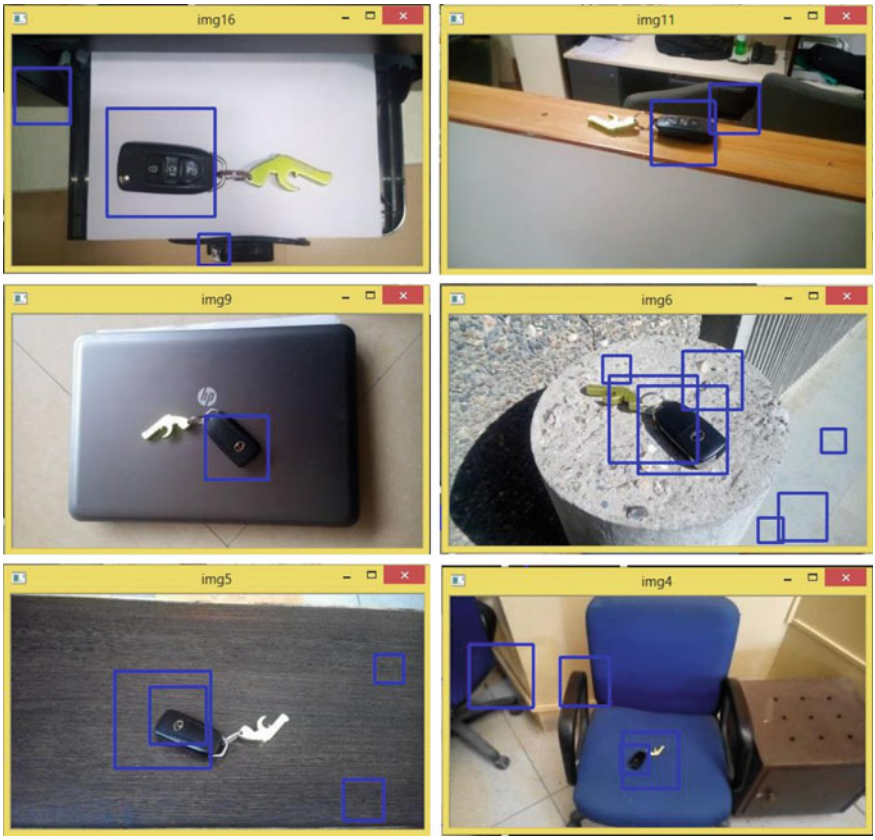


Fig. 2 OpenCV classifier performance

Acknowledgments Authors are thankful to Mr. Bhanprakash for his valuable help in collecting image samples.

References

1. Sonka, Milan, Vaclav Hlavac, and Roger Boyle. Image processing, analysis, and machine vision. Cengage Learning (2014).
2. Documentation for OpenCV, http://opencv.org/documentation.html.
3. Snyder, Wesley E., and Hairong Qi. Machine vision. Cambridge University Press (2010).
4. Viola, Paul, and Michael Jones. "Rapid object detection using a boosted cascade of simple features" In Computer Vision and Pattern Recognition, 2001. CVPR 2001. Proceedings of the 2001 IEEE Computer Society Conference on, vol. 1, pp. I–511. IEEE (2001).

5. Freund, Yoav, and Robert E. Schapire. “A decision-theoretic generalization of on-line learning and an application to boosting” Journal of computer and system sciences 55, no. 1 (1997): 119–139.
6. Cascade Classifier Training, http://docs.opencv.org/3.1.0/dc/d88/tutorial_traincascade.html#gsc.tab=0.
7. OpenCV-Python Tutorials, http://docs.opencv.org/3.1.0/d6/d00/tutorial_py_root.html.

Global Stability of Dynamic Model for Worm Propagation in Wireless Sensor Network

Rudra Pratap Ojha, Pramod Kumar Srivastava, Shashank Awasthi and Goutam Sanyal

Abstract Wireless Sensor is one of the important communication device through which data can be collected and transmitted from any type of terrain. The collection of sensors constitutes a network that is a self-organized autonomous network which is called Wireless Sensor Network (WSN). A number of security challenges are addressed in WSN and one of the security issues is worms or virus attack. To study the attack and analysis of the spread and control of worms, the epidemic mathematical model becomes an important tool. We propose Susceptible (S), Infective (I), Treated (T), Highly infected (H), Recovered (R), SITHR model to describe the nonlinear dynamics of model. In this model, we propose that some infected individuals should move from treated phase to infected phase even after the use of a protection mechanism. The universal dynamics of the transmission of the worms can be analyzed by mathematical model and spreading behavior of a worm in WSN can be determined by the value R_0 basic reproduction number.

Keywords Wireless sensor networks · Basic reproduction number · Equilibrium point · Worms · Stability

1 Introduction

A large number of sensor nodes constitute Wireless Sensor Networks (WSN), which are equipped with limited resources like memory, processing power and coverage area [1]. WSN applications in various area like military, intrusion detection, surveillance, disaster management, monitoring, healthcare, etc. [2]. Basically sensor

R.P. Ojha (✉) · P.K. Srivastava
Galgotias College of Engineering and Technology, Greater Noida, India
e-mail: rpojha@gmail.com

R.P. Ojha · Goutam Sanyal
National Institute of Technology, Durgapur, India

Shashank Awasthi
G.L. Bajaj Institute of Technology & Management, Greater Noida, India

© Springer Science+Business Media Singapore 2017

R. Singh and S. Choudhury (eds.), *Proceeding of International Conference on Intelligent Communication, Control and Devices*, Advances in Intelligent Systems and Computing 479, DOI 10.1007/978-981-10-1708-7_80

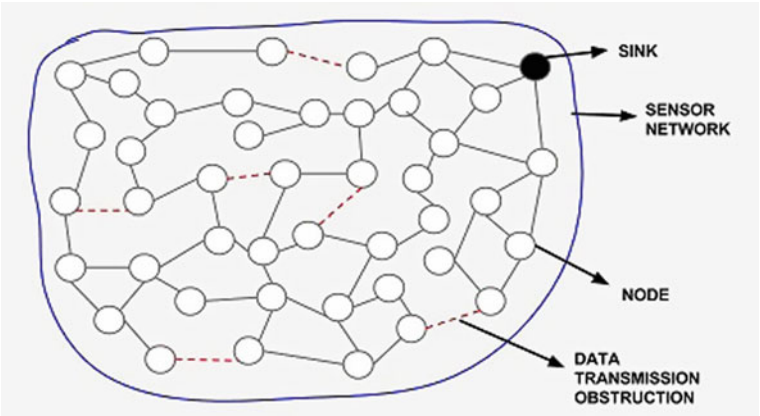


Fig. 1 Wireless sensor network field

nodes are used to create a wireless network in any type of territory. After deployment of nodes it collect data from its surroundings and delivers the collected data to the control node that is called sink node in multihop communication via its neighbor nodes. Sensor nodes have limited energy and it is very difficult to replace its battery because the working areas are very difficult. Therefore, when node exhausts its energy then it has no ability to transmit data in the network.

The WSN is one of the hot topics for academia and industry due to various applications. There are some challenges with sensor nodes such as energy consumption, deployment of nodes, security, etc. Sensor nodes are very soft target for worm attack due to weak defense mechanism. So securities are one of the important concerns for WSNs and need to be more attention. The other challenge is energy saving, for energy saving there are various parameters to be discussed like topology placement of nodes, etc. Working mode of sensor nodes also play an important role to save energy. Sensor nodes are working in two modes, sleep or active mode, in sleep mode, all functional units of the nodes are in an inactive state,ability to transmit directly and when the nodes are in active mode they are fully working and at that time the energy of nodes is dissipated. So cleverly use the nodes to save the energy that means, when no need to transmit or receive data the sensor node goes to sleep mode.

It is found that when worm appears in the sensor networks and nodes are in active mode they can spread it with data or may be independently from one node to another node, this happens due to lack of defense mechanism [3]. Figure 1 shows the sensor field in which sensor nodes are scattered and data transmit between nodes to nodes or from nodes to sink. When the data is transmitted from node to sink it will take more hop to reach at sink by different mechanisms [4]. When the source node sends data to sink via neighbor nodes, during the transmission of data there is some obstruction in WSN such as worms and virus attack.

Computer viruses are self-replicating and they can propagate via network of computer without any manual interference [4, 5]. In the digital world one of the

most dangerous threat is worm attack for communication network and computer. Now day's new types of worms are surfacing specially for portable devices like laptops and phones. They have ability to transmit directly from device to device through wireless technology for example, as Bluetooth or Wi-Fi [4, 5] Wireless devices are targeted by malicious signals, for example Cabir worm and Mabir worm and spreading the behavior of these worms and are epidemic in nature [6]. Therefore, to prevent the malware attacks on sensor nodes security mechanism using epidemic models has been explored by various groups [4, 6–8]. Effect and control of malicious signals on the computer network have been studied by various authors by using the concepts of epidemical model [9–12]. Some researchers have described epidemic models to consider time delay and control mechanism for virus propagation [9–12].

To be able to understand the dynamical characteristics of worm propagation in WSNs to study different epidemic models,it is found that there is a similarity between computer network and WSNs in case of worm propagation. The epidemic models broadly are useful to study worm spread in WSNs by some authors [4, 13]. In [13], the authors proposed a SIRS model with feedback controller and analyzed Hopf bifurcation dynamics of malware prevalence in mobile wireless networks. The authors in [4] proposed an epidemic model with vaccination compartment which includes both temporal and spatial dynamics of worm spreading process, and some mathematical analysis and numerical simulations were done to verify this model. These models do not consider undetected nodes which is harmful for sensor network.

In the present study, we propose SITHR model to study the dynamics of spreading of a virus in WSNs and find the stability of the network. Assume that all the nodes are susceptible towards malicious attack and become infectious and transmit the worm with data or may be spread through wireless communication. It is found that some sensor nodes are not detected early the worm attack, so they are not using any antivirus to prevent malicious attacks. So, it is found that those undetected infectious nodes become highly infected with time. After some time infected nodes are detected, and these nodes are sent immediately into sleep mode. Because they do not spread worms to the neighbor nodes in sleep mode and run the antivirus to remove the worms from nodes. By this method the lifetime of a WSN can be increased. An efficient antivirus is to be used either to recover these infected nodes or to remove them from the network without disturbing network stability, because these infected nodes become dangerous for WSN. Those sensor nodes, which are detected early, are sent to the treated compartment and malicious signals can be eradicated early from sensor network. It may be a possibility that due to slower treatment rate some nodes move to highly infected compartments. Hence, by increasing the treatment rate we may decrease the severity in the WSNs or we may say that overhead occurred due to the malicious signal can be removed. When the transmission overhead of the nodes is minimized, the energy dissipation of nodes can be minimized and it increases the lifetime of WSN. The diagnosed nodes which are not treated timely may move to highly infected state they can remove or

recover to elongate lifetime of a network. This model explores the treatment and control of early and late detected nodes to elongate WSNs life.

2 Model Formulation

Different subclass of sensor nodes at any time *t,* are Susceptible $S(t)$, Infectious $I(t)$, Treatment $T(t)$, Infected $H(t)$, and Recovered $R(t)$ of Total size $N(t)$ i.e.,

$$N(t) = S(t) + I(t) + T(t) + H(t) + R(t), \tag{2.1}$$

In Fig. 2 we describe the dynamical transfer of sub class. The SITHR model is given by:

$$\left.\begin{aligned} \frac{dS}{dt} &= \alpha N - \beta \frac{SI}{N} - \mu S, \\ \frac{dI}{dt} &= \beta \frac{SI}{N} - (\gamma + \lambda + \mu) I, \\ \frac{dT}{dt} &= \lambda I - (\sigma + \mu + \rho) T, \\ \frac{dH}{dt} &= \gamma I + \sigma T - (\delta + \mu + \phi) H, \\ \frac{dR}{dt} &= \rho T + \phi H - \mu R \end{aligned}\right\} \tag{2.2}$$

where $S(0) = S_0,\ I(0) = I_0,\ T(0) = T_0,\ H(0) = H_0 \forall\, t \geq 0$. In order to express system of Eq. (2.2) as a portion of the entire population, and since the recovered class $R(t)$ does not appear in the first four equations of system (2.2), we use the following substitution $s = \frac{S}{N}, i = \frac{I}{N}, z = \frac{T}{N}, h = \frac{H}{N}$. Hence resulting system of equation shall be:

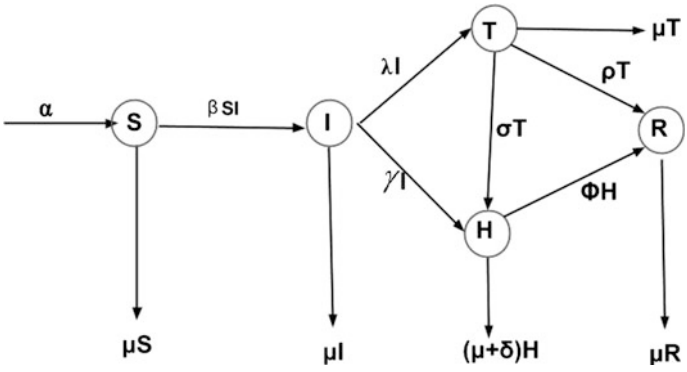


Fig. 2 Malicious signal transmission diagram in wireless system network

$$\left.\begin{aligned}\frac{\mathrm{d}s}{\mathrm{d}t} &= \alpha - \beta si - \mu s,\\ \frac{\mathrm{d}i}{\mathrm{d}t} &= \beta \mathrm{si} - (\gamma + \lambda + \mu)i,\\ \frac{\mathrm{d}z}{\mathrm{d}t} &= \lambda i - (\sigma + \mu + \rho)z,\\ \frac{\mathrm{d}h}{\mathrm{d}t} &= \gamma i + \sigma z - (\delta + \mu + \phi)h,\end{aligned}\right\} \tag{2.3}$$

where α considered to be constant rate for new nodes which connected to the WSN, μ is the crashing rate of sensor nodes, β is coefficient of transmission, σ is the rate of transmission from T class to H class, λ is the rate of treatment, ϕ is the rate of recovery from H class to R class, ρ is the recovery rate from T class to R class, δ is the rate of hardware failure and γ the rate at which the infective individuals move from I class to H class. We will discuss the system in the domain $\Gamma = \left\{(s, i, z, h) \in \Re^4_+\right\}$. Since the model monitors sensor nodes of different class, so all the state variables remain non negative for all t greater than or equal to zero.

3 Existence of Positive Equilibrium

For equilibrium points, we have $\frac{\mathrm{d}s}{\mathrm{d}t} = 0; \frac{\mathrm{d}i}{\mathrm{d}t} = 0; \frac{\mathrm{d}z}{\mathrm{d}t} = 0; \frac{\mathrm{d}h}{\mathrm{d}t} = 0$; and after a straight forward calculation, we get equilibrium points as: $P_0 = (s, i, z, h) = \left(\frac{\alpha}{\mu}, 0, 0, 0\right)$ for worm free state and $P^* = (s^*, i^*, z^*, h^*)$ for endemic state, where,

$$s^* = \frac{\gamma + \lambda + \mu}{\beta},\ i^* = \frac{\mu}{\beta}(R_0 - 1),\ z^* = \frac{\lambda\mu}{\beta(\sigma + \mu + \rho)}(R_0 - 1),$$
$$h^* = \frac{\mu}{\beta}\left[\gamma + \frac{\sigma\lambda}{(\sigma + \mu + \rho)}\right](R_0 - 1);$$

where R_0 [14] is the basic reproduction number given by $R_0 = \frac{\alpha\beta}{\mu(\gamma + \lambda + \mu)}$. It is clear that P^* exist and unique if and only if $R_0 > 1$.

4 The Stability Analysis

In this section we will discuss the stability analysis of the worm free equilibrium and endemic equilibrium

Theorem 1 *The system (2.2) is locally asymptotically stable if basic reproduction number R_0 is less than unity at worm free equilibrium P_0.*

Proof At worm free equilibrium point P_0, the Jacobian matrix is

$$J(P_0) = \begin{pmatrix} -\mu & -\frac{\beta\alpha}{\mu} & 0 & 0 \\ 0 & \frac{\beta\alpha}{\mu} - (\gamma+\lambda+\mu) & 0 & 0 \\ 0 & \lambda & -(\sigma+\mu+\rho) & 0 \\ 0 & 0 & -\sigma & -(\delta+\mu+\phi) \end{pmatrix} \tag{4.1}$$

Eigenvalues of (4.1) are: $\omega_1 = -\mu, \omega_2 = \frac{\beta\alpha}{\mu} - (\gamma+\lambda+\mu)$, $\omega_3 = -(\sigma+\mu+\rho)$, $\omega_4 = -(\delta+\mu+\phi)$. It is clear that $\omega_1 < 0$, $\omega_3 < 0$, $\omega_4 < 0$ and $\omega_2 < 0$ if $\frac{\beta\alpha}{\mu} - (\gamma + \lambda + \mu) < 0 \Rightarrow \frac{\alpha\beta}{\mu(\gamma+\lambda+\mu)} < 1 \Rightarrow R_0 < 1$, therefore the system is locally asymptotically stable at worm free equilibrium point P_0 which proves the theorem.

Theorem 2 *The system (2.2) is globally asymptotically stable if $R_0 \leq 1$ at worm free equilibrium P_0.*

Proof Consider the Lyapunov [15] function $L(t) : \Re^4 \to \Re^+$ defined by $L(t) = \omega i$.
Its derivative w.r.t t

$$\dot{L}(t) = \omega\frac{\mathrm{d}i}{\mathrm{d}t} = \omega(\beta_{\mathrm{si}} - (\gamma+\lambda+\mu)i) \leq \omega\left(\frac{\beta\alpha}{\mu} - (\gamma+\lambda+\mu)\right)i = \omega(R_0 - 1)i,$$

It is clear that $\frac{\mathrm{d}L(t)}{\mathrm{d}t} = 0$ only when $i = 0$. Therefore the maximum invariant $\Gamma = \left\{(s,i,z,h) \in \Re^4_+\right\}$ is the singleton set. Therefore the global stability of worm free equilibrium P_0 when $R_0 \leq 1$ from Lasalle invariance principle [15].

Theorem 3 *The endemic equilibrium is locally asymptotic stable if $R_0 > 1$.*

Proof The Jacobian matrix associated with endemic equilibrium is

$$J(P_0) = \begin{pmatrix} -\mu R_0 & -\frac{\beta\alpha}{\mu R_0} & 0 & 0 \\ \mu(R_0 - 1) & 0 & 0 & 0 \\ 0 & \lambda & -(\sigma+\mu+\rho) & 0 \\ 0 & \nu & \sigma & -(\delta+\mu+\phi) \end{pmatrix} \tag{4.2}$$

Eigenvalues of (4.2) are $\omega_1 = -(\mu+\delta+\phi), \omega_2 = -(\gamma+\lambda+\mu), \omega_3 = -(\sigma+\mu+\rho)$, $\omega_4 = -\mu(R_0 > 1)$. It is clear that $\omega_1 < 0, \omega_2 < 0, \omega_3 < 0, \omega_4 < 0$, if $R_0 > 1$ therefore the system is locally asymptotically stable at endemic equilibrium point P^*.

Theorem 4 *The Endemic equilibrium is globally asymptotically stable.*

Proof Consider the suitable Lyapunov function

$$\begin{aligned}\dot{L} &= \left(\frac{s-s^*}{s}\right)\dot{s} + \left(\frac{i-i^*}{i}\right)i + \left(\frac{z-z^*}{z}\right)\dot{z} + \left(\frac{h-h^*}{h}\right)\dot{h} \\ &= \left(\frac{s-s^*}{s}\right)(b-\beta(s-s^*)(i-i^*)-\mu(s-s^*)) + \left(\frac{i-i^*}{i}\right)(\beta(s-s^*)(i-i^*) \\ &\quad -(\gamma+\lambda+\mu)(i-i^*)) + \left(\frac{z-z^*}{z}\right)(\lambda(i-i^*)-(\sigma+\rho+\mu)(z-z^*)) \\ &\quad + \left(\frac{h-h^*}{h}\right)(\gamma(i-i^*)-\sigma(z-z^*)-(\delta+\mu+\phi)(h-h^*)) \\ &= \left(\alpha - \frac{\alpha s^*}{s}\right) - \frac{(s-s^*)^2}{s}(\beta(i-i^*)+\mu) + \frac{(i-i^*)^2}{i}(\beta(s-s^*)-(\gamma+\lambda+\mu)) \\ &\quad - \frac{(z-z^*)^2}{z}(\sigma+\mu+\rho) - (\delta+\mu+\phi)\frac{(h-h^*)^2}{h} + \lambda\left(i - i^* - \frac{z^*i}{z} + \frac{z^*i^*}{z}\right) \\ &\quad \gamma\left(i - i^* - \frac{h^*i}{h} + \frac{h^*i^*}{h}\right) + \sigma\left(z - z^* - \frac{h^*z}{h} + \frac{z^*h^*}{h}\right)\end{aligned} \tag{4.3}$$

$$\Rightarrow \frac{\mathrm{d}L}{\mathrm{d}t} = P - Q \text{ where,}$$

$$P = \alpha + \frac{\beta(s-s^*)^2 i^*}{s} + \frac{\beta s(i-i^*)^2}{i} + \lambda i + \frac{\lambda z^* i^*}{z} + \gamma i + \frac{\gamma h^* i^*}{h} + \sigma z + \frac{\sigma z^* h^*}{h}$$

$$Q = \frac{\alpha s^*}{s} + \frac{(s-s^*)^2}{s}(\beta i+\mu) + \frac{(i-i^*)^2}{i}(\beta s^* + (\gamma+\lambda+\mu)) + (\sigma+\mu+\rho)\frac{(z-z^*)^2}{z}$$
$$(\delta+\mu+\phi)\frac{(h-h^*)^2}{h} + \lambda i^* + \frac{\lambda i z^*}{z} + \gamma i^* + \frac{\gamma h^* i}{h} + \sigma z^* + \frac{\sigma h^* z}{h}$$

$$\frac{\mathrm{d}L}{\mathrm{d}t} = 0 \Leftrightarrow s = s^*, i = i^*, z = z^*, h = h^*$$

If $P < Q$ then we get $\frac{\mathrm{d}L}{\mathrm{d}t} \leq 0$, and $\frac{\mathrm{d}L}{\mathrm{d}t} = 0$ iff $s = s^*, i = i^*, z = z^*, h = h^*$, therefore the largest compact invariant set $\Gamma = \left\{(s,i,z,h) \in \Re_+^4 : \frac{\mathrm{d}L}{\mathrm{d}t} = 0\right\}$ is the singleton set $\{P^*\}$. Hence by Lasalle's invariance principle [15] P^* globally asymptotically stable in Γ.

5 Simulation and Result

Figure 3 explain the dynamical behavior of susceptible (S), infective (I), treated (T), highly infected (H) and recovered (R) with respect to time (t). It has been observed that the number of susceptible and infected nodes takes non-negative values and

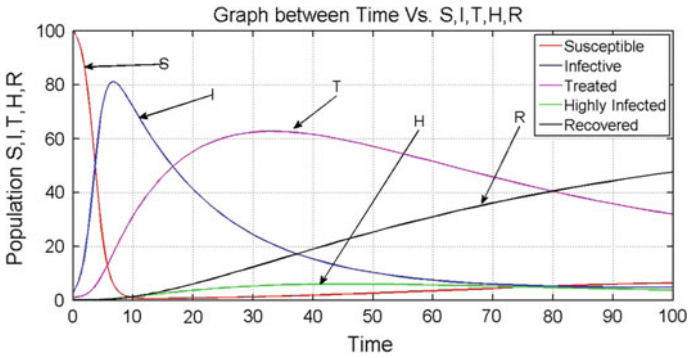


Fig. 3 Shows dynamical demeanor of the system for different classes under the condition ($\alpha = 0.35$; $\beta = 0.01$; $\mu = 0.001$; $\gamma = 0.001$; $\lambda = 0.06$; $\sigma = 0.009$; $\rho = 0.01$; $\delta = 0.08$; $\varphi = 0.01$)

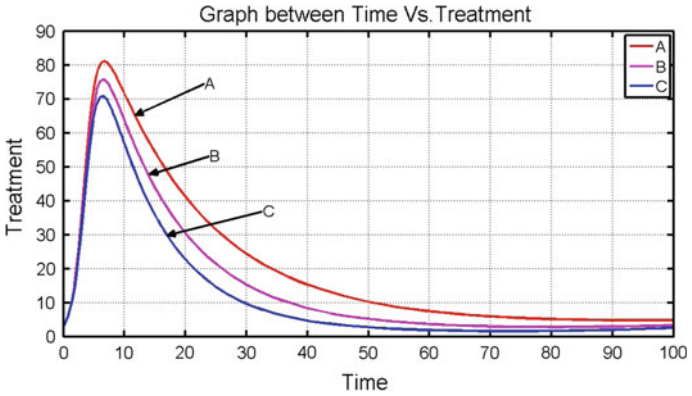


Fig. 4 Shows dynamical demeanor of the system for Treatment classes under the condition A $\alpha = 0.35$; $\beta = 0.01$; $\mu = 0.001$; $\gamma = 0.001$; $\lambda = 0.06$; $\sigma = 0.009$; $\rho = 0.01$; $\delta = 0.08$; $\varphi = 0.01$; B $\alpha = 0.35$; $\beta = 0.01$; $\mu = 0.001$; $\gamma = 0.001$; $\lambda = 0.09$; $\sigma = 0.009$; $\rho = 0.01$; $\delta = 0.08$; $\varphi = 0.01$; C $\alpha = 0.35$; $\beta = 0.01$; $\mu = 0.001$; $\gamma = 0.001$; $\lambda = 0.1$; $\sigma = 0.009$; $\rho = 0.01$; $\delta = 0.08$; $\varphi = 0.01$

approaches to steady state. In this situation the worms persist in the WSN. In this case $R_0 > 1$ this shows asymptotic behavior of endemic equilibrium.

It has been observed from Fig. 4, when treatment rate is high, initially infective nodes are removed quickly and after some time a treatment approach is applied in a steady state.

Figure 5 demonstrates the analysis of susceptible class versus infective class by the variation of different parameters. Initially all nodes are susceptible and becomes infective after some time.

It has been observed from Fig. 6, when treatment rate is high, infective nodes get removed from the network quickly and elongate the lifetime of a network.

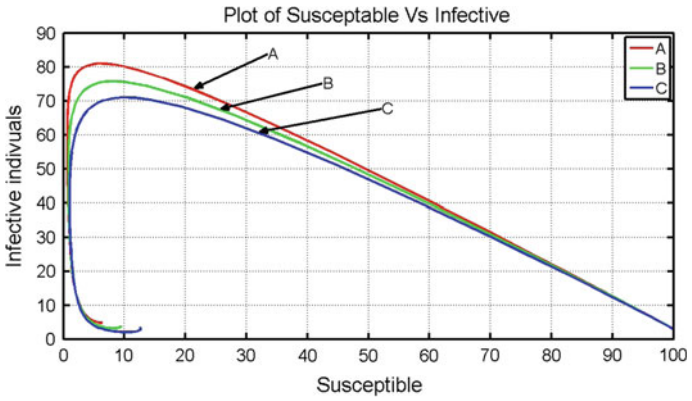


Fig. 5 Shows dynamical demeanor of the system for susceptible versus infective under the condition *A* $\alpha = 0.35$; $\beta = 0.01$; $\mu = 0.001$; $\gamma = 0.001$; $\lambda = 0.06$; $\sigma = 0.009$; $\rho = 0.01$; $\delta = 0.08$; $\varphi = 0.01$; *B* $\alpha = .38$; $\beta = 0.01$; $\mu = 0.001$; $\gamma = 0.001$; $\lambda = 0.08$; $\sigma = 0.01$; $\rho = 0.01$; $\delta = 0.08$; $\varphi = 0.01$; *C* $\alpha = .4$; $\beta = 0.01$; $\mu = 0.001$; $\gamma = 0.001$; $\lambda = 0.1$; $\sigma = 0.014$; $\rho = 0.01$; $\delta = 0.08$; $\varphi = 0.01$

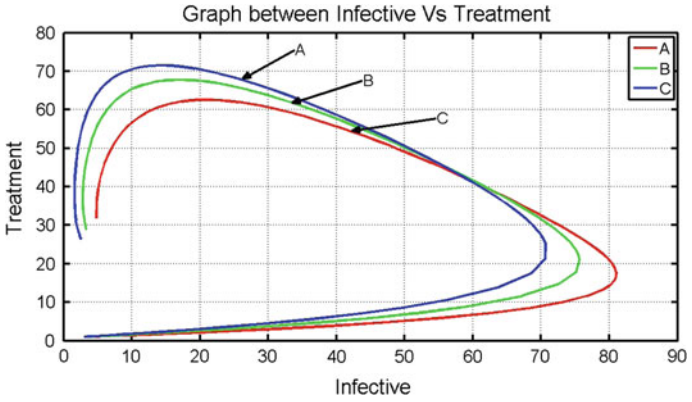


Fig. 6 Shows dynamical demeanor of the system for infective versus treatment under the condition *A* $\alpha = 0.35$; $\beta = 0.01$; $\mu = 0.001$; $\gamma = 0.001$; $\lambda = 0.06$; $\sigma = 0.009$; $\rho = .01$; $\delta = 0.08$; $\varphi = 0.01$; *B* $\alpha = 0.35$; $\beta = 0.01$; $\mu = 0.001$; $\gamma = 0.001$; $\lambda = 0.09$; $\sigma = 0.009$; $\rho = 0.01$; $\delta = 0.08$; $\varphi = 0.01$; *C* $\alpha = 0.35$; $\beta = 0.01$; $\mu = 0.001$; $\gamma = 0.001$; $\lambda = 0.1$; $\sigma = 0.009$; $\rho = 0.01$; $\delta = 0.08$; $\varphi = 0.01$

6 Conclusion

We developed mathematical model to describe the spreading and controlling activities of malicious signals in WSN consisting of ordinary differential equations to study the effect of treatment dynamics of worm transmission. We derive the expression for basic reproduction R_0 for determining the dynamic behavior of worm transmission. The local and global stability of worm free equilibrium and endemic

equilibrium are established by using the Jacobian matrix and Lyapunov function. It is establish that if R_0, is less than or equal to one, then worms can be eradicated and the system becomes globally stable and when $R_0 > 1$ the endemic equilibrium will be globally asymptotically stable. It is also observed that as the treatment rate increases the spreading of malicious signal decreases. It saves energy of the sensor nodes by operating in sleep and active modes and enhances the life of WSN.

References

1. I. F. Akyildiz et al., Wireless sensor networks: a survey, Computer Networks. 38 (4) 393–422, 2002.
2. R. B. Lenin, S. Ramaswamy, Performance Analysis of Wireless Sensor network Using Queuing Network, Department of Mathematics, Technical Report, University of Central Arkansas Conway; 2013.
3. H. Shi, W. Wang, N. Kwok, "Energy dependent divisible load theory for wireless sensor network workload allocation," Mathematical Problems in Engineering, vol. 2012, Article ID 235289, 16 pages, 2012.
4. B. K. Mishra, N. Keshri, "Mathematical model on the transmission of worms in wireless sensor network," Applied Mathematical Modelling, vol. 37, no. 6, pp. 4103–4111, 2013.
5. S. Stantiford, V. Paxton, Weaver, in: Proc. Of the 11th USENIX Security Symposium (Security'02), 2000.
6. J. R. C. Piqueira, B. F. Navarro and L. H. A. Monteiro, Epidemiological model applied to virus in computer networks, J. Comput. Sci. 1 (1) (2005) 31–34.
7. Neha Keshri and Bimal Kumar Mishra, Two time delay dynamic model on the transmission of malicious signals in wireless sensor Network, Chaos Solitons & Fractals 11/2014; 68. doi:10.1016/j.chaos.2014.08.006.
8. Zizhen Zhang, Fengshan Si, Dynamics of a delayed SEIRS-V model on the transmission of worms in a wireless sensor network, Advances in Difference Equations 2014, 2014:295. doi:10.1186/1687-1847-2014-295.
9. S. J. Wang, Q. M. Liu, X. F. Yu, and Y. Ma, "Bifurcation analysis of a model for network worm propagation with time delay," Mathematical and Computer Modelling, vol. 52, no. 3–4, pp. 435–447, 2010.
10. Q. Zhu, X. Yang, L.X. Yang, and C. Zhang, "Optimal control of computer virus under a delayed model," Applied Mathematics and Computation, vol. 218, no. 23, pp. 11613–11619, 2012.
11. L. Feng, X. Liao, H. Li, and Q. Han, "Hopf bifurcation analysis of a delayed viral infection model in computer networks," Mathematical and Computer Modelling, vol. no. 7–8, pp. 167–179, 2012.
12. L. Feng, X. Liao, Q. Han, and H. Li, "Dynamical analysis and control strategies on malware propagation model," Applied Mathematical Modelling, vol. 37, no. 16–17, pp. 8225–8236, 2013.
13. L. H. Zhu, H. Y. Zhao, and X. M. Wang, "Bifurcation analysis of a delay reaction-diffusion malware propagation model with feedback control," Communications in Nonlinear Science and Numerical Simulation, vol. 22, no. 1–3, pp. 747–768, 2015.
14. Diekmann, O; Heesterbeek, J. A. P.; Metz, J. A. J. (1990)."On the definition and the computation of the basic reproduction ratio R_0 in models for infectious diseases in heterogeneous populations". Journal of Mathematical Biology 28 (4):365–382. doi:10.1007/BF00178324.
15. J. P. LaSalle, "The stability of dynamical system" (SIAM, Philadelphia), 1976.

WPAN-Based Energy Efficient Automation System for Buildings

Manish Kumar Mishra, Rajesh Singh, Anita and Rohit Samkaria

Abstract Nowadays the building energy management systems (BEMS) or implementing control automation in buildings is very significant and well known, because they can play an important role in regular energy management and therefore these type of system can achieve the possible both cost and energy savings. The key driver of the building automation market is focused upon better facilitation to the user in terms of comfort at reduced operation cost. Energy efficiency improvement will also contribute to environmental protection. Therefore, there have been regulations and rating systems made that mandates the requirement of energy monitoring and control in a building. For example, the above mentioned building utilities and equipment's control and automation plays an integral role in achieving the green building rating points from certifying authorities such as GRIHA and IGBC. The proposed system includes the control of various active systems such as lighting including artificial lighting (On/Off and dimming control) and day lighting (motorized blinds or shutters), air conditioners and safety features like fire alarm and gas alarm. In future the existing idea can be implemented for the whole building, i.e., various rooms or areas, and then all of them can be integrated on a common platform for monitoring and control of different energy consuming equipment. Also, it can be further extended to the integration of different building systems in a particular area on a single platform.

Keywords Building automation · WSN technology · Arduino · Energy efficiency improvement

M.K. Mishra (✉) · Rajesh Singh · Anita · Rohit Samkaria
University of Petroleum Energy Studies (UPES), Dehradun, India
e-mail: manishmishra14@stu.upes.ac.in

© Springer Science+Business Media Singapore 2017

R. Singh and S. Choudhury (eds.), *Proceeding of International Conference on Intelligent Communication, Control and Devices*, Advances in Intelligent Systems and Computing 479, DOI 10.1007/978-981-10-1708-7_81

1 Introduction

Mostly the building HVAC systems run on set schedules and do not make use of any fine grained control based on in depth occupancy information. Therefore, the design and implementation of a presence sensor platform is needed for accurate occupancy detection at the level of individual offices [1]. The need for the necessary thermal comfort, visual comfort, and indoor air quality are increased, especially in the prevailing situation of price fluctuations and the technology's evolution. Towards this course, the role of the BEMS is well known and important, since these systems can add to the continuous energy management and therefore to the accomplishment of the possible energy and cost savings [2]. The high energy necessary for appliances make our buildings one of the most critical areas for the impact of energy usage on natural environment. Therefore, a wireless sensor network is proposed to monitor and control physical parameters as well as monitoring the presence of users in the rooms [3]. Building automation systems (BAS) present automatic control of the conditions of interior environments. Its prime goal is to recognize significant savings in energy and diminish cost. Yet the reach of BAS has extended to incorporate information from all kinds of building systems, working toward the objective of "intelligent buildings" [4]. To attain a major reduction in energy utilization apart from the typical energy efficiency methods, innovative technologies must be employed. Therefore, logicality of customary and new energy efficiency options becomes necessities. To move towards the thought of sustainable buildings, a small amount of advanced steps are required, regarding energy, water, land, and material management, collectively with environmental loading, and the characteristics of the indoor and outdoor environments [5]. Enabling the behavioral models in superior lighting simulation programs, such as DAYSIM and the Light switch Wizard permits for an additional practical estimation of lighting use under dynamic conditions. A sub-hourly occupancy-based control model (SHOCC), which allows advanced behavioral models inside entire building energy simulation is presented [6]. Present monitoring control modules compute load current and power monitor modules examine power consumed by selected loads, both modules transmitting bus messages signifying load status and status changes. The utility company can access chosen utilization data and control at least a few loads via message exchange to and from microcomputers [7]. User activity and behavior including occupant presence is considered as a main element and has long been used for control of a variety of devices such as artificial lighting and HVAC. The most capable and suitable activity detection technologies and approaches allow in developing principles and perspectives for energy intelligent buildings based on user activity [8]. Wireless sensors and their networks have approached ahead in the field of recently developed technologies. The application of these sensors and the prospects of managing them into networks have discovered many research matters and have emphasized new ways to deal with definite problems [9]. BAS are employed to control and develop indoor building climate at cheaper costs. By incorporating BAS with wireless sensor networks, the requirement for cabling can be detached, and installation and operational expenses significantly diminished [10].

2 Proposed System

The methodology implied over the system is explained in the block diagram as shown in Fig. 1 in which the main central unit is the Arduino Uno platform. The various sensors are connected with the Arduino Unit. Gas and fire sensors are connected for the safety requirements. light dependent resistor (LDR) sensor for sensing the lux level in the concerned area or room, passive infrared (PIR) sensor for sensing the occupancy in the room, a magnetic reed switch door sensor is also used for better and accurate detection of occupancy and LM65 sensor for temperature sensing would be given as the input to Arduino Uno, a microcontroller board having digital input/output pins with analog inputs as well. A seven segment display is connected to the microcontroller for monitoring of the different energy parameters in the area or room. In system programming (ISP) connector is linked for the programming purpose with the controller.

In transmitter, basically six building block of the system are data acquisition unite (sensors), controller unit, display unit, RF modem, power supply unit, and serial communication module. To operate various sensors and controller the power supply is fed through power supply unit which having the regulator IC. The data from various sensor is fed to controller unit and the corresponds data of the sensors unit display over the display unit and at the same time this data is serially provided to RF Modem which wirelessly transmit this data to the surrounding.

In the receiver module basic building blocks of the system are same as used in the transmitter unit. RF Modem receives the data transmitted by the transmitter unit

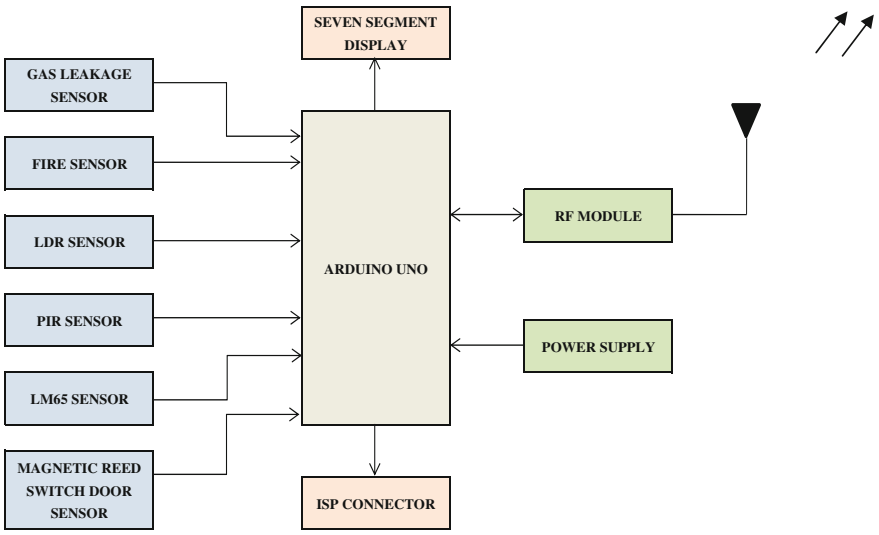


Fig. 1 Block diagram of transmitter unit

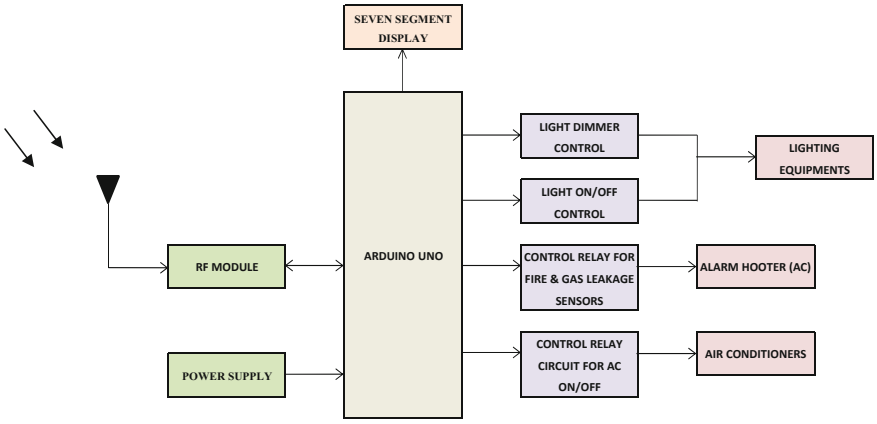


Fig. 2 Block diagram of receiver unit

and this data is processed by the controller unit and according to the sensor data parameters further various controls are activated (Fig. 2).

After the connection of a RF module, on the output side, through the controller different outputs are given, such as the lighting dimmer controlling and ON/OFF circuit, control relay for fire and gas leakage and control relay circuit for switching of AC. The above explained methodology is proposed to be implemented for two different areas or rooms in a building for better analysis in terms of energy efficiency and energy cost savings.

3 Prototype Development

Arduino Uno platform is used as the controller unit of the system through which data is detected through the sensors unit and transmitted to surrounding and another controller unit receives the data and according to the data various control operation are performed at the output.

Figure 3 shows the circuit diagram of the transmitter unit in which the analog sensors are connected to A0–A5 pin of the controller unit. The controller unit having 10 bit ADC which converts the analog input into 1024 level as $2^{10} = 1024$. The fire sensor, PIR sensor and magnetic red sensors are connected to the pin no. 8, 9, 10 of the controller unit.

Power Supply unit consist of four diode 1N4007 followed by the filter capacitor. For the regulated output IC7805 is used which provide 5 V output and the output is provided to various sensors, RF modem and Display Unit. LCD is connected at pin no. 2, 3, 4, 5, 11, 12 of the controller unit. The RF modem is connected at Tx pin of the controller and is fed to the Rx pin of the RF Modem. RF modem receives this data and transmits further.

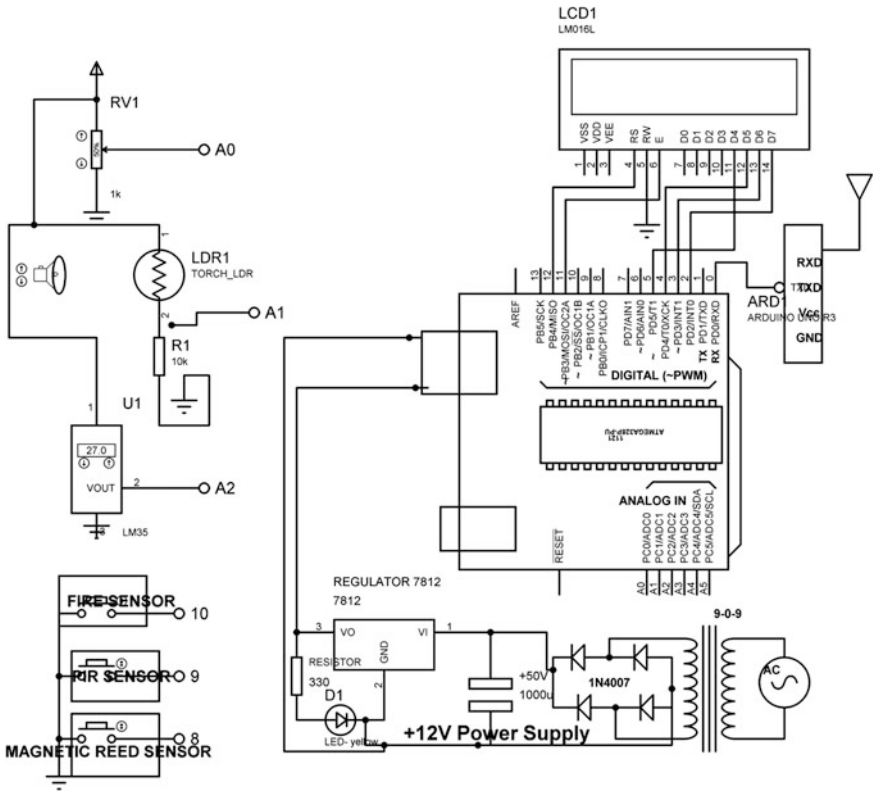


Fig. 3 Circuit diagram at transmitting end

In the receiver circuit diagram as shown in figure RF modem receives the wireless data and put this data to the Rx pin of the controller unit. LCD is connected to the pin no, 2, 3, 4, 5, 11, 12 pin of the microcontroller. To operate the various AC devices the relay based breakout board has used in which the output from the controller is fed to the relay 2N2222 transistor which act as switching circuit to operate the relay. The various AC appliances are connected to this relay board (Fig. 4).

4 Software Development

The software platform being used for the development of the proposed model is Proteus, and following circuits were developed for transmitting as well as receiving side of the model in which various virtual components taken from the Proteus library and placed in the workspace. Arduino platform utilized for the software development of the system. Figure 5 show the step by step flow chart of the system

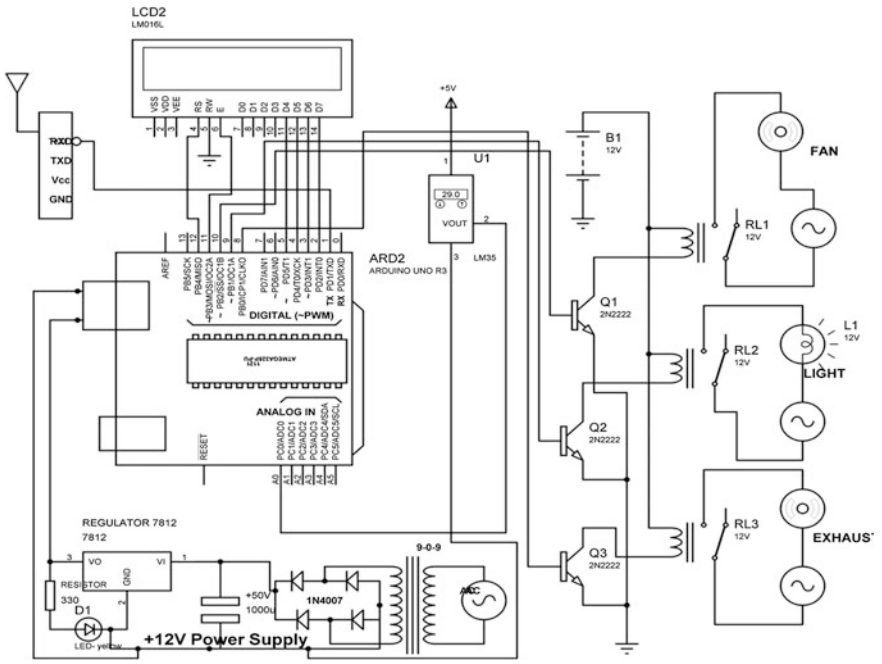
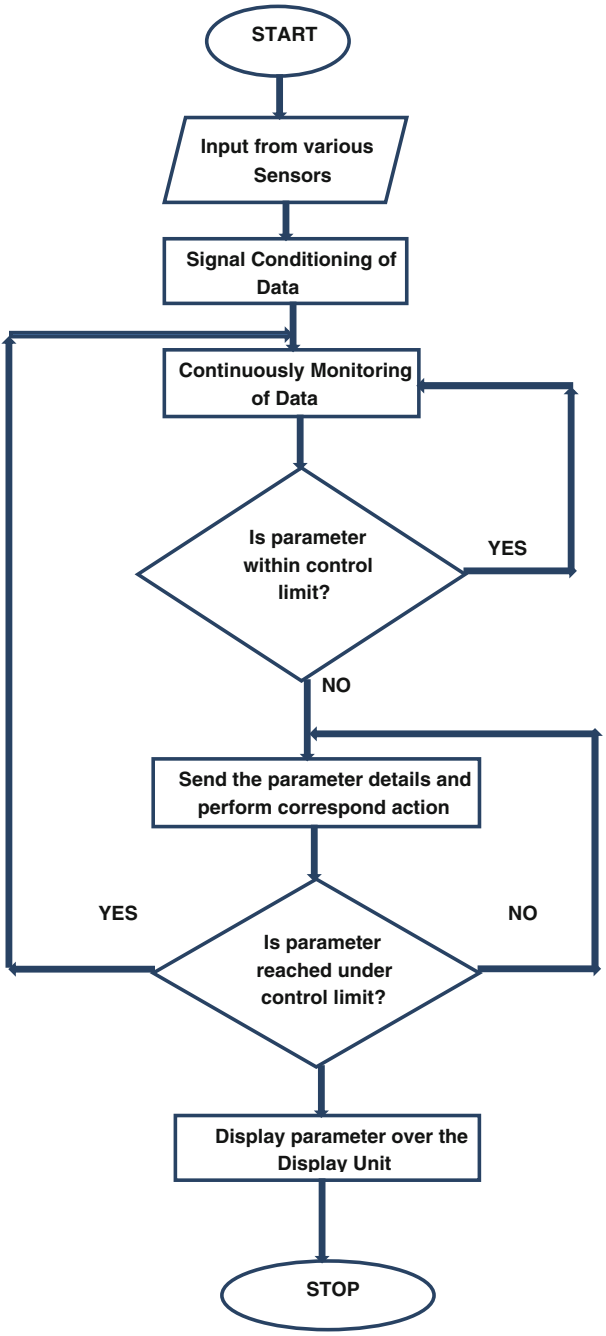


Fig. 4 Circuit diagram receiver unit

where various parameters are continuously monitored and the corresponding data is compared with the predefined limit. If the data rises above the defined limit then the corresponding action occurs and parameters bring back to normal condition.

In the Proteus simulation the virtual components from the Proteus library are taken and placed in the workspace and these various components and the program is dumped into the arduino.

As shown in Fig. 5 the various sensors which are placed in the different location within in the building provides the data corresponds to their operation. Some of the sensors provide digital data and we provide the analog data. The analog data cannot process directly by the arduino for that the signal conditioning to be done. The signal conditioning is done by the internal ADC of the Arduino which is 10 bit. Now the data from the analog sensor is converted to the 1024 levels and the sensors provide this level corresponds to the data of the sensor. Now these levels need to be calibrated according to the sensor data. After calibration this data fed to the arduino unit and sent to the remote location through the wireless medium. In receiver section the data is continuously compared with the defined levels inside the program. Now if any parameter rises above the defined level then the Arduino unit sends a signal and corresponding action is to be taken to normalize the raised condition.


START
Input from various Sensors
Signal Conditioning of Data
Continuously Monitoring of Data
Is parameter within control limit?
YES
NO
Send the parameter details and perform correspond action
YES
Is parameter reached under control limit?
NO
Display parameter over the Display Unit
STOP

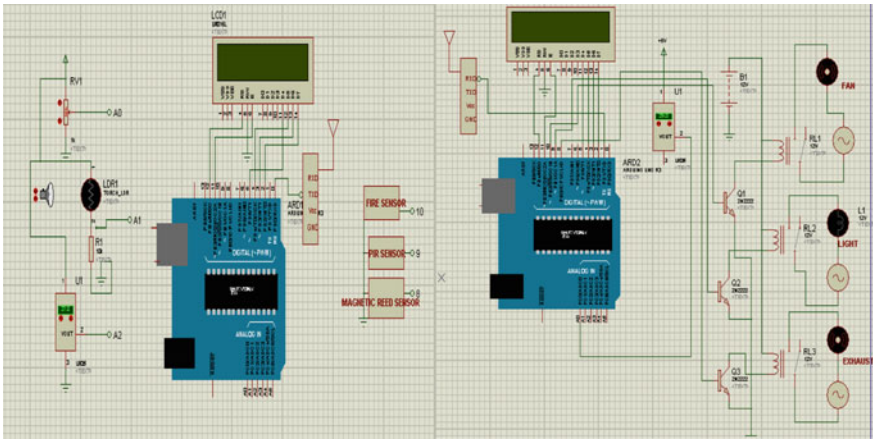


Fig. 5 Proteus simulation of the transmitter and receiver module

5 Result and Conclusion

So, the paper can be concluded with the fact that the combination of controller and information technology into the building energy management system are capable of supervising and controlling many of the actions and services related to buildings. Also, huge reduction over the cost can be taken which occur during installation and maintenance in BAS through wireless sensor networks. The potential use of wireless sensor networks expands over an enormous part of personal activities. Although, most of the functions and applications are still under study and only a small amount of accomplished services and products have developed into as available applications for public use, there is outstanding attempt and advancement. Wireless sensor networks are nowadays measured as mainly the one of the best technology for constructing inexpensive sensor networks similar to intelligent building. Energy intelligent buildings are capable of reacting to their genuine utilization and modifications in their environment. Energy intelligent buildings supported from client work and activity should be capable of identifying occupant actions and building background, and to get used to buildings for reducing energy.

References

1. Agarwal, Yuvraj, et al. "Occupancy-driven energy management for smart building automation." *Proceedings of the 2nd ACM Workshop on Embedded Sensing Systems for Energy-Efficiency in Building*. ACM, 2010.
2. Doukas, H., Patlitzianas, K. D., Iatropoulos, K., & Psarras, J. (2007). Intelligent building energy management system using rule sets. *Building and Environment*, *42*(10), 3562–3569.

3. Barbato, Antimo, et al. “Home energy saving through a user profiling system based on wireless sensors.” *Proceedings of the first ACM workshop on embedded sensing systems for energy-efficiency in buildings*. ACM, 2009.
4. Kastner, W., Neugschwandtner, G., Soucek, S., & Newman, H. M. (2005). Communication systems for building automation and control. *Proceedings of the IEEE*, *93*(6), 1178–1203.
5. Chwieduk, Dorota. “Towards sustainable-energy buildings.” *Applied energy* 76.1 (2003): 211–217.
6. Bourgeois, Denis, Christoph Reinhart, and Iain Macdonald. “Adding advanced behavioural models in whole building energy simulation: a study on the total energy impact of manual and automated lighting control.” *Energy and Buildings* 38.7 (2006): 814–823.
7. Ehlers, Gregory A., Robert D. Howerton, and Gary E. Speegle. “Energy management and building automation system.” U.S. Patent No. 5,572,438. 5 Nov. 1996.
8. Nguyen, Tuan Anh, and Marco Aiello. “Energy intelligent buildings based on user activity: A survey.” *Energy and buildings* 56 (2013): 244–257.
9. Arampatzis, Th, John Lygeros, and S. Manesis. “A survey of applications of wireless sensors and wireless sensor networks.” *Intelligent Control, 2005. Proceedings of the 2005 IEEE International Symposium on, Mediterrean Conference on Control and Automation*. IEEE, 2005.
10. Österlind, Fredrik, et al. “Integrating building automation systems and wireless sensor networks.” *Emerging Technologies and Factory Automation, 2007. ETFA. IEEE Conference on*. IEEE, 2007.

An Intelligent GA-Optimized Fuzzy Controller for Automatic Generation Control for a Two-Area Interconnected System

Vishal Jain, Devendra Saini, K.N. Dinesh Babu and J.S. Saini

Abstract The paper presents an optimized FLC using GA for AGC of a two-area non-reheat thermal system. The design of the FLC is carried out by automatically tuning the parameters of membership functions of the FLC using GA by minimizing the integral time absolute error (ITAE) based fitness function. The effectiveness of GAFLC is shown over GA-tuned PI controller (GAPI) for the same model.

Keywords Genetic algorithm (GA) · Fuzzy logic controller (FLC) · Automatic generation control (AGC) · Membership functions (mfs)

1 Introduction

Automatic generation control (AGC) plays a vital role and operates constantly to balance the generation and load in power systems at a lowest price. In so doing, it provides an efficient means for setting the generation to minimize frequency deviations and to control the power flows on tie-line. From a pragmatic stand point, the problem of frequency control of interconnected areas is imperative than those of isolated areas, and the problem of load-frequency control becomes a joint responsibility. Closely linked is the problem of controlling the power flows on the

Vishal Jain (✉) · Devendra Saini
UPES, Dehradun, India
e-mail: vishal_dehradun@yahoo.com

Devendra Saini
e-mail: dksaini@upes.ddn.ac.in

K.N. Dinesh Babu
General Electrics, Hyderabad, India
e-mail: dineshbabukn@gmail.com

J.S. Saini
DCRUST, Murthal, Haryana, India
e-mail: jssain@redidffmail.com

© Springer Science+Business Media Singapore 2017

R. Singh and S. Choudhury (eds.), *Proceeding of International Conference on Intelligent Communication, Control and Devices*, Advances in Intelligent Systems and Computing 479, DOI 10.1007/978-981-10-1708-7_82

inter-ties. AGC study in power systems has an extensive past and its background literature [1, 2] as well as the current literature [3–9] is ample. The conventional AGC designs are limited for specific operating points, and are not competent for modern power systems. The conventional AGC schemes [10, 11] have sufficiently developed over the years, however, concern continues in proposing new intelligent AGC [6–9] schemes with an improved capacity to keep tie-line power flow and system frequency close to the nominal values. Recent research works [12–15] show that more importance has been put on the collective usage of intelligent technologies for further progress of the operation, control, and management of power systems. FLC's have been successfully used to decipher large control problems in power system control and operations. Numerous studies have been listed for the fuzzy logic-based AGC design scheme [16, 17]. It is shown in [16] that the presence of FLC provides a better dynamic response than that with the conventional PI controllers. There are various levers of FLC that can be fine-tuned to yield good controller performance [12]. Thus, Evolutionary computing technique such as genetic algorithm (GA), being an efficient optimizer, is used to search large solution spaces for solutions that are close to the optimal. In this paper, an automatic procedure of GA tuning the membership functions of FLC for a two-area AGC is used. The effectiveness of GA-tuned FLC (GAFLC) is shown over a GA-tuned PI controller (GAPI) implemented on the same model with identical testing environment.

2 Modeling of System

The model of a two-area non-reheat thermal system [13] with a step perturbation on the load demand in Area 1 is taken. The block diagram is developed in MATLAB Simulink. A separate GA program (.mfile) is used to interface the Simulink model and the fuzzy inference System. The optimized parameter of membership functions based on the objective function in each iteration of the program and for each chromosome of the GA is returned to the FLC in the Simulink model.

3 The Proposed Approach

3.1 PI Controller

A PI-based controller is applied to the AGC model with the optimal integral gains K_{i1}, K_{i2} (in Area 1 and Area 2, respectively) evolved with same fitness function using GA taking a hint from our previous paper [18]. The GA searched the optimal values K_{i1}, K_{i2} as −0.91 and −0.91 respectively for a range (−1 to 1).

3.2 Design of Fuzzy Logic Controller

The fuzzy controller has ACE and d/dt(ACE) as the two inputs. Five membership functions are chosen as (Negative Large, Negative Small, Zero, Positive Small, and Positive Large) for each of the two inputs (ACE and d/dt(ACE)) and one output are defined. The rule set of [14] is used for FLC. A typical rule is interpreted as follows: if ACE is NL and d/dt(ACE) is NL then ACE-out is NL, etc. Initially, the gains of FLC were chosen so as to allow the different variables (such as ACE, d/dt(ACE) and Output) hover within their respective universes of discourse (UODs). An automatic tuning of the input and output membership functions of the FLC is carried out by the GA vis-a-vis a fitness defined in Eq. (1). The optimisation is based on the minimization of ITAE. After the choice of the AGC model [15] in Simulink, FLC is constructed using MATLAB fuzzy logic tool box (all mfs are taken as symmetrical). The lower and upper bounds for the mfs of FLC are specified for the GA to search for optimal parameters within a reasonable time but precluding the possibility of constructing obtuse angles. The GA program is run till the termination criterion is fulfilled.

3.3 Choice of Fitness Function

The fitness function for tuning the FLC parameters is usually chosen based on a performance index that considers the complete closed-loop response. Performance criterion generally used in the control system problems are the integral of squared error (ISE), integral of time multiplied absolute error (IATE), integral of time multiplied squared error (ITSE), and integral of absolute error (IAE). It has been demonstrated in earlier paper [15] that IATE proves to be a better fitness function and, therefore, is used in this paper.

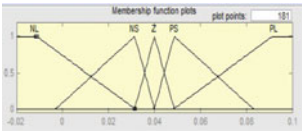
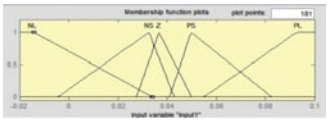
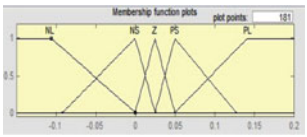
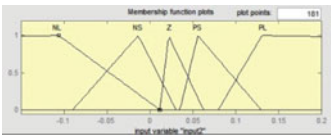
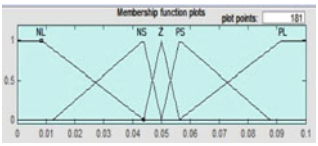
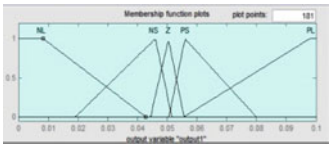
$$J = \text{ITAE} = \int_0^{t_{\text{sim}}} (|\Delta F_1| + |\Delta F_2| + |\Delta P_{\text{tie}}|) \cdot t \cdot \mathrm{d}t \tag{1}$$

ΔF_1 Change in Frequency in area 1
ΔF_2 Change in Frequency in area 2
ΔP_{tie} Change in Tie-Line Power
t_{sim} Simulation time.

3.4 Length of Chromosome

In the current work, initial, symmetrical inputs, and output membership functions of the FLC are taken, however, optimized and evolved by the GA to be as per Table 1

Table 1 Symmetrical and GA-tuned mfs of FLC

	Symmetrical (untuned) mfs of FLC in Area 1	Mfs of GA-tuned FLC in Area 1
(a) ACE		
(b) d/dt (ACE)		
(c) Output		

to improve the controller response. The formation of the chromosome is based on the sets of parameters of the mfs of the FLC. The length of the chromosome used has three alleles for each triangular membership function (trimf) and two for each sigmoidal membership function (smf) and Z-shaped membership function (zmf), thus the length of the chromosome is decided as

$l = [(2 \times 2) \times 3 + ((5 - 2) \times 3) \times 3] = 39$ alleles.

Thirty nine parameters are tuned for FLC in each area, for two-area AGC two FLC's are employed, therefore the length of chromosome becomes: $2 \times l = 78$.

3.5 Selection of Parameter Bounds

Taking a clue from the previous papers [12, 19], it is ensured that the parameters of mfs lie within rational limits. The lower and upper limits on each allele value are set through random trial runs of FLC without applying GA. Thus bounds within which membership functions for inputs and output are evolved by the GA are calculated.

3.6 The GA Program Stopping Criterion

The parameters of FLC by the GA are evolved till a stopping criterion is reached. The standard [18] used in this paper is that the difference between the average of fitness value of $(i - 5)$th and ith generations is less = 0.001 (threshold value of fitness).

4 Results and Discussions

The MATLAB/Simulink is used to develop the AGC model. To begin with, similar FLC controllers are considered for each area. The simulation of the AGC model is carried out through a discretely written program (.mfile) using random generated initial population of solution/membership function parameters of FLCs. The fitness value is computed and passed on to the main GA program through workspace. In the subsequent generations, good fitness values are retained using elitism and the process is continual until termination criterion is met with. For the sake of brevity, however, only the untuned FLC response and GAFLC response statistics are presented along with the GAFLC plots of the frequency deviations and tie-line power deviations (Figs. 1, 2 and 3).

The tuned fuzzy controller parameters are 78.

Parameters chosen for the GA program are: Population Size = 30, Length of chromosome = 78, Probability of Cross over = 0.6, Probability of mutation = 0.03.

The AGC model is simulated; the GA produced some good solutions in different generations (0.0861, 0.0451, and 0.0351). Figures 1, 2 and 3 show the response of GAPI and GAFLC for Δf_1, Δf_2 and $\Delta P_{\text{tie-line}}$, respectively. The performance comparison of the system for a GAPI and GAFLC is shown in Table 2.

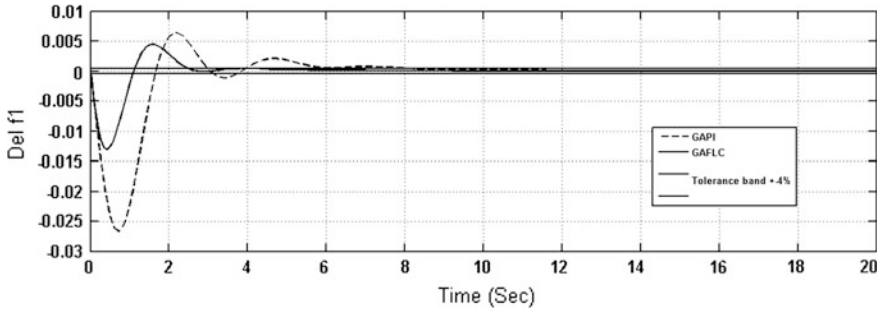


Fig. 1 Plot of change in frequency in Area −1 (Δf_1) with GAPI and GAFLC

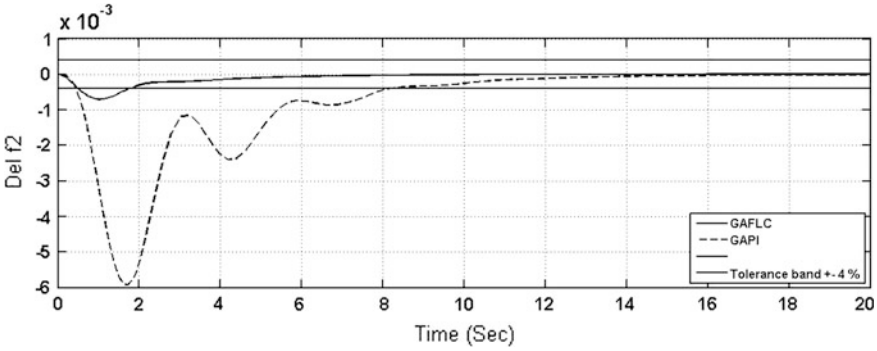


Fig. 2 Plot of change in frequency in Area 2, (Δf_2) with GAPI and GAFLC

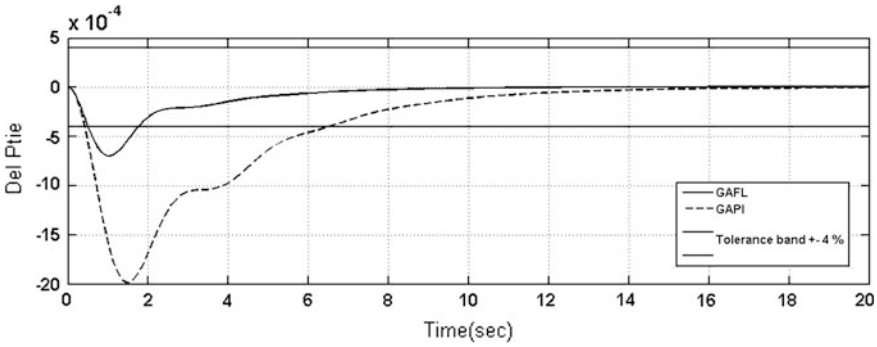


Fig. 3 Plot of change in tie line power ($\Delta P_{\text{tie-line}}$) with GAPI and GAFLC

4.1 Membership Functions

Table 1 shows the hand-tuned FLC with all mfs taken as symmetrical and GA-tuned mfs of FLC attained from the best solution, i.e., best fit chromosome in 32 generations.

Generation 1: *Statistics*

Minimum fitness = 1.7126, Maximum fitness = 0.1425, Mean of Fitness = 0.9501.

Generation 32: *Statistics*

Minimum fitness = 1.7120, Maximum fitness = 0.0733, Best fitness = 0.0351, Mean Fitness = 0.5990.

Table 2 Performance comparision of GAPI and GAFLC response

Controller	Overshoot in Hz ($\times 10^{-3}$)			Undershoot in Hz ($\times 10^{-3}$)			Settling time (ts) with tolerance band = ±4 % in s			IATE
	Δf_1	Δf_2	$\Delta P_{tie\ line}$	Δf_1	Δf_2	$\Delta P_{tie\ line}$	Δf_1	Δf_2	$\Delta P_{tie\ line}$	
GAFLC	4.461	0	0	−13.06	−1.98	−0.7	4.2	2.358	1.81	0.0351
GAPI	6.475	0	0	−26.62	−5.92	−1.98	8.12	8.097	6.624	0.1581

5 Conclusion and Future Direction

It is a challenging task to find a global optimal solution in many applications due to the nonlinear nature of the system and different sources of disturbances. In this regard nature inspired optimization algorithms have gain recognition. In this paper, a standard model of AGC using FLC, automatically tuned by GA has been proposed. GA technique is applied to minimize an IATE-based fitness function. To illustrate the supremacy of the proposed GAFLC, results are compared in Table 2 with that of a GAPI controller implemented on the same model. The comparison is made using performance indices such as undershoot, overshoot and settling time and IATE. Our future research agenda include

- To develop the multi-area AGC scheme on the restructured power system.
- Testing the AGC model with parametric variations.
- Compliance of the NERC standards on the designed controller.

References

1. Hadi Sadat, “Power system analysis”, Tata McGraw-Hill, Edition, 2002.
2. Elgerd OI. Electric energy systems theory an introduction. 2nd ed. New Delhi: Tata McGraw Hill, 2000.
3. Y. Sharma and L. C. Saikia, “Automatic generation control of a multi-area ST – Thermal power system using Grey Wolf Optimizer algorithm based classical controllers,” *Int. J. Electr. Power Energy Syst.*, vol. 73, pp. 853–862, Dec. 2015.
4. S. R. Khuntia and S. Panda, “Simulation study for automatic generation control of a multi-area power system by ANFIS approach,” *Appl. Soft Comput.*, vol. 12, no. 1, pp. 333–341, Jan. 2012.
5. G. Panda, S. Panda, and C. Ardil, “Automatic Generation Control of Interconnected Power System with Generation Rate Constraints by Hybrid Neuro Fuzzy Approach,” *World Acad. Sci. Eng. Technol.*, vol. 52, pp. 543–548, 2009.
6. M. H. Khooban and T. Niknam, “A new intelligent online fuzzy tuning approach for multi-area load frequency control: Self Adaptive Modified Bat Algorithm,” *Int. J. Electr. Power Energy Syst.*, vol. 71, pp. 254–261, Oct. 2015.
7. K. Wadhwa, J. Raja, and S. K. Gupta, “BF based integral controller for AGC of multiarea thermal system under deregulated environment,” in *2012 IEEE Fifth Power India Conference*, 2012, pp. 1–6.

8. Hou Guolian, Qin Lina, Zheng Xinyan, and Zhang Jianhua, "Application of PSO-based fuzzy PI controller in multi-area AGC system after deregulation," in *2012 7th IEEE Conference on Industrial Electronics and Applications (ICIEA)*, 2012, pp. 1417–1422.
9. Y. L. Karnavas, "AGC Tuning of an Interconnected System after Deregulation Using Genetic Algorithms," vol. 2005, pp. 218–223, 2005.
10. D. N. Ewart, L. H. Fink, and A. G. Hoffmann, "UNDERSTANDING AUTOMATIC GENERATION CONTROL," vol. 7, no. 3, 1992.
11. L. C. Saikia, J. Nanda, and S. Mishra, "Performance comparison of several classical controllers in AGC for multi-area interconnected thermal system," *Int. J. Electr. Power Energy Syst.*, vol. 33, no. 3, pp. 394–401, 2011.
12. J. S. Saini and V. Jain, "A Genetic Algorithm Optimised Fuzzy Logic Controller for Automatic Generation Control for Single Area System," *J. Inst. Eng. Ser. B*, 2015.
13. S. Panda, B. Mohanty, and P. K. Hota, "Hybrid BFOA–PSO algorithm for automatic generation control of linear and nonlinear interconnected power systems," *Appl. Soft Comput.*, vol. 13, no. 12, pp. 4718–4730, Dec. 2013.
14. S. Pati, B. K. Sahu, and S. Panda, "Hybrid differential evolution particle swarm optimisation optimised fuzzy proportional–integral derivative controller for automatic generation control of interconnected power system," *IET Gener. Transm. Distrib.*, vol. 8, no. 11, pp. 1789–1800, Nov. 2014.
15. R. K. Sahu, S. Panda, and S. Padhan, "A hybrid firefly algorithm and pattern search technique for automatic generation control of multi area power systems," *Int. J. Electr. Power Energy Syst.*, vol. 64, pp. 9–23, Jan. 2015.
16. G. A. Chown and R. C. Hartman, "Design and experience with a fuzzy logic controller for automaticgeneration control (AGC)," *Proc. 20th Int. Conf. Power Ind. Comput. Appl.*, 1997.
17. S. Africa, R. C. Hartman, and S. Africa, "Design and Experience with a Fuzzy Logic Controller for Automatic Generation Control (AGC)," vol. 13, no. 3, pp. 965–970, 1998.
18. J.S. Saini et al., "Genetic Algorithm Based PID Tuner", Journal of IE (I), Vol 85, pp. 216–221, March 2005.
19. J.S.Saini et al. "Evolving Optimal Fuzzy Logic Controllers by Genetic algorithm", IETE Journal of Research, pp. 179–190, May-June, 2004.

Design and Verification of 16-Bit Vedic Multiplier Using 3:2 Compressors and 4-Bit Novel Adder

K. Venkata Siva Reddy, P. Vishnu Kumar, K. Maheswari and B. Khaleelu Rehman

Abstract This paper describes the implementation of a 16-bit Vedic multiplier enhanced in terms of propagation delay when compared with array multiplier and Vedic multiplier using ripple carry adder. In our design, we have utilized ripple carry adder, 4-bit novel adder, 3:2 Compressor. The propagation delay comparison was extracted from the synthesis report and static timing report as well as circuits have to be designed and simulated using DSCH3.1 and the results are to be compared with different technologies.

Keywords Ripple carry adder · 4-bit novel adder · 3-2 Compressor propagation delay

1 Introduction

Multipliers are an integral part of most processing units hence the performance of processors greatly depends upon the functioning of their multiplication units.

Several new architectures have been proposed for improving the functioning of multiplier units to meet the constraints of reducing the delay, power, layout, and hence small area or even combination of them which makes suitable for various very high speed, low power, and compact VLSI implementations. Though, an efficient multiplier design is yet to come.

K. Venkata Siva Reddy (✉)
Ravindra College of Engineering for Women, Andhra Pradesh, India
e-mail: kvenkatsivareddy@gmail.com

P. Vishnu Kumar · K. Maheswari
G Pullaiah College of Engineering and Technology, Andhra Pradesh, India
e-mail: vishnu4b8@gmail.com

K. Maheswari
e-mail: Kotlamahi435@gmail.com

B. Khaleelu Rehman
University of Petroleum and Energy Studies, Dehradun, India
e-mail: krehman@ddn.upes.ac.in; afridi.1156@gmail.com

© Springer Science+Business Media Singapore 2017

R. Singh and S. Choudhury (eds.), *Proceeding of International Conference on Intelligent Communication, Control and Devices*, Advances in Intelligent Systems and Computing 479, DOI 10.1007/978-981-10-1708-7_83

In order to address the disadvantages associated with multiplier architectures, Vedic mathematic approach was proposed. Multipliers were designed using Urdhwa Tiryagbhyam [1]. In this paper, an even more efficient approach to improve multiplier units compared to the Vedic multipliers is being proposed.

2 Existing Techniques

2.1 Array Multiplier

Array multiplier is an efficient layout of a combinational multiplier [2]. To multiply two unsigned 8-bit integers together, we can produce eight partial products by performing eight 1-bit multiplications one for each bit is multiplicand to produce the product, add all eight partial products. Consider an array multiplier for two binary numbers X and Y, of p bits each as shown in Fig. 1. There will be p^2 partial

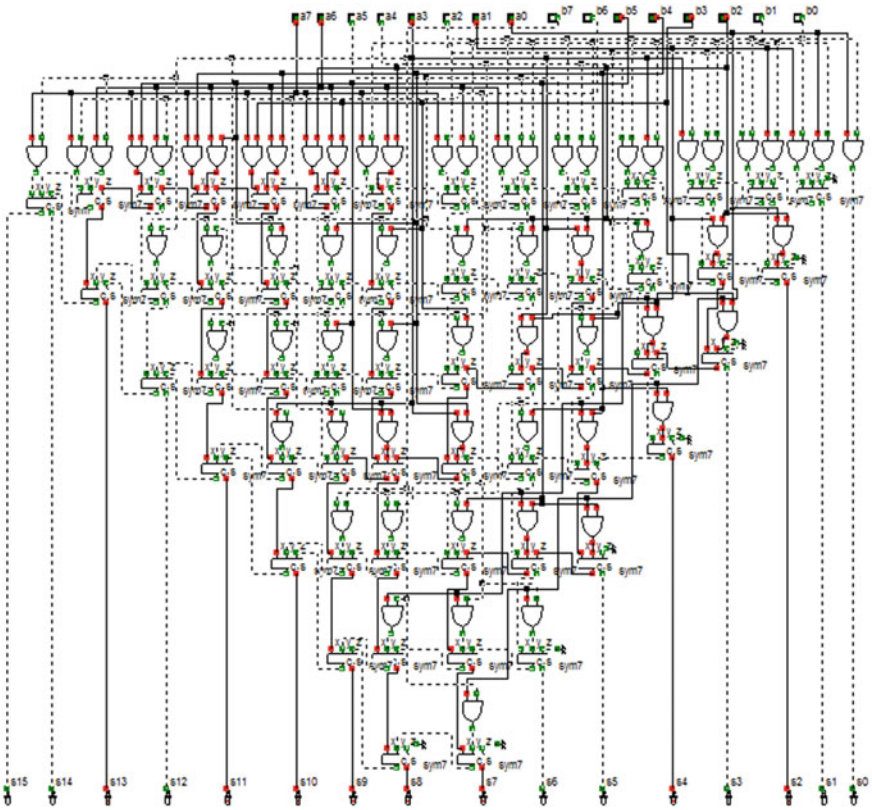


Fig. 1 A 8-bit array multiplier

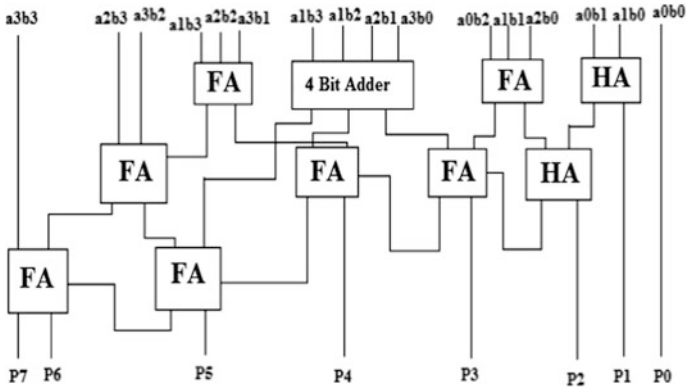


Fig. 2 4-bit novel adder-based multiplier

products that are produced in parallel by a set of p^2 and gates. A $p \times p$ multiplier requires $p\ (p - 1)$ full adders and Sp^2 gates.

The limitations in the array multipliers are high power consumption as well as number of devices utilization. Delay is the time taken by the signals to propagate through the gates and in array multiplier, the worst case delay would be $(2p + 1)\ t_d$ due to the gates that form the multiplication array. Thus array multipliers are less economical with more hardware complexity.

2.2 *Vedic Multipliers: Using Urdhwa Tiryagbhyam Sutra and 4-Bit Novel Adder*

Vedic multiplier designed using Urdhwa Tiryagbhyam sutra and 4-bit novel adder [3] is shown in Fig. 2. The novel 4-bit adder performs the addition of 4 bits at a time and produces three output bits. These three output bits comprise of one sum bit and two carry bits. The 4-bit adder adds the four input bits at a time and the speed of the multiplication increases.

By using this 4×4 multiplier we can design the architecture for 8×8 multiplier also. Though the multiplier reduces the design complexity and power drastically the delay can still be reduced further [4].

3 Proposed Multiplier

In this proposed multiplier design, we are introducing compressors in the existing Vedic multiplier using novel adder. A compressor is a device that reduces the combination of input bits at the output. Shown in Fig. 3, is a 3:2 adder compressor that functions similar to a full adder.

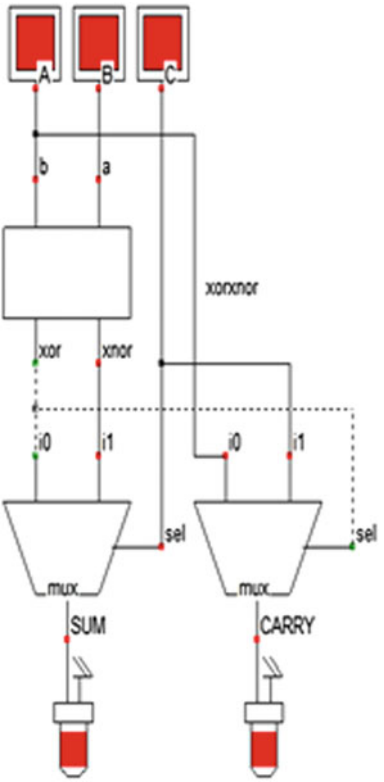


Fig. 3 3:2 compressor

It takes three inputs A, B, and C to generate two outputs, the sum, and the carry bits. Equations for sum and carry bits are governed by 1 and 2

$$\text{Sum} = (\text{A} \oplus \text{B}) * \overline{\text{C}} + \overline{(\text{A} \oplus \text{B})} * \text{C} \tag{1}$$

$$\text{Carry} = (\text{A} \oplus \text{B}) * \text{C} + \overline{(\text{A} \oplus \text{B})} * \text{A} \tag{2}$$

This compressor is built using xor-xnor and multiplexer modules. We are replacing the full adders in the Vedic multiplier design using novel 4-bit adder by 3:2 compressor. Even though a 3:2 compressor works the same as full adder, the difference lies in propagation delay. A full adder needs two half adders which are in turn built using 'xor' and 'and' gates. The delay produced by a full adder is 0.027 ns whereas a 3:2 compressor adder produces a delay of only 0.019 ns (Fig. 4).

Hence we are improving the delay and power consumption very efficiently in the above multiplier architecture though the area constraint can still be improved further using other techniques (Fig. 5).

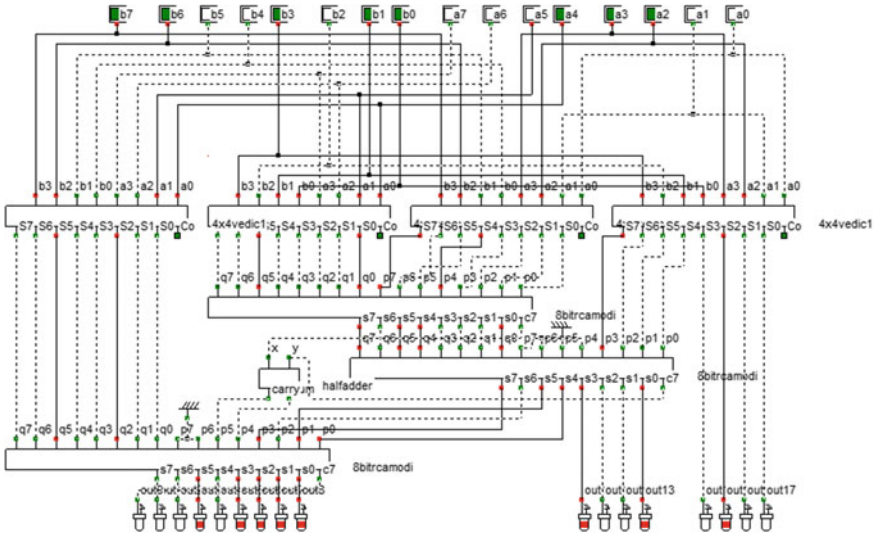


Fig. 4 8-bit Multiplier using 3:2 compressor adder and 4-bit novel adder

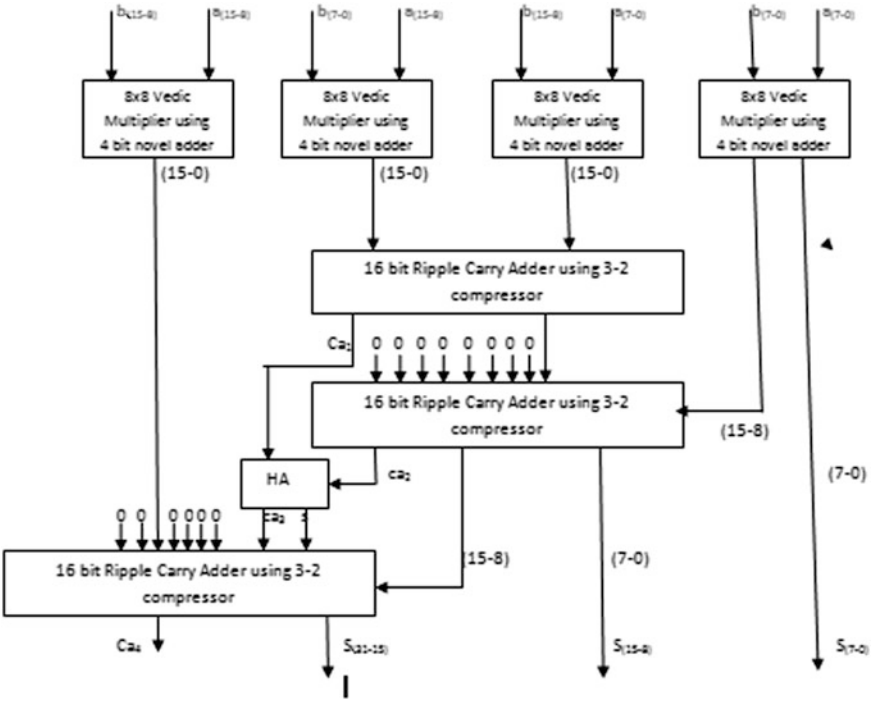


Fig. 5 16-bit Multiplier using 3:2 compressor adder and 4-bit novel adder

4 Results

4.1 Simulation Results

Using the Xilinx 9.2i version the simulation results were found as shown

(i) For 8-bit proposed multiplier (Fig. 6).
(ii) For 16-bit proposed multiplier (Fig. 7).

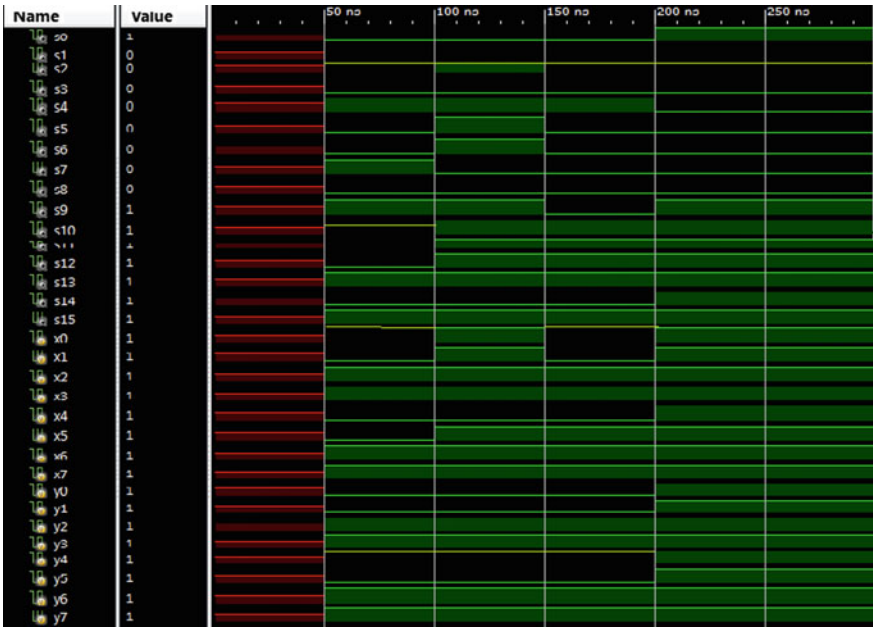


Fig. 6 Simulation output

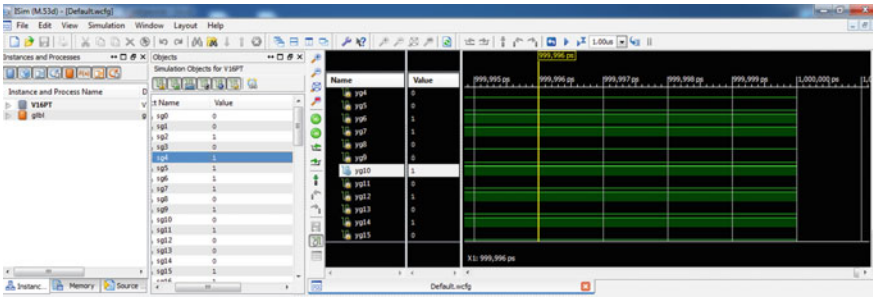


Fig. 7 Simulation output

4.2 Delay Tables and Graphs

(i) For 4-bit proposed multiplier (Fig. 8 and Table 1).
(ii) For 8-bit proposed multiplier (Fig. 9 and Table 2).

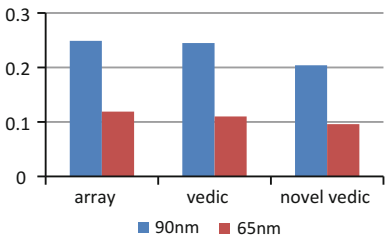


Fig. 8 Delay table, graph for 4 bit

Table 1 Comparison of Delay for various 4-bit multipliers in multiple technologies

	Technology in nm	
Multiplier	65	90
Array multiplier	0.119 ns	0.249 ns
Vedic multiplier	0.110 ns	0.245 ns
Proposed Vedic multiplier	0.096 ns	0.204 ns

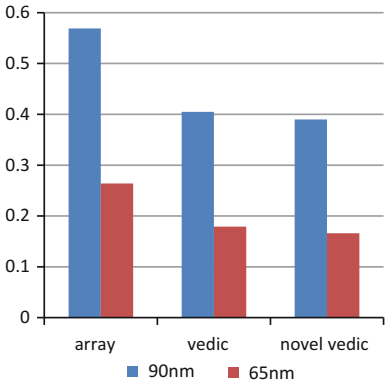


Fig. 9 Delay table, graph for 8 bit

Table 2 Comparison of Delay for various 8-bit multipliers in multiple technologies

	Technology in nm	
Multiplier	65	90
Array multiplier	0.264 ns	0.569 ns
Vedic multiplier	0.179 ns	0.405 ns
Proposed Vedic multiplier	0.166 ns	0.370 ns

4.3 RTL Schematics

(i) For 8-bit proposed multiplier (Fig. 10).
(ii) For 16-bit proposed multiplier (Fig. 11).

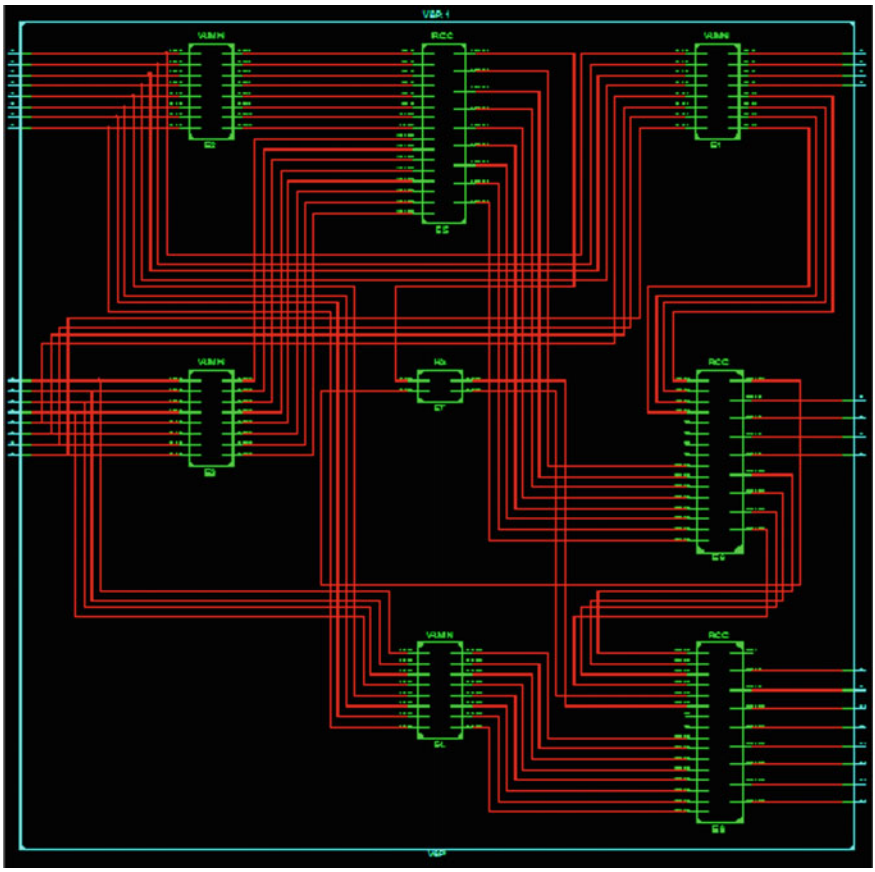


Fig. 10 Schematics for 8 bit

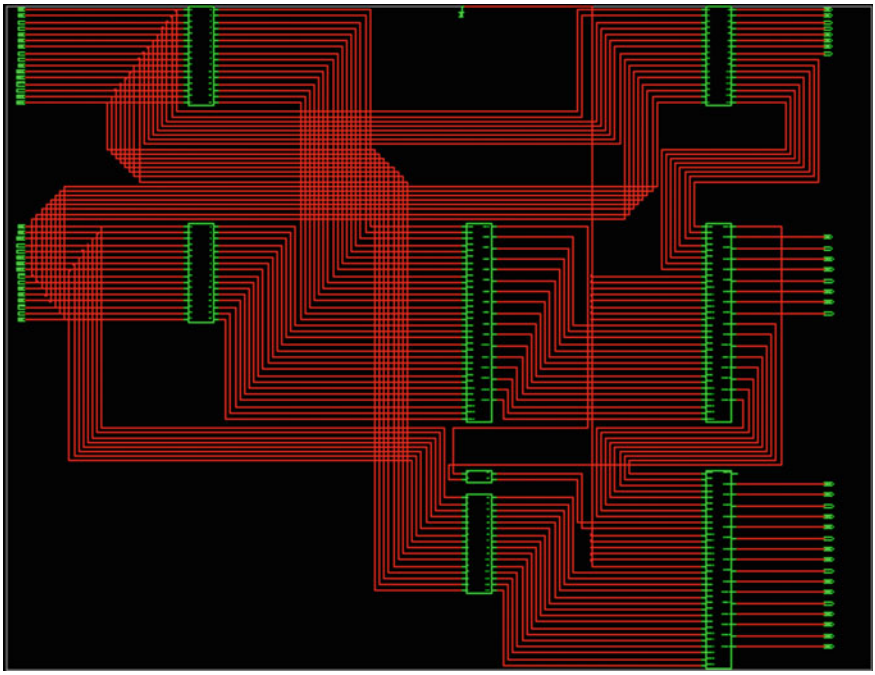


Fig. 11 Schematics for 16 bit

5 Conclusion

The proposed Vedic multiplier using 4-bit novel adder and 3:2 compressors has produced an improved performance compared to its predecessors by reducing the delay. These multipliers can improve the performances of applications in which they are used.

6 Future Scope

The proposed Vedic multiplier using novel 4-bit adder and 3:2 compressors can also be implemented for 32, 64 bits, and for higher bits. The hardware area can be decreased considerably, and it can be further improved.

References

1. MD. Belal Rashid, Balaji B.S. and Prof. M.B. Anandaraju, "VLSI Design and Implementation of Binary Number Multiplier based on Urdhva Tiryagbhyam Sutra with reduced Delay and Area", International Journal of Engineering Research and Technology, ISSN 0974-3154 Volume 6, Number 2 (2013), pp. 269–278.
2. M.Padmaja, A.Saida, "Design and Implementation of High Speed and Low Power Multiplier using Urdhwa Tiryagbhyam Sutra", IJERT, ISSSN: 2278-0181 Vol.3 Issue 3, March-2014.
3. Rajasekhar. N, Shanmuganatham. T, "A Novel 4 Bit Adder Based Urdhwa Tiryakbhyam Multiplier", IJCSMC, Vol. 2, Issue. 10, October 2013, pp. 219–225.
4. Pavan Kumar, Sai Prasad Goud, A.Radhika, " FPGA Implementation of High Speed 8 bit Vedic multiplier using barrel shifter", 978-1-4673-6150-7/13/$31.00 ©2013 IEEE.
5. Sushma R. Huddar and Sudhir Rao Rupanagudi, Kalpana M., Surabhi Mohan, "Novel High Speed Vedic Mathematics Multiplier using Compressors", 978-1-4673-5090-7/13/$31.00 ©2013 IEEE.
6. Hsiao, Shen-Fu, Ming-Roun Jiang, and Jia-Sien Yeh, "Design of high speed low-power 3-2 counter and 4-2 compressor for fast multipliers," IEEE Electronics Letters, vol. 34, no.4, pp. 341–343, Feb. 1998.
7. Prabir Saha, Arindam Banerjee, Partha Bhattacharyya, Anup dandapat, " High speed ASIC design of complex multiplier using vedic mathematics", proceeding of the 2011 IEEE students technology Symposium 14–16 January, 2011, IIT Kharagpur, pp. 237–241.

Brain Tumor Segmentation in Glioma Images Using Multimodal MR Imagery

Shashwat Goel, Aastha Sehgal, Parthasarathi Mangipudi and Anu Mehra

Abstract In this paper, mutlimodal approach has been used for segmenting Tumor core in MRI images using *T*1-Contrast enhanced, *T*2-weighted, and FLAIR imaging modalities. Segmentation techniques working on single modality fails to segment brain tumor where the contrast in MR images is low or when sufficient disparity is not present in the intensity of tumor and background region. The proposed method overcome above stated problems by fusing the images of three modalities to form one image. The entire process is divided into five stages: Image Acquisition, Preprocessing, Segmentation, Tumor Extraction, and Evaluation. Two separate segmentation algorithms, Fuzzy C Means and K Means have been used. The results were evaluated using manually segmented Ground Truth. The average Dice accuracy for 18 real tumors (including 12 high grade Glioma and 06 low grade Glioma) is 86 % using Fuzzy C Means as well as K Means. Hence, the proposed method is highly efficient in segmenting tumor core.

Keywords Multimodal · Segmentation · MRI modalities · Fuzzy C Means · K Means · Ground truth · Dice accuracy · Glioma

Shashwat Goel (✉) · Aastha Sehgal · Parthasarathi Mangipudi · Anu Mehra
Amity University, Sector-125, Noida 201303, Uttar Pradesh, India
e-mail: shashwat.goel@student.amity.edu

Aastha Sehgal
e-mail: aastha.sehgal@student.amity.edu

Parthasarathi Mangipudi
e-mail: psmangipudi@amity.edu

Anu Mehra
e-mail: amehra@amity.edu

© Springer Science+Business Media Singapore 2017

R. Singh and S. Choudhury (eds.), *Proceeding of International Conference on Intelligent Communication, Control and Devices*, Advances in Intelligent Systems and Computing 479, DOI 10.1007/978-981-10-1708-7_84

1 Introduction

Brain tumor segmentation plays a vital role in surgical and treatment planning. In recent years, the number of people suffering from brain tumor has increased multifold. However, the traditional methods of segmenting brain tumor manually by Radiologists are both tedious and prone to bias and error. Hence, there is a pressing need to develop automatic techniques for brain tumor segmentation which are accurate, reliable, and consistent.

The last decade has witnessed a surge of various algorithms for segmenting brain tumors. Most of them focus on Glioma because it is the most frequent type of brain tumor which originates in the glial cells [1]. A good review of recent practices and techniques in this field could be found in [2–4].

The segmentation method proposed by Huang et al. [5] uses local independent projection-based classification approach for labeling each voxel in MRI image into different classes. Sachdeva et al. [6] work was based on content-based active contour in which they used intensity and texture information of contour region for segmentation. Unlike other region growing methods, their algorithm was able to segment homogenous tumor against similar background and in presence of weak or diffused edges. Jiang et al. [7] presented a graph-cut-based method for segmenting brain tumors in multimodal MR images. Diaz et al. [8] segmented Edema and Gross Tumor Volume using four MRI modalities by applying automatic histogram multi-thresholding and geodesic dilation. Menze et al. [1] provides the description of 20 cutting edge tumor segmentation algorithms that were submitted in the MICCAI 2012 and MICCAI 2013 conferences. Ahmed et al. [9] modified the fuzzy c means algorithm to remove the intensity inhomogeneities present due to bias field in the MRI data. A combination of Bayesian–Markov Random Field (MRF) classification technique and Random Forest algorithm was used by Mitra et al. [10] to segment brain tumor using $T1$-weighted, $T2$-weighted and Flair modalities.

It was found in the literature survey that algorithms working on single modality often fail in segregating tumor core when the intensity variation between tumor and background is low or in diffused edges are present due to edema around tumor. The algorithm proposed in this paper overcomes these limitations by fusing images of three modalities ($T1C$, $T2$, and Flair) to get an optimized image for segmenting tumor core. The method works well even for cases the tumor region is not distinctly visible on a particular modality. Neither user input nor any kind of initial estimates were required in the process. Three performance measures, Dice coefficient, Recall and Precision, were calculated to evaluate results by comparing extracted tumor region with the available ground truth with expert annotation for active tumor and edema.

2 Methodology

2.1 Image Acquisition

The MRI image dataset used in this work was obtained from the MICCAI—BRATS 2015 (http://www.miccai2015.org/). *This work has used a total of 18 Glioma images of real patients out of which 12 are for high grade Glioma and 06 are for low grade Glioma.* All images have been aligned to same anatomical template, skull stripped, and interpolated to 1 mm isotropic resolution and stored as signed 16-bit integers, but with only positive values. The manually segmented image (Ground Truth) for each patient has four different labels for Necrosis, Edema, Enhancing tumor and Non-enhancing tumor (Fig. 1).

2.2 Preprocessing

The first step is to remove the bias field in MRI images using *N*3 Algorithm [11] for all three modalities. Bias field is a low intensity signal that may accumulate in MR images during scanning due to magnetic field inhomogeneities [9]. These artifacts may result in poor segmentation output. Hence, it is imperative to remove them. Next, the bias field corrected *T*2 images were subjected to intensity thresholding to eliminate very high intensities. This step is crucial as it eases the tumor extraction stage.

Third, *T*1-contrast enhanced, *T*2 and Flair images for each patient were fused together to get one image. This was achieved by summing *T*1*C* image with the absolute difference of *T*2 and Flair image. Usually, edema appears as high intensity region on Flair and *T*2, while lesion has high *T*1*C* and *T*2 intensities. Hence, it is reasonable to assume the above stated combination of three modalities would be optimal for segmentation of tumor core. Next, the contrast of the image, thus obtained, was enhanced to ease the segmentation process.

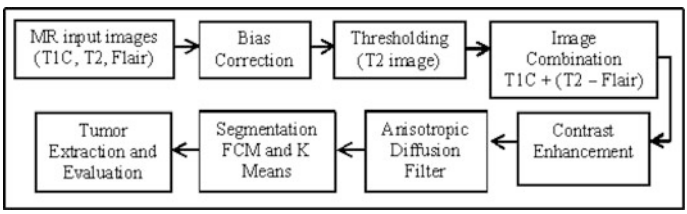


Fig. 1 Generic flow diagram of the proposed method

Further, spatial smoothing was performed using anisotropic diffusion filter [12] to reduce noise and unwanted details from the image, followed by segmentation stage.

2.3 Segmentation and Tumor Extraction

In this paper, two segmentation techniques, Fuzzy C Means and K Means, were used independently. Both the algorithms are fast and reliable. They do not require user inputs or initial estimates. The segmented outputs are labeled images with only three labels present. Generally, segmentation alone is not sufficient to segregate the tumor core from rest of the brain. Hence, post processing techniques were applied after segmentation. This was attained by first measuring the area of regions in segmented image and then applying Circularity criteria selectively to three regions with highest area, using Eq. (1). This eliminates unwanted parts, but the tumor region. The region with circularity closest to 1.0 was selected as tumor. Consequently, tumor core region was successfully extracted for each patient.

$$\text{Circularity} = \left(\text{Perimeter}^{\wedge}2\right) \div (4\pi\,\text{Area}). \tag{1}$$

2.4 Evaluation

Three evaluation parameters Dice coefficient, Recall, and Precision were calculated using the following formulas:

$$\text{Dice} = (2\times|S \cap T|) \div (|S| + |T|), \tag{2}$$

$$\text{Precision} = (\text{TP}) \div (\text{TP} + \text{FP}), \tag{3}$$

$$\text{Recall} = (\text{TP}) \div (\text{TP} + \text{FN}), \tag{4}$$

where, S is the extracted tumor region. T is the ground truth. *TP (True Positive)* is the tumor region correctly identified as tumor. *FP (False Positive)* is the normal brain region incorrectly labeled as tumor. *FN (False Negative)* is the tumor region incorrectly labeled as normal brain region (Fig. 2).

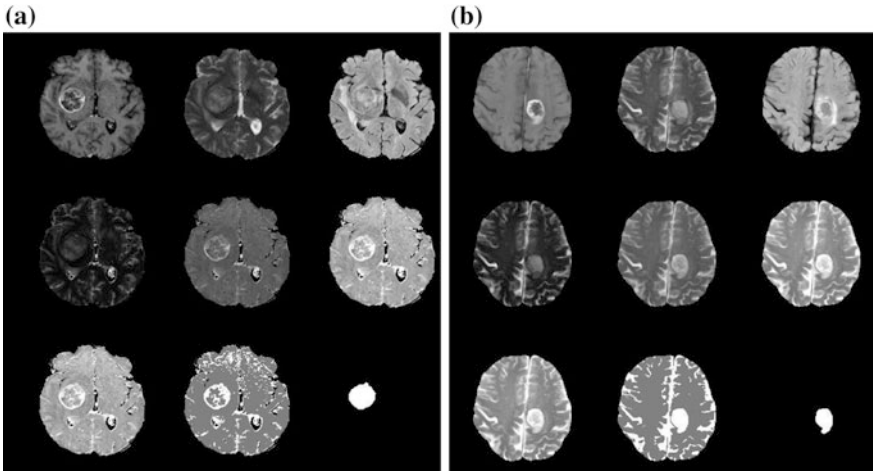


Fig. 2 **a** Result for one patient using Fuzzy C Means segmentation. *Top row* (*L-R*): *N*3 corrected *T*1*C* image, *N*3 corrected *T*2 image, *N*3 corrected flair image. *Middle row* (*L-R*): (*T*2−Flair) image, (*T*1*C* + (*T*2−Flair)) image, contrast enhanced image. *Bottom row (L-R):* Smoothed image using anisotropic diffusion filter, FCM segmented image and extracted tumor region. **b** Result for another patient using K means segmentation. *Top row* (*L-R*): *N*3 Corrected *T*1*C* image, *N*3 Corrected *T*2 image, *N*3 Corrected Flair image. *Middle Row* (*L-R*): (*T*2−Flair) image, (*T*1*C* + (*T*2−Flair)) image, contrast enhanced image. *Bottom row* (*L-R*): smoothed image using anisotropic diffusion filter, FCM segmented image and extracted tumor region

3 Results and Discussion

The algorithm was executed using MATLAB 8.5 (R2015a) on a personal computer with 2.53 GHz CPU and 3 GB RAM. Figure 3a shows the results of using FCM and Fig. 3b shows results using K Means.

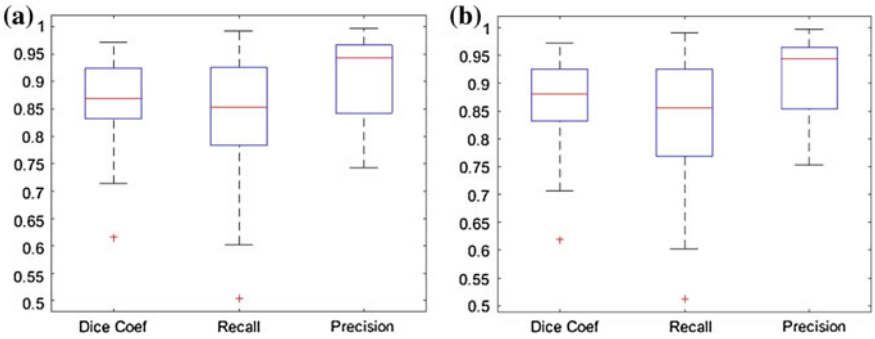


Fig. 3 Box plot showing dice coefficient, recall and precision for eighteen evaluation cases **a** Using *Fuzzy C Means.* **b** Using K Mean

The average value of Dice coefficient, Recall and Precision, using either segmentation algorithm, are 0.86, 0.82 and 0.9, respectively. The minimum and maximum dice accuracy is 62 % and 97 %, respectively. This shows that they have similar performance for segmenting tumor core using the proposed method. The results are quite overwhelming and convey that the algorithm works well for both high-grade and low-grade glioma—the most frequent type of brain tumor.

4 Conclusion

The method presented in this paper uses three MRI modalities (T1C, T2, and Flair) segment the tumor core region. Two segmentation techniques were applied. However, it was later found that they both give almost same performance with same average values of all three performance measures. It is fully automatic and does not require user inputs or initial estimates. The method has been successfully tested on both high-grade and low-grade glioma images. This approach overcomes the shortcomings of segmentation using single modality. The results are comparable with the best works that have been done in this field using various state of the art methods.

References

1. B. H. Menze, A. Jakab, S. Bauer, J. Kalpathy-Cramer, K. Farahani, J. Kirby, Y. Burren, N. Porz, J. Slotboom, R. Wiest, L. Lanczi, E. Gerstner, M. A. Weber, T. Arbel, B. Avants, N. Ayache, P. Buendia, L. Collins, N. Cordier, J. J. Corso, A. Criminisi, T. Das, H. Delingette, C. Demiralp, C. Durst, M. Dojat, S. Doyle, J. Festa, F. Forbes, E. Geremia, B. Glocker, P. Golland, X. Guo, A. Hamamci, K. Iftekharuddin, R. Jena, N. John, E. Konukoglu, D. Lashkari, J. A. Mariz, R. Meier, S. Pereira, D. Precup, S. J. Price, T. Riklin-Raviv, S. Reza, M. Ryan, L. Schwartz, H. C. Shin, J. Shotton, C. Silva, N. Sousa, N. Subbanna, G. Szekely, T. Taylor, O. M. Thomas,N. Tustison, G. Unal, F. Vasseur,M.Wintermark,D. H. Ye, L. Zhao, B. Zhao, D. Zikic, M. Prastawa, M. Reyes, and K. V. Leemput, "The multimodal brain tumor image segmentation benchmark (BRATS)," IEEE Trans. Med. Imag., vol. 34, no. 10, Oct. 2015.
2. Jin Liu, Min Li, Jianxin Wang, Fangxiang Wu, Tianming Liu, and Yi Pan, "A Survey of MRI-Based Brain Tumor Segmentation Methods," Tsinghua Science and Technology, vol. 19, no. 6, pp. 578–595, Dec. 2014.
3. S. Bauer, R. Wiest, L.-P. Nolte and M. Reyes, "A survey of MRI based medical image analysis for brain tumor studies," Phys. Med. Biol., vol. 58, no. 13, pp. R97–R129, Jul. 2013.
4. Nelly Gordilloa, Eduard Montsenyb and Pilar Sobrevillac, "State of the art survey on MRI brain tumor segmentation," Magnetic Resonance Imaging, vol. 31, no. 8, pp. 1426–1438, Oct. 2013.
5. Huang M, Yang W, YaoWu, Jiang J, Chen W and Feng Q, "Brain Tumor Segmentation Based on Local Independent Projection-Based Classification," IEEE Trans. Biomed. Eng., vol. 61, no. 10, Oct. 2014.
6. Sachdeva J, Kumar V, Gupta I, Khandelwal N and Ahuja C K, "A novel content based Active Contour model for brain tumor segmentation," Magnetic Resonance Imaging 30 (2012), pp. 694–715.

7. Jiang J, Wu Y, Huang M, Yang W, Chen W and Feng Q, "3D brain tumor segmentation in multimodal MR images based on learning population- and patient-specific feature sets," Computerized Medical Imaging and Graphics 37 (2013), pp. 512–521.
8. Diaz I, Boulanger P, Greiner R, Hoehn B, Rowe L and Murtha A, "An Automatic Brain Tumor Segmentation Tool," 35th Annual Intl. Conf. IEEE Eng. In Med. Biol. Soc. (EMBC), pp. 3339–3342, 2013.
9. M. N. Ahmed, S. M. Yamany, N. Mohamed, A. A. Farag, and T. Moriarty, "A modified fuzzy c-means algorithm for bias field estimation and segmentation of MRI data," IEEE Trans Med. Imag. Vol. 21, no. 3, pp. 193–199, Aug. 2002.
10. Mitra J, Bourgeat P, Fripp J, Ghose S, Rose S, Salvado O, Connelly A, Campbell B, Palmer S, Sharma G, Christensen S and Carey L, "Lesion segmentation from multimodal MRI using random forest following ischemic stroke," Neuroimage, vol. 98, pp. 324–335, Sept. 2014.
11. Sled J G, Zijdenbos A P and Evans A C, "A nonparametric method for automatic correction of intensity nonuniformity in MRI data," IEEE Trans. Med. Imag., vol. 17, no. 1, pp. 87–97, Feb. 1998.
12. Perona P and Malik J, "Scale-space and edge detection using Anisotropic Diffusion," IEEE Trans. On Pattern Analysis and Machine Intelligence, vol. 12, no. 7, July 1990.

Design and Sizing of Decentralized Grid-Connected Solar Power Plant

Vineet Mediratta, Kamal Bansal, Piyush Kuchhhal and Vinay Chandna

Abstract Power demand of the country is mostly met through conventional plant which generates bulk amount of power centrally. Power generation using photovoltaic (PV) technology is very promising in terms of power generation ranging from kWs to MWs and helps to great extent increasing the installed capacity and can help electric utility companies in meeting increasing load demand along with minimizing distribution losses. The concept of grid-connected solar PV system is mounted on vacant unutilized area of commercial buildings; small-scale industry rooftops are likely to add to generation capacity and thus meet renewables portfolio standard targets of utility. This paper analyzes and designs a PV array and defines inverter sizes for a grid-connected PV system. The proposed site selected is Zirakpur (Punjab) with latitude 30.40° N and longitude 76.50° E. Various inputs like peak power, module voltage, global irradiance and tilt angle are given, and a detailed report on the losses of PV array as well as the inverter are obtained using software PVsyst.

Keywords Photovoltaic · Grid-connected · PVsyst software

1 Introduction

Due to industrial growth and urbanization the power demand is increasing day by day. Addressing to this ever-increasing energy need and power security challenge and to provide ecologically sustainable growth, Government of India had launched Jawaharlal Nehru National Solar Mission during 2010–2011, under the novel initiative of Government of India and state Governments, setting up of small-scale to large-scale solar photovoltaic off-grid as well as grid-connected plants are proposed.

Vineet Mediratta (✉) · Kamal Bansal · Piyush Kuchhhal
UPES, Dehradun, India
e-mail: vmediratta@ddn.upes.ac.in

Vinay Chandna
JECRC, Jaipur, Rajasthan, India

© Springer Science+Business Media Singapore 2017

R. Singh and S. Choudhury (eds.), *Proceeding of International Conference on Intelligent Communication, Control and Devices*, Advances in Intelligent Systems and Computing 479, DOI 10.1007/978-981-10-1708-7_85

This not only will add to capacity but will also contribute toward global effort to meet the challenges of climate change.

By this implementation installation of solar plants, both standalone and grid-connected plants are encouraged to be set up both at centralized level as well as decentralized level. This will help solar technology penetration in the country along with capacity addition under renewable energy portfolio.

The unit price for power generated from standalone photovoltaic (PV) plants is quite high; however, grid-connected power is produced at a rate slightly higher than the commercial tariff charged from consumers by distribution companies, i.e., DISCOMS, but with the advancement of semiconductor technology and improvement in panel design the cost of solar power is on the decline trend while the unit cost of energy is obtained from conventional fossil fuel plants which is increasing day by day.

2 Solar Photovoltaic Energy

Among the various sources of renewable energy, solar energy (thermal and PV put together) is the second largest after wind energy.

- For solar energy conversion, solar panels are used which utilizes PV material. The PV materials can be several individual solar cells or a single thin layer, which make up a larger solar panel.
- Unlike electromechanical energy conversion devices, PV technology converts the energy of sunlight which is widely available (a reliable fuel) into electrical energy using number of moving parts; hence, conventional requirement of burning and consuming fossil fuel is eliminated and thus there is no pollution. Moreover, the maintenance is minimum in solar plant.

2.1 Components of Photovoltaic System

2.1.1 PV Panels

Solar PV modules shall be of polycrystalline technology of 72 cell configurations with wattage ranging from 315 to 320 Wp. Modules are arranged in arrays in the configuration of series and parallel systems. It is proposed to go for 1000 V DC bus system to take care of the high DC current to be fed into the Inverters.

2.1.2 Inverter

Optimum size of inverters in grid-connected PV systems is selected.

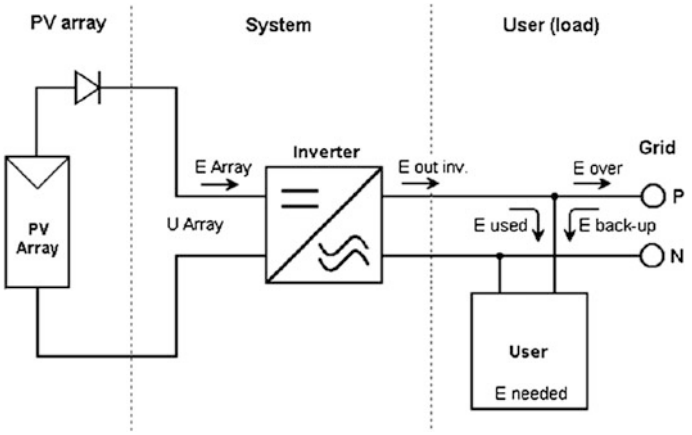


Fig. 1 Schematic layout of a grid-connected solar PV system

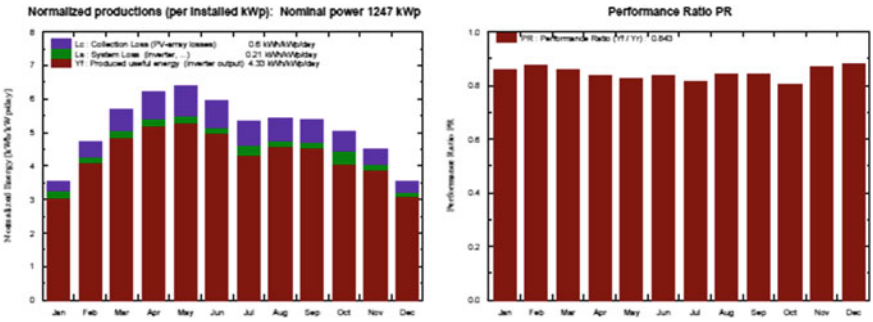
3 Rooftop Grid-Connected Solar Power Plant

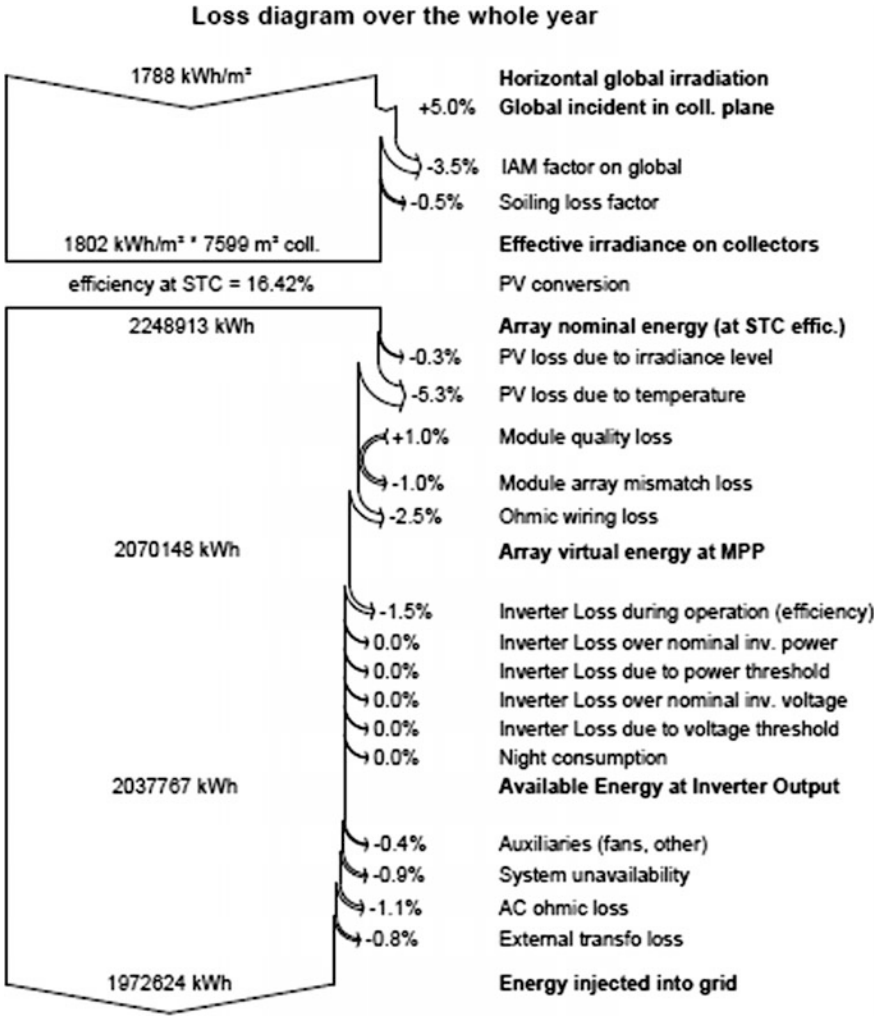
In grid-connected SPV system mounted on rooftop, depending upon the capacity of the system installed at institution/commercial/factory establishment, the solar panel of suitable rating is connected in series to get desired dc voltage and form a string, such that strings are connected in parallel to get the desired DC power output power from the PV array. Depending upon the capacity of the plant, voltage is selected for generation. The resultant DC voltage thus obtained from SPV panel is converted into AC power using inverter which can be stepped up appropriately and fed to the grid either at 33 kV/11 kV three-phase line using ring main unit or directly can be connected to LT panels without stepping up at 440/220 V three-/single-phase line. The power generated during day time is used to cater the connected load and the excess power is fed to the grid as long as the grid is available. In the absence of solar power or in case of less generation due to cloud cover, the captive loads are served by drawing power from the grid. For importing or exporting power, these interactive grid-connected rooftop systems employ net metering concept wherein the beneficiary pays to the utility on net meter reading basis only. The same objective can also be realized by installing two meters to measure the export and import of power separately (Fig. 1).

4 PVsyst and Proposed Work

Designing of 1250 kWp rooftop grid-connected plant is done in PVsyst for proposed site, i.e., Zirakhpur—Bindra 1250 KWp Latitude: 30.4° N; and Longitude 76.5° E.

Simulation parameters			
Collector plane orientation	Tilt 7°	Azimuth 0°	
PV array characteristics			
PV module	Si-Poly	Model CS6X—315P	
		Manufacture Canadian Solar Inc.	
No of PV modules	In series	20 modules	In parallel 198 strings
Total number of PV modules	3960	Unit Nom. Power	315 Wp
Array global power	1247 KWp (Nominal STC)		
Array operating characteristics (50° C)	U mpp	674 V	I mpp 1721 A
Total area	Module Area 7599	Cell area 6940 m^2	
Inverter	Model Sunny Central 1000CP XT		
Manufacturer SMA			
Characteristics	Operating Voltage: 596–850 V		
Unit nominal power	1000 kWac		
Max. power	1100 kWac		
Inverter pack	No. of inverters	1 units	





5 Conclusion

Grid-connected rooftop solar plants providing clean energy offer many advantages compared to off-grid PV system as there is no requirement of battery back up for feeding excess generated power. Moreover, unutilized space is productively used to fulfill own power requirement and extra units generated may be exported/injected into grid. The electricity generation contributes to shorten the demand and supply gap along with revenue generation. Also reliability of distribution network

increases with the use of ring main unit and reduction in distribution losses is achieved as they are located at close to load.

The optimum designing is required in terms of module selection, array sizing and configuration, inverter selection, and location of SPV plant in distribution network to obtain solar energy at economic price. Influential parameters effecting production and losses of energy are studied and evaluated for optimum sizing. A detailed analysis using a software PVsyst which offers good flexibility along with accuracy for optimally designing a PV system therefore becomes important tool for designing a grid-connected PV system. Simulation using onsite parameters such as solar radiation, wind speed, and temperature using PVsyst is thus important computer-based tool for design for power systems requiring a detailed analysis.

References

1. Hongbo Ren, Weijun Ga, Yingjun Ruan. Economic optimization and sensitivity analysis of photovoltaic system in residential buildings. Renewable Energy 2009;34: 883–889.
2. Mohamed A. Eltawil, Zhengming Zhao. Grid-connected photovoltaic power systems: Technical and potential problems—a review. Renewable and Sustainable Energy Reviews 2010; 14: 112–129.
3. Gang Liu, Rasul MG, Amanullah MTO, Khan MMK. Techno-economic simulation and optimization of residential grid connected PVsystem for the Queensland climate. Renewable Energy 2012; 45:146–155.
4. Benatiallah A, Mostefaoui R, Boubekri M, Boubekri N. A simulation model for sizing PV installation. Desalination 2007; 209: 97–101.
5. Blackledge, Jonathan, Rivas Duarte, Maria-Jose, Kearney, Derek Joseph, Murphy, Eamonn. A techno-economic analysis of photovoltaic system design as specifically applied to commercial buildings in Ireland. Journal of Sustainable Engineering Design 2012:1 Iss. 2, article 5.
6. PVsyst SA. PVsyst photovoltaic software 2012. [Internet] accessed from http://www.pvsyst.com/en/.
7. Phil Bolduc, David Lehmicke & Joseph Smith, "Performance of a grid connected PV system with energy storage". IEEE Photovoltaic. Page(s):1159–162, 1993.
8. Eduardo Román, Ricardo Alonso & Pedro Ibañez, "Intelligent PV Module for Grid-Connected PV Systems", IEEE Transactions on Industrial electronics, Vol.53. No.4, Page(s): 1066–1073, August 2006.
9. C.H. Lin, W.L. Hsieh, C.S. Chen, C.T. Hsu, T.T.Ku, and C.T. Tsai, "Financial analysis of a large-scale photovoltaic system and its impact on distribution feeders," IEEE Trans. Ind. Appl., vol. 47, no. 4, pp. 1884–1891, Jul./Aug. 2011.
10. http://www.mnre.gov.in.
11. M. Njozila, S. Chowdhury, S. P. Chowdhury, "Impacts of DG on the operation of auto-reclosing devices in a power network", IEEE Power and Energy Society General Meeting, 2011, pages: 1–8.
12. A Moreno-Muroz, J. J. G. de-la-Rosa, M. A. Lopez-Rodriguez, J. M. Flores-Arias, F. J. Bellido-Outerino, M. Ruiz-de-Adara, "Improvement of power quality using distributed generation", International Journal of Electrical Power and Energy Systems, Vol. 32, Issue 10, 2010, pages: 1069–1076.

Effect of Faults on Power Electronic Devices for ZSI-Fed Induction Motor Drive System

Bhawana Negi, Vivek Sharma, Ankit Bhatt and Pratibha Yadav

Abstract Fault analysis is the main concern for the system configuration and design. Three-phase analysis is required as for the industrial function so that the current signature analysis is performed in the three phase. As ZSI was introduced for the boost and buck operation in the same circuitry. The input cannot change but the output can be modified according to requirement using the passive components. The aim of this inverter is to efficiently transform a DC power source to a high-voltage AC using the two port setup.

Keywords ZSI · MOSFET · THD · Fault

1 Introduction

The current signature analysis in the conversion process is used in the present work; the conversion of low-voltage DC into the high-voltage DC and then conversion of high-voltage DC into the AC voltage using PWM approach. Earlier the analysis of faults in the single-phase ZSI-fed IM drive is compared with the healthy condition. The connection with the nonlinear load, i.e., asynchronous motor generates harmonics which are to be considered while designing the inverter. The study of input supply of induction motor is current signature analysis. The comparison for identifying the faults is done by taking the reference. In this case, reference value is the

Bhawana Negi (✉) · Vivek Sharma · Ankit Bhatt · Pratibha Yadav
Department of Electrical Engineering,
Graphic Era University, Dehradun, India
e-mail: bhawananegi105@gmail.com

Vivek Sharma
e-mail: mail.vivek21@gmail.com

Ankit Bhatt
e-mail: bhatt.ankit.23@gmail.com

Pratibha Yadav
e-mail: pratibhayadavddun@gmail.com

© Springer Science+Business Media Singapore 2017

R. Singh and S. Choudhury (eds.), *Proceeding of International Conference on Intelligent Communication, Control and Devices*, Advances in Intelligent Systems and Computing 479, DOI 10.1007/978-981-10-1708-7_86

value at the time of normal condition of system having no faults. The energy storage component capacitor and inductor used in ZSI is capable to boost the voltage. Failures of switching device can affect the entire system and the failure of system and emergency shutdown of motor be can prevented by knowing the conditions of fault. The current signature analysis is carried out when system is in operating condition. The output of the inverter is sufficient to identify normal and abnormal condition of the switching device. The three faults are considered which are in line to ground fault, open circuit of MOSFET in phase A, and blown off MOSFET in phase A. These different faults are to be inserted to find the spectral response and calculate FFT (Fast Fourier Transform). The FFT calculates the higher order Fourier transform quickly at the frequency of 50 Hz [1]. The THD% in the present work is obtained using the current waveform.

2 Methodology

2.1 Three-Phase ZSI-Fed Induction Motor Load

The circuitry when the motor is operating at normal condition is shown in Fig. 1. There are no faults in the circuit due to the inverter module (Fig. 2).

The input and output voltage is shown by the waveform. Where input is 120 V and output is 260 V. Current output is 190 A and the THD% is 7.99.

2.2 Line to Ground Fault of Z-Source Inverter

This fault is due to the output of inverter connected with the ground (Fig. 3).

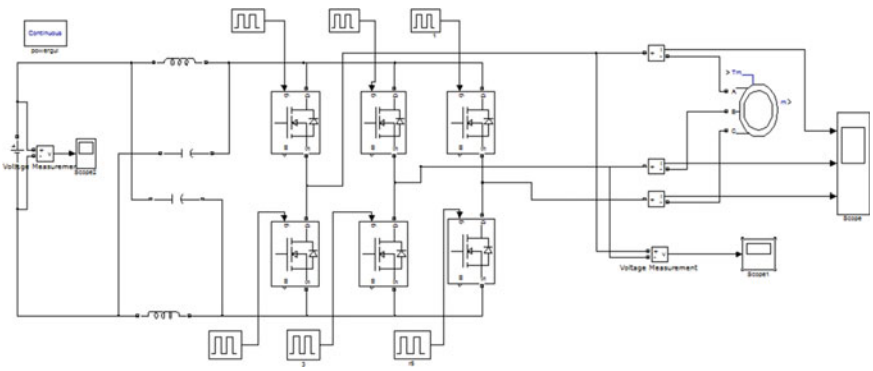


Fig. 1 Simulation circuit of the three phase ZSI fed IM

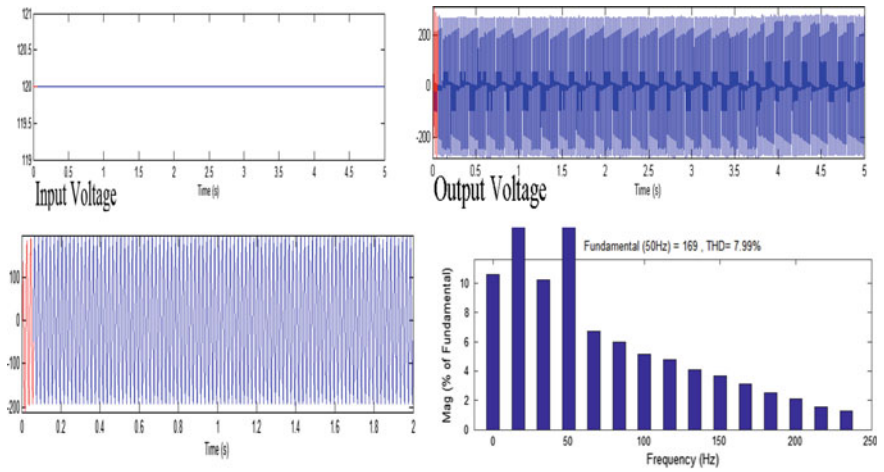


Fig. 2 THD% response at healthy condition of inverter

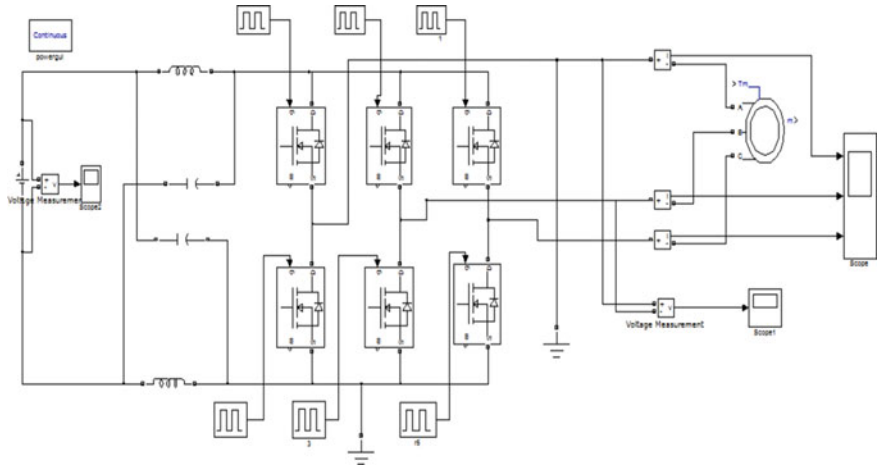


Fig. 3 Simulation circuit of *line* to ground fault on three phase ZSI fed IM

Figure 4 shows the current and THD% when the phase A is connected with the ground. So the current is going to negative side and value of current is −650. The THD% is 39.22.

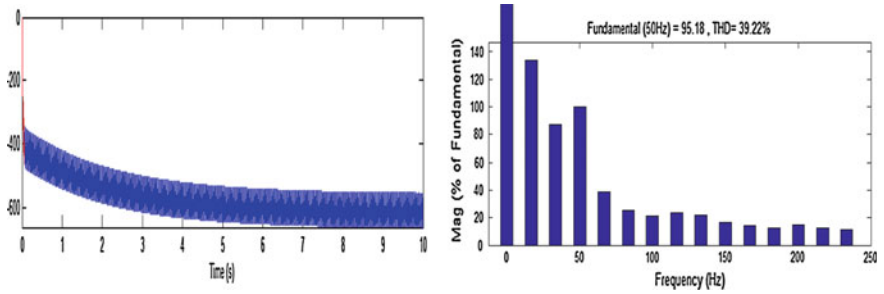


Fig. 4 THD% response at faulty condition of inverter

2.3 *Faults at the One of the Phase of the MOSFET Gate*

Phase A is taken into consideration as the fault is introducing in the phase A. The gate pulse of the MOSFET is open and simulation performed to get the effect of faults in the ZSI which is evaluated by the THD% (Fig. 5).

When the gate is not in the first-phase leg of one MOSFET, the current is −240 and THD% is 34.72 (Fig. 6).

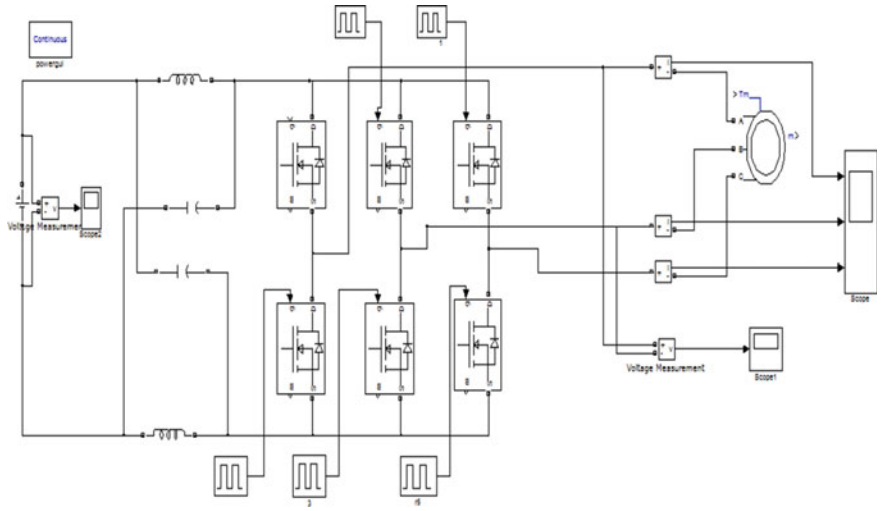


Fig. 5 Simulation circuit of fault at MOSFET gate

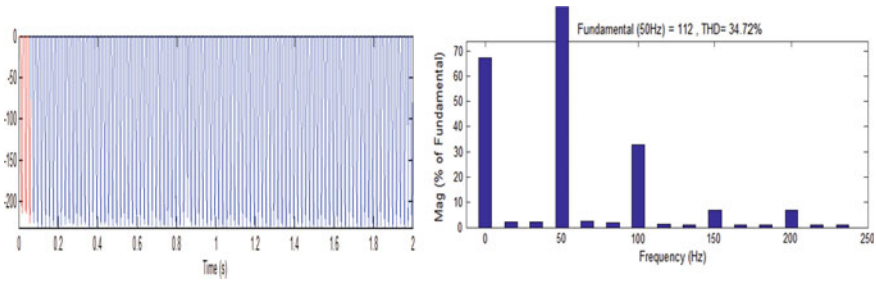


Fig. 6 THD% response of faulty condition of inverter

2.4 *Faults at the One of the Phase of the MOSFET Gate*

This condition is the open-circuit condition for the system. As the open circuit occurs, the MOSFET is removed. This condition can be achieved using high value of resistor in the position of MOSFET (Fig. 7).

This fault due to the open circuit of MOSFET is considered where high-value resistor of 10 k is placed to form open circuit. The current value is −215 and the THD% is 81.35 (Fig. 8 and Table 1).

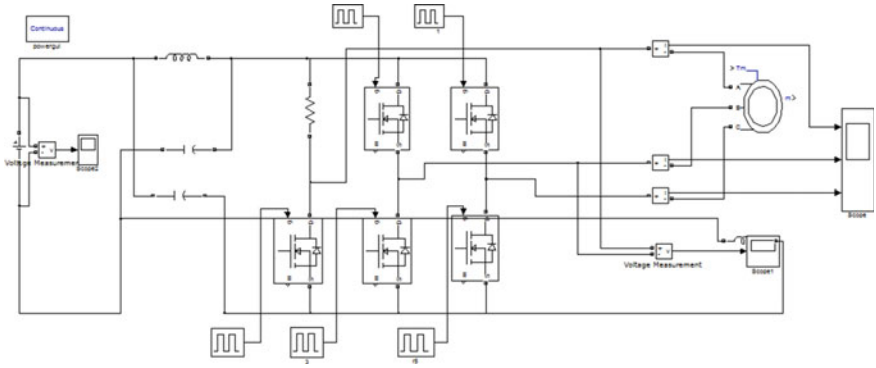


Fig. 7 Simulation circuit three phase ZSI when open circuit occurs in MOSFET Phase A

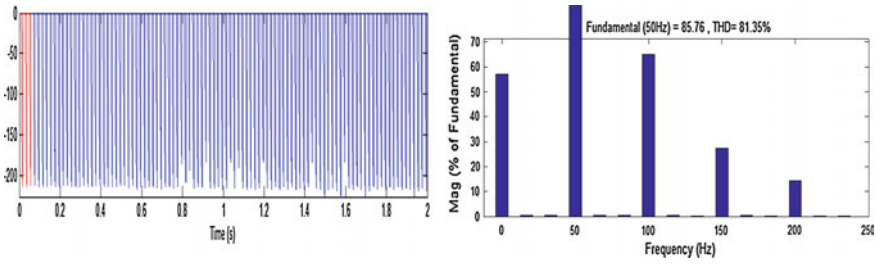


Fig. 8 THD% response of faulty condition of Inverter

Table 1 Analysis of healthy and faulty condition using FFT

Conditions	THD %	Current (Amp)
Without fault	7.99	190
Line to ground fault on Phase A	39.22	−650
MOSFET gate open on Phase A	34.72	−240
MOSFET blown off on Phase A	81.35	−215

3 Conclusion

The simulation studies prove that, due to incorporation of faults, value of fault current increases rapidly which may cause breakdown of device. As of study, it is concluded that the output current also falls to negative value due to faulty conditions which is undesirable for the inverter operation. In future, this study can be extended for multilevel converters.

References

1. Kaumudi Purohit' Vivek Sharma.: Fault Detection of PV Fed DC Converter Fed Induction Motor System. Advanced Research in Electrical and Electronic Engineering. Volume 2, ISSN: 2349–5804, April–June 2015, pp. 40–44.
2. Aashna Hemkumar, Baavana Balaji, V. Rajini.: Fault Diagnosis Of Vsi-Fed Three-Phase Induction Motor. Proceedings of 17th IRF International Conference, 18th October 2015, Bengaluru, India, ISBN: 978-93-85832-22-2.
3. Chaitali S. Kalaskar, Vitthal J. Gond.: Motor Current Signature Analysis to Detect the Faults in Induction Motor. Int. Journal of Engineering Research and Applications. Vol.4, ISSN:-2248-9622, June 2014, pp. 58–61.
4. Vivek Sharma, Nikita Rawat.: Fault Diagnosis of Single phase Z-Source Inverter. IEEE International Conference on Advances Computing & Communication Engineering ICACCE-2015, May 2015.
5. Vivek Sharma, Gaurav Mendiratta.: Harmonic Analysis of CSI-fed Induction Motor Drive. In Proceedings of the 8th INDIA Com 2014 IEEE International Conference on Computing for Sustainable Global Development, March 2014.

Design of a Multiband Filter for Future Wireless Communication

Jagadish Baburao Jadhav and Pramod Jagan Deore

Abstract In recent years, multiband filters have been acquiring more interest in modern wireless communication systems. Here a novel quadband filter design is proposed to produce four passbands with good skirt selectivity. First, second, and fourth passbands are generated due to the external set of a stub-loaded resonators and internal set is responsible to produce third pass band. To make a circuit compact, one set of resonators are surrounded by the one more set of resonators. Due to its simple structure, compact size, and excellent performance, the proposed quadband filter is expected to be good candidates for use in various future wireless communication systems.

Keywords Bandpass filter · Quadband filter · Open stub resonator · Short stub resonators

1 Introduction

Nowadays, multiservice wireless systems are more admired due to the rapid enlargement of mobile and wireless communication systems. Specifically in WLAN, the tasks of designers is to design a multiband bandpass filter and to realize diminishment in the size of the filter, expected high selectivity, assigning various passbands in one design and low insertion loss, and much more. Conventionally, multiband filters were constructed by cascading two or extra single-band filters so the filters become extremely massive and large in size. Using appropriate arrangements of resonators, it is possible to miniaturize the size of the filter. In last decade, various techniques have been invented by authors to design multiband

J.B. Jadhav (✉) · P.J. Deore
Department of E&TC Engineering, RCPIT, North Maharashtra University, Jalgaon, Maharashtra, India
e-mail: jagadish.rcpit@gmail.com

P.J. Deore
e-mail: pjdeore@yahoo.com

© Springer Science+Business Media Singapore 2017

R. Singh and S. Choudhury (eds.), *Proceeding of International Conference on Intelligent Communication, Control and Devices*, Advances in Intelligent Systems and Computing 479, DOI 10.1007/978-981-10-1708-7_87

microstrip bandpass filters utilizing stepped impedance resonators, multiple mode resonators, open circuited stubs, short circuited stubs, ring resonator, etc.

2 Literature Overview

In literature, many efforts were carried out for the multiband filters utilizing the stepped impedance resonator concept. In [1] a triple-band filter is designed using half-wavelength resonator with SIRs. In [2], by using combined quarter wavelength resonators new tri-band bandpass filter was designed. For designing multiband filters, investigators concentrate on multiple-mode stub-loaded resonators [3–10]. In [3], tri-band filter is designed with five transmission zeros. In [4], a quad-mode resonator is employed to design quadband BPF. Two cascading resonators are used which leads to GPS, WIMAX, and WCDMA application. In [5], transmission zeroes are inserted close to the passband edges with the help of spur line to project dual-bandpass filter utilizing an open stub-loaded resonator.

2.1 Main Contribution of This Paper

- We attempt to develop a simple compact quadband filter for multiband wireless communication system using two sets of resonators, i.e., short- and open-ended stub-loaded resonators which are not proposed yet as per our best of my knowledge.
- Unlike most of the methods reported in literature, which use open-ended stub-loaded resonators to produce four passbands with high selectivity, our method directly analyzes the odd mode excitation and even mode excitation to calculate resonant frequencies.

In this paper, the filter operating at 2.017, 2.63, 4.06, and 4.6 GHz is designed by modifying the resonator structure. The theory of the designed quadband filter is discussed and analyzed. By utilizing plus-shaped stub-loaded resonator, quadband filter is realized with five transmission zeroes. The size of whole circuit is 33:7 $\times$ 29:3 mm.

3 Quadband Filter Design

The structure of the microstrip quadband BPF is shown in Fig. 1 with dimensions. Here it is composed of two pair of resonators. Two sets of resonators are inserted into each other, thus the dimension of the filter becomes so compact. Instead of

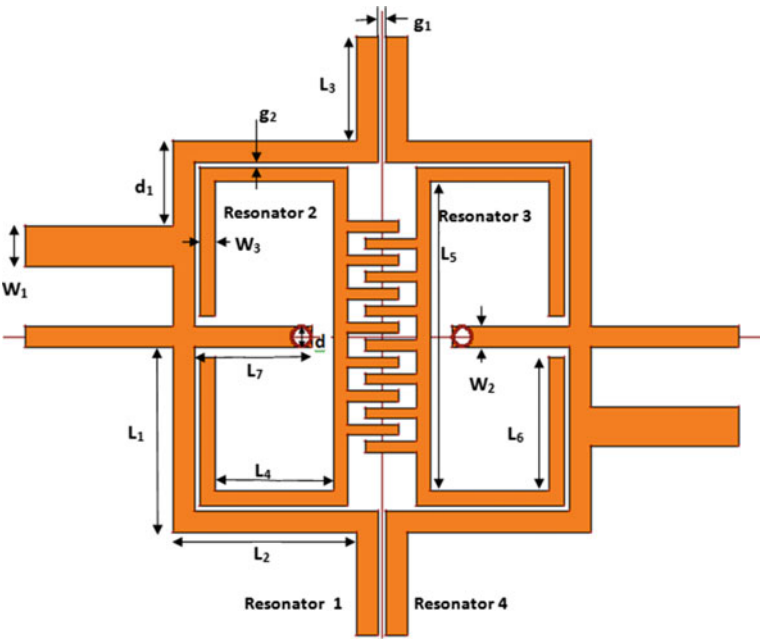


Fig. 1 Proposed quadband filter with dimensions

T-shaped stub-loaded resonator, plus-shaped resonator is utilized. Plus-shaped stub has one open-ended stub and second stub is shorted by using vias. Here frequencies of operation depend upon the dimensions of the lengths of stub. The length of the stub-loaded resonator 1 and resonator 4 controls first, second, and fourth resonant frequency whereas third passband frequency depends upon resonator 2 and resonator 3 as shown in Fig. 1. Here, in this proposed design two vias are added into the inner stub of plus-shaped resonator structure which improves the filter performance. In this proposed design, vias having radius of 0.45 mm are used to short the ground plane and substrate layer. Table 1 tabulates the dimensions for the proposed design.

4 Mathematical Analysis of Proposed Filter

4.1 Preliminary Design of Filter

Dielectric Constant. The substrate utilized in the design of quadband BPF having $\epsilon_r = 2.94$ and height is selected as 0.762 mm. Width of the resonator is 1.9 mm (Table 1).

Table 1 Dimensions of proposed quadband filter (in mm)

Parameters	9_1	9_2	d	d_1	L_1	L_2
Values	0.4	0.25	0.9	4.05	12.55	5.6
Parameters	L_3	L_4	L_5	L_6	L_7	L_8
Values	4.9	8.65	14.6	6.35	5.55	7.05
Parameters	W_1	W_2	W_3	L_c	9_c	W_c
Values	1.9	0.7	1	2.4	0.3	0.5

Effective Dielectric Constant. More precise expressions for the effective dielectric constant as follows, for $W/h \geq 1$,

$$\varepsilon_{\text{reff}} = \frac{\varepsilon_r + 1}{2} + \frac{\varepsilon_r - 1}{2}\left\{1 + 12\frac{h}{w}\right\}^{-0.5} = 2.3723 \tag{1}$$

Length of the Resonator. Extended incremental length of patch,

$$\Delta L = 0.412h\frac{(\varepsilon_{\text{reff}} + 0.3)\left(\frac{w}{h} + 0.264\right)}{(\varepsilon_{\text{reff}} - 0.258)\left(\frac{w}{h} + 0.8\right)} = 0.66\,\text{mm} \tag{2}$$

Actual length of the patch,

$$L = \frac{1}{2f_r\sqrt{(\varepsilon_{\text{reff}}}} - 2\Delta L = 44.94\,\text{mm} \tag{3}$$

Characteristic Impedance. General formula for characteristic impedance is given as

$$Z_0 = \frac{\eta}{\sqrt{(\varepsilon_{\text{reff}}}}\left\{\frac{W}{h} + 1.393 + 0.677\,\ln\left(1.44 + \frac{W}{h}\right)\right\}^{-1} = 50.2\Omega \tag{4}$$

where $\text{Ղ} = 120\Pi = 376.99$.

Transmission Lines Length. Total length of transmission line is given by

$$L = L_1 + 2L_2 + 2L_3 + d + W = 45.6\,\text{mm}. \tag{5}$$

Resonant Frequency Calculations. The filter has four passbands at 2.017, 2.63, 4.06, and 4.6 GHz (Table 2). At first passband frequency f_1, resonators 1 and 4 resonate, so, f_1 depends upon the length of these resonators, mainly on the dimensions of short-ended stub. First passband frequency can be expressed as

$$f_1 = \frac{c}{(2L_1 + 4L_2)\sqrt{\varepsilon_{\text{reff}}}} = 1.817\,\text{GHz} \tag{6}$$

Table 2 Simulated and measured frequency response for quadband filter

Resonant frequency	F_1 in (GHz)	F_2 in (GHz)	F_3 in (GHz)	F_4 in (GHz)
	2.017	2.63	4.06	4.6
3 dB Bandwidth (MHz)	152.03	154.65	201.83	128
S_{11} (dB)	−20.89	−27.086	−20.88	−15.67
S_{21} (dB)	−0.89	−1.28	−1.3	−1.8
Transmission zeros (GHz)	1.9, 2.19	2.52, 2.92	4.37	5

Second passband frequency depends upon overall transmission length of resonator, *L*. According to even-odd mode analysis, second passband frequency can be represented as

$$f_2 = \frac{c}{(2L)\sqrt{\varepsilon_{\text{reff}}}} = 2.183\,\text{GHz} \tag{7}$$

At third passband frequency f_3, resonators 2 and 3 resonate. So f_3 depends upon the length of these resonators. Third passband frequency can be expressed as

$$f_3 = \frac{c}{(2L_4 + 2L_6 + L_5)\sqrt{\varepsilon_{reff}}} = 2.62\,\text{GHz} \tag{8}$$

Fourth passband frequency f_4, resonators 1 and 4 resonate. So f_4 depends upon the length of these resonators, mainly on the dimensions of open-ended stub. Fourth passband frequency can be expressed as

$$f_4 = \frac{c}{(L_1 + 2L_3)\sqrt{\varepsilon_{\text{reff}}}} = 3.26\,\text{GHz} \tag{9}$$

5 Fabricated and Simulated Results of Proposed Filter

For simulations of the proposed structure, IE3D electromagnetic simulator is used. The size of whole circuitry is 33:7 × 29:3 mm. Differential ports are used in the structure to indicate finite plane instead of infinite ground plane for better results (Fig. 2). Figure 3 shows simulated and measured results for S_{11} and S_{21} parameters for the filter. From results, we found that the passband frequencies of the designed filter are centered at 2.017, 2.63, 4.06, and 4.6 GHz, respectively. The 3-dB bandwidths according to resonant frequencies are of 152.03, 154.65, 201.83, and 128 MHz, respectively. S_{11} represents return loss, i.e., how much power reflected from filter. So, for better performance, it should be below −10 dB. The return loss at four resonant frequencies is −20.89, −27.086, −20.88, and −15.67 dB, respectively. S_{21} represents insertion loss of the filter and should be near to 0 dB. The insertion

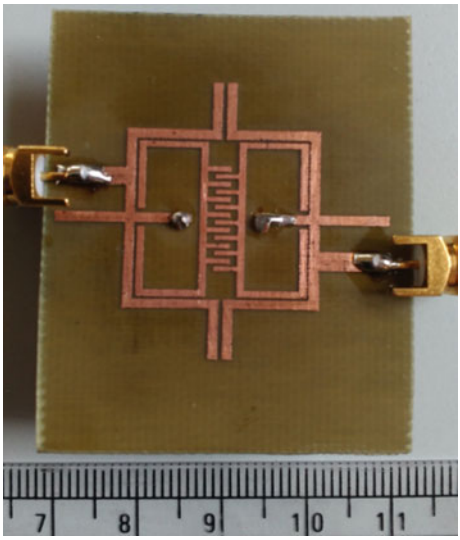


Fig. 2 Front view of fabricated proposed quadband filter

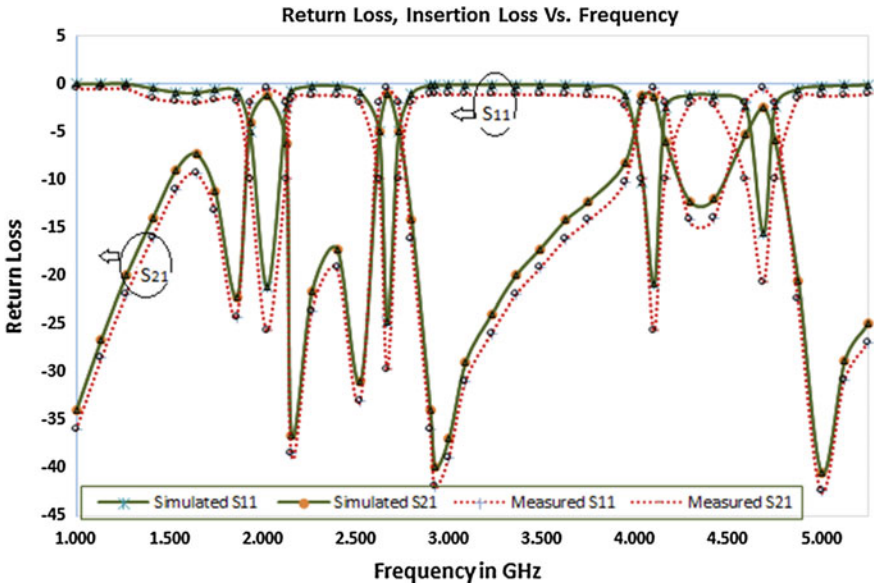


Fig. 3 Simulation and measured results for S-parameters of proposed quadband filter

loss for the proposed design at four centered frequency is −0.89, −1.28, −1.3, and −1.8 dB, respectively which results in high selectivity and low losses. Transmission zeroes have been inserted with each side in passband so as to improve skirt

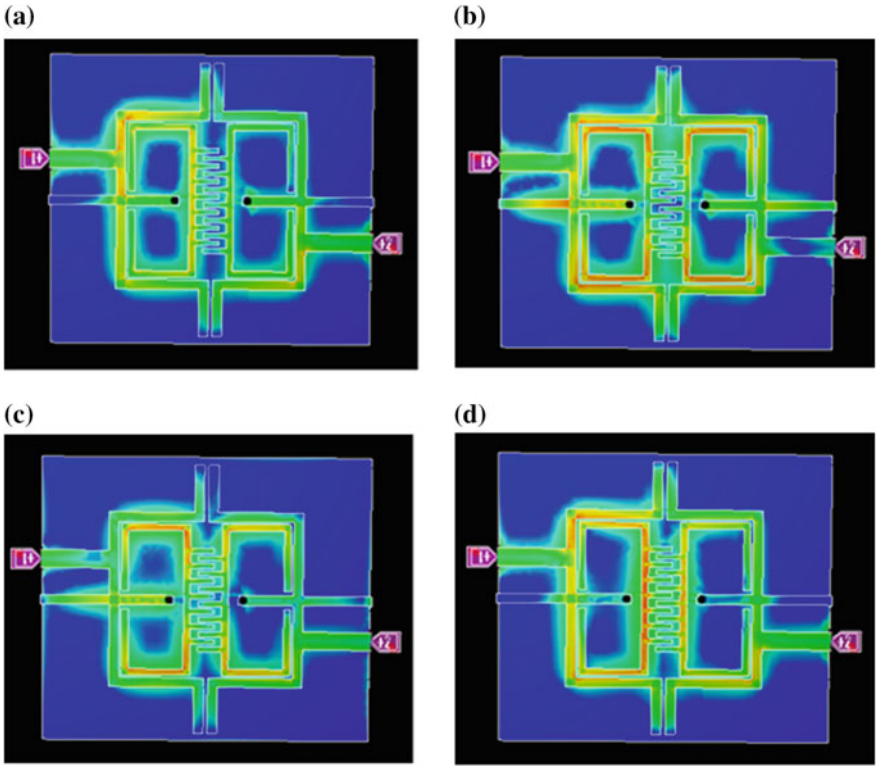


Fig. 4 Current distributions of proposed quadband filter. **a** At 2.017 GHz **b** At 2.63 GHz **c** At 4.06 GHz **d** At 4.6 GHz

selectivity and to enhance the rate of roll-off. Total five Transmission zeroes are created at 1.9, 2.19, 2.52, 2.92, 4.37, and 5 GHz frequencies. The current distribution for proposed quadband filter at four centered frequency is shown in Fig. 4.

6 Conclusion

Since the size reduction and designing low profile structures are a trend in RF circuit design and gaining momentum. Designing of multiband filter is the most challenging issue. By making changes in the stub-loaded resonator, geometry from T-shape to plus-shaped stub-loaded resonator, quadband filter is proposed. Short stub is added in the plus-shaped stub-loaded resonator which is responsible for adding one resonant frequency. Length of the stubs controls operating resonant frequencies. The simulated and measured results are very close to each other which proves the efficacy of proposed design. There are minor mismatches between the simulated and measurement results, it is because of error in measurement system.

References

1. Fu-Chang Chen and Qing-Xin Chu, (2009): Design of Compact Tri-Band Band-pass Filters Using Assembled Resonator, IEEE Transactions on Microwave Theory and Techniques, Vol. 57, No. 1.
2. Ching-Her Lee, Chung-I. G. Hsu and He-Kai Jhuang, (2006): Design of a New Tri-Band Microstrip Bandpass Filter Using Combined Quarter Wavelength SIRs, IEEE Microwave And Wireless Components Letters, Vol. 16, No. 11.
3. Li Gao, Jun Xiang Quan Xue, (2014): Novel Compact Tri-band Bandpass Filter Using Multistub Loaded Resonator, Progress in Electromagnetics Research Vol. 50, 139–145.
4. Haiwen Liu, Xiaomei Wang, Shen Li, Yu long Zhao, Xuehui Guan, (2014): Quadband Bandpass Filter Using Quadmode Stub Loaded Resonator, ETRI journal, Vol 36, pp 690–693, No.4.
5. Xiu Yin Zhang, Jian-Xin Chen, Quan Xue and Si-Min Li, (2007): Dual Band Bandpass Filters Using Stub Loaded Resonators, IEEE Microwave And Wireless Components Letters, Vol. 17, No. 8.
6. Xiu Yin Zhang, Quan Xue and Bin Jie Hu, (2010): Planar TriBand Bandpass Filter With Compact Size, IEEE Microwave and Wireless Components Letters, Vol. 20, No. 5.
7. F.C. Chen, Q.X. Chu, and Z.H. Tu, (2008): Triband Bandpass Filter Using Stub Loaded Resonators, Electron. Lett, vol. 44, no. 12, pp. 747–749.
8. X. Y. Zhang, J.-X. Chen, Q. Xue, and S.-M. Li, (2007): Dual-band bandpass filter using stub loaded resonators, IEEE Microw. Wireless Compon. Lett., vol. 17, no. 8, pp. 583–585.
9. M. D. C. Vellazquez-Ahumada, J. Martel, F. Medina and F. Mesa, (2010): Application of stub loaded folded stepped Impedance resonators to dual band Filter Design, Progress In Electromagnetics Research, PIER 102,pp. 107–124.
10. Yuan Chun Li, Hang Wong, and Quan Xue, (2011): Dual-Mode DualBand Bandpass Filter Based on a Stub-Loaded Patch Resonator, IEEE Microwave and Wireless Components Letters, Vol. 21, no.10.

Gait-Based Human Recognition by Multiple Wavelet Coherence

Sagar Arun More and Pramod Jagan Deore

Abstract In this paper we use Multiple Wavelet Coherence (MWC) for the recognition of human using gait. MWC is analogous to multiple correlation which results coherence of multiple independent signals on dependent one. It describes the region of proportionate wavelet power of independent signals. We extract 1D dependent signals generated due to shoulders and hand movement and independent signals generated due to leg movement. We compute MWC of each sequence of all 20 subjects of CASIA-A gait database walking at an angle 0° to the image plane. Experimental results show that MWC preserves significant discriminant information of walking individual. Finally PCA is used to train the proposed system and for testing we use nearest neighbor method. Cumulative match score is used to evaluate the proposed system.

Keywords Gait recognition · Multiple wavelet coherence · Principle component analysis

1 Introduction

Human identification and recognition at a distance using gait is gaining momentum since last decades. It has numerous advantages like noninvasive, works from a distance, and can work with low quality video. Most of the first generation biometrics require subject's physical contact with the device and willingness to get identified. This second generation biometric technology does not require subject's physical contact with the device and willingness to get identified as well. Because of these advantages lot of researchers get attracted towards this technology. Gait is

S.A. More (✉) · P.J. Deore
Department of Electronics and Telecommunication Engineering,
R. C. Patel Institute of Technology, Shirpur, India
e-mail: sagar.more27@gmail.com

P.J. Deore
e-mail: pjdeore@yahoo.com

© Springer Science+Business Media Singapore 2017

R. Singh and S. Choudhury (eds.), *Proceeding of International Conference on Intelligent Communication, Control and Devices*, Advances in Intelligent Systems and Computing 479, DOI 10.1007/978-981-10-1708-7_88

simply the manner of his or her walking. It is already known that one can recognize a known person by the manner or style of walking, even when no fine details are available. This is best example of human intelligence. Beside of numerous advantages, gait recognition has few challenges also. The factors which affect the gait recognition are called as covariate factors. The gait can be affected by surface of walking, change in shoes, carrying bag, change in weight, pregnancy, injury at joint, drunkenness, etc. Viewing angle is also an important covariate factor. It plays a vital role in multiple camera scenarios. Lot of work has been done in gait-based human recognition. Few state-of-the art methods are discussed next.

2 Literature Overview

Gait-based human recognition can be broadly classified into two approaches.

1. Model free [1–5]
2. Model based [6–10]

In all these approaches, the features are extracted based on shape analysis [5, 10], image geometry analysis [1–3], extracting gait energy image and then find some spectral features [4], wavelet analysis [8] and so on. In model free approach the features are directly extracted from image. In [5], Procrustes shape analysis is used to obtain mean shape. It is also called as eigen gait representation. After extracting silhouettes by using an improved background subtraction method each silhouette then unwrapped. The full Procrustes distance of this unwrapped vector which is the distance between boundary point and centroid of silhouette then used for classification and recognition. In [3], author proposed 3D approach. After background removal, they extract stereo gait feature which is the $L2$-norm of 3D stereo silhouette vector. After finding centroid, they unwrap 3D silhouette. The 3D silhouette vector is obtained by stereo vision method, which exhibits 3D coordinates of 2D scene. The stereo gait feature then obtained by taking $L2$ norm of stereo silhouette vector of each sequence. They extract this feature for each gait cycle which is extracted by autocorrelation function. The gait cycle is the function of ratio of height to width. For classification NN and ENN classifier based on Euclidean distance is used. Similarly soft biometric-based methods also have been proposed [1]. They use height and stride length as soft biometrics. In model based approach, the human body is modeled and various parameters of that model are then extracted for analysis and recognition. This approach is little bit computationally complex than model free. In an earlier approach [9], the gait pattern is detected in XYT spatiotemporal volume. Further they fit it with snake. Snake are used to find the bounding contour of walking subject. These contour then used to control a 5-stick human model. They measure angle signals from complete sequence which is modeled by the 5-stick human model. In [8], author fuses features like wavelet descriptor and human skeleton model for multiple views. First they model human

body by skeleton model which has eight key points including; midpoints of head, neck, shoulder, hip, knees, malleolus. The feature vector is constructed by all these key points. Further they extract boundary–centroid distance of each silhouette. Wavelet is applied to this distance and wavelet descriptor feature is preserved. Finally they fuse these two features to construct feature space. SVM is deployed for classification. Since gait energy image representation is unable to provide dynamic information, [7] modeled gait cycle as a chain of key poses and extracted features like pose energy image. First they estimate key pose by K-means clustering of all the PCA transformed silhouettes across gait cycle followed by pose classification. The state transition model is deployed to form the chain of estimated key poses. Finally they compute pose energy image which preserves dynamic and shape information. NN classifier is then used for classification.

2.1 Wavelet Coherence Overview

Wavelet analysis is always been a useful and famous tool for analyzing localized variations in a signal. It gives time–frequency representation of signal. In [11], author provides a step-by-step guide to wavelet analysis. Here they consider the El-Nino Southern Oscillations (ENSO) and gridded sea level pressure. They analyzed the wavelet spectrum of above said parameters across hundreds of years. The cross wavelet spectrum is analyzed of various meteorological data for future prediction. One of the pioneering works has been done by [12], in which application of cross wavelet transform and wavelet coherence to the geophysical data has been explored. Following this approach, [13] modified the technique of wavelet coherence. Recently, [14] has shown that it can also be applied in biomedical field for ECG pattern analysis and classification. Inspired by the results of [13, 14], we concentrate our research activity towards exploring the significance of wavelet coherence, specifically MWC in gait-based human recognition.

2.2 Main Contribution of this Paper

- We attempt to develop a simple model free gait-based human recognition system using MWC of various body parts which is not proposed yet as per our best of knowledge.
- Unlike most of the methods reported in literature, which use model based approach for extracting dynamic body features, our method directly analyzes the spatiotemporal gait patterns,
- As the features are extracted using movement of body parts from the silhouettes of gait sequences, the system is insensitive to the color and texture.

3 Multiple Wavelet Coherence Based Human Recognition

3.1 Wavelet Coherence of 1D Signals

Wavelet coherence is the measure of relationship between two independent processes which are expressed in terms of time series most often. It gives the area of common frequency band along with the time interval, across which these two signals vary simultaneously. It also reveals phase relationship between these two series. Most of theory in this section is taken as it is from [12, 13] because it is self-contained. Following [13], wavelet coherence between *Xn* and *Yn* can be written as follows:

$$\mathrm{WC}(Xn, Yn) = \frac{|\varsigma[W(Xn;\ Yn)]|}{\sqrt{\varsigma[W(Xn)]X\varsigma[W(Yn)]}} \tag{1}$$

where, ς is smoothing parameter,
$[W(Xn)]$ and $[W(Xn)]$ are wavelet transforms,
$[W(Xn, Yn)]$ is cross wavelet transform of both series.
The cross wavelet transform of two given series is given as follows:

$$W(Xn,\ Yn) = W(Xn) \cdot W(Yn)^{*} \tag{2}$$

where $W(Xn)$ is continuous wavelet transform and * is complex conjugation.
The cross wavelet power can be defined as

$$Wp = |W(Xn, Yn)| \tag{3}$$

The local relative phase between *Xn* and *Yn* can be expressed as complex argument,

$$\Phi n = \arg(W(Xn, Yn)) \tag{4}$$

The complete representation of cross wavelet spectrum is

$$W(Xn, Yn) = |W(Xn; Yn)|e^{i\emptyset n} \tag{5}$$

where Φn is the phase at time *tn*.

3.2 Multiple Wavelet Coherence

MWC is analogous to the multiple correlation which reveals wavelet coherence of multiple independent processes on dependent. It is the localized correlation in time–frequency domain. MWC reveal the fraction of the wavelet power of dependent time series which is fully explicable by independent time series. Let consider three time series *Xn*, *Yn* and *Zn*, assuming *Yn* and *Zn* as independent and *Xn* as dependent time series. Following [13], MWC of these time series or signals can be expressed as

$$\mathrm{MWC} = \frac{WC(Xn,Zn) + WC(Xn,Yn) - 2\sqrt{Re[WC(Xn,Zn)\cdot WC(Xn,Yn)^{*}\cdot WC(Yn,Zn)^{*}]}}{1 - WC(Yn,Zn)} \tag{6}$$

3.3 Proposed Gait Recognition Method

We propose a simple gait recognition method based on MWC of moving body parts using model free approach. We analyze spatiotemporal gait patterns which preserves the MWC of various dynamic body parts which are responsible for gait.

3.4 Pre-processing

For this experiment, we use CASIA A database [15] which has readily available silhouettes of 20 persons walking at angles 0°, 45°, and 90°. It has four sequences for each angle, let us call them as *S*1–*S*4. In total it has 12 sequences of each person. We perform our experiment on these sequences considering the person is walking at an angle 0 with the image plane so that the features can be extracted. In the sequences *S*1 and *S*3 person is walking from right to left in the image plane and in *S*2 and *S*4, the person is walking from left to right. Many of the silhouettes have breaks or holes. Morphological operations like opening and closing are done to fill these breaks and holes. Following [16], we set a quality factor Q and select only a quality gait cycle from each sequence, which further we use for feature extraction.

3.5 1D Signal Extraction

After selecting a quality gait cycle, we divide it into three parts which contain body parts like shoulders, hands and legs. Further we extract 1D signals from each quality gait cycle. Considering *Xn* as 1D signal, generated due to legs movement, i.e., gait cycle. *Yn* is 1D signal, generated due to hands swing and Zn is the 1D

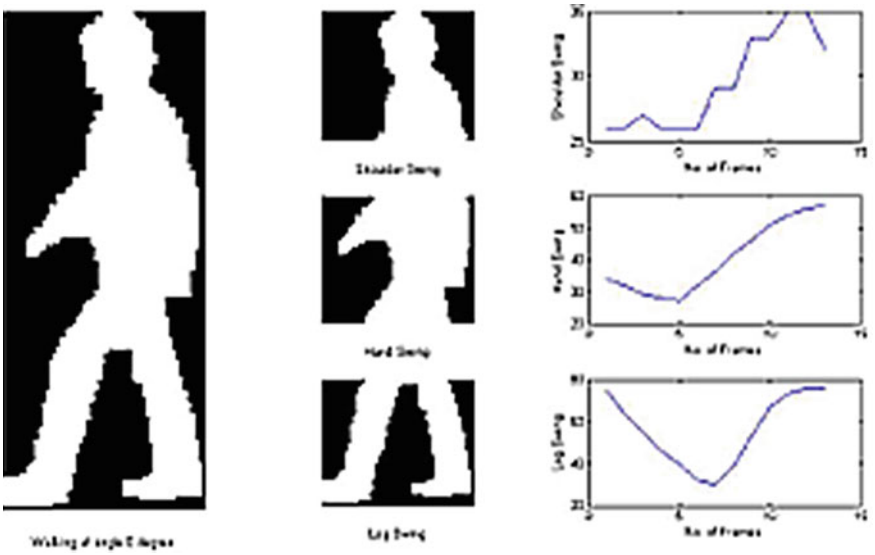


Fig. 1 1D Signals extraction of person 'fyc' from *S*1

signal, generated due to shoulders movement. Three 1D signals extracted are shown in Fig. 1. Here we assume that leg movement is dependent process and shoulders' and hands' swing are independent. Most persons have their unique style of walking with variable swing and extent of hand and shoulder. They have different walking speeds, stance and heal strikes also. In this research work we investigate the coherence among all these body parts with the help of multiple wavelet coherence. We use Morlet function as mother wavelet as it suits better for such application and considering the nature of signals in the regard of time and frequency localization.

The Morlet function,

$$\psi_0(\eta) = \pi^{\frac{-1}{4}} e^{i\omega_0\eta} e^{\frac{-1}{2}\eta^2} \tag{7}$$

where ω_0 is dimensionless frequency.

3.6 MWC of Dynamic Body Parts

Considering all the extracted 1D signals and using Eq. (6), MWC then calculated. We trained the system by all four sequences one at a time and tested on all. Figure 1 shows that the person 'fyc' from *S*1 sequence walking at an angle 0. After dividing the silhouette, the swing of shoulders, hands and legs is captured. The MWC among shoulder, hand and leg swing calculated by using Eq. (6) is shown in Fig. 2.

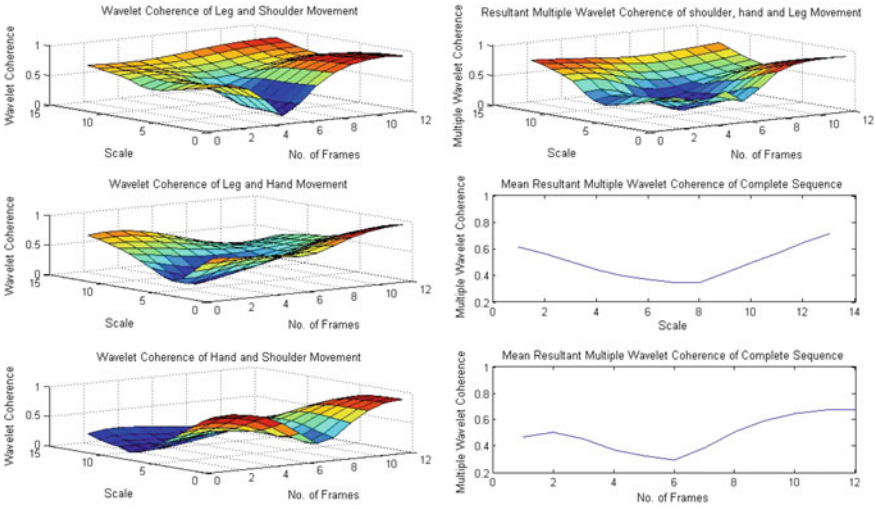


Fig. 2 MWC among shoulder, hand and leg swing of person 'fyc' in *S*1

For the similar person 'fyc' but from sequence *S*4, walking is at an angle 0 from left to right, Fig. 3 shows the person along with its all extracted 1D signals and its MWC among body parts.

We extract 1D signals from all 20 persons walking at an angle of 0° to the image plane followed by calculating the multiple wavelet coherence. Principal component analysis is deployed to train and test the proposed system. PCA is the conventional way for dimension reduction of feature vector and at the same time it preserves maximum variance among the patterns. The eigenvectors shows the direction of highest variance. The eigenvector which has highest eigenvalue is the principle component of the data. The feature vector which contains MWC of all the sequences preserved as template by projecting it on eigenvectors, i.e,. eigenspace of MWC. In testing, first the variance of test sequence is found and then projected on eigenspace of MWC. We use nearest neighbor classifier which has Euclidean distance as similarity measure. To evaluate the proposed method, we use

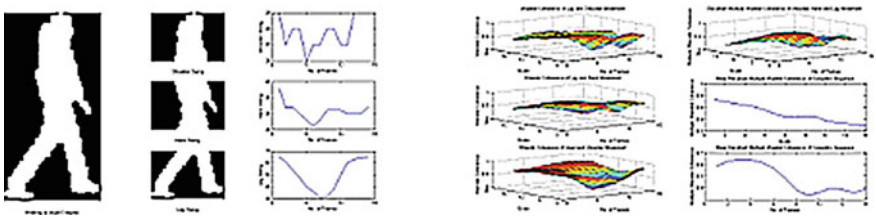


Fig. 3 1D Signals extraction of person 'fyc' in *S*4 and MWC among shoulder, hand and leg

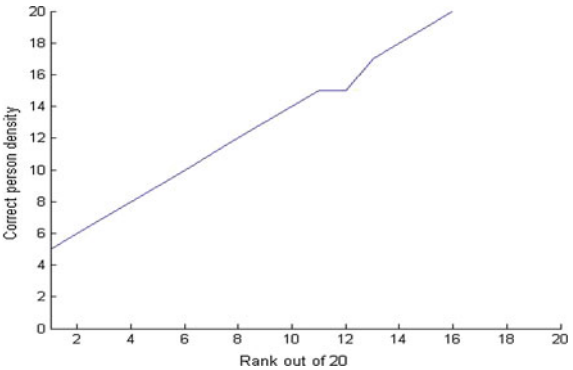


Fig. 4 Trained by sequence *S*1 and tested on sequence *S*3

cumulative match score. We trained the system by all the sequences one at a time and tested on all. Figure 4 shows the cumulative match scores of various training and testing sequences.

4 Conclusion

From experimental results it is observed that the MWC preserve discriminant information about walking person. Hence, it can be used as novel feature for gait-based human recognition. In this work, the sequences in which the person is walking at an angle of 0° to the image plane are considered so that movements of shoulders, hand and legs can be captured. We found that the rank 1 results are average in all combination of training and testing sequences but rank 5 and 10 results are encouraging. This might be because of change of phase angle between the moving body parts of same person in different sequences. This problem can be solved by assigning membership function consists some high and low threshold of phase variation for each person. Further it has been observed that the overall process of walking has certain coherence among the body parts which are responsible for gait. In this work we considered single view only, in future we will try to build a multiview gait recognition system.

Acknowledgments Portions of the research in this paper use the CASIA Gait Database collected by Institute of Automation, Chinese Academy of Sciences.

References

1. Konstantinos Moustakas, Dimitrios Tzovaras and Georgios Stavropoulos,: Gait Recognition Using Geometric Features and Soft Biometrics, IEEE Signal Processing Letters, Vol. 17, No. 4, (2010) 367–370.
2. Nikolaos V. Boulgouris, Konstantinos N. Platamiotis and Drimitris Hatzinakos: Gait Analysis and Recognition using Angular Transforms, In: Canadian Conference on Electrical and Computer Engineering, Vol. 3, (2004) 1317–1320.
3. Haitao Liu, Yang Cao and Zengfu Wang: Automatic Gait Recognition from a Distance, In: Chinese Control and Decision Conference, CCDC, (2010) 2777–2782.
4. Sungjun Hong, Heesung Lee and Euntai Kim: Fusion of Multiple Gait Cycles for Human Identi_cation, In: ICROS-SICE International Joint Conference, (2009) 3171–3175.
5. Liang Wang, Tieniu Tan, Weiming Hu and Huazhong Ning: Automatic Gait Recognition Based on Statistical Shape Analysis, IEEE Transactions on Image Processing, Vol. 12, No. 9, (2003) 1120–1131.
6. Xiaxi Huang and Nikolaos V. Boulgouris: Model-Based Human Gait Recognition using Fusion of Features, In: IEEE International Conference on Acoustics Speech and Signal Processing, Vol. 3, (2009) 1469–1472.
7. Aditi Roy, Shamik Sural and Jayanta Mukherjee,: Gait Recognition using Pose Kinematics and Pose Energy Image, Signal Processing, Elsevier Vol. 92, No. 3, (2012) 780–792.
8. Dong Ming, and Cong Zhang, Yanru Bai, Baikun Wan, Yong Hu and KDK Luk: Gait Recognition Based on Multiple Views Fusion of Wavelet Descriptor and Human Skeleton Model, In: IEEE International Conference on Virtual Environments, Human-Computer Interfaces and Measurement Systems (VECIMS), (2009) 246–249.
9. Sourabh A. Niyogi and Edward H. Adelson: Analyzing and Recognizing Walking Figures in XYT, In: Computer Vision and Pattern Recognition (CVPR), (1994) 469–474.
10. David K. Wagg, and Mark S. Nixon: On Automated Model-Based Extraction and Analysis of Gait, In: Sixth IEEE International Conference on Automatic Face and Gesture Recognition, (2004) 11–16.
11. Christopher Torrence and Gilbert P. Compo: A Practical Guide to Wavelet Analysis, Bulletin of American Meterological Society, (1997) 61–77.
12. A. Grinsted, J. C. Moore and S. Jevrejeva: Application of The Cross Wavelet Transform and Wavelet Coherence to Geophysical Time Series, Nonlinear Processes in Geophysics, Vol. 11, No. 5/6, (2004) 561–566.
13. Eric K. W. Ng and Johnny C. L. Chan: Geophysical Applications of Partial Wavelet Coherence and Multiple Wavelet Coherence, Journal of Atmospheric and Oceanic Technology, Vol. 29, (2012) 1845–1853.
14. Swati Banerjee and Madhuchhanda Mitra: Application of Cross Wavelet Transform for ECG Pattern Analysis and Classification, IEEE Transactions on Instrumentation and Measurement, Vol. 63, No. 2, (2014) 326–333.
15. CASIA Gait Database, http://www.sinobiometrics.com.
16. Sagar More, Pramod Deore: Human Gait Recognition by Silhouette Vector and Principle Component Analysis, International Journal of Computer Applications, (2014) 1–5.

Automatic Segmentation of Brain MRI of Newborn and Premature Infants Using Neural Network

Tushar H. Jaware, K.B. Khanchandani and Anita Zurani

Abstract This paper focuses on the development of an accurate neonatal brain MRI segmentation algorithm and its clinical application to characterize normal brain development and investigate the neuro anatomical correlates of cognitive impairments. Neonatal brain segmentation is more challenging field because of anatomical variation and rapid brain development in the neonatal period. Segmentation of neonatal brain MR images is a fundamental process in the study and assessment of newborn brain development. Adult brain MRI segmentation techniques are not suitable for neonatal brain, because of substantial contrasts in tissue and structure properties between neonatal and adult brains. In this paper, we proposed an atlas free model to segment the newborn brain MRI images, using neural network approach. The segmentation of the neonatal brain in MR Imaging is a prerequisite to obtain quantitative measurements of regional brain structures.

Keywords Automatic segmentation · Cerebra-spinal fluid (CSF) · Gray matter (GM)

1 Introduction

The use of MRI in neuroimaging has revolutionized health care with its potential to obtain noninvasive sectional images of the brain without using ionizing radiations. [1] Brain MRI is used to investigate seizures, strokes, infections and injuries of the

T.H. Jaware (✉) · K.B. Khanchandani · Anita Zurani
Department of Electronics and Telecommunication Engineering,
Shri Sant Gajanan Maharaj College of Engineering, Shegaon, India
e-mail: tusharjaware@gmail.com

K.B. Khanchandani
e-mail: kbkhanchandani@rediffmail.com

Anita Zurani
e-mail: anitazurani@gmail.com

© Springer Science+Business Media Singapore 2017

R. Singh and S. Choudhury (eds.), *Proceeding of International Conference on Intelligent Communication, Control and Devices*, Advances in Intelligent Systems and Computing 479, DOI 10.1007/978-981-10-1708-7_89

brain, hemorrhages, brain tumors, multiple sclerosis, neurodegenerative diseases such as Alzheimer's, and others [2, 3].

Currently, tissue segmentation and clinical interpretation of brain scans is the onus of neuro radiologists with computers being used only to enhance the visualization. Since MR data is voluminous, a completely manual analysis is tedious and time consuming; it is also very subjective and prone to user variability [4].

Automating the segmentation process will favor faster and reproducible results and be the first step toward a volumetric analysis of the brain tissues. Though automated brain extraction and segmentation of the adult brain is a well researched area with plenty of supporting literature [6–12], these approaches cannot be extended to the neonatal brain due to its inverted contrast in white and Gray Matter (GM) [13].

This has led to the development of techniques devoted to segmenting the neonatal brain in the last decade. For neonatal MRI diagnosis it is important to classify the segmented brain tissues. This classification is according to type of brain tissues, and abnormal tissue structures. The volumetric changes in neonatal brain MRI is used to classify, and analyze physiological processes and characterize brain related disease. The segmentation of brain tissues can be done manual as well as automatic. The process of automatic brain tissue segmentation goes through preprocessing, feature extraction, segmentation, and then classification.

Preprocessing of brain MRI images enhances the quality of image by reducing noise and motion artifacts. Image parameters can be extracted using feature extraction process. Segmentation separates the foreground and background pixel which can be use to define the boundaries of effected tissues, i.e., skull striping is performed and brain portion is separated in this process. After segmentation, classification, and labeling of the various brain tissues are performed, this can be used for image analysis purpose.

The aim of the research in this paper is to provide an accurate automatic method for segmentation of the newborn brain MRI. The quantitative analysis of the newborn brain is performed; this can lead to improved understanding of the development of the brain and will enable the impact of aberrant brain growth on subsequent neurodevelopment following preterm birth to be assessed.

Potential challenges in neonatal brain [14] MR image segmentation are as follows:

- Variable imaging parameters
- Overlapping intensities
- Partial voluming
- Nonintensity-based borders
- Shape complexity
- Susceptibility artifacts

2 Method and Material

In neuroimaging MRI provides great source of information for diagnosis and treatment planning of newborn infants. Therefore, it provides good platform for the researchers. Automatic segmentation and classification of brain MR images into tissue types: white matter (WM), gray matter (GM), and cerebra-spinal fluid (CSF) [15] (Fig. 1).

This section elucidates the system design and methodology which concerns its ultimate design and the features of the proposed method. The proposed system design is illustrated in Fig. 2.

The three phase structured model is used for classification of brain MR images into different tissues present in the brain.

2.1 First Segmentation Stage

The aim of the first stage was to label the voxels that can easily be assigned to a tissue class. WM, GM, and CSF can be differentiated based on their spatial characteristics and their intensity values.

2.2 Second Segmentation Stage

The first stage identified voxels for further analysis based on the posterior probability for each class. For these voxels, in addition to the previously computed features, the output of the first stage, i.e., the probabilities of a voxels to belong to each of the three tissues, was transformed into features.

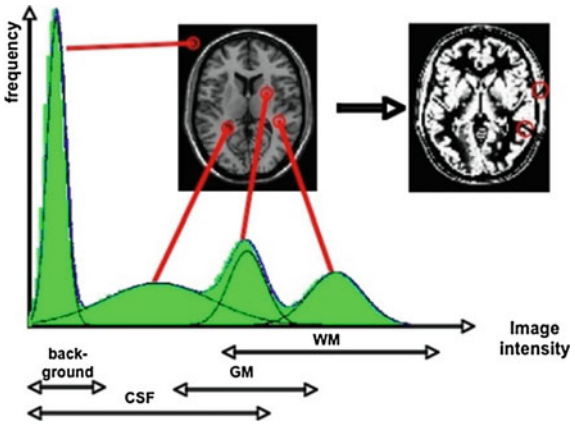


Fig. 1 Distribution of different tissues of brain

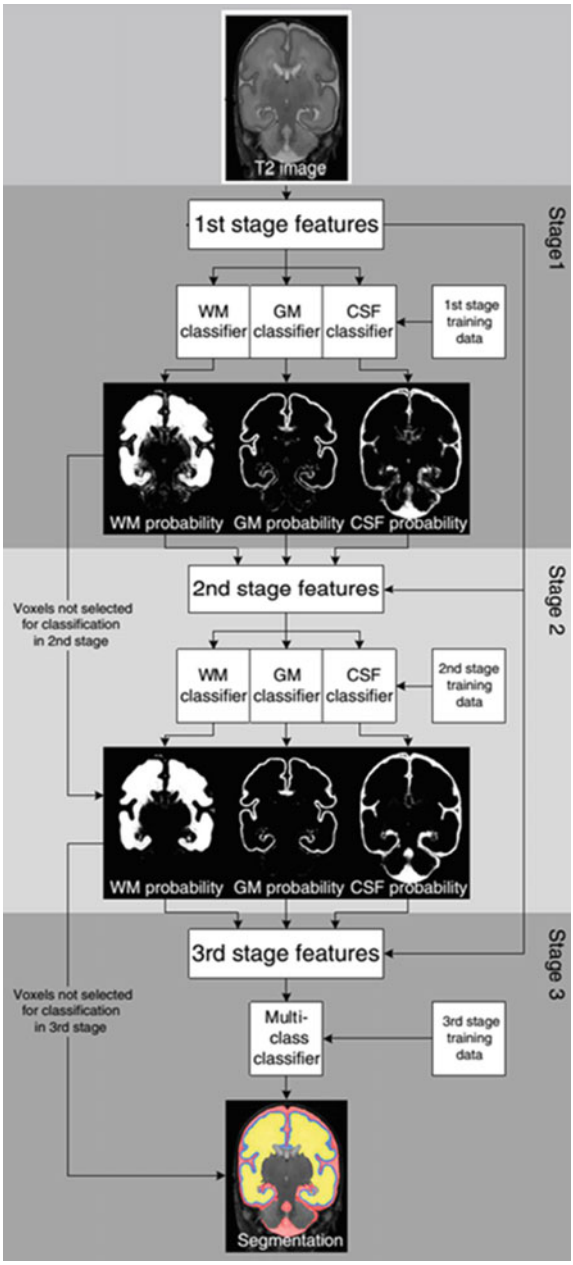


Fig. 2 Proposed three phase structured model

2.3 Third Segmentation Stage

Owing to the independent segmentation of each tissue in the first and second stages, some voxels might have been assigned to more than one tissue class, while others, in between tissue classes might have remained unclassified. These regions were resolved in the third segmentation stage.

3 Results

Figure 3 illustrates the Newborn brain MRI output of the various process used in the proposed system. Figure 3a shows the original Newborn MRI image Fig. 3b shows the Intensity corrected removed MRI, which is obtained by multi model intensity mathematical model. Figure 3c illustrates the preprocessed image. Then the classification of tissues and segmentation process is done by using neural network technique. The segmented image output using neural network technique is illustrated in Fig. 3d.

The performance parameter used here is dice similarity coefficient that can be used to monitor the performance of proposed and expert consensus method. Figure 4 shows evaluation based on the Dice similarity coefficient.

The different monitored parameters are GM—cortical gray matter, SGM—subcortical gray matter, WM—unmyelinated white matter, MWM—myelinated white matter, Bm—brainstem, Std—standard deviation, Cb—cerebellum (Fig. 5).

4 Conclusion

Here in this paper, we have developed a three phase model for newborn brain MR images using automatic segmentation technique. There are various challenges in segmentation of infant MR image than adults and children's MR image. Neonatal brain development is accompanied by large changes in the shape and appearance of structures. In addition, partial volume effects, and limited signal-to-noise ratio introduce challenges in the automatic techniques.

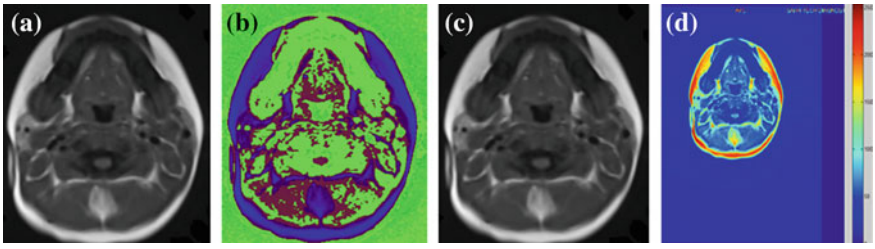


Fig. 3 **a** Original newborn MRI, **b** Intensity corrected newborn MRI, **c** Preprocessed newborn MRI, **d** Fully segmented newborn MRI

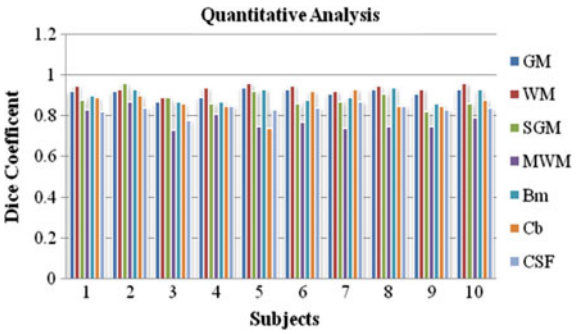


Fig. 4 Evaluation based on the dice similarity coefficient

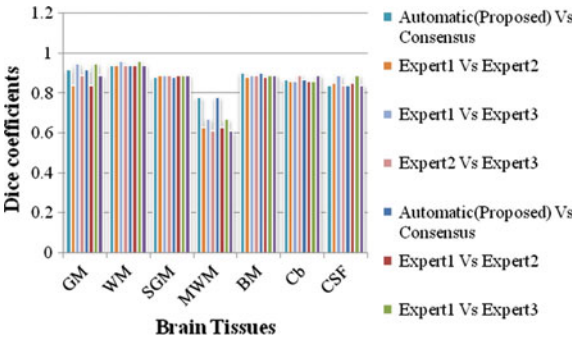


Fig. 5 Represents the comparison of the dice similarity coefficient with different manual segmentation

The presented method accurately segmented WM, CSF, and GM in T2-weighted images and is robust to differences in age and acquisition protocol. Furthermore, the method accurately segmented the images when trained with a limited number of training samples from the given population, without any additional parameter tuning. This reduces the time and effort required to create reference annotations and may therefore extend the applicability of the method. The resulting segmentations can be used for volumetric measurements and quantification of cortical characteristics. This analysis plays an important role for neurologist for early detection of neural disorders. Hence proposed research work will provide more information to neuro Physicians for better treatment of newborn babies.

References

1. Chelli Devi.N, Anupama Chandrasekharan, V. K. Sundararamanand Zachariah C. Alex, "Neonatal brain MRI segmentation: A review", Computers in biology and medicine, Vol. 64, pp. 163–178, 2015.
2. A. G.Kolk, J. Hendrikse, J.J.M. Zwanen burg, F. Visser, P. R. Luijten, Clinical applications of 7T MRI in the brain, Eur. J. Radiol. 82 (2013) 708–718.

3. Magnetic Resonance Imaging (MRI) of the head, Web MD Medical Reference from Health wise. Available: (http://www.webmd.com/brain/magnetic-resonance-imaging-mri-of-the-head), 2015.
4. P. Suetens, Fundamentals of Medical Imaging, seconded. Cambridge University Press (2009) 159–189.
5. J. Ashburner, K.J. Friston, Unified segmentation, NeuroImage 26(2005) 839–851.
6. H. Greenspan, A. Ruf, J. Gold Berger, Constrained Gaussian mixture model framework for automatic segmentation of MR brain images, IEEE Trans. Med. Imaging 25(9) (2006) 1233–1245.
7. Zhang B., Zhu W., Zhu H., Song A., Zhang W., A SVM based automatic segmentation method for brain magnetic resonance image series, in: Proc. of Symposia and Workshops on Ubiquitous, Autonomic and Trusted Computing, 2010, pp. 375–379.
8. H. Zhang, J. Liu, Z. Zhu, H. Li, An automated and simple method for brain MR image extraction, Biomed. Eng. Online 10(81) (2011).
9. S. Datta, P. A. Narayana, Automated brain extraction from T2-weighted magnetic resonance images, J. Magn. Reson. Imaging 33(4) (2011) 822–829.
10. K. Somasundaram, T. Kalaiselvi, fully automatic brain extraction algorithm for axialT2-weighted magnetic resonance images, Computer. Biol. Med. 40 (2010) 811–822.
11. K. Somasundaram, T. Kalaiselvi, Automatic brain extraction methods for T1 magnetic resonance images using region labeling and morphological operations, Computer. Biol. Med. 41 (2011) 716–725.
12. M. Cabezas, A. Oliver, X. Lladó, J. Freixenet, M. B. Cuadra, A review of atlas-based segmentation for magnetic resonance brain images, Computer. Methods Programs Biomed. 104 (2011) e158–e177.
13. H. Xue, L. Srinivasan, S. Jiang, M. Rutherford, A.D. Edwards, D. Rueckert, J.V. Hajnala, Automatic segmentation and reconstruction of the cortex from neonatal MRI, NeuroImage 38 (2007) 461–477.
14. M. Prastawa, J. H. Gilmore, W. Lin, and G. Gerig, "Automatic segmentation of MR images of the developing newborn brain," Med. Image Anal., vol. 9, no. 5, pp. 457–466, Oct. 2005.
15. Bhattacharya S., Manlik U., Dutta P. A pruning algorithm for efficient image segmentation with neighbourhood neural networks. IAENG International Journal of Computer Science 2008.

An Efficient Handoff Using RFID Tags

Sadip Midya, Asmita Roy, Koushik Majumder, Debashis De and Santanu Phadikar

Abstract With the introduction of VANET, inter-vehicular communication and communication between vehicle and network infrastructure has become very convenient. This advancement has brought in challenges with itself. The vehicles are mobile; moving around with very high speed whereas infrastructure is stationary. Thereby handoff plays a critical role in VANET. In our approach, we have used radio frequency identification (RFID) tags for efficient hand off mechanism with reduced delay. RFID tags are deployed in the chassis of every vehicle containing the unique MAC address of that vehicle. RFID scanners are deployed on road which scans the RFID tags and sends the MAC address to the handoff gateway which communicates the information to the nearest access point. This makes the access point aware of the incoming vehicle thereby reducing the delay. Using this novel approach not only the delay in handoff is reduced but also hand off is performed efficiently with minimal information.

Keywords RFID · VANET · Handoff delay

Sadip Midya (✉) · Asmita Roy · Koushik Majumder · Debashis De · Santanu Phadikar
Department of Computer Science and Engineering, West Bengal University of Technology, BF 142 Salt Lake Sector 1, Kolkata, India
e-mail: sadip20@gmail.com

Asmita Roy
e-mail: asmitaroy2002@gmail.com

Koushik Majumder
e-mail: koushikzone@yahoo.com

Debashis De
e-mail: dr.debashis.de@gmail.com

© Springer Science+Business Media Singapore 2017

R. Singh and S. Choudhury (eds.), *Proceeding of International Conference on Intelligent Communication, Control and Devices*, Advances in Intelligent Systems and Computing 479, DOI 10.1007/978-981-10-1708-7_90

1 Introduction

The advancement of wireless communication technology allows accessing internet connection from anywhere anytime. VANET provides a low cost solution for communication network for vehicles. vehicle to vehicle (V2V) and vehicle to infrastructure (V2I) communication is very important to receive emergency warnings, information about heavy traffic locations, finding alternate routes, etc. At the same time seamless connection for video conferencing and voice call is also desired while moving in vehicles [1]. In recent times the number of vehicle on road is increasing gradually. This in turn leads to increase in data rates demand. It is always a crucial decision as to which access point a moving vehicle should be handed over for efficient network coverage. At the same time the delay of the decision system should be minimized. To materialize the IoT concept RFID (Radio Frequency Identification Reader) tags are used. They are small electronic chip with an antenna. The data storage capacity of any RFID tags is up to 2 Kb. They provide a unique identification for every object they are attached to by storing their unique information in its memory. These tags can be scanned from a distance of 20 feet. In this scheme RFID tags are embedded in the moving vehicle containing the MAC address of every vehicle. RFID scanners are placed on road for scanning the moving vehicle. This will reduce the delay in decision as to which access point the vehicle should connect to.

2 Related Works

Among the various handoff schemes available [2] does not make use of CoA and identifies each vehicle with its unique home address. Reference [3] uses two kinds of buses a real bus and a virtual bus to perform handoff more efficiently. It also uses CoA to identify each vehicle in the network, which is assigned using IP passing or IP exchange. References [4, 5] show how RFID tags can be used on the streets for controlling the speed of vehicles and also positioning vehicles on road. Another scheme [6] shows a global vehicle mobility scheme using LVMM and GVMM. In [7] two types of vehicles relay vehicles (RV) and small vehicles (SV) are used where the small vehicles are connected to the relay vehicles and the relay vehicles are connected to the infrastructure. This allowed lesser load on the infrastructure.

3 System Architecture

In this scheme the bottom of every vehicle chassis is equipped with a RFID tag. A RFID tag scanner strip is placed on road. A RFID scanner strip consists of an array of RFID scanners. The RFID scanner strip is placed between two APs, in such

a way that it is equally distant from both the access points. Scanner strips placed on road scans the RFID tags present on the vehicle. Every vehicle's RFID tag contains the MAC address of the vehicle. A collection of access points forms a subnet which is controlled by a single access router. For efficient maintenance of vehicles in a subnet, local vehicle server (LVS) is used as shown in Fig. 1. The local vehicle server maintains a vehicle relation table which has three fields MAC address of vehicle, IPv6 address of access point, IPv6 address of vehicle. The global vehicle server (GVS) stores and maintains a vehicle locality table which has two fields IPv6 address of vehicle and the IPv6 address of the access router (AR). Another table known as the vehicle address table is also maintained by the GVS, which stores the Home Address of vehicles. The Home address is obtained from the Home Agent at the time of startup. The vehicle address table then stores the home IPv6 address along with the MAC address of the vehicle in the vehicle address table. The vehicle relation table manages all the vehicles which fall under the subnet of the particular local vehicle server, whereas the vehicle locality table keeps track of where the vehicle is currently present in the network (Figs. 1 and 2). The Tables maintained is shown in Fig. 2.

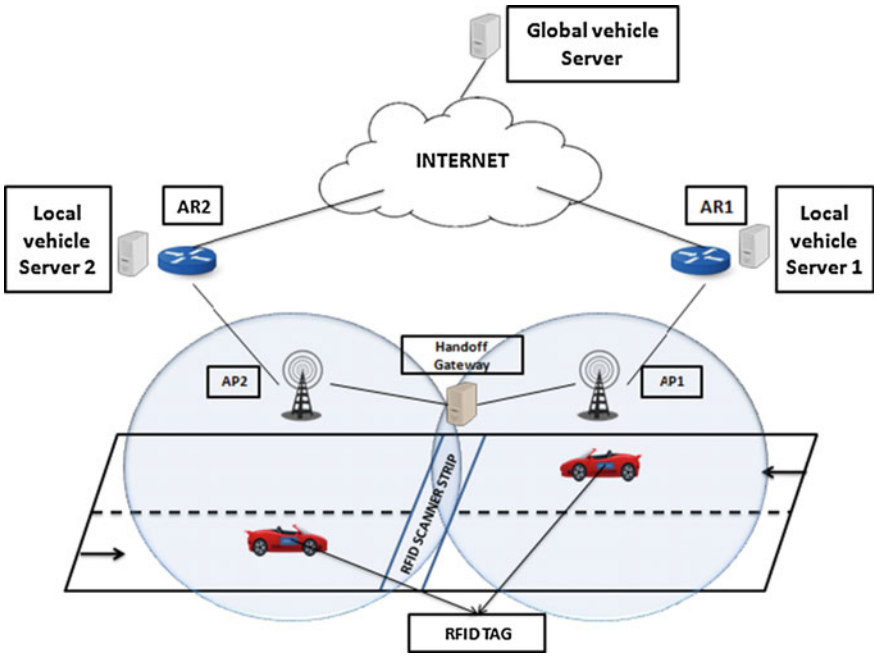


Fig. 1 System architecture

IPv6 address of vehicle	IPv6 address of Access Point	MAC address of vehicle

(a) Vehicle Relation table

IPv6 address of vehicle	IPv6 address of Access Router

(b) Vehicle Locality table

MAC address of vehicle	Home IPv6 address of vehicle

(c) Vehicle Address table

Fig. 2 Tables maintained

4 Handoff Procedure

When a vehicle passes over a scanner strip, the scanner strip scans the RFID tags attached to vehicles and sends the information on to the Handoff gateway. The Handoff Gateway notifies the AP on either side by sending a message containing the MAC address of the vehicle. Then the following operation takes place:

1. The new AP on reception of the MAC address forwards the message to the LVS as VEHICLE_UPDATE message.
2. The LVS then checks whether the MAC address is present in its vehicle relation table or not, if the MAC address is present
   (a) It checks whether the IPv6 address of the AP listed against it is same as the source of the VEHICLE_UPDATE message or not.
   (b) If it is different then it updates the vehicle relation table with the IPv6 address of the new AP.
   (c) If it is the same then nothing is done.
3. If the MAC address is not present it forwards the VEHICLE_UPDATE message to the GVS.
4. The GVS on reception checks its vehicle address table to find the entry of the vehicle with the obtained MAC address
   (a) If no entries are found then the vehicle address table is updated with the MAC address and the new home address of the vehicle.
   (b) If an entry is found then the GVS sends a VEHICLE_REG message back to the LVS containing the MAC address of the vehicle and the Home IPv6 address of the vehicle.
5. The LVS on reception of the VEHICLE_REG updates its vehicle relation table.
6. After updation, when a message arrives at the GVS it is routed to the vehicle via the respective AR and AP (Fig. 3). The message flow Diagram is shown in Fig. 3.

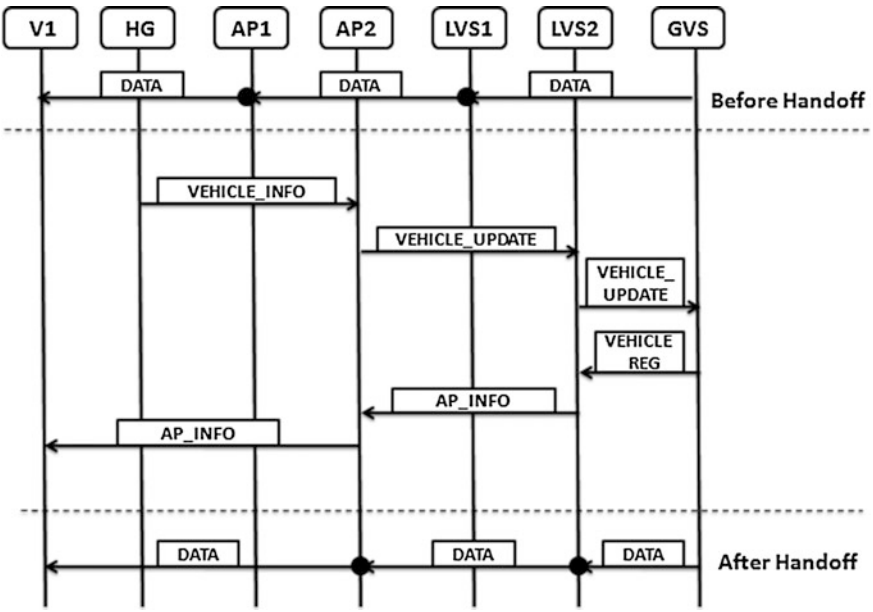


Fig. 3 Message flow diagram

5 Performance Evaluation

We evaluate our scheme by comparing it with GVMM to understand the advantages of our scheme in a better way. Let us say the handoff procedure for any scheme comprises of three phases, which are network detection, address configuration and registration. So, the handoff delay for any scheme is given by

$$T_{\mathrm{HL}} = T_{\mathrm{ND}} + T_{\mathrm{AC}} + T_{\mathrm{RG}}, \tag{1}$$

where T_{ND} stands for the time taken for a vehicle to detect the network. T_{AC} stands for the address configuration time and T_{RG} is the time taken for registration.

T_{AC} can be calculated by multiplying the time taken to exchange message between two nodes and the number of hops (n) required to acquire the message. T_{RG} can also be calculated by the same way, i.e., multiplying number of hops (n) with the time taken to perform update operation as given in (3) and (4).

$$T_{\mathrm{AC}} = n \cdot T_{\mathrm{MSG}} \tag{2}$$

$$T_{\mathrm{RG}} = n \cdot T_{\mathrm{UPD}} \tag{3}$$

Now we compare our scheme with GVMM. In both GVMM and our proposed scheme after a vehicle enters a network, data link layer handover takes place, i.e.,

the vehicle gets connected to the new AP in the data link layer before the network layer. So, T_{ND} remains the same for both GVMM and our proposed scheme.

$$T_{ND(GVMM)} = T_{ND(ProposedScheme)} \tag{4}$$

GVMM requires a care-of-address, so it requires configuring the address at the time of handoff for each vehicle. Acquiring the CoA requires 2 hops in GVMM. While in our scheme no CoA is required at the time of handoff as the vehicle is identified by the unique home address acquired from the home agent. So the value of T_{AC} for GVMM and our scheme is given by

$$T_{AC(GVMM)} = 2 \cdot T_{MSG} \tag{5}$$

$$T_{AC(ProposedScheme)} = 0 \tag{6}$$

The registration phase in both GVMM and our proposed scheme is the same requiring 4 hops for registering the vehicle so

$$T_{RG(GVMM)} = T_{RG(ProposedScheme)} = 4 \cdot T_{UPD} \tag{7}$$

By combining Eqs. (1), (4–7) we get

$$T_{HL(GVMM)} = T_{ND} + 2 \cdot T_{MSG} + 4 \cdot T_{UPD} \tag{8}$$

$$T_{HL(ProposedScheme)} = T_{ND} + 4 \cdot T_{UPD} \tag{9}$$

We can obtain the following graph at Fig. 4 based on the above equation if we take the value of T_{ND}, $T_{MSG,}$ and T_{UPD} to be 10 ms.

5.1 Results and Discussion

In Fig. 4 the performance of the proposed scheme as well as the GVMM scheme [6] is shown. Considering the various network parameters explained above the simulation is being carried out in Matlab 2010b. It is observed from the result that the delay in the network reduces a lot using our proposed scheme compared to GVMM. In VANET delay is critical network parameter so reducing it helps us in enhancing the QoS of the network.

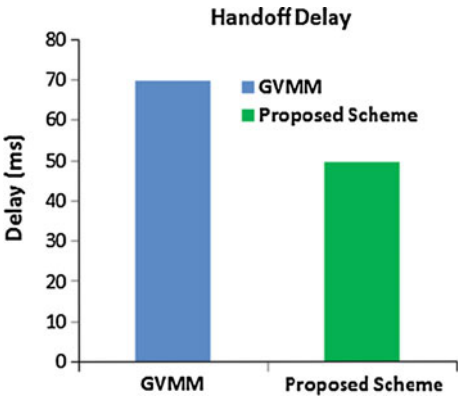


Fig. 4 Performance evaluation

6 Conclusion

This scheme takes the complexity of message transfer from the vehicle to the handoff gateway unlike GVMM where all the vehicles entering a particular network sends binding update messages which causes more packet collision leading to lowering the QoS of the network. Whereas in our scheme the rate of collision is reduced by using a single handoff gateway in between two access points which uses a single channel to communicate with the access point thus reducing packet collision. Also in this scheme the Handoff delay is reduced as this does not use any CoA and each vehicle is identified by its home address. So, compared to GVMM this scheme incorporates faster handoff.

Acknowledgments The authors are grateful to West Bengal University TEQIP II program and DST FIST program with reference number FIST/ETI/296/2011.

References

1. Lee, S., Sriram, K., Kim, K., Kim, Y. H., and Golmie, N.: Vertical handoff decision algorithms for providing optimized performance in heterogeneous wireless networks. Vehicular Technology, IEEE Transactions on (2009) 865–881.
2. Wang, X., and Qian, H.: A mobility handover scheme for IPv6-based vehicular ad hoc networks. Wireless personal communications (2013) 1841–1857.
3. Chen, Y. S., Hsu, C. S., and Cheng, C. H.: Network mobility protocol for vehicular ad hoc networks. International Journal of Communication Systems (2014) 3042–3063.
4. Chowdhury, A., Kumar, J., and Majumder, A.: A solution to speeding related problem in road vehicles using passive RFID tags. In Control, Instrumentation, Energy and Communication (CIEC), IEEE International Conference (2014) 96–100.
5. Lee, E. K., Oh, S. Y., and Gerla, M.: RFID assisted vehicle positioning in VANETs. Pervasive and Mobile Computing (2012) 167–179.

6. Lee, J. M., Yu, M. J., Yoo, Y. H., and Choi, S. G.: A new scheme of global mobility management for inter-vanets handover of vehicles in v2v/v2i network environments. In Networked Computing and Advanced Information Management. IEEE Fourth International Conference (2008) 114–119.
7. Chen, L., Cai, X., Sofia, R., and Huang, Z.: A cross-layer fast handover scheme for mobile WiMAX. IEEE 66th Vehicular Technology Conference (2007) 1578–1582.

A Robust and Fast Technique to Detect Copy Move Forgery in Digital Images Using SLIC Segmentation and SURF Keypoints

Kanica Sachdev, Mandeep Kaur and Savita Gupta

Abstract Digital image forgery is the alteration of an image in any form. Increasing advancements in the quality of image capturing devices and photo editing softwares have made the process of image forgery easy. Copy move forgery is the most frequent type among the various types of forgery. This paper presents a novel technique to detect copy move forgery that uses Speeded Up Robust Features (SURF) keypoints. First, the image is sectioned into nonoverlying blocks using Simple Linear Iterative Clustering (SLIC) algorithm. After this, the feature points are selected using SURF. The matching of the SURF points of different segmented regions is done using cosine similarity. The matched regions represent the forged areas. This method has a low computational complexity and shows good results even if the forged area is rotated or scaled.

Keywords Image forgery · SURF · SLIC · Copy move forgery

1 Introduction

Image forgery has become very popular nowadays. The images are presented as news items, financial records, medical records, or as evidence in the court of law. Thus, forgery of images can cause serious legal, social, and personal consequences. This has caused the development of various methods to establish the authenticity of images, which are collectively known as image forgery detection techniques. It is being used in various fields like computer vision, criminal investigation, biomedical

Kanica Sachdev (✉) · Mandeep Kaur
Department of Computer Science, UIET, Panjab University, Chandigarh, India
e-mail: kanicasachdev@yahoo.co.in

Mandeep Kaur
e-mail: mandeep@pu.ac.in

Savita Gupta
Department of Information Technology, UIET, Panjab University, Chandigarh, India
e-mail: savitagupta@pu.ac.in

© Springer Science+Business Media Singapore 2017

R. Singh and S. Choudhury (eds.), *Proceeding of International Conference on Intelligent Communication, Control and Devices*, Advances in Intelligent Systems and Computing 479, DOI 10.1007/978-981-10-1708-7_91

technology, digital image forensics, etc. [1] Image forgery is of three types; resampling, image splicing, and copy move forgery [2]. Resampling refers to certain geometrical transformations that are applied to the image during the process of forgery like stretching, scaling, rotation, etc. Image splicing is done by combining parts of two or more images. Copy move forgery is performed by duplicating a part of an image of any shape or size, and pasting it on some other area of the same image. Since the pasted portion is from the original image, it has similar properties like texture, noise, color, etc. This makes the detection of replicated region difficult.

The various techniques for detection of copy move forgery can be divided into block-based techniques and keypoint-based techniques. Block-based techniques subdivide the image into overlying segments and match these segments to find similar areas. Fridrich et al. used the Discrete Cosine Transform (DCT) of the image segments to match and find similar blocks [3]. Popescu and Farid used Principal Component Analysis (PCA) to get a reduced dimension representation of the blocks and compared them [4]. Bayram et al. developed a highly efficient approach to detect forgery using Fourier Mellin Transform (FMT) which was robust to different processing operations applied to the images [5]. Another important technique was developed by Ryu et al. which involved the use of Zernike moments to find similar regions [6]. The block-based techniques were computationally expensive as it involved the processing of overlapping blocks. Hence, the proposed method uses nonoverlapping blocks to greatly reduce the complexity.

The other category of techniques is the keypoint-based methods. The most popular keypoint extraction methods are Scale Invariant Feature Transform (SIFT) and Speeded Up Robust Features (SURF). It has been shown that although SURF detects lesser keypoints, it is several times faster than SIFT [7]. Bo et al. used SURF keypoints to detect forgery and used Eucledian distance of the SURF keypoints to find matching areas [8]. Amtullah and Koul also used SURF keypoints and introduced a method to detect multiple replication forgeries [9]. The keypoint-based methods, however, have low recall rate. The proposed algorithm combines both block and keypoint approaches to overcome their drawbacks.

The remaining paper is arranged as given: Sect. 2 describes the proposed algorithm for forgery detection. Section 3 explains the results obtained by applying the proposed method. The conclusion and future work are given in Sect. 4.

2 Proposed Method

The proposed scheme combines the block-based methods and the keypoint-based methods to develop a hybrid technique. First, the image is divided into superpixels using Simple Linear Iterative Clustering (SLIC) algorithm. Then, the SURF method is applied to the image to get the feature points and their descriptors. Subsequently, the superpixels are matched using these SURF keypoints. Figure 1 shows the proposed framework for the forgery detection method.

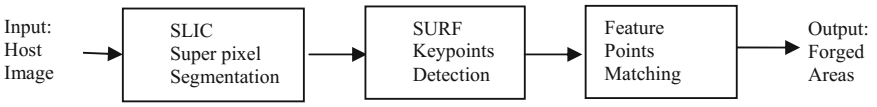


Fig. 1 Flowgraph of the introduced technique

2.1 SLIC Superpixel Segmentation

In the introduced method, the image is sectioned into segments. This step is similar to subdividing the image into blocks, as done in the block based techniques. However, subdividing the image into overlying blocks and comparing them is computationally expensive. Thus the image is sectioned into nonoverlying segments of irregular shape. For this, the technique segments the image into SLIC superpixels because it is memory efficient and faster than the other segmentation methods [10]. Superpixels refer to the relevant granular regions that are acquired by subdividing the image. They separate the source copying region and the target pasting region by dividing the image into segments that are semantically independent to each other. SLIC algorithm uses k-means clustering approach to generate superpixels. Dividing the image into superpixels decreases the computational time considerably. Moreover, irregular meaningful blocks can be efficiently used to detect forgery as compared to regular blocks. SLIC algorithm requires the initial size of the superpixels as an input. By various experiments, the starting size of superpixel is approximately taken to be one-fifth of the image width/height. It can be calculated as:

$$\text{initial_superpixel_size} = \frac{\max(\text{height of image},\ \text{width of image})}{5} \tag{1}$$

2.2 SURF Keypoints Detection

After segmentation, the block features are selected from the image. However, the features extracted by the block-based methods from the image are not resistant to geometrical transformations. Hence, the SURF feature extraction method is employed in the introduced method which is resistant to scaling, blurring, scaling, and compression.

SURF was proposed by Bay et al. [11] SURF algorithm is also computationally faster compared to other feature extraction methods. It uses Hessian matrix approximation. Hessian matrix for a point $X_1 = (x, y)$ can be computed as:

$$H(X_1, \sigma) = \begin{bmatrix} L_{xx}(X_1, \sigma) & L_{xy}(X_1, \sigma) \\ L_{yy}(X_1, \sigma) & L_{yy}(X_1, \sigma) \end{bmatrix} \tag{2}$$

where L_{xx} is the convolution of the Gaussian derivative of second-order given by $d/dx^2(g(\sigma))$ of the image at point X_1 and σ is the scale. Box filters are used to approximate second-order Gaussian derivative. These box filters are used to compute the convolutions of integral images quickly. By deciding the appropriate weights, the determinant of Hessian determinant is calculated as:

$$|H| = D_{xx}\,D_{yy} - (0.9D_{xy})^2 \tag{3}$$

where D_{xx}, D_{yy} and D_{xy} are the approximations of second order Gaussian derivatives in x, y and xy direction, respectively. Then, non-maximum suppression is implemented in a $3 \times 3 \times 3$ surrounding region to localize the interest points. The points associated with the maxima of the calculated determinant are the interest points.

The descriptors of the keypoints are computed by considering the responses of the Haar wavelet of the neighboring areas of the keypoint. A square area is first constructed in the pixels surrounding the interest point to extract the descriptor. It is divided into 4×4 subregions and the responses of Haar wavelet are found out. A descriptor V is calculated for each subregion using the formula:

$$V = \left(\sum d_x, \sum d_y, \sum |d_x|, \sum |d_y|\right) \tag{4}$$

where d_y and d_x are the vertical direction response and the horizontal direction response of the wavelet responses, respectively. A descriptor of length 64 is formed by considering all 4×4 subregions.

2.3 Feature Points Matching

In the last step, the blocks are compared using the block features. Most of the algorithms use Eucledian distance to calculate the distance between the features. However, a more computationally efficient method is to use cosine similarity to compute the correlation between two vectors. In this step, the keypoint descriptors are compared to find the matching keypoints. Typically, the descriptor of each keypoint is compared to every other keypoint in the image. However, since the image has already been divided into superpixels, only the keypoints of every pair of superpixels are compared. In our technique, the matching between the keypoints is described as follows:

1. Consider the set of keypoint descriptors calculated for each superpixel.
2. Calculate the cosine similarity of a keypoint descriptor of a superpixel to all the other descriptors of the other superpixel and obtain a distance vector.
3. Sort the distance vector obtained in increasing order of distances. Calculate the ratio of nearest neighbor of the keypoint to the second nearest neighbor of the keypoint from the sorted list.

4. If the ratio computed in Step 3 is less than a specified threshold T, then the keypoint is considered to be matched, else it is discarded. The threshold T that has been used in our paper is 0.45. If the total number of matched keypoints between two superpixels are greater than 2, we consider the superpixels to contain the copy moved forged regions.
5. Repeat Step 2 to Step 4 for all pairs of superpixels. Store the matched keypoints of the matched superpixels and display them on the forged image to identify the copy move forged areas.

3 Experiments and Analysis

The introduced technique has been executed in MATLAB environment. vlFeat library has been used to perform SLIC segmentation [12]. The images used in the experiments have been taken from the CoMoFoD database [13]. This database contains semantically meaningful images taken under different conditions and provides good images to objectively evaluate our method. Table 1 presents the details of the database.

The results of applying the introduced algorithm on different images from the CoMoFoD database are depicted in Fig. 2. Figure 2a–g shows the authentic images from the database. The copy move tampered images are shown in Fig. 2h–n. Areas of various sizes and shapes have been copied from the original images and pasted at some other location on the image. Figure 2o–u displays the results of applying the introduced method.

The matched points have been shown on the image through the lines between them. The technique successfully finds keypoints in the original and pasted region. Figure 2k, l shows the forged images in which the copied regions have been rotated and pasted on the image. Figure 2s, t depicts the results of applying the technique on rotated forged images. Figure 2m, n presents copy move images that have been scaled and their detection results are displayed in Fig. 2t, u.

The limitation of the scheme is that the image is first divided into various segments and then the keypoints of these segments are matched. However, if the copy moved blocks are in the same segment, the method will not be able to detect

Table 1 Details of CoMoFoD database

	Description
Source	Canon EOS 7D camera
Forgery done by	Photoshop CS3 and CS5
Size	Recorded images of 5202 × 3465 pixels were resized
Format	Portable Network Graphics (PNG) format
Image topic	Various

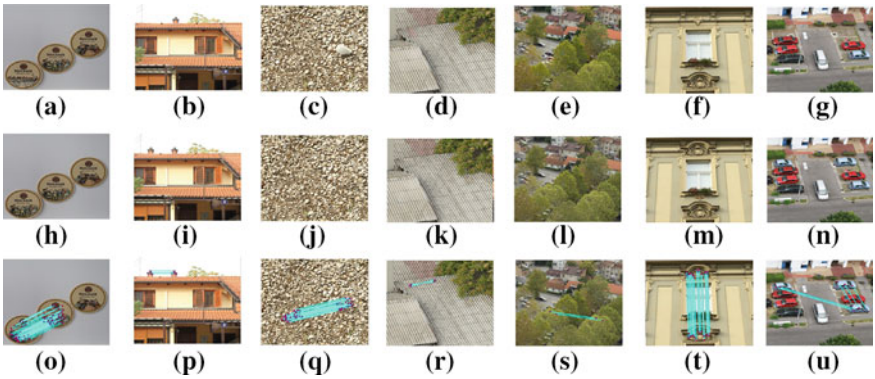


Fig. 2 Results of proposed technique: **a–g** Original images, **h–n** Copy move forged images **o–u** Detection results of the introduced method

those regions. In this case, the image needs to be divided again with a smaller initial superpixel size and then detect the forged areas.

4 Conclusion

A fast yet robust technique to detect copy move forgery using SURF keypoints is introduced in this paper. The image is subdivided into nonoverlying superpixels and their SURF keypoints are compared. The method has a very low computational complexity. It even detects copy moved areas even in the presence of processing operations like scaling, rotation, etc. Future work can emphasize on localizing the forged areas using the keypoints to find the exact boundary of the pasted region.

References

1. Bayram, Sevinc, Husrev Taha Sencar, and Nasir Memon. "A survey of copy-move forgery detection techniques." In IEEE Western New York Image Processing Workshop, pp. 538–542. 2008.
2. Ali Qureshi, M., and M. Deriche. "A review on copy move image forgery detection techniques." In Systems, Signals & Devices (SSD), 2014 11th International Multi-Conference on, pp. 1–5. IEEE, 2014.
3. Fridrich, A. Jessica, B. David Soukal, and A. Jan Lukáš. "Detection of copy-move forgery in digital images." In Proceedings of Digital Forensic Research Workshop. 2003.
4. Popescu, A. C., and H. Farid. "Exposing digital forgeries by detecting duplicated image region [Technical Report]. 2004-515." Hanover, Department of Computer Science, Dartmouth College. USA (2004).

5. Bayram, Sevinc, Husrev Taha Sencar, and Nasir Memon. "An efficient and robust method for detecting copy-move forgery." In Acoustics, Speech and Signal Processing, 2009. ICASSP 2009. IEEE International Conference on, pp. 1053–1056. IEEE, 2009.
6. Ryu, Seung-Jin, Min-Jeong Lee, and Heung-Kyu Lee. "Detection of copy-rotate-move forgery using Zernike moments." In Information Hiding, pp. 51–65. Springer Berlin Heidelberg, 2010.
7. Panchal, P. M., S. R. Panchal, and S. K. Shah. "A comparison of SIFT and SURF." International Journal of Innovative Research in Computer and Communication Engineering 1, no. 2 (2013): 323–327.
8. Bo, Xu, Wang Junwen, Liu Guangjie, and Dai Yuewei. "Image copy-move forgery detection based on SURF." In Multimedia Information Networking and Security (MINES), 2010 International Conference on, pp. 889–892. IEEE, 2010.
9. Amtullah, Salma, and Dr Ajay Koul. "Passive Image Forensic Method to detect Copy Move Forgery in Digital Images." IOSR Journal of Computer Engineering (IOSR-JCE) 16, no. 2: 96–104.
10. Achanta, Radhakrishna, Appu Shaji, Kevin Smith, Aurelien Lucchi, Pascal Fua, and Sabine Susstrunk. "SLIC superpixels compared to state-of-the-art superpixel methods." Pattern Analysis and Machine Intelligence, IEEE Transactions on 34, no. 11 (2012): 2274–2282.
11. Bay, Herbert, Tinne Tuytelaars, and Luc Van Gool. "Surf: Speeded up robust features." In Computer vision–ECCV 2006, pp. 404–417. Springer Berlin Heidelberg, 2006.
12. Vedaldi, Andrea, and Brian Fulkerson. "VLFeat: An open and portable library of computer vision algorithms." In Proceedings of the 18th ACM international conference on Multimedia, pp. 1469–1472. ACM, 2010.
13. Tralic, Dijana, Ivan Zupancic, Sonja Grgic, and Mislav Grgic. "CoMoFoD—New database for copy-move forgery detection." In ELMAR, 2013 55th International Symposium, pp. 49–54. IEEE, 2013.

VPBC: A Varying Probability-Based Clustering for Energy Enhancement in WSN

Shaveta Gupta, Vinay Bhatia and Vishal Puri

Abstract Nowadays, the performance of wireless sensor network (WSN) in a variety of applications plays a pivotal role in the research field and variety of parameters is used for its functioning. While designing WSN, some issues may arise out of which one issue is energy consumption. Energy efficiency is a serious issue for distributed WSNs deployed in varied environments. The energy efficient cluster-based protocols play a vital role for energy saving in hierarchical WSN. In modelling, probability plays its important role. While selecting the CH at the beginning of the network, one important parameter used is distance. The probability definition is different for different approaches. Most of the protocols consider probability of all the nodes to become CH at the beginning of the network is fixed but the present paper is an approach to consider varying probability of the nodes to become CH at the beginning on the basis of distance from BS. These results show that the present approach has improved performance when compared to existing algorithms with their results. Simulations are carried out to demonstrate and compare the performance of the proposed algorithms.

Keywords Clustering · Cluster heads · Non-cluster heads · Hierarchical routing · Energy efficiency · Variable probability · WSN

Shaveta Gupta (✉) · Vishal Puri
Baba Ghulam Shah Badshah University,
Rajouri, J&K, India
e-mail: shavetaqca@gmail.com

Vishal Puri
e-mail: vishal_puri28@yahoomail.com

Vinay Bhatia
Baddi University of Emerging Sciences and Technology,
Baddi, HP, India
e-mail: vinay4research@gmail.com

© Springer Science+Business Media Singapore 2017

R. Singh and S. Choudhury (eds.), *Proceeding of International Conference on Intelligent Communication, Control and Devices*, Advances in Intelligent Systems and Computing 479, DOI 10.1007/978-981-10-1708-7_92

1 Introduction

Wireless networks have gained tremendous popularity in deployment as well as usage. Despite several limitations such as vulnerability to various attacks, these networks have gained research thrust owing to several advantages such as mobility and ease of installation [1, 2]. Wireless sensor network (WSN) is the network that has many applications in many practical situations. With the advancement and utility of practical applications of WSN, it becomes very important for researchers to investigate the environmental conditions of remote and esoteric regions. Wireless is an advancement of science and technology that enables us to send the signals to one or more devices without using wired connections and reduces the complexity of the system. A WSN is a spatially deployed network to monitor the surrounding or environmental conditions and then pass the collected data to the main location called BS through the network. In recent or advanced networks information transfer is bi-directional, which are also used to control the activity of the sensors. WSN comprises of a collection of hundreds or thousands of nodes connected to one another and used to sense the environmental or surrounding conditions, collects the data from the environment and transmits the information to BS via wireless links. Recently WSNs have become popular owing to its low cost, small size, adoption to harsh environment and many others. One of the serious issues discussed in the present paper is energy consumption. Most of the energy gets consumed while collecting, transmitting, and receiving the data. Because of limited energy of the batteries, energy efficiency becomes a serious issue. To overcome this problem, number of algorithms has been developed to enhance the energy efficiency and the lifetime of the WSN [1].

One of the approaches used for energy enhancement is clustering where clusters of sensor nodes are formed then the CHs are selected within every clusters and followed by data transmitted from non-CHs to CHs [2].

2 Existing Hierarchical Routing Techniques

Hierarchical or cluster-based routing is an efficacious protocol to perform high energy efficient routing technique in WSNs. In this technique, there are two types of nodes: CH nodes and non-CH nodes and these are categories on the basis of energies. The nodes having high energy become CH nodes and nodes having lower energy comparatively become non-CH nodes. This technique contributes to increase the lifetime and enhance the energy efficiency of the network. Hierarchical routing has two phases where in one phase CHs are selected and the other phase is used for routing [3–5]. Some of them are described below:

LEACH. The **Low Energy Adaptive Clustering Hierarchy** protocol randomly selects some sensor nodes as CHs and rotates this role to the nodes to evenly distribute the energy load among the sensors in the network [6, 7]. In this protocol

few nodes in a cluster are randomly selected with a certain/fixed probability to become CHs per round. It is also considered that all the nodes have equal amount of energy in each round and all the nodes are electing themselves to become CH with a fixed predefined probability.

LEACH-C. Low Energy Adaptive Clustering Hierarchy—Centralized is a centralized approach where BS has the energy level and distance information of all the nodes. The probability of CH selected is fixed by the BS [8].

SEP. In Stable Election Protocol, weighted election probabilities based on residual energy of each node decides the node to become CH [9].

DEEC. In Distributed Energy Efficient Clustering, CHs are formed on the basis of the ratio between residual energy of each node and the average energy of the network [10, 11].

The above-mentioned protocols assumes that at the first and the foremost round all the nodes have same probability for CH formation but practically it is not possible because of various reasons. First, it is not necessary that all the nodes in a cluster are in range with the BS, which may cause more energy consumption due to longer distance between CH and the BS. Second, some nodes might be at the boundary of the cluster which may cause high intra-cluster energy consumption. Third, the nodes might have different energy levels depending upon different power sources that may cause different probability for each node to become CH.

In this paper, we calculate the probabilities of all the sensor nodes of a cluster to become CH on the basis of their distance from the BS.

3 First-Order Radio Model

This model calculates the amount of energy consumed for transferring the data from simple node to CH, from CH to intermediate CH, from CH to BS and also from node to BS. The radio dissipation energy model (Fig.1) consists of transmitter having transmit electronics (E_{elec}) and amplifier that depends on the distance to the receiver and the tolerable bit-error rate. If the distance between transmitter and receiver is less than the threshold distance (say d_o), then free space (d^2 power loss) channel model is used and if distance between transmitter and receiver is greater than threshold distance (say d_o) then multipath fading (d^4 power loss) channel model is used [12].

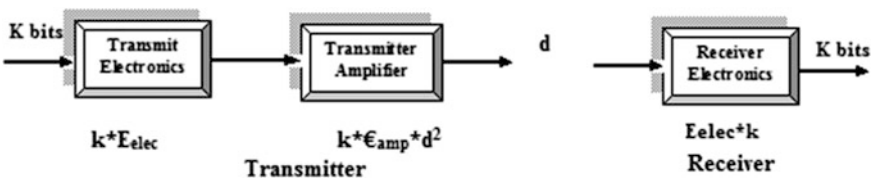


Fig. 1 Radio energy dissipation model

Table 1 Radio parameters

Parameters	Operation	Values
Tx/Rx electronics	E_{elec}	50 nJ/bit
Transmit amplifier (if d to BS < d_o)	E_{fs}	10 pJ/bit/4 m^2
Transmit amplifier (if d to BS > d_o)	E_{mp}	0.0013 pJ/bit/m^4
Data aggregation	E_{DA}	5 nJ/bit/signal

The energy consumed by the specific nodes/CH for transmitting k bits of data is Energy consumed by transmitter (for $d < d_o$)

$$d_o = \sqrt{\left(E_{\text{fs}} \backslash E_{\text{mp}}\right)} \tag{1}$$

$$E_{\text{tx}}(k,\ d) = E_{\text{elec}} * k + k * \left(E_{\text{fs}} * d^2\right) \tag{2}$$

Transmission energy for intermediate node

$$E_{\text{tx}}(k,\ d) = \left((E_{\text{elec}} + E_{\text{DA}}) * k\right) + \left(E_{\text{fs}} * k * d^2\right) \tag{3}$$

Energy consumed by transmitter (for $d \geq d_o$)

$$E_{\text{tx}}(k,\ d) = E_{\text{elec}} * k + k * \left(E_{\text{mp}} * d^4\right) \tag{4}$$

Transmission energy for intermediate node

$$E_{\text{tx}}(k,\ d) = \left((E_{\text{elec}} + E_{\text{DA}}) * k\right) + \left(E_{\text{mp}} * k * d^4\right) \tag{5}$$

Energy consumed by receiver

$$E_{\text{rx}}(k) = E_{\text{elec}} * k \tag{6}$$

Table 1 contains first-order radio model parameter that is used to calculate the energy consumed by each node in a cluster at various distances [12].

4 Proposed Methodology

Varying Probability. At the beginning of the network, the clusters are formed. The size of the clusters has different sizes and they have correlation with each other. Then the corresponding posterior probabilities for each node have been evaluated and describe that how each node relates to each cluster. The mixing coefficient is considered as the prior probabilities of the data and for a given number of the clusters the corresponding posterior probabilities can be calculated using following equations:

$$\mu = \frac{1}{N}\left(\sum_{n=1}^{N} x_n\right) \tag{7}$$

$$\sum = \frac{1}{N}\sum_{n=1}^{N}(x_n - \mu)(x_n - \mu)^T \tag{8}$$

$$p(x) = \sum_{k=1}^{K}\prod_{k} N\left(x_k|\mu_k, \sum_{k}\right) \tag{9}$$

where Π_k is the mixing coefficient, i.e., the weightage of each Gaussian distribution and K is the number of clusters.

Cluster Head Formation. After the evaluation of the probabilities, the nodes select themselves to the CH on the basis of threshold value, $T_{s(i).}$ The sensor node chooses a random number r between 0 and 1. The node becomes CH for that current round, if the value of r is less than the threshold value, $T_{s(i).}$ The threshold value is evaluated by

$$T_{s(i)} = \begin{cases} \frac{p(i)}{1-p(i)(r \bmod \frac{1}{p(i)})} & \text{if } s(i) \in G \\ 0 & \text{otherwise} \end{cases} \tag{10}$$

Cluster Formation. After the selection of CHs, the CH nodes send an advertisement (ADV) message to the whole network which contains the CH's ID and a header which specifies the type of the message. After receiving the message, the non-CH nodes choose the CH on the basis of minimum communication distance by calculating the signal strength of the ADV message from different CHs. After selecting the CH by the non-CH nodes they send a join-request (JOIN-REQ) to their corresponding CH for which they form the cluster. Again the join message is a short message consisting of the CH node's ID, non-CH node's ID and the header. The clustering done in this algorithm is a soft clustering where the nodes are not restricted to a cluster but in every round the clusters changes dynamically.

Data Transmission. The data is then sensed by the environment and transmits to the CH. The CHs close to the BS uses single hop or direct transmission where as the CHs far away from the BS uses multi-hop transmission/communication, i.e. they transmit there data to the next CH close to the BS and soon.

5 Results

The results are analyzed between DEEC, DDEEC and VPBS using MATLAB tool (Table 2).

Table 2 Shows the comparison of different parameters to compare three protocols

Parameters	DEEC	DDEEC	VPBC
First node dead	1300 rounds	1085 rounds	1600 rounds
Tenth node dead	1450 rounds	1340 rounds	1870 rounds
All node dead	3000 rounds	2757 rounds	4700 rounds
Packets sent to BS	64,214 packets	67,759 packets	2.8×10^5 packets

Fig. 2 Network lifetime

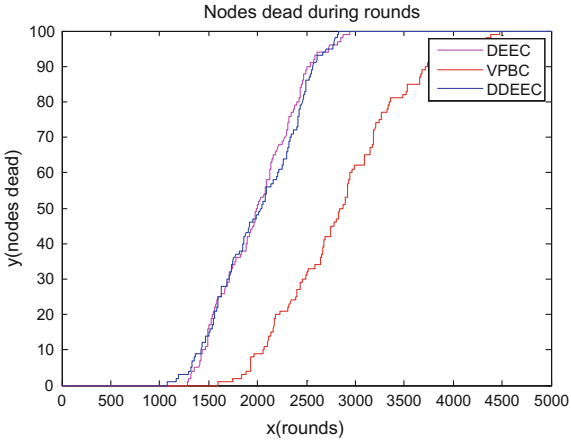


Figure 2 shows the comparison between of the network lifetime on the basis rounds in WSN. In DEEC first node is found dead at 1300th round, tenth node at 1450th round and all nodes die at 3000th rounds, in case of DDEEC first node is found dead at 1085th round, tenth node at 1340th round and all nodes die at 2757th round and in case of VPBC first node dead at 1600th round, tenth node dead at 1870th round and all nodes dead at 4700th round. This shows that the lifetime of VPBC has been improved over DEEC and DDEEC.

Figure 3 shows the comparison between the packets reached at BS from CHs. In DEEC 64,214 packets has been transmitted to BS from CHs, in case of DDEEC 67,759 packets has been transmitted to BS from CHs and in case of VPBC 2.8×10^5 packets has been transmitted to BS from CH. This show the increased efficiency of packet transfer from CHs to BS in case of VPBC as compared to the DEEC and DDEEC protocols.

Figure 4 shows that more nodes are alive in case of VPBC than in DEEC and DDEEC protocols. In DEEC the nodes starts decaying at 1300th rounds and finally all alive are nodes dead at approx. 3000th round, in DDEEC the nodes starts decaying at 1100th rounds and finally all alive nodes are dead at approx. 2700th round while in case of VPBC the nodes starts decaying at 1600th rounds and finally all alive nodes are dead at approx. 4700th round. This result depicts that VPBC has more network lifetime than other two protocols.

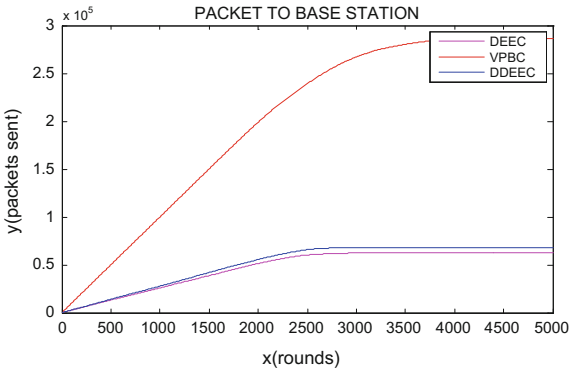


Fig. 3 Packets to BS

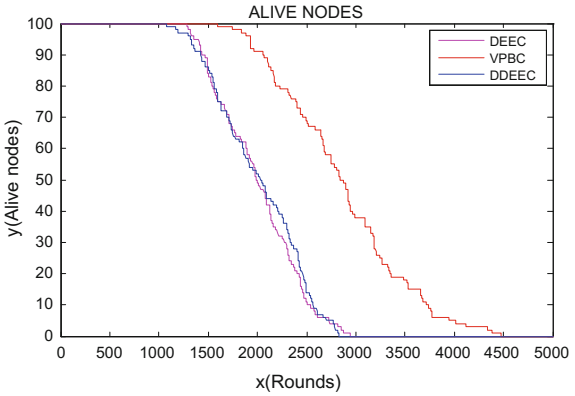


Fig. 4 Alive node

6 Conclusion

Wireless technology is nowadays surpassing wired technology. Many factors attribute to change of applicability from wired to wireless, one of them being freedom of coordinates. Now a person can roam around fully connected to the network. The needs and demands driven results wireless technology as an alternative to wired one. Every technology has its boons and flaws and an engineer is working on efficiency parameter to improve its model in order to make it more practical. The work is an attempt to improve energy efficiency of wireless system by varying the probability during the first round for CH selection on the basis of distance into a wireless system. Taking on design issues and taking practical constraints into account, the attempt is made to develop an application-oriented system to increase energy efficiency and improve the performance of WSN.

References

1. Nikolaos, Pantazis, A., Stefanos, Nikolidakis, A., and Dimitrios, Vergados, D.: Energy Efficient Routing Protocols in Wireless Sensor Networks: A Survey. IEEE communication survey & tutorials, VOL. 15, No.2, second quarter 2013.
2. Shaveta, G., Vinay, B.: A Manhattan Distance Approach for energy optimisation in wireless sensor network. IEEE Conference (NGCT.2015.7375112) pp. 203–206.
3. Mehdi T., Kavian Y. S., and Saman S."SEECH: Scalable Energy Efficient Clustering Hierarchy Protocol in Wireless Sensor Networks". IEEE SENSORS JOURNAL, VOL. 14, NO. 11, Nov. 2014.
4. Heinzelman W. B., Chandrkasan A. P., and Balakrisnan H.: An application-specific protocol architecture for wireless microsensor networks. IEEE Trans. Wireless Commun., vol. 1, no. 12, pp. 660–670, Oct. 2002.
5. Qing Q., Zhu, Wang M.: Design of a distributed energy-efficient clustering algorithm for heterogeneous wireless sensor networks. In ELSEVIER, Computer Communications, 2006.
6. Youssef M.A.: Wireless sensor networks part II: routing protocols and security issues. Canadian Conference on Electrical and Computer Engineering 2005, 2005.
7. Liu B., Brass P., Dousse O., Nain P., and Towsley D.: Mobility improves coverage of sensor networks. Proceedings of the 6th ACM International Symposium on Mobile Ad Hoc Networking and Computing (MobiHoc), 2005.
8. Nikolaos A., Pantazis, Stefanos, A., Nikolidakis and Dimitrios D., Vergados: Energy Efficient Routing Protocols in Wireless Sensor Networks: A Survey. IEEE communication survey & tutorials, VOL. 15, NO.2, second quarter 2013.
9. Heinzelman W. B., Chandrakasan A. P., and Balakrishnan H.: An application-specific protocol architecture for wireless microsensor networks. IEEE Trans. Wireless Communication, vol. 1, no.4, pp. 660–670, Oct.2002.
10. Smaragdakis G. and Ibrahim M.: SEP: A Stable Election Protocol for Clustered Heterogeneous Wireless Sensor Networks, 2004.
11. Akbar, M., Javaid N., Yousaf S., Khan A.H., Khan Z.A., U. Qasim, and A.A. Khan.: TRP: Tunneling Routing Protocol for WSNs. 2014 IEEE 28th International Conference on Advanced Information Networking and Applications, 2014.
12. Saadat M., Saadat R., and Mirjalily G.: Improving threshold assignment for cluster head selection in hierarchical wireless sensor networks. Proc. 2010 Int'l Symposium on Telecommunications, pp. 409–414.

Biosignal Acquisition of Stress Monitoring Through Wearable Device

Ritika Saxena, Sushabhan Choudhary, Rajesh Singh and Anshuman Prakash

Abstract Due to hectic and running lifestyle nowadays most of the people in the world are suffering from several physiological disorders such as hypertension, emotional stress, and cardiac diseases. Hence it becomes necessary to have a device that monitors our physiological parameters in day-to-day life which is portable and handy. This paper proposes a wearable device to monitor stress by the acquisition of skin resistance (GSR), standing for Galvanic Skin Response. GSR sensors allow to spot such strong emotions by simply attaching two electrodes to two fingers on one hand. There are mainly two types of stress like Physical stress and Physiological stress which can also be a cause of degradation in performance and also leads to higher psychological stress levels. The major cause of stress can be from lifestyle, daily living activities like visual stress, car driving, gaming control. These signals were procured using Data Acquisition System, then interfaced to the LabVIEW using microcontroller. Experimental setup is done using GSR connection with LabVIEW for data logger.

Keywords GSR (Galvanic skin response) · Arduino · LabVIEW · MATLAB · Bluetooth · LCD (Liquid crystal display)

1 Introduction

In today's world, mental health has gradually moved to priority positions in public health. Joydeep et al. has proposed that heart rate, eye-blink rate increases in stressful situations which determine the stress levels of a person [1]. Stress is one of the main reasons for this sympathetic division of the autonomic nervous and the hypothalamo-hypophyseal portal systems is activated. Salafi et al. has proposed that the skin temperature, Galvanic Skin Response (GSR), heart rate are the three

Ritika Saxena (✉) · Sushabhan Choudhary · Rajesh Singh · Anshuman Prakash
University of Petroleum and Energy Studies, Dehradun, India
e-mail: saxenaritika04@gmail.com

© Springer Science+Business Media Singapore 2017

R. Singh and S. Choudhury (eds.), *Proceeding of International Conference on Intelligent Communication, Control and Devices*, Advances in Intelligent Systems and Computing 479, DOI 10.1007/978-981-10-1708-7_93

physiological signals to classify the stress and is performed using stress monitoring patch prototype with mobile app user interface and conducted experiment with 50 participants [2]. Neurotoxic damages, emotional and vegetative reactions, and ultimately, behavioral and mental disorders and somatic diseases occurred due to secretion of hormones, including cortisol. Dosinas et al. have proposed that the main aim of those systems—enable human physiological parameters to be registered and analyzed continuously during his work activities [3]. Krupinski et al. have proposed that high levels of efficiency regardless of task complexity and workload is operated consistently by an individual provider [4]. Ren et al. has proposed that The pupil diameter (PD), controlled by the autonomic nervous system, seems to provide a strong indication of affective arousal, as found by previous research, but it has not been investigated fully yet [5]. Sysoev et al. has proposed that some of the body features used for these purposes: Heart Rate (HR), heart rate variability (HRV), Electro Dermal Activity (EDA), Electrocardiogram (ECG), Electromyogram (EMG), Skin Temperature (ST), Pupil Dilation (PD), Blood Volume Pulse (BVP), Respiration, Voice Features, Facial Expression, Eye Gaze, Blink Rates [6].

1.1 GSR

GSR, refers to Galvanic Skin Response. Electrical conductance of the skin is measured by the GSR. Strong emotion is stimulated by the Sympathetic Nervous System (SNS), which results in secreting of more sweat from sweat glands. GSR consists of two electrodes which are attached to two fingers on a hand, and are used to detect strong emotions.

1.2 GSR Schematic

Figure 1 shows the basic schematics of the GSR amplifier which amplifies the conductive voltage of the skin. It is basically an instrumentation amplifier in which the gain is cascaded. Through the input pin *J*1 the electrode is placed on the body mainly on index and middle finger. When the circuit is powered, the amplified voltage comes out as signal pin at *J*2.

1.3 Proteus Simulation

See Fig. 2.

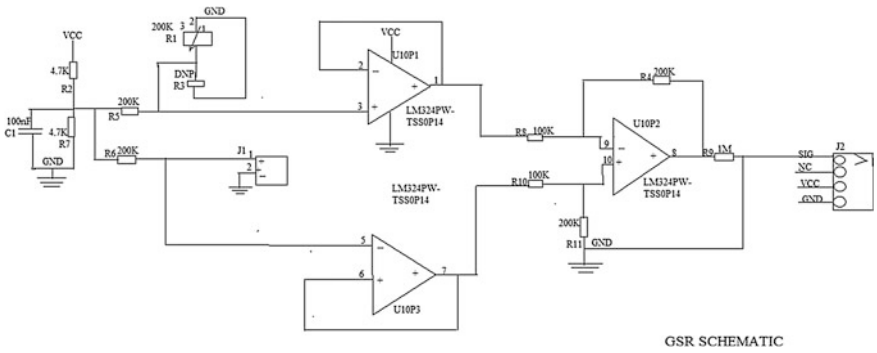


Fig. 1 GSR schematic

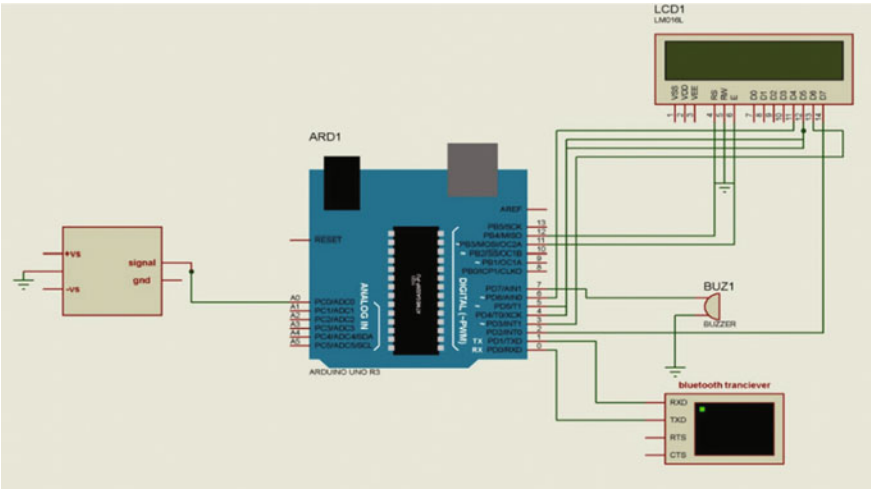


Fig. 2 Proteus simulation

2 Materials and Methods

2.1 Methods

Galvanic Skin Response (GSR) or EDA is the measurement of the skin conductance and skin resistance of the body, which is directly connected to the SNS. As the persons' mood or emotion changes the sweat gland over the skin secretes some amount of sweat, which causes change in the skin resistivity. As from the Ohm's law

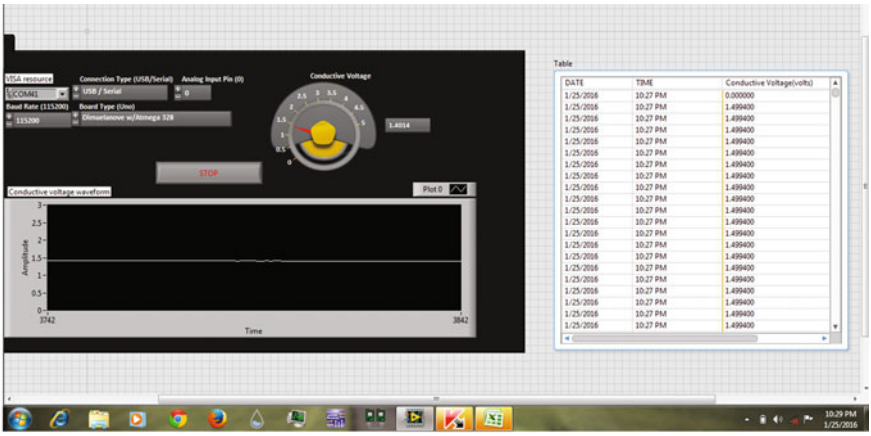


Fig. 3 Front panel of LabVIEW

that voltage is directly proportional to resistance, hence as the resistance increases the voltage increases. With reference to this, when the person is in stressed condition the skin resistance decreases due to sweat and hence conductivity increases.

Data Acquisition System: The data logger of the GSR is made up with the help of GSR grove sensor purchased from Protocentral and interfaced with Arduino UNO at analog pin0. The Arduino Firmware was used to link the Arduino IDE and LabVIEW as shown in the Fig. 3 and its programming is in Fig. 4.

3 Results and Discussion

Threshold value detection using histogram technique of subjects is done by taking samples between number of amplitudes and number of conductive voltage in MATLAB.

Based on the histogram technique the range of conductive voltage has been determined. As shown in the Fig. 4, histogram of four different subjects has been represented. The data has been collected for 13 different persons for 1 min gaze paradigm. With reference to Fig. 4, it can be inferred that the conductive voltage varies with person to person so taking the average value of all histogram it has been concluded that the maximum conductive voltage ranges from 1.75 V and above and minimum conductive voltage ranges from 1.44 V.

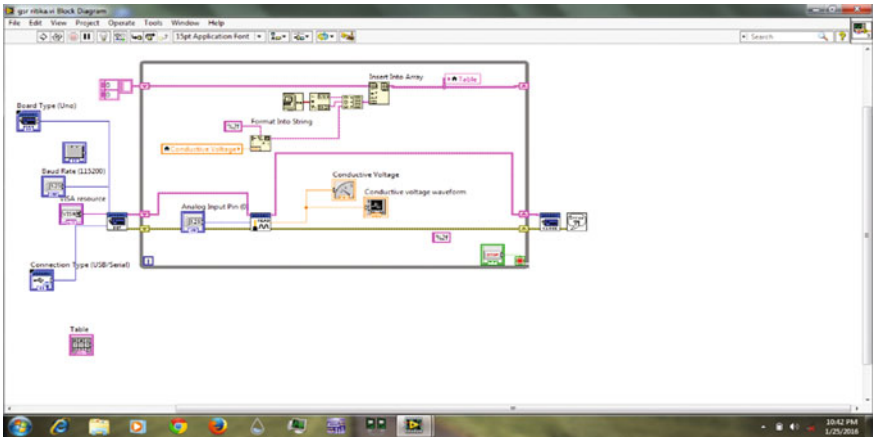


Fig. 4 Back panel of LabVIEW

Based on these values the person GSR voltage can be categorized as

i. Relaxed: <1.75 V.
ii. Normal: between 1.75 and 1.44 V.
iii. Stressed: >1.44 V.

These threshold values are fed into microcontroller through Arduino coding and the persons stress condition is displayed on the device as shown in the Figs. 5 and 6.

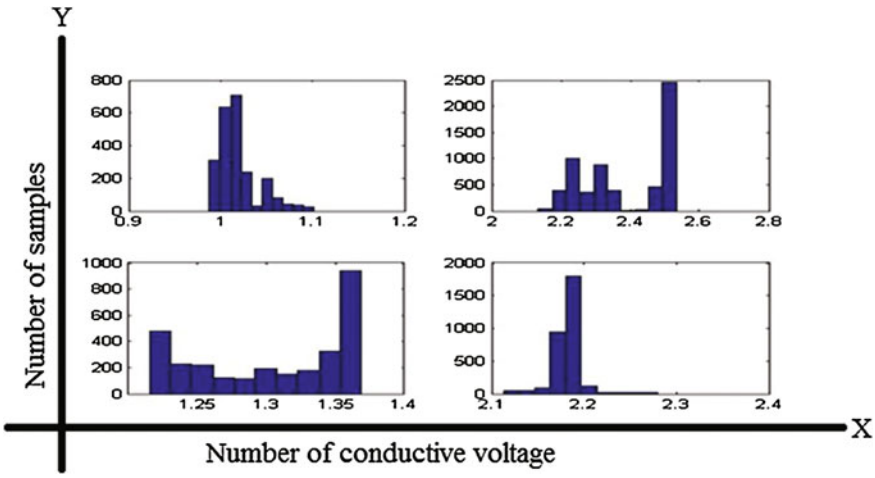


Fig. 5 Histogram of four different subjects

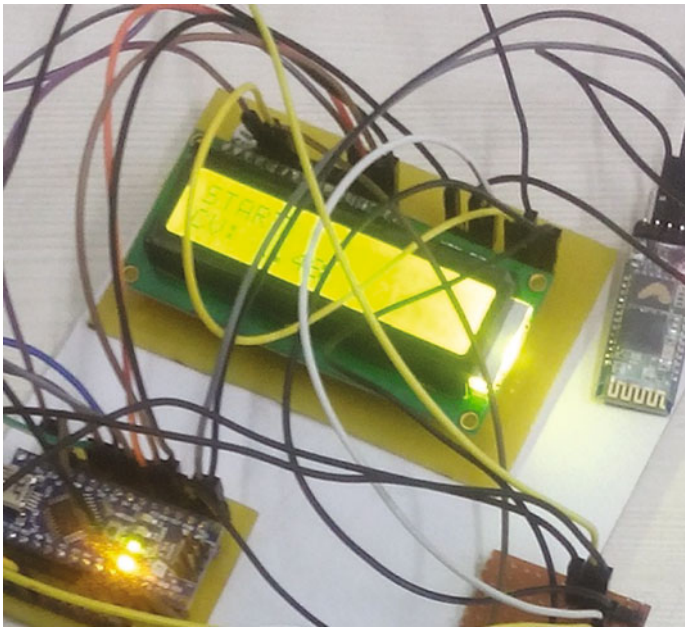


Fig. 6 Hardware showing conductive voltage on the LCD

4 Conclusion

Based on the study and observation of the threshold detection technique it is concluded that the GSR threshold value is 1.44 V in stressed condition, 1.75 V in relaxed condition and in between 1.44 and 1.75 V is moderate condition. These values are fed into the microcontroller and programmed to analyze the stressed condition. The condition of the stress is transmitted to android smart phone through Bluetooth communication, so that user can see his/her stress condition on his smart phone.

References

1. Sengupta Joydeep, Nupur Baviskar, and Surbhi Shukla. "Biosignal Acquisition System for Stress Monitoring." *Mobile Communication and Power Engineering*. Springer Berlin Heidelberg, 2013. 451–458.
2. Salafi, T., and J. C. Y. Kah. "Design of Unobtrusive Wearable Mental Stress Monitoring Device Using Physiological Sensor." 7th WACBE World Congress on Bioengineering 2015. Springer International Publishing, 2015.
3. Dosinas, A., M. Vaitkūnas, and J. Daunoras. "Measurement of Human Physiological Parameters in the Systems of Active Clothing and Wearable Technologies." *Elektronika ir Elektrotechnika* 71.7 (2015): 77–82.

4. Krupinski, Elizabeth, and Bruce I. Reiner. "Real-time occupational stress and fatigue measurement in medical imaging practice." Journal of digital imaging 25.3 (2012): 319–324.
5. Peng Ren, Armando Barreto, Jian Huang, Ying Gao, Francisco "Off-line and On-line Stress Detection Through Processing of the Pupil Diameter Signal" based on Annals of Biomedical Engineering, Vol. 42, No. 1, January 2014.
6. Mikhail Sysoev, Andrej Kos, Matevž Pogačnik "Noninvasive stress recognition considering the current activity" based on the Author(s) 2015. This article is published with open access at Springerlink.com.
7. Lowe Shane A., and Gearóid ÓLaighin. "Monitoring human health behaviour in one's living environment: a technological review." Medical engineering & physics 36.2 (2014): 147–168.

Implementation of Heartbeat Sensing Using PSoC3

Ramesh Babu Chukka, D. Madhavi, N. Jyothi and Ch Sumanth Kumar

Abstract Electrocardiogram is a register of heart's electrical activity. A wide range of heart conditions can be interpreted using ECG. It is increasingly used in medical sciences and technologies as a valuable medical diagnostic tool. For interpretation of ECG, amplifiers play an important role for such instrumentation systems. There is a growing demand for affordable, portable ECG machine. So by choosing the appropriate components suitable for portable applications, portable ECG machines can be developed. The objective is to develop a 3-lead portable feasible user-friendly and economical ECG system which can be managed by a common man.

Keywords Electrocardiogram · Medical diagnosis · Portable design

1 Introduction to ECG

Digital data acquisition system plays a very important role in the design of biomedical gadgets used in medical diagnosis. A compact, economically feasible and safe to use ECG system employing a PSoC-based data acquisition system was realized and presented. The system consists of buffered electrodes connected to first stage instrumentation amplifier with differential output and later forwards to PSoC for further analysis. The system is energized by two 9 V batteries and is absolutely safe to use and the cost of the system excluding the PC around $100.

R.B. Chukka (✉)
Department of Electronics and Communication Engineering, Vignan's Institute of Engineering for Women, Visakhapatnam 530002, Andhra Pradesh, India
e-mail: rameshbabuchukka@gmail.com

D. Madhavi · N. Jyothi
Department of Electronics and Communication Engineering, GITAM University, Visakhapatnam Campus, Visakhapatnam, Andhra Pradesh, India

Ch Sumanth Kumar
Department of Electronics and Communication Engineering, GITAM University, Bengaluru Campus, Bengaluru Rural District 561203, Karnataka, India

© Springer Science+Business Media Singapore 2017

R. Singh and S. Choudhury (eds.), *Proceeding of International Conference on Intelligent Communication, Control and Devices*, Advances in Intelligent Systems and Computing 479, DOI 10.1007/978-981-10-1708-7_94

2 Materials and Methods

The ECG system as shown in Fig. 1 consists of input stage with right leg drive followed by an amplifier, a signal conditioner, a conversion and a serial communication interface. The whole system is realized on the PSoC except the input stage. The input stage consists of a preamplifier with right leg drive, realized around TL084/LM324, a quad operational amplifier. The gain of the input stage is kept to a minimum (around 10) and a DC restoration stage is incorporated to minimize the output offset voltage in the final output.

The output of this is applied as input to the amplifier, realized on the PSoC.

The signal conditioner unit has a low-pass filter with a cutoff frequency of 200 Hz and a notch filter to minimize the 50 Hz pick up. A 12-bit ADC was realized for our application and the digital data is transferred through the serial communication interface. PSoC Creator is used to program the chip to suit our application. After assigning different user modules, the PSoC creator generates a project. Each user modules has its application programming interface (API) (Fig. 2).

2.1 Instrumentation Amplifier

The output recorded by the electrodes is in milli volts. In order to further process this bio-potential signal there is a need to use a bio-potential amplifier possessing the characteristic of high input impedance, high CMRR, low offset voltage. The ECG amplifier is realized around LM324 quad amplifier. Typical bio-potential amplifiers have high input impedance and are designed for safety first. This is due to the fact that the signal amplified is being drawn from a living organism so precautions must be taken in order to prevent macro and micro shock. Isolation and protection circuitry are used to limit current through electrodes to safe levels. This is achieved through instrumentation and differential amplifier.

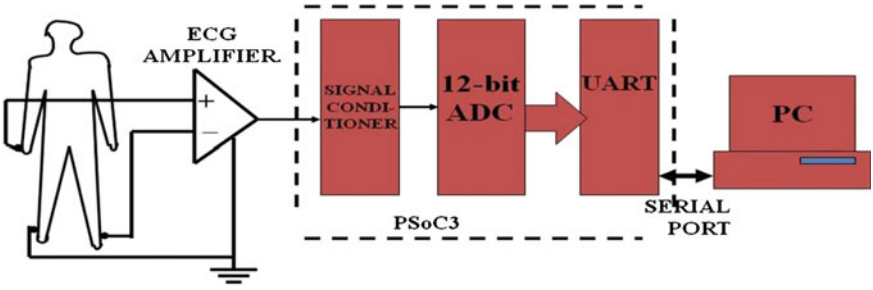


Fig. 1 ECG system block diagram

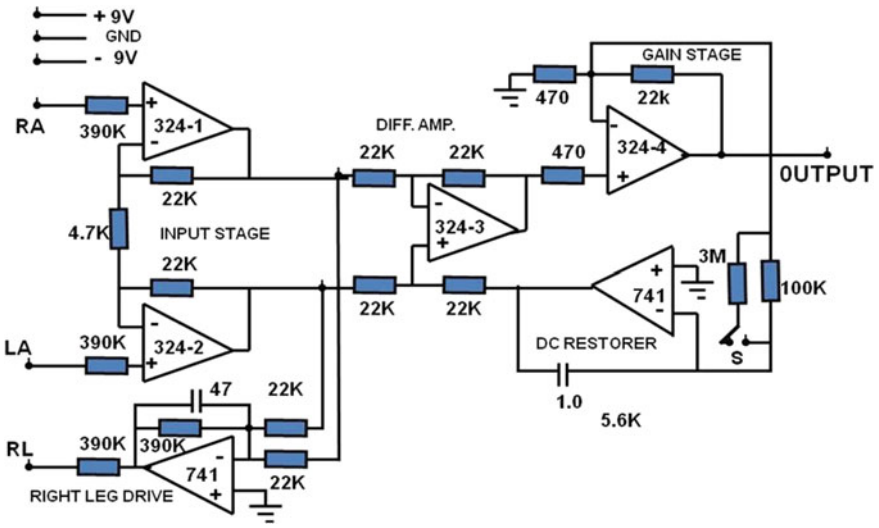


Fig. 2 ECG amplifier realized on LM324

2.2 Gain Stage with Feedback

The output resulting from the instrumentation amplifier has gain which is not sufficient enough for interpreting the data so in order to improve this, gain stage is used.

2.3 DC Restorer

DC Restorer function is to restore the baseline of a DC coupled signal to zero DC level. To reduce interference from the amplifier right leg drive is used.

2.4 Low-Pass Filter

ECGs are subject to many different kinds of noise internally and externally. Low-pass filters with a cutoff frequency of 200 Hz are used to remove high frequency muscle artifact and external interference. So, low-pass filter is used limit the bandwidth to reject interference signals and noises.

2.5 Notch Filter

Due to difference in surface-mounted electrodes impedance notch filter is used to reduce the power line interferences at a 50/60 Hz.

3 PSoC Hardware and Software Implementation

In selecting ADC we output in Digital Format. The digital equivalent of the analog input is obtained in the range 0–4095 (2^12) for 0–5 V input to ADCINC12. This digital equivalent can be viewed with the use of standard library function **itoa**(), and to convert the digital equivalent into analog using the source code the function **ftoa** () is used. The input parameters of this function are floating value and *status where status indicates the range of input digital value.

The equation for digital to analog conversion in the API is given as

$$V_o = (V_{\text{in}} * \text{value})/\text{pow}(2, 12)$$

where value = Digital equivalent in the range 0–4095 for 0–5 V analog input. The floating value of *Vo* is converted to ASCII with the use of **ftoa**() function.

4 Results

Finally it is logged into the PC through an MAX232 serial communication port based on UART in PSoC. In PC we observe the analog values output we used HYPER TERMINAL window and further generated in excel sheet as shown in Figs. 3 and 4.

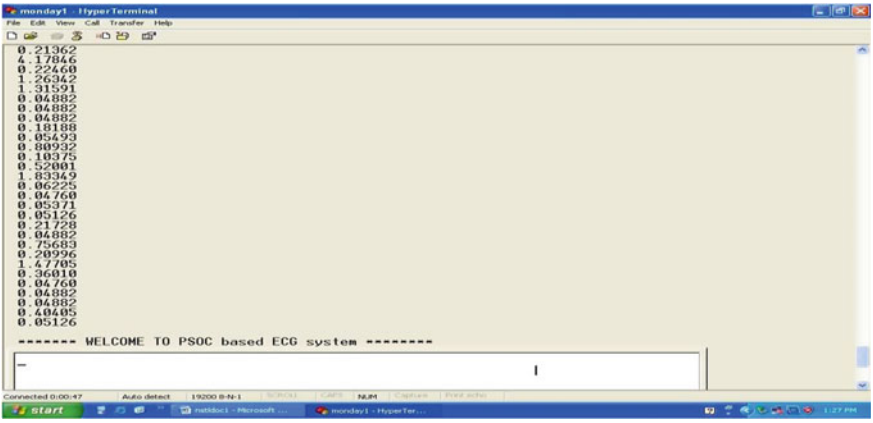


Fig. 3 Hyper terminal output

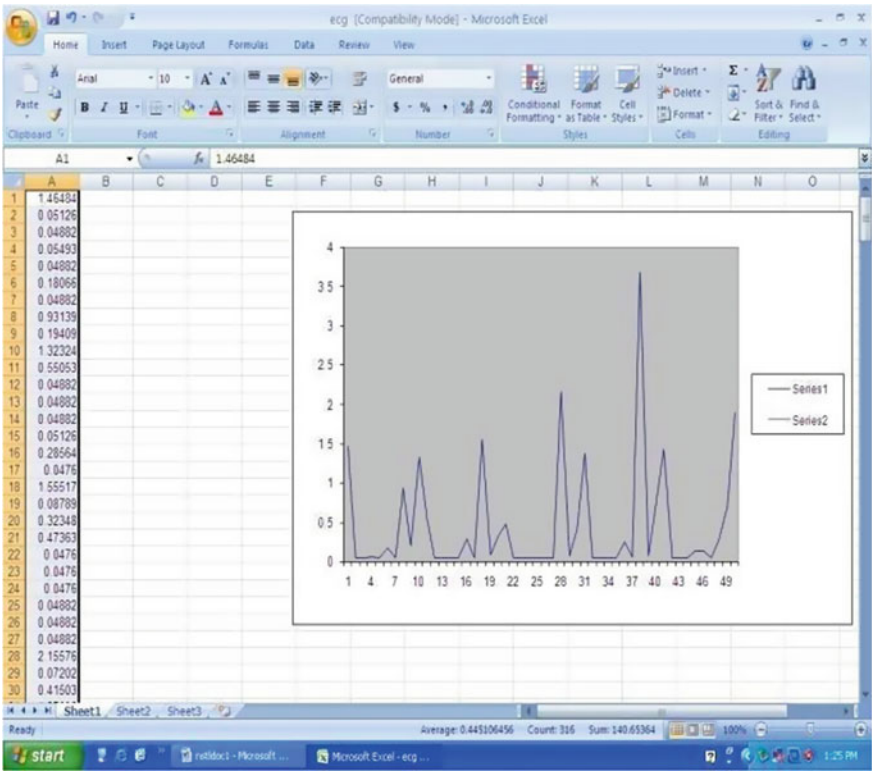


Fig. 4 Generated signal in excel sheet

Acknowledgments The authors are thankful to Dr. Lavu Rathaih, Chairman Vignan's Group and Prof. A Sesha Rao, Principal of Vignan's Institute of Engineering for Women, Visakhapatnam for giving support in doing the work.

References

1. K Krishna Bai, SC Prasanna Kumar, Canadian Journal on Bio Medical Engineering and Technology, Vol. 3 No. 2, February 2012.
2. E Frank, An accurate, clinically practical system for spatial Vectorcardiography. Circ., 1: 737–749, 1956.
3. Ch Ramesh Babu, Vineesha K, T Soumya, Padmaja M, " Realization of ECG using MSP430", International Journal of Electronics, Electrical and Computational System (IJEECS-March 2015), Volume 4, ISSN 2348-117X.
4. Ch Ramesh Babu, AV Nageswara Rao, Puvvada Ramesh, "PSoC Based ECG System", National Journal of Instrumentation Society of India, Vol. 40 No. 1, March 2010.
5. Massot B, Gehin C, Nocua R, Dittmar A, McAdams E, "A wearable, low-power, health-monitoring instrumentation based on a Programmable System-on-Chip", EMBC, Annual International Conference of the IEEE, pp. 4852–55, 2009.

6. Ch Ramesh Babu, Hemalatha, Divya Vani," 12-Lead Portabele ECG using Programmable system on chip", IEEE International Conference on System Engineering and Emerging Systems (ICSEES-2014).
7. Serhiy Matviyenko, Cypress application note AN2284, "Low Cost EKG Pulsometer", Document no. 001-25719, 2006.
8. Ch Ramesh Babu, M Srinanvasa Rao "Design and development of Automatic Test setup for On Board Computer using PSoC and MEMS", 2nd IEEE International Conference on Parallel Distributed and Grid Computing (PDGC-2012), ISBN 978-1-4673-2922-4, 2012.

Design and Implementation of Wearable Device for Water Management System for Household Usage

Manpreet Kaur Khurana, Rajesh Singh, Vivek Kaundal and Nikhil Gupta

Abstract India being the second largest populated country, it has become difficult to keep a track of the basic necessities of every individual. This research describes a device monitoring the water level as well as quality of the water supply in households. The system is automated using a microcontroller for the process of pumping water and monitoring the quality of water. This is an IOT-based system in which the different sensor nodes communicate via RF module and Wi-Fi technology. The data has been sent on the Internet using Wi-Fi module.

Keywords Water management system · RF module · Wi-Fi module · Hall Effect · Transmitter · Receiver · Sensors

1 Introduction

For proper water supply, water management is required for wise use of water resources. The main problems are poor water allocation, degraded water health and lack of adequate water management. This problem is the motivation of this research to eliminate water wastage and improve water health. Abdullah-Al-Mamun et al. proposed a multi sensor Wireless Data Acquisition System for a water-level monitoring system that can communicate using RF module [1]. Gutierrez et al. proposed an algorithm with threshold values of temperature and soil moisture to control water quality. The photovoltaic panels power the system based on a cellular–internet interface [2]. Zia et al. reviewed the role of nonpoint sources with respect to contributions of nutrient and contaminant [3]. Ning et al. proposed a wireless water environment monitoring system. The sensor nodes measure the PH, dissolved oxygen, conductivity, and temperature and communicate via RS232 or 3

M.K. Khurana (✉) · Rajesh Singh · Vivek Kaundal
University of Petroleum and Energy Studies, Dehradun, India
e-mail: manpreetkhurana26@gmail.com

Nikhil Gupta
Larsen & Toubro Limited, Bangalore, India

© Springer Science+Business Media Singapore 2017

R. Singh and S. Choudhury (eds.), *Proceeding of International Conference on Intelligent Communication, Control and Devices*, Advances in Intelligent Systems and Computing 479, DOI 10.1007/978-981-10-1708-7_95

G/GPRS [4]. Rasin et al. proposed that a water flow control wireless monitoring system like Zigbee technology reduces the cost as well provide flexibility in distance or location [5]. System has a facility to auto-monitor the water temperature and pH value environment of an artificial lake online [6]. Jiang et al. proposed a wireless water environmental monitoring system for complex and large scale monitoring. Zhou et al. proposed a wireless solution for large-scale remote intelligent field irrigation based on Zigbee protocol [7]. Lin et al. proposes a communication model for water distribution network monitoring system. The validation of the system was done by flat earth two-ray model [8]. Kim et al. proposed a real-time wireless sensor network for in-field sensing of an irrigation system [9]. O'Flyrm et al. proposed a multi sensor system "Smart Coast" that is used to monitor water quality by measuring the temperature, phosphate level, dissolved oxygen level, conductivity value, pH value, turbidity, and water level [10]. Panchard et al. proposed a method to design the ICT tools targeted at the resource poor to be new [11].

2 Proposed System

The system includes three nodes: two transmitters and one receiver. The data from the transmitters to the receiver is transmitted using RF modules. The data from one transmitter is sent to the server via Wi-Fi module.

2.1 Block Diagram

Figure 1 depicts the block diagram of two transmitter nodes. One of the transmitter nodes includes a top tank from where the water enters the household, microcontroller, level sensor, flow sensor, PH sensor, RF module, Wi-Fi module, and display unit. The data of the sensors are transmitted to the receiver via RF module and also to server via Wi-Fi module. The second transmitter node includes the lower tank, microcontroller, level sensor, RF module, and motor and display unit. Whenever the water level in upper tank is less than a decided value, the motor pumps the water from lower tank to upper tank automatically. The data of both nodes is displayed on their respective LCD display.

Figure 2 shows the block diagram of receiver node which includes a microcontroller, RF module, and a display unit.

2.2 Prototype Development

Arduino mega 2560 is used as the microcontroller at the transmitter nodes to get the data from the sensors and sent to the receiver wirelessly. Arduino Uno is used as the

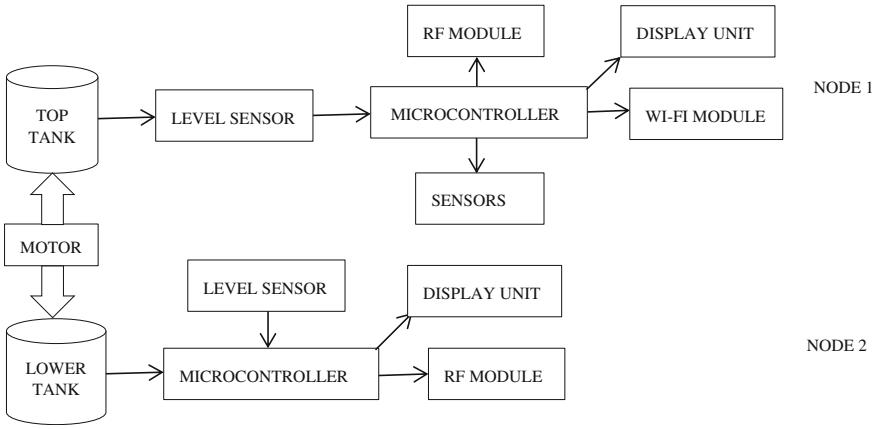


Fig. 1 Block diagram—transmitter node 1 and node 2



Fig. 2 Block diagram—receiver node 3

microcontroller at the receiver node to receive the data wirelessly and display on the LCD. The main modules that are used in the system circuit are as follows:

1. PH sensor: The sensor consists of a probe and an electronic circuit. It gives a value between 0 and 14 PH.
2. Ultrasonic sensor (HC-SR04): The sensor is used to measure the distance and in this case the level of water in tank.
3. Flow sensor: It is a sensor used to measure water consumed in liters per min. It works on the principle of Hall Effect.
4. RF module: It is a module that works on 2.4 GHz frequency in half duplex mode.
5. Wi-Fi module: The module used is ESP 8266 to send the sensor data on the server so that the user can access the data on the mobiles.
6. LCD: LCD (16 × 2) is used at the transmitter nodes to display the sensor data and LCD (20 × 4) is used at the receiver node to display the received sensor data.

2.3 Circuit Diagram

Node 1 transmitter unit Fig. 3 shows the circuit diagram of node 1 and node 2. Node 1 consists of flow sensor, ultrasonic sensor, RF module, ESP 8266, Arduino mega, PH sensor, and LCD. The flow sensor is connected to the digital pin 8 of the

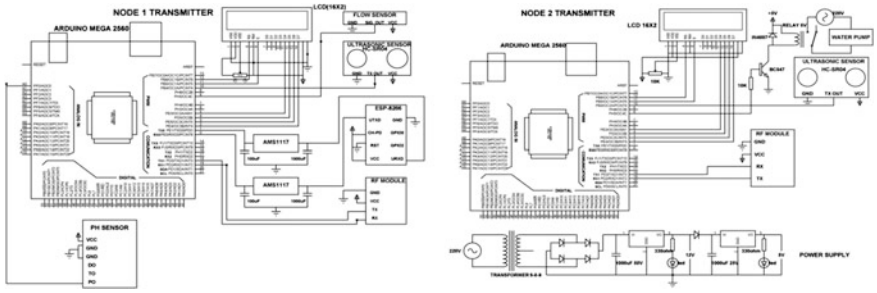


Fig. 3 Circuit diagram for node 1 and node 2 transmitter

microcontroller. The Ultrasonic senor is connected to the 10 pin of the microcontroller. Esp8266 is connected to the Rx0 and Tx0 pin of the microcontroller via AMS1117 to provide a voltage of 3.3 V. RF module is connected to the Rx1 and Tx1 pin of the microcontroller. PH sensor pin P0 is connected to A0 pin the microcontroller. Node 2 transmitter consists of a relay circuit to drive the motor, ultrasonic sensor, RF module, Arduino Mega 2560 and LCD. The relay circuit is connected to pin 8 of the microcontroller. The ultrasonic senor is connected to pin 8 of the microcontroller. RF module is connected to the Rx1 and Tx1 of the microcontroller.

Figure 4 shows the circuit diagram of node 3 receiver which consists of RF module, Arduino uno, and RF module.

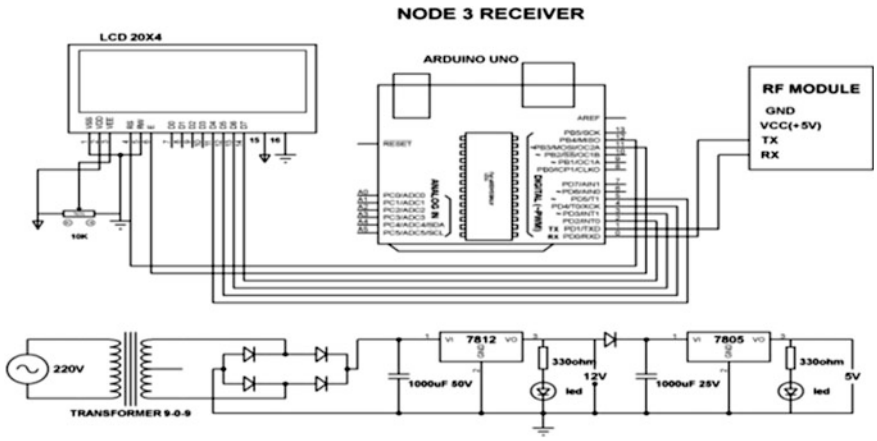


Fig. 4 Circuit diagram for node 3 receiver

2.4 Algorithm

See Fig. 5.

3 Software Development

Software for the nodes has been developed using Arduino IDE 1.6.7 and Proteus simulator. The basic steps are (Fig. 6):

3.1 Proteus Simulation

It is used as hardware simulation software. Before the hardware implementation, its feasibility is checked through this software (Figs. 7 and 8).

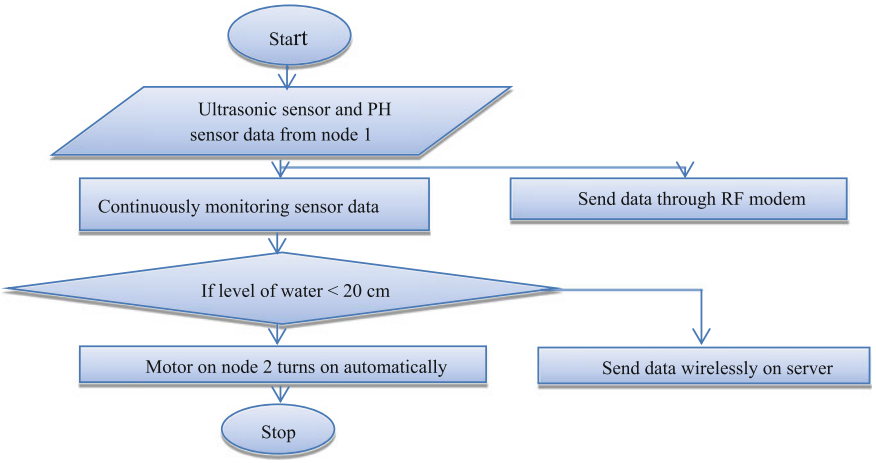
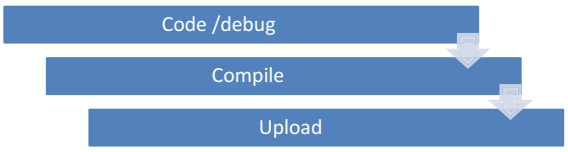


Fig. 5 Flow chart of the proposed system

Fig. 6 Coding steps



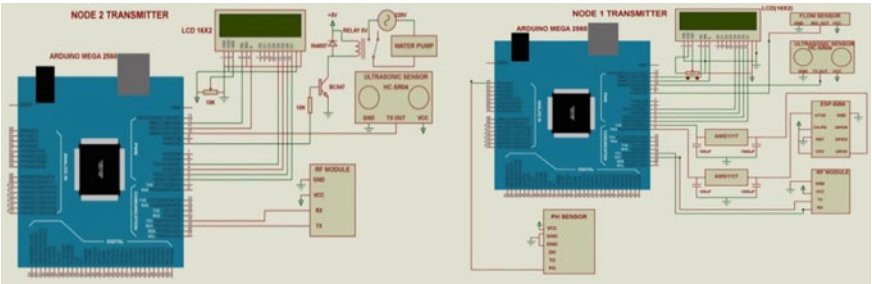


Fig. 7 Shows the Proteus model for node 1 and node 2 transmitter

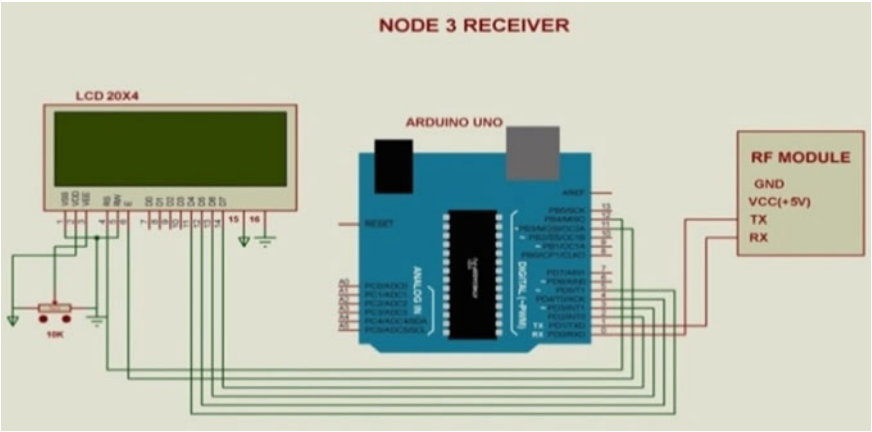


Fig. 8 Node 3 receiver

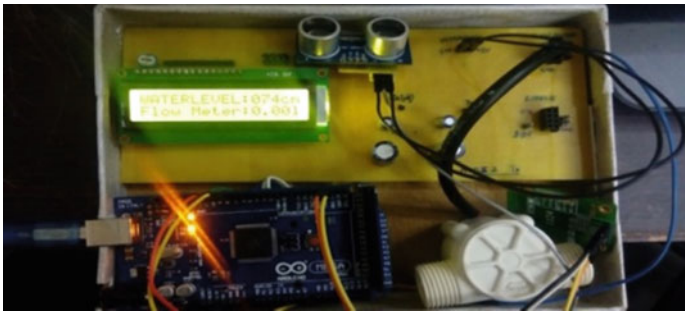


Fig. 9 Hardware prototype of the proposed system

4 Result and Conclusion

The data is being transmitted to the receiver via RF modules and data is being received on the server using ESP8266 Wi-Fi module, thus the proposed prototype is the hand held device through which a user can check the amount of water consumption and its quality from any place (Fig. 9).

It has been observed that PH of water varies from 6.5 to 8.5 for different water types and any value below this or above this will mean contamination of water. Also, it was observed that ESP8266 has more current consumption than RF modules since it draws a minimum of 500 mA of current. So, due to this the circuit on whole requires a min of 1A of current supply. Also, Esp8266 requires a separate power supply of 3.3v which cannot be provided by Arduino board.

References

1. Abdullah-Al-Mamun, et al. "Use of Wireless Sensor and Microcontroller to develop Water." Vol. 7(9), 1321–1326, September 2014.
2. Gutierrez, Jessica, et al. "Automated irrigation system using a wireless sensor network and GPRS module." *Instrumentation and Measurement, IEEE Transactions on* 63.1 (2014): 166–176.
3. Zia, Huma, et al. "The impact of agricultural activities on water quality: A case for collaborative catchment-scale management using integrated wireless sensor networks." *Computers and electronics in agriculture* 96 (2013): 126–138.
4. Jin, Ning, et al. "A novel design of water environment monitoring system based on wsn." *Computer Design and Applications (ICCDA), 2010 International Conference on*. Vol. 2. IEEE, 2010.
5. Rasin, Zulhani, Hizzi Hamzah, and Mohd Shahrieel Mohd Aras. "Application and evaluation of high power zigbee based wireless sensor network in water irrigation control monitoring system." *Industrial Electronics & Applications, 2009. ISIEA 2009. IEEE Symposium on*. Vol. 2. IEEE, 2009.
6. Jiang, Peng, et al. "Design of a water environment monitoring system based on wireless sensor networks." *Sensors* 9.8 (2009): 6411–6434.
7. Zhou, Yiming, et al. "A wireless design of low-cost irrigation system using ZigBee technology." *Networks Security, Wireless Communications and Trusted Computing, 2009. NSWCTC'09. International Conference on*. Vol. 1. IEEE, 2009.
8. Lin, Min, Yan Wu, and Ian Wassell. "Wireless sensor network: Water distribution monitoring system." *Radio and Wireless Symposium, 2008 IEEE*. IEEE, 2008.
9. Kim, Yunseop, Robert G. Evans, and William M. Iversen. "Remote sensing and control of an irrigation system using a distributed wireless sensor network."*Instrumentation and Measurement, IEEE Transactions on* 57.7 (2008): 1379–1387.
10. O'Flyrm, B., et al. "SmartCoast: a wireless sensor network for water quality monitoring." *32nd IEEE Conference on Local Computer Networks, 2007. LCN 2007*. IEEE, 2007.
11. Panchard, Jacques, et al. "Common-sense net: Improved water management for resource-poor farmers via sensor networks." *Information and Communication Technologies and Development, 2006. ICTD'06. International Conference on*. IEEE, 2006.

High Speed-Low Power Divide-by-16/17 Dual Modulus Prescaler Using C^2MOS

Anupriya Chakraborty, Akanksha Agrawal, Snehil Gupta, Sachin Kumar Rajput and Anu Mehra

Abstract A low power-high speed C^2MOS, divide-by-16/17 dual modulus prescaler design is presented. By adopting C^2MOS designing technique over simple CMOS implementation, the power dissipation is reduced by 29.48 % and the speed of the circuit is improved by 77 %. It also reduces the chip area as the overall number of transistors used in the proposed circuit is reduced. The circuit is implemented in 0.18 μm CMOS technology. The frequency of operation of the circuit is 10 MHz and it operates at a supply voltage of 2 V.

Keywords Dual modulus prescaler · C^2MOS · High speed · Low power · Divide-by-16/17

1 Introduction

Dual modulus prescaler is useful for PLL (Phase Locked Loop) design. Injection locked frequency prescaler with CMOS technology gives frequency of hundreds/tens GHz. Other prescalers like TSPC (True Single Phase Clock) dual modulus prescaler is used in many GHz operations with the help of CMOS technology because TSPC prescaler has the advantage of single phase clock in addition

Anupriya Chakraborty · Akanksha Agrawal · Snehil Gupta · S.K. Rajput (✉) · Anu Mehra (✉)
ECE Department, ASET, Amity University, Noida, Uttar Pradesh, India
e-mail: skrajput@amity.edu

Anu Mehra
e-mail: amehra@amity.edu

Anupriya Chakraborty
e-mail: chakrabortyanupriya.ac@gmail.com

Akanksha Agrawal
e-mail: akanksha.agrawal1411@gmail.com

Snehil Gupta
e-mail: snehilgupta311@yahoo.com

© Springer Science+Business Media Singapore 2017

R. Singh and S. Choudhury (eds.), *Proceeding of International Conference on Intelligent Communication, Control and Devices*, Advances in Intelligent Systems and Computing 479, DOI 10.1007/978-981-10-1708-7_96

with low power, chip area and large output variation [1–3]. In this case, using a forward biasing technique improves the speed of the circuit by reducing the voltage i.e. threshold on NMOS transistor [1]. At the cost of speed it suffers from very large minimum frequency and an increase in cost. If we opt for ETSPC (Extended True Single Phase Clock) it improves the operating speed of the circuit but the leakage of current becomes a major issue and thus limits the performance [1, 4, 5]. TSPC and ETSPC require a large chip area, due to larger number of transistors [4, 6, 7], thus it is beneficial to design the circuit with C^2MOS technology. C^2MOS has many advantage like insensitive to overlap, speed, used to build low power dissipation circuits, operation is simple and so on. Its applications are found in signal processing, radar systems and so on. This work aims to design a 16/17 dual modulus prescaler with the help of C^2MOS technology, to improve the speed and the delay of the prescaler circuit. This whole paper is organized in the following manner—Sect. 2 discusses the D-FF (D-Flip Flop) designs, simple CMOS prescaler circuit design and its results and the C^2MOS prescaler circuit design and its result. In Sect. 3, the operational working of the prescaler circuit is given and Sect. 4 provides a comparative study of the performance characteristics and results of the circuits.

2 Prescaler Design

The prescaler circuit used in this paper essentially uses five D-FFs to perform a divide-by-16 or divide-by-17 operation [8]. The first two D-FFs act as a divide-by-2/3 prescaler and the other three act as an asynchronous divide-by-8 prescaler [9]. This structure allows the circuit to perform dual mode division, based on a control signal MC (Mode Control).

2.1 C^2MOS D-Flip Flop

Figures 1 and 2 show the D-FF circuits using simple CMOS and C^2MOS respectively.

Due to the use of C^2MOS technology the numbers of transistors are reduced which in turn reduces the chip area. The benefits of the proposed circuit can be seen from its comparison with the simple CMOS D-FF circuit (simple CMOS D-FF (Fig. 1)) and Table 1. Both the circuits, the conventional C^2MOS D-FF and the CMOS D-FF are fabricated in 0.18 μm technology and have an operating frequency of 10 MHz.

C^2MOS is a dynamic circuit designing technique that employs the use of two phased clocking system which is insensitive to clock skew. It makes use of two clock signals, CLK and CLKBAR (complement of signal CLK) to make the designed circuit immune to overlapping.

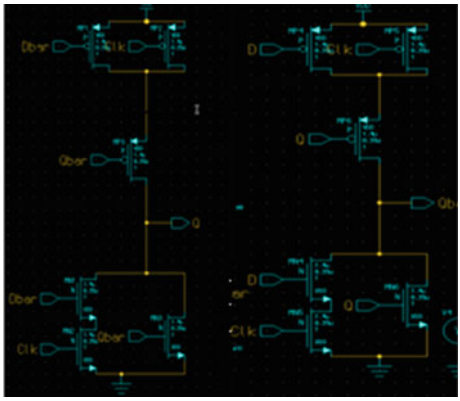


Fig. 1 Simple CMOS D-FF circuit

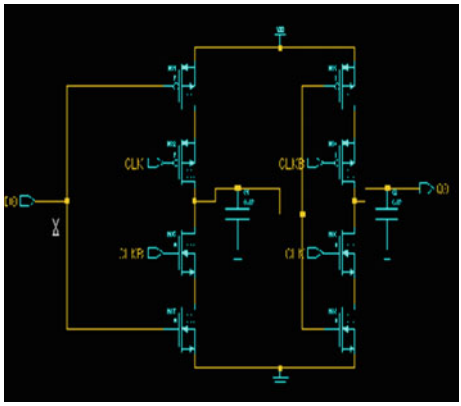


Fig. 2 C^2MOS D-FF circuit

Table 1 Comparison of performance characteristics of simple D-Flip Flop and C^2MOS D-Flip Flop

Type	CMOS	C^2MOS
Circuit	D-Flip Flop	D-Flip Flop
Frequency	10 MHz	10 MHz
Power (mW)	0.007	0.002
Supply (V)	2	2
Process (μm)	0.18	0.18
Delay (ns)	50.186	31.3
Total number of transistors	12	10

2.2 Divide-by-16/17 CMOS Prescaler

The design for the divide-by-16/17 prescaler is shown in Fig. 3. In the given circuit a simple CMOS prescaler is designed. It has a four input NAND gate with its inputs as QN1, QN2, QN3 and MC (Mode Control). Fin is fed as clock to the first two flip

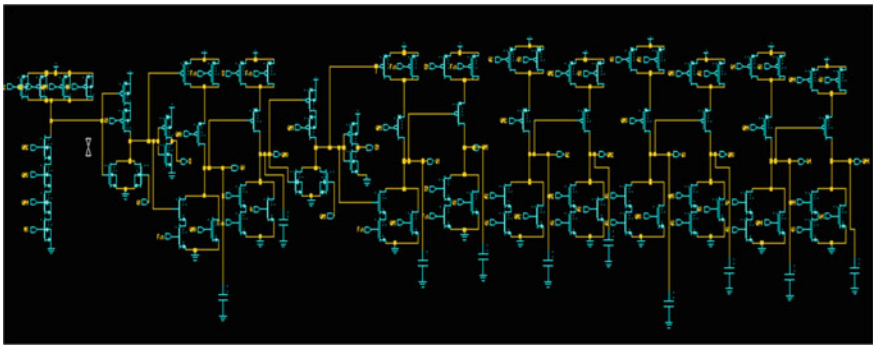


Fig. 3 CMOS divide-by-16/17 prescaler circuit

flops and the other three flip flops act as an asynchronous divide-by-8 prescaler [1]. The function of the signal MC is to decide whether the prescaler divides by 16 or 17. And the output is observed at QN4. The prescaler circuit performs frequency division of 16 if MC = 0 and of 17 if MC = 1. The performance characteristics of the circuit can be observed in Table 2. The circuit has been implemented using 0.18 μm CMOS technology.

2.3 Divide-by-16/17 C^2MOS Prescaler

Figure 4 illustrates the schematic design of divide-by-16/17 frequency divide constructed from divide-by-2/3 prescaler and an Asynchronous divide-by-8 prescaler [10]. It consists of five D-FFs designed using C^2MOS technology with two OR gates and a four input NAND gate [1]. In the circuit designed, the signal MC (mode control) is used to control the dividing operation of the prescaler.

On comparison of generic D latch with C^2MOS D latch there is an effective reduction of two transistors per flip flop which ultimately reduces the number of transistors employed to design the whole prescaler circuit by ten. As a result of which the power dissipation values of the prescaler design reduces to 0.55 mW for the C^2MOS prescaler as compared to 0.78 mW for the simple CMOS prescaler.

Table 2 Comparison of performance characteristics of simple 16/17 prescaler and C^2MOS 16/17 prescaler

Type	CMOS	C^2MOS
Divide ratio	16/17	16/17
Frequency	10 MHz	10 MHz
Power (mW)	0.78	0.55
Supply (V)	2	2
Process (μm)	0.18	0.18
Delay (ns)	61.215	13.773
Total number of transistors	80	70

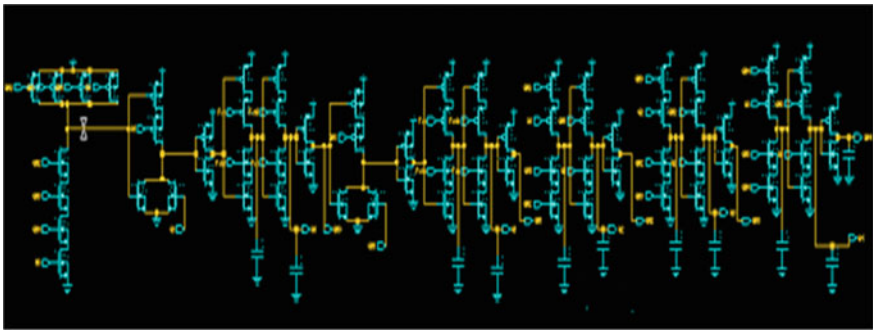


Fig. 4 C^2MOS divide-by-16/17 prescaler circuit

In the prescaler design the operating frequency is 10 MHz. There has also been a considerable reduction in the delay value from 61.215 to 13.773 ns.

2.4 Divide-by-16/17 C^2MOS Prescaler Operation

As illustrated in Fig. 4, the divide-by-16/17 dual modulus prescaler consists of a divide-by-2/3 prescaler and an asynchronous divide-by-8 prescaler. The mode of operation of the circuit is controlled by the input MC (mode control). For MC = 0 the circuit operates in divide-by16 mode and for MC = 1 the circuit operates in MC = 1. The operation of the illustrated circuit is explained a follows. When MC = 0, irrespective of values of QN2, QN3, QN4 the input which feeds into DFF0 is low (D0 = 0). The divide by 2/3 prescaler controlled by D0, performs divide-by-2 operation eight times in a cycle. Therefore the whole circuit performs an operation of divide-by-16 [1].

Similarly when the value of Mode Control (MC) = 1, value of input of DFF0 changes in accordance with the values of QN4, QN3, QN2. The divide by 2/3 prescaler is controlled by D0 and performs divide-by-2 operation seven times and divide-by-3 operation once in a given cycle. The whole circuit hence performs an operation of divide-by-17 [1]. It is also noted that the determination of maximum working frequency of the prescaler design is done by its divide-by-17 operational mode.

In reference to the timing diagram as shown in Fig. 5, it can be observed that for first rising edge of the Fin, output of QN2 and QN1 switched from high to low. For the second rising edge of the Fin, the signal QN1 switches its value from low to high and holds it for two pulse values. For the third rising edge, QN2 switches from low to high and holds the values for two periods. Hence an inference can be made that for MC = 0 the prescaler performs operation in divide-by-16 mode. Similarly it can also be observed that for MC = 1 the prescaler circuit works in divide-by-17 operation mode.

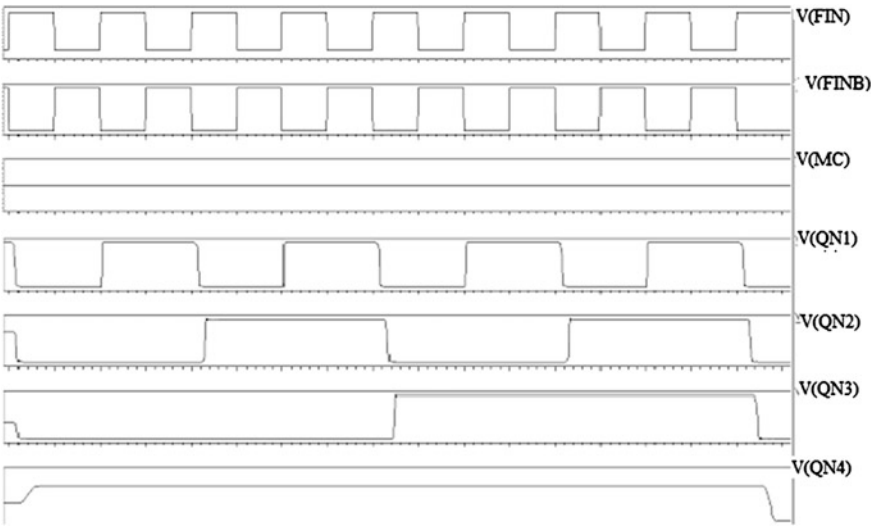


Fig. 5 Timing diagram of the C^{2}MOS prescaler

3 Analysis and Simulation

The circuits shown in Figs. 3 and 4 are simulated using Mentor Graphics ELDO spice simulator. A conventional dual modulus divide-by-16/17 prescaler is designed in an 0.18 µm CMOS technology. The circuit is implemented using a supply voltage of 2 V. A comparison of the performance parameters of simple D-FFs implemented with and without C^{2}MOS technique is provided in Table 1.

As a result the circuit is further modified using C^{2}MOS technique to yield better results. The two circuits are further analyzed and this comparison is provided in Table 2.

The proposed C^{2}MOS design uses 70 transistors which results in a smaller chip area. It further shows a reduction in delay from 61.215 ns to 13.773 ns. The power dissipation is also reduced from 0.78 mW to 0.55 mW. Thus the proposed C^{2}MOS circuit shows a reduction in delay of about 77 % whereas there is a reduction in power dissipation of about 29.48 % (Table 3).

Table 3 Comparision of proposed circuit with previous work

	[11]	[1]	This work
Publication	TVLSI	IEEE	–
Year	2012	2015	–
Type	TSPC	TSPC	C^{2}MOS
Divide ratio	32/33/47/48	16/17	16/17
Power (mW)	2.2	2.6	0.55
Supply (V)	1.8	1.6	2
Process (µm)	0.18	0.18	0.18

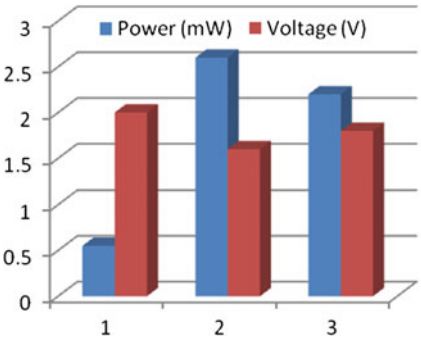


Fig. 6 Power comparison

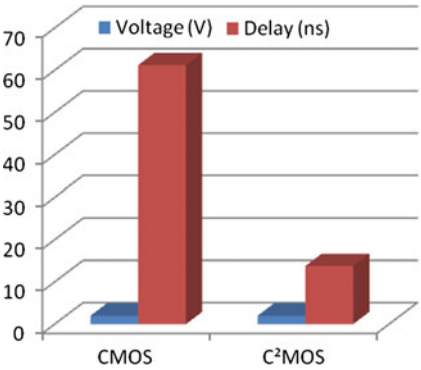


Fig. 7 Delay comparison

The operating frequencies of both the circuits are 10 MHz at an operating voltage of 2 V (Figs. 6 and 7).

4 Conclusion

In this paper, a low power-high speed divide-by-16/17 dual modulus prescaler using C^2MOS is presented. By adopting a C^2MOS designing technique over simple CMOS implementation, the power dissipation is reduced by 29.48 % and the speed of the circuit is improved by 77 %. The total number of transistors are also reduced from 80 (CMOS prescaler) to 70 (C^2MOS prescaler), which thereby reducing the chip area. The circuit is implemented in 0.18 µm CMOS technology operating at 2 V supply. The operating frequency of the circuit is 10 MHz. The modified circuit leads to better performance parameter values for the prescaler.

References

1. Wenrui Zhu, Haigang Yang, Tongqiang Gao, Fei Liu, Tao Yin, Dandan Zhang, and Hongfeng Zhang, "A 5.8-GHz Wideband TSPC Divide-by-16/17 Dual Modulus Prescaler": IEEE Transactions on Very Large Scale Integration (VLSI) Systems (Volume: 23, Issue: 1), January 2015.
2. Wu-Hsin Chen, Byunghoo Jung, "High-speed low-power true single-phase clock dual-modulus prescalers": IEEE Transactions on Circuits and Systems II: Express Briefs (Volume: 58, Issue: 3), 24 February 2011.
3. Ching-Yuan Yang, Guang-Kaai Dehng, June-Ming Hsu, Shen-Iuan Liu, "New dynamic flip-flops for high-speed dual-modulus prescaler": IEEE Journal of Solid-State Circuits (Volume: 33, Issue: 10), October 1998.
4. Seungsoo Kim and Hyunchol Shin, "An E-TSPC Divide-by-2 with Forward Body Biasing in 0.25 μm CMOS. Microwave and Wireless Components Letters, IEEE (Volume: 19, Issue: 10), 09 September 2009.
5. X. P. Yu, W. M. Lim, M. A. Do, X..L. Yan, and K. S. Yeo, "6.1 GHz 4.6 mW CMOS divide-by-55/56 Prescaler": Electron. Lett. (Volume: 44, Issue: 24), pp. 1402–1403, November 2008.
6. Amin Bazzazi, Abdolreza Nabavi, "Design of a low-power 10 GHz frequency divider using Extended True Single Phase Clock (E-TSPC) logic": Emerging Trends in Electronic and Photonic Devices and Systems, 2009. ELECTRO '09. International Conference, 22–24 December 2009.
7. Melanie Jung, Joerg Fuhrmann, Alban Ferizi, Georg Fischer, Robert Weigel, Thomas Ussmueller, "Design of a 12 GHz Low-Power Extended True Single Phase Clock (E-TSPC) Prescaler in 0.13 μm CMOS technology": Microwave Conference Proceedings (APMC), 2011 Asia-Pacific.
8. Shilin Yan, Song Jia, Wenyi Tang, Jiyu Chen, Ziyi Wang, Weiting Li, "A 16/17 prescaler based on novel TSPC 2/3 devider scheme": Solid-State and Integrated Circuit Technology (ICSICT), 2014 12th IEEE International Conference.
9. Siraphop Tooprakai, Apirak Tudsorn, "A 1.2 V low-power true single-phase clock CMOS 2/3 prescalers": Information Science, Electronics and Electrical Engineering (ISEEE), 2014 International Conference (Volume: 3).
10. Yin-Tsung Hwang and Jin-Fa Lin, "Low Voltage and Low Power Divide-by-2/3 Counter Design Using Pass Transistor Logic Circuit Technique": IEEE Transactions on Very Large Scale Integration (VLSI) Systems (Volume: 20, Issue: 9), September 2012.
11. Vamshi Krishna Manthena, Manh V. Do, Chirn Chye Boon, and Kiat Seng Yeo, "A low-power single-phase clock multiband flexible divider": IEEE Transactions on Very Large Scale Integration (VLSI) Systems (Volume: 20, Issue: 20), February 2012.

Design and Optimization of Luggage Tracking System on Airport

Varun Gupta, Roushan Kumar, Raj Gaurav Mishra, Anirudha Semwal and Sweety Siwach

Abstract The loss or mishandling of luggage in airports is increasing nowadays, tremendously raising its associated costs. It is expected that the constant monitoring detects possible errors in a timely manner, allowing a proactive attitude when correcting this kind of situations. There are several devices in the market but all have some problems such as power consumption, location, portability, etc. The current research provides a novel idea to track the luggage in real time with the help of a microcontroller system, which is wearable and handy. Using wireless communication techniques the proposed system has been designed. Power consumption is the most important feature in the luggage tracking system. With the inclusion of accelerometer, the device consumes less power. The proposed system increases the monitoring detail when compared to current monitoring systems because it allows the individual tracking of luggage. It has also a web application to know about location of luggage and GSM module for the text application.

Keywords Luggage tracking system · Luggage handling process · Real-time event processing · Flexible luggage monitoring · Wearable

1 Introduction

The luggage handling process in the airports is very complex and uncertainty factors in most of the passenger's opinion. Many passengers feel uncomfortable when they see their luggage disappearing behind the check-in. In the current scenario, the luggage tracking is done with the help of RFID. Chung [1] medication tracking and medical assistance device and method comprises an RFID tag coder for reading from and/or writing to an RFID. The tracking device, which fits inside or is attached to luggage, pinpoints the identity of a bag in real time. The method of

Varun Gupta (✉) · Roushan Kumar · R.G. Mishra · Anirudha Semwal · Sweety Siwach
University of Petroleum and Energy Studies, Dehradun, India
e-mail: varun.gupta5may@gmail.com

© Springer Science+Business Media Singapore 2017

R. Singh and S. Choudhury (eds.), *Proceeding of International Conference on Intelligent Communication, Control and Devices*, Advances in Intelligent Systems and Computing 479, DOI 10.1007/978-981-10-1708-7_97

tracking through RFID is popular earlier but now the method of tracking in my project has something new technology from RFID. RF identification system for identifying objects by communication between a RF transceiver, mounted on luggage and a RF receiver. The preferred electronic signaling chip or device is an RFID tag that is affixed to luggage. RFID tag contains a transponder, which is energized by the excitation signal to transmit a response signal which contains identifying information back to the interrogator. Every RFID has a unique identity. With this unique identity when we touch this RFID with the luggage, then person can find their luggage. Chadil et al. [2] proposed the system which has GPS/GPRS module that can easily track the location and sends the message though web server. Peijiang and Xuehua [3] proposed the system which has remote monitoring system based on SMS of GSM.

In this paper luggage tracking system has no RFID. It is ARDUINO processor based. In which we have ARDUINO processor, GSM module, Wi-Fi module, GPS module, and accelerometer for the power factor and the device is chargeable (can run without power supply). The working procedure of this device is that it has been kept in the luggage at the airport though which user can get the SMS or he can get a message from android app in his phone regarding their location. As this device is chargeable it is automatically turned off when the plane takes off. This is so because plane generates acceleration and accelerometer prepares the device to enter in airplane mode. And after that when the plane is landing the device is automatically turned ON with the help of accelerometer (plane generates acceleration during landing also) and sends the location via SMS or message on the android application. Thus user can find their luggage.

2 Proposed System

The system comprises of a luggage tracking device that tracks the luggage using a GPS module and sends the location of the luggage using GSM module. The GSM module sends a text message to the user's mobile specifying the location of the misplaced luggage.

2.1 Block Diagram

Figure 1 shows the system block diagram. The system includes a GPS module, a GSM module, and a microcontroller.

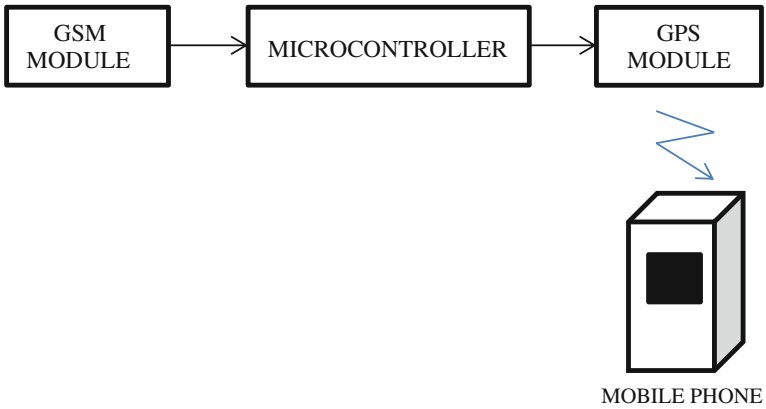


Fig. 1 System block diagram

2.2 Prototype Development

The main modules of the system are as follows:

1. **GSM module**: GSM SIM 900 module is used to send text message to the user mobile. It operates at 12 V DC.
2. **GPS module**: This module is used to get the coordinates of the location of the luggage.
3. **Control unit**: Control unit comprises Arduino UNO microcontroller. It is a 8-bit microcontroller and operates at 16 MHz frequency.

2.3 Circuit Diagram

Figure 2 shows the circuit diagram which includes the GSM module, GPS module, and Arduino UNO. GSM module is connected to the microcontroller via a RS-232 module. TX and RX pin of GPS module is connected to RX and TX pin of the microcontroller.

3 Proteus Simulation

This software is used to check the feasibility of the circuit before it is implemented (Fig. 3).

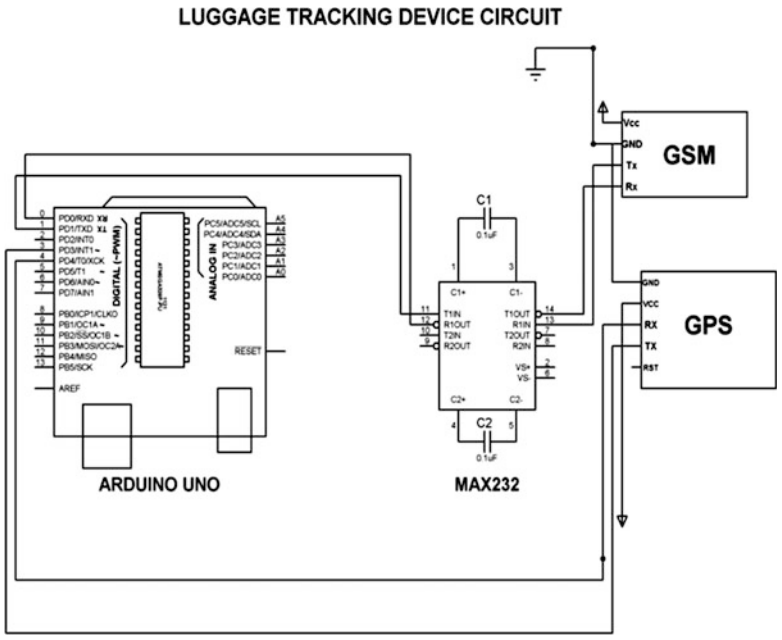


Fig. 2 System circuit diagram

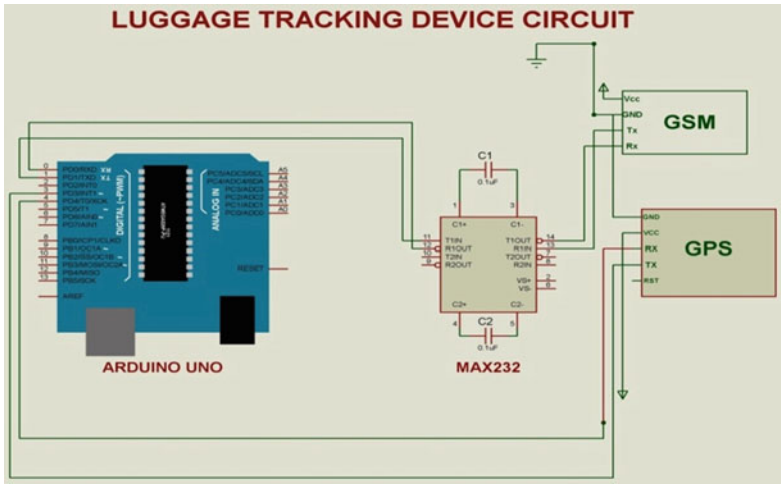
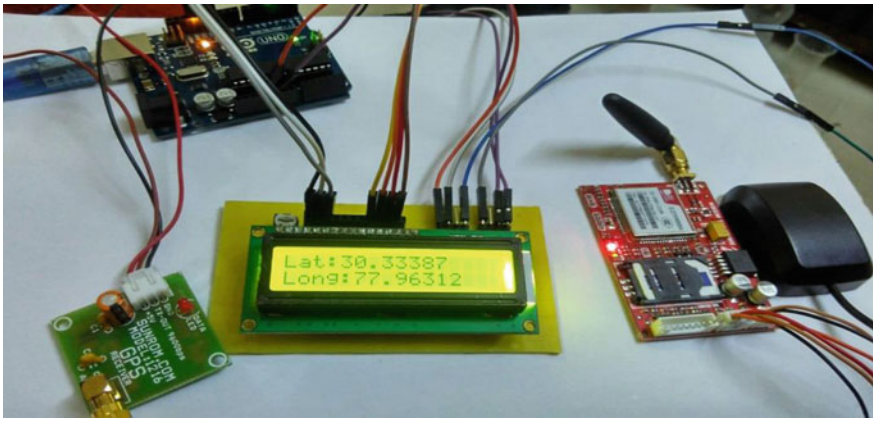


Fig. 3 Proteus simulation of the system circuit diagram

4 Result and Conclusion

In this paper, an efficient controller-based luggage tracking system for airport luggage was proposed. A number of technologies have been implemented to speed these processes but one technology that has the potential to revolutionize baggage handling technique is controller-based technique. This system helps us to find the luggage in real-time with the help of user mobile. This system is different from RFID system. User can track their luggage from anywhere from world. The system provides significant improvement in communication between user and luggage. This will improve passenger security and satisfaction as well as reducing delays in flight caused by mishandled luggage.



References

1. Chung, Kevin Kwong-Tai. "Medical assistance and tracking system and method employing smart tags." U.S. Patent No. 7,158,030, 2 Jan. 2007.
2. Chadil, Noppadol, Apirak Russameesawang, and Phongsak Keeratiwintakorn. "Real-time tracking management system using GPS, GPRS and Google earth." Electrical Engineering/Electronics, Computer, Telecommunications and Information Technology, 2008. ECTI-CON 2008. 5th International Conference on, Vol. 1. IEEE, 2008.
3. Peijiang, Chen, and Jiang Xuehua. "Design and Implementation of Remote monitoring system based on GSM." Computational Intelligence and Industrial Application, 2008. PACIIA'08. Pacific-Asia Workshop on, Vol. 1. IEEE, 2008.
4. W. El-Medany, Wael, et al. "A cost effective real-time tracking system prototype using integrated GPS/GPRS module." Wireless and Mobile Communications (ICWMC), 2010 6th International Conference on. IEEE, 2010.
5. Yuchun, Ma, et al. "General application research on GSM module." Internet Computing and Information Services (ICICIS), 2011 International Conference on. IEEE, 2011.

6. Al-Khedher, Mohammad A. “Hybrid GPS-GSM localization of automobile tracking system.” arXiv preprint arXiv:1201.2630 (2012).
7. Chung, Kevin Kwong-Tai. “Tracking system and method employing plural smart tags.” U.S. Patent No. 7,098,793, 29 Aug. 2013.
8. Collotta, Mario, Giovanni Pau, and Salvatore Tirrito. “A preliminary study to increase baggage tracking by using a RFID solution.” Proceedings Of The International Conference On Numerical Analysis And Applied Mathematics 2014 (ICNAAM-2014), Vol. 1648. AIP Publishing, 2015.
9. Lee, Brian, et al. “Asset tracking system with data ping based on asset movement.” U.S. Patent No. 9,020,527, 28 Apr. 2015.

Contact Thickness Variation Effect on Performance of Novel Organic Thin Film Transistor

Aanchal Verma and Poornima Mittal

Abstract This paper shows the difference in device performance of a novel structure namely Top Source Bottom Drain (TSBD) organic transistor in comparison with the existing Bottom Gate Bottom Contact (BGBC) device structure. The novel structure showed advanced performance in terms of mobility and threshold voltage than the BGBC structure. The TSBD structure also showed an upright control over the drain current henceforth a good saturation of its drain current is obtained. The drain current improved 4–5 times as compared with the novel structure. Even without changing the device parameters and materials this large difference in the electrical parameters shows that, the structure of the device can also play a very important role in affecting the parameters of the device. The analysis by varying the thickness of the contact for the novel structures has also been done with thickness varied from 1 to 50 nm.

Keywords Organic thin film · Bottom gate · Bottom structure · Organic semiconductor

1 Introduction

Organic thin film transistors (OTFTs) are gaining high attention over the past few decades because of their potential in large as well as small area of electronics. In 1976 Shirakawa et al. [1] were the first one to present organic materials that are conducting paving a new path for the researchers. The first OTFT was reported by Tsumura et al. [2] which consisted of organic semiconductor material that acted as a conducting medium for the flow of current. The major advantage of organic thin film transistor is their direct fabrication on flexible and bendable low price substrate [3].

Aanchal Verma (✉) · Poornima Mittal
Department of Electronics and Communication Engineering,
School of Engineering and Technology, Graphic Era University, Dehradun 248002, India
e-mail: aanchaldit@gmail.com

Poornima Mittal
e-mail: poornima2822@ieee.org

© Springer Science+Business Media Singapore 2017

R. Singh and S. Choudhury (eds.), *Proceeding of International Conference on Intelligent Communication, Control and Devices*, Advances in Intelligent Systems and Computing 479, DOI 10.1007/978-981-10-1708-7_98

OTFTs are grabbing great attention in today's scenario since they posses many coolest properties like light weight, low cost, flexibility, low temperature fabrication/processing, and high throughput. Organic devices are made from materials like polymers and small molecules which are carbon based, therefore they are biodegradable and enable disposal integrated circuits, thus avoiding the formation of junks [3–5]. These devices are fabricated on flexible substrates like plastic, paper fiber, and glass [6, 7]. OTFTs have been used for variety of applications such as display drivers, display switches, sensors, radio frequency identification (RFID) tag, solar cell panels, SRAM, and e-paper (electronic paper) [8–14]. The first large-scale complementary circuit with 864 transistors has been fabricated, therefore increasing the complexity of circuits with organic transistors [15].

The discrepancy between the conventional MOSFET structure and OTFT lies basically in the material usage for the semiconductor layer present in both the transistors. The MOSFET uses SiO_2, Al_2O_3, etc. as the conducting material, whereas OTFT uses organic materials such as pentacene, CuPc (copper phthalocyanine) etc. The working principal OTFT is similar to that of a MOSFET structure, i.e., conduction between source and drain will take on application of suitable gate voltage. However there exists a major difference when formation of channel is considered, the channel region in OTFT is formed by the accumulation of charge carrier at the interface of OSC (organic semiconductor) and dielectric layer while in MOSFET it is formed by the formation of the inversion layer.

The basic structure of OTFT is basically a layered structure with layers of substrate, dielectric, and OSC and electrodes source, drain and gate. The structure of OTFT is mainly divided into top gate structure and bottom gate structure. These structure gets further divided into top contact and bottom contact, thus getting four basic structures Top gate Bottom Contact (TGBC), Top Gate Top Contact (TGTC), Bottom Gate Top Contact (BGTC) and BGBC.

A novel structure namely TSBD is described in this paper. When the drain is placed on the insulator and the source is placed on the OSC, the structure formed is TSBD. The schematic of these structures is shown in Fig. 1. This structure is simulated on the basis of performance parameters of BGBC structure. They showed improved performance in drain current (I_{DS}), mobility (μ), and threshold voltage (V_{th}). Therefore, this structure can also be implied in various applications.

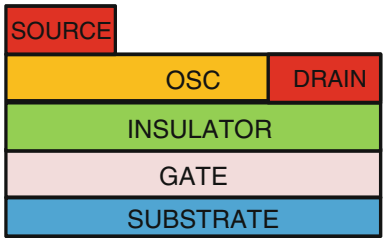


Fig. 1 Schematic of TSBD structure

2 Simulation Setup

The BGBC and TSBD structures are simulated using industrial numerical 2-d simulator ATLAS by Silvaco version 3.44.1.R. This tool also allows the usage of user-defined materials for the devices therefore any material with identified properties can be used for the simulation of the device [16]. All these three structures are simulated with the similar parameters and materials as for the fabricated device. Table 1 shows the dimensions used for the simulation process.

Poole–Frenkel mobility model was adopted and is given by Eq. (1), where μ_0 is the zero field mobility, μ is the field dependent mobility, Δ is the zero field activation energy having the value of 1.792×10^{-2} eV, γ is the fitting parameter, β is the hole Poole–Frenkel (PF) factor given as 7.758×10^{-5} eV $(\text{cm/V})^{0.5}$, T is the temperature and γ is the fitting parameter [13]. The material properties with which structures BGBC and TSBD are simulated have been listed in Table 2.

$$\mu(E) = \mu_0 \exp\left[-\frac{\Delta}{kT} + \left(\frac{\beta}{kT} - \gamma\right)\right] \tag{1}$$

3 Results and Discussion

The output characteristics of BGBC were analyzed with V_{GS} varied from 0 to −100 V. Table 2 shows the simulated values of BGBC structure obtained and its comparison with the experimental value. The simulated values matched up to a certain extent with the experimental value. Thus the TSBD structure is simulated keeping all these parameters into consideration. Figure 2 shows the output characteristics of the novel structure which show improved performance than the BGBC structure. We get a lower V_{th} for the TSBD structure in comparison with the BGBC structure which is important because lower V_{th} results in lower power consumption of the device. Mobility obtained is higher for the TSBD structure, in a conducting path how efficiently charge carriers move defines the mobility of the device. Large on

Table 1 Materials and dimensions used for the simulation of BGBC and TSBD [17]

Material	Usage	Thickness
poly-3,4-ethylenedioxythiopene:styrene sulphonic acid (PEDOT:PSS)	Gate insulator	20 nm
Pentacene	Organic semiconductor	50 nm
Polyethylene-therephthalate (PET)	Dielectric	1.8 μm
PMMA (Poly(methyl methacrylate))	Source/drain	40 nm
Plastic or any flexible material	Substrate	

Table 2 Simulated and experimental values of BGBC

Parameter	Simulated value	Experimental value
Threshold voltage (V_{th})	−30.6358 µA	−32 µA
Drain current (I_D)	−32.76 V	−32 V
Field effect mobility (μ)	0.09 cm^2/Vs	0.1 cm^2/Vs

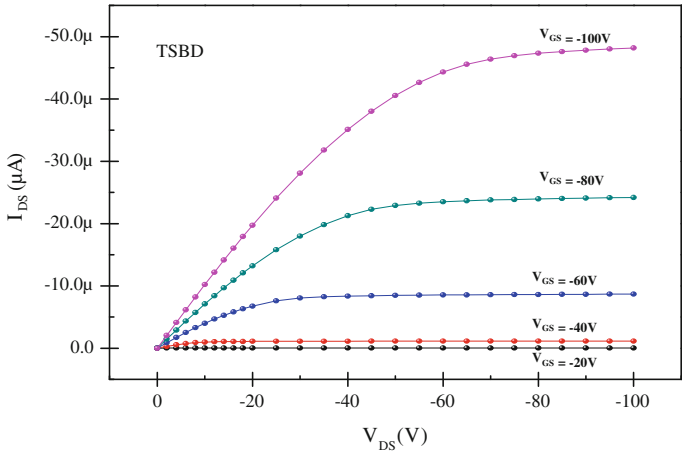


Fig. 2 Output characteristics of TSBD structure

Table 3 Simulated values of TSBD

Structure	I_{DS} (µA)	V_{th} (V)	μ (cm^2/Vs)
TSBD	48.16	31.76	0.21

current is possible with high mobility that is needed for high switching and memory applications.

The simulated TSBD structure showed much better performance than the BGBC structure. Table 3 shows the simulated values of both the structure for I_{DS}, μ and V_{th}.

Thus we can see from table that simulation results for the novel structure showed much higher values than the BGBC structure. The current obtained was 48.16 µA from the novel structure which is higher than 8 µA obtained from BGBC structure. Therefore this showed productive results and this structure thus can be used in variety of applications.

This device is now analyzed by varying the thickness of the drain and hence varying the contact thickness. The contact thickness is varied from 1 to 50 nm taking a step size of 10. The transfer characteristics of TSBD for different contact thicknesses are shown in Fig. 3. The curve is calculated keeping the value of V_{DS} as 10 V. Figure 4 shows the maximum drain current obtained for different values of V_{DS} keeping the gate voltage constant at −100 V.

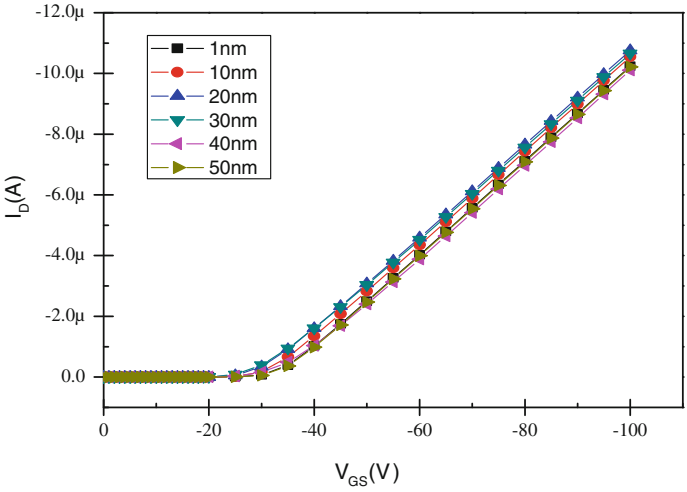


Fig. 3 Transfer characteristics of TSBD at different contact thickness

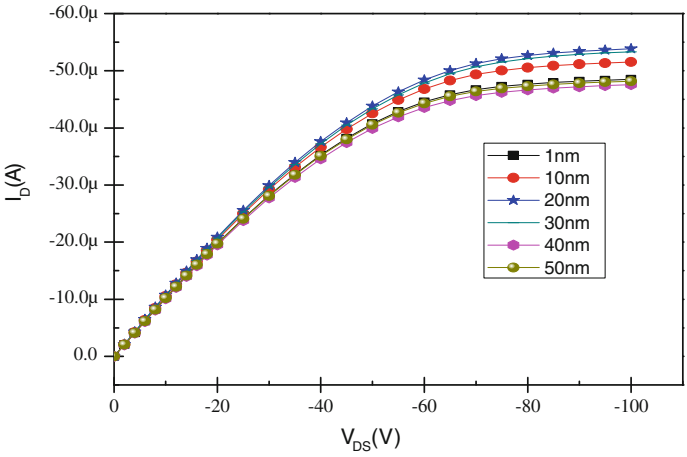


Fig. 4 Output characteristics with maximum drain voltage of $V_{DS} = -100$ V

Table 4 shows the comparison between different parameters obtained by varying the contact thickness of TSBD structure.

Table 4 Simulated values obtained by varying the contact thickness of TSBD

Contact thickness (nm)	I_{DS} (μA)	V_{th} (V)	μ (cm^2/Vs)
1	48.50	31.5148	0.210
10	47.21	32.5895	0.211
20	53.84	27.5222	0.208
30	53.32	27.5351	0.206
40	47.56	31.8757	0.208
50	48.16	31.7652	0.211

4 Conclusion

The parameters of TSBD structure were analyzed using materials and properties of already fabricated device BGBC. TSBD device showed higher performance with value of I_{DS} being 48.01, the threshold voltage achieved was 27.4, and mobility also improved 4 times as compared to the conventional BGBC structure. The variation in the drain thickness was done with the drain varying from 1 to 50 nm and the values for $I_{DS,}$ μ and V_{th} are calculated. The highest performance was shown by the devices at 20 nm contact length with I_{DS} being 53.84 μA. 30 nm contact thickness also showed same performance as that by the 20 nm contact length.

References

1. Shirakawa, H., Louis, E.J., MacDiarmid, A.G., Chiang, C.K., Heeger, A. J.: Synthesis of electrically conducting organic polymers: Halogen derivatives of polyacetylene, $(CH)_x$. Vol. 16. J. Chem. Soc. Chem. Commun. (1977) 578–580.
2. Tsumura, A., Koezuka, H., Ando, T.: Macromolecular electronic device: Field effect transistor with a polythiophene thin film. Appl. Phys. Lett. (1986) 1210–1212.
3. Kumar, Brijesh, Kaushik, B.K., Negi, Y.S.: Organic thin film transistors: structures, models, materials, fabrication, and applications: A review. Vol. 54. no.4. Polymer Reviews (2014) 33–111.
4. Kumar, B., Kaushik, B.K., Negi, Y.S.: Perspectives and challenges for organic thin film transistors: Materials, devices, processes and applications. J. Mater. Sci. Mater. Electron. 25 (1) (2014) 1–30.
5. Jacob, S., et al.: High performance printed N and P type OTFTs for CMOS applications on plastic substrate. IEEE. ESSDERC. (2012) 173–176.
6. Klauk, H., Halik, M., Zschieschange, U., Eden F., Schmid, G.: Pentacene Organic Transistors and using osscillators on glass and on flexible polymers substrate. Vol. 82. Apply Phy. Lett. (2003).
7. Moore, S. K.: Just one word-Plastic. Vol. 39. IEEE Spectrum (2002).
8. Mittal, P., Negi, Y.S., Singh, R.K.: A depth analysis for different structures of organic thin film transistors: modeling of performance limiting issues. Microelectron Engineering, 150 (2016) 7–18.
9. Kumar, B., Kaushik, B.K., Negi, Y.S.: Design and analysis of noise margin, write ability and read stability of organic and hybrid 6-T SRAM. Microelectron. Rel. 54 (12) (2014) 2801–2812.

10. Singh, R.P., Choi, J.W.: Biosensors developments based on potential target of conducting polymers. Vol. 104. Sens. Transducers Journal. (2009).
11. Noguchi, Y., Sekitani T., Someya, T.: Organic transistor based flexible pressure sensors using ink jet printed electrodes and gate dielectric layers. Appl. Phy. Lett. 89 (2006) 253507-1-253507-3.
12. Liu, P.T., L.W.: Innovative voltage driving pixel circuit using organic thin film transistor for AMOLEDs. Vol. 5. J. Display. Techn. (2009) 224–228.
13. SILVACO International: Atlas User's manual. SILVACO International, Santa Clara (2014).
14. Kumar, B., Kaushik, B.K., Negi, Y.S, Goswami, V.: Single and dual gate OTFTs based robust organic digital design. Microelectron. Rel. 54 (1) (2014) 100–109.
15. Crone, B.K., et al.: Organic oscillator and adaptive amplifier circuits for chemical vapour sensing. Nature. Apply Phy. Lett. 91 (2002).
16. Sapp, S., Luebben, S., Losovyj, Y.B., Jepsson, P., Schulz D.L, Carusa, A.N.: Work function and implications of doped poly (3, 4-ethylenedioxythiophene)-co-poly (ethylene glycol). Appl. Phys. Lett. 88 (2006) 152107-1-152107-3.
17. Mittal, P., Negi, Y.S., Singh, R.K.: Mapping of performance limiting issues to analyze top and bottom contact organic thin film transistors. J. of comp. Elect. 13 (2015) 10825–10840.

Comparative Analysis of Various Adaptive Filter Structures Using Simulink

Mahesh B. Dembrani, K.B. Khanchandani and Anita Zurani

Abstract Adaptive digital filter finds its prime applications in the field of science and industry. It is a core technology in the field of Digital Signal Processing. Adaptive digital filter plays a vital role to enhance the performance of the system as well as to reduce the resource utilization. Digital signal processing processes with the digital signal using complex techniques from basic filters and signal transform. The design is implemented using the MATLAB tools which had enabled the design of basic building block faster and more accurate. In this paper, we have implemented the various adaptive filter structures using Simulink. Adaptive filter structure such as NLMS-, RLS-, and BLMS-based model is implemented and error is estimated based on it. Original signal and noisy signal are added together and applied as an input to various adaptive filter modela. Thus, the desired signal that is the original signal is recovered by using NLMS, RLS, and BLMS.

Keywords Adaptive filter structures · Simulink · NLMS · RLS · BLMS

1 Introduction

In data transmission, it is difficult to achieve high-speed data transmission at low error rates. From multiple paths, the transmitted signal usually arrives at the receiver side due to which distortion and noise appear in the received signal, which results in the overlap of the received symbols that is often referred to as inter-symbol-interference (ISI), limiting the maximum data rate. When the size of a cell

M.B. Dembrani (✉) · K.B. Khanchandani · Anita Zurani
Department of Electronics and Telecommunication Engineering,
Shri Sant Gajanan Maharaj College of Engineering, Shegaon, India
e-mail: mahesh.dembrani@gmail.com

K.B. Khanchandani
e-mail: kbkhanchandani@rediffmail.com

Anita Zurani
e-mail: anitazurani@gmail.com

© Springer Science+Business Media Singapore 2017

R. Singh and S. Choudhury (eds.), *Proceeding of International Conference on Intelligent Communication, Control and Devices*, Advances in Intelligent Systems and Computing 479, DOI 10.1007/978-981-10-1708-7_99

decreases, co-channel interference (CCI) becomes another factor which degrades the system performance. The removal of these strong interfering signals can improve the coverage and radio transmission quality.

1.1 Adaptive Filters

When an information signal is transmitted to the receiver from the transmitter through a communication channel, there is a possibility to add multiple interference signals due to multipath propagation in the channel. Such interference cancelation is one of the applications where adaptive filters are used. In this paper, we have proposed various adaptive digital filter designs, which are based on NLMS, RLS, and BLMS algorithm for error estimation and cancelation. This adaptive filter design is based on stable FIR filters. The design and performance of such adaptive filters based on the following trade-off parameters such as the convergence rate and filter coefficient [1, 2].

The source signal is corrupted by the noise signal when it is transmitted through the communication channel. Such mixed signals are passed through our proposed various adaptive filter structure designs. By utilizing the adaptive design and the LMS algorithm, the filter separates the error signal from the information signal. Based on the reference signal, the decision device sends the signal to the receiver or else to the feedback circuit. This paper focuses on comparative analysis of various adaptive filters structures such as NLMS, RLS, and BLMS and recovers the original signal and also estimation of the error signal [3].

Figure 1 shows the adaptive digital filter design structure proposed for analysis of the various algorithms for error estimation and calculation.

1.2 NLMS Algorithm

LMS algorithm has a fixed step size parameter value for each iteration; for fixed size parameter it requires complete information of the input signal for adaptive

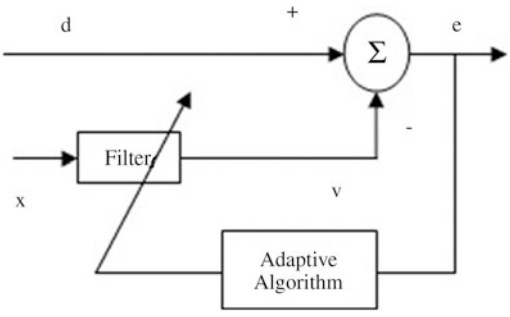


Fig. 1 Adaptive digital filter design structure

digital filter operation. In a real-time application, it is not possible. NLMS algorithm is a modified version of LMS algorithm which removes the logic of calculation of fixed step size parameter. The coefficient of the input vector is inversely proportional to the step size value. The dot product of the input vector and auto correlation matrix is equal to the sum of the coefficients of the input [4, 5].

1.3 RLS Algorithm

RLS algorithm is designed to find filter coefficients which minimizes the linear least squares of the input signal. As compared to LMS algorithm which reduces the mean square error. The simplified algorithm of RLS considers the input signal as the deterministic whereas LMS algorithm considers it as the stochastic. RLS algorithm is faster in terms of convergence rate and filter coefficient. Hence reduces the computational complexity of the system and response speed increases [6].

1.4 BLMS Algorithm

BLMS algorithm is designed from block of input parameters to calculate the finite set of output filter parameters. In BLMS, for each output block the filter coefficients are adjusted according to the LMS algorithm. Analysis of the BLMS algorithm provides fast computational speed, fast implementation higher to that of LMS algorithm [7, 8].

2 Implementation

The design has been implemented using MATLAB/Simulink. DSP Sine Wave generating a sine wave signal is acting as an original signal. The Gaussian noise generator is usually used to generate the noisy signal. The original signal and noise signal are added together as shown in Fig. 2.

This signal is applied as an input to various adaptive filter structures such as NLMS, RLS, and BLMS filters. The error signal is estimated and the original signal is recovered using this adaptive filters. The simulation results of various structures are shown in simulation results and are compared.

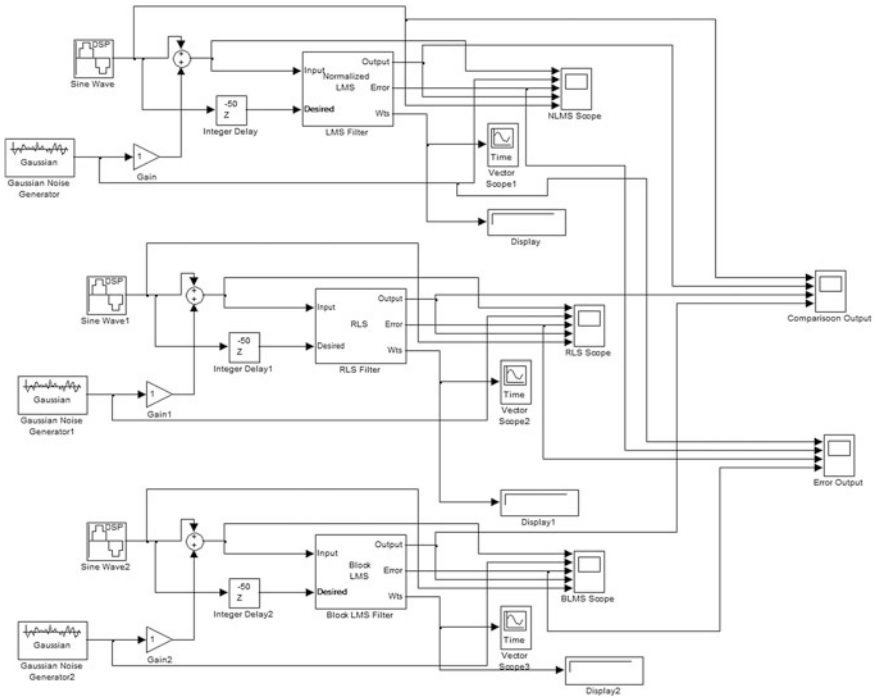


Fig. 2 Designed filter structure

3 Results

The NLMS scope shows the output of NLMS filter as shown in Fig. 3. The first output shows the original signal along with Gaussian noise. The second output on scope shows the Gaussian noise signal which is added with original signal. The third output shows the estimated error signal. The fourth output shows the recovered original signal using the NLMS filter. And the last output shows the original input signal which is compared with recovered original signal.

The RLS scope shows the output of RLS filter as shown in Fig. 4. The first output shows the original signal along with Gaussian noise. The second output on scope shows the Gaussian noise signal which is added with original signal. The third output shows the estimated error signal. The fourth output shows the recovered original signal using the RLS filter. And the last output shows the original input signal which is compared with recovered original signal.

The BLMS scope shows the output of BLMS filter as shown in Fig. 5. The first output shows the original signal along with Gaussian noise. The second output on scope shows the Gaussian noise signal which is added with original signal. The third output shows the error signal estimated. The fourth output shows the

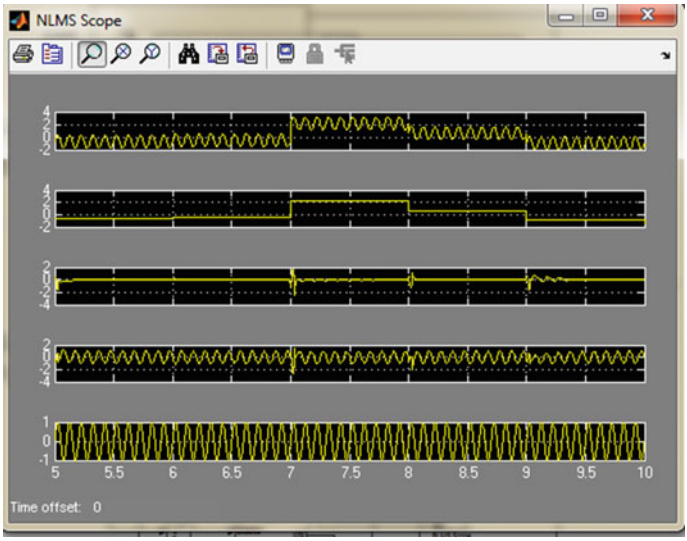


Fig. 3 NLMS filter response

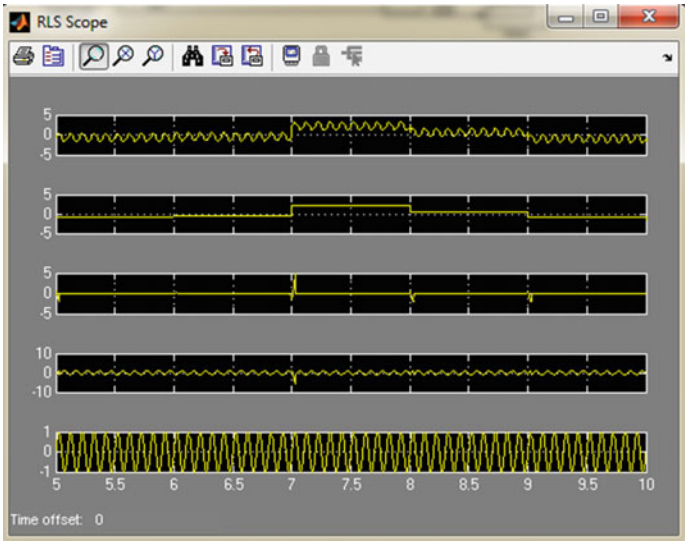


Fig. 4 RLS filter response

recovered original signal by using the BLMS filter. And the last output shows the original input signal which is compared with recovered original signal.

The comparison of output scope compares the various output responses of the filters. The comparison output scope shows the output of NLMS, RLS, and BLMS

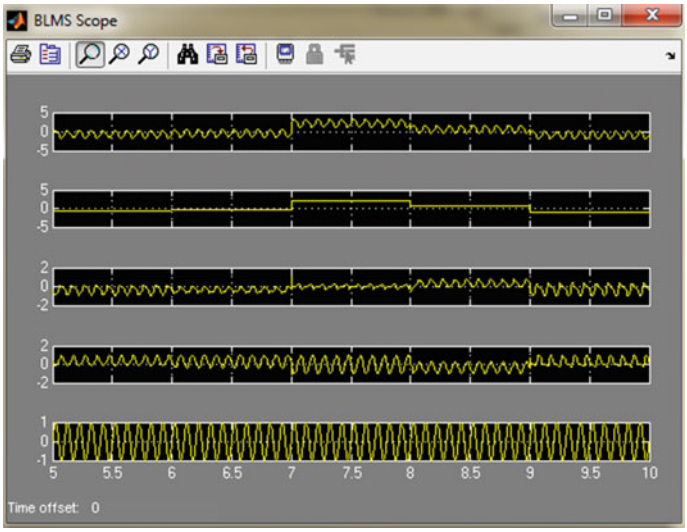


Fig. 5 BLMS filter response

filter as shown in Fig. 6. The first output shows the original signal. The second output on scope shows the output of NLMS filter. The third output shows the RLS filter output. The fourth output shows the output of BLMS filter.

The error output scope compares the various output responses of errors of the filters. The error output scope shows the error signal of NLMS, RLS, and BLMS

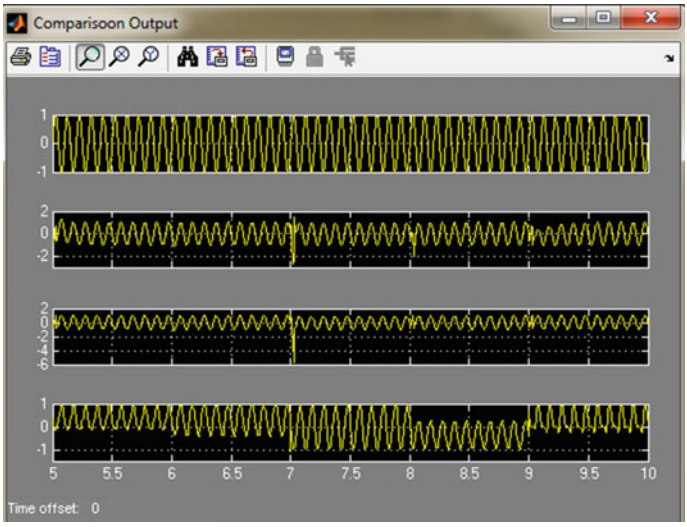


Fig. 6 Comparison of different filter responses

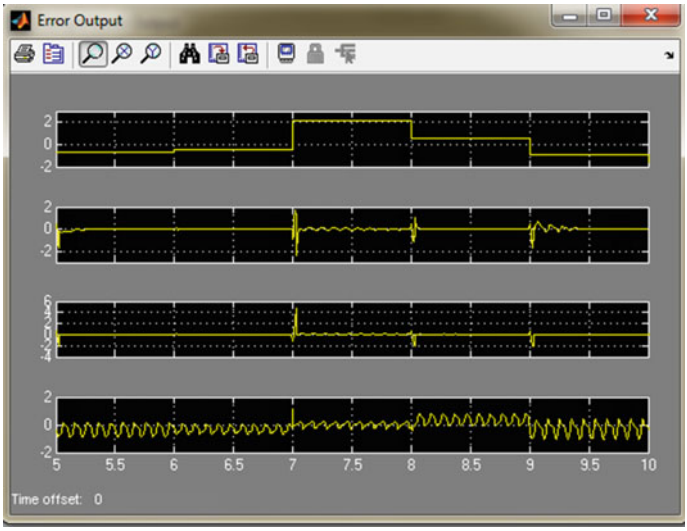


Fig. 7 Error response

filter as shown in Fig. 7. The first output shows the noisy signal. The second output on scope shows the error of NLMS filter. The third output shows the error of RLS filter. The fourth output shows the error of BLMS filter.

4 Conclusion

In this paper, we have implemented the adaptive filters such as NLMS, RLS, BLMS, and FBLMS. We have recovered the original signal and estimated the error signal based on these structures. The error signal can be minimized and the more improved recovered original signal can be obtained.

References

1. Keshab K. Parhi and Darren N. Pearson: Low-Power FIR Digital Filter Architectures, IEEE International Symposium on Circuits and Systems (1995).
2. Fred J Taylor: An Analysis of the Distributed Arithmetic Digital Filter, IEEE Transactions On Acoustics, Speech, and Signal Processing, Vol. 5, (1986) 163–178.
3. K. D. Kammeyer: Quantization Error Analysis of the Distributed Arithmetic, IEEE Transactions on Circuits And Systems, Vol. CAS-24, No. 12 (1997).
4. J. Shynk: Frequency-domain and multirate adaptive filtering, IEEE Signal Processing Mag., vol. 9, Jan. 1992, 15–37.

5. Ahmed I. Sulyman and Azzedine Zerguine: Echo Cancellation Using a Variable Step-Size NLMS Algorithm, Electrical and Computer Engineering Department Queen's University.
6. E. Ferrara: Fast implementation of LMS adaptive filters, IEEE Trans. Acoust. Speech Signal Process., vol. 28, Aug. 1980, 474–475.
7. J.C. Lee, C.K. Un: Block Realization of Multirate Adaptive Digital Filters, IEEE Trans. Acoust. Speech Signal Process., vol. 34, Feb. 1986, 105–117.
8. G.A. Clark, S.K. Mitra, S.R. Parker: Block implementation of adaptive digital filters, IEEE Trans. Circuits Syst., vol. 28, Jun. 1981, 584–592.

Experimental Investigations on the Effects of Dust Fouling on PV Module

Ankit Batra, Ankit Gupta, Rupendra Kumar Pachauri and Athar Hussain

Abstract Accumulation of environmental dust on PV module reduces the solar radiations. The results of this phenomenon are observed in terms of reduction in efficiency of PV module. Various types of dust samples at different weights have been considered for study, presented in this paper. For the investigations, the dust samples such as Badarpur-1, Badarpur-2, Fly Ash, and Rice Husk are taken. An artificial lightening source of radiation is designed to maintain the constant radiation levels for the experimental study. The investigation is carried out with all dust samples and it is observed that the Rice Husk dust sample has maximum impact on PV module performance among the considered dust samples.

Keywords Photovoltaic system · Scanning electron microscopic · Dust fouling

1 Introduction

The demand of solar energy sources is increasing exponentially in stand-alone applications. It is the most preferable source among the various renewable energy sources [1]. But the dust particles reduce the solar module performance. Dust may be defined as crushed form minute particles having size less than 500 μm. Dust

Ankit Batra (✉) · R.K. Pachauri
Civil Engineering Department, School of Engineering,
Gautam Buddha University, Greater Noida 201308, India
e-mail: ankitbatra412@gmail.com

R.K. Pachauri
e-mail: rupendra.gbu@gmail.com

Ankit Gupta · Athar Hussain
Electrical Engineering Department, School of Engineering,
Gautam Buddha University, Greater Noida 201308, India
e-mail: guptaankit299@gmail.com

Athar Hussain
e-mail: athariitr@gmail.com

© Springer Science+Business Media Singapore 2017

R. Singh and S. Choudhury (eds.), *Proceeding of International Conference on Intelligent Communication, Control and Devices*, Advances in Intelligent Systems and Computing 479, DOI 10.1007/978-981-10-1708-7_100

may come in the environment from many sources such as constructional sites, various industries, and pollution. The reduction in solar efficiency due to dust on PV module is approximately 40 %, in this context, various PV module cleaning methods are adopted currently [2].

The authors of [2, 3] reported a comprehensive review on effect of dust on PV performance. The authors of [4] investigated the effect of dust accumulation on PV modules surface and power decreased up to 50 % for a six months' study. In [5], the authors investigated the performance of a solar collector drops progressively as dust is accumulated on its surface. The authors of [6] selected five identical pairs of roof-top PV panels to evaluate the PV performance, the influence of different dust deposition densities on the energy yield and the economic performance of the small power station is estimated. In [7], the authors analyzed the effect of three air pollutants, i.e., red soil, limestone, and fly-ash particles varying in composition, size, and type on PV performance. In [8], the authors proposed a concept of the dust fouling on PV module surface is reduced the efficiency from 16 to 40 % in one-month study. The authors in [9] considered two identical PV modules; the first PV module being clean and the second module being polluted artificially with three types of dust samples such as red soil, limestone and fly-ash. Performance of PV module is highly affected by the deposition of red soil among all the dust samples. Accumulation of dust particles deteriorates the performance of solar cells and results in loss in PV power due to the irradiance scattering effects on the PV surface [10]. In [11], sand particles are used for same investigation on a PV surface.

2 Experimental Analysis

2.1 Apparatus Description

For the investigation of dust fouling on a PV module, the experimental system is comprised various apparatus to obtain the results as, (i) A 60 W polycrystalline PV module (TATA green power-model no. 1260) has been placed under a mounted artificial lightening source, which has comprising total 16 numbers of electric lamps (100 W each). The artificial lightening setup is used to avoid inconsistency in radiation for investigation (ii) A multi-meter (MASTECH, M3900) and a resistive load of 50 Ω (iii) Pyranometer (DT-1307). (iv) Dust samples (a) Badarpur-1 (b) Badarpur-2 (c) Fly Ash (d) Rice Husk. (v) Weighing machine to determine the dust quantity (Fig. 1).

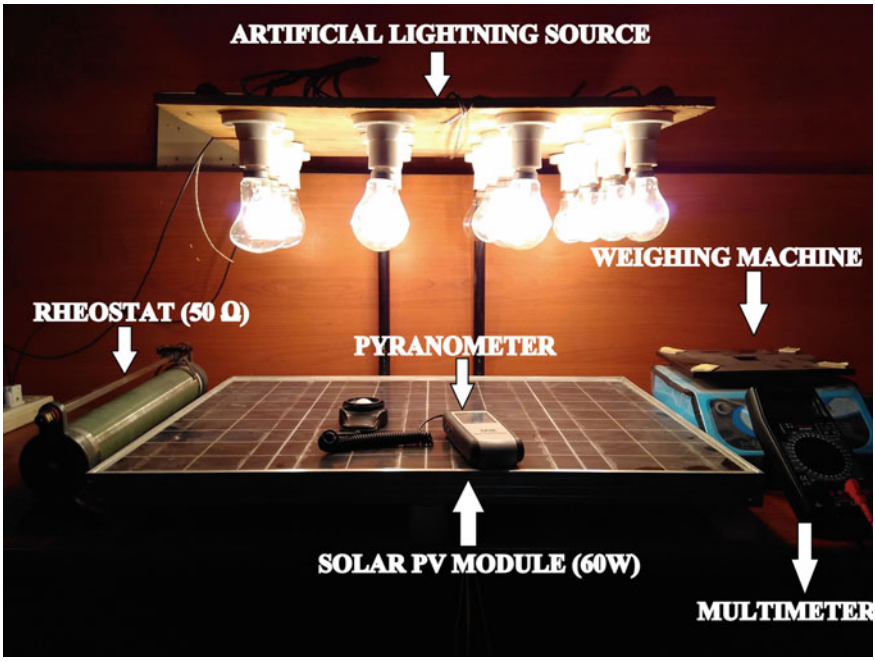


Fig. 1 Experimental setup

2.2 PV Module Specification

In this paper, a 50 W monocrystalline PV module is used for the investigation and the specifications are as shown in (Table 1).

2.3 Dust Samples

Total four types of dust samples are considered such as Badarpur-1, Badarpur-2, Fly Ash, and Rice Husk with different weights. All the dust samples are analysed

Table 1 PV module (TATA green power) specifications at STC

Peak power (P_{max})	60 W
Voltage (V_{min})	18.0 V
Current (I_{mp})	2.72 A
Open circuit voltage (V_{oc})	16.0 V
Short circuit current (I_{sc})	9.5 A
Minimum by pass diode	15 A
Maximum series fuse	15 A

under scanning electron microscope (SEM) to obtain the particle size and bonding density. In Fig. 2a–d, the SEM images are shown for all the dust samples.

3 Results and Discussion

The data is obtained for dust samples of different weights versus power of solar panel at three radiations, i.e., 650, 750 and 850 W/m^2.

From Fig. 3a, it is observed that the minimum power obtained for Badarpur-1 is 7.09 W at 50 gm and radiation 650 W/m^2 and maximum power is 14.88 W at 10 gm and radiation 850 W/m^2. From Fig. 3b, it is observed that the minimum power obtained for Badarpur-2 is 6.509 W at 50 gm and radiation 650 W/m^2 and maximum power is 14.1208 W at 10 gm and radiation 850 W/m^2. From Fig. 3c, it is found that the minimum power obtained for the case of Fly Ash dust is 9.27 W at 25 gm and radiation is 650 W/m^2 and maximum power is 14.773 W at 5 gm and radiation is 850 W/m^2. From Fig. 3d, it is observed that the minimum power

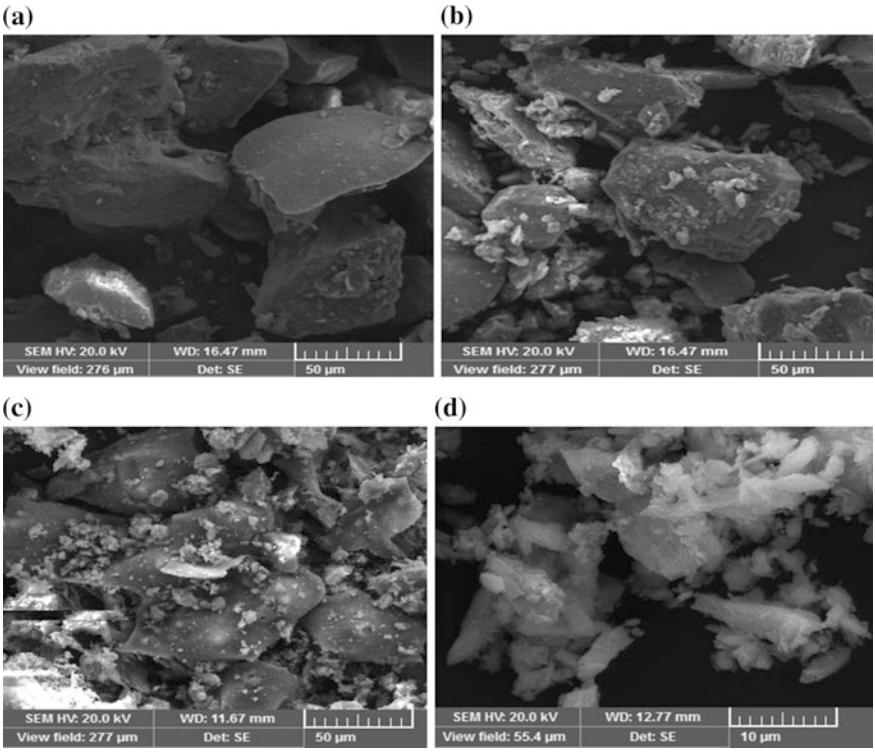


Fig. 2 SEM images for **a** Badarpur-1 (50 µm), **b** Badarpur-2 (50 µm), **c** Fly Ash (50 µm) and **d** Rice Husk (10 µm)

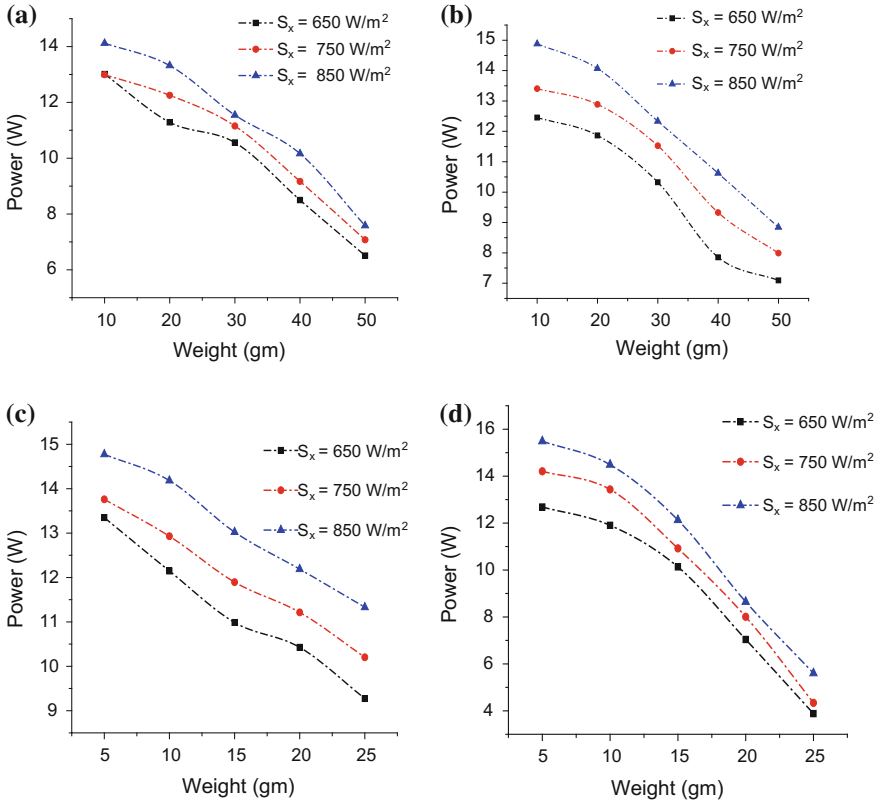


Fig. 3 Analysis of considered four dust samples. **a** Power to weight responds of Badarpur-1, **b** Power to weight responds of Badarpur-2, **c** Power to weight responds of Fly Ash, **d** Power to weight responds of Rice Husk

obtained for Rice Husk is 3.88 W at 25 g and radiation 650 w/m^2 and maximum power is 15.48 W at 5 gm and radiation 850 W/m^2. Overall minimum power obtained is from Rice Husk at 25 gm and radiation 650 W/m^2. The comparative analysis of experimental results for all dust samples are shown in Table 2.

4 Conclusion

In this paper, a study of dust fouling effect on solar PV module has been carried out. An artificial lightening setup is used to maintain constant radiation on PV module for investigation. Power output of PV module has obtained at different weights for all considered dust samples, i.e., (a) Badarpur-1 (50 µm), (b) Badarpur-2 (50 µm), (c) Fly Ash (50 µm), and (d) Rice Husk (10 µm). From the obtained results, the

Table 2 Comparative analysis of experimental results

Radiation	650 W/m^2					750 W/m^2					850 W/m^2				
Dust sample	Badarpur-1														
Weight (gm)	10	20	30	40	50	10	20	30	40	50	10	20	30	40	50
Voltage (V)	18.86	18.2	17.6	17	16.69	18.3	18.02	17.99	17.3	16.85	18.58	18.5	17.76	17.52	16.85
Current (A)	0.69	0.62	0.6	0.5	0.39	0.71	0.68	0.62	0.53	0.42	0.76	0.72	0.65	0.58	0.45
Power (W)	13.01	11.28	10.56	8.5	6.50	12.99	12.25	11.15	9.16	7.07	14.12	13.32	11.54	10.16	7.58
Dust sample	Badarpur-2														
Weight (gm)	10	20	30	40	50	10	20	30	40	50	10	20	30	40	50
Voltage (V)	18.87	18.25	17.8	17.45	16.89	18.36	18.15	18.01	17.6	17	18.6	18.51	17.87	17.7	16.85
Current (A)	0.66	0.65	0.58	0.45	0.42	0.73	0.71	0.64	0.53	0.47	0.8	0.76	0.69	0.6	0.52
Power (W)	12.45	11.86	10.32	7.85	7.09	13.40	12.25	11.52	9.32	7.99	14.88	14.06	12.33	10.62	8.84
Dust sample	Fly Ash														
Weight (gm)	5	10	15	20	25	5	10	15	20	25	5	10	15	20	25
Voltage (V)	19.07	18.13	18.01	17.67	17.17	18.85	18.21	18.02	17.8	17.29	18.7	18.42	18.34	18.19	17.7
Current (A)	0.7	0.67	0.61	0.59	0.54	0.73	0.71	0.66	0.63	0.59	0.79	0.77	0.71	0.67	0.64
Power (W)	13.34	12.14	10.98	10.42	9.27	13.76	12.92	11.89	11.21	10.20	14.77	14.18	13.02	12.18	11.33
Dust sample	Rice Husk														
Weight (gm)	5	10	15	20	25	5	10	15	20	25	5	10	15	20	25
Voltage (V)	18.38	18.31	17.47	17.17	13.86	18.69	18.4	17.9	17.4	14	19.12	18.34	18.1	17.29	15.56
Current (A)	0.69	0.65	0.58	0.41	0.28	0.76	0.73	0.61	0.46	0.31	0.81	0.79	0.67	0.5	0.36
Power (W)	12.68	11.90	10.13	7.03	3.88	14.21	13.43	10.91	8.00	4.34	15.48	14.48	12.12	8.64	5.61

power loss of PV module is investigated. It is concluded that as the particle size of dust samples decreases and it covers more surface area with high density and hence it blocks the maximum radiation from sunlight. Due to this cause, the performance of PV module is most affected by Rice Husk dust sample. The obtained results recommended the necessity of dust cleaning system at solar array power plant.

References

1. Meral, M. E., Dinçer, F.: A review of the factors affecting operation and efficiency of photovoltaic based electricity generation systems. Renewable and Sustainable Energy Reviews, 15 (2011) 2176–2184.
2. Qaraghuli, T. A. A., Kazmerski, L. L.: A Comprehensive review of impact of dust on the use of solar energy, history, investigations, results, literature, and mitigation approaches. Renewable and Sustainable Energy Reviews, 22 (2013) 698–733.
3. Mani, M., Pillai, R.: Impact of dust on solar photovoltaic (PV) performance, research status, challenges and recommendations. Renewable and Sustainable Energy Reviews, 14 (2010) 3124–3131.
4. Adinoyi, M. J. S., Said A. M.: Effect of dust accumulation on the power outputs of solar photovoltaic modules. Renewable energy; 60 (2013) 633–636.
5. Elminir, H. K., Ghitas, A. E., El-Hussainy, R. H. F., Beheary M. M., Abdel, K. M.: Moneim. Effect of dust on the transparent cover of solar collectors. Energy Conversion and Management 47 (2006) 3192–3203.
6. Kaldellis, J. K., Kokala, A.: Quantifying the decrease of the photovoltaic panels energy yield due to phenomena of natural air pollution disposal. Energy 35 (2010) 4862–4869.
7. Kaldellis, J. K., Kapsali M.: Simulating the dust effect on the energy performance of photovoltaic generators based on experimental measurements. Energy 36 (2011) 5154–5164.
8. Ghosh, B., Ghosh A. K.: Effect of dust on solar PV modules efficiency. Science & Culture 80 (2014) 290–297.
9. Kaldellis, J. K., Fragos P., Kapsali, M.: Systematic experimental study of the pollution deposition impact on the energy yield of photovoltaic installations. Renewable Energy 36 (2011) 2717–2724.
10. Saidan, M., Albaali, A. G., Alasis E., Kaldellis, J. K.: Experimental study on the effect of dust deposition on solar photovoltaic panels in desert environment. Renewable Energy 92 (2016) 499–505.
11. Beattie, N. S., Moir, R. S., Chacko, C., Buffoni, G., Roberts, S. H., Pearsall, N. M.: Understanding the effects of sand and dust accumulation on photovoltaic modules. Renewable Energy 48 (2012) 448–452.

Study of Parametric Effects on Solid Oxide Fuel Cell

Kevi Singh, Rupendra Kumar Pachauri, Yogesh K. Chauhan and Ankit Gupta

Abstract In this paper, the mathematical analysis of electrochemical model of Solid Oxide Fuel Cell (SOFC) system has been done for MATLAB/Simulink modeling. Furthermore, the possible mechanism of the parameter influences effects and their interrelationships are discussed comprehensively. To investigate the performance of SOFC, the V and I characteristics, power density, current density, etc., analyzed by the influence effect of the important parameters. For this investigation, various important parameters, e.g., reactants' flow pressure, operating temperature, membrane resistance, etc., are considered. This study is very helpful to predict the performance of the SOFC.

Keywords Solid oxide fuel cell · Distribution generation · Fuel cell · Power density

1 Introduction

Today, energy consumption is increasing because of the depletion of fossil fuels. This situation forces researchers to develop alternative energy sources to meet the energy requirements. A FC is an electrochemical device which is used to convert chemical energy directly into electrical energy. FC requires pure fuel to produce electricity. FCs are compact in size and are highly efficient [1, 2].

Kevi Singh (✉) · R.K. Pachauri · Y.K. Chauhan · Ankit Gupta
Electrical Engineering Department, School of Engineering,
Gautam Buddha University, Greater Noida 201308, India
e-mail: kevi.singh1990@gmail.com

R.K. Pachauri
e-mail: rupendra.gbu@gmail.com

Y.K. Chauhan
e-mail: chauhanyk@yahoo.com

© Springer Science+Business Media Singapore 2017

R. Singh and S. Choudhury (eds.), *Proceeding of International Conference on Intelligent Communication, Control and Devices*, Advances in Intelligent Systems and Computing 479, DOI 10.1007/978-981-10-1708-7_101

FC systems are classified based upon the electrolyte, operating temperature, efficiency, and type of fuel used. Solid Oxide Fuel Cell (SOFC) is used in cogeneration because it works on high temperature [3].

In [4], the authors gave the analysis on V and I characteristics for FC model is developed for different input parameters and its transient behavior is also presented. The authors [5], presented the effects of parameters on FC performance and also discussed about their interrelationship behavior. In [6], authors gave an emphasis on different operating parameters and FCs are compared based on these parameters.

2 Modeling of SOFC

SOFC generally gives best performances at its operating temperature range and specified reactants flow pressure [7]. FC voltage (V_{FC}), at any instance, can be expressed using Eq. (1). No load voltage, known as Nernst voltage (E_{Nerst}), is reduced by three categories of voltage drop during loading condition, shown in Eq. (1) as

$$V_{FC} = E_{Nenst} - V_{act} - V_{ohmic} - V_{con}, \quad E_{Nerst} = E_0 + \frac{RT}{nF} \ln\left(\frac{P_{H_2} P_{O_2}^{0.5}}{P_{H_2O}}\right) \tag{1}$$

where, T is the cell temperature, P_{H_2} and P_{O_2} are hydrogen and oxygen flow pressures, R is the gas constant, and F is Faraday's constant [9]. E_0 is reference or ideal voltage taken as 1.229 in this paper. The activation voltage drop (V_{act}) can be represented by Tafel's equation which gives the activation voltage drop in Eq. (3) as

$$V_{act} = -k_1 + k_2 T - k_3 T \ln[(I)] + k_4 T \ln[(\text{Conc.O}_2)] \tag{2}$$

where, I is the cell current (A) and k_1, k_2, k_3, *and* k_4 are constants, Conc.O_2 is the concentration of oxygen which is a function of stack temperature shown in Eq. (3) as

$$\text{Conc.O}_2 = -\left(\frac{P_{o_2}}{5.08 \times 10^6 e^{(-498/T)}}\right) \tag{3}$$

The Ohmic voltage drop (V_{ohmic}) is almost linear in nature and obtained in Eq. (4) [8] as

$$V_{ohmic} = IR_{mem}, \quad R_{mem} = \frac{t_m}{\sigma} \tag{4}$$

where, R_{mem} represents the resistance of the membrane, t_m is membrane thickness (cm), and σ is the conductivity of membrane.

At higher current densities, the cell potential decreases rapidly due to mass limitations [9]. This linearity is termed as the concentration over potential which is shown in Eq. (5) as

$$V_{\text{con}} = C_1 - C_2(T - 273)\text{e}^{C_3 I}, \quad V_{\text{stack}} = NV_{\text{FC}} \tag{5}$$

where, C_1, C_2, C_3 are constants. With the help of the above equations, cell potential is determined. If all the FCs are in series, stack output is the product of FC voltage and number of cells in the stack (N) is shown.

Hydrogen, oxygen, and water flow pressure are shown in Eq. (6) as,

$$P_{\text{H}_2} = \left(\frac{m_{\text{H}_2} R_{\text{H}_2}}{V_{\text{anode}}}\right) T,\ P_{\text{O}_2} = \left(\frac{m_{\text{O}_2} R_{\text{O}_2}}{V_{\text{cathode}}}\right) T,\ P_{\text{H}_2\text{O}} = \left(\frac{m_{\text{H}_2\text{O}}{}^{0.5} Q_{\text{H}_2\text{O}}}{k_{\text{cathode}}}\right) \tag{6}$$

Current and power density of the FC can be calculated using Eq. (7) as

$$J = \frac{I}{A},\ P_d = \frac{P_{\text{FC}}}{A},\ \eta = \frac{U_f V_{\text{FC}}}{1.48} \tag{7}$$

where, J is the current density (A/cm^2), I is the FC current (A) A is the FC area (cm^2), and P_d is the power density in W/cm^2 [5]. The fuel cell efficiency (η) is computed and expressed in Eq. (7) as above; U_f is the fuel utilization factor, normally kept in the range of 95 %.

3 Results and Discussion

The parametric effects on developed Simulink FC model is investigated and following test cases are considered as

3.1 Effect of Temperature, Reactants Flow Pressure, and Membrane Resistance

The variation in temperature, hydrogen, and oxygen flow pressure and membrane resistance affect the V and I characteristics. These effects on V and I characteristics are shown in Fig. 1a–d as

Figure 1a–d shows V and I characteristics for different temperature, H_2 flow pressure, O_2 flow pressure, and membrane resistance (R_{mem}), respectively, for SOFC. It is evident from Fig. 1a that the step increment in operating temperature (T = 873 + 20 and 873 + 40 %) results into the decrement of polarization voltage while the decrement in operating temperature (T = 873−20 and 873−40 %) results into the voltage increment.

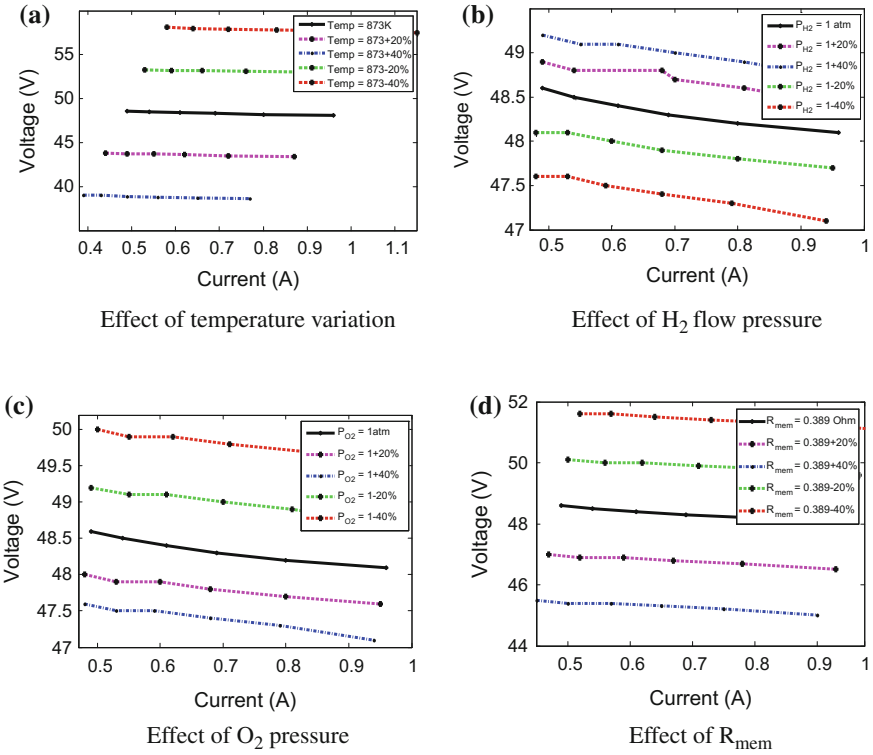


Fig. 1 *V* and *I* characteristics of SOFC for **a** Temperature variation **b** H_2 flow pressure **c** O_2 flow pressure **d** Membrane resistance

3.2 *Effect of Activation Voltage Drop Constants k_1, k_2, k_3, and k_4*

These effects on *V* and *I* characteristics are shown in Fig. 2a–d as

Figure 2a–d shows the effects on *V* and *I* characteristics for varying coefficient values $(k_1, k_2, k_3$ and $k_4)$ which are involved to calculate activation voltage drop (V_{act}). Furthermore, it is observed that the coefficient k_3 and k_4 have the same nature according to k_2 and k_1 coefficients, respectively, shown in Fig. 2c, d.

3.3 *FC Efficiency, Power Density, and Voltage at Fixed Temperature and Different Reactants Flow Pressure*

Figure 3a–d shows the dual *Y* axis curves for efficiency and voltage with power density for single SOFC.

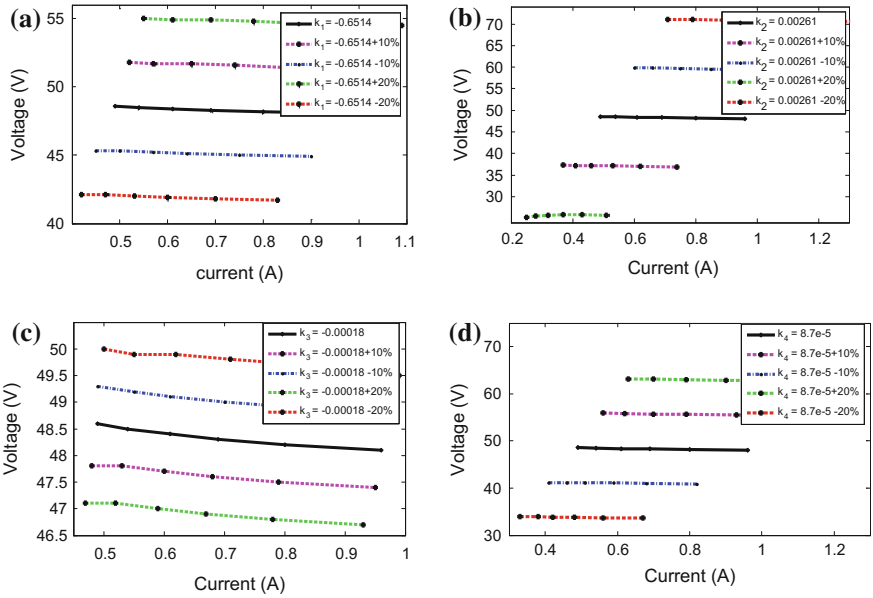


Fig. 2 Effect of **a** k_1, **b** k_2, **c** k_3 **d** k_4 coefficients on V and I characteristics

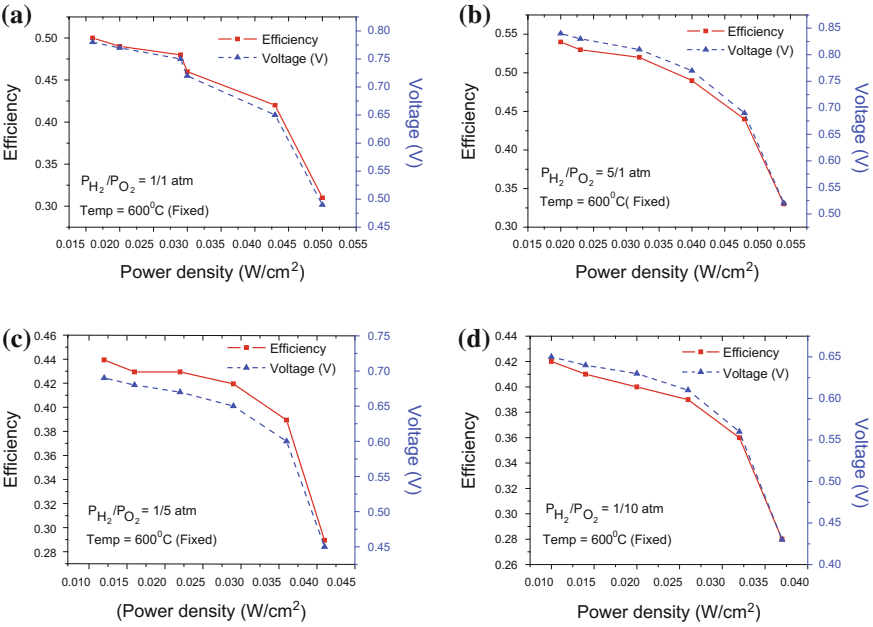


Fig. 3 **a–d** FC efficiency, power density, and voltage at fixed temperature and different reactants' flow pressure

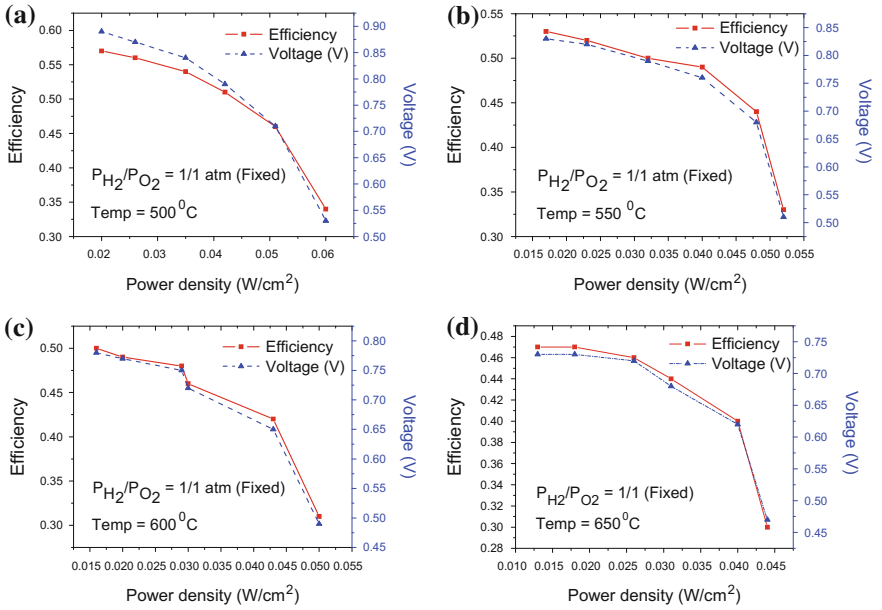


Fig. 4 **a–d** FC efficiency, power density, and voltage at fixed reactants flow pressure and different operating temperature

It is clear from Fig. 3a–d that if operating temperature of FC is considered fixed (600 °C) and reactants flow pressure are increased in a defined ratio 1/1, 5/1. 1/5, and 1/10 atm. At anode and cathode, so efficiency and voltage of FC are changed.

3.4 FC Efficiency, Power Density, and Voltage at Fixed Reactants Flow Pressure and Different Operating Temperature

Figure 4a–d show the dual *Y* axis curves for efficiency and voltage with power density for single SOFC.

It is clear from Fig. 4a–d that if a step increment in operating temperature of FC (500, 550, 600 and 650 °C) is created and reactants flow pressure kept constant (1/1 atm. At anode and cathode), there will be the decrement in the single FC efficiency and voltage.

4 Conclusion

In this paper, a study on parametric effects of various parameters on SOFC performance is investigated. The operating parameters are considered in dynamic in nature. It is found that the SOFC shows the best performance according to variation of operating parameters. This parametric effect is shown on V and I characteristics clearly. This parametric study is helpful to operate the FC system and the difficulties can be encountered in the FC manufacturing.

References

1. Rao, T. S., Turaga, U. T.: Opportunities and Challenges for Fuel Cells in India. Journal of the American Chemical Society, 48(2) (2003) 795–796.
2. Mekhilef, S., Saidur, R., Safari, A.: Comparative Study of Different Fuel Cell Technologies. Renewable and Sustainable Energy Reviews, 16(1) (2012) 981–989.
3. Pachauri, R. K., Chauhan, Y. K.: Study and Performances Analysis of Fuel Cell Assisted Vector Control Variable Speed Drive System Used for Electric Vehicles. International Journal of Sustainable Energy, 35(1) (2015) 1–25.
4. Pachauri, R. K., Chauhan, Y. K.: Various control schemes of power management for phosphoric acid fuel cell system. International Journal of Electrical Power & Energy Systems, 74 (2016) 49–57.
5. Wang, L., Hussar, A., Zhou, T., Liu, H.: A Parameteric Study of PEM Fuel Cell Performances. International Journal of Hydrogen Energy, 28(11) (2003) 1263–1272.
6. Pachauri, R. K., Chauhan, Y. K.: A study, Analysis and Power Management Schemes for Fuel Cells. Journal of Renewable and Sustainable Energy Reviews, 43 (2015) 301–319.
7. Zabihian, F., Fung, A.: A Review on Modeling of Hybrid Solid Oxide Fuel Cell Systems. International Journal of Engineering, 3(2) (2009) 85–119.
8. Laosiripojana, N.: Reviews on Solid Oxide Fuel Cell Technology. Engineering Journal, 13(1) (2009) 65–83.
9. Akikur, R. K., Ullah, K. R., Ping, H. W., Saidur, R.: Application of Solar Energy and Reversible Solid Oxide Fuel Cell in a Co-generation System. International Journal of Innovation, Management and Technology, 5(2) (2014) 134–138.

Performance Investigation of ANN Controller-Assisted Small Hydro Power Generation System

Durgesh Kumar, Ankit Gupta, Rupendra Kumar Pachauri and Yogesh K. Chauhan

Abstract In this paper, the performance investigation of artificial neural network (ANN) controller-assisted small hydro power generation system (SHPGS) has been presented. The mathematical modeling of SHPGS is implemented in MATLAB/Simulink software. As the turbine speed and output power are directly proportional to the water flow rate and net head, an ANN controller has been implemented to control these parameters under varying load demand. A comprehensive investigation of the system under steady state and dynamic state has been done in terms of demand power, water flow rate, net head, turbine power, load voltage and current. The results validate that the ANN controller has satisfactory performance under dynamic conditions.

Keywords Hydro-turbine · Synchronous machine · Artificial neural network

1 Introduction

The small hydro power generation system (SHPGS) is an efficient and reliable source of renewable energy (RE). Kinetic energy of water moves the turbine systems; the turbine rotates to produce electricity. Small hydro is the largest distributor of the electricity from RE sources [1].

The authors of [2], modeled an autonomous variable speed mini hydro power generation system with doubly fed induction generator. In [3, 4], the authors proposed a concept on advanced structure of mini hydro power plant (MHPP) assisted

Durgesh Kumar (✉) · Ankit Gupta · R.K. Pachauri · Y.K. Chauhan
Electrical Engineering Department, School of Engineering,
Gautam Buddha University, Greater Noida 201312, India
e-mail: durgesh11kumar@gmail.com

R.K. Pachauri
e-mail: rupendra.gbu@gmail.com

Y.K. Chauhan
e-mail: chauhanyk@gmail.com

© Springer Science+Business Media Singapore 2017

R. Singh and S. Choudhury (eds.), *Proceeding of International Conference on Intelligent Communication, Control and Devices*, Advances in Intelligent Systems and Computing 479, DOI 10.1007/978-981-10-1708-7_102

with a novel electric grid synchronization technique. The authors of [5] present an approach for modeling and control of MHPP using fuzzy logic system.

From the above literature review, the research addition of this paper is the novelty of this paper is to present a detailed study of artificial neural network (ANN) controller-assisted SHPGS under varying load demand.

2 System Description

The complete system comprises of three major parts: (a) hydro-turbine (b) synchronous machine (c) ANN controllers for the controlling of water flow rate and gross head. The system layout is shown in Fig. 1.

The paper is outlined as follows. In Sect. 3, the mathematical modeling of hydro-turbine is reported. In Sect. 4, ANN controllers are proposed for SHPGS. The results are discussed in Sect. 5 and Sect. 6 concludes the paper.

3 Mathematical Modeling of System

3.1 Small Hydro-Turbine

The small Francis turbine (FT) is a type of water turbine. FTs are commonly used for water head of 30–150 m and are primarily used for electrical power generation.

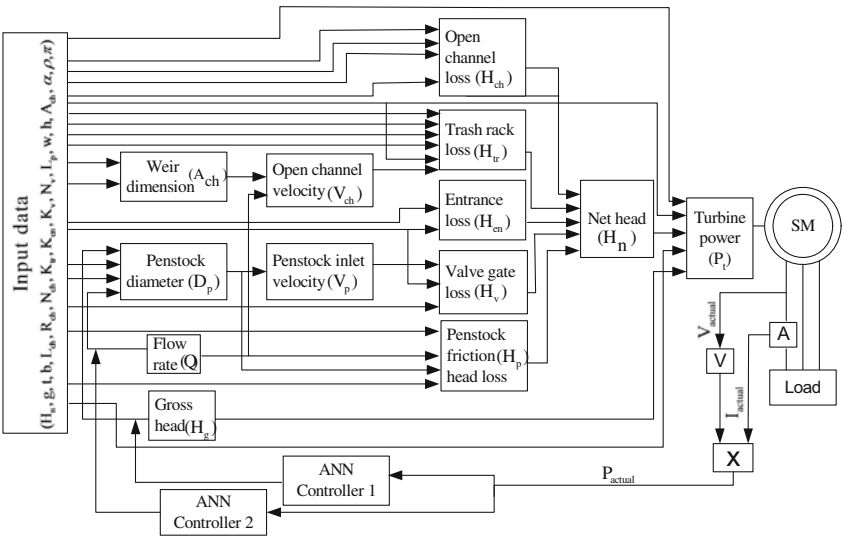


Fig. 1 System layout of ANN controller-assisted small hydro power plant using ANN control system

The electric generator, which utilizes this type of turbine and a penstock diameter of 0.92–10.05 m, has a power output in the range of few kilowatts to 100 MW. The rotor speed range of these type turbines is from 75–1400 rpm. Turbine speed and turbine power of the rotating system are expressed in Eq. (1) as [6],

$$\frac{\mathrm{d}w}{\mathrm{d}t} = \frac{1}{Jw}(P_\mathrm{T} - P_\mathrm{L} - Bw), \quad P_\mathrm{T} = \rho g H_\mathrm{n} Q \eta_t \tag{1}$$

where w is the turbine speed, P_T is turbine power, P_L is load power, J is moment of inertia of whole rotating system, ρ is water density, H_n is net head, and Q is the water flow rate. Net head and open channel losses can be calculated using Eq. (2)

$$H_\mathrm{n} = H_\mathrm{g} - (H_\mathrm{ch} + H_\mathrm{tr} + H_\mathrm{en} + H_\mathrm{v} + H_\mathrm{p}), \quad H_\mathrm{ch} = \left(\frac{Q n_\mathrm{ch}}{A_\mathrm{ch} R_\mathrm{ch}^{2/3}}\right)^2 L_\mathrm{ch} \tag{2}$$

where H_g is gross head, H_ch is open channel loss, H_tr is trash rack loss, H_en is entrance loss, H_v is valve gate loss, H_p is penstock friction head loss, n_ch is manning factor of an open channel, R_ch is open channel of hydraulic radius, and L_ch is length of open channel. Trash rack loss and entrance losses are shown in Eq. (3) as

$$H_\mathrm{tr} = K_\mathrm{tr}\left(\frac{t}{b}\right)^{4/3} \frac{V_\mathrm{ch}^2}{2g \sin\alpha}, \quad H_\mathrm{en} = \frac{K_\mathrm{en} V_\mathrm{p}^2}{2g} \tag{3}$$

where K_tr is trash rack loss, t is bar thickness of trash screen, b is bar width of trash rack screen, V_ch is water flow velocity of an open channel, g is gravity acceleration constant, and V_p is penstock inlet velocity. Valve gate loss and penstock friction head loss are expressed in Eq. (4) as

$$H_\mathrm{v} = \frac{K_\mathrm{v} V_\mathrm{P}^2}{2g}, \quad H_\mathrm{p} = \left(\frac{10.29 n_\mathrm{p}^2 Q^2}{D_\mathrm{P}^{5.33}}\right) L_\mathrm{p} \tag{4}$$

where K_v is gate valve factor, L_p is length of penstock, D_p is penstock diameter. Penstock inlet velocity and internal penstock diameter can be expressed in Eq. (5) as

$$V_\mathrm{p} = \frac{4Q}{\pi D_\mathrm{P}^2}, \quad D_\mathrm{p} = \frac{2.69 n_\mathrm{P}^2 Q^2 L_\mathrm{P}}{H_\mathrm{g}} \tag{5}$$

where V_p is penstock inlet velocity, Q is water flow rate and H_g is gross head. The Eq. (1) to (5) can be used for the modeling of hydro-turbine in MATLAB/Simulink.

3.2 Synchronous Machine

The electrical system for each phase consists of a voltage source in series with RL impedance, which implements the internal impedance of the machine. The value of R can be zero but the value of L must be positive.

The simplified synchronous machine implements the mechanical system as

$$\Delta\omega(t) = \frac{1}{2H}\int_0^t (T_\mathrm{m} - T_\mathrm{e})\mathrm{d}t - K_\mathrm{d}\Delta\omega(t), \quad \omega(t) = \Delta\omega(t) + \omega_0 \tag{6}$$

where $\Delta\omega(t)$, H, T_m, T_e, K_d, $\omega(t)$, and ω_0 are represented as speed variation with respect to speed of operation, inertia constant, mechanical torque, electromagnetic torque, damping factor of damper windings and speed of operation, respectively.

4 ANN-Based Water Flow Rate and Gross Head Control Strategy

ANN controller is a controller with a feedback mechanism which is commonly used in industrial control operations. For the control of water flow rate and gross head of SHPGS two simple feed forward ANNs are generated and trained for operation under varying demand power. The reference demand power is taken as input for both the controllers and the control parameters, i.e., water flow rate and net head are computed as output for ANN controller 1 and 2 respectively as shown in Fig. 1. The input and output of an ANN can be represented using Eq. (7) as [7]

$$y_j^h = f\left(\sum_{i=1}^{N} A_{ji}X_i + \delta_j^h\right), \quad y_k^o = f\left(\sum_{j=1}^{N} A_{kj}Y_j^h + \delta_k^o\right) \tag{7}$$

where A_{ji} and A_{kj} denote the value of weights between the three layers. δ_j^h and δ_k^o denote the bias values of the output and hidden layer, respectively,. X_i and Y_j^h are the input and output signal line values.

5 Results and Discussion

5.1 Steady-State Analysis

The steady-state analysis of the modeled system is shown in Fig. 2a–e in terms of water flow rate (Q), gross head (H_g), turbine power (P_t), load voltage (V_L), and load

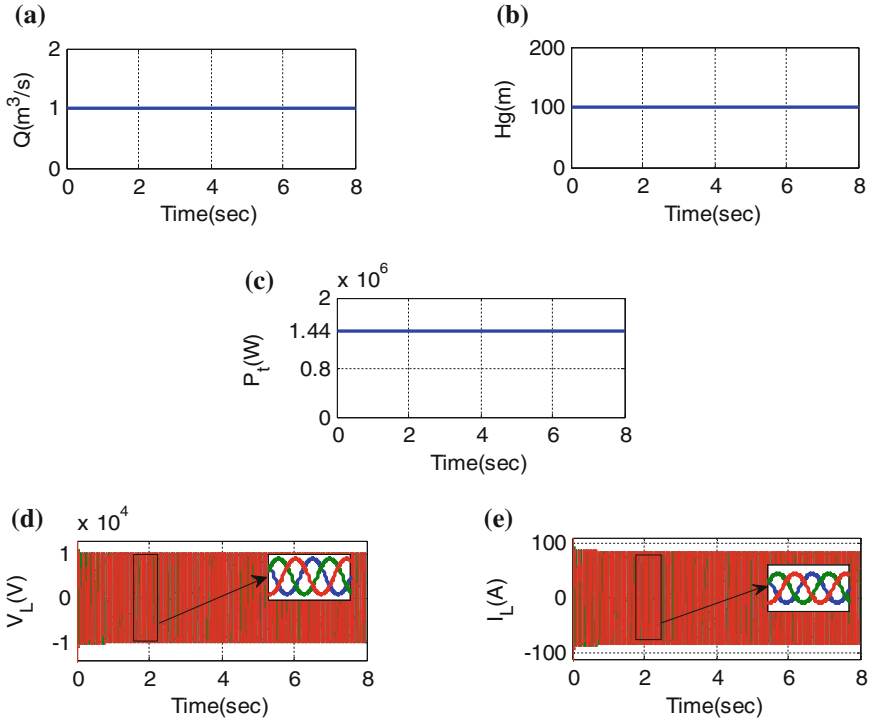


Fig. 2 System parameters under steady-state analysis. **a** Water flow rate response, **b** gross head response, **c** turbine power response, **d** load voltage response, **e** load current response

current (I_L). The Q and H_g are kept constant at rated values of 1 m/s and 100 m, respectively. The steady-state values of P_t, V_L, and I_L are observed to be 1.44×10^6 W, 1.03×10^3 V, and 86 A, respectively.

5.2 *Dynamic Analysis*

For dynamic analysis of the system step variation in the P_{ref} is considered as shown in Fig. 3a. Initially at $t = 0$ s, the P_{ref} is set at 885.8×10^3 W. The Q, H_g, P_t, V_L, and I_L are observed to be 1 m^3/s, 100 m, 1.44×10^3 W, 1.04×10^4 V and 86 A, respectively. Further, at $t = 2$ s P_{ref} is increased to 1835.2×10^3 W and corresponding Q, H_g, P_t, V_L and I_L are noted to be 1.6 m^3/s, 160 m, 2.91×10^5 W, 1.48×10^4 V and 123 A, respectively. Further, at $t = 5$ s P_{ref} is decreased to 190×10^3 W and corresponding parameters are 0.40 m^3/s, 40 m, 3.39×10^5 W, 5×10^3 V, and 42 A. Furthermore, at $t = 6$ s P_{ref} is step increased to 885.8×10^3 W. The values of Q, H_g, P_t, V_L, and I_L are settled at 1 m^3/s, 100 m, 1.43×10^6 W, 10.3×10^3 V and 86 A.

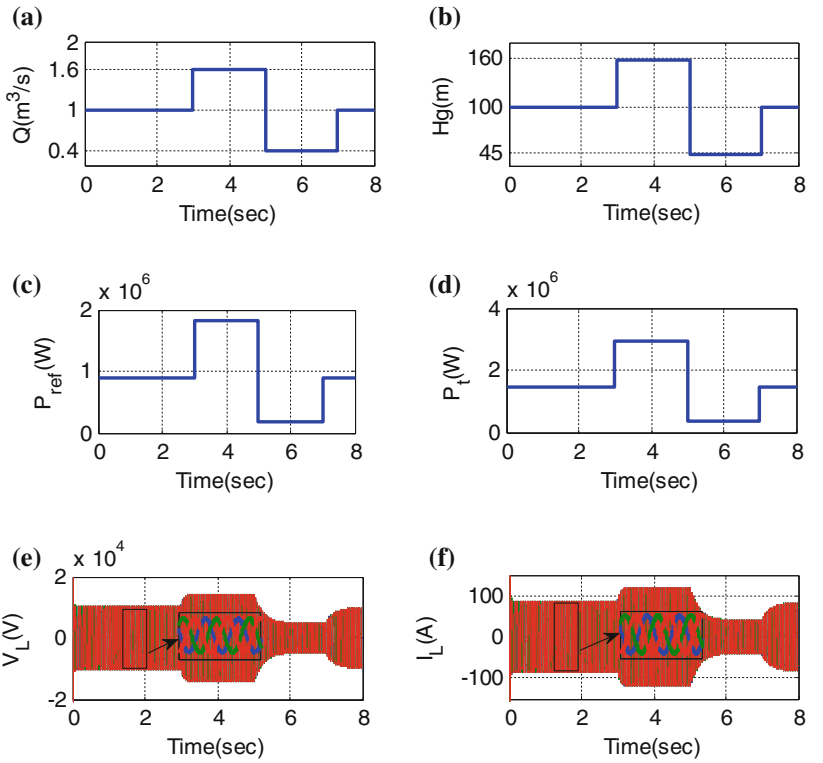


Fig. 3 System parameter under dynamic analysis. **a** Water head response, **b** gross head response, **c** reference power response, **d** turbine power response, **e** load voltage response, **f** load current response

The comparative study of the system parameters (Q, H_g, P_t, V_L, I_L) under static and dynamic analysis in terms of steady state values, rise time and fall time is reported in Table 1. It is observed that performance of the ANN controller-assisted SHPGS is satisfactory.

Table 1 Comparative analysis of system parameters

Factors	Steady state values (t = 4 s)	Rise time (t = 3 s)	Fall time (t = 5 s)
Q	1 m^3/s	1.60 m^3/s	0.40 m^3/s
H_g	100 m	160 m	40 m
P_t	1.44 × 10^6 W	2.91 × 10^6 W	3.39 × 10^5 W
V_L	1.03 × 10^4 V	1.48 × 10^4 V	5 × 10^3 V
I_L	86 A	123 A	42 A

6 Conclusions

In this paper, a study of ANN controllers-assisted SHPGS has been carried out. The modeling of the entire system has been done in MATLAB/Simulink software. The reported results validated the satisfactory performance for the model of SHPGS. The designed system can be used for future studies.

Appendix

Water density (ρ) = 1000 kg/m^3, Length of penstock (L_P) = 66 m, Valve gate factor (K_V) = 0.15, Entrance factor (K_{en}) = 0.04, Length of open channel (L_{ch}) = 10–30 m, Manning factor of open channel (N_{ch}) = 0.014, Penstock water velocity (V_P) = 3–5 m/s, Track rack coefficient (K_{tr}) = 0.8–2.4, Bar thickness of trash rack screen (t) = 9 mm, Bar width of trash rack screen (b) = 0.0015 mm, Gravity acceleration constant (g) = 9.8 m/s^2.

References

1. Ansel, A., Robyns, B.: Modeling and Simulation of an Autonomous Variable Speed Micro-Hydro Power Station. Mathematics and Computer in Simulation. 71 (2006) 320–332.
2. Vyas, A., Gupta, N. K., Gupta, S. K., Gautam, P., Jethoo, A. S.: Micro Hydel Power System Design and its Implementation in Rajasthan. Aquadic Procedia 4 (2005) 1537–1544.
3. Molina, M. G., Marques, J. L., Pacas, J. M.: Dynamic Modeling, Simulation and Control Design of Advanced Micro-Hydro Plant for Distributed Generation Applications. International Journal of Hydrogen Energy. 35 (2010) 5772– 5777.
4. Mishra, S., Sighal, S. K., Khatod, D. K.: Costing of a Small Hydro Power Project. International Journal of Engineering and Technology. 4 (2012) 239.
5. Salhi, I., Doubabi, S., Essounbouli, N., Hamzaoui, A.: Application of Multi-Model Control with Fuzzy Switching to Hydro-electrical Power Plant. Renewable Energy. 35 (2010) 2071–2079.
6. Ekanayake, J. B.: Induction Generator for Small Hydro Schemes. Power Engineering Journal 16 (2002) 61–67.
7. Gupta, A., Kumar, A., Pachauri, R. K., Chauhan, Y. K.: Performance Analysis of Neural Network and Fuzzy Logic Based MPPT Techniques for Solar PV System. in Proc. of Power India International Conference (2014) 1–6.

GA-Tuned 2DOFPID-Based Biomass Concentration Control of Bioreactor

Nikhil Pachauri, Asha Rani and Vijander Singh

Abstract The present work is focused on efficient control of biomass concentration in continuous bioreactor. A two degree of freedom PID (2DOFPID) controller is therefore designed for the purpose. The controller parameters are optimized with the help of genetic algorithm (GA). The proposed controller may provide good control performance as it utilizes the advantages of GA and 2DOFPID. The optimization is also carried out using pattern search (PS) and simulated annealing (SA) for comparative analysis. The performance of designed controllers is analyzed for set point tracking, and disturbance rejection. Results reveal that GA-2DOFPID outperforms the other implemented controllers.

Keywords Bioreactor · PID · Two degree of freedom PID (2DOFPID) · Genetic algorithm (GA)

1 Introduction

Biochemical industries have ascended considerably in the last few decades for industrial production and bioconversions. Microorganisms are used to produce vital products like life-saving vaccines, antibiotics in pharma industries, beer and wine, etc., in agro-food industries and for treatment of urban and industrial waste water. Bioprocesses are one of the most difficult processes in biochemical industries, it is difficult to control a bioprocess precisely and automatically due to its nonlinear and uncertain nature [1]. Literature reveals that several controllers are designed for

Nikhil Pachauri (✉) · Asha Rani · Vijander Singh
Instrumentation and Control Engineering Division, NSIT,
Azad Hind Fauz Marg, Sec-3, Dwarka 110078, New Delhi, India
e-mail: nikhilpchr@gmail.com

Asha Rani
e-mail: ashansit@gmail.com

Vijander Singh
e-mail: vijaydee@gmail.com

© Springer Science+Business Media Singapore 2017

R. Singh and S. Choudhury (eds.), *Proceeding of International Conference on Intelligent Communication, Control and Devices*, Advances in Intelligent Systems and Computing 479, DOI 10.1007/978-981-10-1708-7_103

control of bioreactors; Dowd et al. [2] proposed a controller based on predictive modeling and loose loop control for production of recombinant protein, monoclonal antibodies in perfusion bioreactor. Results show that proposed nonlinear controller responds effectively to the rapid changes in set point and at the same time maintains the quality of product concentration. Valentinotti et al. [3] proposed an adaptive control technique based on internal model principle for maintaining the ethanol concentration at its desired set point and at the same time good rejection of perturbation is achieved. Results show that proposed controller not only maintains the ethanol at desired set point but also increases the biomass productivity. Nagy [4] proposed a model predictive controller based on artificial neural network (NNMPC) for temperature control of yeast fermentation bioreactor. Optimal ANN structure is derived with the help of pruning algorithm and resulting ANN is acquainted with model predictive control scheme. The proposed controller is compared with linear model predictive control (LMPC) and conventional PID controller. The results reveal that NNMPC is more robust and competent in comparison to other controllers. Liu et al. [5] suggested a novel nonlinear guided intelligent controller (NGIC) inspired by the directive features of glucose in human body and its application to bioreactor system. Results show that NGIC controls the temperature of bioreactor efficiently in comparison to PID, ANN, and IMC. In this article 2DOFPID controller is proposed for biomass control of bioreactor. The performance of 2DOFPID is compared with integer order PID in terms of set point tracking and disturbance rejection. An evolutionary optimization technique is used to estimate the best values of 2DOFPID parameters. The paper is organized as follows: in Sect. 2 problem formulation and mathematical modeling of bioreactor are discussed. Section 3 explains the structure of 2-DOF-PID and in Sect. 4 genetic algorithm is described. Sections 5 and 6 describe the results and conclusion of the paper.

2 Problem Formulation and Mathematical Modeling of Bioreactor

Continuous bioreactors are extensively used for large-scale production due to its ease of operation. But it faces the problem of cell wash away with effluent which directly affects the quality of final product. Hence to control the quality of final product it becomes essential to control biomass concentration which is the prime motive of this research work. The mathematical model for continuous fermentation bioreactor under consideration and the parameter values are taken from Liu et al. and Nagy [4, 5]. A schematic diagram of bioreactor is shown in Fig. 1.

$$\frac{dV}{dt} = (F_i - F_e) \tag{1}$$

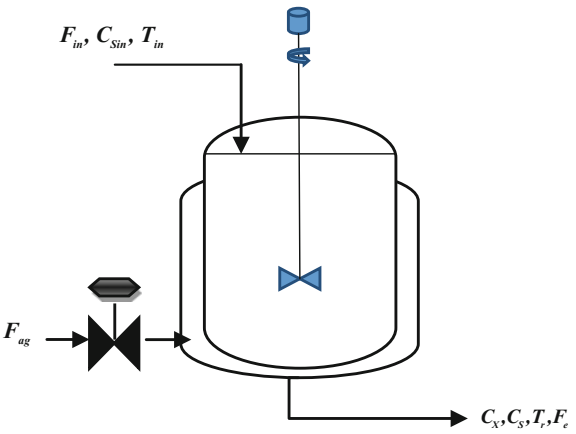


Fig. 1 Schematic diagram of bioreactor

$$\frac{dc_X}{dt} = \mu_X c_X \frac{c_S}{K_{S1} + c_S} e^{-K_{P1} c_P} - \frac{F_e}{V} c_X \tag{2}$$

$$\frac{dc_P}{dt} = \mu_P c_X \frac{c_S}{K_{S1} + c_S} e^{-K_{P1} c_P} - \frac{F_e}{V} c_P \tag{3}$$

$$\frac{dc_S}{dt} = -\frac{1}{R_{SX}} \mu_X c_X \frac{c_S}{K_S + c_S} e^{-K_{P1} c_P} - \frac{1}{R_{SP}} \mu_P c_X \frac{c_S}{K_{S1} + c_S} e^{-K_{P1} c_P} + \frac{F_i}{V} c_{S_{in}} - \frac{F_e}{V} c_S \tag{4}$$

$$\frac{dT_r}{dt} = \frac{F_i}{V}(T_{in} + 273) - \frac{F_e}{V}(T_r + 273) + \frac{r_{O_2} \Delta H_r}{32 \rho_r C_{heat,r}} + \frac{K_T A_T (T_r - T_{ag})}{V \rho_r C_{heat,r}} \tag{5}$$

$$\frac{dT_{ag}}{dt} = \frac{F_{ag}}{V_j}(T_{in,ag} - T_{ag}) + \frac{K_T A_T (T_r - T_{ag})}{V_j \rho_{ag} C_{heat,ag}} \tag{6}$$

$$\frac{dc_{O_2}}{dt} = (k_l a)\left(c^*_{O_2} - c_{o_2}\right) - r_{O_2} \tag{7}$$

3 Two Degree of Freedom PID (2DOFPID) Controller

The problem discussed in the last section may be well addressed, with the flexible control algorithm known as 2-DOF-PID. The problem discussed in the last section may be well addressed, with the flexible control algorithm known as PID (2DOFPID) is mathematically defined by the following equation.

$$U(s) = E(s)\left(K_p(\mathrm{d}R(s) - Y(s)) + \frac{K_i}{s}(R(s) - Y(s)) + \frac{(K_d\, s\,(eR(s) - Y(s)))}{(1 + s\,K_d/K_pN)}\right) \tag{8}$$

Equation (9) can be rewritten as

$$U(s) = R(s)L(s) - Y(s)H(s) \tag{9}$$

where

$$H(s) = K_p + \frac{K_i}{s} + \frac{s\,K_d}{(1 + s\,K_d/K_pN)} \tag{10}$$

$$L(s) = K_p d + \frac{K_i}{s} + \frac{s\,K_d\,e}{(1 + s\,K_d/K_pN)} \tag{11}$$

K_p, K_i, and K_d are proportional, integral and derivative gain, respectively. $E(s)$ is the control error, $U(s)$ is the control signal, $Y(s)$ is the process output, $R(s)$ is the set point, N is derivative filter, d and e are the weights which affect the set point. The functions, $H(s)$ and $L(s)$, maintain a decent output response along with good regulatory performance. The proposed control scheme is used to manipulate the flow rate of cooling agent (F_{ag}), by maintaining the temperature of reactor which in turn controls the biomass concentration [7].

4 Genetic Algorithm (GA)

The efficiency of any control scheme solely depends on the tuning of controller parameters, due to this reason commonly used evolutionary algorithm known as GA is used to optimize the controller parameters. The steps for implementing the GA are as follows [6].

(a) Generate the preliminary individuals with chromosomes of fixed size, where each chromosome represents the probable solution.
(b) Estimate the fitness of every chromosome in the population.
(c) Choose the fittest element of the population.
(d) Replicate using a probabilistic method.
(e) Execute crossover operation on the reproduced chromosomes.
(f) Apply mutation operator.
(g) Reiterate from Step b until a predefined convergence condition is met.

5 Results and Discussion

The mathematical model of continuous bioreactor discussed previously is simulated on Intel® Core™ i5 CPU with 2.4 GHZ frequency and 4 GB RAM in MATLAB version 8.0.1.604. 2DOFPID and traditional PID are designed for biomass concentration control of bioreactor. The primary requirement of any control approach is to obtain the optimal values of its parameters. The tuning of controllers has become an easy assignment because of the development in the area of optimization. An evolutionary optimization technique, i.e., GA is used to evaluate the parameter values of 2DOFPID. The main step in optimization is to select an appropriate cost function. Therefore in order to obtain the desired response weighted sum of Integral Absolute Error (IAE) and settling time (T_s) is chosen.

$$\mathrm{J} = 0.4 * \mathrm{IAE} + 0.6 * T_s \tag{12}$$

The weights of objective function are decided after rigorous experimentation. This cost function is chosen to minimize the settling time and error between the reference variable and process variable.

Six controller parameters (K_p, K_I, K_D, N, d and e) of 2DOFPID are to be optimized. GA, PS, and SA are simulated for 50 generations using the same cost function and the values of objective function obtained are shown in Fig. 2. The comparison of convergence rate for the optimization techniques shows that GA converges significantly faster as compared to PS and SA. The minimum values of fitness function are 7.48, 7.49, and 8.15 for GA, PS, and SA, respectively. The optimum values of 2DOFPID and PID with the help of the three optimization techniques are given in Table 1.

The robustness of the controllers is tested by analyzing the performance of bioreactor for changes in set point. Figure 3 demonstrates the comparison between GA-2DOFPID, PS-2DOFPID, SA-2DOFPID, and PID for biomass concentration control at different set points. Initially fixed set point of 1 g/l is given for first 100 h

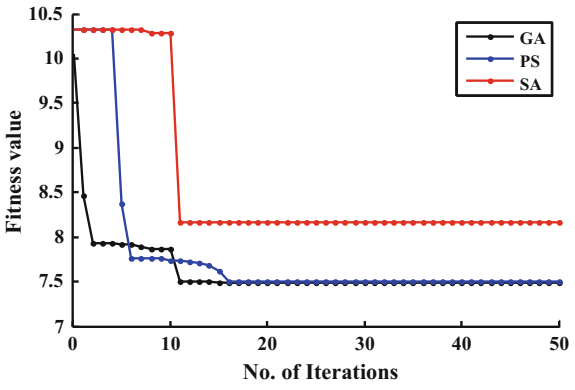


Fig. 2 Comparison of convergence for GA, PS, and SA

Table 1 Optimal parameter values for PID and 2-DOF-PID

Controllers	K_P	K_I	K_D	N	d	e
ZN-PID	100	5.086	280.43	–	–	–
GA-2DOFPID	135	4.48	601.4	0.1984	0.9982	0.9945
PS-2DOFPID	125	4.95	571	0.2145	0.9891	0.9573
SA-2DOFPID	120	4.44	400	0.2536	0.9953	0.9874

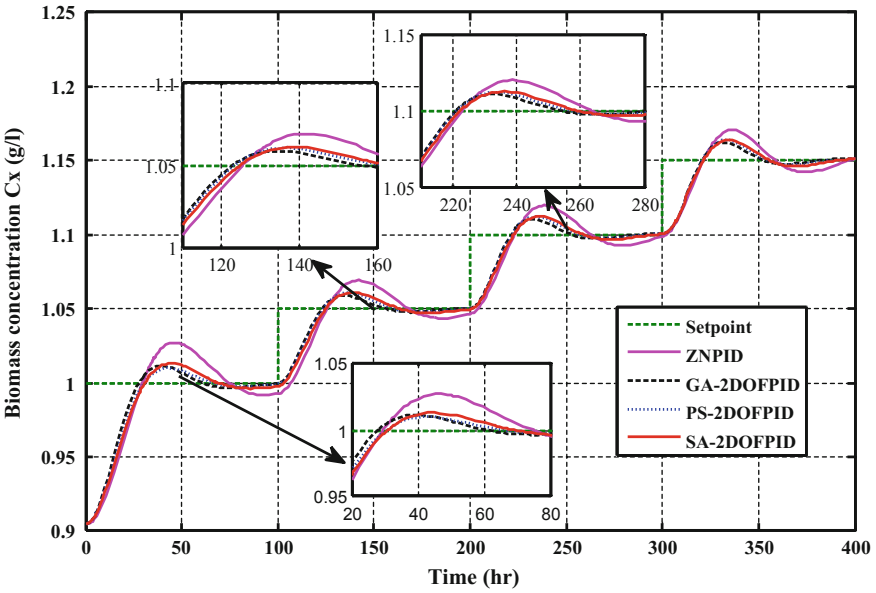


Fig. 3 Biomass composition control by the designed controllers

then it is varied from 1 to 1.05 g/l, 1.05 to 1.1 g/l, and 1.1 to 1.15 g/l at an interval of 100 h. GA-2DOFPID precisely controls the biomass concentration with minimum overshoot and settling time. It is also verified that the performance of PID degrades with the change in set point whereas GA-2DOFPID tracks efficiently the given set points. Hence, it is obvious that the transient and steady state performance of GA-2DOFPID is better than the other designed controllers.

The controllers are also tested for ±5 % disturbance in input temperature T_{in}. The performance of designed controllers is evaluated in terms of Integral Squared Error (ISE) between the set point and controlled biomass concentration. It is verified from Table 2 that GA-2DOFPID is more competent as compared to other designed controllers under the facets of disturbance and set point changes.

Table 2 ISE for set point tracking and disturbance rejection

Controllers	Set point tracking (ISE)	+5 % change in T_{in} (ISE)	−5 % change in T_{in} (ISE)
ZN-PID	0.2536	0.1783	0.1597
GA-2DOFPID	**0.1789**	**0.1200**	**0.1315**
PS-2DOFPID	0.1878	0.1277	0.1401
SA-2DOFPID	0.1989	0.1303	0.1474

6 Conclusion

In this article a 2DOFPID controller is designed for biomass concentration control of bioreactor. The parameters of 2DOFPID controller are optimized with the help of GA, PS, and SA. It is observed that GA converges fast and minimizes the objective function significantly as compared to the other two algorithms. The biomass concentration of bioreactor process is controlled with the help of designed controllers. The designed controllers are analyzed for set point tracking and disturbance rejection. It is concluded from the results that GA-based 2DOFPID is more robust and efficient as compared to other designed controllers.

References

1. Bastin G., Dochain D., On-line Estimation and Adaptive Control of Bioreactors, Elsevier, Amsterdam (1990).
2. Dowd J. E., Kwok K. E., Piret J. M., Predictive modeling and loose-loop control for perfusion bioreactors, Biochemical Engineering Journal, 9 (2001) 1–93.
3. Valentinotti, Srinivasan B., Holmberg U., Bonvin D., Cannizzaro C., Rhielb M., Stockar U., Optimal operation of fed-batch fermentations via adaptive control of overflow metabolite, Control Engineering Practice 11 (2003) 665–67.
4. Nagy Z. K., Model based control of a yeast fermentation bioreactor using optimally designed artificial neural networks, Chemical Engineering Journal 127 (2007) 95–109.
5. Liu B., Ding Y., Gao N., Zhang X., A bio-system inspired nonlinear intelligent controller with application to bio-reactor system, Neurocomputing 168 (2015) 1065–1075.
6. Singh R., Sen I., Tuning of PID controller based AGC system using Genetic Algorithm, in IEEE region 10 Conference TENCON, 3 (2004) 531–534.
7. Vilanova, Alfaro V., Arrieta O., Analytical robust tuning approach for two degree-of-freedom PI/PID controllers, Eng. Lett. 19 (2011) 204–214.

Microcontroller and FPGA-Based Analysis of 8 × 48 LED Matrix Display with Keyboard Interface

Adesh Kumar, Vivek Kaundal, Rajesh Singh, Anita Gehlot, Nikhil Gupta and Mohit Suyal

Abstract Increasing population is demanding to convey the information in an easy way to access the information in less time. In a large volume of population, it is impossible to provide any kind of information via mouth regularly, so there is a need for some substitute, which would easily convey the message to the crowd without any regular human/PC interference. The paper focuses on the design, and hardware implementation of LED matrix-based display system, which is developed to display information regularly or the message in scrolling form. The system takes input directly from the keyboard and the typed message is displayed. The intelligence and control are done using ATMEGA 16 microcontroller to display the message. The same is targeted with the help of SPATAN 6 FPGA and comparative results are estimated with frequency and timing.

Keywords ATMEGA 16 · Light-emitting diode (LED) · Alfa vizard RISC (AVR)

1 Introduction

The LED matrix information system is an output device used to display information in the limited resolutions on various places such as metro trains, clocks, machines, notice boards, train arrival/departure indicators, hotels, shops and flight information display, and many more where ordinary display is required. The matrix is a combination of LED lights [3] arranged in dot matrix manner in a rectangular config-

Adesh Kumar · Vivek Kaundal · Rajesh Singh · Anita Gehlot
Departments of Electronics, Instrumentation and Control (EIC) Engineering, University of Petroleum and Energy Studies (UPES), Dehradun, India

Nikhil Gupta (✉)
Embedded Hardware, Larsen & Toubro Limited (HED), CV Raman Nagar, Bangalore, India
e-mail: gupta.nikhilece@gmail.com

Mohit Suyal
R&D Division, Simon Electric Pvt. Ltd., IHDP Business Park, Sector-127, Noida, India

© Springer Science+Business Media Singapore 2017

R. Singh and S. Choudhury (eds.), *Proceeding of International Conference on Intelligent Communication, Control and Devices*, Advances in Intelligent Systems and Computing 479, DOI 10.1007/978-981-10-1708-7_104



Fig. 1 Scrolling message LED display system

uration. The LED display can have other shapes also and configured in a manner that graphics or text is visualized and displayed by simple action of switch on and off of the LED lights. The signals and device inputs can be controlled using microcontroller-based system or FPGA device that converts instructions from a microcontroller or FPGA to turn on and off LEDs in the matrix form, so that the required information is displayed on the board. The matrix device consists of a 2D LED matrix in which the cathodes of each are joined in rows and the anodes of the diodes are joined in columns. It is also possible to connect vice versa. The amount of current in each LED is controlled with the help of electricity flow through each pair row wise and column wise. The display device multiplexes and scans row wise that flashes the LEDs very fast and the pictures or the characters are displayed on matrix board. The brightness of display can vary by varying the pulse rate per LED. The multicolor LEDs or RGB colored LEDs are considered as display of colored images [6]. The human eye does not feel flicker because the refresh rate is sufficient and always fast. All modern computers can have output data in dot matrix display or it can be said that the data is stored either in dot matrix manner or in vectored form. The paper focuses on design a scrolling textual display system, based on LEDs dot matrix array. The display system is controlled and programmed for ATMEGA 16 AVR series of microcontroller. The example of dot matrix display system is shown in Fig. 1.

2 System Description

The system block diagram is shown in Figs. 2 and 3, in which the microcontroller is energized with the help of 5 V/1 A power supply. The input is given to ATMEGA 16 microcontroller with the help of keyboard. The data is shifted using six shift register arrays connected to the 8×48 LED panel. The concept is derived by cascading six multiplexed one shift register controlled 8×8 LED panel. The proposed system uses an ATMEGA 16 AVR microcontroller for receiving the data from keyboard and transmitting it serially to the shift registers. In the given system the PS2 keyboard is generating the data in standard ASCII format. This data in

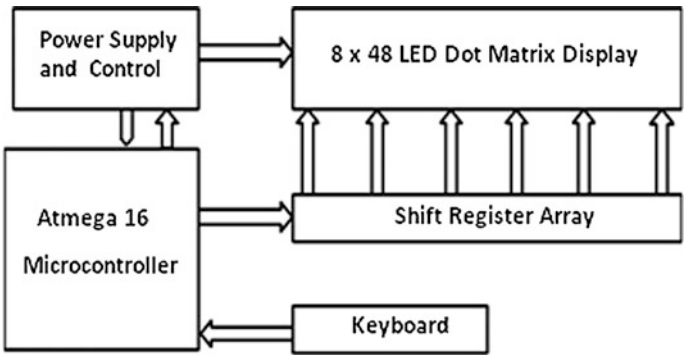


Fig. 2 Block diagram description

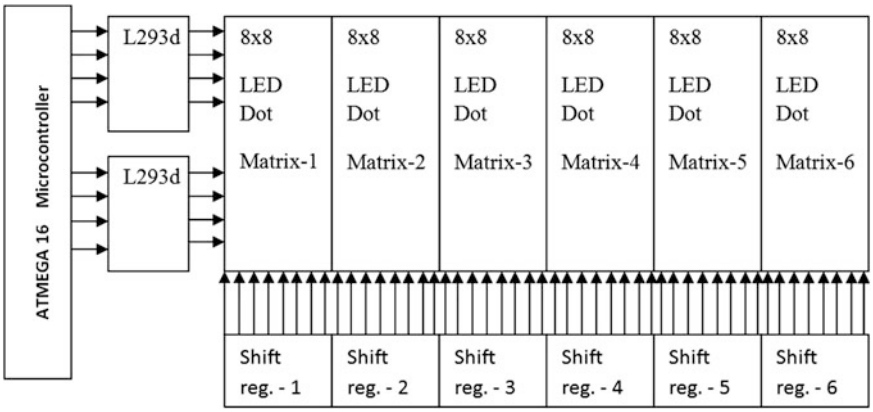


Fig. 3 System block diagram description

ASCII format is then received by the AVR microcontroller which is further stored in an array. After that each character is converted into the 5 × 7 hexadecimal codes [4]. The hexadecimal data is then transmitted serially to the shift registers in bitwise manner. The shift registers are SIPO (serial input parallel output). Hence the bitwise serial data is then transmitted to the LED matrix [1] byte wise. As the shift registers are cascaded, so the data shifts from one matrix to another matrix. The switching time of LED from ON to OFF is very less such that each alphabet appears precisely due to the persistence of vision. Figure 4 shows the bitwise transfer within microseconds and finally due to persistence of vision it appears as an alphabet as indicted in last in Fig. 4.

Power Supply Unit—Power supply is the main part of the system and basically designed to provide sufficient current to the LED matrix display which consists of 384 LED's. The unit provides 5 V, 1 A output to drive the LED's.

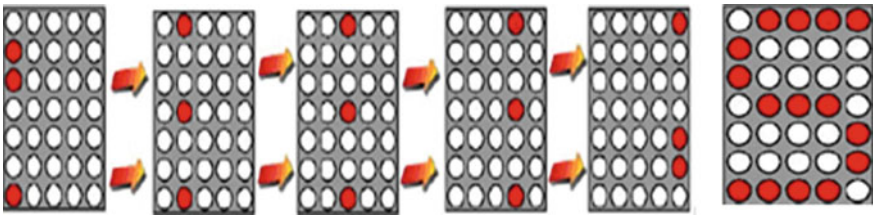


Fig. 4 Hardware pictorial view

LED Matrix Display—This section includes the hardware for the 8 × 48 LED matrix display which consists of the 384 LED's soldered on a zero size PCB.

Microcontroller—In the design ATMEGA 16 microcontroller from AVR RISC-based architecture is used. It is a low-power 8 bit CMOS technology-based microcontroller. ATMEGA 16 provides 1 MIPS per MHz in one clock cycle and executes powerful instructions. It allows the system for optimal power requirement versus speed.

LED's—It requires a low-cost, easily available 5 mm LED which has a low power consumption giving us maximum intensity of 500–900 mcd.

Shift Register (74HC595)—Shift register 74HC595 is the part that follows an 8-bit serial in, parallel—out operation with synchronized D flip flops as storage unit.

L293D—The L293D is half H drivers and provides quadruple high current. It is designed for bidirectional current control and voltages from 4.5 V to 36 V with drive currents of up to 600-mA.

Firmware for the system is developed using Eclipse Galileo and wins AVR software. The complete program is written in Embedded 'C' language and compiled using the *avr-gcc,* an open source compiler. The microcontroller is programmed by the Eclipse software only. The program includes the standard library "avr/io.h", "avr/interrupt.h". As the keyboard works on synchronous mode so the USART mode of the controller is used to get the data from the keyboard. So to have access to the USART mode of the ATMEGA 16 microcontroller, we have created the USART libraries [5]. The program simply takes the data from the keyboard and forms an array and finally converts that array character by character into its equivalent 5 × 7 [2] hexadecimal code. The shift register consists of two clocks, one is the shift register clock and the other is the storage register clock. Both the clocks are synchronized at time period of 1 ms. The code is simulated in Proteus software to test the circuit and the firmware.

3 Flow Chart of Simulation Model

The flow diagram of the developed model is depicted in Fig. 5. Initially, the display is switched ON with the help of switch button and the keyboard is connected to the display. The text is entered with the help of the keyboard and the controller will check for the pressed keys continuously. If the key pressed is "Enter," then the entered data will be copied to display array. The input data from the keyboard are ASCII codes, the codes are then converted into their equivalent 5 × 7 hex codes. The hex codes are transferred bitwise into the shift registers and then the shift register transfers the data byte wise onto the LED Display.

4 FPGA Synthesis

The design is developed using VHDL programming language and the same is synthesized on SPARTAN-6 FPGA, manufactured by Diligent. FPGA has the input switches and output LEDs. The input switches are used to assign the *keyboard_input [7:0]* in ASCII data format, and output of one character is displayed on *LEDs [7:0]*. The logged data is also displayed on the motherboard of the personal computer, when scrolling message is passing, more than one character. The DATA-V5 is strongly integrated with the main/host computer with the help of 8-lane PCI Express connection, which can support the sustainable bandwidths of up to 2 Gbytes/s. The SPARTAN-6 FPGA board has high end peripherals and interfacing, like HDMI video, Gbit Ethernet, DDR2 memory array of 128 Mbyte, USB and audio ports make the board an ideal host for complete system design. The block diagram of the FPGA synthesis is shown in Fig. 6. In the block diagram, input switches are used to control the input sequence and scrolled data is flashed on board developed in matrix form already. The FPGA board, Spartan-6 LX45 is having 324-pin BGA package, 128 Mbyte DDR2 memory-based 16-bit data size 10/100/1000 Ethernet, Physical USB2 ports for on board data transfer and programming, USB-HID port for keyboard interfacing or mouse, USB-UART with two HDMI video input ports and two HDMI output ports, Codec AC—97, with line in line out, headphones with mic, power monitors on all power rails, in real time, with 16 Mbyte × 4 SPI flash configuration and data string capability. It has CMOS oscillator that provides 100 MHz frequency, 48 inputs/outputs, which can be routed with general purpose input/outputs (GPIO) expansion connectors. It includes 8 LEDs, 8 slide switches ships, 6 buttons with power supply of a 20 W and USB cable. The results of FPGA synthesis and comparative analysis is listed in Table 1.

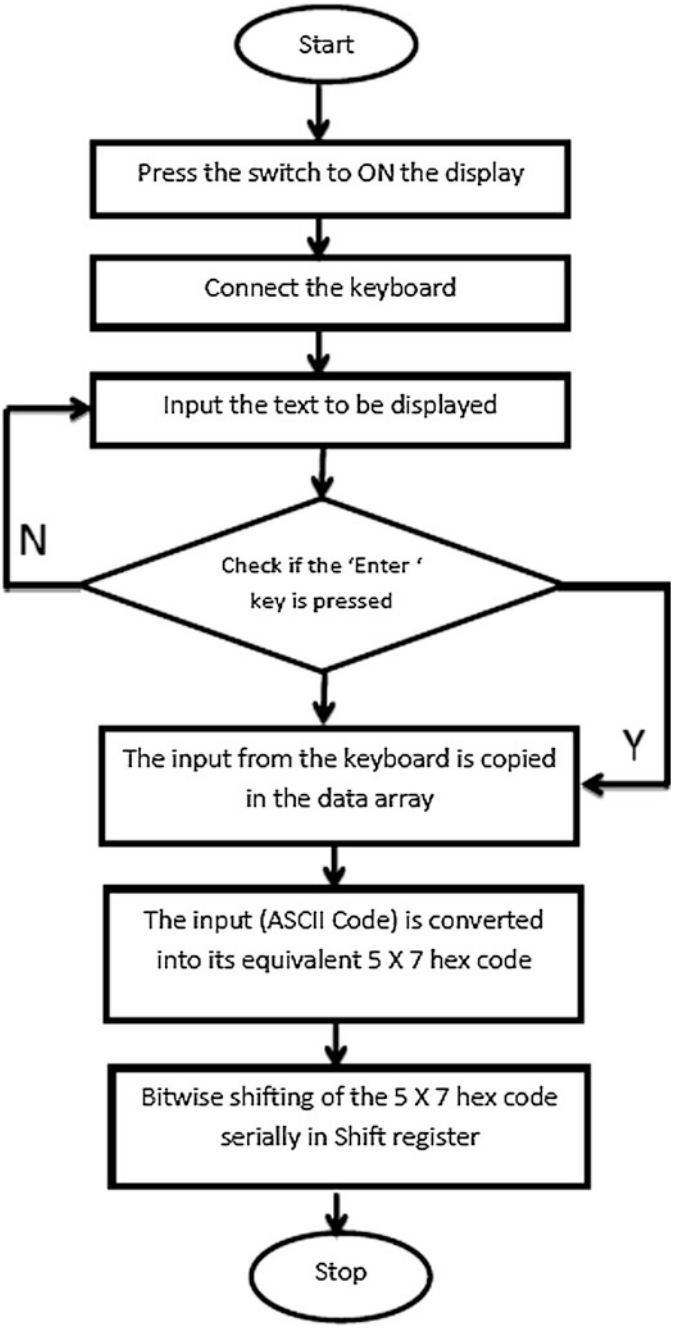


Fig. 5 Flow chart of functional module

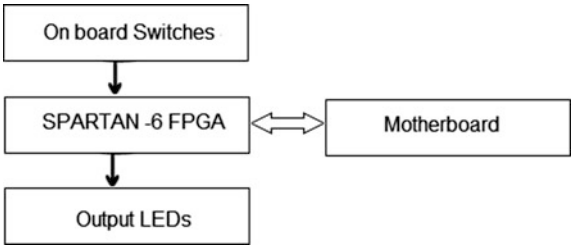


Fig. 6 FPGA block diagram

Table 1 Comparative analysis of ATMEGA 16 and SPARTEN-6 FPGA

Parameter	ATMEGA-16	SPARTEN-6
Minimum time	2.3 ns	1.198 ns
Frequency	16.00 MHz	400.00 MHz

5 Results and Discussions

The system design and code development of the hardware are done successfully with the help of using Eclipse software and functionality is verified on Proteus software. The simulation in Proteus is shown in Fig. 7. The hardware design and development of the system are done using all hardware components as discussed above. It is a cost-effective, economic and simple microcontroller-based hardware used to display real-time messages/information. This system can be used in any public areas, universities, colleges, companies, and metro trains. The interfacing of the serval components to the ATMEGA 16 microcontroller is very important part. The developed prototype reduces the human effort, addresses the group people

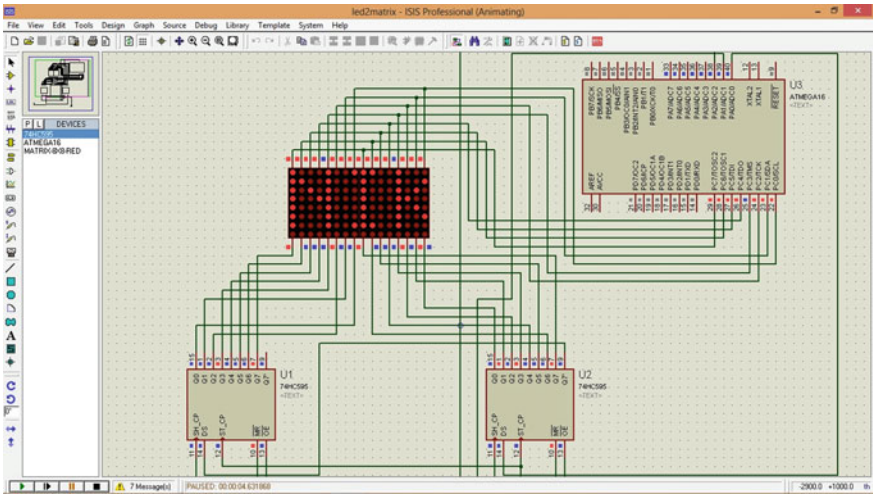


Fig. 7 Protecus simulation model for message display in 8 × 16 matrix display

and convey of messages/information. The developed design and verified different test cases on the hardware as experimental results stress the relevance of the novel approach in the field of LED's.

6 Conclusion

Hardware design and implementation of 8 × 48 LED matrix display with keyboard interface is done successfully and tested for the different test cases. The greatest advantage of the developed hardware is that, any text can be displayed on the LED matrix without reprogram the controller. The code is burned in the controller once and the text is typed with the help of keyboard which is feasible to display any text in real time. FPGA synthesis shows the optimized results in terms of frequency and minimum time of display. Therefore, FPGA control of matrix or scrolling display is an optimal solution to achieve higher speed and throughput.

References

1. A. Zidouri, M. Deriche, M. Al-Otaibi, M. Al-Shahrani, M. Al-Mutairi, T. Al Maleki, S. Al-Ghunaim, A. Al-Nutaifi, H. Al-Issa, F. Al-Anazi "Design and Implementation of a Bilingual LED Message Board". Electrical Engineering Department KFUPM, Dhahran, 31261, Saudi Arabia.
2. D. Indra, Journal ILKOM, ISSN, 2010, journal.umi.ac.id. Abstract: Development of the existing microcontroller has been very fast. A lot of electronic equipment's exploits microcontroller. One other applicable at microcontroller that is making the application of physic for presents character by using dot matrix led display 5 × 8.
3. E. T. Lisuwandi, 2002, mtlweb.mit.edu. Abstract: A feedback circuit for an Organic Light Emitting Diode (OLED) based display is proposed and demonstrated. An OLED-based flat panel display is brighter, much lower power, has no viewing angle limitation and potentially cheaper compared to available LCD/CRTs.
4. Michael Costa, "In-Vehicle Display System". University of Southern Queensland, Faculty of Engineering and Surveying, Oct. 2005.
5. Richard Barnett, Larry O'Cull, Embedded 'C' Programming and the Microchip PIC. Thomson learning, 2004.
6. W. He, Y. Guo, Society of Photo-Optical Instrumentation, 1994, letters. Abstract: In this paper, the author conducted the research how to measure automatically the image point homogeneity of the high density matrix LED display, gave the measuring plan of the integrating sphere—photoelectric multiplex tube (PMT).

Software Reliability Prediction Based on Ensemble Models

Pravas Ranjan Bal, Nachiketa Jena and Durga Prasad Mohapatra

Abstract Software reliability is the determinant factor of software reliability prediction and software quality estimation during software testing period. This report offers an ensemble technique model of different artificial neural networks for forecasting of software reliability. The experimental results of the proposed model are compared with other states of the traditional models and it is noted that the proposed architectural model outperforms its competent models. The proposed architectural ensemble model has been adequately tested on three benchmark datasets and its results tested with an artificial neural network approach and a mathematical linear model. The experimental result demonstrates that the ensemble model yields better performance than other models.

Keywords Ensemble model · Feed forward neural network · Radial basis function · Statistical model and software reliability

1 Introduction

According to ANSI, software reliability is determined as the probability of software failure-free operation for a specific point of time in a conditioned environment [1, 2]. In the last four decades, most of the linear prediction models such as Software Reliability Growth Models (SRGMs) have been designed for software reliability prediction, weather forecasting, cost estimation and its time factors. Parametric neural network models are established on the linear Non-Homogeneous

P.R. Bal (✉) · Nachiketa Jena · D.P. Mohapatra
Department of Computer Science and Engineering,
National Institute of Technology, Rourkela, Rourkela 769 008, India
e-mail: pravasranjan90@gmail.com

Nachiketa Jena
e-mail: nachiketa.jena@gmail.com

D.P. Mohapatra
e-mail: durga@nitrkl.ac.in

© Springer Science+Business Media Singapore 2017

R. Singh and S. Choudhury (eds.), *Proceeding of International Conference on Intelligent Communication, Control and Devices*, Advances in Intelligent Systems and Computing 479, DOI 10.1007/978-981-10-1708-7_105

Poisson Process (NHPP). Lastly, it has been concluded that all parametric linear models cannot predict efficiently in all circumstances. Most of the nonparametric statistical prediction models such as artificial neural networks like Feed Forward Neural Network (FFNN) can predict different types of software reliability metrics like availability, time between failures and cumulative failures, etc. At last, it is concluded that the ensemble prediction architectural model is superior to other types of the parametric linear models and has also better prediction capability [3–5].

This work presents a non-parametric architectural model for software reliability forecasting based on ensemble techniques which can predict efficiently software reliability data than other neural network approach and linear mathematical parametric model like Duane growth model [6].

The remainder of the paper is organized as follows. In Sect. 2, some related works for forecasting of software reliability of cumulative failure data are presented. Section 3 discusses the proposed ensemble approach for software reliability forecasting. The experimental results and discussion is presented in Sect. 4. Finally, Sect. 5 concludes the paper.

2 Literature Survey

This section briefly discusses some related works based on various types of artificial neural network models for prediction of software reliability.

Karunanithi et al. [5] presented connectionist model based on feed forward and recurrent neural network. They observed that this model works well in all circumstances for different types of software reliability datasets than some analytical models.

Su et al. [4] proposed an artificial neural network modeling approach such as Dynamically Weighted Combinational Model (DWCM) for prediction of software failure history data and software reliability estimation. He compared his proposed model with some mathematical models and proved that his proposed model accurately predict than other linear mathematical models.

Sitte [7] used two types of software reliability prediction growth models such as FFNN and recalibration of analytical growth model for prediction. He claimed that both prediction models have better prediction capability for common datasets in all circumstances.

Tian and Noore [8] proposed an evolutionary connectionist approach for forecasting of cumulative software failure data. He used multiple delayed input and single output neural network architectural model. He observed that his proposed model performs efficiently than other prediction model.

Cai et al. [9] observed the effectiveness of an artificial neural network for software reliability prediction from software failure history data and found several new things such as the neural network modeling approach is the best approach to handling software failure data and smoothly trends than other traditional models. The training results of neural network modeling approach are more appropriate than

other linear models. He also observed that neural network modeling approach is quantitatively bad for prediction of software defect prone and qualitatively good for classifying different modules of software.

Related work reveals that most of the prediction growth models used SRGMs. However, use of ensemble technique is limited. So, this work specially focuses only on ensemble technique of three standard artificial neural network models with a goal to obtain efficient and accurate prediction.

3 Proposed Work

This section portrays the proposed model for prediction of software failure data which utilizes ensemble techniques of the artificial neural network.

3.1 Ensemble Model

The prediction model based on the Ensemble technique is depicted in Fig. 1. Ensemble model is a three layer single input and single output architectural model such as an input layer, a component layer consists of feed forward, radial basis function neural network and an output layer is an average combination of output of all component layers. The component layer consists of three components and have used three types of activation functions for three components. The cumulative software failure data are organized in pair $\{T_i, N_i'\}$, where T_i is the execution time of software failure dataset as input of the ensemble model and $N_i^{'}$ is the cumulative

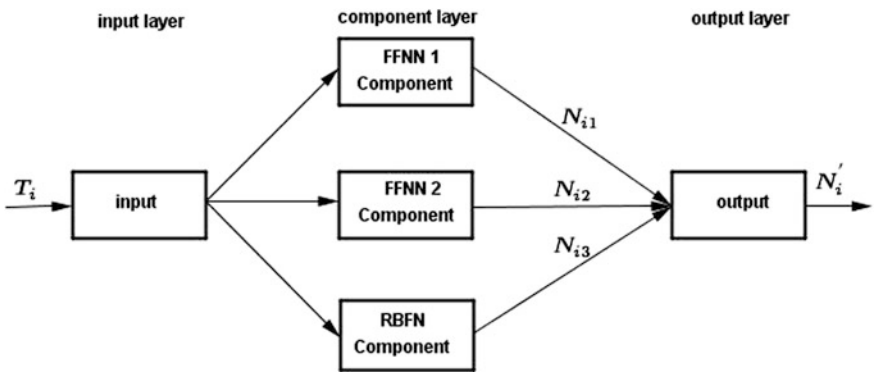


Fig. 1 The architecture of ensemble model

number software failure data as output of the ensemble model. The output of the Ensemble model is the mean of all three neural network components and is defined as follows.

$$N_i' = \frac{N_{i1} + N_{i2} + N_{i3}}{3} \tag{1}$$

3.2 FFNN Component

Two types of FFNNs have been used for our Ensemble model such as FFNN1 and FFNN2. The FFNN model is shown in Fig. 2.

The node in the FFNN model is computed as the sum of weighted sum of input data and bias value and the mathematical definition of this process is defined in Eq. (2)

$$\begin{aligned} a_i &= \sum_{j=1}^{n} w_{ij} x_j + b_i \\ y_i &= f_i(a_i) \end{aligned} \tag{2}$$

where a_i is the linear combination of input data and bias value b_i and w_{ij} is the weight matrices of FFNN model.

For FFNN1 we have used the transfer function such as log sigmoid as activation function and is defined in Eq. (3)

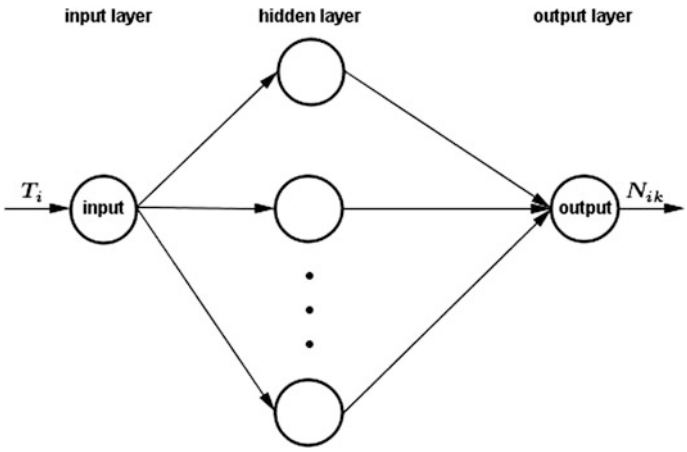


Fig. 2 FFNN model

$$f(n) = \frac{1}{1 + e^{-n}} \tag{3}$$

For FFNN2 we have used the transfer function such as tan sigmoid as activation function and is defined in Eq. (4)

$$f(n) = \frac{2}{1 + e^{-2*n}} - 1 \tag{4}$$

3.3 RBFN Component

Instead of using sigmoid function in FFNN, we have used the transfer function as radial basis function in the hidden layer of FFNN [10, 11] and defined as follows

$$f(y) = \sum_{i=1}^{k} w_i \emptyset(x - c_i) \tag{5}$$

where k is the number of neurons in the hidden layer, x is the number software failure data as input, w_i is the weight matrices of respective neuron i and c_i is the centroid vector for neuron i.

The radial basis function $\emptyset(x - c_i)$ as given by

$$\emptyset(x - c_i) = \sqrt{\sum_{i=1}^{k} (x - c_i)^2} \tag{6}$$

3.4 Performance Measures

Two types of meaningful performance measures have been used to compare the reliability prediction error of ensemble model and its competent models. Here, the proposed ensemble model is trained with some part of software failure data and the rest of software failure data is used for testing purpose. For performance measurement we have used two types of errors called Relative Error (RE) and Average Error (AE) are defined as

$$RE = \frac{(\hat{y}_i - y_i)}{y_i} * 100 \tag{7}$$

$$AE = \frac{1}{n}\sum_{i=1}^{n} RE_i \tag{8}$$

where, n is the total number of data samples, $\hat{y}_i$ is the predicted value and y_i is the actual value.

4 Experimental Results and Comparison

In our experiment, this model is trained and tested with three benchmark datasets DS1, DS2 and DS3 [1] for software reliability forecasting. The dataset DS1 consists of 21,700 numbers of assembly instructions and 136 numbers of failures and collected from real-time command and control application. The dataset DS2 consists of 10,000 assembly instructions and 118 numbers of failures and collected from flight dynamic application. The dataset DS3 consists of 22,500 assembly instructions and 180 numbers of failures and collected from flight dynamic application. All these datasets have been normalized in the range between [0, 1] by min max formula.

The ensemble model is trained with 60, 60 and 55 % for DS1, DS2 and DS3, respectively, in our experiments. The remaining software data for each software failure history dataset is used for testing. We have used different training ratio of different datasets for better prediction results.

We compare our proposed ensemble model with one artificial neural network such as FFNN and another linear mathematical parametric model [6] called Duane growth model: The Duane growth model is given by $\beta(t) = bt^a$ $b > 0$, $a > 0$, where a is the is shape of the growth curve and b is the parameter size of the curve.

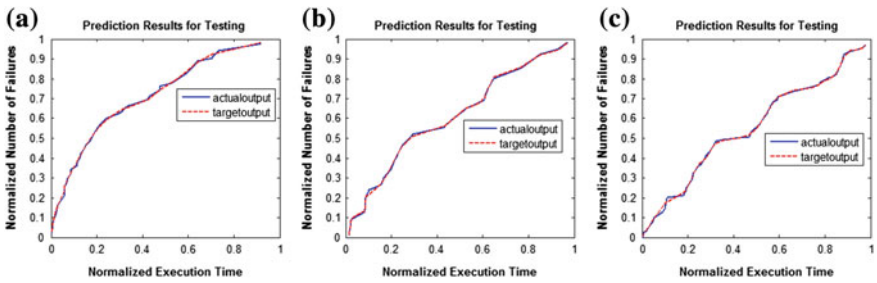


Fig. 3 Prediction results of ensemble model for **a** DS1, **b** DS2 and **c** DS3

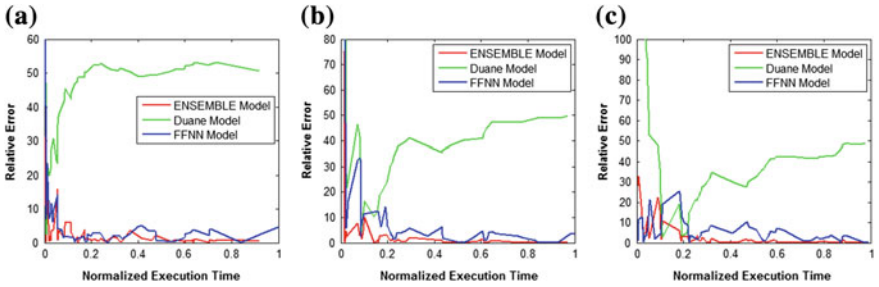


Fig. 4 Relative error of different models for **a** DS1, **b** DS2 and **c** DS3

Table 1 AEs for different models

Dataset	Average error		
	Ensemble model	FFNN	Duane model
DS1	1.1519	2.2156	47.2190
DS2	1.2540	3.1169	30.4239
DS3	1.1236	4.2752	21.1891

4.1 Performance Comparison

For ensemble model, we have chosen three components such as FFNN1, FFNN2, RBFN and each component consists of 5 neurons in the hidden layer. For FFNN model, we have taken five neurons in the hidden layer. The prediction results of Ensemble model for DS1, DS2 and DS3 are depicted in Fig. 3. The REs of different model on three datasets DS1, DS2, and DS3 are depicted in Fig. 4. The AEs on three datasets are shown in Table 1. It is concluded that ensemble modeling approach shows better performance than FFNN model and another linear mathematical modeling approach. For all datasets linear parametric growth model called Duane model shows worse performance than others. It is observed from the above results and discussion the Ensemble model is better than alternate traditional growth models.

5 Conclusion

In this paper, a non-parametric prediction approach has been proposed such as ensemble technique of three different artificial neural networks for software reliability prediction. The proposed ensemble model shows better prediction than other artificial neural network model and another traditional parametric mathematical model. It is observed that from the experimental results and discussions the proposed assembling approach proves the best model and shows lower prediction error than other competent model.

References

1. Lyu, M. R.: Handbook of software reliability engineering. New York: McGraw-Hill (1996).
2. Musa, J. D.: Software reliability engineering. More reliable software, faster development and testing. New York: McGraw-Hill (2004).
3. Zheng, J.: Predicting software reliability with neural network ensembles. Expert System with applications 36.2. (2009) 2116–2122.
4. Su, Y. S., Huang, C. Y.: Neural-network-based approaches for software reliability estimation using dynamic weighted combinational models. Journal of Systems and Software, 80, (2007) 606–615.
5. Karunanithi, N., Whitley, D., Malaiya, Y. K.: Using neural networks in reliability prediction. IEEE Software, 9 (1992) 53–59.
6. Malaiya, Y. K., Li, M. N., Bieman, J. M., Karcich, R.: Software reliability growth with test coverage. IEEE Transactions on Reliability, 51 (2002) 420–426.
7. Sitte, R.: Comparison of software-reliability-growth predictions: neural networks vs. parametric recalibration. IEEE Transactions on Reliability, 48(3) (1999) 285–291.
8. Tian, L., Noore, A.: On-line prediction of software reliability using an evolutionary connectionist model. Journal of Systems and Software, 77 (2005) 173–180.
9. Cai, K. Y., Cai, L., Wang, W. D., Yu, Z. Y., Zhang, D.: On the neural network approach in software reliability modeling. Journal of Systems and Software, 58 (2001) 47–62.
10. Orr, Mark, J. L.: Introduction to radial basis function networks (1996).
11. Leonard, J. A., Kramer, M. A., Ungar, L. H.: Using radial basis functions to approximate a function and its error bounds. IEEE transactions on neural networks/a publication of the IEEE Neural Networks Council, 3(4) (1991) 624–627.

Wireless Sensor Network Based Patient Health Monitoring and Tracking System

Amitabh Yadav, Vivek Kaundal, Abhishek Sharma, Paawan Sharma, Deepak Kumar and Pankaj Badoni

Abstract Hospitals need to be equipped with facilities and services to monitor the patients at all times. Due to large number of patients and limited number of doctors, it gets difficult for the doctors to visit each and every patient, and keep track of their improving or deteriorating health condition. This paper presents the structure of an embedded system that could monitor and keep a track of the patients' position and health condition at all times. It makes use of a Wireless Sensor Network of Xbee radios to acquire data, which is then saved in a local database of the central system and simultaneously, also uploaded on an online database to be made available for the doctors to access at all times. The system makes use of active RFID cards to track the position of the patients and along with it the data from the heart beat sensor is transmitted, for each patient separately.

Keywords Arduino · Internet of things · Wireless sensor network · Xbee · Wearable sensors · Wi-Fi

Amitabh Yadav (✉) · Vivek Kaundal · Abhishek Sharma · Paawan Sharma · Deepak Kumar · Pankaj Badoni
University of Petroleum and Energy Studies, Dehradun, India
e-mail: amitabhydv@gmail.com

Vivek Kaundal
e-mail: vkaundal@ddn.upes.ac.in

Abhishek Sharma
e-mail: abhishek.sharma@ddn.upes.ac.in

Paawan Sharma
e-mail: paawan.sharma@ddn.upes.ac.in

Deepak Kumar
e-mail: dkumar@ddn.upes.ac.in

Pankaj Badoni
e-mail: pbadoni@ddn.upes.ac.in

© Springer Science+Business Media Singapore 2017

R. Singh and S. Choudhury (eds.), *Proceeding of International Conference on Intelligent Communication, Control and Devices*, Advances in Intelligent Systems and Computing 479, DOI 10.1007/978-981-10-1708-7_106

1 Introduction

The advancements in the wearable sensor technology have increased in the recent decades and it is also one of the most thriving areas of research. Often in mental care and healthcare hospitals, patients need to be continuously kept under observation. All their activities need to be kept as a record. For the patients suffering from sleep disorders such as somnambulism (sleepwalking), their movements need to be tracked at all times so that they may not reach any place where they may harm themselves. Similarly, in old age homes and hospitals; there is a need to keep a track of patients' location, monitor their vital signs and maintain it in their records.

Thus, there arises a need for a system to keep a track of movement of the patients, i.e., their location, and at the same time also keep a record of their condition at all times in the form of a database. Such a system also needs to be fully self-sufficient and provides the doctor with the ease of monitoring his patients irrespective of his presence in the hospital; thus, the data must be accessible from any place and at all times.

For acquiring data from multiple sources (nodes) and arranging it together in a central system, it requires setting up of a weireless sensor network (WSN). The data is acquired on a central system, along with the information about the source of origin of each data and saved in an optimized way. Thus, a WSN can be created in a large-scale healthcare center to optimize and automate the task of patient tracking and health monitoring. The data can be made available to the doctor by connecting the overall system to the internet and sending the acquired data to be saved in an online database, the access to which can be provided by simply logging into the user account.

Such a system finds application in many domains of health monitoring, such as in hospitals, tracking and health monitoring at home for infants and elderly, sports training, military, etc.

2 Related Works

The research in the area of wearable sensor technology has been booming in the past few years, employing various biomedical sensors; and it has also proved to gain a lot of scientific attention. The outlook provided by researchers and clinic officials of the recent advancements made in the field of wearable technology has intrigued the ideas of the possibility offered by gathering data from sensors [1, 2]. Wearable computing has originated from placing sensors on the body and interfacing them wirelessly to create a body area network (BAN) that can sense and report the user's attributes [3, 4]. A variety of system's shortcomings have been addressed in biomedical wearable sensor technology, regarding reliability, privacy issues, user interface, etc., and still the continuous development in wearable sensor

based system will advance and be a transforming motivation for the future of healthcare [5, 6, 7].

Previously, systems were integrated with vital sign sensors and location sensors to create ad hoc network and gather patient data for applications at disaster struck areas [8]. The monitoring of the posture and activities can be performed using shoe-based wearable sensors that enable monitoring of energy exhausted, thus, proving to be an aid in checking obesity [9]. Intelligent health monitors that are portable can also be employed, like ECG and ischemia [10]. Researchers have focused to develop on the design of sensors so that they are minimally obtrusive and record the physiological signals. The work to develop algorithms for extracting required information from wearable technology is a flourishing area of research [11]. Employing wearable sensors that are permanently implanted, along with wearable monitoring, has the ability to provide continuous data of critical physiological terms for pre-identifying major adverse conditions in health. UbiMon Body Sensor network is also developed and investigated for activity recognition and health monitoring [12].

The developments in the sensor network technology have been brought about by the putting together the electro-mechanical systems at miniature level, wireless communication technology and digital electronics [13]. Recent developments in the analysis of signal processing of the time-domain signals have shown improvement in measurement of SpO_2 [14]. The miniaturization, the prolonged time of operation of medical sensors and integrating them with medical systems have enabled the patients to get a real-time data of their health condition [15]. The concept of using multiple layer distributed network for data acquisition has been implemented in biomedical systems [16, 17]. WSN of a large number of sensor nodes with the capability of multi-hop networking can be implemented to record sensor data, such as temperature [18], habitat monitoring [19]; and can also be used easily for monitoring in military, sports and biomedical applications [20]. There are many options to do this, such as by using Bluetooth, Xbee protocol and Wi-Fi systems, etc. [21].

However, lack of reliable communication and a limited bandwidth create challenges for implementing a sensor network. Studies to determine the performance of Xbee based WSN have been conducted in indoor environment, and extended study for enhancing the performance needs to be conducted [22]. But, low-power wireless sensor networks hide within it the potential to impact tremendously in the field of healthcare [23]. Systems have been developed using the mobile or PDA systems to provide health data acquired from wearable sensors, by making use of wireless telecommunications technology and the communication devices [24] and synchronizing the records that are collected with records that previously exist on the centralized server [25] or by comparatively easier way of creating a MATLAB based graphical user interface (GUI) [26, 27] or Microsoft Visual Studio based computer interfacing [28]. Techniques to gather data by creating a personal area network (PAN) of the employed sensors are used. However, it proves not very useful for data acquisition for a longer duration [29]. A GSM and Internet of Things (IoT) based system is employed that functions by sending messages and email for

real-time monitoring [30]. Another method is by using Bluetooth enabled wearable sensor, which is suitable for health monitoring at home [31].

Tracking of personal in a building can be done using various techniques ranging from RF-based systems [32], LANDMARC system employing radio frequency identification (RFID) [33, 34], active RFID based indoor localization [35], active badges for tracking in the office environment [36], GPS tracking, etc. The approach to indoor localization of the person has been studied in detail previously using active RFIDs; and enhanced approach to achieve higher accuracy than LANDMARC system has also been studied [37, 33, 35].

WSN, the IoT and machine to machine (M2M) interaction are some of the topics that have developed in the recent years and there is a need for module based, low-cost and easy-to-use platforms to creating network systems for developing software applications of WSN, IoT and other related technologies [38].

3 Proposed System

The idea behind the development of such a system is to automate the process of examining patients. Continuous monitoring of each patient is the most important aspect of designing the system. The system must be able to correctly identify each patient, and must be able to correctly match the data with the corresponding patient's details. In this section, we will elaborate on the subsystems and the block diagram of operation.

The overall system comprises of the following subsystems:

a. **Patient Module**
The patient module is a wearable device for the patients, comprising of (1) an active RFID card, which transmits a unique address for each patient; (2) a heartbeat (HB) sensor to read information of their vital signs and blood pressure levels; (3) an RF module, to transmit the readings to the data receiver unit; and (4) a microcontroller (Arduino), to acquire data from the HB-sensor via the ADC port and transmit using the RF module via the UART protocol. These patient modules act as end points in the proposed wireless sensor network (WSN). They are provided to each patient, who is then identified by their unique RFID addresses. The data is transmitted to the data receiver unit, which act as Routers to our gathered data, and route the collected data to the central system module clubbed with the unique RFID address of the patients.

b. **Data Receiver Unit**
The data receiver modules are systems that are installed in each room/corridor of a healthcare center. It comprises of (1) an RF Receiver, to receive data from the patient modules (end points); (2) an active RFID reader module, which continuously scans the area within 25 m range for presence of any patient, identified by their unique RFID address; (3) an Xbee S2 module, to resend the final data packets to the central system module, (4) an SD-Card module, which has the

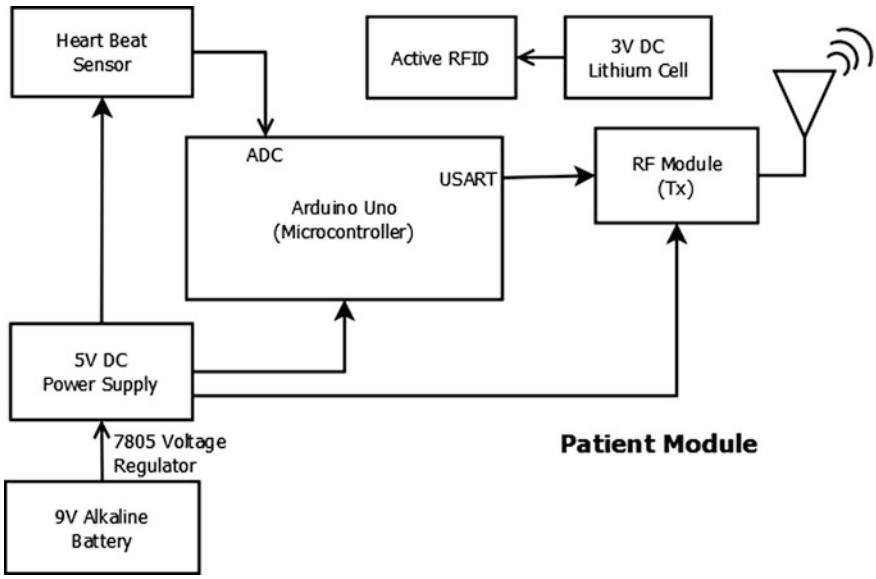


Fig. 1 Block diagram—patient module

information of each patient stored with their corresponding RFID address; and (5) microcontroller (Arduino) that acts as the interface for all the connected modules and runs the program for data receiving, patient identification and re-transmitting (Figs. 1, 2, 3, 4, 5 and 6).

c. **Central System Module**
The central system module is the center of the WSN. It is the central system, where all the data is received and tabulated in a local database on the PC. It is also responsible for uploading the acquired data on the internet to be made accessible to the doctors at all times. It comprises of (1) an Xbee S2 receiver module, i.e., the coordinator Xbee, placed in the form of star topology, which receives the data from all the data receivers in the healthcare center; (2) a Wi-Fi module that acts as the interface for uploading the data on the internet via the 802.11 b/g/n Wi-Fi protocol; and (3) microcontroller (Arduino), which acts as the interface for the PC, Xbee, Wi-Fi module and runs the code to identify the location of the transmitters in the network, and using this information, identifies the location of the patients in the healthcare center.

3.1 Hardware Development

The hardware development of the system can be divided for the comprising three subsystems—the patient module, the data receiver unit and the central system.

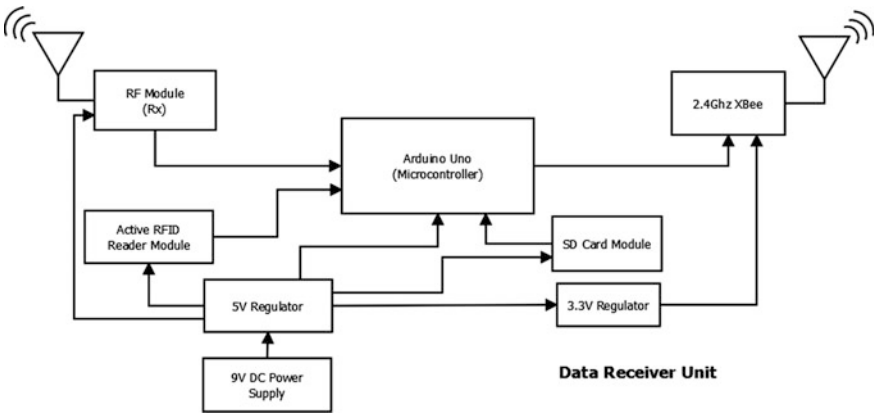


Fig. 2 Block diagram—data receiver unit

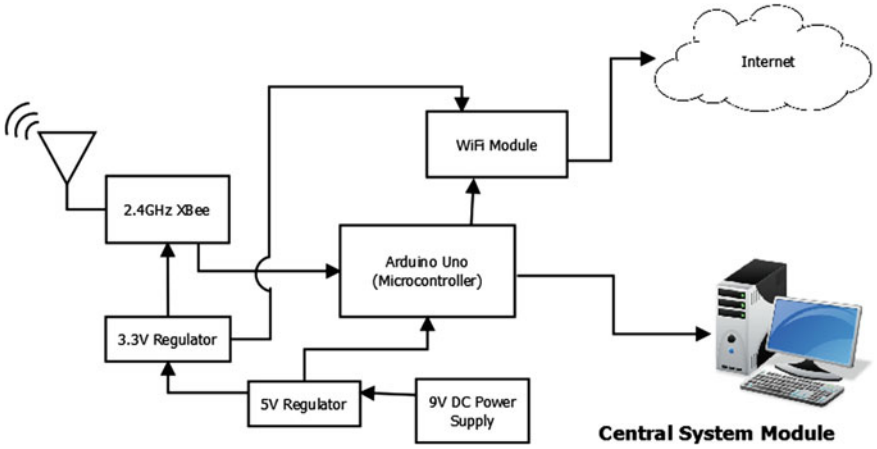


Fig. 3 Block diagram—central system module

Patient Module. The main components of the Patient module are:

- Active RFID Transmitter: Powered by a 3 V mounted battery and transmits a 16-bit unique code every 6 s on 433 MHz frequency in a range of 25 m.
- Pulse Sensor: It is a well-designed heart-rate sensor. Operates on +3 to +5 V, consumes 4 mA of current and provides analog output.
- Arduino Uno: It is the microcontroller board that is employed. It is based on ATmega328P, has 14 digital input/output pins (6 PWM outputs) and 6 analog inputs. A +5 V regulated DC current form a 9 V alkaline battery is used to power the components
- RF Serial Data Link UART, 2.4 GHz: It is a data modem operating in half duplex communication mode. It transmits serial data at baud rate 9600 bps.

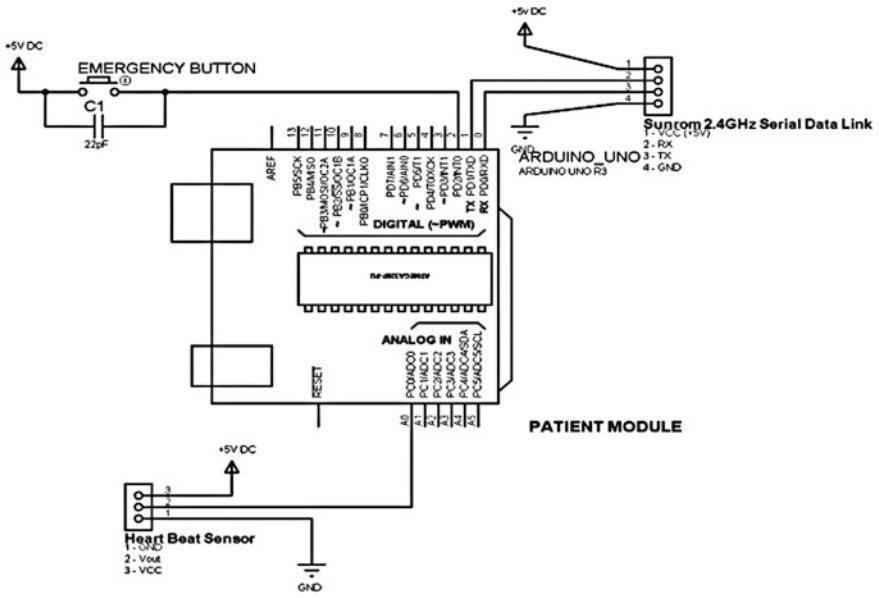


Fig. 4 Circuit diagram—patient module

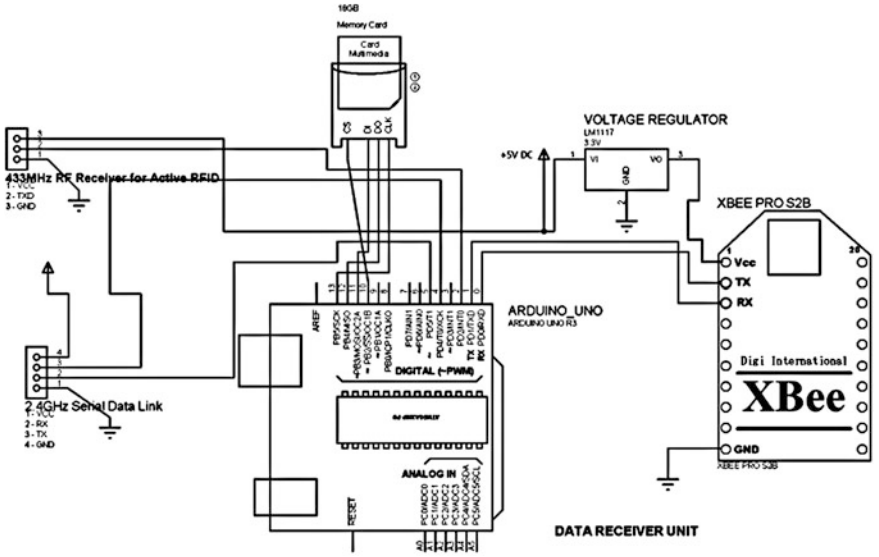


Fig. 5 Circuit diagram—data receiver unit

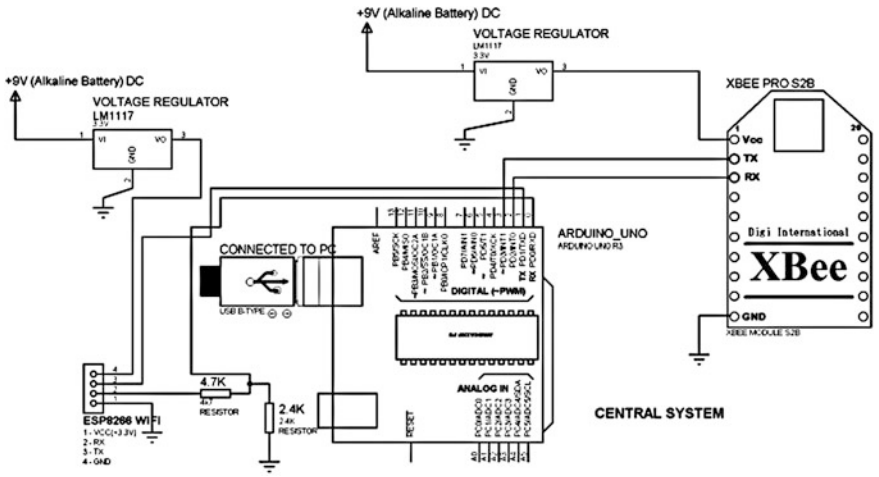


Fig. 6 Circuit diagram—central system

Data Receiver Unit. The main components of the data receiver unit are as follows:

- RF Receiver for Active RFID: It receives on 433 MHz frequency for active RFID and outputs the unique 16 bit ID in serial ASCII format at 9600 bps baud rate. RF Serial Data Link UART, 2.4 GHz: It receives serial data at baud rate 9600 bps.
- Micro SD Breakout Board: Used to store the details of the active RFIDs with corresponding allotted values (See Sect. 3.5 for details.)
- 2.4 GHz Xbee Pro S2B: These are used to re-transmit the data to the central system and allow a very reliable and simple communication. It operates on 3.3 V@ 295 mA, with 250 kbps Max data rate, 63 mW output (+17 dBm) and gives 1500 m indoor range.
- Arduino Uno: It is the microcontroller board that is employed. It receives data from the RF Serial Data Link and RF Receiver for active RFID, binds in a string and retransmits to the central system via the Xbee radio. A +5 V regulated DC current form a 9 V alkaline battery is used to power the components. A separate +9 V Alkaline battery is used to meet the power requirements (+3.3 V/63 mW) of the Xbee Pro S2B.

Central System Module. The main components of the central system module are as follows:

- 2.4 GHz Xbee Pro S2B: It is used as the receiver at the central system module.
- Arduino Uno: It is the microcontroller board that is employed. It runs the code for receiving data from the Xbee on various nodes (Xbee on the Data Receiver Unit), sending it to the PC and simultaneously uploading it on the internet database.

- ESP8266 ESP-12 Wi-Fi Module: It is a self-contained System-On-Chip (SOC) with integrated TCP/IP protocol stack that gives the microcontroller, access to a Wi-Fi network.
- Power Supply: The microcontroller is powered from the PC itself via the USB connection. The Xbee Pro S2B and ESP8266 Wi-Fi are powered with +3.3 V DC by regulating the voltage from a 9 V Alkaline Battery using an LM1117 IC.
- PC: PC or personal computer is the system which is used as an interface to gather the acquired data. The system uses a GUI built in MATLAB environment, which continuously displays the data for each patient, saves in a database (a comma-separated-value (CSV) file).

3.2 Algorithm and Software Development

The proposed algorithm for various subsystems is implemented in Arduino IDE software. In this section, the flow of operations using a methodical approach using a flowchart is explained.

3.3 Patient Module

The Arduino Uno on the patient module is concerned with the acquisition of data from the health sensors (pulse sensor) and transmitting to the data receiver unit. It makes use of the analog input pin for reading the data from the pulse sensor and transmits the data on the serial link set at a baud rate of 9600 bps using the 2.4 GHz RF Serial Data Link UART module, which can be regarded as the end node of the sensor network. The flowchart for the same is demonstrated in Fig. 7.

The patient module also consists of an active RFID Transmitter Tag which is an independent module i.e. it has not been interfaced with the Arduino and does not require programming. It transmits a unique 16-bit ID every 6 s, to the receiver at the Data Receiver Unit.

3.4 Data Receiver Module

The data receiver unit has multiple serial devices—RF receiver for active RFID, RF Serial Data Link 2.4 GHz and Xbee Pro S2B—connected to the Arduino Uno. Since, Arduino Uno has only one serial communication port (digital pins 0 and 1), it requires to make two extra serial ports using the 'SoftwareSerial' library. Second, a Micro SD card is used with the data receiver unit to store the addresses of all the

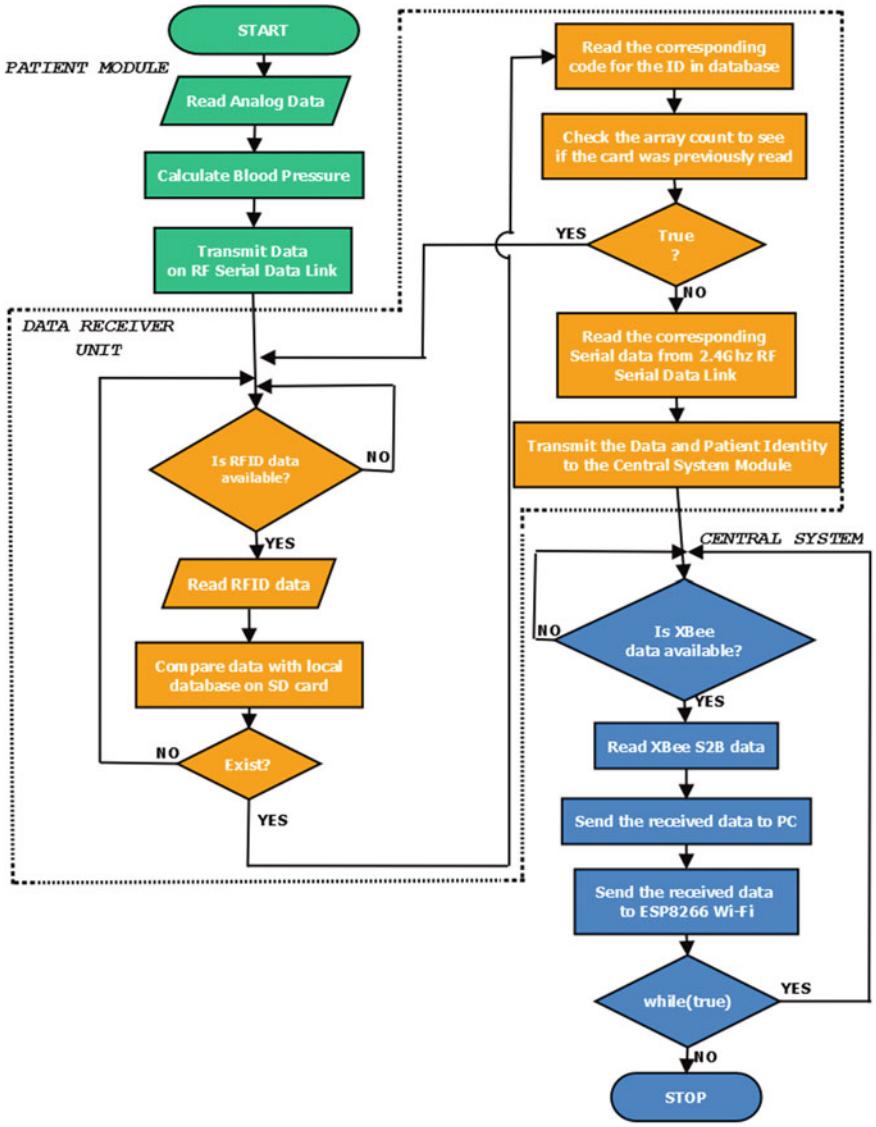


Fig. 7 Flowchart for the algorithm of overall system

Active RFID Transmitter Tag, and then used to identify the patients' identity, through the algorithm. The flowchart for the same is demonstrated in Fig. 7.

3.5 Central System Module

The Xbee Pro S2B at the central system acts as the Coordinator Xbee in the WSN and receives the data from all the Router Xbee Pro S2B placed in various wards/corridors/rooms in the healthcare center. It receives the data from all the Router Xbee and also identifies the source of origin of the data. The data along with the source information is wrapped as a string and sent to the PC. Simultaneously, it is also uploaded to the internet via ESP8266 Wi-Fi module in the optimized format. The flowchart for the algorithm for central system is demonstrated in Fig. 7.

3.6 Graphical User Interface (GUI) Development

A GUI developed in MATLAB is used as a Serial terminal. It makes use of push button option to open/close COM port and receive data. The string of data which is received contains the source of origin, patient's identity information and the pulse sensor reading. The GUI (developed in MATLAB) runs the algorithm which separates the relevant information from the received string, and displays it to the user in an optimized and precise format. Simultaneously, it also saves the received data in a CSV file on the local system.

4 Results and Discussions

The proposed system has been designed, evaluated and data acquired. It was realized on a small scale using two patient modules, two data receiver units and one central system module. In this paper, we have presented the findings based on the overall system performance, power consumption and error in the readings.

The data received from the pulse sensor was accurate, and provided substantial information about health from the obtained beats-per-minute (bpm) readings. The waveform of the readings is as shown in the Fig. 8d.

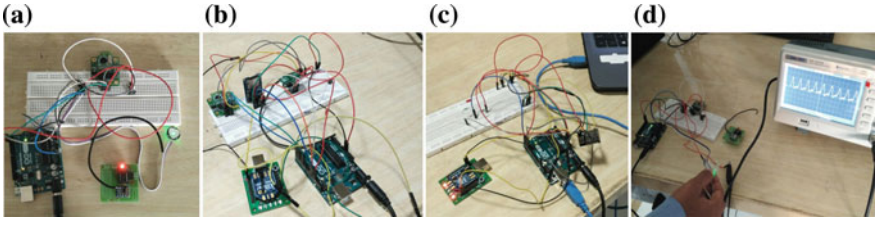


Fig. 8 Experimental Setup—**a** Patient module. **b** Data receiver unit. **c** Central system. **d** Data transmission testing and heat beat readings (each crest on waveform represents a heartbeat)

The active RFID cards transmit the associated ID every 6 s and each RFID was uniquely identified. Errors were identified to have occurred at the receiver, when more than 1 reading was obtained. So the problem was diagnosed by bypassing the extra reading in the algorithm on the data receiver unit. According to the datasheet, a total of 64 active RFID transmitter tags can exist together in same region, with each automatically occupying its own time slot without interfering with another. Thus, it limits the maximum number of patients that can be detected in a room to 64.

The 2.4 GHz Serial Data Link is used as transmitter and receiver at the end nodes of the sensor network, which perform well when a limited number of patients are present in the room. However, when dealing with large number of patients, it causes the problem of interference. Thus, readings are not obtained precisely. However, a solution to this problem has been identified to use 2.4 GHz Xbee Radio. It offers less interference compared to 2.4 GHz Serial Data Link, and can be ideally used for dealing with large number of patients. The disadvantage with using an Xbee radio is that, it highly increases the cost of the system.

The ESP8266 was used to connect to the internet via an open Wi-Fi network, which sends the readings to *thingspeak.com*, which is an online data platform for Internet of Things. The acquired readings are saved online without error. These readings can be accessed by any authorized personal (doctors) by logging into the online account using the correct credentials.

5 Conclusion and Future Work

The proposed system is intended to help the hospitals in better treatment of its patients and also to make it convenient for the doctor to check up his patients. The system can further be improved in many terms, some of which are stated as follows:

i. It is a simplified and cheap version of an advanced patient monitoring system. Using apt wireless technology, the system could be further developed to spread and work over several hospitals, i.e., in a wide range, using a free wireless network. Also, the system can be extendedly be used for home monitoring of the patients.
ii. More number of health issues can be investigated, as per requirement using adequate sensors. For example, muscle activity can be measured by its electric potential, referred to as electromyography (EMG), using a Muscle Sensor; the ECG sensor module AD8232 can be used to measure electrical activity of heart by attaching ECG electrodes to the patient's body etc.
iii. The GUI can be further upgraded to let the doctors have the ease to make specific appointments with a particular patient, set reminder for attending a patient, keep a proper database and remarks for every patient. Further, database encryption can also be implemented to restore the privacy rights of the patients.

References

1. Bonato, P., R. Hughes, D. Sherrill, R. Black-Schaffer, M. Akay, B. Knorr, and J. Stein. "Using wearable sensors to assess quality of movement after stroke." *Proceedings of the 65th Annual Assembly American Academy of Physical Medicine and Rehabilitation 2004* (2004).
2. Park, Sungmee, and Sundaresan Jayaraman. "Enhancing the quality of life through wearable technology." *Engineering in Medicine and Biology Magazine, IEEE* 22, no. 3 (2003): 41–48.
3. Jurik, Andrew D., and Alfred C. Weaver. "Remote medical monitoring." *Computer* 41, no. 4 (2008): 96–99.
4. Jovanov, Emil, Amanda O'Donnell Lords, Dejan Raskovic, Paul G. Cox, Reza Adhami, and Frank Andrasik. "Stress monitoring using a distributed wireless intelligent sensor system." *Engineering in Medicine and Biology Magazine, IEEE* 22, no. 3 (2003): 49–55.
5. Pantelopoulos, Alexandros, and Nikolaos G. Bourbakis. "A survey on wearable sensor-based systems for health monitoring and prognosis." *Systems, Man, and Cybernetics, Part C: Applications and Reviews, IEEE Transactions on* 40, no. 1 (2010): 1–12.
6. Shih, E., V. Bychkovsky, D. Curtis, and J. Guttag. "Demo abstract: Continuous, remote medical monitoring." In *Proc. Second Annual International Conference on Embedded Networked Sensor Systems*. 2004.
7. Martin, Thomas, Emil Jovanov, and Dejan Raskovic. "Issues in wearable computing for medical monitoring applications: a case study of a wearable ECG monitoring device." In *Wearable Computers, The Fourth International Symposium on*, pp. 43–49. IEEE, 2000.
8. Gao, Tia, Dan Greenspan, Matt Welsh, Radford R. Juang, and Alex Alm. "Vital signs monitoring and patient tracking over a wireless network." In *Engineering in Medicine and Biology Society, 2005. IEEE-EMBS 2005. 27th Annual International Conference of the*, pp. 102–105. IEEE, 2006.
9. Sazonov, Edward S., George Fulk, James Hill, Yves Schütz, and Raymond Browning." Monitoring of posture allocations and activities by a shoe-based wearable sensor." *Biomedical Engineering, IEEE Transactions on* 58, no. 4 (2011): 983–990.
10. Jovanov, Emil, Pedro Gelabert, Bryan Wheelock, Reza Adhami, and Paul Smith. "Real time portable heart monitoring using low power dsp." In *International Conference on Signal Processing Applications and Technology ICSPAT*, pp. 16–19. 2000.
11. Bonato, Paolo. "Advances in wearable technology and applications in physical medicine and rehabilitation." *Journal of NeuroEngineering and Rehabilitation* 2, no. 1 (2005): 2.
12. Van Laerhoven, Kristof, Benny PL Lo, Jason WP Ng, Surapa Thiemjarus, Rachel King, Simon Kwan, Hans-Werner Gellersen et al. "Medical healthcare monitoring with wearable and implantable sensors." In *Proc. of the 3rd International Workshop on Ubiquitous Computing for Healthcare Applications*. 2004.
13. Akyildiz, Ian F., Weilian Su, Yogesh Sankarasubramaniam, and Erdal Cayirci. "Wireless sensor networks: a survey." *Computer networks* 38, no. 4 (2002): 393–422.
14. Rusch, T.L., R. Sankar, and J.E. Scharf. "Signal processing methods for pulse oximetry." *Computers in biology and medicine* 26, no. 2 (1996): 143–159.
15. Raskovic, Dejan, Thomas Martin, and Emil Jovanov. "Medical monitoring applications for wearable computing." *The Computer Journal* 47, no. 4 (2004): 495–504.
16. Bauer, Peter, Mihail Sichitiu, Robert Istepanian, and Kamal Premaratne. "The mobile patient: wireless distributed sensor networks for patient monitoring and care." In *Information Technology Applications in Biomedicine, 2000. Proceedings. 2000 IEEE EMBS International Conference on*, pp. 17–21. IEEE, 2000.
17. Barro, S., J. Presedo, D. Castro, M. Fernandez-Delgado, S. Fraga, M. Lama, and J. Vila. "Intelligent telemonitoring of critical-care patients." *Engineering in Medicine and Biology Magazine, IEEE* 18, no. 4 (1999): 80–88.

18. Boonsawat, Vongsagon, Jurarat Ekchamanonta, Kulwadee Bumrungkhet, and Somsak Kittipiyakul. "XBee wireless sensor networks for temperature monitoring." In *the second conference on application research and development (ECTI-CARD 2010), Chon Buri, Thailand*. 2010.
19. Szewczyk, Robert, Alan Mainwaring, Joseph Polastre, John Anderson, and David Culler. "An analysis of a large scale habitat monitoring application." In *Proceedings of the 2nd international conference on Embedded networked sensor systems*, pp. 214–226. ACM, 2004.
20. Rashid, Rozeha, Sharifah Hafizah Syed Arifin, Mohd Rozaini Abd Rahim, Mohd Adib Sarijari, and Nur Hija Mahalin. "Home healthcare via wireless biomedical sensor network." In *RF and Microwave Conference, 2008. RFM 2008. IEEE International*, pp. 511–514. IEEE, 2008.
21. Nugroho, Eko, and Alvin Sahroni. "ZigBee and wifi network interface on Wireless Sensor Networks." In *Electrical Engineering and Informatics (MICEEI), 2014 Makassar International Conference on*, pp. 54–58. IEEE, 2014.
22. Ibrahim, Ahmad Shahran, Zairi Ismael Rizman, and Nur Hafizah Rabi'ah Husin. "Performance Analysis of Xbee-Based WSN in Various Indoor Environments." *J. Basic Appl. Sci. Res* 3, no. 11 (2013): 20–27.
23. Shnayder, Victor, Bor-rong Chen, Konrad Lorincz, Thaddeus RF Fulford Jones, and Matt Welsh. "Sensor networks for medical care." In *SenSys*, vol. 5, p. 314. 2005.
24. Kroc, S., and Vlado Delic. "Personal wireless sensor network for mobile health care monitoring." In *Telecommunications in Modern Satellite, Cable and Broadcasting Service, 2003. TELSIKS 2003. 6th International Conference on*, vol. 2, pp. 471–474. IEEE, 2003.
25. Jovanov, Emil, Amanda O. Donnel, Andy Morgan, Brent Priddy, and Rick Hormigo. "Prolonged telemetric monitoring of heart rate variability using wireless intelligent sensors and a mobile gateway." In *Engineering in Medicine and Biology, 2002. 24th Annual Conference and the Annual Fall Meeting of the Biomedical Engineering Society EMBS/BMES Conference, 2002. Proceedings of the Second Joint*, vol. 3, pp. 1875–1876. IEEE, 2002.
26. Gupta, R., J.N. Bera, and M. Mitra. "Development of an embedded system and MATLAB-based GUI for online acquisition and analysis of ECG signal."*Measurement* 43, no. 9 (2010): 1119–1126.
27. Schultz, Robert C., and Robert W. Ives. "Biometric data acquisition using MATLAB GUIs." In *Frontiers in Education, 2005. FIE'05. Proceedings 35th Annual Conference*, pp. S1G-1. IEEE, 2005.
28. Ling, Tonny Heng Yew, Lim Jin Wong, Jocelyn Ee Hung Tan, and Chong Kee Lee. "XBee Wireless Blood Pressure Monitoring System with Microsoft Visual Studio Computer Interfacing." In *Intelligent Systems, Modelling and Simulation (ISMS), 2015 6th International Conference on*, pp. 5–9. IEEE, 2015.
29. Jovanov, Emil, Dejan Raskovic, John Price, A. Krishnamurthy, J. Chapman, and A. Moore. "Patient monitoring using personal area networks of wireless intelligent sensors." *Biomedical Sciences Instrumentation* 37 (2001): 373–378.
30. Prakash, R., Siva V. Girish, and A. Balaji Ganesh. "Real-Time Remote Monitoring of Human Vital Signs Using IoT and GSM Connectivity." In *Proceedings of the International Conference on Soft Computing Systems*, pp. 47–56. Springer India, 2016.
31. Barnes, G. Edward, and Steve Warren. "A wearable, Bluetooth-enabled system for home health care." In *Engineering in Medicine and Biology, 2002. 24th Annual Conference and the Annual Fall Meeting of the Biomedical Engineering Society EMBS/BMES Conference, 2002. Proceedings of the Second Joint*, vol. 3, pp. 1879–1880. IEEE, 2002.
32. Bahl, Paramvir, and Venkata N. Padmanabhan. "RADAR: An in-building RF-based user location and tracking system." In *INFOCOM 2000. Nineteenth Annual Joint Conference of the IEEE Computer and Communications Societies. Proceedings. IEEE*, vol. 2, pp. 775–784. IEEE, 2000.
33. Ni, Lionel M., Yunhao Liu, Yiu Cho Lau, and Abhishek P. Patil. "LANDMARC: indoor location sensing using active RFID." *Wireless networks* 10, no. 6 (2004): 701–710.

34. Weinstein, Ron. "RFID: a technical overview and its application to the enterprise." *IT professional* 7, no. 3 (2005): 27–33.
35. Jin, Guang-yao, Xiao-yi Lu, and Myong-Soon Park. "An indoor localization mechanism using active RFID tag." In *Sensor Networks, Ubiquitous, and Trustworthy Computing, 2006. IEEE International Conference on*, vol. 1, 4 pp. IEEE, 2006.
36. Want, Roy, Andy Hopper, Veronica Falcao, and Jonathan Gibbons. "The active badge location system." *ACM Transactions on Information Systems (TOIS)* 10, no. 1 (1992): 91–102.
37. Jiang, Xuejing, Ye Liu, and Xiaolei Wang. "An enhanced approach of indoor location sensing using active RFID." In *Information Engineering, 2009. ICIE'09. WASE International Conference on*, vol. 1, pp. 169–172. IEEE, 2009.
38. Dobrilovic, Dalibor, Zeljko Stojanov, and Borislav Odadzic. "Teaching application development for RFID/ZigBee networks using open source hardware." In *Telecommunications (BIHTEL), 2014 X International Symposium on*, pp. 1–6. IEEE, 2014.

Maple Leaf Planar Fractal Antenna for Energy Harvesting Applications

Ila Verma, Pratima Singh, Hemant Kumar and Malay Ranjan Tripathy

Abstract The design mentioned in this paper represents a three-sided maple leaf planar fractal antenna. A prototype of the antenna has been designed on FR4-Epoxy substrate with dielectric constant 4.4 and thickness h = 1.6 mm with a microstrip feed of length L = 1.6 mm and slot width W = 2 mm. The simulation result of this antenna exhibits super wide band characteristics from frequency 5 to 32 GHz (S11) and has the VSWR < 2. The proposed antenna has the maximum gain of 8 at 23 GHz. This antenna can be used for energy harvesting. The E-plane and H-plane radiation patterns of the proposed antenna are nearly omnidirectional. The resistive part and reactive part which affects the impedance matching can be balanced by the slots and cuts. The antenna band exhibits the characteristics of three major bands used worldwide—X band (8–12 GHz), Ku band (12–18 GHz) and K Band (18–26 GHz). The ultra wide band (UWB) system, microwave imaging, precision position system, radar tracking system, TV transmission, satellite transmission and 5G communication systems are the common applications of this proposed maple leaf planar fractal antenna.

Keywords Fractal antenna · Maple leaf planar antenna · Super wide band · RF energy harvesting · X band · Ku band · K band

1 Introduction

Nowadays lots of efforts are being made to design antenna for RF energy harvesting application [1–5]. RF harvesting is becoming more demanding for energy-aware wireless sensor network applications to drive tiny circuits at far-off locations. Apart from this it is being used for power charging of wireless systems in satellites,

Ila Verma · Pratima Singh · Hemant Kumar · M.R. Tripathy (✉)
Amity University, Noida, Uttar Pradesh, India
e-mail: mrtripathy@amity.edu

Pratima Singh
e-mail: psparul3522@gmail.com

© Springer Science+Business Media Singapore 2017

R. Singh and S. Choudhury (eds.), *Proceeding of International Conference on Intelligent Communication, Control and Devices*, Advances in Intelligent Systems and Computing 479, DOI 10.1007/978-981-10-1708-7_107

mobile phones [6, 7] and other RF devices employed in an energy-constraint environment. Energy harvesting circuits is proposed by Mickle in US patent [1]. For wireless sensor network applications the details are described in the paper [2, 7]. Antenna with high efficiency is proposed to be used for energy harvesting at 2.45 GHz [8], Zhou et al. reported novel antenna techniques for RF energy harvesting [9]. Different types of fractal antennas are proposed in the literature [10–12] for RF energy harvesting. Rectenna is designed for K band RF harvesting and reported in the paper [13]. For satellite application antenna is reported for rectenna purpose [14]. Antenna is being designed for ISM band energy harvesting purpose [15]. However, a much detailed work on RF energy harvesting is not reported in the literature.

The motivation for this particular design was to obtain the super wide band antenna with significant return loss (<–10 dB) and VSWR (<1.02). The design mentioned in this paper represents a three-sided maple leaf planar fractal antenna. The super wide band characteristics are obtained from frequency 5 to 32 GHz (S11). The E-plane and H-plane radiation pattern of the proposed antenna are seen to be nearly omnidirectional. The maximum gain is obtained as 8 dB at 23 GHz.

The paper is organized as follows. Section 2 describes design parameters of the proposed antenna. The results and discussion is done in the Sect. 3. The conclusion is made in the Sect. 4.

2 Antenna Structure Design

The geometrical configuration of the microstrip feed maple leaf fractal antenna is described in Table 1. The substrate used for this antenna is FR4 with dielectric permittivity (ε_r) as 4.4. The three twigs of the leaf consist less than ¾ area. The dimension of the substrate is 116 × 140 × 1.6 mm^3. The designed antenna is shown in Fig. 1.

Table 1 Geometrical parameter of the maple leaf fractal antenna

SI. no.	Parameter	Dimensions (mm)
1	Ground plane	116 × 40
2	Substrate	116 × 40 × 1.6
3	L	65
4	W	65
5	H	30
6	A	5
7	B	15
8	C	20
9	D	5
10	E	30
11	F	2

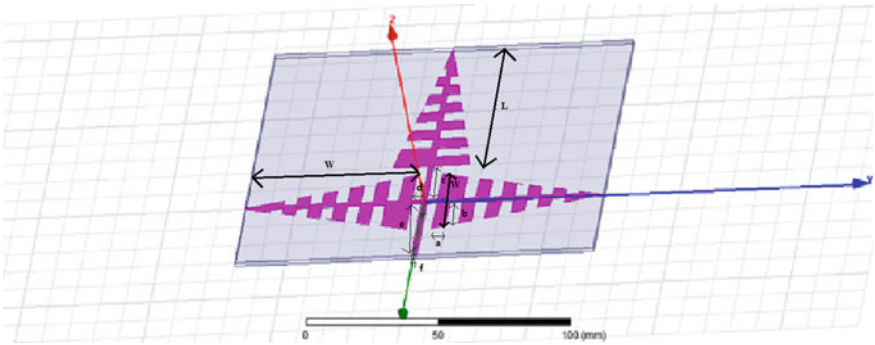


Fig. 1 Antenna specifications

3 Discussions and Results

The simulation of this antenna is carried out by using HFSS version 13. It has a super wide band response spanning from 5 to 32 GHz in S11 versus frequency graph as shown in Fig. 2. This band covers the complete frequency range of X, Ku and K band. The maximum return loss is –23.2 dB at 15.7 GHz. Details are mentioned in the Table 2.

Figure 3 shows the VSWR versus frequency plot. It shows the behavior of super wide band from 5 to 32 GHz with VSWR < 2. The lowest VSWR is seen at 15.7 GHz as 1.0967. Other values of VSWR are mentioned in the Table 2.

Table 2 describes return loss, VSWR, gain of the antenna at different frequencies. The lowest return loss and VSWR is seen at 15.7 GHz. The maximum gain of 8 dB is seen at 23 GHz.

For proposed multiband antenna Fig. 4a shows the simulated E-plane radiation pattern at 23 GHz. The pattern is directional for $\Phi = 0$ but the pattern is nearly omnidirectional at $\Phi = 90$. At 23 GHz Fig. 4b illustrates H-plane radiation pattern. The gain is less than the E-plane pattern with radiation pattern as omnidirectional at $\theta = 0$. Improved gain is achieved at the radiation pattern at $\theta = 90$ which is directional.

For the proposed multiband antenna in Fig. 5a, b, the simulated E- and H-plane radiation patterns at 15.7 GHz are shown respectively. The patterns for $\Phi = 0$ is seen to be nearly omnidirectional but, for $\Phi = 90$ it is seen to be directional. The gain in both the cases is lesser than the Fig. 4a, b. The radiation pattern in Fig. 5b is omnidirectional for $\theta = 0$ and for $\theta = 90$ is directional. But the relative gain is lesser in comparison to corresponding pattern at 23 GHz.

Figure 6 shows the graph of gain versus frequency. In this plot the maximum gain of 8 dB is observed at 23 GHz. In general the gain is good in the frequency range of 5–32 GHz. But this needs further improvements.

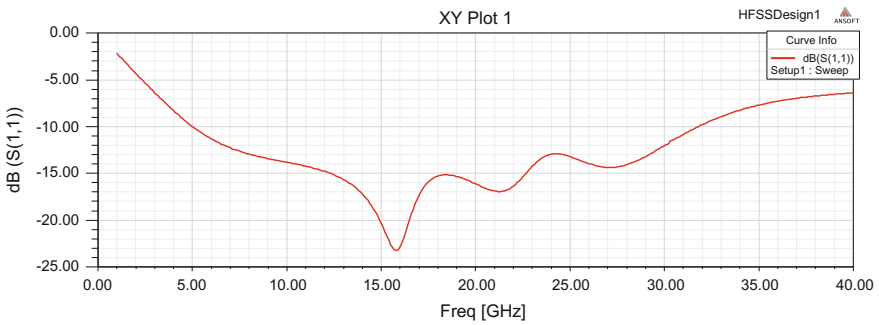


Fig. 2 Frequency versus return loss

Table 2 S11, VSWR and gain of maple leaf fractal antenna at different frequencies

SI. no	Frequency (GHz)	Return loss (dB)	VSWR	Gain (dB)
1	5	–10	1.9	–11.1
2	10	–13.8	1.463	–7.28
3	15	–19.89	1.21	–9.3
4	15.7	–23.2	1.0967	–6.85
5	20	–16.23	1.39	2.45
6	23	–14	1.48	8
7	25	–13.1	1.56	–3.99
8	32	–10.6	1.97	–1.5

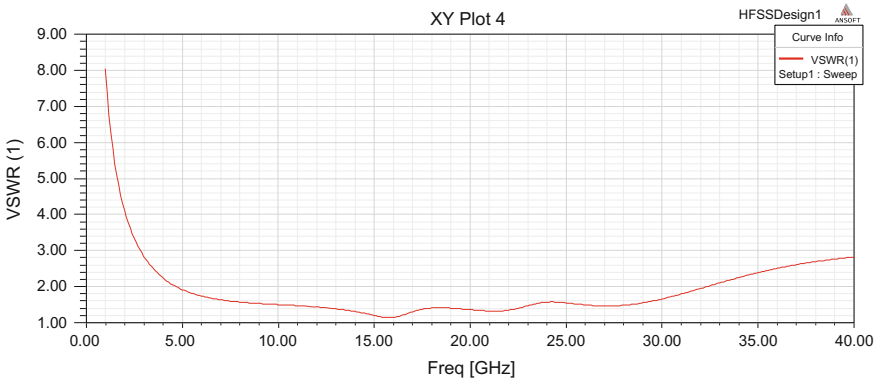


Fig. 3 Frequency versus VSWR

The surface current density distribution at 1 GHz on radiating patch is shown in Fig. 7. The current density is distributed throughout the radiating patch. The coupling between feedline and rest of the patch is very strong. However, the current

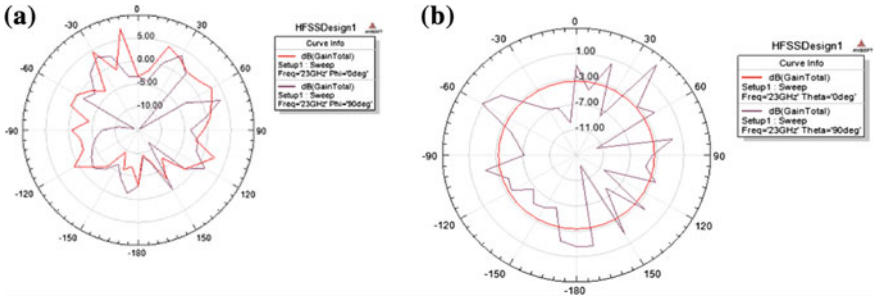


Fig. 4 **a** E-plane pattern at 23 GHz. **b** H-plane pattern at 23 GHz

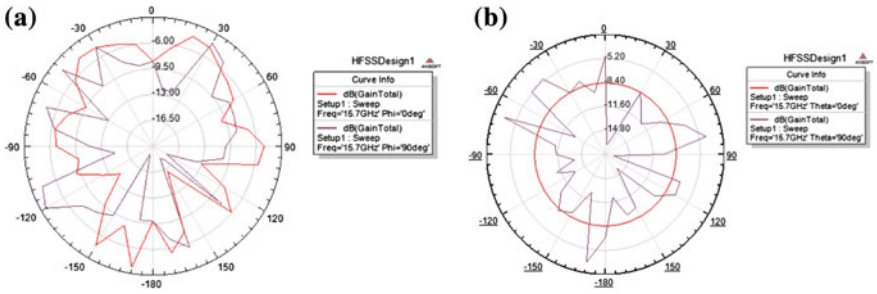


Fig. 5 **a** E-plane pattern at 15.7 GHz. **b** H-plane pattern at 15.7 GHz

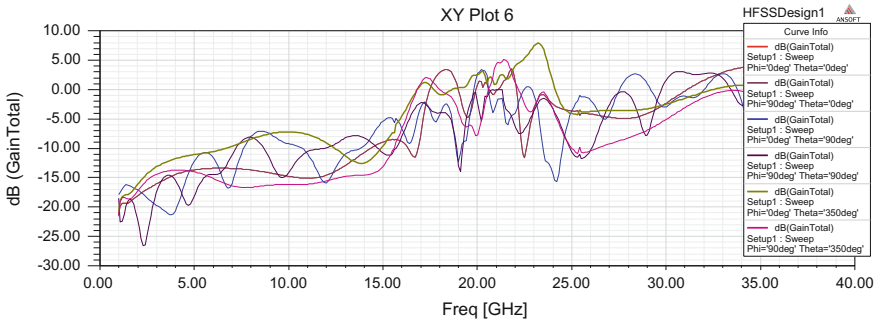


Fig. 6 Frequency versus gain

distribution is stronger at lower part of the split ring resonator region of the patch. By adjusting ground plane and design parameters of proposed simple, miniaturized multiband and compact antenna the gain and other parameters can be improved.

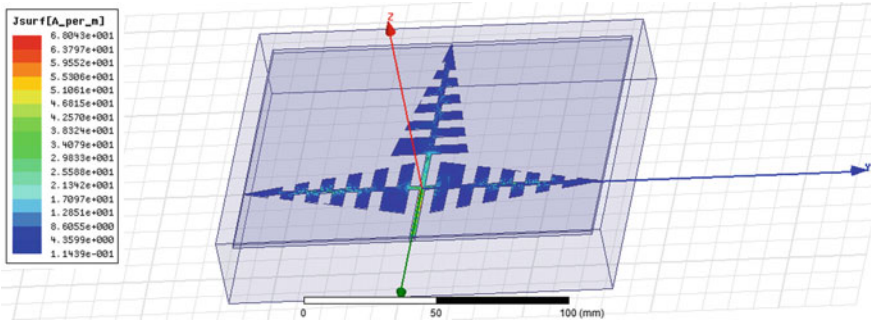


Fig. 7 Current surface density

4 Conclusions

The proposed antenna is a fractal antenna that provides the super band from 5 to 32 GHz. The antenna is able to achieve maximum gain of 8 dB at 23 GHz. It is suitable for applications of X, Ku and K bands. It supports energy harvesting applications. The various applications are wireless LAN, optic links, airborne weather and ground mapping radar, satellite downlink, broadband local wireless facilities and satellite uplink.

References

1. Mickle MH, Capelli CC, Swift H, inventors; University Of Pittsburgh-Of The Commonwealth System Of Higher Education, assignee. Energy harvesting circuits and associated methods. United States patent US 6,856,291. 2005 Feb 15.
2. Visser HJ, Vullers RJ. RF energy harvesting and transport for wireless sensor network applications: Principles and requirements. Proceedings of the IEEE. 2013 Jun;101(6): 1410–23.
3. Georgiadis A, Andia Vera G, Collado A. Rectenna design and optimization using reciprocity theory and harmonic balance analysis for electromagnetic (EM) energy harvesting. Antennas and Wireless Propagation Letters, IEEE. 2010;9:444–6.
4. Dolgov A, Zane R, Popovic Z. Power management system for online low power RF energy harvesting optimization. Circuits and Systems I: Regular Papers, IEEE Transactions on. 2010 Jul;57(7):1802–11.
5. Jabbar H, Song YS, Jeong TT. RF energy harvesting system and circuits for charging of mobile devices. Consumer Electronics, IEEE Transactions on. 2010 Feb;56(1):247–53.
6. Sim ZW, Shuttleworth R, Alexander MJ, Grieve BD. Compact patch antenna design for outdoor RF energy harvesting in wireless sensor networks. Progress In Electromagnetics Research. 2010;105:273–94.
7. Sun H, Guo YX, He M, Zhong Z. Design of a high-efficiency 2.45-GHz rectenna for low-input-power energy harvesting. Antennas and Wireless Propagation Letters, IEEE. 2012;11:929–32.

8. Zhou Z, Peng M, Zhao Z, Li Y. Joint power splitting and antenna selection in energy harvesting relay channels. Signal Processing Letters, IEEE. 2015 Jul;22(7):823–7.
9. Shrestha S, Lee SR, Choi DY. A new fractal-based miniaturized dual band patch antenna for RF energy harvesting. International Journal of Antennas and Propagation. 2014 Jan 29;2014.
10. Choi DY, Shrestha S, Park JJ, Noh SK. Design and performance of an efficient rectenna incorporating a fractal structure. International Journal of Communication Systems. 2014 Apr 1;27(4):661–79.
11. Taghadosi M, Albasha L, Qaddoumi N, Ali M. Miniaturised printed elliptical nested fractal multiband antenna for energy harvesting applications. Microwaves, Antennas & Propagation, IET. 2015 Apr 22;9(10):1045–53.
12. Takacs A, Aubert H, Luca A, Charlot S, Fredon S, Despoisse L. Rectenna design for K band application. InMicrowave Conference (EuMC), 2014 44th European 2014 Oct 6 (pp. 648–651). IEEE.
13. Takacs A, Aubert H, Despoisse L, Fredon S. Design and implementation of a rectenna for satellite application. In Wireless Power Transfer (WPT), 2013 IEEE 2013 May 15 (pp. 183–186). IEEE.
14. Zhang F, Liu X, Meng FY, Wu Q, Lee JC, Xu JF, Wang C, Kim NY. Design of a Compact Planar Rectenna for Wireless Power Transfer in the ISM Band. International Journal of Antennas and Propagation. 2014 Feb 20;2014.

Performance of Dual Metal-Double Gate Tunnel Field Effect Transistor with Different Dielectrics

Deepak Kumar and Prateek Jain

Abstract The performance of dual metal-double gate tunnel field effect transistor (DMG-DGTFET) with different dielectric gate materials is discussed. The dual metal gate technique (DMG) when applied to a DGTFET boosts the I_{ON} current and simultaneously decreases the OFF state current, which results in a substantial increase in the I_{ON}/I_{OFF} ratio. In DMG-DGTFET, gate consists of two different metals with different work function which can be used to modulate the width of tunneling barrier at the source to body junction. It is shown in this paper that by appropriately engineering the work function of the metals at the gate the good performance can be achieved for low-power design applications. All the simulations were done in 2-D TCAD. Nonlocal tunneling model is been used to calculate band-to-band tunneling (BTBT) tunneling current across the junction.

Keywords DMG (Dual metal gate) · SMG (Single metal gate) · DGTFET (Double gate tunnel field effect transistor) · BTBT (Band-to-band tunneling) · Drain induced barrier lowering (DIBL) · WKB (Wentzel–Kramers–Brillouin)

1 Introduction

Factors responsible for high leakage current during dimension reduction of MOSFET are short channel effects, such as DIBL. Thus the need arises for an alternative device other than MOSFET which consumes less power and can be operated at lower voltages [1, 2]. In this respect Tunnel FET (TFET) seems to be the most dominant for

Deepak Kumar (✉)
Department of Electronics and Instrumentation Control Engineering,
University of Petroleum and Energy Studies, Dehradun 248007, India
e-mail: deepakkumar18207@gmail.com

Prateek Jain
Department of Electrical Engineering,
Indian Institute of Technology Kanpur, Kanpur 208016, India
e-mail: prateekjain1587@gmail.com

© Springer Science+Business Media Singapore 2017

R. Singh and S. Choudhury (eds.), *Proceeding of International Conference on Intelligent Communication, Control and Devices*, Advances in Intelligent Systems and Computing 479, DOI 10.1007/978-981-10-1708-7_108

low-power applications devices. Tunnel Field Effect Transistor (TFET), because of its low subthreshold swing and excellent reduction in leakage current [3, 4] is gaining attention in the VLSI industry. TFET can be operated at much lower voltage than the conventional MOSFET and consume less power than conventional MOSFET, but the mechanisms in which both operate are quite different. In TFET it is the band-to-band tunneling (BTBT) carrier injection to the channel, which is responsible for the current while in MOSFET its normal drift diffusion. The biggest drawback of TFET is its low ON state current (I_{ON}). To employ TFET for lower power application it is essential to improve the I_{ON} current [5].

The I_{ON} can be increased significantly by using a narrow band gap material (e.g., Ge, SiGe) at the source side. In the other way to improve the ON state current (I_{ON}), we can employ double gate technique [6]. Dielectric plays a very crucial role in Tunnel FET optimization. Using high dielectric constant materials such as hafnium oxide (HfO_2) silicon nitride (Si_3N_4) *and* silicon dioxide (SiO_2) having dielectric constant of 25, 7.5 and 3.9 respectively at the gate to improve the coupling between gate and tunneling junction which results in high I_{ON} current. DMG-DGTFET [7, 8] uses metals with different ϕ_M (work function) at the gate to control the different sections of transfer characteristics.

This paper includes the DMG-DGTFET device structure based on silicon nitride (Si_3N_4) as gate dielectric material is simulated and compared with SMG-DGTFET. DMG technique [7, 8] is then applied to DGTFET based on different dielectric, since the dielectric constant of silicon nitride is more compared with silicon dioxide, better coupling between the gate and tunneling junction which results in a good improvement in the ON state current. The simulations were done in 2-D TCAD with nonlocal tunneling model [9].

2 Schematic of DMG-DGTFETs

The schematic of DMG-DGTFETs is shown in Fig. 1. The gate consists of two metals with different ϕ_M. The auxiliary gate is near to the drain end, and tunnel gate is near to the source, t_{si} is the body thickness of silicon material, t_{ox} is the thickness of gate oxide, $L_{aux.}$ is the auxiliary gate length and $L_{tun.}$ is the tunnel gate length.

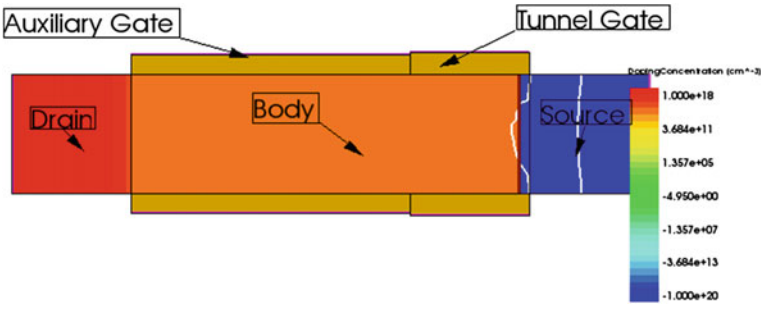


Fig. 1 Schematic view of DMG-DGTFET based on silicon nitride gate dielectric

Table 1 Showing simulated device parameters

Chanel length	Source doping (p+)	Drain doping (n+)	Body region doping	$L_{aux.}$	$L_{tun.}$	t_{si}	Gate oxide (t_{ox})
20 nm	Boron 1×10^{20} cm^{-3}	Arsenic by 1×10^{18} cm^{-3}	Arsenic by 1×10^{16} cm^{-3}	14 nm	6 nm	8 nm	1 nm

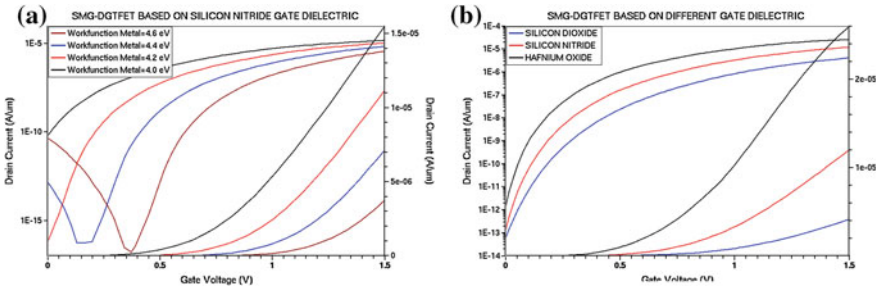


Fig. 2 Transfer characteristics of SMG-DGTFET both on semilog and linear scale. **a** Silicon nitride gate dielectric for different ϕ_M. **b** With different dielectric calculated at ($V_{DS} = 1.0$ V and $\phi_M = 4.2$ eV)

The fabrication process of DMG-DGTFET is already reported in the literature [7, 10]. The doping profile is uniform in the region. All the device structures are simulated in TCAD for following device parameters shown in Table 1.

3 SMG-DGTFET's

This section includes the simulated results of SMG-DGTFET based on different dielectric were discussed. The ϕ_M of the metal at the gate plays a very crucial role in SMG-DGTFET, by changing the ϕ_M of the metal the transfer characteristics changes significantly as shown in Fig. 2a for silicon nitride dielectric. The best possible value of ϕ_M is selected, which ensures high I_{ON}/I_{OFF} ratio. It can be seen from the simulation result that by the use of high-k dielectric material, the ON state current can be increased significantly. Figure 2b shows the transfer characteristics for different dielectric.

4 DMG-DGTFET's

To investigate the effect of $\phi_{aux.}$ (*auxiliary work function*) on the transfer characteristics $\phi_{tun.}$ (*tunnel work function*) is kept constant at 4.0 eV, and $\phi_{aux.}$ is varied from 4.0 to 4.6 eV at OFF and ON state. It is evident from the result as shown in Fig. 3c that as $\phi_{aux.}$ is varied at OFF state, the tunneling width at the source side

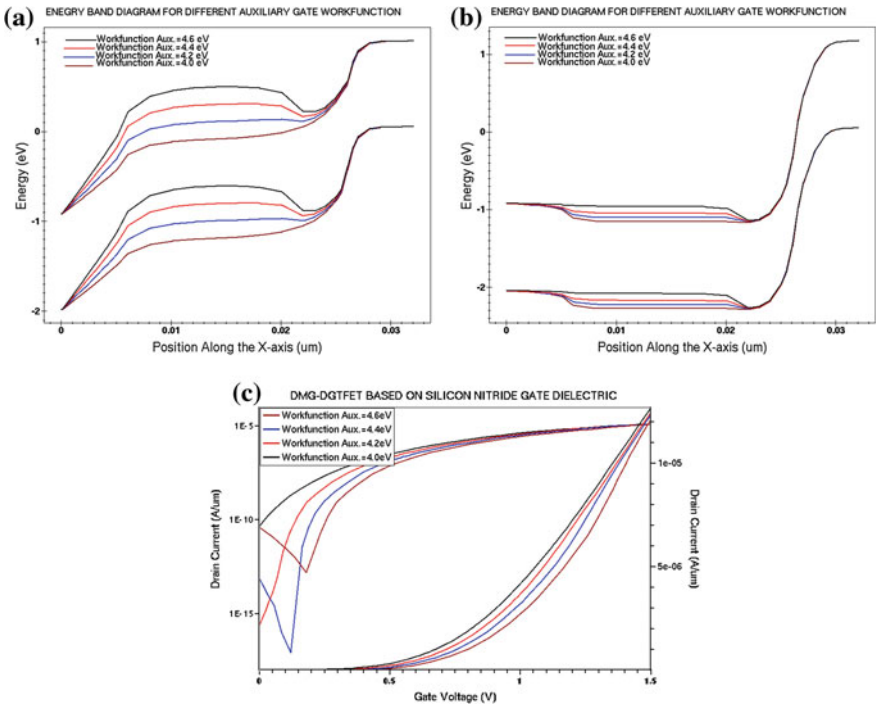


Fig. 3 DMG-DGTFET based on silicon nitride, its energy band diagram along the device length near the surface at, **a** OFF state ($V_{gs} = 0$ V and $V_{DS} = 1.0$ V), and **b** ON state ($V_{gs} = 1.5$ V and $V_{DS} = 1.0$ V) state, **c** transfer characteristics ($\phi_{tun.} = 4.0$ eV)

increases as shown in Fig. 3a which results in the decrease of the OFF state current. When $\phi_{aux.}$ increases beyond 4.4 eV the increase in the OFF state current can be seen. At ON state the effect of $\phi_{aux.}$ on tunnel barrier width is not significant as shown in Fig. 3b as a result the ON state current does not change by much.

Next the same analysis is carried out for $\phi_{tun.}$. To analyze the effect of $\phi_{tun.}$ on the transfer characteristics, $\phi_{tun.}$ is varied from 4.0 to 4.6 eV at OFF and ON states, while keeping $\phi_{aux.}$ constant at 4.4 eV. As $\phi_{tun.}$ is varied from 4.0 to 4.6 eV at OFF state, there is no energy band overlapping on the source side as a result the OFF state current does not change much, Fig. 4a. At ON state band starts to overlap which results in the increase in the tunnel barrier width, Fig. 4b. The BTBT current decreases because of increase in tunneling barrier width, as shown in Fig. 4c along with energy band diagram. Thus it can be concluded from the analysis that the best possible value of $\phi_{tun.}$ to have higher I_{ON}/I_{OFF} ratio is 4.0 eV. When the DMG technique is applied to DGTFET based on silicon nitride dielectric results in high I_{ON} and low I_{OFF}, where SMG-DGTFET fails to perform.

For SMG-DGTFET based on silicon nitride dielectric with best optimized value of $\phi_M = 4.2$ eV, the best optimized value of I_{ON}/I_{OFF} (about 1×10^{11}) is achieved. For DMG-DGTFET the ratio I_{ON}/I_{OFF} is in the range of 1.2×10^{12}

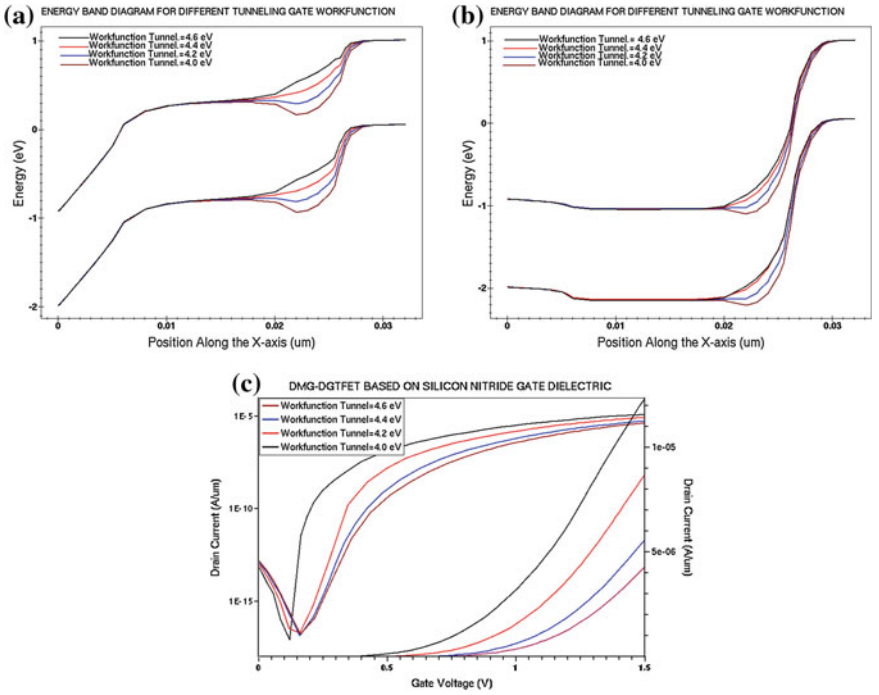


Fig. 4 DMG-DGTFET based on silicon nitride dielectric, its energy band diagram along device length near to the surface in, **a** OFF state $(V_{gs} = 0\ \text{V}, \quad V_{DS} = 1.0\ \text{V})$, and **b** ON $(V_{gs} = 1.5\ \text{V}, V_{DS} = 1.0\ \text{V})$ state, **c** transfer characteristics $(\phi_{aux.} = 4.0\ \text{eV})$

based on silicon nitride. This significant improvement in DMG-DGTFET is mainly due to the average subthreshold slope SSAVG improvement. The average subthreshold slop is calculated as the inverse of slope between threshold voltage (V_T) and V_{OFF}.The SS_{AVG} improves from 60 mV/decade in an SMG-DGTFET to 48 mV/decade in the DMG-DGTFET based on silicon nitride dielectric. Thing to be noticed here is that, by changing ϕ_M of the metal in SMG-DGTFET changes the transfer characteristics. SSAVG does not improve much as the transfer characteristics curve just shift parallel to the *X*-axis.

5 DMG-DGTFET with Different Dielectrics

In this section, the application of DMG technique to DGTFET based on different gate dielectric is carried out. The same analysis for Auxiliary and Tunnel gate is carried out for DMG-DGTFET based on different materials for gate dielectric, as it is done for DMG-DGTFET based on silicon nitride, and the results that were

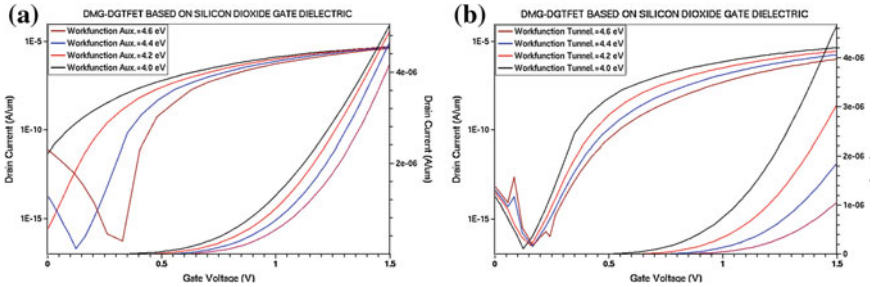


Fig. 5 DMG-DGTFET based on silicon dioxide dielectric its transfer characteristics. **a** For different $\phi_{aux.}$ while $\phi_{tun.} = 4.0$ eV. **b** For different $\phi_{tun.}$ while $\phi_{aux.} = 4.0$ eV

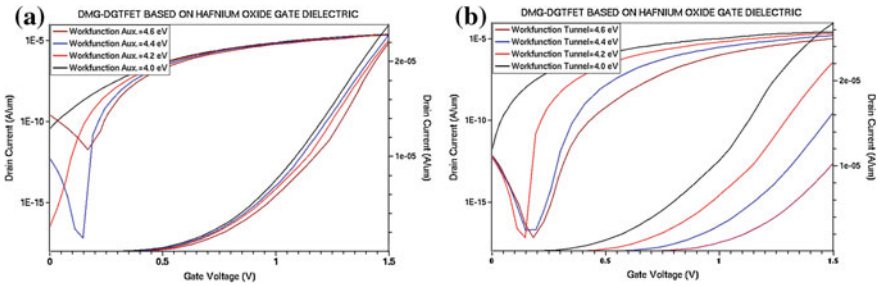


Fig. 6 DMG-DGTFET based on hafnium oxide dielectric its transfer characteristics. **a** For different $\phi_{aux.}$ while $\phi_{tun.} = 4.2$ eV. **b** For different $\phi_{tun.}$ while $\phi_{aux.} = 4.4$ eV

Table 2 Showing behavior of device with different dielectrics

Technique	Dielectric	I_{OFF}	I_{ON} A/μm	SS_{AVG} mV/decade
DMG-DGTFET	Silicon nitride	1×10^{-17}A/μm	1.23×10^{-5}	48
DMG-DGTFET	Hafnium oxide	1.8×10^{-17}A	2.23×10^{-5}	41
DMG-DGTFET	Silicon dioxide	2×10^{-17} A/μm	4.8×10^{-6}	70

obtained were shown in Figs. 5 and 6. Thus we can infer that by appropriately selecting the metal ϕ_M at the two gates it is possible to control the tunneling current.

The different metals for desired $\phi_{aux.}$ (4.4 eV) are Ta, W, and Mo and $\phi_{tun.}$ (4.0 eV) are Mo, Ni-Ti, and Sc can be used in this discussed technique [11, 12]. Different gate dielectrics with $\phi_M = 4.2$ eV the devices are simulated to obtain the better subthreshold slope shown in Table 2.

6 Conclusion

The application of DMG technique when applied to double gate TFET based on different dielectric gate material boosts the ON state current and decreases the OFF state current simultaneously and also improves the average subthreshold slope which cannot be achieved by SMG-DGTFET. Fabrication difficulties were there with DMG-DGTFET, also using a high-k dielectric material at the gate also leads to the degradation in the carriers' mobility near the interfaces. The use of high-k dielectric material at the gate in SMG-DGTFET ON and OFF current simultaneously increases.

References

1. C. Hu, et al., "Prospect of tunneling green transistor for 0.1 V CMOS." IEDM Tech. Dig., pp. 387–390, 2010.
2. Q. Zhang, W. Zhao, and A. Seabaugh, "Low-subthreshold-swing tunnel transistors," *IEEE Electron Device Lett.*, vol. 27, no. 4, pp. 297–300, Apr. 2006.
3. M. Luisier, G Klimeck, "Performances comparisons of tunneling field effect transistors made of InSb, Carbon and GaSb-InAs broken gap heterostructures," IEDM Tech. Dig., pp. 913–916, 2009.
4. Semiconductor Industry Association (SIA), International Technology Roadmap for Semiconductors, 2009 Edition.
5. P.-F. Wang, K. Hilsenbeck, T. Nirschl, M. Oswald, C. Stepper, M. Weis, D. Schmitt-Landsiedel, and W. Hansch, "Complementary tunneling transistor for low power application," *Solid StateElectron.,* vol. 48, no. 12, pp. 2281–2286, Dec. 2004.
6. K. Boucart and A. M. Ionescu, "Double-gate tunnel FET with high-κ gate dielectric," *IEEE Trans. Electron Devices*, vol. 54, no. 7, pp. 1725–1733, Jul. 2007.
7. W. Long, H. Ou, J. M. Kuo, and K. K. Chin, "Dual-material gate (DMG) FET," *IEEE Trans. Electron Devices*, vol. 46, no. 5, pp. 865–870, May 1999.
8. A. Chaudhary and M. J. Kumar, "Investigation of the novel attributes of a fully depleted dual-material gate SOI MOSFET," *IEEE Trans. Electron Devices*, vol. 51, no. 9, pp. 1463–1467, Sep. 2004.
9. Synopsys, TCAD Sentaurus device, ver. D2010-03, 2010.
10. W. Long, H. Ou, J. M. Kuo, and K. K. Chin, "Dual-material gate (DMG) TFET," *IEEE Trans. Electron Devices*, vol. 46, no. 5, pp. 865–870, May 1999.
11. K. Y. Na and Y. S. Kim, "Silicon CMOS with dual work function gate," *Jpn. J. Appl. Phys.*, vol. 45, no. 12, pp. 9033–9036, Dec. 2006.
12. P. Ranade, Y. C. Yeo, Q. Lu, H. Takeuchi, T. J. King, and C. Hu, "Molybdenum as a gate electrode for deep sub-micron CMOS technology," in *Proc. MRS Symp.*, 2000, vol. 611, pp. C3.2.1–C3.2.6.
13. M. Hasan, H. Park, H. Yang, H. Hwang, H. S. Jung, and J. H. Lee, "Ultralow work function of scandium metal gate with tantalum nitride interface layer for n-channel metal oxide semiconductor application," *Appl. Phys. Lett.*, vol. 90, no. 10, pp. 103 510-1–103 510-3, Mar. 2007.

An In-Memory-Based Big Data Analytics with Two-Level Storage on Private Cloud

Nikkita Shekhar and Ambika Pawar

Abstract With growing capacity of main memory, in-memory big data management and processing is developing and being used in many big data applications. It supports interactive data analysis by improving I/O throughput. Memory-centric distributed file systems such as tachyon and in-memory data clustering framework like Apache Spark are being used in analytical problems where both speed and fault tolerance are mandatory. In order to achieve high-speed big data processing, we proposed a system design which involves two-tier storage architecture which is the combination of HDFS and in-memory-based file system tachyon. Also, our architecture involves Apache Spark, an open-source in-memory-based data processing tool to analyse the big data. In this framework we would utilise the main memory by integrating caching algorithm to improve the data processing time. As the experimental result, we would demonstrate the comparison between performance of traditional Hadoop MapReduce and this in-memory-based framework. In this paper, we survey the existing storage and computation infrastructures, their performance while integrating together and contribution of such infrastructures in solving many I/O intensive analytical issues.

Keywords Big data · Analytics · In-memory · Spark · Hadoop · Parallel computing · Distributed system · I/O throughput · Computation speed

1 Introduction

In this digital era, society is becoming more instrumented and as a result of that, a large amount of data is getting generated each and every second. Today, the main sources of data are electronic devices, social network, business data, sensors, stock

Nikkita Shekhar (✉) · Ambika Pawar
Department of Computer Science, SIT, Symbiosis International University, Pune, India
e-mail: nikkita.shekhar@sitpune.edu.in

Ambika Pawar
e-mail: ambikap@sitpune.edu.in

© Springer Science+Business Media Singapore 2017

R. Singh and S. Choudhury (eds.), *Proceeding of International Conference on Intelligent Communication, Control and Devices*, Advances in Intelligent Systems and Computing 479, DOI 10.1007/978-981-10-1708-7_109

markets, etc. This large volume of data does not make any sense until it gets analysed and give some informative output. With this explosion of big data, the requirements of efficient solution to deal with the aspects like data storage, real-time processing and information reorganisation have become mandatory. Big data analytics is the field of research to uncover hidden pattern and information from a large volume of random data in structure, unstructured or semi-structure format. This is usually accomplished through implementation of large data storage and high-performance computation engine with suitable iterative algorithm. To perform any analysis on such huge amount of complex data, a suitable hardware and software platform is required. Two things are need to be considered while choosing the right resources: (i) How big is the data to be processed? and (ii) How quickly the data need to be processed?

In private Cloud where storage and computation are done at separate machine, to perform analysis on big data, following points are need to be kept in mind: system scalability, CPU and computing, data volume and storage and network bandwidth. This system should be elastic to scale up and scale out as per the requirement. It should be capable to handle huge data in storage and computation engine should be strong enough to compute the data processing in time. Although there are many successful traditional tools and technology available to perform the same [1], with the growth in volume and velocity of data generation, a faster and reliable system is required. With growing capacity of main memory, in-memory big data management and processing is developing and being used in many big data applications. It supports interactive data analysis by improving I/O throughput [2].

In analytical system, RAM can be used as data storage as well as temporary location for intermediate result of data computation process. Using RAM as middleware removes I/O overhead between the machines. This improves the speed of analysis as the time taken by the I/O requests has been removed. Also, for an iterative algorithm, keeping the intermediate result in main memory enhances the overall performance of analytical engine.

In memory, feature can be implemented in an analytical project as IMDB (in-memory database) and in-memory-based analytical engine. Memory-centric distributed file systems such as tachyon and in-memory data clustering framework like Apache Spark are being used in analytical problems where both speed and fault tolerance are mandatory. In this paper, we are proposing a system design for big data analytics problem utilising in-memory features as storage as well as in analytical engine in order to improve the data computation speed. In Sect. 2, we have given literature review of the related components. In Sect. 3, proposed idea and system design is discussed, and Sect. 4 gives a brief detail about experimental setup and preliminary results.

2 Literature Review

In this section, we will give brief introduction about our system component and literature survey about them. First, we will discuss about Hadoop and its limitation in big data analytics, importance of in-memory technology and existing works on them.

2.1 Apache Hadoop

Apache Hadoop is an open-source framework for storing and processing big data sets using clusters. Hadoop platform contains two major components: 1. Distributed file system, and 2. Hadoop YARN that manages the job schedules across cluster. MapReduce is a programming model in Hadoop that breaks the task into small parts and process them in parallel. One major drawback of Hadoop MapReduce is its inefficiency in running iterative processes [3]. After each iteration, data is read/write to disc which increases i/o overhead and degrades the performance [4].

2.2 Apache Spark

Apache spark is a next-generation in-memory-based paradigm developed by researchers at university of California at Berkeley. It is developed to overcome the i/o limitation and an alternative for Hadoop MapReduce. Spark allows the data to be cached in memory and thus removes disc overhead and increases the processing speed by 100× [5]. Also, it generates RDD and DAG graph to keep track of job scheduling [3].

2.3 Tachyon

For distributed storage, the read throughput can be improved using caching; however, the write throughput is limited by both disc and network bandwidth due to data replication for fault tolerance. Tachyon is a memory-centric, fault tolerant distributed file system which enables reliable data exchange at in-memory speed across cluster frameworks [6]. Tachyon uses a master–slave architecture similar to other cluster file systems, where each worker manages local blocks and shares them with applications through a RAMFS. Files in Tachyon are organised in a tree hierarchy and identified by their paths. Hence, it provides fault tolerance in case of system failure [7].

2.4 Survey

Various research approaches are proposed by scholars and researchers for in-memory utilisation in big data analytics.

In Xuan et al. [7], on a HPC cluster, two-level storages with parallel file system OrangeFS and in-memory file system Tachyon are integrated together to enhance the I/O throughput and fault tolerance for a scalable system. They characterise the I/O behaviour of proposed system and compare the performance with HDFS and OrangeFS using TeraSort benchmark.

Jorge et al. [8] utilised the memory to speed up the computation by integrating Spark on Hadoop. They implemented iterative algorithm like KNN and Pegasus SVM on Spark framework and compare its performance with MPI. As a result, they conclude that Spark give speed but MPI is more reliable for fault tolerance.

Yan et al. [9] researcher suggested a domain-specific seismic analytical Cloud as a service. They used Spark and YARN to create a cloud platform for the processing of seismic dataset which is very complex to deal with. SAC, seismic analytical cloud, as a service provides simple and better platform to work on seismic data.

Khan et al. [3] demonstrated the effectiveness of the analytics service for future smart city implementation. They identify correlation between different environmental indicators of city datasets using Hadoop and Spark. They compare the result on the basis of computation speed between Hadoop MapReduce and Apache Spark.

Recently, during our research, we found Baidu, a search engine in china, and also used Tachyon and collaborated with research team of TachyonFS [10]. They have achieved 30× to 60× speedups. They are also working on some limitations like block size issue, memory swapping, etc.

3 Proposed Idea

In order to achieve high-speed big data processing, this framework would involve two-tier storage architecture which is the combination of HDFS and in-memory-based file system Tachyon as shown in Fig. 1. Also, our design involves Apache Spark, an open-source in-memory-based data processing tool to analyse the big data. In this framework we would utilise the main memory by integrating caching algorithm to improve the read/write request miss and hit ratio [7]. As the experimental result, we would demonstrate the comparison between performance of traditional Hadoop MapReduce and proposed in-memory-based framework. Our system design involves integrating main memory features integration with tradition

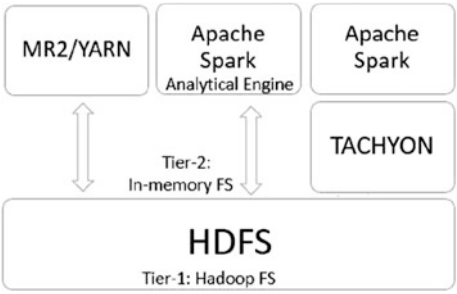


Fig. 1 System design of two-level storage framework

data processing techniques. Such framework would contribute in solving many I/O intensive analytical issues.

4 Proposed Architecture

In the proposed architecture, we describe our framework for two-level storage system in which we have integrated an in-memory file system like Tachyon at name node on the top of traditional distributed file system HDFS at data node of the distributed cluster. Also, we have combined in-memory-based computation engine which is supposed to enhance the aggregate I/O throughput efficiently for an iterative algorithm (Fig. 2).

We implemented a prototype of two-level storage system by integrating tachyon-7.1.0 with HDFS-2.6.1 on Apache Spark-1.5.0. Here HDFS works as disc

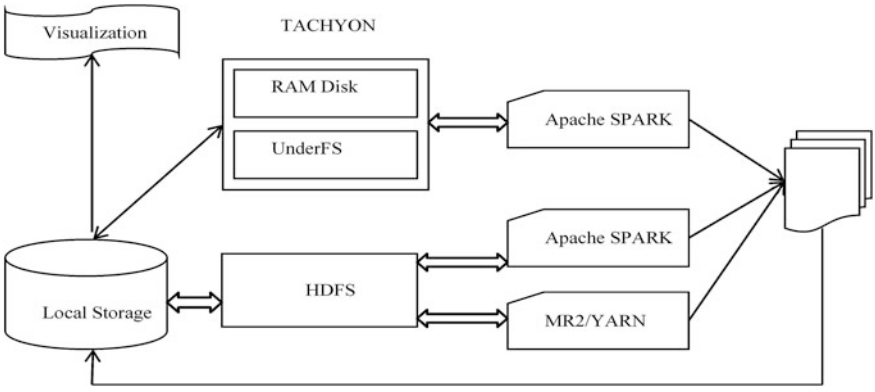


Fig. 2 System architecture of proposed framework

storage where data is stored in distributed manner, and Tachyon acts like cache memory between disc and analytical engine Spark. In this architecture, a set of fix-sized logical blocks are considered for input file in Tachyon. It controls parallel granularity and also RDDs generated by analytical engine Spark are managed here. In order to enhance the I/O throughput and speed up the computation, Spark and Tachyon work together at compute node while input files are distributed over Hadoop file system in cluster. Tachyon manages the cached file from HDFS as well as the intermediate output result from spark. In our system, we have removed the read/write overhead of reading data from remote data nodes, especially when the nodes are overloaded with request, by applying priority policy. A cache I/O buffer is applied between Spark and Tachyon to set the priority of data that are being stored in Tachyon from different sources, i.e., Spark RDD [4] and input file from disc.

5 Experimental Evaluation and Preliminary Result

In this section, we are evaluating prototype for our two-level storage-based analytical setup and further we are comparing it with the traditional Hadoop MapReduce. For this, two experimental setups are established: First, traditional Hadoop MapReduce, and another is a two-layer storage architecture with Tachyon over HDFS. In private cloud where resources are limited [11], we have used the following configuration as shown in Table 1. We have setup a five-node Hadoop cluster, each with 2 GB RAM and 1 TB storage. As Apache Spark and Tachyon are memory sensitive, 8 GB of memory is allocated for both at master node.

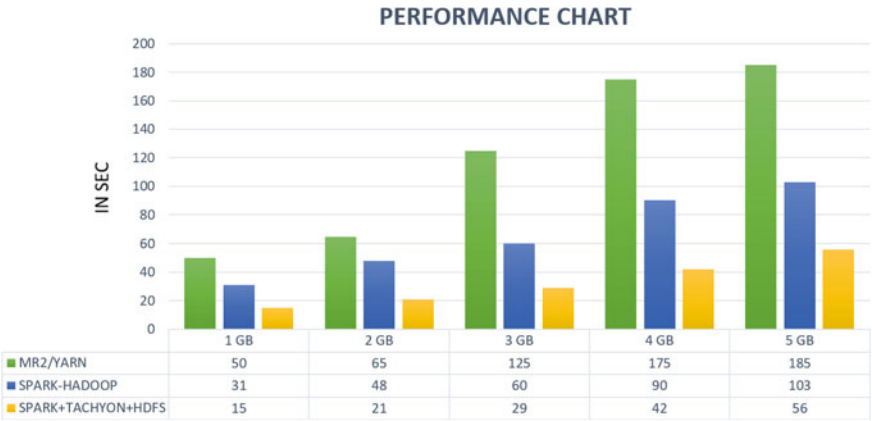
We have chosen anomaly detection problem for Wikipedia datasets of different sizes. We used supervised learning technique to find the outliers. We used 10 MB of cache buffer between Spark and Tachyon on compute node.

Three experiments are performed using traditional Hadoop MapReduce, Spark on Hadoop and out two-level storage system with HDFS, Tachyon and Apache Spark. We compared our tentative result in the form of graph as shown in Graph 1. Here we can see that our proposed system gives high-speed performance for particular problem.

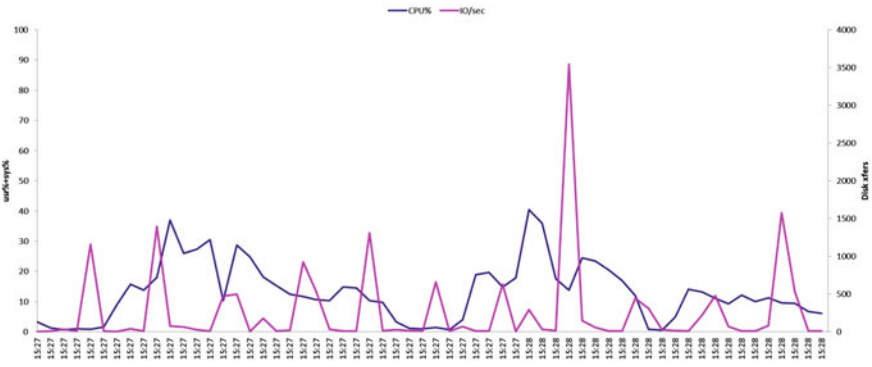
In other Graph 2 we can see that the comparison between read and write operation time with integrated file systems is used in our framework.

Table 1 Experimental setup configuration

Master node			
CPU	Memory	Storage	Network
Intel i7 2.5 GHz	8 GB	1 TB	10 MBPS
Data node			
CPU	Memory	Storage	Network
Intel i5 2.5 GHz	2 GB	1 TB	10 MBPS



Graph 1 Performance analysis



Graph 2 CPU I/O analysis for proposed design

6 Conclusion

With a brief discussion we have proposed an experimental framework for big data analytics especially for iterative problems. To make our framework efficient we have used the caching concept in two ways. First, we use i/o cache buffer between analysis process and main memory for data read operation and also providing caching for data write operation using TachyonFS. We have used in-memory features to remove I/O request overhead, increase fault tolerance and finally improve the speed of data processing. We compared our result with traditional Hadoop. In future, we are looking forward to make our framework more suitable for real-time problems in a small private Cloud environment where resources may be limited.

References

1. Dilpreet Singh and Chandan K Reddy: A survey on platforms for big data analytics. Singh and Reddy Journal of Big Data 2014, 1:8.
2. Hao Zhang, Gang Chen, Member, IEEE, Beng Chin Ooi, Fellow, IEEE, Kian-Lee Tan, Member, IEEE, and Meihui Zhang, Member, IEEE: In-Memory Big Data Management and Processing: A Survey. IEEE TRANSACTIONS ON KNOWLEDGE AND DATA ENGINEERING, VOL. 27, NO. 7, JULY (2015).
3. Zaheer Khan, Ashiq Anjum, Kamran Soomro and Muhammad Atif Tahir: Towards cloud based big data analytics for smart future cities. Khan et al.; licensee Springer Journal of Cloud Computing: Advances, Systems and Applications 4:2 (2015).
4. M. J. Franklin, S. Shenker, and I. Stoica. Resilient distributed datasets: A fault-tolerant abstraction for in-memory cluster computing. In NSDI, 2012.
5. Juwei Shiz, Yunjie Qiuy, Umar Farooq Minhasx, Limei Jiaoy, Chen Wang; Clash of the Titans: MapReduce vs. Spark for Large Scale Data Analytics. Proceedings of the VLDB Endowment, Vol. 8, No. 13 (2015).
6. H. Li, A. Ghodsi, M. Zaharia, S. Shenker, and I. Stoica. Tachyon: Reliable, memory speed storage for cluster computing frameworks. In SOCC, pages 1–15 2014.
7. Pengfei Xuan, Feng Luo, Pradip K Srimani: Big Data Analytics on Traditional HPC Infrastructure Using Two-Level Storage. School of Computing, Clemson University (2015).
8. Jorge L. Reyes-Ortiz, Luca Oneto, and Davide Anguita: Big Data Analytics in the Cloud Spark on Hadoop vs MPI/OpenMP on Beowulf. The Scientific Programme Committee of INNS-BigData conference (2015).
9. Yuzhong Yan, Mahsa Hanifi, Liqi Yi, Lei Huang: Building a Productive Domain-Specific Cloud for Big Data Processing and Analytics Service. Journal of Computer and Communications, 3, 107–117 (2015).
10. https://www.oreilly.com/ideas/accelerating-big-data-analytics-workloads-with-tachyon (Online).
11. Ahsan Javed Awan, Mats Brorsson, Vladimir Vlassov and Eduard Ayguade; Performance Characterization of In-Memory Data Analytics on a Modern Cloud Server. SIGMOD'15 Proceedings of the 2015 ACM SIGMOD International Conference on Management of Data Pages 631–646 ACM New York, NY, USA (2015) ISBN: 978-1-4503-2758-9.

Drive Current Boosting Using Pocket Implant Near to the Strained SiGe/Si Source with Single-Metal/ Dual-Metal Double-Gate Tunnel Field-Effect Transistor

Prateek Jain and Deepak Kumar

Abstract Heterojunction double-Gate tunnel field-effect transistor based on strained SiGe/Si source and pocket implant near to the source is simulated in TCAD using the non-local band-to-band tunnelling (BTBT) model. The dual-metal gate (DMG) and single-metal gate (SMG) technique were discussed separately for the proposed device structure. The use of strained SiGe/Si source and halo/pocket implant near to the source to boost the I_{ON} state current in SMG-DGTFET. The DMG technique results in a better performance when compared to SMG-DGTFET, and as in DMG, we have two different metals which are used at the gate to control the different portions of the transfer characteristics. The SMG and DMG-DGTFET are analysed for different dielectrics as well. The I_{ON}/I_{OFF} ratio comes out to be in the ratio of 4.12×10^{10} in SMG-DGTFET, and the average subthreshold slope also improves from 41.1 mV/decade in SMG-DGTFET to 23.7 mV/decade in DMG-DGTEFT. All the simulations were done in Synopsys TCAD for a channel length of 25 nm using the non-local tunnelling model.

Keywords Dual-metal gate (DMG) · Single-metal gate (SMG) · Double-gate (DG) · Tunnel field-effect transistor (TFET) · Band-to-band tunnelling (BTBT)

Prateek Jain (✉)
Department of Electrical Engineering,
Indian Institute of Technology Kanpur, Kanpur 208016, India
e-mail: prateekjain1587@gmail.com

Deepak Kumar
Department of Electronics and Instrumentation Control,
University of Petroleum and Energy Studies, Dehradun 248007, India
e-mail: deepakkumar18207@gmail.com

© Springer Science+Business Media Singapore 2017

R. Singh and S. Choudhury (eds.), *Proceeding of International Conference on Intelligent Communication, Control and Devices*, Advances in Intelligent Systems and Computing 479, DOI 10.1007/978-981-10-1708-7_110

1 Introduction

Tunnel field-effect transistor (TFETs) are widely focussed recently for low-power VLSI devices [1], because of its exceptional leakage power performance [2] and low OFF current [3]. However, the main drawback with TFETs is its low I_{ON} current as compared to ITRS requirements and stringent fabrication steps required for extracting performance. The methods reported which can be used to increase I_{ON} in TFETs include structural modifications (heterojunction source [4, 5], etc.), doping optimization (retrograde doping, pocket implant source, etc.), gate metal work function engineering (double-gate, dual-metal gate [6]) improving electrostatics (gate all around structures), dielectric optimization (with one or multiple dielectrics), etc. Strain at the source and drain end can also be used to increase the I_{ON} current [7, 8].

2 Schematic of DMG-DGTFET Based on SiGe/Si Source and Pocket Implant

The schematic cross section of the device is shown in Fig. 1. The drain side metal gate is referred as auxiliary gate, while the source side metal gate is referred as tunnel gate. The source consists of a layer of SiGe on top of silicon and additional pocket implant were used below the tunnel gate on the source side to boost the I_{ON} current as shown below.

We have not considered the strain effect in SiGe, which is due to the difference in lattice constant of SiGe and Si. The fabrication of DMG-DGTFET [9] based on strained SiGe/Si source and halo/pocket implant near the source can be done by the technique already available in the literature [10, 11]. For strained SiGe/Si source, it can be made by the technique already reported [12]. The doping profile is uniform in the drain, source, and body region.

2.1 Simulation Model and Structure Parameters

All the simulation was done using Synopsys 2D-TCAD [13]. The band-to-band tunnelling (BTBT) current is calculated using the non-local BTBT tunnelling

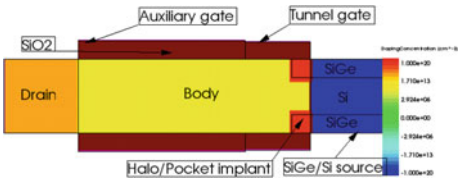


Fig. 1 The schematic of n-type DMG-DGTFET with the proposed device structure

model. The values of the non-local BTBT model parameters are calibrated according to the practical results [14]. The recombination model that is used in the simulation is SRH (Shockley–Read–Hall) recombination and surface SRH recombination. Band gap and Fermi-Dirac statistics were used to account for high doping effects.

Device simulation had been done for the discussed structure with drain doped with 1×10^{18} cm^{-3}(Arsenic n+), source is doped with 1×10^{20} cm^{-3} (Boron p+), and body is doped with arsenic concentration of 1×10^{16} cm^{-3} (n–). The gate dielectric material thickness is 2 nm and the gate length is 25 nm. The auxiliary gate length $(L_{aux.})$ is 18 nm and that of tunnel gate is $L_{tun.} = 7$ nm. The silicon body thickness t_{si} is 8 nm with pocket implant of 1×10^{20} cm^{-3} (Arsenic) and 2 nm thickness.

2.2 SMG-DGTFET Based on Strained SiGe/Si Source and Pocket Implant

As the metal work function increases at ON state, the BTBT probability decreases due to the increase in the barrier thickness at the junctions as shown in Fig. 2a, which results in the decrease in the BTBT current.

Increasing the work function of the metal results in the transfer characteristics, which are shifted parallel to the *x*-axis, and as a result threshold voltage increases as shown in Fig. 2b. The use of strained SiGe/Si source reduces the band gap of the source material with increase in the Ge mole fraction, which increases the BTBT probability and the use of halo implants results in the steeper energy band characteristics, which results in the increase in the BTBT current. The best possible value of work function, which ensures high I_{ON}/I_{OFF}, is selected $\phi_M = 4.3$ eV. The work function of the gate metal is set to $\phi_M = 4.3$ eV for other combination of dielectric and the results are shown in Fig. 2c. The SS_{AVG} comes out to be from 41.1 mV/decade in an SMG-DGTFET based on the above-mentioned device structure. In Table 1 we have mentioned the results with different dielectrics.

3 DMG-DGTFET Based on Strained SiGe/Si Source and Pocket Implant

In this section, the analysis of DMG-DGTFET based on SiO_2 dielectric, strained SiGe/Si source, and the above-mentioned structure is carried out for both the metal gates to set the values of the work function. The effect of $\phi_{aux.}$ (Auxiliary gate work function) on the transfer characteristics is studied by keeping $\phi_{tun.}$ (Tunnel gate work function) constant at 4.0 eV at both OFF and ON states. As $\phi_{aux.}$ is varied from 4.0 to 4.4 eV at OFF state, the OFF state current decreases due to the increase

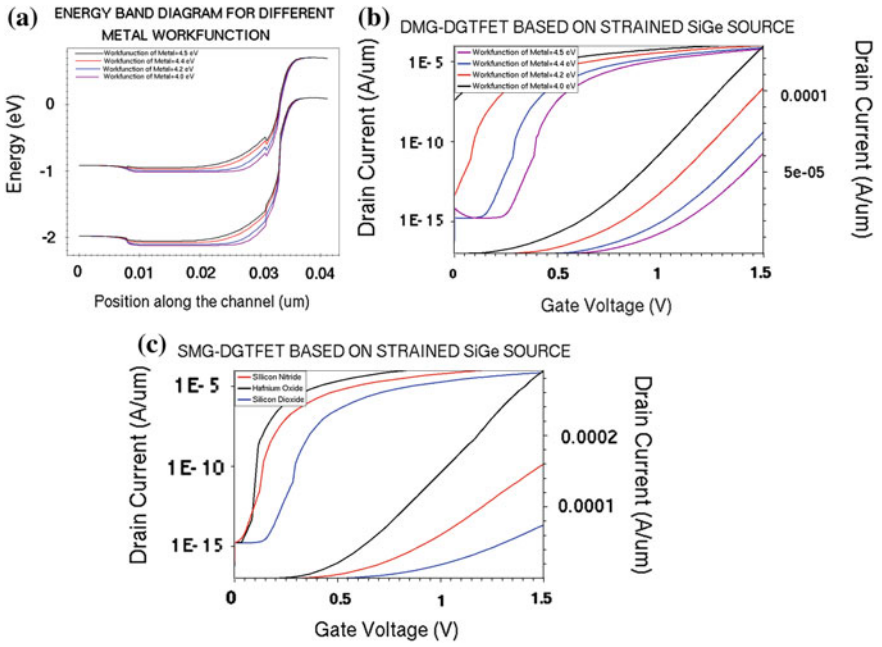


Fig. 2 SMG-DGTFET ($L = 25$ nm, $t_{ox} = 2$ nm) based on the strained SiGe/Si source, 0.5 Ge mole fraction and pocket implant near to the source, and energy band diagram along device length near to the surface. **a** For different values of ϕ_M calculated at ON state ($V_{gs} = 1.5$ V and $V_{ds} = 1$ V). **b** The transfer characteristics at $V_{DS} = 1.0$ V. **c** For different dielectric ($\phi_M = 4.3$ eV) materials

Table 1 SMG results for different dielectrics at $\phi_M = 4.3$ eV

	I_{on} (μA/μm)	I_{off} (A/μm)	SS_{avg} mV/dec
SiO_2	75	1.8×10^{-15}	41.1
Si_3N_4	160	2×10^{-15}	30
$Hf0_2$	291	8×10^{-15}	23.5

I_{ON} is enhanced as the dielectric constant increases, because of better coupling of gate

in the barrier width at the junction as shown in Fig. 3a, and further increase in $\phi_{aux.}$ results in increase in the OFF state current. The increase in $\phi_{aux.}$ at ON state does not bring significant changes in the barrier width as shown in Fig. 3b; as a result the ON state current (I_{ON}) is not changed by much as shown in Fig. 3c.

Next the value of $\phi_{tun.}$ is selected which gives the best ON state current (I_{ON}). The same analysis is carried out for $\phi_{tun.}$ as it is carried out for $\phi_{aux.}$. In this analysis $\phi_{aux.}$ is constant at 4.4 eV and $\phi_{tun.}$ is varied from 4.0 to 4.6 eV and the results are shown in Fig. 4c. It is evident from the results that as $\phi_{tun.}$ is varied from 4.0 to 4.6 eV at ON state, the BTBT current decreases because of increase in the barrier width as shown in Fig. 4b and decrease in the BTBT probability. At OFF state

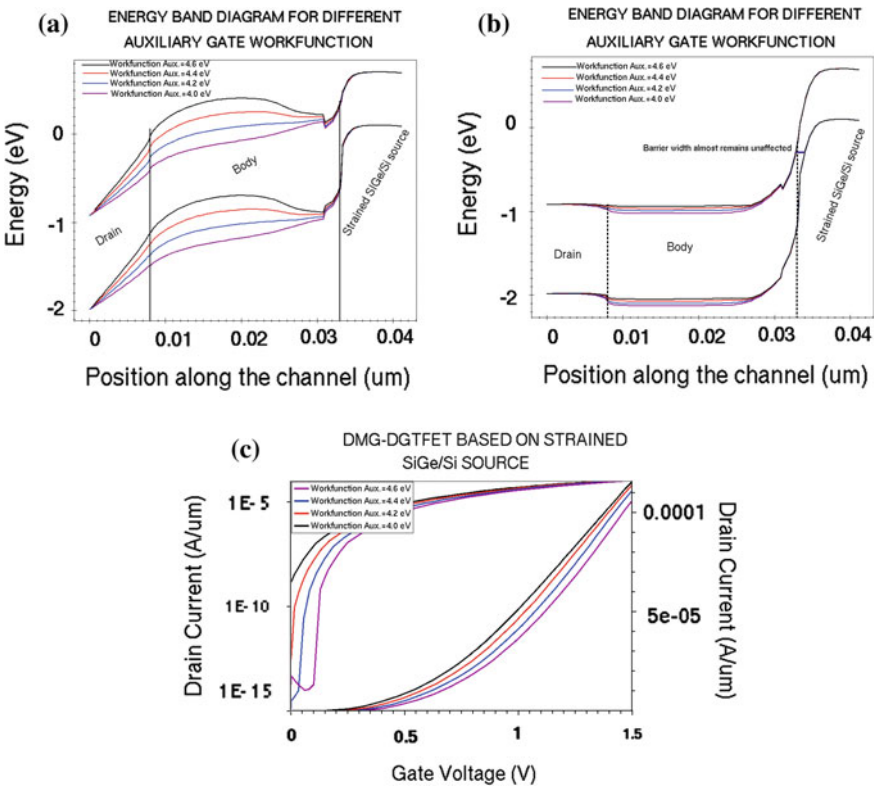


Fig. 3 DMG-DGTFET based on strained SiGe/Si on the top of source, 0.5 Ge mole fraction and halo implant near to the source, and its energy band diagram along a horizontal cut line near to the surface shown at, **a** OFF state $\left(V_{gs} = 0\,\text{V}, V_{DS} = 1.0\,\text{V}\right)$, and **b** ON state $\left(V_{gs} = 1.5\,\text{V}, V_{DS} = 1.0\,\text{V}\right)$, **c** transfer characteristics $(\phi_{aux.} = 4.0\,\text{eV})$ shown on both semi-log and linear scale

increased in $\phi_{tun.}$ does not change the OFF state current by much as shown in Fig. 4a.

The best possible value for $\phi_{aux.}$ is 4.4 eV which gives the best OFF state current (I_{OFF}); the metals which can be used at the gates to provide 4.4 eV work function are W, Ta, and Mo. The best possible value of $\phi_{tun.}$ which gives the best ON state current is 4.0 eV and the metals which can be used are Mo, Ni–Ti, and Sc [15].

The results that were obtained for SMG/DMG-DGTFET for the mentioned device structure are compared. The value of SS_{AVG} improves from 41.1 mV/decade in single-metal gate (SMG) to 23.7 mV/decade in DMG-DGTFET for 0.5 Ge mole fractions. The application of dual-metal gate (DMG) technique boots the ON state current (I_{ON}) and lowered the I_{OFF} as compared to SMG-DGTFET. The best possible value of I_{ON}/I_{OFF} (about 4.1×10^{10}) is achieved at $\phi_M = 4.3$ eV in the

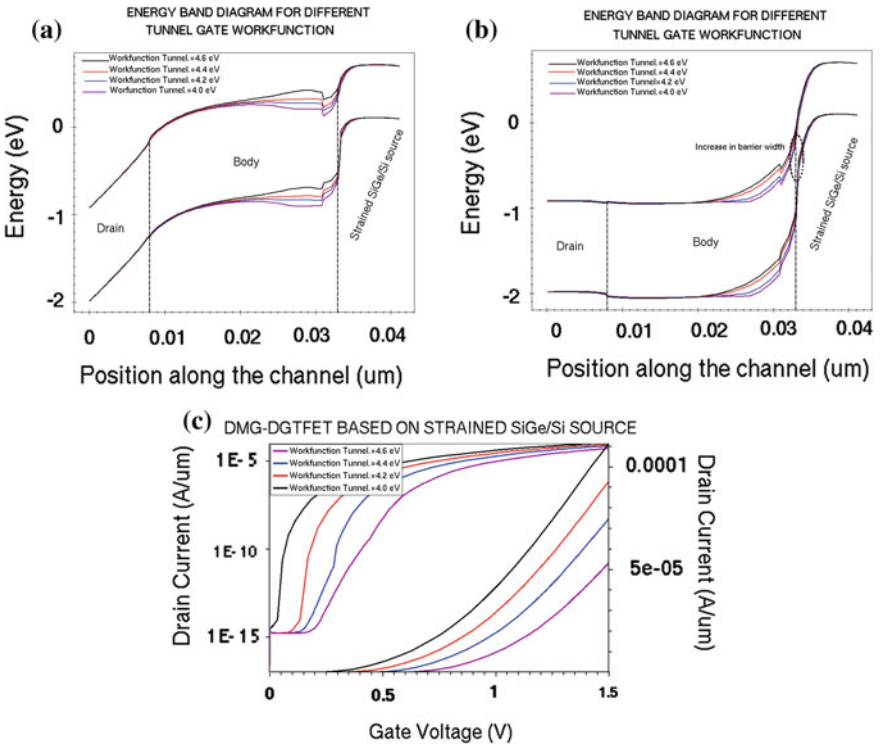


Fig. 4 DMG-DGTFET based on strained SiGe/Si on the top of source, with Ge mole fraction(x) 0.5, and pocket implant near to the source, and its energy band diagram along a horizontal cut line near to the surface shown at, **a** OFF state $\left(V_{gs} = 0\,\text{V}, V_{DS} = 1.0\,\text{V}\right)$, and **b** ON $\left(V_{gs} = 1.5\,\text{V}, V_{DS} = 1.0\,\text{V}\right)$ state, **c** transfer characteristics $(\phi_{aux.} = 4.0\,\text{eV})$ shown on both semi-log and linear scale

SMG-DGTFET. The ratio of I_{ON}/I_{OFF} is in the range of 9.25×10^{10} for a DMG-DGTFET.

4 Effect of Ge(x) Mole Fraction in Strained SiGe Source

Varying the Ge mole fraction in SiGe layer results in the modulation of the energy band gap of the source material with Ge mole fraction, and band gap reduces with increase in Ge mole fraction in SiGe layer as shown in Fig. 5a; as a result barrier thickness reduces, which increases the BTBT probability and BTBT current as shown below in Fig. 5b.

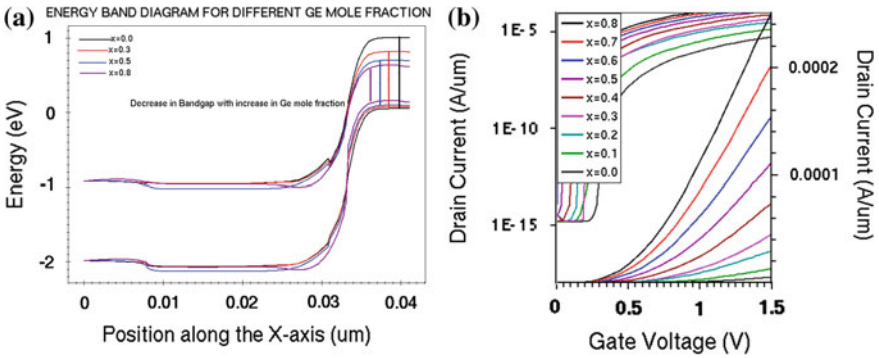


Fig. 5 The effect of different mole fractions of Ge(x) in DMG-DGTFET based on strained SiGe/Si source, silicon dioxide dielectric, and its energy band diagram along a horizontal cut line near to the surface shown at, **a** ON $\left(V_{\mathrm{gs}} = 1.5\ \mathrm{V},\ V_{\mathrm{DS}} = 1.0\ \mathrm{V}\right)$ state, **b** transfer characteristic shown on both the scales while $\phi_{\mathrm{tun.}} = 4.0\ \mathrm{eV}$ and $\phi_{\mathrm{aux.}} = 4.4\ \mathrm{eV}$

5 Conclusion

The DMG technique takes the advantage of two metals at the gate to control the BTBT current and results in better performance, when compared to SMG-DGTFET. The use of halo/pocket implant near to the source further boosts the ON state current. Fabrication difficulties were there to fabricate SMG/DMG-DGTFET based on SiGe/Si source and pocket implant near to the source, but the results that we got from the simulation are significant.

References

1. Adrian M. Ionescu and Heiki Riell. "Tunnel Field Effect Transistor as Energy efficient switches". Nature 479, pp. 329–337, Nov. 2011.
2. M. Luiser, G. Klimeck, "Performance comparison of tunneling field effect transistors (H-TFET) for steep subthresholdswing," IEDM Tech. Dig., pp. 785–788, 2011.
3. Zhang, W. Zhao, and A. Seabaugh, "Low-subthreshold-swing tunnel transistors," *IEEE Electron Device Lett.*, vol. 27, no. 4, pp. 297–300, Apr. 2006.
4. Method of Fabricating a Silicon TFET with high drive current, by M. Zhu, S.S. Tan, E.H. Toh, E. Quek, (2013, Feb.5). Patent, US 8,368,127 B2.
5. P. Y. Wang and B. Y. Tsui, "Band Engineering to Improve Average Subthreshold Swing by Suppressing Low Electric Field Band-to-Band Tunneling With Epitaxial Tunnel Layer Tunnel FET Structure," *IEEE Trans. Nanotechnol.*, vol. 15, no. 1, pp. 74–79, Jan. 2016.
6. *P. Jain, V. Prabhat and B. Ghosh. "Dual Metal Double Gate Tunnel Field Effect Transistor with mono and hetero dielectric gate". Journal of computational electronics, Volume 14, Issue 2, pp 537–542, Jun. 2015.*
7. Osama M. Nayfeh, Cait Ni Chleirigh, John Hennessy, Leonardo Gomez, Judy L. Hoyt, and Dimitri A. Antoniadis. "Design of Tunneling Field-Effect Transistors Using Strained-Silicon/Strained-Germanium Type-II Staggered Heterojunctions" IEEE ELECTRON DEVICE LETTERS, VOL. 29, NO. 9, SEPTEMBER 2008.

8. Paul M. Solomon, I. Lauer, A. Majumdar, J. T. Teherani, M. Luisier, J. Cai, and S. J. Koester "Effect of Uniaxial Strain on the Drain Current of a Heterojunction Tunneling Field-Effect Transistor" IEEE ELECTRON DEVICE LETTERS, VOL. 32, NO. 4, APRIL 2011.
9. A. Yagishita, T. Saito, K. Nakajima, S. Inumiya, Y. Akasaka, Y. Ozawa, K. Hieda, Y. Tsunashima, K. Suguro, T. Arikado, K. Okumura, High performance damascene metal gate MOSFETs for 0.1 m regime, IEEE Trans. Electron Devices 47 (5) (2000) 1028–1034.
10. Gibong Lee, Jung-Shik Jang "Dual-Dielectric-constant spacer hetero-gate-dielectric tunneling FETs" Semicond. Sci. Technol. **28** (2013) 052001 (5 pp).
11. . W. Long, H. Ou, J. M. Kuo, and K. K. Chin, "Dual-material gate (DMG) field effect transistor," *IEEE Trans. Electron Devices*, vol. 46, no. 5, pp. 865–870, May 99.
12. G. Hock, E. Kohn, C. Rosenblad, H. von Kanel, H.-J. Herzog, U. Konig, High hole mobility in Si0.17Ge0.83 channel MOSFET grown by plasma-enhanced chemical vapor deposition, Appl. Phys. Lett. 76 (26) (2000) 3920–3922.
13. Synopsys, TCAD Sentaurus device, ver. D2010-03,2010.
14. Jiao Yipeng, Wei Kangliang, Wang Taihuan, Du Gang and Liu Xiaoyan "Comparision of band-to-band tunnel model in Si and Si-Ge junctions" Journal of semiconductor *et al* 2013 *J. Semicond.* **34** 092002.
15. P. Ranade, Y. C. Yeo, Q. Lu, H. Takeuchi, T. J. King, and C. Hu, "Molybdenum as a gate electrode for deep sub-micron CMOS technology," in *Proc. MRS Symp.*, 2000, vol. 611, pp. C3.2.1–C3.2.6.

Distributed Intrusion Detection System for TCP Flood Attack

Deepak Kshirsagar, Suraj Sawant, Ravi Wadje and Pravin Gayal

Abstract Nowadays, there is an increase in the number of users to use different web services for various activities such as online shopping and online payment transactions. Currently, most of these web servers are suffering from distributed denial-of-service (DDoS) attacks, which results in unavailability of services to valid users. Intrusion detection system (IDS) is one of the best solutions adopted by various organizations for these types of attack detection. This paper proposes the distributed intrusion detection mechanism (DIDM) for efficient DDoS attacks. The proposed intrusion detection takes place with the help of server IDS and client IDS placed on a central server and individual clients, respectively. This type of mechanism extends the scalability and overcomes the limitation of central server failure in a distributed environment.

Keywords Distributed DoS · Distributed intrusion detection mechanism · TCP flood · Scalability and client–server architecture

Deepak Kshirsagar (✉) · Suraj Sawant
College of Engineering Pune (COEP), Pune, India
e-mail: kdeepak83@gmail.com

Suraj Sawant
e-mail: suraj.t.sawant@gmail.com

Ravi Wadje
Citrus Payment Solutions, Pune, India
e-mail: wadje.ravi@gmail.com

Pravin Gayal
Vignet IT Solutions, Pune, India
e-mail: gayalpravin777@gmail.com

© Springer Science+Business Media Singapore 2017

R. Singh and S. Choudhury (eds.), *Proceeding of International Conference on Intelligent Communication, Control and Devices*, Advances in Intelligent Systems and Computing 479, DOI 10.1007/978-981-10-1708-7_111

1 Introduction

Denial-of-service (DoS) attack does not hamper user's confidential information or any other security issues. Loss of service is defined as the inability of a network service to be temporary unavailable of predefined network connectivity and services. The result of DoS attacks has contributed to forced shutdown of the system [1].

Akamai State of the Internet Security Report 2014 [2] states that distributed DoS attacks have steeply increased in volume from last quarter. There is an increase of 57 % as compared to earlier year and 90 % increase of attacks in the fourth quarter as compared to the third quarter. In United States 45.8 % of hosted websites were suffered from distributed denial-of-service (DDoS) [3].

1.1 Distributed DoS

In DoS attack, hacker uses a single connection of the Internet to exploit the vulnerability by sending large volume of malicious traffic towards the victim. The hacker usually makes an attempt to exhaust the resources of the server, such as memory and CPU utilization.

A distributed DoS attack is an attempt which makes web services unavailable to genuine users with the help of malicious overwhelming traffic from various connected devices over the Internet. These types of attack mainly target e-commerce resources from banking, online shopping, and news websites. The hackers use botnets which creates large volume of malicious traffic for DDOS which targets towards network infrastructure.

1.2 Classification of DDoS

DDoS is broadly classified [4] into the following types:

1.2.1 Network Layer Attacks

This layer provides the description of internetwork and used for routing and switching packet information to other networks. A hacker generates malicious traffic using ARP, IP, and ICMP protocols. ICMP flooding is the most common DDoS that overloads firewall and bandwidth of the victim.

1.2.2 Transport Layer Attacks

A hacker uses TCP and UDP protocols for the generation of malicious traffic. This type of vulnerability effects on networking devices and bandwidth. SYN Flood, Smurf, and UDP flood are some of the examples of DDoS.

1.2.3 Application Layer Attacks

The attacker uses HTTP, SMTP, and FTP for generation of DDoS at the application layer. The attacker sends large number of malicious traffic for resource requests. The examples of DDOS attack are Slowloris and HTTP flood.

This work adds the following contributions:

1. This paper proposes the distributed intrusion detection mechanism (DIDM) for efficient detection of TCP flood attacks.
2. The proposed solution extends the scalability of intrusion detection system (IDS) based on server and client IDS placed on a central server and individual clients, respectively.

The remainder of the paper is organized as follows: Section 2 presents related work in the area of DoS attacks in a distributed environment. Section 3 provides proposed intrusion detection mechanism. Section 4 deals with system implementation. Section 5 describes comparative analysis and Sect. 6 concludes followed by future scope.

2 Related Work

This section describes the literature survey carried out in the area of IDS in network and distributed environment for DoS attacks.

2.1 Network IDS

IDS [5] detects attacks based on the common intrusion detection framework. The pattern-based IDS consists of capturing, decode, detection, known attack, and action module. This system captures data over the network and with the help of predefined signatures detects various attacks.

A multivariate correlation analysis [6] is used for detection of land, back, Smurf, and pod attacks. This approach provides correlative information present between the features of network data records. This system compares incoming traffic with profile generated in training phase using normal traffic records. Euclidean distance is used for inner correlation analysis. This approach produces a high false negative rate.

Feature selection algorithm [7] based on entropy is used for ID. Initially, training dataset is used to determine the entropy for U2R, R2L, probing, and DoS attack. This entropy is used for testing dataset and used for attack classification.

Hybrid intelligent systems [8] are used to model ID. This system uses decision tree (DT) and support vector machines (SVM) combined for the detection of SYN flood and ping of death attacks. DT algorithm produces better results than SVM.

Data mining-based IDS (DM-IDS) [9] was used for detection of TCP and UDP flood attacks. This framework contains packet capturing, feature extraction, known attack database, and detection module.

Agent-based IDS (A-IDS) [10] is used for land and UDP flood attacks' detection. Agent-based architecture is used and based on pattern-based rules these attacks are detected.

Network IDS [11] is proposed for the detection of web attacks. This paper mainly covers a brief overview of different security mechanisms used by researchers. This paper suggests that the ontology is useful for detection process. This paper proposes the use of ontology for XSS, buffer overflow, and SQL injection attacks' detection.

2.2 Distributed IDS

An optimized scalable distributed architecture [12] is used to detect DoS attacks for high-speed networks. The proposed architecture is effectively decreasing the bottleneck problem due to ID process. This architecture with its switch-based splitting structure provides flexibility and scalability. Snort rules are used for ID. This system produces high false alarms.

Distributed IDS (DIDS) [13] detects DoS attacks for high-speed networks based on log analysis. This system is implemented using field-programmable gate array (FPGAs) hardware. This system has central and host IDS components, which detects attacks at network level. The central IDS collects information from individual host IDS and takes decision based on it. The central IDS takes decision and informs all other hosts. This system provides partial reconfigurability and flexibility.

Distributed anomaly ID platform [14] is proposed with alert processing. This framework consists of centralized correlation and detection entity distributed over the network. All local probes are controlled by detection entity. This IDS uses an alert scoring system based on the common vulnerability scoring system (CVSS) for the efficient detection of Targa3 and UDP flood attacks.

DIDS [15, 16] is implemented along with firewall for DoS and web service attack detection. Scalability of the system is extended with the help of agent-based architecture. The proposed architecture consists of monitor, analysis, executive, and manager agent. Ontology and semantic rules are used for detection of Smurf, mail bomb attacks. The accuracy is increased, but produces a high false alarm rate.

3 Proposed Intrusion Detection Mechanism

The proposed intrusion detection mechanism uses client–server architecture for intrusion detection. IDSs are deployed on each client and server machine of the distributed environment. Each IDS interacts with other by exchanging messages. Each IDS consists of packet sniffer, feature extraction, and rule-based detection and message exchange module.

3.1 Packet Sniffer

The incoming traffic is captured with the help of packet sniffer. This raw data is captured in promiscuous mode. The traffic consists of various information fields related to various protocols.

3.2 Feature Extraction

The captured raw data contains various fields of communication protocols. The necessary features are identified, extracted, and stored in the database.

3.3 Detection Policy

Rule-based policy is used by this detection system. The extracted features are used for rule generation and used for intrusion detection mechanism.

3.4 Message Exchange

Message exchange module is used for interaction between two IDSs.

4 System Implementation

System captures the packets that are approaching the network with the help of packet sniffer. This packet sniffer is shown in Fig. 1 which is developed with the help of Jpcap API. Packet sniffer captures TCP, UDP, and ICMP packets for intrusion detection. These packets are captured and made available for the feature extraction. The important features are identified, extracted, and stored in a database.

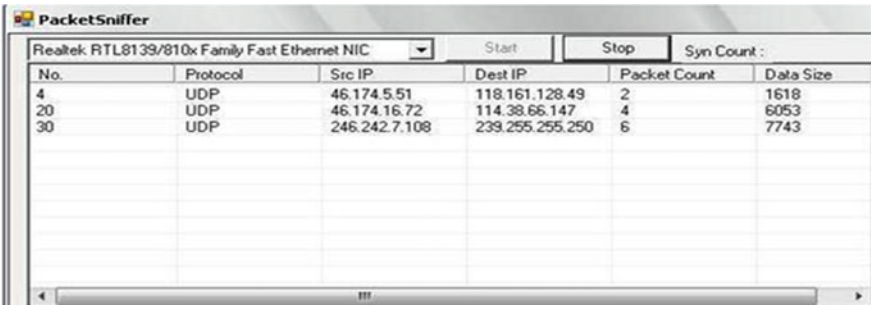


Fig. 1 Packet sniffer

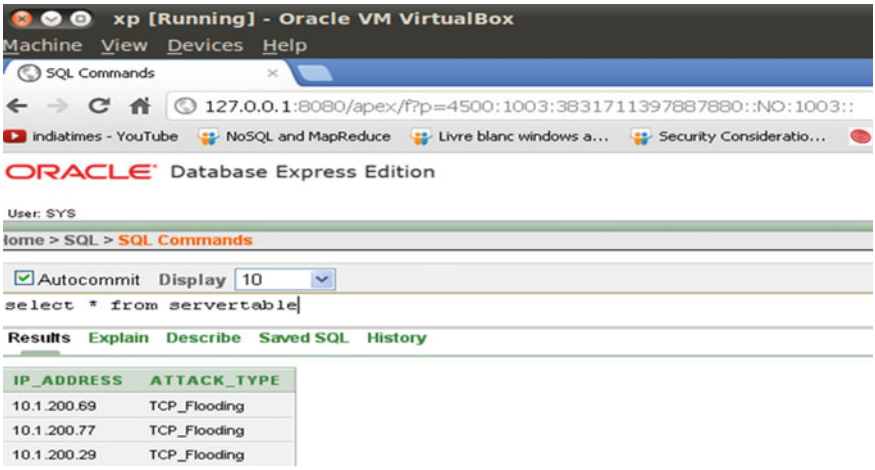


Fig. 2 TCP flood attack detection on server machine

These features are used to define intrusion policy in terms of rules. The intrusion is detected by the server and client IDS based on these rules. Each IDS detects attacks and information regarding that attack is stored in the database. Figure 2 shows that TCP flood attack is detected by server machine. This attacker information is stored and communicated to others with the help of message exchange. Client server socket programming is used for the message exchange module.

5 Comparative Analysis

The proposed detection mechanism is useful for efficient detection of DoS attack in a distributed environment. This paper uses client and server IDS which is placed on individual clients and a central server. The proposed detection mechanism detects

Table 1 Comparative analysis with state–of-the-art systems

Work	Distributed IDS	Architecture used	Scalability	Central IDS failure
Anomaly IDS [6]	No	NA	No	NA
NIDS [11]	No	NA	No	NA
DIDS [13]	Yes	Server and host IDS	Yes	Yes
MA-IDS [16]	Yes	Agent	Yes	NA
DIDS [15]	Yes	Agent	Yes	NA
Presented work	Yes	Client and server IDS	Yes	No

host and network-based intrusions. The key contribution of this paper is that it has no effect of central IDS failure because each IDS is communicating with every other system, i.e., client–client, server–client, and client–server.

Table 1 shows comparative analysis of proposed work with the current state-of-the-art. NA entry in the table denotes that respective parameter is not applicable for the corresponding work.

6 Conclusions

This paper has proposed and implemented DIDM for efficient detection of DDoS attack, i.e., TCP flood. The proposed mechanism uses server IDS and client IDS for intrusion detection. The message exchange module is used for communication with other IDS, which does not affect the central server failure. However, this detection system detects only DDoS attack, i.e., TCP flood. The further task is to test the system for different DoS attacks and distributed as well as Cloud computing environment.

References

1. Mathew, R., Katkar, V.: Software based low rate dos attack detection mechanism. Int. J. Computer Applications, 20(6), (2011) 14–18
2. Dave, L.: DDoS Attacks Continue To Rise. (2015)
3. Joseph, S.: Denial of Service Attacks Are Growing Increasingly Problematic: Here's What You Need to Know. SecureMySocial, New York, NY, USA
4. DDoS Quick Guide. National Cybersecurity and Comm. Integration Center (2014)
5. Kshirsagar, D., Tagad, D., Sale, S., Khandagale, G.: Network Intrusion Detection based on attack pattern. Extc. Comp. Tech. Int. Conference IEEE (2011) 283–286
6. Tan, Z., Jamdagni, A., He, X., Nanda, P., Liu, R.: Denial-of-service attack detection based on multivariate correlation analysis. Neural Information Processing. Springer Berlin Heidelberg, (2011) 756–765
7. Gautam, S., Om, H.: Anomaly detection system using entropy based technique. Next Generation Computing Technologies Int. Conference IEEE (2015) 738–743

8. Peddabachigari, S., Abraham, A., Grosan, C., Thomas, J.: Modeling intrusion detection system using hybrid intelligent systems. Int. J. Network and Computer Applications. 30(1), (2007) 114–132
9. Kshirsagar, P., Holambe, A., Kshirsagar, D.: Data mining based intrusion detection system (dm-ids). Int. Conference on Comp. Sci. and IT, (2012)
10. Malik, A.: Agent-based Network Intrusion Detection System Using K-Means clustering algorithm. Int. Conference on Computing and Control Engg. (2012)
11. Khairkar, A., Kshirsagar, D., Kumar, S.: Ontology for Detection of Web Attacks. Communication Systems and Network Technologies, International Conference IEEE (2013) 612–615
12. Sallay, H., AlShalfan, K.: A scalable distributed IDS Architecture for High speed Networks. Int. J. Comp. Sci. and Network Security, Vol. 9. (2009)
13. Tummala, A., Patel, P.: Distributed ids using reconfigurable hardware. Parallel and Distributed Processing Symposium International IEEE (2007) 1–6
14. Aussibal, J., Gallon, L.: A new distributed IDS based on CVSS framework. Web-Based Information Tech. and Distributed Systems, Atlantis Press, (2010) 189–206
15. Brahmkstri, K., Thomas, D., Sawant, S., Jadhav, A., Kshirsagar, D.: Ontology based multi-agent intrusion detection system for web service attacks using self learning. Networks and Comm., Springer International Publishing, (2014) 265–274
16. Thomas, D., Brahmkstri, K., Jadhav, A., Sawant, S.: Multi-Agent Distributed Intrusion Detection System Using Ontology. Int. J. Recent Advances in Engineering and Technology, (2013) 5–7

An Optimized Approach: Air Energy Trap System in Railways for Power Generation

Nikhil Raj, Rohan Sharma, Sagar Majumdar, Rajesh Singh and Anita Gehlot

Abstract In order to have sustainable development, we should focus more toward the renewable energy resources. A high-relative velocity between wind and train causes more air drag to the moving train. The drag is produced because of the energy delivered by the engine to move forward. This paper is all about the harvesting of energy from the air drag and utilizing it into useful applications. The proposed system is highly efficient with an approximate efficiency of around 72.56 %. In this system, air drag is used to rotate the fans, which are mounted on the roof top of the trains, inclined at an angle of 10° to maximize the harvested energy from the air drag.

Keywords Sustainable development · Air drag · Energy harvesting

Nikhil Raj (✉) · Rohan Sharma
Power System Engineering, University of Petroleum and Energy Studies,
Energy Acres, Dehradun, India
e-mail: nikhil.raj110@gmail.com

Rohan Sharma
e-mail: rohansharma0394@gmail.com

Sagar Majumdar
Electronics Engineering, University of Petroleum & Energy Studies,
Energy Acres, Dehradun, India
e-mail: sagarnandim@gmail.com

Rajesh Singh · Anita Gehlot
Department of Electronics Engineering, University of Petroleum and Energy Studies,
Energy Acres, Dehradun, India
e-mail: rsingh@ddn.upes.ac.in

Anita Gehlot
e-mail: anita@ddn.upes.ac.in

© Springer Science+Business Media Singapore 2017

R. Singh and S. Choudhury (eds.), *Proceeding of International Conference on Intelligent Communication, Control and Devices*, Advances in Intelligent Systems and Computing 479, DOI 10.1007/978-981-10-1708-7_112

1 Introduction

According to economists by the end of twenty-first century, dependency on these fuels, such as, oil, gas, and coal will be increased by 20 %, i.e., so high that threat will occur on their existence, by that time [1]. The concept of extracting the "*free abundant energy*" of this universe, i.e., *air* and converting it to power to extend the lifetime of the system or to provide an endless power supply to the system has motivated a lot of researchers toward this field [2]. Previously, a number of free energy extraction devices were constructed, but they could not work effectively [3].

These are also one of the greatest consumers of these natural energy resources. In the coming future, it is just not possible to transmit huge megawatts of power to accelerate the train as well as fulfill the extra power requirements for internal coach's lights, fans, and other activities [4].

According to the Dutch railways, since 2005, approximately 80 % is the energy consumption per passenger per kilometer and that green power for rail has been preferred by the 80 % of its riders [5]. German railway has made many remarkable strides toward sustainability in the past few years. It currently uses 2 % of the country's total electricity but still dependent upon fuels [6]. Deutsche Bahn said that, to become carbon-free by 2050, wind, hydro, and solar energy used for powering the trains should be raised from 20 % now to 28 % by 2014—higher thoughts than the German government's already ambitious national goals [7]. Electric trains are so efficient that a single 300 W solar panel, i.e., about 4 $\times$ 6 feet is sufficient provide up to 5–20 miles per day. Based on the National Transportation Database data on efficiency of the various U.S. electric train systems, the national average is about 4000 miles per year for each 300 W solar panel. 1–3 MW of solar panels is supported by one mile of train tracks, resulting in 2 million and 6 million passenger miles of train travel [8].

In all of the above approaches, somewhere such costly setups are used to overcome this crisis and somewhere just a dream of getting green railway is seen while somewhere only proposals are given for the implementation of energy efficient system [9]. Here, we are trying to introduce a new concept in railways, that not only will minimize the use of fossil fuels, but is also easy to relocate and quite inexpensive [10]. Air drag is the phenomenon occurring all the time around running train. The air drag is directly proportional to the square of speed of train [11]. Aerodynamic drag on the traveling train is categorized into two type, i.e., pressure drag and friction one. Hence, the energy consumption of high-speed train and reduction of aerodynamic drag are one of the essential issues related to the development of the desirable train system [12].

2 Theory and Principle Involved

Selection of a model for design is put for further process after judging the main principle and its long-term benefits with respect to mankind. The Principle of Operation for the proposed system can be elaborated using key terms as—Motion, Air, Drag Force, Rotation, Inclination and Efficiency, etc. The moving air in the direction opposite to the motion of the object tends to go waste, besides having a potential of being utilized for better applications, as air—a renewable energy source, can help in producing power, ranging from certain KW-MW. The principle involved in the working of our model is an amalgamation of many small phenomenon of the nature.

Air drag is that component of the surface force which is parallel to the direction of flow of air [13]. This air drag makes the rotor to spin just the way propeller does and the generator is made to spin by the turning shaft, in order to produce required amount of electricity [14]. This drag equation can be formulated below, mathematically, as:

$$D = C_d \times A \times 0.5 \times r \times V^2, \tag{1}$$

[15] where D = Drag, C_d = Drag Coefficient, r = Density, V = Velocity, A = Referenced Area.

2.1 EMF Equation

Let, Φ = useful flux per pole in webers (Wb), P = total number of poles, Z = total number of conductors in the armature, n = speed of rotation of armature in r.p.s, A = number of parallel paths through the armature between brushes of opposite polarity, Z/A = number of armature conductors in series for each parallel path. Thus, total voltage generated = (average voltage per conductor) x (number of conductors in series per path).

That is,

$$E = nP\Phi Z/A, \tag{2}$$

where $A = P$ (Lap Winding); $A = 2$ (Wave Winding) [16].

Thus, these two basic principles along with Newton's Third Law of Motion constitute the basic working of our system and it could be exercised for feeding internal requirements of the train in our contrast.

3 Fabrication and Methodology

A flexible fabrication process has been used to fabricate the system. The system consists of a free moving blade mounted on the top of a moving train at an elevation of 10 degrees from the plane surface of the roof top of the train, inclined in the direction of the moving train (Fig. 1).

The fans are further connected with a generator, which is attached just below the fans. All the fan systems, installed in particular coaches, are integrated to have high-output values of power. Now, as train starts to move in the horizontal direction, an air drag will be created in the direction, which is opposite to that of the moving train. The aerodynamic drag will hit the blade with the relative velocity between moving train and the speed of the wind. As the opposing air strikes the blade of the fans because of the aerodynamic property, fan reduces its kinetic energy and converts that to the rotational energy of the fan system. As stated earlier there is a generator which is connected with the fan, hence as the fan rotates by the

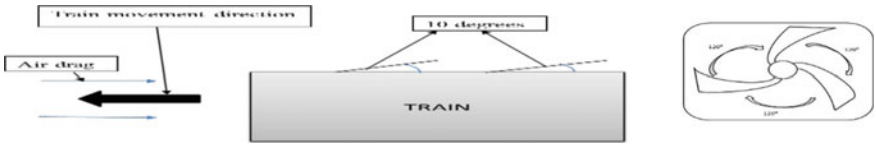


Fig. 1 Angle of elevation of blades with respect to roof top of the train, geometry of fans, which are to be installed on the roof top of the train

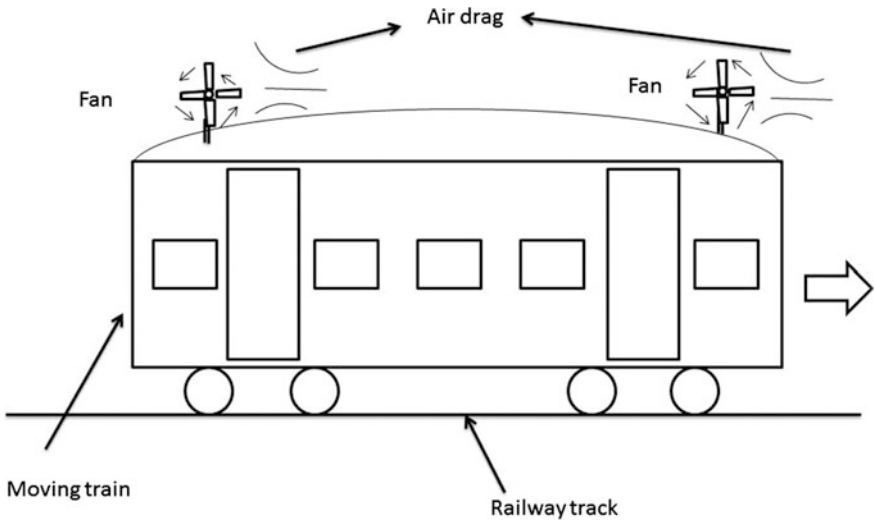


Fig. 2 The arrangement showing the fan and its position on the train for installation

effect of the air, generator shaft also starts rotation. With each complete rotation of generator shaft, an EMF is produced and a corresponding power is produced in the generator which is sent to the storage bank. The storage bank consists of Li-Po battery which is installed beneath the bottom of the train's floor. The adjustment of fan and generator system is so designed that it optimizes the space in the train. The system will not affect the space inside the train. The efficiency of the system was calculated and found out to be 72.56 % (Fig. 2).

4 Mathematical Calculation

Width of Indian Railways = 3.25 m; Diameter of each fan = 1.5 m, Range of Speed of Train (in India) (v) = 65–90 km/hr.

Now, Swept Rotor Area (A) = $3.14*(1.5/2)^2$ = 1.766 m^2 (radius of blade = 0.75 m).

From the relation,

$$\text{Power } (P) = 0.5*\varrho*A*C_p*v^3. \tag{3}$$

where P = Total Power that is Produced, ϱ = Air Density in kg/m^3, A = Rotor Swept Area, C_p = Coefficient of Performance (Taking, 0.59), v = Wind Velocity in m/s.

On substituting the values above, we get,

For v = 25 m/s;

$$P = (0.5 * 1.23 * 1.766 * 0.59 * 15625)\,\text{Watt} = 10.012\ \text{kW}$$

4.1 System Efficiency

It is defined as the ratio of total power produced (P) to the power contained by the wind (p).

$$\eta_s = P/p. \tag{4}$$

Here,

$$p = 0.5 * \hat{w} * v^2. \tag{5}$$

where $\hat{w}$ = Mass flow Rate (m^3/s), v^2 = Velocity of wind (m/s).

And

$$\hat{w} = A * v. \tag{6}$$

On substituting the values,
For v = 25 m/s, A = 1.766 m^2;
p = 0.5 * 1.766 * $(25)^3$ = 13.796 kW.
From above formulation, we get,
η_s = (10.012 kW/13.796 kW) * 100 %.

ηs = 72.56 %

5 Conclusion

The good response from the system efficiency calculations for the different speed range of train will certainly help us to switchover to this alternate source of energy. The installation cost is also minimal as it only requires a rigid design, construction, and alignment of the fan in a way that it extracts and produces better results.

Thus, if appreciated it can act very beneficial and ease for each one in the country as it involves 'CLEAN AND GREEN ENERGY' with minimum basic requirements.

References

1. http://instituteforenergyresearch.org/topics/encyclopedia/fossil-fuels/
2. https://www.google.com/patents/US2715912
3. http://www.sensaphone.com/pdf/DataCenterEbook.pdf
4. http://www.bloomberg.com/news/articles/2016-02-04/biggest-human-migration-to-greet-year-of-monkey-is-boon-for-fuel
5. http://cleantechnica.com/
6. http://inhabitat.com/german-trains
7. http://www.nytimes.com/2011/08/22/business/energy-environment/trains
8. http://www.greentechmedia.com/articles/read/railway
9. Market Barriers to Energy-Efficiency Investments, Ronald J. Sutherland, The Energy Journal, Vol. 12, No. 3 (1991), pp. 15–34
10. http://www.sciencedirect.com/science/article/pii/S0965856403000752
11. SAO/NASA Astrophysics Data System (ADS), Second-order solution of artificial satellite theory without air drag, Kozai, Y., Astronomical Journal, Vol. 67, p. 446 (1962)
12. http://physics.info/drag/
13. https://en.wikipedia.org/wiki/Drag_(physics)
14. http://energy.gov/eere/energybasics/articles/wind-turbine-basics
15. https://www.grc.nasa.gov/www/K-12/airplane/drageq.html
16. http://yourelectrichome.blogspot.in/2012/08/emf-equation-of-dc-generator.html

Implementation of Ladder Logic for Control of Pipeline Inspection Robot Using PLC

Varnita Verma, Roushan Kumar and Vivek Kaundal

Abstract In the modern world, the transportation of goods and services plays an important role in establishing good connections between the nations. The main source of transportation of major energy sources like fuel gases, petroleum, and other flow of gases and liquid has been done through pipelines, any crack, blow-holes, or damage inside the pipe may lead to major economic loss and can catches fire therefore the internal inspection of pipelines is needed. For inspection of narrow, deep, and hazardous environment inside the pipeline the robots is used. The control of robot has been done by programmable logic controller (PLC) and internal control of robot has been through human–machine interface (HMI). The control of robot has two parts in terms of programming. First, the development of ladder logic is done in Indraworks Engineering Software according to the sequence of operations and then simulates it on software itself to check the fulfillment of objectives. Second, developing the HMI Interface is for internal control of robot and easy access of operation. Touch screen has been used as HMI which is helpful in opting the size of pipe accordingly pipeline inspection robot will adjust its arms.

Keywords Pipeline inspection robot · Rexroth PLC · Industrial automation · HMI · Indraworks Engineering

Varnita Verma (✉) · Roushan Kumar · Vivek Kaundal
University of Petroleum and Energy Studies, Dehradun, India
e-mail: varnitaverma@yahoo.in

Roushan Kumar
e-mail: rkumar@ddn.upes.ac.in

Vivek Kaundal
e-mail: vkaundal@ddn.upes.ac.in

© Springer Science+Business Media Singapore 2017

R. Singh and S. Choudhury (eds.), *Proceeding of International Conference on Intelligent Communication, Control and Devices*, Advances in Intelligent Systems and Computing 479, DOI 10.1007/978-981-10-1708-7_113

1 Introduction

The flow of gases and liquid has been done through pipelines and the inspection of pipeline is must for proper transportation of gases and liquids and related to safety issues, for internal inspection of pipe conventionally, humans go inside the pipe which is harmful to the health of human. Therefore, the device has been created which was inserted in pipes to check for obstruction or damage [1–3]. This robot is capable of adjusting its arm from 30 to 40 cm and able to detect the intensity of damage inside the pipe this could be done through inspection camera mounted on the robot which helps in capturing the real-time images and processes the image through image processing. This robot is very useful for internal inspection of underground pipeline, sewage pipes, gas pipes, ac vent, etc., and easy repair of pipeline can be done after knowing the defect location of pipeline. The most popular nondestructive testing (NDT) techniques has been done with the help of camera, ultrasonic sensor, microwave technique, and 3D optical sensor. The size and shape of robot are dependent on the layout of entire pipeline structure [2]. Many pipeline inspection robots have been implemented before like PIRAT robot which is a nonautonomous tethered robot for the quantitative and automatic assessment of sewer conditions. Visual camera and laser scanner have been used as a sensory device. A human operator can operate the robot from a surveillance unit via a cable, with a length of 250 m (maximum). An expert system running on a workstation was responsible for data interpretation and damage classification [1]. For sewer inspection, a platform has been developed which is semi-autonomous and connected with surveillance unit by a cable named as Kanalroboter (KARO), it is having an inclinometers which will correct the tilt poses by wheel of robot and balanced them accordingly [2]. Kanal–Untersuchungs–Roboter-testplatform (KURT) is a six-wheeled autonomous un-tethered robot. A map of pipe net is needed for the navigation. Ultrasonic sensor, inclinometer, and CCD camera are used for inspection [3]. For drain pipe inspection, wireless radio communication system has been used by Ishikawa Tekkousyo in "The robot was developed based on drain pipe inspection robot, Mogurinko 250" [4]. Rotating probes with piezo-electric element have been used by "The Indian Institute of Technology Kanpur for internal inspection robot [4]. There are many nondestructive techniques which have been mentioned above along with non-contact inspection technique [5]. Classification of non-contact inspection techniques results into two techniques optical and no optical techniques. Non-contact optical inspection techniques include machine vision system, conventional optical instruments (optical comparators and microscopes), laser system (scanning laser device), linear array devices, and optical triangulation techniques. Non-contact non-optical inspection techniques include: electrical field techniques, radiation techniques, and ultrasonic inspection methods. In in-pipe inspection, robot has used machine vision (computer vision) in most of them because of the distinction is that machine vision tends to imitate the capabilities of the human optical sensory system. This includes not only the eyes, but also the complex interpretive powers of the brain [6]. CCD-based technique that is

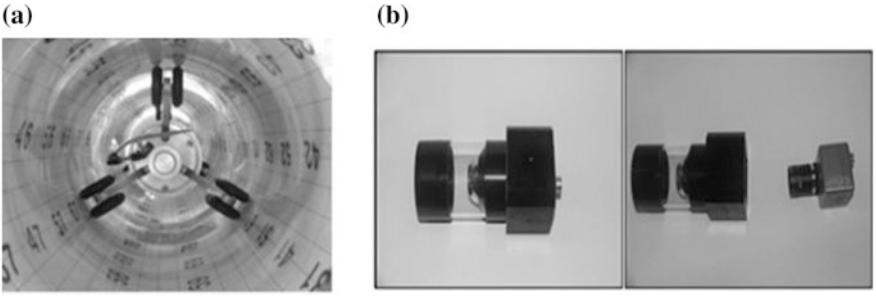


Fig. 1 **a** Image acquisition test pipe [7]. **b** CCD Camera and lens system

embedded in in-pipe inspection robot structure has some limitations that restrict their implementation like: (1) the lack of visibility in the interior of the pipes and (2) the poor quality of the obtained images because of difficult lighting conditions Fig. 1a, b.

2 Hardware System

The pipeline inspection robot is using the cable to control the robot and to transfer the information data to detect the defects inside the robot. Robot is controlled by wired remote to get a direct view to the pipe wall. PLC connection is also possible through wire and in case of failure of power we can easily access the robot. For control of robot, the Rexroth PLC L20 is needed along with Indraworks engineering software installed in laptops or PC's and the connection established between PLC and Indraworks engineering software can be used in many ways like Profibus, Ethernet cable, etc., after establishing the connections, the control of PLC input and output devices can be done by developing Ladder logic. Wall-pressed caterpillar-shaped robot consists of six motors in which three motor is used to control the length of arms and another three motors are used for linear motion control of robot. For each motor pushbutton switches have been provided. If Switch 1 is pressed then switch 4 cannot be true because at a time relay can move in single direction, this problem is been rectified with in the ladder logic program. In the motor switching Table S2 symbolizes the Switch_2 and, respectively, others have the same extension. The robot will have 3 DOF in X and Z direction and one rotatory shaft will rotate along 360 along with linear motion in x direction. Hence three motors which drive the standard wheel rotate in two directions that make robot to move in $+x$ and $-x$ direction and other three motor is used to adjust the arms of robot according to the size of pipe diameter which gave linear motion in $+z$ and $-z$ direction. The $+x$ and $-x$ direction motion can be done by developing the motor control circuitry which helps motor to rotate in clockwise and anticlockwise direction. The motor control circuitry consists of 24 V SPDT relay. For control of

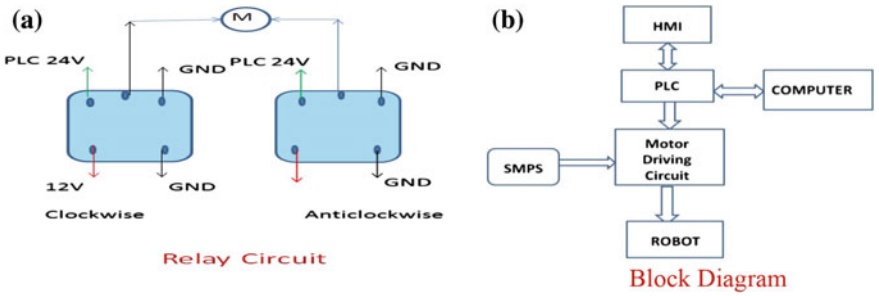


Fig. 2 **a** Relay circuit and **b** block diagram

each motor in clockwise and anticlockwise direction, two SPDT relays are used where common of two relays is connected to the motor and normally closed terminal (NC Terminal) has been grounded and normally open terminal (NO Terminal) has been connected to 12 V power supply and PLC output terminal has been connected to the one terminal of relay coil and other was grounded. When PLC output is high then accordingly relay got energized and rotates motor in either of direction (Fig. 2a).

3 Software Algorithms

Software algorithms are used to run the system according to the requirement. In this paper, the system has been controlled using Ladder Logic, which has been developed in Indraworks Engineering Software which is compatible with Rexroth L20 PLC. Software algorithms consist of two states naming of variables and Ladder logic implementation. The location of input switches and output port which are used in the ladder logic has been mentioned in the Figs. 3 and 4 with their data types.

The Ladder Logic for control of three arm motor in clockwise and anticlockwise direction in order to move the robot in clockwise and anticlockwise direction and three thread screw motor are used to adjust the size of robot. Start and stop switches are used to switch ON and OFF the device but the motor will run according to Switches allotted to them.

Control of each motor consists of a TON Timer and a TOF Timer to produce the square pulses which will run the DC motor attached to the arms and thread screw. The speed of motor can be controlled by adjusting the preset time of the timer which controls the pulse width and accordingly the speed of the motor is controlled. The flow chart of the system has been showed in Fig. 3.

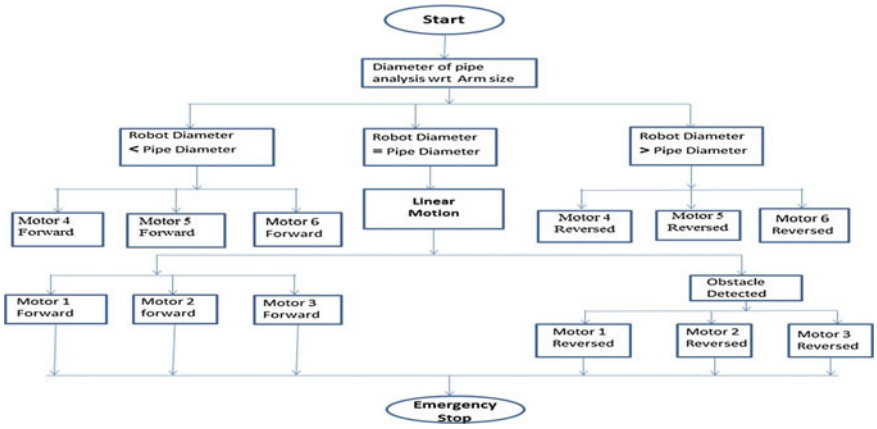


Fig. 3 System flow chart

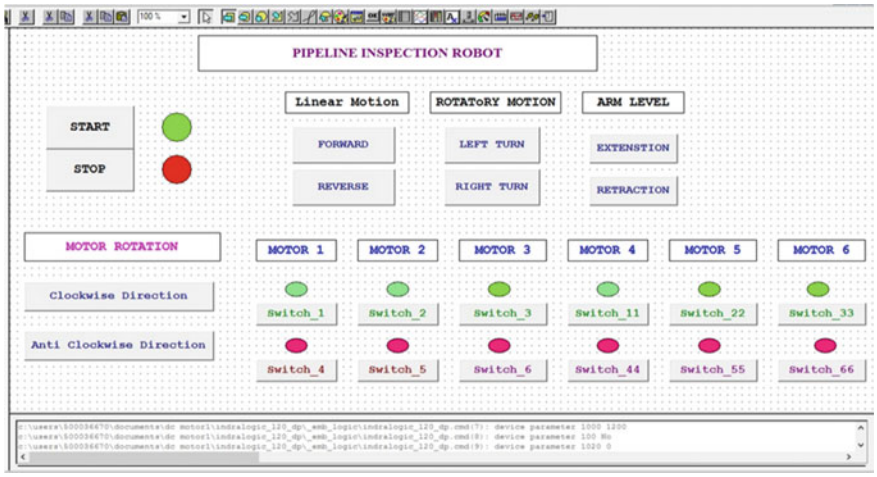


Fig. 4 HMI interface

4 Visualization and HMI

In Indraworks Engineering Software, the visualization tool provides an easy understanding of system parameters and gave visual platform to user to monitor the system and able to extract the useful content out of it. It works similarly as the SCADA software which builds the graphic user interface (GUI) between man and machine. It is used as indicator to know the status of switch whether the switch is pressed or not, various indicators are used in HMI to know the real-time operation. Monitor and control of robot can be done through HMI by pressing the pushbutton

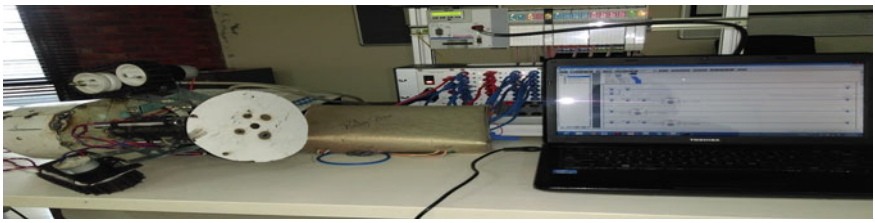


Fig. 5 Experimental setup

S.No.	Motor Driver Type	Torque of Motor (oz-in)	Speed of Motor (RPM)	Time Latency (ms)
1	Relay Circuit	0.05	10,786.3	26ms
2	L293d motor Driver	0.075	10,324.85	40ms
3	Variable Speed driver	0.1	9,863.6	82ms
4	IXDN404PI	0.125	9,402	150ms
5	SCR Dc Driver	0.15	8,940.9	350ms

Fig. 6 Comparison table of motor driver wrt to time latency

on HMI. Hence it gave an advance safety feature to the system. The layout of HMI has been shown below in Fig. 4.

In the HMI displayed, the motor 1, motor 2, motor 3 are used for linear and rotatory motion of robot while motor 4, motor 5, motor 6 have been used for adjusting the arms of robot according to the size of pipelines. Switches are the manual control of robot and indicator will show the status of switches.

5 Result and Discussions

The experiment setup of pipeline inspection robot has been shown in Fig. 5 which consists of Rexroth L20 PLC, RS232 cable, Onboard and Inline I/O's, wall-pressed caterpillar-shaped pipeline inspection robot, motor driver circuit, different push-buttons, and toggle switches and HMI. The control robot through HMI has been properly done.

The total machine cycle used in ladder logic is of 13 rungs each rung will take 2 ms with timer hence total time taken by robot to complete one Scan cycle is 26 ms and comparison of different motor driver types with each other's is shown in Fig. 6. Hence implementation of ladder logic will control the pipeline inspection robot more effectively with less duration of time.

References

1. R. Kirham, P.D. Kearney, K.J. Rogers, J. Mashford, PIRAT: "A system for quantitative sewer pipe assessment", The International Journal of Robotics Research 19 (11) (2000) 1033–1053.
2. H.B. Kuntze, H. Haffner: "Experiences with the development of a robotvb for smart multisensoric pipe inspection", in: Proceedings of the IEEE International Conference on Robotics and Automation, Leuven, Belgium, 1998.
3. F. Kirchner, J. Hertzberg: A prototype study of an autonomous robot platform for sewerage system maintenance, Autonomous Robots 4 (1997) 319–331.
4. H. Schempf, Explorer-ii: Wireless Self-powered Visual and NDE Robotic Inspection System for Live Gas Distribution Mains, Tech. Rep., Carnegie Mellon University, 2006.
5. Zin, Md Raziq Asyraf Md,Sahari, Khairul Salleh Mohamed, Saad, Juniza Md, Anuar, Adzly, Zulkarnain, Abd Talip, Development of a Low Cost Small Sized In-Pipe Robot, Procedia Engineering 41, (2012), 1469–1475.
6. Skjelvareid, M.H., Birkelund, Y. and Larsen, Y., 2013. Internal pipeline inspection using virtual source synthetic aperture ultrasound imaging, NDT & E International, 54(0), 2013, pp. 151–158.
7. Choi, H.R. and Ryew, S.M., Robotic system with active steering capability for internal inspection of urban gas pipelines, Mechatronics, 12(5), 2002, pp. 713–736.

Design of Wearable Device for Muscle Fatigue Monitoring

Sweety Siwach, Anita Gehlot and Anshuman Prakash

Abstract Exercise is very beneficial to our health but evidence show that intense training and heavy exercises out by fortitude athletes can cause skeletal muscle damage, which is known as muscle fatigue. For athletes, muscle fatigue is perhaps one of the major causes of degradation in their performance. There are various methods to monitor the muscle fatigue, of which surface electromyography is an important one. In this research work, a system is proposed to monitor muscle fatigue continuously and transmit the data wirelessly to a handheld portable device using RF module. A threshold point is set by calculating the average mean and in case of any danger a notification will be given by the device indicating onset of fatigue.

Keywords Muscle fatigue monitoring · sEMG · Microcontroller · Wearable sensor

1 Introduction

In the nineteenth century the prevailing view was that fatigue was caused by processes in the central nervous system. Mosso (1892) has been quoted as advocating this view, but actually he clearly demonstrated that muscle fatigue could be entirely peripheral. Mosso was the first to record the decrease in muscle force by means of an "ergograph" during fatiguing contractions in humans, and he found a comparable decline in force both during voluntary contractions and during stimulation of the muscle. There are mainly two types of fatigue, high frequency and low frequency fatigue. In high frequency fatigue, the muscle fatigues very rapidly on continuous workout but also recovers after a short rest while low frequency fatigue is one in which fatigue develops more slowly with low intensity. Fatigue represents a reduction in the capability of muscle to generate force. So far two main causes of

Sweety Siwach (✉) · Anita Gehlot · Anshuman Prakash
University of Petroleum and Energy Studies, Bidholi via Prem Nagar, Dehradun, India
e-mail: ssiwach112@gmail.com

© Springer Science+Business Media Singapore 2017

R. Singh and S. Choudhury (eds.), *Proceeding of International Conference on Intelligent Communication, Control and Devices*, Advances in Intelligent Systems and Computing 479, DOI 10.1007/978-981-10-1708-7_114

muscle fatigue are discovered, first one was observed when nerve's ability to generate a sustained signal is limited and second comes the declined ability of the muscle fiber to contract while some other causes lack of essential nutrients and oxygen in muscle and also accumulation of waste products mainly lactic acid.

Many systems are developed based on different techniques to monitor the muscle fatigue. [1] Dayan, et al. proposed a system a signal spike and peak counter system which is then correlated with median frequency for monitoring the muscle fatigue [2] Ahamed, et al. proposed a system in which muscle fatigue is monitored by calculating average EMG, the highest peak of the signal and root mean square (RMS) values after recording the EMG values. [3] Tanaka, et al. proposed a system which uses myoelectric signals to monitor the muscle condition. [4] Pioggia, et al. proposed a system in which a wearable platform is developed to monitor the muscle fatigue by observing the sEMG in absence and presence of fatigue after which STFT of signal is calculated in absence and presence on fatigue. [5] Karagözoğlu, et al. proposed a system which used FFT on platform MATLAB to calculate the power spectrum of the signals obtained. [6] Na, et al. developed a muscle fatigue monitoring system by observing the variation in the muscles before the fatigue is approached and after the fatigue is approached. [7] Cifrek, et al. proposed a system were classical and modern signal processing techniques are explained which includes frequency domain, time domain, time–frequency, and time scale representations. [8] Kang-Ming, et al. proposed a system in which (DWT), (EMD), and (EEMD) are calculated to monitor the muscle fatigue progression.

1.1 Proposed System

The system consists of a real-time monitoring of muscles and wirelessly transmit the data using RF module to a handheld portable device and also will notify the user when the fatigue is approached (Fig. 1).

2 Methodology

The methodology behind this work started from developing a data logger in lab VIEW. The data logger consists of a wave form diagram indicating EMG values in amplitude and time relationship form other part consists of a table having EMG value in volts with date and time of recording data. Next step started by collecting muscle fatigue data of two specific groups, one those who were suffering from muscle fatigue and other who were not suffering from muscle fatigue and after collecting data it was observed that the average mean values of both the groups were different. After observing the average mean values, a range was set with the lowest value of muscle fatigue and the maximum value of muscle fatigue, i.e.,

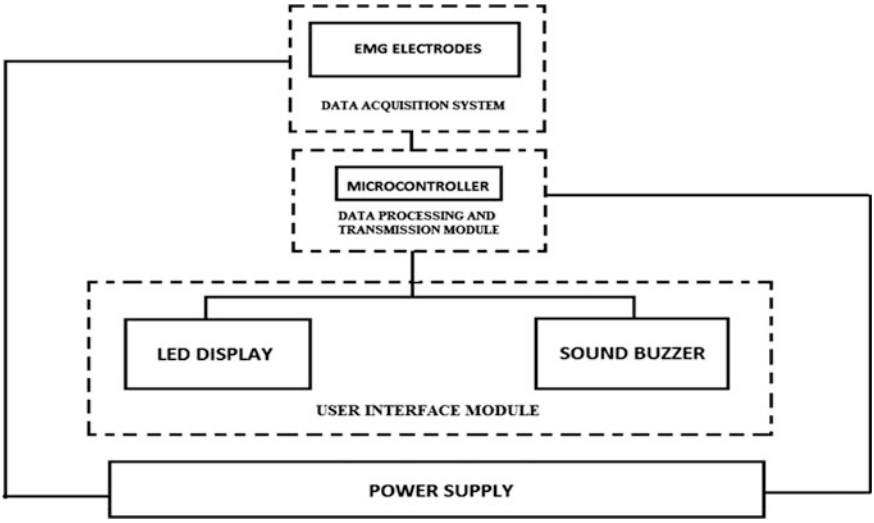


Fig. 1 System block diagram showing the main modules used in the system. The data acquisition system consists of EMG electrodes through which data is recorded. Data processing and transmission module consists of arduino uno which is a 8 bit microcontroller and works on 16 MHz frequency. Next part consists of user interface module containing led display or sound buzzer depending on user requirement

indicating onset of fatigue. Now when the real-time monitoring of muscles will be carried out, if the value exceeds the specified range, a notification will be sent to the user or the coach regarding the danger.

3 Algorithm

The flow chart shows the working model of the proposed system in which data from EMG sensor is continuously monitored and wirelessly transmitted through RF module to a handheld device to indicate the status of subject. A threshold value is set after careful examination of both the groups, first group having person affected of muscle fatigue and second group having persons suffering from muscle fatigue. If the recorded value is same as the threshold value, a notification in the form of led or buzzer is sent to the subject. This process is continually repeated (Fig. 2).

4 Result and Simulation

Figure shows the two different waveforms of recorded EMG values. After obtaining the couple of readings through electromyography sensor from a group of people suffering from muscle fatigue and other group of people who are free from muscular

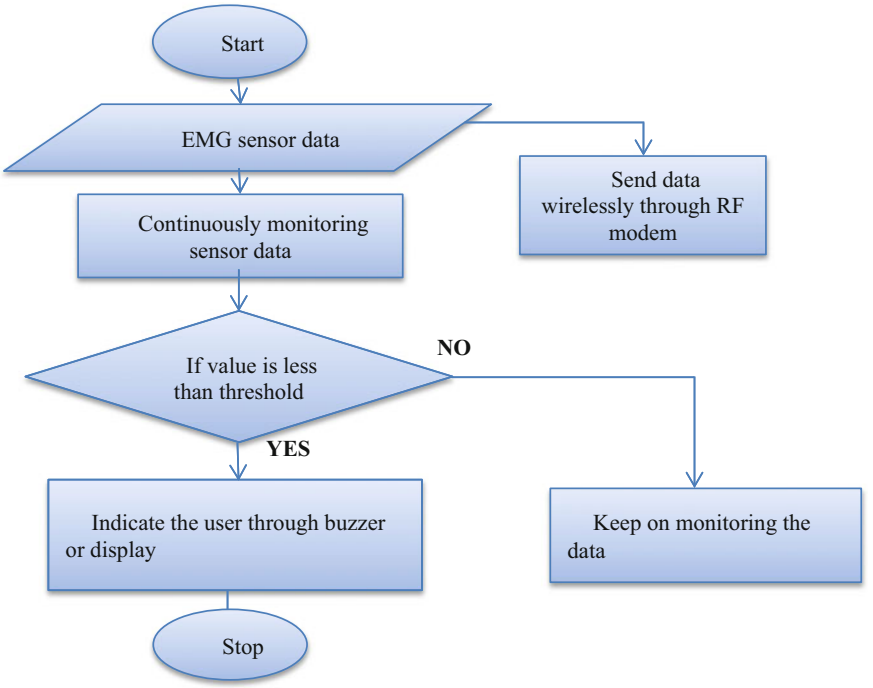


Fig. 2 Flow chart of the proposed system

fatigue, a threshold value is set. This value is decided. Now when the real-time monitoring is carried out, the data is continuously transferred to a handheld portable device with the help of RF module which is connected on both the end, i.e., transmitter and receiver end. When the value from the sensor is crossed above the threshold value, an indication in form of alarm or led is given as output (Figs. 3 and 4).

5 Discussion and Conclusion

Muscle fatigue has not only been observed in athletes but also in elderly people. Monitoring the muscle fatigue can also be useful in rehabilitation, because excessive exercises can be very dangerous to our muscles. Many technics are used to monitor the muscle fatigue some of them are using power spectrum, STFT, mean and median frequency observation and many more. The technique used here is to observe the average mean between the two groups (first group is for people where no muscle fatigue is observed and second one consists of people suffering muscle fatigue). So it is concluded that a wearable device is developed which can give the status of person's muscle contraction activity and can also alert them of the danger.

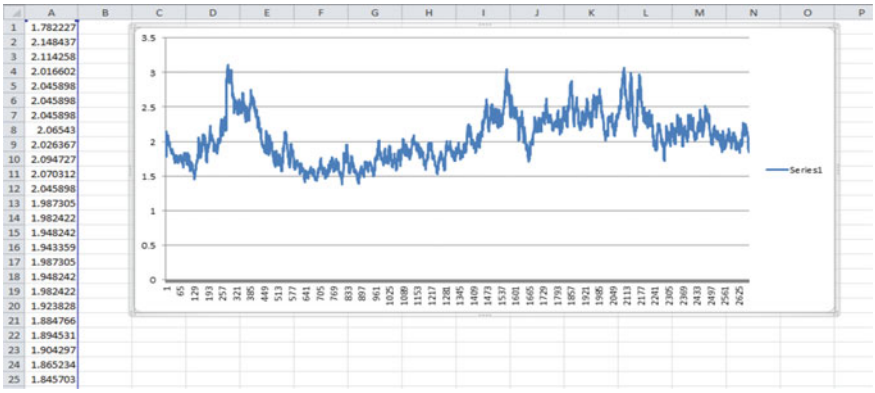


Fig. 3 shows waveform in presence of fatigue. As the waveform shows that the amplitude is decreasing at every instant which means person suffering from muscle fatigue cannot withstand more muscle contraction and failed to sustain the force. From initial stage to the final stage of recording procedure their muscles witness in pain

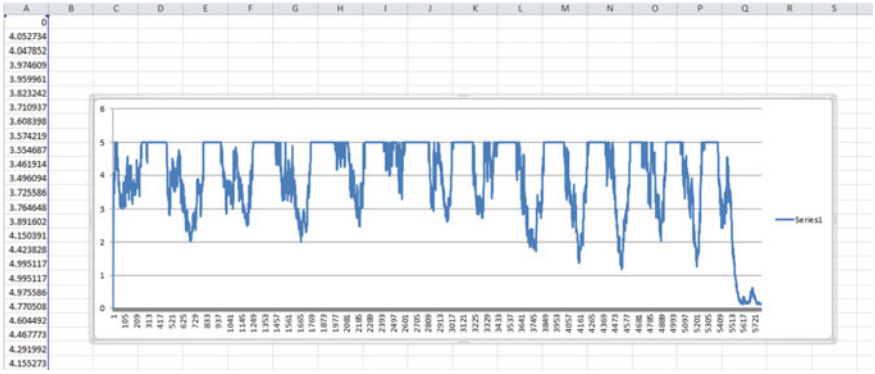


Fig. 4 shows the EMG values and the recorded amplitude waveform of persons not suffering from muscle fatigue. As the waveform shows here that after a particular value the graph is gradually falling down which shows the decline in muscle activity also referred to as initial stage of muscle fatigue

Of course, further experiments are required to confirm the validity of the monitoring system.

The research can be further extended from monitoring to controlling. Until now, a handheld portable monitoring system is developed but further these EMG signals can be used to control mechanical systems like robotic moments or automate home, i.e., it can control the turning on and off of lights, fans, or other gadgets. There are systems which can use EMG signals to control the forward and backward moment of the robot similarly further actions of the robot can be controlled.

References

1. Dayan, O., Spulber, I., Eftekhar, A., Georgiou, P., Bergmann, J., & McGregor, A. (2012, November). Applying EMG spike and peak counting for a real-time muscle fatigue monitoring system. In *Biomedical Circuits and Systems Conference (BioCAS), 2012 IEEE* (pp. 41–44). IEEE.
2. Ahamed, N., Sundaraj, K., Ahmad, R. B., Rahman, M., Islam, A., & Ali, A. (2012, November). Non- invasive electromyography-based fatigue detection and performance analysis on m. biceps brachii muscle. In *Control System, Computing and Engineering (ICCSCE), 2012 IEEE International Conference on* (pp. 302–306). IEEE.
3. Tanaka, Mami, Takeshi Okuyama, and Kazuhiro Saito. "Study on evaluation of muscle conditions using a mechanomyogram sensor." *Systems, Man, and Cybernetics (SMC), 2011 IEEE International Conference on*. IEEE, 2011.
4. Pioggia, G., Tartarisco, G., Ricci, G., Volpi, L., Siciliano, G., De Rossi, D., & Bonfiglio, S. (2010,November). A wearable pervasive platform for the intelligent monitoring of muscular fatigue. In *Intelligent Systems Design and Applications (ISDA), 2010 10th International Conference on* (pp. 132– 135). IEEE.
5. Karagözoğlu, Bahattin, Waleed H. Sindi, and Ahmed A. Al-Omari. "Design and development of a practical muscle fatigue monitor." *GCC Conference & Exhibition, 2009 5th IEEE*. IEEE, 2009.
6. Na, Y., Kwon, S., Kim, J., & Choi, C. (2013, October). Variation of dynamic muscle model during fatigue-inducing voluntary contraction. In *Systems, Man, and Cybernetics (SMC), 2013 IEEE International Conference on* (pp. 4854– 4859). IEEE.
7. Cifrek, M., Medved, V., Tonković, S., & Ostojić, S. (2009). Surface EMG based muscle fatigue evaluation in biomechanics. *Clinical Biomechanics*, *24*(4), 327–340.
8. Chang, Kang-Ming, et al. "Exercise muscle fatigue detection system implementation via wireless surface electromyography and empirical mode decomposition." *Engineering in Medicine and Biology Society (EMBC), 2013 35th Annual International Conference of the IEEE*. IEEE, 2013.

A Novel Design of Inexpensive, Heavy Payload and High Mobility ORQ Robot

Praveen Kumar, Parag Verma, Rajesh Singh and Ravi Kumar Patel

Abstract This paper presents the novel design of an Off Road Quadruped (ORQ) Robot having multiple purposes to be applied in uneven terrain. The proposed design is characterized by modular design, heavy payload and high mobility capabilities. The design includes the four 2-DOF Flipper, the robot body and its controlling electronics components. The proposed robot is able to smoothly traverse on simple tracks and off road tracks as well while carrying additional payloads with high mobility. Through this paper we have been induced a quadruped robot design, energy stored by robot and its sufficient used to perform critical actions like uneven terrain. We proved mathematically the design mobility and compared the ORQ robot with other existing quadruped robots w.r.t. speed, payload, navigation technique, accessibility range, design cost, working locations, etc.

Keywords Quadruped robots · Off Road Quadruped (ORQ) robot design · Flipper · Walking in off road terrain · Robot mobility mathematical calculation · Off Road Quadruped robot compressions

Praveen Kumar (✉)
Robotics Engineering, University of Petroleum and Energy Studies, Dehradun 248007, Uttarakhand, India
e-mail: kmrpraveen89@gmail.com

Parag Verma
Computer Science and Engineering, Neelkanth Institute of Engineering & Technology, Meerut 250110, Uttar Pradesh, India
e-mail: parag_verma@yahoo.com

Rajesh Singh
Robotics Institute R&D, University of Petroleum and Energy Studies, Dehradun 248007, Uttarakhand, India
e-mail: rsingh@ddn.upes.ac.in

R.K. Patel
Department of Electronics and Telecommunication, Government Polytechnic College, Waidhan 486886, Madhya Pradesh, India
e-mail: ravikumarpatel28@gmail.com

© Springer Science+Business Media Singapore 2017

R. Singh and S. Choudhury (eds.), *Proceeding of International Conference on Intelligent Communication, Control and Devices*, Advances in Intelligent Systems and Computing 479, DOI 10.1007/978-981-10-1708-7_115

1 Introduction

In various conditions, there is high requirement of mobile platforms that able to move in areas with uneven terrain, where normal wheeled vehicles cannot be travel [1, 2]. Examples include military search, patrol, surveillance operations, and rescue tasks and carrying payloads as well. Some patrol and surveillance robots use small size models for accessing easy site tasks [3–5]. However, the small size robots can face problems while climbing or alighting over the steps higher than their heights and wants high response [6, 7]. There are some walking and jumping robots which try to move over the high obstacles by using pneumatic cylinders that are effectively used in better patrol and surveillance purpose, but they persevere some problems like gravity and stability. Unlike or walking robots or flipper-based robot are characterized by high mobility and heavy payload carrying in rough terrains [8, 9].

The main goal of this paper is to present a high responsive innovative, modular and inexpensive design of a four-flipper (2-DOF). It gives the details to the hardware design and controlling system as well. In section two, the mechanical design of 2-DOF flippers are explained. In section three, details about the uneven terrain and strategies of ORQ robot over them. In section four, mathematically prove the design response and ORQ robot acceptability over other petrol and survey robot used under military and defense agency. Section five shown the experimental result and last section gives the conclusion and future scope of the ORQ robot.

2 Mechanical Design of ORQ Robot

The ORQ Robot tracked with wheel vehicle. They are quite active, fast in uneven terrains and relatively light weight. The structure is constructed in mild steel and all the mechanical joints are effectively works with gears.

2.1 Body and Driving System

A rectangular hollow square pipe of cast iron with three-sided wrapped by thick aluminum sheet to be the base frame. The rectangle hollow pipe gives the high strength with low weight to the base frame. The locomotion driving system, all motors and the mechanical joints sets and motor driven batteries are placed in this base frame in order to have the low level center of gravity principal [8, 10]. The gears, flippers, external sensor, and electrical components are mounted on this chassis.

The typical design of ORQ robot is simple, modular, and built from off-the-shelf components. It consist four-flippers that are walking as stiff legs based on the momentum transfer principle. Each of its flippers is composed of one drive wheel controlled via electric motor. Six DC motors are used four used by each flipper to

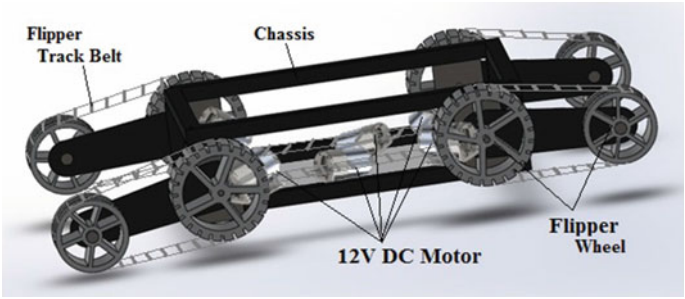


Fig. 1 Model design of ORQ robot

control the flipper action and two 12 V DC motors are used for driving base frame separately and each are controlled bidirectionally. The ORQ robot design is shown in Fig. 1.

Whenever, a solid body slides over a rough or smooth stationary surface then a force is exerted at the surface of contact by the moving body [7, 11]. This applied force is frictional force and is always acting in the opposite direction of moving body. If the slope of climbing is 45° as shown in Fig. 2, then the minimum torque required can be calculated by second law of Newton [6].

The ORQ Robot can cover the steps up to 45° because the height of the large wheel in flipper is 18 cm.

$$F = ma \tag{1}$$

Assume the linear acceleration and thus the rotational acceleration of the wheels to be zero.

$$a = 0 \tag{2}$$

The frictional forces

$$\begin{aligned} F &= \mu R \\ &= 0.35 \times 20 \times 9.81 \times \cos 45^\circ \left\langle \begin{array}{l} \text{The estimated mass of the ORQ Robot is } 20\,\text{Kg} \\ \text{Coefficient of friction is } \mu = 0.05 \end{array} \right. \\ &= 48.55\,\text{Nm} \end{aligned}$$

and the weight component $(W_m) = \text{Mg}\sin\emptyset = 20 \times 9.81 \times \sin 45^\circ = 138.73\,\text{Nm}$

$$\begin{aligned} \text{The force at the large wheel of the robot} &\geq \text{weight component} + \text{Frictional Forces} \\ &= 138.7 + 48.55 = 87.25\,\text{Nm} \end{aligned}$$

so the torque required by the motor $T = 187.25/2 = 93.62\,\text{Nm} \approx 100\,\text{Nm}$.

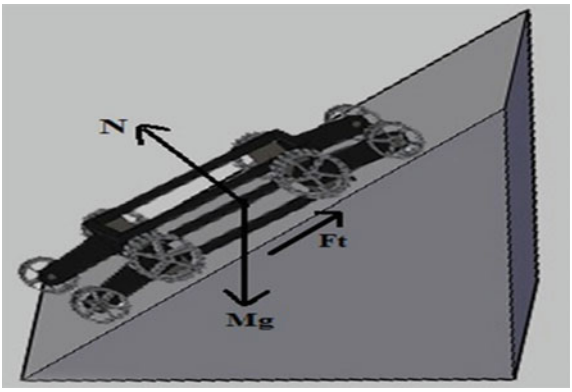


Fig. 2 Free body diagram of force applied on ORQ robot

The locomotion system consists of two separate sides mounted with the rectangular body frame while a motor independently drive the track at each side. So the desired torque is obtained as; the required torque of the motor is = $T/2 \approx 50$ Nm.

2.2 2-DOF Flippers and Driving System

The flippers are designed in order to raise the charging terminal up for better connectivity. In ORQ robot flipper used the track belt system. Track belt system provides higher griping over slipping track and provides high stability during robot climb over vertical and horizontal obstacles. The robot flipper consist two wheel and one track belt, which is shown in Fig. 3. Another 12 V DC motors and transmission chains are required for controlling the driving motion of flipper. For this action separate commands are generated by the controller. In this system, the each large wheel (18 cm in diameter) direct connected with its own individual small wheel (12 cm in diameter) and uses the principal of direct transmission with connected via track belt and free moving capability.

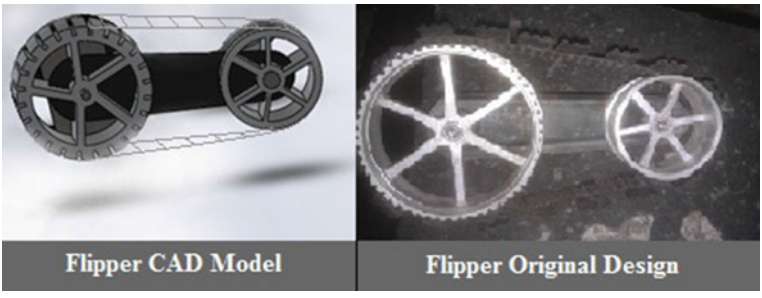


Fig. 3 2-DOF ORQ robot flipper

2.3 Mechanical Joints

In ORQ robot the flipper is reacting as the mechanical arms. These allow the ORQ to expand its flippers whenever it needs to lift up or down the base frame. In Fig. 12 shown the drawing of flipper works as mechanical arm [2, 12]. Because the heavy payload at the top of the base and the flipper weight is fixed, DC motor with gear set still can regulate the joint angle quite well. Let 'h_1' be the height form large wheel bottom to base joint and 'h_2' be the height form small wheel bottom to the base joint. The angle of rotation is determined by 'θ_1' and 'θ_2'. If the angle could change between 0° and 360° then the work space should be cylindrical at the height form h_1 to h_2. It takes four steps to takes complete one 360° rotation of the flipper.

3 Working Methodology of ORQ Robot

ORQ Robot is a novel design that characterized by a set of arms (flippers) that position pulleys to the front or back of the robot with equal agility that to provide the mobility of the robotics technology that works in uneven terrain and smooth surface as well.

3.1 Off Road Terrain

An Off Road terrain or uneven ground considers when an obstacle over average height 'h' (where h = ½ Length of flipper) traps the robot movement (Fig. 4).

ORQ Robot is able to climb or alight of height greater than its flipper length. To be tracked out the vertical obstacle and horizontal gap on the ORQ robot path, takes an example of robot climb and alight on stairs.

The vertical obstacles or the horizontal gap in the path of the robot may vary in sizes then ORQ Robot can climb the vertical obstacles up to slightly greater than its flipper length [13, 14]. In our design, we used the rubber belt over the flipper that

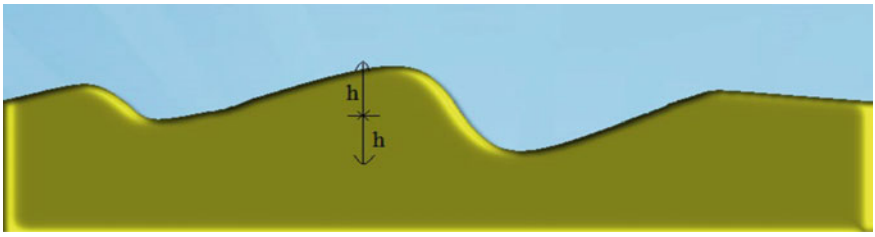


Fig. 4 Off road terrain

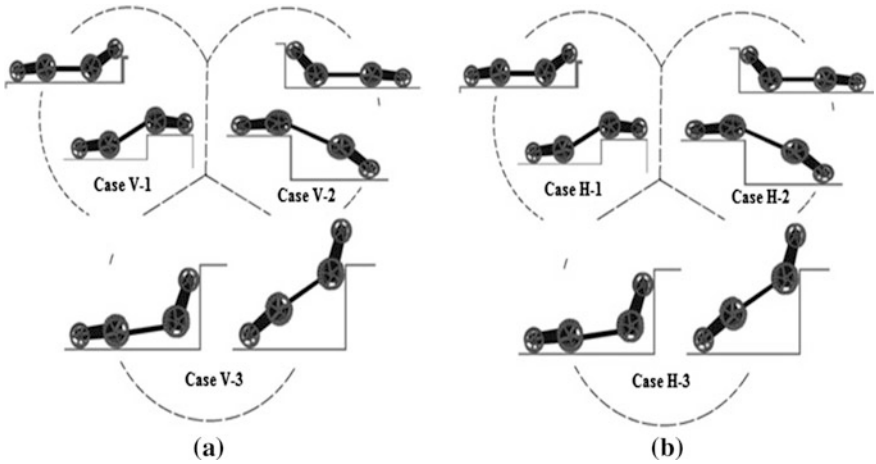


Fig. 5 Three wondering cases of vertical obstacle **a** and horizontal gap. **b** in ORQ robot path

helps to the robot to easily climb the vertical obstacle and alights horizontal gap of height up to its length (Fig. 5).

Cases of vertical obstacle: Three wondering cases of vertical obstacle in robot path as follow:

- Case V-1: If the height of vertical obstacle is less than length of flipper.
- Case V-2: If the height of vertical obstacle is equal to the length of flipper.
- Case V-3: If the height of vertical obstacle is greater than length of flipper.

Cases of horizontal gap: Three wondering cases of horizontal gap in robot path as follow:

- Case H-1: If the length of horizontal gap is less than length of flipper.
- Case H-2: If the length of horizontal gap is equal to the length of flipper.
- Case H-3: If the length of horizontal gap is greater than length of flipper.

Due to its modular design ORQ Robot is capable to track the gap of greater than twice of the flipper's length. But in this case it happen the robot consider vertical obstacle track as well.

4 Mathematical Operation of the Design Response

The ORQ Robot design is high responsive in various factors based in its compact design their responsive factor mathematical proves areas.

4.1 Maximum Speed of ORQ Robot

Let the maximum speed of motor used under ORQ Robot is 1000 rpm and the gear ratio is 1:15. So the speed to wheel is 65 rpm.

- The diameter of large wheel in flipper of the robot = 180 mm or 18 cm or 0.18 m
- The circumference of wheel = π × diameter of wheel = π × 0.18 m = 0.5654867 m

$$= \text{Circumference of Wheel} \times \text{Speed of Motor}$$

- The speed of the robot $= 0.5654867\,\text{m} \times 65\,\text{rpm} = 36.7566\,\text{m/min}$
$= 2.2054\,\text{km/h}$

4.2 Energy of the ORQ Robot

The energy factor is a leading feature to explain robot workability. Energy is not only related to the battery (electricity) attached with robot, three different ways of energies that improves the ORQ robot performance, i.e., potential energy and kinetic energy [7, 15].

4.2.1 Potential Energy

The energy stored by a robot at its ideal condition. If a robot is at height 'h' or in static position at any point when it alight, than it contains some energy known as Potential Energy consumed by robot. Let us consider at certain height the potential energy absorbed by the robot is as (Figs. 6 and 7):

$$\text{Potential Energy of ORQ Robot} = \text{Mass of robot} \times \text{Gravity} \times \text{Height} = \text{mgh}\left(\text{kg-m/s}^2\right).$$

This energy required by ORQ Robot to travel over a certain height "*h*" is equal to the potential energy of the robot at height "*h*".

4.3 Kinetic Energy

The amount of energy required to accelerate or decelerate a robot is referred to kinetic energy. It is the resultant energy which absorb by robot motion.

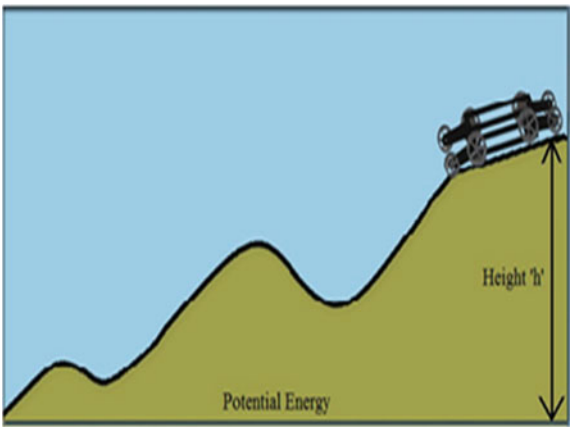


Fig. 6 Potential energy

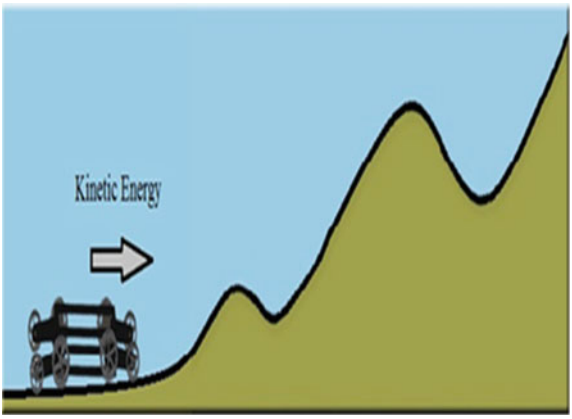


Fig. 7 Kinetic energy

The kinetic energy of ORQ Robot $= \frac{\text{mass of robot (kg)} \times \text{Velocity}^2\left(\frac{\text{m}}{\text{s}}\right)}{2}$ (where velocity is the desired maximum velocity).

5 Experimental Result

Experiments were conducted to demonstrate and verify the design and computations. In order to determine actual speed and quantify the result of ORQ Robot different trails performed over different terrains. To determine experimental speed for each terrain time taken to travel for 30 m was took as observation and than a mean time is decided with all four result to decide speed of the ORQ Robot.

5.1 Normal Terrain

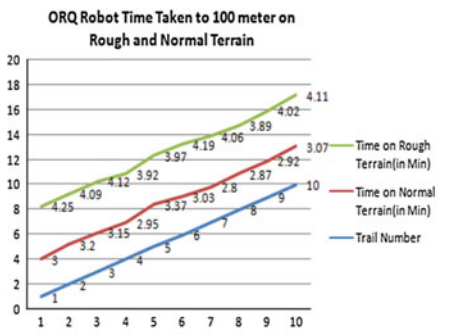
The ORQ Robot can travel at 90 % of its maximum speed on the normal terrain. Because of its design of four tracked and in normal terrain there is no use of flipper movement.

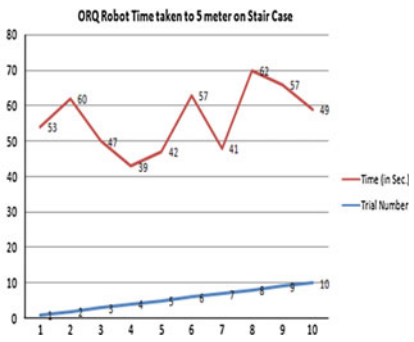
5.2 Rough Terrain

The ORQ Robot is specially designed to travel on the rough terrain with maximum vertical obstacle of 17 cm. But the speed of the ORQ Robot decreased on the rough terrain due to use of flipper to climb over obstacles.

5.3 Staircase

With the help of the Flipper ORQ ROBOT can climb stair case very easily but during climbing a gravitational force acting downward that reduces the speed of the robot. Also the problem of slipping on staircase causes the decrease in speed of the robot.





Maximum slope tested for the ORQ ROBOT is 55° on the plane terrain and 45° on rough terrain.

6 Comparison with Other Quadruped Robot

Factors	ASI-Chaos	Avatar-II	Daksh	Dominator	ORQ robot
Speed	6.5 kmph	3 kmph	N/A	6 kmph	2.3 kmph
Payload	50 lb	N/A	N/A	N/A	25 lb
Navigation	Remote controlled	Vision	Remote controlled	Remote controlled	Remote controlled
Range	500 m	300 m	500 m	30 km (LOS)	300 m
Locomotion	Track + flipper	Track + flipper	Track	Tracks	Track + flipper
Cost*	2 M $	9855 $	3 M$	N/A	1400$
Dimensions (l × w×h) in.	51.6 × 26.2 × 9.1	24.41 × 15.35 × 6.14	N/A	27.5 × 26 × 8.4	33.6 × 33.6 × 8

*Cost may vary as per the size

After comparing from above table with other robots ORQ ROBOT is much better if we take cost as factor. Because all other robots are much costly than ORQ ROBOT.

7 Conclusions

We introduced a novel design of ORQ robot for military purpose. We presented the model framework and the mathematical responsive acceptability of the robot performance. The robot performance and its vertical obstacle or horizontal gap successfully tracking has been briefly described. Its performance was observed to be excellent in uneven terrains. The development of ORQ robot can be easily adapted to fit in several other applications by adding more sensor and robotic arms on the top part of the robot. For better to access of its performance any Wifi/Internet module can be easily attach with it and high amount of memory storage can be use to enhance its information storage power.

References

1. Geva, Yam, and Amir Shapiro. “A Novel Design of a Quadruped Robot for Research Purposes”, International Journal of Advanced Robotic Systems, 2014.
2. K. Iagnemma and S. Dubowsky. Mobile Robots in Rough Terrain Estimation, Motion Planning, and Control With Application to Planetary Rovers, Volume 12 of Springer Tracts in Advanced Robotics. Springer, New York, USA, 2004.
3. iRobot’s Packbot 510 http://www.irobot.com/us/learn/defense/packbot/Specifications.aspx.
4. SD ATR http://www.superdroidrobots.com/shop/custom.aspx/all-terrain-robots/42/.
5. Robotex’s Avatar-II http://robotex.com/products/?n=avatar-ii.
6. Ioannis Chochlidakis, Yiannis Gatsoulis and Gurvinder S. Virk, “Open Modular Design for Robotic Systems”, Intelligent Systems Group, Department of Mechanical Engineering, University of Leeds, Woodhouse Lane, Leeds, West Yorkshire, UK.

7. Hirose S. (2001) Super mechano-system: new perspective for versatile robotic system. In: Rus D, Singh S (eds) Experimental robotics VII. Springer, Berlin, Heidelberg.
8. Hirose S., Kato K. (2000) Study on quadruped walking robot in Tokyo institute of technology —past, present and future. In: Proceedings of the IEEE international conference on robotics and automation, San Francisco, CA, pp 414–419.
9. QuadTrack-II: "A Remotely Operated Mobile Robot with Four Articulated Tracks", By;-Youngsoo Choi, Kyungmin Jeong, Yongchil Seo, Sung-uk Lee, Jaiwan Cho, Seungho Jung, Seungho Kim, Korea Atomic Energy Research Institute, Daejeon, Korea.
10. ASI's high mobility robot "Chaos" http://www.asirobots.com/ "Chaos an Intelligent Ultra-Mobile SUGV: Combining the Mobility of Wheels, Tracks, and Legs" Paul J Lewis1, Dr. Nicholas Flann2, Mitchel R. Torrie3, Eric A. Poulson4, Thomas Petroff Autonomous Solutions, Inc. 1946 South 1600 West, Young Ward, UT, USA 84339 Dr. Gary Witus6 Turing Associates, Inc. 1392 Honey Run Drive, An Arbor, MI, USA 48103.
11. Paul E. Sandin, "Robot Mechanism and Mechanical devices", McGraw-Hill.
12. Jeong, K., Kang J., Lee, G., Lee S., Seo Y., Jung S. and Kim S. (2006)"A Remotely Operated Robotic System for Urban Search and Rescue", ICCAS 2006.
13. J. Estremera and P. G. de Santos. Generating continuous free crab gaits for quadruped robots on irregular terrain. IEEE Transactions on Robotics, 21(6):1067–1076, 2005.
14. Oren Y. Kanner, Aaron M. Dollar, "Kinematic Design of an Underactuated Robot Leg for Passive Terrain Adaptability and Stability", Dept. of Mechanical Engineering, Yale University, New Haven, Connecticut, 06511.
15. I. M. Koo, T. D. Trong, Y. H. Lee, H. Moon, and H. R. Choi. Control of quadruped walking robot aidin-iii based on biomimetic inspired approach. In The 6th Asian Conference on Multibody Dynamics (ACMD), August 2012.
16. T. Kang, H. Kim, T. Son, and H. Choi. Design of quadruped walking and climbing robot. In Intelligent Robots and Systems, 2003. (IROS 2003). Proceedings. 2003 IEEE/RSJ International Conference on, volume 1, pages 619–624, 2003.

Hindi Dialect (Bangro) Spoken Language Recognition (HD-SLR) System Using Sphinx3

Virender Kadyan, Amitoj Singh and Parth Wadhwa

Abstract A Hindi dialect (Bangro) Spoken Language Recognition (HD-SLR) System is designed to recognize language from a given spoken utterance. Paper focuses on the influence of Hindi dialects, i.e., Haryanvi spoken by males and females of different age groups ranging from 18 to 40 years. The system is trained and tested with the help of Sphinx3 toolkit on Linux platform. Also, it has been tried with semicontinuous speech corpus in clean environment of around 5 h that includes 1000 distinct Hindi dialect words spoken in different parts of Haryana. The dialectal information of the input speech signals is extracted with the help of MFCC technique and the same system is then tested on the basis of utterance level. The Speaker Independent Semicontinuous (SISC) word recognition system has an average of 75–85 % accuracy rate by native and nonnative speakers of Hindi dialect.

Keywords Dialect recognition · Prosodic extraction · Feature extraction · Hindi speech recognition

1 Introduction

The Indian Constitution recognizes 22 official languages and 122 dialects that are spoken in different parts of the country. Many researchers and engineers are day by day thinking and trying to implement their thoughts to build a machine that can understand speech. After successful implementation of ASR in many European language, researchers and engineers are in a queue of making a perfect system for Indian language. In this study, a very small portion of Hindi Dialect Spoken Language Recognition system has been taken into account for making a machine that can understand people's native language and then respond accordingly. This is primarily because the impact of dialect plays an important role in an ASR system

Virender Kadyan (✉) · Amitoj Singh · Parth Wadhwa
CURIN, Chitkara University, Rajpura, Punjab, India
e-mail: Virender.kadyan@chitkara.edu.in

© Springer Science+Business Media Singapore 2017

R. Singh and S. Choudhury (eds.), *Proceeding of International Conference on Intelligent Communication, Control and Devices*, Advances in Intelligent Systems and Computing 479, DOI 10.1007/978-981-10-1708-7_116

which was not well considered in most of the researches till date. A dialect is basically a form of a language that is spoken in a particular area and that uses some of its own words, vocabulary, grammar, and pronunciations. The system has been trained with a small set of words from Haryanvi dialect which are spoken most commonly.

2 Literature Review

Until now, most of the studies focused on development of large or small vocabulary on Speech to Text (STT) interfaces for mobile devices and other hand held devices using sphinx tool [1]. The research which is being done in development of STT systems mainly focuses on standard pronunciation and does not consider various dialects. This work is also built on previous research work, but mainly targets dialectal feature of Hindi language along with the other parameters of Speech Technology. Sreenivasa Rao et al. [2] have explored speech features to identify different Hindi dialects and emotions. The author has considered spontaneous speech corpus which was spoken by male and female speakers. The techniques used to collect speech corpus were Auto Associative Neural Network (AANN), Support Vector Machine (SVM), Mel-Frequency Cepstrum Coefficient (MFCC), and these techniques help in extracting the prosodic features and spectral features to discriminate dialects and emotions. The prosodic features are represented with the help of duration of syllables, pitch, and energy contours. The AANNs were used to capture the nonlinear relations specific to dialects and on the other hand SVM performed dialects and emotion classification on the basis of discriminative characteristics. Results showed that dialect identification accuracy achieved around 81 % and emotions accuracy around 78 %. Shweta Sinha et al. [3] have explored four major dialects of speech corpus collected from 15 speakers (including both male and female) and used syllable of CVC structure as a processing unit. The prosodic and spectral features were considered to discriminate the dialects. The studies showed that the system performed well when they used spectral and prosodic features combined during training phase and achieved recognition rate of 79 %. Huang et al. [4] proposed a word-based dialect modeling technique for English language for a LVCSR-based system. The system consisted of three different dialect corpuses and a significant improvement was achieved using context adapted training algorithm which adapts the universal phoneme GMMs (Gaussian Mixture Model) to dialect dependent word using linear regression. Liu Mingkuan et al. [5] focused on a pronunciations variation modeling technology for Mandrian accent to get a context-independent and context-dependent accent specific confusion matrix. The suggested system was tested on an INTEL Shangai Mandrian corpus.

The target of research is to make a user friendly device or system that can interact with the user in his/her native language along with its dialectal information. Also, there are various other sections which are emphasized upon while making this Hindi dialect spoken language system. Some of the sections are:

- Phonetics description of Hindi dialect.
- Introduction of more phonetic distribution for a single word.
- Automation of system functionality using perl script and shell script on Linux Environment.

3 Hindi Dialect Spoken Language Recognition System

The proposed Hindi Dialect Spoken Language Recognition System (HD-SLR) is implemented using CMU-SPHINX consisting of cmuclmtk-0.7, sphinx3-0.6.3, sphinxbase-5perealpha, and sphinxtrain-5prealpha. The Linux operating system, Ubuntu of version 14.04 LTS has been used for the purpose of development. The proposed framework of HD-SLR system consists of two phases (Fig. 1).

3.1 Training Phase

This is the phase in which HMM-based system analyses the characteristics of the set of input sounds. It comprises three models.

3.1.1 Acoustic Analyzer

The main purpose of Acoustic (interdisciplinary science related to the study of physics of sound) Analyzer is to analyze the audio files and convert them into Feature Extractor files (MFCC). Initially, input sound waves are recorded as RAW (.raw) files with frequency of 16 kHz mono using dictate-phone. After this, Fileids files (for testing and training) are created which contain names and addresses of

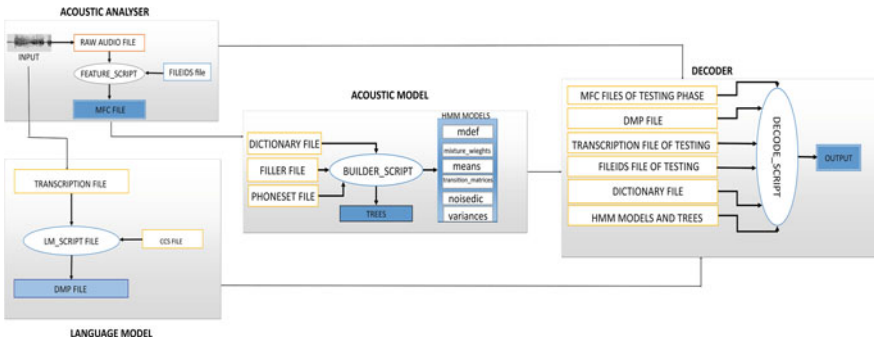
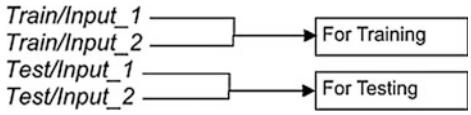


Fig. 1 Architecture of HD-SLR system

RAW audio files (that are to be trained and decoded, respectively) without extensions. They were written in the format of:



A feature script file is created by using a tool of sphinxbase. This tool converts RAW file in a feature extractor file, i.e., mel-frequency cepstrum file (.mfc) with the help of Fileids files. The most important thing which needs to be ensured is that the discriminatory information of the dialect should not be lost. Another factor of consideration during feature extraction is that the compact features must enable real time analysis [3].

3.1.2 Language Model Builder

The major requirement for speech recognition system is Language Model Builder. Technically, the major action performed by Language Model Builder is to convert the training transcription (transcription) file to DMP file, i.e., a binary format language model in the standard ARPA (Advanced Research Projects Agency) format. Basically, a transcription file for the training phase consists of all the letters and the words that are trained to generate word-frequency and vocabulary files. These files in turn are trained to generate unigrams, bigrams, trigrams, or n-grams models. These grams are then used to create binary format files, i.e., DMP files. These DMP files are further used in decoding section. The transcription file is also written for testing phase but is not trained, it actually calculates the accuracy and Word Error Rate (WER) of the input sound given for testing. The format of the transcription file is as follows:

<s > IS MEHANGAI NAY MHARAY DESH KEE CHARO KUON HILADEE </s > (Input_1)

A CCS file is also required by the system which contains phones of nonlinguistic sound (filler phones), i.e.,

<s>
</s>

The functionality of Language Model Builder is associated with the output of acoustic model. Then, a LM_SCRIPT file is created which comprises of commands from cmuclmtk tool.

3.1.3 Acoustic Model Builder

Acoustic models link the statistical representations of the speech signal with the expected phonetics of the hypothesis sentence. These speech signals are used in the forms of mfcc for the purpose of training of system. Phones are taken from two files, i.e.,

Filler file consists of representation of filler phones:

<s> SIL
</s> SIL
SIL SIL

Phoneset file contains all the phones that are used in the dictionary file:

AI
AH
AO
IX

The main purpose of Acoustic Model is to create HMMs (hidden Markov models) [6] which provide an effective framework of many algorithms or techniques to evaluate the probability of occurrence of sequence of observations. In HD-SLR system, Baum–Welch Algorithm is used to estimate the transition probabilities of Context-Independent (CI) HMMs. Next, refined context-defined phones are generated and HMM is built for every phone. The HMM distributions are combined to form similar state distributions. Baum–Welch Algorithm was executed with the help of sphinxtrain tool. BUILDER_SCRIPT is created that executes the scripts in a specific order. In HD-SLR system, CI-HMMs were built and the following files were obtained-mdef, variances, mixture_weights, transition_matrices, noisedict, and means for different grams. Decision Trees were also formed by training senons (group of similar states) that were formed and trained during the building process of CI-HMM models. Such a training of the system leads to the recognition of even those words which are not completely present in it, rather present as a part of some other word. After successful training of the system, it is ready for being tested.

3.2 Testing Phase

3.2.1 Decoder

This model uses the knowledge of Acoustic Analyzer, Language Model Builder, and Acoustic Model Builder. The decoder model recognizes the speech signal taken as input during testing phase as formulated by [7]:

$$W = \arg\max P(X|W)P(W)\ldots w.$$

In this model a dictionary file is used which contains the words along with their phonemes representations as:

AAG AAG
ARAB AE R AH B
ARAB(2) EY R AH B

Then DECODE_SCRIPT file is created that takes MFCC file from Acoustic Analyser, DMP file, testing transcription file, Dictionary, Trees, and HMM models from Acoustic Model Builder to generate the required pattern. Execution of DECODE_SCRIPT creates an output file that consists of the decoded part of the given speech signal.

4 Result

The performance of the proposed HD-SLR system is calculated by:

$$\text{Tested Signal Percentage Accuracy} = (N - I - S - D/N) * 100,$$

where N is the total number of words, I is the insertion error, S is the substitution error, and D is the deletion error in a spoken dialectal sentence. The result analysis of the system is done in two scenarios—one with same semicontinuous sentence that are used in the training and testing phase and the other which has not been used in training. The second factor on which the performance of the system is analyzed is type of speaker, i.e., native or nonnative speaker of Hindi sentences that contain dialectal information. The native speakers' accuracy comes out to be 100 % for small length sentences whereas nonnative speakers' accuracy comes out to be above 90 % when the input is same sentences used for training and testing both, as shown in Fig. 2. On the other hand Fig. 3. shows the performance of system for different sentences that are not involved in training phase but contain words present in system database.

The native speakers' accuracy is adjudicated to be around 82 % whereas non-native speakers' accuracy comes out to be in a range of 72–76 %; again less than that of the native speakers.

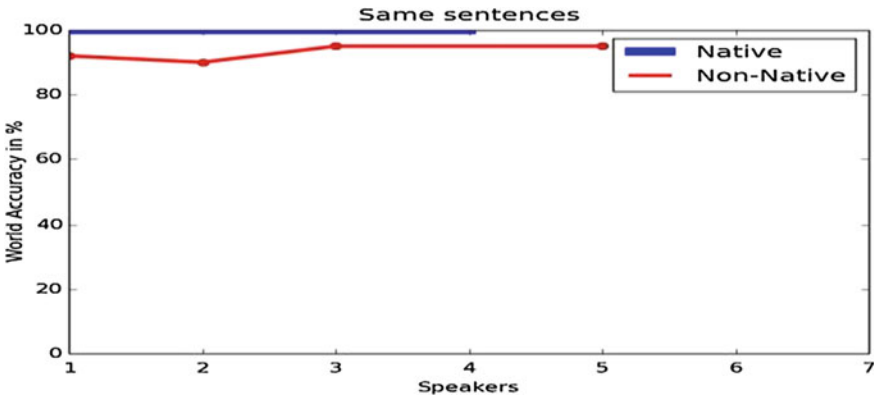


Fig. 2 Shows the graph plotted for same sentences which were used in training as well as testing phase

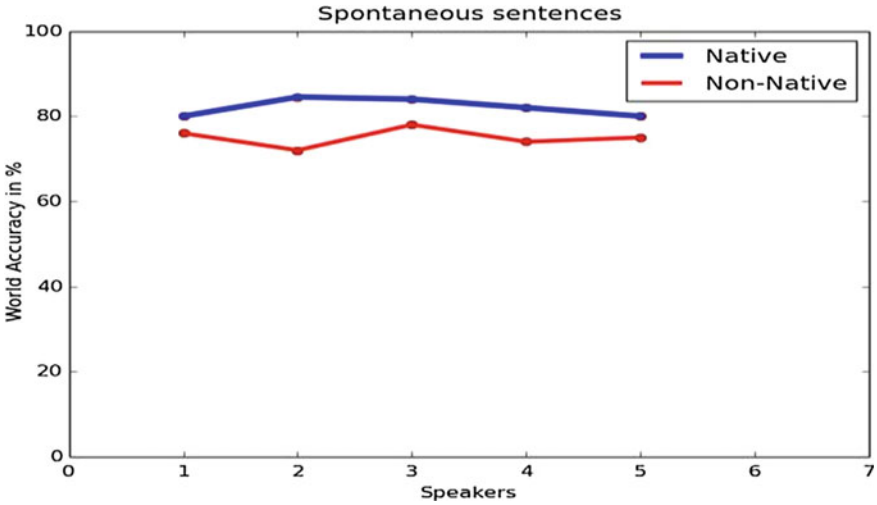


Fig. 3 Shows the graph plotted for different sentences (i.e., spontaneous sentences) which were used in testing as compared to those in training

5 Conclusion

In a country like India, with diverse languages, such a device/system becomes an indispensable part to provide people with a highly interactive environment. The goal of HD-SLR system is to make it nearer to the state of the art of other Hindi Dialect ASR systems. The system performed well for around 5 h of Hindi dialectal semicontinuous words. Future target will be to improve the recognition rate for large vocabulary of commonly spoken Hindi dialect. The system can also be

expanded by including large masses of different age groups in building of speech corpus and also by including more dialectal area of Hindi so that we are able to make a robust, accurate, and fast automatic speech recognition system.

Acknowledgments The authors would like to thank Ms. Nitika Gupta for her kind cooperation and support in building speech corpus.

References

1. Huggins-Daines, D., Kumar, M., Chan, A., Black, A. W., Ravishankar, M., and Rudnicky, A. "Pocketsphinx: A free, real-time continuous speech recognition system for hand-held devices." IEEE International Conference on Acoustics, Speech and Signal Processing, ICASSP, Vol. 1. IEEE, (2006) 1–1.
2. Rao, K. S., and Koolagudi, S. G. "Identification of Hindi dialects and emotions using spectral and prosodic features of speech". IJSCI: International Journal of Systemics, Cybernetics and Informatics 9.4 (2011) 24–33.
3. Sinha, S., Jain, A., and Agrawal, S. S. "Speech processing for Hindi dialect recognition." Advances in Signal Processing and Intelligent Recognition Systems. Springer International Publishing, (2014) 161–169.
4. Huang, R., Hansen, J. H., ***n*** Angkititrakul, P. "Dialect/accent classification using unrestricted audio." Audio, Speech, IEEE Transactions and Language Processing, 15(2) (2007) 453–464.
5. Liu, M., Xu, B., Hunng, T., Deng, Y., and Li, C. "Mandarin accent adaptation based on context-independent/context-dependent pronunciation modeling." IEEE International Conference, Acoustics, Speech, and Signal Processing. ICASSP. Proceedings Vol. 2. IEEE, (2000) 1025–1028.
6. Rabiner, L. R. "A tutorial on hidden Markov models and selected applications in speech recognition." Proceedings of the IEEE 77.2 (1989) 257–286.
7. Aggarwal, R. K., and Dave, M. "Acoustic modeling problem for automatic speech recognition system: conventional methods (Part I)". International Journal of Speech Technology, 14(4), (2011) 297–308.

Fingerprint-Based Attendance System Using MATLAB

Anushka Swarup, Kottapalli Dheeraj and Adesh Kumar

Abstract Finger prints are the one of the many forms of biometrics used to verify an individual's identity. Finger print identification refers to the automated system of verifying a match between two human finger prints. This research aims at extracting the primary uniqueness of the images obtained from the finger print. A finger print constitutes of a series of grooves/ridges on the surface of the finger. The uniqueness of a finger print can be determined by these patterns. Minutiae points are local groove characteristics that occur at either a groove bifurcation or a groove ending. Here an approach of identification of minutia in terms of ending, bifurcation, and region of interest (ROI) has been proposed. Extraction of minutiae from the image is attained using termination and bifurcation process and then elimination of false minutia is done from the image using the distance formula. The ROI, i.e., the region which is most densely concentrated with minutiae is extracted.

Keywords Minutiae points · Ridges · Bifurcation · Thinning · Feature detection · Region of interest (ROI)

1 Introduction

As life is getting more digital, security systems are gaining more importance. The rapid progress in biometrics makes information more susceptible to abuse. A type of human biometrics, the finger print has been widely used for individual identification in judicial and civilian purposes because of its uniqueness. A finger prints identification system is based on pairing an input finger print with a considerable amount of finger print in a database.

Biometric data required for recognition is called feature, and features appearing in finger prints are especially called minutia. The minutia is subdivided into two

Anushka Swarup (✉) · Kottapalli Dheeraj · Adesh Kumar
Department of Electronics and Instrumentation, University of Petroleum and Energy Studies, Energy Acres PO Bidholi via Premnagar, Dehradun 248007, Uttarakhand, India
e-mail: anushaasw17@gmail.com

© Springer Science+Business Media Singapore 2017

R. Singh and S. Choudhury (eds.), *Proceeding of International Conference on Intelligent Communication, Control and Devices*, Advances in Intelligent Systems and Computing 479, DOI 10.1007/978-981-10-1708-7_117

types: ending and bifurcation. Ending applies to the area where the movement of ridges is cut, and bifurcation is the point where two ridges become one. One finger print image can have many endings and bifurcations.

Although there has been a significant progress in designing autonomous finger print identification systems, a number of design factors such as low image quality difficulty in defining a reliable match, identification speed, etc., require new higher performance factor finger print recognition systems.

2 Related Works

Gnanasivam et al. [1], the paper presents a Multimodal Biometric system using Ear and fingerprint which has been designed and tested on 75 samples. EIPD systems were initially proposed for feature extraction of the ear. Fingerprint features are identified and a corresponding feature matrix has been generated. The paper makes use of authentication using fingerprint only when one using ear alone fails. Feature level union of ear and fingerprint features is done with the help of concatenation. The system requires less memory as compared to pattern developing methods of templates.

Mohd Rizal Mohd Isa et al. [2], this paper presents a novel idea of finger print verification by embedding it into a smart card which can be the scanned over a finger print sensor for various security reasons. With the wide acknowledgement of Biometric identification such unique ideas are going to widely replace traditional identification methods. The purpose of the research paper was to show the basic characteristics and possibilities of merging smart card and finger print biometrics in identification and authentication process.

Musa et al. [3], proposed a system which is a simple model for the combination of finger print recognition and conventional password technologies. Their system awarded enhanced levels of computer user authorization security needed to preserve access to sensitive information and to assist recognize approved system users in the greater education environment.

3 Methodology

The grayscale image read is converted into binary and the output binary image has all its pixels replaced by 1 or 0 according to the luminance. The pixels with luminance greater than level are replaced by 1 (i.e., white color and all other pixels with 0 (i.e,. black color). Level basically lies in the range of [0–1]. The default value of level is 0.5. Converting to binary is used in order to find a ROI—a portion of the image that is going to be used for further processing. Thinning is a morphological operation which is generally used to remove selected foreground pixels from binary images which is generally used for skeletonization. The thin image can be morphed n times which is infinity in this case which means the thinning operation is repeated until the lines are reduced to single pixel thickness.

3.1 Feature Extraction and False Feature Detection and Removal

In this we filter the thinner ridge map by the filter "minutiae" and compute the number of 1-value of each 3×3 window. If the central pixel has only 1-value neighbor then the central pixel is the termination (red dots) and if central is one and has three one-value neighbor, then the central pixel is a bifurcation (Green dots). The spurious minutiae are removed by performing the following processes:

1. If the distance between a termination and a bifurcation $\leq D$ then we remove this minutiae.
2. If the distance between two bifurcations $\leq D$ we remove the minutiae.
3. If the distance between two terminations $\leq D$ then we remove this minutiae where $D = 6$.

3.2 Region of Interest and Validation

The ROI is to be determined which is done by applying a closing on the image and an erosion. With the help of the GUI we can use ROI tools if MATLAB to manually define the ROI. In the next step we validate the obtained minutiae which are done using an algorithm which one by one compares the input with all the finger prints in database of the system to decide whether the person is authentic or not (Fig. 1).

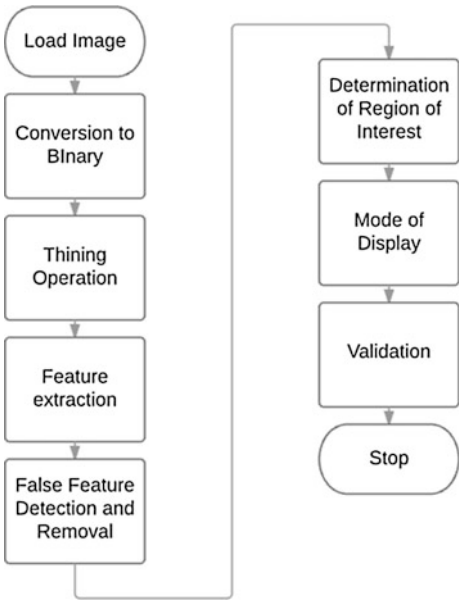


Fig. 1 Block diagram

4 Result

The final system is a graphical user interface as shown in Fig. 2. The interface provides an efficient platform for users to quickly validate their finger prints.

Step-1 Load Image
The load image function is created to provide users to input an image for validation.

Step-2 Binary Conversion and Thinning Operation
The input image is then converted into binary as shown below. Thinning operation is then carried out so that the edges in the binary image is made single pixel thick. This is used to refine the output for edge detection. Figure 3 shows the image after thinning operation.

Step-3 Feature Extraction and False Feature Detection and Removal
The features like ridge ending, bifurcation, and short ridge are detected as shown below. As there is a lot of false features detection, a quality check measure is done and the result is shown in Fig. 4.

Step-4 Region/Area of Interest
The region/area of interest is detected as shown in Fig. 5.

Step-5 Validation
At this point the user can either choose to add the input image to the database or to validate it. In case of validation, the system compares the

Fig. 2 .



Fig. 3 .



Fig. 4 .

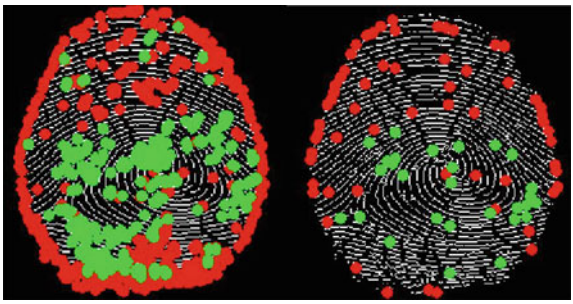


Fig. 5 .

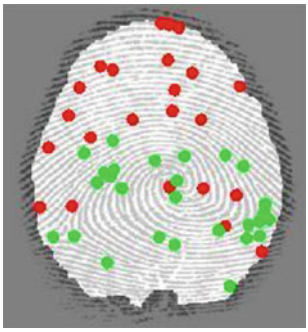
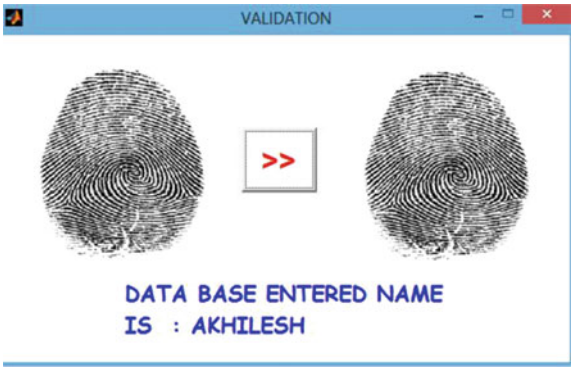


Fig. 6 .



output of the previous step with all the images present in the database and the output is as shown in Fig. 6.

5 Conclusion

The proposed work is centered at marking the attendance of a candidate by taking his finger print and then comparing some specific features with those of the finger prints present in a predefined database.

References

1. P. Gnanasivam, Dr. S. Muttan, "Ear and Finger print Biometrics for Personal Identification" in: Proceedings of 2011 International Conference on Signal Processing, Communication, Computing and Networking Technologies (ICSCCN), pp. 347–352, 2011.
2. Mohd Rizal Mohd Isa, Yuhanim Hani Yahaya, Mohd Hazali Mohamed Halip, Mohammad Adib Khairuddin, Kamaruzaman Maskat, "The Design of Finger print Biometric Authentication on Smart Card for PULAPOT Main Entrance System(PMES)" IEEE, pp. 1–4, 2010.
3. S M. Musa, T. de Q. Jefferson, M.N.O. Sadiku, "A Simple Model for Biometric Identification Technology Using Finger print Scanning" IEEE, pp 1–4, 2012.
4. Dr. S. Ravi, Dattatreya P. Mankame "Multimodal Biometric Approach Using Finger print, Face and Enhanced Iris Features Recognition" in: 2013 International Conference on Circuits, Power and Computing Technologies [ICCPCT], pp. 1143–1150, 2013.
5. Teddy Ko, "Multimodal Biometric Identification for Large User Population Using Finger print, Face and Iris Recognition" in: Proceedings of the 34th Applied Imagery and Pattern Recognition Workshop (AIPR), 2005.
6. Zin Mar Win, Myint Myint Sein "Texture Feature based Finger print Recognition for Low Quality Images" ©IEEE, pp 333–338, 2011.
7. Yuhanim Hani Binti Yahaya, Mohd Rizal Bin Mohd Isa, Mohammad Indera Bin Aziz, "Finger print Biometrics Authentication on Smart Card" in: 2009 Second International Conference on Computer and Electrical Engineering, pp. 671–673, 2009.
8. Wang Yuan, Yao Lixiu, Zhou Fuqiang, "A Real Time Finger print Recognition System Based On Novel Finger print Matching Strategy" in: The Eighth International Conference on Electronic Measurement and Instruments (ICEMI), pp. 1-81–1-85, 2007.
9. Gabriel Babatunde Iwasokun, Oluwole Charles Akinyokun, "Finger print Singular Point Detection Based on Modified Poincare Index Method" in: International Journal of Signal Processing, Image Processing and Pattern Recognition, Vol.7, No.5 (2014), pp. 259–272, 2014.
10. Seung-Hoon Chae, DaesungMoon, Kyeong-Ri Ko, JuHyun Shin, Sung Bum Pan, "Security Enhancement for Smartphone Using Biometrics in Cyber-Physical Systems" in: Hindawi Publishing Corporation-International Journal of Distributed Sensor Networks, 9 pages, 2014.
11. Jing Luo, Dan Song, Chunbo Xiu, Shuze Geng, Tingting Dong, "Finger print Classification Combining Curvelet Transform and Gray-Level Cooccurrence Matrix", Hindawi Publishing.

Investigations on the Effects of Partial Shading and Dust Accumulation on PV Module Performance

Pankaj Yadav, Amit Kumar, Ankit Gupta, Rupendra Kumar Pachauri, Yogesh K. Chauhan and Vinod Kumar Yadav

Abstract In this paper, a self-designed PV module of Series–Parallel (SP) configuration has been developed using mono-crystalline solar cells for performance investigations under partial shading and dust accumulation conditions. For this study two moving shading patterns (horizontal and diagonal) and four dust samples of different particle properties have been considered at three irradiation levels. Comprehensive investigations are carried out on the considered system and results are obtained in terms of *I–V*, *P–V* characteristics, PV power, weight of dust accumulated on PV panel and irradiation level. The results show that diagonal partial shading pattern and ash dust sample have more significant effect on the PV module performance among all the considered shading patterns and dust samples.

Keywords Array configuration · Dust accumulation · Partial shading · PV module

1 Introduction

Solar photovoltaic (PV) module is combination of several PV cells. A single PV cell cannot produce sufficient power, in order to increase power of PV cells they are connected together called modules. [1] PV system can be designed to fulfill almost any electric power need small or large. Shadow cast of trees, chimney or buildings, etc., cause the partial shading of solar panels which affects the output of whole

Pankaj Yadav (✉) · Amit Kumar (✉) · Ankit Gupta · R.K. Pachauri · Y.K. Chauhan
Department of Electrical Engineering, School of Engineering, Gautam Buddha University, Greater Noida 201312, Uttar Pradesh, India
e-mail: pankajgbu091@gmail.com

Amit Kumar
e-mail: amitkumar2495@gmail.com

V.K. Yadav
Department of Electrical Engineering, Galgotias University, Greater Noida 201312, Uttar Pradesh, India

© Springer Science+Business Media Singapore 2017

R. Singh and S. Choudhury (eds.), *Proceeding of International Conference on Intelligent Communication, Control and Devices*, Advances in Intelligent Systems and Computing 479, DOI 10.1007/978-981-10-1708-7_118

system. Bypass diodes are used to minimize the effects of partial shading. Also the accumulation of dust on the solar PV system is obvious which also reduces the power of solar PV system [2].

In [3], the author's investigation of solar PV system performance is based on MATLAB/Simulink on the existing and some proposed Solar PV configurations. In [7–9] partial shading conditions has been studied on different or single configuration with the help of Software's on tested solar panels. In [4] the investigation is based on different orientation angles of modules and dust accumulation on glass samples over a period and are investigated considering the impact on transmittance. In [5, 6] the effect of environment conditions like temp, humidity, dust, and rain has been analyzed.

From above literature review, the novelty of this paper is to study the effect of partial shading conditions under two different shading patterns and effects of dust accumulation on PV module using four dust samples of different particle properties.

2 Experimental Setup

In this work, a SP PV module is self-assembled as shown in Fig. 1. It is connected to a system which consists of a multimeters (TRINITY TDM-3020), pyranometer (CEM DT-1307), weighing balance (Citizen CY204) for dust sample weight measurement, diode (IN5408) and Rheostat (50 Ω) for the measurement of electrical quantities.

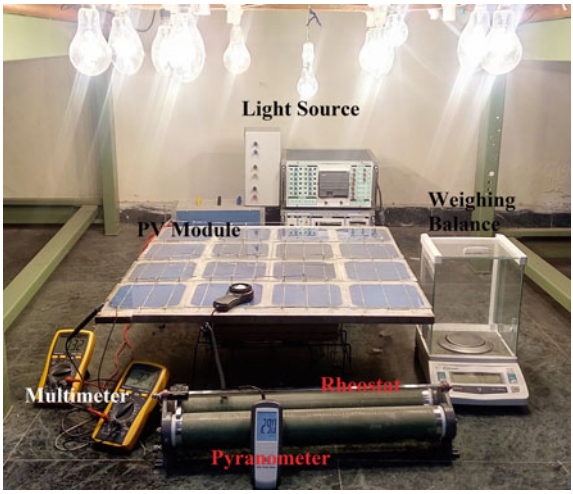


Fig. 1 Experimental setup

3 PV System

The PV cell voltage (V_c) is function of photocurrent, depends upon the solar irradiation level and can be represented using Eq. (1) as

$$V_c = \frac{AkT_c}{e} \ln\left(\frac{I_{ph} + I_0 - I_c}{I_0}\right) - R_s I_c, \quad (1)$$

where, A is curve fitting factor, k is boltzman constant, T_c is reference cell operating temperature, e is electron charge, I_{ph} is photocurrent, I_o is reverse saturation current of diode, I_c is cell output current and R_s is series resistance of cell (Fig. 2 and Table 1).

4 Results and Discussion

The typical I–V and P–V characteristics of the designed PV module under irradiation level of 360 W/m^2 and STP are shown in Fig. 3.



Fig. 2 Designed SP PV module

Table 1 Specifications of PV module

Irradiation level	360 W/m^2
Open circuit voltage (Voc)	2.2 V
Short circuit current (Isc)	3.96 A
No of cells	16 (4 × 4)
Type of cells	Mono
Max. reverse current(diode)	5 A

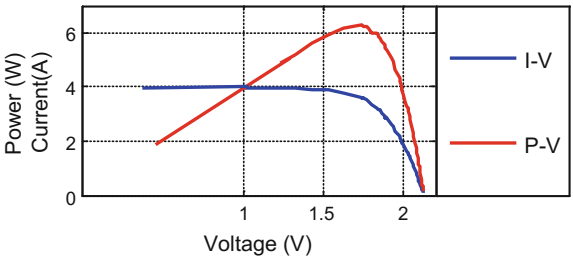


Fig. 3 Ideal *I–V* and *P–V* of the panel

4.1 Partial Shading

For the study of effects of partial shading on PV module two shading patterns, namely, horizontal shading pattern and diagonal shading pattern are considered. A black paper of thickness 0.125 mm is used to shade the cells as it blocks the irradiation level up to 95 %. The *I–V* characteristic response of horizontal shading pattern and diagonal shading patterns are shown in Figs. 4 and 5 respectively.

From Figs. 4 and 5 it is observed that both the shading patterns reduces the PV performance significantly but diagonal shading pattern has more effect on PV module performance. In horizontal shading pattern P_{mpp} for ideal and SP4 are reported to be 6.31 W and 1.21 W, respectively. Further for diagonal shading pattern P_{mpp} for ideal and SP4 are observed to be 6.31 W and 0.12 W, respectively.

4.2 Dust Accumulation

The effect of dust particles on the PV module has been studied in detail. In this study four dust samples namely normal dust, clay, ash, and sand are considered. For each dust sample three weights $W_1 < W_2 < W_3$ of dust accumulation are taken and each dust accumulation is analyzed under three level of irradiation ($Ir_1 < Ir_2 < Ir_3$) incident on the PV module. For each dust samples *I–V* curve and power versus weight of dust accumulation are obtained as shown in Figs. 6, 7, 8 and 9.

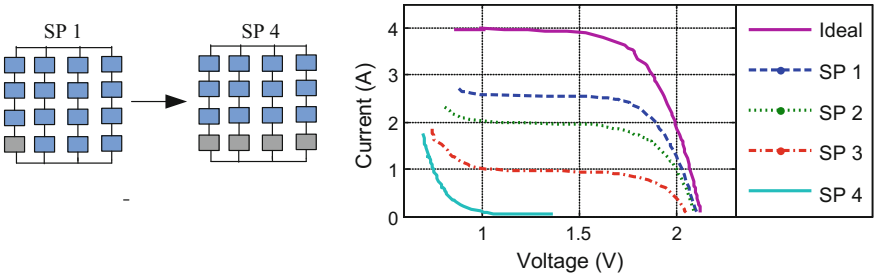


Fig. 4 *I–V* characteristics of horizontal shading pattern (SP1—SP4)

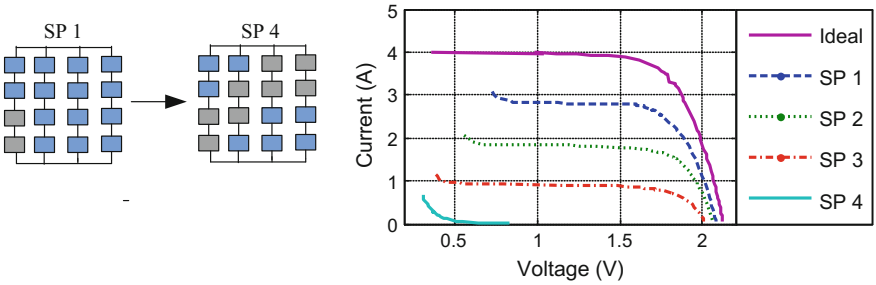


Fig. 5 *I–V* characteristics of diagonal shading pattern (SP1—SP4)

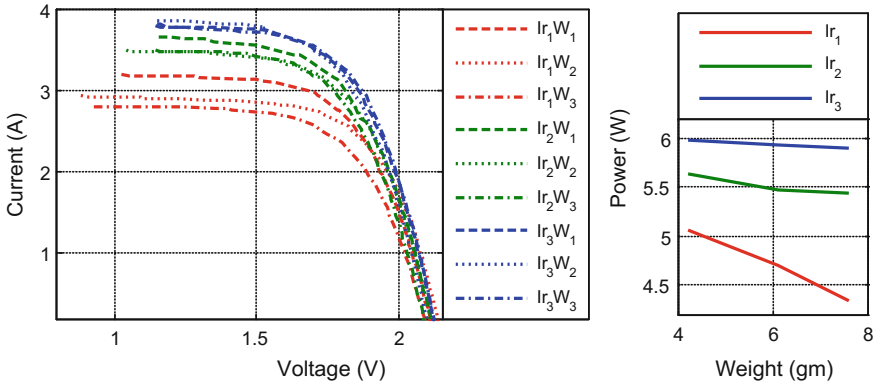


Fig. 6 *I–V* characteristics and power vs weight curve of normal dust

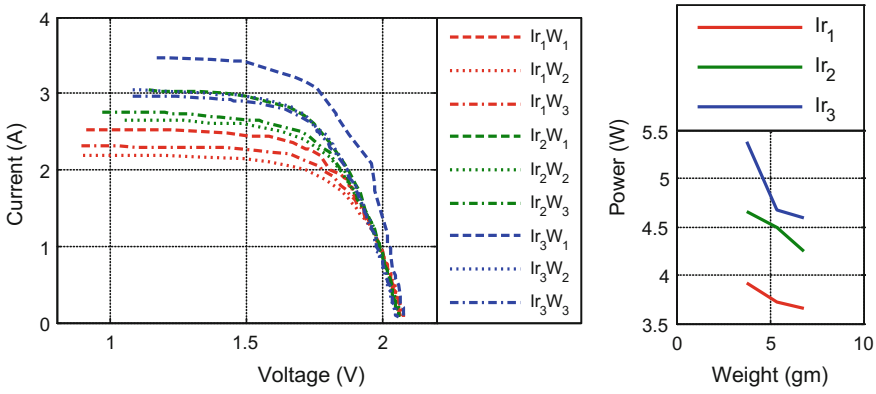


Fig. 7 *I–V* characteristics and power vs weight curve of clay

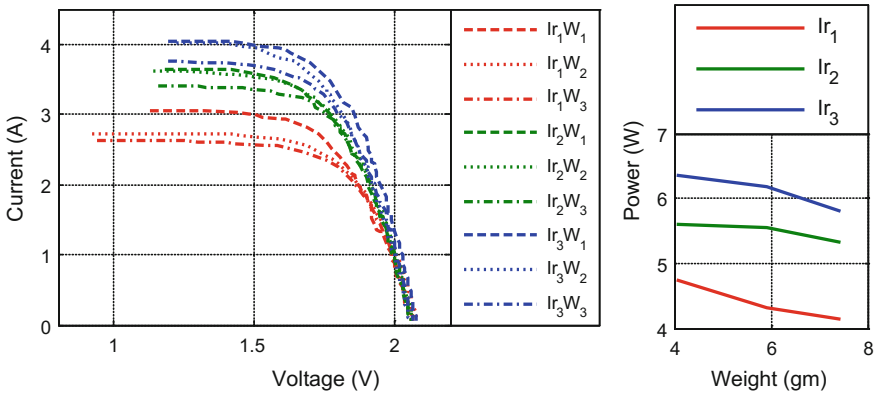


Fig. 8 *I–V* characteristics and power vs weight curve of sand

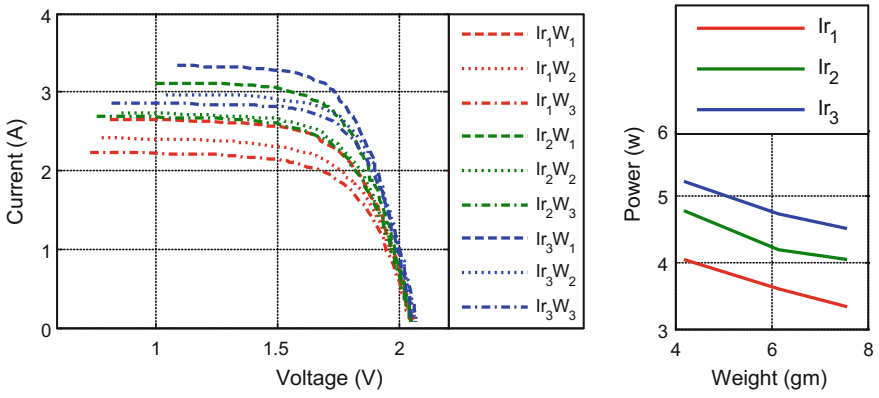


Fig. 9 *I–V* characteristics and power vs weight curve of ash

From Figs. 6, 7, 8 and 9 it is evident that accumulation of ash on PV modules has most significant effect on PV performance among the considered samples. The comparative analysis of the samples is shown in Table 2.

5 Conclusion

In this paper a comparative study of the effects of partial shading and dust accumulation on a self-assembled PV module at different irradiation level is presented. A comprehensive investigation has been carried out and the obtained results show that both partial shading and dust accumulation have significant reduction in the performance of PV module. Following are the salient points of this study:

Table 2 Comparative analysis of experimental results

Parameters		Normal dust	Clay	Sand	Ash
Ir_1W_1	I_{sc} (A)	3.19	2.52	3.06	2.64
	P_{mpp} (W)	5.057	3.921	4.748	4.041
Ir_1W_2	I_{sc} (A)	2.93	2.19	2.73	2.42
	P_{mpp} (W)	4.692	3.722	4.326	3.591
Ir_1W_3	I_{sc} (A)	2.80	2.31	2.63	2.22
	P_{mpp} (W)	4.339	3.652	4.136	3.343
Ir_2W_1	I_{sc} (A)	3.66	3.04	3.64	3.11
	P_{mpp} (W)	5.6416	4.651	5.594	4.794
Ir_2W_2	I_{sc} (A)	3.49	2.64	3.62	2.74
	P_{mpp} (W)	5.471	4.486	5.543	4.182
Ir_2W_3	I_{sc} (A)	3.49	2.76	3.40	2.70
	P_{mpp} (W)	5.430	4.250	5.332	4.052
Ir_3W_1	I_{sc} (A)	3.81	3.47	4.04	3.33
	P_{mpp} (W)	5.992	5.385	6.358	5.215
Ir_3W_2	I_{sc} (A)	3.86	3.04	4.02	2.97
	P_{mpp} (W)	5.933	4.6704	6.187	4.734
Ir_3W_3	I_{sc} (A)	3.79	2.96	3.75	2.86
	P_{mpp} (W)	5.889	4.590	5.814	4.524

- Among the considered two shading patterns diagonal shading pattern is observed to have greater effect on PV module power response.
- Similarly, amongst the four dust samples of dust accumulation, ash is more effective as compared to other samples because of its smaller particle size.
- Partial shading is reported to have greater reduction in PV module output power as compared to dust accumulation.

References

1. Gupta, A., Kumar, P., Pachauri, R. K., Chauhan, Y. K.: Effect of Environmental Conditions on Single and Double Diode PV System: A Comparative Study. International Journal of Renewable Energy Research. 4 (2014) 563–569.
2. Kumar, P., Gupta, A., Pachauri, R. K., Chauhan, Y. K.: Utilization of Energy Sources in Hybrid PV/FC Power Assisted Water Pumping System, IEEE conference on Computational intelligence & Communication technology. (2015) 548–553.
3. Yadav, A. S., Pachauri, R. K., Chauhan, Y. K.: Comprehensive Investigation of PV arrays with puzzle shade dispersion for improved performance. Solar Energy. (2016) 256–285.
4. Pareek, S., Dahiya, R.: Output Power Maximization of Partially Shaded 4 × 4 PV fields by altering its Topology. Energy Procedia. 54 (2014) 116–126.
5. Gao, L., Roger A.D., Liu, S., Alben, P. L.: Parallel-Connected Solar PV System to Address Partial and Rapidly Fluctuating Shadow Conditions. IEEE Transactions on Industrial Electronics. 56 (2009) 1548–1556.

6. Karatepe, E., Boztepe, M., Colak, M.: Development of Suitable Model for characterizing photovoltaic arrays with shaded solar cells. Solar Energy. 81 (2007) 977–992.
7. Gandhi, A. T., Gupta, A., Vijay, B. S.: Investigations of the effects of Dust Accumulations and Performance for Mono and Polycrystalline Silica Modules. International Journal of Renewable Energy Research 4 (2014) 628–634.
8. Ahmed, Z., Hussen, A. K., Sopian, K.: Effect of Dust on Photovoltaic Performance: Review and Research Status. Latest trends in Renewable Energy and Environmental Infromatics. 1 (2013) 193–199.
9. Muhammed, J.A., Syed, A. M. S.: Effect of dust accumulation on the power outputs of solar photovoltaic modules. Renewable Energy. 60 (2013) 633–636.

Design and Development an Embedded System for Multichannel Data Acquisition for Use in Networked Monitoring System

Ashi Rastogi and Aastha Dadheech

Abstract In industry data acquisition covers the most demanding applications of real-time monitoring. The multi-channel data acquisition is used for the acquisition and monitoring of various industrial sensor signals. The data obtained are processed in real-time execution. For future work, we can access the stored data from an external memory. The proposed design is implementing by combination of EDA tools and nios II Processor. This processor provides an ideal embedded solution that includes the following: flexibility, high performance, low cost, long life for real-time processing. This document entails the design of a network data acquisition system which consists of a number of links RS 422 to communicate with various devices connected to it. The hardware development is to generate VHDL code for implementing the hardware inside the FPGA. Real-time processing and signal processing of data acquisition attains by FPGA. It also involves the development of test routines for simulation and verification of VHDL code.

Keywords Data acquisition system · RS 422 · Nios II processor · Qsys · Uart

1 Introduction

In recent years, industrial I/O interface products are reliable, accurate, and cost effective. Data acquisition systems are widely used in industrial and laboratory applications such as monitoring, communication, control, data acquisition, and automated testing. The purpose of data acquisition system is to measure physical phenomena such as light, temperature, pressure, sound, etc. The data acquisition system convert the analog signal into a digital signal than it is control by A/D

Ashi Rastogi (✉)
Bhabha Atomic Research Centre, Mumbai, India
e-mail: ashirastogi83@gmail.com

Aastha Dadheech
Banasthali Vidhapth, Jaipur, India
e-mail: aasthaec26@gmail.com

© Springer Science+Business Media Singapore 2017

R. Singh and S. Choudhury (eds.), *Proceeding of International Conference on Intelligent Communication, Control and Devices*, Advances in Intelligent Systems and Computing 479, DOI 10.1007/978-981-10-1708-7_119

convertor plug-in board and then sent to the computer using RS-422 serial communication for real-time monitoring. It also involves the collection of data for analysis and process documentation. Accuracy, reliability, and versatility are playing a leading role in modern electronics. Data acquisition system can acquire multichannel or a single channel signals. Many applications require a multi channel Data acquisition system. In particular, simultaneous multichannel data acquisition system is used in many applications such as monitoring of the industrial and environmental radiation. If the signal can be detected at the same time, the simultaneous capture of additional data can be used to provide additional information at the same acquisition time. It usually includes multiple sampling of analog signals, and converts them into digital format so they can be processed either on board or outside.

1.1 The Overall Design of the System

Our design's goal is founded on embedded Nios II processor which provides smallest possible logic utilization of FPGA and it is very efficient for low cost FPGA applications. Altera FPGA provides the platform for developing the soft-core processor with their peripheral component interfaces [1]. The design offers interconnection with the internal hardware and external hardware like ADC and sensor. The Cyclone III Development Board offers a hardware platform for developing and high functionality, feature-rich designs. Cyclone III Device contains on-chip memory and the Nios II embedded soft processor. This kit is built on 65 nm process technology and we use this kit to provide low static and dynamic power consumption [2] (Fig. 1).

1.2 RS-422 Serial Communication Over RS-232

We use RS 422 for interfacing between pc and hardware. RS 422 known as EIA/TIA 422. It is a technical standard developed by the electronics industries alliances that specify the electrical circuit. RS 422 provides communication up to

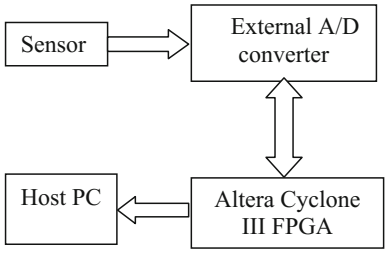


Fig. 1 Design of system

1.2 km and data can be transmitted at the rate of 10 Mbits/s. We can transmit the data using balanced or differential signaling as well as unidirectional and terminated or non terminated transmission lines in RS 422. The data can be transmitting each signal with two wires to increase the maximum baud rate and cable length. It uses differential electrical signal in contrast to unbalanced signal referenced to ground with RS 232. There is two line transmission, each for transmit and receive signal which give the results in greater noise immunity. RS 422 is better than RS 232 because this standard was designed for high speed Communication.

1.3 Interfacing DAQ with RS-422

To establish the communication link between the PC and the data acquisition module, it is necessary to use the channel either serial or parallel communication [3]. The information can be transferred in a digital format which is transmitted in the serial mode or in parallel. We use the parallel communications to provide connections between instruments or computers and printers test the series is frequently used between computers and other devices. On a single communications line, serial transmission sends the data one bit at a time [3]. On the other hand, the parallel communication requires many lines to transmit the data. In the asynchronous serial communication is the date transmitted by a bit in order that two transition lines are necessary for achieving a bidirectional communication. Serial communication is used in the data acquisition system to simplify the equipment and save the cost.

1.4 Nios II Processor

Nios II is an integrated 32-bit RISC processor designed specifically for the Altera FPGA family. It is a reconfigurable Soft-core processor. Nios II processor is a flexible peripheral set (Fig. 2).

Altera nios II processor supports 50 MHz frequency. For connecting the peripheral component we use Avalon memory-mapped interface. Avalon MM Interface is a read/writes address based interface which is used in master slave connection. There is no on-chip ADC peripheral in altera cyclone III; therefore, we have to manage the ADC to a certain extent. The analog signal is coming from ADC plug-in board that provides digital data and this digital data can be detected by the input–output port (PIO) of the Nios II core. The Nios II system can also communicate with a host computer, enabling the logical host control inside the FPGA.

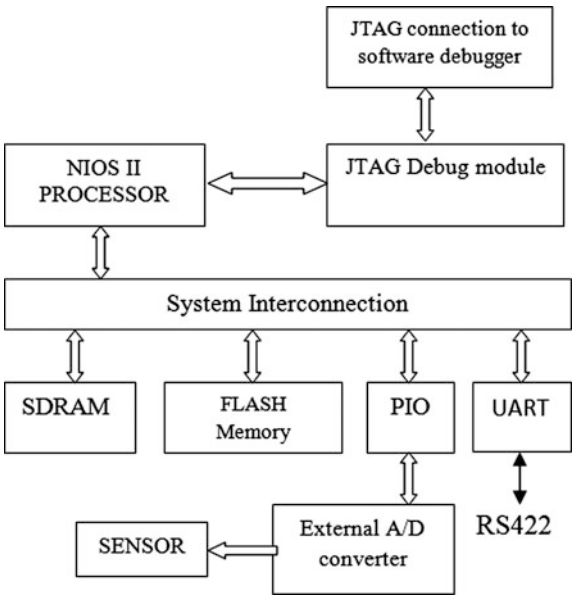


Fig. 2 Architecture of nios II processor

2 Design Implementation

For transmitting and receiving the data, we designed the Nios II processor with necessary peripheral interface. Whole implementation process is taken in two steps.

2.1 Hardware Generation System

The Nios II processor is generated in the Quartus II software environment and Qsys manufacturer. Nowadays many applications need a variety of devices so they are integrated on a single chip thus increasing complexity. The Qsys is used for system hardware design. This tool is used to save the valuable time and endeavor in the FPGA design process [4] and we take all the input–output peripherals from the SOPC internal library. It directly generates interconnect logic optimized and time consuming (Fig. 3).

2.2 Software Generation System

The software development tool for Nios II processor is Nios II integrated development environment (IDE) consists of C/C++ compiler [5]. C language is preferred language to write a program in nios II IDE tool like Embedded C coding for a microcontroller. When the Nios II receives an interruption of the general block of

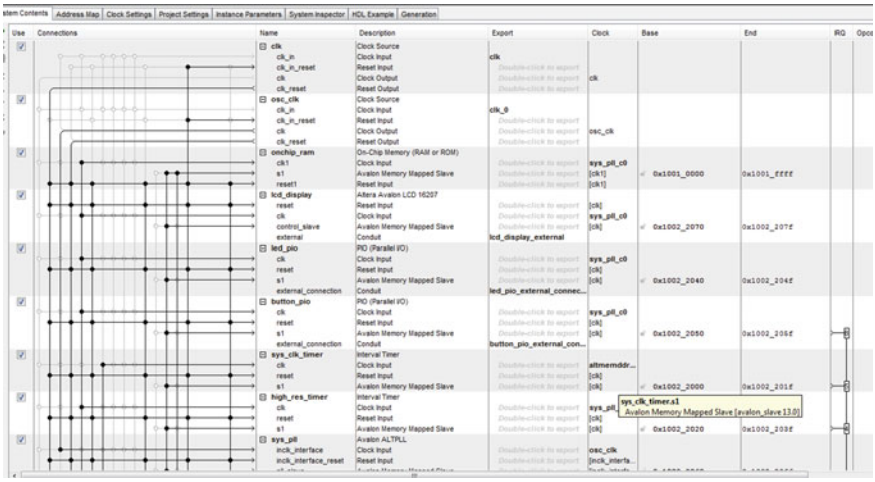


Fig. 3 Qsys interconnections

the ADC, the processor reads and uses it as per the requirement and we also write a c code for serial port to provide communication between pc and nios II processor.

3 Result

We have designed multichannel data acquisition system which receives digitized data and the digital data coming through the ADC. The data can be processed by the processor and displayed on LCD (Fig. 4).

Flow Status	Successful - Wed Dec 16 02:31:28 2015
Quartus II 32-bit Version	13.0.0 Build 156 04/24/2013 SJ Web Edition
Revision Name	niosII_processor
Top-level Entity Name	niosII_processor
Family	Cyclone III
Device	EP3C120F780C7
Timing Models	Final
Total logic elements	7,256 / 119,088 (6 %)
Total combinational functions	6,507 / 119,088 (5 %)
Dedicated logic registers	4,588 / 119,088 (4 %)
Total registers	4664
Total pins	101 / 532 (19 %)
Total virtual pins	0
Total memory bits	608,304 / 3,981,312 (15 %)
Embedded Multiplier 9-bit elements	4 / 576 (< 1 %)
Total PLLs	2 / 4 (50 %)

Fig. 4 Compilation result

References

1. Yi Wu, Yu Huang, Yao Wang, Ruixia Yang and Xiaojuan Liu. "Design of Embedded Web Module Based on SOPC", 2012 International Conference on Solid State Devices and Materials Science
2. Cyclone III reference kit handbook. [Online]. Available: http://www.altera.com
3. Serial communication. [Online]. Available: http://en.wikipedia.org/wiki/serial-communication
4. Design a qsys system tutorial. [Online]. Available: http://www.altera.com
5. NIOS-II processor handbook. [Online]. Available: http://www.altera.com/
6. Hae-Seung Lee, Charles G. Sodini, "Analog-to-Digital Converters: Digitizing the AnalogWorld", Proceedings of the IEEE, Vol. 96, No 2, February 2008
7. Nios II software developer handbook. [Online]. Available: http://www.altera.com
8. R. Ramachandran, J. Thomas Joseph Prakash, "Design and implementation of SOC in NIOS II soft core Processor for Secured Wireless Communication", International Journal of Computer Application, 2012
9. F. M. Sun, et al., "FPGA-based Embedded System Design", 2008 IEEE Asia Pacific Conference on Circuits and Systems (Apccas 2008), Vols 1–4, pp. 733–736, 2008
10. Aditya M Gulkotwar, Sachin K. Meshram "Implementing an Application of Data Acquisition System using NIOS –II Soft Core Processor" International Journal of Computer Applications, International Conference on Quality Up-gradation in Engineering, Science and Technology (ICQUEST-2014)

Early Stage Identification of Localized Brain Atrophy Using Bioimage Processing Algorithms

Abhishek Raj and Swati Kadlag

Abstract Mind deviation from the normal is a noteworthy cause of handicap and passing in person. Mind Abnormality is an unusual development of cells inside the cerebrum. It is the mass of tissue in which a few cells become wildly. For right on time conclusion of abnormality in tissue tests innovative work exercises are focused on the investigation of programmed picture examination. Attractive Resonance Tomography (ART) or Magnetic Resonance (MR) imaging is one of the significant systems utilized by the radiologist to analyze mind inner structure. This strategy utilizes radiofrequency beats of the attractive field to inspect diverse organs. The yield of this method is MR picture in Digital Imaging and Communications in Medicine (DICOM) position that can be seen on a computer. This paper audits some momentous works from writing alongside the essential ideas identified with programmed cerebrum variation from the norm recognition procedures using k-means and Support Vector Machines (SVM).

Keywords K-means clustering · SVM · MRI · DICOM · Interpolation

1 Introduction

In this image get ready to field, the information is deciphered using pictures as a part of the kind of the pixel (power, force) where we take data as an image and we get yield which is moreover a image. The guideline goal of this image is evacuating the part without angering the whole picture using best frameworks. For therapeutic picture taking care of examinations of Magnetic Resonance Imaging (MRI), pictures

Abhishek Raj (✉) · Swati Kadlag
Department of Electronics and Telecommunication,
Symbiosis Institute of Technology,
Symbiosis International University, Pune 412115, India
e-mail: abhishek.raj@sitpune.edu.in

Swati Kadlag
e-mail: swatik@sitpune.edu.in

© Springer Science+Business Media Singapore 2017

R. Singh and S. Choudhury (eds.), *Proceeding of International Conference on Intelligent Communication, Control and Devices*, Advances in Intelligent Systems and Computing 479, DOI 10.1007/978-981-10-1708-7_120

are crucial for perception the human body. Remedial imaging modalities as in MRI, Computed Tomography (CT) check which regularly depends on CT scan to make mechanized photos of within organs of the body help the authorities to examine the inside parts of the body. CT scanner, Ultrasound, and MRI accepted control standard X-shaft imaging by allowing the masters to see the body's third estimation that is three-dimensional perspective.

1.1 Magnetic Resonance Imaging

For an MRI test, the zone of the body being considered is put inside a phenomenal machine that contains a solid magnet. Pictures from an MRI are electronic pictures that can be spared and set away on a computer for later study. The photographs beside can be evaluated remotely in a working room, MRI with an open machine is also taken sometimes that does not encase your body. Yet, open MRI machines are not accessible all around. The photos from an open MRI may not be on a standard with those from a standard MRI machine.

1.2 DICOM Images

This part is intended to present an energizing picture information representation standard known as Digital Imaging and Communications in Medicine (DICOM) in restorative imaging group. DICOM is a worldwide data standard that is utilized and soon will be utilized by practically every restorative calling that uses pictures inside of social insurance industry. It is intended to guarantee the interoperability of frameworks used to create, store, show, send, recover, inquiry, or print medicinal pictures, for example, registered tomography (CT) checks, MRI, and ultrasound. DICOM standard has likewise been created to address the issues of producers and clients of restorative imaging hardware for interconnection of gadgets on standard systems. The day-by-day operations of DICOM standard is at present oversaw by the National Electrical Manufacturers Association (NEMA).

2 Challenges in Bioimages Handling and Processing

Nowadays, many clinical centers or hospitals that maintain a large database of Magnetic Resonance (MR) images finds the task of indexing the available database according to size or location or other attributes is very difficult. To date, automated brain abnormality segmentation from MR images remains a challenging, computationally intensive task. There are numerous difficulties from which the majority of the specialists are battling. In any case, the genuine issue is that consider the

possibility that the variations from the norm are little like truly immaterial or not ready to recognize in ahead of schedule stages so here falsehoods genuine test. This can be overcome by utilizing computerized image preparing and medicinal image handling also by utilizing programming recreation.

3 Proposed Approaches for Atrophy Detection

In this paper less and subjective measure of work described or represented which will be very usefull in bio medical image processing. The work done is confined to some region such as around hippocampus where the long haul recollections framed in the cerebrum. Current strategies tell about decay or loss of cell by plaque and tangles. A proposed algorithm for atrophy detection [1–3] is based on clustering [k-means] given an arrangement of perceptions $(x_1 x_2 \ldots x_n)$, where every perception is a d-dimensional genuine vector, K-implies grouping plans to segment the N perceptions into K ($\leq N$) sets $S = \{s_1 s_2 \ldots s_k\}$ in order to minimize the inside of Within-Cluster Sum of Squares (WCSS) (the entirety of separation elements of every point in the bunch to the K focus). In other words, its objective is to find

$$\arg_S \min \sum_{i=1}^{k} \sum_{x \in S_i} \|X - \mu_i\|^2 \tag{1}$$

where μ_i is the mean of points in S_i. As recorded in the data picture arrangement in framework structure to perform K-implies grouping is the least difficult type of order in the view of specific parameters.

Second likely approach [4–6] depends on the standard of basic danger amplification. Rather than minimizing a target capacity in view of the preparation tests, (for example, mean square blunder), the SVM endeavors to minimize the bound on the speculation mistake. Therefore, SVM has a tendency to perform well when connected to information outside the preparation set. SVM accomplishes this favorable position by concentrating on the preparation illustrations that are most hard to order. These "marginal" preparing illustrations are called bolster vectors. In this paper, we regard picture arrangement as a two-class design order issue. We apply the entire MRI picture to the classifier to figure out if the anomalies are available or not. We allude to these two classes all through as "white" and "non-white" pictures. The issue is the means by which to develop a classifier [i.e., a choice capacity $f(x)$] that can accurately arrange an info design x that is not as a matter of course from the preparation set. For a given preparing set, while there might exist numerous hyperplanes that amplify the isolating edge between the two classes, the SVM classifier depends on the hyperplane that augments the isolating edge between the two classes. At the end of the day, SVM finds the hyperplane that causes the biggest division between the choice capacity values for the "marginal"

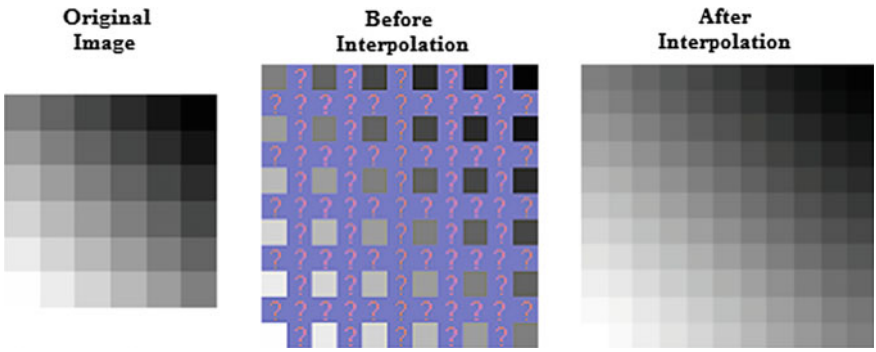


Fig. 1 Interpolation of an image

cases from the two classes. The SVM grouping with a hyperplane that minimizes the isolating edge between the two classes are shown by information focuses set apart by "white" and "nonwhite". Bolster vectors are components of the preparation set that lie on the limit of hyperplanes of the two classes.

Interpolation works using known data to estimate values at unknown points. For example, if you want to know the temperature at noon, but only measured it at 11 am and 1 pm, you could estimate its value by performing a linear interpolation. Unlike air temperature fluctuations and the ideal gradient above, pixel values can change far more abruptly from one location to the next as shown in Fig. 1.

4 Applied Methodologies

Two different approaches as explained above in section second proceeding are discussed and results are produced. This method includes the preprocessing feature which will remove succeeding noise of the image and make it executable for further image feature detection. Image smoothing is done for taking the significant part of the image and then applied the algorithm (k-means/SVM) which detects the atrophy part by locating boundary box. The proposed algorithm for atrophy detection is shown in Fig. 2 which includes clustering as well as support vector machine algorithms.

5 Results

Initiating centroid process of classification using the minimal distance from the center to the clusters $N = 3$, where N denotes number of cluster assign for image. Figure 3 represents the clustering of image using k-means algorithm.

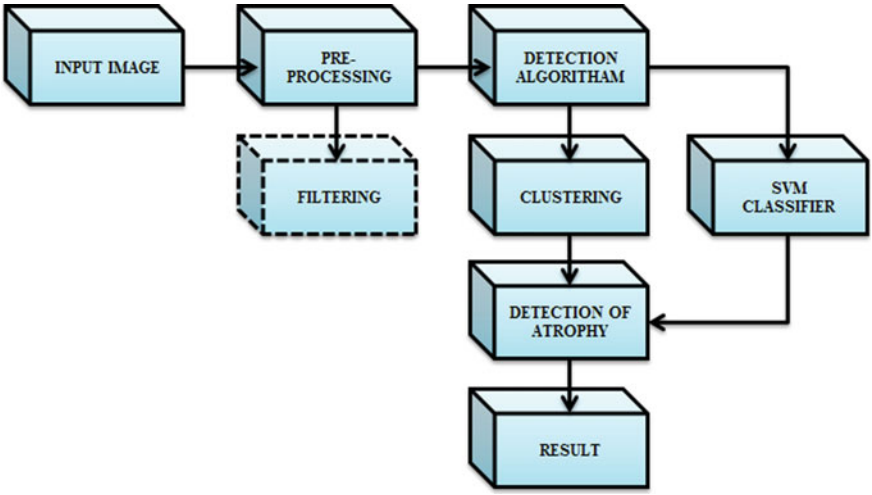


Fig. 2 Proposed algorithm for atrophy detection

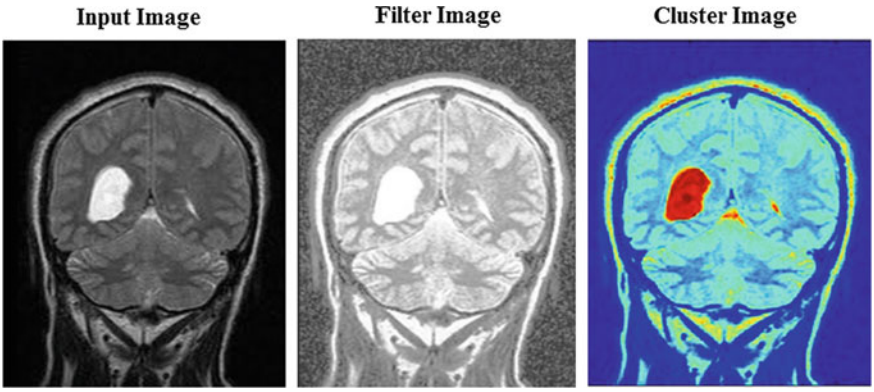


Fig. 3 Illustrate the detection of target atrophy result of *k*-means with $k = 3$

Here Fig. 4 elaborates support vector machine [5] classification which gives brief information about images that one cannot see by naked eyes. By taking input image in which filtering operation is performed then hidden features will appear clearly where we can locate area/region of interest in the image after which is formed by locating image boundary box, and then SVM [6, 7] comes into the picture by location boundary box. The boundary between the white region and gray region appears prominently. Linear classifier with minimal distance from the hyperplane is then used for extracting defected portion and its location is shown in Fig. 4.

X-ray picture is initially changed into grayscale picture. A cluster of class pixel values indicates force values. For single and twofold exhibits, values range from

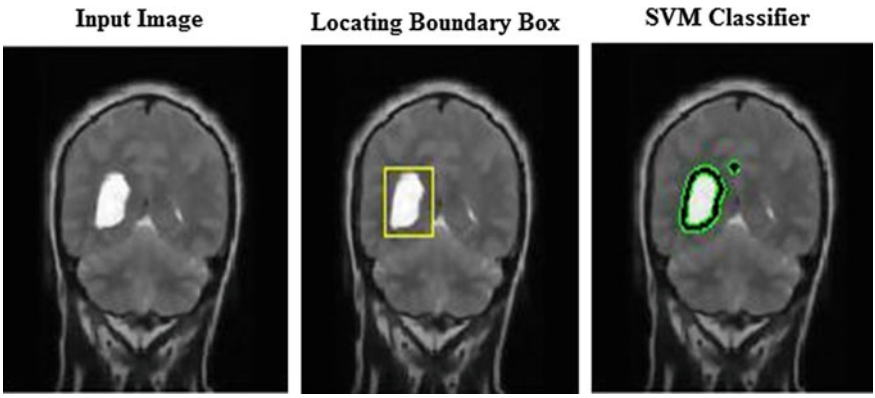


Fig. 4 Result after applying linear SVM classifier

[0, 1]. For uint8, values range from [0, 255]. For uintl6, values range from [0, 65535]. For intl6, values range from [−32,768, 32,767]. Force or brilliance of a picture as two-dimensional nonstop capacity is $F(x, y)$, where (x, y) signifies the spatial directions at the point when just the shine of light is considered. Separating is the procedure of expelling commotion from MRI pictures. Edges are huge nearby changes of power in a picture. Edges ordinarily happen on the limit between two distinct areas in a picture. The objective of edge identification is to deliver a line drawing of a scene from a picture of that scene and to remove essential components from the edges in images. Watchful edge detector algorithm is utilized for edge detection. Division is the procedure which separates a picture into its constituent districts or questions. Sectioning unimportant pictures are one of the troublesome undertakings in picture handling. Division exactness decides the inevitable achievement or disappointment of mechanized investigation method. Division calculations depend on one of the two fundamental properties of power qualities irregularity and comparability. Classification depends on dividing a picture into areas that are comparative as per predefined criteria.

6 Conclusion

Genuine treatment related to the brain is always a challenge, no doubt it is essential with the help of k-means clustering and SVM classifier the location of atrophy can be detected with great accuracy survey. It is helpful for mild cognitive impairment which is otherwise the only challenge for MCI. It is a ray of hope for patients who suffer from loss of memory and life for them become miserable.

Acknowledgments It is of great pleasure to thank one and all from Symbiosis Institute of Technology for their deep insights and expertise that greatly assisted the research and made the journey easy.

References

1. Patil, M., Kshirsagar, P., Samata Prabhu, Sonal Patil, Sunilka Patil: Brain Tumor Identification Using K-Means Clustering. International Journal of Engineering Trends and Technology. 4(3), pp 354–357 (2013)
2. Dhanalakshmi, P., Kanimozhi, T.: Automatic Segmentation of Brain Tumor using K-Means Clustering and its Area Calculation. International Journal of Advanced Electrical and Electronics Engineering. 2(2), pp 130–134 (2013)
3. Dubey, S.K., Ghosh, S.: Comparative Analysis of K-Means and Fuzzy C Means Algorithms. International Journal of Advanced Computer Science and Applications. 4(4), pp 35–39 (2013)
4. Vapnik, V.: The Nature of Statistical Learning Theory. Springer, New York (1995)
5. Scholkopf, B., Kah-Kay, S., Burges, C.J., Girosi, F., Niyogi, P., Poggio, T., Vapnik, V.: Comparing support vector machines with Gaussian kernels to radial basis function classifiers. IEEE trans Signal Processing. 45, pp. 2758–2765 (1997)
6. Wan, V., Campbell, W.M.: Support vector machines for speaker verification and identification. Presented at IEEE Workshop Neural Networks for Signal Processing, Sydney, Australia, pp. 775–784 (2000)
7. Pontil, M., Verri, A.: Support vector machines for 3-D object recognition. IEEE Trans. pattern anal. Machine Intel. 20. pp. 637–646 (1998)

Dual Gate Organic Inverter Circuit Behavior Analysis Based on Diode Load Logic Configuration

Yamini Pandey, Shubham Negi, Srishti, A.K. Baliga and Brijesh Kumar

Abstract The dual gate organic thin film transistor (DG-OTFT), at present is one of the most attractive devices in the field of organic electronics because of its overall better performance in comparison to single gate (SG) organic transistors. Organic electronics have shown good mechanical flexibility, lower temperature fabrication at lower cost in comparison to conventional MOSFET devices. They may not stand as a challenge for the MOS devices as of now but still due to their numerous advantages they are being chosen alternative future candidate by the industries, academia and R and D sections. The dual gate OTFT device analysis and its performance parameters extraction has been done in this paper. Besides this, comparison of different modes of operation of the dual gate device has been made, that justifies our working in the dual gate-based devices and circuits. The dual gate organic inverter circuit that has been analyzed is in the diode load logic (DLL) configuration because of its delay is small and speed of operation is better in comparison with zero-Vgs load logic (ZVLL) configuration.

Keywords Organic inverter · OTFT · DLL configuration

1 Introduction

Dual gate organic thin film transistors (DG-OTFT), since their advent in the year 2005 by Cui and Liang [1], have improved the performance of the OTFT immensely. Earlier, it was believed that due to their low mobility the OTFT would

Yamini Pandey (✉) · Shubham Negi · Srishti ·
A.K. Baliga · Brijesh Kumar (✉)
Department of Electronics and Communication Engineering,
School of Engineering and Technology, Graphic Era University,
Dehradun 248002, India
e-mail: yamini.yami5@gmail.com

Brijesh Kumar
e-mail: brijesh_kumar@ieee.org

© Springer Science+Business Media Singapore 2017

R. Singh and S. Choudhury (eds.), *Proceeding of International Conference on Intelligent Communication, Control and Devices*, Advances in Intelligent Systems and Computing 479, DOI 10.1007/978-981-10-1708-7_121

not be able to make an impact on a large scale until some new high mobility organic semiconducting materials (OSC) could be found, but it was with the device innovations like DG-OTFT [2] that the performance was improved. DG-OTFT posses numerous advantages over the conventional SG-OTFT such as higher device mobility, better subthreshold slope, lower threshold voltage, more robust device to name a few [3, 4]. Along with this, the secondary gate helps to put an external bias control over the threshold voltage. To add on to this the DG-OTFT being an organic transistor possesses the advantage of flexibility, lower temperature fabrication, and large roll to roll device size, over the conventional metal oxide semiconductor (MOS) devices [5–7].

The DG-OTFT works almost like a single gate with the exception of the bias on the secondary gate. The source drain electrodes perform their functioning of injecting and taking out the charge carriers, respectively, from the OSC layer. The gate electrodes which are separated from the OSC layer by means of a dielectric forms a conducting channel, when an adequate biasing is applied to them. The channel in the OTFT is formed by the accumulation, thus on proper biasing conditions two channels will be formed and they will be electrostatically interacted with each other to enhance the performance of the device and thus the threshold voltage is reduced.

2 Simulation Setup

Atlas by Silvaco, that is a 2-D numerical simulator, has been used for the study of the device and its application in the inverter circuit. It employs the Poole and Frenkel mobility model [6–9] for analyzing the devices and circuits. The dual gate device that has been analyzed here has the channel length (L) of 50 μm and a device width of 1600 μm.

The device fabrication [6] starts with a bottom gate electrode of thickness 50 nm of titanium followed by Al_2O_3 of 200 nm which acts as bottom dielectric material. It has a capacitance of 41 nF/cm^2 [7]. On top of it, there are patterned source drain contacts which are bilayer of titanium and gold of 3 and 80 nm, respectively. The titanium layer here acts just as an adhesion layer. Now the OSC material Pentacene, of 150 nm, is deposited by low temperature process such as vacuum evaporation. After this the top dielectric is deposited. This dielectric is often organic because OSC cannot withstand the high temperature processes. Here Parylene has been used as a top dielectric material with the capacitance 7.15 nF/cm^2 [7]. Its thickness is 30 nm. At last but not the least the top gate is deposited which is of Gold of the thickness 50 nm. The structure of the dual gate OTFT is shown in Fig. 1.

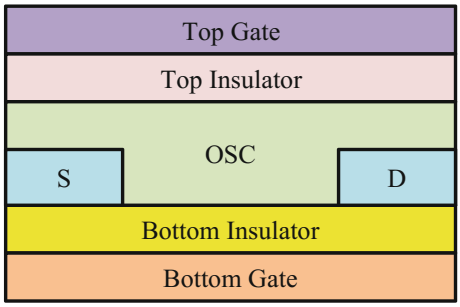


Fig. 1 Dual gate OTFT: structure

3 DG-OTFT: The Electrical Characteristics and Extraction of Parameter

The dual gate OTFT-based device, simulated through DeckBuild Atlas, has been shown in Fig. 2a. The layers of different materials used have been clearly shown in this figure. It is followed by the transfer curve for the device in Fig. 2b. At last the output curve of the device has been plotted in Fig. 2c.

A dual gate device can be operated in three different modes of operation which can be summed-up as follows: Top gate mode, Bottom gate mode and a dual gate mode [2]. The top gate is biased and the bottom gate is grounded in the top gate mode of the DG-OTFT, whereas it is vice versa in the bottom gate mode. In the dual gate mode both the gates are biased. The performance of the dual gate mode is superior in every aspect in comparison to the other two modes which is clearly apparent from the curves shown in the Fig. 3. The performance parameters for the dual gate device have been discussed in the Table 1.

4 DG-OTFT Inverter Circuit

In this section, analyses of the all-*p* (both driver and the load transistor are of the *p*-type) dual gate based inverter have been made. The inverter is in DLL configuration as shown in Fig. 4. In this configuration the gate and the drain of the load transistor are shorted [10–14]. This is done in order to preserve a steady drain–source current leading to the diode connected transistor [10, 13]. This helps to get better pull down of the circuit, thus reducing the circuit delay and increasing the speed of the circuit.

Also to be noted here is that the load as well as the driver transistor in this configuration works in the enhancement mode thus the ratio of the driver to the load transistor is 5:1. The W_D (driver transistor width) = 16,000 µm and W_L (load transistor width) = 3200 µm. The supply voltage V_{DD} is varied from 0 to 10 V for this analysis. The 0 V indicates the logic "0" and 10 V indicates the logic "1" [11].

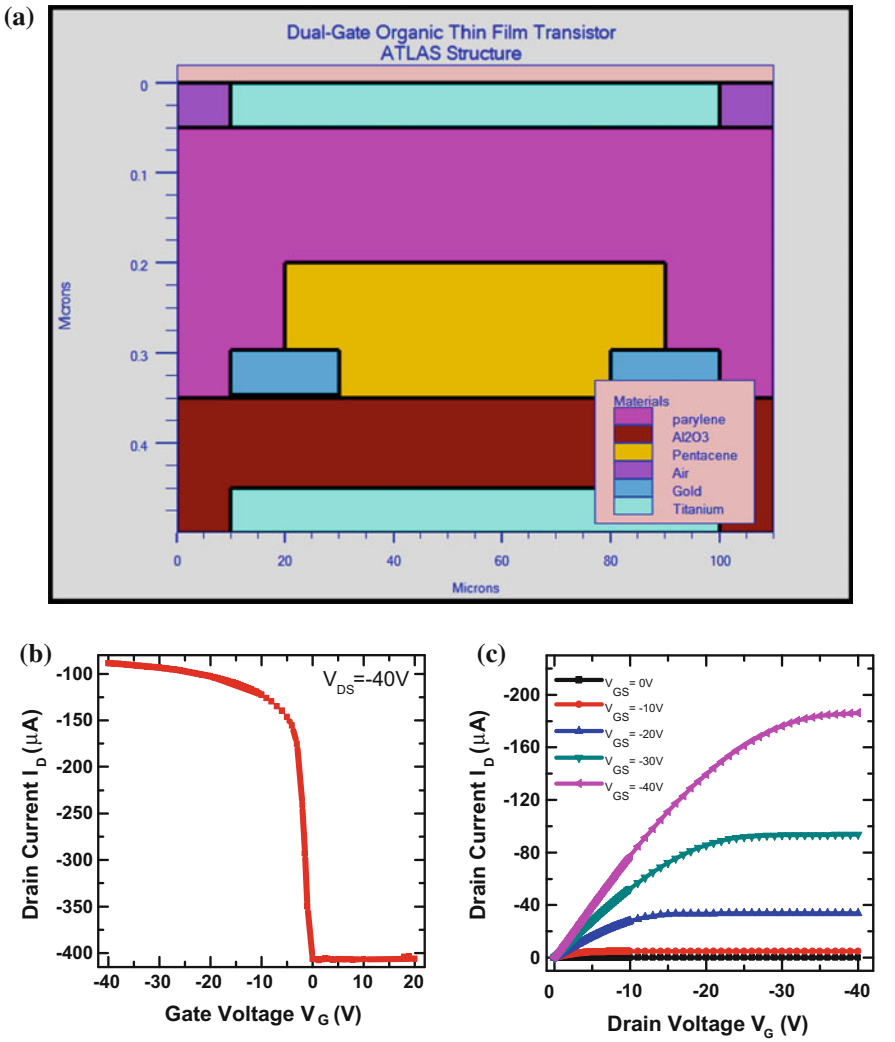


Fig. 2 **a** Simulated device structure, **b** Transfer characteristic curve and **c** Output characteristic curve for the device

The V–T characteristic and the transient response for the inverter circuit are shown in Fig. 5a, b. The V_{OH} of the device is 9 V and the V_{OL} of the device is 0.25 V. Therefore, the output swing of the device so obtained is 8.75 V. The plot of gain against input voltage and voltage transfer characteristics at different voltages are shown in Fig. 6a, b, respectively.

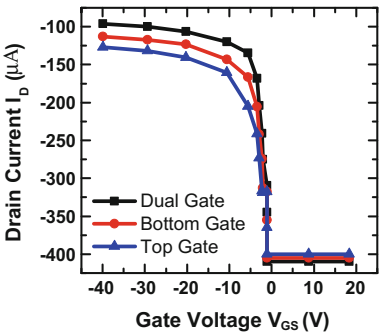


Fig. 3 Comparison of different modes of operation of dual gate OTFT

Table 1 Extracted performance parameters of dual gate OTFT

Name of the parameter	Simulated value
V_T (threshold voltage in V)	−4.53
S.S. (subthreshold voltage in V/Dec.)	0.202
I_{ON}/I_{OFF} (current on–off ratio)	10^8
μ (field effect mobility in cm^2/Vs)	0.69

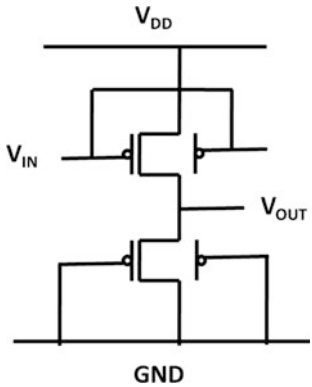


Fig. 4 Schematic of inverter circuit in DLL configuration

5 Conclusion

This paper analyzes the Pentacene-based dual gate device and organic inverter circuit based on this device. The device shows an overall excellent performance. Along with it a comparison has also been made between the different modes of operation of the DG-OTFT, wherein the dual gate mode was best. The inverter circuit based on DG-OTFT is realized in the DLL configuration. This circuit shows good pull down and high output swing of 8.75 V.

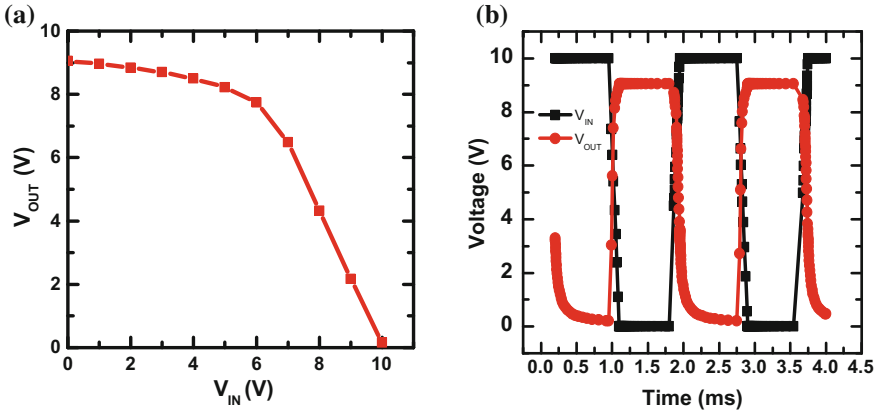


Fig. 5 Inverter circuit. **a** V–T characteristic curve and **b** Transient response

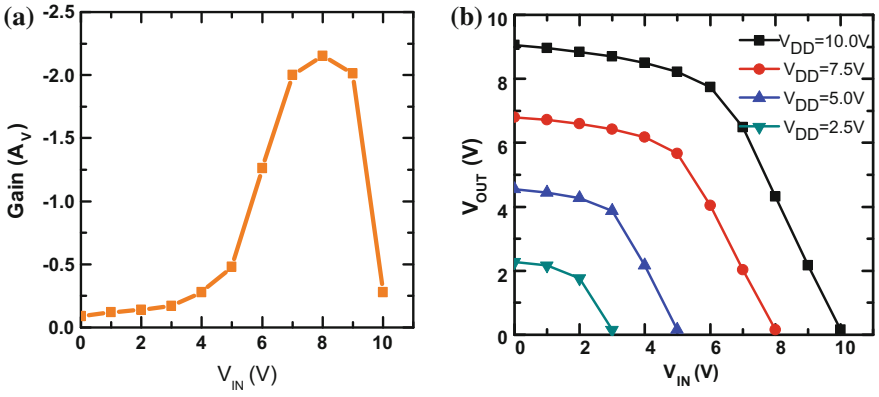


Fig. 6 **a** Plot of gain against V_{IN} **b** Variation of V_{OUT} with V_{IN} at different values of V_{DD}

References

1. Cui, T., Liang, G.: Dual gate pentacene organic field-effect transistors based on a nanoassem-bled SiO_2 nanoparticle thin film as the gate dielectric layer. Appl. Phys. Lett. 86 (2005) 064102–064105
2. Kumar, B., Kaushik, B.K., Negi, Y.S.: Organic thin film transistors: structures, models, materials, fabrication, and applications: A review. Polymer Reviews 54 (4) (2014) 33–111
3. Kumar, B., Kaushik, B.K., Negi, Y.S, Goswami, V.: Single and dual gate OTFTs based robust organic digital design. Microelectron. Rel. 54 (1) (2014) 100–109
4. Spijkman, M., Mathijssen, S.G.J., Smits, E.C.P., Kemerink, M., Blom, P.W.M., de Leeuw, D.M.: Monolayer dual gate transistors with a single charge transport layer. Appl. Phys. Lett. 96 (2010) 143304

5. Kumar, B., Kaushik, B.K., Negi, Y.S.: Perspectives and challenges for organic thin film transistors: Materials, devices, processes and applications. J. Mater. Sci. Mater. Electron. 25 (1) (2014) 1–30
6. Lin, Y.Y., Gundlach, D.J., Nelson, S., Jackson, T.N.: Stacked pentacene layer organic thin film transistors with improved characteristics. IEEE Electron Device Lett. 18 (1997) 606–608
7. Mittal, P., Kumar, B., Negi, Y.S., Kaushik, B.K., Singh, R.K.: Channel length variation effect on performance parameters of organic field effect transistors. Microelectron. J. 43 (2012) 985–994
8. Mittal, P., Negi, Y.S., Singh, R.K.: A depth analysis for different structures of organic thin film transistors: modeling of performance limiting issues. Microelectron Engineering, 150 (2016) 7–18
9. ATLAS User's Manual Device Simulation Software. Silvaco International Ltd., Santa Clara, USA (2013)
10. Koo, J.B., Ku, C.H., Lim, S.C., Lee, J.H., Kim, S.H., Lim, J.W., Yun, S.J., Yang, Y.S., Yuh, K.S.: Threshold voltage control of pentacene thin film transistor with dual gate structure. Journal of Information Display 7 (2010) 27–30
11. Kumar, B., Kaushik, B.K., Negi, Y.S.: Static and dynamic analysis of organic and hybrid inverter circuits. Journal of Computational Electronics 12 (2013) 765–774
12. Kumar, B., Kaushik, B.K., Negi, Y.S.: Static and dynamic characteristics of dual gate organic TFT based NAND and NOR circuits. Journal of Computational Electronics 13 (2014) 1–12
13. Kumar, B., Kaushik, B.K., Negi, Y.S.: Design and analysis of noise margin, write ability and read stability of organic and hybrid 6-T SRAM. Microelectron. Rel. 54 (12) (2014) 2801–2812
14. Goswami, V. Kumar, B., Kaushik, B.K., Negi, Y.S, Yadav, K.L.: Analysis of static and dynamic performance of organic inverter circuits based on dual and single gate OTFTs. IET Circuits, Devices & Systems. 7(6) (2013) 345–351

Substrate Integrated Waveguide Leaky Wave Antenna with Backward to Forward Scanning Capability

Anumeha Badoni, Nitin Kumar and S.C. Gupta

Abstract Leaky wave antennas (LWA) have inherent property of beam scanning. As the energy travels from one end to another end of waveguide, it leaks/radiates from the discontinuity introduced in it. In this communication, substrate integrated waveguide (SIW) LWA is proposed, showing scanning properties in backward direction (−41° to −24°) and in forward direction (+11° to +53°), with a wide bandwidth of 3.6 GHz. SIW is designed with cutoff frequency at 11 GHz with a tapered T slot which radiates energy in both backward and forward directions. Simulated results are reported for an array of 7 unit cells operating partial in Ku band (11.3–14.9 GHz). The model is designed and simulated using Ansys.

Keywords Leaky wave antenna (LWA) · Substrate integrated waveguide (SIW) · Beam scanning

1 Introduction

Leaky wave antennas (LWAs) have found much attention in last few decades. LWA is basically a waveguide structure that permits it to leak power along its length. These antennas produces narrow beam from discontinuity along its length [1]. Earlier LWAs offered scanning in forward direction but after some decades backward scanning become achievable using metamaterials and slots [2]. Recent LWAs antennas have the capability to scan from backfire to endfire directions [3–6]. Slots in the antennas provide forward as well as backward scanning. LWAs are widely used for millimeter and microwave applications because of only their property of scan with frequency [7–11]. The radiation of LWA occurs in approximately at a angle of [12]

Anumeha Badoni (✉)
Digital Communication, DIT University, Dehradun, India
e-mail: anumehabadoni33@gmail.com

Nitin Kumar · S.C. Gupta
Department of ECE, DIT University, Dehradun, India

© Springer Science+Business Media Singapore 2017

R. Singh and S. Choudhury (eds.), *Proceeding of International Conference on Intelligent Communication, Control and Devices*, Advances in Intelligent Systems and Computing 479, DOI 10.1007/978-981-10-1708-7_122

$$\theta = \cos^{-1}(\beta/k_0) \tag{1}$$

LWA based on substrate integrated waveguide (SIW) found attention in recent years for its advantages of low profile, low cost, easy integration with other devices. It has replaced conventional rectangular waveguide used in earlier antennas. LWA using SIW proposed recently with many advantages over earlier antennas [12, 13].

Usually nontapered LWAs have a radiation pattern with high sidelobe level, which are restricted for radar and satellite application. Tapering of slots have been done to reduce side lobe level [14, 15] and to enhance the performance of antenna to obtain directive beam [16].

2 Design of SIW-Based LWA Design

2.1 Proposed Structure

The proposed structure consists of an array of tapered T slot in SIW-based LWA as shown in Fig. 1. Duroid with relative permittivity 2.2 and loss tangent 0.0009 is taken as the substrate of the antenna. Ansys HFSS software is used to design and simulate the structure. Tapered feed is used to obtain wide bandwidth from 11.3 to 14.9 GHz and a 50 Ω transmission line is used in order to watch the port impedance. The thickness of substrate is 0.787 and a 0.035 mm layer copper is used for simulation purpose. Slots of the antenna are placed at quarter of guided wavelength distance from center of each other. Length of slots is approximately equal to quarter of guided wavelength. The design of unit cell and SIW is discussed in the next section.

2.2 SIW and Unit Cell Design

Design parameters of substrate integrated waveguide at 11 GHz cut-off frequency can be calculated using following mathematics equations [17]:

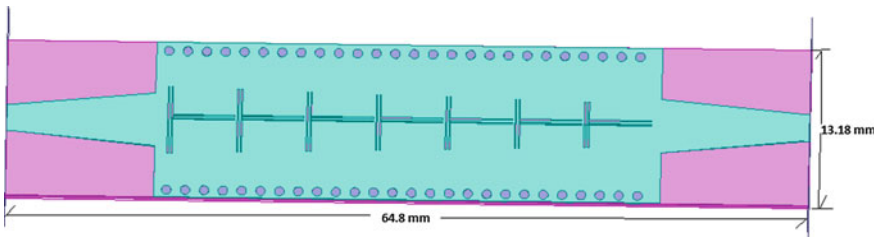


Fig. 1 Proposed structure of SIW leaky wave antenna

$$w = 0.5\left[a + \sqrt{(a+0.54)^2 - 0.4d^2}\right] + 0.27d, \tag{1}$$

where d = diameter of via, w = effective width which can be calculated by Eq. (1), total width of patch 'a' is given by

$$a = w - \frac{1.08d^2}{2d} + \frac{0.1d^2}{w}. \tag{2}$$

And width of SIW, length of taper and end fed are calculated by the following formulas:

$$W_{\text{siw}} = w + d. \tag{3}$$

$$L_{\text{tap}} = 10d. \tag{4}$$

$$L_p = 5d. \tag{5}$$

A SIW with taper feed and unit cell of antenna is shown in Fig. 2a, b. Slots are inserted in the antenna as discontinuity which radiate energy at fast wave mode. The distance between the slots is chosen as quarter of guided wavelength. Tapering is done to reduce sidelobe level of antenna. A comparison is shown in Fig. 6 between radiation pattern of nontapered slots and tapered slots at frequency 14.8 GHz. The various dimensions after calculation and optimization are presented in Table 1.

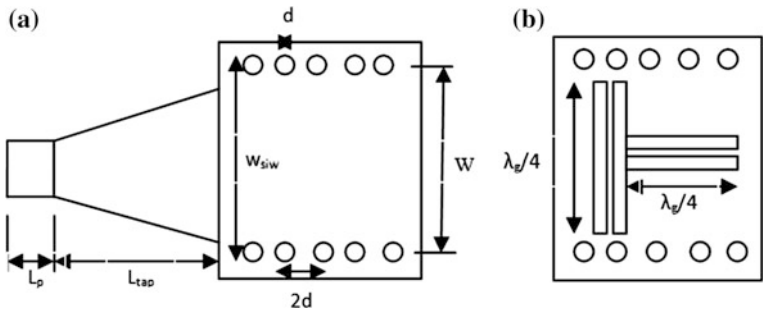


Fig. 2 **a** Design of SIW. **b** Unit cell structure of antenna

Table 1 Various dimensions of LWA

S. No.	Properties	Dimensions (mm)
1	Width of patch	13.18
2	Center to center distance (w)	11.8
3	Diameter of via (d)	0.76
4	Spacing between diameter ($2d$)	1.52
5	With of each slot	0.1
6	Distance between slots	0.2
7	Taper length	7.6
8	Taper fed box length	3.8

3 Simulated Results

3.1 S Parameters

The results for S_{11} and S_{21} are shown in figure, which shows the bandwidth of the proposed antenna. S_{11} is assured less than −10 db and band is achieved from 11.3 to 14.9 GHz. Similarly, S_{21} in this range also gives an idea how electromagnetic waves are leaked from the structure. Bandwidth of the antenna from S_{11} calculated of 3.6 GHz, a wide bandwidth of antenna is achieved due to taper feeding of substrate integrated waveguide (Fig. 3).

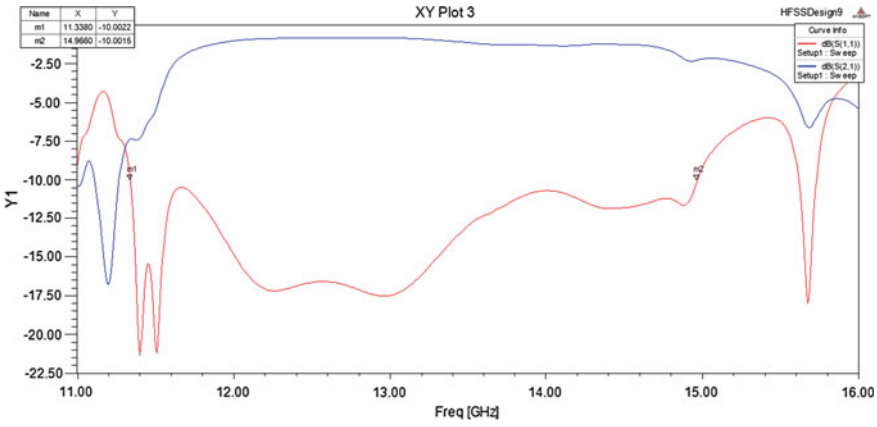


Fig. 3 Simulated S parameters of leaky wave antenna (LWA)

3.2 Radiation Patterns

The simulated results show beam scanning at simulated frequency range in forward direction (+11° to +53°) scanning and in backward direction (−24° to −41°) are as shown in figure. Normalized pattern of antenna gain is shown giving directions of maximum radiated power. It is shown in figures that antenna shows left-hand scanning from 11.3 to 12.8 GHz of 17°. While from 12.9 to 14.9 GHz it shows right-hand scanning of 42°.

Tapering in transverse slots reduces side lobe level in forward direction. In Fig. 4 patterns are shown at different frequencies 13.3 and 14.8 GHz with scanning angles 11° and 53°. Similarly in Fig. 5, it shows scanning at different frequencies and some of them are 11.8 and 12.8 GHz with −41° and −24°.

A comparison between nontapered and tapered results is shown in Fig. 6.

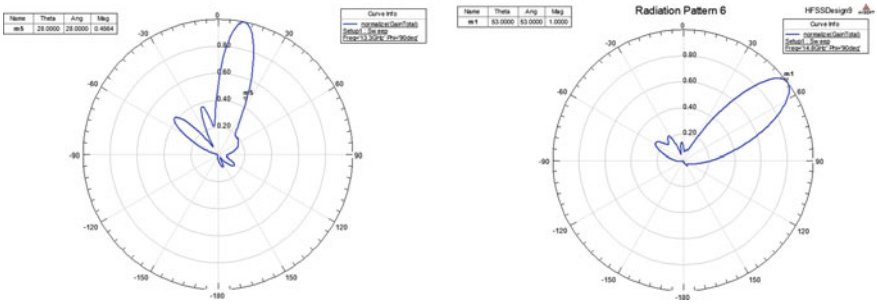


Fig. 4 Normalized pattern of forward scanning of LWA

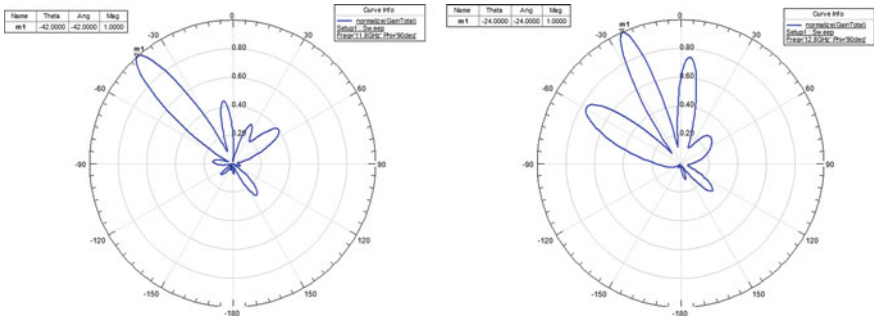


Fig. 5 Normalized pattern of backward scanning of LWA

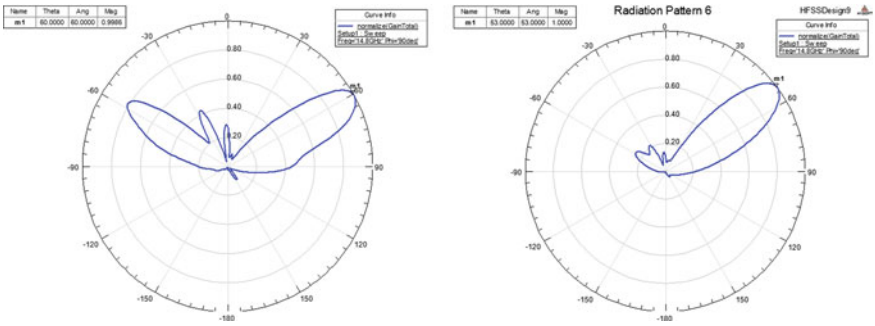


Fig. 6 **a** Radiation pattern with nontapered slot. **b** Radiation pattern of tapered slot

4 Conclusion

Backward and forward scanning shown with in Ku band simulated in the paper. Tapering of the slots is used to reduce sidelobe level in order to enhance antenna performance. Because of its beam scanning capability, it may be used for many millimeter and microwave applications. Frequency-scanned antennas may be used in radar and in smart antennas for communication purpose.

Acknowledgments This work is supported by Defence Research and Development Organization of India under grant ERIP/ER/1403170/M/01/1555.

References

1. L. O. Goldstone and A. A. Oliner, “Leaky-wave antennas I: rectangular waveguides,” IRE Transactions on Antennas and Propagation, vol. 7, no. 4, pp. 307–319, 1959.
2. David R. Jackson,, Christophe Calo, and Tatsuo Itoh, “ Leaky-Wave Antennas” Proceedings of the IEEE| Vol. 100, No. 7, July 2012.
3. W. W. Hansen, “Radiating electromagnetic waveguide,” U.S. Patent no. 2,402,622, 1940.
4. L. O. Goldstone and A. A. Oliner, “Leaky wave antennas II: Circular waveguides,” IRE Transactions on Antennas and Propagation, vol. 9, no. 3, pp. 280–290, 1961.
5. J. L. Gómez-Tornero, A. D. L. T. Mart´ınez, D. C. Rebenaque, M. Gugliemi, and A. Álvarez-Melcón, “Design of tapered leaky-wave antennas in hybrid waveguide-planar technology for millimeter waveband applications,” IEEE Transactions on Antennas and Propagation, vol. 53, no. 8, pp. 2563–2577, 2005.
6. Y. J. Cheng, W. Hong, K. Wu, and Y. Fan, “Millimeter-wave substrate integrated waveguide long slot leaky-wave antennas and two-dimensional multibeam applications,” IEEE Transactions on Antennas and Propagation, vol. 59, no. 1, pp. 40–47, 2011.
7. A. A. Oliner and D. R. Jackson, “Leaky-wave antennas,” in Antenna Engineering Handbook, 4th ed., J. L. Volakis, Ed. New York: McGrawHill, 2007.
8. A. Krauss, H. Bayer, R. Stephan, and M. A. Heim, “A dual-band circularly-polarised leaky-wave antenna for mobile ka-band satellite communications,” IEEE Antennas and Propagation in Wireless Communications (APWC), 2011IEEE-APS Topical Conference on, pp. 203–206, September 2011.

9. J. L. G6mez, A. de la Torre, D. Cafiete, M. Gugliemi,, and A. A. Melc6n,"Design of tapered leaky-wave antennas in hybrid waveguide-planar technology for millimeter waveband applications," IEEE Transactions on Antennas and Propagation, vol. 53, pp. 2563–2577, August 2005.
10. A. Martinez, J. L. G6mez, and G. Goussetis, "Holographic pattern synthesis with modulated substrate integrated waveguide line-source leaky-wave antennas," IEEE Transactions on Antennas and Propagation, vol. 61, pp. 3466–3474, July 2013.
11. S. Otto, A. Rennings, K. Solbach, and C. Caloz, "Transmission line modeling and asymptotic formulas for periodic leaky-wave antennas scanning through broadside," IEEE Transactions on Antennas and Propagation, vol. 59, no. 10, pp. 3695–3709, October 2011.
12. D. Deslandes and K. Wu, "Integrated microstrip and rectangular waveguide in planar form," IEEE Microwave and Wireless Components Letters, vol. 11, no. 2, pp. 68–70, 2001.
13. D. Deslandes and K. Wu, "Substrate integrated waveguide leaky-wave antenna: concept and design considerations," in Proceedings of the Asia-Pacific Microwave Conference (APMC'05), December 2005.
14. A. Krauss, H. Bayer, R. Stephan, and M. A. Heim, "A dual-band circularly-polarised leaky-wave antenna for mobile ka-band satellite communications," IEEE Antennas and Propagation in Wireless Communications (APWC), 2011IEEE-APS Topical Conference on, pp. 203–206, September 2011.
15. J. L. G6mez, A. de la Torre, D. Cafiete, M. Gugliemi,, and A. A. Melc6n, "Design of tapered leaky-wave antennas in hybrid waveguide-planar technology for millimeter waveband applications," IEEE Transactions on Antennas and Propagation, vol. 53, pp. 2563–2577, August 2005.
16. A. Martinez, J. L. G6mez, and G. Goussetis, "Holographic pattern synthesis with modulated substrate integrated waveguide line-source leaky-wave antennas," IEEE Transactions on Antennas and Propagation, vol. 61, pp. 3466–3474, July 2013.
17. F. Xu and K. Wu, "Guided-wave and leakage characteristics of substrate integrated waveguide," IEEE Trans. Microwave Theory Tech., vol. 53, pp. 66–73, Jan. 2005.

Optimal Power Dispatch in Competitive Market

Aayush Shrivastava, Manjaree Pandit, Devender Saini and Raj Gaurav Mishra

Abstract This paper presents the solution of dynamic load dispatching problem using particle swarm optimization (PSO) evolutionary technique. The PSO is used for minimizing the cost with subject to constraints such as capacity of generation and analyses the two different cases on IEEE 30 bus, 6-generator data. It found that the proposed method is capable to provide feasible results for the generating power.

Keywords Power dispatch · Power limits · PSO · Dynamic economic dispatch (DED)

1 Introduction

In competitive market, continuous power supply is very essential for consumers at minimum cost [1, 2]. The generation of power should satisfy the demand of consumer at optimal cost. In power system, security is an important constraint while dispatching power to consumers because of time-dependent demand [3]. To reach optimal cost of generation, generators must be dynamically scheduled according to the hourly demand of the consumers by satisfying complex constraints [1]. In static dispatch, all generators will be operated on full load condition. Compared to dynamic dispatch where generators are scheduled dynamically according to demand, static economic dispatch will become costlier in terms of generation.

A. Shrivastava (✉) · D. Saini · R.G. Mishra
CoES, University of Petroleum and Energy Studies, Dehradun, Uttarakhand, India
e-mail: mr.aayushshrivastava@gmail.com

D. Saini
e-mail: dksaini@ddn.upes.ac.in

R.G. Mishra
e-mail: rgmishra@ddn.upes.ac.in

M. Pandit
Madhav Institute of Technology and Science, Gwalior, Madhya Pradesh, India
e-mail: manjaree_p@hotmail.com

© Springer Science+Business Media Singapore 2017

R. Singh and S. Choudhury (eds.), *Proceeding of International Conference on Intelligent Communication, Control and Devices*, Advances in Intelligent Systems and Computing 479, DOI 10.1007/978-981-10-1708-7_123

Conventionally, the cost function of the generators is minimized using sequential quadratic programming (SQP) [1], function minimization constraints, and line search algorithm. This paper optimizes the cost of generation including complex constraint using evolutionary technique, particle swarm optimization (PSO).

2 Dynamic Energy Dispatch

The load dispatch problem is mostly functionalized in the area of power system to search the feasible and optimal scheduling of generating units which satisfy the complex and noncomplex constraints [4]. Power system control is essential to keep a continuous stability between electrical generation and a variable consumer load demand, and to preserve system frequency, level of voltages, security at least cost [5]. Scheduling of power is done in such a way that the system constraints and network are matched. Unit commitment of each generator will be changing dynamically according to the need of electricity. Hence, there is a need to satisfy the hourly generation and hourly demand. Various traditional and evolutionary algorithms are functionalized to solve this problem to reach a feasible power generation with minimum cost [6]. The key goal of dynamic energy dispatch problem is to dispatch the power from generating station to consumer optimally and to provide power at lowest cost to the consumer. Optimal dispatch plan strains to sustain the equilibrium between the power generation and power demand by optimizing the fuel cost and losses in transmission. Traditional technique is a very efficient way to reach the optimal results but it is applied only when the objective function is quadratic [6, 7]. Interior point and SQP, proved to be feasible in finding the optimal cost [8]. Nature-inspired evolutionary techniques are also very popular for solving convex problems. PSO, memetic algorithm, genetic algorithm (GA) [9], harmony search algorithm, differential evolution (DE) proved capable to give efficient result for energy dispatch problem. PSO is very efficient and found to be an attractive implementation in MATLAB platform. In this paper, dynamic economic dispatch problem is solved by considering (i) curves of generator cost swapped by bids price, (ii) dispatch carried out concurrently in the place of "traditional dispatch", (iii) energy limits, (iv) generator contingencies. The proposed approach is tested on 6-generator system and IEEE 30 bus system.

2.1 Objective Function

The important aim of DED problem is to reduce energy cost of generating units. The total cost of N unit of generators at time interval "t" is given as

$$\text{Cost} = \sum_{t=1}^{T} \sum_{i=1}^{N} \left[F(P_i(t)) \right] \tag{1}$$

where $(P_i(t))$ is power generation for ith unit at time interval "t". $F(P_i\,(t))$ is the bid price of energy dispatch.

2.2 Inequivalent Constraints

(1) Unit power generation capacity constraints

$$P_i^{\min} \le P_i(t) \le P_i^{\max} \tag{2}$$

where $P_i^{\min}$ is the minimum capacity of generators, $P_i^{\max}$ is the maximum capacity of generator, and $P_i(t)$ is the actual power generated by generators.

(2) Unit generating power coupling constraints

$$P_i(t) \le P_i^{\max} \tag{3}$$

Here, $P_i^{\min}$, $P_i^{\max}$ are restrictions of power generating units.

2.3 Equality Constraints

(1) Power equality constraint for time intervals (t) is given as:

$$\sum_{i=1}^{N} P_i(t) = P_D(t) \tag{4}$$

Consumer demand for time intervals' is given by $P_D(t)$ and $P_i(t)$ is power generated by generator.

3 Particle Swarm Optimizing

PSO technique was proposed by Kennedy and Eberhart in 1995. It is the technique which is inspired by nature such as the behavior and movement of birds and insects, and the theory is based on searching of food to fulfill needs of groups. Fitness value plays a very important role in searching food for whole group. The method of

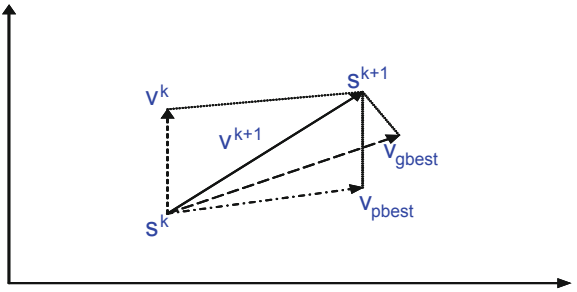


Fig. 1 Concept of modification of a searching point by PSO

searching called the global gradient and less stochastic search method is suitable for the continuous variable problem [10, 11] (Fig. 1).

s^k = "current searching point", s^{k+1} = "modified searching point", v^k = "current velocity", v^{k+1} = "modified velocity", v_{pbest} = "velocity based on pbest", v_{gbest} = "velocity based on *g*best".

The modification of the particle's position can be mathematically modeled according to the following equation:

$$V_i^{k+1} = wV_i^k + c_1 \,\text{rand}_1(\ldots)x(\text{pbest}_i - s_i^k) + c_2 \,\text{rand}_2(\ldots)x(\text{gbest}_i - s_i^k) \qquad (5)$$

4 Result and Discussion

Case 1: Power generation without outage condition

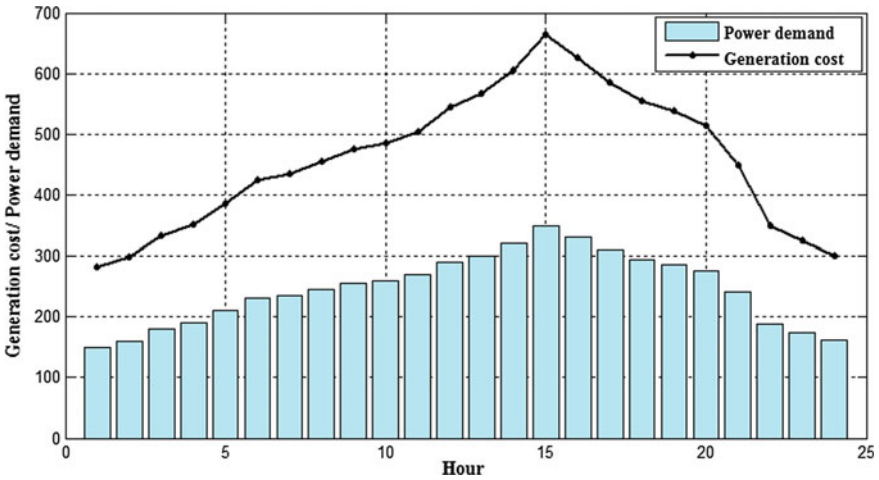


Fig. 2 Variation of generation cost with respect to load variation

Here, we analyze the generation cost with respect to the load variation or consumer demand. Figure 2 shows the variation of generation cost with respect to load. Power dispatch by every generator is shown in Table 1. This is found that all the constraints are satisfied with power generation and capable to fulfill the demand of the consumer.

Case 2: Power generation with outage condition

In this case, one generator is shut down due to maintenance. The cost of generation is affected due to generator shut down. The variation is shown in Fig. 3. This generation cost in outage condition of generator is given in Table 2. It shows that the third generator is in outage position and it will not generate any power.

Figure 3 shows the variation of cost for the outage case condition with load variation. It shows the cost variation between Cases 1 and 2 and found that the generation cost of outage case condition is more.

Table 1 Power generated by every generators for 24 hr (Case 1)

S. no	P1 MW	P2 MW	P3 MW	P4 MW	P5 MW	P6 MW	Power demand MW/H	Generation cost $/H
1	50	20	48	10	10	12	150	281.5858
2	50	28	50	10	10	12	160	297.5858
3	50	48	50	10	10	12	180	332.5858
4	50	57.9999	50	10	10	12	190	350.0871
5	50	78	50	10	10	12	210	385.0858
6	67.9998	80	50	10	10	12	230	424.5912
7	72.6393	80	50	10	10.3118	12	235	435.0135
8	83.1005	79.8992	50	10	10.0003	12	245	454.6114
9	93.3424	79.5495	50	10.0152	10	12.0928	255	474.8118
10	97.8712	80	50	10	10	12.1288	260	484.7147
11	l08	80	50	10	10	12	270	504.5858
12	128	80	50	10	10	12	290	544.5858
13	136.9981	79.9666	50	10.8316	10.1392	12.0638	300	565.8829
14	158.4806	79.3895	50	10.1298	10	12	320	604.9027
15	188	80	50	10	10	12	350	664.5858
16	168.9529	79.0472	50	10	10	12	330	624.8247
17	148	80	50	10	10	12	310	584.5858
18	133	80	50	10	10	12	295	554.5858
19	120.1738	80	49.8291	10.0074	10	14.9899	285	537.7629
20	113	80	50	10	10	12	275	514.5858
21	80.6976	79.3018	50	10	10	12	242	448.7915
22	50	56.9995	50	10.0004	10	12	189	348.3374
23	50	43	50	10	10	12	175	323.8358
24	50	30	50	10	10	12	162	301.0858

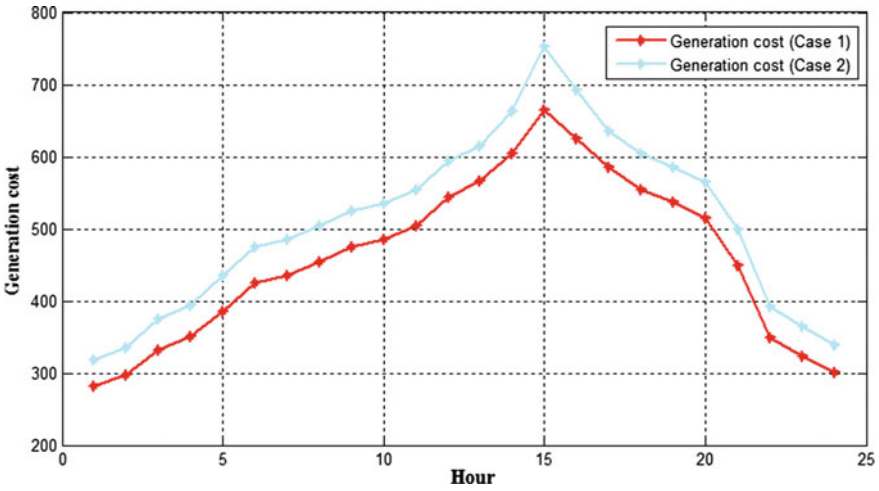


Fig. 3 Variation of generation cost for generator outage case

Table 2 Power generation cost for outage case condition (Case 2)

H	P1	P2	P3	P4	P5	P6	Power demand MW/H	Generation cost $/H
1	50	68	0	10	10	12	150	317.5858
2	50	78	0	10	10	12	160	335.0858
3	68	80	0	10	10	12	180	374.5858
4	78	80	0	10	10	12	190	394.5858
5	98	80	0	10	10	12	210	434.5858
6	118	80	0	10	10	12	230	474.5858
7	123	80	0	10	10	12	235	484.5858
8	133	80	50	10	10	12	245	504.5858
9	143	80	0	10	10	12	255	524.5858
10	148	80	0	10	10	12	260	534.5858
11	158	80	0	10	10	12	270	554.5858
12	178	80	0	10	10	12	290	594.5858
13	188	80	0	10	10	12	300	614.5858
14	200	80	0	10	18	12	320	662.5858
15	200	80	0	10	20	40	350	752.5858
16	200	80	0	10	28	12	330	692.5858
17	198	80	0	10	10	12	310	634.5858
18	183	80	0	10	10	12	295	604.5858
19	173	80	0	10	10	12	285	584 5858
20	163	80	0	10	10	12	275	564.5858
21	130	80	0	10	10	12	242	498.5858
22	77	80	0	10	10	12	189	392.5858
23	63	80	0	10	10	12	175	364.5858
24	50	80	0	10	10	12	162	338.5858

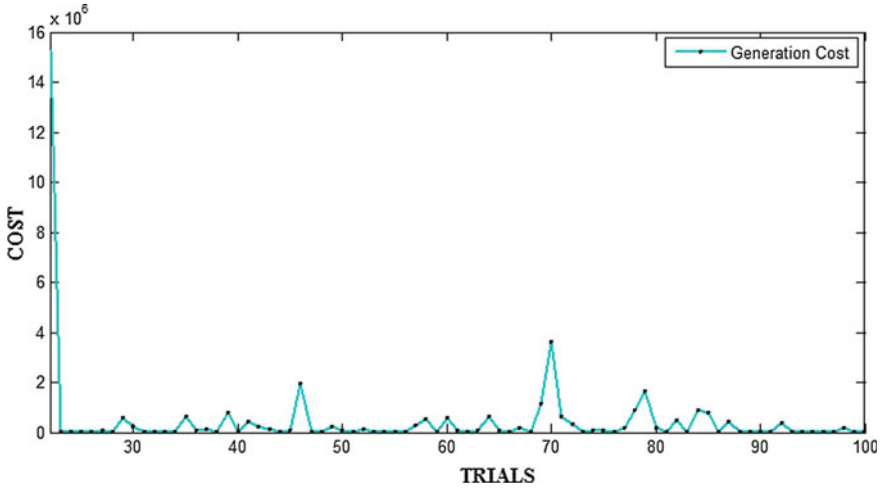


Fig. 4 Convergence graph of power dispatch (Case 1)

Figure 4 shows the convergence characteristic of PSO and feasible results are found for the optimal generation by satisfying all the equality constraints. PSO has good convergences behavior and found feasible result in 100 trials.

5 Conclusions

The paper presents solution of energy dispatch model for deregulated market of electricity using PSO algorithm. The proposed solution found the result for two cases: (1) without outage (2) with outage condition. The obtained results are feasible and capable to handle the behavior of stable convergence.

References

1. M. Pandit, L. Srivastava and K. Pal, "Static/dynamic optimal dispatch of energy and reserve using recurrent differential evolution", IET Generation, Transmission & Distribution, vol. 7, Issue 12, pp. 1401–1414, 2013 doi:10.1049/iet-gtd.2013.0127
2. David, A. K., & Wen, F. (2000). Strategic bidding in competitive electricity markets: a literature survey. In Power Engineering Society Summer Meeting, 2000. IEEE (Vol. 4, pp. 2168–2173). IEEE.
3. Alsac, O., Bright, J., Prais, M., & Stott, B. (1990). Further developments in LP-based optimal power flow. Power Systems, IEEE Transactions on, 5(3), 697–711.
4. Rao, R., & Patel, V. (2012). An elitist teaching-learning-based optimization algorithm for solving complex constrained optimization problems. International Journal of Industrial Engineering Computations, 3(4), 535–560.

5. Panigrahi, B. K., V. Ravikumar Pandi, and Sanjoy Das. "Adaptive particle swarm optimization approach for static and dynamic economic load dispatch." Energy conversion and management 49.6 (2008): 1407–1415.
6. Shrivastava, A., Bhatt, A., Pandit, M., & Dubey, H. M. (2014, April). Dynamic energy and reserve dispatch solutions for electricity market with practical constraints: Intelligent computing technique. In Communication Systems and Network Technologies (CSNT), 2014 Fourth International Conference on (pp. 990–994). IEEE.
7. Bhatt, A., Shrivastava, A., Pandit, M., & Mohan Dubey, H. (2014, May). Dynamic scheduling of operating energy and reserve in electricity market with ramp rate constraints. In Recent Advances and Innovations in Engineering (ICRAIE), 2014 (pp. 1–6). IEEE.
8. Shrivastava, A., Bhatt, A., Pandit, M., & Dubey, H. M. Optimal Dispatch of Energy/Reserve in Restructured Electricity Market with Demand Variations. constraints, 27, 28.
9. Fonseca, "Multiobjective Genetic Algorithms with Application to Control Engineering Problems", PhD Thesis, Department of Automatic Control and Systems Engineering. The University of Sheffild, September 1995.
10. http://www.swarmintelligence.org/tutorials.php.
11. Eberhart, R. C. and Kennedy, J. A new optimizer using particle swarm theory. Proceedings of the sixth international symposium on micro machine and human science pp. 39–43. IEEE service center, Piscataway, NJ, Nagoya, Japan, 1995.

Improvement in Performance of OLED by Introducing Additional Hole Blocking Layer

Akanksha Uniyal and Poornima Mittal

Abstract Organic Light Emitting Diode (OLED) is one of the most recent emerging area of research that are very popular among the researcher from industries and academia. OLED possess many advantages like larger viewing angle, many times thinner than LCD and are brighter, hence it does not require backlight. In this paper, we have analyzed the improvement in the performance of OLED's in terms of current by introducing an additional layer. This additional layer is used to increase the recombination rate by reducing the mobility of the injected holes. The balanced recombination can be achieved by matching the mobility of the injected holes and electrons. Now as the Langevin recombination is directly proportional to the number of photons produced, hence, efficiency increases.

Keywords Organic LED · Hole blocking layer · Recombination rate · Organic semiconductor

1 Introduction

Organic Light Emitting Diodes (OLEDs) are gaining numerous attention at present because of their various benefits that they hold over the conventional LEDs. OLEDs, to name a few, have a large viewing angle, low power consumption, less fabrication cost, and large area (roll to roll) applications. OLEDs have possible applications in the flat panel displays and in lightning applications [1–6].

The generation of exciton, is a major problem in the OLEDs, which causes the charge carriers to skip, due to which proper recombination does not occur. So here

Akanksha Uniyal (✉) · Poornima Mittal
Department of Electronics and Communication Engineering,
School of Engineering and Technology, Graphic Era University,
Dehradun 248002, India
e-mail: akankshauniyal00@gmail.com

Poornima Mittal
e-mail: poornima2822@ieee.org

© Springer Science+Business Media Singapore 2017

R. Singh and S. Choudhury (eds.), *Proceeding of International Conference on Intelligent Communication, Control and Devices*, Advances in Intelligent Systems and Computing 479, DOI 10.1007/978-981-10-1708-7_124

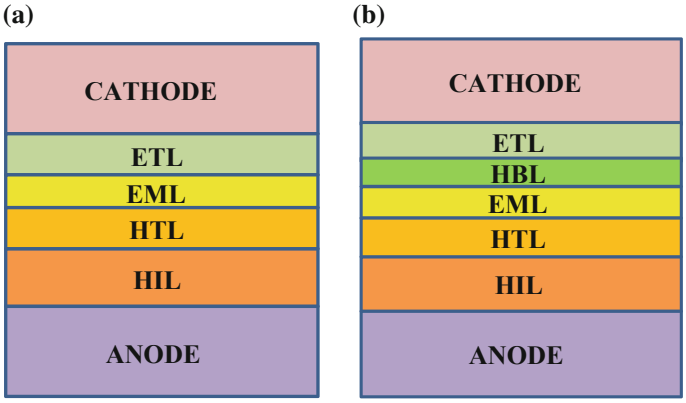


Fig. 1 Structures of the devices. **a** Structure of the multilayered OLED. **b** Structure of Device 2 containing an additional HBL layer [1]

an additional hole blocking layer (HBL) is being introduced, which makes the confinement of the excitons possible [2], because of this, balanced recombination of the charge carriers are possible. In OLEDs, the efficiency is the total number of photons generated to the total number of injected carriers. This maximal efficiency can be achieved through the proper recombination and high efficiency of the carrier injection. This gives the external quantum efficiency (EQE), so a proper recombination should be present there in the emissive layer (EML) [7–11] for achieving this maximal efficiency.

However, commonly used OLEDs does not provide such balanced injection and transportation of the charge carriers. One of the reasons for this is that in organic material the mobility of the injected holes is more than the mobility of the injected electrons. Hence for proper recombination an additional HBL is introduced [8], which blocks the holes and confines them, to give the proper recombination of the electrons and holes. So additional layer introduced here can improve the performance by putting a restriction on the holes and thus providing proper injection and transportation. The HBL is placed after the EML layer closer to the cathode.

In this paper, the performance enhancement is shown of the conventional OLED by the introduction of an additional HBL layer [5–9]. The structures taken here are shown in Fig. 1, Fig. 1a is the structure of Device 1 and Fig. 1b is showing the structure of Device 2.

2 Simulation Setup

The OLED structures in this paper are simulated using industrial standard numerical 2-D Atlas simulator by Silvaco. The emissive area is 16 mm^2 in both the devices. Device 1 starts with a cathode made of aluminium, which is followed by the

Table 1 Materials and dimensions used for the simulation of OLED Device 1 [1]

Material	Usage	Thickness (nm)
Indium Tin Oxide	Anode	150
CuPc	Hole injection layer	100
TPD (N,N′-diphenyl-N,N′-bis(3-methylphenyl), 1′-biphenyl-4,4′-diamine)	Hole transport layer	30
MEH-PPV (Poly[2-methoxy-5-(2-ethylhexyloxy)-1,4-phenylenevinylene])	Emissive layer	30
Alq3(tris(8-Hydroxyquinolinate)aluminium)	Electron transport layer	25
Cathode	LiF	1
Cathode	Aluminium	150

electron transport layer (ETL). Over this an EML of MEH_PPV is deposited by low temperature processes. Then a hole transport layer is added over it which is of TPD (N,N′-diphenyl-N,N′-bis(3-methyl phenyl),1′-biphenyl-4,4′-diamine). The function of this layer is to provide ease of transportation of the holes. Then, a hole injection layer of CuPc has been deposited which is followed by the top electrode of ITO which acts as an anode. Same setup is there for the Device 2 except for the HBL, the HBL added between the emission layer (EML) and the ETL as shown in Fig. 1b.

In Atlas simulation process, at first dimensions, structure, and mesh are defined and then, the physical models are defined and at last the material parameters are extracted after applying operational bias conditions. The model used in the simulation of this device is Langevin PF model. This model of the simulator helps in accepting the device physics in a well-explained way [3, 4]. In this simulator user-defined materials can also be used. The dimensions of the device used are shown in Table 1. Figure 2a is showing the simulated structure of the Device 1.

Table 2 given above is showing the dimensions of the device with the additional hole blocking layer. To predict the results under proper boundary conditions, The Langvin recombination model is used and it can be expressed as shown in Eq. (1) [1, 5, 12].

$$R = e^{\frac{(\mu_n + \mu_p)}{\varepsilon_o \varepsilon}} \tag{1}$$

where, R is the rate of recombination, e is the charge of electron which is 1.6×10^{-19}, μ_e = Mobility of electron, μ_h = Mobility of hole, ε = Permittivity of material, ε_o = Permittivity of air which is 8.85×10^{-12} F/cm. For Device 2 the only difference is of an additional layer as shown in Fig. 2b.

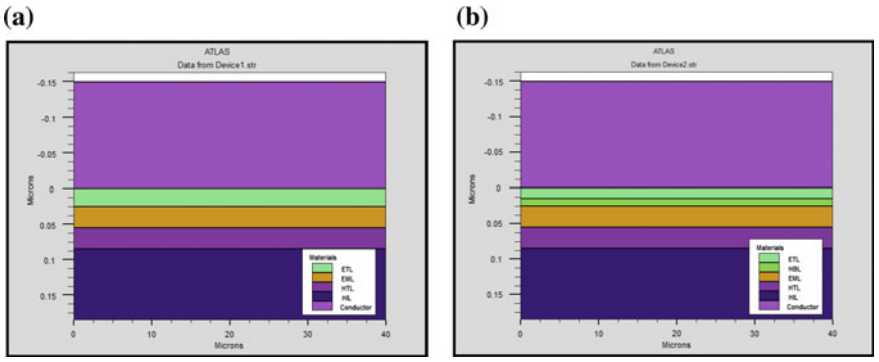


Fig. 2 Simulated structures of the devices. **a** Structure of the multilayered OLED. **b** Structure of Device 2 containing an additional HBL layer [1]

Table 2 Materials and dimensions of the OLED Device 2

Material	Usage	Thickness (nm)
Indium Tin Oxide	Anode	150
CuPc	Hole injection layer	100
TPD (N,N′-diphenyl-N,N′-bis(3-methyl phenyl), 1′-biphenyl-4,4′-diamine)	Hole transport layer	30
MEH-PPV (Poly[2-methoxy-5-(2-ethylhexyloxy)-1,4-phenylenevinylene])	Emissive layer	30
Lithium Floride (LiF)	Hole blocking layer	10
Alq3(tris(8-Hydroxyquinolinate)aluminium)	Electron transport layer	15
LiF	Cathode	1
Aluminium	Cathode	150

3 Results and Discussion

In this paper the simulation of two devices have been done. The Device 2 with the additional HBL whose purpose is to improve the recombination has shown the better results. The increased current can be shown in the simulated results of the anode current versus anode voltage of the Device 1 and Device 2. As shown in Fig. 3a, b.

Here, the current achieved in Device 1 is 2.47 mA while in Device 2 the current is 28.35 mA. Hence the current is being increased by adding the HBL. The current attained here shows that the current density has also been increased [13].

Figure 4 is showing the Luminescence of Device 1 and Device 2, the Luminescence decay here in Device 1 is occurring 6.89 V while in Device 2 it is

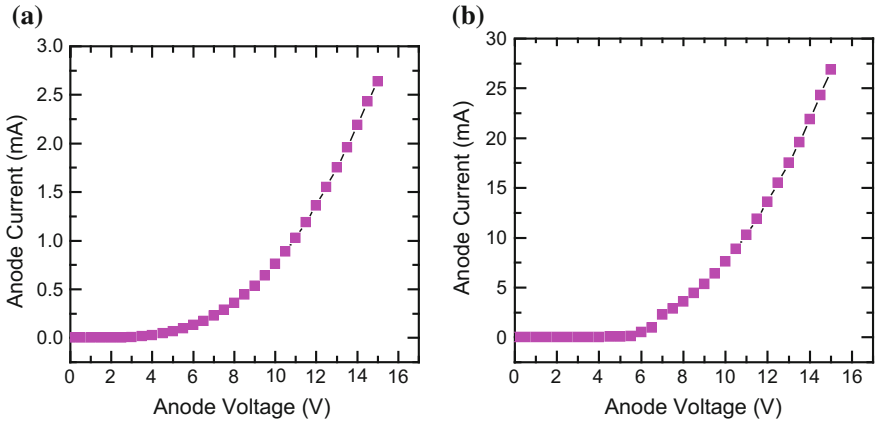


Fig. 3 Simulated anode current versus anode voltage of **a** Device 1 **b** Device 2

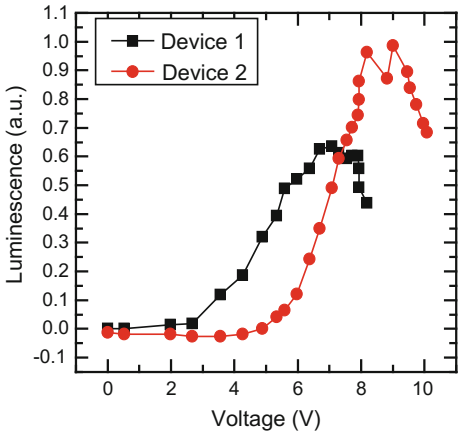


Fig. 4 Simulated luminescence versus anode voltage of Device 1 and Device 2

occurring at 9.12 V and the luminescence attained in Device 1 is of 0.654 a.u. while in Device 2 is 1.42 a.u. hence in terms of luminescence also improvement is shown.

4 Conclusion

The performance improvement of the conventional multilayered OLED is achieved through the introduction of the additional HBL layer. The balanced recombination is achieved as the mobility of the injected holes is higher than the injected electrons. The probability of the recombination is increased by the introduction of the respective layer. The current has increased nearly up to two times while luminescence is also

improved more than twice. The decay of luminescence is also improved. Luminescence achieved here in Device 2 is for a longer time as its decaying time larger so luminescence will be there for a longer time.

References

1. Samal, G. S., Narayanan, K. N., Bharat, S., Gupta, S., Gupta, D.: Improved efficiency in fluorescent blue organic light emitting diode with a carrier confining structure. Org. Electron. 10 (2009) 1201–1208.
2. Tetsuka, H., Ebina, T., Tsunoda, T., Nanjo, H., Mizukami, F.: Fabrication of flexible organic light-emitting diodes using transparent clay films as substrate. Japanese Journal of Applied Physics. 47 (2008) 1894–1896.
3. Mittal, P., Negi, Y. S., Singh, R. K.: Impact of source and drain thickness on the performance of organic thin film transistors. J. of Semiconductors. 35 (2014) 124002-1–124002-7.
4. Kumar, B., Kaushik, B. K., Negi, Y. S.: Perspectives and challenges for organic thin film transistors: Materials, devices, processes and applications. J. Mater. Sci. Mater. Electron. 25 (1) (2014) 1–30.
5. Mittal, P., Kumar, B., Kaushik, B. K., Negi, Y. S., Singh, R. K.: Channel length variation effect on performance parameters of organic field effect transistors. Microelectron. J. 43 (2012) 985–994.
6. Burroughes, J. H., Bradley, D. D. C., Brown, A. R., Marks, R. N., Mackay, K., Holmes, A. B.: Light emitting diodes based on conjugated polymers. Nature. 347 (1990) 539–541.
7. Chung, D. H., Kim, S. K., Oh, H. S., Hong, J. W., Lee, W. J., Lee, J. U., Kim, T. W.: Conduction mechanism and stability of organic light-emitting diodes depending on the Al-based cathodes. Inter. Conf. on Properties and Applications of Dielectric Materials, Nagoya. 13 (2003) 1–5.
8. Kumar, B., Kaushik, B. K., Negi, Y. S.: Organic thin film transistors: structures, models, materials, fabrication, and applications: A review. Polymer Reviews 54 (4) (2014) 33–111.
9. Lin, C. L., Tsai, T. T., Chen, Y. C.: A novel voltage-feedback pixel circuit for AMOLED displays. J. Display Techn. 4 (2008) 54–60.
10. Park, J.: Speedup of dynamic response of organic light emitting diodes. J. of Lightware Techn. 28 (2010) 2873–2880.
11. Kim, J. Y., Kiry, D., Kim, D. H., Choi, K. C.: Analysis of out-coupling mechanism in organic light-emitting diodes. IEEE Photonics Technology Letters. 26 (2014) 896–899.
12. Chang, Y. L., Lu, Z. H.: White organic light emitting diodes for solid-state lighting. J. Display Techn. 9 (2013) 459–467.
13. Qi, Q., Wu, X., Hua, Y., Hou, Q., Dong, M., Mao, Z., Yin, B., Yin, S.: Enhancement of performance for blue organic light emitting devices based on double emission layer. J. Organic Elect. 11 (2010) 503–507.

Background Subtraction Method for Object Detection and Tracking

Satrughan Kumar and Jigyendra Sen Yadav

Abstract Video object extraction and its tracking is one of the fundamental tasks of computer vision that require a close observation on video content analysis. However, these tasks become sophisticated due to spatial and temporal changes in the video background. In this work, we have proposed a background subtraction algorithm that efficiently localizes the object in the scene. In the next stage, a regional level process is integrated by calculating the Shannon energy and entropy to correctly examine the nonstationary pixels in the frames. In order to extract the object efficiently, the background model is updated to the dynamics changes that reduces the false negative pixels on foreground. Further, an adaptive Kalman filter is integrated to track the object in consecutive frames. Qualitative and quantitative analysis on some experimental videos shows that the method is superior to some existing background subtraction methods used in tracking.

Keywords Background subtraction · Shannon entropy · Energy · Object tracking

1 Introduction

Video object segmentation has been a motivating area of computer vision system in the last decade. It solves the varieties of problem in target localization, tracking, and action analysis [1–3]. However, the varying nature of video background due to rippling water, waving tree, quasi-stationary motion, and its changing appearance due to bad resolution or illumination make the object segmentation and extraction tasks more exigent. In [3], Hu et al. categorized the moving object detection methods into three basic classes that are frame difference [4], optical flow [5], and

Satrughan Kumar (✉) · J.S. Yadav
Department of Electronics and Communication, MANIT,
Bhopal 462003, India
e-mail: satrughankumar@gmail.com

J.S. Yadav
e-mail: jsyadav74@gmail.com

© Springer Science+Business Media Singapore 2017

R. Singh and S. Choudhury (eds.), *Proceeding of International Conference on Intelligent Communication, Control and Devices*, Advances in Intelligent Systems and Computing 479, DOI 10.1007/978-981-10-1708-7_125

background subtraction [1–3]. The temporal difference method uses the pixel-wise difference between the two or three consecutive frames in the video to localize the moving object especially in sudden or gradual illumination changes, but the object extraction fails when the object becomes stationary in the scene. It is also affected due to serious hole, ghost, and aperture distortion. The optical is computationally complex and its smoothness constraint limited to few pixels movement in the successive frame.

In this concern, we proposed a background subtraction algorithm that has the capability to provide the sufficient sample size to tracking module without the any prior assumption and suitable under static camera arrangement. The article is structured as follows: Sect. 2 explains some methods related to object extraction and tracking. In Sect. 3, the proposed algorithm is explained. Experimental results are shown in Sect. 4, while the concluding remarks are given in Sect. 5.

2 Related Work

Some of the existing background subtraction methods are reviewed in this section. Many tracking frameworks use these models to trace the object in the scene.

In [2], Manzanera and Richefeu proposed Σ-Δ method (SDE and utilized the difference image and time variance to calculate the foreground pixels. The method is suitable for real-time application but produces insufficient accuracy in case of multiple objects in a scene. In [6], a Gaussian mixture model (GMM) method handles a single pixel using at least three Gaussian components that are updated adaptively over a time in the consecutive frames. Although GMM can work well under gradual illumination conditions and local background motion, but it has greater time complexity. A statistical method proposed in [7], does not update the background pixels that makes it less useful under changing illumination. In [8], Jing et al. integrate spatial-temporal processing to get the moving pixels, but the update of background model is done according to traditional schemes. In [9], a recursive filter is used in updating the background that solely depends on the learning parameters. The dependency on the learning parameters may cause either trails or delay to update the background model. In order to extract the object, a frame difference method is proposed in [10]. However, the frame difference method stops the extraction procedure when the target becomes stationary. In [11], Yao and Ling proposed an improved version of GMM, but it fails to detect the object near camouflage region.

Previous studies reveal that the sample size of object either is lost or buried under the noise under complex condition. Even though some methods are applicable in real-time scenario, but most of them suffer from either ghost effect or aperture distortion. Methods depend on fast learning parameter causes trails behind the object and reduce the accuracy, while methods having low learning rate, do not update the background accurately. Therefore, a regional level processing may be beneficial to update only the changing background pixels and for detecting the

actual non-stationary pixels. In this paper, we integrate the regional level processing by evaluating the block wise entropy and energy that provided the actual moving pixels on the foreground.

3 Proposed Method

The section explains the proposed method into two stages. The first stage or phase describes the object extraction phase using the background subtraction technique, while the next stage works on tracking the trajectory of object using an adaptive Kalman filter. We have utilized the gray scale videos for the experimental set up, which are recorded under static camera arrangement.

3.1 Background Subtraction and Object Extraction

Initially, some 'K' frames are taken to generate the reference background model using the modified moving approach. These initial frames consist of no foreground object. The reference background $B_r(x, y)$ is given as follows:

$$B_r(x, y) = I_0(x, y) + \frac{(I_t(x, y) - I_0(x, y))}{K} \tag{1}$$

where $I_0(x, y)$ and $I_t(x, y)$ are the first and current frame of the video. The 'x' and 'y' are the height and width of the frame.

Further, it creates a difference image by subtracting reference background from the current frame. The moving pixels in the difference image are filtered out by selecting the proper threshold function. Finally, it updates the reference background model over a time to adapt the temporal variation due to environmental changes. The difference image $D_t(x, y)$ is computed as

$$D_t(x, y) = \left| I_t(x, y) - B_t^R(x, y) \right| \tag{2}$$

However, the state of pixels in $D_t(x, y)$ may be affected due to the dynamic or illumination changes in the background, which may lead to the appearance of irrelevant pixels on the foreground. In this concern, block wise Shannon entropy and Shannon energy are evaluated to examine the actual moving pixels in the initial motion field. The moving pixels that belong to the constant intensity area have low entropy and energy as compared to the fluctuating intensity region. The entropy and energy depict the information content present in the video. As seen, the lower gray level distributed region has higher energy. Taking these assumptions, the gray levels inside the block of $D_t(x, y)$ having size $c \times c$ are taken to evaluate the

probability density function 's'. The value of 'c' is taken as 8. The 'R' are gray levels inside the block. The Shannon entropy 'E_t' and energy 'EN_t' are computed as follows:

$$E_t = -\sum_{R=R_{\min}}^{R_{\max}} s \log_2(s) \tag{3}$$

$$EN_t = -\sum_{R=R_{\min}}^{R_{\max}} s^2 \log_2(s^2) \tag{4}$$

Based on the ratio of energy to entropy, the approximate moving region is defined and the background update is done.

$$B_t(x,y) = \left\{ \begin{array}{ll} B_{t-1}(x,y) + \text{signum}(I_t(x,y) - I_{t-1}(x,y)), & \text{if } \left(\frac{EN_t}{E} < \tau_1\right) \\ B_{t-1}(x,y), & \text{else} \end{array} \right\} \tag{5}$$

The corresponding motion mask is evaluated as follows:

$$M_t(x,y) = \left\{ \begin{array}{ll} 1 & \text{if } (D_t(x,y) > \tau_2 \text{ or } \frac{EN_t}{E_t} < \tau_1 \\ 0 & \text{otherwise} \end{array} \right\} \tag{6}$$

where 'τ_1' and 'τ_2' are user defined thresholds. Signum is a mathematical function.

3.2 Object Tracking Using Kalman Filtering

The Kalman filter has the capability to estimate tracking positions using the minimum sample size of the detected object. The adaptive Kalman filtering method proposed in [10] is integrated for tracking in the object extraction module. As seen, the tracking may be affected due to unconstrained measurement and local disturbance in the background. These difficulties may be overcome using the accurate predicted sate. The Kalman filter utilizes a state model that requires current input and previous output to estimate the next location in the successive frames.

The matrices that belongs state $\hat{T}(t)$ and measurement $m(t)$ model are defined as

$$\hat{T}(t) = B\hat{T}(t-1) + p(t) \tag{7}$$

$$m(t) = H(t)\hat{T}(t) + q(t) \tag{8}$$

where 'B' stands for the state transition matrix and $H(t)$ refers to measurement matrix used in the estimation procedure. The Gaussian noise $p(t)$ and $q(t)$ having the zero mean may arise in the system model due to unconstrained measurement. The white noise is assuming in this experiment.

The filter predicts the next state $\hat{T}^+(t)$ by incorporating the prior estimate of state $\hat{T}^-(t)$. The prior state used for the actual measurement in the system.

$$\hat{T}^+(t) = \hat{T}^-(t) + K(t)(m(t) - H(t)\hat{T}^-(t)) \tag{9}$$

'$K(t)$' stands for the Kalman gain and is expressed as

$$K^+(t) = \hat{P}^-(t)H(t)^T(H(t)\hat{P}^-(t)H(t)^T + R(t))^{-1} \tag{10}$$

The Kalman gain includes a prior error covariance matrix $\hat{P}^-(t)$ and $\hat{P}^+(t)$.

The aim is to estimate correct state using Eq. (9) through correcting the Kalman gain using Eq. (10). As seen, higher would be the Kalman gain, it will reduce the measurement error. The final aim is to get a posterior covariance matrix using Eq. (11). The previous posterior estimate is utilized to compute a new prior estimate in order to correct the measurement.

$$\hat{P}^+(t) = (I - K(t)H(t))\hat{P}^-(t) \tag{11}$$

4 Experimental Analysis

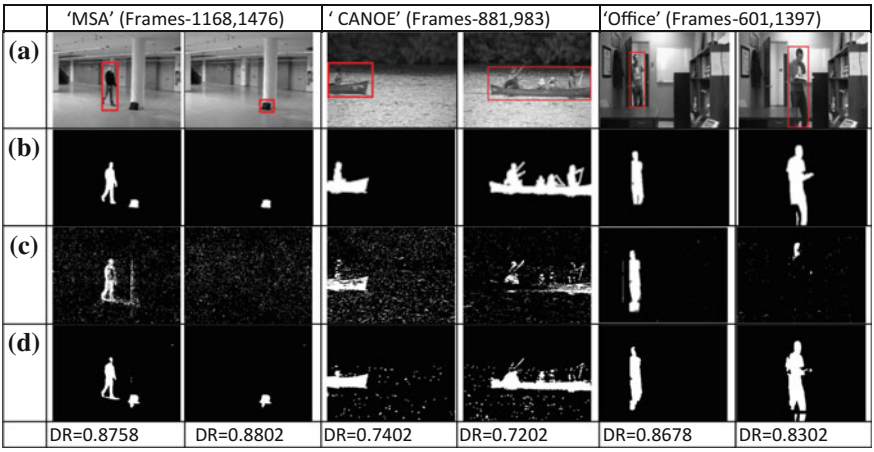
In this section, we have shown the visual and quantitative performance on some experimental video sequences. In this regard, we consider 'MSA,' 'CANOE,' and OFFICE sequences that consist some deviations in the background. All the experiment results are simulated on MATLAB 7.1 on a desktop with configuration 3.2 GHz Intel CPU, 2 GB RAM.

In Fig. 1, first row shows the sampled video frames. The first row of Fig. 1 also shows tracking results through the proposed method, while the last row shows the segmented results of this method. As one can observe, the proposed method classifies accurately between the foreground and background in both static and dynamic background conditions. Moreover no ghost effect, over-segmentation error and aperture distortion are seen on the foreground mask.

The parameters Similarity, F1, and Detection rate are the quantitative metrics. These metrics explain the output image with respect to its ground truths. These metrics depend on '*tn'*, '*fp'*, '*fn,'* and *'tp',* which are true negative, false positive, false negative, and true positive pixels, respectively. The '*fp'* and '*fn*' are the mistakenly detected foreground and background pixels, respectively. The '*tp*' and '*tn*' are accurately detected foreground and background pixels, respectively.

The parameters Detection Rate, Similarity, and F1 are computed as

$$\text{Detection Rate} = \text{tp}/(\text{tp} + \text{fn}) \tag{12}$$



DR*=Detection rate

Fig. 1 **a** Sample frames with tracking results **b** Ground truth **c** Results using GMM method **d** Foreground output using proposed method

$$\text{Similarity} = \text{tp}/(\text{tp} + \text{fp} + \text{fn}) \tag{13}$$

$$\text{F1} = 2 \times \text{Precision} \times \text{Recall}/(\text{Precision} + \text{Recall}) \tag{14}$$

where precision and recall are the irrelevant and relevant true positive pixels, respectively. Figure 1 presents the detection rate on sampled frames through this proposed method. Table 1 shows the comparison between GMM and proposed method. Here, GMM [6] initially have good detection rate, but its performance is tainted on subsequent frames when object either becomes stationary or moves near camouflage region. However, the detection rate through our method is far better than GMM for each video sequence. The average similarity and F1 obtained through this method is up to 60 % greater than GMM for the MSA sequence. However, in dynamic background of CANOE sequence, it is approximately 21 % greater than GMM method. The visual inspection and quantitative analysis exemplify that the method provide enough cues to meet the requirement of video surveillance.

Table 1 Performance comparison between proposed method and GMM method

Sequences	Evaluation	Proposed method	GMM
MSA	Similarity	0.8551	0.2726
	F1	0.9219	0.3001
Canoe	Similarity	0.6834	0.4420
	F1	0.8119	0.6370
Office	Similarity	0.8248	0.2721
	F1	0.9040	0.4279

5 Conclusion

In this work, a background-updating scheme is reported to update the dynamic background pixels, which in turn provided a sufficient sample size to the tracking module and enhanced the results. Based on the ratio of Shannon energy to entropy, the relevant moving pixels are accessed on the foreground. The proposed method efficiently reduces the over-segmentation error, aperture distortion, and ghost effect. The accurately segmented object on the foreground may provide important cues to many postprocessing applications. One can focus to extend this work for multiple object detection and tracking in unconstrained videos. Experimental results on some challenging video sequences show that the method outperforms the other state-of-the-art background subtraction methods used in tracking.

References

1. R. Cucchiara, C. Grana, M. Piccardi, A. Prati: Detecting moving objects, ghosts, and shadows in video streams. IEEE Transactions on Pattern Analysis and Machine Intelligence 25, 1337–1342 (2003).
2. Antoine Manzanera, Julien C. Richefeu: A new motion detection algorithm based on Σ-Δ background estimation. Pattern Recognition Letters 28, 320–328 (2006).
3. Weiming Hu, Tieniu Tan, Liang Wang, S. Maybank: A Survey on Visual Surveillance of Object Motion and Behaviors. IEEE Transactions on Systems Man and Cybernetics 34, 334–352 (2004).
4. Mandellos N. A., Keramitsoglou I., Kiranoudis C. T.: A background subtraction algorithm for detecting and tracking vehicles. Expert Systems with Applications 38, 1619–1631 (2011).
5. Lucas B. D., Kanade T.: An iterative image registration technique with an application to stereo vision. IJCAI 81, 674–679 (1981).
6. Stauffer C., Grimson W. E. L.: Learning patterns of activity using real-time tracking. IEEE Transactions on Pattern Analysis and Machine Intelli. *22*, 747–757 (2000).
7. M. Oral, U. Deniz: Center of mass model: A novel approach to background modeling for segmentation of moving objects. Image and Vision Computing 25, 1365–1376 (2007).
8. Jing G., Siong C. E., Rajan D.: Foreground motion detection by difference-based spatial temporal entropy image. IEEE Conference 2004 379–382 (2004).
9. Fu Z., Han, Y.: Centroid weighted Kalman filter for visual object tracking. Journal of Measurement 45, 650–655 (2012).
10. Weng S. K., Kuo C. M., Tu S. K.: Video object tracking using adaptive Kalman filter. Journal of Visual Communication and Image Representation 17, 1190–1208 (2006).
11. Yao, Li, Ling, M.: An Improved Mixture-of-Gaussians Background Model with Frame Difference and Blob Tracking in Video Stream. The Scientific World Journal 2014, 1–9 (2014).

Impact of Gate Thickness Variation and Dielectric on the Performance of Vertical Organic Thin Film Transistor

Srishti, Yamini Pandey, A.K. Baliga and Brijesh Kumar

Abstract This research paper emphasizes on the impact of gate thickness variation and gate dielectric on the performance of an organic static induction-type vertical organic thin film transistor (VOTFT). The electrical behavior of VOTFT is analyzed and performance parameters extraction is carried out using Atlas 2-D numerical device simulator. VOTFTs have high-speed operation in comparison to conventional organic thin film transistor (OTFT) due to shorter channel length that corresponds to thickness of organic semiconductor (OSC) layer. Majority carrier flow from source to drain is controlled by varying gate voltage (V_G) applied to Schottky gate electrode. Effect of gate thickness variation is analyzed by varying gate thickness of device from 10 to 50 μm with a step size of 20 μm. Pentacene is used as OSC channel material. A device having additional thin layers of Al_2O_3 dielectric above and below buried grid-type gate electrode has also been analyzed. The results obtained demonstrate that with 80 % reduction in gate electrode thickness, I_{on}/I_{off} ratio increases by 48 %. This analysis shows control of drive current (I_{DS}) with gate electrode thickness variation. Device having gate dielectric layers has shown very low off current of 7.01×10^{-9} A that can be attributed to reduction in leakage between gate and source due to use of gate dielectric.

Keywords VOTFT · Gate electrode thickness variation · Gate dielectric impact

Srishti (✉) · Yamini Pandey · A.K. Baliga · Brijesh Kumar
Department of Electronics and Communication Engineering,
School of Engineering and Technology, Graphic Era University,
Dehradun, India
e-mail: srisparandiyal27@gmail.com

Brijesh Kumar
e-mail: brijesh_kumar@ieee.org

© Springer Science+Business Media Singapore 2017

R. Singh and S. Choudhury (eds.), *Proceeding of International Conference on Intelligent Communication, Control and Devices*, Advances in Intelligent Systems and Computing 479, DOI 10.1007/978-981-10-1708-7_126

1 Introduction

The discovery of a highly conductive polymer in 1977 by Shirakawa et al. [1] had led to origin of a new field of electronics, i.e., organic electronics. Over the last few decades, organic thin film transistors (OTFTs) have emerged as a suitable alternative to inorganic materials based TFTs. OTFTs are considered suitable for large-area, flexible, low-temperature and low-cost devices due to their processing characteristics and performance. Wide range of OTFT applications covers display devices such as organic light-emitting diodes (OLEDs) to advance devices like radio frequency identification (RFID) tags, sensors, digital circuits and memory devices [2, 3].

However, OTFTs have some demerits like lower drive current and higher voltage operation due to lower mobility of OSC materials as compared to inorganic TFTs. For performance enhancement of OTFTs, both device structure and electrical properties of OSCs have to be improved.

The improved device structure of vertical channel OTFT (VOTFT) is used for high-speed applications due to their shorter vertical channel. Conventional lateral and improved vertical OTFT device structures are shown in Fig. 1.

Organic static induction-type VOTFTs widely known as OSITs have been analyzed in this research paper. Inorganic SITs were firstly proposed by Nishizawa et al. [4] in 1975. Thereafter in 1998, OSC-based (copper phthalocyanine films) SIT (OSIT) was proposed by Kudo et al. [5].

2 Organic Static Induction Transistor—A Type of VOTFT

An OSIT, having a buried grid-type Al gate electrode as shown in Fig. 1, has ohmic contact between OSC and source/drain electrode while a Schottky barrier contact between OSC and gate electrode. The injected majority carrier flow from source to drain electrode is controlled by potential barrier height depending on applied gate voltage (V_G).

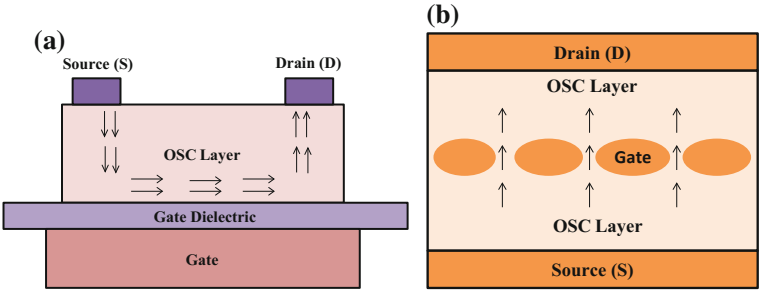


Fig. 1 Cross-sectional view of **a** lateral channel OTFT, **b** vertical channel OTFT

OSITs operate somewhat like depletion-type transistors (like JFET). On application of a positive V_G less than breakdown voltage of Schottky barrier formed between gate and source, majority carrier flow between source to drain is hindered by spreading of the depletion layer around gate electrode. When a negative V_G is applied until a built-in voltage of Schottky barrier, majority carrier flow from source to drain is improved by augmented electric field at interface between OSC and source.

The current in the device [6] is given by

$$I_{DS} = I_o \exp(-qV_G^*/kT) \tag{1}$$

where I_o is reverse saturation current, k is Boltzmann constant, q is electronic charge, T is absolute temperature, and V_G^* is the effective gate voltage.

$$V_G^* = \eta\left(V_{GS} - \frac{V_{DS}}{\mu}\right) \tag{2}$$

where μ is voltage amplification coefficient, V_{GS} is the gate bias, V_{DS} is the drain bias, and gate voltage ratio $\eta = \partial V_G(0)/\partial V_{GS}$.

Voltage amplification factor μ is given as

$$\mu = g_m \times r_D = \eta\mu^* \frac{\partial V_{DS}}{\partial V_G(0)} = \frac{W}{W_G} \tag{3}$$

where g_m is transconductance, r_D is the output resistance, μ^* is intrinsic voltage amplification factor, W_G is the distance between source and gate, and W is the distance between gate and drain. Transconductance is $g_m = \partial I_{DS}/\partial V_{GS}$ at constant V_{DS} value while output resistance is $r_D = \partial V_{DS}/\partial I_{DS}$ at constant value of V_{GS}.

Equation (1) represents current equation of OSIT with no effect of series channel resistance (r_s). Due to voltage drop across series resistance r_s, drive current equation can be modified as

$$I_{DS} = I_o \exp\left[-\frac{q}{kT}\eta\left\{\left(V_{GS} + \frac{1+\mu}{\mu} r_s \cdot I_{DS}\right) - \frac{V_{DS}}{\mu}\right\}\right]. \tag{4}$$

Equation (4) shows that *I–V* characteristics tend to deviate from exponential form with increasing I_{DS}.

Equivalent series resistance is given by

$$r_S = \frac{\mu}{1+\mu}\frac{\Delta V_{GS}}{I_{DS}} \tag{5}$$

Table 1 Materials and dimensions used for the simulation of OSIT Devices

Material	Usage	Thickness (in nm)	
		OSIT without gate dielectric	OSIT with gate dielectric
Indium tin oxide (ITO)	Source electrode	30	30
Pentacene	1st OSC layer	100	100
Al_2O_3	Gate insulator below gate electrode	–	50
Aluminum (Al)	Gate electrode	10	30
Al_2O_3	Gate insulator above gate electrode	–	30
Pentacene	2nd OSC layer	100	100
Gold (Au)	Drain electrode	30	30

3 Simulation Setup, Device Dimensions, and Material Properties

Simulation analysis is carried out using organic module of Atlas 2-D numerical device simulator provided by Silvaco [7]. The dimensional parameters of devices under consideration are listed in Table 1. The schematic structures of simulated devices are shown in Fig. 2a–d.

Poole–Frenkel mobility model is used as mobility model for device simulation. It can be given by

$$\mu_{\text{eff}} = \mu_0 \exp\left(-\frac{\Delta E_a - \beta\sqrt{E}}{kT}\right) \tag{6}$$

where μ_0 is zero field mobility, ΔE_a is zero field activation energy, E is electric field and β is Poole–Frenkel factor. Zero field activation energy with a value of 1.792×10^{-2} eV and hole Poole–Frenkel factor (β_h) of value 7.758×10^{-5} eV $(\text{cm/V})^{0.5}$ are considered for device simulation. The electrical properties of pentacene used as OSC material in the devices [8–11] are listed in Table 2. Work function of 4.8 eV is considered for ITO. Work function of Au on the surface of pentacene is 4.3 eV while that of Al is 4.3 eV. Al_2O_3 is used as gate dielectric with a permittivity of 3.9.

4 Results and Discussion

This section includes detailed discussion of OSIT device performance in terms of its transfer characteristics for different devices analyzed through simulation.

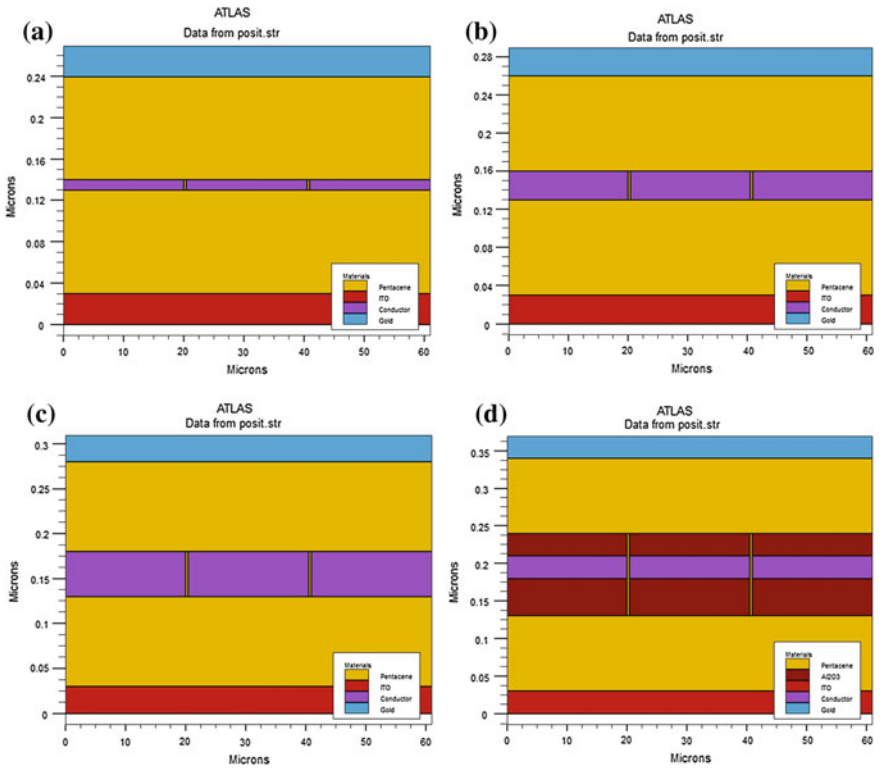


Fig. 2 Simulated schematic structures of pentacene-based OSITs with **a** gate thickness (t_g) = 10 nm, **b** gate thickness (t_g) = 30 nm, **c** gate thickness (t_g) = 50 nm, **d** gate dielectric layers. All devices have effective area of 2.25 × 10^{-2} cm^2, gate line spacing of 0.5 µm and gate line width of 20 µm

Table 2 Electrical properties of pentacene used as OSC material

Property	Pentacene material
Bandgap (E_g)	2.4 eV
Permittivity (ε)	4.0
Hole mobility (μ_h)	0.85 cm^2/Vs
Electron mobility (μ_n)	5 × 10^{-5} cm^2/Vs
Doping concentration (N_A)	10^{17} cm^{-3}

4.1 Influence of Gate Electrode Thickness on OSIT Transfer Characteristics

Gate dimensions play an important role in controlling current flow in an OSIT [5, 8]. A very thick gate electrode forms double Schottky barriers thereby blocking carrier flow from source to drain. On the other hand, a very thin gate electrode does

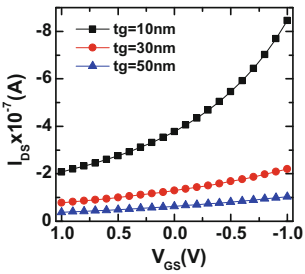


Fig. 3 Transfer characteristics of pentacene-based OSIT with variation in gate electrode thickness (t_g) from 10 to 50 nm with a step size of 20 nm at $V_{DS} = -3$ V

not work effectively due to its discontinuous nature. Therefore, ideal Al gate electrode should be of mesh type with proper thickness. Transfer characteristics of pentacene-based OSIT with gate electrode thickness variation from 10 to 50 nm with a step of 20 nm are shown in Fig. 3. Transfer characteristics exhibit rectifying properties due to Schottky barrier formed between gate and OSC layers. OSIT with gate thickness of 10 nm has better performance as compared to OSIT with thicker gate thickness in terms of I_{on}/I_{off} ratio. OSIT with gate thickness of 50 nm has shown degraded transistor operation due to very thick continuous film nature of gate electrode.

4.2 *Influence of Using Gate Dielectric on OSIT Transfer Characteristics*

Transfer curve of OSIT with gate dielectric layers is shown in Fig. 4. Thickness of dielectric layer (Al_2O_3) used below and above gate electrode is 50 nm and 30 nm, respectively.

A thicker oxide layer is used between gate and source to effectively reduce gate leakage current. A low I_{off} of 7.01×10^{-9} A is obtained due to proper pinch off achieved as a result of thin gate spacing during off state and use of dielectric layers. A comparative tabular form of extracted parameters of all devices is shown in Table 3.

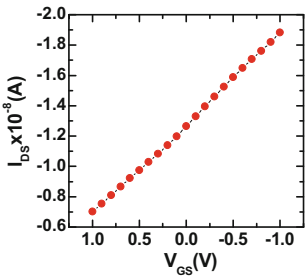


Fig. 4 Transfer characteristics of OSIT having additional dielectric layers above and below gate electrode at $V_{DS} = -3$ V

Table 3 Comparison of extracted parameters of simulated OSITs

Parameters	Extracted values			
	OSIT (t_g = 10nm)	OSIT (t_g = 30nm)	OSIT (t_g = 50nm)	OSIT with dielectric
Maximum current (I_{DSMAX})	0.84 μA	0.22 μA	0.1 μA	0.02 μA
Minimum current (I_{DSMIN})	0.21 μA	0.07 μA	0.03 μA	7.01 nA
Threshold voltage (V_T)	0.09 V	0.85 V	1.12 V	1.90 V
Subthreshold slope (SS)	2.40 V/dec	4.15 V/dec	4.57 V/dec	4.50 V/dec
Transconductance (g_m)	0.77 μS	0.1 μS	0.04 μS	6.63 nS
Current on-off ratio (I_{on}/I_{off})	4.06	2.82	2.75	2.68

5 Conclusion

Current conduction in OSIT is mainly affected by depletion region formed around gate with applied gate bias and gate electrode dimensions. The results obtained demonstrate that with 80 % reduction in gate electrode thickness, I_{on}/I_{off} ratio increases by 48 %. Therefore, drive current (I_{DS}) can be controlled effectively by optimizing gate electrode thickness. Thereafter, OSIT with gate dielectric layers has shown very low off current of 7.01×10^{-9} A that can be attributed to effective pinch off obtained in off state due to thin gate spacing of 0.5 μm and use of gate dielectric.

The results obtained promise efficient use of high performance OSITs in fast switching novel devices like sensors and memories.

References

1. Shirakawa, H., Louis, E.J., MacDiarmid, A.G., Chiang, C.K., Heeger, A.J.: Synthesis of electrically conducting organic polymers: Halogen derivatives of polyacetylene, $(CH)_x$. J. Chem. Soc. Chem. Commun. 16 (1977) 578–580.
2. Kumar, B., Kaushik, B.K., Negi, Y.S.: Organic thin film transistors: structures, models, materials, fabrication, and applications: A review. Polymer Reviews 54 (4) (2014) 33–111.
3. Kumar, B., Kaushik, B.K., Negi, Y.S, Goswami, V.: Single and dual gate OTFTs based robust organic digital design. Microelectron. Rel. 54 (1) (2014) 100–109.
4. Nishizawa, J., Terasaki, T., Shibata, J.: Field-effect transistor versus analog transistor (static induction transistor). IEEE Trans. Electron. Devices 22 (4) (1975) 185–197.
5. Kudo, K., Wang, D.X., Iizuka, M., Kuniyoshi, S., Tanaka, K.: Schottky gate static induction transistor using copper phthalocyanine films. Thin Solid Films, 331 (1998) 51–54.

6. Wang, D.X., Wang, X., Wang, C., Pang, C., Yin, J.H., Zhao, H.: Fabrication and characteristics of sub-micrometer vertical type organic semiconductor copper phthalocyanine thin film transistor. IEEE 10th Int. Conf. on the Properties and Applications of Dielectric Materials, Bangalore, July 24–28 (2012).
7. ATLAS User's manual device simulation software. Silvaco Int. Ltd., Santa Clara, USA (2013).
8. Rawat, S., Ramola, V., Baliga, A.K., Mittal, P., Kumar, B.: Performance analysis of vertical channel organic thin film transistors through 2-D device simulation. Proc. IEEE Int. Conf. on Computing, Communication and Automation (ICCCA 2015) (2015) 1038–1043.
9. Kumar, B., Kaushik, B.K., Negi, Y.S.: Perspectives and challenges for organic thin film transistors: Materials, devices, processes and applications. J. Mater. Sci. Mater. Electron. 25 (1) (2014) 1–30.
10. Mittal, P., Kumar, B., Kaushik, B. K., Negi, Y. S., Singh, R. K.: Channel length variation effect on performance parameters of organic field effect transistors. Microelectron. J. 43 (2012) 985–994.
11. Kumar, B., Kaushik, B.K., Negi, Y.S.: Design and analysis of noise margin, write ability and read stability of organic and hybrid 6-T SRAM. Microelectron. Rel. 54 (12) (2014) 2801–2812.

Depth Analysis of Organic Bilayer Solar Cell and Their Performance Parameters Extraction

Kamlesh Kukreti, Arun Pratap Singh Rathod and Brijesh Kumar

Abstract This research paper is an attempt to present a depth study and performance parameters extraction of organic solar cell. Subsequently, this paper also discusses various recent advancements in organic solar cells in terms of material, structures, and other performance influencing factors. Furthermore, analysis of organic solar cells is included in terms of transmittance of PEDOT: PSS material, Absorption spectrum of PCBM film, photocurrent at different thickness of CuPc, Dark and light *I*–*V* characteristics of CuPc/PCBM bilayer. Besides this, depth performance analysis of organic solar cell is carried out using 2-D numerical device Atlas simulator; subsequently, impact of thickness variation of bilayer organic solar cells on performance parameters is also analyzed.

Keywords Organic solar cell · Bilayer OPV · PEDOT · Bulk hetero junction OPVs

1 Introduction

Organic solar cells have the ability that can be efficient solar energy convertors which proves favorable in light tracing and exciton generation properties. Organic material-based devices and circuits can be processed using low cost and lower temperature solution process method of fabrication [1, 2] to reduce the overall cost of the end user products. Polymer materials are generally processed with solution method that intern use of flexible substrate and light weight for solar energy conversion with the potential to be used as roll to roll processing techniques for low temperature. The conversion to electrical energy from light energy is known as

Kamlesh Kukreti (✉) · A.P.S. Rathod · Brijesh Kumar
Department of Electronics and Communication Engineering, School of Engineering and Technology, Graphic Era University, Dehradun 248002, India
e-mail: kamlesh.kukreti23@gmail.com

Brijesh Kumar
e-mail: brijesh_kumar@ieee.org

© Springer Science+Business Media Singapore 2017

R. Singh and S. Choudhury (eds.), *Proceeding of International Conference on Intelligent Communication, Control and Devices*, Advances in Intelligent Systems and Computing 479, DOI 10.1007/978-981-10-1708-7_127

photovoltaic effect which is traced by Becquerel's in 1839 as studies of liquid electrolyte [3] has been studied for broad range of material. In the modern world the tipping point as it transformed photovoltaic technology to convert sunlight into electricity was reported in 1954 by Chapin et al. [4] based on silicon p-n junction with 6 % of solar energy conversion. Calvin and Kearns [5] in 1958 utilized magnesium phthalocyanines (MgPh) to generate 200 mV photo voltage.

This area of organic solar cell reached a significant level in 1970s and in the 1980s. In 1986, Tang [6] explained two-layer device, i.e., copper phthalocyanine as the donor and perylene tetracarboxylic derivative as the acceptor which gives the power efficiency of 1 %. In the year 1992, Scriciftci et al. [7] used material polyphenylene fullerene for charge generation assistance (acceptor) and further to get better result he used polyphenylene vinylene (PPV) and PCBM (1-(3-methoxy-carbonyl) propyl-1-phenyl[6,6]C_{61}) because of more soluble fullerene derivative, further researchers in 2001 Shaheen et al. [8] used polyphenylene vinylene (PPV) and PCBM (1-(3-methoxy carbonyl propyl-1-pheny[6,6]C_{61}) for adjusting phase separation by means of selecting solvents having higher boiling point which allows for slower drying as positive and better self organization as by the year 2003 Padinger et al. P3HT (poly(3-hexyl-thiophene)) and PCBM (1-(3-methoxy-carbonyl) propyl-1-phenyl[6,6]C_{61}) uses semi crystalline form which resembles improvement in phase separation by treating it thermally and electric field after deposition this improved the efficiency from 0.42 to 3.51 %. In preceding decades, many important changes have been carried out on the enlightenment of the working mechanism of OSC, the inventory and the efficiency processing techniques, the examination of novel of OSC architectures and to increases the device stability, synthesis and design of new materials which are working towards improving the Power Conversion Efficiency (PCE) of OSC [9]. Presently, the highest reported PCEs are in the range of 6.71–8.72 % for small molecule, 8.40–10.61 % for polymer OSCs and 7.1–15.2 % for perovskite OSCs which is a breakthrough towards, environmentally friendly, low cost, and renewable power source [10].

2 Simulation Setup

The organic bilayer solar cell (OBOPV) structures are simulated using industrial numerical 2-d simulator ATLAS by Silvaco. ATLAS provides general capabilities for physically based two- (2D) and three-dimensional (3D) simulation of semiconductor devices. This tool also allows the usage of user defined materials for the devices therefore any material with identified properties can be used for the simulation of the device [11]. All these three structures are simulated with the similar parameters and materials as for the fabricated device. Table 1 shows the dimensions used for the simulation process.

The *I–V* characterization of the organic devices was done using the Keithley 4200 semiconductor characterization system. The dark *J–V* characterization should be done in complete dark room. For the measurement of the light characteristics, the

Table 1 Materials and dimensions used for the simulation of bilayer solar cell

Material	Usage	Thickness (nm)
CuPc (Copper Thalocyanine)	Organic semiconductor	12–24
([6, 6]-phenyl-C_{61}-buytricacid- methyl ester) PCBM	Organic semiconductor	31
PEDOT:PSS (Polyethylenedioxythophene Polystyrene sulphonic acid)	Dielectric	10
Aluminium (Al)	Cathode	20
Indium Tin Oxide (ITO)	Anode	20

devices were illuminated by a calibrated solar simulator having a 150 W Quartz Tungsten Halogen Lamp (QHT lamp) from OSRAM. Usually, these sources of light are developed particularly and it is used for simulating solar radiation. They have the ability to generate a parallel output beam which is uniform (with close spectral match to sun light) incident on device.

Spectral Response: It is used to measure the incident photon to the current efficiency (IPCE) or the external quantum efficiency (EQE) which gives the spectral resolution of the photocurrent. The light coming from a Xe lamp is optically chopped. After passing through a monochromator the light is focused onto a sample using a light fiber.

Poole–Frenkel (PF) mobility model was adopted and is given by Eq. (1), where μ_o is the zero field mobility, μ is the field dependent mobility, Δ is the zero field activation energy having the value of 1.792×10^{-2} eV, γ is the fitting parameter, β is the hole PF factor given as 7.758×10^{-5} eV $(\text{cm/V})^{0.5}$, T is the temperature and γ is the fitting parameter [11].

$$\mu(E) = \mu_0 \exp\left[-\frac{\Delta}{kT} + \left(\frac{\beta}{kT} - \gamma\right)\right] \tag{1}$$

3 Results and Discussion

Thickness Variation of active layer in CuPc/PCBM Bilayer Organic solar cell. The structure of the device investigated and corresponding energy levels is shown in Fig. 1. At the electrode ITO/PEDOT: PSS the work function is well aligned with the HOMO level of CuPc, the holes generated in the CuPc will be preferentially extracted through the ITO/PEDOT: PSS contact. The Al back electrode, the C60 derivative PCBM LUMO, and serves as a back reflector to increase the optical path of the incident light.

To study the compatibility of PEDOT: PSS and PCBM layer on organic bilayer solar cell, we study the transmittance of PEDOT: PSS and absorption coefficient of PCBM as shown in Fig. 2. To study the influence of the thickness of active layer different thicknesses on the photo generated current simulations were done.

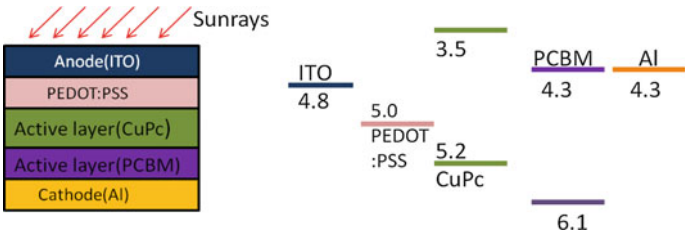


Fig. 1 Structure of organic bilayer solar cell and corresponding energy levels

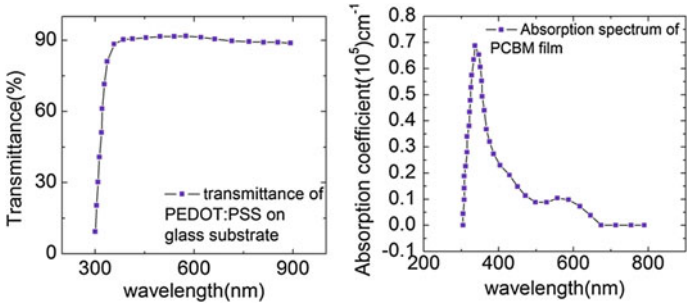


Fig. 2 Simulated result of transmittance of PEDOT: PSS and absorption spectrum of PCBM film

Figure 3 shows the simulation results of the variations in exciton generation at different thickness of CuPc in a bilayer cell. The peak is obtained due to the exciton diffusion length limitation of CuPc layer and the larger absorption with higher thickness of CuPc. The maximum photocurrent 18.2 mA cm^{-2} was obtained at 24 nm of CuPc thickness. Owing to the absence of recombination model and interference, the value of current is exaggerated. If recombination was taken into account, the peak would have been obtained at a lower thickness. Based on the simulations, different thickness of CuPc layers were deposited on PEDOT: PSS and ITO coated glass substrate.

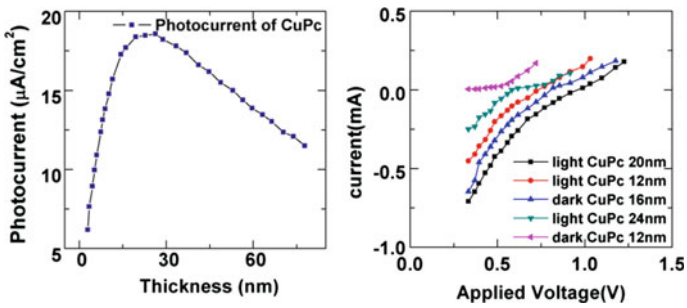


Fig. 3 Simulation result of the variation of photocurrent at different thickness and dark and light *I–V* characteristics of CuPc/PCBM bilayer solar cell

Figure 3 shows the *I–V* characteristics of the device in dark and light. As expected of this material combination, an open circuit voltage (V_{oc}) of 0.53 V is obtained which is proportional to the difference level of the HOMO and the LUMO level as of the CuPc and PCBM layer and maximum Jsc is obtained at 20 nm thickness of CuPc.

The exciton diffusion length of CuPc is reported between 10–20 nm approximately above this thickness, the trade-off between absorption and exciton recombination acts as a limiting factor on the current and the efficiency. Table 2 summarizes the changes in the parameters with the change in CuPc thickness. Due to the absorption and the exciton diffusion length trade-off, it was found that 20 nm of CuPc thickness shows the best performance in CuPc/PCBM bilayer device and degrades on increasing thickness further the devices showed the best efficiency of 0.36 % Also, it is shown that these solar cells show lesser degradation with time as compared to P3HT: PCBM cells.

In a bilayer cell, the crossing point between the donor and the acceptor leads to exciton breaking as the holes and the electrons move across the donor and the acceptor, respectively, to the electrodes as lower the thickness of the acceptor, lesser is the series resistance for the electrons to the move to the cathode and better will be the fill factor. The reduced thickness of PCBM (31 nm) was used by using a lower concentration (10 mg/ml) in chlorobenzene.

Figure 4 shows that Dark current at varying thickness of CuPc in CuPc/PCBM bilayer solar cell. The built-in voltage of all the solar cells lies close to 0.70 V which is proportional to the difference level of the HOMO and the LUMO level for CuPc and PCBM, respectively. In light, the decrease in the fill factor with the increasing thickness can be attributed to the increase in series resistance which hampers the charge carrier transport requiring high fields for charge extraction. The Jsc is low for thinner device and then increases with increase in thickness due to enhancement of absorption inside the active layer, peaks at 20 nm and at the excitons and the generated charge carriers. In the thicker device before recombining as it is not able to leave the device before recombining as it is generated too far away from the electrode. As PCBM is known as one of the best electron transporting organic materials, the most likely explanation is that the collection of holes at organic/PEDOT: PSS interface is the current determining.

Table 2 Efficiency parameters of CuPc/PCBM bilayer OSCs (1 sun illumination)

CuPc thickness (nm)	J_{sc} (mA/cm^2)	V_{0C} (V)	Fill factor	Efficiency
12	2.82	0.53	0.16	0.22
16	3.81	0.53	0.15	0.30
20	4.29	0.53	0.14	0.36
24	1.53	0.53	0.14	0.11

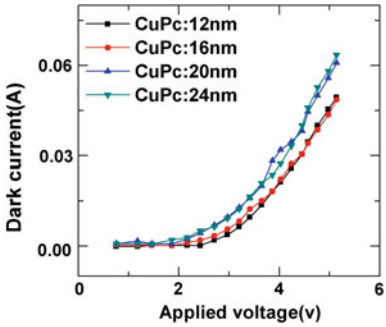


Fig. 4 Dark current at varying thickness of CuPc in CuPc/PCBM bilayer solar cell

4 Conclusion

The parameters of bilayer organic solar cell structure have analyzed using different layer of different organic materials such as CuPc/PCBM. Bilayer solar cell device has shown better performance in comparison to convention organic solar cells. Depth study of bilayer organic solar cell and their performance influencing factors has discussed that are very informative to the beginners of organic material-based solar cell analysis and fabrications. Organic solar cell with bilayer of CuPc/PCBM is simulated and performance parameters are extracted for their further applications.

References

1. Kumar B., Kaushik B.K., Negi Y.S.: Organic thin film transistors: structures, models, materials, fabrication, and applications: A review. Polymer Reviews 54 (4) (2014) 33–111.
2. Kumar B., Kaushik B.K., Negi Y.S.: Perspectives and challenges for organic thin film transistors: Materials, devices, processes and applications. J. Mater. Sci. Mater. Electron. 25 (1) (2014) 1–30.
3. Coakley K. M., and McGehee M. D.: Conjugated Polymer Photovoltaic Cells. Chem. Mater., 16 (2004) 4533–4542.
4. Chapin D.M., Fuller C. S., Pearson G. L.: A New Silicon P-N Junction Photo Cell for Converting Solar Radiations into Electrical Power. J. Appl. Phys., 25 (5) (1954) 676.
5. Spanggaard H., Krebs F.C.: A brief history of the development of organic and polymeric photovoltaics. Solar Energy Materials & Solar Cells, 83 (2004) 125–146.
6. Tang C.W.: 2-layer Organic Photovoltaic Cell. Appl. Phys. Lett., 48 (2) (1986), 183.
7. Sariciftci N.S et al.: Photo induced electron transfer from conducting polymers on to buckminsterfullerene, Science, 258 (1992) 1474.
8. Shaheen Sean E., Brabec, C. J., Sariciftci, N. S., Padinger F., Fromherz T., Hummelen J. C.: 2.5 % efficient organic plastic solar cells, Applied Physics Letters 78 (2001) 841.
9. Yu Junsheng et al.: Towards high performance organic photovoltaic cells: A review of recent development in organic photovoltaics. Polymers, 6 (2014) 2473–2509.
10. Park Nam-Gyu: Perovskite solar cells: An emerging photovoltaic technology. Materialstoday, 18 (2) (2015) 65–72.
11. ATLAS User's Manual Device Simulation Software. Silvaco International Ltd., Santa Clara, USA (2013).

Four-Stage Telecommunication Switching Design and Synthesis

Adesh Kumar, Piyush Kuchhal and Sonal Singhal

Abstract The research article presents the hardware chip design and FPGA implementation of the four-stage telecommunication switching system. The switching capacity of the exchange is increased with the implementation of the programmable multistage network. In multistage network, there are alternate paths to provide the availability of the network. The four-stage switching provides more capacity in comparison to three-stage switching. Modular design approach is used to build the large-scale network, which can be fabricated easily using VLSI technology. The design is carried for 8 × 8 switching network. The work is carried out in Xilinx ISE 14.2 software using VHDL programming language and synthesized on Vitex-5 FPGA.

Keywords Very large scale of integration (VLSI) · Field programmable gate array (FPGA) · Very high speed integrated circuit hardware description language (VHDL) · Integrated system environment (ISE)

1 Introduction

Telecommunication networks demands high speed switching to deploy and create new and novel services. High speed switching does not depend on the service provider's operational infrastructure but it depends on the flexibility of the software architecture. Current telecommunication networks are based on the network structure based on architecture over 30 years in age [2, 3]. The architecture has less computational capabilities and bandwidth is a factor for degree of flexibility.

Adesh Kumar (✉) · Piyush Kuchhal
Department of Electronics Instrumentation and Control (EIC) Engineering, University of Petroleum and Energy Studies (UPES), Dehradun, India
e-mail: adeshmanav@gmail.com

Sonal Singhal
Department of Electrical Engineering, Shiv Nadar University (SNU), G.B Nagar, NCR, India

© Springer Science+Business Media Singapore 2017

R. Singh and S. Choudhury (eds.), *Proceeding of International Conference on Intelligent Communication, Control and Devices*, Advances in Intelligent Systems and Computing 479, DOI 10.1007/978-981-10-1708-7_128

Network switching can be increased using cluster-based models where large processors are distributed over the network and to provide distributed services [1, 5]. Dedicated processors used monolithic software, which control the response, necessary data and coordinate with the services modules. Traditional communication fabrics [1, 6] have scalability issues because of physical circuit design and performance issues. Moreover, the designs of telephone exchanges are complex in structure due to non-programmability and crossbar switches are larger in size. These factors lead to the traffic congestion [6, 8] in a network. Network switching capacity [4, 7] depends on the number of route available for inlet to outlets. Till today, conventional telephone switching is limited to three-stage switching. Increasing number of stages in a conventional network is not the feasible solution as it further adds to the hardware complexity along with larger crossbar switches. This limitation can be overcome by the increasing the number of stages such as utilizing four- and five-stage with programmable network configurations and switching capacity [4] of a network can be enhanced considerably.

2 Four-Stage Switching

In single-stage there is only one link from source inlet to destination inlet. In case of any failure of connection, there is not alternative path to communicate with destination subscriber. In multistage space division switching network, multiple connections are available because of intermediate stage cross-point. Let us consider a four-stage $N \times N$ network, shown in Fig. 1, having N number of inlets and N number of outlets. N inlets are segmented into a blocks and each block is carrying x inlets ($N = a \times x$). In the same way, N outlets are also segmented into a blocks carrying x outlets ($N = a \times x$). The structure of four-stage network is configured with intermediate switching matrices. The size of switching matrices in first-stage, second-stage, third-stage, and four-stage is ($x \times b$), ($a \times b$), ($b \times a$), and ($b \times x$) respectively. The calculation of total number of cross-point depends on Eqs. (1)–(3).

$$S = axb + ab^2 + ab^2 + bxa \tag{1}$$

$$S = 2axb + 2ab^2 \tag{2}$$

The number of cross-point are estimated, with the help of Eq. (3) and putting the value of ($N = a \times x$)

$$S = 2\left(Nb + ab^2\right) \tag{3}$$

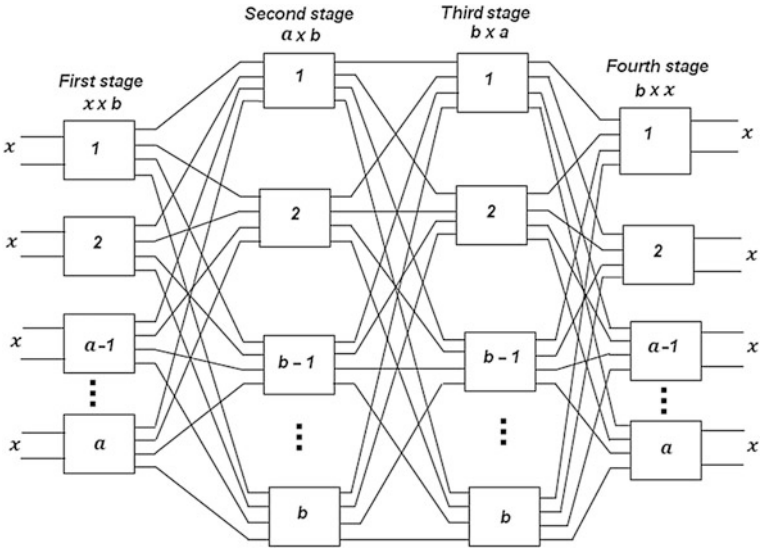


Fig. 1 Four-stage switching

The switching capacity of four-stage network is calculated, with the help of Eq. (4) when the network is full available and all the cross-point are utilized.

$$\text{Switching Capacity} = abba = a^2b^2 \tag{4}$$

3 Design Considerations

The four-stage network with 8×8 configuration is shown in Fig. 2. The Switching Capacity $= a^2b^2 = 4^2 \times 4^2 = 256$. It means, four-stage ($8 \times 8$) network is capable to maintain 256 calls simultaneously. The numbers of cross-points in four-stage (8×8) networks are determined with the help of Eq. (2). The value of cross-point, $S = 2axb + 2ab^2 = 2 \times 4 \times 2 \times 4 + 2 \times 4 \times 4^2 = 64 + 128 = 192$. The addressing and routing of the same network is discussed with the help of Table 1. The table suggests that if any inlet wants to communicate to outlet, the call can be routed by 16 alternate paths. Therefore, the network cannot be blocked. In the same way, the five-stage switching can provide more alternate paths in comparison to three and four-stage networks.

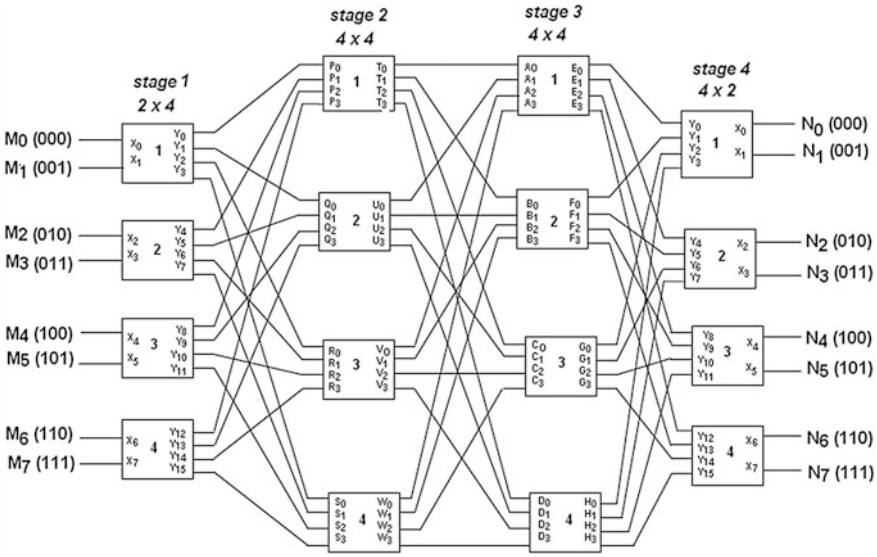


Fig. 2 Four-stage switching network (8 × 8) design

Table 1 Four-stage network (8 × 8) with routing

Inlet	Outlet	Routing
$M_0(000)$	$N_0(000)$	$M_0(000) \rightarrow X_0 \rightarrow Y_0 \rightarrow P_0 \rightarrow T_0 \rightarrow A_0 \rightarrow E_0 \rightarrow Y_0 \rightarrow X_0 \rightarrow N_0(000)$
		$M_0(000) \rightarrow X_0 \rightarrow Y_0 \rightarrow P_0 \rightarrow T_1 \rightarrow B_0 \rightarrow F_0 \rightarrow Y_1 \rightarrow X_0 \rightarrow N_0(000)$
		$M_0(000) \rightarrow X_0 \rightarrow Y_0 \rightarrow P_0 \rightarrow T_2 \rightarrow C_0 \rightarrow G_0 \rightarrow Y_2 \rightarrow X_0 \rightarrow N_0(000)$
		$M_0(000) \rightarrow X_0 \rightarrow Y_0 \rightarrow P_0 \rightarrow T_3 \rightarrow D_0 \rightarrow H_0 \rightarrow Y_3 \rightarrow X_0 \rightarrow N_0(000)$
		$M_0(000) \rightarrow X_0 \rightarrow Y_1 \rightarrow Q_0 \rightarrow U_0 \rightarrow A_1 \rightarrow E_0 \rightarrow Y_0 \rightarrow X_0 \rightarrow N_0(000)$
		$M_0(000) \rightarrow X_0 \rightarrow Y_1 \rightarrow Q_0 \rightarrow U_1 \rightarrow B_1 \rightarrow F_0 \rightarrow Y_1 \rightarrow X_0 \rightarrow N_0(000)$
		$M_0(000) \rightarrow X_0 \rightarrow Y_1 \rightarrow Q_0 \rightarrow U_2 \rightarrow C_1 \rightarrow G_0 \rightarrow Y_2 \rightarrow X_0 \rightarrow N_0(000)$
		$M_0(000) \rightarrow X_0 \rightarrow Y_1 \rightarrow Q_0 \rightarrow U_3 \rightarrow D_1 \rightarrow H_0 \rightarrow Y_3 \rightarrow X_0 \rightarrow N_0(000)$
		$M_0(000) \rightarrow X_0 \rightarrow Y_2 \rightarrow R_0 \rightarrow V_0 \rightarrow A_2 \rightarrow E_0 \rightarrow Y_0 \rightarrow X_0 \rightarrow N_0(000)$
		$M_0(000) \rightarrow X_0 \rightarrow Y_2 \rightarrow R_0 \rightarrow V_1 \rightarrow B_2 \rightarrow F_0 \rightarrow Y_1 \rightarrow X_0 \rightarrow N_0(000)$
		$M_0(000) \rightarrow X_0 \rightarrow Y_2 \rightarrow R_0 \rightarrow V_2 \rightarrow C_2 \rightarrow G_0 \rightarrow Y_2 \rightarrow X_0 \rightarrow N_0(000)$
		$M_0(000) \rightarrow X_0 \rightarrow Y_2 \rightarrow R_0 \rightarrow V_3 \rightarrow D_2 \rightarrow H_0 \rightarrow Y_3 \rightarrow X_0 \rightarrow N_0(000)$
		$M_0(000) \rightarrow X_0 \rightarrow Y_3 \rightarrow S_0 \rightarrow W_0 \rightarrow A_3 \rightarrow E_0 \rightarrow Y_0 \rightarrow X_0 \rightarrow N_0(000)$
		$M_0(000) \rightarrow X_0 \rightarrow Y_3 \rightarrow S_0 \rightarrow W_1 \rightarrow B_3 \rightarrow F_0 \rightarrow Y_1 \rightarrow X_0 \rightarrow N_0(000)$
		$M_0(000) \rightarrow X_0 \rightarrow Y_3 \rightarrow S_0 \rightarrow W_2 \rightarrow C_3 \rightarrow G_0 \rightarrow Y_2 \rightarrow X_0 \rightarrow N_0(000)$
		$M_0(000) \rightarrow X_0 \rightarrow Y_3 \rightarrow S_0 \rightarrow W_3 \rightarrow D_3 \rightarrow H_0 \rightarrow Y_3 \rightarrow X_0 \rightarrow N_0(000)$
⋮	⋮	⋮
$M_7(111)$	$M_7(111)$	$M_7(111) \rightarrow X_7 \rightarrow Y_{12} \rightarrow P_3 \rightarrow T_0 \rightarrow A_0 \rightarrow E_0 \rightarrow Y_0 \rightarrow X_0 \rightarrow N_0(000)$
		⋮
		$M_7(111) \rightarrow X_7 \rightarrow Y_{15} \rightarrow S_3 \rightarrow W_3 \rightarrow D_3 \rightarrow H_3 \rightarrow Y_{15} \rightarrow X_7 \rightarrow N_7(000)$

4 Simulation Results and Synthesis

The simulation of four-stage network is carried in ModelSim 10.1 b software. The RTL diagram of developed design is shown using Fig. 3. The inlet subscribers are presented as $M_0(7:0)$ to $M_7(7:0)$ and outlet subscribers are $N_0(7:0)$ to $N_7(7:0)$. The address of source and destination subscribers is presented with *in_node_address* [2:0] and *out_node_address* [2:0]. The memory unit has two control signals: *write_en* and *read_en* are used for write and read operations. *Clk* is the default input to provide clock pulse and reset is used to reset all the contents of destination subscribers. The summary report extracted directly from the Xilinx software about device utilization is the details of utilized Field programmable gate array (FPGA) device hardware parameters such as logic gates, flip flops, slices, LUTs, memory etc. Table 2 describes the hardware parameters and timing parameters utilization for the four-stage network. The target device is selected xc5vlx20t-2-ff323, which is programmed for Virtex 5 FPGA.

The functional simulation is verified using modelsim software and corresponding simulation is shown in Fig. 4. The data is analyzed on the rising edge of clock pulse. In the result the data is communicated from node 2 to node 6. The details of timing parameters are descripted by frequency support (maximum), arrival time as input before clock signal, output time after clock signal, and total path delay as combinational delay.

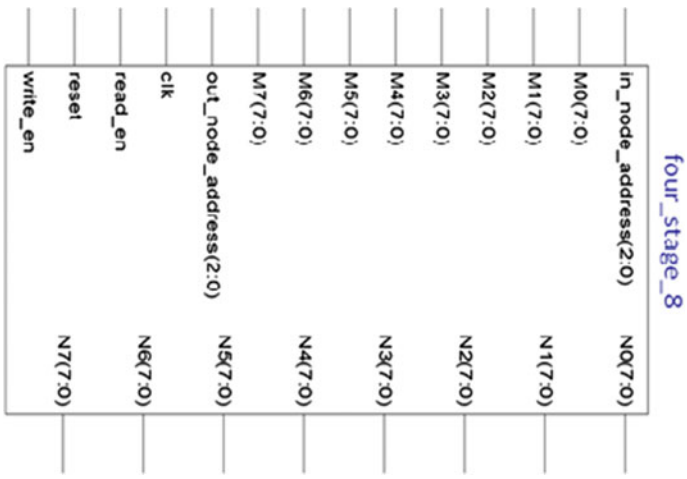


Fig. 3 Four-stage network with RTL view

Table 2 Device and time utilization summary for four-stage network

Device part	Utilization (%)	Parameter for timing	Utilization
Slices utilization	160/12,480 1	Frequency (maximum)	535.733 MHz
Slice flip flops utilization	229/12,480 1	Arrival time before clk (minimum)	4.090 ns
4 input LUTs utilization	160/229 67	Time after clk (maximum)	2.830 ns
Bonded IOBs utilization	138/172 80	Total path delay (combinational)	12.000 ns
GCLKs utilization	1/32 3	Memory utilization	263,208 kB

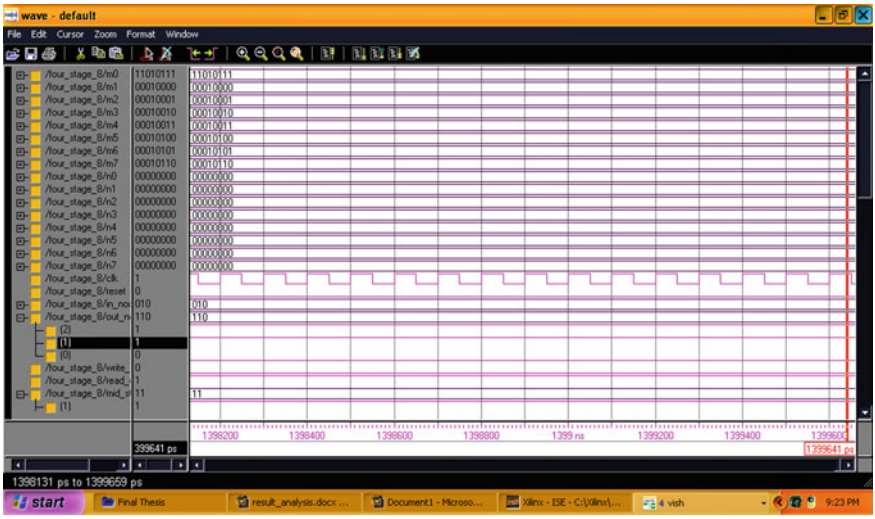


Fig. 4 Simulation waveform

5 Conclusions

The chip design and synthesis of the four-stage telecommunication switching is done using Very high speed integrated circuit hardware description language (VHDL) programming. The cluster size of the design is chosen (8 × 8), which guarantees the full duplex commutation of 8 inlets at input side and 8 outlets at output side. The simulation results are validated on Virtex-5 FPGA, manufactured by Digilent. The intercommunication among the nodes is verified on the same kit. The design and implementation of the expandable structure of four-stage telecommunication network is to configure the entire whole switching system as programmable to enhance the switching capability, and reduction in routing delay. The developed structure facilitates 256 calls simultaneously under full available network. In future work, the cluster size of the four-stage network can be increased.

References

1. Alfaraj N, Xu Y, Chao H.J "A Practical and Scalable Congestion Control Scheme for High-Performance Multi-Stage Buffered Switches" IEEE 13th international conference on high performance switching and routing, pp (44–51), 2012.
2. Chaudhari S.K., Ingale H.T., Rane K.P., "Novel Approach of Hybrid Switching System using Combined SPC and VLSI technology" International Journal of Recent Trends in Engineering, 2, 303–310, 2009.
3. John. C. Bellamy, "Digital Switching, Chapter 5 pp 225– 245" Digital Telephony, Wiley India Pvt. Ltd, India, 2011.
4. Kumar. A, Kuchhal. P, and Singhal. S "Design and FPGA Synthesis of Three Stage Telecommunication Switching in HDL Environment" Procedia Computer Science, Elsevier 48, 454 – 460, 2015.
5. N. Chrysos, "Request - grant scheduling for congestion elimination in multistage networks," Ph.D. dissertation, Univ. of Crete, Greece, 12–28, 2006.
6. Rajala M "Heavy Loading Effects in Networked Systems", "IEEE Conference on Soft Computing in Industrial Applications (SMCia/08)", 199–121,2008.
7. Vishwanathan T, Bhatnagar M "Electronics Space Division Switching, Ch-4", "Telecommunication Switching Systems and Networks" 2nd Ed. PHI India, 143–157, 2015.
8. Varatkar G, Marculescu R "On-chip traffic modeling and synthesis for MPEG-2 video applications". IEEE Transaction VLSI, Vol. 12, No. 1, pp (108–119), 2004.

Nanoferrite Embedded in Poly(O-Toluidine) and Polyaniline Matrix for EMI Shielding

Preeti, M. Farukh, Balesh Vasisth, Shaily Singhal, Lalit Gaur, Vivek Verma, S.P. Gairola and S.K. Dhawan

Abstract Nanoparticles of barium ferrite were synthesized by citrate precursor method and nanocomposite of barium ferrite@poly(o-toluidine) and barium ferrite@polyaniline were prepared by in situ polymerization. The electromagnetic properties were investigated in the frequency range of 8–12 GHz. Shielding effectivenesses of nanoferrite/poly(o-toluidine) and nanoferrite/polyaniline composites were obtained as 10.9 dB and 42.5 dB, respectively. The value of SE suggests that the barium ferrite@polyaniline composite shows much better electromagnetic interference (EMI) shielding results than barium ferrite@poly (o-toluidine).

Keywords Nanoferrites · Polyaniline · Poly(O-Toluidine) · Shielding effectiveness

1 Introduction

The ambient usage of electronic gadget procreates a different mode of disturbance well familiars as electromagnetic interference (EMI), caused by EM waves, consists of magnetic (H) and an electric (E) vector component. Electromagnetic shielding

Preeti (✉) · Balesh Vasisth · Lalit Gaur · S.P. Gairola (✉)
Uttaranchal University, Prem Nagar, Dehradun, India
e-mail: preeti10090@gmail.com

S.P. Gairola
e-mail: spgairola10@gmail.com

M. Farukh · S.K. Dhawan
National Physical Lab, CSIR, K.S. Krishnan Marg, New Delhi, India

Vivek Verma
Department of Physics, Hindu College, University of Delhi, Delhi, India

Shaily Singhal
University of Petroleum and Energy Studies, Bidholi, Prem Nagar, Dehradun, India

© Springer Science+Business Media Singapore 2017

R. Singh and S. Choudhury (eds.), *Proceeding of International Conference on Intelligent Communication, Control and Devices*, Advances in Intelligent Systems and Computing 479, DOI 10.1007/978-981-10-1708-7_129

[1–7] is competent redresses for the EMI issue [8]. The conducting polymer and ferrimagnetic composites enhance the shielding efficiency [9–11]. The fusion of ferromagnetic-conducting polymer composite [12] leads special amalgamation of magnetic as well as electrical characteristics. The electromagnetic waves originated from an electric origin can be shielded by conducting ferromagnetic substance, whereas EM waves [13] from a magnetic origin can be actively shielded by magnetic materials.

2 Experimental

2.1 Formation of $BaFe_{12}O_{19}$

For the preparation of BF, citrate precursor method [14] was used. Ferric nitrate, barium nitrate, and $C_6H_8O_7$ were taken as beginning raw ingredients. Required quantities of $Ba(NO_3)_2$ and $Fe(NO_3)_3$ were liquidized in least amount of distilled water. The proportion of barium to iron was taken as 1:12. An aquatic emulsion of $C_6H_8O_7$ was combined with mixture of $Fe(NO_3)_3$ and $Ba(NO_3)_2$. The molar ratio of total nitrate ions to citric acid was determinate at 1:1. NH_3 was added gradually to balance the pH at 9. In the end, the mixed emulsion was allowed to vaporize through heating at 100 °C with constant agitation and finally brown gel was obtained, with continuous heating and increasing the temperature to form a brown porous powder. This yield was calcinated at 900 °C for 2 h to get the $BaFe_{12}O_{19}$ [15]. The final powder of the combustion was milled by mechanical ball mill.

2.2 Formation of PANI/BF Nanocomposite

PANI/BF nanocomposite was formed by in situ polymerization method with DBSA and ammonium dioxypersulphate. Dodecyl benzene sulphonic acid was liquidized in deionized water with cogent agitation for 30 min. Then $BaFe_{12}O_{19}$ nanoparticles were mixed with DBSA for 1 h with constant stirring. Thereafter, aniline monomer was mixed. APS liquefied in 100 ml deionized water was gradually added drop wise under continuous agitation. Polymerization was permitted at 0 °C for 4 h. The final product was mixed-up thoroughly with iso-propanol, filtered, and dried in oven. The sample was scrunched in pestle mortar to use for further characterization (Fig. 1).

2.3 Preparation of Poly(O-Toluidine)/BF Nanocomposite

Poly(O-Toluidine)/BF compound was formed by in situ polymerization method with DBSA and APS. DBSA was liquidized in deionized water for 30 min with cogent stirring, and then $BaFe_{12}O_{19}$ was mixed to the DBSA for 1 h with constant

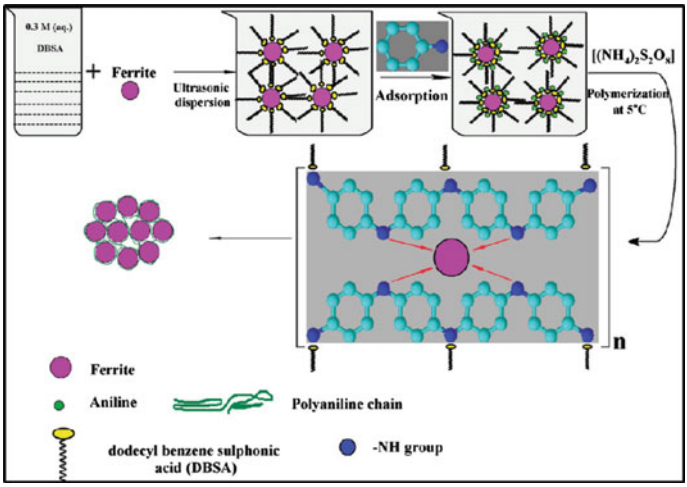


Fig. 1 $BaFe_{12}O_{19}$/PANI nanocomposite formation

agitation. Later on, o-toluidine was mixed and agitated for 30 min. APS liquefied in 100 ml deionized water was gradually added drop wise under continuous agitation. Polymerization was permitted at 0 °C for 4 h. The final product was mixed-up thoroughly with iso-propanol, filtered, and dried in oven. The sample was scrunched in pestle mortar to use for further characterization.

3 Characterizations

The crystalline size of barium ferrite was analyzed using HRTEM model Tecnai G2 F30 Stwin, USA. $BaFe_{12}O_{19}$ in polymer matrix was confirmed by XRD, Bruker, and D8 ADVANCE ECO, and pure barium ferrite by Rigaku, miniflex-II, and X-ray diffractometer. The M–H measurements were performed by VSM, PAR 155, USA at room temperature. SEM, FEI Quanta 200 was employed to examine the surface morphology. The shielding measurements were analyzed by VNA, E8263B Agilent Technologies in X-band (8–12 GHz) using two port measurement techniques [16, 17].

4 Results Analysis

The $BaFe_{12}O_{19,}$ XRD patterns have been shown in Fig. 2a. The XRD peaks was observed at 2θ value of 30.55(d = 2.923), 32.37(d = 2.763), 34.19(d = 2.620), 37.30(d = 2.407), 40.42(d = 2.228), and 42.76(d = 2.112), 55.49(d = 1.654),

57.05(d = 1.612), 63.28(d = 1.467) which correspond to hexagonal-structured $BaFe_{12}O_{19}$ nanoparticles (JCPDS 12047-11-9). The diffraction peaks of $BaFe_{12}O_{19}$ are very intense which indicates a high crystallinity.

Figure 2b shows the patterns PANI@BaF and Poly(O-Toluidine)@BaF composite. $BaFe_{12}O_{19}$ crystalline size is calculated by the equation $D = k\lambda/\beta \cos\theta$.

The surface morphologies of $BaFe_{12}O_{19}$ nanoparticles were investigated using SEM. Figure 3 shows SEM images of $BaFe_{12}O_{19}$ nanoparticles. It can be seen that $BaFe_{12}O_{19}$ nanoparticles are highly aggregated.

The morphology and particle size distribution were determined by means of TEM. Figure 4 shows the typical TEM image of the pure ferrite nanoparticles obtained from citrate precursor method. It can be seen in Fig. 4a that $BaFe_{12}O_{19}$ particles (40–60 nm) are extremely aggregated, and Fig. 4b shows the d-spacing of $BaFe_{12}O_{19}$ particles, which is near about 0.37 nm.

The magnetization curve of $BaFe_{12}O_{19}$ is shown in Fig. 5. The value of magnetization (Ms) for $BaFe_{12}O_{19}$ was obtained to be 51.76 emu/g.

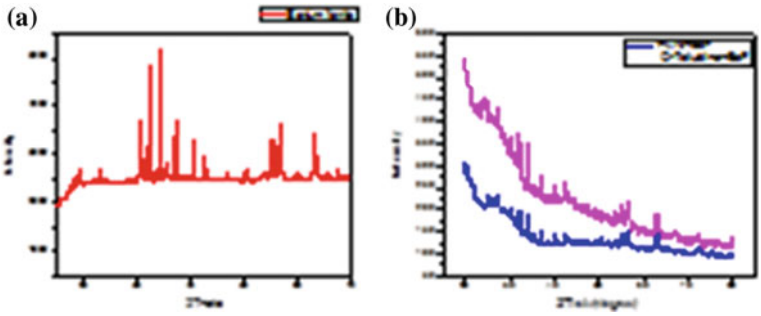


Fig. 2 XRD graph of **a** $BaFe_{12}O_{19}$ **b** PANI@BaF and Poly(o-toluidine)@BaF composite

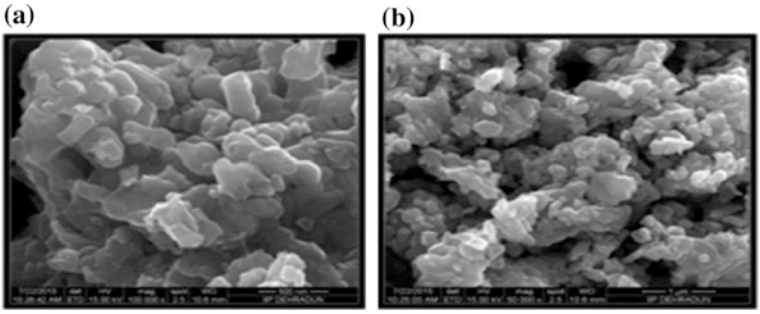


Fig. 3 SEM images of $BaFe_{12}O_{19}$ nanoparticles

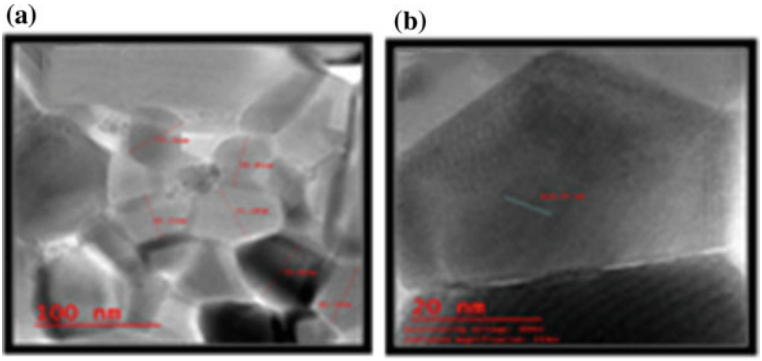


Fig. 4 HRTEM images of barium ferrite nanoparticles

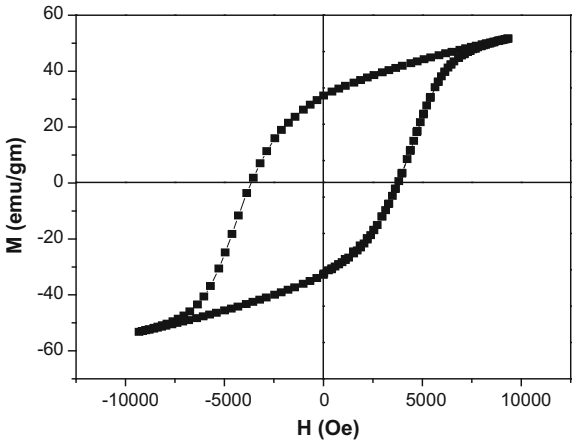


Fig. 5 VSM of $BaFe_{12}O_{19}$ nanoparticles

5 Electromagnetic Shielding Studies

The shielding efficiency (SE) of a substance is articulated as the proportion of incident and transmitted power expressed as

$$\mathrm{SE(dB)} = -10\ \log(P_T/P_I) = \mathrm{SE_R} + \mathrm{SE_A} + \mathrm{SE_M}$$

whereas SE_A, SE_R, and SE_M describe the shielding efficiency due to absorption, reflection, and multiple reflections, respectively, and can be expressed as [18]

$$\mathrm{SE_R} = -10\log(1-R)$$

$$\mathrm{SE_A} = -10\log(1-A_{\mathrm{eff}}) = -10\log(T/1-R)$$

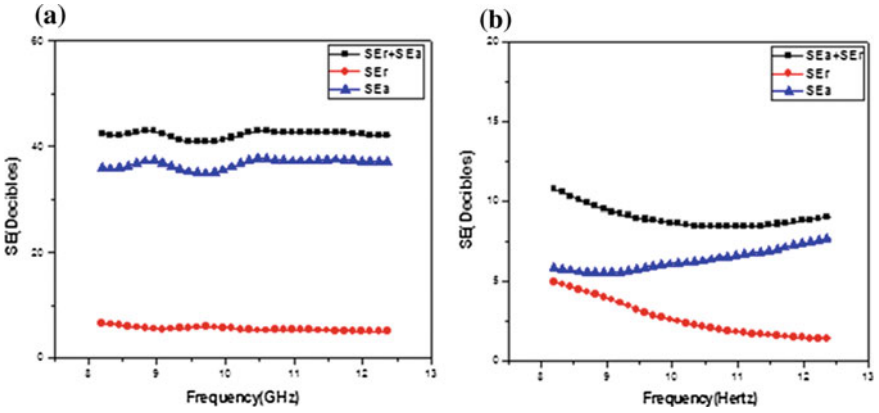


Fig. 6 Shielding effectiveness, **a** PANI@Barium Ferrite, **b** o-Toluidine@Barium Ferrite composite

$$SE_M = -20\log\left(1-e^{-2t/\delta}\right) = -20\log\left(1-10^{-SE_A/10}\right)$$

whereas SE_M is the multiple reflection that can be neglected when $SE_A > 10$ dB [19, 20].

Figure 6a exhibits shielding effectiveness of the PANI@Barium Ferrite. Total shielding effectiveness has been found to be 42.5 dB in the composite while 10.9 dB for the Poly(O-Toluidine)@BaF composite as shown Fig. 6b. The total SE of the PANI@BaF composite is much higher than the Poly(O-Toluidine)@BaF composite. It was seen that PANI@BaF composite, SE, is mostly influenced by absorption.

6 Conclusions

Barium ferrite nanoparticles were synthesized by citrate precursor method, and its composites with polyaniline and with Poly(o-toluidine) have been prepared by in situ polymerisation method. PANI@Barium Ferrite composite shows higher shielding effectiveness (SE = 42.5 dB) as compared to Poly(O-Toluidine)@Barium Ferrite composite. As a result PANI@Barium Ferrite composite is more promising microwave absorption materials as compared to Poly(O-Toluidine)@Barium Ferrite.

Acknowledgments This research work was endorsed in part by a grant from the DST, Government of India.

The authors wish to thank Director, Indian Institute of Petroleum (I.I.P), Dehradun, for providing the SEM characterization facility.

References

1. T. Mokela, J. Sten, A. Hujanen, H. Isotalo, Synth. Met. 101(1999)707.
2. X. Huang, Z. Chen, L. Tong, M. Feng, Z. Pu and X. Liu, Mater. Lett., 2013, 111, 24–27.
3. T.A. Ezquerra, F. Kremer, M. Mohammadi, J. Ruhe, G. Wegner, B. Wessling, Synth. Met. 28 (1989)83.
4. A. P. Singh, A. Chandra and S. Dhawan, AIP Adv., 2011, 1, 022147.
5. T. Taka, Synth. Met. 41 (1991) 1177.
6. M. Mishra, A. P. Singh and S. K. Dhawan, J. Alloys Compd., 2013, 557, 244–251.
7. A. Ohlan, K. Singh, A. Chandra, V. N. Singh and S. K. Dhawan, J. Appl. Phys., 2009, 106,044305–044311.
8. D. D. L. Chung, Carbon, 2012, 50, 3342–3353.
9. K. Chen, C. Xiang, L. Li, H. Qian, Q. Xiao and F. Xu, J. Mater. Chem., 2012, 22, 6449–6455.
10. B. Yuan, L. Yu, L. Sheng, K. An and X. Zhao, J. Phys. D: Appl. Phys., 2012, 45, 235108.
11. G.-S. Wang, X.-J. Zhang, Y.-Z. Wei, S. He, L. Guo and M.-S. Cao, J. Mater. Chem. A, 2013, 1, 7031–7036.
12. Ramanathan T, A. A. Abdala, Stankovich S, D. A. Dikin, M. Herrera Alonso, R. D. Piner, D. H. Adamson, H. C. Schniepp, Chen X, R. S. Ruoff, S. T. Nguyen, I. A. Aksay, R. K. Prud'Homme and L. C. Brinson, Nat Nano, 2008, 3, 327–331.
13. K. Singh, A. Ohlan, V. H. Pham, B. R, S. Varshney, J. Jang, S. H. Hur, W. M. Choi, M. Kumar, S. K. Dhawan, B.-S. Kong and J. S. Chung, Nanoscale, 2013, 5, 2411–2420.
14. C. Mao, X. Dong, T. Zeng, G. Wang and S. Chen, Mater. Res. Bull., 2007, 42, 1602–1610.
15. A. Ohlan, K. Singh, A. Chandra and S. K. Dhawan, Journal of Applied Polymer Science, 2008, 108, 2218–2225.
16. A.M. Nicolson, G.F. Ross, IEEE Trans. Instrum. Meas. 19 (1970) 377.
17. W.B. Weir, Proc. IEEE 62 (1974) 33.
18. N. C. Das, D. Das, T. K. Khastgir and A. C. Chakrraborthy, Composites A., 2000, 31, 1069–1081.
19. M. Ashokkumar, T. N. Narayanan, B. K. Gupta, A. Leela, Mohana Reddy, P. Avanish, S. K. Dhawan, C. Bangaru, D. S. Rawat, S. Talapatra and P. M. Ajayan, ACS Sustainable Chem. Eng., 2013, 619–626.
20. N. F. Colaneri and L. Schacklette, Instrumentation and Measurement, IEEE Transactions on, 1992, 41, 291–297.

Design and Performance Analysis of Bowtie-Shaped Slotted Rectangular Patch Antenna for Terahertz (THz) Applications

Devesh Kumar, Malay Ranjan Tripathy, Sachin K. Rajput, Amit Kumar and Manish Sharma

Abstract The paper comprises the design and simulation of a bowtie-shaped slotted rectangular patch antenna at frequency 1.56 THz for frequency range of 1.2–1.8 THz. GaAs material is used as substrate to achieve better antenna performance. The performance characteristic parameters (return loss, VSWR, gain, and radiation pattern) of proposed design have been portrayed and analyzed to show the performance of antenna. The analyzed results exhibit that the antenna designed shows multiband nature. The overall maximum gain of 7.13 dB is obtained at 1.60 THz and maximum return loss of 32.27 dB is at frequency 1.73 THz. HFSS simulation tool is used to provide platform for simulating the proposed design.

Keywords Bowtie · Multiband · Return loss · Gain · Terahertz

1 Introduction

Over the number of decade, as exponential increases the prestigious demand of wireless applications, any other demands in the field of electronics have been outgrown and these changes create green platform for upgrading the antenna size as well as power efficiency. The system parameters like modulation scheme, operating

Devesh Kumar (✉) · M.R. Tripathy · S.K. Rajput · Amit Kumar · Manish Sharma
Amity University, Noida, Uttar Pradesh, India
e-mail: dvshkmr@gmail.com

M.R. Tripathy
e-mail: malay.amity@gmail.com

S.K. Rajput
e-mail: skrajput@amity.edu

Amit Kumar
e-mail: amitkumar5555@gmail.com

Manish Sharma
e-mail: manish.nsit07@gmail.com

© Springer Science+Business Media Singapore 2017

R. Singh and S. Choudhury (eds.), *Proceeding of International Conference on Intelligent Communication, Control and Devices*, Advances in Intelligent Systems and Computing 479, DOI 10.1007/978-981-10-1708-7_130

frequency, and power have to be supposed to adapt as there are different applications for so many tasks. But there are many more characteristics such as large bandwidth, high efficiency, and low cost which are independent of them and they are always sought after and play important role. There have been different forms of message communication between two places which may be very far from each other. The basic reason for these different forms of communication is to enhance the transmission capabilities, transmission range, or the data rate. The use of higher frequencies is always preferred such as frequency which is higher than microwave that offers up gradation in the areas of directivity, bandwidth, and resolution. The terahertz (THz) region is more preferable as having so important properties like improved data rate, operating bandwidth, and so many. The THz region which lies between the microwave and the infrared region extends from frequency 0.1 to 10 THz. THz band has also numerous advantages over microwave as well as far-infrared wave communication. Some of these are as follows:

- It has low diffraction in comparison with microwave band and it is profitable in the line of sight and point-to-point communication links.
- It has low attenuation of the signal in comparison to IR, in certain atmospheric condition like fog.
- It has noticeable reduction of the scintillation effect in the THz wave communication link in comparison to IR links.

The THz antennas with different structures and techniques have been presented in [1–7]. A bowtie-shaped antenna with a finite ground plane and AMC (artificial magnetic conductor) structure is designed to achieve greater directivity [1]. The different bowtie-shaped antennas are presented in [6–9]. Terahertz application based photoconductive optoelectronics by incorporating plasmonic contact electrodes for significant performance enhancement is described in [10]. Novel Design of Key-Shaped Fractal Antenna for UWB Applications is presented in [11]. Modified Ring Shaped Sierpinski Triangle Fractal Antenna for C-Band and X-Band Applications is presented in [12]. THz communication can be described as a secure point-to-point, short distance, and high data rate system line communication which can go up to Gb/s. The transmission of THz waves through water and objects is still a concern but its upside is enormous with huge advantages for wireless communication. A lot of researches have been done on antennas for THz applications but there is always room for better designs and upgraded characteristics.

This research paper contributes research context in THz frequency range. A bowtie antenna has been created which is giving acceptable results in the THz frequency range. This paper work is dedicated to analyzing of antenna design. The use of a semiconductor substrate (GaAs) makes it even more convenient for the commercial part. Also the antenna is also confined in an airbox, thus increasing its radiating power. The whole antenna has been designed on high-frequency structure simulator software.

The paper is organized as follows. Antenna design parameters are detailed in Sect. 1. Section 2 includes simulated results and discussions on results. The conclusion part is detailed in Sect. 3.

2 Antenna Design

The bowtie-shaped slotted terahertz antenna is designed for frequency span of 1.2–1.8 THz. The solution frequency of design is taken as 1.56 THz. The microstrip line feed is used. Gallium arsenide material of dielectric permittivity 12.9 is used as substrate which is a semiconductor. The dimension of the substrate is 90 × 152 22 μm^2. A main radiating patch of dimension 64 × 142 μm^2 is placed on top of the substrate. A bowtie-shaped slots are created on radiating patch which covers 2/3 area of the patch. The strip lines which connect bowtie slot are of dimension 16 × 4 μm^2. The dimension of ground is 90 × 152 μm^2. The various pictorial views of designed antenna are depicted in Fig. 1 and (Table 1).

3 Simulated Results and Discussions

The simulation of proposed antenna design has been performed on HFSS for frequency 1.56 THz. The design shape of the antenna is a bowtie and all the results are analyzed and presented for the frequency range of 1.2–1.8 THz.

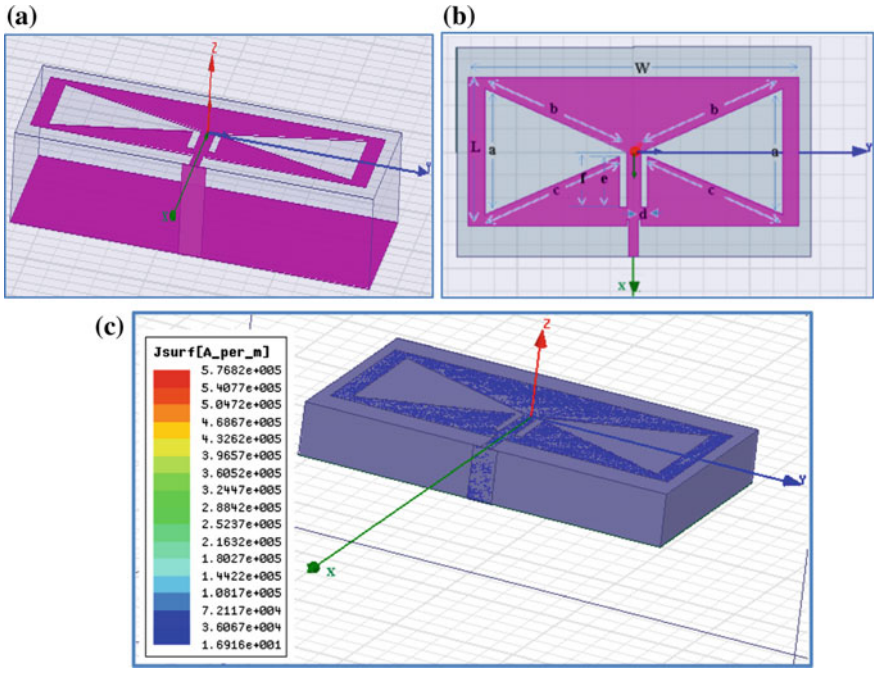


Fig. 1 The different views of bowtie-shaped slotted antenna, **a** 3-D view, **b** Top, **c** Current distribution in main patch

Table 1 Physical parameters of metamaterial-based bowtie-shaped slotted antenna

Parameters	Values (μm)				Parameters	Values (μm)
Radiating patch ($L \times W$)	64 × 142				Substrate ($L_S \times W_S \times H_S$)	90 × 156 × 22
Bowtie-shaped slots	a	54.00	d	3	Ground ($L_g \times W_g$)	90 × 156
	b	66.70	e	22	Wave port ($W_W \times H_W$)	10 × 22
	c	63.16	f	24	Feed ($L_f \times W_f$)	16 × 4

3.1 Return Loss

The return loss of the antenna is pictured in Fig. 2. The four proper resonance peaks are obtained at frequencies 1.2794 THz (RL = –23.75 dB), 1.5784 THz (RL = –23.74 dB), 1.6874 THz (RL = –13.01 dB), and 1.7296 THz (RL = –32.27 dB). The observed impedance bandwidths corresponding to resonance peaks obtained are 14.5, 20.9, 11.8, and 31.8 GHz, respectively, for RL = –10 dB (VSWR = 2).

3.2 VSWR

The VSWR of the antenna designed is shown in Fig. 3. It is observed from the figure that each impedance bandwidth is measured for the value of VSWR $\leq$ 2 (abs) to achieve better impedance matching at feeding point.

3.3 Gain

The plot of variation of total gain of the antenna is shown in Fig. 4. In Fig. 4a variation gain is depicted in Φ-plane for various values of θ angle for frequency 1.56 THz. It can be observed that the maximum gain obtained is 4.09 dB in radial

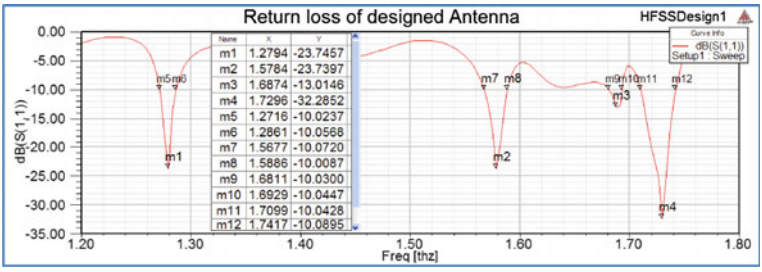


Fig. 2 Return loss of antenna designed

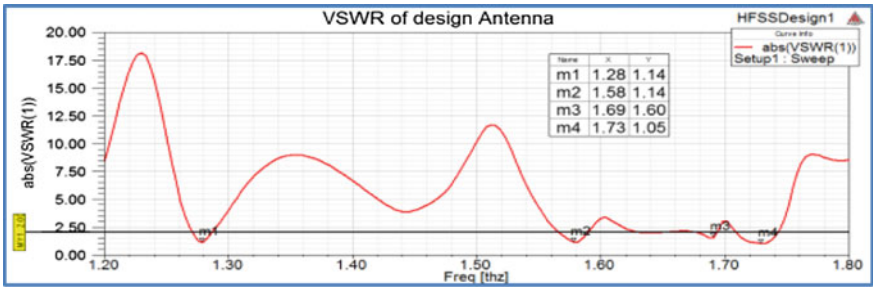


Fig. 3 VSWR of antenna designed

directions denoted by angles $\theta = 94°$, $\Phi = 84°$ and $\theta = 95°$, $\Phi = 279°$ at frequency of 1.56 THz. Figure 4b shows the variation of gain as frequency and it is notified that maximum gain of 7.13 dB ($\theta = 170°$ and $\Phi = 360°$) is achieved at 1.60 THz. The gains of 6.38, 2.39, 3.93, and 5.23 dB are obtained at frequencies 1.2794, 1.5784, 1.6874, and 1.7296 THz, respectively.

3.4 Radiation Pattern

The E-plane and H-plane radiation patterns of the antenna are shown in Fig. 5 for frequency 1.56 THz and frequencies at which maximum RL obtained with different impedance bandwidths. The simulated radiation patterns show that the E-Plane and

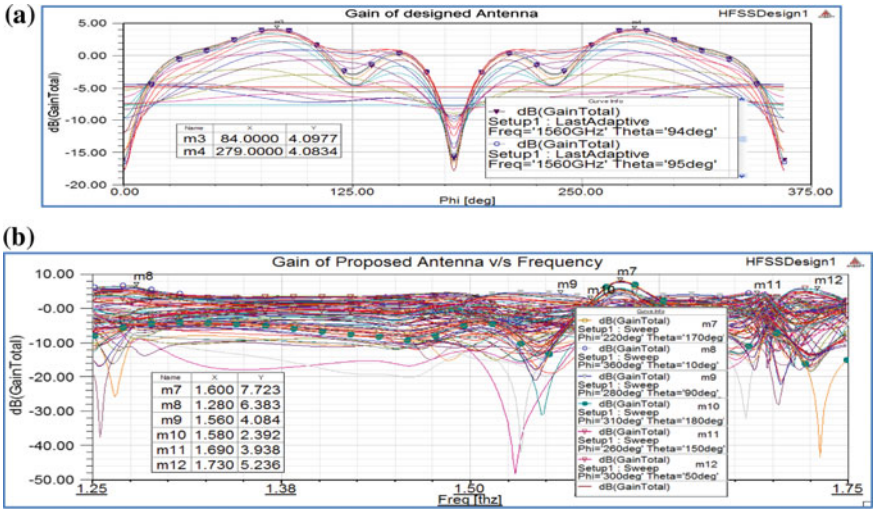


Fig. 4 Total gain of the antenna **a** verses angle Φ for various angles θ **b** verses frequency

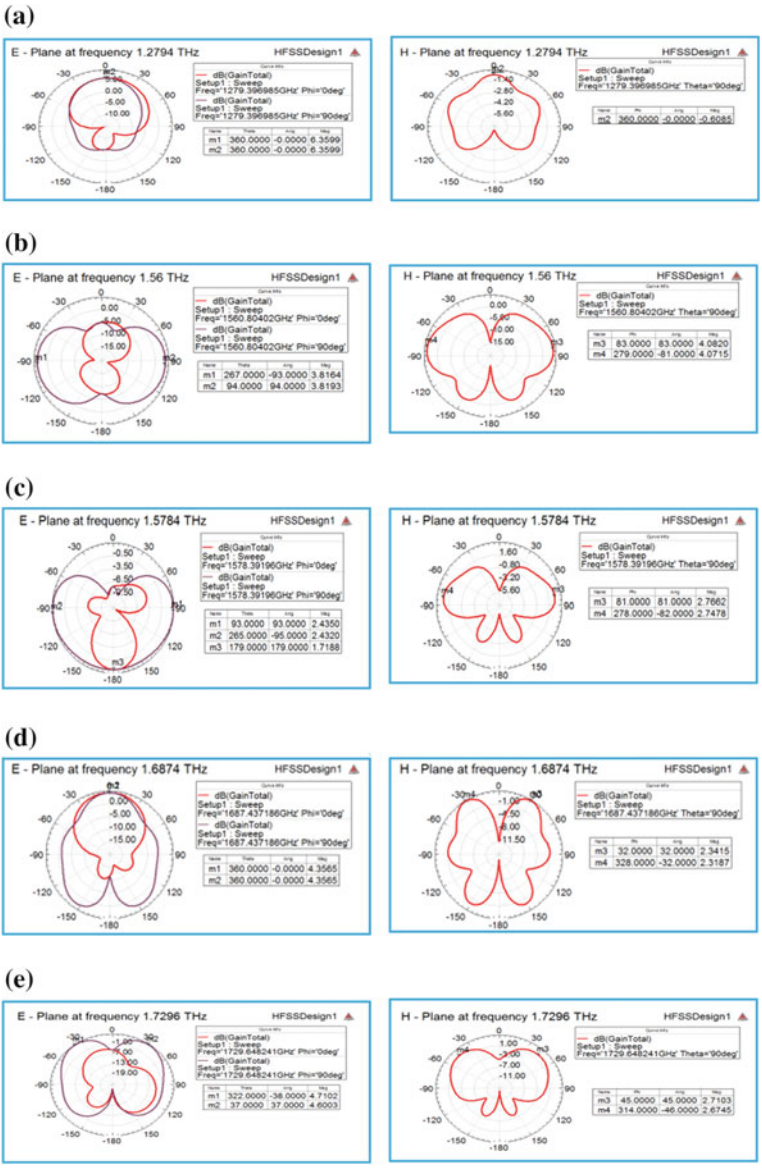


Fig. 5 Simulated radiation patterns in E- and H-plane of the antenna at **a** 1.2794 THz **b** 1.5600 THz **c** 1.5784 THz **d** 1.6874 THz **e** 1.7296

H-Plane radiation patterns are directional patterns. It is notified that maximum gain obtained is 5.90 dB in both vertical planes $\Phi = 0°$ and $\Phi = 90°$ at frequency 1.28 THz.

4 Conclusion

The conclusion of this paper is that the proposed design of bowtie-shaped slotted rectangular patch antenna can work efficiently in the THz frequency range, thus opening doors to a vast field of applications at THz frequencies such as THz aerospace, THz imaging, defense range sectors, etc. The design proposed has the substantial advantages of its compact size (in μm) and wide bandwidth (maximum obtained is 31.8 GHz for resonance peak at 1.7296 THz (RL = –32.27 dB)). The maximum gain of 4.09 dB is obtained in radial directions at different angles $\theta = 94°$, $\Phi = 84°$ and $\theta = 95°$, $\Phi = 279°$ for frequency 1.56 THz. The overall maximum gain of 7.13 dB ($\theta = 170°$ and $\Phi = 360°$) and maximum return loss of –32.27 dB are obtained at frequencies 1.60 and 1.7296 THz, respectively. GaAs substrate is used for this design.

References

1. N. Zhu and R. W. Ziolkowski, "Progress toward THz antenna designs with high directivity and high efficiency," in Proc. IEEE Antennas Propagat. Soc. Int. Symp., Orlando, FL, USA, 2013, pp. 2271–2272.
2. N. Zhu, R. W. Ziolkowski, "Photoconductive THz Antenna Designs With High Radiation Efficiency, High Directivity, and High Aperture Efficiency," IEEE Transactions on Terahertz Science and Technology, vol. 3, no. 6, pp. 721–730 (2013).
3. A. Sharma, V. K. Dwivedi, G. Singh, "THz Rectangular Patch Microstrip Antenna Design Using Photonic Crystal as Substrate," Progress in Electromagnetic Research Symposium, USA, July 2–6, 2008.
4. H. Liu, H. Jiang, X. Guan, "Single-Feed Slotted Bowtie Antenna for Triband Applications," Antennas and Wireless Propagation Letters, IEEE, vol. 12, pp. 1658–1661 (2013).
5. Z. Popovic, and E. N. Grossman, "THz metrology and instrumentation," IEEE Transaction on Terahertz Science and Technology, vol. 1, No. 1, pp. 133–144, September 2011.
6. I. Woo, T. K. Nguyen, H. Han, H. Lim, and I. Park, "Four-leaf-clovershaped antenna for a THz photomixer," Optics Express, vol. 18, pp. 18532–18542, August 2008.
7. R. Singh, and C. Rockstuhl, "Spiral-type terahertz antennas and the manifestation of the Mushiake principle," Optics Express, vol. 17, pp. 9971–9980, May 2009.
8. H. Harde and D. Grischkowsky, "Coherent transients excited by subpicosecond pulses of terahertz radiation," J. Opt. Soc. Amer. B, vol. 8, no. 8, pp. 1642–1651, Aug. 1991.
9. M. Tani, S. Matsuura, K. Sakai, and S.-I. Nakashima, "Emission characteristics of photoconductive antennas based on low-temperature-grown GaAs and semi-insulating GaAs," Appl. Opt., vol. 36, no. 30, pp. 7853–7859, Oct. 1997.
10. C.W. Berry, N. Wang, M. R. Hashemi, M. Unlu, and M. Jarrahi, "Significant performance enhancement in photoconductive terahertz optoelectronics by incorporating plasmonic contact electrodes," Nature Commun., vol. 4, pp. 1622, Mar. 2013.

11. Devesh Kumar, Sakshi Bansal and Manish Sharma “Novel Design of Key-Shaped Fractal Antenna for UWB Applications” IEEE CICN 2014, Nov 2014, pp 41–45.
12. Devesh Kumar, Samira Ahmed “Modified Ring Shaped Sierpinski Triangle Fractal Antenna for C-Band and X-Band Applications” IEEE CICN 2014, Nov 2014, pp 78–82.
13. H. Liu, J. Yu, P. Huggard, and B. Alderman, “A multichannel THz detector using integrated bow-tie antennas,” Int. J. Antennas Propag., vol. 2013, Article ID 417108, Apr. 2013.

FPGA Implementation of UDP/IP Stack Using TSE IP Core and Transfer Data at 1 Gbps

Deeksha Jain and Swati Shrivastava

Abstract High-speed VHDL interfaces are used for transmission of huge amount of data. This paper deals with the development of VHDL code for interfacing with high-speed serial data link: Triple-Speed Ethernet (TSE) IP core. It includes the use of high bandwidth structure, Qsys system as System On Programmable Chip (SOPC) builder system for connecting components. Qsys interconnects the components either available in library or the customized components developed by user with VHDL or Verilog code (using Avalon interface interconnect). Modelsim simulator is used to simulate the developed code, and generated Qsys structure is verified and tested with TCL script in system console. Signal Tap II analyzer is used to analyze the behavior of signals used internally in the design. Data packets are generated using data packet module from the processed data and transmitted over communication channel in order to attain the high-speed data transmission. Transfer of these data packets to data archiving server on Ethernet over open core UDP/IP stack at 1 Gbps data rate.

Keywords TSE IP core · UDP/IP stack · Altera Quartus II · Qsys · Signal Tap II analyzer · System console · FPGA

1 Introduction

Transmission of huge amount of data within a short period of time is a demand of today's world. Thus need of high-speed interfaces arise. High-speed serial data link, Altera Triple-Speed Ethernet (TSE) mega core function, is accomplished with the IEEE 802.3 standard. Previously, when connecting this standard with LAN or

Deeksha Jain (✉)
Bhabha Atomic Research Centre, Mumbai, India
e-mail: Deeksha.jain1991@gmail.com

Swati Shrivastava
Banasthali Vidhyapith, Jaipur, India
e-mail: swatiashwanishri92@gmail.com

© Springer Science+Business Media Singapore 2017

R. Singh and S. Choudhury (eds.), *Proceeding of International Conference on Intelligent Communication, Control and Devices*, Advances in Intelligent Systems and Computing 479, DOI 10.1007/978-981-10-1708-7_131

Internet, there is a need of additional network circuits with more functionality than required which was not cost-effective. But with the use of FPGA technology the application of UDP/IP stack can be implemented economically [1]. TSE mega core function offers various levels of support for each Altera device family. Here we are using Cyclone IV (GX) which fulfills higher bandwidth requirement while lowering the cost.

In this paper, in order to achieve high-speed data transmission, UDP/IP core on 1000 MB Ethernet is introduced. Ethernet side uses Reduced Gigabit Medium Independent Interface (RGMII) which provides support to 10/100/1000 MB Ethernet MAC (media access controller). Open-source IP cores are available for different communication speeds. Here we are using Open core UDP/IP stack and make some changes in order to get the required objective [2]. The UDP/IP protocol is used here to fulfill the requirement of transmission of huge data at high speed. This paper presents the implementation of UDP/IP stack using TSE on Cyclone IV GX FPGA device and compares the results with previous studies. Quartus II is used which is a PLD design software and provide support Cyclone IV FPGA and platform for analysis and synthesis of hardware description language based designs. It provides Qsys system which interconnects the components either available in library or developed by the user with VHDL or Verilog code (using Avalon interface interconnect). The captured packets are analyzed in Wireshark. In this paper, Sect. 2 presents the theoretical concept of communication layers which provide support for implementation of 1000 MB Ethernet communication. Then Sect. 3 describes the structure of core and proposed systems necessary for implementation and Sect. 4 shows the evaluation and results.

2 Ethernet Communication

2.1 OSI MODEL and TCP/IP MODEL

The Open System Interconnection (OSI) is a standard model that covers all the network related aspects. It is a layered architecture with seven layers: Application, Presentation, Session, Transport, Network, Data link and Physical layer. In TCP/UDP/IP model, the Session and Presentation layers come under Application layer. For a detailed description of protocols and layer, see [3].

Application Layer: The Application layer in TCP/IP combines the three layers of OSI model. It provides control on the issues related with representation and encoding. These issues combine together form a single layer in the TCP/IP model.

Host-to-Host: This layer provides a host-to-host layer protocol in the TCP/IP model. The services provided by this protocol are almost equivalent to the transport protocol of OSI model. It provides error and flow control, data segmentation, reliability in transmission. Transmission Control Protocol (TCP) and User Datagram Protocol (UDP) are the protocols known as host-to-host protocols.

Internet: The services provided by the Internet layer of TCP/IP model are equivalent to the services of Network layer of OSI model. It routes the packets to their destination without knowing the path taken. Delivery of packets from source to destination is performed by the protocol known as Internet Protocol (IP). UDP module called this protocol to take the UDP packet as data and transmit datagram.

Network Access: This layer provides all the services related to the physical and network media and manages issues like data termination on network. Physical layer defines relation between protocols and also hierarchy of protocols. Physical layer uses PHY device to make Ethernet connection with FPGA using RGMII interface. Data Link layer manages delivery of packets over shared network.

2.2 UDP/IP Protocol

It is transport-layer protocol and used for communication between process. It uses IP services to deliver datagrams to the correct host. UDP/IP uses a protocol port, i.e., source port and destination port which are identified by a positive integer. UDP/IP is considered to be a connectionless protocol. It provides fast transmission but Packets may be misplaced or delivered out of order. The packet produced by the UDP is called a user datagram. UDP transmitter communicates with IP transmitter on whether it is ready to accept user datagram packets. UDP receiver communicates with IP receiver to acknowledge that it is ready to accept IP datagram packets.

2.3 Internetwork Protocol (IP)

IP is the mechanism used for transmission by the host-to-host layer protocols. Error checking or tracking service is not provided by IP. The data is transmitted in packets called datagrams. A datagram is a packet of different length having header and data. The header contains information essential to routing and delivery. IP address gives the information related to the network on which receiving host is active.

3 Structure of Core

In this project Component Based Software Engineering (CBSE) is used because of various advantages associated with it (Fig. 1).

In presented work, there is top layer in FPGA application which composed of other component. The top level component consist of UDP transmitter, UDP receiver, IP transmitter, IP receiver, ARP transmitter, ARP receiver and other necessary components that are written in VHDL. Phase Locked Loop (PLL) available in Mega Wizard Plug-in manager is used for generating clocks by customized their parameters.

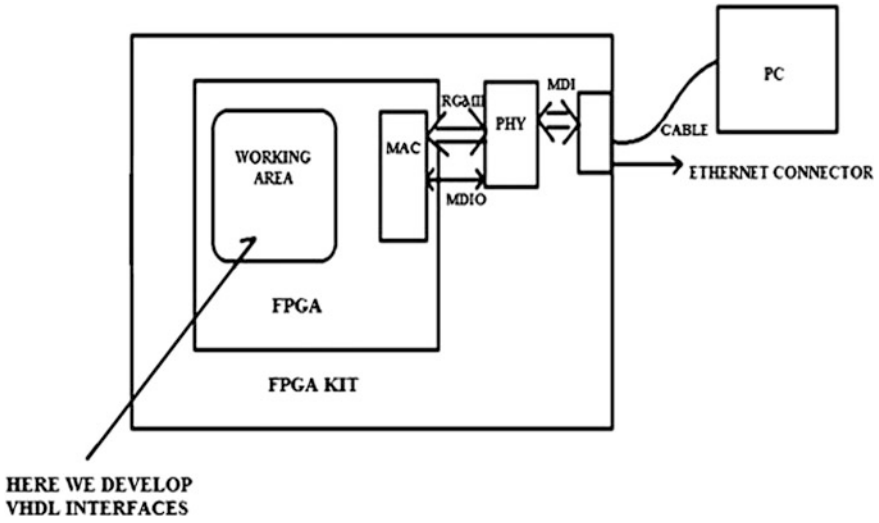


Fig. 1 Proposed design

3.1 PHY Management (MDIO)

PHY device is controlled by writing and reading the PHY control and status registers through MDIO interface. PHY connect to Ethernet cable through RJ-45 connector. The gigabit Ethernet PHYS connect to MAC via GMII and RGMII interface, and data is transmitted on Ethernet over UDP/IP. Here we are using RGMII interface [2]. At RGMII interface that operates at 1000 Mbps, PHY provides 2.5 MHz clock and for 1000 Mbps speed it provides 125 MHz clock.

3.2 Triple-Speed Ethernet (MAC)

Altera offered TSE MAC mega core function with high capability and variety of operating modes. It is configured to operate at half-duplex or full-duplex with minimum possible resource consumption. The 10/100/1000-Mbps Ethernet MAC and 1000 BASE-X/SGMII physical coding sub layer (PCS) with optional physical medium attachment (PMA) combines to form a complete triple-speed Ethernet IP. Ethernet MAC with 1000 Mbps is used in order to make Ethernet communication with gigabit PHY device using RGMII in full-duplex mode with 1000 Mbps speed. Different aspects of MAC can be configured by writing the MAC configuration registers and retrieve its status and statistics counter. TSEMAC features and operations are illustrated in [4].

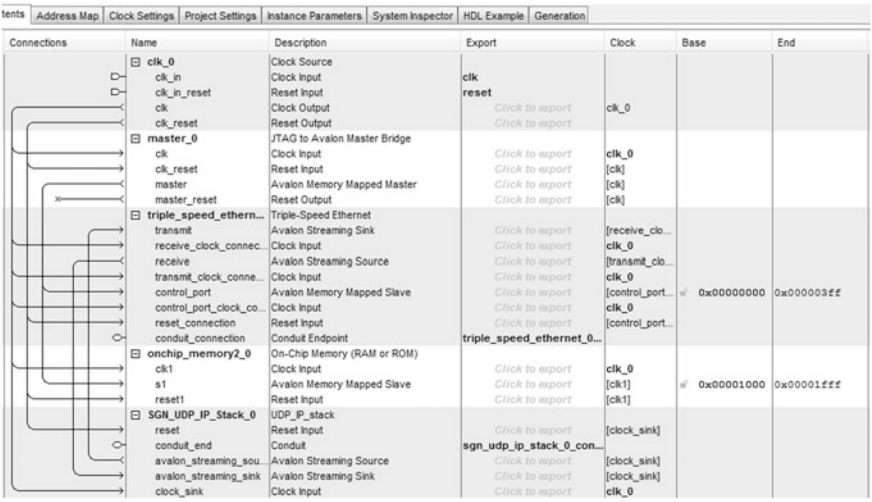


Fig. 2 Qsys interconnections

3.3 Qsys Interconnects

Altera provides Qsys interconnect which is a high bandwidth structure for connecting components. Qsys supports various standards; Avalon is used in the presented work. The Mega core function is constructed from transmitter and receiver units. Here we have UDP transmitter which transmits the data packets and receive these packets by using UDP receiver. Here we are using a single open core UDP stack component which is connected with TSE JTAG master, clock, reset, and on-chip memory as shown in Fig. 2.

4 Evaluation and Results

The designed Qsys structure using TSE and composed UDP_IP_Stack component are connected through Avalon-Streaming and with on-chip memory through Avalon-MM(memory mapped) interface. The peripheral system consisting of JTAG to Avalon master bridge to connect with main system, system clock source and JTAG UART for serial communication and debugging System Console application using TCL script through on board USB blaster circuitry. In Packets, the Memory-mapped transactions are encapsulated between master and slave. These transactions are transmitted on a network that carries these packets between master and slave. Avalon-ST interface is used to provide high throughput data path to the high bandwidth components with streaming data and these streaming interfaces also

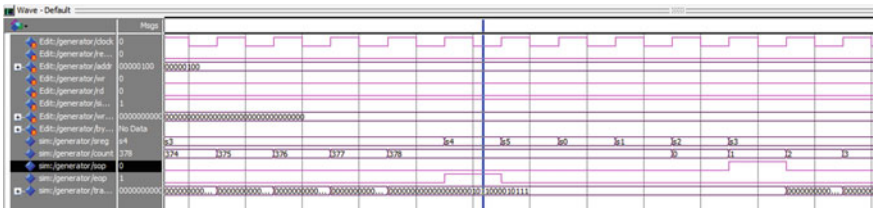


Fig. 3 Transmitter waveform on Modelsim



Fig. 4 Receiver waveform on Modelsim

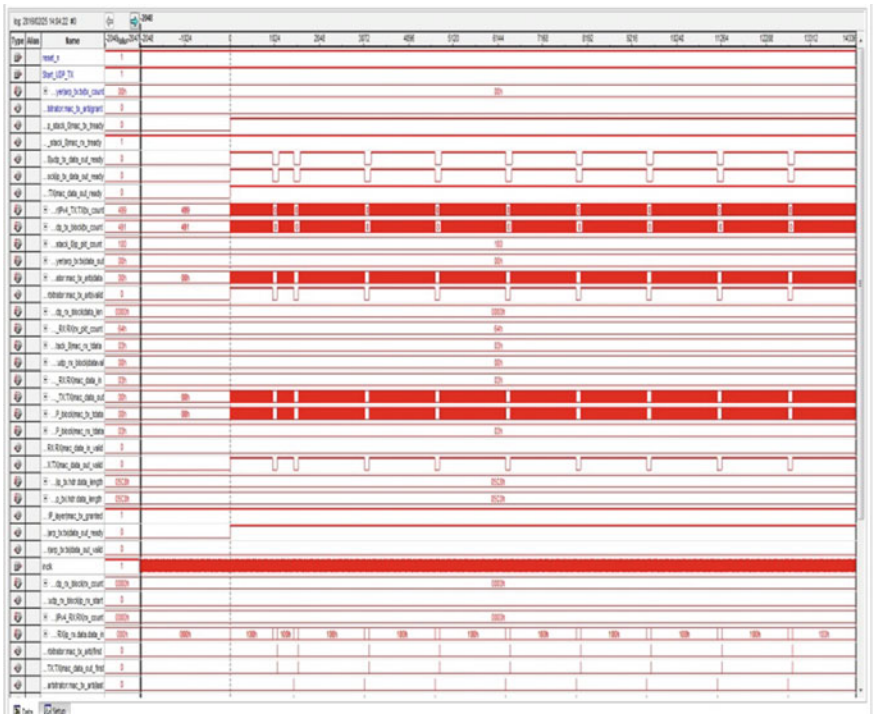


Fig. 5 Signal Tap II analyzer

```
Info: Applying Software Reset on Marvell PHY
PHY read Extended PHYSpecific Control Register      = 0x00000cea
PHY read Status Register                            = 0x00007949
PHY Link Up.
PHY Speed and Duplex Resolved.
PHY operating in Full Duplex mode.
PHY operating Speed 1000Mbps

% master_read_32 $jtag_master 0x00000068 1
0x0097bf28
% master_read_32 $jtag_master 0x00000068 1
0x0099fd88
% master_read_32 $jtag_master 0x00000068 1
0x009b9fa0
% master_read_32 $jtag_master 0x0000006c 1
0x00014b88
% master_read_32 $jtag_master 0x0000006c 1
0x00014cb5
% master_read_32 $jtag_master 0x0000006c 1
0x00014d7f
% master_read_32 $jtag_master 0x0000006c 1
0x00014e48
% master_read_32 $jtag_master 0x00000070 1
0x00000000
%
```

Fig. 6 System console results

provide an access point for control using memory-mapped connection [5]. The connections in Qsys are shown in Fig. 2.

The generator as transmitter and monitor as receiver are being evaluated and simulated using Modelsim, the resulting waveform is shown in Figs. 3 and 4. The maximum frame length in bytes for MAC is 1518 so in both generator and monitor counter counts up to 1518 times in order to transmit and receive packets.

To transmit data, assert Start_UDP_TX signal, UDP_TX waits for UDP_tx_dataout_READY and when it comes the UDP_TXIS.data.data_out_valid signal goes high and counter cntr counts up to 1468 times as UDP header data length is taken as 05C0(1472). The total length = user data length + header length (bytes), thus 1472 + 8 = 1480. When ip_tx.hdr.data_length is less than 1480 then IP_TX sends Ethernet header and it starts transmit user data when it gets mac_-data_out_ready, ip_data_out_ready and udp_data_out_ready goes high with data_out_valid signal. The first and last byte of frame can be seen through arbitrator first and last signal as shown in waveform. Using packet builder module we send some customized packets and analyze them on Signal Tap II analyzer. Signal Tap II analyzer is used to analyze signals of the design internally.

The proposed design is tested and verified using TCL script in system console. Statistics counter describes the read-only registers that collect the statistics on transmit and receive datapaths. A number of frames that are successfully transmitted are checked using Dword offset 0x1A, since the data length used in the presented

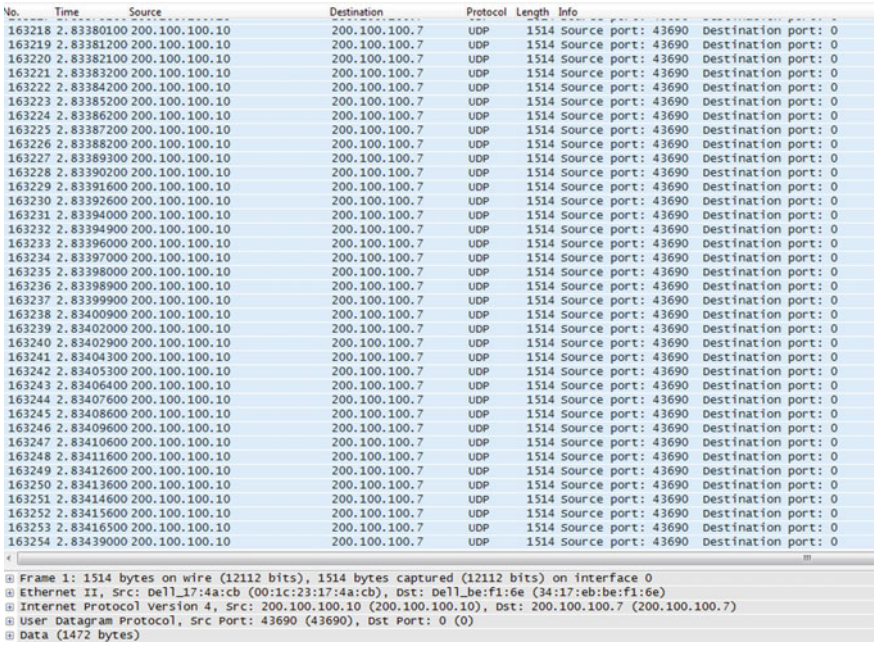


Fig. 7 Packets on Wireshark

work is 32 bit, so 0x00000068 is used in system console. Similarly the number of frames that are successfully received are checked using Dword offset 0x1B, which is further calculated as 0x0000006c and 0x00000070 to check for number of receive frames with CRC error (Figs. 5 and 6).

Figure 7 shows the UDP packets communication in Wireshark. The UDP destination IP address is set as 200.100.100.7 and source IP address is set as 200.100.100.10 along with source port as x "AAAA" and destination port as x "0000".

5 Conclusion

This paper shows the implementation of UDP/IP stack using TSE soft IP Core on FPGA. Here a UDP/IP stack is implemented and verified in Altera Cyclone IV GX. It uses 8 % of total logic elements of FPGA and can operate at maximum frequency of 125 MHz. Design uses Qsys system to make interconnections between components. The design is tested and verified in signal Tap II analyzer and Wireshark. We also compare our design with other work in terms of speed and maximum Ethernet speed [6]. The result shows that our design gives higher speed, i.e., 1 Gbps among other designs in term of data transmission.

References

1. Bhavika A. Vithalapara, Abhimanyu Dhiman, Sudhir Agrawal and Shailendrasinh Parmar "Design and Implementation of TSEMAC and UDP/IP network stack on FPGA", *International Journal of. Engineering and Technical Research (IJETR) ISSN: 2321-0869, Volume-3, Issue-5, May 2015.*
2. Nima Moghaddami Khalilzad, Sheida Pourshakour, "FPGA implementation of Real-time Ethernet communication using RMII Interface", *3rd International conference on Communication Software and Networks (ICCSN),* IEEE 2011.
3. A. S. Tanenbaum, *Computer Networks*, 4th ed. Prentice Hall, August 2002.
4. San Jose, "Triple Speed Ethernet Mega Core Function User Guide", *ALTERA, 101 Innovation Drive, Software Version 13.1,* December 2013.
5. San Jose, "Avalon Interface Specifications", *ALTERA, 101 Innovation Drive, Software Version 13.1,* December 2013.
6. N. Alachiotis, S. Berger, and A. Stamatakis, "Efficient PC-FPGA Communication over Gigabit Ethernet," Computer and Information Technology (CIT), 2010 IEEE 10th International Conference on. IEEE, 2010.

Channel Capacity in MIMO OFDM System

Nishu Baliyan, Manish Verma and Adesh Kumar

Abstract Orthogonal frequency division multiplexing (OFDM) is the technology used to encode the data on multiple carrier frequencies in 4G mobile communication, digital TV, power line communications and broadband applications. The paper discusses the channel capacity and cumulative distribution function (CDF) simulation with MIMO OFDM system with different cluster size in MATLAB. The channel capacity of the multiple-input multiple-output (MIMO) system increases with increment in the transrecievers. The theoretical and simulated values are estimated with additive white Gaussian noise (AWGN) channel at signal-to-noise ratio (SNR) of 3 dB.

Keywords Multiple-input multiple-output (MIMO) · Orthogonal frequency division multiplexing (OFDM) · Additive white Gaussian noise (AWGN) · Signal-to-noise ratio (SNR)

1 Introduction

Orthogonal frequency division multiplexing (OFDM) [1, 2] is used for multicarrier transmission in which the available spectrum is divided into many subcarriers that each carrier is modulated by a low-rate data stream. It utilizes efficiently the existing spectrum by using orthogonal subcarriers that makes the available spectrum of individual carrier has a null at the center of one another. Thus the carriers are coming very close to each other without inter carrier interference (ICI). The nature of OFDM is capable to convert frequency-selective channels into different

Nishu Baliyan (✉) · Manish Verma
Sobhasaria Engineering College (SEC), Rajasthan Technical University (RTU), Sikar, Rajasthan, India
e-mail: nishubaliyan4@gmail.com

Adesh Kumar
Department of Electronics Instrumentation and Control (EIC) Engineering, University of Petroleum and Energy Studies (UPES), Dehradun, India

© Springer Science+Business Media Singapore 2017

R. Singh and S. Choudhury (eds.), *Proceeding of International Conference on Intelligent Communication, Control and Devices*, Advances in Intelligent Systems and Computing 479, DOI 10.1007/978-981-10-1708-7_132

independent flat fading subchannels, also mitigates the problem of multipath in wireless communication. Multiple-input multiple-output (MIMO) [3] and OFDM are the modern wireless technologies at physical layer which are used in 4G wireless cellular technology standards such as worldwide interoperability for microwave access (WiMAX), long-term evolution (LTE/LTEA) 3GPP, wireless LAN standards for high speed. The 4G technology in cellular supports the high data rates such as 100 Mbps using MIMO OFDM [2, 4] and enables high-throughput applications for multicast video, broadband communications, internet access at high speed, gaming interactive, HDTV, etc. The technology demands the researchers to develop MIMO OFDM based wireless network, which are proved with 4G wireless technology IEEE 802.16, and IEEE 802.11n as one of the best technologies. It provides high data rate because the technology has low computational complexity, frequency-selective fading and high spectral efficiency. OFDM with MIMO [3] transceivers has increased diversity [2] and channel capacity because it uses many parallel narrowband channels in exploration with spatial domain.

2 Block Diagram of OFDM

The block diagram of OFDM system is shown in Fig. 1 the data input stream is as input data serially taken by transmitter. So serial to parallel conversion is required to get the data symbols and signal mapper maps the parallel data to modulator. To inverse fast Fourier transformer (IFFT) that gives parallel outcome and cyclic prefix can be added to check error. The modulated data is transferred using channel so parallel to serial conversion is required, and then it is passed to additive white Gaussian noise (AWGN) channel where white noise can be added. In the receiver

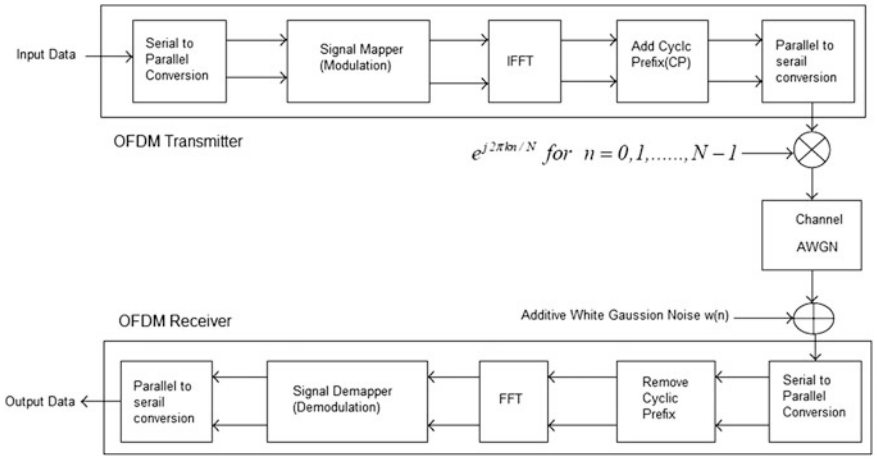


Fig. 1 Block diagram of OFDM [2, 5]

side the modulated and channel data is converted from serial to parallel because the demodulator works on FFT that takes parallel data. In the parallel data cyclic prefix is removed and decoded by FFT demodulator. Signal demapper takes the demodulated data and parallel data is converted to serial to achieve the output data. In the signal mapper and demapper QAM modulator or demodulator can be used.

3 MIMO OFDM

The block diagram presentation of MIMO OFDM system is shown in Fig. 2, which has four transmitters and four receivers. The same configuration of the MIMO OFDM can be applied for multiple transmitter antennas. In MIMO OFDM each signal has many data symbols which can be transmitted and received in concurrent or parallel way. Considering a random signal vector $f = (f_1, f_2, f_3 \ldots f_n)^T$. The probabilities of the random signal are given by

$$P_i = P(f = f_k)\ k = 1, 2, 3 \ldots \tag{1}$$

The entropy [4] of f is given by

$$H(f) = -\sum_i p_i \log p_i \tag{2}$$

The function f is continuously distributed with probability density function (PDF) $p(f_1, f_2, f_3 \ldots f_n)$. The expression for the differential entropy will be

$$H(f) = -\int \ldots \int p(f_1, f_2, f_3 \ldots f_n) \log p(f_1, f_2, f_3 \ldots f_n) \mathrm{d}f_1 . \mathrm{d}f_2 \ldots \mathrm{d}f_N \tag{3}$$

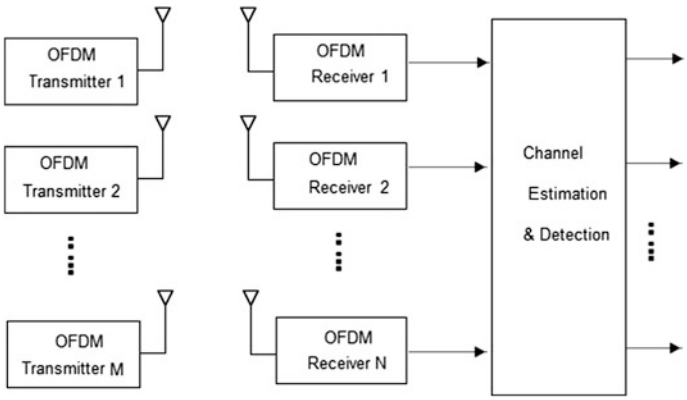


Fig. 2 MIMO OFDM system with $M \times N$ transmitter and receivers

The diagonal vector f covariance matrix is given by

$$C_f = E\{(f-\mu)(f-\mu)^T\} \tag{4}$$

where μ is the mean. The expression of the differential entropy is given by

$$H(f) = \frac{1}{2}\left[N \cdot \log(2\pi e) + \log\ \det(C_f)\right] \tag{5}$$

The mean value μ is not affecting the random vector the $\mu = E\{f\} = 0$

The real values variables which are having zero mean should satisfy the condition

$$C_f = \mathrm{Cov}(f, f^T) = E\{ff^T\} \tag{6}$$

Then

$$\max_{P_f(f)\,:C_f=\mathrm{Cov}\,(f,f^T)=E\{ff^T\}} H(f) = \frac{1}{2}\left[N \cdot \log(2\pi e) + \log\ \det(C_f)\right] \tag{7}$$

The maximum entropy is presented by Gaussian vector among all vectors from the same covariance matrix. In a flat MIMO fading channel the matrix gain G. In the MIMO OFDM with $N \times M$ channel matrix, the output is expressed as

$$y = G \cdot f + w \tag{8}$$

Here, w is the AWGN. The matrix gain G connects $M_t \times 1$ input vector to f and $N_r \times 1$ connects output vector y to $N_r \times 1$. The MIMO system with M transmitters and N_r receivers is shown in Figs. 2 and 3. The MIMO channel matrix G is presented as

$$G = \begin{bmatrix} g_{11} & g_{11} & \cdots & g_{1N} \\ g_{21} & g_{22} & \cdots & g_{2N} \\ & & & \vdots \\ g_{N1} & g_{N2} & \cdots & g_{N_r,M_t} \end{bmatrix} \tag{9}$$

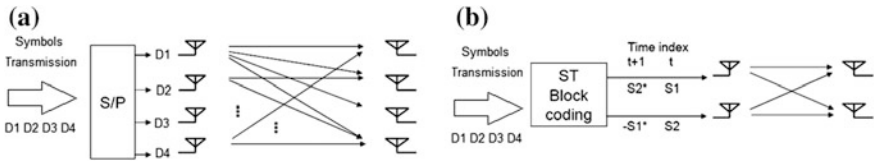


Fig. 3 **a** MIMO system with data symbols. **b** With block coding

The capacity of the channel is described as the maximum value of information which is transmitted within bandwidth. In a single input antennas system, the channel capacity is estimated using Shannon's formula to calculate channel capacity

$$C = B \log_2(1 + \text{SNR})$$

where, B is bandwidth, P is transmitted power and SNR is signal-to-noise ratio and channel is assumed white Gaussian. The value of channel capacity is changed with respect to several number of transmit and receiver antennas. In the MIMO channel matrix G is considered with respect to unit variance and zero mean value. For random number on transmitters and receivers the expression of the channel capacity [4] is given as

$$C = \frac{1}{2}\log\left[I_N + \frac{\sigma_f^2}{\sigma_w^2}\text{GG}^T\right] \tag{10}$$

where σ_f^2 variance of signal and σ_w^2 variance with AWGN.

The capacity of MIMO link in OFDM can be increased using spatial multiplexing in which data streams are transmitted independently within same time slot from each transmit antenna and frequency band simultaneously. Multiple data streams are differentiated at the OFDM demodulator with the help of channel information over individual propagation path. In contrast to multiplexing in spatial domain, the main objective of spatial diversity is to mitigate the fading of channel by coding a signal across time and space to enhance the diversity order for the same MIMO link for fading channel. The demodulator in OFDM receiver replicas of output signal and grouped together all received signals to obtain diversity gain.

MIMO system offers enormous capacity upsurge but the biggest problem is channel fading because the signal travels multiple paths among many transmitter antennas and receiver antennas. The mitigation of signal diversity can be solved by fading techniques that the data is transmitted not only one time but many times that at least once to all replicas and prevents to undergo several fading.

4 Results and Discussions

The results are extracted from MATLAB 13.0 signal processing tool. Figure 4 shows the results of simulation of channel capacity with respect to four transmit antennas. The theoretical and simulated values of the system with different transmit antennas and receive antennas are listed in Table 1. The theoretical and simulated values are 10.00 and 9.00 bps/Hz for single antenna (1 × 1). In the same way for 2 × 2, 3 × 3 and 4 × 4 antenna the theoretical values are 10.00 bps/Hz, 15.00 bps/Hz and 20.00 bps/Hz, and simulated values are 15.76 bps/Hz, 20.2 bps/Hz, and

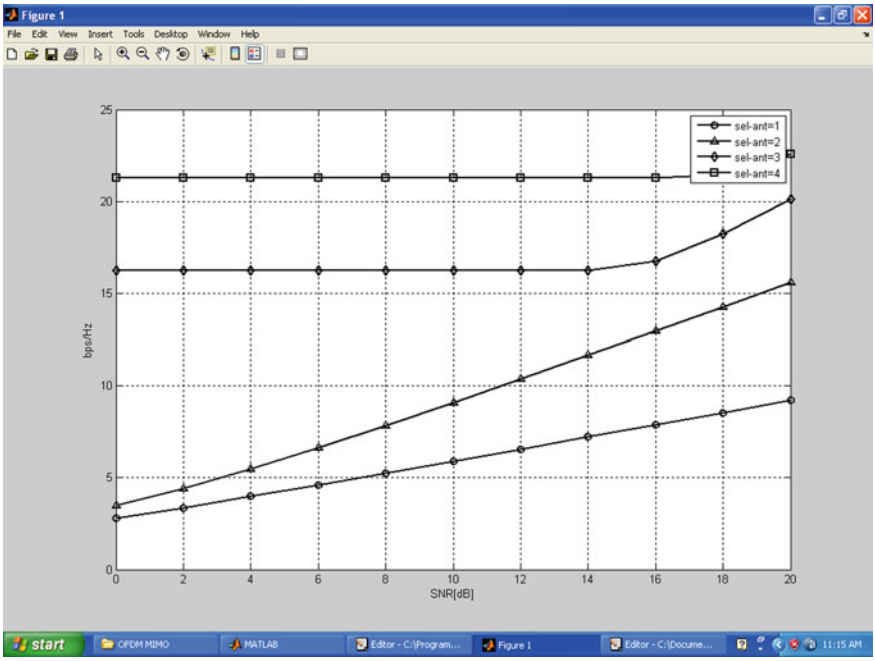


Fig. 4 Channel capacity of MIMO OFDM with four antennas

Table 1 Channel capacity with different antennas

No. of antennas	Capacity value Bps/Hz (simulated)	Capacity value Bps/Hz (theoretical)
1	9.00	10.00
2	15.76	15.00
3	20.2	20.00
4	22.5	25.00

22.5 bps/Hz respectively. The results are satisfactory to meet the theoretical values. From the simulated results it is clear that the channel capacity is increasing as the MIMO transceivers are increasing. The simulation is also carried for cumulative distribution function (CDF) in case of different configurations of MIMO system.

Figure 5 shows the simulated value of CDF for cluster size 1 × 1, 2 × 2, 4 x 2, 2 × 4, 4 × 4, and 8 x 4 respectively. The value of CDF concentrated is increasing with more no of transmitter and receivers ate higher rate or capacity. The probability for 2 × 2 MIMO is 1.0. The value of probability is dropped to 0.2 and 0.05 for 4 × 4 and 8 x 4 MIMO systems.

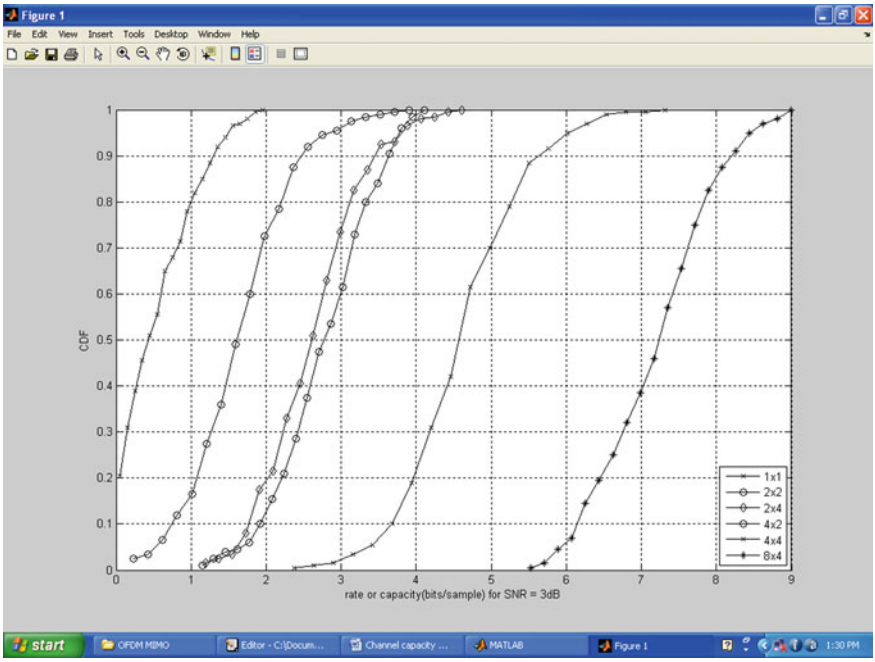


Fig. 5 CDF of MIMO OFDM

5 Conclusions

In the paper the channel capacity MIMO OFDM for 1×1, 2×2, 3×3 and 4×4 is simulated in MATLAB. The simulated values and theoretical values are compared and simulated values are approaching the theoretical values. The capacity of the MIMO OFDM system is increasing with the increment in the transceivers. The CDF is also estimated with data rate capacity for six different cluster sizes (1×1, 2×2, 2×4, 4×2, 4×4 and 8×4). The CDF is more concentrated with high rate with multiple transrecievers. The Probability ($C_{\text{MIMO}} \leq$ Rate). The value of CDF decreases with 1×1 to 2×2 and then 4×4. The increment value of channel capacity with increment in MIMO transceivers and decrement value of CDF with increment in MIMO transceivers estimates that MIMO OFDM provides higher capacity, which is a boon for the 4G wireless communication system.

References

1. A. Raghunathan, S. Dey, N. K. Jha, "High-level macro-modeling and estimation techniques for switching activity and power consumption", Very Large Scale Integration (VLSI) Systems, IEEE Transactions on, Vol. 11, Issue 4, Aug. 2003 Page(s):538–557.
2. Abdeldime Mohamed Salih Abdelgader, and Lenan Wu "Design of a Multiorder OFDM Frequency Diversity Approach" Hindawi Publishing Corporation Mathematical Problems in Engineering Volume 2015, Article ID 291625, 9 pages. http://dx.doi.org/10.1155/2015/291625, pp. (1–10).
3. N. Prasad and M. K. Varanasi, "Analysis and optimization of diagonally layered lattice schemes for MIMO fading channels," *IEEE Transactions on Information Theory*, vol. 54, no. 3, pp. 1162–1185, 2008.
4. B. P Lathi Zgi Ding "Modern Digital and Analog Communication Systems" Fourth Edition Oxford University Press, Ch-13, pp. (780–796).
5. S. Sood, A. Singh, A. Kumar "*VHDL Design of OFDM Transreceiver Chip using Variable FFT*" Journal of Selected Areas in Microelectronics (JSAM), Singaporean Journal of Scientific Research (SJSR) Vol. 5. No. 2 2013 pp. (47–58).

Digital Image Processing-Based Water Pollution Control System

Ramandeep Singh, Toolika Srivastava, Anuj Sharma, Sandeep Sharma and Santosh Kumar

Abstract Pollution in water caused by sewage, industrial waste, oil pollution, and various bacteria and viruses damage inhabitants in water and affects the entire biosphere. As water is one of the major resources which we consume directly and indirectly, so it must be protected. To avoid this water quality degradation, it is required to construct the real-time monitoring system which determines the quality of water by assessment of pollutants present. In this study, the real-time monitoring system which consists of computer, image processing toolbox which takes images of polluted water as input has been developed and examined to assure the adaptability of monitoring the pollutants in water. The results of examining will lead to monitoring the pollutants and estimating the pollutants.

Keywords Real time · Pollutants · Environmental

Ramandeep Singh (✉) · Toolika Srivastava · Anuj Sharma · Sandeep Sharma · Santosh Kumar
Advance Signal Processing Lab, Department of Electronics and Communication Engineering, DIT University, Dehradun, Uttrakhand, India
e-mail: ramankhurana01@gmail.com

Toolika Srivastava
e-mail: tashurocksatdit@gmail.com

Anuj Sharma
e-mail: shaanuj@gmail.com

Sandeep Sharma
e-mail: tek.learn@gmail.com

Santosh Kumar
e-mail: santoshrus@yahoo.com

© Springer Science+Business Media Singapore 2017

R. Singh and S. Choudhury (eds.), *Proceeding of International Conference on Intelligent Communication, Control and Devices*, Advances in Intelligent Systems and Computing 479, DOI 10.1007/978-981-10-1708-7_133

1 Introduction

Recently, our attention is on the environmental problems such as the water pollution, greenhouse effect, acid rain, deforestation, etc. While these are the global issues, some local environmental problems such as noises, air pollution, red tides, and turbid water have also become to obstruct the lives of humans. So, it is required to take correct action or build some monitoring systems which help in examining quality of these various resources. In this study, various images of polluted water will be taken and with the help of image processing, detect the impurities present in that polluted water. Here, the pollution causing microorganisms are taken into consideration. Various kinds of microorganisms live in water and make living beings (fish, animals, and humans) ill. Many serious diseases such as cholera can be caused by these microorganisms that live in water. Since in poorer countries, they do not have facilities of water treatment, people living in these countries are affected more. They are derived from human sewage and other sources. It is important to keep in mind the sea water contains approximately 1 billion bacteria and 1 trillion viruses that are not pathogenic to humans. Our work is to identify some specific disease causing pathogens in water bodies.

2 Pathogens

Pathogen is a Greek word formed by combining two words pathos (means suffering) and genes (means producer of). So, a pathogen is an agent (biological) that can cause disease or illness to its host. The agents which affect multicellular organisms (plants and animals) generally are referred to as pathogens. However, pathogens also infect unicellular organisms from all biospheres. There are several ways by which a pathogen can infect a host. The human body has immune system which fights against various common pathogens with the help of useful bacteria present in human body, but up to a level. There are some bacteria which our body cannot fight. At present, medical technology has developed to protect humans against infections caused by pathogens, by using vaccinations, antibiotics; still pathogens continue to threaten human life. Social awareness such as safe food, good hygiene, and treated water [1] has reduced the affect of some pathogens [1] (Fig. 1).

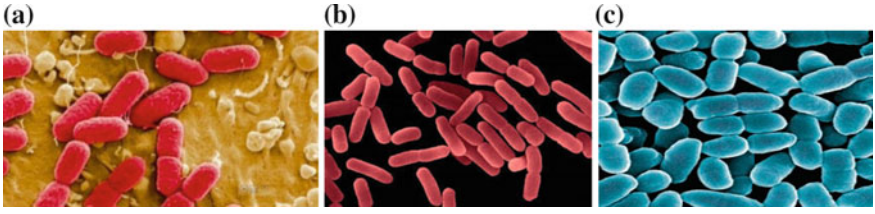


Fig. 1 **a** Escherichia. **b** Bacillus. **c** Boredetella

Our system basically deals with analysis of morphological features of

- Bacillus
- Boredetella
- Escherichia.

3 Morphology

Morphology is a tool in MATLAB which contains various image processing operations to process an image on the basis of shapes. In morphology, the value of pixels in an image (output) is calculated by comparing their counterpart in the input image with pixels in its neighbour. Morphological operations depend on relatively ordered pixels, not on numerical values of pixels. So, these operations are best suited for binary image processing [2].

There are two basic operations in morphology, i.e., dilation and erosion. When pixels are added to boundary of any object in an image, it is called dilation and when pixels are removed from the boundary of an object in an image, it is known as erosion. The number of pixels to be added or removed from the objects' boundary in an image depends on size and shape of the structuring element which is used to process that image. A structuring element is a matrix which is centred at any pixel. It is shifted to each pixel in an image. In the morphological operations, i.e., dilation and erosion, the state of any pixel in the output image is calculated by applying some rule (mathematical) to corresponding pixel and its neighbours in the input image. Morphological operations are determined by these rules used in calculating output pixel value [3].

4 Other Helpful Algorithms

4.1 Image Deblurring

In image processing toolbox of MATLAB, image deblurring algorithms are there which include regularized filter, Lucy–Richardson filter, blind filter, and Wiener filter deconvolution [4], and conversions between optical transfer and point spread functions. With the help of these functions, correction of blurring caused by out of focus, camera movement, environmental conditions, and other factors is done. All the functions of deblurring work on multidimensional images [4] (Fig. 2).



Fig. 2 Image deblurring



Fig. 3 Image segmentation on the basis of colour with live image acquisition

4.2 Image Segmentation

Image segmentation algorithms analyze boundaries of different regions in an image. It is the process by which one can divide a digital image into various segments. These segments are set of pixels which are also called superpixels [4]. It is basically done to simplify our image or to focus on any area in an image, so that better computation can be done. There are many methods to achieve image segmentation like morphological methods, edge-based methods, automatic thresholding, etc. (Fig. 3).

4.3 Image Enhancement

With the help of image enhancement function in image processing toolbox of MATLAB, one can increase SNR of an image, i.e., increase signal power or reduce noise power and emphasize image features by changing the colour or intensity of an image. The toolbox includes specialized filter and a generalized multidimensional filter function that operates on integer image types and performs correlation and convolution [4].

Using predefined filters and routines one can perform filtering with morphology, deblurring, sharpening, removing noise with linear or adaptive filtering, histogram equalization, contrast adjustment, gamma value adjustment.

5 Functions Used in System

Function	Description
Uigetfile()	It displays a model dialog box that lists files in current folders and enables you to select or enter the name of a file
Imopen(IM, SE)	It performs morphological opening on grey scale or binary image IM with structuring element SE
strel(shape, parameter)	Creates structuring element SE of the type specified by shape
imadjust(I)	It maps the intensity values in grayscale image I to new values in J such that 1 % of data is saturated at low and high intensities of I. This increases the contrast of output image J
graythresh(I)	Computes a global threshold(level) that can be used to convert a intensity image to a binary image with im2bw level in normalized intensity value that lies in the range [0, 1]
bwareaopen (BW, P)	It removes from a binary image all connected components (objects) that have fewer than P pixels, producing another binary image. BW2. This operation is known as an area opening

6 Flow Chart of System

See Fig. 4.

7 Result and Discussion

An image is given as input to this program which is shown in Fig. 5a. As a result of this, the system is fully able to detect the shape of bacteria present in image. The output image of the system after the detection is shown in Fig. 5b. All the bacteria and pollutant elements are separated on the basis of their shapes and classifications except the shape of bacteria and plotted that shape as output. The system is designed to simulate the stores and static images of the pollutant water, for the future scope, it could be extended for real time images: static as well dynamic, of the water.

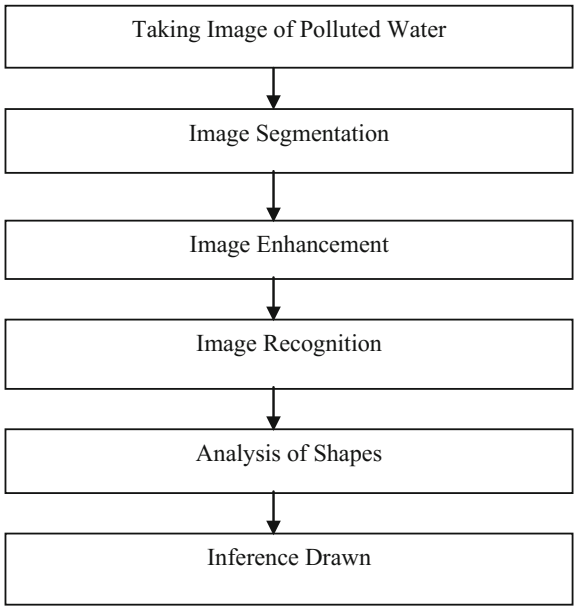


Fig. 4 Flowchart of the process [5, 6]

7.1 Input Image

See Fig. 5a.

7.2 Output Image

See Fig. 5b.

8 Conclusion

This paper presents in detail working of the system that is designed to detect pollutants in water. Though there are large number of pollutants present, it could not be detected easily because of their small size and undefined shapes. But now as this system is based on digital image processing, identifiable shapes of some of the pathogens are detected. This system can be extended to other shapes (regular or irregular), covering most of illness causing pathogens which can be present in water.

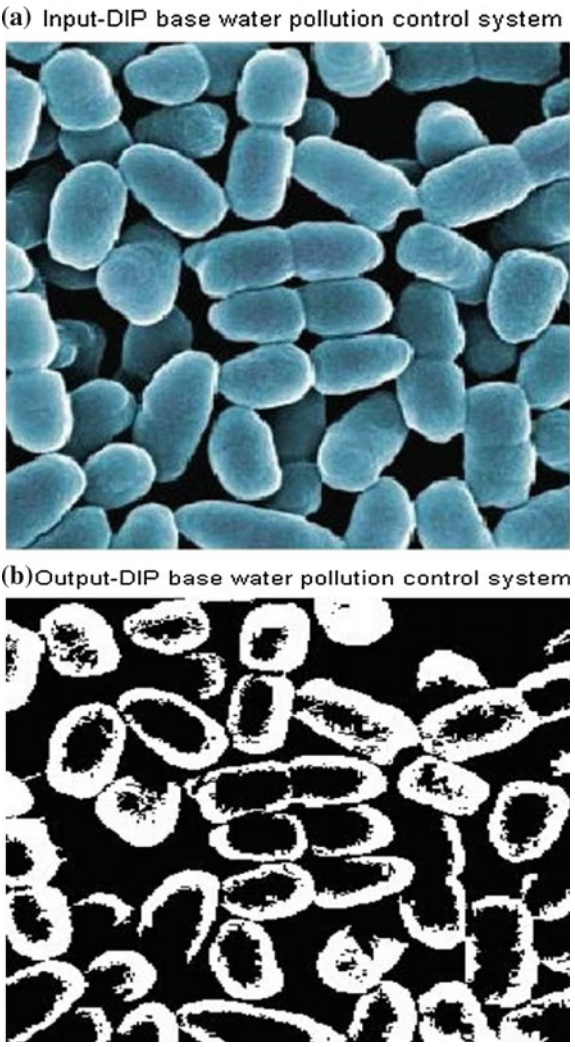


Fig. 5 **a** Input image. **b** Output image

Further, this system can be extended to find hardness of water. As it is one of the major problems in water which cannot be seen by naked eyes and also it is calculated through a long chemical process, it will be very easy and time saving if it can be detected through images. This project can also be implemented to dynamic images captured of any river (like Ganga).

References

1. https://www.sciencedaily.com/terms/pathogens.htm
2. https://www.cs.auckland.ac.nz/courses/compsci773s1c/lectures/ImageProcessing-html/topic4.htm
3. http://in.mathworks.com/help/images/morphology-fundamentals-dilation-and-erosion.html?s-tid=gn.loc_drop
4. http://in.mathworks.com/products/image/features.html
5. Digital Image Processing by Rafael C. Gonzalez (Author), Richard E. Woods
6. CMEIAS: A Computer-Aided System for Image Analysis of Bacterial Morphotypes in Microbial Communities

Switched Capacitor Circuit Realization of Sigma-Delta ADC for Temperature Sensor

Abhishek Pandey, Mohd. Javed Khan, Deepak Prasad, Vijay Nath, S.S. Solanki and L.K. Singh

Abstract In this article the basic operating principles of CMOS smart temperature sensors are demonstrated. In this article a CMOS temperature sensor with sigma-delta analog to digital converter (ADC) is proposed, which have widespread use due to their low cost, low power consumption and small size. The sigma-delta ADC was implemented by the switch capacitor circuit. For the implementation of sensor high-performance signal conditioning circuits are required as interfacing circuit and for these bias circuits have been designed. The accuracy of sensor is mainly limited by offset and 1/*f* noise, which is canceled by the autozeroing circuit with the help of switch capacitor circuit. The sensor circuit is designed with biasing subcircuit for controlling the curvature correction.

Keywords Temperature sensor · Threshold voltage · Switch capacitor circuit · Sigma-delta · Analog to digital converter (ADC)

1 Introduction

Many years ago people had great desire to know about temperature. However, many types of temperature sensors are invented, but in recent years the automatic operated instrument demanded for temperature controller [1, 2]. In aerospace to reduce the fuel consumption in central heating and cooling system is essential for monitoring the temperature. To communicate with computer, a digital signal is required and this is done by Analog to digital converter (ADC) [3]. This kind of

Abhishek Pandey (✉) · M. Javed Khan · D. Prasad · Vijay Nath · S.S. Solanki
Department of Electronics and Communication Engineering, Birla Institute of Technology Mesra, Ranchi 835215, Jharkhand, India
e-mail: a.p.bitmesra@gmail.com

L.K. Singh
Department of Physics and Electronics, Dr. RML Avadh University, Faizabad 224001 UP, India

© Springer Science+Business Media Singapore 2017

R. Singh and S. Choudhury (eds.), *Proceeding of International Conference on Intelligent Communication, Control and Devices*, Advances in Intelligent Systems and Computing 479, DOI 10.1007/978-981-10-1708-7_134

temperature sensor is called integrated smart temperature sensor, which consists of temperature sensor cell and ADC. It was attempted in mid-seventieth century which is widely used in industrial, aerospace, biomedical application. With the development of integrated circuit, it was also the time to develop the BJT-based temperature sensor. It was much accurate than other types of temperature sensor. On the basis of literature report, the smart temperature sensor further designed into parasitic BJT-based temperature sensor, delay-inverter-based temperature sensor and threshold voltage-based temperature sensor [4–6]. The CMOS smart temperature sensor described here perfectly fits in this low-cost, high-performance, and low-power market. It has its application in the automotive industry, where it is meant to measure the temperature in car tires. This is first for safety reasons and second to compensate for the temperature sensitivity of a pressure sensor which is also located in the tire.

Designing of smart temperature sensor is quite challenging task in today's world. Due to the low magnitude of analog signal of temperature sensors flicker noise ($1/f$ noise) is generated. Due to its conditioning circuit offset voltage is generated and it varies with temperature. The noise and offset can be canceled by auto-zeroing circuit. Now output of the CMOS temperature sensor convert into a digital through ADC, which is linear with the temperature. There are number of temperature sensors exist in which some of them are [6] (i) CMOS-based temperature sensor (ii) Propagation delay-based temperature sensor, and (iii) Thermal diffusivity-based temperature sensor. Combined three types of temperature sensors block diagram are depicted in Fig. 1.

Sigma-delta (SD) ADC which oversamples the signal and, employing a feedback system, is able to filter the quantization noise. The structure can have several stages, increasing the resolution at the output. EA converter is very suitable in low-frequency, high-performance applications. Analog switched capacitor circuits play a critical role in mixed-signal, analog-to-digital interfaces. They include a large number of functions sampling, filtering, and digitization. It makes suitable for integration with complex digital signal processing circuit.

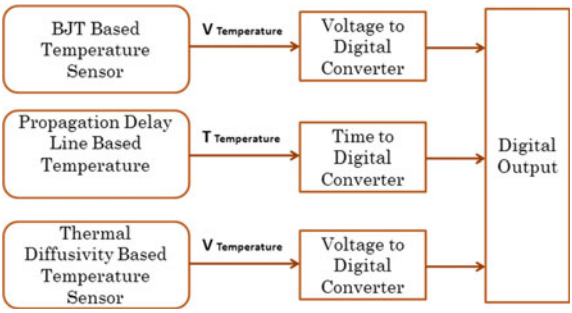


Fig. 1 Block representation of temperature sensors

The *W/L* ratios of the transistors are configured as active resistors for suitable adjustment for linearizing the output voltages. The threshold voltage of MOS device is linear with temperature [7], which is demonstrated in Eq. (1).

$$V_T(\text{Device}) = V_T(\text{Nom}) + \left(KT_1 + \frac{KT/L}{L_{\text{eff}}} + KT2 \cdot V_{\text{BS}}\right) \times \left(\frac{T}{T(\text{Nom})} - 1\right) \quad (1)$$

where

V_T Threshold voltage
K Boltzmann constant
T Absolute temperature
V_{BS} Substrate voltage
L Channel length
L_{eff} Effective channel length.

2 Sigma-Delta Analog to Digital Converter

In analog sample data techniques were used for MOSFET switches, capacitor and op-amp in place of the resistor, these circuits called as switch capacitor amplifier. One of the important reasons for that success of switch capacitor circuit is that the accuracy of capacitor ratio is proportional to the signal processing function. Also, a capacitor can store the charge proportional to the analog signal of interest. Since the capacitor is infinite at dc. To overcome this problem, switches controlled by a two phase nonoverlapping clock are used to control the operation of the above circuit.

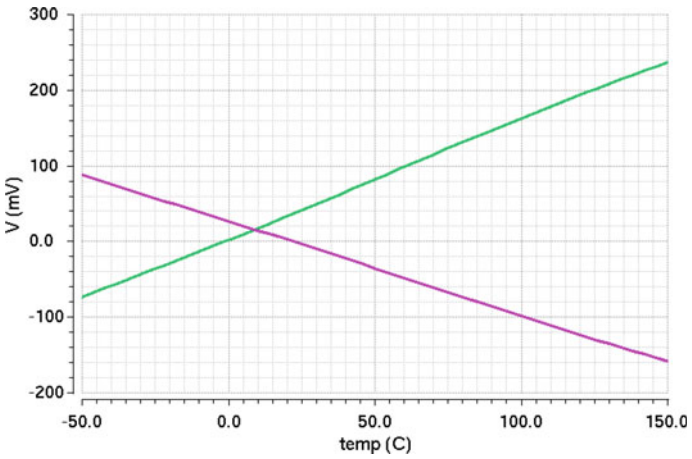


Fig. 2 Temperature directly proportional voltage and inversely proportional voltage

Table 1 Performance comparison of proposed sensor with recently designed temperature sensors

Parameter	[5]	[6]	[7]	Result
Technology (nm)	90	90	180	90
Power supply (V)	1	1	1.8	1
Temperature range (°C)	−60 to 150	−60 to 150	−10 to 100	−50 to 150
Inaccuracy (°C)	±1.3	±1.8	±0.15	±0.5
Power consumption (nW)	862	40	–	157

The sigma-delta ADC is one of the important applications of switched capacitor circuit [8]. In oversampling the quantization noise of sigma-delta ADC is shifting into high frequency. Then quantization noise is removed with the help of digital filter. The first order sigma-delta ADC is depicted in Fig. 2. The sigma-delta shows low frequency representation of the analog input. If the signal bandwidth is smaller than the sampling frequency then the quantization noise can be separated and removed with the help of low-pass filter (LPF).

In the switch capacitor circuit, nonoverlapping clocks φ_1 and φ_2 are used. For unity gain, clock φ_1 should be on. For storing voltage difference ($V_{\text{in}} - V_X$) in capacitor C_S, the end of the first phase of input voltage V_{in} is sampled over capacitor C_1 with respect to the virtual ground signal V_X. C_S is discharged to V_X, when the second clock φ_2 is on, and then feedback capacitor C_{fb} will be charged through feedback path. As a result, the following charge is created [2, 3] (Table 1).

$$Q = C_S\{V_{\text{in}}(t_1) + [(V_x(t_2) - V_x(t_1)]\} \tag{7}$$

3 Result and Discussion

The temperature sensor has been designed to sense between −50 and 150 °C with an inaccuracy of ±0.5 °C which is shown in Fig. 2. A sigma-delta modulator circuit is shown in Fig. 3. An auto-zeroed offset cancelation circuit has been

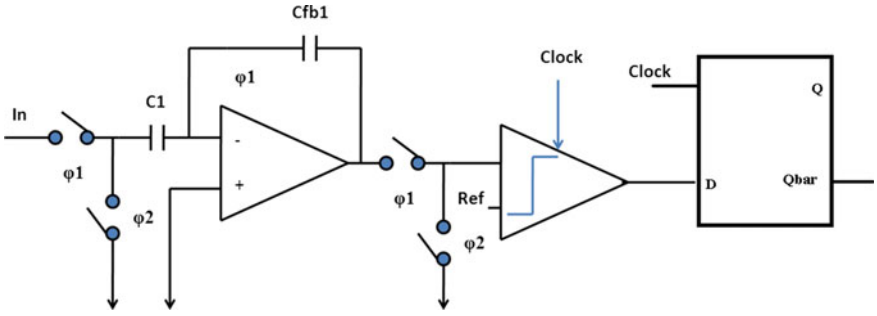


Fig. 3 Sigma-delta modulator

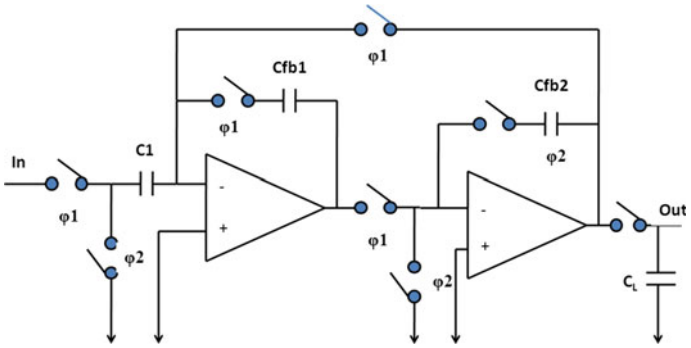


Fig. 4 Autozeroing circuit

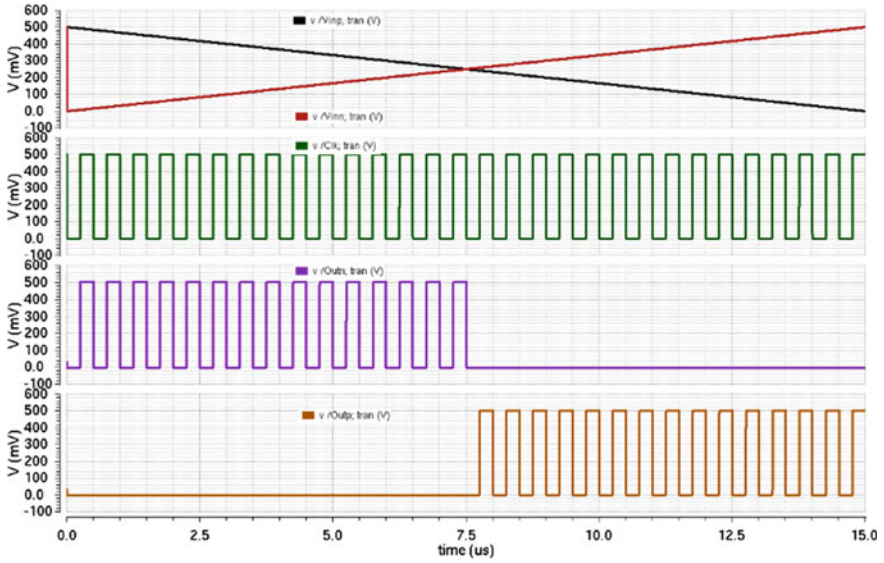


Fig. 5 Output of clocked comparator

designed and simulated in UMC 90 nm library, which is shown in Fig. 4. In the proposed design amplifier is used to stabilize the output and reduce ripples in the output when dc input voltage is applied. It is quite important block for ADC design. The output of clocked comparator, integrator and sigma-delta modulator is depicted in Figs. 5, 6 and 7 respectively.

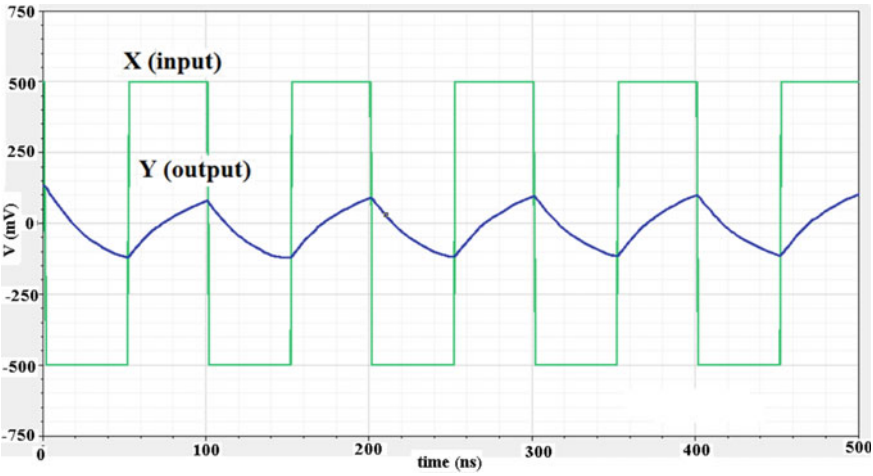


Fig. 6 Output of integrator

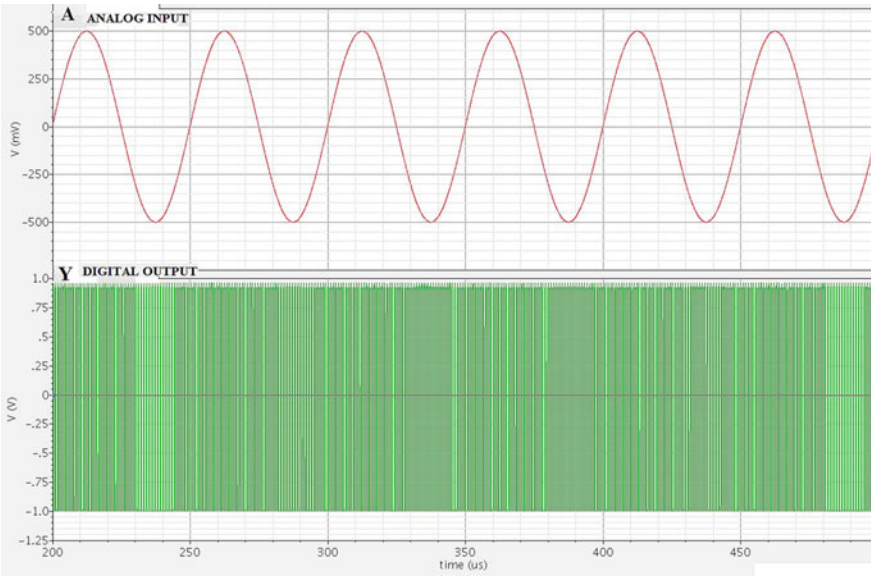


Fig. 7 Output waveform of sigma-delta ADC

4 Conclusion

In this article, temperature sensor integrated with sigma-delta ADC has been designed and simulated using UMC 90 nm CMOS technology in cadence environment. It is applicable to sense in between −50 and 150 °C with an inaccuracy of ±0.5 °C while consuming just 157 nW power. Since the proposed sensor senses for a widespread range of temperature with satisfactory accuracy, therefore it is more useful for in military and aerospace applications.

Acknowledgments We are thankful to RESPOND ISRO, Bangalore for funding this research work. We are also thankful to Prof. V.R. Gupta, HOD ECE and Prof. M.K. Mishra, Vice-chancellor, BIT Mesra Ranchi for providing infrastructure facility to carry out this research work.

References

1. Bakker, A. and Huijsing, J.: Micropower CMOS temperature sensor with digital output. IEEE Journal Solid State Circuits (1996) 933–937.
2. Anton Bakker A. and Huijsing J.H.: High-Accuracy CMOS Smart Temperature Sensors, 1st edn. Springer, Science Business Media, Boston (2000).
3. Michiel A.P. Pertijs and Johan H. Huijsing. Precision Temperature Sensors in CMOS Technology, Springer, Dordrecht, Netherland, 2006.
4. Subhra Chakraborty, Abhishek Pandey, Vijay Nath.: A CMOS Temperature Sensor with −60 °C to 150 °C Sensing Range and ±1.3 °C Inaccuracy. ARPN Journal of Engineering and Applied Sciences vol. 10 (8): (2015) 3588–3592.
5. Subhra Chakraborty, Abhishek Pandey and Vijay Nath.: A 1.37 nW CMOS Temperature Sensor with Sensing Range of −25 °C to 65 °C. IEEE International Conference GCCT. 23–24 April (2015). Kanyakumari TamilNadu.
6. Abhishek Pandey*, Vijay Nath.: Study and Design of 40 nW CMOS Temperature Sensor for Space Applications Telkomnika, Vol. 13, No. 3 (2015) pp. 813–819. doi:10.12928/TELKOMNIKA.v13i3.1426.
7. Jun He, Chen Zhao, Sheng-Huang Lee, Karl Peterson, Randall Geiger, Degang Chen.: Highly linear very compact untrimmed on-chip temperature sensor with second and third order temperature compensation. 53rd IEEE International Midwest Symposium on Cicuit and Systems (MWSCAS) (2010). 288–291. Seattle, WA. doi:10.1109/MWSCAS.2010.5548802.
8. Chen, Chung-Yuan, and Tai-Ping Su.: CMOS, Delta-Sigma pH-to-Digital Converter as New Integrated Device for Potentiometric Biosensors Applications, New Perspectives in Biosensors Technology and Applications (2011).

Calculation of Aircraft Altitude Using RADAR Dataset: A Basic Study and Implementation of FM Concept

Shagun Bishnoi, Hutanshu Kamal, Sudhir Kumar Chaturvedi and Anirudh Katyal

Abstract The main focus of this study is the altitude estimation are based on FM based 2-D Radar. This method carries out the measurements of desecrate signals mathematically based on the algorithms provides for the 2D principles. By applying airborne RADAR altimeter technique, centimeter level of accuracy can be measured. The 2-D method can be employed to estimate the height information. The method is completely based on the assumption that the target aircraft has enough velocity so that the variation of signal transmission and receptions can further be calculated and estimated. The method shows the good result and can be able to distinguish between high and low targets on normal 2D radars. The results provide the good estimate for the resolution of 100 m which can be considered as the optimized result for the height calculation.

Keywords Airborne RADAR · 2-D search RADAR · Altimeter · 2-D method

1 Introduction

Altitude estimation plays an important role in any aircraft this estimation using RADAR give a better and precise values for the same.2-D RADARS are relatively cheaper and efficient sensors that form the first line of defense in airspace control. In its military applications these are often employed as long range search RADAR that locate and track aircrafts [1].

With frequency modulation, the term airborne radar-altimeter can be understood as a altimetry radar type that uses high frequency dataset, harmonic and FM signal

Shagun Bishnoi · Hutanshu Kamal · S.K. Chaturvedi (✉)
Department of Aerospace Engineering, University of Petroleum and Energy Studies, Dehradun 248007, India
e-mail: sudhir.chaturvedi@ddn.upes.ac.in

Anirudh Katyal
Department of EICAS, Rockwell-Collins, Hydrabad, India
e-mail: anirudh.katyal@yahoo.co.in

© Springer Science+Business Media Singapore 2017

R. Singh and S. Choudhury (eds.), *Proceeding of International Conference on Intelligent Communication, Control and Devices*, Advances in Intelligent Systems and Computing 479, DOI 10.1007/978-981-10-1708-7_135

datasets to measure the altitude of the aircraft target above the mean sea level. The measured range of altitude is found from 0 to 1.5 km. On-board radar-altimeters are mostly used. For, at low altitudes and by time of final phases of flight such as approach for landing or touchdown, The systems used for indication and estimation of actual altitude of the aircraft are onboard radar altimeters which provides information about altitude through output signal of radar-altimeter and it can also be utilized to control continuous correction of subsystem through aircraft flight control system.

2 RADAR Altimeter Principle

RADAR altimeter works on the principle that the altimeter produces the radar wave and the return signal which bounces back from the surface is analyzed. The alteration among the position of satellite on orbit of the Earth, with respect to a subjective surface of reference (an utmost approximation of the surface of the Earth or the center of the Earth: the reference ellipsoid) and the range at the satellite surface which is measured by calculating the time period to travel the trip around for the signal, is called the surface height. Besides the height of the surface can be determined, by observing at the waveform and amplitude of the signal returned.

The radar-altimeters have the major disadvantage of the error caused methodically. Because of this error the altitude value is constantly varying whereas all the signals determined by the altimeter are shown in considerate moves. The process of investigating differential signal frequency is the main cause of the same [2].

The other varieties of altimetry radar usually functions with a frequency of carrier of 444 MHz in addition to shift of frequency of 8.5 MHz. The precision is of about ±4.4 m. The present altimetry radar usually functions on a frequency of carrier as 4.4 GHz and a shift of frequency of 50 MHz. The precision is of about ±0.75 m. For man operated landing the precision is sufficient but it is not satisfactory for automatic landing procedure. To raise the precision level to ±0.2 m, one way shall be to utilize the carrier frequency of 12 GHz in addition to shifting of frequency of 200 MHz. As they are not in standard production because of the complex technicality of these altimetry radar. This paper describes about to improve precision significantly of shallow altitudes measurement with no requirement for increasing values of the shift of frequency and carrier frequency, in a much easier way. The experimental procedure was purposely carried out on the RV-UM altimetry radar, with an absolute accuracy of ±4.4 m [3].

Suppose the airborne FMCW radar-altimeter is transmitting signal $u(t)$. It can be represented as given in Eq. (1).

$$u_t(t) = U_t \sin\left(\omega_0 t + \frac{\Delta\omega_0}{\Omega}\sin(\Omega t)\right) \tag{1}$$

where U_t is the amplitude, $\omega_0 = 2\pi\ f_0$ and f_0 is the transmitted signal central frequency, $\Omega m = 2\pi$ Fm and Fm denotes the modulation frequency, $\Delta\omega_0 = 2\pi\Delta f_0$ and Δf_0 represents the shifting of frequency of transmitter, t is time. Equation (1) it can be solved further by substituting as shown in Eq. (2) [3].

$$\varphi = \left(\frac{\Delta\omega_0}{\Omega m}\right)\sin(\Omega m t) \tag{2}$$

Then modulated frequency of the transmitter signal is found equal to as denoted in Eq. (3) [1].

$$U_t(t) = U_t \sin(\omega_0 t + \phi t) \tag{3}$$

$$U_r(t) = U_r \sin\left(\acute{\omega}_0(t-\tau) + \frac{\Delta\omega_0}{\Omega m}\sin(\Omega m(t-\tau))\right) \tag{4}$$

$$\varphi_r = \frac{\Delta\omega_0}{\Omega m}\sin(\Omega(t-\tau)) \tag{5}$$

$$U_r(t) = U_r \sin(\omega_0 t + \psi_r) \tag{6}$$

$$U(t) = u_t(t) + U_r(t) \tag{7}$$

$$U = \sqrt{\left((Ut)^2 + (U_r)^2 + 2U_t U_r \cos(\psi_r - \psi_t)\right)} \tag{8}$$

$$\Phi_d = 2\pi\Delta f_0 \frac{2h}{c} \tag{9}$$

$$F_d = \frac{8\Delta f \mathrm{Fmh}}{c} \tag{10}$$

$$T_d = \frac{c}{8\Delta f \mathrm{Fmh}} \tag{11}$$

3 2-D RADAR Concept

A single 2-D radar source will not straight forwardly calculate the aircraft altitude, hence, the presented procedure in this paper is combined with a variety of limitations and suppositions.

3.1 Consideration

Three limitations are imposed on the method described. The Aircraft speed is known: The speed of the aircraft is instrumental in calculating the altitude of the aircraft more specifically the aircraft horizontal speed. The meticulously of the observed speed is directly proportional to that of the exactness to the determined altitude.

Aircraft flies at a level altitude: for the level flight, it should be noted that the Doppler speed measurements underestimate the horizontal speed of the target, which corresponds to an underestimate of the altitude of the target. However, since aircraft are generally further away from the radar horizontally than vertically, the Doppler measurement for speed is a sufficiently close approximation for the horizontal speed [4] (Figs. 1 and 2).

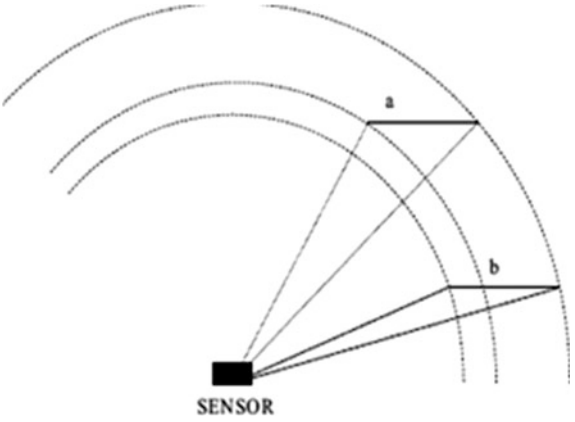


Fig. 1 Range spheres of a 2-D radar

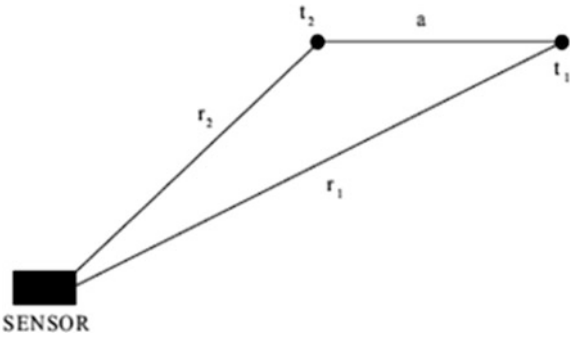


Fig. 2 Distance travelled by aircraft in different time intervals

3.2 Using a 2-D RADAR for Altitude Estimation

The circles represent the range spheres of a 2-D radar as seen from the side, thus **a** is higher than **b**. It was observed that the horizontal lines labeled **a** and **b** are of the same length and both touch the outer sphere, however, they both do not end at the same inner sphere [5].

The point marked as t_1 represents the first measurement of the aircraft by the sensor and t_2 represents the second measurement. The r_1 and r_2 correspond to the slant ranges measured by the sensor at t_1 and t_2; and a represents the estimated speed v of the aircraft times the time interval between t_1 and t_2 as given in Eq. (12).

$$a = v(t_1 - t_2) \tag{12}$$

Figure 3 shows the height h that one wishes to compute. Since the lengths of the sides of the measurement triangle are known, it is possible to compute the angle $\hat{a}$. Furthermore, noting that due to the assumption of level flight the angle between a and h is 90°, it follows that $\alpha = 90–\beta$. Finally the height h can be computed as given in Eq. (13).

$$h = c \cdot \cos(\alpha) \tag{13}$$

Given the computational triangle shown in Fig. 3, the angle α is computed as given in Eq. (14).

$$\beta = a \cos \frac{(b2 - c2 - a2)}{-2ac} \tag{14}$$

Thus the height is determined as

$$h = c \cdot \cos\alpha = c \cdot \cos(\pi/2 - \beta) \tag{15}$$

$$h = c \cdot \cos\left(\pi/2 - a \cos \frac{(b2 - c2 - a2)}{-2ac}\right) \tag{16}$$

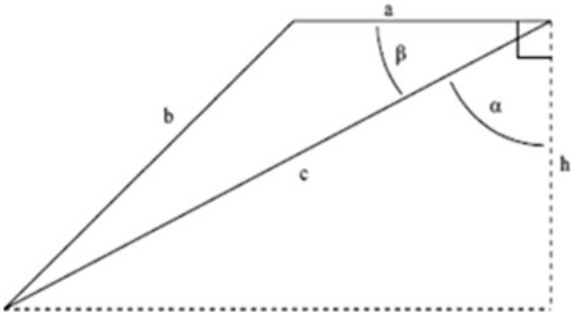


Fig. 3 Calculation of aircraft's height from ground

4 Results and Discussion

Using the Airborne RADAR altimetry approach we can see the variation of transmitted and received power with respect to time. MATLAB programming has been done for the purpose of simulation used in this study.

Figure 4 shows variation of the combined transmitted and power received versus time and indicates the lagging of received power in contrast to the transmitted power. The blue lines indicate the transmitted power and the redlines indicate the received power. Figure 5 shows that the height varies linearly with the change in frequency (Table 1).

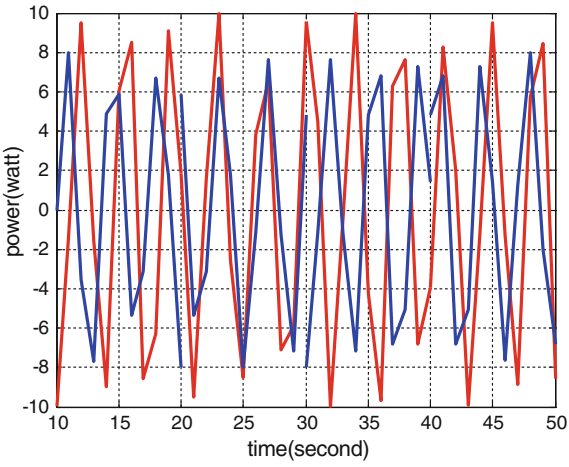


Fig. 4 Variation of combined transmitted and power received versus time

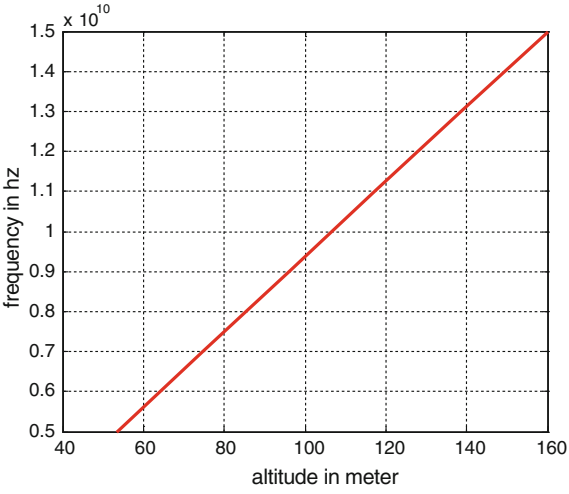


Fig. 5 Variation of height with change in frequency

Table 1 Result for altitudes for various frequencies

Frequency (Hz)	5×10^9	7×10^9	9×10^9	11×10^9
Altitude (*m*)	53.3	74.6	96	117.3

5 Conclusion

As it can be clearly seen from the results an Airborne RADAR altimeter gives better results rather than a two dimensional RADAR. The graph between the frequency and altitude show that they are linearly proportional. We also get to know the difference between the transmitted and received power by taking into consideration the comparison graphs by looking at the difference between the two. It has been observed that, the simulation has been carried out over MATLAB interface and comparative study can be implemented in the future scope work with the real time data acquisition.

References

1. Milos S. and Jan L.: The new approach of evaluating differential signal of airborne FMCW radar altimeter, Aerospace Science and Technology, Elsevier Masson SAS, (2011).
2. Hakl, H., Davies, E. and Roux, W.H., Aircraft height estimation using 2-D RADAR, Defence Science Journal, Vol. 60, No. 1, (2010) 100–105.
3. Skolnik I. Merrill.: Introduction to RADAR Systems. Mcgraw-Hill, Singapore (1980).
4. Ming-Jiu, G., Xiao, Y., You, H., and Bao, S.: An approach to tracking a 3D-target with 2D-radar, in Proc. IEEE International Radar Conference, Crystal Gateway Marriott Arlington, VA, May 9–12, (2005) 763–768.
5. Wood, T. E., Ager, R. S., Fleury, R. B. and Heuer, G. D.: Methods and apparatus for providing target altitude estimation in a two dimensional radar system, (2008), 417–583.

Development and Analysis of FSR and RFID Based Authentication System

Anita Gehlot, Piyush Kuchhal, Adesh Singh and Rajesh Singh

Abstract The increase in number of deaths after accident with two-wheeler is due to the negligence towards wearing helmet. So it is required to develop a system to limit this negligence at the manufacturer end. The concept is to develop a RFID and FSR based system, which doesn't allow the rider to start two-wheeler unless he wears helmet. The ignition of the vehicle is controller through the cumulative decision from RFID reader placed on vehicle and FSR located in the helmet. The whole system is analysed with LabVIEW and real prototype is developed to prove the concept. The analysis is done for FSR sensors and RFID reader to encode the system with required values.

Keywords FSR · RFID · Two-wheeler · LabVIEW · Zigbee

1 Introduction

To avoid the accidents occurs due to negligence of two-wheeler rider, a system is designed that uses RFID and FSR sensors to recognize human activities [1]. Sensors have proven helpful in maintenance of injuries due to accidents [2]. The system comprises FSR sensors and RFID technology employed for bringing the automatic ignition system [3]. Wireless Identification and Sensing Platform is used to perform sensing and operating from RF energy [4]. To ensure the safety equipment wears by the human FSR sensors are used and these sensors are often implemented only with the two parameters that are maximum resistance and minimum resistance [5]. When force appears on them there resistance reduces towards the zero and when there is no force they provides a high value of resistance. RF technologies are the more attractive to many application domains [6]. The system has designed a novel read out method for wireless RFID architecture [7]. Wireless Identification and sensing platform promises the ability to infer human

Anita Gehlot (✉) · Piyush Kuchhal · Adesh Singh · Rajesh Singh
University of Petroleum and Energy Studies, Dehradun, India
e-mail: anita@ddn.upes.ac.in

© Springer Science+Business Media Singapore 2017

R. Singh and S. Choudhury (eds.), *Proceeding of International Conference on Intelligent Communication, Control and Devices*, Advances in Intelligent Systems and Computing 479, DOI 10.1007/978-981-10-1708-7_136

activity directly from sensor readings [8]. RFID technology employed to form a remote system for the monitoring of the bike rider [9] and used for real time data collection and synchronization with bike node [10]. The RFID based technologies can be employed to provide the necessary information [11]. The information from RFID based technologies is of great value to the building and improving the utilization and maintenance of facilities [12]. For the helmet node the correlations of various data from pressure sensors with known values taken and ignite the engine after getting high value predefined in program [13]. LabVIEW provide displays of all pressures sensors as real-time bar graphs or as analog pressure versus time curves [14].

2 Proposed System

The system is proposed with the two-wheeler at industry end. Here a special helmet is proposed to design with each two-wheeler. At initial stage all the nodes are designed with required components. The FSR sensor nodes are placed at appropriate place in the helmet and receiver section placed on the vehicle comprises of RFID reader. The rider is to first wear the helmet, then the pressure sensor values is transmitted to receiver section, here AND operation is performed on pressure value and RFID tag values. If both the values are matched with predefined values, stored in the controller then only vehicle is ignited through a relay connected to engine. Two different boards are developed one within the helmet (sensor node) and another placed on Vehicle. In the sensor node there are four FSR sensors inside the helmet. When rider wears helmet these sensors provides some output voltage corresponds to the pressure on them and an average value is taken from these sensors (Fig. 1).

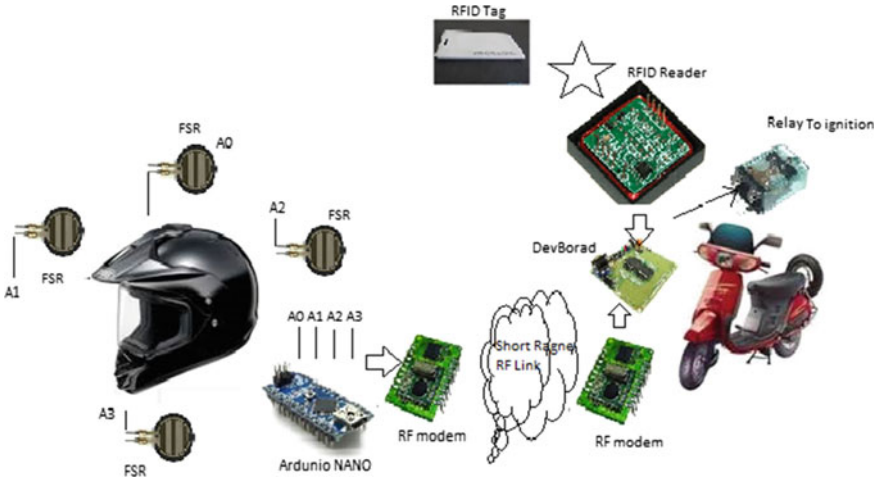


Fig. 1 Generalized block diagram

2.1 Initializing the System

At the time a customer comes to buy two-wheeler. The vendor is responsible to encode the RFID tag with the RFID card reader placed at two wheeler. The vendor is to store all the information about user in the LabVIEW as data logger. LabVIEW is also used to process and analysed the data with RFID reader. To encode RFID tag, the data bytes from tag is received and stored into the flash memory of RFID reader as authentic user and same is processes and analysed with LabVIEW. Any number of RFID tags can be encoded and synchronized at the time of purchasing of the vehicle. The data logger comprises of the data with details of RFID **tag issued to a particular user.** The working of FSR sensors is also analysed with LabVIEW. A frontend is designed to analyse the pressure measured by sensors before, vehicle is handed over to customer.

For FSR Analysis-

$$V+/(\mathrm{RM}+\mathrm{RFSR}) = \mathrm{VOUT}/\mathrm{RM} \tag{1}$$

$$\mathrm{RFSR} = \mathrm{RM} * ((V+/\mathrm{VOUT}) - 1) \tag{2}$$

FSRs show power law behavior within the force range from 0 to 20 *N* (Fig. 2).

2.2 Block Diagram of Helmet Node

Figure 3 shows the block diagram for helmet/sensor node section. It comprises of FSR sensors, control unit and Zigbee. The four different FSR sensors detects, whether the helmet is wear by the rider or not. The Arduino uno is the controlling unit of the system. The four FSR sensors are connected to the ADC pins of the Arduino, as FSR provides analog value corresponds to the pressure on the sensor. Arduino detects the four different values and create an average value, which is transmitted to receiver section. To operate the whole system a power supply of 5 V is required.

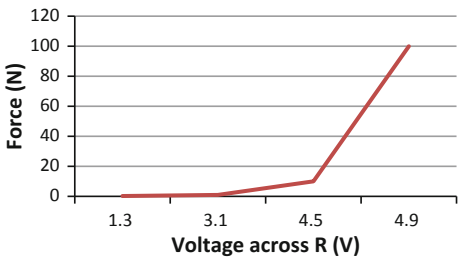


Fig. 2 FSR relation between force and voltage across output resistance

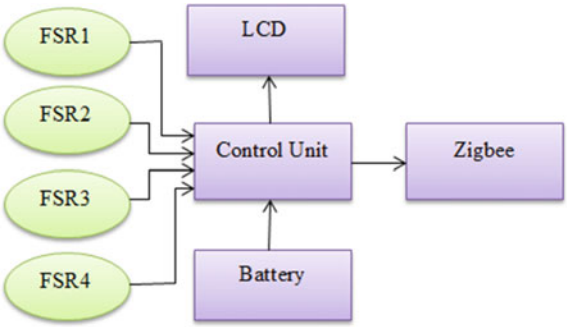


Fig. 3 Block diagram of helmet node

2.3 Block Diagram of Receiver Section

Figure 4 shows the block diagram of receiver section which comprises of control unit, LCD, RFID reader and Zigbee. The Zigbee receives the average data sent by helmet node and RFID unit sense the RFID tag. The control unit for this section is ATmega16 microcontroller which receive these two data and perform the AND operation. If both data meets the predefined requirements then only ignition through relay is permitted.

3 Software Development

The software for sensor node is developed by Arduino Development Board and for the receiver section ATmega16 Board is used. Simulation is performed for both the sections through Proteus Simulator. RFID and FSR.

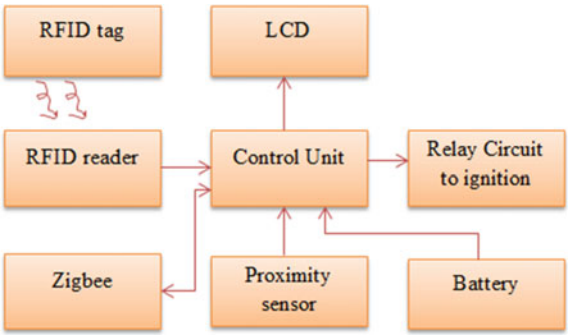


Fig. 4 Block diagram of bike node

3.1 Proteus Simulation

Proteus platform is used for the hardware development which provides the real time simulation. Figure 5 shows the Proteus simulation model. To view the data with the LabVIEW the virtual serial port COMPIM is used in the Proteus Simulator (Fig. 6).

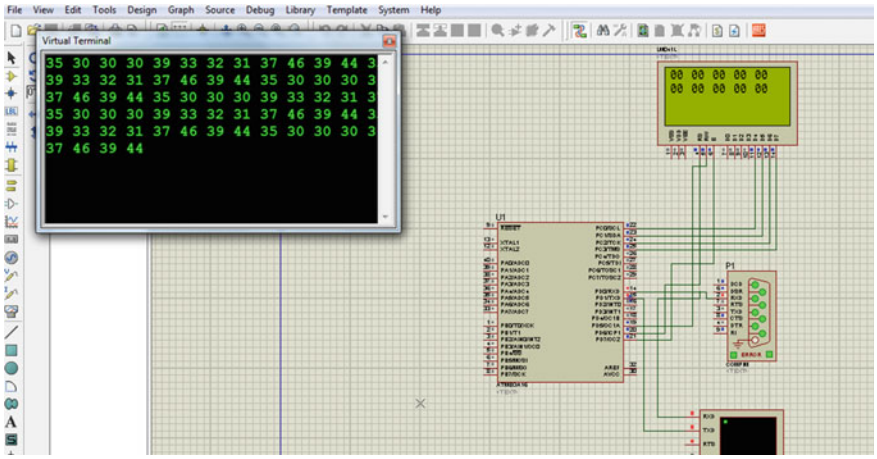


Fig. 5 Proteus simulation of model

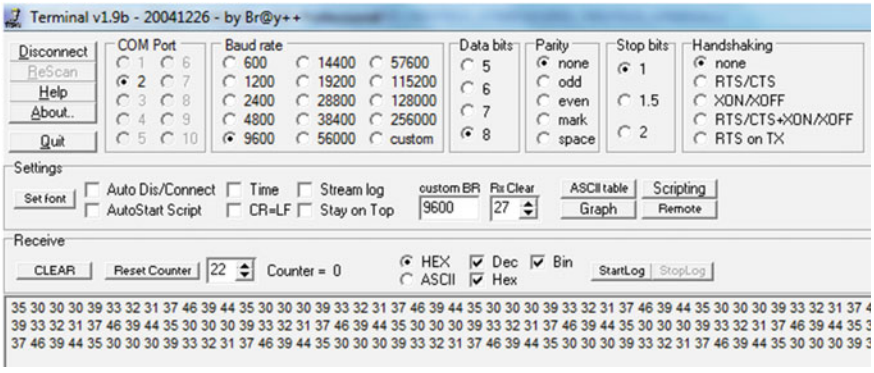


Fig. 6 Terminal v1.9 for 12byte data process from RFID tag



Fig. 7 Snapshot of developed system

4 Results and Discussion

Smart helmet for safe ride on two-wheeler is designed with radio frequency link (Zigbee). As user wears the helmet a RF signal is transmitted from sensor nodes, which carries average value of pressure on all the four sensors. The data from sensor node and RFID are synchronized with the help of predefined data by the receiver section placed with the ignition system of the vehicle (Fig. 7).

5 Conclusion

This system is very effective for the safety purpose of the user. User has to wear helmet to ride two wheeler. This system is low budget and easy to operate. It provides a better security to the rider. The Analysis shows proper working of the developed system.

References

1. Ko, Chien-Ho. "RFID-based building maintenance system." Automation in Construction 18.3 (2009): 275–284.
2. Buettner, Michael, et al. "Recognizing daily activities with RFID-based sensors." Proceedings of the 11th international conference on Ubiquitous computing. ACM, 2009.
3. Sample, Alanson P., et al. "Design of an RFID-based battery-free programmable sensing platform." Instrumentation and Measurement, IEEE Transactions on 57.11 (2008): 2608–2615.

4. Chowdhury, Belal, and Rajiv Khosla. “RFID-based hospital real-time patient management system.” Computer and Information Science, 2007. ICIS 2007. 6th IEEE/ACIS International Conference on. IEEE, 2007.
5. Zhao, Yiyang, Yunhao Liu, and Lionel M. Ni. “VIRE: Active RFID-based localization using virtual reference elimination.” Parallel Processing, 2007. ICPP 2007. International Conference on. IEEE, 2007.
6. Darianian, Mohsen, and Martin Peter Michael. “Smart home mobile RFID-based Internet-of-Things systems and services.” Advanced Computer Theory and Engineering, 2008. ICACTE’08. International Conference on. IEEE, 2008.
7. Smith, Joshua R., et al. “RFID-based techniques for human-activity detection.”Communications of the ACM 48.9 (2005): 39–44.
8. Zhou, Shouqin, Weiqing Ling, and Zhongxiao Peng. “An RFID-based remote monitoring system for enterprise internal production management.” The International Journal of Advanced Manufacturing Technology 33.7 (2007): 837–844.
9. Huang, George Q., Y. F. Zhang, and P. Y. Jiang. “RFID-based wireless manufacturing for real-time management of job shop WIP inventories.” The International Journal of Advanced Manufacturing Technology 36.7–8 (2008): 752–764.
10. Parlikad, Ajith Kumar, and Duncan McFarlane. “RFID-based product information in end-of-life decision making.” Control engineering practice 15.11 (2007): 1348–1363.
11. Li, Nan, and Burcin Becerik-Gerber. “Performance-based evaluation of RFID-based indoor location sensing solutions for the built environment.” Advanced Engineering Informatics 25.3 (2011): 535–546.
12. Hollinger, Avrum, and Marcelo M. Wanderley. “Evaluation of commercial force-sensing resistors.” Proceedings of International Conference on New Interfaces for Musical Expression, 2006.
13. Morley Jr, Robert E., et al. “In-shoe multisensory data acquisition system.”Biomedical Engineering, IEEE Transactions on 48.7 (2001): 815–820.
14. Zhu, Hongsheng, et al. “An umbilical data-acquisition system for measuring pressures between the foot and shoe.” Biomedical Engineering, IEEE Transactions on 37.9 (1990): 908–911.

Author Index

A
Aakanksha Devrari, 285, 425
Aanchal Verma, 839
Aastha Dadheech, 1013
Aastha Gupta, 197
Aastha Sehgal, 733
Abhas, 251
Abhimanyu Nain, 279
Abhinav Shukla, 251
Abhishek Gandhar, 407
Abhishek Pandey, 519, 1129
Abhishek Raj, 1019
Abhishek Sharma, 435, 653, 903
Adesh Kumar, 285, 425, 601, 661, 887, 999, 1079, 1113
Adesh Singh, 1145
Aditya Agarwal, 451
Agarwal, S.K., 367
Aghwariya, Mahesh Kumar, 471, 581
Akanksha Agrawal, 825
Akanksha Uniyal, 1051
Akash Gupta, 601
Ambika Pawar, 935
Ambujaksh Shah, 591
Amit Bhattacharyya, 1
Amit Gupta, 143
Amit Kumar, 285, 383, 425, 1005, 1095
Amit Mondal, 653
Amitabh Yadav, 903
Amitoj Singh, 991
Amod Kumar, 135
Anamika, 633
Anand Mohan, 27
Anasuya Devi, H.K., 417
Anirudha Semwal, 833
Anirudh Katyal, 1137
Anish Chopra, 9
Anita, 705
Anita Gehlot, 251, 267, 537, 569, 887, 959, 973, 1145
Anita Ghelot, 451
Anita Zurani, 771, 847
Ankit Batra, 855
Ankit Bhatt, 747
Ankit Gupta, 317, 855, 863, 871, 1005
Ansari, M.A., 617
Anshuman Prakash, 625, 803, 973
Anu Chaudhary, 89
Anu Mehra, 733, 825
Anuj Sharma, 1121
Anumeha Badoni, 1035
Anupriya Chakraborty, 825
Anushka Swarup, 999
Apoorva Nimbargi, 519
Apurv Thakur, 461
Archit Agarwal, 343
Arora, Tajinder Singh, 511
Arpit Jain, 661
Arpita Sengupta, 127
Arya, Sandeep K., 227
Asha Rani, 879
Ashi Rastogi, 1013
Ashish Gupta, 673
Ashish Kumar, 617
Ashish Ranjan, 151
Ashutosh Bhatt, 259
Ashutosh Pranav, 519
Asmita Roy, 211, 779
Ateev Agarwal, 569
Athar Hussain, 855
Ayush Agarwal, 343

B
Bal, Pravas Ranjan, 895
Balesh Vasisth, 1087
Baliga, A.K., 1027, 1065
Balwinder Singh, 407

© Springer Science+Business Media Singapore 2017

R. Singh and S. Choudhury (eds.), *Proceeding of International Conference on Intelligent Communication, Control and Devices*, Advances in Intelligent Systems and Computing 479, DOI 10.1007/978-981-10-1708-7

Barma, Mrinal Kanti Deb, 105
Bharath, Kurukuru Varaha Satya, 299
Bhaskar, Data Ram, 243
Bhawana Negi, 747
Bhumika Gupta, 309
Bhupinder Singh, 591
Brijesh Kumar, 1027, 1065, 1073

C
Chamandeep Kaur, 97
Charu Narula, 167
Chaturvedi, Sudhir Kumar, 1137
Chauhan, Y.K., 617
Chauhan, Yogesh K., 317, 863, 871, 1005
Chukka, Ramesh Babu, 811

D
Debashis De, 211, 779
Deeksha Jain, 1103
Deepak Kshirsagar, 951
Deepak Kumar, 903, 927, 943
Deepak Prasad, 519, 1129
Dembrani, Mahesh B., 847
Deore, Pramod Jagan, 753, 761
Devendra Rawat, 561
Devendra Saini, 715
Devesh Kumar, 383, 1095
Dhawan, S.K., 1087
Dinesh Babu, K.N., 715
Dinesh Ganotra, 443
Dinesh Prasad, 243
Divya Asija, 51
Diwaker Pathak, 317
Dolly Sharma, 537
Durgesh Kumar, 871

E
Eesh Mehandiratta, 569

F
Farukh, M., 1087

G
Gairola, S.P., 1087
Garima Mahendru, 197
Ghanshyam Singh, 243
Ginne Rani, 581
Gitanjali Mehta, 527
Gola, Kamal Kumar, 309
Goutam Sanyal, 695
Gulista Khan, 309
Gupta, Manish, 511
Gupta, Mukul K., 689
Gupta, Mukul Kumar, 601, 653
Gupta, S.C., 1035

H
Harry Garg, 135
Hemant Kumar, 919
Huirem Tarunkumar, 151
Hutanshu Kamal, 1137

I
Ila Verma, 919
Isha Adhikary, 553
Ishita Bhakta, 335

J
Jadhav, Jagadish Baburao, 753
Javed Khan, Mohd., 1129
Jaware, Tushar H., 771
Jeevanshi Mittal, 375
Jigajinni, Vijaylakshmi S., 391
Juneja, Pradeep K., 375
Jyothi, N., 811
Jyoti Sharma, 479
Jyoti Singh, 519

K
Kamal Bansal, 741
Kamlesh Kukreti, 1073
Kamlesh Pandey, 299
Kanchan Bahukhandi, 451
Kancherla, Anitha Sheela, 59
Kanica Sachdev, 787
Kapil Shukla, 653
Kevi Singh, 863
Khaleelu Rehman, B., 723
Khanchandani, K.B., 771, 847
Khurana, Manpreet Kaur, 817
Kottapalli Dheeraj, 999
Koushik Majumder, 211, 779
Kritika Bansal, 561
Kuldeep Singh, 227
Kumar, Ch Sumanth, 811
Kunal Jain, 9
Kushwah, Mukul Singh, 9

L
Lalit Gaur, 1087

M
Madhavi, D., 811
Madhu Kumari Ray, 519
Madhu Sharma, 667
Maheswari, K., 723
Mainak Mukherjee, 553
Mandeep Kaur, 787

Manish Kumar, 519
Manish Mishra, 519
Manish Sharma, 9, 383, 1095
Manish Verma, 1113
Manoj Bisht, 643
Marvi Grover, 189
Mayank Chaturvedi, 161, 375
Mayank Ranakoti, 653
Mayank Srivastava, 243
Meenakshi Pundir, 553
Meera, C.S., 601
Mishra, Manish Kumar, 705
Mishra, Raj Gaurav, 683, 833, 1043
Mohammad, Sheikh Suhail, 545
Mohan Kashyap, 89
Mohapatra, Durga Prasad, 895
Mohit Suyal, 887
Mondal, Amit K., 689
Mondal, Amit Kumar, 435, 553
More, Sagar Arun, 761

N
Nachiketa Jena, 895
Nalini Rajput, 351
Naveen Singhal, 667
Navneet Dayal, 293
Neeru Rathee, 443
Nidhi Garg, 135
Nikhil Gupta, 817, 887
Nikhil Pachauri, 879
Nikhil Raj, 959
Nikita Gupta, 219
Nikita Rawat, 259
Nikkita Shekhar, 935
Niranjan Kumar, 527, 633
Nishu Baliyan, 1113
Nitin Chandola, 503
Nitin Kumar, 1035
Nitin Sundriyal, 161

O
Ojha, Mukesh Kumar, 625
Ojha, Rudra Pratap, 695

P
Paawan Sharma, 601, 689, 903
Pachauri, Rupendra Kumar, 317, 855, 863, 871, 1005
Palanisamy, P., 643
Pallavi Choudekar, 51
Pandey, Alok Kumar, 561
Pandey, Purnendu Shekhar, 471, 581
Pandit, Manjaree, 1043
Pankaj Aswal, 461
Pankaj Badoni, 903
Pankaj Yadav, 1005
Parag Verma, 979
Pardeep Kaur, 143, 189, 293
Parmod Kumar, 219
Parthasarathi Mangipudi, 733
Parth Sharma, 489
Parth Wadhwa, 991
Parul Gaur, 609
Parvesh Saini, 351
Patel, Ravi Kumar, 979
Patil, Jayantrao Bhaurao, 325
Patil, Nitin Namdeo, 325
Pattabiram, Sampath Kumar Karai, 19
Peyush Pande, 127, 489
Piush Verma, 495
Piyush Kuchhal, 27, 683, 1079, 1145
Piyush Kuchhhal, 741
Poornima Mittal, 839, 1051
Prabhavathi, D., 69, 113
Praful Ranjan, 471, 581
Prakasam, K., 69, 113
Prasad, Deepak, 1129
Prasanthi, N., 471
Prateek Jain, 927, 943
Pratibha Yadav, 161, 747
Pratima Singh, 919
Praveen Kumar, 979
Pravin Gayal, 951
Preetam Suman, 173
Preeti, 143, 1087
Preeti Singh, 97, 181, 189, 293, 609
Priti Deb, 211
Priyanka Sharma, 351
Puja Bharti, 617

R
Rachana Garg, 219
Rajagopal Peesapati, 527
Rajan Sharma, 667
Rajeev Gupta, 495
Rajesh Kumar, 351
Rajesh Singh, 251, 267, 451, 569, 705, 803, 817, 887, 959, 979, 1145
Rajib Chowdhuri, 105
Rajkumar, T., 39
Rajput, Sachin K., 1095
Rajput, Sachin Kumar, 825
Rakesh Dwivedi, 661
Ramandeep Kaur, 135
Ramandeep Singh, 1121
Rani, Varkha, 511
Ranjan Mishra, 683
Rathod, Arun Pratap Singh, 1073

Ravi Kumar, 151
Ravi Wadje, 951
Rawat, Rohit Singh, 503
Rintu Khanna, 407
Ritika Saxena, 803
Ritu Gupta, 181
Rohan Sharma, 959
Rohit Samkaria, 591, 705
Rohit Sanket, 569
Rohit Singh, 489
Roshan Jahan, 173
Roushan Kumar, 833, 965
Ruchira, 51
Ryait, Hardeep S., 135

S
Sachi Bansal, 367
Sachin Mishra, 235, 545
Sadip Midya, 211, 779
Sagar Majumdar, 959
Saini, Devender, 1043
Saini, Devender Kumar, 495
Saini, J.S., 715
Saini, Raj Kumar, 495
Samar Ansari, Md., 479
Sandeep Sharma, 1121
Sandhya Rachamalla, 59
Sanjeev Sharma, 661
Sanjiv Kumar, 167
Sankara Narayanan, A., 39
Santanu Phadikar, 335, 779
Santosh Kumar, 1121
Sarkar, Bikash Kanti, 673
Saruchi Attri, 167
Satish Kansal, 89
Satrughan Kumar, 1057
Savita Gupta, 787
Sen, Santanu Kumar, 105
Senthil Kumar, S., 417
Shagun Bishnoi, 1137
Shailey Singhal, 667
Shaily Singhal, 1087
Sharma, M.G., 27
Shashank Awasthi, 695
Shashwat Goel, 733
Shaveta Gupta, 795
Shelly Singla, 279
Shilpi Agarwal, 667
Shival Dubey, 435
Shobhit Garg, 259
Shraddha Singh, 285, 425
Shrivastava, Aayush, 1043
Shubham Negi, 1027
Siddiqui, Anwar S., 367
Singh, Amit Kumar, 235
Singh, H.P., 235
Singh, L.K., 1129
Singh, Raj Pratap, 489
Singh, Suyash Kumar, 461
Sinha, Sanjay Kumar, 545
Snehil Gupta, 825
Sobhana, N.V., 39
Solanki, S.S., 1129
Sonali Agrawal, 203
Sonal Singhal, 1079
Srishti, 1027, 1065
Srivastava, Pramod Kumar, 695
Subrahmanyam, P., 151
Sudipta Roy, 105
Sunori, Sandeep Kumar, 375
Surajit Mondal, 553
Suraj Sawant, 951
Suresh Kumar, 279
Surya Kalavathi, M., 69, 113
Sushaban Choudhury, 569, 591
Sushabhan Choudhary, 803
Swati Kadlag, 1019
Swati Shrivastava, 1103
Sweety Siwach, 833, 973

T
Tanisha Gupta, 569
Tanvi Mehta, 537
Tayal, Vijay Kumar, 545
Toolika Srivastava, 1121
Tripathy, Malay Ranjan, 197, 383, 919, 1095

U
Umesh Kumar, 383

V
Vanam Upendranath, 391
Varchas Choudhry, 267
Varnita Verma, 601, 965
Varun Gupta, 833
Venkata Siva Reddy, K., 723
Venkateswaran, P.S., 435
Verma, Yajvender Pal, 609
Vijander Singh, 879
Vijay Nath, 519, 1129
Vimal Upadhyay, 203
Vinay Bhatia, 795
Vinay Chandna, 741
Vinay Chowdary, 553
Vindhya Devalla, 435
Vineet Mediratta, 741
Vipin Choudhary, 197
Virender Kadyan, 991

Vishal Jain, 715
Vishal Puri, 795
Vishal Sharma, 451
Vishnu Kumar, P., 723
Vivek Kaundal, 435, 653, 689, 817, 887, 903, 965
Vivek Sharma, 259, 747
Vivek Verma, 1087

Y
Yadav, Jigyendra Sen, 1057
Yadav, Vinod Kumar, 527, 1005
Yamini Pandey, 1027, 1065